Proceedings Volume 2

11th International Conference on Clouds and Precipitation

11ième Conférence Internationale sur les nuages et les précipitations

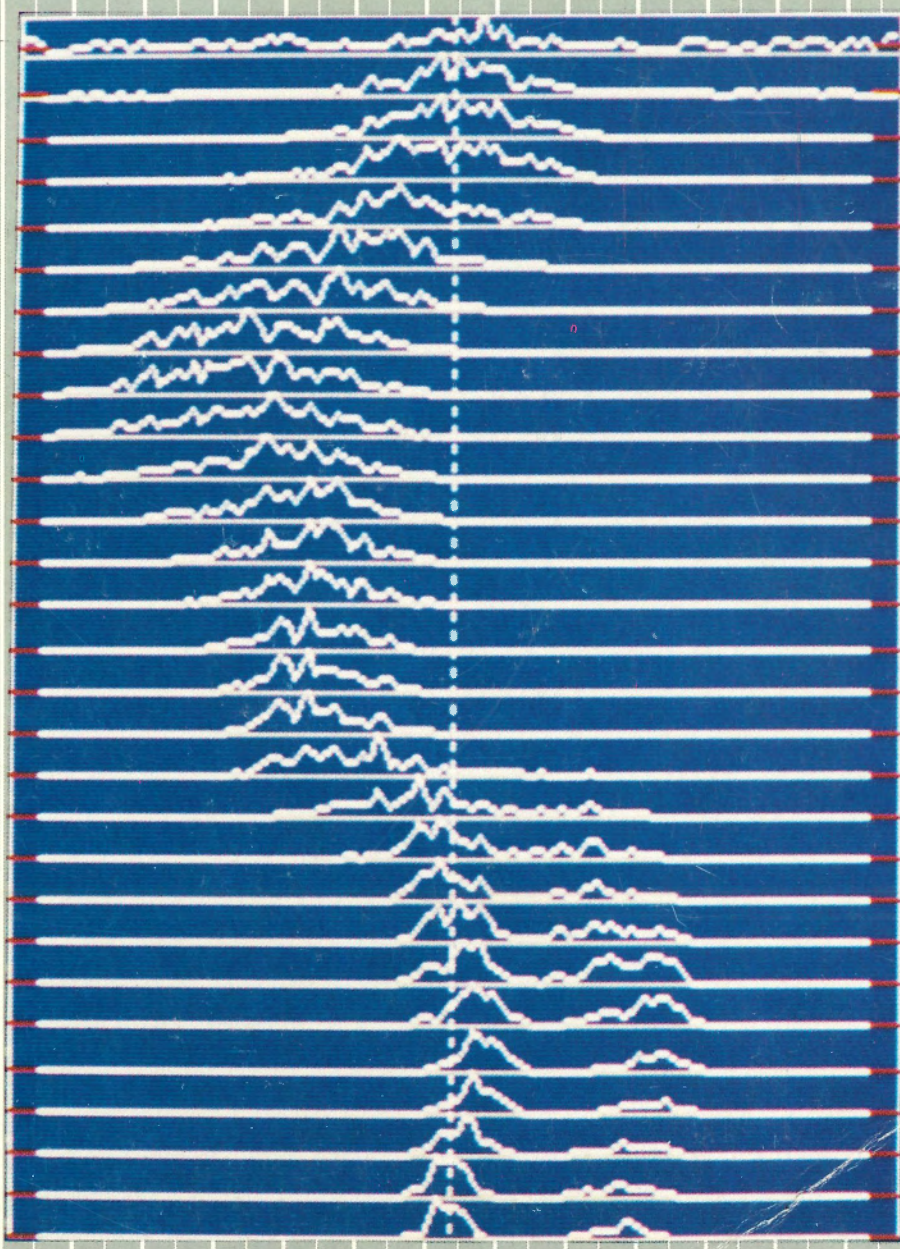

GREG McFARQUHAR

Proceedings Volume 2

11th International Conference on Clouds and Precipitation

11ième Conférence Internationale sur les nuages et les précipitations

Sponsored by

International Commission on Clouds and Precipitation
International Association of Meteorology and Atmospheric Physics

Major Financial Support from

Atmospheric Environment Service of Canada
World Meteorological Organization
Particle Measuring Systems, Inc.
l'Université du Québec à Montréal
McGill University
Elsevier Science Publishers

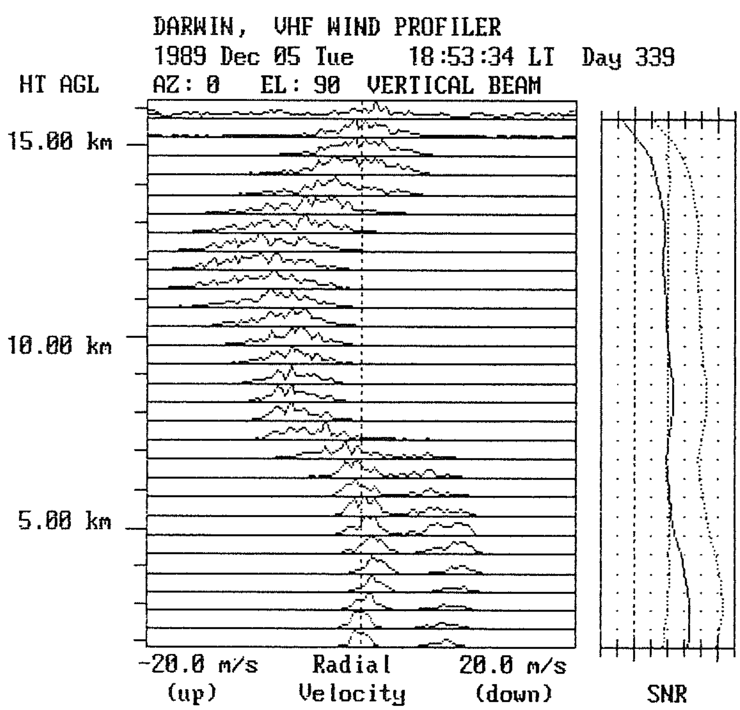

Front Cover: Doppler spectra, stacked in altitude, measured by a radar wind profiler in a thunderstorm. These are the same data as plotted in contour form on the cover of Volume 1. The figure at the left is the cover illustration, with scales of velocity and height indicated. See paper by Ecklund et al., pp. 1009-1012, for explanation.

ORGANIZATION OF THE CONFERENCE

International Program Committee

P.V. Hobbs, Chairman (USA)
T.W. Choularton (UK)
T.L. Clark (USA)
K.E. Haman (Poland)
K. Kikuchi (Japan)
I.P. Mazin (Russia)
G. Ohring (USA)
H.D. Orville (WMO Representative)
H.R. Pruppacher (FRG)
F. Prodi (Italy)
R.R. Rogers (Canada)
R. Rosset (France)
S. Rutledge (USA)
A.-S. Wang (PRC)

National Organizing Committee

R.R. Rogers, Chairman
R.G. Humphries
G.A. Isaac
Roland List
E.P. Lozowski
John Maybank

Local Organizing Committee

H.G. Leighton, Chairman
Roger Davies
Mary Ellen Rogers
Enrico Torlaschi
M.K. Yau
I.I. Zawadzki

PRESIDENTIAL ADDRESS

I wield the flail of the lashing hail,
And whiten the green plains under,
And then again I dissolve it in rain,
And laugh as I pass in thunder.

Percy Bysshe Shelley
"The Cloud"

In my introductory remarks to the proceedings of the 10th Conference I reviewed briefly the history of research on clouds and precipitation, discussed the growing importance of the subject, and made some prognostications as to likely developments (see also the Bulletin of the American Meteorological Society, 70, 282 and 72, 184). The last four years have seen no letup in either the pace of research or in the growing recognition of the importance of clouds and precipitation in atmospheric processes and in the future of planet earth.

The International Conference on Clouds and Precipitation (ICCP) (or the Cloud Physics Conference, as it used to be called) reflects the evolution of the subject. The exponential rise in the number of papers continues with the 11th Conference, to which 613 papers were submitted (Fig. 1). This, despite the fact that over the past several decades the International Commission on Clouds and Precipitation has spawned international conferences, workshops and symposia on Atmospheric Aerosol and Nucleation, Atmospheric Electricity, Weather Modification, Cloud Modeling, and Aerosol-Cloud-Climate Interactions. However, of much greater importance than mere increases in numbers of papers (which are a mixed blessing!) are the quality and diversity of the papers.

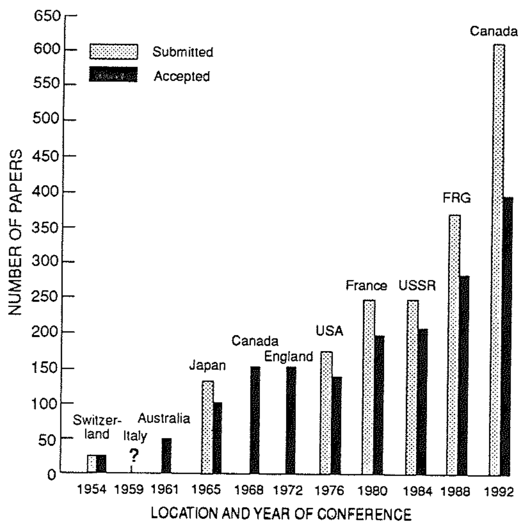

Fig. 1. Trends in number of papers submitted and accepted for the International Conference on Clouds and Precipitation. (Note: in some cases data is not available.)

I believe that the quality, or more accurately, perhaps, the relevance, of the papers submitted to the ICCP has improved over the years. This is due, in large part, to the increasingly powerful observational and numerical modeling capabilities that we can bring to bear on a wide variety of problems; these capabilities are beginning to approach the sophistication required to match the complexities of cloud and precipitation processes.

The need for increasingly diverse, and inter-disciplinary, research on clouds and precipitation processes was a subject that I dwelled on in my introductory remarks to the 10th Conference. Figure 2 compares the distribution of papers by methodology (field, laboratory, theoretical and numerical modeling) and by scale ("microscale" – defined as precipitation size and below – and "larger scale") for the 1968, 1988 and 1992 ICCP. The significant change in trends between 1968 and 1988 are seen to be maintained in 1992. (The relatively small differences in the statistical results for 1988 and 1992 are probably due more to changes in the way the papers were classified – see note to caption of Fig. 2 – than to any significant trends since 1988.) Thus, compared to twenty-five years ago, the 1992 conference has significantly more papers on field studies and numerical modeling, and dramatically fewer papers on laboratory studies (unfortunately almost a dying breed!). Comparing the scales of phenomena with which the papers are primarily concerned, we see that there has been a significant decrease in papers devoted to microscale studies from 1968 to 1992 but not a correspondingly large increase in papers devoted to larger scale studies. Instead, and this is most encouraging, in 1992 multiscale studies account for nearly one third of the papers presented at the ICCP.

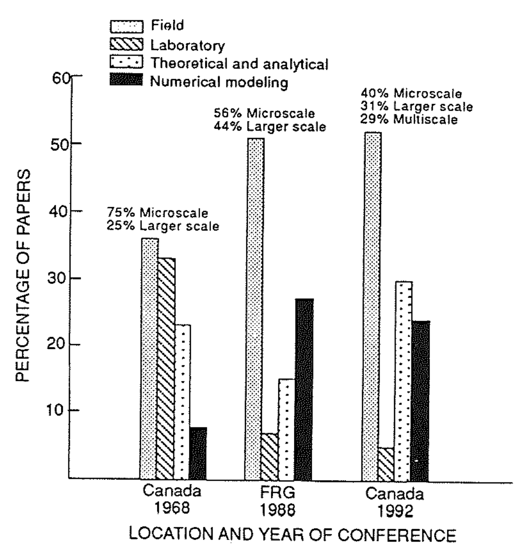

Fig. 2. Division by methodology (histograms) and scale of the phenomenon studied (percentages above the histograms) of the papers presented at the 1968, 1988 and 1992 International Conferences on Clouds and Precipitation. (Papers in the 1992 conference that used more than one methodology are included in more than one of the four categories, consequently the percentages do not add to 100. This is not the case for the 1968 and 1988 conference, where papers were assigned to just one dominant methodology. Also, papers in the 1992 conference that encompassed both microscale and larger scales are classified as "multiscale"; this was not done for the 1968 and 1988 conferences.)

In addition to traditional topics covered in the ICCP (e.g. microphysics, dynamics, modeling, severe storms, instrumentation), and topics that have become common in more recent years (e.g. clouds and radiation, cloud chemistry, satellite studies), sessions on forecasting, general circulation and climate are included in the 11th Conference. I hope that these subjects, which are intimately involved with clouds and precipitation and are likely to become increasingly important in the future, will figure even more prominently in the next ICCP.

Only those who have organized an international conference realize how much work is involved in bringing it to fruition. In the two ICCP conferences for which I have been Chairman of the International Program Committee I have had the support and help of excellent committee members at the international, national and local organizing levels. In the case of the 11th Conference, I would like to thank, in particular, Professor Roddy Rogers, Chairman of the National Organizing Committee, and Professor Henry Leighton, Chairman of the Local Organizing Committee, for their outstanding work.

At the end of this conference my term as President of the International Commission on Clouds and Precipitation will come to an end. I have been fortunate to occupy this position during a period of great scientific excitement and progress in our subject. The remainder of this century should see similar advances (beyond that my crystal ball cannot see). I trust that the International Commission will continue to play an important role in helping to foster these advances and in providing means for communicating them among the nations of the world.

Peter V. Hobbs
President of the International Commission on Clouds and Precipitation (1984–1992)

TABLE OF CONTENTS

Volume 1 contains Sessions 1 - 10, pp. 1 - 596.
Volume 2 contains Sessions 11 - 19 and the Appendix, pp. 597 - 1162.

VOLUME 1

SESSION 1: MICROPHYSICS: LABORATORY STUDIES

SESSION 6: FOGS AND STRATIFORM CLOUDS

SESSION 7: MARINE STRATOCUMULUS CLOUDS

SESSION 8: CUMULIFORM CLOUDS

SESSION 9: OROGRAPHIC CLOUDS; CIRRUS CLOUDS

VOLUME 2

SESSION 11: PRECIPITATION BANDS

SESSION 12: HAILSTORMS AND CONVECTIVE DYNAMICS

SESSION 13: MESOSCALE CONVECTIVE SYSTEMS

SESSION 14: CLOUDS AND RADIATION

SESSION 15: CLOUD CHEMISTRY

SESSION 16: MEASURING AND ANALYSIS TECHNIQUES I: GROUND BASED AND AIRBORNE

SESSION 17: MEASURING AND ANALYSIS TECHNIQUES II: RADAR AND LIDAR

SESSION 18: SATELLITE OBSERVATIONS OF CLOUDS AND PRECIPITATION

APPENDIX: LATE PAPERS

AUTHOR INDEX

MICROPHYSICS AND THERMODYNAMICS IN FRONTAL RAINBANDS OBSERVED DURING MFDP/FRONTS 87 EXPERIMENT

Virginie Marécal and Danièle Hauser

CNET/CNRS, Centre de Recherches en Physique de l'Environnement
Issy les Moulineaux, France.

1. INTRODUCTION

Research concerning fronts is mainly devoted to dynamics. Nevertheless, it appears that interactions between microphysics and thermodynamics or dynamics can play an important role in the organization and the development of frontal rainbands (Thorpe and Clough 1991, Lemaître and Scialom 1991, Lemaître and Scialom 1992). In order to study quantitatively interactions between microphysics and thermodynamics, a powerful way is to introduce radar observations (and in particular wind fields) into a diagnostic model, called in that case a retrieval model (Rutledge and Hobbs 1984, Ziegler 1985,...). In this paper, we analyse and discuss the results obtained with a microphyscal retrieval model in two different cases: a narrow cold frontal rainband (NCFR) and a rolls meso-scale circulation associated with Conditional Symmetric Instability (CSI).

2. MODEL DESCRIPTION

The microphysical retrieval model (Marecal *et al.*, 1991) is based upon the resolution of four continuity equations of the form:

$$\frac{\partial X}{\partial t} + V.\nabla X - \nabla(K\nabla X) = S \qquad (1)$$

where the X variable represents q_r, q_g, q_i or q_T which are respectively the mixing ratio (m.r.) of rain, precipitating ice particles, non-precipitating ice crystals and total water. **V** is the wind vector, K the eddy mixing coefficient (taken as a constant into the model) and S the source or sink term corresponding to each variables.

The total water substance is defined as:

$$q_T = q_r + q_g + q_v + q_i + q_c \qquad (2)$$

where q_v is the mixing ratio of water vapor and q_c the mixing ratio of cloud water (non-precipitating droplets). The q_c and q_v variables are diagnosed following Cotton *et al.* (1982): if air is not saturated with respect to liquid water, then q_c is zero and q_v is derived from Eq.(2); otherwise, q_v equals the saturation mixing ratio with respect to liquid water (q_{sw}) and q_c is calculated as:

$$q_c = q_T - q_R - q_G - q_i - q_{sw} \qquad (3)$$

where q_{sw} is given by the Tetens' (1930) formulation (as a function of temperature and pression).

To quantify interactions between microphysics and thermodynamics, the following thermodynamic equation for potential temperature (θ) is solved jointly to the equations of type (1):

$$\frac{\partial \theta}{\partial t} + V.\nabla\theta - \nabla[K\nabla(\theta - \theta_0)] = S_\theta \qquad (4)$$

θ_0 is the potential temperature of the environment (state of reference) and S_θ the source or sink term associated with exchanges of latent heat involved in microphysical processes.

Equations (1) and (4) are solved with the assumption of stationarity ($\partial/\partial t$=0), and using the successive overrelaxation method SOR (Young 1954).

Microphysical variables and processes introduced in the model are described in Fig. 1. Dashed lines corresponds to the variables or processes which are not explicitly solved. In particular, condensation is implicitly included in the model through the equation of the mixing ratio of total water.

The parameterizations used to describe the different microphysical processes come from Kessler (1969), Lin *et al.* (1983), Rutledge and Hobbs (1984) and Cotton *et al.* (1982). They are based on the assumption that size-distributions (N(D)) for the two types of precipitating particles have an exponential form:

$$N(D) = N_0 \exp(-\lambda D)dD \qquad (5)$$

where D is the diameter of the hydrometeors. N_0 is taken as a constant in the model.

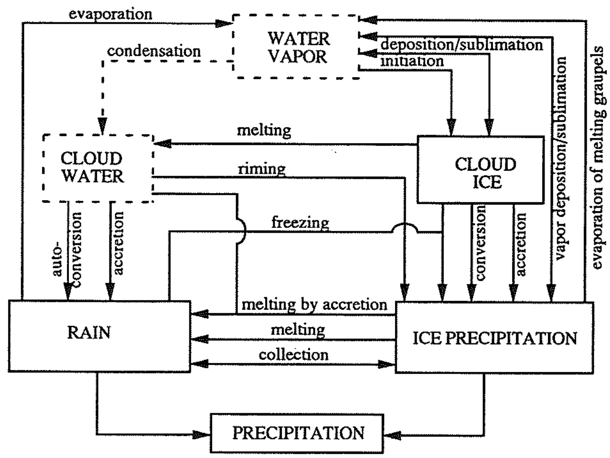

Fig. 1. Schematic of the various microphysical processes and variables included in the model.

In the NCFR case, *in situ* data (aircraft microphysical measurements and disdrometer) have shown that the exponential hypothesis for N(D) was valid, and allowed us to fix N_0 values (for rain, for ice). In both studies, the aircraft data were used to choose the type of precipitating ice particles, which has to be fixed in the model: graupel of low density in the NCFR case (type 1 from Locatelli and Hobbs, 1974) and rimed aggregates in the rolls meso-scale circulation case (type 10 from Locatelli and Hobbs, 1974).

3. NCFR CASE STUDY

During the night of 12 to 13 January 1988 a cold front passed over the French experimental site of the MFDP/FRONTS87 experiment (Bessemoulin *et al.* 1989). The combined data of the dual-Doppler radar system RONSARD have shown the existence of a narrow cold frontal rainband (NCFR) associated with the cold front (Roux and Hauser 1989). It was characterized by a rather two-dimensional and time-steady structure. Consequently, the retrieval model has been applied in a 2D-version to a vertical cross-section perpendicular to the NCFR, and Eqs. (1,4) have been solved neglecting time variations. The domain studied is 16km long in the direction quasi-perpendicular to the cold front and 4.0km high. The horizontal and vertical resolutions are 400 and 200m, respectively. The wind and reflectivity fields derived from the radars observations and used in the retrieval model are shown in Fig. 2 where the X-axis is perpendicular to the line joining the two radars, *i.e.* here, quasi-perpendicular to the surface front. The wind field depicts relative wind (calculated in a frame moving with the NCFR). The observed updraft has a maximun intensity of 7ms^{-1} and is located at about 1.2 km altitude. It induces the formation of a high precipitation content region which

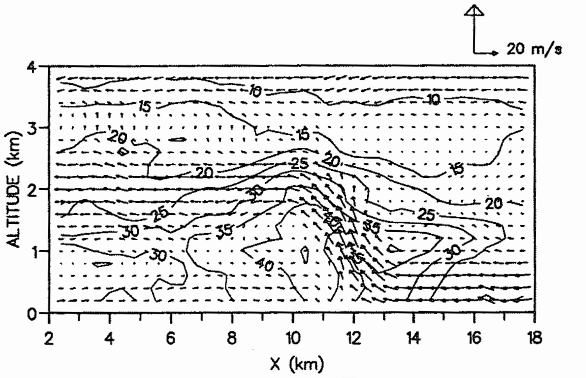

Fig. 2: Wind field (arrows) and reflectivity field (isolines in dBZ) observed the 12 January 1988.

corresponds to high reflectivity values. Two weak downdrafts are located behind and in front of this zone.

The retrieved precipitation field (q_r+q_g) (Fig.3a) is characterized by a region of intense precipitation located just behind the updraft. The results indicate that the most important part of precipitation is formed by solid particles, *i.e.* graupel. The growth of graupel is largely dominated by riming acting in the updraft region where condensation is active. Graupel is carried behind the updraft zone by wind and to the ground by their own fallspeed. Rain observed at ground level is formed through different processes: in the updraft region part of the domain (8km<X<11km), liquid phase processes (accretion) are the most important, whereas behind the updraft region rain is formed from melting of ice precipitation.

Fig. (3a) can be compared to Fig. (3b) which represents the precipitation field directly derived from radar reflectivity, using Z-q_r and Z-q_g relationships obtained from *in situ* observations of particle-size distributions (aircraft and disdrometer). A good agreement is found between the two, with the same kind of structure and the same localization of the region of maximum of precipitation. The order of magnitude of the precipitation maximum is the same: 2.4gkg^{-1} given by the retrieval model and 3.0 gkg^{-1} derived from reflectivity. This good agreement indicates that the retrieval

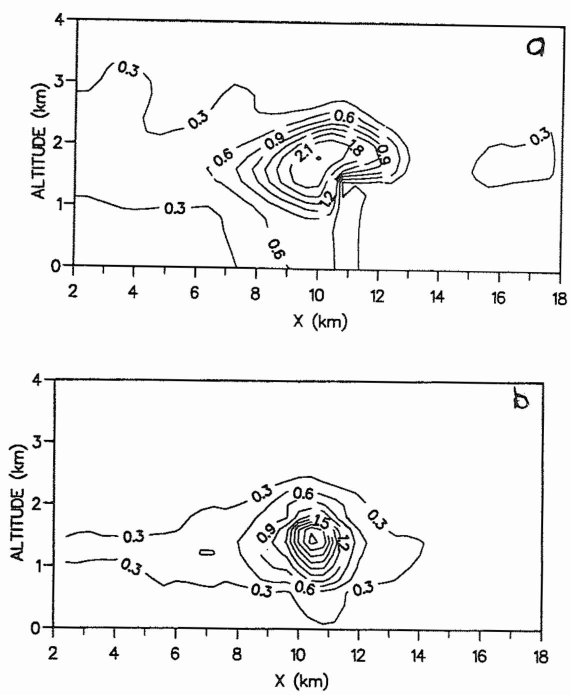

Fig. 3(a-b). Precipitation content (g kg^{-1}) (a) result of the retrieval model (b) directly derived from radar reflectivity.

model is well-adapted to the case studied here.

The temperature perturbations with respect to the pre-frontal conditions are shown in Fig.(4). A cooling is found nearly everywhere. This can be explained by two effects. In the updraft region, it is due to the quasi-neutral state of the prefrontal atmosphere: the latent heat flux due to microphysical processes, particularly condensation which is much greater than the freezing processes (rain freezing and riming) (Fig. 5a), does not counterbalance the adiabatic cooling; at the rear of the frontal discontinuity the cooling is due to microphysical effects (precipitation evaporation and

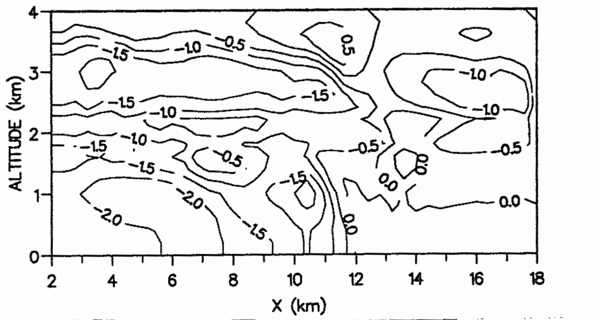

Fig. 4: Result of the retrieval model: potential temperature perturbations (in K) with respect to prefrontal conditions.

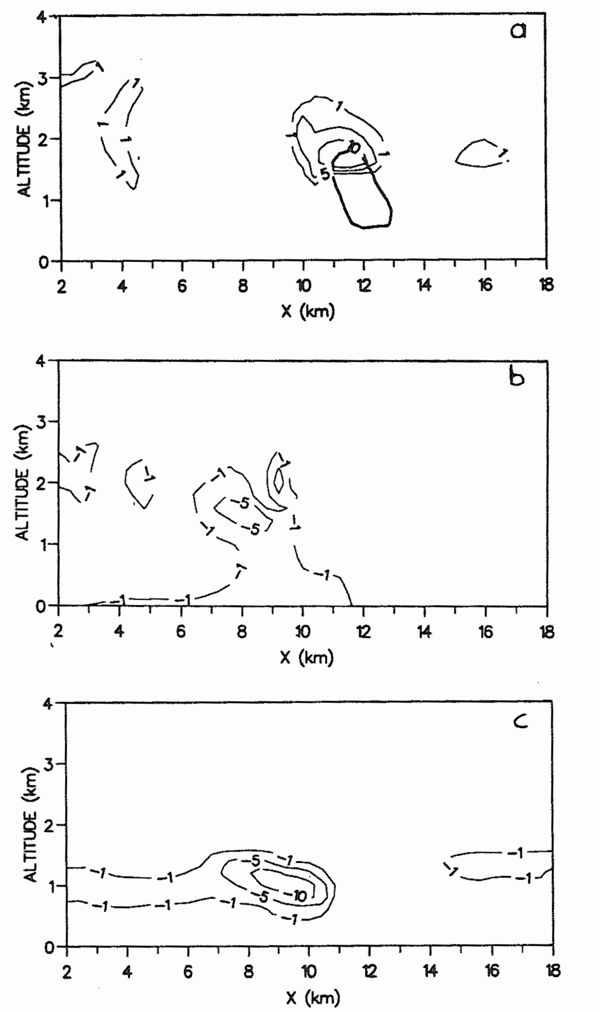

Fig. 5: (a) Warming rate due to 'freezing' terms (rain freezing processes and riming) in solid lines (in K h^{-1}). The heavy contour corresponds to the 50 K h^{-1} warming rate due to condensation. Cooling rate in K h^{-1} due to (b) the evaporation of precipitation terms and (c) the melting terms.

graupel melting). At ground level, the retrieved cooling of about 2°C is consistent with ground-stations observations (Fig. 6). This indicates that microphysical processes are sufficient to explain the temperature gradient associated with the frontal discontinuity, and that in the case studied here large-scale forcing is quasi-inexistent. This last hypothesis seems to be comfirmed by the radiosounding analysis (Lagouvardos *et al.*, 1992).

The most important processes leading to air cooling at low levels are graupel melting (Fig 5b) and precipitation evaporation (Fig 5c). The cooling rate induced by these two processes is of the same order of magnitude and acts approximately in the same region. This is confirmed by the results obtained with three different runs of the retrieval model in which we suppressed in the resolution of the potential temperature equation (Eq. 4) first graupel melting, then precipitation evaporation and at last both processes. In all these runs (Fig.7), a warming is observed at ground level instead of the cooling actually observed.

Hence, this study has shown that microphysical processes can play an important role on the thermodynamics in a NCFR.

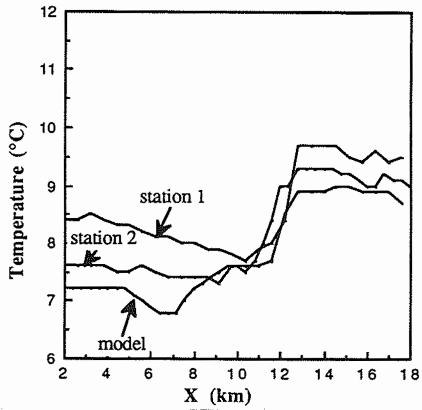

Fig. 6: Ground temperature (in K) as a function of the X-axis recorded by ground-stations 1 and 2 of the observational network of FRONTS 87 experiment and retrieved with the model.

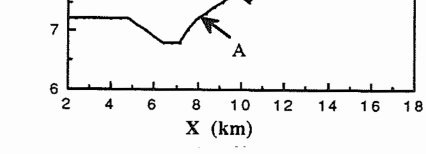

Fig. 7: Ground temperature (in °C) as a function of the X-axis: retrieved with different versions of the model: curve (A) reference case (corresponding to fig. 4), curve (B) when the melting terms are omitted in the thermodynamic equation, curve (C) when the evaporation of precipitation terms are omitted, and curve (D) when both melting and evaporation terms are omitted.

4. ROLLS MESO-SCALE CIRCULATION CASE STUDY

In this part, the retrieval microphysical model has been applied to a meso-scale wind field (Fig. 8a) associated with a cloud band observed around 1820 UTC the 9 January 1988. This wind field is relative to the large scale flow and has been obtained by combining the observations of conical scans from the two Doppler radars RONSARD, using a method proposed by Scialom and Lemaître (1990). Note that small scale motions (less than 15 km horizontally) are filtered out in this circulation. The considered domain is 90 km long and 4.2 km high. The vertical and horizontal resolutions are 0.35 km and 5 km, respectively. The wind field is caracterized by a rolls structure moving with the large scale flow. The corresponding observed reflectivity field is depicted in Fig. (8b). Three precipitation structures can be identified: the NCFR associated with the front (50km<X<60km), a wide cold frontal rainband (WCFR) located in front of the NCFR (70km<X<90km) and a convective cell aloft (5km<X<25km).

The precipitation field structure does not seem to be correlated with the wind field: the mesoscale updraft is associated to a reflectivity minimum and high reflectivity values do not correspond to ascent motions zones. This can be partly explained by two reasons. It is likely that high reflectivity values observed in Fig. (8b) are associated with convective motions which have been filtered out in the wind field determination. It is at least the case of the NCFR and of the cell located aloft. The second reason concerns the WCFR. Radar observations have shown that this precipitation band is not stationary in the frame of the rolls circulation. It is probable that precipitation in the WCFR is first created in the meso-scale updraft region of the rolls circulation, then intensified and horizontally advected into the downdraft region located in the right-hand side of the domain. More radar observations aloft before 1820 UTC are needed to confirm this interpretation.

Lemaître and Scialom (1992) have studied the dynamics of the meso-scale rolls circulation (Fig. 8a). They found that this wind field shows several characteristics predicted by the CSI theory. Only one point differs from the CSI theory. It concerns the downdraft region of the roll (in the left-hand part of the domain here). Although it is predicted unsaturated by the CSI theory, it appears nearly saturated according to the radiosounding measurements. In the present study, the

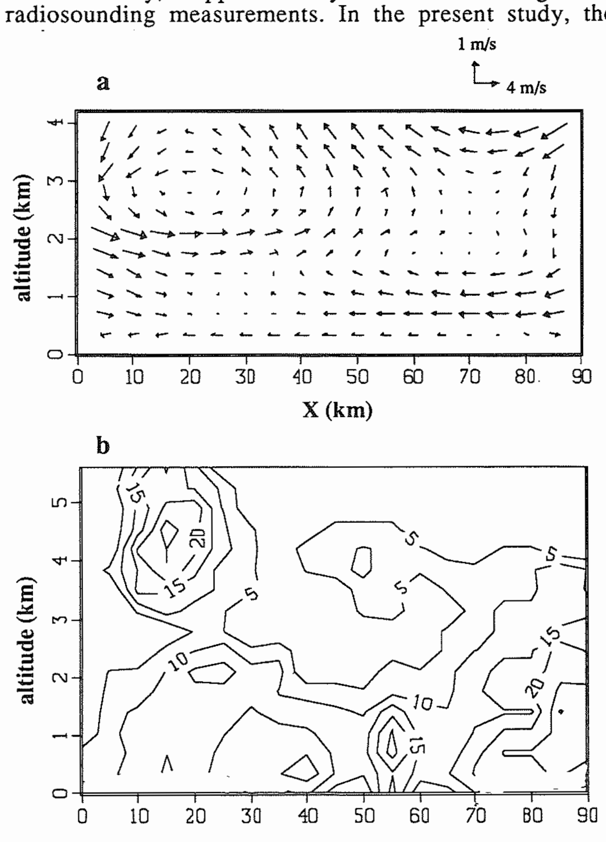

Fig. 8: (a) Meso-scale wind field relative to the large scale flow observed the 9 January 1988 and (b) corresponding reflectivity field.

retrieval model has been applied for one main objective which was to investigate the role of the microphysical processes in the subsiding part of the roll. Can microphysical effects explain the nearly saturated state of the air as suggested by Clough and Franks (1991)' study?

The retrieval microphysical model has been applied to the meso-scale rolls circulation (Fig. 8a). This wind field shows a 2D structure in the chosen frame so that the retrieval microphysical model has been applied in a 2D version. No observations before and after 1820 UTC are available. Nevertheless, the rolls structure observed at 1820 UTC corresponds to the development stage predicted stationary by CSI theory. Hence, Eqs. (1, 4) were solved neglecting time variations.

Results from four different runs of the microphysical model are analysed; In the first one (run 0), an ice precipitation profile derived from reflectivity observations was fixed at altitude 4.2 km between X=5 km and X=30 km. In the retrieved relative humidity (RH) field (Fig. 9), air is found nearly saturated in the downdraft region. Does RH depend on the intensity of the ice precipitation flux and/or on the type of ice-precipitating particles used in the model as suggested by Clough and Franks (1991)? To answer this question, three other runs of the model have been done. In the first one (run 1), we have set a constant flux corresponding to 5 mmh^{-1} between X=5km and X=30 km at 4.2 km altitude. Between run 0 and run 1, RH has increased in the downdraft zone (Fig. 9). When ice particles flux increases, evaporation and consequently RH also increase (Fig 10). Below the 0°C level, cooling due to melting acts by decreasing the saturation m. r. and hence by increasing RH. This effect is more pronounced when the precipitation flux is increased. In the two other runs, graupel particles have been used in the model instead of rimed aggregates. In run 2 (resp. run 3), precipitation flux at altitude 4.2 km is the same as that used in run 0 (resp. run 1). The results (Fig. 9) show that RH is smaller when graupel particles are assumed because evaporation is less active. This conclusion is consistent with the results obtained by Clough

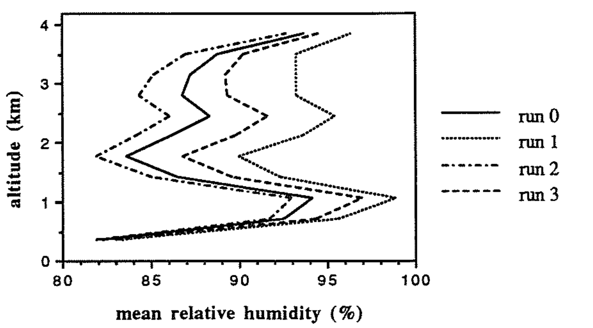

Fig. 9: Altitude as a function of mean relative humidity (RH) between X=5km and X=20 km (downdraft zone). The saturation mixing ratio is calculated with respect to ice when temperature less than 0°C and otherwise with respect to water. The terms run 0, run 1, run 2 and run 3 are definied in the text.

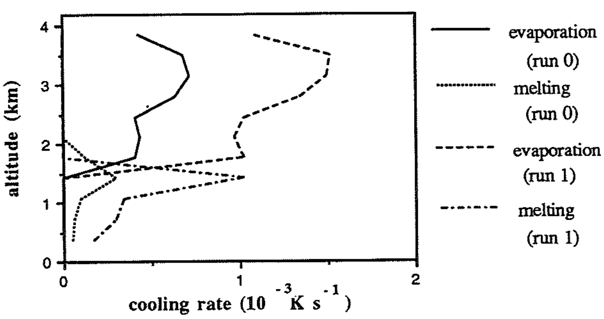

Fig. 10: Altitude as a function of cooling rate in 10^{-3} K s^{-1} due to ice precipitation evaporation and melting. The terms run 0 and run 1 are defined in the text.

and Franks (1991). Hence, RH depends on the type of ice particles and of the precipitation flux imposed. The convective cell located above the downdraft region of the roll probably plays an important role in the maintenance of nearly saturated conditions thanks to evaporation of ice precipitation and melting.

5. CONCLUSION

This study has shown the potential interest of using retrieval techniques for the study of interactions between microphysics and thermodynamics in precipitation systems.

Interesting results have been obtained in a case of NCFR. We have shown that the cooling observed at ground can be explained by microphysical processes: melting of graupel and evaporation of precipitation. The cooling rate due to these two processes is of the same order of magnitude.

The microphysical model has also been used to study the effects of the precipitation falling from a convective cell in the downdraft zone of a meso-scale circulation associated with CSI. Evaporation of ice precipitating particles and melting (in a lesser vertical extend) seem to allow the maintenance of nearly saturated conditions in the downdraft region.

REFERENCES

Bessemoulin, P., M. Petitdidier, V. Pircher, F. Roux, and B. Urban, 1989: Mesoscale structure of the cold front on 12-13 January 1988 during The MFDP/FRONTS 87 experiment. *Prep. 24th Conf on Radar Meteorology, Tallahassee, Amer. Meteor. Soc.*, 451-454.

Clough, S. A. and R. A. A. Franks, 1991: The evaporation of frontal and other stratiform precipitation. *Quart. J. Roy. Meteor. Soc.*, 117, 1057-1080.

Cotton, W.R., M.A. Stephens, T. Nehrkorn and G.J. Tripoli, 1982 : The Colorado State University three-dimensional cloud/mesoscale model. Part II: An ice phase parameterization. *J. Rech. Atmos.* , 16, 295 - 320.

Kessler, E., 1969 : On the Distribution and Continuity of Water Substance in Atmospheric Circulation.. *Meteor. Monogr.* , No. 32, Amer. Meteor. Soc., 84pp.

Lagouvardos, K., Y. Lemaître and G. Scialom, 1992, Mesoscale ageostrophic circulations of two fronts observed during the Fronts 87 experiment: diagnosis and interpretation. *Meteor. and Atmos. Physics*, to be published.

Lemaître, Y. and G. Scialom, 1991: Three dimensional mesoscale circulation within a convective post-frontal system: possible role of CSI for triggering convective motions. *Quart. J. Roy. Meteor. Soc*, 118, 71-99.

Lemaître, Y. and G. Scialom, 1992: Relevance of conditional symmetric instability and frontogenetic forcing to explain the banded organization of frontal precipitation observed on 9 January 1988 during the MFDP/FRONTS 87 experiment. *submitted to J. Atmos. Sci.*

Lin, Y-L., R.D. Farley and H.D. Orville, 1983 : Bulk parameterization of the snow field in a cloud model. *J. Climate Appl. Meteor.* , 22, 1065 - 1092.

Locatelli, J.D. and P.V. Hobbs, 1974 : Fallspeeds and masses of solid precipitation particles. *J. Geophys. Res.*, 79, 2185 -2197.

Marecal, V., D. Hauser and F. Roux, 1991: The narrow cold frontal rainband observed on 12-13 January 1988 during the MFDP/FRONTS 87 experiment: Part II: microphysics,. *submitted to J. Atmos. Sci.*

Roux, F. and D. Hauser, 1989: Kinematics, thermodynamics, and microphysics of a narrow cold frontal rainband. *Prep. 24th Conf. on Radar Meteorology, Tallahassee, Amer. Meteor. Soc.*,494-497.

Rutledge, S.A., and P.V. Hobbs, 1984: The mesoscale and microscale structure and organization of clouds and precipitation in midlatitude cyclones. PartXII: A diagnostic study of narrow cold frontal rainbands. *J. Atmos. Sci.*, 41, 2949-2972

Scialom, G. and Y. Lemaître, 1990: A new analysis for the retrieval of three-dimensional mesoscale wind fields from multiple Doppler radar. *J. Atm. and Oceanic Technol.*, 7, 640-665.

Tetens, O., 1930 :Uber einige meteorologische begriffe. *Z.Geophys.*, 6, 297 - 309.

Young, D., 1954: Iterative methods for solving partial difference equations of elliptic type. *Trans. Amer. Math. Soc.*, 76, 92-111.

Thorpe, A. J. and S. A. Clough, 1991: Mesoscale dynamics of cold fronts: structures described by dropsounding in FRONTS 87. *Quart. J. Roy. Meteor. Soc.*, 117, 903-941.

Ziegler, C.L., 1985 : Retrieval of thermal and microphysical variables in observed convective storms. Part I: Model development and preliminary testing. *J. Atmos. Sci.*, 42, 1487 - 1509.

SOME PECULIARITIES OF THE MESOSTRUCTURE OF FRONTAL CLOUDS FIELD

S.M. Shmeter

Central Aerological Observatory,
Dolgoprudny,Moscow Region 141730,RUSSIA

The mesostructure of a frontal cloud systems (FCS) depends on the large-scale flow type and thermodynamical characteristics. Mesoscale structure observed in FCS is always a combination of banded and cell-like features (Hobbs, 1981; Shakina, 1985; Bezrukova , Shmeter, 1989). The latter may cover several tens of percent of FCS' total area. The bands and, especially, cells are characterized by the local enhancement of micro- and meso-fluctuations of wind and temperature as well as a widespread vertical motion (w) and associated cloud liquid water content (W). The resulting augmentation of precipitation development (and therefore, of precipitation intensity) produces bands and cells ("spots") in frontal precipitation patterns. The mesoscale cloud features dimensions do not necessarily coincide with those of precipitation. However, the dimensions, lifetime and trajectories of cloud and precipitation features can't differ considerably.

The studies of the structure and evolution of cloud and precipitation mesofeatures made it possible to draw a number of conclusions. In particular, it has been established that the cells present embedded Cu,Cb. They often form clusters. Sometimes, cells are lining up,with minor bands and lines being embedded into larger ones. The spatial orientation of cell clusters and lines mainly coincide with that of bands in which they are embedded. That is why the cloud lines, as a rule are approximately parallel to surface fronts. The distance between the adjacent precipitation cells is $10^0...10^2$ km , while in a cross-front direction it varies from tens to 150-200 km. Sometimes "regular" structures are formed, with the distance between the cells in along and across the front line being almost equal (Bezrukova , Shmeter 1989; Bezrukova,1991) . Near cold fronts and occlusions the cells are moving both with and along the bands in which they are embedded.

Judging from precipitation mesostructure studies, the larger the mesoscale features within FCS are,the longer they live. The larger bands endure for tens of hours, while individual cells seldom survive for more than 1-1.5 hours (Livshits 1989; Sergeev, 1991; Shmeter,1990). Only large clusters live longer. Finally, it is worth mentioning that bands and cells precipitate havier than "pure" Ns and As, due to a stronger uplifting and larger liquid water content. Precipitation forms not only in Cb, but also in Cu cong, because within Ns, As the latter is less affected by entrainment, since the entrained air is saturated. Rainfall from cells contributes 20-40% to the total rainfall amount near warm fronts and occlusions and up to 60% near cold fronts (Bezrukova , Shmeter ,1989).

This paper summarizes the Central Aerological Observatory's studies of FCS mesostructure over European Russia, in transitional and winter seasons. The studies made use mainly of airborne data.

a. DIMENSIONS OF MESOSCALE FEATURES WITHIN FCS.

Table 1 displays the airborne, satellite and radar observational data available on the dimensions of mesoscale features within FCS.

Table 1

Characteristics of bands and cells within frontal cloud systems (FCS)

	Dimensions km			W cm/s
	Along-front length	Cross-front width	Spacing between adjacent	
Bulk of FCS	$1 - 5.10^3$	$1 - 5.10^2$	—	$10^0 - 10^1$
Mesoscale cloud bands including lines of embedded convective clouds	100 - 500	50 - 100	$10^1 - 10^2$	$10^2 - 10^3$
Cells	5 - 40	5 - 40	$10^0 - 10^2$	$10^2 - 10^3$
Clusters	100 - 200	100 - 200	$10^1 - 10^2$	$10^2 - 10^3$

The vertical motion velocity was calculated from (1), using radar data on the precipitating rate J_Z at Z_0 level

$$\bar{J}_{Z_0} = - \int_{Z_0}^{Z} \bar{\rho}\, \bar{w}\, \frac{\partial q_{max}}{\partial z}\, dz \qquad (1)$$

where q_{max} is maximum saturated mixing ratio within $(Z_0\ ,\ Z)$, $\bar{\rho}$ and $\bar{W}$ are layer-averaged air density and vertical velocity, respectively.

Fig.1 presents frequencies of individual cells and clusters dimensions.

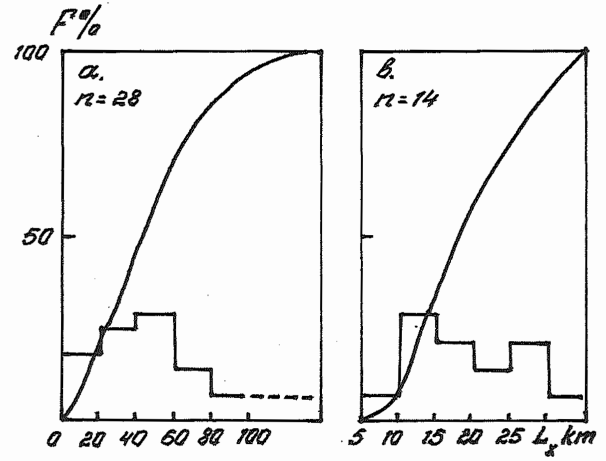

Fig.1 Frequency of occurrence of clusters (a) and cells (b) dimensions. n - number of cases.

In majority of cases, the longer the bands, the wider they are. Due to the scarcity of data, figures given in Table 1 and Fig.1 are approximate, with the largest distortions reffering to the smallest cells. Judging by individual measurements, the depth of the cells in winter and transitional seasons reaches several km (see Table 2). In summer, the cells are deeper than in other seasons. Thus, the tops of Cu, Cb are often doming above the upper deck of Ns, As, while in winter they are entirely embedded (Brylev et.al, 1989). The mean annual maximum height and the standard deviations of radar echo tops are 4.4±0.96 km for convective cells and 5.5±0.50 km for As. The cells may be based in the lower, middle or upper portions of Ns, As.

b. CELL STRUCTURE

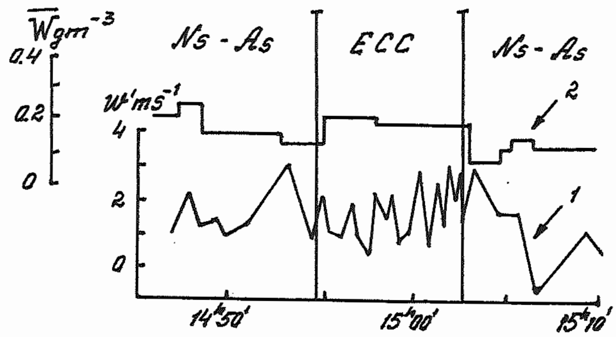

Fig.2 Profiles of vertical pulsation velocity (1), liquid water content (2) in embedded cloud cells (ECC) and in their environment. Warm front, Smolensk region, Dec.15, 1979, Z=2600m.

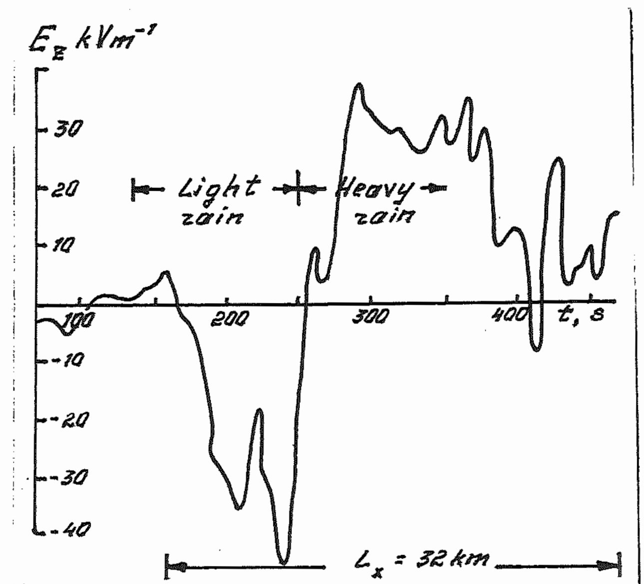

Fig.3 Variations of E_z within ECC on October 27, 1969, Simferopol-Krasnodar region, Z=300m. L_x - width of zone with increased $|E_z|$ (B.F.Evteev, private communication)

Table 2

Average values ($\bar{H}$) and standard deviations (σ_H) of radar echo top height over the European Russia. ECC - embedded convective cell

	ECC			As, Ns		
	$\bar{H}$km	σkm	number of cases	$\bar{H}$km	σkm	number of cases
Summer	6.4	2.1	797	5.6	2.0	310
Winter	4.2	1.9	542	4.3	1.8	1833

Fig.2,3 show the typical horizontal distributions of liquid water content (W), vertical pulsation velocity (w'), and vertical component of electric field strength (E_z) within embedded convective cells (ECC). It can be seen that within ECC, W, w' and E_z values grow drastically. Within ECC, the mesoscale uplifting velocity (w) and ε_z are by 10-100 and 3-4 orders of magnitude greater, respectively, than those in the adjacent portions of Ns, As, So, the distribution of meteorological parameters within ECC is similar to that observed in Cu cong, but unlike Cu, which are not encountered at middle latitudes in winter, ECC occur all the year round. They cause the winter thunderstorms.

Table 3 gives root mean-square velocity pulsations (σ_w), coefficient turbulence (K), and the rate of dissipation of turbulent kinetic energy (ε_z) in ECC and Ns, As. The bar denotes averaging over the bulk of realizations and the index "max" indicates the maximum value of the relevant characteristic. The methods of σ_w ,ε_z and k calculations are described by Shmeter (Shmeter,1990).

$$\varepsilon_w = \alpha_w S_w^{3/2}(k)\, k^{5/2}$$

where $k = \frac{1}{\lambda}$ is a wave number , $\alpha_w \approx 35.3$

$$S_w(k) = 2\int_0^\infty \cos(2\pi k\xi) R_w(\xi)\, d\xi$$

is the vertical pulsation spectral density, R_w is the autocorrelation function.

The turbulence characteristics for ECC (as well as ε_w) were found to be very close to those in Cu cong.

The energy spectra for both ECC and Cu cong have shown a "plateau" or a local maximum at the wavelength λ=600-800m. This reveals a source of turbulent kinetic energy at the aforementioned λ ,which is likely to be caused by convective updrafts, responsible for cells formation.

Vertical and horizontal pulsations' distribution functions in spatially homogeneous portions of Ns, As obey a normal law, while within ECC they are described by the sum of 3 normal distributions with various dispersions. The latter apparently manifests the presence of pulsations of different nature within ECC (Mazin , Khrgian Eds.,1989).

The formation and evolution of bands and cells have been studied inadequately. The present day understanding of this problem is as follows. A very stable stratification produces a spatially homogeneous layer of frontal Ns , As. The vertical lapse rate ($\bar{\gamma}$) in FCS,which is less than the moist adiabatic one (γ_m) by 0,1...0.2°C/100m , causes an internal gravity wave with $\lambda \approx 10^4...10^5$ m. The waves are induced by periodic oscillations at the rate of the latent heat release resulting from precipitation particles growth and deposition out.The most intensive cloud development occurs in the wave crests, thus forming a banded structure.

If $\bar{\gamma} > \gamma_m$,either a cell-like or banded convection emerges. These conclusions are valid for fronts of all types , but the exact form of mesoscale features also depends on the characteristics of wind field deformation (Sergeev,1991).

If a strong frontal baroclinicity is present the bands are formed due to the realization of a large-scale baroclinic instability (slantwise convection). As parameters of the bands formed by waves and baroclinic instability are often similar ,it is difficult to infer the physical machanism of a given band formation, only using observational evidence.

The cells are formed by elevated convection. Their emergence within FCS is facilitated by the fact that $\bar{\gamma}$ within Ns, As is very close to a moist adiabatic one (γ_m).The values of γ in frontal Sc,Ac are still greater.Even spatially averaged $\bar{\gamma}$ is equal or greater than γ_m in more than 50% of cases (provided that FCS temperature is below zero) (Mazin, Khrgian,Eds.,1989). In some FCS portions, $\bar{\gamma} \gg \gamma_m$.

Local convectively unstable layers are often produced by the interpenetration of mesoscale tongues of cold and warm air through the frontal surface (Bezrukova , Shmeter , 1989). Such tongues are several tens of km long and hundreds of meters deep. If a cold tongue overruns a warm one , thus forming a convectively unstable layer. Such process may develop at several levels, resulting in multilayered ECC.

Table 3

Characteristics of turbulence within embedded cloud cells (ECC) and in Ns,As in transitional and winter seasons over European Russia (Shmeter,1990)

	Height, km	Number of cases	$\bar{\sigma}_w$ m/s	$\bar{\sigma}_{w\,max}$ m/s	$\bar{K}$ m^2/s	$\bar{K}_{max}$ m^2/s	$\bar{\varepsilon}$ cm^2/s^3	$\bar{\varepsilon}_{max}$ $cm^2/$
Ns,As	1.0 - 6.3	85	0.21	0.67	12.7	50.7	3.8	98.
ECC	1.0 - 2.7	58	0.42	1.15	26.5	74.4	27.5	309.

REFERENCES

1. Bezrukova N.A. The pecularities of frontal precipitation field morphology. Moscow, Trudi CAO,1991 iss.178, pp.47-60.(in Russian)

2. Brylev G.B. et al. Characteristics of electricaly active zones in stratiform clouds. Leningrad, Hydrometeoyzdat, 1989, p.157.(in Russian)

3. Livshyts E.M. Time and spatial variability of precipitation based on the data of digitized radar and the esmitation of seeding effect of winter clouds in Moldova (Modification of atmospheric process in Moldova-Kishinev,Shteentsa) , 1989, pp.111-120.(in Russian)

4. Mazin J.P. and Khrgian A.Kh. (Editors) Handbook of Clouds and Cloudy Atmosphere. Leningrad , Hydrometeoyzdat, 1989,p.647. (in Russian)

5. Sergeev B.N. On investigation of frontal precipitation structure and quantity dependence on large scale flow parameter. Moscow, Trudi CAO, 1991,iss.178,pp.79-84.(in Russian)

6. Shakina N.P. Dynamics of atmospheric fronts and cyclones. Leningrad, Hydrometeoyzdat, 1985,p.263.(in Russian)

7. Shmeter S.M. Characteristics of embeded convection in frontal clouds and conditions for its formation. Moscow, Meteorogya and Hydrologya, 1990, N 11,pp.36-43.(in Russian)

8. Shmeter S.M. Some features of frontal cloud system mesostructure. Moscow,Trudi CAO, 1991, iss.178, p.3-20.(in Russian)

9. Bezrukova N.A.,Shmeter S.M. Cloud and precipitation structures in frontal zones. Beijing, Proc. 5-th Int. Weather Modification Conf.,1989, pp.471-474.

10 Hobbs P.V. Mezoscale structure in midlatitude frontal systems, Humburg, Proc. IAMAP Symposium, 1981, pp.251-259.

STRUCTURE OF MESOSCALE SNOW BANDS OVER THE SEA OF JAPAN

Y. Yamada, T. Matsuo, M. Murakami, and H. Mizuno

Meteorological Research Institute, Tsukuba, Ibaraki 305, Japan

1. INTRODUCTION

In winter monsoon season, "sea-effect snow clouds" develop over the Japan Sea as a result of modification of cold air mass passing over the warm sea surface. These clouds produce much snowfall in coastal regions facing the Japan Sea. They sometimes do serious damage to regional activities and economics.

Several observational studies of "sea-effect snow clouds" have been made so far about airflow structures in the clouds using a single Doppler radar: for example, Ishihara et al. (1989) described the air flow pattern in the snow bands induced by land-sea breeze circulation, and Sakakibara et al. (1988) revealed a flow structure in some clouds similar to that in a tropical squall line. Ikawa et al. (1987), on the other hand, theoretically simulated the clouds using a two-dimensional numerical cloud model with microphysical processes.

Similar snow clouds, well known as "lake-effect snow clouds" around and over the lake Michigan, have been extensively studied by observations with a single Doppler radar and numerical models (Kelly, 1982; Braham, 1983; Hjelmfelt, 1983; Hsu, 1987). Recently, Kristovich (1990) reported a dual-Doppler radar observation of "roll-convection" over the lake Michigan combined with aircraft observations.

Although the above studies provided good information on air flow structures in the "sea-effect snow clouds", there still remain some problems unsolved on three-dimensional structures of various "sea-effect snow clouds" because of a limitation of a single Doppler observations. Dual-Doppler radar observations combined with specially designed drop sondes were carried out in the winters of 1989-1992 on the western coast of the Tohoku District of Japan in order to investigate the three-dimensional structures of the "sea-effect snow clouds". This paper describes mesoscale structures and maintenance mechanisms of the snow clouds, and presents conceptual models of some clouds.

2. RADAR OBSERVATIONS AND DATA PROCESSING

Dual-Doppler observations were carried out using two X-band Doppler radars. The detection range of the radars was 64 km. In 1989 the vertical resolution was rather low because the rotating speed of antenna was slow at 1 rpm for the two radars. After that, the rotating speed of antenna was increased to 2 rpm for one radar and 3 rpm for the other so that the vertical resolution has improved since 1990. During the period of 1989-1992, the data acquisition time for one sequence of the dual-Doppler observation was several minutes.

The raw radial data were interpolated onto common grids. The grid spacings are 1 km in the horizontal and 0.5 km in the vertical direction with the lowest level 0.8 km ASL in 1989, while in 1990, 0.8 km in the horizontal and 0.3 km in the vertical direction with the lowest level 0.6 km ASL (hereafter all levels are in ASL). The vertical winds were calculated by integrating the anelastic continuity equation upward assuming w=0 at the sea surface. Although it is common in the dual-Doppler technique that the vertical winds are adjusted by variational methods (Ray et al., 1980; Chong and Testud, 1983), no adjustment has been made in these cases because a software is not available at present.

3. RESULTS OF OBSERVATION

Several types of snow clouds were identified from the radar observations and they usually appeared in a form of band, typically 3 km deep and persisting for several hours. The two types of the snow cloud bands, oriented parallel (L-type) to and perpendicular (T-type) to the prevailing northwesterly surface wind, will be discussed below.

a. L-type band

Several L-type bands, about 50 km long and 10 km wide, appeared on 10-11 Feb. 1989. They almost alined parallel to the prevailing northwesterly surface wind. The synoptic situation was favorable for development of snow clouds: a high over the Siberia Continent and a low over the Pacific Ocean. The precipitation intensity was 1-4 mm/hr in water equivalent and graupel was dominant around the radar site.

Shown in Fig.1 is the aerological data of Akita at 2100 JST on 10 Feb., 100 km north of the MRI (Meteorological Research Institute) radar site. The environmental wind direction changed slightly with height between the surface and 800 hPa. The environmental air stratified convectively unstable below 1.5 km level.

Figure 2 shows the horizontal system-relative airflows and the reflectivity fields at the levels of 0.8 and 1.8 km from the dual-Doppler observations. The band was in the mature stage, and it moved southeastward at a speed of 8 m/s. At the 0.8 km level,

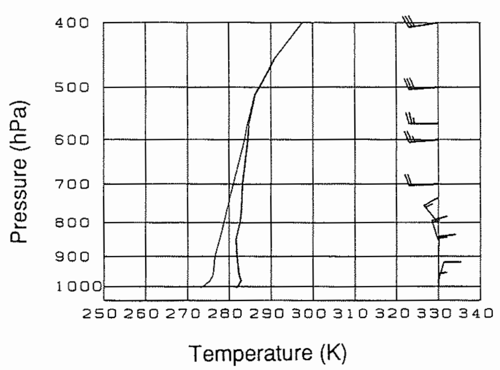

Fig. 1 Vertical profile of potential temperature (thin line) and equivalent potential temperature (thick line) of Akita at 2100 JST on 10 Feb. 1989. A full barb denotes 10 knots.

the overview of the horizontal divergence fields is that convergence and divergence exist, respectively, at the northeastern edge and at the southwestern edge, suggesting upward and downward air motion existing there. The magnitude of the horizontal convergence was greater at the lower levels, say around $3\times10^{-3}\ s^{-1}$. The flow pattern was characterized by the ascending inflow around the northeastern edge and the descending outflow around the southwestern edge of the band. At the 1.8 km level, the flow pattern bears a resemblance to that at 0.8 km level, though vertical air velocities are greater.

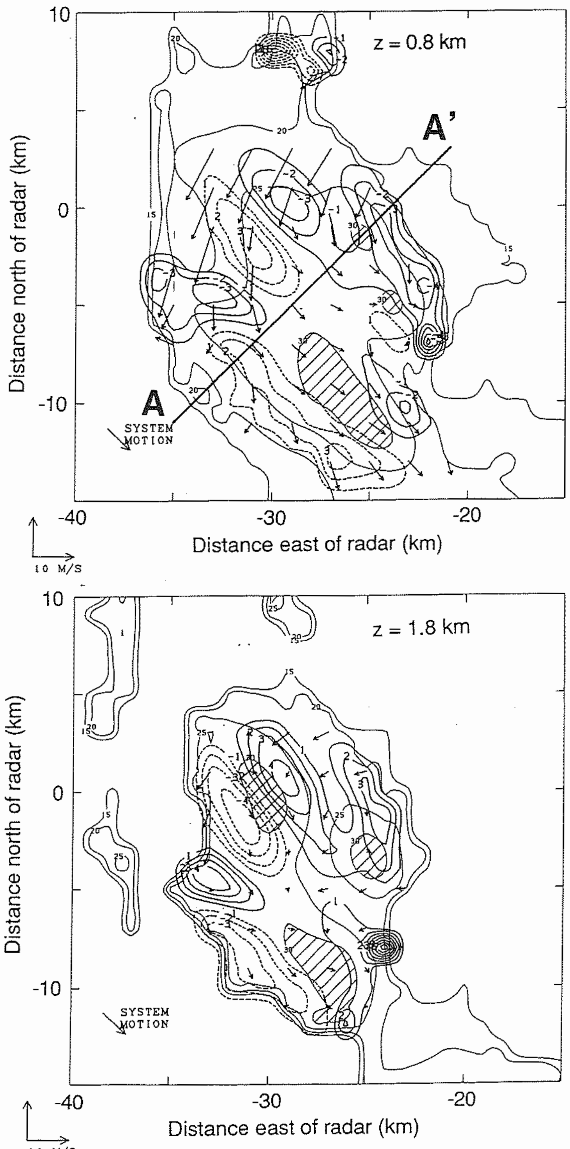

Fig.2 System-relative horizontal airflow and reflectivity fields in the band at 0.8 km and 1.8 km levels at 0046 JST on 11 Feb. 1989. Wind arrows are drawn every two grids. Location of the vertical cross section in the Fig. 3 is also shown. Thin solid lines are contours of reflectivity at 5-dBZ_e intervals. Reflectivity values exceeding 30 dBZ_e are hatched. At 0.8 km level, thick solid and dashed lines are, respectively, contours of horizontal convergence and divergence at $1\times10^{-3}\ s^{-1}$ interval. At 1.8 km level, Thick solid and dashed lines are, respectively, contours of positive and negative vertical air velocity at 1 m/s interval .

The circulation in the vertical cross section perpendicular to the band orientation is shown in Fig. 3. From the northeastern edge, the convectively unstable air flows into the band as updraft. Around the southwestern edge, on the contrary, the downdrafts originated around the middle-level enter the band and then flow out around the southwestern boundary at the lower levels. The magnitude of vertical motions are several meters per second.

A conceptual model of the structure of the L-type band can be deduced from the above results (see Fig. 4). The circulation in the band demonstrates a typical long-lasting updraft-downdraft couplet: the inflow of unstable air outside the band continuously ascends over the cold downdraft. The cold air created by the downdraft seems to play an important role on maintenance of the band, although no in-situ observation was made of the thermal structure in and around the band. The cold air would be continuously supplied around the sea surface by evaporative cooling of snow particles falling in the downdraft.

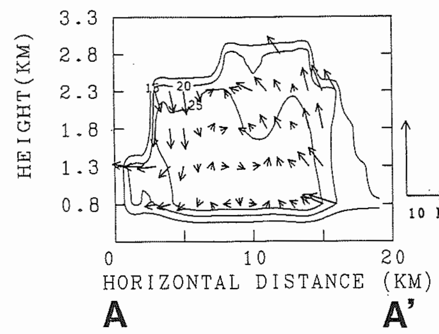

Fig. 3 Vertical cross section along the A-A' line in Fig.2. Reflectivity contours are indicated at 5-dBZ_e intervals. Horizontal wind vectors indicate system-relative winds.

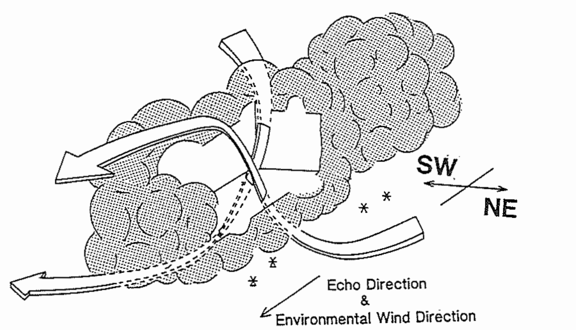

Fig. 4 A conceptual model of a L-type snow band. The air flows are relative to the system motion.

b. T-type band

A T-type band, about 100 km long and 20 km wide, appeared following the passage of an extratropical cyclone on 12 Feb. 1990. The band sometimes appears in the winter monsoon, but not common. It moved east-southeastward at a speed of 13 m/s. Radar reflectivity depicted that the band was consisted of two or three band-like echo regions aligned parallel to the band orientation; hereafter we refer to these echo regions as "subbands". The surface wind analysis on that day at Tobishima Island, 30 km off shore, suggests that the band was associated with a convergence zone in large scale. Wind speeds drastically increased from 8 to 16 m/s after the passage of the band, while the surface wind directions hardly changed from west-northwest. The environmental wind measured at Akita is shown in Fig. 5. The wind changed the direction with height from west-northwest at lower levels to west-southwest at 700 hPa. The precipitation intensity at Tobishima was very weak, 1mm/hr in water equivalent and graupel was dominant.

Figure 6 shows the vertical profiles of equivalent potential temperatures in and outside of the band, measured by meteorological drop sondes. The observation of the outside was made 90 km west of the MRI radar. The thermal field is characterized by colder air inside and unstable air outside of the band in the lower layer.

Horizontal wind fields relative to the system motion and the reflectivity fields are shown in Fig. 7. Here we will describe only the features of the subband 1 situated around the trailing edge of the band because the subband 2 had similar features to it. At the 0.6 km level, horizontal convergence exists around the trailing edge, and divergence is situated in the forward portion of the subband. The system-relative wind fields are, therefore, characterized by the ascending low-level inflow around the trailing edge and outflow of downdraft in the forward portion of the subband. Similar pattern is also seen at 1.8 km level. The TV-drop sonde observation was also carried out around (x,y)=(-50 km, -39 km) at 1451 JST. Although the dropping position is situated a little beyond the limitation of dual-Doppler processing, the PPI display of the radar indicated that the position was inside of the subband with reflectivity values 20-25 dBZ_e. Plenty of supercooled droplets were observed in the band.

Figure 8 shows a vertical cross section perpendicular to the band orientation. The line crosses a matured cell embedded in the band. This circulation was found to take place in most of area in the subband. From the trailing edge, the air flows into the band as updraft. The downdraft originated around the middle-level exists in the forward portion.

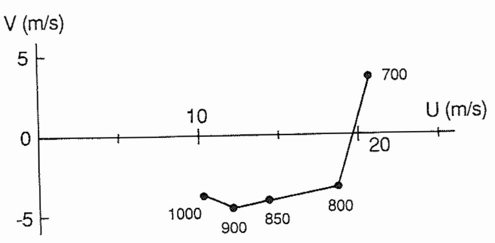

Fig. 5 Wind hodograph observed at Akita, 40 km north of the MRI radar, at 1500 JST. Numbers near darkened circles indicate pressure (hPa).

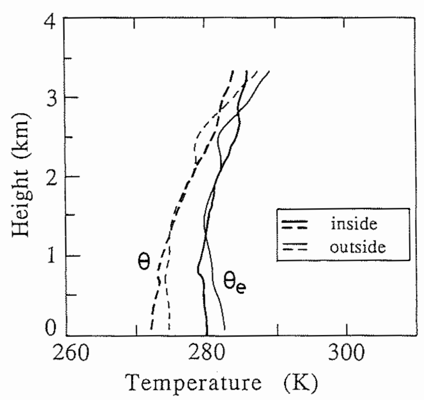

Fig. 6 Vertical profile of potential (Θ) and equivalent potential temperature (Θ_e) in and outside the band.

Around the trailing edge of the band at middle- and higher levels, there exists a reverse flow toward the trailing edge with relatively weak updraft.

A conceptual model of the subband in the T-type snow band is illustrated in Fig. 9. The inflow of unstable air from the trailing edge ascends over the cold air on the sea surface. The vertical air velocity is about 2 m/s. In the forward portion the downdraft originates around the 1.8 km level and then flows out of the subband at the lower levels. As the cold air on the sea surface are continuously supplied ahead of the subband by the downdraft, the inflow is free to ascend over it. The surface observations of snow particles at Tobishima supports the conceptual model: at first graupel was observed and then precipitation changed to snowflake as the band passed. Probably the graupel grows in the updraft in the forward portion

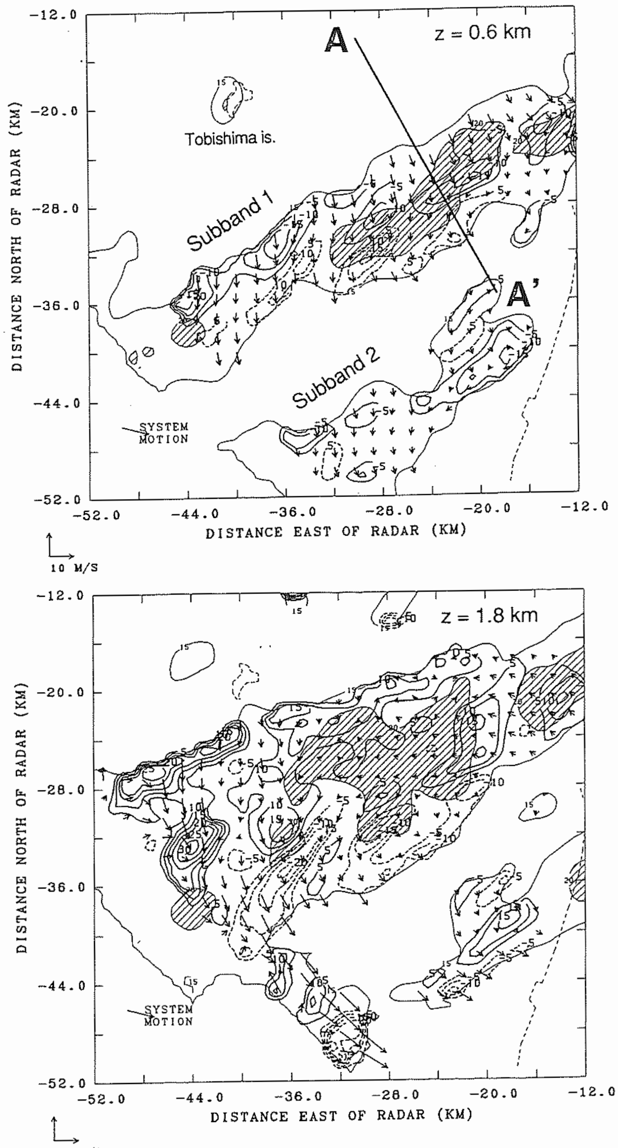

Fig. 7 Same as in Fig. 2 except for 1442 JST on 12 Feb. 1990. In this case reflectivity values exceeding 20 dBZ_e are hatched and that contours of horizontal divergence and vertical air velocities are drawn at 5×10^{-4} s^{-1}, 0.5 m/s intervals, respectively. Thin dotted lines show shore lines. Position of Tobishima is. also shown.

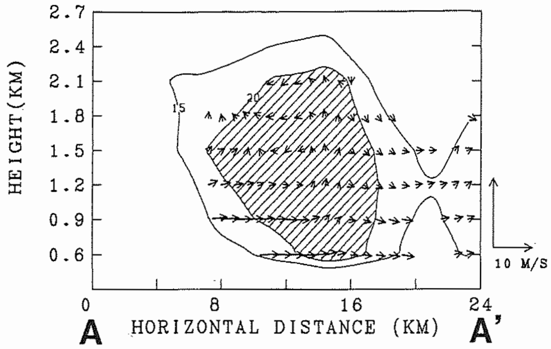

Fig. 8 Vertical cross section of the subband along the line A-A' in Fig. 7. Horizontal wind vectors indicate system-relative winds. Reflectivity contours are drawn at 5-dBZ_e intervals. Reflectivity values exceeding 20 dBZ_e are hatched.

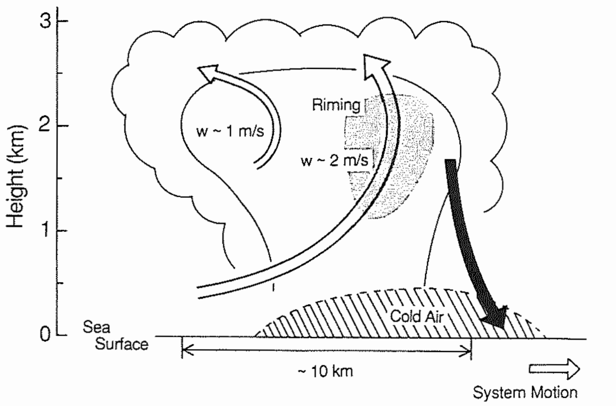

Fig. 9 Same as in Fig. 4, except for subband in the T-type snow band. The inner thin solid line indicates the radar echo region.

of the subband, and the snowflake is formed in the relatively weak updraft around the trailing edge.

5. DISCUSSION

Both types of bands, L-type and T-type, have long-lasting updraft-downdraft circulations with preferable thermal structures: convectively unstable air ascends over the cold air on the sea surface in the band, and the downdraft originated around the middle-level falls down being cooled by evaporation of graupel or snow. It spreads out on the sea surface and makes a cold pool. This contrast between the unstable warm air and the cold air around the sea surface seems to be important for the maintenance of the band. The existence of the contrast was successfully confirmed in the observations of 1991 and 1992.

In general, with respect to the difference in configuration between L-type and T-type, vertical wind shear is likely to be important although the large scale convergence may affect in part its configuration in the T-type case. In fact, the vertical shear was significantly different between the L-type and the T-type: wind direction changed less with height for the L-type than for the T-type. Since the cold downdrafts originate at middle- and higher levels and transport the momentum at that level toward the lower levels, the interaction in the lower levels between the ambient air and the downdrafts becomes important. The style of the interaction, associated with vertical shear, would determine the configuration of the bands.

Another different types of bands were observed in 1991 and 1992. Their airflow structures were significantly different from those described in this text. The results of the analyses are reserved for the future paper.

6. CONCLUSION

Two types of snow bands, L-type and T-type, were analyzed from the data of dual-Doppler radars and special drop sondes. Based on the results, the conceptual models are presented. Circulations in the snow bands, both L-type and T-type, are long-lasting types with temperature contrast at the low levels between the unstable warm air outside and the cold air inside. This contrast is considered to be important for maintenance of the snow bands. It is also suggested that the vertical wind shear is important for the band configuration.

Acknowledgements The authors are grateful to Dr. Y. Fujiyoshi, Dr. M. Maki, and Mr. S. Nakai for cooperative dual-Doppler observations. The authors also would like to thank the members of the third laboratory of the Typhoon Division of Meteorological Research Institute, Messrs. H. Sakakibara, M. Ishihara, A. Tabata, K. Akaeda, and K. Mori for their supporting the Doppler radar observations.

REFERENCES

Braham, R. R. JR., 1983: The midwest snow storm of 8-11 December 1977. *Mon. Wea. Rev.*, **111**, 253-272.

Chong, M., and Testud, J., 1983: Three-dimensional wind field analysis from dual-Doppler radar data. part III: The boundary condition : An optimum determination based on a variational concept. *J. Climate and Appl. Meteor.*, **22**, 1227-1241.

Hjelmfelt M. R. and Braham R. R. Jr., 1983 : Numerical simulation of the airflow over lake Michigan for a major lake-effect snow event. *Mon. Wea. Rev.*, **111**, 205-219.

Hsu Hsiao-Ming, 1987 : Mesoscale lake-effect snowstorms in the vicinity of lake Michigan: linear theory and numerical simulations. *J. Atmos. Sci.*, **44**, 1019-1040.

Ikawa, M., Sakakibara, H., Ishihara, M., and Yanagisawa, Z., 1987: 2-Dimensional simulation of the convective snowbands observed over the Japan Sea: - the structure and time evolution of the organized multicellular convection -. *J. Meteor. Soc. Japan*, **65**, 605- 633.

Ishihara, M., Sakakibara, H., and Yanagisawa, Z. 1989: Doppler radar analysis of the structure of mesoscale snow bands developed between the winter monsoon and the land breeze. *J. Meteor. Soc. Japan*, **67**, 503-520.

Kelly, R. D., 1982: A single Doppler radar study of horizontal-roll convection in a lake-effect snow storms. *J. Atmos. Sci.*, **39**, 1521-1531.

Kristovich, D. A. R., 1990: Aircraft and radar observations of the three-dimensional flow fields of boundary layer rolls. *Conference on Cloud Physics*, San Francisco, Amer. Meteor. Soc., 706-711.

Ray, P. S., Ziegler, C. L., Bumgarner, W., and Serafin, R. J., 1980 : Single- and multiple-Doppler radar observations of tornadic storms. *Mon. Wea. Rev.*, **108**, 1607-1625.

Sakakibara, H., Ishihara, M., and Yanagisawa, Z., 1988: Squall line like convective snowbands over the Sea of Japan. *J. Meteor. Soc. Japan*, **66**, 937-953.

MESOSCALE RAINBANDS IN CYCLONIC STORMS OF NORTH CHINA

Peng-Yun Wang[1] and Zi-Xiu Xu
Chinese Academy of Meteorological Science,
Beijing, People's Republic of China

1. INTRODUCTION

It is well known that mesoscale rainbands are common and that they make a considerable contribution to precipitation in midlatitude cyclones (e.g. Hobbs, 1978; Browning, 1986). Studies over the past two decades in the Beijing area of North China show that the basic characteristics of mesoscale rainbands are similar to those described by Hobbs (1978) for the Pacific Northwest of the United States. However, since the Beijing area is located on the eastern side of Eurasia, and on the western coast of the Pacific Ocean, many of the fronts passing through this region have been affected by the topography of the continent. Thus, their structures and organization are sometimes more complex than those observed in the west United States and Britain. A brief description of our findings is given below.

2. MAJOR CHARACTERISTICS OF THREE TYPES OF RAINBANDS

a. Cold-Frontal Rainbands

Two types of cold-frontal rainbands are often associated with cold fronts. One is the narrow cold-frontal rainband. These bands are about 200–400 km long and 10–20 km wide. The surface cold front is generally located along the narrow cold-frontal rainband. However, an exceptional example is shown in Fig. 1a in which a narrow band was located about 16 km behind the surface cold front. It arrived 65 mins after the surface cold front passed. The band was associated with the steep edge of the cold air mass at upper levels, but the surface cold front (defined by wind shear and temperature decrease) was located along the leading edge of the cold air mass.

Wide cold-frontal rainbands have widths generally greater than 50 km, and are generally located behind the surface cold front. Although they may appear to consist of homogeneous stratus precipitation, they actually contain rain clusters.

b. Warm-Sector Rainbands

Warm-sector rainbands are situated ahead of most surface cold fronts, especially when there is a cold low to the west and a blocking high to the east. Xu and Wang (1989) observed warm-sector rainbands ahead of thirty-three cold fronts. About 50% of these bands were oriented parallel to the cold front and moved in same direction as the front (Fig. 1a). The bands were one hundred to several hundreds of kilometers long and tens to a hundred kilometers wide. The average distance between the bands was ten to tens of kilometers, with a maximum spacing of 100 km. Many case studies showed that the warm-sector rainbands originated 10–20 km ahead of the surface cold front. Single convective cells first appeared near the front, then, within 10–30 mins, banded echoes formed and moved forward faster than the cold front. They typically propagated forward as younger, more convective bands formed ahead of older, less convective bands.

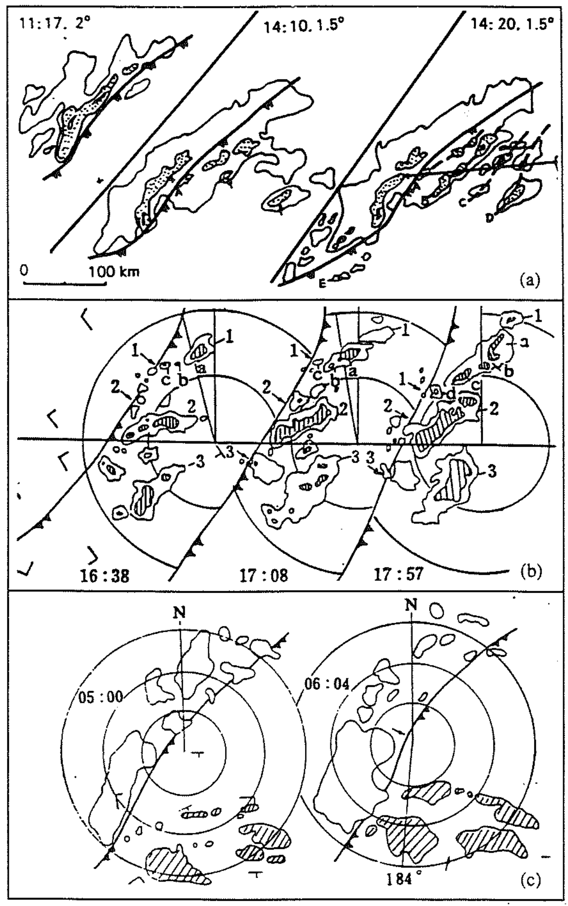

Fig. 1 Three types of warm-sector rainbands based on PPI scopes taken with a C-band weather radar at Beijing on (a) 22 July 1985, (b) 18 July 1980, (c) 18 July 1979. The range markers are at intervals of 100 km in (b) and 50 km in (c); the radar echoes are contoured at 20 dB(Z) in (a), and 0 dB(Z) in (b) and (c), with shaded areas representing 30 and 40 dB(Z) in (a), and 30 dB(Z) in (b) and (c). The surface cold fronts are from synoptic analyses.

The other 50% of the warm-sector rainbands form either at an angle to the cold front (Fig. 1b) or perpendicular to it (Fig. 1c). The former were generally at an angle of 30^{o}–60^{o} to the cold front. They were typically tens to two hundreds of kilometers long, ten to tens of kilometers wide, and spaced 10–50 km. The frequency of this type of band was about 36%. The bands as a group move together at a similar speed to the cold front. Radar observations indicate that the cells in these bands originate at the surface cold front. New cells that form on the front move downwind with the wind velocity at mid- and low- levels ahead of the front. Cells farthest from the front are older than those near the front.

The third type of warm-sector rainband is perpendicular to the cold front and they move in a different direction from the front. Rainbands of this type generally

[1]Visiting Scholar, Department of Atmospheric Sciences, University of Washington, Seattle.

contain 2–6 sub-bands. The frequency of this type of rainband is about 14%. The bands are tens to one hundred kilometers long, and ten to tens of kilometers wide. This type of band does not originated on or near the front. Instead it is associated with mesoscale interactions of warm and wet airflows from the ocean. The bands sometimes have an arc shape, which reflects cyclogenesis in the region.

c. Warm-Frontal Rainbands

Since the cyclonic center is often located north of 45°N in North China, warm-frontal rainband are seldom observed in the Beijing area. Only when the Hetao cyclone moves from the northwest into the North China Plain, or there is cyclogenesis, are warm-frontal rainbands observed. Figure 2 shows an example of such a band.

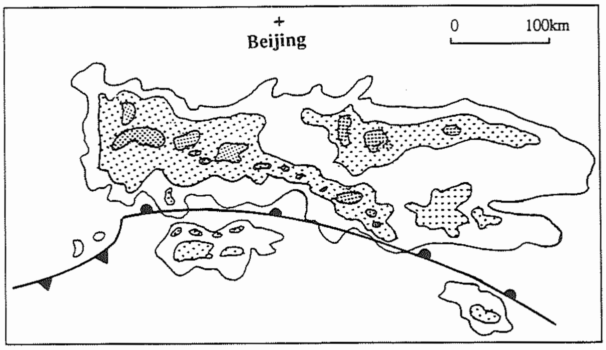

Fig. 2 Warm-frontal rainband observed at Beijing at 1454 Z on 6 July 1990. The shadings are the same as in Fig.1 (a).

3. SUB-STRUCTURES OF RAINBANDS

a. Cells on Rainbands

All of the rainbands discussed above consist of cells. The cells have their own life cycle. New cells form as older cells dissipate. In the case of warm-sector rainbands that are oriented parallel to and at an angle to the cold front, the cells move forward with the band, but they also move along the band. Therefore, the rainfall produced by these band depends on the motion of both the band and the cells.

b. Cyclogenesis on Pre-Existing Rainbands

When cold fronts move from the mountains of Northwest China down into the North China Plain, cyclogenesis sometimes occurs on pre-existing bands. These new cyclones generally dissipate quickly. Sometime, however, they develop into a local cyclone and produce heavy rainfall. For example, a new cyclone developed on warm-sector rainband shown in Fig. 3, it produced 75 mm of rain in 24 hours in Beijing.

c. Reformation of Rainbands

When rainbands associated with a cold front move to the east coast of China, they may be blocked by high pressure to the east, and therefore slowly dissipate. However, if there is a transformed tropical depression of a typhoon moving up toward the north, the rainband may reform along the previous location of the dissipated rainband.

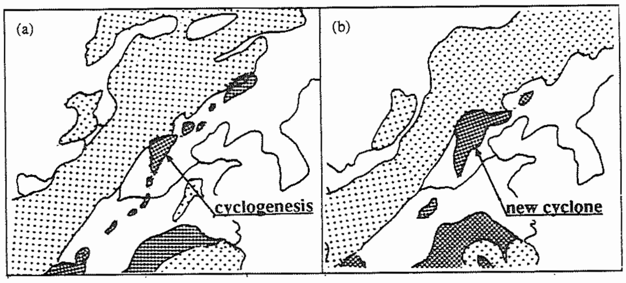

Fig. 3 Sketches from a satellite photograph on 1 August 1990 (a) 1730 Z and (b) 2030 Z. The dotted and hatched areas represent cloud top temperatures from –20° to –40°C and –60° to –80°C, respectively.

4. SYNOPTIC ANALYSES

Xu (1977 and 1981) and Wang and Yu (1989) investigated the synoptic situations associated with the formation of warm-sector rainbands in the Beijing area. They found that a "cold low to the west and a blocking high to the east" is the major synoptic background for the formation of warm-sector rainbands. Warm-sector rainbands are often associated with the mesoscale shear lines in front of cold fronts. The convergence of two mesoscale shear lines can produce a significant strengthening of the rainband and at their connecting point there may be severe convective weather. Gravity waves, caused by the acceleration of cold fronts as they move from the mountains area to the west into the North China Plain, may stimulate the formation and development of mesoscale rainbands.

5. DIAGNOSTIC ANALYSES AND NUMERICAL SIMULATIONS

Xu and Wang (1989) and Wang et al. (1990) studied the three types of warm-sector rainbands and showed that the parallel, angular and perpendicular types were associated with symmetric instability, Kelvin-Helmholtz instability and vertical shear instability overturning, respectively.

6. REFERENCES

Browning, K. A., 1986: Conceptual models of precipitation systems. Weather & Forecasting, I, 23–41.

Hobbs, P. V., 1978: Organization and structure of clouds and precipitation on the mesoscale and microscale in cyclonic storms. Rev. Geophys. Space Phys., 16, 741–755.

Wang, Pengyun, Xu Zixiu and Pan Zeitao, 1990: A case study of warm sector rainbands in North China. Adv. Atmos. Sci., 7, 354–365.

Wang, Muwei and Yu Zimin, 1989: Analysis on the band-like echoes in Beijing-Tianjin-Hebei area (I) Statistical characteristics of convectical echo bands. Collected Papers of Beijing-Tianjin-Hebei Experimental Base for Mesoscale Meteorology, 2, 104–116 (in Chinese).

Xu, Zixiu and Wang Pengyun, 1989: Mesoscale rainbands ahead of cold fronts in North China and their dynamical mechanisms. Acta Meteor. Sinica, 3, 516–525.

Xu, Zixiu, 1977: The analyses of mesoscale weather processes in summer in Beijing, Tianjin and Tangshan area. Collected Papers on Radar Meteorology of Chinese Academy of Meteor. Sci., 17–39 (in Chinese).

———, 1981: Study on mesoscale rainbands and their interactions with convergence in boundary layer in Beijing-Tianjin-Hebei area. Collected Papers on Radar Meteorology of Chinese Academy of Meteor. Sci., 17–27 (in Chinese).

FRONTAL TOPOGRAPHY AND PRECIPITATION

John D. Locatelli, Jonathan E. Martin and Peter V. Hobbs

Atmospheric Sciences Department, University of Washington, Seattle, Washington 98195

1. INTRODUCTION

Several theories have been proposed to explain rainbands in extratropical cyclones (e.g. Bennetts and Hoskins 1979; Matejka et al. 1980; Emanuel 1983; Parsons and Hobbs 1983; Sanders and Bosart 1985; Locatelli and Hobbs 1987; Moore and Blakely 1988; Knight and Hobbs 1988). In this paper we will show that, for at least one wide cold-frontal rainband, the velocity of the frontal surface and topographical features on this surface were closely related to the movement of the rainband and its sub-structure.

2. OVERVIEW

Four hours after a surface cold front passed eastward over Cape Hatteras, North Carolina, on 26 January 1986 a wide cold-frontal rainband (WCFR) passed through a region of dual-Doppler radar coverage adjacent to Cape Hatteras. This coverage was provided by the NCAR CP-3 and CP-4 Doppler radars, which were part of a larger array of instruments deployed for the Genesis of Atlantic Lows Experiment (GALE).

Figure 1 shows the area over which reflectivity data were available from the dual-Doppler radars, and the region (90 km x 36 km x 9 km) in which three-dimensional wind fields could be derived from the dual-Doppler radars. The insert in Figure 1 shows the WCFR (defined by the 31 dBZ contour at 1 km altitude) and the surface cold front at approximately 0045 UTC 27 January. The WCFR was located 120 km behind and parallel to the cold front.

In common with other WCFRs (e.g. Hobbs et al. 1980) the WCFR depicted in Figure 1 had internal substructure. The smallest and strongest elements of this substructure, which we refer to as "precipitation cores" (Hobbs and Locatelli 1978), are denoted by the letters X and Y in Figure 1. The velocity of the precipitation cores was 30 m s^{-1} toward 13°. We will refer to larger, organized elements of the rainband as "sub-bands".

3. MESOSCALE STRUCTURE

Shown in Figure 2 is a vertical, time-space, cross section of temperature, equivalent potential temperature (θ_e) and winds in the region of dual-Doppler radar coverage. A sloping region of increased stability is evident by the vertical gradient of the θ_e lines. In this same region there is a sloping region of backing winds with height and a decrease in the horizontal temperature. We conclude that this region is the elevated cold-frontal surface; the top of this zone is the cold-frontal surface, which is marked by a heavy dashed line in Figure 2.

We can also objectively locate the cold-frontal zone by calculating frontogenesis values given by:

$$F=\frac{\left[\frac{\partial\theta}{\partial x}\left(-\frac{\partial u}{\partial x}\frac{\partial\theta}{\partial x}-\frac{\partial w}{\partial x}\frac{\partial\theta}{\partial x}\right)+\frac{\partial\theta}{\partial z}\left(-\frac{\partial u}{\partial z}\frac{\partial\theta}{\partial x}-\frac{\partial w}{\partial z}\frac{\partial\theta}{\partial z}\right)\right]}{\left[\left(\frac{\partial\theta}{\partial x}\right)^2+\left(\frac{\partial\theta}{\partial z}\right)^2\right]^{1/2}} \quad (1)$$

where, x is the west-east direction, u the wind velocity in this direction, and w the vertical air velocity.

Shown in Figure 3 are the values of F in an east-west cross section, located at 12 km in the south-north direction. This cross section of F is similar to all other cross sections of F within the region where winds were derived from the dual-Doppler radar data. The top of the zone of positive frontogenesis is marked with a heavy dashed-dot line in Figure 3. A comparison of Figures 2 and 3 show that the zone of positive F corresponds closely to the cold-frontal zone defined previously.

Figure 4 shows a cross section of the wind relative to the velocity of the precipitation cores. The heavy solid line in Figure 4 is the center of the region where the total horizontal

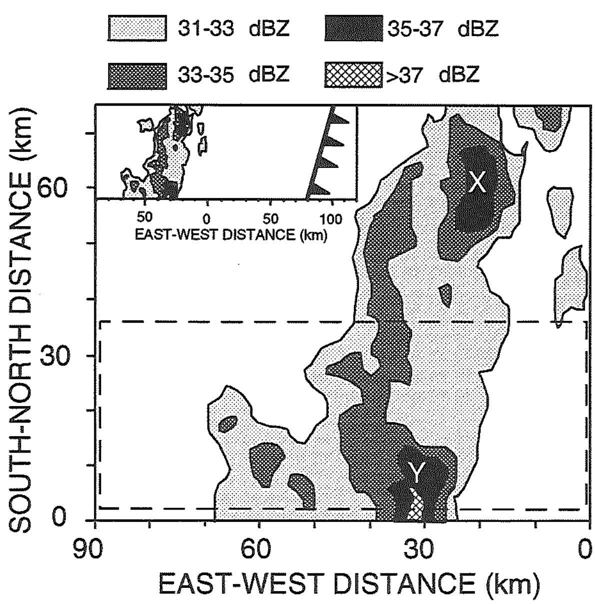

Fig. 1. Radar reflectivity values for the wide cold-frontal rainband (WCFR) at an altitude of 1 km at 0045 UTC 27 January 1986. The dashed rectangle shows the region over which winds were derived from dual-Doppler radars. Precipitation cores within the WCFR are designated by X and Y. Sub-bands are the south-north oriented regions defined by the 33–35 dBZ level. The inset shows the rainband (shaded area) relative to the position of the surface cold front.

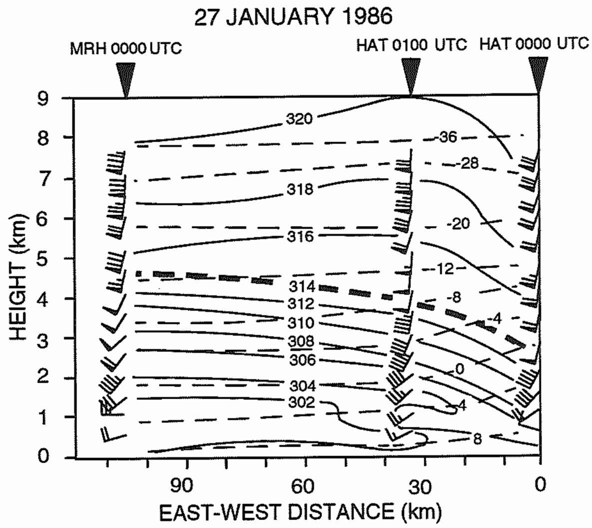

Fig. 2. Time-space cross section of equivalent potential temperature, θ_e (solid lines, labeled in degrees Kelvin), temperature (dashed lines, labeled in degrees Centigrade), and winds (conventional symbols) in the region where winds were derived from the dual-Doppler radars. The locations of the radiosondes (HAT = Cape Hatteras, NC; MRH = Morehead City, NC) are indicated by the heavy arrows. The heavy dashed line is the top of the cold-frontal zone defined by wind shear, temperature gradient and θ_e.

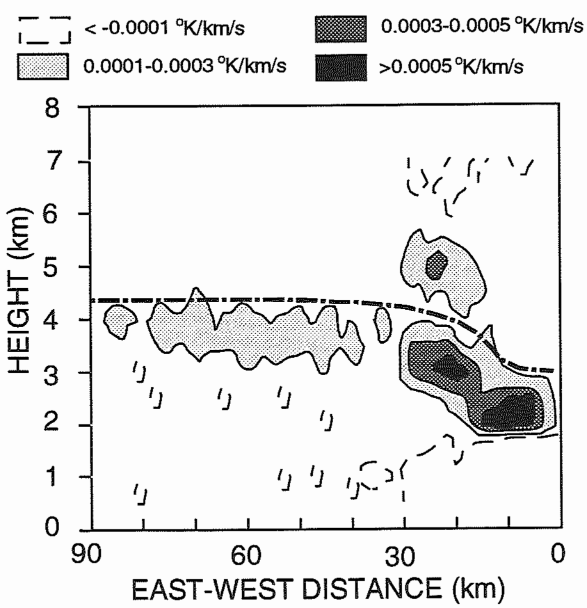

Fig. 3. Frontogenesis values (F) across the rainband in an east-west vertical cross section located at 12 km in the south-north direction at 0045 UTC 27 January 1986. The heavy dashed-dot line is the top of the layer of positive frontogenesis.

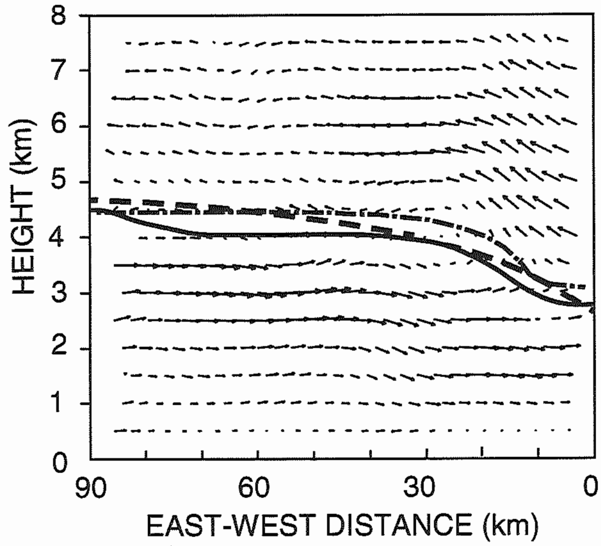

Fig. 4. Vector airflow relative to the velocity of the precipitation cores in an east-west vertical slice located at 12 km in the south-north direction at 0045 UTC 27 January 1986. The heavy dashed-dot line is at the top of the layer of positive frontogenesis; the heavy dashed line is the top of the layer defined by wind shear, temperature gradient and θ_e; and the heavy solid line shows the region along which the winds derived from the dual-Doppler radars were closest to the velocity of the precipitation cores.

wind (as derived from the dual-Doppler radar measurements) was less than 2 m s^{-1} relative to the velocity of the precipitation cores. This line divides the cross section into an upper region of rising westward airflow from a lower region of sinking eastward airflow. Also shown in Figure 4 are the positions of the cold-frontal surface from Figure 2 (heavy dashed line) and Figure 3 (heavy dashed-dot line): all three lines are similar in shape and position.

Similar computations for the whole region in which winds were derived from the dual-Doppler radars produced an undulating surface on which the winds had a similar velocity to the precipitation cores; we take this to be the cold-frontal surface. This cold-frontal surface is shown in Figure 5a; it is steeper toward the east, but it also contains smaller regions of even steeper slope toward the south-east.

Shown in Figure 5b are three vertical cross sections through the rainband oriented in the east-west direction. Pronounced regions of higher radar reflectivity are located at the eastern portion of each cross section, where fallstreaks of precipitation particles were descending from aloft. Comparing Figure 5a with 5b, we see that the WCFR formed in the region where the slope of the cold-frontal surface was large. Also, the steeper the topography of the cold-frontal surface the stronger the fallstreaks. All of the other cross sections through the rainband showed the same correspondence between radar reflectivity, fallstreak strength and steepness of the cold-frontal surface.

Shown in Figure 5c are vertical air velocities derived from the dual-Doppler data. A comparison of Figure 5a and 5c shows that the steeper the slope of the frontal surface the greater the vertical velocity of the air in the upper regions of the fallstreaks. This explains why the radar reflectivity and the fallstreaks were greater in the regions of greater frontal slope.

4. MOVEMENT OF THE RAINBAND

Shown in Figure 6 are a series of radar reflectivity patterns for the WCFR. The series is aligned along the thin horizontal lines that pass through two of the precipitation cores. The result of such an alignment is to view the time evolution of the WCFR from the perspective of these precipitation cores.

The WCFR was composed of groups of precipitation cores and sub-bands (labeled A, B and C in Figure 6). For example, sub-band A decreased in strength as sub-band B developed to the east of it. Similarly, sub-band B decreased in strength as sub-band C developed, all within 30 min. The net result was that speed of the WCFR was greater than the band-normal speed of either the precipitation cores or the sub-bands. For example, as sub-band B developed between 0022-0052 UTC on 27 January, it moved northward faster than the speed of the new precipitation cores that formed on its northern edge.

5. MOVEMENT AND GENERATION OF THE PRECIPITATION FEATURES IN RELATION TO FRONTAL TOPOGRAPHY

In Section 2 we showed that the precipitation cores within the WCFR moved with the same velocity as the winds on the frontal surface. We also showed that the WCFR was located beneath a region of the frontal surface that had a relatively steep slope, and that the steepness of the frontal surface affected the strength of the updraft above and along its surface and the resulting radar echo strength. The sub-bands within the WCFR were associated with smaller scale and steeper regions on the frontal surface, and the precipitation cores were associated with still smaller scale and even steeper regions of the frontal surface. Hence, the movement and generation of the WCFR, and its sub-bands and precipitation cores, are simply explained by the movement and evolution of the frontal surface and "topographical" features on this surface.

Figure 7 illustrates these points. Here, a portion of the cold-frontal surface is depicted with regions of varying steepness. The steepest regions produce precipitation cores, the next steepest produce sub-bands, and a region of somewhat less steepness defines the rainband itself. This is because the warm air flowing toward the frontal surface (black and hatched flat arrows in Figure 7) is lifted at a rate proportional to the steepness of the frontal surface. If the frontal topography moves at the velocity of the frontal surface (3-D arrow in Figure 7), the precipitation cores and sub-bands will also move at this velocity (cross-hatched flat arrow).

Figure 4 shows the warm, westward moving air rising above the cold-frontal surface. This implies the front acted as a barrier to the warmer air ahead of it. The θ_e pattern in Figure 2 shows that a parcel of warm air moving toward the cold air beneath the frontal surface could not have easily penetrated this surface, because the potential temperature differences would force it to rise. The speed of the wind in the east-west direction, eastward of the dashed box in Figure 1, was computed from the 0000 UTC 27 January Nested Grid Model initialization using a weighted average of the three closest 700 mb model data points. This was subtracted from the speed of the frontal surface, giving a relative speed of 3 m s^{-1} toward the frontal surface. The resulting vertical velocity was calculated at 12 km south-north in the box by assuming that $w = -v_r \nabla h$, where v_r is the relative air velocity toward the front and ∇h the frontal slope. This gave an updraft of 0.2 m s^{-1}, compared to the maximum updraft of <0.5 m s^{-1} computed from the dual-Doppler data for the same region.

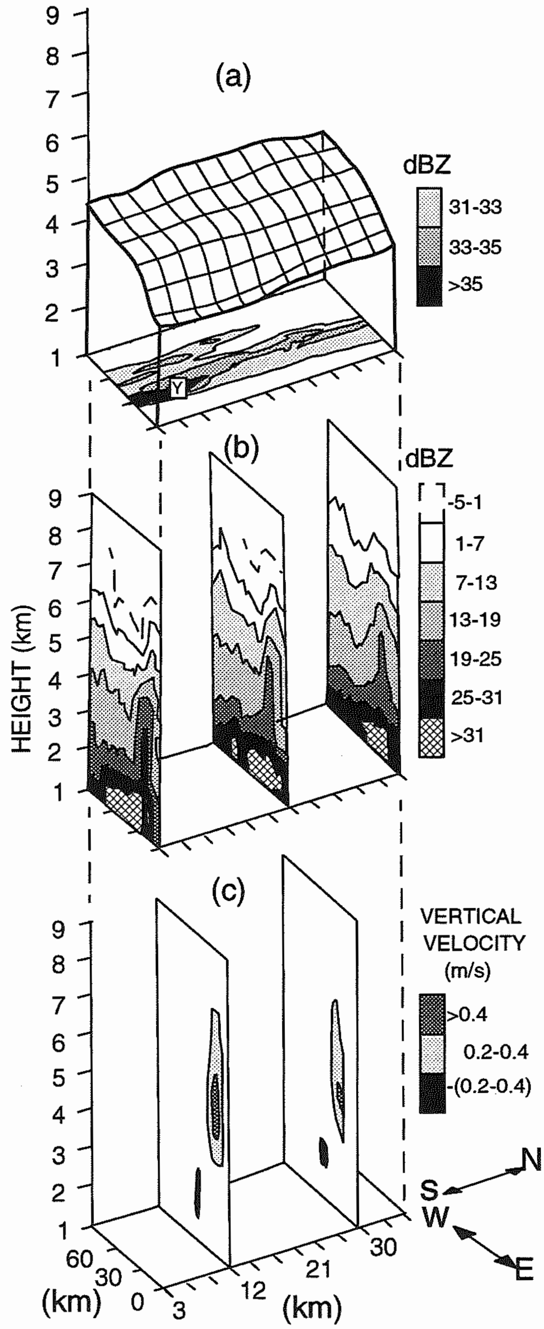

Fig. 5. a) The hatched surface shows the region aloft where the horizontal winds were closest in velocity to that of the precipitation cores in the WCFR (i.e. the cold-frontal surface). Radar reflectivities at 1 km are also shown. b) Radar reflectivities of the WCFR on three vertical planes. c) Vertical air velocities in the WCFR on two vertical planes. For 0045 UTC 27 January 1986.

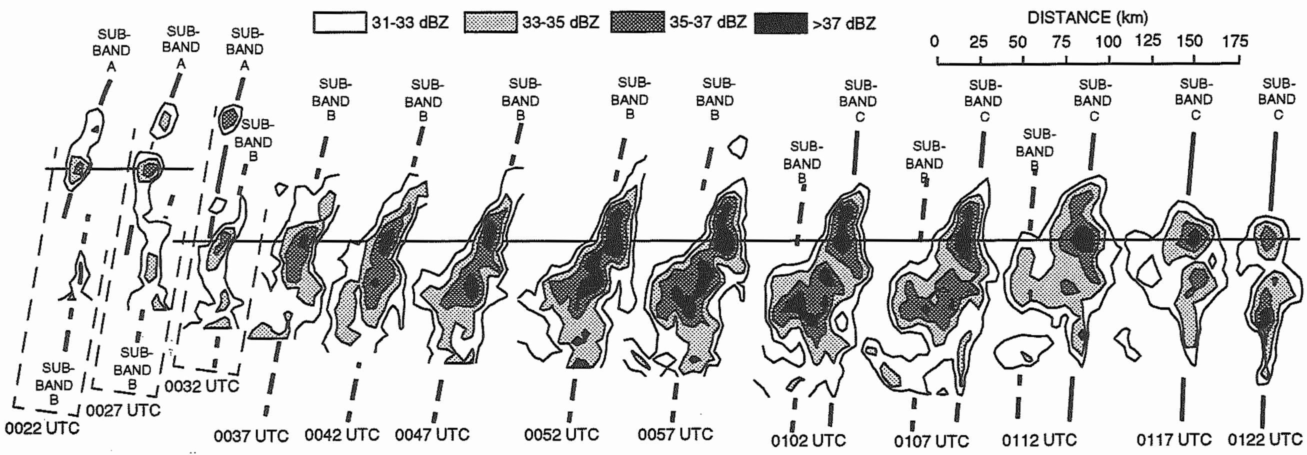

Fig. 6. Radar reflectivities at five minute intervals for the WCFR taken from the 0.5-0.7° scans of the National Weather Service WSR-57 radar.

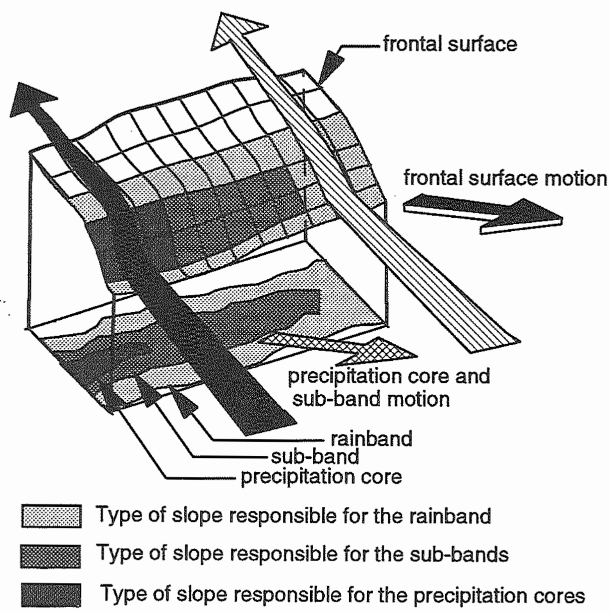

Fig. 7. Schematic illustrating the connection between the slope and motion of the frontal surface, the upward air motions, and the positions and motions of a rainband and its sub-structure.

Since the radar reflectivity pattern of the WCFR was coupled to the topography of the frontal surface, the results discussed in Section 4 shed light on the rate of changes of this topography. Based on the observed evolution of the sub-bands, the topographical features on the frontal surface responsible for the sub-bands must have grown and died within ~30 min; older topographical features flattening out as new ones ahead became steeper. The features on the frontal surface that were responsible for the sub-bands must have moved northward faster than the steepest features on the frontal surface, which were responsible for the precipitation cores.

(At the Conference, this paper was presented non-verbally by means of an animated, colored video.)

Acknowledgements.This research was funded by NSF grant ATM-8809061.

6. REFERENCES

Bennetts, D. A., and B. J. Hoskins, 1979: Conditional symmetric instability: A possible explanation for frontal rainbands. Quart. J. Roy. Meteor. Soc., 105, 945–962.

Emanuel, K. A., 1983: Lagrangian parcel dynamics of moist symmetric instability. J. Atmos. Sci., 40, 2368–2376.

Hobbs, P. V., and J. D. Locatelli, 1978: Rainbands, precipitation cores and generating cells in a cyclonic storm. J. Atmos. Sci., 35, 230–241.

______, T. J. Matejka, P. H. Herzegh, J. D. Locatelli, and R. A. Houze, Jr., 1980: The mesoscale and microscale structure and organization of clouds and precipitation in midlatitude cyclones. I: A case study of a cold front. J. Atmos. Sci., 37, 568–596.

Knight, J. D., and P. V. Hobbs, 1988: The mesoscale and microscale structure and organization of clouds and precipitation in midlatitude cyclones. Part XV: A numerical modeling study of frontogenesis and cold-frontal rainbands. J. Atmos. Sci., 45, 915–930.

Locatelli, J. D., and P. V. Hobbs, 1987: The mesoscale and microscale structure and organization of clouds and precipitation in midlatitude cyclones. XIII: Structure of a warm front. J. Atmos. Sci., 44, 2290–2309.

Matejka, T. J., R. A. Houze, Jr., and P. V. Hobbs, 1980: Microphysics and dynamics of clouds associated with mesoscale rainbands in extratropical cyclones. Quart. J. Roy. Meteor. Soc., 106, 29–56.

Moore, J. T., and P. Blakely, 1988: The role of frontogenetical forcing and CSI in the Midwest snowstorm of 30-31 January 1982. Mon. Wea. Rev., 116, 2155–2171.

Parsons, D. B., and P. V. Hobbs, 1983: The mesoscale and microscale structure and organization of clouds and precipitation in midlatitude cyclones. XI. Comparisons between observational and theoretical aspects of rainbands. J. Atmos. Sci., 40, 2377–2397.

Sanders, F., and L. F. Bosart, 1985: Mesoscale structure in the megalopolitan snowstorm of 11–12 February 1983. Part I: Frontogenetical forcing and symmetric instability. J. Atmos. Sci., 42, 1050–1061.

NUMERICAL SIMULATION OF THE FORMATION AND EVOLUTION OF THE MESOSCALE FRONTAL RAINBANDS

B.Ya.Kutsenko, V.V.Ivanov and S.A.Vladimirov

Central Aerological Observatory, Dolgoprudny, Moscow Region 141700 , Russian Federation

1. INTRODUCTION

It is well known from the numerious observations that some frontal cloud,rain and precipitation systems have band structure. There have been many efforts of theoretical explanation of the appearance such band structures (Parsons and Hobbs, 1983). In particular as one of the possibilities for the initiation of frontal rainbands symmetric instability and especially conditional symmetric instability have been shown in a number of publications to have many attractive features. Numerical simulation have played the essential role among these publications. Most numerical investigations of this problem (e.g. Bennets and Hoskins, 1979) have dealt with simulation of some small disturbances grouth in conditions of spatially uniform symmetric or conditionally symmetric instability. However , there are some numerical investigations (Knight and Hobbs, 1988) in which the development of some cloud and rainband mesostructures was simulated in situations close to real atmospheric frontal conditions with the regions of conditional symmetric instability.

The main purpose of the reported work was the numerical simulation of the appearance and evolution of mesoscale structures inside frontal cloud and rain systems in the cases of the presence conditionally symmetric unstable regions. We have used in our simulations both the hydrostatic numerical model (Kutsenko, 1984) and nonhydrostatic one (Vladimirov and Pastushkov, 1984.)

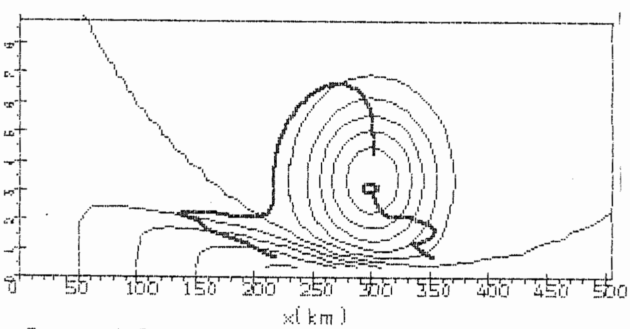

Figure 1 Initial conditions

Uy(x,z) Step= 5.0 **Instability region**

2. THE FORMULATION OF PROBLEM

To simulate the situation of atmospheric frontal zone having the regions which are characterized by the presence of conditional symmetric instability we have used the formulation in which the frontal distribution of calculated fields is posed in the initial conditions. The frontal formating processes have not been regarded. The parameters of analytical formula used for calculation of initial along front velocity component and the temperature stratification were chosen so that there was the region of conditional symmetric instability (CSI). See Fig.1.

The model is initialized with a cross-front circulation. This circulation is obtained by solving some elliptic equation for streamfunction. This equation is a version of the Sawyer-Eliassen equation. The obtained circulation and the temperature distubance which is geostrophically balanced with along front velocity component are shown in the Fig.2. As we can see the updraft region and CSI region from Fig.1 are intercepted. So if there is the layer of sufficiently high relative humidity the stratiform frontal cloud is formed and some unstable disturbances may grow inside this cloud.

The models have used the smooth and rigid top and buttom boundary conditions and open lateral boundary conditions. The horizontal resolution was 20 km for the hydrostatic model and 3 km for nonhydrostatic one. The time step was 30 s.

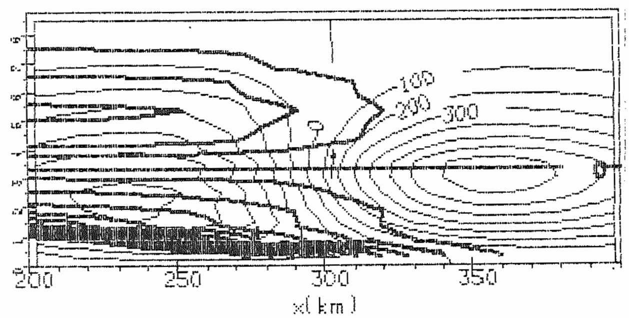

Figure 2. Initial Circulation

T(x,z) Step= 1.0

Streamfunc.F(x,z) Step= 100

3. NUMERICAL SIMULATIONS

Some preliminary testing numerical experiments have been conducted for simulation of evolution of small distubances in symmetrically unstable uniform atmosphere. The initial conditions and the main model parameters have been taken the same as them in previously published paper (Bennets and Hoskins, 1979). The obtained results (the slower grouth rate compare to lineary predicted one and more steeper then potential temperature isosurfaces circulation slope (See Fig.3)) principally coinside with results of Bennets and Hoskins.

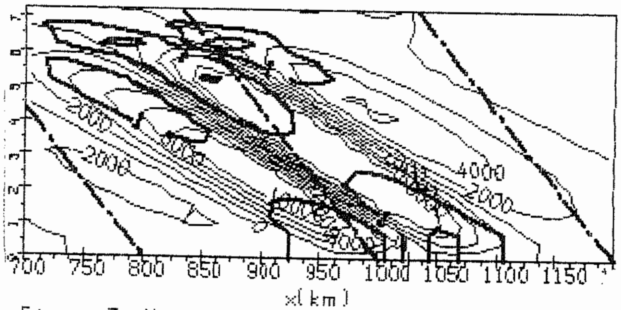

Figure 3. Uniform SI circulation

T(x,z) Step= 2.0 Streamfunc.F(x,z) Step= 2000

Potential temperature Step= 10.0

The resuls of numerical experiments in previously described conditionally symmetric unstable situation are shown in Figs.4 and 5. Shown in these figures are liquid water content L (g/kg,thick lines) and perturbation streamfunction F (m**2/s thin lines) at the time 5 Hrs for different z - eddy diffusion coefficients Kz. It was obtained that the appearance of band structure in cloud and rain fields in presence of CSI regions depends on turbulent viscosity properties of atmosphere.

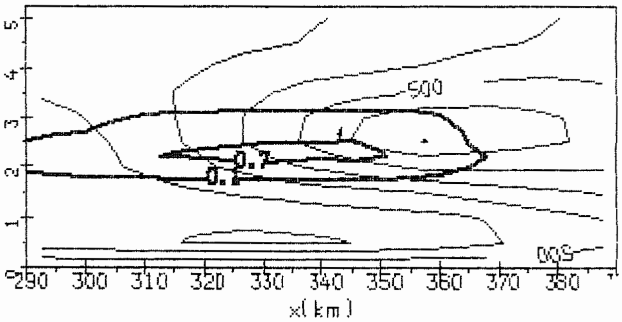

Figure 4. CSI case for t=5 Hs with Kz= 15 m**2/s

L(x,z) Step= 0.6 Streamfunc.F(x,z) Step= 500

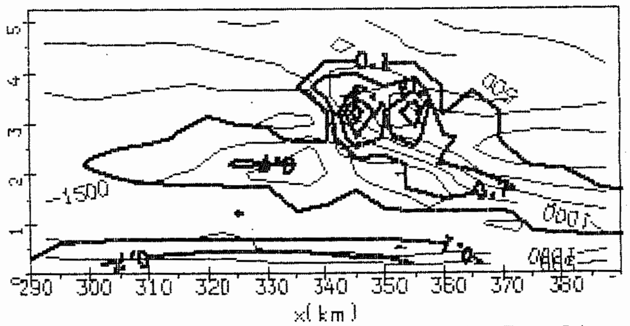

Figure 5. CSI case for t=5 Hs with Kz= 5 m**2/s

L(x,z) Step= 0.6 Streamfunc.F(x,z) Step= 500

4. REFERENCES

1.Bennetts D.A.and Hoskins B.J,1979,Conditional symmetric instability - Possible explanation for frontal rainbands.,Quart. J.Roy.Meteor.Soc.,105,945-962.

2.Knight D.J.and Hobbs P.V.,1988,The mesoscale and microscale structure and organization of cloud and precipitation in midlatitude cyclones.Part XV: A numerical modelling study of frontogenesis and cold frontal rainbands., J.Atmos.Sci.,45 ,915-931.

3.Kutsenko B.Ya.,1984, Numerical simulation of the formation and evolution of frontal stratiform cloudiness.,Proc. 9-th International Cloud Physics Conference., 629-632.

4.Parsons D.B. and Hobbs P.V., 1983, The mesoscale and microscale structure and organization of cloud and precipitation in midlatitude cyclones. Part X: Comparisons between observational and theoretical aspects of rainbands., J.Atmos.Sci. ,40, 2377-2397.

5.Vladimirov S. A. and Pastushkov R. S., 1984, Numerical model of cold front convective clouds., Proc. 9-th International Cloud Physics Conference.,647-650.

COLD-FRONTAL RAINBAND SIMULATIONS USING HYDROSTATIC AND NONHYDROSTATIC MODELS WITH EXPLICIT ICE-PHASE MICROPHYSICS

Jong-Jin Baik [1], Michael C. McCumber [2], V. Mohan Karyampudi [1], and Steven E. Koch [2]

[1] Universities Space Research Association
[2] Laboratory for Atmospheres
NASA / Goddard Space Flight Center
Greenbelt, MD 20771

The physical processes associated with fronts and frontal rainbands have been studied extensively since the early work by Bjerknes (1919) because of their spectacular and unusual nature in the atmosphere. Theoretical studies (e.g., Hoskins and Bretherton 1972) have shown that some features of observed fronts such as a maximum gradient of cross-frontal potential temperature at the surface can be produced using the semigeostrophic equation set in an adiabatic, inviscid framework. The inclusion of the turbulent mixing of sensible heat and momentum in the planetary boundary layer (PBL) in the dry primitive-equation numerical model resolves additional realistic features of frontal structure such as a narrow updraft at the top of PBL above the surface pressure trough (Keyser and Anthes 1982; Koch et al. 1992). Using a moist semigeostrophic model with a wave-CISK parameterization for latent heating, Mak and Bannon (1984) showed that condensational heating can further strengthen and narrow the vertical motion field of surface fronts. These studies indicate that frictional and diabatic processes are important in the surface frontal structure and dynamics.

Observational studies (e.g., Browning and Harrold 1970; Parsons and Hobbs 1983) have documented three classes of precipitation bands associated with cold fronts – narrow cold-frontal rainband, wide cold-frontal rainbands, and warm-sector rainbands. A number of possible physical mechanisms [e.g., conditional symmetric instability (CSI), gravity waves, differential advection] has been proposed to explain the formation of frontal rainbands. CSI is believed to be the most probable cause for the wide cold-frontal rainbands.

There are several studies which have investigated frontogenesis and cold-frontal rainbands using two-dimensional, moist, primitive-equation, hydrostatic (Hsie et al. 1984; Knight and Hobbs 1988) or nonhydrostatic (Benard et al. 1992a and b) numerical models initialized with the analytic solutions to the Hoskins-Bretherton horizontal shear model of frontogenesis. Hsie et al. (1984) started model integration with conditionally unstable conditions to ensure early development of convection by specifying an initial relative humidity of 98% throughout the domain and simulated convective rainbands in the warm sector ahead of the surface cold front, which resemble observed warm-sector rainbands. Knight and Hobbs (1988) simulated frontal circulations and rainbands in a convectively stable atmosphere by decreasing the initial relative humidity (80%) and increasing the vertical stability. The first wide cold-frontal rainband intensified in a region of CSI. The second (third) wide cold-frontal rainband was forced by convergence behind the first (second) and intensified as it moved into the region of CSI. Some of the characteristics of these rainbands appear to agree with the theory of CSI. The control experiment with an initial relative humidity of 98% by Benard et al. (1992a and b) produced an upright convection stage and then non-upright convection. In addition to the three classes of rainbands, they simulated narrow free-atmosphere rainbands whose characteristics are well explained by the linear stationary hydrostatic gravity wave theory. These numerical modeling studies indicate that the initial moisture distribution and vertical stability are important factors in characterizing frontal rainbands.

The idealized modeling studies mentioned above included explicit water-phase microphysics, but ignored the effects of ice-phase processes. Since the inclusion of explicit water-ice phase microphysics can parameterize almost 30 individual microphysical process terms (Lin et al. 1983), more plentiful microscale and mesoscale features are expected to be revealed in the frontogenesis and cold-frontal rainband simulations than those when only explicit water-phase microphysics are included, hence contributing further understanding of the formation mechanisms and characteristics of rainbands associated with midlatitude cold fronts, and cold season cyclones. A main objective of this study is to investigate the role of ice-phase microphysics on simulated cold-frontal rainbands in the presence of frontogenetical forcing. For this purpose, two-dimensional hydrostatic and nonhydrostatic numerical models with ice-phase microphysical processes included are used, which are initialized with the analytic solutions to the Hoskins-Bretherton horizontal shear model of frontogenesis.

The dry version of the hydrostatic model is a two-dimensional (x, σ) version of the Goddard Mesoscale Atmospheric Simulation System (GMASS), which is a primitive-equation, incompressible, finite difference model with high resolution Blackadar PBL physics and a surface energy balance equation (Kaplan et al. 1982). For moist simulations, prediction equations for water vapor, cloud water, cloud ice, rain water, snow, and graupel are added, and explicit water-ice phase microphysical processes are parameterized following the cloud microphysics module in the Goddard Cumulus Ensemble Model (GCEM) (Tao and Simpson 1989). The hydrostatic water-ice loading effect is included into the hydrostatic equation to allow for the effects of water-ice on buoyancy. The longitudinal (y direction) boundary condition terms are added according to Keyser and Anthes (1982) and Hsie et al. (1984). The longitudinal gradient of water vapor mixing ratio is calculated assuming that the longitudinal gradient of relative humidity is zero on isobaric surfaces (Hsie et al. 1984). This allows for warm, moist advection in the southerly flow and cold, dry advection in the northerly flow. The model has a horizontal resolution of 10 km and 15 layers in the vertical with higher resolution in the lowest layers to represent PBL processes more properly.

Special attention is paid to the computation of terminal velocity for hydrometeors in the hydrostatic model. Since the terminal velocity calculation in mesoscale models follows that in cloud models, the calculated fallspeed sometimes appears to be too large in mesoscale models with weaker vertical motions to take into account the hydrostatic water loading effects (Zhang 1989). The computed mass-weighted mean terminal velocity for rain water, for example, may be large even for low rain mixing ratios (Lin et al. 1983). For this reason, the terminal velocity for any precipitating particle in the present hydrostatic model is represented by

$$V_{TM} = (\Delta x_C / \Delta x_M)^{\beta} \, V_{TC} \ , \qquad (1)$$

where V_{TM} and V_{TC} are terminal velocities in mesoscale and cloud models with corresponding horizontal resolutions of Δx_M and Δx_C, respectively, and β is a non-negative exponent. Although the value of β may be different for each precipitating particle, we presently use the same value of β for rain water, snow, and graupel.

The nonhydrostatic model used for this study is the same as the two-dimensional (x, z) GCEM, which is a primitive-equation, anelastic, finite difference model with explicit water-ice phase microphysics. The Blackadar PBL physics and surface energy balance equation from the GMASS are added to the GCEM. The model has a horizontal resolution of about 2 km and has 30 vertical layers with higher resolution in the lowest layers. This high horizontal resolution will especially enable us to examine details of the narrow cold-frontal rainband, which has a characteristic width of O (1 km) in nature.

The hydrostatic and nonhydrostatic models are both initialized with the same analytic solutions to the Hoskins-Bretherton horizontal shear model of frontogenesis at 60 h based on the semigeostrophic theory (Hoskins and Bretherton 1972; Keyser 1981). The horizontal domain size is equal to the wavelength of the most unstable baroclinic wave and periodic boundary conditions are used. The computed wavelength and phase speed of the baroclinic wave are 3507 km and 14.35 m s^{-1}, respectively. Since we are mainly interested in the development of frontal circulations and their associated rainbands in a convectively stable atmosphere, we initially suppress convective instability by specifying an initial relative humidity of 80% and a high vertical stability of 3.5°K km^{-1}. This results in model initial conditions similar to Knight and Hobbs (1988), but different from Hsie et al. (1984) and Benard et al. (1992a and b). The sensible and latent heat fluxes across the surface can play an important role in the frontal circulations. However, in this study the surface heat fluxes are turned off (insulated lower boundary condition) to interpret model results in a simpler context and make direct comparisons with the previous work along this research line.

Through the extensive intercomparative numerical model experiments, we will address the following issues at the conference.

1. What kind of rainbands do the models produce ?
2. What are the formation mechanisms for the simulated cold-frontal rainbands ?
3. What is the role of ice-phase microphysics on the simulated rainbands and how does the microphysics interact with the circulations arising from CSI ?
4. What are the similarities and differences in the simulated rainbands with the hydrostatic and nonhydrostatic models ?

ACKNOWLEDGMENTS

This research was supported by NASA under RTOP 461-53-51. The computations for this research were performed using the CRAY Y-MP at NASA / Goddard Space Flight Center.

REFERENCES

Benard, P., J.-L. Redelsperger and J.-P. Lafore, 1992a: Nonhydrostatic simulation of frontogenesis in a moist atmosphere. Part I: General description and narrow rainbands. Submitted to J. Atmos. Sci.

_____, J.-P. Lafore and J.-L. Redelsperger, 1992b: Nonhydrostatic simulation of frontogenesis in a moist atmosphere. Part II: Moist potential vorticity budget and wide rainbands. Submitted to J. Atmos. Sci.

Bjerknes, J., 1919: On the structure of moving cyclones. *Geofys. Publ.*, **1**, 1-8.

Browning, K. A., and T. W. Harrold, 1970: Air motion and precipitation growth at a cold front. *Quart. J. Roy. Meteor. Soc.*, **96**, 369-389.

Hoskins, B. J., and F. P. Bretherton, 1972: Atmospheric frontogenesis models: Mathematical formulation and solution. *J. Atmos. Sci.*, **29**, 11-37.

Hsie, E.-Y., R. A. Anthes and D. Keyser, 1984: Numerical simulation of frontogenesis in a moist atmosphere. *J. Atmos. Sci.*, **41**, 2581-2594.

Kaplan, M. L., J. W. Zack, V. C. Wong and J. J. Tuccillo, 1982: Initial results from a mesoscale atmospheric simulation system and comparisons with the AVE-SESAME I data set, *Mon. Wea. Rev.*, **110**, 1564-1590.

Keyser, D., 1981: Frontogenesis in the planetary boundary layer of an amplifying, two-dimensional baroclinic wave. Ph. D. dissertation, The Pennsylvania State University, 285 pp.

_____, and R. A. Anthes, 1982: The influence of planetary boundary layer physics on frontal structure in the Hoskins-Bretherton horizontal shear model. *J. Atmos. Sci.*, **39**, 1783-1802.

Knight, D. J., and P. V. Hobbs, 1988: The mesoscale and microscale structure and organization of clouds and precipitation in midlatitude cyclones. Part XV: A numerical modeling study of frontogenesis and cold-frontal rainbands. *J. Atmos. Sci.*, **45**, 915-930.

Koch, S. E., J. McQueen and V. M. Karyampudi, 1992: A numerical study of the influence of differential sensible heating and momentum mixing on surface frontogenesis. J. Atmos. Sci. (in preparation)

Lin, Y.-L., R. D. Farley and H. D. Orville, 1983: Bulk parameterization of the snow field in a cloud model. *J. Climate Appl. Meteor.*, **22**, 1065-1092.

Mak, M., and P. R. Bannon, 1984: Frontogenesis in a moist semigeostrophic model. *J. Atmos. Sci.*, **41**, 3485-3500.

Parsons, D. B., and P. V. Hobbs, 1983: The mesoscale and microscale structure and organization of clouds and precipitation in midlatitude cyclones XI: Comparisons between observational and theoretical aspects of rainbands. *J. Atmos. Sci.*, **40**, 2377-2397.

Tao, W.-K., and J. Simpson, 1989: Modeling study of a tropical squall-type convective line. *J. Atmos. Sci.*, **46**, 177-202.

Zhang, D.-L., 1989: The effect of parameterized ice microphysics on the simulation of vortex circulation with a mesoscale hydrostatic model. *Tellus*, **41A**, 132-147.

PRECIPITATION BANDS IN THE MESOSCALE VORTICES

Yuichi Miura

Faculty of Science and Technology, Science University of Tokyo
2641 Yamazaki, Noda-city, Chiba 278 Japan

1. INTRODUCTION

It usually observed by the radar that mesoscale vortices generated under the winter monsoon have been constructed by two or three spiral precipitation bands where wind into the center drawing cyclonic curvature. It is suggested that these precipitation bands have brought as a result of organized cumulus convection associated with the vortices, same time, there are release of latent heat and produce a certain wind to maintain the vortices. But we don't know much about what physical processes are existent. Therefore we made the investigation on some physical process for the construction of spiral precipitation bands, released latent heat and produced winds using meteorological observation and remote sensing data such as AMeDAS, radar and satellite.

Mesoscale vortices generated under the winter monsoon have been found a wide range of 20 to 300 km horizontal scale, above all, there are a pick of mountainous distributions at these of 35, 70 and 150 km (Miura and Asai, 1987; Miura, 1990; Miura, 1992). Consequently, we will report formation process of three typical scale of mesoscale vortices viewed from the construction of spiral precipitation bands.

Figure 1 shows a series of mesoscale vortices generated under the winter monsoon over the sea of central Japan Sea and west Hokkaido revealed by the GMS-4 satellite (IR, 15Z 23 January 1990). These vortices are found in a cold air outbreak accompanied convergence zone laid between transverse and longitudinal convective rolls. We shall notice to these vortices on the next chapter.

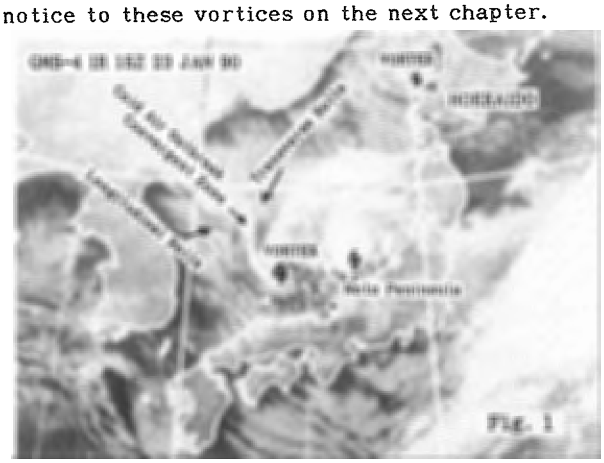

Figure 2 shows surface weather chart made by JMA at 12Z 23 January 1990. We can see what pressure arrangement is possible to find mesoscale vortices generated under the winter monsoon.

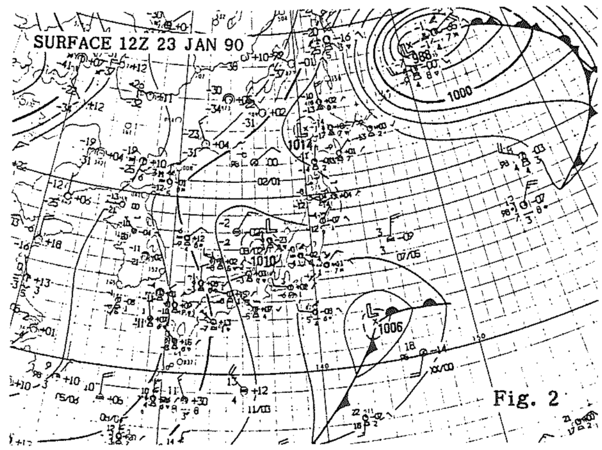

Fig. 2

2.1 PRECIPITATION BANDS OF SMALL-SCALE VORTEX

Figure 3 shows digitalized PPI radar echo for small-scale vortex taken at 12:00 GMT on 22 January 1990 by the Keifu (JMA research vessel) located at 44.11° N and 139.57° E of the Japan sea.

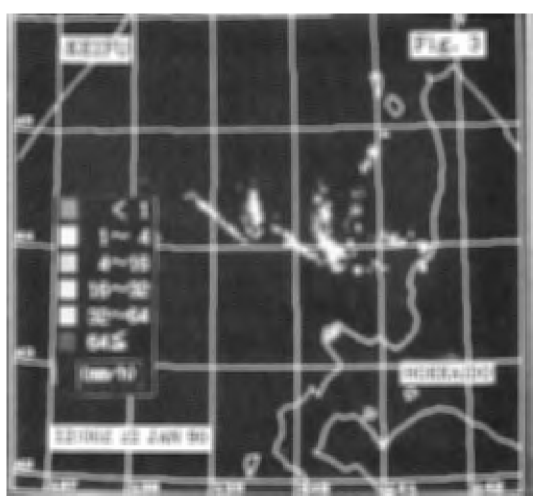

As shown in the figure, these vortices have been formed under the cold air outbreak accompanied with convergence zone by constructing three spiral precipitation bands produced by cumulus.

We can recognize such convergence zone as vortex line in Fig. 3. The reflective intensity for white-plastered spiral precipitation bands equivalent to 1-4 mm/hour and total regime of precipitation bands is $\sim 1\text{x}10^3$ km^2. The diameter of ring-like echo encircled spiral bands is about 20 km.

A characteristic of mesoscale vortices generated under the winter monsoon is realized that the pressure depression amounting to ~1 mb at the center is comparable to one to be expected from the cyclostrophic wind balance between pressure gradient force and centrifugal force (Asai and Miura, 1981; Miura, 1990, 92).

2.2 PRECIPITATION BANDS OF MIDDLE-SCALE VORTEX

Figures 4, 5 and 6 show digitalized PPI radar echoes taken at intervals of 30 minutes from the initial until reach to the mature stage of middle-scale vortex by the Keifu detected at the Japan Sea of west Hokkaido where is the road of cold air outbreak accompanied with convergence zone.

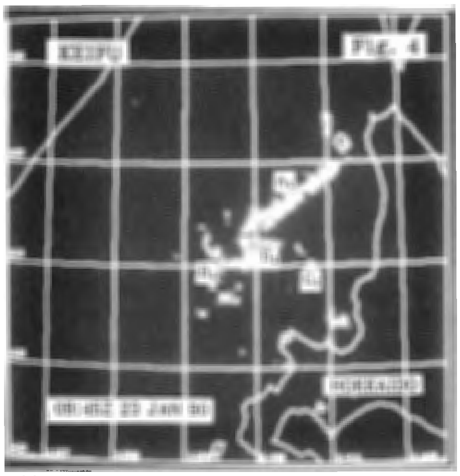

The position and time taken a picture of radar echo for Fig. 4 was at 44.25° N, 139.50° E and 09:45 GMT on 23 January 1990. The diameter of ring-like echo encircled three spiral echoes is about 20-30 km, and then a hour later, it will enlarge about 30-40 km as normal size. As compared Fig. 2 with 4, the domain of spiral echoes with 1-4 mm/h for the early stage of middle-scale vortex is about two times larger than small-scale vortex.

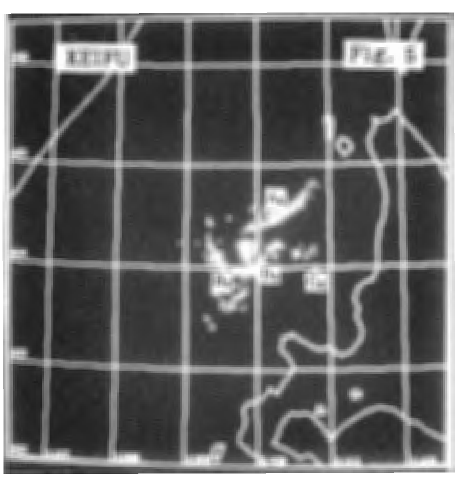

Figure 5 shows same digitalized PPI radar echo as Fig. 4 except taken at 10:15 GMT on 23 January 1990 by the Keifu located at 44.24° N and 139.50° E.

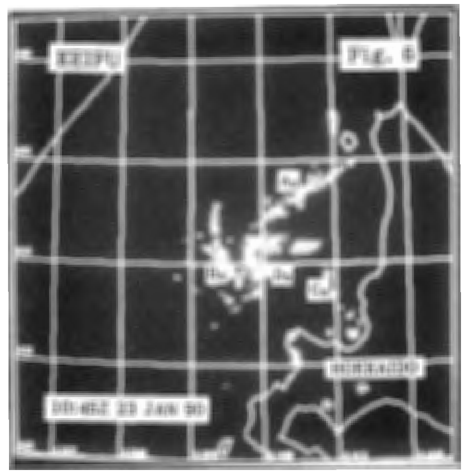

Figure 6 shows same digitalized PPI radar echo as Fig. 4 except taken at 10:45 GMT on 23 January 1990 by the Keifu located at 44.24° N and 139.50° E.

As shown in Figs. 4, 5 and 6, The transformation of echo patterns of three spiral bands in company with the formation of middle class mesoscale vortex is as follows.

First, A line-like cluster echoes A_1 attributed to the cumulus convection increases as much as shown in Fig. 4. Total domain of the echoes corresponding to 1-4mm/h is about $\sim 1\text{x}10^3$ km^2. We will find a lump of echoes D_1 drawing cyclonic curvature between line echo A_1, spiral echo B_1 and C_1. Also line echo, spiral echoes B_1 and C_1 are jointed to a partial ring-like echo together. The line echo shows a shape to be penetrated into convergence zone where is constructed by a convergent air currents carrying strong ascending motion. Above cluster echo D_1 is growing to a ring-like echo.

Second, after 30 minutes, above line echo A_2 decreases in half value of first stage A_1. Spiral echo B_2 and a cluster echoes D_2 increase as much as decrease of the line echo in Fig. 5. A lump of convection D_2 more grow into ring-like echo.

Third, after one hour, spiral echoes B_3 and C_3 increase as much as decrease of a line echo A_1. At same time, partial ring echo grow to be a ring echo. Total precipitation domain slightly increases than first stage in Fig. 6.

As seen in Figs. 4, 5 and 6, spiral echoes A, B and C increase in turn to counter-clockwise, respectively. And ring-like echo has been intensified successively cyclonic curvature increases with cumulus convection increase .

According to the rawinsonde observation data of the Keifu at the same time of radar echoes, the domain of precipitation bands increases with the wind speed around the vortex, for instance, ~8 m/s for small scale vortex and ~12 m/s for middle scale vortex. This is about 4 m/s larger than small scale vortex. The relation of area of precipitation between middle scale and large scale vortices also consist with $\sim 2\text{x}10^3$ and $\sim 4\text{x}10^3$ km^2 and wind speed around vortex is ~16 m/s for large-scale.

The heights of vortices also increase with the area of precipitation and wind speed encircled the vortices, for instance, ~ 2.5 km for small one, ~ 3.5 km for middle one and ~ 4.5 km for large scale vortex (Miura, 1990, 1992).

2.3 PRECIPITATION BANDS OF LARGE-SCALE VORTEX

Figure 7 shows digitalized PPI radar echo for large-scale vortex taken at 11:52 GMT on 09 February 1988 by Fukui (Tojinbo; dark dot in Fig. 1) radar site (JMA) in the Hokuriku district.

Figure 8 shows PPI radar echo same as Fig.7 except taken at 12:52 GMT on February 1988.

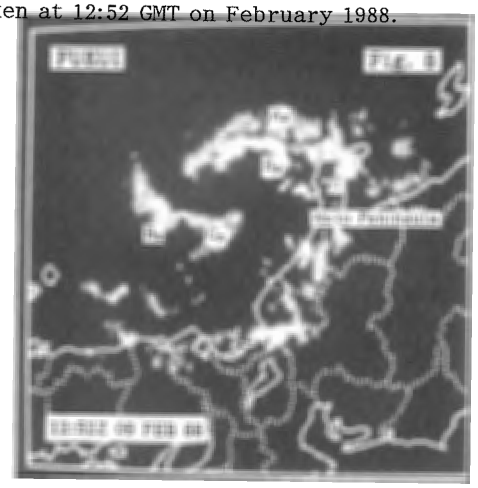

Figs. 7, 8 and 9 show the radar echoes of one hour interval through the formative period of the vortex. Figure 9 shows PPI radar echo same as Fig.7 except taken at 13:52 GMT on February 1988. The intensity of white-plastered radar echoes for the line and spiral bands around vortex equivalent to 1-4 mm/h and total regime of precipitation bands is $\sim 4.5\text{x}10^3$ km^2. The diameter of ring-like echo encircled three spiral band echoes is 60-70 km. The vortex has not formed yet in Fig. 7. The picture shows some traces of precipitation line echoes A_1 due to the longitudinal convective rolls across to the transverse rolls where intersect to the convergence zone B_1. Basically, the formation process attributed to the horizontal shear instability is same as middle-class vortex.

But the construction of echo patterns to form large-scale vortex is slightly different. The transformation of echo patterns of three spiral bands in company with the formation of large class mesoscale vortex is as follows.

First, cluster-like echoes A_1 are gradually concentrated into spiral band, but total area of precipitation for amount of 1-4mm/h around A_1 is not much change through the formative period. The area A_1 is about 2/3 of total precipitation area ($\sim 4.5\text{x}10^3$ km^2) around the vortex. Second, spiral band B_2 in Fig. 8 became two time (2/7) bigger than first stage after a hour passed. It's area is about 1/7 of total precipitation area at the first. And cleared ring-like echo D_2 appear around the vortex. Third, after one hour from the second stage, spiral band C_2 was separated from B_2 and merely intensified in Fig. 9. Both A_2 and B_2 get into the shape of spiral bands to support the vortex rotation. While, spiral band A_3 is intensified again. These alternately intensification of spiral bands will work to increase of cyclonic curvature.

Finally, we will introduce an example of large-scale vortex occurred over the sea of west Hokkaido as like as shown in the small and middle scale vortices.

Figure 10 shows digitalized PPI radar echo for the early stage of large scale vortex taken at 11:15 GMT 25 January 1990 by the Keifu located 44.28° N and 139.49° E of the Japan sea.

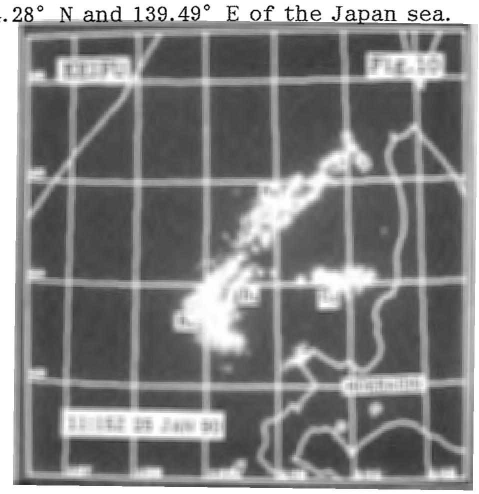

The diameter ring-like echo encircled spiral echoes is 60-70 km.

Fig.11 shows PPI radar echo same as Fig.10 except taken at 12:15 GMT 25 January 1990 by the Keifu located 44.29° N and 139.46° E of Japan Sea.

As seen in Fig.10 and 11, we can see all most same construction patterns in the case of Hokkaido as the case of west Noto peninsula. Through Figs.10 and 11, line band A_1 decreases as much as the value of 5/12 to 3/12 and at the same time, B_1 increases from 5/12 to 7/12. Total amount of precipitation with 1-4mm/h for A_1, B_1, C_1 and D_1 around vortex is 4.3-4.7x10^3 km^2. Also a cluster of dot-like echoes B_1 produced by the convergence zone is arranged into spiral band in order to increase of cyclonic curvature. The case of large scale vortex, spiral band C_1 and C_2 don't appear clearly because the vortex may be occur much approach to the land. At last in this case, we can see alternately intensification of the spiral bands, i.e., the increase of precipitation area. The band structure of the mesoscale vortices are merely different where the vortices occur, but primary structures to form the vortices are same mechanism attributed to the horizontal shear instability.

Note: We wrote that 'As seen in Figs. 4, 5 and 6, spiral echoes A, B and C increase in turn to counter-clockwise, respectively. And ring-like echo has been intensified successively cyclonic curvature increases with cumulus convection increase' in page two of the extend abstract. The mean of 'intensified successively' is not intensity of reflective radar echo. It means increase of the amount of precipitation per unit area.

3. SUMMARY

Structure of the spiral precipitation bands varying with the formation process of the mesoscale vortices has been studied by the remote sensing data of satellite and radar. From the structure and environmental atmosphere of the vortices, it is confirmed that the vortices have been formed where three spiral precipitation bands around vortex are intensified successively into counter-clockwise as cyclonic curvature increases with cumulus convection increase in cold air outbreaks accompanied with convergence zone.

ACKNOWLEDGEMENTS

This work was supported in part by funds from the Cooperative Program (91049) Provided by Ocean Research Institute University of Tokyo.

REFERENCES

1) Asai, T. and Y. Miura, 1981: An analytical study of Meso-scale vortex-like disturbances observed around Wakasa bay area. J. Meteor. Soc. Japan, 59, 832-843.

2) Miura, Y. and T. Asai, 1987: Formation process of the mesoscale vortices generated under the winter monsoon. Proc. of 3rd Conference on Mesoscale Processes, Vancouver, Canada, AMS, 139-140

3) Miura, Y., 1990: Mesoscale vortices generated under the winter monsoon. Proc. of 4th Conference on Mesoscale Processes, Boulder, USA, AMS, 110-111.

4) Miura, Y., 1992: Observed structual characteristics of mesoscale vortices generated under the winter monsoon. Proc. of 5th Conference on Mesoscale Processes, Atlanta, USA, AMS, 137-141.

STRUCTURES OF CONVECTIVE SNOW BANDS AT FORMATION STAGE IN NORTHWEST COAST OF HOKKAIDO, JAPAN

Hiroshi Uyeda, Akio Takemoto, Naonori Osaki*, Katsuhiro Kikuchi

Faculty of Science, Hokkaido University, Sapporo 060 JAPAN
*The Graduate School of Environmental Science, Hokkaido University, Sapporo 060

1 Introduction

Active cloud bands over the Japan-Sea, the so-called Convergent Cloud Band (CCB) by Nagata (1992) and others, produce sometimes heavy snowfalls along the west coast of northern Japan in the winter monsoon season. One of the CCBs which is elongated from the west of Sakhalin southward along the west coast of Hokkaido Island is a significant cloud band, since when the southern tip of it comes into Ishikari Bay and Sapporo with a cyclonic curvature it brings heavy snowfalls (Kobayashi, 1991). Internal structures of narrow cloud bands which merges with the CCB are also interesting to be studied.

Many of the studies on the general features of the CCBs are based on the GMS images. On the other hand, observational studies of snow clouds along the west coast of Japan with radars were made by Sakakibara et al. (1989), Ishihara et al. (1989), Tsuboki et al. (1989), and Shirooka and Uyeda (1990). In their analyses, it was revealed that downdrafts (assumed to be associated with soft hail) in convective snow clouds plays an important role for the development of snow clouds. In many cases, soft hails were observed on the sea coast when snow clouds land and snowflakes follow it. Therefore, types and shapes of snow crystals in snow clouds are very interesting for the understanding of the structure of snow clouds. However few observations with radar on the cloud bands of the formation stage have been carried out.

In order to study the formation mechanism of snow bands and convergence cloud bands along the west coast of Hokkaido, observations were carried out at Rebun Island with dual-linear-polarization Doppler radar.

2 Observational

A map around the observation site Rebun Island is shown in Fig.1. The site is a suitable place to observe the cloud bands in winter monsoon surges without the orographic effects since it is located in the ocean about 60 km apart from the west coast of Hokkaido island. The radar observation range from Rebun Island is known as the area of initiation of long lasting and active cloud bands in winter as suggested by Kobayashi(1991) and others.

Internal structures of convective snow clouds were observed with a dual-linear-polarization Doppler radar (λ= 3.2 cm, ϕ=1.2 m). The specification of the radar is on the paper by Uyeda et al. (1991). Rawinsonde data and surface weather data were corrected at the radar site. Satellite data of GMS and NOAA and rawinsonde by Japan Meteorological Agency at Wakkanai were utilized in the analyses.

In order to obtain a two dimensional wind field in a vertical cross section of radar echo, wind components across the plane are ignored and integrations of vertical winds are made from the lowest height. The method used to calculate the values of Z_{DR} is the same as that of Uyeda et al. (1991). Radar reflectivity of PPI used was slightly weakend by MTI ground clutter canceler.

3 Results

During the period from 21 to 28 January several types of cloud bands were observed in the radar observation range (r=60km). A time-height cross section of wind and equivalent potential temperature at Wakkanai from 21 to 28 January 1991 is shown in Fig.2. The observation site was covered by a cold air mass twice during the period. Three cases of snow bands were analyzed; The periods of analyses are shown by the arrows in Fig.2. On 23 January and 28 January significant convergent cloud bands were observed. From 25 to 26 January, stratiform snow clouds and narrow cloud bands were observed at the

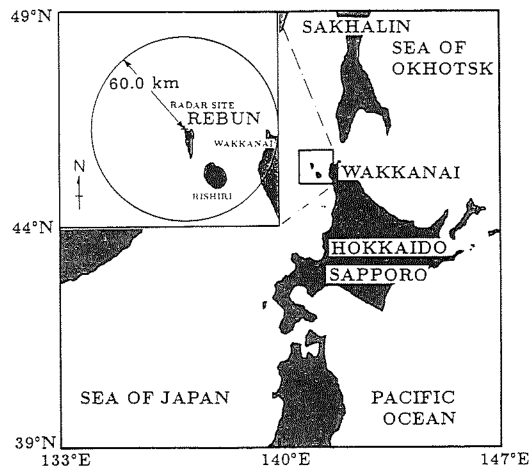

Fig.1 Map around Rebun Island, Hokkaido. The inset shows an expanded view of radar observation randge (r=60 km).

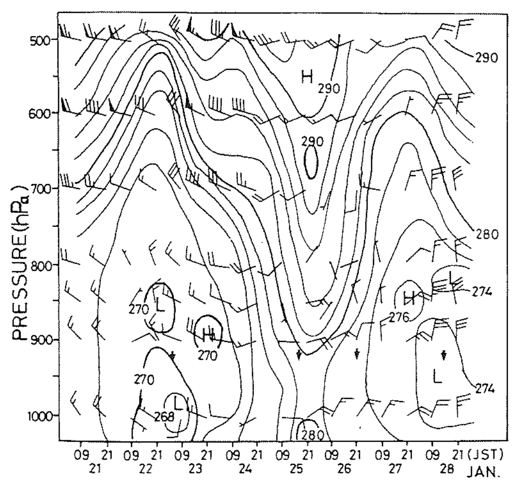

Fig.2 Time-height cross section of equivalent potential temperature and winds derived from serial rawinsondes launched from Wakkanai from 21 to 28 January 1991. The interval of the isotherms is 1 K. A half barb, a full barb and a flg indicate 2.5, 5 and 25 m/s respectively.

radar site. The differences of internal structures between the two clouds were analyzed by a dual-linear-polarization Doppler radar.

3.1 Structures and evolution of the CCB of 23 January 1991

Echo evolution and movement at about one hour intervals from 20 JST 22 January 1991 are shown in Fig.3. From 21 JST, linear echoes extending from north-northwest(NNW) to south-southeast(SSW) moved toward the radar site. Around 0030 JST a strong echo passed the radar site. Around 00 JST 23 January, bending of the echo became prominent. After 02 JST, the echo extending from NNE to SSW was weakened and receded to the east. However the echo intensity was enhanced again around 7 JST. The infrared imagery of NOAA/AVHRR (Fig. 4) shows the signatures of convergence cloud band.

Time sequence of vertical cross sections perpendicular to the approaching echoes are shown in Fig.5. Arrows show winds calculated assuming two dimensionarity on the plane. The solid line on the echo in each frame indicates the boundary between the westerly and easterly. The easterly at the lower altitude implies cold outflow from the east. The surface temperature at the radar site decreased about $1°C$ after the passage of the head of the easterly winds with the shift of wind direction from northwesterly to northeasterly. However the wind speed of the northeasterly behind the head was a few meters per second smaller than that of general northwesterly (7 m/s in average). Ahead of the echo movement, strong updrafts were analyzed and downdrafts were analyzed behind the enhanced echo elevated up to 2.5 km in altitude.

In the sounding (not shown) at Rebun at 2000 JST 22 January before the approach of the CCB, below 600 m it was stable and unstable layers formed were from 600 to 1,100 m and from 1,300 to 1800 m. Propagation speed U of gravity current is calculated to be 6 m/s by taking the values of measured temperatures drop of 1 K, the depth of the layer (1000 m) and Fr=1 into consideration. The observed propagation speed of the cloud band coincided well with the calulated value of U; This supports a possibility of a gravity current.

As shown in Fig.6, when a very strong echo covered the observation site, soft hails were observed and rimed snowflakes were observed when echoes were weakened.

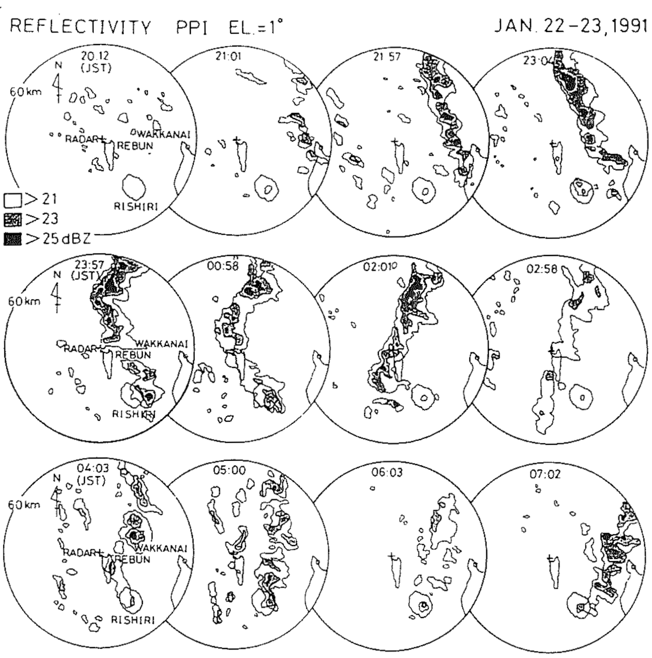

Fig.3 Time sequence of the PPI radar echo patterns.

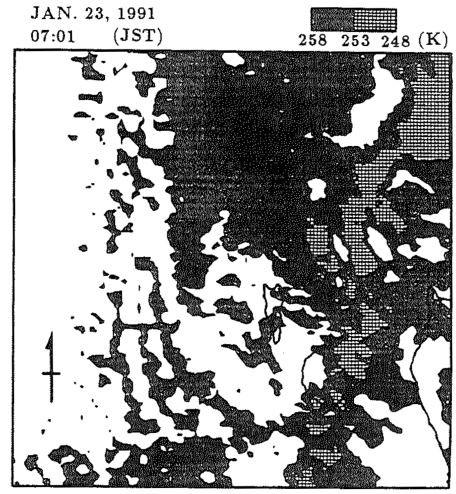

Fig.4 Infrared NOAA/AVHRR imagery of brightness temperature below 258 K at 0701 JST 23 January 1991.

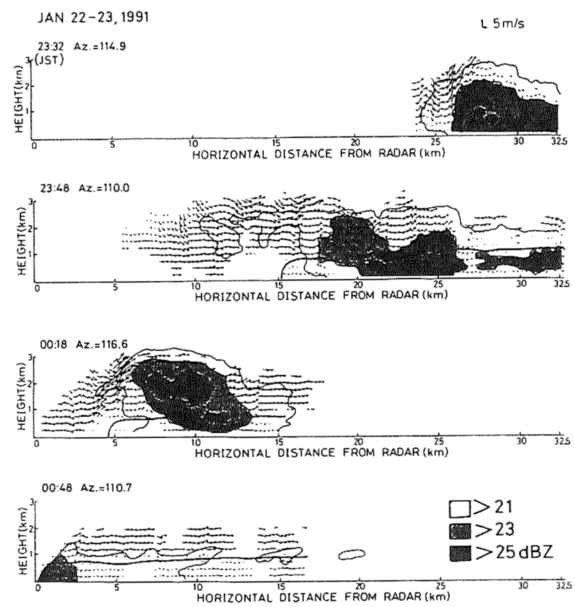

Fig.5 Vertical cross sections of radar reflectivity and wind field in the direction (azimuth is about 110° perpendicular to the convergence cloud band. Boundary between easterly and westerly is drawn by a thick solid line.

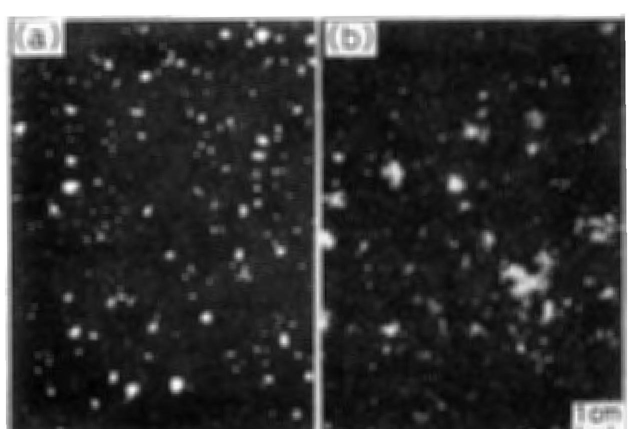

Fig.6 Examples of snow particles collection on a board with a black velvet cloth on 23 January 1991. (a) soft hails at 0033 JST, (b) snowflakes at 0215 JST.

3.2 Comparison of internal structures of snow cloud

The differences of internal structures of narrow cloud bands (21 JST 26 January) and stratiform clouds (14 JST 25 January) are compared. Vertical structures of a narrow cloud band (in Fig. 7) were analyzed. Fig. 8 shows a vertical cross section of the echo along the solid line in Fig.7. The reflectivity of Fig. 8 is the value of Z_{HH} and is not passed the filter of the canceler of ground clutter.

Two regions are named as Cell A (from 17 to 20 km in the distance from the radar site) and Cell B (from 21 to 24 km). In the cell A, reflectivity is rather large and the updraft is strong. At the altitude higher than 1 km, the value of Z_{DR} is large up to 2.0 dB and below 1 km the value is small close to 0 dB. In the rear of the cell A, the value of Z_{DR} is small and somwhat negative where a weak downdraft prevails. Here soft hails are expected. In cell B, reflectivity is not large and the updraft is weak.

For the comparison, the vertical cross section of stratiform snow clouds on 25 January is shown in Fig. 9. Reflectivity is small and the values of Z_{DR} are large in average. Whole range from 10 to 25 km from the radar site is named Cell C for convenience.

Vertical characteristics of the internal structure of the cells A and B in Fig.8 and the cell C in Fig.9 are summarized in Table 1. Reflectivity Z_{HH}, differential reflectivity factor Z_{DR}, divergence and vertical wind speed, at each grid of 250m x 250m, are averaged for three vertical layers; below 500m (LOWER), from 500 to 1000 m (MIDDLE) and higher than 1000 m (UPPER). In the active convective cell A, convergence is large (7.7 x $10^{-4}s^{-1}$) in the lower altitude and divergence is large in the upper part of the snow cloud as expected in general. The value of Z_{DR} is small and variation of Z_{DR} in height is very small in average; It implies that by the strong updraft, snow crystals of forming stage is mixed vertically, though a region of large Z_{DR} is clearly seen in Fig.8.

In the weak convective cell B, small divergence in the lowest layer and convergence in the upper layer are analyzed. The values of Z_{DR} are larger in the upper layer and smaller in the lower layer. This implies that the particles in the lower layer are densely rimed snow crystals or soft hails having a shape close to sphere.

In stratiform snow clouds the values of Z_{DR} are larger than 1 dB through the layer; Major snow particles here are considered to be plates, dendrites or snow flakes with flat shapes. Temperatures in the upper layer are around $-15°C$ and minus a few degrees Celsius in the lower layer.

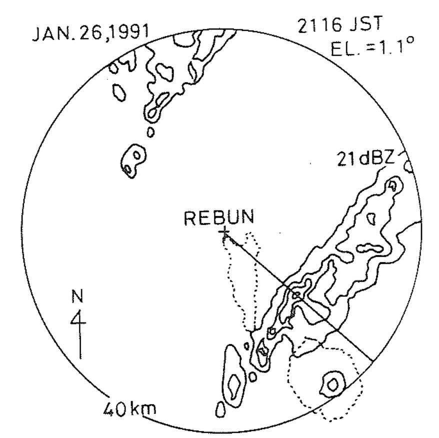

Fig.7 Radar reflectivity PPI display at the elevation angle of 1.1° at 2116 JST 26 January 1991. The range of 40 km is shown. The line is the direction of RHI scan in Fig. 8.

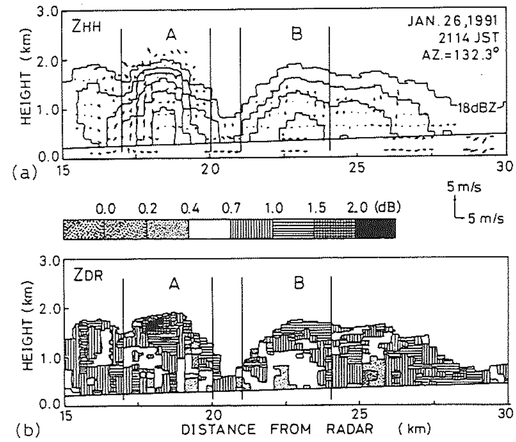

Fig.8 Vertical cross section of (a) radar reflectivity and (b) differential reflectivity factor at 2114 JST 26 January 1991 at the azimuth of 132.3° on Fig.7. Two dimensional winds are superposed on the figure. Analysis regions of cells A and B are shown by vertical solid lines.

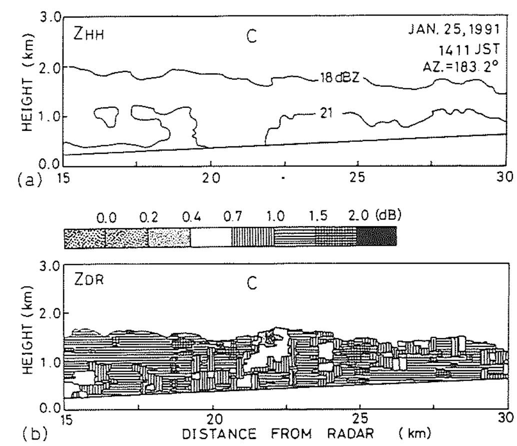

Fig.9 Vertical cross section of (a) radar reflectivity and (b) differential reflectivity factor at 1411 JST 25 January 1991. Two dimensional winds are superposed on the figure. Whole region of the figure is analyzed as cell C.

Table 1 Reflectivity, differential reflectivity factor Z_{DR}, divergence (one dimensional: 250 m in horizontal length) and vertical velocity of cells A, B and C at three different altitudes. Numbers of each frame at the top is averaged values in the area and that at the bottom in parentheses is standard deviation of the value in the area.

CELL	LAYER	REFLECTIVITY (dBZ)	Z_{DR} (dB)	DIVERGENCE (x $10^{-4} s^{-1}$)	VERTICAL VEL. (m/s)
A	UPPER	24.2 (4.07)	0.91 (0.31)	1.98 (13.6)	0.55 (0.83)
	MIDDLE <1000m	28.1 (3.78)	0.68 (0.31)	0.65 (7.42)	0.63 (0.99)
	LOWER <500m	29.7 (3.30)	0.71 (0.29)	−7.66 (12.3)	0.56 (0.72)
B	UPPER	22.0 (1.75)	0.87 (0.20)	−1.20 (4.58)	−0.21 (0.74)
	MIDDLE <1000m	24.0 (3.00)	0.68 (0.15)	2.38 (10.2)	−0.12 (0.51)
	LOWER <500m	25.7 (2.57)	0.54 (0.21)	0.49 (5.33)	0.02 (0.24)
C	UPPER	19.7 (0.60)	1.13 (0.32)	−2.46 (5.08)	0.13 (0.26)
	MIDDLE <1000m	20.9 (0.68)	1.10 (0.23)	−0.83 (3.12)	0.05 (0.20)
	LOWER <500m	21.5 (0.88)	1.08 (0.22)	−0.49 (4.22)	0.01 (0.10)

3.3 Structures of the CCB of 28 January 1991

Infrared NOAA/AVHRR imagery of brightness temperature below 258 K at 0646 JST 28 January 1991 is shown in Fig.10. Northern tip of a prominent convergence cloud band, extending for several hundred kilometers from north to south, passed over the radar site. Corresponding PPI radar echo at the elevation angle of 1.0° is shown in Fig.11. These two figures coincide well in the major cloud bands extending from north-northeast to south-southwest. This indicates that in most convective snow clouds, the cloud is prominent tall and has strong snowfalls.

However in the narrow cloud bands extending from north west to the radar site, even if TBB is low and the cloud top is high, strong snowfalls are not necessarily expected, since the radar reflectivity is not necessarily large there.

In the strong echo cells of snow band, major precipitation is estimated to be soft hails and plate, dendrite and their snowflakes are expected around them, taking into consideration Fig.10 and 11 and vertical structures of Z_{DR} by Uyeda et al. (1991) for the case of 28 January.

4 Concluding remarks

General features of snow clouds in narrow cloud bands and convergence cloud bands are summarized as follows. The radar echo heights were less than 3 km, as in the case of winter storms in this region. The value of Z_{DR} is small where the reflectivity

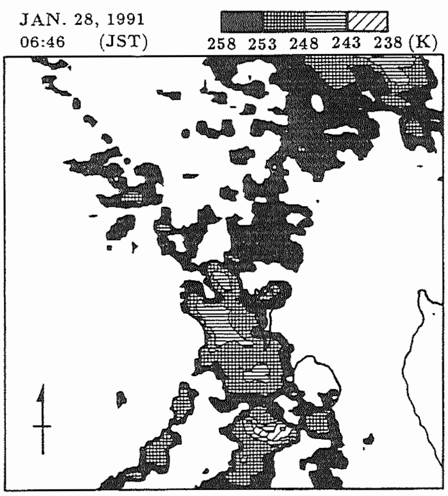

Fig.10 Infrared NOAA/AVHRR imagery of brightness temperature below 258 K at 0646 JST 28 January 1991.

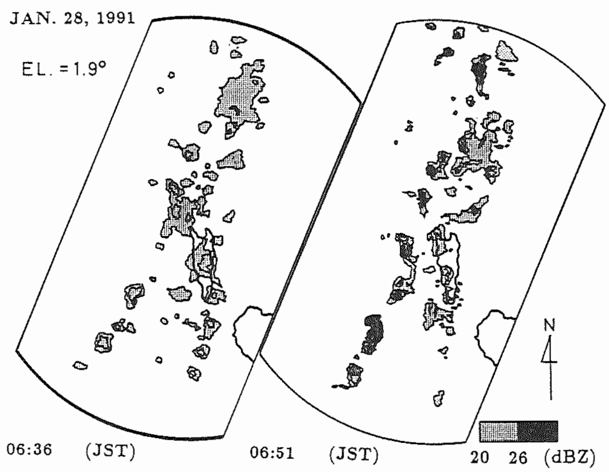

Fig.11 Radar reflectivity PPI displays at the elevation angle of 1.9° at 0636 and 0651 JST 28 January 1991. Radar reflectivity larger than 20 dBZ is shown by shades.

is large and Z_{DR} is large at the top of the echoes where reflectivity is small. The major precipitations are considered to be dendrites or plates and snowflakes of them in the region of large differential reflectivity factor Z_{DR} (1-2 dB). Soft hails are estimated in the region of small Z_{DR} about 0. This distribution of the types of precipitations were confirmed by surface observation of precipitation types. The region of small Z_{DR} coincided with the head of the updrafts. Rapid formation of graupel in the lower altitude, drift of precipitations to the rear of northeasterly and downdraft with the soft hails are considered to make the life of the convective snow clouds very short.

The width of convergent cloud bands were narrow for about 10 to 20 km in the PPI radar echo. The narrow bands composed of convective cells were formed in the horizontal convergence region of this northeasterly wind and northwesterly general wind. Northeasterly winds below 500 m were confirmed by the VAD analysis (not shown in this paper), RHI velocity fields and rawinsonde data.

For the formation of convergent cloud band, northeasterly or easterly gravity current or cold outflow with the depth of 500 m is essential in the westerly winter monsoon surges. Strong updraft at the convergence zone of cloud bands produce rapid evolution of convective snow clouds. The life of the clouds are from 30 to 60 minutes, though the cloud band itself lasts several hours. Though downdraft by soft hail loading leads the clouds to the dissipating stage, movement of outflow forward or supply of cold air flow maintain continuous formation of the strong updrafts ahead of the old echo cells.

Acknowledgements. The authors express their thanks to N. Takahashi and the students of Meteorological Laboratory, Hokkaido University for their assistance in the observation, to the Rebun Town Hall for their cooperation and providing of installations and facilities, and to Japan Meteorological Agency for permission of using meteorological Data. NOAA data were recorded by the Research Center for Atmospheric and Oceanic Variations, Tohoku University. The expense of this study was supported by the Grant-in Aid for Scientific Research of the Ministry of Educa- tion, Science and Culture of Japan. This study was partly sup- ported by Research Development Fund of Foundation of River and Basin Integrated Communication, Japan.

References

[1] Ishihara, M., H. Sakakibara and Z. Yanagisawa, 1989: Doppler radar analysis of the structure of mesoscale snow bands developed between the winter monsoon and the land breeze. *J. Meteor. Soc. Japan*, **67**, 503-519. Meteor. Soc. Japan, 67, 503-519.

[2] Kobayashi, F., 1991: Observational and analytical studies on the convergence band clouds occurring along the west coast of Hokkaido, Japan. *Hokkaido Univ.*, pp. 131. (Doctor's thesis).

[3] Nagata, M., 1992: Modeling Case Study of the Japan-Sea Convergent Cloud Band in a varying large-scale environment: Evolution and upscale effect. *J. Meteor. Soc. Japan*, **70**, 649-671.

[4] Sakakibara, H., M. Ishihara and Z. Yanagisawa, 1988: Squall line like convective snowbands over the Sea of Japan. *J. Meteor. Soc. Japan*, **66**, 973-953.

[5] Shirooka, R. and H. Uyeda, 1990: Morphological structure of snowburst in the winter monsoon surges. *J. Meteor. Soc. Japan*, **68**, 677-686.

[6] Tsuboki, K., Y. Fujiyoshi and G. Wakahama, 1989: Doppler radar observation of convergence band cloud formed on the west coast of Hokkaido Island. II: Cold front type. *J. Meteor. Soc. Japan*, **67**, 985-999.

[7] Uyeda, H., R. Shirooka, K. Iwanami, A. Takemoto, K. Kikuchi, G. Yoshida and M. Okazaki, 1991: Observation of vertical structures of convective snow clouds with a dual-polarization radar in Hokkaido, Japan. *Preprint 25th Intern. Conf. on Radar Meteor., Paris France, American Meteor. Soc.*, 717-719.

Dual Doppler Radar Observation of Convergence Band Cloud

Shinsuke Satoh[1], Yasushi Fujiyoshi[2], Gorow Wakahama[1], Ryuichi Shirooka[3] and Hiroshi Uyeda[3]

[1]Institute of Low Temperature Science, Hokkaido University, Sapporo, Japan
[2]Water Research Institute, Nagoya University, Nagoya, Japan
[3]Department of Geophysics, Hokkaido University, Sapporo, Japan

1.Introduction

Convergence band clouds often form on the west coast of Hokkaido Island of Japan during cold air outbreaks from the Eurasia Continent, and are known to bring heavy snowfall locally. It has been recognized that convergence band clouds develop on the shear front between the north-westerly winter monsoon and the easterly land breeze. Fujiyoshi et al.(1988) and Tsuboki et al.(1989) have examined the structure of the convergence band cloud using a Doppler radar. They have described that the land breeze is a few hundred meters deep, and is relatively colder and dryer than the monsoon. The shear front is dynamically similar to a gravity current.

Similar cloud bands are found in several places. Over Lake Michigan, shore line parallel bands are observed (Passarelli and Braham, 1981; Braham, 1983; Schoenberger, 1984). In the western Hokuriku district of Japan, Ishihara et al.(1989) have investigated the structure of snow bands using a Doppler radar. In these studies, however, the detail of the structure was only obtained in a two-dimensional (vertical) section, since a single Doppler radar was used.

The purpose of this study is to determine the three-dimensional kinematic structure of the convergence band cloud from dual-Doppler radar measurements and to clarify the mechanism of concentrated snowfall in the shear front region.

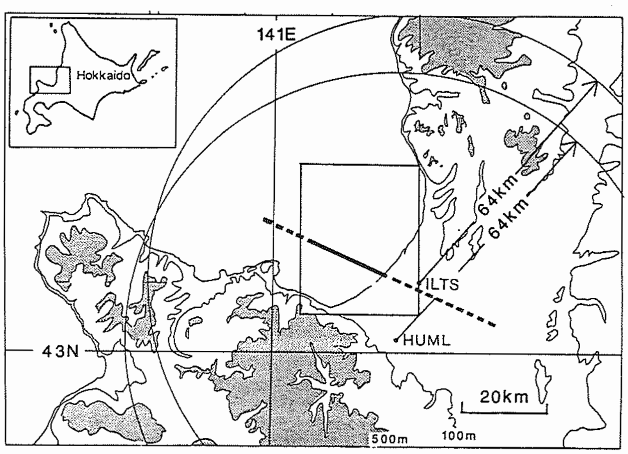

Fig. 1. Locations of dual Doppler radar analysis domain (rectangle) and vertical cross sections (heavy solid line and dashed line).

2.Observation and data processing

Observations of a convergence band cloud above Ishikari Bay in Hokkaido were carried out on 23 January 1990. The band cloud shifted eastward and accompanied a retracting land breeze. The band cloud was a typical warm frontal type, which was classified by Fujiyoshi et al.(1987).

The Institute of Low Temperature Science (ILTS) 3cm Doppler radar and the Hokkaido University Meteorological Laboratory (HUML) 3cm Doppler radar were used for the measurement. Fig.1 shows the location of these radars and an analysis domain. The principal method for dual-Doppler data processing introduced by Armiji(1969) was used. Determining w field from the horizontal divergence integration, the downward scheme was adopted according to the result by Ray et al.(1980).

3.Kinematic structure

Fig.2a shows reflectivity contours and stream lines in a horizontal plane at height 0.25km. To the west of an about 20km wide (defined by 29dbZ contour) band echo which lies almost north-south, are some line echoes about 5km wide, which are oriented in the direction of north-westerly or north-north-westerly flow. The line echoes are associated with convective rolls along the monsoon flow. They merge into the band echo. The north-westerly flow and easterly flow converge forming a shear front with flow southward. Before and behind the front, the extent of the air stream changed its direction is 3-5 km long. At the south of the front, a small vortex is formed by the horizontal shear. A horizontal convergence region at the front is shown in Fig.2b. There are three cores of convergence with peaks values of $5*10^{-4}$ s^{-1}. The location of these cores coincide with the merging place. These cores can be identified as convective cells as they have a high-reflectivity at the upper

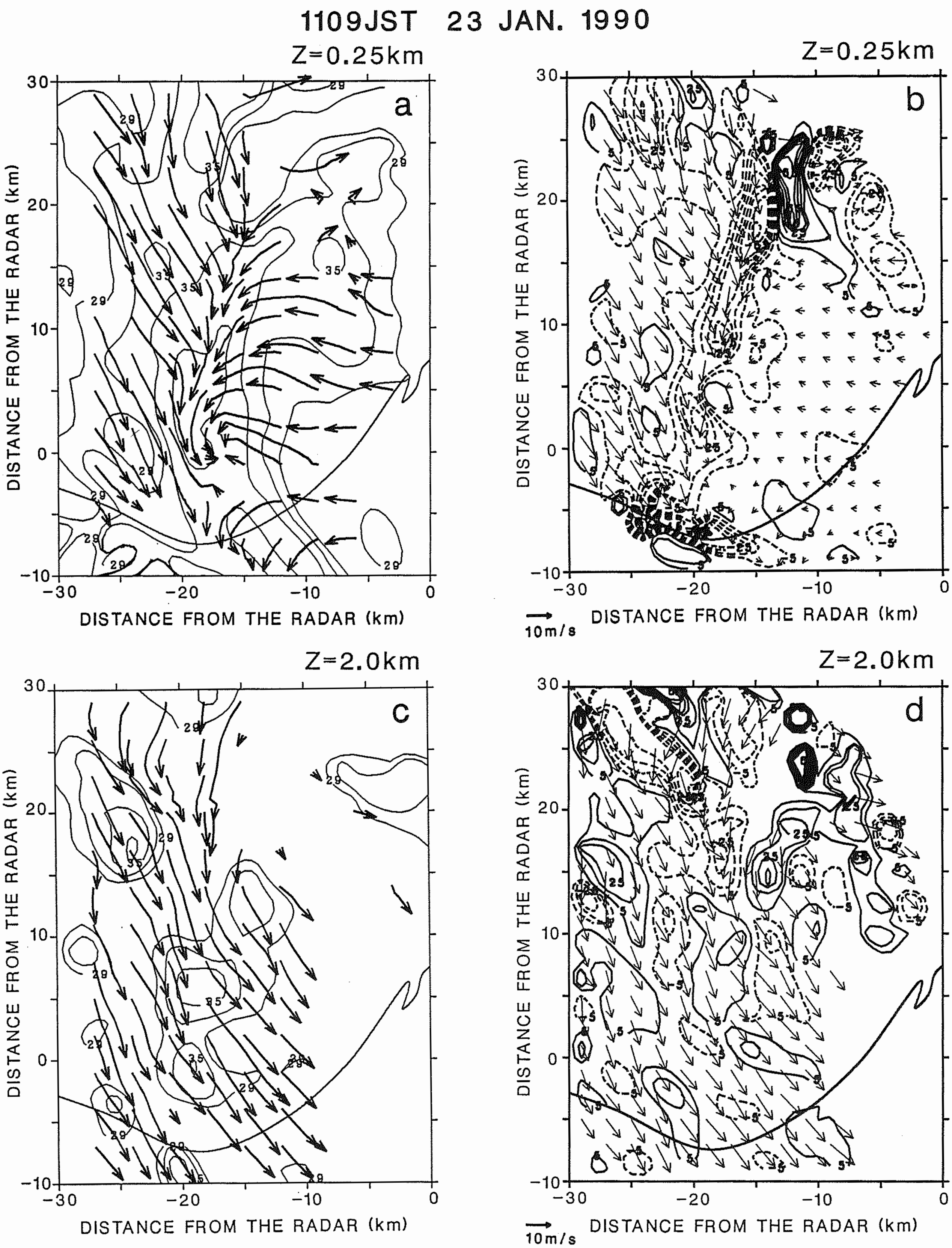

Fig. 2. Horizontal cross section of (a)(c) reflectivity contours and stream lines, (b)(d) divergence contours and wind field at height 0.25, 2.0km respectively. The divergence contour interval is $1*10^{-4}\ s^{-1}$ with negative value dashed.

level (Fig.2c). At height 2.0km, the air stream curves from the northward to the south-eastward in Fig.2c. This air stream is almost coincident with the shape of the convergence band cloud. Superimposed on this flow are alternate regions of divergence and convergence, as shown in Fig.2d. This distribution is not relate to the shape of the band cloud. The each location of divergence and convergence is independent of the cell in the band echo. Since the distribution of divergence or convergence lies in line along the monsoon flow, it suggests an internal gravity wave excited by convective cells in the line echoes.

Fig.3 displays a vertical cross section transverse to the front. The easterly land breeze is about 0.5km deep, as shown in Fig.3a; the monsoon flow climbs above the land breeze. The updraft and downdraft regions appear in about 10km wavelength, and the maximum vertical velocity is over the front, as shown in Fig.3b. The horizontal convergence at the surface is also a maximum on the front, as shown in Fig.3c. These aspect relative to the front will remain with time passes, since the large convergence by the shear front maintains the circulation. Fig.3a also shows two cells; the one is stands erect, the other is tilted downstream. The erect cell is evolving depend on updraft, while the tilted cell is further decaying caused by downdraft (see Fig.4).

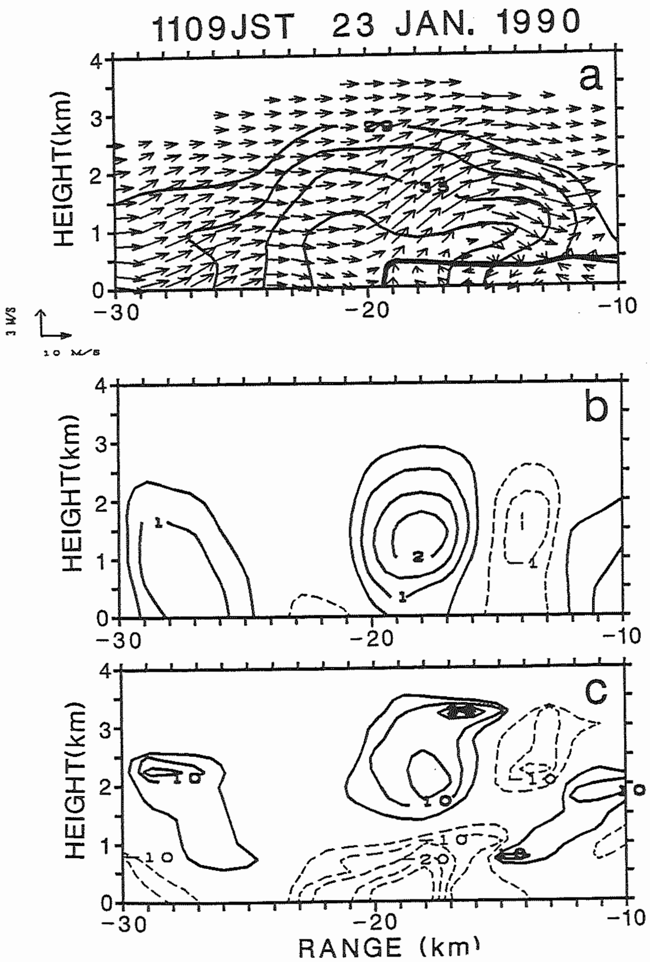

Fig. 3. Vertical cross section of (a) reflectivity contours (dbZ) and wind field, (b) vertical velocity (ms^{-1}), (c) divergence contours ($*10^{-5}$ s^{-1}). The thick line indicates the depth of the land breeze.

4.Mechanism of concentrated snowfall

According to the time series of the vertical cross section of radar reflectivity (Fig.4), we found that the velocity relative to the ground

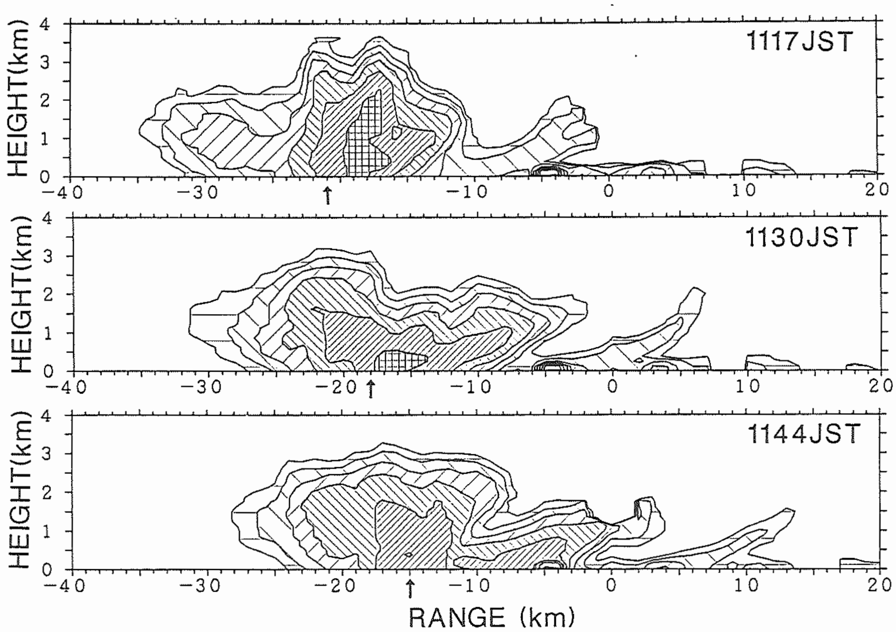

Fig. 4. Time series of vertical cross sections of reflectivity contours at 18, 21, 24, 27, 30 and 33dbZ at 1117JST, 1130JST and 1144JST. Arrows indicate the location of the front.

of the front is 1.9 m s^{-1} and that of the cell top is 9.8 m s^{-1}. In consequence of the difference of the velocity, convective cells pass over the front successively. When a cell approaches the front, it evolves rapidly and brings snowfall, that is mainly composed of graupel and densely rimed crystal with large fallspeeds. Due to the shear between the monsoon and the land breeze, the convective cell located on the east side of the front tilts eastwards. There is little convection in this cell, and so the already formed snowfall, composed of snowflakes with small fallspeeds, is swept back towards the front by the land breeze. At the same time, another convective cell has moved over the front. This leads to a persistent heavy snowfall in the frontal region.

Furthermore, since the land breeze is cold and unsaturated, some of snow particles from the decaying cell will evaporate, so that the land breeze is cooled by the release of a latent heat. The larger difference in the air temperature between the monsoon and the land breeze will lead to a strengthening the front.

5.conclusion

A kinematic structure of a convergence band cloud is revealed by using dual-Doppler radar. A convergence region at the lowest level along the shear front between north-westerly monsoon and easterly land breeze is a main cause of the band cloud development. There are three cores of convergence in the convergence region. These are a result of line echoes, which parallel the monsoon flow, merge into the band echo. Over these cores, there are developing convective cells. A band echo, that consists of some convective cells, is 20-30km wide. However an extent of a air stream changed by the shear front is no more than 3-5km long before and behind the front. While, at the upper level, there are alternate regions of divergence and convergence, suggesting an internal gravity wave excited by convective cells in the line echoes.

A mechanism of concentrated snowfall in the shear front region is represented by the following. Since a line echo cell moves south-eastwards faster than the front, it reaches the front. And it evolves rapidly and brings snowfall there. At the east side of the front, the cell decays and the already formed snow particles are swept back towards the front by the land breeze. Furthermore, snow particles from the decaying cell will evaporate in the land breeze, so that the land breeze cooling will lead to a strengthening the front.

Reference

Armijo, L., 1969: A theory for the determination of wind and precipitation velocities with Doppler radars. J.Atmos.Sci., **26**, 570-573.

Braham,R.R.,Jr., 1983: The midwest snow storm of 8-11 December 1977. Mon.Wea.Rev., **111**, 253-272.

Fujiyoshi,Y., K.,Tsuboki, H.,Konishi and G.,Wakahama, 1988: Doppler radar observation of convergence band cloud formed on the west coast of Hokkaido Island (1): warm frontal type. Tenki, **35**, 427-439(in Japanese).

Ishihara,M., H.,Sakakibara and Z.,Yanagisawa, 1989: Doppler radar analysis of the Structure of mesoscale snow bands developed between the winter monsoon and the land breeze. J.Meteor.Soc.Japan, **67**, 503-520.

Passarelli,R.,E.,Jr. and R.R.Braham,Jr., 1981: The role of the winter land breeze in the formation of Great Lake snow storms. Bull.Amer.Meteor.Soc., **62**, 428-491.

Ray,P.S.,C.L.Ziegler,W.Bumgarner and R.J.Serafin, 1980: Single- and multiple-Doppler radar observations of tornadic storms. Mon.Wea.Rev., **108**, 1607-1625.

Schoenberger, L.M., 1984: Doppler radar observation of a land-breeze cold front. Mon.Wea.Rev., **112**, 2455-2464.

Tsuboki,K., Y.,Fujiyoshi and G.,Wakahama, 1989: Doppler radar observation of convergence band cloud formed on the west coast of Hokkaido Island (2): cold frontal type. J.Meteor.Soc.Japan,**67**, 985-999.

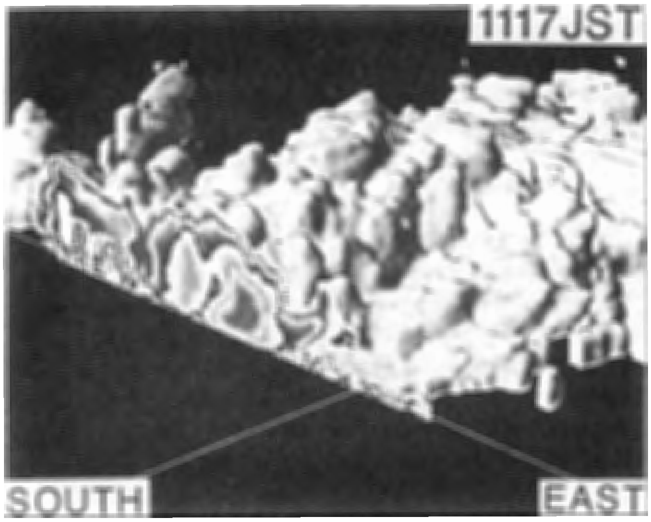

Fig. 5. Three-dimensional display of radar echoes with a vertical cross section. The surface is specified by 15dbZ.

Precipitation Band Structure in the Front Range Blizzard of March 5-7, 1990

Greg J. Stossmeister and Roy M. Rasmussen

National Center for Atmospheric Research* Boulder,
Colorado 80307

1. Introduction

The March 5-7 Blizzard of 1990 was responsible for snow accumulations between 12 and 30 inches in a corridor between Denver, Colorado and Cheyenne, Wyoming extending eastward from the foothills about 30 km. On the plains to the east of this area, only rain was observed. Along the foothills, strong northerly winds developed in response to the strong easterly flow over the plains (Parrish, 1982, Schwerdtfeger, 1975). Surface winds as high as 25 ms^{-1} created drifts as high as 7 feet around the Boulder area and buried more than a hundred cars on U.S. 36 between Boulder and Denver. In this paper we will examine the evolution of the storm from a radar perspective and attempt to determine the focusing mechanisms for heavy snow along the Front Range.

2. Dataset

This paper will present data collected during the Winter Icing and Storms program (WISP) (see figure 1 for project area). The first field season of WISP took place between February 1 and March 31, 1990 (see Rasmussen, et al, 1992). This project employed numerous measurement platforms including, PAM mesonet stations, PROFS mesonet stations, CLASS soundings, 2 Doppler radars, aircraft, profilers, radiometers, and others in the pursuit of an improved understanding of the production and depletion of supercooled liquid water in winter storms. The project also has the goal of improving forecasts of aircraft icing in winter storms.

3. Storm overview

The storm was categorized by a 500 mb cutoff low, whose center was skirting the southern border of Colorado on the morning of March 6. This pattern brought deep upslope flow to Northeast Colorado with easterly winds extending up to 250 hPa. This low moved very slowly eastward, bringing precipitation to Northeast Colorado for a period of approximately 36 hours.At the surface, a low developed in East-Central Colorado of 994 hPa. This helped to focus the low-level upslope flow at the Front Range. The moisture availability in Northeast Colorado was high with dewpoints near and above 0 C, making the potential high for heavy precipitation.

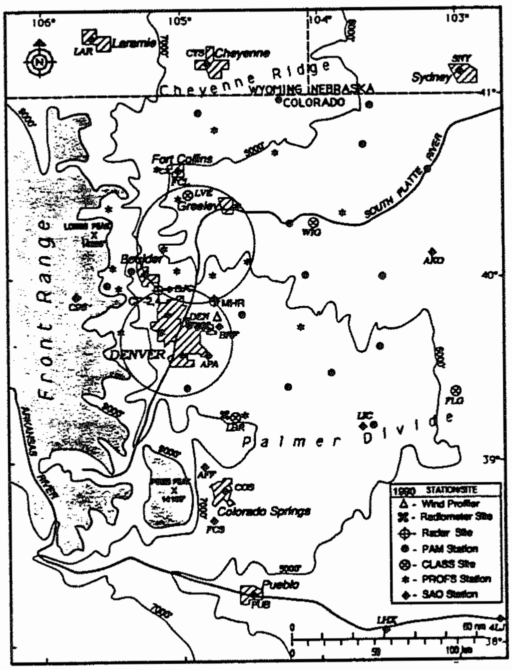

Fig. 1 The WISP 90 project area. Elevation contours are every 2000 ft. The approximate dual-Doppler lobes for CP3 and MHR are shown by the circles.

4. Observations

After the field season a radar movie was put together from the 0.5° elevation scans for this storm, covering the period: 02 UT/6th - 11 UT/7th. The following observations are the result of a detailed study of the movie. It is apparent that there are distinct phases during the storm between which the character and intensity of the precipitation change. These different phases will be discussed below and will be followed by a more detailed discussion of one of them.

Phase 1

This phase begins with the start of precipitation along the Front Range around 02 - 03 UT on the 6th. It is characterized by widespread stratiform precipitation containing

---

* The National Center for Atmospheric Research is supported by the National Science Foundation.

large areas with reflectivity greater than 40 dBz. The movement of these echoes was from south to north, while the surface winds were generally southeasterly at 10-15 ms^{-1}. Two hours prior to this time, a N-S boundary developed along the foothills and began moving east (Maurwitz and Day, 1991). At 03 UT, this boundary is just east of Denver and extends south towards the Palmer Divide. West of this boundary, winds are calm to light westerly. Northerlies are not present at this time but do begin to develop around 04 UT.

Phase 2

After 10 UT on the 6th the stratiform precipitation becomes less widespread and a separate N-S band of precipitation develops 90 km east of Denver. The band is at least 200km in length and moving to the north. The stratiform precipitation is closer to the Front Range at this time and is moving toward the northwest. At the surface, northerly winds are present along the Front Range. The boundary between the northerlies and easterlies has changed its orientation from N-S to NW-SE. This could be due to a weaker easterly component south of Denver. To the north of Denver, the boundary remains along the 5000 ft contour as the opposing easterlies are strong. Surface temperatures in the northerlies and along the south side of the Cheyenne Ridge have now dropped to near 0 C (See Maurwitz and Day, 1991 for a discussion of the melting processes leading to the observed cooling).

Phase 3

After 1530 UT on the 6th a WNW-ESE line of convective cells develops just south of Denver. Over the next 2 hours this band rotates to a N-S orientation over Denver. As the band moves across the boundary between the northerly and easterly flow, it intensifies and increases in areal coverage. As it continues to move westward, its intensity decreases. At this time, the easterly surface flow has become northeasterly and continues to blow at 10-15 ms^{-1}. The northerlies are of similar strength.

Phase 4

By 1730 UT on the 6th, a dry slot has wrapped in to 80 km east of Denver. At this time, convection is developing along the northern and western edges of this region with maximum reflectivities in some of the cells near 50 dBz. Convective cells are also apparent trailing the northern edge of the band discussed in the previous phase. Cloud top temperatures determined from GOES infrared imagery are in the -30 to -35 C range for the convective clouds. An 18 UT CLASS sounding shows this temperature range to correspond to a top near 7.5 km MSL (5.0 km AGL). These convective cells all move westward at an approximate speed of 16 ms^{-1}. They also appear to intensify when they reach the boundary, although the increase in areal coverage doesn't occur until they are nearly 20 km west of the boundary. The surface flow remains at this time northeasterly over the plains, northerly near the foothills.

Phase 5

By 04 Ut on the 7th, surface pressures have generally risen 10 hPa in northeast Colorado since 1730 UT. Weaker convective cells are moving westward and developing into bands as they near the boundary. The surface winds are generally from the north everywhere (except for near the Palmer Divide) with the winds east of the boundary containing a small easterly component.

By 0930 UT on the 7th, the storm is pretty much over for the Front Range. Small areas of low reflectivity drift slowly southwestward. Surface winds are generally northerly and temperatures have fallen another 3 - 4 C since 04 UT.

Some common features occurred throughout most of the phases described above. Some bands were observed to form in place (frequently west of the boundary) while others were the result of an interaction between a convective cell(s) and the boundary. Some bands were persistent over the foothills for several hours while others moved quickly across. Some of the bands reached their maximum linear extent as they reached the boundary while others were 20 km beyond it. Aspects of the boundary and the development of the northerly flow behind it are discussed in Maurwitz and Day, 1991, and Maurwitz, et al 1992.

5. Phase 4 - A Closer Look

Phase 4 is a time of particular interest for studying the interaction between the convection and the boundary separating the northerly flow from the easterlies. The northerly flow is called a Barrier Jet and is thought to be the result of blocking of a statically stable flow with a component perpendicular to a barrier (Parrish, 1982; Schwerdtfeger, 1975). In this case, the barrier is the Front Range and the flow is the easterlies. The boundary actually slopes westward with height over the barrier flow as the easterlies overrun the barrier jet.

The convection that develops near the edges of the dry slot begins to reach the boundary just after 19 UT on the 6th. Figure 2 shows the mesonet winds for 1920 UT.

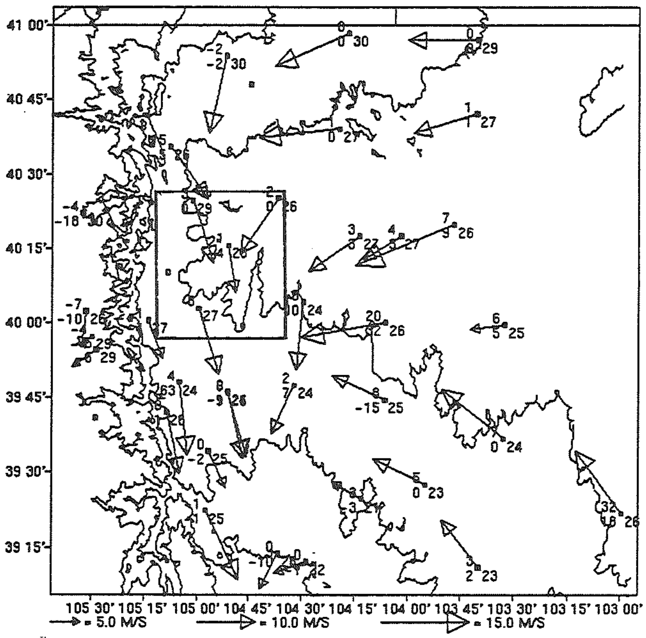

Fig. 2. Mesonet data from both PAM and PROFS networks at 1920 UT on 6 March 1990. Elevation contours are at 1000 ft intervals with 4000 ft contour in the upper right. Station model is temperature (C) top left, dewpoint (C) bottom left, pressure minus 900 (hPa) bottom right (corrected to 1600 m). Box denotes region of dual-Doppler analysis.

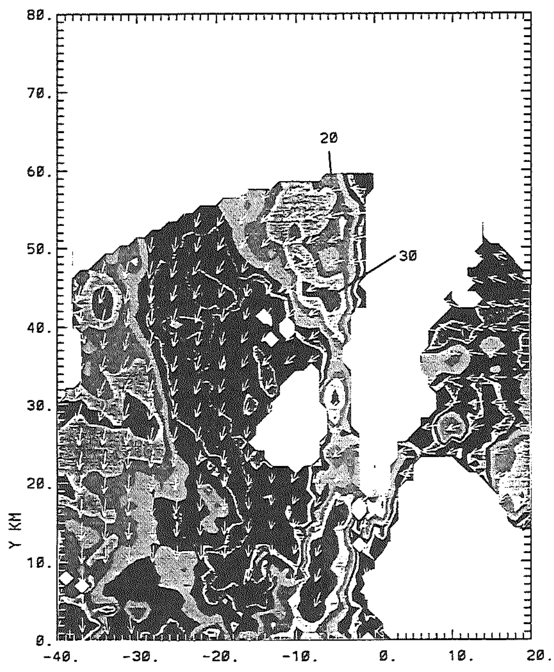

Fig. 3. Reflectivity and horizontal wind vectors at 0.5 km AGL from dual-Doppler analysis. Center time of volume is 1915 UT 6 March 1990. Scale of wind vectors is 10 ms^{-1} per km. Coordinates are km relative to Mile High Radar (MHR).

A dual-Doppler analysis was performed at this time in the region shown by the box. Figure 3 depicts a horizontal slice of reflectivity and horizontal wind vectors at 0.5 km AGL. These data show a line containing several convective elements almost coincident with the boundary at this time. Notice that the winds turn from easterly to northerly in a very short distance at 0.5 km AGL. The strongest northerlies at this level are found along the western side of the box and are blowing at 20 - 30 ms^{-1}. The foothills begin their abrupt rise approximately 3 km west of this box at 0 km north and are at the edge of the box by approximately 38 km north.

The northerly flow is shallow, being less than 1 km deep, as shown by figure 4. As was suggested by figure 3 the strongest northerlies occur at the lowest level above the ground and closest to the foothills. The depth of the northerly flow also decreases to the east.

An E-W cross-section through the reflectivity core at 44 km north is shown in figure 5. The structure of this convective element is similar at first glance to summertime convection. The slope of the core is approximately 45°. GOES visible imagery at this time shows an overshooting top, while at the ground several observers are reporting heavy snow with the predominant crystal type being graupel ranging in size from 1-10 mm. Curiously, the updraft is

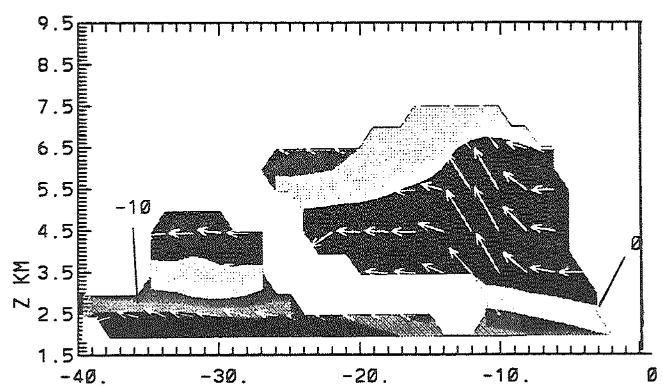

Fig. 4. East west cross-section of v-component in the X-Z plane. Note vertical scale exaggeration, 1 km in vertical equals 3 km in horizontal. Y = 44 km.

downwind from the reflectivity core. Figure 6 shows the vertical velocity field and the relative air motion in the X-Z plane. The updraft is aligned vertically which would

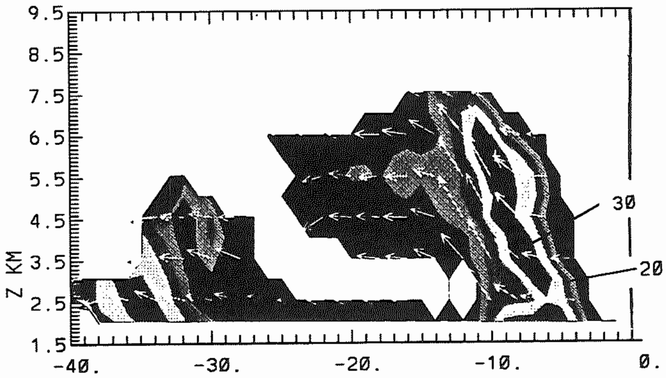

Fig. 5. East west cross-section of reflectivity and velocity in the X-Z plane (U + W, W component is multiplied by 10 to improve visibility). Y= 44 km.

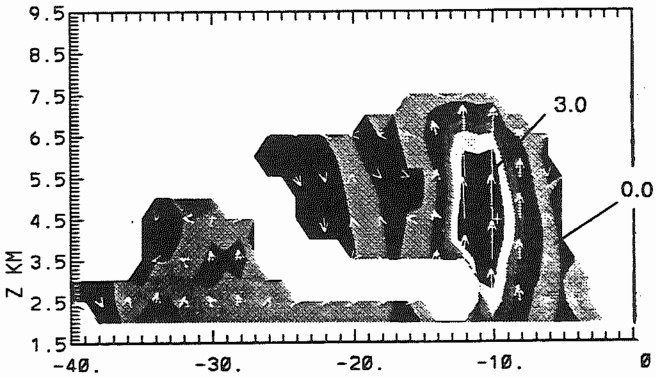

Fig. 6. East west cross-section of vertical velocity in the X-Z plane, superimposed with vectors of relative U compo nent plus W.(W component is multiplied by 10 to improve visibility). Y= 44 km.

be expected from the shear profile, which is unidirectional and nearly constant in speed with height. The interesting thing is that the slope of the reflectivity core cannot be explained by simply taking into account storm relative horizontal motion and the fall speed of the particles. It may be that the slope of the reflectivity core is changing as the convection encounters the boundary.

6. Conclusions

Detailed study from a radar movie of this case show that this storm could be categorized into 5 different phases between which the precipitation structure and intensity change. It is also evident that the dry slot played an important role in this storm by triggering convection which moved westward and interacted with the Barrier Jet. Precipitation along the foothills was enhanced by this interaction over what would have been obtained by the overrunning of the Barrier jet alone. Further research will center on examination of the convection prior to its encounter with the Barrier Jet boundary.

REFERENCES

Maurwitz, J. and D. Day, 1991: The effect of melting on a Denver snow dump. *Proceedings, First International Symposium on Winter Storms*, New Orleans, La., p. 241-244.

Parrish, T. R., 1982: Barrier winds along the Sierra Nevada Mountains. *J. Appl. Meteor.*, **21**, 925-930.

Rasmussen, R., M. Politovich, j. Maurwitz, W. Sand, J. McGinley, J. Smart, R. Pielke, S. Rutledge, D. Wesley, G. Stossmeister, B. Bernstein, K. Elmore, N. Powell, E. Westwater, B. Stankov, and D. Burrows, 1992: Winter icing and storms project (WISP). *Bull. Amer. Meteor. Soc.*, in press.

Schwerdtfeger, W., 1975: The effect of the Antarctic Peninsula on the temperature regime of the Weddell Sea. *Mon. Wea. Rev.*, **103**, 45-51.

NUMERICAL STUDIES OF THE DYNAMICS AND CLOUD MICROPHYSICS OF THE FRONTAL RAINBANDS

A.M. Pirnach

Ukrainian Hydrometeorological Research Institute,
Kiev, Ukraine

1. INTRODUCTION

Three-dimensional numerical models of atmospheric front were constructed to study the dynamical and microphysical structure of the frontal bands in the winter frontal cloud systems.

The above bands were examined considesing 1) the feature of the cloud formation process and evolution of cloudness and precipitation in bands allocated in different regions of the various frontal systems, 2) the relationship of the bands to the fronts, 3) the relationship of the bands to the surface pressure field, 4) the air motion associated with the frontal cloud systems, 5) the interaction of the dynamical and microphysical processes in frontal cloud bands.

2. DESCRIPTION OF THE MODEL

The formation and development in space and time of clouds and rainbands in the frontal zones are simulated by integration of the following set of primitive equations:

$$\frac{\partial u}{\partial x} + \frac{\partial v}{\partial y} + \frac{\partial w}{\partial z} = 0, \qquad (1)$$

$$p = \rho RT, \qquad (2)$$

$$\frac{\partial s_i}{\partial t} + u\frac{\partial s_i}{\partial x} + v\frac{\partial s_i}{\partial y} + w_i\frac{\partial s_i}{\partial z} = F_i + K_x\frac{\partial^2 s_i}{\partial x^2} + K_y\frac{\partial^2 s_i}{\partial y^2} + K_z\frac{\partial^2 s_i}{\partial z^2}, \qquad (3)$$

$$i = 1,2,\ldots,7,$$

$$(s_1,s_2,\ldots,s_7) = (u,v,w,q,T,f_1,f_2), \qquad (4)$$

$$(w_1,w_2,\ldots,w_7) = (w,w,w,w,w-v_1,w-v_2), \qquad (5)$$

$$F_1 = lv - \rho^{-1}\frac{\partial p}{\partial x}, \qquad (6)$$

$$F_2 = -lu - \rho^{-1}\frac{\partial p}{\partial y}, \qquad (7)$$

$$F_3 = -\rho^{-1}\frac{\partial p}{\partial z} - g, \qquad (8)$$

$$F_4 = -\mathcal{E}_1 - \mathcal{E}_2, \qquad (9)$$

$$F_5 = \alpha_1\mathcal{E}_1 + \alpha_2\mathcal{E}_2 - \gamma_a w, \qquad (10)$$

$$F_6 = \frac{\partial f_1 r_{1k}}{\partial r} + I_a - I_f, \qquad (11)$$

$$F_7 = -\frac{\partial f_2 r_{2k}}{\partial r} + I_s + I_f \qquad (12)$$

There is an assumption that a coordinate system itself is moving and its velicity is u_f. u_f is horisontal velocity of a front at $t=0$.

x,y,z,r,t are respectively horisontal coordinates perpendicular and parallel to a front, height above sea level, cloud particle size and time.

u,v,w are wind components in the x,y,z direction respectively.

The other symbole defined as follows:

- T,P air temperature, air pressure
- ρ,q air density, specific humidity
- f_i size distribution of drops ($i=1$) and ice particles ($i=2$)
- v_i terminal velocity of drops ($i=1$) and ice particles ($i=2$)
- $\mathcal{E}_i$ rate of the change of r due to condensation or evaporation
- I_a,I_s sources of the origin of drops and ice particles, respectively (Ref.3)
- I_f freezing rate of drops (Ref.3)
- α_i, l, g,R,γ_a,K_x,K_y,K_z constants (Ref.3)

Two metods were used to compute the initial data: 1) the time-independent three-dimensional theoretical models of the frontal systems (Ref.3), 2) the serial rawin-sonde data were used to construct the three-dimensional models of the frontal systems passing over the area (Refs.2,5).

A complete description of model is given in Ref.3 and the solution schemes of nonsteady differential Egs. 1-12 were given in Ref.3.

3. RESULTS OF NUMERICAL EXPERIMENTS

The present paper provided a brief review of our current understanding of mesascale rainbands in theoretical atmospheric fronts and fronts passing under Ukraine, which were study with aid numerical modeles.

Numerical integration of the model equations has been carried out and analysed for many frontal situations associated with warm, cold and occluded fronts.

There were found that vertical motion, high gradient temperature, cloud and precipitation which develops along the front exhibits a bands structure.

At warm fronts were found three types of rainbands: 1) occur ahead front, 2) coincides with the ground front line, 3) lag behind it (Refs.2, 4,6).

In case study of the cold front were indentified four bands: two bands were situated in warm air; a rainband straddle the surface cold front or lag behind it; a postfrontal rainbands (Ref. 6).

It partially agree with Ref.1. The mesoscale less 30 km there were not considered.

In present paper the modeling studies have focused on occluded frontal system. In the interest of space, only one case will be discussed at length here. The analysis is based on the results obtained with numerical model described above in section 2.

The vertical cross-section through the occluded frontal system on 11 junuary at 09 MST, 1976 were used to construct of the initial distribution. This frontal system was embeded in a westerly upper-level flow and passed over Ukraine on 11-12 junuary 1976. A broad zone of precipitation and cloudiness was encom passing it. It more detail discription is given in Ref.5.

The evolution of the dynamics and cloud microphysics of three rainbands in an occluded frontal system were examined by numerical simulation. Its presented in Fig. 1-2, Tabl. 1-2. Two of the rainbands occured in the leading portion of the frontal cloud shield and were oriented parallel to the warm front. The third band occured in the trailling portion of the cloud shield and had cold frontal orientation.

Table 1. Change in spase and time of pressure (P-700 mb) in both cases, with (1) and without cloudiness (2). z = 2.7 km.

y (100 km)	No	x (100 km): 1	2	3	4	4.5	5	6	7	8	9.5
						t= 12h					
	1	13	17	20	12	11	12	15	9	5	17
12	2	13	17	19	12	11	12	15	9	4	17
	1	14	19	21	13	12	13	15	8	3	17
9	2	14	19	22	14	13	13	14	9	4	17
	1	16	21	23	16	14	15	17	10	5	18
6	2	16	21	24	16	15	15	17	11	6	18
						t= 24h					
	1	12	16	17	11	10	13	16	10	7	18
12	2	12	17	18	10	8	11	14	9	5	16
	1	10	15	18	11	9	8	10	5	1	17
9	2	11	17	18	10	9	9	12	8	4	16
	1	12	17	19	11	10	8	9	5	3	20
6	2	14	18	20	13	11	10	13	8	5	18

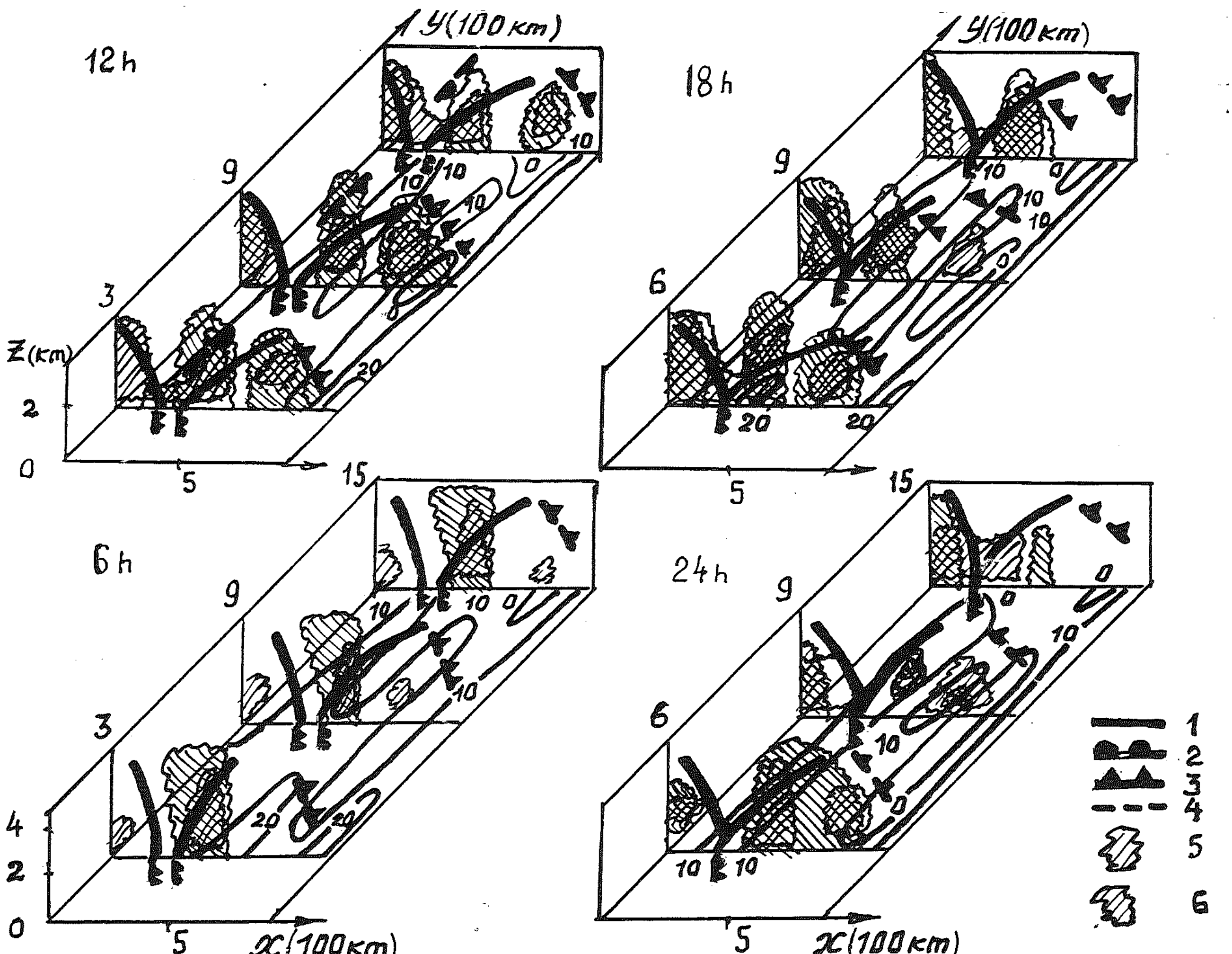

Figure 1. Three dimensional structure of cloud frontal system at various t. 1) P 1000mb, 2) warm front, 3) cold front, 4) HBZ, 5) liquid-water cloud, 6) ice cloud.

Table 2. Evolution of cloud microstructure. q_1) water content, N_2) ice consentration,-) cloudless

t (h)	y (100 km)	z (km)	x(100 km) 1	2	3	4	4.5	5	6	7	8
			q_1 $(10^{-2}$g/kg)								
6	12	1.8	3	-	-	19	41	0	-	-	1
	6		8	-	-	24	40	-	-	18	39
18	12	1.2	-	-	3	24	6	-	0	12	18
	6		20	-	1	30	46	-	-	14	20
			$N_2(g^{-1})$								
6	12		1	0	0	0	11	0	0	0	-
	6	3.6	6	0	0	3	13	-	0	8	13
18	12		2	-	1	6	1	-	-	-	-
	6	3.0	9	0	0	1	3	-	-	-	-

The temperature field feature has a wave-like structure. A few lines of the high temperature gradients occured in the frontal system: warm front, cold front, cold HBZ, warm HBZ. HBZ is zone with relatively large baroclinicity, so called hyperbaroclinic zone. In during time with its were associated the high vertical motion bands, the high ice and water content bands, precipitation bands.

The initial pressure distribution was included two trough and two peak in the pressure field.

The cold front and cold HBZ favoured the development of the closed regions of the low pressure. The warm front and warm HBZ favoured the development of the closed redions of the high pressure. In during time prefrontal trough of low pressure was transformed into the closed regions of low pressure. Prefrontal peak of pressure was trasformed into the closed region of the high pressure. Mesoscale pressure feature were parallel to the rainbands (Fig.1, Tabl.1).

The maximum values water and ice content were associated with regions of low pressure (Tabl.2). Maximum water content were found at x= 450 km in middle frontal band. It exited for many hours. Two either bands were less stability.

The pattern of vertical air motions in rainbands reveals that deep updrafts were associated with the precipitation shafts shown in Fig.2. There was found three stable peak updraft bands. In initial period of time (t≤18h)

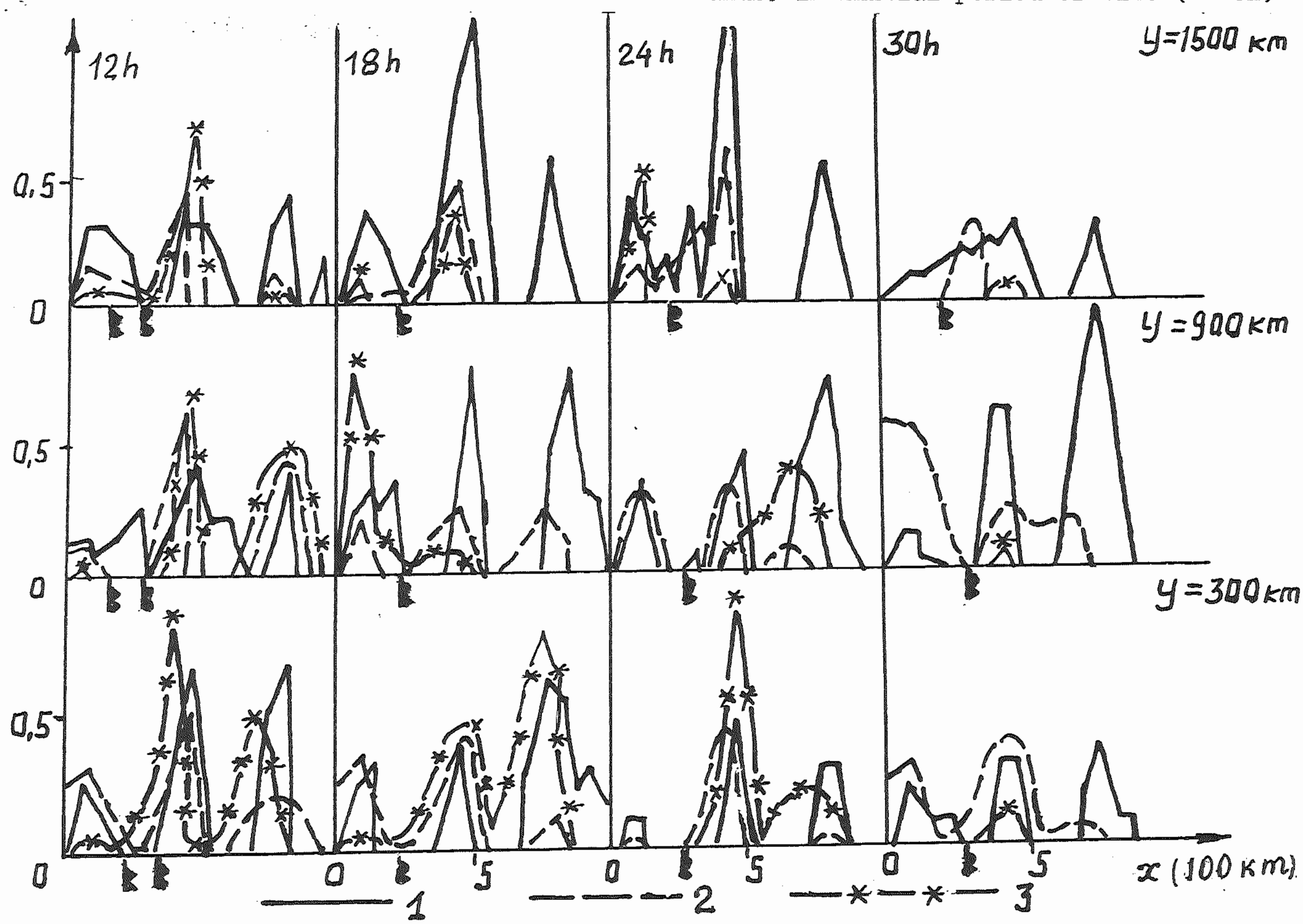

Figure 2. Distribution of vertical motion, water content and precipitation rate at various t. 1) z-maximum w, 2) z-maximum water content q_1, 3) precipitation rate.

the maximum vertical motion and precipitation were associated with middle rainband (warm-frontal rainband).

In the begining the warm-frontal band arise with the large area cloudiness produced by wide spread lifting associated with the warm frontal surface. There were maximal values of water content in "feeder" zone and maximal values of ice concentration in "seeder" zone (Tabl.2). Evidence that in many cases precipitation rate associated with this rainband are enhanced due to "seeding" from above by ice particles (Ref.1).

The dynamic, cloud microphysic and precipitation of the band were oscillated in space and time.

After 18 h development, when the cold and warm fronts approached the rainband associated with the cold front (cold-frontal band) exetended and reached a steady-state. Precipitation and microstructure feature in it increased. This rainband reached about 100km wide. At $t \geqslant 18$h main sources of moisture with $\Delta_2 \leq 0.25$g/kg and $q_1 \leq 0.5$g/kg were accumulated behing the cold front. Δ_2- ice supersuturation. The cloudiness exited for many hours.

The prefrontal rainband was associated with cold HBZ which was allocated in cold air ahead warm front. This band were the most nonstable in time. The period oscillations of dynamic and microstructure feature was most short that the both warm and cold front rainbands. Evidence the both high gradients temperature and pressure were is main cause of the short-period oscilations.

The free-cloud atmosphere was simulated by condition $f_i(t)=0$. δs_i noted the difference between cloud and free-cloud values of s_i.

It is noted that at x=450 km in the band of the stable condensation the cloudiness was intensifying ascending motion. In prefrontal nonstable cloud band at x=700 km where condensation processes were often changing to the evaporation the ascending motion in the cloud were found to be weakening most.

The period of oscillation w in both cases cloudinnes and cloudless atmosphere was different from each other. The greatest value of δw may be explained by coincidence of both the maximum and minimum of w in time or space.

The maximum cloudiness effect on temperature were found at $450 \leq x \leq 500$km and $800 \leq x \leq 900$km in bands of the maximum water content. There is $\delta T > 0$ relationship. The cloudiness effect on temperature T was $-1 \leq \delta T \leq 3^{\circ}$; mainly $\delta T > 0$ relationship was found as the effect of condensation was more intensive. The cloud effect pressure was $-4 \leq \delta P \leq 2$. The time and space oscilations of $\delta w, \delta u, \delta P, \delta T$ were found.

4. CONCLUSIONS

Three-dimensional time-dependent models of atmospheric fronts were constructed.

Modeling studies for the evolution of rainbands associated with warm, cold and occluded fronts indicated, that every frontal system may to include a few rainbands. At warm and cold fronts the most steady-state bands with mixed clouds and high precipitation rate associated with warm front and warm hyperbaroclinic zones. At occluded front its associated in different period time development with warm-frontal rainband and postfrontal band.

The dynamics, cloud microphysics and precipitations of the frontal cloud bands may oscillate in the time and space. The period and amplitudes of these oscillations were found to depend on a type of front, model parameters and on the location of bands in frontal system.

The cloudiness may both intensity and weaken the dynamics feature in the cloud and in the near cloud enviroment in dependence on the phase of the cloud.

REFERENCE

1. Houze R.A. jr. and Hobbs P.V. Organization and structure of precipitation cloud system, 1982. Advance in Geophysics, v.24,53p.

2. Palamarchuk L.V.,Pirnach A.M. Study of the atmospheric front structure with aid semiempirical three-dimensional models, 1992. Trudy of Ukrainian Res. Ins.,N_0 243.

3. Pirnach A.M. Numerical simulation of the frontal cloud involves dynamical and microphysical processes (three-dimensional model), 1987. Trudy of Ukrainian Res. Ins., N_0 221,71-82.

4. Pirnach A.M. Numerical simulation of the cloud and precipitation bands in atmospheric fronts, 1988. Meteorology and Hydrology, N_0 8, 20-32.

5. Pirnach A.M., Palamarchuk L.V., 1988. Numerical simulation of the interaction of dynamical and microphysical processes in frontal cloud. Proc. the All-Union seminar,Kiev, 22-25 April, 1985, 54-61.

6. Pirnach A.M. Numerical simulation of the evolution of frontal rainbands, 1991. Proc. the All-Union conf. active influence on meteorological processes. Kiev, November, 1987, 313-317.

Raindrop formation in Hawaiian rainbands

Robert M. Rauber[1], Kenneth V. Beard[1,2], Harry T. Ochs III[2], and L. Jay Miller[3]

[1]Department of Atmospheric Sciences, University of Illinois, Urbana, IL, USA 61081
[2]Illinois State Water Survey, Office of Cloud and Precipitation Research, Champaign, IL, USA 68820
[3]National Center for Atmospheric Research, Boulder CO, USA 80307

1. INTRODUCTION

Raindrops with diameters exceeding 4 mm are common in thunderstorms where drops form from melting ice particles, but, until recently, have not been observed in clouds whose summit temperatures are warmer than 0°C (e.g. Blanchard, 1953; Bringi et al., 1984). The existence of giant raindrops (4-8 mm) in warm convective clouds was first confirmed in shallow convective rainbands off the coast of Hawaii in 1985 (Beard et al., 1986). More recently the presence of giant drops in warm convection over the southeast U.S. was inferred from differential reflectivity radar measurements (Illingworth, 1988). These observations were quite surprising, since model and laboratory results support the view that collisional breakup rapidly destroys larger drops in natural clouds and generally limits drop diameters to a maximum of about 2.5 mm (List and Gillespie, 1976; Gillespie and List, 1978; Low and List, 1982). In the absence of ice, large raindrops must form by collision with other drops; however, raindrops exceeding 3 mm diameter are known from experiments to disintegrate upon collision with neighboring drops provided the neighbor's diameter exceeds 1 mm (McTaggart-Cowan and List, 1975; Low and List, 1982). Since millimeter sized raindrops are generally abundant in natural clouds, the survival time of a giant drop in a field of millimeter sized raindrops is exceedingly short. How giant raindrops form and survive within these warm clouds remains an open question.

One mechanism proposed to explain giant raindrop formation is that exceptionally large aerosol particles act as nuclei for the largest droplets near cloud base which then grow rapidly by accretion of smaller cloud droplets in the updraft (Johnson, 1982; Beard et al., 1986; Caylor and Illingworth, 1987; Illingworth,1988). Under very favorable conditions of high liquid water content and strong updraft velocity it has been shown that giant raindrops indeed can form from these embryonic droplets by accretion as they rise and fall through a cloud (Beard et al., 1986; Caylor and Illingworth, 1987). An alternate mechanism is that giant raindrops result when selected small raindrops recirculate from downdrafts into updrafts within eddies generated along updraft/downdraft shear zones near cloud top. In this paper, we will examine these mechanisms using data from the Joint Hawaiian Warm Rain Project (JHWRP) and the Hawaiian Rainband Project (HaRP).

2. EXAMPLE MEASUREMENTS FROM AIRCRAFT

Example JHWRP measurements from a series of penetrations through a cloud on July 23, 1985, shown in Figs. 1-4, demonstrate fundamental aspects of the data. Fig. 1 shows examples of raindrop images taken by the 100 μm resolution 2DP probe. The environmental winds, measured during a takeoff sounding on the island side of the rainband, are shown on Fig. 2. In the boundary layer, offshore flow associated with island blocking and cold air drainage is evident, a typical feature observed on the windward side of the island. The trade wind layer extends to 2400 m, which was the base of the trade wind inversion and very close to the top of convective cells within the rainband. The trade wind layer shown on Fig. 2 roughly corresponds to the depth of the cloud (1.9 km), since cloud base was near 500 m. Within the layer, the wind direction was constant and variations in the horizontal wind, except at the inversion, were less than 3 ms^{-1}.

Figure 3 shows the raindrop size spectra for each of eight cloud passes at various altitudes. Also shown are the computed rainfall rate, radar reflectivity factor and liquid water content averaged for each pass. The aircraft was considered to be in cloud if any of the following criteria were met for 10 consecutive seconds: 1) droplet concentrations measured with the Forward Scattering Spectrometer Probe were greater than 10 cm^{-3}; or 2) the 2DP or 2DC optical array probe concentration was greater than 1 L^{-1}. The optical array probes must have individually filled their buffers within 1.5 s. Figure 4 contains detailed measurements of drop size, air motion, and turbulent energy dissipation for Passes D-G. The cloud was initially sampled four times at a constant altitude (1600 m). The first penetration occurred just below cloud top, with each successive penetration farther below cloud top as the cloud grew vertically. All raindrops were smaller than 3.0 mm on each of the first three passes; however, broadening of the raindrop spectra was evident (Passes A-C). On the fourth pass, 3.2, 3.8 and 4.5 mm raindrops were found (Pass D). These large raindrops were embedded within an updraft that had a peak velocity of 8.3 m s^{-1}, liquid water content of 0.8 g m^{-3} and cloud drop concentration (3-48 μm diameter) of 119 cm^{-3}. The largest drops were isolated from the bulk of the 1-2 mm precipitation drops, which were located primarily in weak downdrafts on the flanks of the core updraft. A key characteristic of the cloud at this time was the existence of a strong shear zone (18.4 m s^{-1} km^{-1}) between the core updraft and downdraft. The largest drops resided within this zone. A strong fluctuation of the horizontal component of the wind along the direction of flight (u, see Fig. 4), was measured within the shear zone as well as the largest turbulent energy dissipation rates. The structure of the cloud on Pass E at 1300 m was similar in many respects to Pass D. The largest raindrops were again within the strongest updrafts, in the vicinity of the strong horizontal shear zone, and relatively removed from high concentrations of smaller raindrops. The updrafts, downdrafts and horizontal wind shear were very weak at the lower altitude, a general characteristic of our data.

Penetrations of the cloud were made at 810, 480 (cloud base), and 140 m immediately following the Passes at 1600 and 1300 m. These latter penetrations (Passes F-H) were made during the mature stage of cloud development near the time the cloud top approached the trade wind inversion at 2300 m. Giant raindrops, observed on all but the lowest pass, were

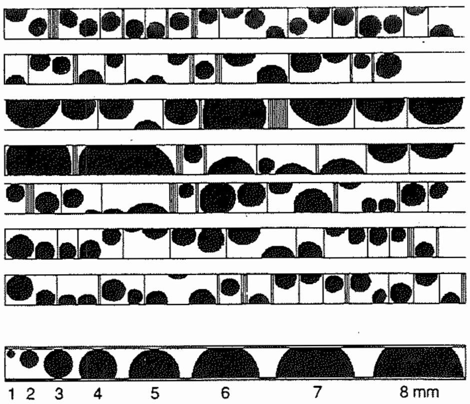

FIG. 1. Raindrop images from a rainband that contained giant raindrops, including a raindrop with diameter of 8.2 mm, the largest recorded. The magnified record is a time sequence with each vertical line denoting the passage of 0.1 seconds. The scale at the bottom shows relative size.

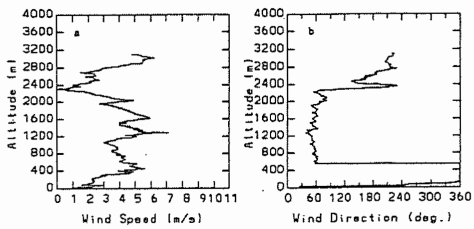

FIG. 2. (a) Wind speed vs altitude and (b) wind direction vs altitude for the 23 July 1985 takeoff sounding. The trade wind inversion is located at 2300 m.

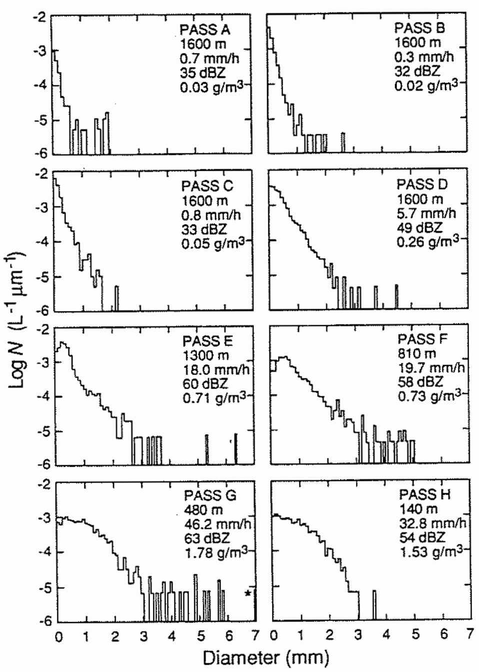

FIG. 3. Raindrop size spectra for eight passes at five elevations through a rainband cell on 23 July 1985. The total elapsed time between the first and last passes was 15 min. The star shown in pass G denotes the largest raindrop recorded, which lies off the diagram at 8.2 mm. Calculated rainfall rates, radar reflectivity factors, and measured liquid water contents averaged for each pass are also shown.

found only in regions deficient of small raindrops. Key features of these and our other measurements at lower altitudes in the rainbands include the segregation of the giant raindrops into narrow regions of the cloud and the lack of substantial updraft/downdraft structure. The lack of vertical air motion at low levels later in the cloud lifetime implies that the giant raindrops were falling rapidly (~9 m s^{-1}) from higher regions of the cloud. In order to avoid disruptive collisions, these drops must have fallen through vertical channels within the cloud in which the concentration of raindrops with diameters > 1 mm was small. We believe these channels develop in regions occupied by weakening updraft circulations. The majority of the rain, as evident from Fig. 4, falls earthward on the flanks the former core updraft circulation. Despite the fact that these smaller raindrops possess lower terminal velocities (4-7 m s^{-1}) than giant raindrops, simple calculations show that they arrive at cloud base at nearly the same time because they primarily reside outside the core updraft area. The largest raindrops appeared from our data to fall in the developmental stage of the rainshaft shortly after the cloud reached its mature stage.

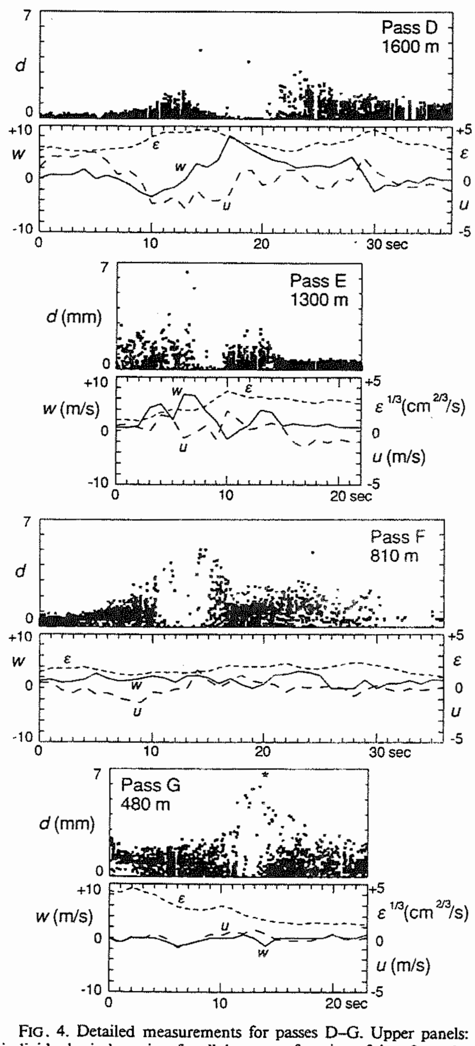

FIG. 4. Detailed measurements for passes D–G. Upper panels: individual raindrop sizes for all drops as a function of time from the beginning of each cloud pass. The density of the dot pattern is indicative of the drop concentration. The star shown in pass G denotes the largest raindrop observed, which lies off the diagram at 8.2 mm. Lower panels: air motion measurements; w is the vertical air motion (updrafts and downdrafts), u is the fluctuation from the mean horizontal air motion, and ϵ is the turbulent intensity. For convenience, turbulent intensity is plotted in units of $\epsilon^{1/3}$ ($cm^{2/3}$ s^{-1}). (A value of 0.01 m^2 s^{-3} is equivalent to 4.6 $cm^{2/3}$ s^{-1}.)

3. DISCUSSION

Many JHWRP penetrations through rainband clouds exhibited features common to those described above. Near cloud top, larger raindrops were found either within the core updraft or the shear zone associated with the updraft/downdraft boundary. The magnitude of the shear was typically strong. The large drops were relatively isolated from the bulk of the smaller precipitation drops, which typically were located on the flanks of the core updraft. Lower in the cloud and near cloud base, the updraft structure was substantially weaker or non-existent and downdrafts were seldom observed. When giant raindrops were observed, they were segregated into small regions of the rainshaft away from the higher concentrations of 0.1-2.5 mm drops. Our data suggest that giant raindrops appear first high in the clouds suspended in updrafts which are rich in cloud droplets but largely devoid of precipitation drops. How they arrive at this location is less clear.

A popular hypothesis forwarded to explain the initiation and rapid growth of precipitation drops in warm clouds is that exceptionally large aerosol particles act as nuclei for select cloud drops near cloud base (Johnson, 1982; Beard et al., 1986; Caylor and Illingworth, 1987; Illingworth, 1988). These cloud drops, because of their initial large size, are thought to grow rapidly by accretion of smaller cloud droplets in the updraft and arrive near cloud top as precursor giant raindrops. The drops then fall back through the updraft to cloud base growing by accretion into giant raindrops. Beard et al. (1986) used a continuous collection model of the kind introduced by Bowen (1950) to determine the maximum raindrop size likely to be produced by this process as a function of cloud depth and updraft velocity. In the model, use was made of realistic collection efficiencies containing reduction factors for both aerodynamic deflection and drop bounce. Figure 5, from Beard et al., shows the results of the model for the case of a cloud with droplet concentrations of 100 cm^{-3} and half adiabatic water content, conditions that approximate those found in Hawaiian rainbands (e.g., Raga et al., 1990). A constant updraft was assumed in time and over the entire depth of the cloud. Their calculations (Fig. 5) showed that, *with very strong, persistent updraft velocities over the entire cloud depth*, giant raindrops can form from embryonic droplets by accretion as they rise and fall through a cloud of depth 2-3 km.

Our data in Fig. 4 shows that such strong updrafts may indeed occur locally in the upper portion of the cloud, but are not persistent and do not extend over the cloud depth. Raga et al. (1990) have compiled statistics concerning the magnitude of updrafts in developing "main turrets" of Hawaiian rainband clouds similar to those where giant raindrops occur. A main turret was defined by Raga et al. as (1) a region of cloud that showed active growth as characterized by peak liquid water content and vertical velocity and (2) a cloud where inspection of the aircraft tracks showed that regions of active growth belonged to the same turret. Their statistics were based on penetrations of 17 rainband clouds. Their results are reproduced in Fig. 6. Their analysis shows that typical updrafts averaged well less than 2 m s^{-1} over the depth of actively growing clouds.

The cloud on 23 July presented here extended through a depth of 2 km. In the lower part of the cloud, during the maturing stage when the giant raindrops were falling, updrafts were weak or non-existent. Although the lower part of the cloud during its development stage was not sampled in this case, Raga et al.'s analysis suggests that updrafts during the early stage of development of this cloud were less than 5 ms^{-1}. Only near cloud top did the vertical velocity exceed 5 ms^{-1} and only in narrow regions of the cloud. If we apply this information to the model presented by Beard et al. (Fig. 5), we find that the maximum drop size predicted by the model for continuous growth on ultra-large aerosol would probably be less than 2 mm, and certainly less than 3 mm. Even if giant raindrops could be produced by this mechanism, they would be subjected to rapid collisional breakup, since diffusional and accretional growth *across the nuclei spectrum* must result in orders of magnitude more small raindrops in the updraft. Thus, an additional set of circumstances appears to be required to explain the existence of giant raindrops in these clouds, one which prolongs their growth and separates them from smaller raindrops.

Returning to Fig. 4, we note that the observed air motion within the zone containing the giant raindrops is characteristic of shear induced eddy circulations. The largest scale of eddy motion from the data presented in Fig. 4 and other cases appears to be related to the width of the shear zone, as evident in the wind fluctuations (u) for Pass D. Smaller scale eddy and turbulent motions clearly exist simultaneously in the 23 July cloud. Analogous eddy circulations along cumulus cloud boundaries in two-dimensional cloud simulations indeed show similar scale selection (Klaassen and Clark,1985; Grabowski, 1989). Eddy circulations between the downdraft, an environment rich in small raindrops, and the updraft, an

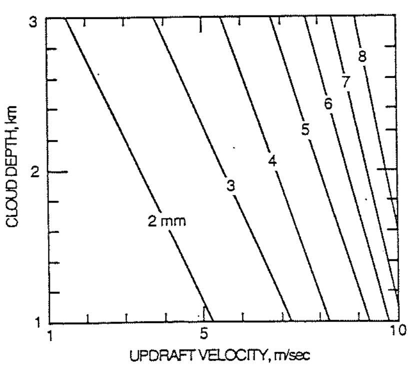

FIG. 5. Maximum raindrop diameter predicted by a collection model (cloud base temperature 20°C, half adiabatic water content, 100 drops per cm^3) as a function of cloud depth and updraft velocity (from Beard et al. 1986).

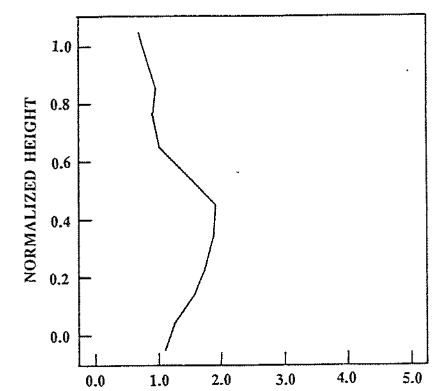

FIG. 6. Mean vertical velocity measured in active cloud turrets of Hawaiian rainbands as a function of normalized height, z^*, given by $z^* = (z - z_b)/(z_i - z_b)$, where z_b is the cloud base height and z_i is the inversion height (from Raga et al. 1990).

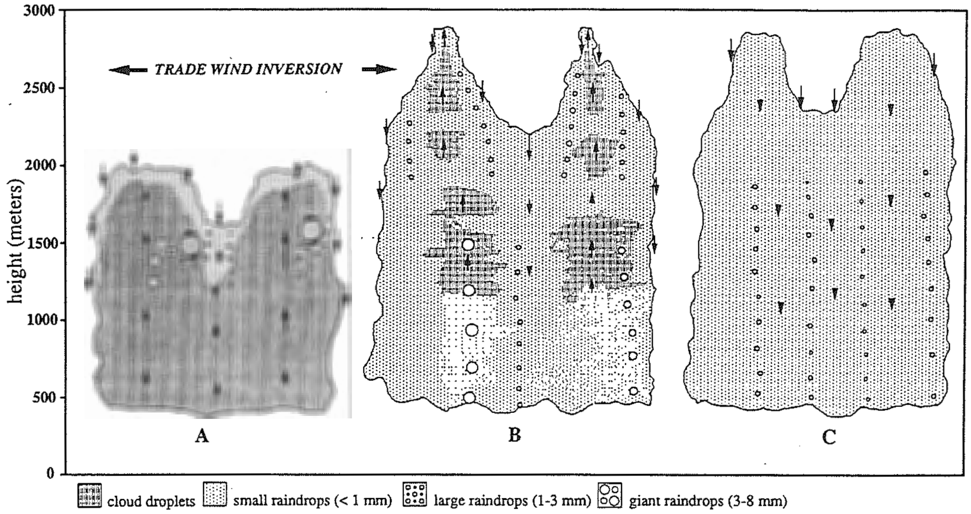

FIG. 7. Conceptual model of giant raindrop formation and evolution within a Hawaiian rainband cell as the cell passes through its developing (A), mature (B), and dissipating (C) stages. The length of the arrows denote relative updraft and downdraft strengths. The density of shading of the small raindrops denotes relative small raindrop concentrations.

environment rich in small cloud droplets but initially free of raindrops, should result in transport of small raindrops and cloud droplets between the primary updraft and downdraft circulations. Our calculations of turbulent transport for the measured intensity of $\varepsilon \sim 0.01$ m^2 s^{-3} show that it is only the shear-zone scale eddies which are capable of moving the drops hundred of meters within a few minutes. This type of motion is basically a raindrop recirculation mechanism, since selected small raindrops are transported from the edge of the downdraft rather directly into the updraft. Such a mechanism can allow select raindrops to re-enter the updraft, an environment rich in cloud water that supports rapid accretional growth. Once in the updraft, these few drops can grow in the absence of disrupting smaller raindrops. Our data show that the narrow regions of the updraft in the upper part of the cloud that have sufficient velocity to suspend the larger raindrops are also associated with the strongest shear. Once drops enter the updraft core, their residence time in this rapid growth environment is increased since they will rise with, or fall slowly against the updraft.

We have constructed a simple conceptual model from our measurements (Fig. 7) that we believe characterizes the initiation, growth, and fallout of giant raindrops within Hawaiian rainbands. The model shows three stages of evolution of a cloud cell. Updrafts dominate the cloud except near the cloud top and edges in the initial stage of development (A). Near cloud boundaries, dry air entrainment and vorticity generation (Klaassen and Clark 1985) induce downdrafts which transport small raindrops downward into the cloud. Eddy circulations induced by shear instabilities along updraft/downdraft boundary simultaneously transport selected raindrops horizontally back into the updraft. A few of these raindrops, by chance, are carried into the updraft core. Within this high liquid water content environment composed largely of cloud droplets, these selected raindrops grow rapidly, suspended in space by the strong upward air motion. Precursor giant raindrops first appear here, high in the cloud embedded within updrafts. As the updrafts weaken (B), the giant raindrops fall to the ground through the relatively raindrop-free channel provided by the weakening updraft. Smaller raindrops, falling outside the updraft channel are not suspended during their growth, and consequently reach cloud base at nearly the same time. As the cloud matures (C), collision and breakup processes become dominant throughout the cloud and giant raindrops no longer develop.

In 1990, the Hawaiian Rainband Experiment collected an extensive set of dual Doppler radar data in Hawaiian rainbands. We are now attempting to verify this hypothesis using the dual Doppler radar data and aircraft measurements from HaRP. The radar data provide a means to observe individual cells within rainbands over the course of their evolution and to draw more quantitative conclusions regarding the evolving updraft structure within the rainbands. On August 10, 1990, a particularly strong rainband cell was observed by both radar and aircraft throughout its lifetime. At the conference, we will present an analysis of the structure and evolution of this cell.

4. ACKNOWLEDGEMENTS

We thank Mr. A. Tokay of the University of Illinois and Drs. D. Baumgardner and D. Johnson of NCAR for assistance. This research was supported by the NSF under grant NSF-ATM-8719498.

5. REFERENCES

Beard, K. V., D. B. Johnson, and D. Baumgardner, 1986: *Geophys. Res. Lett., 19,* 991-994.
Blanchard, D. C., 1953: *J. Meteor., 10,* 457-473.
Bowen, E. G., 1950: *Aus. J. Sci. Res., A3,* 193-213.
Bringi, V. N., T. A. Seliga and W. A. Cooper, 1984: *Radio Science, 19,* 157-167.
Caylor, I. J. and A. J. Illingworth, 1987: *Quart. J. Roy. Meteor. Soc., 113,* 1171-1191.
Gillespie, J. R. and R. List, 1978: *Pure Appl. Geophys., 117,* 599-626.
Grabowski, W. W., 1989: *J. Atmos. Sci., 46,* 3513-3541.
Illingworth, A., 1988: *Nature, 336,* 754-756.
Johnson, D. B., 1982: *J. Atmos. Sci., 39,* 448-460.
Klaassen, G. P. and T. L. Clark, 1985: *Atmos. Sci., 42,* 2621-2642.
List, R. and J. R. Gillespie, 1976: *J. Atmos. Sci., 33,* 2007-2013.
Low, T. B., and R. List, 1982: *J. Atmos. Sci., 39,* 1591-1606.
McTaggart-Cowan, J. D. and R. List, 1975: *J. Atmos. Sci., 37,* 1401-1411.
Raga, G. B., J. B. Jensen and M. B. Baker, 1990: *J. Atmos. Sci., 47,* 338-355.

Mesosale Structure Characteristics Of Mei-Yu Frontal Torrential Rain Over China

Xunchang Tang and Huijun Guo
Jiangsu Provincial Meteorological Bureau, China

I. Introduction

The lower reach of Changjiang River has been influenced by Mei-yu front from June to July every year, producing frequenty a torrential rain process one after another. As for the feature of macroscale, Mei-yu front is formed at the westnorth edge of Pacific horse latitude high and results from the seasonal adjustment of East-Asia general circulation of atmosphere. It produces a long time still rain belt from the lower reach of Chang-Jiang River to the south of Japan. A stationary front meaning Mei-yu front is shown on the surface chart. At 850 and 700 hpa. There is a shear line formed of the tropic air current in the west of Pacific horse latitude high and the cold high air current of mid-high latitude. There is no jet stream in upper air but a great deal of vapour sent from strong southwest jet stream in downer air. So Mei-yu front has half-tropic characteristic fallout system.

II. The feature of mesoscale and disturbance machanism produced over Mei-yu front

Torrential rain produced over Mei-yu front in fact results from mesoscale disturbance. During Mei-yu westerly jet move northward to about 40 N. The centre of jetstream is always formed on the axis of jetstream and moves from west to east When Mei-yu front cloud bar lies at the entrance on the right, there exists diver gence over the upper air. Inside the troposphere is ascending motion which makes low-level jet underthe troposphere develop and leads to Meso-α scale depres sion over the Mei-yu front. Sometimes the depression in the form of eddy appears on 850 and 700 hpa and produces tor rential rain. Torrential rain area is the left forepart at the top of low-level jet(Fig.1)

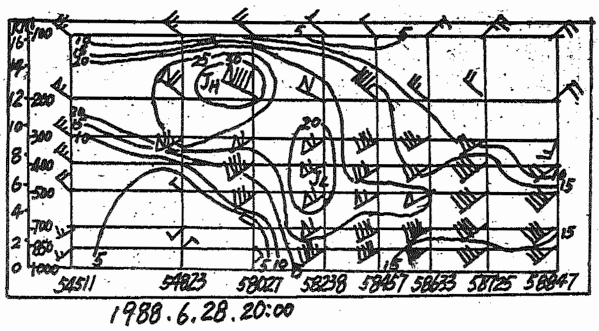

Fig.1. The wind cross-section in the derection of meridion

The torrential rain in the Fig.1 is over the Mei-yu front near Nanjing, over which there is a deep and thick ascending stream area(Fig.2).

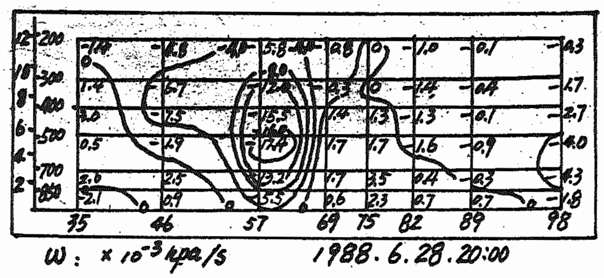

Fig.2a. ω cross-section in meridional derection

The desencending area is on both sides of the Mei-yu area. In the Fig. 2b. can see convergence and divergence over the torrential rain area. The depression is shown on the satellite cloud picture as a white and bright cloud cluster and shown on the radar echo as a floccus ech cluster, in which short-band meso-β scale strong echo is constantly produced and its instensity can reach to over 50 dbZ, moving eastward with propagation along the Mei-yu front (Fig.3a). Meso-β scale depression is coordinate with strong ech area(Fig.3b). The direction pointed by the trough of mesoscale depression front means the movement of futuristic strong echo. The trough is corresponding with divergence field, field of vorticity, divergence field of moisture flux and the convergence zone of divergence field of energy flux. The trough is also high tempearture and high humidity area and high area. The strong echo is in the form of merging cloud on RHI, which has both sheet cloud ecgo with plain echo top and convection echo formed of meso-γ sclae convection system (Fig.4)

Fig.2b. ζ and D normal profile in torrential rain area

Fig.3a. Mei-yu front echo belt (3Km CAPPI)

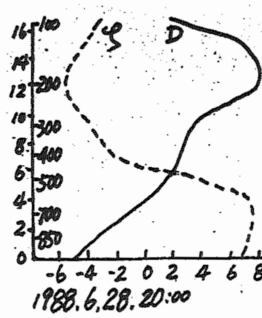

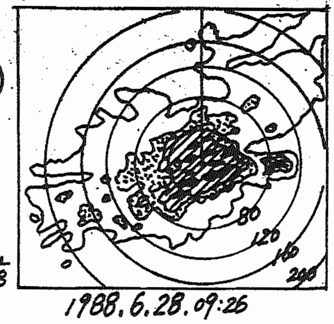

(Fig.3b and 4. are on the bottom of P.3)

Fig.3b. It is corresponding with surface pressure field and divergence field of Fig.3a.

Fig.4. The RHI echo of the Mei-yu Front

The top of echo highness is usually about 10Km high. 50 dbZ strong echo mucleus lies in warm area inside the cloud and clearly shows the feature of warm cloud precipitation. It has obvious zero temperature level bright band, whose upper bound is about 5.0 Km high and 600—850m thick and its temperature is 0.6°C; whose downer bound temperature is 4° C. These mesoscale system usually have the character of internal gravity wave, leading to continual mesoscale disturbance . When they move eastward in propagation, the course of torrential rain and several torrential rain centres result again and again.

Sometimes in the east of Xizang plateau is a southwest China vortex. When the trough of short wave from the north with southwest China vortex moves to the east along the shear line of Mei-yu front produced strong wave motion over Mei- yu front forms meso-α scale Changjiang-huaih cyclone. With the effect of CISK mechanism the cause of Changjiang-huaihe cyclone is mostly the dynamic effect sent from latent heat. The development of Changjiang - huaihe cyclone depends on barolinicity.

III. The feature of the mesoscale of Changjiang-Huaihe cyclone terrentical

The feature of the change of Changjiang-Huaihe cyclone can be seen on the satellite cloud chart (Fig. 5)

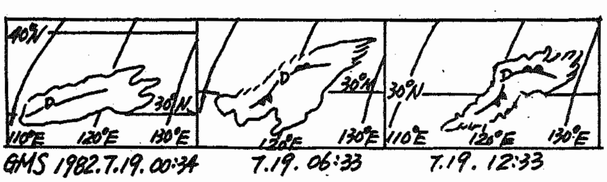

Fig.5. The change feature on the satellite cloud chart.

The feature of badar echo is in Fig.6. In front of the centre and hearby the centre of Changjiang-Huaihe cyclone is floccus echo cluster being eddy, whose diameter is 150-300 Km at least. In RHI the echo top is about 10 Km high, there is zero-temperture level bright band and columns of convection echo . Precipitation shower and the rainfall amount can reach to 20 — 50 mm/h.

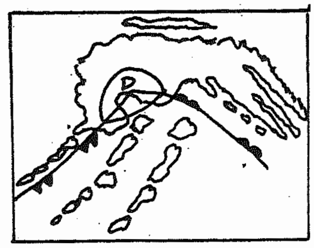

Fig. 6. The feature of the badar echo of Changjiang-Huaihe cyclone

Before warm front is fleccus echo belt area. The echo belt area is 100 Km away from warm front. Its width is one or two hundredKm. The forepart is sheet cloud echo at the fore. Near warm front the convection echo is more obviously. Its intencity of echo is only 40-50 dbZ. Just then the precipitation is only shower, but sometimes is thunder rain. The rainfall amount is 10-20 mm/h at the most Zone of convective precipitation echo belt may come into being over cold front of cyclone whose intencity can reach over 55 dbZ. While developing up to high high ness, it will leave cold front and move to the east quickly in warm area. If cold front moves slower, quite a few convec - tion echo belts can be produced over cold front continuously and move to the east at a distance in warm area one by one (Fig.7). Its distance between them is

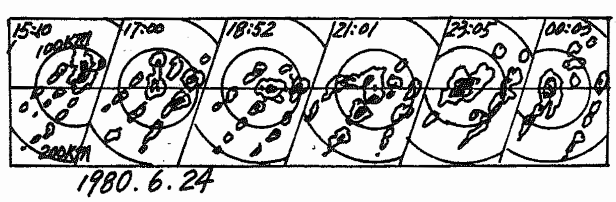

Fig.7. The change of cyclone cold front echo belt

about 80-100Km and the time between them is one hour when they move. The length of the echo belt is hundreds Km and the width is 30-40Km. Once even 8 convection echo belts appear over cold front. A single echo belt can produce about 20mm/h rainfall amount when it passes some places. If there is more exuberant convective contition afternoon, meso-β scale depression appears over zone of convective echo of cold front, which makes the part echo belt develop more exuberantly and its top may be over 18 Km high. The rainfall amount adds up to 50 mm/h and leads to thunderstorm and even tornado weather. After the last convection echo belt move, the whole course of torrential rain is over.

In fornt of Changjiang-Huaihe cyclone there always exists a shear line of mesoscale with east - west direction(Fig.8).

1980.6.24.10:00

Fig.8. The M -β S system of Changjiang Huaihe cyclone

At the earliest, in the north of cyclone centre there is a meso-β scale depression With the effect of internal gravity wave on mesoscale shear line, more meso-β scale depression is forned. It may produce 50-80 mm/h torrentical rain. In the north of the shear line is colder wet air on Yellow Sea sent from east wind. In the south of the shear line is warm wet air on East Sea sent from southeast wind. In the low-level there is more water-vapour sent by southwest jet. Three-ply gathering, must produce torrentical rain. The whole course of Changjiang-Huaihe cyclone weather lasts more than 20 or 30 hours. In a certain course of Changjiang- Huaihe cyclone there causes 8 meso-β scale depressions; making the distribution of the centre of torrential rain rath differential.

IV. The discussion about the judder produced over the Mei-yu front

Mei-yu front is usually neuter and weak judder. But the cause of disturban may be reasearched with the theory of symmetry instability. It is regarded as finite moist air over Mei-yu front. The criterion of symmetry instability is Richardson num.

$Ri < 1$, that is to say, $Ri = F^2 N^2 / S^4$.

To moist air,

$$F^2 N_{se}^2 - S^2 S_{se}^2 < 0, \quad \text{among of them,}$$

$$F^2 = f \left(f - \frac{\partial u}{\partial y} \right)$$

$$S_{se}^2 = \frac{g}{\theta_{se}} \frac{\partial \theta_{se}}{\partial y}$$

$$S^2 = - f \frac{\partial u}{\partial z}$$

$$N_{se}^2 = \frac{g}{\theta_{se}} \frac{\partial \theta_{se}}{\partial z}$$

To the moist air, including cumulus convective latent heat effect, it is,

$$F^2 N_{se_1}^2 - S^2 S_{se}^2 < 0$$

$$N_{se_1}^2 = \left[1 - Q_0 G(z) \right] \cdot N_{se}^2$$

Taking $Q_0 = 1.14$ (empirical value)

$$G(z_0) = \sin \frac{z_0}{H}$$

H is the highness of tropopanse, z_0 is the count storey, on Y - Z level, Y is the meridinal direction of meeting trontal surface at a right angle. According to parameter of ambient atmosphere, the count can be carried out. When the over criterion is founded slantwise convection will be formed. The disturbance will be also produced over Mei-yu front.

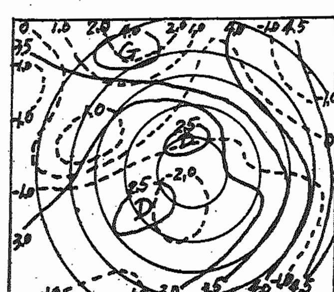

1988.6.28.08:00
----- D: $\times 10^{-5}$/s

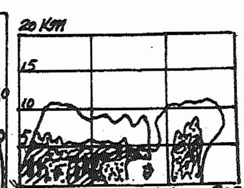

1988.6.28.09:25

PHYSICAL CONDITIONS OF HAILSTONE GENERATION AND GROWTH IN DIFFERENT TYPES OF HAIL CLOUDS (THE RESULTS OF COMPLEX HAIL EXPERIMENT)

L.M. Fedchenko, M.I. Tlisov

High-Mountain Geophysical Institute, Nalchik, 360030, RUSSIA

In the framework of Complex Hail Experiment (Fedchenko et al.,1989) the special large hail network was created in the foothills of Central Caucasus with total area of $3.5x10^3 km^2$ and spacing of 3 km. The micro-network with area of 900 km^2 and spacing of 1.25 km was within the large one. There were 600 hail-pads, 13 automatic hail samplers and 7 special hail recorders on the network territory. To measure the liquid precipitation we placed regularly 40 pluviographs. One half of this territory was the target area and another was the controlled one. During 8 years the network recorded more than 70 hailfalls, 41 cases of them were with seeding and 31 without it. The hail samples from 31 hailstorms with and without seeding were gathered and processed.

The analysis of the theoretical estimation of true number of hail-streaks for the network and the comparison with measured hail-streak number showed the difference of not more than 1 hailstorm. The aircraft-laboratories "IL-18 Cyclon" and "YAK-40" with special equipment were used for measuring of microphysical and dynamical characteristics of the initial stage of cumulonimbus clouds.The sounding was made in the days with hail forecast. The characteristics of clouds from which hail fell subsequently were analized in the first place (Myakonkii et al.,1991). Besides, a series of investigations on laboratory modelling of generation, growth and fallout of hail in aerodynamical units were carried out by freely weighting of different hydrometeors (Tlisov et al.,1992). The general formulae for heat and mass transfer and for the time of rain-drop freezing and growth and melting of hail particles from real forms were obtained.The investigation results of physical character of hailstone embryos showed that total ratio of hail embryo types of grauple-freezing drop had the values (68:32÷65:35).

Hailstone samples from supercell processes are characterized by close content of drop and grauple embryos and in singlecell processes the predominance of one type over the other was observed. In the Fig.1 these samples correspond to the lower and upper values of the curve. In other words in autumn-spring months the hailstone embryos form due to Bergeron-Findeisen mechanism and in summer months the role of warm-rain mech-

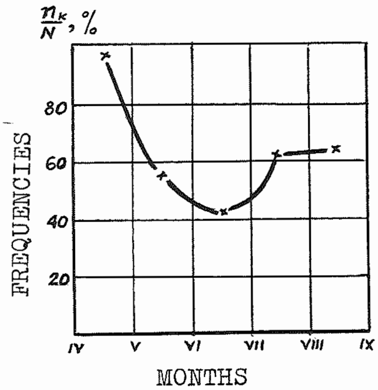

Fig.1 Average seasonal changes of a part of grauple hail embryos.

anism sufficiently increases. Maximum relative amount of drop embryos within the separate hail storm corresponds to the right margin of hail-streak along the hailstorm movement. In time the maximum relative amount of drop embryos conforms with the stage of maximum values of hail cloud parameters. Besides, the maximum relative amount of drop embryos according to its space-time variations coincides with maximum values of surface density of point kinetic energy of hail. In hailstorms with kinetic energy of less than 50 J m^{-2} in spring-autumn months the Bergeron-Findeisen mechanism is prominent in hail-generation process and in hail clouds with more than 50 J m^{-2} the warm-rain mechanism is of more importance.

A set of investigations confirmed the different physical character of drop and grauple embryos. The different aerosol structure of drop and grauple embryos (Tlisov et al.,1984)is defined by different on dispersiveness the aerosol medium in which the embryos form. It may be related to the different parts of hail clouds or different stages of development. The drop embryos have wider size spectrum of aerosol particles with higher ice-forming threshold and activity than aerosol depositions of grauple embryos. The analysis of bubble structure of drop embryos of hailstones showed that near 70% of their total number generate at the temperature interval from -6°C to -12°C and 30% - at the temperature higher than -10°C. The drop and grauple embryos have different elemental composition (Tlisov et al.,1988). The concentration of sodium and chlorine in drop embryos reaches 2.4×10^{-8} g and 1.7×10^{-8} g, respectively, and in grauple embryos it by an order or two orders of magnitude lower. The sodium-chlorine ratio in drop embryos agrees with that of rains, but in grauple embryos this ratio is violated. Such heavy elements as iron, zink and others mainly associated with giant and supergiant particles in grauple embryos of hailstones and practically didnot observe. (Tlisov et al., 1989).

The silver iodide detection in hail stones which fell out from the storms seeded by a new method (Abshaev,1989) showed the accumulation of agent particles in ice layers of hailstones and grauple embryos. In drop embryos the agent particles were not detected. It may be explained by the fact that a new seeding method does not take into account the warm-rain mechanism in hail formation absolutely.

The aircraft measurements of the initial stage of hail clouds showed that size spectrum of large cloud drops successfully approximated by the relationship $N(R)=N_1(R_1/R_{max})^{-1}$, where N_1 is the concentration (m^{3}) of drops with radius $R_1=100$ m, R_{max} is the radius of largest drops in size spectrum. For cumulus congestus clouds $=2.5\div3$. The concentration of these drops by an order of magnitude greater than similar characteristics of cumulus congestus clouds on the Europian part of Russia. Besides, in June-August the precipitation fallout of warm-rain type was observed.

The study of isotopic composition of ice layers and hail embryos by hydrogen showed that drop embryos form at higher temperatures than grauple embryos and layers of dry growth (Tlisov et al.,1988). The drop embryos form at the upward trajectory and the grauple embryos form at the downward one.

The numerical simulation of growth and movement of hail particles in the clouds showed that the less the initial size of embryos the more spread their trajectories independent of embryo type and level of agent injection. There is a critical size of embryos if being less of which they are carried away into the anvil and do not convert into the hail. The drop embryos generate hailstones with the most short trajectories. These hailstones fall out near the updraft. The comparative analysis showed that according to their physical characteristics the hailfalls on the North Caucasus are similar to the Alberta hailfalls (Dessens,1988). But in our region the part of the most severe hailfalls is greater.

In 70% of hailfalls the kinetic energy was not more than 50 J m^{-2} that meant the absence of crop damage of corn and wheat, for example. The statistical estimation of seeding influence on spectral and energetic characteristics of hailfalls was carried out. Some non-parametric methods were used: -criterion, Vandervarden-criterion and Wilcoxon-Mann-Whitney-criterion. The differences of mean, maximum and global characteristics of hailfalls such as mass, concentration, size and kinetic energy were not important at the 0.05% confidence level, though the quality differences conformed with the expected ones. In other words the seeding does not sufficiently affect the hail precipitation regime. The comparison of our data with similar data of "Grossversuch IV" was made. The changes of global kinetic characteristics as a result of seeding in "Grossversuch IV"were more substantial than in Complex Hail Experiment at a new seeding method.

CONCLUSION

1. The investigation of aerosol and bubble structure, the isotopic and elemental composition of hail embryos and aircraft measurements of microphysical and dynamical characteristics of initial cloud stage showed that the drop embryos were not the secondary ones after the melting of grauple particles or the blowing off from the surface of wet-growing hailstones but formed by the action of warm-rain mechanism.
2. In the total sample the hail generates predominantly on the grauple and in the samples of individual hailfalls the relationship of different types of hail embryos experiences the spatial-time and seasonal changes. In singlecell hailstorms may act the mechanism of warm rain or Bergeron-Findeisen mechanism as a function of season. In multicell hailstorm mainly Bergeron-Findeisen mechanism works. In supercell hailstorms frequently two mechanisms have enough time to work.
3. According to our measurements of more than 70 hailstorms it was found that a new seeding method without taking into account the warm-rain mechanism did not substantially affect the regime of hail precipitation.

REFERENCES

1. Abshaev M.T.,1989:O novom metode vozdejstviya na gradovye protsessy,Trudy VGI, 72, 14-28.
2. Fidchenko L.M., M.T.Abshaev, M.I.Tlisov, 1989: Complex Hail Experiment: objectives, technical instrumentation and preliminary results, 5th WMO Sci. Conf. on Weath.Modif. and Appl. Cloud Phys., Beijing, China, 595-597.
3. Myakonkii G.B., M.I.Tlisov, L.M.Fedchenko, 1991: Issledovaniya mikrofizicheskikh i dinamicheskikh kharakteristik nachalnoi stadii kuchevodozhdevykh oblakov na samolete IL-18 Ci-

klon, Trudy seminara" Aktivnye vozdejstviya na gradovye protsessy i perspektivy usovershenstvovaniya ldoobrazuyushchikh reagentov dlya praktiki aktivnykh vozdejstvii," 77-84.
4. Tlisov M.I.,1989: Physical characteristics and mechanism of hail formation, 5th WMO Sci. Conf. on Weath. Modif. and Appl. Cloud Phys.,Beijing, 337-338
5. Tlisov M.I., V.G.Khorguani, Microphysics conditions of hail formation in clouds, 9th Intern. Conf. on Cloud Phys., Tallin, USSR, 1984, 1, 287-290.
6. Tlisov M.I.,V.G.Khorguani, 1988:Microphysical concept of hailstorms,10th Cloud Phys. Conf.,Bad Homburg, F.R.G. 2, 554-556.
7. Tlisov M.I., V.N.Filatkin, I.I.Pilip, 1992: Heat and mass transfer of drops and growth and melting of freely floating hailstones, J. Atmos. Res.,27.

POLARISATION AND DOPPLER OBSERVATIONS OF A TORNADIC STORM IN CENTRAL ALBERTA

A.R.Holt[1], E.Torlaschi[1,2], R.McGuinness[1], D.A.Holland[1], F.Bergwall[3], T.Nichols[4], P.Joe[5]

1 Department of Mathematics, University of Essex, Wivenhoe Park, Colchester, CO4 3SQ, U.K.
2 on leave from:- Department de Physique, UQAM, Montreal, Quebec, Canada, H3C 3P8
3 Environmental Res. and Eng., Alberta Research Council,Edmonton,Alberta,Canada, T6H 5X2
4 Atmospheric Environment Service, 4999-98 Avenue, Edmonton, Alberta , Canada, T6B 2X3
5 King Weather Radar Station, AES, RR#1, Jane St., King City, Ontario, Canada, L0G 1K0

1.Introduction

For a period of three weeks from 17th July 1991, the Alberta Research Council (ARC) ,Canada, and the University of Essex, U.K., jointly conducted a field experiment using the ARC S-Band polarisation radar situated at Red Deer Industrial Airport, nr Penhold Alberta. The object of the experiment was to collect further polarisation data from convective storms together with concurrent ground observations of rainfall, hail etc, and to attempt to obtain a real-time display of the polarisation data. The ARC radar is situated approximately 150km south of Edmonton. The Atmospheric Environment Service of Environment Canada has an operational C-Band doppler radar situated at Carvel, some 45km west of Edmonton. From the ARC radar, Carvel is at a range of approximately 155km at azimuth 352°. The range of the Carvel radar in doppler mode extends to 110km. There was thus a considerable region in which both radars overlapped. It was intended that the field experiment be restricted to within a distance of 70km from Red Deer.

In this paper we describe observations on the 29th July. At 0800MDT a short wave trough oriented north-south over central British Columbia was moving eastward at 13 m/s. Winds from the surface to 2000m above sea level (ASL) were light and variable while winds above were west southwesterly and increasing to more than 40 m/s at the tropopause. Although a surface front was not evident, a west to east baroclinic zone lay across central Alberta.

By early afternoon, the low pressure centre associated with the short wave had moved eastward away from the mountains allowing a 10m/s northwesterly flow to become established in the low levels over western Alberta. As the air was already quite unstable (Lifted Index of -7 degrees) in the morning, the increasing divergence aloft with the short wave and the intensification and southeastward motion of the front, allowed strong convection to develop during the afternoon. The strong wind shear that developed (northwest 10 to 15 m/s in the low levels with southwest 15 m/s at 3000m ASL and stronger southwesterly aloft) meant that well developed long lived supercells were generated. These cells produced very large hail (greater than 6cm) and possibly one tornado.

A series of convective storms moved across the region between the two radars, their tracks being from the West in a direction just South of East; we shall describe observations on the three most intense storms [see fig. 1, where range rings are at 20km intervals]. The information from the two radars is seen to be complementary. As well as the radar observations, the field experiment had two chase vehicles equipped with both wedge and tipping bucket gauges. In addition, observations were made by several of a small network of volunteer observers, and rainfall measurements were made by two permanent tipping-bucket gauges belonging to AES and Alberta Environment.

2.Theory

The AES radar at Carvel is a C-Band radar manufactured by Enterprise Electronics Corporation. It was Dopplerized for the 1991 severe weather season. It is a coherent on receive magnetron system with a twelve foot dish and has a nominal 1° beam. Reflectivity, mean radial velocity and mean Doppler spread are computed via the pulse pair technique using a RVP6 Doppler signal processor from Sigmet Inc. The dual PRF velocity unfolding technique is used to extend the unambiguous velocity interval to $\pm\cdot 48$m/s. Radar image products are produced at the radar site by a microvax (Digital Equipment Corporation) processing system developed by the King City radar group (Crozier et al 1991). Scanning strategy consists of a 24 elevation reflectivity-only volume scan with 2km resolution to a range of 256km taking 5 minutes to perform, and then a 3 elevation Doppler scan (0.5°, 1.5°, 3.5°) with 1km resolution to a maximum range of 110km occupying the next 5 minutes.

The ARC S-Band radar has already been carefully described (English et al 1991). It measures 4 items of data from each 1.05km range bin - the complex correlation, W , of the signals in the "main" and "orthogonal" receive channels, and the powers, W_1, W_2 of these two signals. From these can be obtained a number of different radar parameters:-(circular) reflectivity, Z; differential reflectivity Z_{DR}, (total) differential phase Φ, circular depolarisation ratio (CDR), circular correlation (ORTT or ρ), and degree of polarisation (p). However, since the propagation characteristics of linear vertical and linear horizontal polarisations are different, resulting in both differential propagation phase and differential attenuation, the circularly polarised waves are progressively depolarised as they propagate through rain (Humphries 1974). The data collected thus relate to a combination of propagation and backscatter.

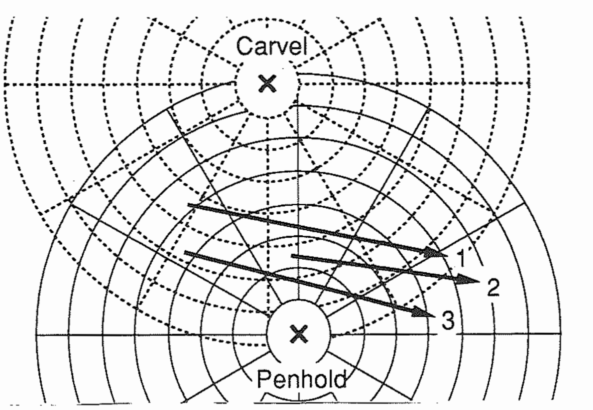

Fig. 1: The relative positions of the Carvel and Penhold radars showing the storm tracks of the three cells considered. Range rings are at 20km intervals.

However, the differential propagation phase can be extracted and used to retrieve the backscatter data (Holt 1988, McGuinness & Holt 1989, Torlaschi et al. 1989). This is possible at S-Band since the backscatter phase in rain is negligible, and thus the total phase and the propagation phase are the same. Recently a measurement scheme has been proposed which enables the total differential phase to be resolved into its separate propagation and backscatter components (Holt & Tan 1992). Although this measurement scheme was not available in 1991 , nevertheless the data can be processed to simulate it and thus to give an indication of regions (eg where hail is present) where the backscatter phase is significant.

3.Ground Observations

The field experiment had two mobile chase crews, in radio contact with the control at the radar site. The crews were equipped with both wedge and tipping bucket rain gauges. One crew also had a video camera. Radar control was equipped with oscilloscopes giving PPI displays of reflectivity and CDR, albeit not range corrected. A small network of some 27 volunteer observers had been established for the duration of the experiment, each measuring rainfall twice a day. We subsequently were given access to the data recorded by the AES network of observers, and data from tipping-bucket gauges in the project area (radius 70km) belonging to AES and Alberta Environment. Red Deer College also gave us access to their data. The AES Weather Office at Edmonton provided forecast information, and regular contact was made between the Weather Office and ARC radar control on the day being discussed. Furthermore, we have subsequently been given statistics of claims for hail damage.

4.Radar Observations

All times are given in MDT. The radar data showed large isolated cells with storm structure (Fig. 2 & 3) typical of Alberta hailstorms (Chisholm & English 1973)

(i)The first storm Due to essential maintenance, the S-Band was not operational until 1549hrs, at which time the first convective cell was approximately 45km from the radar along azimuth 350°. At this stage, heavy hail had already been experienced by one chase crew, and the second chase crew was also experiencing hail. The ARC radar data shows that there were reflectivities in excess of 55dBZ at 1° elevation, whilst the differential reflectivities were less than 1dB throughout the high reflectivity region. This is indicative of hail (cf Al-Jumily et al 1991). It is also noteworthy that the circular correlation was less than 30% in the same region. Viewed from Carvel the storm was at range 100km and azimuth 175° at 1550. The largest low level reflectivities were located in the southwest side of the storm. The highest reflectivity gradients and a reflectivity notch were located in the right front quadrant, indicative of the storm inflow region. The anvil from the storm streamed towards the northeast with a low reflectivity region extending in two directions. This is shown in fig. 2, which shows the S-Band reflectivity. The doppler data from Carvel shows a weak rotational structure (radial velocity difference of about 12 m/s over a distance of 3 km) was observed within the weak echo region, indicative of a mesocyclone. This storm was at the maximum range of the Doppler radar. It was tracking in the direction shown in fig. 1 at a speed of 70km/hr. At this time also a weak line echo is visible in the ARC reflectivity data (Z typically 10dBZ), but there is virtually no polarisation return at this time. The second storm is also visible, situated at range 100km and azimuth 320°.

(ii)The second storm The second storm had a similar reflectivity structure to the first. At 1648hrs the second storm was centred on a position at azimuth 340° and range 72km. One of the chase crews observing this storm from a distance of approximately ten miles observed a possible touch-down. A funnel was observed to drop below tree level for 30-60secs. The third convective cell was positioned 85km from the radar at azimuth 303°.

During 1730-1745hrs this second storm passed over a chase crew positioned at range 57km, azimuth 13°. As it approached at 1723hrs the crew reported strong rotation visible. In the early stages of the sampling there was little rain, but sparse soft hail, **baseball** sized was experienced, as the video record shows. By 1734 the hail had reduced in size to grape-size, and to pea-size by 1741.

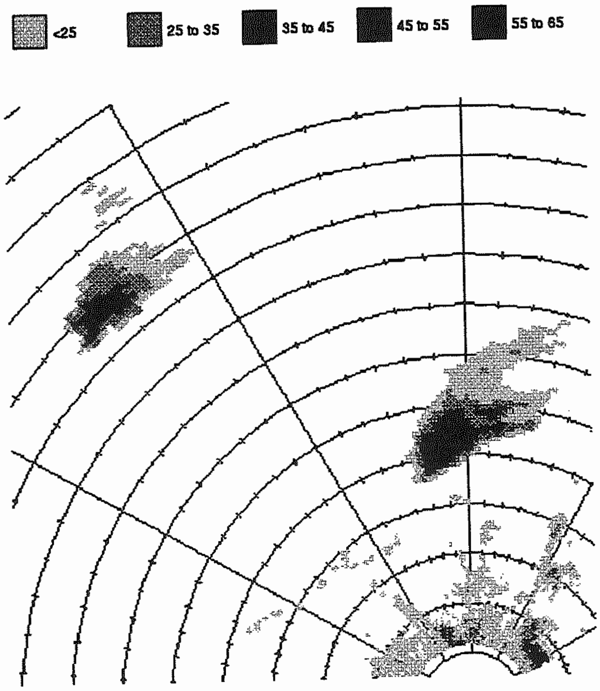

Fig. 2: The ARC radar PPI reflectivity map at 1° elevation at 1551hrs, in units of dBZ. Range rings at 10km intervals.

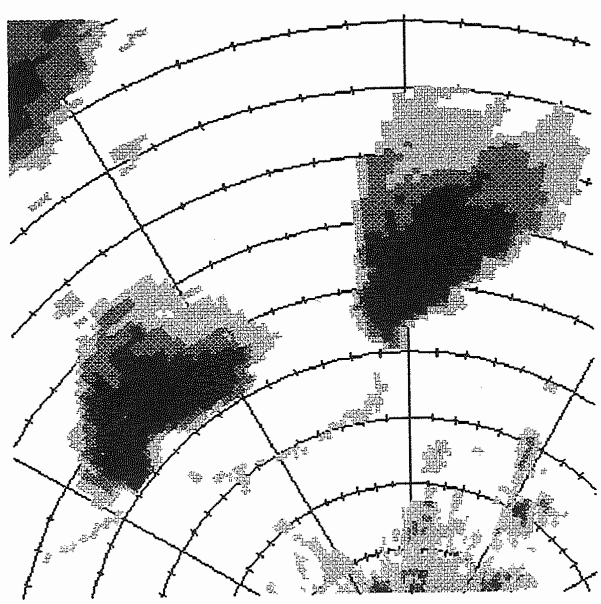

Fig. 3: As Fig 2, but 1721hrs.

The ARC radar data shows that a line echo first became evident around 1720hrs, seeming to start from the second cell, link to the third cell, and then stretch out to the SW again. This is shown in fig. 3. At 1723 the reflectivities in the line echo were generally in the range 10-20dBZ. Such line echoes are typical of regions of strong convergence (Wilson & Schreiber 1986). Whereas the first line echo was hardly noticeable as it passed over the radar site, the second line echo caused an abrupt change in wind speed and considerable turbulence. It passed through the radar site around 1805. At 1800 the log at the airport control tower records the wind-speed as 8 knots (15 km/hr), whilst at 1900 the mean speed was 25 knots (46 km/hr) with gusts of 43 knots(80km/hr). The record at Red Deer College, situated 8km NNE of the radar, is almost exactly the same. There was a drop in dew-point temperature from 13.4^{0}C to 6.9^{0}C, and in dry bulb temperature from 21.9^{0}C to 12.6^{0}C between 1800 and 1900 at the radar site. As the line echoes passed through the region in which the radar detects them, they initially had little polarisation return, but finally had strong differential reflectivity. As they passed through the radar, some long pieces of wild grass were deposited, and the radar picture is consistent with the possibility that grasses sheared off by the turbulent winds were the scattering mechanism on this occasion. Certainly there was no evidence of insects on the ground.

The doppler data at 1730hrs (fig. 4) showed a velocity difference of 42 m/s over a distance of about 7km within the weak echo region of the storm. The extrema were azimuthally offset and the inflow region of the storm showed strong inbound radial velocities. Both of these observations are consistent with strong convergence into the storm. This is consistent with the interpretation of the ARC radar data as showing a line of convergence existing on the southern edge of this cell.

(iii)The third storm This cell was unfortunately beyond the range of the Carvel doppler radar. The storm structure was similar to cells 1 & 2. As seen in Fig.3 the line echo linked to this cell at a region of high low-level reflectivity. As the storm developed, a hook echo became evident on the southwest corner, with the line echo linked in this region. Its ARC radar image became less distinct in the low-level elevation since it entered the ground clutter region. A chase crew observed mesocyclonic activity at 1746hrs, and experienced hail up to golfball in size. Hailshafts in this storm were visible from the radar site.

5.Analysis

To date polarisation has been shown to be useful for two purposes. These are firstly the identification of regions containing hail, and secondly the measurement of rainfall during periods of high rainrate. The cells on this day turned out to produce many reports of hail, but the accompanying rainfall was relatively light. To demonstrate the value of the polarisation returns we therefore consider (i) the radar record at the same location and time as reports from a chase crew sampling a cell (ii) the plot of all radar locations in which the radar parameters suggest hail, together with locations in which hail was recorded as having fallen to the ground.

In Table 1 we give values of Z, Z_{DR}, ORTT , K_{DP}(Differential propagation phase per km), and rainrate derived from K_{DP} for the period 1730 -1745 at the location where the chase crew was monitoring the second cell. We also give the notes of the chase crew about the precipitation being experienced. In the early part of the storm, there was little rain, but then there was a part when there was heavier hail when it is difficult to estimate rainrate by eye. We also give the total rainfall over the period. It can be clearly seen that in the early part of the storm when there was sparse but very large hail, the reflectivity is less than 50dBZ, but Z_{DR} and ORTT are very low. Reflectivity alone could not have identified the region as containing hail, but the polarisation parameters are telling, since in rain ORTT should be greater than 75%, and Z_{DR} should be larger than 1.5 for that value of Z. As the record progresses we see that first Z increases with Z_{DR} and ORTT remaining small, but then Z reduces again to 53dBZ and Z_{DR} and ORTT both increase, indicative of rain. The rainfall predicted from the radar is in quite good agreement with that measured.

In Fig 5a,b we plot regions in which the radar data predicts that hail may well have fallen together with the locations of ground reports of hail. It should be stressed that since a limited set of ground reports of hail was available, there has been no attempt to seek the best combination of radar variables- that will be a matter of further research. In fig.5a we plot regions in which Z > 45dBZ, Z_{DR} < 1.3dB, and ORTT < 60%. The density of plot indicates the number of radar records in which the above criteria were satisfied. In fig.5b we plot the locations at which hail was reported, giving the maximum size at each location ("X" = shot or pea, "Δ" =grape or walnut, "+" = golfball or larger). Almost all the reports of hail occur at points at which the criterion was satisfied, although no attempt at time correlation has been made.(It should be noted that the locations of the reports in the far east are not known quite as accurately as those in the central region). This agreement provides further indication of the value of polarisation (at S-band) in the identification of hail.

An interesting feature of the polarisation echoes is that the *degree of polarisation, p* which is normally greater than 95% in both rain and hail, displays regions in storms 2 & 3 in which p lies less than 90%, sometimes as low as 70%. (In the first storm there is just a hint of such a region.)

Table 1: Observations at 17:30-17:45 hrs 1991 July 29. Position re ARC radar: Az 12°, range 57km.

Time	Z dBZ	Z_{DR} dB	ORTT %	K_{DP} °/km	Rainrate mm/hr	Ground time	Ground Information
17:30:27	48.2	1.03	15.6	-	-	17:31	Baseball hail
17:31:47	49.7	0.74	13.3	-	-	17:32	Hail>golfball
17:33:15	59.8	0.33	16.4	1.3	26		
17:34:49	61.1	0.28	18.7	0.1	3	17:35	Grape-size hail
17:36:17	57.1	0.48	28.9	1.7	34		
17:37:37	53.9	0.75	44.8	1.9	37	17:37	Grape/pea hail and light rain
17:39:05	53.9	1.52	72.3	3.7	66		
17:40:32	49.3	2.10	71.1	4.3	75		
17:42:07	41.7	2.14	87.5	0.1	2	17:42	Pea hail and light rain
17:43:27	28.5	1.36	50.3	-	-	17:45	Rain stopped

K_{DP} estimate of rainfall 6mm

Wedge gauge measured 8mm

These regions are seen at low-level, and on the south-east edge of the storms. They may well indicate a region of turbulence. The feature requires further investigation.

6.Acknowledgements

We are indebted to several people for assistance with the project. In particular, from the Alberta Research Council, C.Richmond, B.Kochtubajda, F.D.Barlow, M.Stanley-Jones, R.Morris, and members of the radar group, and from the University of Alberta, Dr R.Charlton. Dr R.G.Humphries gave us some of his own time to help check the calibration of the radar. We are also grateful for the support of the Atmospheric Environment Service both through its Western Region and through its Cloud Physics Research group. We also thank Red Deer College, Alberta Environment, and Alberta Hail and Crop Insurance for the use of data.

7.References

Al-Jumily K., R.B.Charlton & R.G.Humphries 1991: Identification of Rain and Hail with Circular Polarization Radar. *J. Appl. Meteorology,* **30** 1075-87

Chisholm A.J. & English M. 1973: Alberta Hailstorms *Met. Mono.,* **14** no 36, (Boston: AMS) 98pp

Crozier C.L.,P.I.Joe, J.W.Scott, H.N.Herscovitch & T.R.Nichols 1991: The King City Operational Doppler Radar: Development, All-Season Applications and Forecasting *Atmosphere-Ocean* **29** 479-516

English M.,B.Kochtubajda, F.D.Barlow, A.R.Holt, & R.McGuinness 1991: Radar Measurement of rainfall by differential propagation phase: a pilot experiment *Atmosphere-Ocean* **29** 357-380

Holt A.R. 1988: Extraction of differential propagation phase from data from S-band circularly polarised radars. *Electron Lett.* **24** 1241-2

Holt A.R. & Tan J. 1992: Separation of differential propagation phase and differential backscatter phase in polarisation-diversity radar. *Electron. Lett.* (in the press)

Humphries R.G. 1974: Observations and calculations of depolarization effects at 3GHz due to precipitation. *J.Rech. Atmos.* **8** 155-161

McGuinness R. & A.R.Holt 1989: The extraction of rainrates from CDR data. *Preprints 24th Conf. on Radar Meteorology, Tallahasse (Boston: AMS)* 338-41

Torlashi E., B.Pettigrew, & J.St-Pierre 1989: Circular polarization: Correction of propagation effects and comparison between radar fields and ground precipitation pattern *Preprints 24th Conf. on Radar Meteorology, Tallahasse (Boston: AMS)* 599-601

Wilson J.W. & W.E.Schreiber, 1986: Initiation of Convective Storms at Radar-Observed Convergence Lines *Mon. Wea. Rev* **114** 2516-36

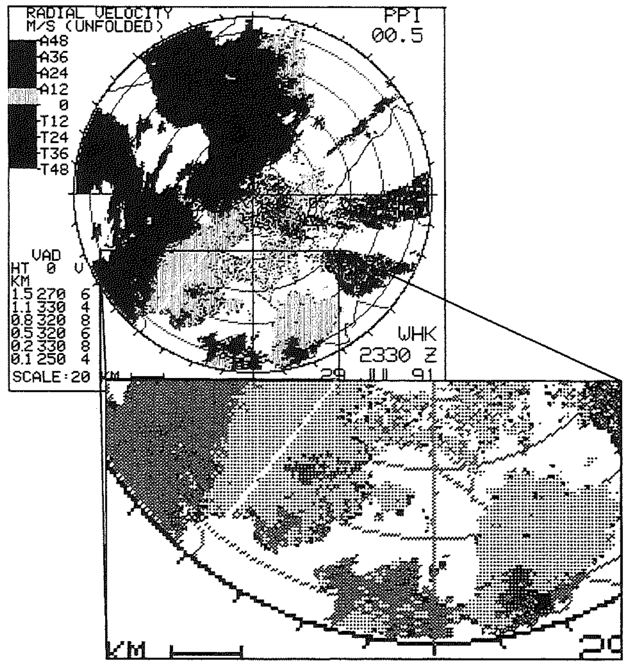

Fig 4: Map of radial velocity seen by AES radar at Carvel at 1720hrs. Range rings at 20km intervals.

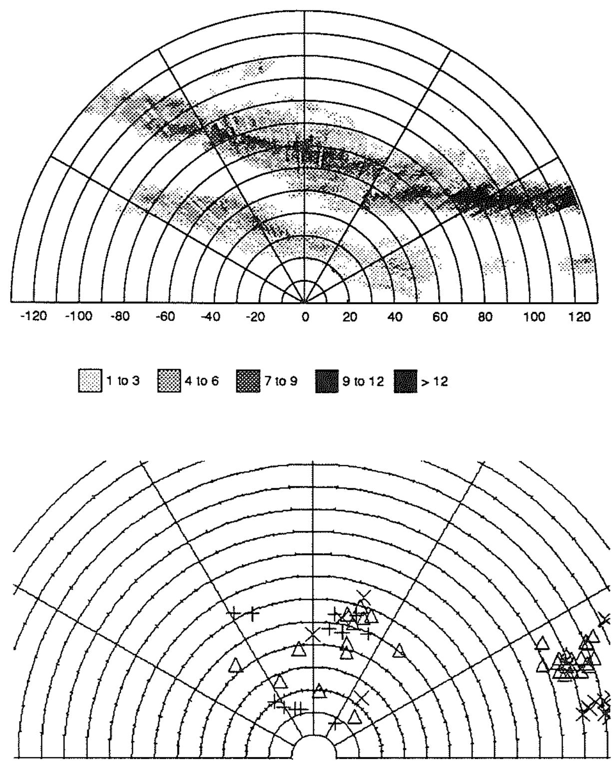

Fig 5.(a) Cumulative plot of locations where [Z > 45dBZ, Z_{DR} < 1.3dB, and ORTT < 60%] during period 1550-1850hrs. Density gives the number of times the criterion is exceeded at a given location.

(b) Locations at which hail was reported on the ground. See text for symbols.

THE ROLE OF BOUNDARY LAYER CONVERGENCE IN INITIATING DEEP CONVECTION IN A SEMI-TROPICAL ENVIRONMENT

J. C. Fankhauser, J. W. Wilson, G. B. Foote, C. K. Mueller
and C. G. Wade

National Center for Atmospheric Research [1]
Boulder, Colorado 80307

1. INTRODUCTION

Most of the work relating convection initiation to clear-air boundary-layer convergence lines is based on observations over the semi-arid High Plains of the United States (Wilson and Schreiber, 1984; Wilson et al., 1988; Fankhauser and Rodi, 1989). The Convection and Precipitation/Electrification Experiment (CaPE) conducted along Florida's east-central coast in the summer of 1991 (see Fig. 1) afforded the opportunity to study such correlations in a moist and generally more unstable semitropical environment. The ocean-land sea-breeze front is a recurring feature of the coastal circulation and its interaction with thunderstorm outflows and with convergence zones of other origins was a primary focus of the CaPE research. The daily development of sea-breeze fronts along both coasts accounts for a high frequency of thunderstorm days (15 to 20 in the months of July and August; Watson, 1990) and insured a plentiful number of research opportunities during the six weeks of field operations.

The case described here involves a westward moving sea-breeze front and an outflow boundary moving eastward across the peninsula. In addition to the enhanced convergence at the point where these boundaries eventually merged, convective rolls within the intervening air mass appear to influence the timing and location of earliest convective development. The study uses data from two Doppler radars, a surface mesonet, two aircraft, NCAR CLASS fixed and mobile rawinsondes, and rapid scan satellite imagery to investigate the evolving boundary layer structure leading to the development of deep convection. Dual Doppler radar data are used to delineate the position of air-mass boundaries and associated boundary-layer airflow structures while soundings and multilevel aircraft traverses provide the fine scale kinematic and thermodynamic structure across the convergence lines that separate them.

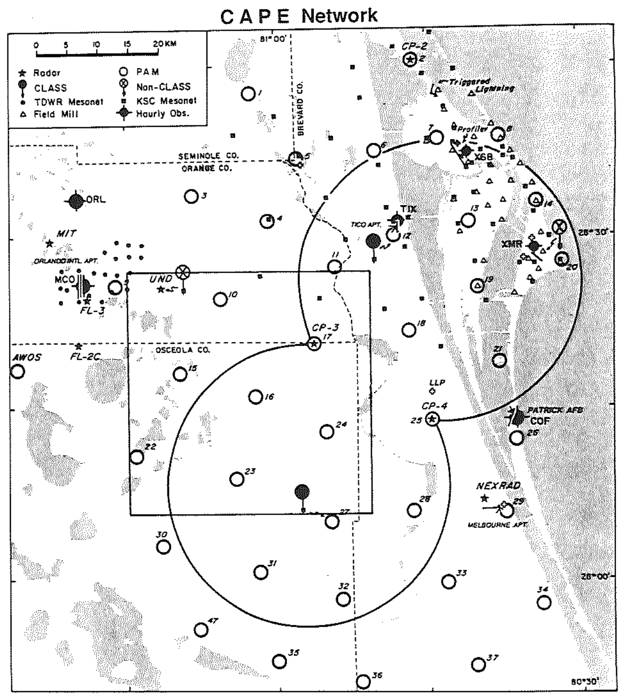

Figure 1. *CaPE mesonetwork situated along Florida's east-central coast. The legend at upper-left identifies various observing systems and shaded areas represent water bodies. Interlocking circles indicate region of optimum dual-Doppler scans from the NCAR CP-3 and CP-4 C-band radars. Square box shows location of grid in Fig. 2. (Figure courtesy of R. Wakimoto).*

2. MESOSCALE FEATURES

Shading in Fig. 2 represents radar reflectivity observed on a low level (EL. = 0.3°) PPI scan from the NCAR CP4 C-band radar (located at coordinates 0,0) at 2215 UTC on 2 August 1991. Two lines of enhanced reflectivity extending from north to south across the

[1] The National Center for Atmospheric Research is sponsored by the National Science Foundation.

grid mark the locations of converging eastward and westward moving air mass boundaries. The eastern line represents the east coast sea-breeze front which was moving westward at a speed of 3.5 m s^{-1} and at the time shown it was located some 30 km inland from the coast. Surface airflow behind the front was southeasterly at a speed of 3 to 5 m s^{-1} and it was comparatively cool ($\theta \approx 303$ K) and moist (mixing ratio, $q \geq 18$ g kg^{-1}).

Air approaching from the west had similar thermodynamic properties and may have originated as the west coast sea breeze, but as indicated by the high reflectivity cores evident over the northern part of the grid the air mass has been modified by downdrafts and outflow from earlier inland convection. The western air mass was spreading eastward at a rate of 4 m s^{-1}. The intervening air was warmer and drier ($\theta \approx 305$ K and $q \leq 17$ g kg^{-1}) than the converging air masses and airflow varied from southerly to southwesterly from east to west across this intermediate zone.

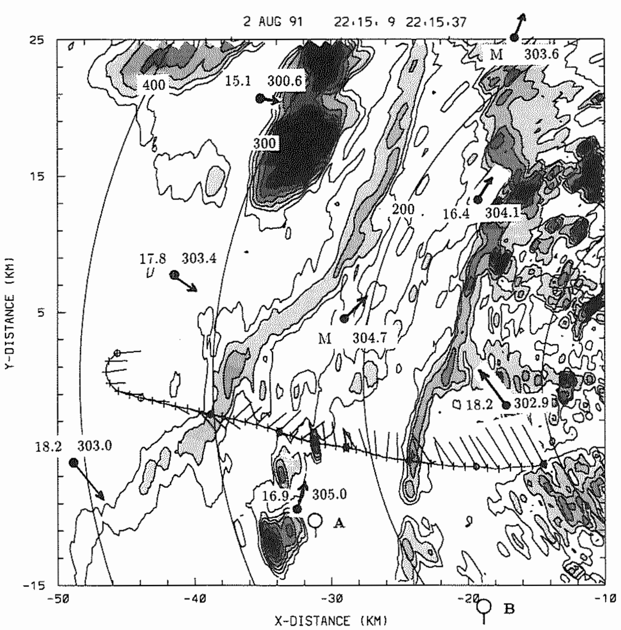

Figure 2. *PPI scan at 0.3° elevation at time indicated from CP-4 radar located at coordinates (0,0). Circular arcs labelled in meters show beam height above ground. Gray-shade represents reflectivity beginning at 0 dBZ and increasing in 5-dB steps. Dots with wind vectors designate locations of PAM mesonet sites with potential temperature and mixing ratio plotted on the right and left, respectively. Line segment with circles at 1-min intervals shows the flight track of the University of Wyoming King Air flown at 300 m AGL between 2212 and 2219 UTC. Wind vectors measured by the aircraft are plotted at 10-s intervals, originate on the track and point in the direction of airflow. Vector scale for both the mesonetwork and aircraft winds is 1 m s $^{-1}$ per km. Balloon symbols show locations of soundings made at ~2230 UTC and plotted in Fig. 3.*

Soundings made at the locations of the balloon symbols in Fig. 2 around 2230 UTC are plotted in Fig. 3. Temperature and moisture profiles indicate that the boundary layer was very well mixed within the intermediate air mass (Sounding A) where the adiabatic lapse rate had $\theta = 305$ K. In agreement with mesonet data in this sector, mixing ratio was around 17 g kg^{-1} in a shallow layer near the surface but decreased to ~14 g kg^{-1} just off the ground and retained that value upward through the boundary layer. The Lifted Condensation Level (LCL) for this air was 836 mb or ~1.6 km MSL. The air behind the sea breeze front was more moist (q ~16 g kg^{-1}), somewhat cooler and more stable with θ increasing from ~ 303 K near the surface to between 304 K and 305 K aloft.

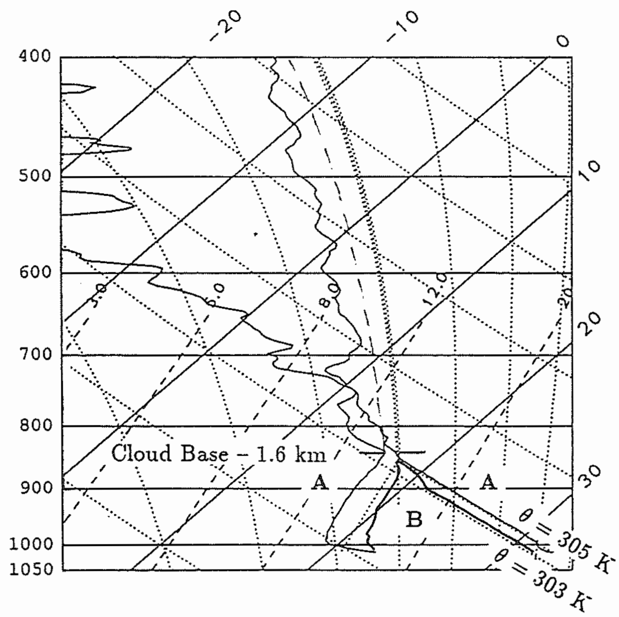

Figure 3. *Skew-T plots of soundings made at locations designated in Fig. 2. Sounding A represents conditions within the intermediate air mass and sounding B shows boundary layer profiles through the sea-breeze air mass. The moist adiabat passing through the LCL on sounding A is indicated as a dashed line.*

3. FINE-SCALE STRUCTURES

Horizontal wind vectors are plotted in Fig. 2 at 1-s intervals along the track flown at 300 m above ground level (AGL) by the University of Wyoming King Air (N2UW) between 2212 and 2219 UTC. Airflow at this level reflects surface conditions with transitions from southeast to south, through southwest to west northwesterly as the aircraft flew from east to west through the various air masses. It can be seen that the sharpest wind shifts occur at the boundaries between the air masses and at a zone of confluence near the middle of the intervening air mass. This is shown more graphically in the analog plot of wind direction illustrated with other kinematic and thermodynamic

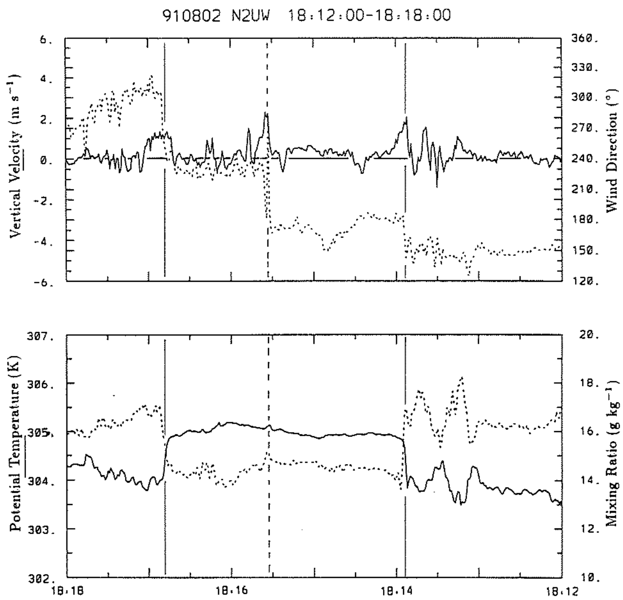

Figure 4. *Analog traces of vertical velocity (top, solid), horizontal wind direction (top, dashed), potential temperature (bottom, solid), and mixing ratio (bottom, dashed) measured between 1812 and 1818 LDT (2212 and 2218 UTC) at 300 m AGL along aircraft track plotted in Fig. 2. Note that time progresses from right to left to match east-to-west direction of flight.*

parameters in Fig. 4. A near instantaneous shift in wind direction from 150° to 180° occurs when penetrating the sea breeze front. At the confluence zone midway through the intermediate air mass a sharp shift from ~180° to ~230° is encountered and at the western air-mass boundary the shift is from ~240° to ~300°. Convergence concentrated in the windshift zones produces three distinct peaks in vertical velocity with the one near the middle of the intermediate air mass being the narrowest and strongest.

Thermodynamic variables in Fig. 4 clearly distinguish the three air masses and the sharpest gradients are found to coincide with the windshift zones. Potential temperature in the converging air masses is ~ 304 K and mixing ratio generally exceeds 16 g kg^{-1}. Air in the intermediate zone is well mixed horizontally and vertically since average temperature and moisture values across the zone (θ = 305 K and q = 14 g kg^{-1}) agree well with those found on the sounding made through this air.

A second aircraft (the NCAR King Air, N312D) simultaneously flew the track illustrated in Fig. 2 but at an altitude of 600 m. At that level a gradual shift from southeasterlies to southwesterlies was observed but neither the wind shears nor the thermodynamic gradients were as great as those illustrated in Fig. 4. Although horizontal velocity gradients at the upper flight level were not as large the vertical velocity peaks were stronger, particularly over the intermediate confluence zone where w $\geq$ 3 m s^{-1}. Potential temperature at the 600-m level in the intermediate zone was near 305 K which agrees with temperatures at the surface and at the lower flight level and supports the neutrally buoyant conditions found on the sounding in this sector.

The horizontal wind field at 2217 UTC derived from dual-Doppler radial velocities is given in Fig. 5 at an altitude of 400 m. The overall airflow characteristics at this level corroborate conditions at the surface and the lower flight level. As in Fig. 2 continuous lines of enhanced radar reflectivity coincide with wind shift zones at the leading edges of the advancing peripheral air masses. However, some spotty radar echo is also found along the intermediate confluence line and when horizontal air mass convergence is calculated from the wind field in Fig. 5 the strongest organized convergence is found to be concentrated along this line.

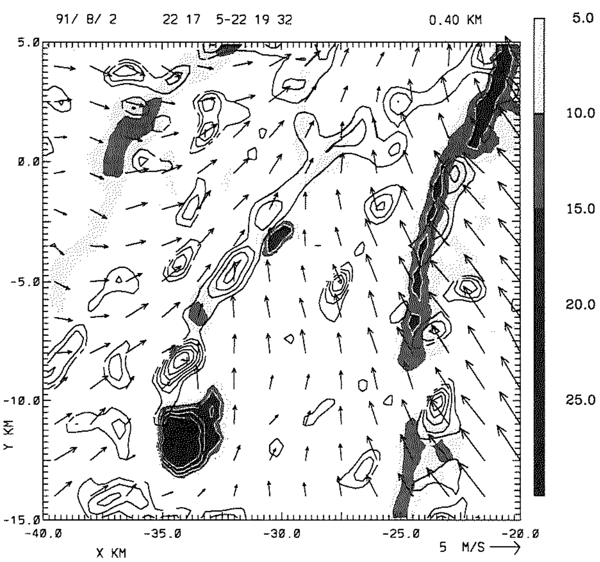

Figure 5. *Horizontal wind field at 400 m derived from radial velocity measured by the CP-3 and CP-4 radars at ~2217 UTC. Gray-shade represents radar reflectivity from CP-3 radar beginning at 5 dBZ and increasing in steps of 5 dB. Vector scale is given at lower right. Grid coordinates as in Fig. 2. Solid contours show horizontal air mass convergence ($\geq$ 1 x 10^{-3} s^{-1} at intervals of 0.5 x 10^{-3} s^{-1}).*

4. CONVECTIVE DEVELOPMENT

Conventional wisdom would predict that boundary layer forcing might be most favorable when the converging air masses eventually merge, which does not take place until $\geq$15 min after the time illustrated in Fig. 5. However, strongest radar echoes within the intermediate air mass in Fig. 5 are from precipitating convection which had already begun to form along the intermediate convergence line. Given the neutral stability and strong organized convergence in this sector this early development is not surprising. Major convective development eventually occurs with the merger of the opposing air masses, but from the standpoint of predicting the earliest convection in the present case it is the origin of the confluence line that becomes important.

Gray-shade in Fig. 6 represents reflectivity from a low level PPI scan at 2134 UTC, some 50 min prior to analyses presented above. As in Figs. 2 and 5 enhanced bands of reflectivity in the east central and extreme northwest sectors of the grid identify the advancing air masses discussed above. Also evident are bands of weaker reflectivity oriented from south southwest to north northeast within the intervening air mass. It is thought that these features result from the presence of horizontal convective rolls. Given a boundary layer depth of ~1.5 km their horizontal spacing (~ 5 km) matches theoretical expectations (Kuettner, 1971 and Lemone, 1973). In a study of thunderstorm initiation over the High Plains, Wilson et al. (1992) found that storms tended to form where convective rolls intersected a pre-existing convergence line. The focus of our ongoing research will be to investigate the importance of horizontal roll phenomena in preconditioning the boundary layer for deep convection in the present case.

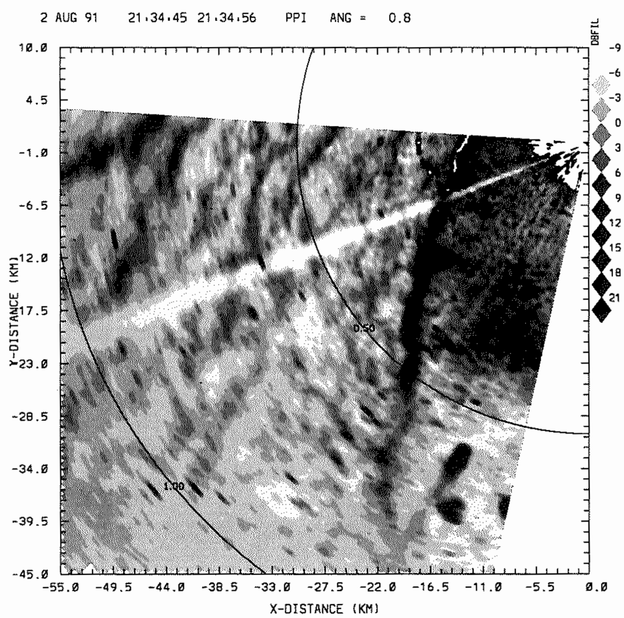

Figure 6. *PPI scan from CP-4 radar at 0.8° elevation at time indicated at top. Circular arcs labelled in kilometers show beam height above ground. Gray-shade represents reflectivity increasing from -9 to 24 dBZ in increments of 3 dB. Bands of highest reflectivity through the east-central and extreme northwest sectors identify air mass boundaries as in Figs. 2 and 5. Other bandedness over western portions of the intermediate air mass is believed to result from horizontal convective rolls.*

5. REFERENCES

Fankhauser, J. C., and A. R. Rodi, 1989: Kinematic and thermodynamic structure of radar-detectable clear-air boundary-layer convergence zones. Preprints, 24th Conference on Radar Meteorology, Amer. Meteor. Soc., Boston, 130-133.

Kuettner, J. P., 1971: Cloud bands in the earth's atmosphere: Observations and theory. *Tellus*, **23**, 404-425.

LeMone, M. A., 1973: The structure and dynamics of horizontal roll vortices in the planetary boundary layer. *J. of Atmos. Sci.*, **30**, 1077-1091.

Watson, A. I., 1990: Percentage frequency of thunderstorms at Kennedy Space Center. Unpublished figures and tables prepared by Mesoscale Research Division, NSSL, ERL, NOAA, Boulder, CO.

Wilson. J. W., G. B. Foote, N. A. Crook, J. C. Fankhauser, C. G. Wade, J. D. Tuttle, C. K. Mueller, and S. K. Krueger, 1992: The role of boundary layer convergence zones and horizontal rolls in the initiation of thunderstorms: A case study. *Mon. Wea. Rev.*, (in press).

Wilson, James W., James A. Moore, G. Brant Foote, Brooks Martner, Alfred R. Rodi, Taneil Uttal, and James M. Wilczak, 1988: Convection Initation and Downburst Experiment (CINDE), *Bull. Amer. Meteor. Soc.*, **69**, 1328-1348.

Wilson. J. W., and W. Schreiber, 1986: Initiation of convective storms at radar-observed boundary layer convergence lines. *Mon. Wea. Rev.*, **114**, 2516-2536.

ORGANIZATION OF CLOUD AND PRECIPITATION IN A SEVERE ALBERTA STORM

Gerhard W. Reuter[1] and Chi D. Nguyen[2]

[1] Dept of Geography, University of Alberta, Edmonton, Canada
[2] Climate Center, Louisiana State University, Baton Rouge, LA

1. INTRODUCTION

We investigate the organization of cloud and precipitation for the Alberta rain storm of 17-18 July 1986 that caused extensive flooding. A large area of western and central Alberta received in excess of 50 mm in 24 hours. Carrot Creek recorded 104.5 mm in 24 hours which was the greatest amount reported in the last 45 years The first two weeks of July 1986 had already substantial rain so that the ground was saturated, the catchments and storage basins full and the rivers high. When the 17-18 July storm dumped copious amounts of rain, the water masses could not be stored, resulting in wide-spread flooding of the North Saskatchewan, the Athabaska, the Red Deer rivers.

Satellite digital data, radar measurements and sounding data have been analyzed to document the evolution of this storm. The emphasis is on identifying the organization of cloud and precipitation and to relate this to the synoptic, mesoscale and convective circulations.

2. LEE CYCLOGENESIS

Nguyen (1987) examined the synoptic forcing for the Alberta storm, based on surface and upper-air charts. Only a brief summary is given here. The 500 mb height analysis valid at 0000 UTC July 16, 1986 indicated the presence of an upper-level low located near Port Angeles in Washington, USA (Fig. 1). Within the next 12 hours the cold low moved to central Washington at about 8 knots and deepened to 556 dam. During the next 24 hours, the cold low drifts slowly northeastwards filling back to 558 dam. When the upper cold low passed over the Rocky Mountain range (between 1200 UTC July 17 and 0000 UTC July 18) it deepened from 558 to 552 dam. This significant intensification is closely associated with surface cyclogenesis. The 0000 UTC 17 July surface map provides the first hint for some organization: A NW-SE trough is stretched from Central British Columbia to Southern Alberta with steadily falling pressures. By early morning (1200 UTC 17 July) a cyclonic circulation had developed around a 1001 mb low centred just south of Coronation. The cloud and precipitation area had expanded north of the centre, as north easterly upslope winds near the surface and over-running warm air aloft increased the flux of moisture into the system. By 1800 UTC the surface low had deepened rapidly to 996 mb in response to the vigorous positive vorticity advection to the east of the cold core. In phase with the cold-core intensification, the surface centre had reached its lowest pressure by 0600 UTC July 18. Thereafter the low entered a quiescent stage.

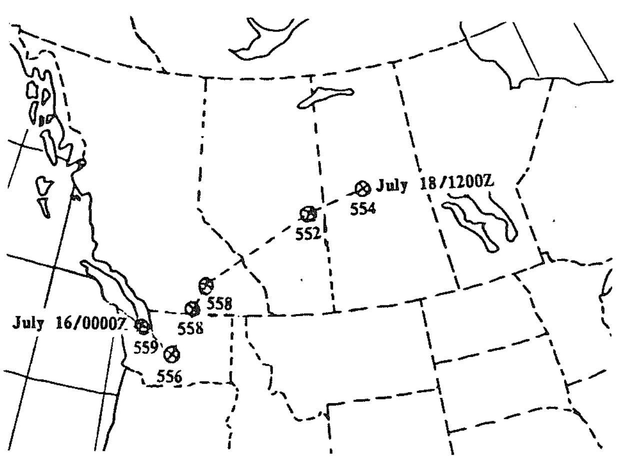

FIG.1. Twelve-hour interval track positions of the 500 mb low from 0000 UTC 16 July to 1200 UTC 18 July 1986. Geopotential height values are given in decameters.

3. ORGANIZATION OF CLOUD

Our classification of clouds is based on a simple scheme using digital data received from the polar-orbiting NOAA-9 satellite. This satellite moves in a sun-synchronous orbit at an average height of 865 km above the earth with a nodal regression of 25.51^0. The satellite carries on board an Advanced Very High Resolution Radiometer (AVHRR) instrument which provides imagery at five separate wavelengths. The resolution is 1 km. We received the data from the visible and infrared channel by processing the Automatic Picture Transmission (APT) signal.

The digital counts of the infrared data were converted to temperature values using standard infrared calibration techniques. The temperature field is presented by contouring isotherms. As the thermal gradients are very tight near the edges of the clouds, the relatively large contour interval of 20^{0}C is used. This judicious choice of "principal" isotherms roughly displays the three basic cloud types in their ascending hierarchy of elevation:

0^0C - low cloud (St, Sc, Cu)
-20^0C - middle cloud (As, Ac, Ns)
-40^0C - high cloud (Ci, Cs, TCu, Cb).

We did not attempt to convert the digital counts (DC) of the visible-wavelength data to absolute values of brightness. Instead relative brightness isopleths were chosen at a 20 DC interval, which resulted in a few classes of "equivalences" between brightness, cloud albedo and cloud

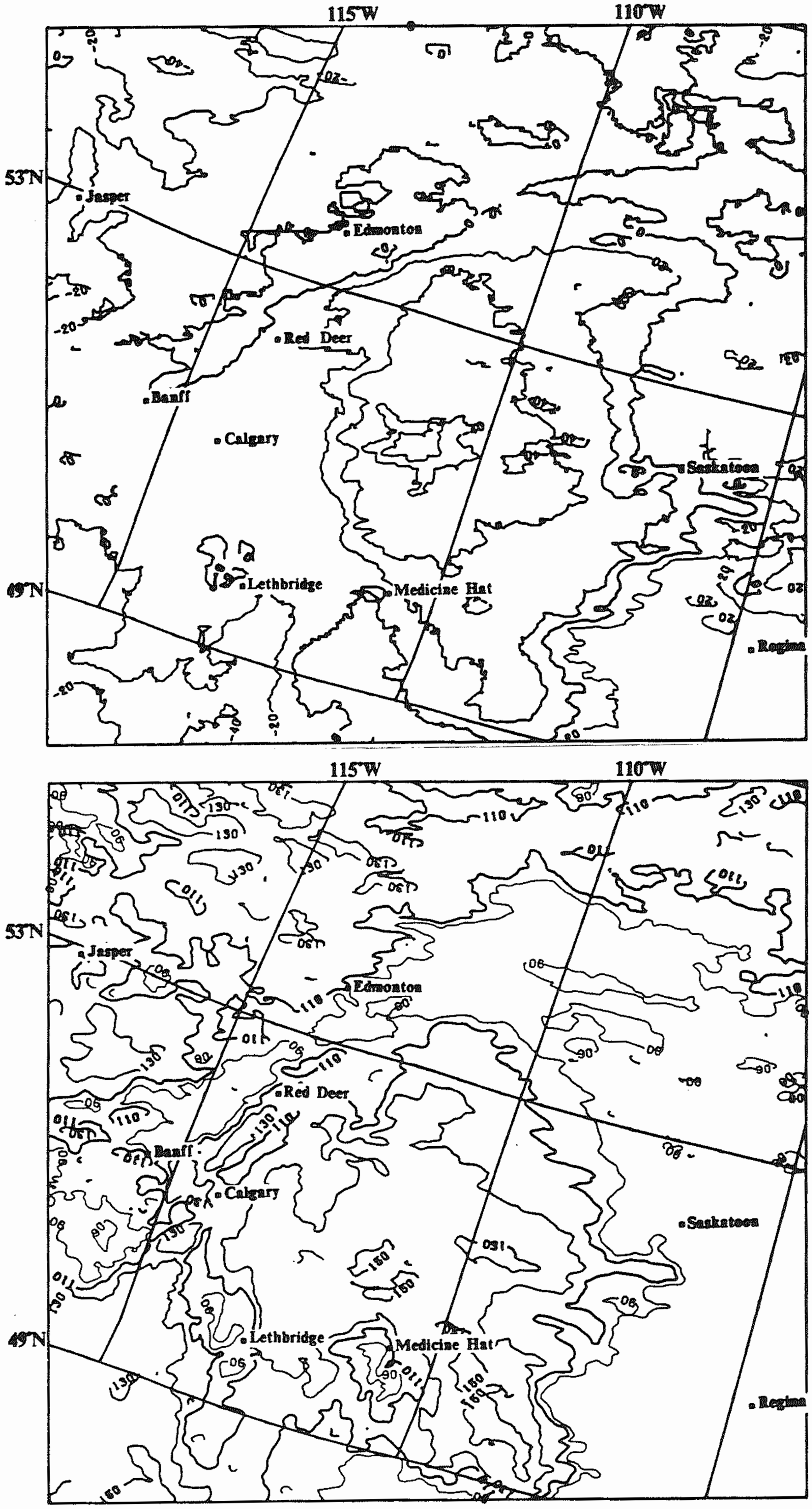

FIG. 2. Data collected during 2054-2110 UTC July 1986 by the NOAA-9 polar orbiting satellite. The temperature field (top) is contoured at -40, -20, 0 and 20 °C. The brightness field is contoured at 90, 110, 130 and 150 digital counts.

thickness:

90 DC - thin clouds broken or in patches
110 DC - opaque cloud layers
130 DC - solid cloud layer
150 DC - thick cloud or anvils of TCu and Cb.

Combining the information of the temperature and brightness fields, gives a practical aid for nephanalysis. Comparison with surface reports suggest our scheme is quite reliable, provided the ground has no snow-covered. Problems also arise with shadows cast by deep cloud towers.

Fig. 2 shows the temperature and the brightness fields as observed by the satellite at about 2100 UTC 16 July 1986. The cloud mass east of Calgary was "bright" on both infrared and visible images. This thick and very bright mass had cloud-top temperatures as low as -55°C, an indication that most of it extends right to the tropopause level. Judging by the synoptic reports from nearby weather stations, the cloud complex was made up of a thick layer of Ac and Acc, interspersed with TCu and Cbs. The "scalloped" western edge of this cloud mass (on the IR image) outlined individual convective cells. The cloud mass over Edmonton was bright in the visible range but had cloudtop temperatures only around -5^0C. Surface reports suggested layers of As and Sc. The isotherm and brightness patterns also hint at the formation of the comma cloud. The broad, warm sector in Saskatchewan narrows and curves westward toward Edmonton and Banff, indicating the presence of a southeasterly circulation in advance of the approaching cold low, and the influx of warm, moist air. The cloud edge east of Red Deer marks the incipient head of the comma cloud of the developing storm.

A similar analysis of the cloud cover was made at the maturing stage (2100 UTC 17 July) and the decaying stage (2100 UTC 18 July). The results have not been depicted here because of the four page limitations of the preprints. A detailed description can be found in Nguyen (1987).

4. PRECIPITATION BANDS

The C-band radar located at Carvel (about 100 km west of Edmonton) recorded the radar reflectivity patterns associated with rain field. Nguyen (1987) presents a time series of low-level scans. Significant rainfall started at about 1010 UTC in the western quadrant. New cells were generated on the southern flank of the echoes moved eastward. As the new cells intensified they tended to amalgamate with the main body of rain. By 1315 UTC rain fell over most of central Alberta with the heaviest precipitation to the south and west of the radar site.

In the next few hours the heavy precipitation became organized in a banded structure essentially in the north-south direction. By 1740 UTC two distinct parallel bands of heavy precipitation (> 15 mm/h) were formed and they remained distinct up to 2130 UTC, while drifting eastward. Throughout their life time, these bands were aligned in the direction of the windshear as observed from the sounding Stony Plain (20 km east of the radar site) at about 2340 UTC. The heavy precipitation core were about 10 km wide and the separating distance was 40-60 km. The two bands of heavy rain were aligned parallel to the direction of the wind shear as observed by the radiosonde.

5. SLANTWISE CONVECTIVE INSTABILITY

The upward air motion that produced the large rainfall rate was certainly larger than the synoptic-scale ascent associated with the baroclinic wave. Using the observations from a balloon sounding released at 2340 UTC 17 July from Stony Plain (20 km east of the radar site) at about 2340 UTC on 17 July, the potential of upright cumulus convection was examined. The profile of equivalent potential temperature (θ_e) indicated are stable conditions for cumulus instability except for two shallow layers of conditionally unstable stratification: 90-85 kPa and 80-75 kPa (Fig. 3). Furthermore, the Convective Available Potential Energy (CAPE) was about 50 J/kg which can hardly account for the radar echo intensity and observed rainfall amounts.

Since the heavy precipitation was banded in the direction of the mid-tropospheric flow (blowing from 220^0), we investigated the potential for Moist Symmetric Instability using the Richardson number criterion (Seltzer et. al. 1985; Reuter and Yau 1990). Provided the vertical component of the relative vorticity is small compared to Coriolis parameter, the flow of saturated air becomes unstable whenever

$$1 < (Ri)^{-1}$$

where Ri denotes the moist Richardson number. Ri is here defined by

$$Ri = (N_m / U_z)^2$$

where U_z is the vertical shear and N_m the moist buoyancy frequency given by

$$N_m^2 = \frac{\Gamma_m}{\Gamma_d} \frac{g}{\theta_{ref}} \frac{\partial \theta_e}{\partial z}$$

where θ_{ref} is a reference potential temperature, g the gravitational acceleration, z the altitude and Γ_d and Γ_m are the dry and moist adiabatic lapse rates, respectively.

When estimating the shear, the component of the wind parallel to the precipitation bands (220^0) has been used. The vertical resolution is 50 mb. The computed profiles of Ri, U_z and relative humidity (RH) are shown in Fig. 3. The airflow in the 60-40 kPa layer strong wind shear in excess of 5 $ms^{-1}km^{-1}$ was found. Within this sheared environment, Ri^{-1} exceeds 1 in the layers 60-55 kPa and 45-40 kPa, indicating the potential for slantwise convection. The release of this potential instability requires that the air becomes saturated. The presence of 100% relative humidity at 60 kPa suggests that moisture is available for condensation. Note that within the layer from 55 to 45 kPa, the air was close to its state of neutrality (Ri=1) for slantwise convection. This should allow for an organized slantwise ascent from 60 kPa to at least 40 kPa. Most likely, the circulation will extend beyond the 40 kPa layer due to slantwise overshooting of its level of zero slantwise buoyancy. This is consistent with infrared satellite data showing cloud top temperature values of about -50°C, which is the ambient temperature at about 200 kPa.

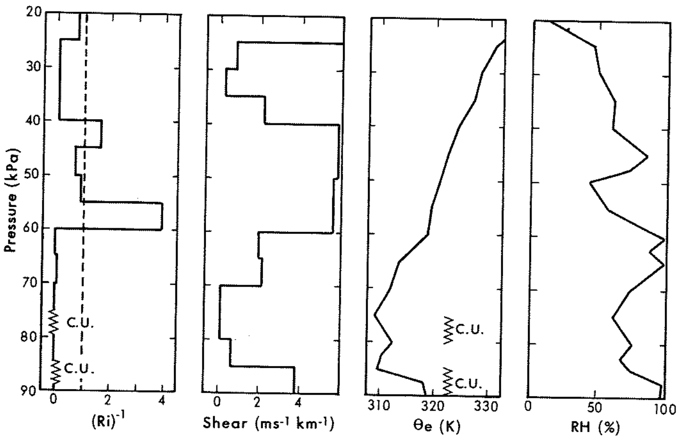

FIG. 3. Plots of the inverse Richardson number, the magnitude of the band-parallel wind shear, equivalent potential temperature and relative humidity as functions of pressure. The sounding is taken from the radiosonde at Edmonton Stony Plain (WSE) at 0000 UTC 18 July 1986.

6. CONCLUSION

This storm was a good example of the occurrence of summertime lee cyclogenesis driven by strong positive vorticity advection aloft. This synoptic event is rather seldom as it requires a strong upper cold low. The easterly airflow north of the cold low forced the airmass to lift over increasingly higher ground creating an extensive layer of nimbo-stratus clouds. Satellite imagery were analyzed and we found that the thick cloud layer was interspersed with "convective" outbreaks that reached up to the tropopause level.

The radar data showed large variations in the echo pattern. The strongest rain downpours occurred in two narrow bands pointing in the direction of major wind shear as estimated from a nearby sounding. The airmass was found to be stable for vertical convective instability, except for two very shallow layers that exhibited a decrease of equivalent potential temperature with height. However, the flow was unstable for moist symmetric instability in the region of large vertical wind shear. The slantwise instability most likely produced the observed series of roll circulations with the axis along the wind shear that produced the strongest rainfall rates. This case study confirms the notion that slantwise convection can contribute to heavy precipitation (Donaldson and Stewart 1989, Reuter and Yau 1990). Also it reaffirms the strength of combining satellite data, radar measurements, soundings and synoptic observations to examine precipitation formation.

We presently attempt to quantify the statistical significance of moist symmetric instability in producing rainfall over the Canadian Prairies for different seasons.

REFERENCES

Donaldson, N.R., and R.E. Stewart, 1989: On the precipitation regions within two storms affecting Atlantic Canada. Atmos. Ocean, **27**, 108-129.

Nguyen, C.D., 1987: Synoptic study of two intense cold-core cyclonic storms. M.Sc. Thesis, Univ. of Alberta, Edmonton, Canada, 176pp.

Reuter, G.W., and M.K. Yau, 1990: Observations of slantwise convective instability in winter cyclones. Mon. Wea. Rev., **118**, 447-458.

Seltzer, M.A., R.A. Passarelli and K.A. Emanuel, 1985: The possible role of symmetric instability. Mon. Wea. Rev., **42**, 2207-2219.

HAILSTONE SIZE DISTRIBUTIONS IN SOUTHWESTERN FRANCE

J. Dessens

Centre de Recherches Atmosphériques, 65300 Campistrous, France

1. INTRODUCTION

Hail is one of the rare notable meteors which is generally not the subject of any regular physical measurement. This lack does not favor the development of the knowledge of the phenomenon, in particular concerning its forecast. The highly hazardous character of hailfalls ("the lottery of hell", as they call it in Spain) is of course at the origin of their measurement.

In 1987, the "Association Nationale d'Etude et de Lutte contre les Fléaux Atmosphériques (A.N.E.L.F.A., i.e. The National Association for the Study and Prevention of Atmospheric Calamities) decided to set up a permanent network of hailfall ground measurement in the Southwestern departments which partake in the program of storm seeding from ground generators releasing silver iodide nuclei. The measurement network was set up progressively and will reach its final extension in 1992.

The results presented in this paper are concerned with the global distribution of the hailstones fallen on a large area during a day, a season or a year. This approach is different from the study of the distributions related to a point hailfall on a single station, because it smooths the effect of the dynamical sorting of the hailstones during their fall. The global distribution parameters are more likely to be correlated with the atmospheric environment than those of a point distribution.

2. DESCRIPTION OF THE MEASUREMENT NETWORK AND DATA PROCESSING

The method chosen for the ground measurement of hailfalls was developped in Alberta by Lozowski and Strong (1978). It consists in setting horizontally 1.5 m above the ground an extruded polystyrene pad whose area, measuring 1044 cm^2, approximately corresponds to the A3 paper. The pads are protected against solar radiations by a coat of white lacquer paint. After the hailfall, the impact dents are revealed by a black inking made with a ink roller. For the calibration of the pads, steel balls of various diameters are released from different heights. The detailed operational procedure of this method was described by Admirat (1987).

The processing of the pads is semi-automatic. The pads are photocopied on ordinary A3 paper and the smallest diameter of each impact is measured with a digitizer linked to a computer. The summation of the number of hailstones, by ranges of 0.2 cm of diameter, from 0.5 cm on, is automatic. After several investigations, this semi-automatic technique is, for the moment, prefered to a determination by computer of the hailstone shapes. Only one technicist is in charge with the pad analysis, which insures a better data homogeneity.

In 1991, the network was composed of 830 hailpads distributed over an area of about 40,000 km^2 spreading North of the Pyrenees from the Atlantic Ocean to the Mediterranean Sea. The network is not homogeneous since it approximately coincides with the ground generator network whose density varies according to the interest taken in hail in the various zones of the area. In practice, the network mesh insures the proper recording of any significant hailfall and avoids the redundant information that a tighter network would give. The scientific aims to be expected from the operating of this network must, of course, take account of its structure. Sharp studies of the hailfalls will thus be possible only in the areas of intensified density such as those located around Cognac, Mont-de-Marsan and Toulouse.

3. NORMALIZATION OF THE RESULTS

It is admitted that, except for the smallest hailstones which are likely to be systematically undercounted, the hailstone size distributions deduced from the hailpad measurements follow an exponential form (Crow *et al.*, 1979). The same result is found in Southwestern France, and we will see that the exponential form is all the better observed since it corresponds to a greater number of hailpads hit. The real distribution deviates notably from an exponential distribution only for the smallest and largest hailstones :

- For the minor diameters, the real distribution deviation is visible in the 0.5-0.7 cm range. The processing of an ordinary hailfall simulated with steel balls shows, indeed, that about 10 % of the impacts of the 0.6 cm balls are not found on the pad because their dents are covered with those of the bigger hailstones.

- For the major diameters, the deviation is observed to start with the diameters for which the mean number of hailstones for each measurement range is smaller than 1 per pad, that is to say about 10 per m^2. It is obvious that the hailspads are not adapted to the counting of such hailstones.

The dimensional distribution parameters will thus be calculated with the data corresponding to the hailstones of the 0.7-0.9 cm, 0.9-1.1 cm, ... ranges, up to the range for which it is still possible to find an average of at least 1 hailstone per pad.

The exponential relation most often used to represent a dimensional distribution of raindrops or hailstones is the following :

$$\Delta N/\Delta D = N_0\, e^{-\lambda D} \quad (1)$$

ΔN is the number of hailstones whose diameter ranges from D to D + ΔD. λ is the slope of the regression line, and N_0 is defined by the intersection between this line and the ordinate axis. N_0 is the theoretical number of hailstones (or rather of particles) with a 0 diameter, thus corresponding physically to nothing.

Since the regression is established with hailstones having a 0.8, 1, 1.2, ... cm diameter, N_0 would be extrapolated with the regression outside the measurement range. In fact, the corresponding values of N_0 would be strongly correlated with λ and this artificial correlation would conceal any weaker, although real, correlation with meteorological parameters. For this reason, it seems, more judicious to use an equation of the type suggested by Crow *et al.* (1979) :

$$\Delta N/\Delta D = N_{D_{min}}\, e^{-\lambda(D-D_{min})} \quad (2)$$

where $N_{D_{min}}$ represents the number of hailstones in the first range, fitted to the regression.

The form of the exponential distribution finally chosen for the standardization of the hailpad data in southwestern France is thus :

$$N = N_{0.8}\, e^{-\lambda(D-0.8)} \quad (3)$$

The correlation coefficient r will be noted in each case, since it checks the validity of the approximation to an exponential distribution.

4. HAIL DAY DISTRIBUTIONS

Table 1 gives the mean hailfall parameters for the days when at least 5 hailpads were hit by hailstones with diameters over 1 cm in either the Atlantic zone (AT) or the Midi-Pyrenees (MP) zone. The recent installation of the hailpads in the Méditerranean zone does not yet enable the presentation of significant results. The hailfall parameters are the following :

- Maximum diameter measured on a pad, D_{max},
- Mean maximum diameter for all the pads, $\overline{D}_{max}$,
- Mean mass of the hail for all the pads, M,
- Mean kinetic energy for all the pads, E,
- Distribution parameters for all the pads, $N_{0.8}$, λ and r

The right-hand side column gives the altitude of the 0°C isotherm, according to the radiosounding made at Bordeaux at 12.00 UTC.

It can be noticed that the correlation coefficient of the exponential regression is excellent, except for August 31. A close examination of the data for that day shows

Table 1 : Characteristics of the main hail days during the years 1987 to 1991 in the Midi-Pyrénées (MP) and Atlantic (AT) areas.

Year (number of hailpads)	Date	Area	Number of pads hit	D_{max} (cm)	$\overline{D}_{max}$ (cm)	M (kg)	E (J/m2)	$N_{0.8}$ (cm-1m-2)	λ (cm-1)	r	h0°c (km)
1987	4 Jul.	MP	5	1.35	1.13	0.115	8.4	867	6.72	0.999	4.0
(100)	31 Aug.	MP	6	2.64	1.48	0.917	113.3	2412	2.92	0.946	4.0
1988	2 May	MP	11	3.59	1.54	0.388	59.0	879	3.37	0.975	2.0
(350)	19 Oct.	MP	6	2.15	1.50	1.219	123.5	4173	4.70	0.974	2.4
1989	9 Jun.	MP	5	1.70	1.30	0.239	22.2	981	3.53	0.991	3.0
(648)	6 Jul.	AT	39	2.40	1.29	0.355	39.0	1815	3.58	0.968	4.0
	23 Jul.	MP	11	4.07	2.01	1.190	207.8	1777	2.12	0.996	4.1
	-	AT	9	1.76	1.31	0.622	65.1	2141	2.78	0.997	4.1
	16 Aug.	AT	8	1.44	1.29	0.220	18.6	1556	4.62	0.977	3.7
	19 Aug.	AT	5	1.17	1.09	0.140	10.6	1438	7.17	0.997	3.9
1990	6 Apr.	MP	13	1.68	1.25	0.889	66.7	7111	7.37	0.999	1.9
(730)	17 May	MP	20	2.47	1.31	0.628	54.6	3649	5.24	0.998	3.2
	13 Aug.	MP	11	1.45	1.24	0.270	20.0	1572	5.68	0.999	3.8
	-	AT	9	2.85	1.68	0.571	68.3	1878	3.18	0.986	3.8
	24 Aug.	AT	5	2.51	1.71	0.823	79.4	4510	4.66	0.979	3.9
1991	5 Apr.	AT	12	1.66	1.21	1.056	79.0	5588	5.81	0.999	1.3
(830)	31 May	AT	5	1.76	1.29	0.430	37.9	2682	4.97	0.973	2.7
	21 Jun.	MP	13	3.64	1.97	0.795	110.1	2976	3.85	0.999	4.0
	5 Jul.	AT	10	2.61	1.41	0.490	44.1	2750	6.31	0.998	3.3
	31 Aug.	AT	15	3.33	1.70	0.767	79.4	3872	4.63	0.998	3.7
	10 Sept.	MP	8	2.77	1.70	0.550	72.2	1879	3.74	0.993	3.6

Table 2 : Correlations between the parameters of a hail day as calculated from the data of Table 1.

	D_{max}	$\overline{D}_{max}$	M	E	λ	$N_{0.8}$	$h_{0^\circ C}$
$N_{0.8}$	- 0.04	+ 0.01	+ 0.56	+ 0.30	- 0.04		- 0.54
λ	- 0.61	- 0.62	- 0.26	- 0.53		- 0.04	- 0.33

that the pad of Latoue, 21.00, is very different from the other 5, so that the mean distribution represents correctly neither the pad of Latoue not the other 5.

Table 2 presents the correlation coefficients between $N_{0.8}$ or λ and various parameters. For a sample of 21 couples of data, the significance level reaches 0.01 for $r = 0.52$. The results give rise to the following comments.

- Correlation between D_{max} or $\overline{D}_{max}$ and $N_{0.8}$ or λ : obvious results, since it can be seen from (3) that the observed maximum diameter is nearly in direct relation with log $N_{0.8}$ and in opposite relation with λ.

- Correlation between M and D_{max} or $\overline{D}_{max}$, and between λ and E : computing M and E by integration of (3) also shows that these correlations are obvious.

- No correlation between $N_{0.8}$ and λ : this results suggest that the significant correlations found by others (Cheng and English, 1983) probably resulted from the artifact in the determination of N_0 with the regression itself (Note for example that $\log N_0 = \log N_{0.8} + 0.8\ \lambda$).

- Correlation between $N_{0.8}$ or λ and $h_{0^\circ C}$: it is known that the melting of hailstones between the 0°C level and the ground can strongly modify the distribution. From our data, the linear fitting between $N_{0.8}$ and λ is:

$$N_{0.8} = 6217 - 1052\ h_{0^\circ C},\ h_{0^\circ C} \text{ in km},$$

while there is no significant correlation between λ and $h_{0^\circ C}$.

This regression between $N_{0.8}$ and $h_{0^\circ C}$ is consistent with the determination of the $N_{0.8}$ variations due to melting made according to the Ludlam hypotheses (1980). By contrast, the λ variations are found to be small.

The mean values of $N_{0.8}$ and λ as computed from Table 1 lead to the following size distribution :

$$N = 2691\ e^{-4.62\ (D-0.8)}, \qquad (4)$$

with a corresponding mean value of 3.35 km for $h_{0^\circ C}$. This distribution may be considered as a standard for Southwestern France.

5. YEARLY AND SEASONAL DISTRIBUTIONS

A total of 335 pads have been examined for the two zones during the period 1987-1991. The yearly distributions are presented in Table 3. The 1989 and 1990 values for Midi-Pyrenees are very different from the other yearly values in this zone. The high $N_{0.8}$ values in 1990 may be partly explained by the fact that 46 out of the 63 hailfalls for that year occurred in April and May, when the 0°C level is at a low altitude.

The mean values of $N_{0.8}$ for the whole period are similar in the two zones, but the mean value of λ is greater in the Atlantic zone.

The seasonal distributions are given in the table 4 for a total of 356 pads hit in the two precedent zones and in the Mediterranean one. The values of $h_{0^\circ C}$ are computed from the mean temperatures at Bordeaux. The seasonal variations of $N_{0.8}$ with $h_{0^\circ C}$ corroborate the daily variations.

In a general way, it can be noticed that the exponential distribution is perfectly adapted to the real distribution of the hailstones, and this is all the more accurate since the distribution is calculated on an important number of pads.

6. CONCLUSION

The main result of this study is that there is no correlation between the 2 parameters of the exponential form which represents a distribution of the hail of the ground, provided that the parameter related to the absolute number of the hailstones is not calculated by extrapolation, far from the range of the real dimensions of the hailstones. The two parameters $N_{0.8}$ (number of hailstones with a 0.8 cm diameter) and λ (slope of the fitting line) thus are the two significant parameters of a hailfall.

$N_{0.8}$ being significantly correlated to $h_{0^\circ C}$, the altitude of the 0°C isotherm, the standard distribution of a hailfall on the ground in Southwestern France must be given taking into account this correlation :

$$N = (6217 - 1052\ h_{0^\circ C})\ e^{-4.62\ (D-0.8)}$$

The correlation between $N_{0.8}$ and $h_{0^\circ C}$ corroborates the hypotheses made by Ludlam (1980) for the melting of hailstones during their fall. By contrast, the melting effect on λ is secondary, which is also in agreement with the Ludlam hypotheses.

The mean values of $N_{0.8}$ along the Atlantic and in the inner zone are similar, but the mean values of λ are greater along the

Table 3 : Yearly hailstones diameter distributions in the Midi-Pyrénées (MP) and Atlantic (AT) areas and in both areas (MP + AT). n is the number of pads hit and r is the correlation of the best-fitting exponential distribution $N = N_{0.8}\, e^{-\lambda(D-0.8)}$.

Year	MP				AT				MP and AT			
	n	$N_{0.8}$	λ	r	n	$N_{0.8}$	λ	r	n	$N_{0.8}$	λ	r
1987	16	2467	4.33	0.983	0				16			
1988	28	2892	4.60	0.989	3				31	2926	4.78	0.992
1989	34	2217	2.92	0.998	75	2391	4.64	0.995	109	2238	3.83	0.998
1990	63	4460	6.36	0.998	28	3477	4.70	0.988	91	4482	6.14	0.999
1991	29	3230	3.85	0.998	59	3499	4.96	0.999	88	3311	4.42	0.999
5 years	170	2951	4.18	0.997	165	3140	4.97	0.999	335	2958	4.45	0.999

Table 4 : As in Table 3 except for all areas (including the Mediterranean area) and for seasons.

Saison	n	$N_{0.8}$	λ	r	$h_{0°C}$
D - F - J	9	6967	7.91	0.947	0.9
M - A - M	95	4558	6.33	0.999	1.9
J - J - A	213	2187	4.01	0.998	3.0
S - O - N	39	4147	4.15	0.992	2.1
Year	356	3129	4.73	0.999	2.6

Atlantic (less large hailstones). It would be important to confirm this result which may have implication with the growing process of hailstones in a maritime atmosphere. More generally, it will be interesting to consider the distributions which deviate the most from the standard distribution in order to analyse the associated meteorological parameters.

REFERENCES

Admirat, P., 1987 : Grêlimétrie 1987. Rapport de synthèse, Convention ANELFA/S2A 8701.

Cheng, L. and M. English, 1983 : A relationship between hailstone concentration and size. *J. Atmos. Sci.*, 40, 204-213.

Crow, E.L., A.B. Long, J.E. Dye and C.W. Ulbrich, 1979 : Results of a randomized hail suppression experiment in northeast Colorado. Part III : Analysis of hailstone size distributions for seeding and yearly effects. *J. Appl. Meteor.*, 18, 1559-1568.

Lozowski, E.P., and G.S. Strong, 1978 : Further reflections on the calibration of hailpads. *Atmosphere-Ocean* , 16, 69-80.

Ludlam, F.H., 1980 : Clouds and storms. The behavior and effect of water in the atmosphere. The Pennsylvania State University Press, University Park and London, 405 pp.

Analysis of Hailstorm and Hailstones

Guo Enming Tu Dubin Liu Yanggang Ma Deming
(Institute of Weather Modification, AMS, Beijing 100081 PRC)

Gong Fujou Yang hejun
(ShenYang Regional Central Meteorological Research Institute, ShenYang, PRC)

ABSTRACT

With 3cm radar echo, radiosonde and stone photographs, analysis is made of hailstone occuring at Shuizhong, Liaoling on ser.4,1989. Combined with other observations a hailstorm model is formalated. In addition using QUANTIMET 900, the squares, length, width and perimeter are measured. The hailstone size distribution could be fitted with gamma distribution.

1. INTRODUCTION

A cold–tough appeared on 08:00 500 hpa weather map over Hebei and Inermogonia. At 14:00, the surface cold front was near Huhehaote Region. Thunders occured in the warm sector, located over Beijing–Tianjin–Shandong sea shores. On 14:00 Noaa–10 satellite graph, a mass of clouds occured over Beijing–Tianjin–Shandong sea shores, and the thunderstorms and hailstorms could be clearly identified, which was the hailstorms falling stones in vicinity of ShueiZhong, LiaoLing.

2. ATMOSPHERIC STABILITY

A radiosonde was launched at 06:33 locally; the results are shown in Fig1. It is shown that there is a temperature inversion in lower atmosphere; there is a stability energy layer below 850hpa and above 380hpa, but a unstability energy layer between 850–380hpa. The wind field shows 5 ms^{-1}at 293 ° angle on 850hpa, increasing to 6 ms^{-1}at 276 ° on 600hpa and then falling down to 5 ms^{-1}at 260 ° on 400hpa, but increasing again on 300hpa (21ms^{-1}at 273 °). Fig.1 also shows a gradual

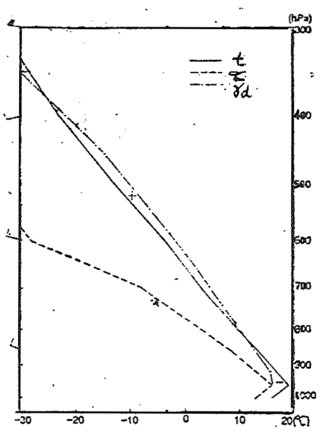

Fighre1. Atmospheric vertical structure

unstability intensifying from morning, up to 279.37 $J.Kg^{-1}$. This weather condition is helpful for the hailstorms.

3. SURFACE OBSERATIONS

At 13:00 here existed strong cumulus moving toward the station, the anvil developing fast. At 14:08, a little stone falling occured but stoped in short time and rain begans. At 14:15 stone began agin, and after 23minutes, rain again substitute stone.

4. RADAR ECHO

Radar observations is consistent with the above results. Apart from the common echo features (void, anvil etc). We should point out a remarkable feature: V–echo in RHI whish could be another criteria judging the hailstone falling. (see Fig.2)

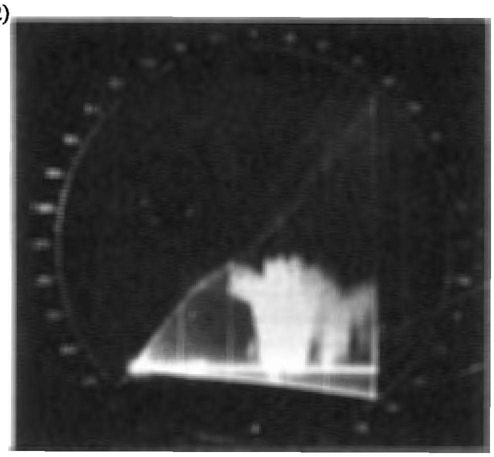

Figure2. Radar echo

5. CONCEPTUAL MODEL of HAILSTORMS

Fig.3 is given as graphial show of conceptual hailstorm model, which is based on the integration of various observations. As shown in Fig.3 the cloud top is about 11000m (–45 ° c temperature); echo top is about 9000m; the strong echo top is about 6000m; the 0 ° c–level is 4000m; strong up current occures in the front but the down current in the hail and / or

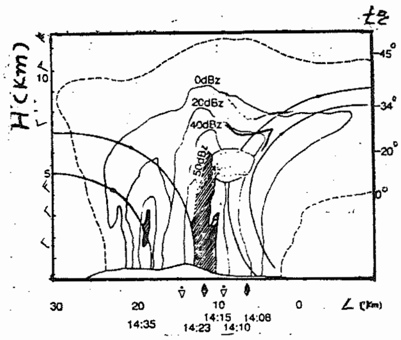

Figure3. Conceptual hailstorm model

rain region. The maximum hail density area covers about 1000 × 500.Squre meters.

6. MICROPHYSICAL FEATURES

A classifications of hailstone shapes and the hail emblrgos have been done and given in Table 1. Table 2. respectively.

Table 1. Stone Shape Frequency

Number / Shape	1	2	3	4	Total	%
Cone	11	14	18	4	47	6.8
Ellipse	6	9	5	5	25	3.6
Sphere	38	145	202	234	619	89.6
Total	55	168	225	243	691	100

Table2. Embryo Frequency

Kinds	freezendrop	graupel	multi–nuclei	Total
Count	57	632	2	691
%	8.2	91.5	0.3	100

7. STONE SHAPE PARAMETERS

Using Q–900, the length, width, square and perimeter, etc. of every stones are obtained, and shown in Table 3.

Table3. Shape Parameters

Parameter	Surface area mm^2		Length mm		Width mm		A	
Value	max.	min.	max.	min.	max.	min.	max.	min.
	136.2	49.6	17.5	12.1	15.6	10.5	1.21	1.03

In table 3, A represents "circularity" which is defined as:

$A = \frac{L^2}{4\pi S}$ in which L is perimeter; S is surface area. Apperantly for spheres A is equal to 1.

8. SIZE DISTRIBUTIONS

Four sets of hail size distributions are analysed, which reveals that the gamma distribution $n(D) = N_0 D^{\mu} e^{-\Lambda D}$ could be best approximation and the cases all have a large μ value see Fig.5.

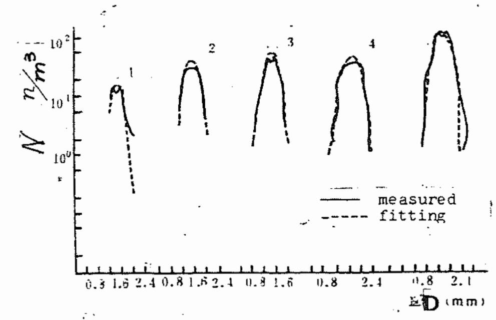

Figure4. Stone size distributions

Their corresponding fitting curve as.

$n_1(D) = 2.34 \times 10^{20} D^{7.33} \exp(-48.8D)$

$n_2(D) = 3.66 \times 10^{14} D^{37.29} \exp(-30.37D)$

$n_3(D) = 6.07 \times 10^{12} D^{29.72} \exp(-25.64D)$

$n_4(D) = 2.81 \times 10^{8} D^{17.87} \exp(-15.58D)$

References (Omitted)

On Vortex Formation in Multicell Convective Clouds in a Shear-Free Environment

Alan Shapiro
Center for the Analysis and Prediction of Storms
University of Oklahoma, Norman, Oklahoma, USA 73019

Yefim L. Kogan
Cooperative Institute for Mesoscale Meteorological Studies
University of Oklahoma, Norman, Oklahoma, USA 73019

1. Introduction

The development of storm rotation has been a subject of intense interest in the meteorological community in recent years. Observational and numerical modeling studies suggest that a prime environmental condition favoring vortex formation is a pronounced vertical wind shear, especially at low levels. For example, the analytical model of Rotunno (1981) and the numerical cloud model simulations of Klemp and Wilhelmson (1978) and Schlesinger (1978) revealed that an updraft growing in the presense of vertical wind shear tends to split into two counter-rotating vortical updrafts which propogate to the left and right of the wind shear vector.

However, ample observational evidence suggests that interactions between convective updrafts and downdrafts, as well as storm inflows and outflows are also important factors in vertical vorticity generation. In many cases atmospheric vortices form in regions of strong horizontal gradients of vertical velocity such as in the interface between a convective storm's main updraft and its rear flank downdraft (e.g., Lemon and Doswell, 1979) and are not necessarily related to the mesoscale circulation of a parent storm (Davies-Jones, 1985).

While most numerical cloud modeling investigations have focused on single-cloud evolutions in complex environments (e.g., vertically varying wind shears), relatively little work has been devoted to the modeling of multicell clouds. In this paper we examine the structure of a developing three-cloud system in a shear-free environment. A significant result is the production of vertical vorticity and vertical motion as a consequence of cloud-cloud interactions.

2. Model description and initialization

We now briefly summarize some of the more important aspects of the model. Detailed descriptions of the equations, boundary conditions, discretizations and numerical solution techniques can be found in Kogan (1991).

The model's dynamical equations are the nonhydrostatic anelastic equations of motion with the Coriolis force neglected. Sub-grid scale mixing is parameterized with a conventional Smagorinsky formulation. The microphysical description is based on the prediction of local size distribution functions for cloud condensation nuclei (19 categories from 0.0076 to 7.6 μ) and cloud/rain drops (30 categories from 4 to 3250 μ). Warm rain processes include nucleation, condensation/evaporation, coalescence, breakup and sedimentation. The model does not, at present, include an ice phase.

The computational domain consists of a large Cartesian grid of 50 x 50 horizontal points and 30 vertical levels on which the dynamical variables are carried and a smaller grid of 30 x 30 x 25 points enbedded in the larger grid on which both dynamical and microphysical variables are carried. Both grids have a uniform horizontal and vertical grid spacing of 250 m.

The simulation described in this paper was deliberately idealized to facilitate analysis of the physical mechanisms involved in multicell cloud interactions. With this in mind we initially specified three thermal perturbations or "bubbles" of equal strengths and dimensions. The vertical depth of each bubble was 2.0 km with a maximum strength of 1° C reached at z = 1.0 km. The e-folding bubble radius was ~ 0.75 km. In plan form the bubbles mark the vertices of a (nearly) equilateral triangle 2.5 km on a side.

The idealized thermodynamic profile employed in this study was quite moist and unstable from low to mid-levels with vigorous convection anticipated in the model run. An inversion layer imposed at 4 km served as a natural upper boundary on updraft growth about 2 km below the upper boundary of the integration domain.

3. Results

The hot air bubbles imposed in the model's initial state immediately began to rise and, by 200 s, reached their condensation level. The formation and merger of the individual clouds is apparent in the horizontal cross-sections of the velocity field depicted in Figs. 1 - 3 for 600, 1200 and 1800 s.

Typical pre-merger updrafts were ~ 0.75 km in radius with maximum vertical velocities of ~ 10 m/s. A peak value of ~ 17 m/s occurred at 1200 s at 3.0 km (not shown). An asymmetric inflow into each of the individual clouds was indicated on the 0.75 km level. At 600 s the 1.75 km level was characterized by outflow. At later times the outflow layer began at higher elevations, indicating that the clouds and their associated in-up-out circulations had developed vertically.

These figures also revealed counter-rotating vortices on the periphery of the updrafts. At 1200 s these vortices were ~ 1 km deep and strongest at the 1.75 km level (Fig. 2(b)). At 1800 s the clouds merged and the vortices intensified and moved up to the 2.75 km level (Fig. 3). Figs. 4 and 5 depict the vertical vorticity and the tilting term of the vertical vorticity equation at 1200 s on the 1.75 km plane. Peak vorticity values of $\pm$ 0.004 s^{-1} were colocated with the vortex circulation centers. A high correlation was apparent between the vertical vorticity and tilting fields at this time and elevation.

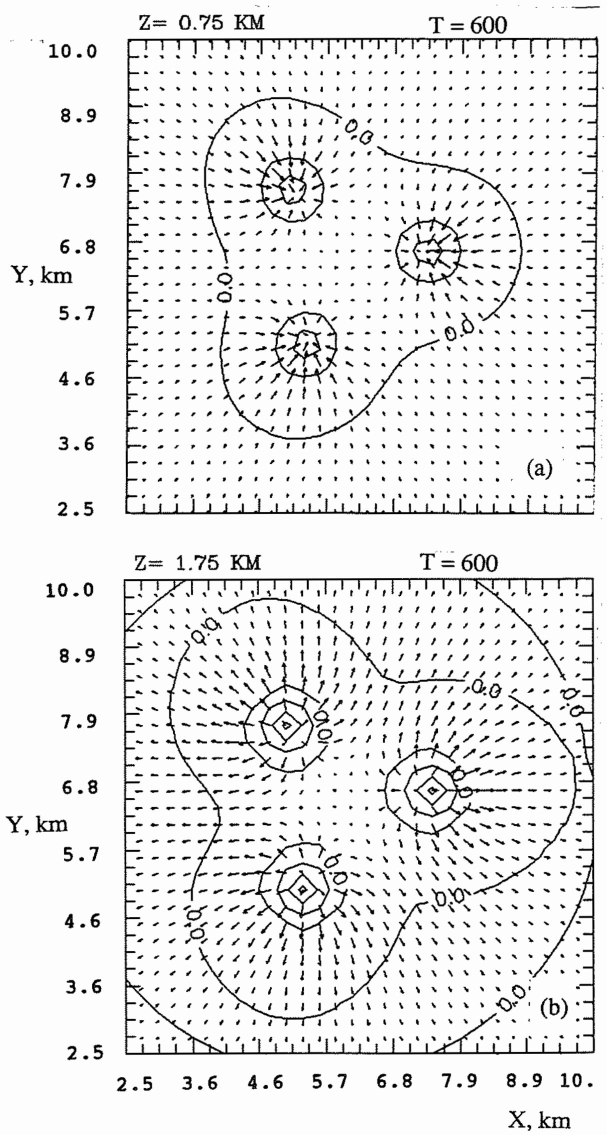

Fig. 1. Horizontal velocity vectors with superimposed vertical velocity isolines at 600 s. Horizontal cross-sections at (a) 0.75 km and (b) 1.75 km. 2 m/s vertical velocity contour interval.

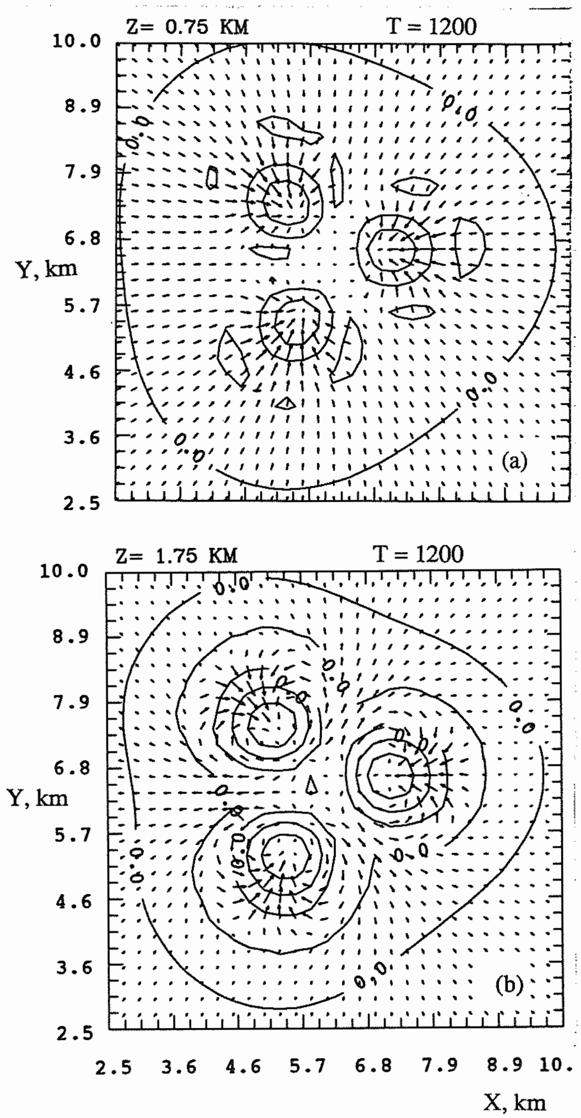

Fig. 2. (a), (b) Same as Fig. 1 but at 1200 s. 2 m/s velocity contour interval at z = 0.75 km but 4 m/s contour interval at z = 1.75 km.

To better understand the physical mechanisms involved in vortex formation we diagnosed the vertical vorticity budget for over 50 air parcels originating near the base of one of the clouds. The relevant vertical vorticity equation (neglecting friction) can be written as,

$$\frac{D\zeta}{Dt} = \underset{\text{tilting}}{\vec{\omega}_H \cdot \nabla w} + \underset{\text{stretching}}{\zeta \frac{\partial w}{\partial z}}$$

where w is the vertical velocity component and $\vec{\omega}_H$ is the horizontal vorticity vector.

In the interest of brevity we present a trajectory characterized by one of the larger observed values of vertical vorticity. Other trajectories were characterized by pronounced trajectory curvature but somewhat smaller vertical vorticity. Fig. 6 traces the selected parcel's trajectory from its entrainment into the base of the northernmost cloud at 600 s until its expulsion from the top of the cloud after 1800 s. Fig. 7 describes the evolution of the vertical vorticity and horizontal divergence associated with this parcel. The corresponding stretching and tilting terms of the vertical vorticity equation are shown in Fig. 8.

It is apparent that the tilting term was responsible for initially generating the parcel's (negative) vertical vorticity. Once generated, the vorticity was augmented by further tilting and amplified by the stretching mechanism. Before leaving the cloud, the parcel was "squashed" in the strongly divergent flow near the cloud top and the vorticity decreased in magnitude. Since the parcel was close to the 1.75 km level at 1200 s, one may return to Figs. 2 (b), 4 and 5 to place the

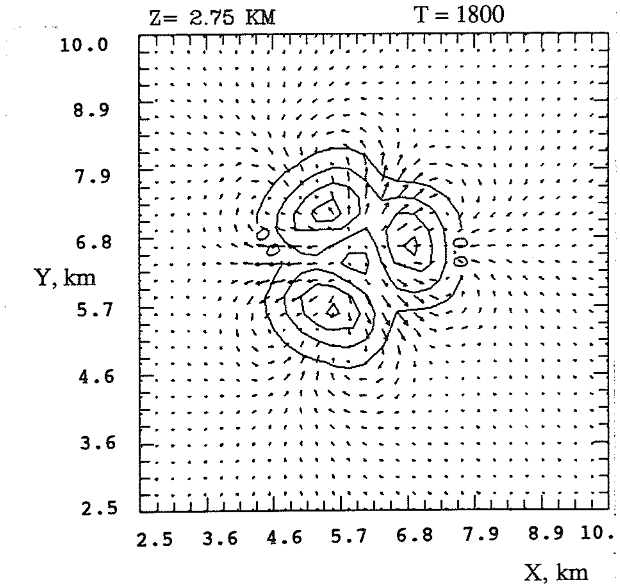

Fig. 3. Same as Fig. 1 but at 1800 s and for z = 2.75 km. 4 m/s vertical velocity contour interval.

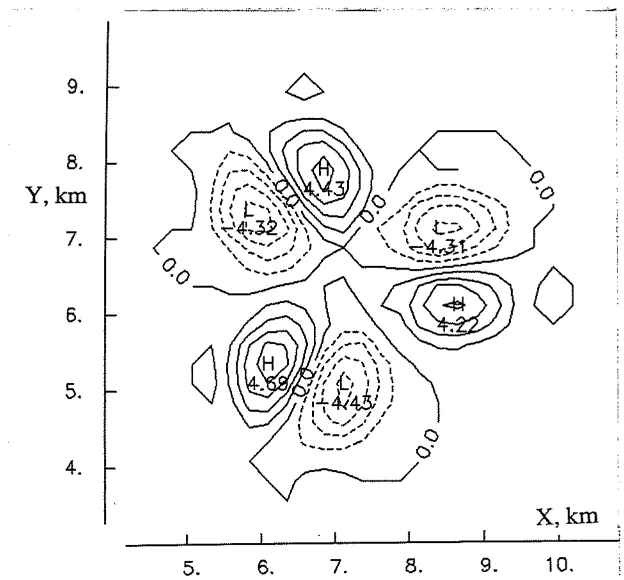

Fig. 4. Vertical vorticity at 1200 s, z = 1.75 km. Units are 10^{-3} s^{-1}. Negative contours dashed.

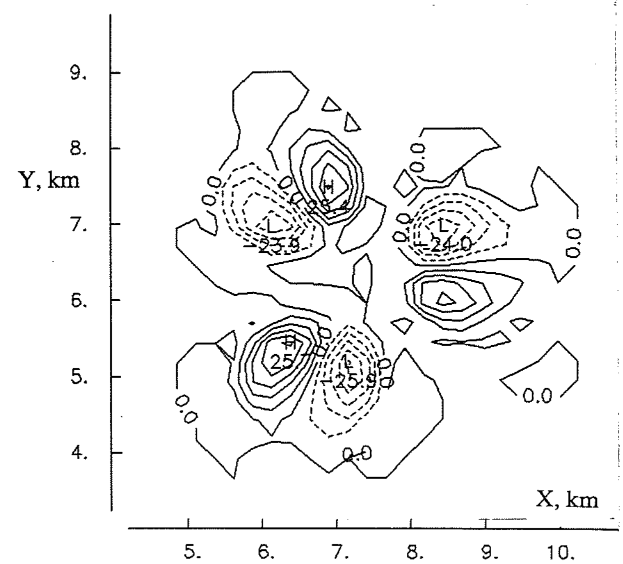

Fig. 5. Tilting term of vertical vorticity equation at 1200 s, z = 1.75 km. Units are 10^{-3} s^{-1}. Negative contours dashed.

parcel in an Eulerian frame. The parcel was located inside a lobe of negative vorticity and clockwise rotation to the southwest of the northernmost updraft.

We now examine the importance of the tilting term in this simulation and in some simpler idealized flows. First note that for a single cloud growing in a shear-free environment, growth and decay occur axisymmetrically and the azimuthal vorticity is associated with a baroclinically-generated "ring" circulation. The vorticity vector has no component crossing isolines of vertical velocity so the tilting mechanism cannot operate. No matter how large the "reservoir" of baroclinically generated azimuthal vorticity, vertical vorticity cannot be generated.

Next consider the case of a single convective element rising in a unidirectionally sheared environment (e.g., Lilly, 1986). For definiteness, we suppose the environmental vorticity vector points toward the north. In such a case an axisymmetric updraft tilts horizontal vorticity into the vertical, generating positive vertical vorticity to the south of the updraft and negative vertical vorticity to the north of the updraft.

In the case of the simulated multicell clouds described in this study, the horizontal vorticity is initially generated baroclinically. Based on the simulated updraft size and velocity scales we estimate a typical value of this horizontal vorticity as ~ 0.013 s^{-1}. If this horizontal vorticity was manifested as an environmental wind shear rather than a ring circulation, the environmental wind would change by 65 m/s over 5 km. The magnitude of the baroclinically generated azimuthal vorticity is thus quite large and can easily rival (or exceed) the magnitude of horizontal vorticity present in a strongly sheared atmosphere. On the other hand the vertical velocity isolines and horizontal vorticity vector must become skewed with respect to each other if any of this horizontal vorticity is to be tilted into the vertical. A single cell in a shear free environment cannot do this but, as demonstrated in this study, multicell clouds are capable of tilting the horizontal vorticity into the vertical. The skewing of the ring-like circulation/updraft geometry by cloud-cloud interactions is the crucial intermediate step by which the horizontal vorticity reservoir is tapped. These multicell processes are undoubtedly complex and warrant further investigation.

4. Conclusion

The purpose of this paper is to draw attention to a phenomenon observed in numerical simulations of multicell cloud mergers: the production of counter-rotating vortices on the periphery of merging convective cells. These vortices are novel in that they develop in a shear-free non-rotating environment without the agency of the Coriolis force. The vertical vorticity associated with these vortices originates from the tilting of each cloud's baroclinically generated azimuthal vorticity into the vertical. Multicell cloud interactions are crucial for this tilting mechanism to operate in a shear-free environment. It is suggested that the cloud merger/vortex production mechanism identified in this study may be an important means of vorticity production in multicell clouds.

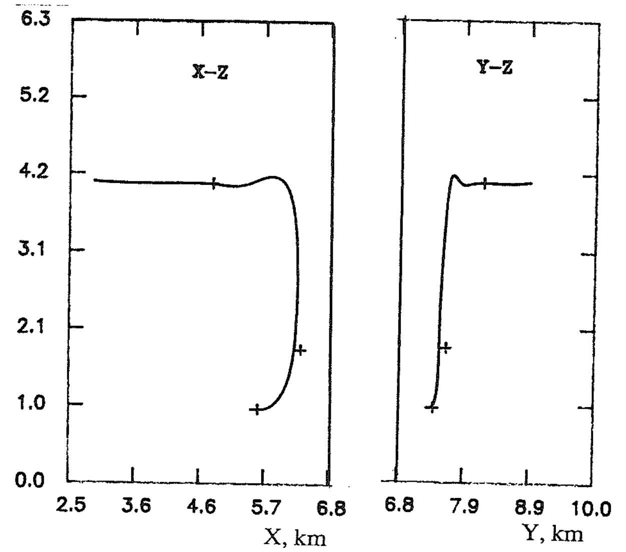

Fig. 6. xz and yz projections of the trajectory of a selected air parcel. The motion is upward with tick marks at 600, 1200 and 1800 s.

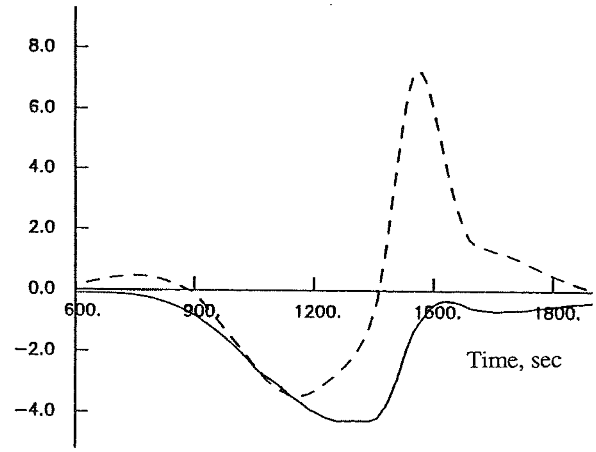

Fig. 7. Evolution of a parcel's vertical vorticity (solid line) and divergence (dashed line). Units are 10^{-3} s^{-1}.

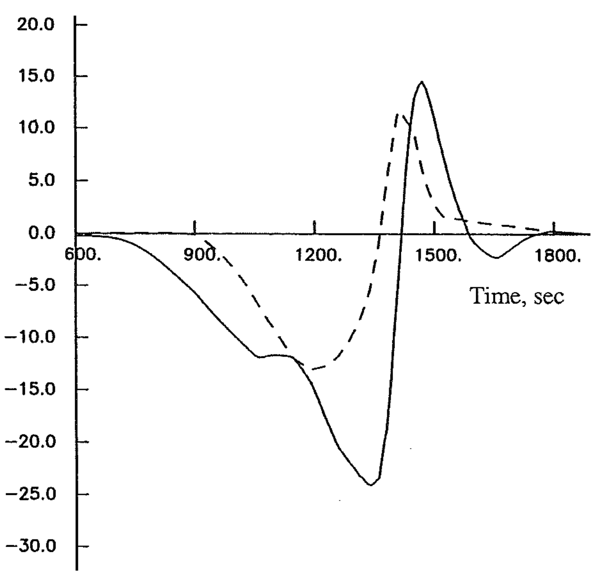

Fig. 8. The parcel's vertical vorticity budget: tilting term (solid line), stretching term (dashed line). Units are 10^{-6} s^{-2}.

Acknowledgments. The numerical simulation and analysis were performed with the facilities of the University of Oklahoma's Geosciences Computing Network. Jeff Castle assisted with the figure preparation. Partial support for this investigation was provided by NASA under Grant NAG 5-1528 and by NSF/FAA-CAPS under Grant ATM 88-09862.

REFERENCES

Davies-Jones, R. P., 1985: Tornado dynamics. *Thunderstorm morphology and dynamics, second edition.* Volume 2 of *Thunderstorms: A social, scientific and technological documentary*, E. Kessler, Ed., University of Oklahoma Press, 197-236.

Klemp, J. B., and R. B. Wilhelmson, 1978: Simulations of right- and left-moving storms produced through storm splitting. *J. Atmos. Sci.*, **35**, 1097-1110.

Kogan, Y. L., 1991: The simulation of a convective cloud in a 3-D model with explicit microphysics. Part 1: Model description and sensitivity experiments. *J. Atmos. Sci.*, **48**, 1160-1189.

Lemon, L. R., and C. A. Doswell, 1979: Severe thunderstorm evolution and mesocyclone structure as related to tornadogenesis. *Mon. Wea. Rev.*, **107**, 1184-1197.

Lilly, D. K., 1986: The structure, energetics and propagation of rotating convective storms. Part I: Energy exchange with the mean flow. *J. Atmos. Sci.*, **43**, 113-125.

Rotunno, R., 1981: On the evolution of thunderstorm rotation. *Mon. Wea. Rev.*, **109**, 577-586.

Schlesinger, R. E., 1978: A three-dimensional numerical model of an isolated thunderstorm: Part I. Comparative experiments for variable ambient wind shear. *J. Atmos. Sci.*, **35**, 690-713.

THE KINEMATIC STRUCTURE OF A MELTING INDUCED GUST FRONT

John Marwitz, Ellen Eakins, and James Toth
University of Wyoming, Laramie 82071

1. INTRODUCTION

During the early stages of the Denver blizzard of 1990, a line of convective clouds developed south of Denver and rapidly extended northward into the Winter Icing and Storms Project (WISP) area. This line of deep convection produced a mesoscale front which progressed slowly towards the east at 1-2 m/s for about 15 hours. Marwitz and Toth (1992) have hypothesized that the front resulted from the diabatic process of melting.

This convective line/band developed about 10 km west of the Mile High Radar (MHR) and moved slowly over and towards the east of this Doppler radar. The PPI volume scans have been analyzed using a variety of single Doppler analysis techniques.

2. VVP ANALYSIS RESULTS

Waldteufel and Corbin's (1979) Volume Velocity Processing (VVP) method is an extension of the VAD method for processing the data in a cylinder centered on the radar. The method uses all the data in the cylinder rather than only those data from a single PPI scan. No assumptions about the hydrometeor fall speeds are required.

The PPI volume scans on 6 March 1990 from 01Z to 18Z have been processed at 1-3 hourly intervals using the VVP method. The size of the cylinder was set at 50 km and the vertical interval was set at 0.3 km. The wind hodographs for the PPI volume scans are presented in Fig 1. The hodographs prior to 04Z displayed a linear wind shear from the SE below 1.5 km and linear shear from the WSW above 1.5 km. Assuming geostrophic balance the thermal advection from 2 to 6 km was ~+1.5 °C/hr. From 06Z to 12Z there was linear wind shear from the SE below 5.0 km. After 12Z the winds were from the E and displayed little wind shear.

During those times and within those levels containing linear wind shear, it would appear that the flow might well be 2-dimensional and, therefore, that the Band Velocity Processing (BVP) single Doppler analysis technique described by Johnston et al. (1992) may well be applicable. Some preliminary results using the BVP analysis technique are presented below. More extensive results will be presented at the conference.

3. BVP ANALYSIS RESULTS

Fig 2 is the PPI reflectivity for 0.5° at 0357Z. The range rings are at 20 km intervals. Note the 335° oriented band of high reflectivity just east of the radar. The BVP analysis was applied to the data within the 40 km by 60 km box. The results are presented in Fig 3. The coordinate convention is x toward the warm air (normal to the band), y toward the downshear direction (band parallel), and z is zenith direction. The individual boxes were oriented along 335° and their sizes were Dx = 8 km, Dy = 60 km and Dz = 0.7 km. Note that the linear wind shear below 2 km was also toward ~335° (Fig 1a).

The reflectivity contours are presented Fig 3a. The center of the band was located 6 km east of the radar. The peak reflectivities at the surface were 40 dBZ and decreased to 20 dBZ at 6 km. The reflectivities from 10 km west of the radar were below 0 dBZ.

The mass stream functions are presented in Fig 3b. The mass stream function is expressed as follows:

$$\Psi_x = -\int_{p_s}^{p} U dp \qquad (1)$$

where p_s is the surface pressure. The stream function field is contoured at 1,000 kg/s^3 intervals. Strong low level convergence was present from both sides of the band with most of the inflow coming from the east side and from below 2 km. Above 2 km there was divergence to east of the band. The indicated magnitude of the ascending motion above the radar is in question because this is the cone-of-silence region were few Doppler scans were obtained. The strongest ascending corresponded with the highest reflectivities, suggesting that the stream functions are qualitatively correct.

The wind direction and wind speed are presented in Fig 3c and Fig 3d, respectively. East of the band the low level winds are from the SE at 22 m/s. Beneath and to the west of the band the winds were < 2 m/s in agreement with the hypothesis of Marwitz and Toth (1992) that the diabatic process of melting resulted in a stable, stagnant boundary layer with frontal characteristics. West of the band and above the frontal boundary layer, the winds are from the S at 10 m/s.

The u and v component of the winds are presented in Fig 3e and Fig 3f, respectively. The east side of the band displays a -12 m/s inflow velocity (u) at the lowest levels which ascends upward into the band. Beneath the band the u component is 0 m/s. The band parallel component (v) displays a 22 m/s low level jet to the east of the band. The v component of the winds within the frontal boundary layer is < 2 m/s.

4. TESTS FOR GEOSTROPHIC BALANCE

If one assumes quasi-steady state, then it is possible to estimate the Rossby number (Ro) for air parcels which move along individual stream functions. Ro is the ratio of acceleration (DV/Dt) to Coriolis force (fV). The estimated Rossby numbers for some stream functions are summarized in Table 1. Ro along the -100 stream function into, the -100 stream function out of, and the 50 stream function into the band were 0.33, 5.30, and 0.80, respectively. Therefore, the inflow air into the band was not in geostrophic balance, but the outflow air to the east of the band was in quasi-geostrophic balance.

Table 1. Test for geostrophy in 6 March 1990 snow band.

Trajectory	DV/Dt	fV	Ro
-100 Out	.0006/s	.0018/s	0.33
-100 In	.0090/s	.0017/s	5.30
50 In	.0008/s	.0011/s	0.80

Acknowledgements: The participants in WISP are greatly appreciated for collecting these data under the most adverse conditions. The authors were funded under NSF grant ATM-9014763.

REFERENCES
Johnson, B., J. Marwitz, and R. Carbone, 1990: JAOT, **7**, 866-875.
Marwitz, J. and J. Toth, 1992: The Denver blizzard of 1990, Part I: Surface and sounding data. Submitted to MWR.
Waldteufeld, P. and H. Corbin, 1979: JAM, **18**, 532-542.

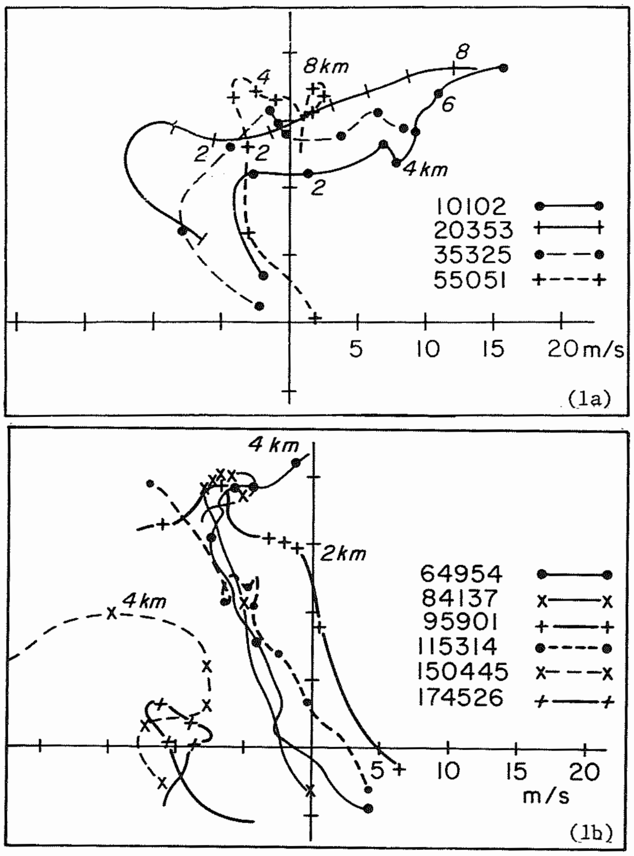

Fig 1. Hodograph for VVP analysis at a) 0101Z, 0204Z, 0353Z, and 0551Z and b) 0650Z, 0841Z, 0959Z, 1153Z, 1505Z, and 1745Z.

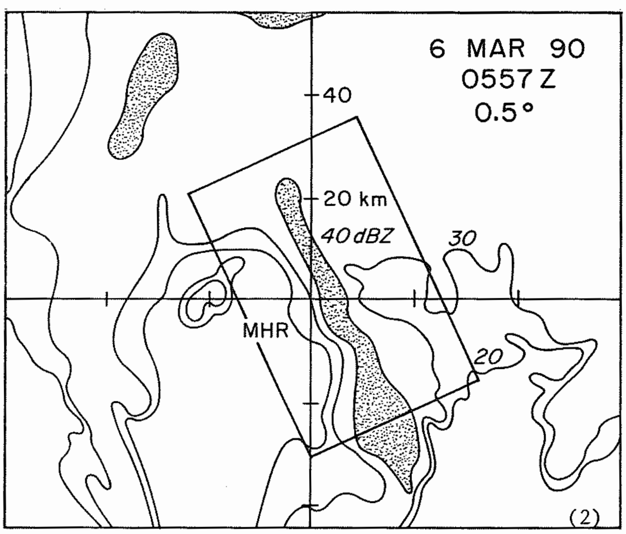

Fig 2. PPI scan at 0357Z at elevation of 0.5°. Contours at 10, 20 30, and 40 dBZ.

Fig 3. (adjacent column ⟶) BVP results from PPI volume scan from 0356Z to 0359Z. A dot indicates that valid results were determined for that BVP box. a) Reflectivity, b) Mass stream function, c) Wind direction, d) Wind speed, e) U component, and f) V component.

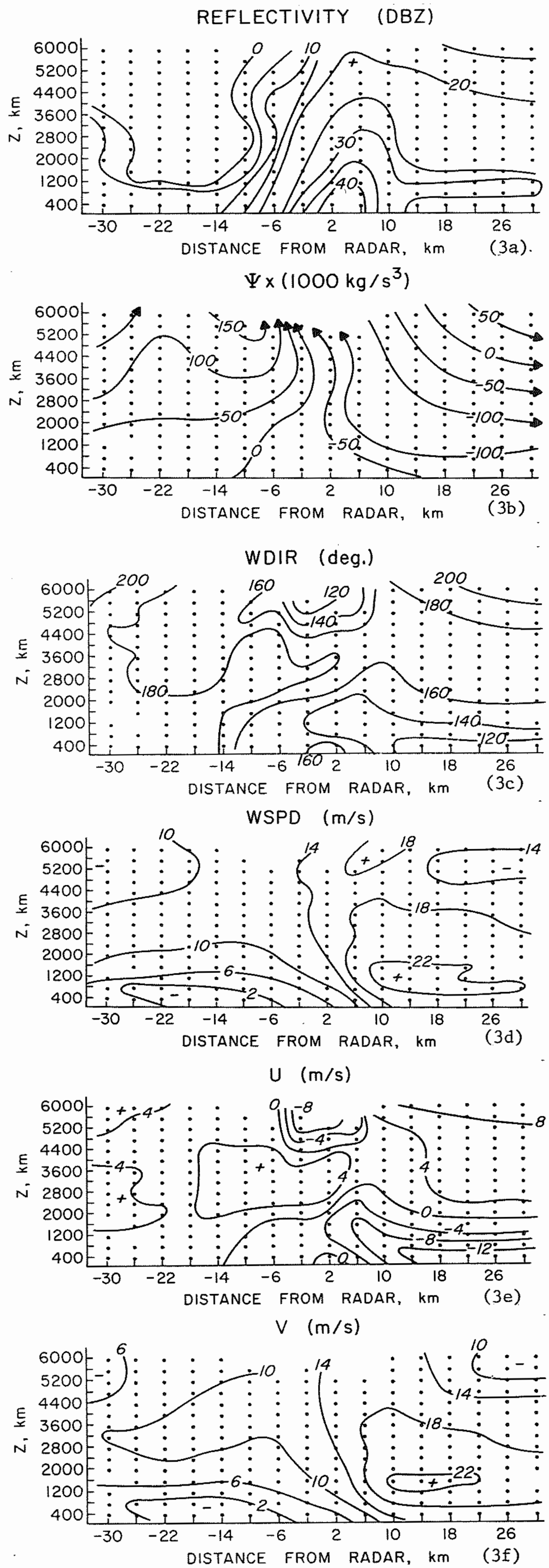

ESTIMATES OF PRECIPITATION IN SUMMER STORMS IN CENTRAL ALBERTA

E.Torlaschi[1,2], D.A.Holland[1], A.R.Holt[1], R.McGuinness[1], B.Kochtubajda[3].

1. Department of Mathematics University of Essex, Wivenhoe Park, Colchester, CO4 3SQ, U.K.
2. On leave from:- Department of Physique, UQAM, Montreal, Quebec, H3C 3P8, Canada.
3. Environmental Res. & Eng., Alberta Research Council, Edmonton, Alberta, T6H 5X2, Canada.

1.Introduction

A polarisation radar-rain experiment was conducted jointly by the Alberta Research Council (ARC),Canada, and the University of Essex, U.K., during the period 18 July to 7 August 1991. The field experiment involved observing storms within about a 70km radius from Red Deer, Alberta, with the ARC S-band polarisation diversity radar, and measuring rainfall at the ground through a small network of fixed, volunteer observers, a mobile storm-chase operation and automatic recording stations belonging to the Atmospheric Environment Service (AES) and Alberta Environment.

One of the objectives of this experiment as to collect further polarisation data from convective storms together with concurrent ground observations of rainfall, hail, etc..., in addition to the data set already available from a previous measurement campaign conducted in the summer of 1989 and reported by English et al. (1991).

This paper presents the estimation of rain rates for four days during the field experiment using the full polarisation information from the ARC S-band radar.

2. The Field Experiment

The ARC S-band polarisation diversity radar was the primary observing system for the experiment. The characteristics of this radar have already been carefully described by English et al (1991). A small network of some 27 volunteer observers had been established for the duration of the experiment. Each volunteer was provided with a TRU-CHEK wedge raingauge, and was instructed to read the gauge twice a day.

The field experiment had two vehicles equipped with maps, a radio, a tipping-bucket raingauge connected to a data logger and a wedge-type raingauge. Each vehicle included a driver and a navigator who could record position and information about the precipitation encountered by the vehicle. The vehicles in radio contact with the control at the radar site were deployed into oncoming storms as opportunities arose. The chase-vehicle controller had at his disposal a radio, an analogue PPI displaying reflectivity and circular depolarisation ratio, albeit not range corrected, and road maps.

Weather forecasts were obtained from (AES) Western Region Office in Edmonton to help in planning the daily operations. Additional weather information was obtained from the staff in the control tower at Red Deer Industrial Airport. The ARC C-band conventional weather radar was operated 24 hours a day to monitor rainfall in the area. Data from this radar were recorded as well. The ARC S-band polarisation diversity radar was operated only when suitable weather occurred in the project area.

3. Extraction of Rainrates from the Radar Data

The principle of the ARC S-band polarisation diversity radar is to transmit left hand circular (LHC) polarised radiation, and to make four measurements of the return signal. These are the powers in the main and orthogonal channels, $\tilde{W}_2$ and $\tilde{W}_1$ respectively, and the magnitude and phase of the complex correlation, $\tilde{W}$, of the main and orthogonal fields.

Because precipitation particles are generally nonspherical, not only will the transmitted radiation be depolarised when reflected by precipitation, but also the polarisation state of the transmitted wave will change as the radar beam penetrates the region of precipitation. The intrinsic scattering properties of the target are, therefore, coupled with the properties of the propagation medium, and both effects contribute to establish the return signal.

According to Torlaschi and Holt (1991) when S-band LHC polarisation is transmitted, the intrinsic radar observables can be estimated by

$$\phi_{DP} = \arg(\frac{\tilde{W}_2 - \tilde{W}_1}{2} + j\,\mathrm{Im}\,[\tilde{W}]) = \arg(\tilde{W}_3) \qquad (1)$$

$$W_2 = e^A[\cosh\Delta a\,(\frac{\tilde{W}_2 + \tilde{W}_1}{2}) + |\tilde{W}_3| - \sinh\Delta a\,\mathrm{Re}(\tilde{W})] \qquad (2)$$

$$W_1 = e^A[\cosh\Delta a\,(\frac{\tilde{W}_2 + \tilde{W}_1}{2}) - |\tilde{W}_3| - \sinh\Delta a\,\mathrm{Re}(\tilde{W})] \qquad (3)$$

$$\text{and} \quad |W| = e^A[\sinh\Delta a\,(\frac{\tilde{W}_2 + \tilde{W}_1}{2}) - \cosh\Delta a\,\mathrm{Re}(\tilde{W})] \qquad (4)$$

where ϕ_{DP} is the two-way propagation differential phase, Δa is the two-way differential attenuation in Np units, and A is the two-way mean attenuation of the radar signal.

McGuinness and Holt (1989) suggested that it is possible to estimate the two-way attenuation at horizontal polarisation, A_h , and the two-way differential attenuation, ΔA ,

by means of $A_h(dB) = \phi_{DP}(rad)$ (5)

and $\Delta A(dB) = 8.686\,\Delta a(Np) = 0.26\,\phi_{DP}(rad)$ (6)

The radar parameters which can be obtained from the radar observables are:

(i) the equivalent reflectivity factor for circular polarisation

$$Z_c = \frac{\lambda^4}{\pi|K|^2}\frac{4\pi r^2}{|C|^2}W_2 \qquad (7)$$

where $|K|^2 = 0.93$, and λ is the wavelength;

(ii) the circular depolarisation ratio

$$CDR = 10\log_{10}(W_1/W_2); \qquad (8)$$

(iii) the differential reflectivity

$$Z_{DR} = 10\log(\frac{\tilde{W}_2+\tilde{W}_1-2\mathrm{Re}(\tilde{W})}{\tilde{W}_2+\tilde{W}_1+2\mathrm{Re}(\tilde{W})}) + \Delta A; \qquad (9)$$

(iv) the correlation for circular polarisation

$$\rho = \frac{|W|}{(W_1W_2)^{1/2}}; \qquad (10)$$

(v) the gradient of the two-way propagation differential phase, K_{DP}, in gate n of length L

$$K_{DP}^{(n)} = (\,\phi_{DP}^{(n+1)} - \phi_{DP}^{(n)}\,)/L. \qquad (11)$$

In this paper we have derived rainfall amounts from the differential propagation phase K_{DP} using

$$K_{DP} = \frac{R^{1.15}}{3.172\ \lambda(\mathrm{cm})} \tag{12}$$

suggested by Zrnic (priv. commun., 1989). This is the procedure adopted by English et al (1991), but with one important difference. In the former paper it was assumed that the total differential phase, the quantity obtained from equation(1) was totally differential propagation phase, since the differential backscatter phase in rain is negligible. To minimise the error due to noise, English et al obtained the value ofK_{DP} by averaging over three radial bins, centred on the location being monitored. Since hail does not generally have negligible differential backscatter phase, this procedure will be open to error in regions containing hail or melting particles. In this paper we have followed the algorithm of Holt & Tan (1992) who showed how the differential propagation phase may be extracted from the total phase by measuring concurrently over double-length bins. Although the measurements were not made this way in 1991, it is possible to simulate measurements over double- length bins, and this is the process adopted. In order to provide some measure of the accuracy, we have provided estimates of rainfall by considering both one-bin and average-over-three-bin estimates. The latter will not be as accurate when the location is at the edge of a storm.

Even though the ability of polarisation radar parameters to identify regions likely to contain hail has been demonstrated (c.f. Al-Jumily et al 1991; Torlaschi and Holt, 1991), this topic will not be addressed in this paper.

4.Results

Data collected on five days during the experiment (26th,27th,29th July, and 6th,7th August) have been analysed. On the 29th July 1991, mesocyclonic activity and a possible tornado touchdown was also reported by the chase crews. For polarisation and Doppler radar observation of these events, see Holt et al (1992).

A total of 26 samples of total rainfall amount were collected on these days and they are summarized in Table 1, where we also give the type of recording station, its distance from the radar, and the duration of the radar record of the storm at that location. The radar estimates were obtained by multiplying the derived rainrate for each first elevation PPI by the time between PPI's (88sec).

The wedge gauges can be read accurately to 0.1mm up to an accumulation of 5mm, and to 0.2mm up to 20mm. Since the use of differential propagation phase should be limited to significant rainrates, it is to be expected that records 8,9,10,14,15,19,22,25 should have the best agreement with ground measurements, since they have average rainrates in excess of 50mm/hr. However, since 10,19,22 record hail as well as rain, these may be expected to be in poorer agreement. However, it can be seen that the 1 bin radar estimates lie within a factor of 2 of the gauge record for all but 5 records, and the 3 bin estimates for all but 6 records. Generally the agreement is much better than a factor of 2. Bearing in mind that the bin length is 1.05km, and the angular width is 1°, this is very encouraging agreement.

5.Acknowledgements

We are indebted to several people for assistance with the project. In particular, from the Alberta Research Council, C.Richmond, F.Bergwall, F.D.Barlow, M.Stanley-Jones, R.Morris, and members of the radar group, and from the University of Alberta, Dr R.Charlton. Dr R.G.Humphries gave us some of his own time to help check the calibration of the radar. We are also grateful for the support of the Atmospheric Environment Service both through its Western Region and its Cloud Physics Research group. We also thank Alberta Environment for the use of data.

6.References

Al-Jumily, K.J., R.B. Charlton, and R.G. Humphries, 1991: Identification of rain and hail with circular polarisation radar. *J. Appl. Meteor.*, **30** 1075-1087.

English, M., B. Kochtubajda, F.D. Barlow, A.R. Holt, and R. McGuinness, 1991: Radar measurement of rainfall by differential propagation phase: A pilot experiment. *Atmosphere-Ocean,* **29** 357-380.

Holt, A.R., E. Torlaschi, R. McGuinness, D.A. Holland, F. Bergwall, T. Nichols, and P. Joe, 1992: Polarisation and Doppler observations of a tornadic storm in central Alberta. *This volume.*

Holt A.R. and J.Tan 1992: Separation of Differential Propagation phase and differential backscatter phase in polarisation diversity radar. *Electron. Lett.* (in the press)

McGuinness, R., and A.R. Holt, 1989: The extraction of rainrates from CDR data. *Preprints, 24th Conference on Radar Meteorology,* Tallahasse, Amer. Meteor. Soc., 338-341.

Torlaschi, E., and A.R. Holt, 1991: Separation of propagation and backscattering effects in circular polarisation diversity S-band radars. Submitted for publication in *J. Atmos. Oceanic Technol.*

TABLE 1
Radar predicted and measured rainfall

Date	No.	Type	Dist. (km)	Rainfall(mm) radar 1bin	radar 3bin	grnd.	Duration mins
JY26	1	ch(w)	26	5.9	9.2	6.5	20
	2	EC(t)	32	6.5	5.6	4.9	27
	3	net	58	4.9	9.4	7.6H	12
	4	net	58	7.0	7.0	10.2	22
	5	net	47	13.2	12.1	12.7H	39
	6	net	42	8.7	6.3	6.1H	13
	7	net	38	0.5	1.4	2.5	6
	8	net	23	15.5	16.3	20.3	16
	9	net	50	5.8	5.2	10.2	10
	10	net	48	16.1	23.2	25.4H	16
	11	net	30	11.4	10.5	14.0	26
JY27	12	ch(w)	93	4.4	2.9	6.5H	29
	13	ch(w)	28	7.6	4.5	3.0	13
	14	EC(t)	28	10.0	6.9	8.8	6
	15	net	23	16.2	16.9	12.7	12
	16	net	18	6.1	6.8	6.4	10
	17	net	30	4.1	3.0	4.1	7
JY29	18	ch(w)	57	5.9	6.2	8.0H	15
	19	ch(w)	54	2.3	2.1	5.0H	5
	20	ch(w)	80	5.7	5.7	9.8	20
	21	EC(t)	32	13.5	10.7	5.0	19
	22	net	23	4.6	1.8	6.4H	7
	23	net	30	11.5	10.1	5.1H	18
AU06	24	ch(w)	45	9.6	7.1	10.0	22
	25	net	56	8.5	1.3*	10.2	7
AU07	26	AE(t)	58	12.2	8.7	5.6	30

w: wedge gauge
t: tipping-bucket
*: estimate unreliable;location at front edge of storm
ch: chase vehicle
ae: Alberta Environment Station
EC: Environment Canada (AES) Station
net: Volunteer Network (wedge gauge)
H: Hail reported

HAILSTONE SIZE CHARACTERISTICS OF THE HAILFALLS IN THE *PÁRAMO LEONÉS* (SPAIN)

R. FRAILE, J. L. SÁNCHEZ AND A. CASTRO

Laboratorio de Física de la Atmósfera, Universidad de León, 24071 León, Spain.

1. INTRODUCTION

In the northwest of the regions of Old Castile and León (Spain), a Project is been developed since 1985 in order to analyze the incidence of the hail on the agriculture. One of the aspects we are working on is the characterization of the hailfalls. To determine the physical parameters of the hailstones when on the ground, we have set up a network of hailpads. There is a wide bibliography about the use of this type of network in many countries (for example Schleusener and Jennings, 1960; Changnon, 1969, Morgan *et al.*, 1980; Federer *et al.*, 1986; Sackiw, 1989; Morgan, 1990). In this paper we will show some of the results relating to the distribution of the stones sizes and a discussion about them.

2. DESCRIPTION OF THE SYSTEM AND METHODOLOGY

The network covers an area of 1,000 km². The system makes use of a Styrofoam plate as a material sensible to the impact. The 250 hailpads have been placed following a regular network with a 2 km side square unit cell. The position of the sensors can be observed in figure 1. The specifications of the sensor, its calibration, the characteristics of the network and the measure method of the dents have been described in a previous paper (Fraile *et al.*, 1991a).

Between May 15 and September 15, 1990, 10 hail days have been detected in the area of hailpads. We have picked up 151 plates altogether where more than 20,000 hail dents have been measured by a manual method. However, for this work, we have taken the sample of the hailfalls that have affected more than three adjacent hailpads. We started from a total sample of 13 different hailfalls, since the hailfalls have affected different parts of the network on the same day. In each hailfall we have taken the sample of all the hailstones which hit the hailpads affected. Some of the parameters of the hailfalls are shown in table 1. With these data, we have determined the distribution of sizes for each hailfall.

Table 1. Some parameters of the thirteen hailfalls tabulated in the study zone during the summer of 1990. We point out the number of impacted sensors and the affected area, supposing a representativeness of 4 km² sensor. The other columns contain the maximum size of the recorded hail, the number of fallen stones (m^{-2}), the density of energy, the total energy of the hailfall and the total mass of ice.

Hailfall	Sensors	Area (km²)	Dmax (mm)	Density (m^{-2})	Density of energy (J/m²)	Total energy (MJ)	Total mass (Mg)
6.10.90 /1	4	16	10.7	647	6.71	107.3	1776
6.13.90 /4	5	20	16.4	800	14.79	295.7	3988
6.13.90 /7	9	36	12.7	4031	39.01	1404.5	22988
6.13.90 /8	23	92	19.1	1656	14.47	1331.2	22192
6.13.90 /9	6	24	17.0	1690	31.65	759.6	9740
6.27.90 /1	17	68	18.6	575	13.67	929.2	10772
8.2.90 /6	8	32	12.4	353	3.88	124.2	1948
8.2.90 /8	4	16	16.5	808	16.91	270.6	3448
8.20.90 /1	14	56	16.8	1213	18.14	1016.0	14544
8.20.90 /2	10	40	14.2	671	7.35	294.0	4652
8.20.90 /3	5	20	9.9	777	3.98	76.9	1604
8.20.90 /4	14	56	10.6	658	4.87	272.9	4904
8.20.90 /6	5	20	12.1	823	8.87	177.5	2880

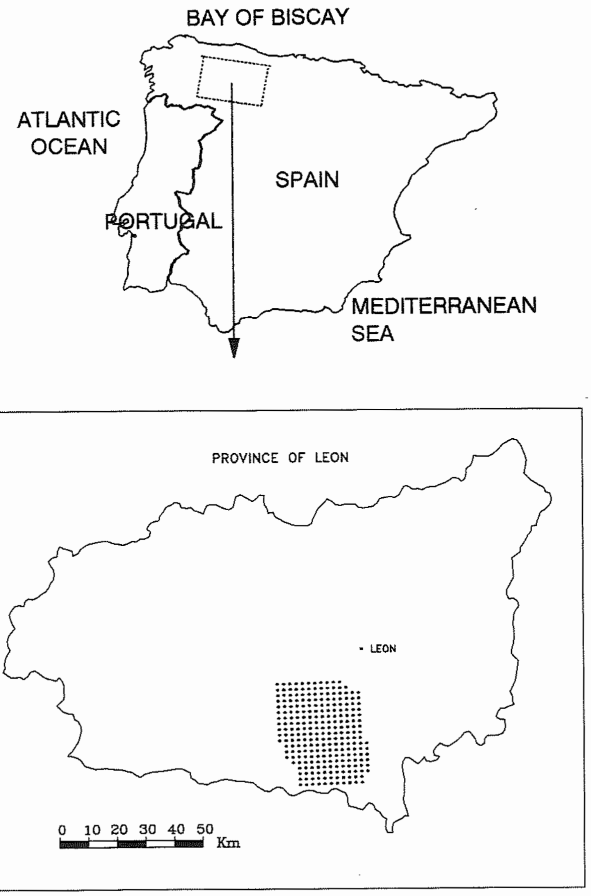

Fig. 1. The network of 250 hailpads (dots) and its position in the province of León (lower map). Location of this province in the Iberian Peninsula (upper map).

In order to do this distribution, we have taken into account only those hailstone sizes bigger than 5 mm, as, by convention, the precipitation in the form of ice is called hail only when its size exceeds this border (WMO, 1966). Besides, the instrument of measurement used, the hailpad, is unable to discern sizes less than about 3 mm, due to the value of the intercept of the calibration straight line. In consequence, we have used the transformation $x = d - 5$ mm to fit the data to probability density functions defined for $x > 0$.

Supposing that the number of hailstones decreases exponentially with the size (Marshall and Palmer, 1948), we have tried to fit the data to an exponential probability density function $f(x) = \beta\, e^{-\beta x}$. Previously (Fraile *et al.*, 1991b), we have discussed some methods of fitting, and chosen that of moments (Sneyers, 1990). In the case of the exponential law, the method of moments coincides with the maximum likelihood method. In order to make this fitting, we have to take into account that the first-order moment (mean) of an exponential distribution is $\overline{x} = 1/\beta$.

Once calculated the value of β for each hailfall, we have applied the Kolmogorov-Smirnov test of goodness-of-fit (Essenwanger, 1986). Taking the value of $\alpha = 0.05$ as the threshold level of significance, we come to the conclusion that only two of the thirteen hailfalls studied offer good fits to an exponential distribution. In most of the cases, the biggest differences between the experimental data and the exponential law, are located on the region of the smallest hailstone sizes; this type of hail is less frequebt than we could expect if the sizes were distributed in an exponential way.

This result has led us to try the fitting to another type of distribution. The form taken by the frecuency histogram approaches in a way to the shape of a gamma probability density function, of which, besides, the exponential law is a particular case. On the other hand, the gamma distribution has been proposed before for the distribution of both water drops and hailstone sizes (for example Ulbrich, 1983; Wong *et. al.*, 1988).

We have used the gamma probability density function, as

$$f(x) = \nu^{\mu}\, x^{\mu-1} \exp(-\nu x) \,/\, \Gamma(\mu)$$

defined for $x>0$, where Γ is the Euler factorial, or gamma, function. This distribution is a function of two parameters, μ and ν, and has a maximum in $x = (\mu-1)/\nu$ if $\mu>1$. We can see that the exponential is a gamma distribution for which $\mu=1$. As in the former case, we have to bear in mind that we have made the fitting of the values x, obtained by substracting 5 mm from the diameter of the hailstone, and that the first-order moment with respect to zero and the second-order central moment of the gamma distribution are respectively $\overline{x} = \mu/\nu$ and $\mathrm{var}(x) = \mu/\nu^2$.

The results of fitting the exponential and gamma distributions by the method of moments are shown on table 2, together with the goodness-of-fit according to the Kolmogorov-Smirnov test.

Table 2. Parameters of the exponential and gamma distributions, fitted by the method of moments, for each hailfall. The goodness-of-fit (g. o. f.), after the Kolmogorov-Smornov test for a significance level $\alpha = 0.05$, is also shown.

		EXPONENTIAL		GAMMA		
Hailfall	Sample	β(mm^{-1})	g. o. f.	μ	ν(mm^{-1})	g. o. f.
6.10.90 /1	202	0.514	ns	2.818	1.448	s
6.13.90 /4	312	0.374	ns	2.355	0.880	s
6.13.90 /7	2830	0.598	ns	1.547	0.925	ns
6.13.90 /8	2970	0.673	ns	1.306	0.879	ns
6.13.90 /9	79	0.419	ns	1.350	0.566	s
6.27.90 /1	762	0.389	s	1.167	0.454	s
8.2.90 /6	220	0.545	s	1.600	0.871	s
8.2.90 /8	252	0.368	ns	1.781	0.655	s
8.20.90 /1	1325	0.439	ns	1.793	0.786	ns
8.20.90 /2	523	0.536	ns	1.722	0.923	ns
8.20.90 /3	303	1.088	ns	1.382	1.503	s
8.20.90 /4	718	0.727	ns	1.631	1.185	s
8.20.90 /6	321	0.509	ns	2.543	1.295	s

In this table we can see that, in most of the cases, the gamma distribution fits better than the exponential to the experimental data.

3. DISCUSSION

What may the explanation be for this "anomaly" in relation to the exponential? If we consider the exponential distribution of the hailstone sizes inside the cloud as appropriate, that alteration can appear in the measure instrument, the hailpad, when certain overlapping of the dents is produced. This sometimes can make the smallest hailstones unnoticed.

On the other hand, let us remember that the hail starts its melting on going through, in its falling, the 0° C isotherm. The rate of melted ice, which will be just an anecdote on the biggest stones, can become important on the region of smallest sizes. However, a most accurate analysis of this aspect will be the subject to develop in a later work.

REFERENCES

Changnon, S. A., Jr., 1969: Hail evaluation techniques. Part 1, Final Rept. NSF GA-482, Illinois State Water Survey, Urbana, 88 pp.

Essenwanger, O. M., 1986: *General Climatology, 1B. Elements of statistical analysis,* Elsevier, Amsterdam, 424 pp.

Federer, B., A. Waldvogel, W. Schmid, F. Hampel, M. Schweingruber, W. Stahel, J. Bader, J. F. Mezeix, N. Doras, G. D'Aubigny, G. DerMergreditchian and D. Vento, 1986: Main results of Grossversuch IV. *J. Climate Appl. Meteor.,* **25,** 917-957.

Fraile, R., J. L. Sánchez, J. L. de la Madrid and A. Castro, 1991a: A network of hailpads in Spain. *J. Wea. Mod.,* **23,** 56-62.

Fraile, R., A. Castro, A. Vega and J. Rodríguez, 1991b: Analysis of hailstones from a hailpad network. II International Meeting on Agriculture and Weather Modification, Zamora, 87-100.

Morgan, G. M., 1990: La grandine. E.R.S.A., Gorizia, 148 pp.

Morgan, G. M., Jr., D. Vento, J.F. Mezeix, P. Admirat, B. Federer, A. Waldvogel, L. Wojtiv, and E. Wirth, 1980: A comparison of hailfall intensity and spatial variability in the United States, and Europe based on data from instrumental networks. Preprints, *Third WMO Sci. Conf. on Weather Modification,* Clermont-Ferrand, 607-613.

Sackiw, C., 1989: Dense network analysis. In "Greek national hail suppression program. 1988 annual report". National Agricultural Insurance Institute, Athens.

Schleusener, R. A. and P. C. Jennings, 1960: An energy method for relative estimates of hail intensity. *Bull. Amer. Meteor. Soc.,* **41,** 372-376.

Sneyers, R., 1990: *On the statistical analysis of series of observations,* WMO, Technical note No. 143, Geneva, 192 pp.

Ulbrich, C. W., 1983: Natural variations in the analytical form of the raindrop size distribution. *J. Climate Appl. Meteor.,* **22,** 1764-1775.

WMO, 1966: *International Meteorological Vocabulary,* Geneva, 276 pp.

Wong, R. K. W., N. Chidambaram, L. Cheng and M. English, 1988: The sampling variations of hailstone size distributions. *J. Appl. Meteor.,* **27,** 254-260.

NUMERICAL MODELING OF REGIONAL PRECIPITATION IN WESTERN COLORADO

by
David A. Matthews
Bureau of Reclamation
and
Gary Bates and Filippo Giorgi
National Center for Atmospheric Research[1]

1. INTRODUCTION

This paper describes a plan to study precipitation over the Rocky Mountains in Colorado. Bureau of Reclamation (Reclamation) research includes a collaborative effort in its Global Climate Change Response Program (GCCRP) described by Matthews et al., (1991) and Medina (1991). This collaboration involves scientists from the National Center for Atmospheric Research (NCAR) and the U. S. Geological Survey (GS). The GCCRP is designed to understand and predict precipitation over selected Western drainage basins. Reclamation and the GS are jointly examining the precipitation and hydrologic characteristics of the Gunnison River Basin to determine streamflow properties and reservoir management needs in present and future climates. This drainage basin is typical of other headwaters for the Upper Colorado River and other major river systems in the West. Therefore, Reclamation is interested in understanding the physical mechanisms that produce precipitation and is developing a method to describe the spatial and temporal evolution of precipitation from various types of winter and summer precipitation events.

Reclamation's GCCRP modeling approach involves two phases. Phase one will evaluate the nested regional modeling method in current climate to determine its capability to accurately simulate existing conditions in well-documented cases. As confidence in the large-scale, general circulation model results improves, phase two will apply this approach to future climate simulations that use a general circulation model, regional model and local-scale nested modeling system. This paper focuses on the early stage of research in phase one.

2. THE NESTED MODELING APPROACH

The nested modeling approach uses a regional model to provide the regional-scale forcing that largely controls the evolution of local-scale clouds and precipitation, which is simulated in a local-scale model. The regional model is the Pennsylvania State University/NCAR Mesoscale Model Version 4 (MM4). The standard MM4 model is described in Anthes et al. (1987); however, in this study we use results from an augmented version for regional climate studies described by Giorgi and Bates (1989). This version of the MM4 model includes a sophisticated surface physics-soil hydrology package. The model is a compressible and hydrostatic model with primitive equations written in terrain-varying sigma vertical coordinates.

Figure 1 shows the three-dimensional terrain surface from MM4's 3000 by 3000 km domain having 60-km grid spacing over the Western United States from the Pacific to the High Plains and from northern Mexico to southern Canada. Note that MM4's terrain fails to clearly define the Colorado River Basin, hence the need for higher resolution. Yet even the somewhat coarse 10-km resolution terrain (fig. 1), used in our sensitivity test of Clark's model, resolves major drainages on the Gunnison River.

[1]NCAR is sponsored by the U. S. National Science Foundation.

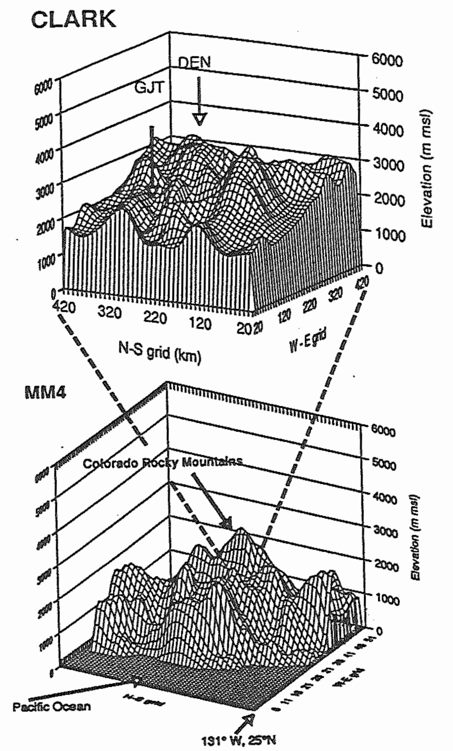

Figure 1. Three-dimensional topography used in the MM4 and Clark model simulations as viewed from the southwest corner of the grids. Dashes show the nesting of the local-scale Clark model into MM4's regional domain. Relative locations of Denver (DEN) and Grand Junction (GJT) rawinsonde sites are shown. Note that MM4's coarse 60-km resolution fails to resolve major river basins; however, the 10-km resolution of the Clark model defines the major rivers and tributaries within the Gunnison Basin.

Reclamation is using the sophisticated, three-dimensional, local-scale Clark model to simulate the local evolution of clouds and precipitation over complex terrain in the central Colorado Rockies. The Clark model is used extensively throughout the research community to simulate phenomena ranging from airflow over complex terrain to deep convection (Clark, 1979). The model is an anelastic, finite difference model with one- and two-way interactive nesting described by Clark (1977), and Clark and Hall (1991). It uses a terrain-following coordinate system to accurately describe orographic effects on the flow. The version of the model used here includes Kessler's warm rain and Murray-Koenig ice microphysical parameterizations.

3. INITIALIZATION AND VALIDATION OF MODEL SIMULATIONS

A set of heavy precipitation cases from the wet 1983 and the dry 1988 spring storms and summer monsoon periods will be used in the evaluation of this nested approach. The Grand Junction, Colorado (GJT), National Weather Service (NWS) rawinsonde and representative soundings from grid points in the MM4 model analyses will be used to initialize the Clark model for sensitivity tests. Later a four-dimensional dynamic data assimilation method, currently under development by scientists at the Mesoscale and Microscale Meteorology Division of NCAR, will be used to assimilate the MM4 dynamics into the Clark model initialization process.

Surface precipitation network data from NWS offices and cooperative stations, and the Soil Conservation Service "Snotel" remote high elevation automatic stations, will be used to validate model predictions of precipitation.

4. CLARK MODEL SIMULATIONS OVER THE GUNNISON BASIN -- AN EXAMPLE

The Clark model was adapted to the Gunnison Basin and tested using the terrain shown on Fig. 1 and the 1200 UTC December 19, 1983 GJT rawinsonde. This case was selected to test the model simulation of typical airflow flow during conditions of moderate precipitation over the basin when data (from the University of North Dakota's cloud-physics aircraft) were available. The preliminary sensitivity analyses used a 42 x 42 x 24 (x,y,z) grid-point domain with a coarse 10-km horizontal grid spacing and an expanding 0.5 to 2.0 km vertical grid spacing. The model was run in the nonhydrostatic mode with a time-step of 60 s using Murray-Koenig parameterized microphysics. Figure 2 shows the spatial distribution of cloud water - supercooled liquid water (SLW) in the surface layer after 120 minutes of integration. This SLW water appeared to be transient and moved from one ridge to another in this simulation; however, ice crystals (stippled pattern) developed over the major ridges and generally increased to concentrations of about 1 to 10 L^{-1}. The vertical structure of ice crystal concentration along line AB is shown on Fig. 2a. These spatial cloud patterns closely matched the terrain and propagated into the wind on the upwind sides of ridges. This cloud evolution is consistent with observations.

Aircraft observations, at 3.7 km msl (-13°C), indicated winds veered from 290 to 300° and accelerated from 7 to 10 m s^{-1} over the Grand Mesa. The modeled winds within the surface layer over the Mesa (marked M in fig. 2b) also indicated veering and acceleration. Aircraft measurements indicated a cloud with SLW; however, initial model simulations indicated ice developing at 5 km and falling through SLW that was confined from the surface to 1 km agl. These characteristics and the transient nature of SLW are consistent with Holroyd and Super's (1984) observations of significant amounts of transient SLW near the upwind slopes and over the Mesa in the winter of 1983.

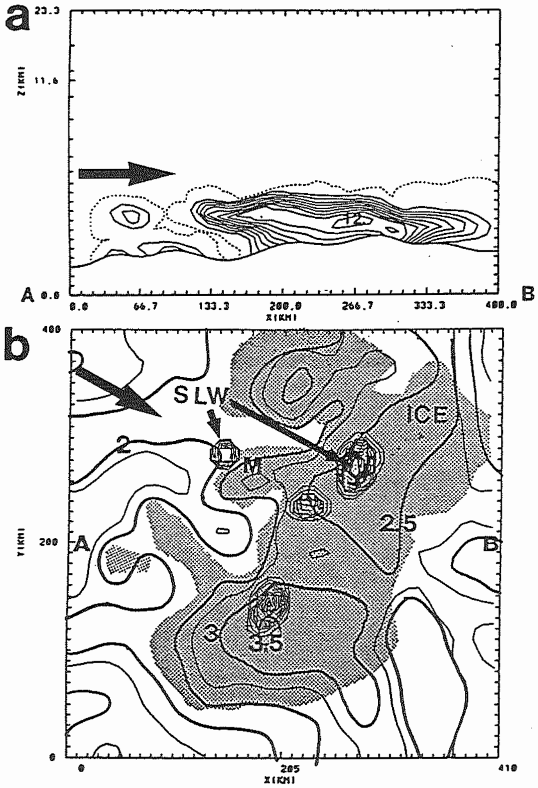

Figure 2. Vertical cross-section (a) of ice particle concentrations (number per liter) through the cloud, and corresponding horizontal pattern of cloud water mixing ratio (g kg^{-1}) contours and ice crystal concentration > 2 l^{-1} (stippled) in the surface layer (b). The cross-section passes along line AB shown on fig. 2b. Bold lines indicate elevation contours (km msl). Grand Mesa is marked by the bold M. Note the cloud development along the major ridges and its propagation into the wind shown by bold vectors.

5. SUMMARY AND FUTURE STUDIES

This paper presents an overview of Reclamation's approach to numerical modeling of precipitation in western Colorado. The example of modeled cloud development over complex terrain shows the model's capability to simulate strongly forced orographic cloud development that closely resembles observed clouds and airflow.

Our next step in sensitivity testing will perform higher resolution nested Clark model simulations of this case and begin simulations of summer monsoon conditions for more complex convective clouds and precipitation. Detailed comparisons of the predicted and observed spatial and temporal distributions of precipitation will be used to assess model validity. Further examination of the three-dimensional airflow and evolution of cloud structure will help us better understand and predict the physical mechanisms leading to precipitation in this region.

6. ACKNOWLEDGEMENTS

Sincere thanks is expressed to Drs. Terry Clark and Bill Hall of NCAR's MMM Division for their assistance in providing the model code and instruction regarding its operation and interpretation. The computing was performed at NCAR, which is sponsored by the National Science Foundation. Our appreciation is extended to Drs. Arlin Super and Ed Holroyd of Reclamation for providing aircraft cloud physics data.

7. REFERENCES

Anthes, R. A., E. Y. Hsie, and Y. H. Kuo, 1987: Description of the Penn State/NCAR Mesoscale Model Version 4 (MM4). NCAR Tech. Note, NCAR/TN-282+STR, 66 p.

Clark, T. L., 1977: A small-scale dynamic model using a terrain-following coordinate transformation. *J. Computational Physics*,**24**, 186-215.

____,1979: Numerical simulations with a three-dimensional cloud model: Lateral boundary condition experiments and multicellular severe storms simulations. *J. Atmos. Sci.* **36**,2191-2215.

___,W. D. Hall,1991: Multi-domain simulations of the Navier-Stokes equations: Benchmark error analysis of some nesting procedures. *J. Computational Physics*, **92**, 456-481.

Giorgi, F. and G. T. Bates, 1989: On the climatological skill of a regional model over complex terrain. *Mon. Wea. Rev.*,**117**, 2325-2347.

Holroyd, E. W. ,III, and A. B. Super, 1984: Winter spatial and temporal variations in supercooled liquid water over the Grand Mesa, Colorado. Preprints, *Ninth Conference on Weather Modification*, AMS Boston, MA. pp. 59-60.

Matthews, D. A., F. Giorgi, and G. Bates, 1991: Modeling regional controls of watershed precipitation for climate change studies. Preprints, *Second Symposium on Global Change Studies*, AMS Boston, MA. pp. 63-67.

Medina, J. G., 1991: Application of a simple local-scale numerical model in the study of altered climate impacts on watershed precipitation. Proc., *Second Symposium on Global Change Studies*, AMS Boston, MA. pp. 68-71.

Mesoscale Vorticity Structure of an Intense Midlatitude Squall Line

Da-Lin Zhang

Department of Atmospheric and Oceanic Sciences, McGill University
Montreal, Quebec, Canada H3A 2K6

1. Introduction

Recent observational studies have provided ample evidence on the development of mesovortices in the stratiform region of mesoscale convective systems (MCSs). However, there have been some ambiguities on whether midlevel mesovortices are induced by latent heating or cooling, and develop in the descending or ascending portion of MCSs. In this study, we examine a cooling-induced midlevel mesovortex associated with a midlatitude squall line, that occurred on 10 - 11 June 1985 during PRE-STORM, using a 20-h high resolution simulation of the squall system (see Zhang et al. 1989; Zhang and Gao 1989). Of particular interest is that this mesovortex developed in a descending rear inflow jet, as opposed to warm-core mesovortices that form in ascending flow of MCSs (e.g., Bosart and Sanders 1981; Zhang and Fritsch 1987).

Sections 2 and 3 briefly describe the model used for this study and the case. Section 4 shows vertical cross sections of the mesoscale vorticity structure associated with the squall system. Section 5 presents vorticity budgets and a summary is given in the final section.

2. Numerical model

The model used for this study is an improved version of the Penn State/NCAR three-dimensional mesoscale model (Anthes et al 1987). The following model features are considered to be important for the simulation:

- a two-way interactive nested-grid procedure which allows incorporation of realistic terrain (Zhang et al. 1986);
- an improved version of the Fritsch-Chappell (1980) convective scheme for the fine mesh and the Anthes-Kuo scheme for the coarse mesh;
- an explicit scheme containing predictive equations for cloud water (ice) and rainwater (snow) (Zhang 1989);
- a modified version of the Blackadar planetary boundary layer parameterization (Zhang and Anthes 1982).

The nested-grid model uses a fine-mesh length of 25 km and a coarse-mesh length of 75 km. The number of grid points for (x, y, σ) dimensions of coarse and fine meshes are 49 x 41 x 19 and 61 x 49 x 19, respectively. The model is initialized at 1200 UTC 10 June 1985 using conventional observations. No balancing between mass and wind fields is performed; however, the vertically integrated divergence in a column is removed to minimize noise early in the model integration. The reader is referred to Zhang et al. (1989) for more details.

3. Case description

The squall line was initiated at 2100 UTC 10 June 1985 as a weak surface front moved toward the PRE-STORM network and interacted with a thermal boundary. Then the system intensified rapidly within a widespread convectively unstable environment over the network and advanced southeastward at a speed of 14-16 m s^{-1}. The mesovortex under investigation was observed to develop to the north of the convective line. Both the satellite imagery and radar echoes display rapid expansion of stratiform cloudiness over the area where the mesovortex was located (Rutledge et al. 1988). The squall system entered the mature and nearly steady state around 0300 UTC 11 June.

The nested-grid model reproduced extremely well many internal structures and evolution of the 10-11 June 1985 squall system with *conventional data*, as verified against observational analyses by Johnson and Hamilton (1988) and Rutledge et al. (1988). These features include the timing, location and propagation of the squall system, the relative flow configuration of front-to-rear (FTR) motion at both upper and lower levels with an intermediate rear-to-front (RTF) inflow.

4. Kinematic analysis

Figures 1a-e show vertical cross sections of absolute vorticity, superposed with divergence and relative flow vectors taken from the incipient (a,b), mature (c) and dissipation (d,e) stages of the squall system. There are two regions of cyclonic vorticity concentration: one along the leading line and another to the rear of the system, with an intermediate anticyclonic vorticity zone. This vorticity structure conforms well to the composite vorticity analysis of the same case by Biggerstaff and Houze (1991). These two cyclonic vorticity concentrations will be hereafter referred to as "the leading vortex" and "the wake vortex", respectively. At 2200 UTC, the leading cyclonic vorticity concentrates along a shallow surface cold front, in coincidence with a favorable convergence zone with continued convective development (Fig. 1a). In contrast, the wake vortex is embedded in a weak convergence zone associated with a midlevel meso-α-scale short wave. Both vortices are evidently weak to begin with at this time. However, once the squall system intensifies, this vortex couplet assumes totally different characteristics of evolution. Of particular interest is that the development of the leading vortex is strongly linked to the ascending motion along the leading convective line, whereas *the wake vortex intensifies in a descending rear inflow* (Figs. 1b-d). Specifically, the leading vortex strengthens rapidly as the leading upward motion increases; it also dissipates rapidly as the system advances into a convectively less unstable environment. On the contrary, the most rapid development of the wake vortex occurs during the system's decaying stage, when it has come into phase with the convergence zone along the interface. At 0600 UTC, the wake vortex is nearing its maximum intensity and spatial coverage, while the leading line and its attendant vortex are dissipating rapidly. This feature explains why the wake vortex tends to be better observed during the decaying stage of MCSs (Smull and Houze 1985; Stirling and Wakimoto 1989).

Several other interesting phenomena in Fig. 1 are also worthwhile to mention. First, the wake vortex advances gradually into the leading edge of descending rear inflow from far behind, and during the decaying stage it comes into phase with the convergence zone along the interface (Fig. 1d). The maximum convergence occurs above the core of the wake vortex. Second, a region of anticyclonic vorticity occurs in a deep layer of the middle to upper troposphere centered along the interface during the intensifying stage. The middle portion of the anticyclonic vorticity rapidly diminishes as the system enters into the decaying stage, but not the upper portion (Fig. 1d). Third, beneath the wake vortex is a shallow layer of relative anticyclonic vorticity close to the surface that is associated with divergent outflow. At the end of the squall's lifecycle, both the wake and the leading vortices have nearly merged into one entity that tilts rearward along the interface (Fig. 1e). The rearward tilt of the wake vortex in the present case is due to the presence of strong vertical shear associated with FTR and RTF flows that tends to distort the vortex slantwise into a deeper (up to 250 mb) and wider region. Of particularly significance is that the wake vortex becomes the only remaining element of the squall system that can be observed at a larger scale in the troposphere at the end of the squall's lifecycle.

Figs. 2a and 2b shows the midlevel absolute vorticity structure during the incipient and decaying stages. At 0000 UTC, the relative flow shows little sign of a closed circulation associated with the wake vortex (Fig. 2a). As the system matures, the intensity of the wake vortex increases (not shown), as well as the FTR and RTF flows. As the system enters into the decaying stage, the vortex-related wind circulation occurs over an area much larger than that occupied

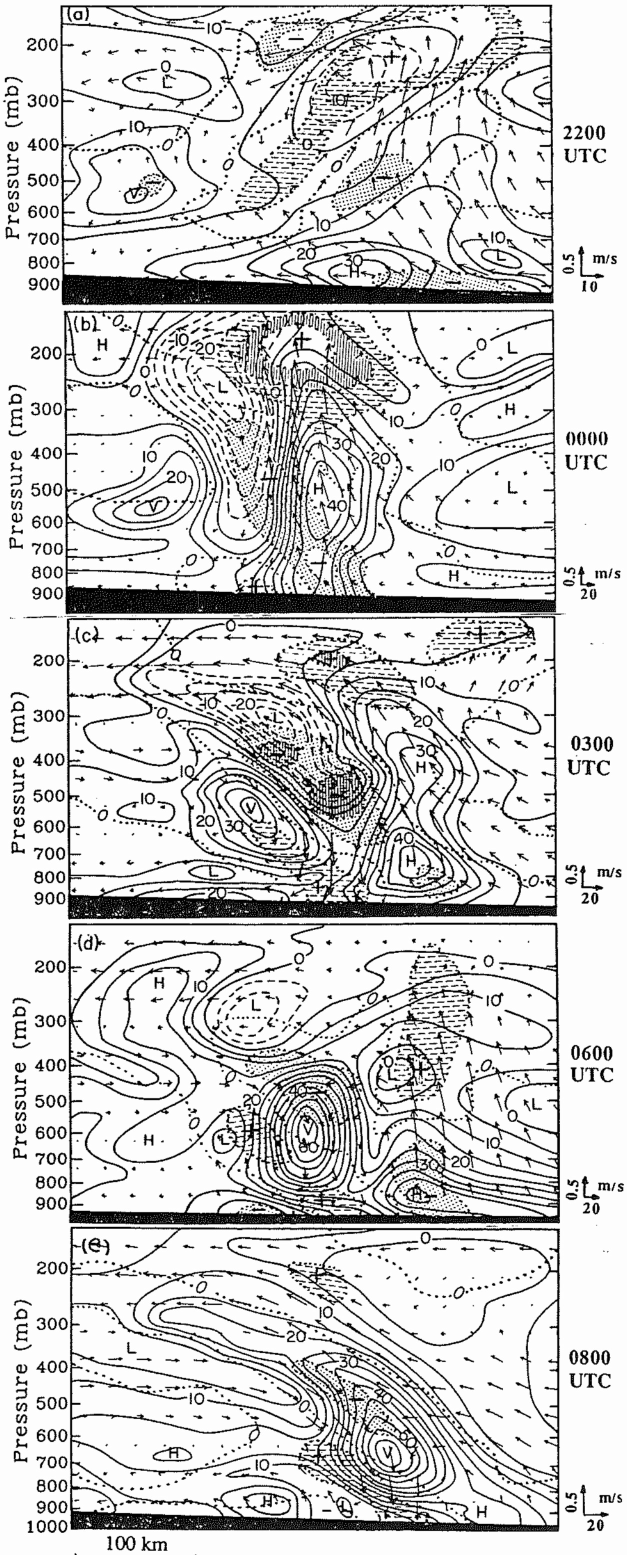

Fig. 1 Vertical cross sections of absolute vorticity (solid lines/positive, dashed lines/negative) at intervals of 5 x 10^{-5} s^{-1}, divergence (dotted lines) at intervals of 2 x 10^{-4} s^{-1} superposed with relative across-line flow vectors from a) 10 h; b) 12h; c) 15 h; d) 18 h and e) 20 h simulations, valid at 2200 UTC 10, 0000, 0300, 0600 and 0800 UTC 11 June 1985, respectively. Shadings and hatchings represent areas of convergence and divergence larger than 2 x 10^{-4} s^{-1}, respectively, with their centers denoted by the respective signs of "-" and "+".

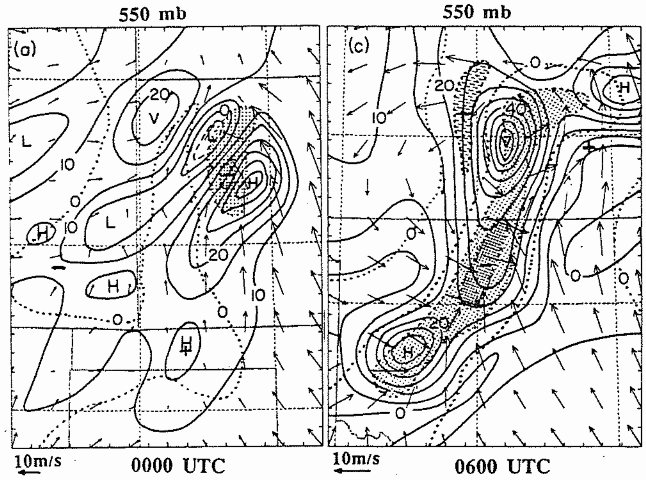

Fig. 2 Horizontal distribution of absolute vorticity (solid lines/positive, dashed lines/negative) at intervals of 5 x 10^{-5} s^{-1}, divergence (dotted lines) at intervals of 2 x 10^{-4} s^{-1} superposed with relative wind vectors from a) 12h and b) 18 h simulations, valid at 0000 and 0600 UTC 11 June 1985, respectively.

by the squall system. This larger-scale wind circulation apparently results from the development of extensive RTF inflow, in conjunction with the cyclonic flow occurring to the northern edge of the system. It is evident that the intensification of the RTF flow assists the concentration of cyclonic vorticity along the interface. On the other hand, the amplification of the wake vortex would in turn help enhance the RTF inflow. This complementary process can be evidenced by the fact that the RFT descending flow is relatively stronger to the south of the vortex whereas to its north, the RTF flow is both weak and elevated (see Fig. 5 in Zhang and Gao 1989).

5. Vorticity budget

With the dynamically consistent model dataset, a complete 3D vorticity budget for the mesovortices at different stages can be performed to provide an understanding of the processes that lead to the midlevel mesocyclogenesis. The equation describing the time rate of change in absolute vorticity following a parcel in isobaric coordinates may be written as

$$\frac{D(\zeta + f)}{Dt} = -(\zeta + f)\cdot\left(\frac{\partial u}{\partial n} + \frac{\partial v}{\partial s}\right) - \left(\frac{\partial \omega}{\partial n}\frac{\partial v}{\partial p} - \frac{\partial \omega}{\partial s}\frac{\partial u}{\partial p}\right)$$

where ζ is the vertical component of relative vorticity; f is the local Coriolis parameter; u, v and ω are the relative wind components in the right-hand coordinates (n, s, p), respectively, with n-axis normal to the line, positive in its direction of propagation.

Because of the space constraint, Figs. 3 and 4 only show vorticity budget during the squall's mature and dissipation stages, respectively. At 0300 UTC, the FTR ascending and RTF descending currents in the squall system have fully developed, as well as the leading vortex and the anticyclonic vorticity along the interface (Fig. 1c). Thus, a deep layer (up to 300 mb) of net cyclonic vorticity production associated with the wake vortex occurs along the leading edge of descending RTF inflow. This cyclonic vorticity tendency is produced by weak stretching followed by strong tilting (Fig. 3). Of striking significance is that *the contribution from the tilting of horizontal vorticity to the wake vortex by the descending rear inflow is about one order of magnitude larger than that from the stretching*. This finding, to a certain extent, agrees with conclusion obtained by Biggerstaff and Houze (1991). It is evident that stronger descending motion or strong mid- to upper-level cooling will likely intensify the wake vortex through tilting, revealing that the wake vortex is cooling-induced. Because the RTF descending flow is highly divergent (see Fig. 1c), *the stretching effect in most of the RTF flow*

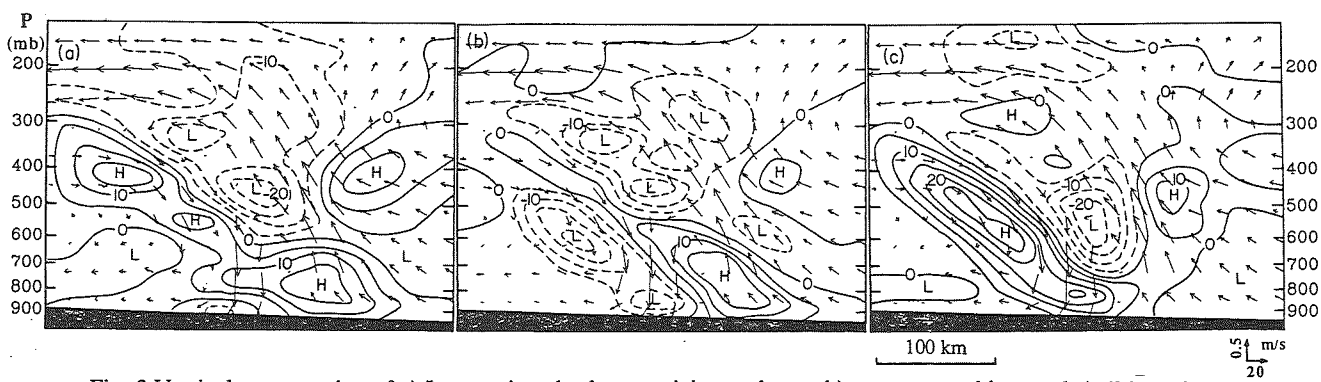

Fig. 3 Vertical cross section of a) Lagrangian absolute vorticity tendency; b) vortex stretching; and c) tilting of horizontal vorticity at intervals of 5 x 10^{-5} s^{-1} hr^{-1}, superposed with relative flow vectors from 15 h simulation, valid at 0300 UTC 11 June 1985. Solid (dashed) lines are positive (negative) tendencies.

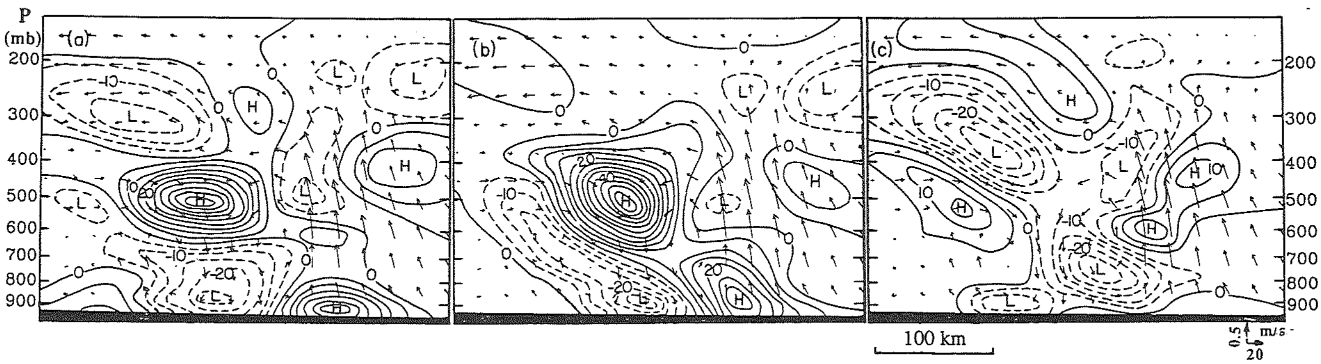

Fig. 4 As in Fig. 3 but from 18 h simulation, valid at 0600 UTC 11 June 1985.

tends to locally destroy the wake vortex during the system's development stage. This negative effect offsets a significant fraction of the positive contribution from the tilting in the lower half of the vortex layer. Despite this significant offset, the net Lagrangian tendency still shows that the tilting of horizontal vorticity by the descending flow determines the depth and magnitude of the wake vortex during this stage. It follows that *vortex tilting by the descending RTF flow can create a strong wake vortex without requiring pre-existing cyclonic vorticity*, as in the present case, associated with a midlevel meso-α-scale short wave.

As the system enters into the dissipating stage, the wake vortex propagates into the strong convergence zone along the interface (Fig. 1d). Thus, the stretching of the wake vortex itself gives rise to extremely large concentration of cyclonic vorticity along the interface (Fig. 4b). This rate considerably overcompensates the negative tilting effect along the interface for the amplification of the wake vortex (Fig. 4a). The tilting effect changes its role in the intensification of the wake vortex at this time because the vortex advances into the interface where the tilting always generates anticyclonic vorticity. Even behind the wake vortex, the tilting effect is much smaller than that during the formative stage, owing to the weakening of both the shears and descending motion. The net Lagrangian cyclonic vorticity tendency associated with the wake vortex, located at 500 mb, exceeds 45 x 10^{-5} s^{-1} hr^{-1} which is much greater than ever occurred during the formative stage. This further reveals that this type of mesovortex has better-defined circulation characteristics during the decaying stage of MCSs. Nevertheless, in the lower half portion of the vortex layer, the stretching associated with the divergent outflow again tends to destroy the wake vortex locally. Hence, the roles of the vortex stretching are to enhance the upper portion but weaken the lower portion of the wake vortex. Then, the descending rear inflow advects the cyclonic vorticity surplus in the upper layers downward to make up the vorticity deficit in the lower layers, such that the wake vortex is maintained within a deep layer.

It is extremely important to point out that the amplification of the wake vortex as the system decays by no means implies that the system's dissipation has positive or no effects on the intensity of the vortex. Rather, it reflects the increasing importance of the stretching as the wake vortex approaches the convergence zone along the interface. In fact, as the FTR ascending flow weakens, the convergence along the interface decreases rapidly because of less latent heat release occurring in the FTR ascending flow and less condensate available for subsequent diabatic cooling in the stratiform region [see Zhang and Gao (1989) for more details]. Thus, by 0800 UTC, the wake vortex has weakened from its peak intensity (which occurred roughly between 0630 and 0700 UTC), and its core has shifted from 550 to 650 mb after the upper-level vorticity sources diminished.

6. Summary and conclusions

In this study, the structure and evolution of a cooling-induced midlevel mesovortex, referred to as the wake vortex, that developed in the descending rear inflow of the 10-11 June 1985 squall line has been examined, primarily based upon a 20-h real-data simulation of the case.

Figure 5 summarizes the 2D structure of relative vertical vorticity in association with the across-line circulations during the mature stage of the 10-11 June 1985 squall system. A deep layer of strong cyclonic vorticity is generated along the leading convective line, owing to the concurrent positive contributions of tilting and stretching. This vortex is warm-cored, and extends to the trailing stratiform region. In a certain sense, the warm-core vortex plays an important role in organizing mesoscale flows from the low to upper troposphere through convective and FTR updrafts. Based on the conservation of moist potential vorticity, anticyclonic vorticity should be expected in the upper portion of overturning updrafts after air parcels from the convectively unstable boundary layer pass their equilibrium levels in the upper troposphere. Similarly, another local maximum of anticyclonic vorticity should appear to the rear of the stratiform precipitation region. The wake vortex develops in the descending rear inflow beneath the active stratiform cloudiness, with its maximum intensity

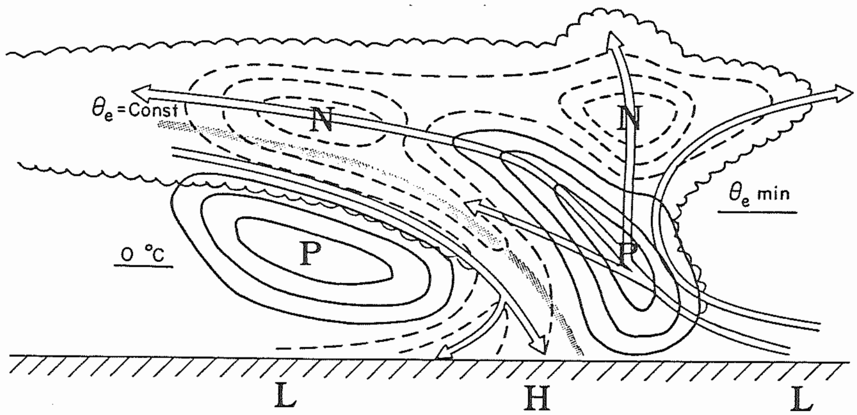

Fig. 5 The two-dimensional conceptual distribution of relative vertical vorticity in a cross section taken normal to the leading convective line during the mature stage of system. Solid (dashed) lines denote relative cyclonic (anticyclonic) vorticity, with its local maxima represented by the letter, "P (N)". Open arrows indicate the internal circulations of the squall system. A shaded line is used to represent the FTR and RTF flow interface. The letters, "H" and "L", denote surface meso-high and low pressure centers, respectively.

occurring above the melting level. The wake vortex has a scale of 120 - 150 km in its across-line dimension, but its longitudinal dimension during the decaying stage is more than 300 km. There is a constant θ_e surface situated along the flow interface that acts to separate the FTR from the RFT flow. Thus, the wake vortex decouples from the upper-level FTR ascending and anticyclonic flow during this formative stage.

As the squall system enters its decaying stage, the above conceptual model needs to be substantially modified. Specifically, the wake vortex is advected into the flow interface and comes into phase with the major convergence zone, thus causing the rapid spinup of the midlevel vortex through stretching. In contrast, because deep convection along the leading line dissipates, the leading vortex rapidly decays, shrinking in both depth and width, and eventually merging into the wake vortex. The midlevel anticyclonic vorticity zone also rapidly dissipates, primarily owing to the horizontal vorticity 'mixing' by the FTR and RTF flows. At the end of the lifecycle, the wake vortex becomes the only remaining element of the internal squall-line circulation that can be observed in a deep layer and at a larger scale in the low to midtroposphere.

In conclusion, we may state that midlevel mesovortices, large or small, strong or weak, deep or shallow, are ubiquitous in MCSs, since they can be induced by either latent heating or cooling; and that their pertinent mesoscale rotational flow may be one of the basic dynamic effects of MCSs on their larger-scale environments. The results suggest that vertical (or potential) vorticity should be considered as a fundamental variable to diagnose the structure and evolution of MCSs, because vorticity is a more persistent variable in the atmospheric flow. Finally, the present modeling results pose a serious challenge for future field experiments to obtain 4-D high-resolution datasets for a lifecycle of MCSs, and to mesoscale analysts for correctly attaining the internal structure of MCSs if scientific understanding of MCSs is to continue to advance.

Acknowledgments

The author is very grateful to Kun Gao for his assistance in preparing the hourly model output for the present study. The model integration was performed on CRAY X-MP of the National Center for Atmospheric Research which is sponsored by National Science Foundation. The research was partly supported by the Natural Science and Engineering Research Council and Atmospheric Environmental Service of Canada.

References

Anthes, R.A., E.-Y. Hsie and Y.-H. Kuo, 1987: Description of the Penn State/NCAR mesoscale model version 4 (MM4). Tech. Note, NCAR/TN-282, 66pp.

Biggerstaff, M.I., and R.A. Houze, Jr., 1991: Midlevel vorticity structure of the 10-11 June 1985 squall line. *Mon. Wea. Rev.*, **119**, 3066-3079.

Bosart, L.F., and F. Sanders, 1981: The Johnstown flood of July 1977: A long-lived convective storm. *J. Atmos. Sci.*, **38**, 1616-1642.

Fritsch, J.M., and C.F Chappell, 1980: Numerical prediction of convectively driven mesoscale pressure systems. Part I: Convective parameterization. *J. Atmos. Sci.*, **37**, 1722-1733.

Johnson, R.H., and P.J. Hamilton, 1988: The relationship of surface pressure features to the precipitation and air flow structure of an intense midlatitude squall line. *Mon. Wea. Rev.*, **116**, 1444-1472.

Rutledge, S.A., R.A. Houze, Jr., M.I. Biggerstaff and T. Matejka, 1988: The Oklahoma-Kansas mesoscale convective system of 10-11 June 1985: Precipitation structure and single-Doppler radar analysis. *Mon. Wea. Rev.*, **116**, 1409-1430.

Smull, B.F., and R.A. Houze, Jr., 1985: A midlatitude squall line with a trailing region of stratiform rain: Radar and satellite observations. *Mon. Wea. Rev.*, **113**, 117-133.

Stirling, J., and R.M. Wakimoto, 1989: Mesoscale vortices in the stratiform region of a decaying midlatitude squall line. *Mon. Wea. Rev.*, **117**, 452-458.

Zhang, D.-L., 1989: The effect of parameterized ice microphysics on the simulation of vortex circulation with a mesoscale hydrostatic model. *Tellus*, **41A**, 132-147.

------, and J.M. Fritsch, 1987: Numerical simulation of the meso-β scale structure and evolution of the 1977 Johnstown flood. Part II: Inertially stable warm-core vortex and the mesoscale convective complex. *J. Atmos. Sci.*, **44**, 2593-2612.

------, and R.A. Anthes, 1982: A high-resolution model of the planetary boundary layer - sensitivity tests and comparisons with SESAME-79 data. *J. Appl. Meteor.*, **21**, 1594-1609.

------, H.-R. Chang, N.L. Seaman, T.T. Warner and J.M. Fritsch, 1986: A two-way interactive nesting procedure with variable terrain resolution. *Mon. Wea. Rev.*, **114**, 1330-1339.

------, K. Gao, and D.B. Parsons, 1989: Numerical simulation of an intense squall line during 10-11 June 1985 PRE-STORM. Part I: Model verification. *Mon. Wea. Rev.*, **117**, 960-994.

------, and ------, 1989: Numerical simulation of an intense squall line during 10-11 June 1985 PRE-STORM. Part II: Rear inflow, surface pressure perturbations and stratiform precipitation. *Mon. Wea. Rev.*, **117**, 2067-2094.

NUMERICAL SIMULATION OF A NOCTURNAL MICROBURST OBSERVED DURING THE 1989 TDWR PROJECT IN KANSAS CITY, MISSOURI

J. P. Searles, R. D. Farley, M. R. Hjelmfelt and F. J. Kopp

Institute of Atmospheric Sciences
South Dakota School of Mines and Technology
501 E. St. Joseph Street
Rapid City, South Dakota 57701-3995

1. INTRODUCTION

An intense microburst was produced by one of a series of small, but strong, nocturnal thunderstorms that developed during the early morning of 30 July 1989. Radar analysis from the Lincoln Laboratories FL-2 Doppler radar showed that cells developed to the northwest of Kansas City and moved east southeast, with each successive cell and microburst becoming more intense. Radar also revealed a strong low-level jet oriented southwest to northeast, with speeds exceeding 20 m s^{-1} less than 1 km above ground. The strongest microburst occurred at 0930 UTC (0430 CDT) with maximum outflows observed by the University of North Dakota Doppler radar exceeding 24 m s^{-1} and a velocity differential of 47 m s^{-1}. Damage occurred to the suburban area of Claycomo, Missouri, with trees uprooted and trailers overturned. Cloud tops with this cell exceeded 15 km AGL, indicating an intense updraft as well. This is the first purely nocturnal microburst of such intensity to be analyzed by Doppler radar.

The Terminal Doppler Weather Radar (TDWR) project was in operation in Kansas City, Missouri, during the 1989 summer thunderstorm season. During the project, many different windshear events were recorded and archived, but this nocturnal case was the most intense. Several factors played a role in determining thunderstorm and microburst intensity -- the outflows from the early cells and their role in further development, precipitation microphysics that contributed to microburst intensity, and the effects of the low-level jet on the overall process. Another point to be investigated is the possibility of warm air advection in the jet regime that destabilized the lower level portion of the atmosphere, allowing for greater instability in the microburst production region.

These issues are addressed through use of two- and three-dimensional numerical cloud model simulations. There were four experiments run in 2D, consisting of 1) a thermodynamic and wind profile only slightly modified from the 12 UTC Topeka sounding to compensate for post squall changes; 2) same thermodynamics but no jet; 3) a double strength jet case; and 4) same as 1 but with a 3°C warming in the levels affected by the jet regime. An example of the wind speeds for the first three cases is given in Fig. 1. Similar cases were run with the 3D model except the double jet case was omitted.

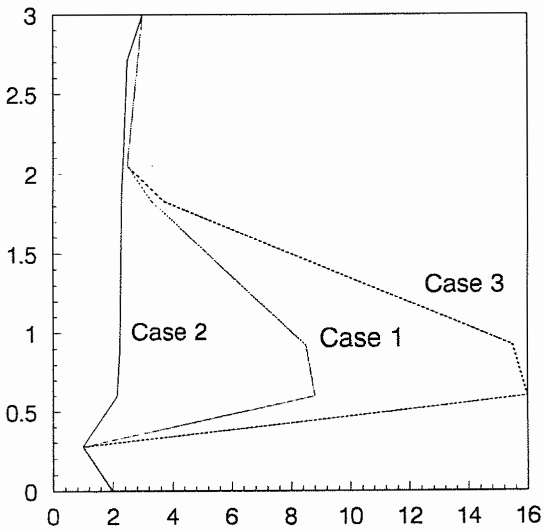

Figure 1: Variation of low-level jet speed in m s^{-1} with height in km for 3 cases in the 2-D experiments.

The 2D cloud model used in this study is the IAS deep-convection, slab-symmetric, two-dimensional, time-dependent cloud model with bulk water microphysics (*Orville,* 1965; *Orville and Kopp,* 1977; *Lin et al.,* 1983; and *Chen and Orville,* 1980). The three-dimensional anelastic nested grid cloud model developed by Clark and associates (*Clark,* 1977, 1979; *Clark and Gall,* 1982; *Clark and Farley,* 1984) has been modified to use the bulk water parameterization scheme of *Lin et al.* (1983), as explained by *Farley et al.* 1992).

The closest soundings available for this study were from Topeka, Kansas, at 00 and 12 UTC 30 July 1989. Neither of these were considered representative of the storm environment. However, by using both soundings, and the synoptic analysis, it was possible to derive a sounding that is believed to be representative of the atmosphere at the time of convection. This sounding is shown in Fig. 2. It has a temperature and moisture profile through the mid and upper levels similar to the 12 UTC Topeka sounding, but with added moisture and some temperature smoothing in the lowest 200 mb. The models were initiated in each case with a thermal bubble, centered at 3 km AGL, because the nocturnal nature of the storms rules out surface heating as the primary forcing mechanism.

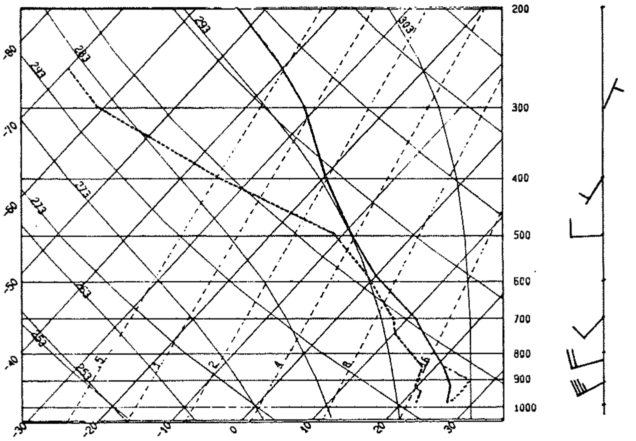

Figure 2: Atmospheric sounding diagram used in model experiments plotted on a skew-T log*P* with temperature, moisture, and wind barbs. One full wind barb equals 5 m s^{-1}. The dashed portion of the temperature sounding indicates modifications applied for the isothermal cases.

2. SIMULATION RESULTS

The first run (Case 1) produced an initial outflow peaking at 36 min with a differential of 7 m s^{-1}. This outflow initiated further convective events which, in turn, produced further microburst outflows. Each cell grew more vigorously than the previous one, and the subsequent outflows at 55 min and 66 min had peak differential velocities of 17 and 19 m s^{-1}, respectively. This indicates the model's ability to recreate the rhythmic nature of the cells as seen in the observations. The timing of microburst production in the model is also in close agreement with radar observations of descending reflectivity cores and the microburst events. Maximum cloud top approached that observed by the radar for the third cycle of cloud growth. However, the model does not reproduce the observed outflow intensities.

When the jet was removed (Case 2), the initial microburst outflows were more symmetric in nature and, as a result, so was the subsequent convection. Microburst intensity was also less in the no jet case. The most significant difference appears to be in the shape of the clouds themselves and the orientation of the updraft. In Case 1, the model portrays a leaning or tilting and merging of updrafts after being initiated by earlier outflows, resulting in a larger cloud and thus more intense precipitation. In the no jet case (Case 2), this feature disappears as the updrafts are vertical and result in an overall symmetric pattern to the convection. The symmetric outflow produces a new regime of convection characterized by two cells, one on each side of the outflow, which experience similar growth cycles and subsequently multiple outflows existing simultaneously. These concurrent microbursts are individually weaker than those in Case 1, but the net velocity differential is comparable. This is not realistic when compared with the actual radar observations.

The double intensity jet case (Case 3) also produces microbursts similar in strength to Case 1. The microburst outflows act to initiate convection, but the updraft and downdraft velocities do not reach the intensities seen in Case 1 for the third cycle of cloud growth and decay. The overall pattern and timing of the convection is much different from Case 1 beyond 42 min. Maximum cloud top height is also adversely affected, being limited to 13 km as in Case 2.

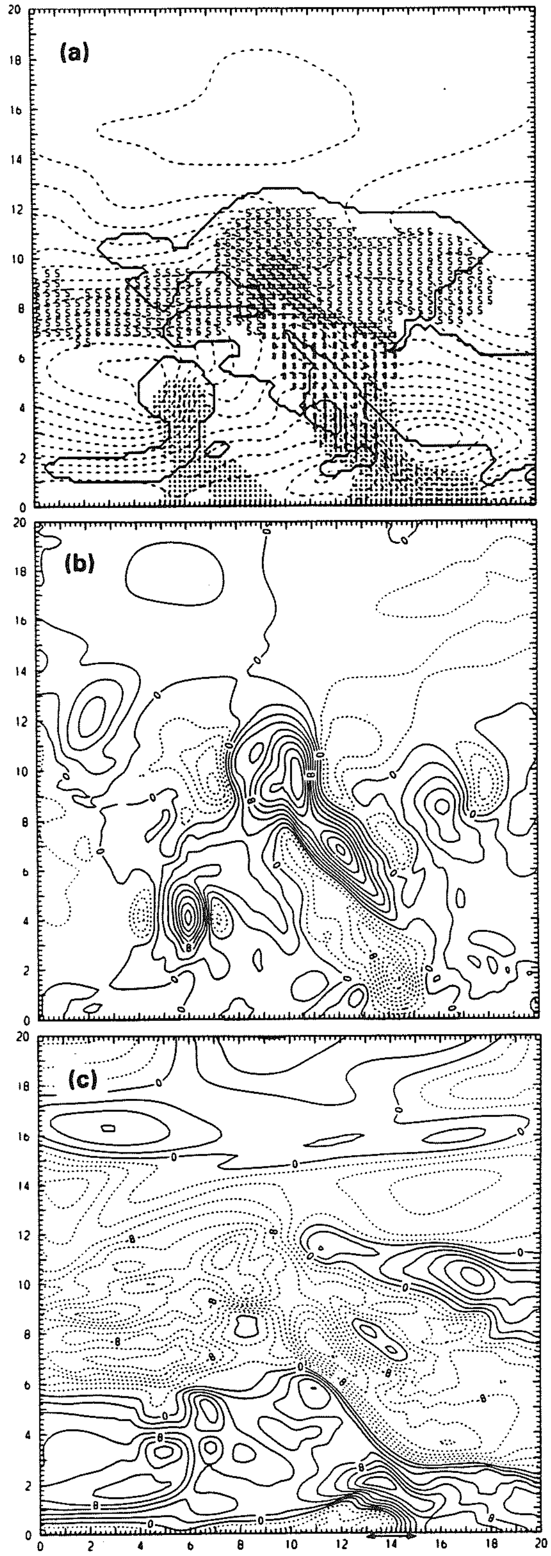

Figure 3: Two-dimensional model results for Case 4 at 66 min. a) cloud and precipitation depiction with dots and asterisks indicating rain and graupel/hail, respectively, greater than 1 g kg^{-1}. The letter s indicates snow greater than 0.5 g kg^{-1}. Cloud outline is given by the bold solid line. Dashed lines are streamlines. b) vertical velocity field and c) horizontal velocity field. Contour interval is 2 m s^{-1} in b) and c) with solid lines for positive values and dashed lines for negative. The microburst is indicated by the arrow below c).

The final simulation was carried out because the synoptic pattern suggested that the low-level jet was advecting a layer of the warm air observed over Kansas into the Kansas City area. The lowest 1 km of the sounding was warmed, producing an isothermal layer and a 3°C increase at 900 mb. The results show that this caused an increase in the simulated storm strength and produced the strongest downdrafts (17 m s^{-1}) and microburst outflows (21 m s^{-1}) observed in all the 2D simulations for the third cycle of development. A sample of the results for this case is shown in Fig. 3.

When compared to radar observations, Case 1 has the most realistic appearance, with the rhythmic nature and cloud precipitation characteristics well modeled. Sensitivity to warming of the lowest levels was revealed by stronger downdrafts and outflows attained in Case 4. The moderate jet strength in Case 1 gave more realistic results than weaker or stronger jets (Cases 2 and 3). However, none of the simulations have been able to reproduce the intensity of the observed microbursts. This may have been due to the limitations of the two dimensionality of the simulations. Therefore, three-dimensional simulations were performed so that the circulations and full wind field could be more accurately represented.

Three numerical experiments were carried out using the 3D cloud model. They are the equivalent of cases 1, 2, and 4 of the 2D model experiments, and were terminated at 39 min, following the occurrence of the initial microburst. All three displayed the presence of microburst precursors in horizontal cross sections 4 to 6 min before surface outflows were initiated. Radar analysis indicates that these precursors were present in all the microbursts for the case day at least 6 min before the onset of observed outflows. This indicates that the model was accurate in reproducing the circulation processes involved with microburst production.

Table 1 summarizes the processes and intensities of the three 3D model simulations showing similarities and differences in rain and hail formation and updraft, downdraft, and outflow strength. It helps illustrate that the mere presence of the low-level jet has only a small impact on model generated convection and subsequent outflows. Updraft and downdraft velocities are marginally stronger in Case 6 (no jet) as compared to Case 5 (full jet). Case 7 (isothermal) produces the strongest updraft of 38 m s^{-1} due to the added instability by the warm layer. Microburst production is also only slightly stronger in the no jet case, but much stronger in Case 7, with a downdraft of -17.6 m s^{-1} and a velocity differential of 20 m s^{-1} over a 4 km distance. This is consistent with the greater precipitation loading in Case 7.

A stronger microburst was observed when the warm layer was added to the lower levels due to a combination of several effects. These are: 1) production of a more vigorous updraft and

TABLE 1: Precipitation types and amounts, vertical velocities and outflow differentials for five time periods of the 3-D model results for each case.

Case #	Run Time in Minutes	Graupel/Hail (g/kg)	Rain (g/kg)	Updraft (m/s)	Downdraft (m/s)	Velocity Differential (m/s)
5	24	12.6	0.7	34.8	-3.4	0.0
	27	15.2	2.9	26.0	-5.6	0.0
	30	10.7	7.2	21.0	-12.9	3.2
	33	4.7	7.1	15.6	-14.5	13.8
	36	3.7	3.4	15.2	-5.6	8.8
6	24	12.3	0.8	34.4	-2.9	0.0
	27	14.6	3.1	23.9	-5.3	0.0
	30	9.8	7.5	22.7	-15.3	3.8
	33	4.8	5.9	17.2	-13.7	16.2
	36	3.3	3.6	12.0	-5.8	7.4
7	24	14.7	1.1	38.0	-3.3	0.0
	27	15.6	3.9	26.2	-5.8	0.0
	30	8.9	9.9	29.4	-17.6	7.1
	33	4.1	5.5	17.5	-13.6	20.3
	36	2.9	3.7	12.5	-6.8	13.2

increased precipitation allowing for a greater downward acceleration due to loading; 2) a greater amount of melting of graupel/hail producing more rain and subsequent evaporation; and 3) more negative buoyancy when the microburst descends through the lower warm layer allowing for continued acceleration and stronger impact on reaching the surface. Thus, the low-level jet is not enhancing the microbursts directly, but more indirectly, by providing strong warm air advection that resulted in a layer of low-level instability.

3. CONCLUSIONS

1) A strong microburst occurred during early morning hours despite a stable boundary layer.

2) Microburst precursors were observed and simulated, confirming that the microburst precursors used in TDWR algorithms will still be useful for detection in a nocturnal environment. A more complete discussion is provided in *Searles* (1992).

3) The 2D model results capture the rhythmic nature of convective activity and microburst production.

4) Both models indicate that direct transfer of momentum from the jet to the microburst does take place with stronger winds on the opposite side of jet entrance, but that the net effect on microburst intensity is small.

5) Strongest microbursts are produced when warm air advection is taken into consideration to produce a low-level warm layer in the jet regime.

ACKNOWLEDGMENTS

This research was sponsored by the National Science Foundation, Division of Atmospheric Sciences, under Grant No. ATM-8821119. The computations were performed using the facilities of the Scientific Computing Division of the National Center for Atmospheric Research, which is sponsored by the National Science Foundation. Radar data was provided by the Lincoln Laboratory of the Massachusetts Institute of Technology under sponsorship of the Federal Aviation Administration. We gratefully acknowledge the assistance of Joie Robinson in the preparation of the manuscript.

REFERENCES

Chen, C-H., and H. D. Orville, 1980: Effects of mesoscale convergence on cloud convection. *J. Appl. Meteor.*, **19**, 256-274.

Clark, T. L., 1977: A small scale dynamic model using a terrain following coordinate system. *J. Compute. Phys.*, **24**, 186-215.

Clark, T. L., 1979: Numerical simulation with a three-dimensional cloud model: Lateral boundary condition experiments and multicellular severe storm simulations. *J. Atmos. Sci.*, **36**, 2191-2215.

Clark, T. L., and R. Gall, 1982: Three-dimensional numerical model simulations of airflow over mountainous terrain: A comparison with observations. *Mon. Wea. Rev.*, **110**, 766-791.

Clark, T. L., and R. D. Farley, 1984: Severe downslope windstorm calculations in two and three spatial dimensions using anelastic interactive grid nesting: A possible mechanism for gustiness. *J. Atmos. Sci.*, **41**, 329-350.

Farley, R. D., S. Wang and H. D. Orville, 1992: A comparison of 3D model results with observations for an isolated CCOPE thunderstorm. [Accepted for publication *Meteor. Atmos. Phys.*]

Lin, Y. L., R. D. Farley and H. D. Orville, 1983: Bulk parameterization of the snow field in a cloud model. *J. Clim. Appl. Meteor.*, **22**, 1065-1092.

Orville, H. D., 1965: A numerical study of the initiation of cumulus clouds over mountainous terrain. *J. Atmos. Sci.*, **22**, 684-699.

Orville, H. D., and F. J. Kopp, 1977: Numerical simulation of the life history of a hailstorm. *J. Atmos. Sci.*, **34**, 1596-1618.

Searles, J. P., 1992: Numerical simulation of a nocturnal microburst as observed during the 1989 TDWR project in Kansas City, Missouri. Master's Thesis, Dept. of Meteor., South Dakota School of Mines and Technology, Rapid City, SD. 90 pp.

A NUMERICAL STUDY OF THE MICROBURST DOWNDRAFT AND OUTFLOW: THE INTERACTION OF PRECIPITATION MICROPHYSICS AND DYNAMICS

Janice L. Coen

Laboratory for Atmospheric Probing, Department of the Geophysical Sciences,
The University of Chicago, Chicago, IL 60637

1. Introduction

Microbursts are small, sudden, severe downdrafts that produce strong outbursts of damaging winds near the ground. They have been implicated in several large aircraft crashes and caused much loss of life and property (Fujita, 1985). However, although we now know the general conditions that favor microbursts and believe we know the mechanisms by which they develop, we still cannot predict precisely which clouds will produce them. Sometimes, in conditions which appear to be very similar, one cloud produces a microburst while a similar cloud nearby does not. Therefore, there must be something about the nature of the clouds which is different or some mechanism that we do not completely understand.

To date, factors that have been used to explain strong downdrafts and the sudden, brief nature of microburst outflow include a subcloud lapse rate of temperature near the dry adiabatic and large precipitation mixing ratios. Here, I test other characteristics of the environment and the precipitation produced by the cloud that could determine whether or not a microburst would occur and also could resolve some unexplained aspects of microburst behavior.

2. Description of the Numerical Model

In this time-dependent model of the subcloud region, a system of finite difference equations for the conservation of momentum, mass, thermodynamic energy, water vapor, and condensed water are solved numerically in an axisymmetric domain. The model is anelastic, nonhydrostatic, and uses a simple, discrete representation of the raindrop size distribution. The microphysical scheme used in this study assumes that raindrops are distributed in a discrete set of 20 size categories. The drops in the kth size category have radius R_k and are present in a concentration of n_k per unit mass. Two prognostic equations describe each size category - one for n_k:

$$\frac{\partial n_k}{\partial t} = -\frac{1}{\rho r}\left[\frac{\partial(\rho r u n_k)}{\partial r} + \frac{\partial(\rho r (w - v_k) n_k)}{\partial z}\right] + S_{n_k} \quad (1)$$

where u and w are the radial and vertical components of the air velocity, respectively, v_k is the fall speed for drops of the kth size category. The second equation for raindrops, which yields the drop size, is for the quantity $(nR^2)_k$:

$$\frac{\partial (nR^2)_k}{\partial t} = -\frac{1}{\rho r}\left[\frac{\partial(\rho r u (nR^2)_k)}{\partial r} + \frac{\partial(\rho r (w - v_k)(nR^2)_k)}{\partial z}\right] + S_{nR^2_k} \quad (2).$$

In (1) and (2), $S_{nR^2_k}$ is the rate of change of $(nR^2)_k$ due to evaporation, and since no raindrops are created in this simple model, S_{n_k} represents only drops evaporating completely. $S_{nR^2_k}$ is derived from the traditional diffusional growth equation written in terms of drop radius for drops of size category k:

$$S_{nR^2_k} = \frac{2 D_v}{\rho_L} n_k f_{v_k} (\rho_{v_\infty} - \rho_{v_R}) + R_k^2 S_{n_k} \quad (3)$$

where f_{v_k} is the ventilation coefficient for a drop of radius R_k, and ρ_{v_∞} and ρ_{v_R} are the vapor densities in the ambient air and at the drop surface, respectively. The term S_{n_k} in (1) and (3) is 0, except in locations where all the drops of category k evaporate completely, in which case it is calculated as:

$$S_{n_k} = \frac{n_k}{\Delta t} \quad (4)$$

where Δt is the time step.

To close the set of equations, the subgrid scale fluxes were parameterized using the eddy viscosity method with an eddy viscosity coefficient that is a function of the local velocity deformation and the local Richardson number (Clark, 1979). I assume that the turbulent transport of scalar variables can be expressed similarly in terms of a scalar eddy mixing coefficient, which is assumed to be equal to the viscosity coefficient.

The domain is a cylinder 4 km in radius whose height is the depth of the subcloud region (1-4 km). The boundary conditions on the model are a closed, free slip upper boundary, a no-slip lower boundary, and an open lateral boundary. The numerical scheme is a forward-time, modified upstream method suggested by Soong and Ogura (1973), which conserves scalar variables in a closed domain, is positive definite, and advects quantities only downstream, but suffers numerical diffusion. These experiments use a grid interval of 50 m and a time step of 1 second.

The numerical experiments begin with the release of raindrops into the domain at cloud base, the top of the domain, in an atmosphere at rest. Raindrops are initially distributed in a Marshall Palmer distribution. The subsequent motions in the subcloud region show the descent of a microburst to the surface, driven by water loading and the evaporation of rain, and its expansion in a ring vortex-type manner at the ground. The steady source of precipitation used in these experiments is not realistic for simulating microbursts, but allows the effects of the onset and end of precipitation to be separated.

The current model is limited in that (1) it only models the

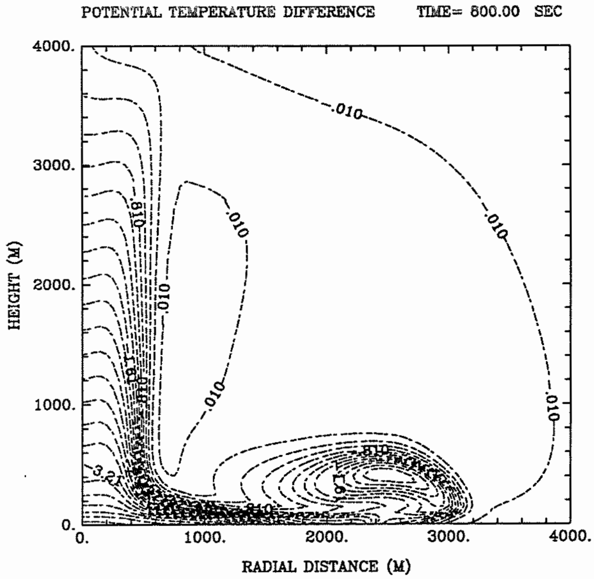

Fig. 1a. The difference in potential temperature between the downdraft air and the environment at 800 sec. (Rainwater mixing ratio = 4 g/kg; lapse rate = 9.5 K/km; Cloud radius = 800 m). Dashed lines indicate contours with negative values. Contours intervals are 0.2 K.

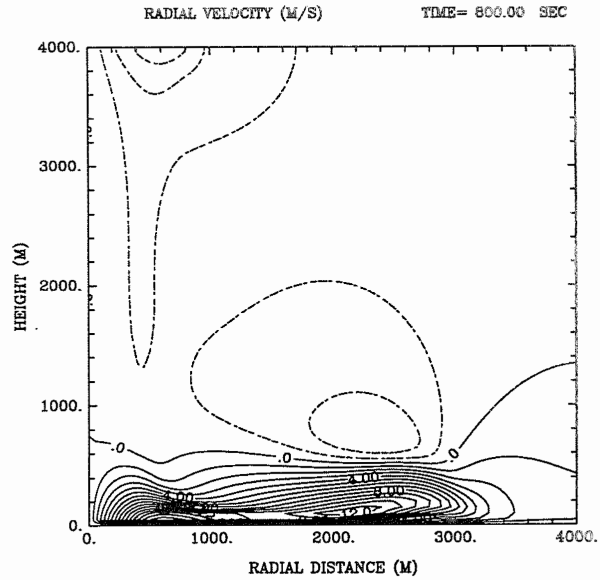

Fig. 1b. Radial velocity at the same time as (a). Dashed lines indicate contours with negative values. Contours intervals are 1 m/s.

dissipating stage of the cloud, (2) it does not allow raindrop interactions that could be important at larger precipitation rates, (3) it does not include ice, so it cannot assess how melting contributes to the strength of the downdraft, and (4) the model is axisymmetric and therefore cannot take surrounding wind shear into account, nor can it explore microburst asymmetry.

3. Effect of Rainwater Characteristics on Microburst Behavior

In a typical numerical experiment, raindrops fall from a cloud with a radius of 800 m into the top of the domain from the beginning to the end of the experiment. The raindrops evaporate, cooling the air, and drive a downdraft that builds toward the ground. Under the downdraft, a dome of high pressure builds and accelerates the descending, cooled air outward near the surface (fig. 1a). Figure 1b shows that as the cold outflow begins to spread near the ground, two regions of strong outflow exist - one that remains steady and fixed near the downdraft base and another that weakens as it expands outward with the leading edge of the evaporatively-cooled air. With a constant source of rain, the burst of winds at the head of the outflow expands out of the domain, and the downdraft and outflow peak at its base reach a steady state.

In order to reveal how a time-dependent rainwater source influences microburst strength, I varied the time it took the rainwater source to reach its maximum of 4 g/kg, from 0 (a sudden gush of rain) to 1500 sec. (the rain increases linearly throughout the experiment). Although the downdraft and outflow velocities in each case eventually reach the same steady state (Figs. 2a and 2b), the paths to the steady state are quite different. Cases in which the cloud reaches maximum rainfall rate quickly (0 - 600 sec.) have a strong initial burst of winds, whereas cases with a slowly building source of rain (900, 1500 sec.) only grow slowly to the steady state. This suggests that the burst-like nature of microbursts is enhanced by the rapid onset of precipitation.

To test how long rain must fall to develop microburst-strength outflow, I varied the length of time that the cloud provided rain from 100 sec. (a short pulse of rain) to 1500 sec. (the entire experiment) (Figs. 3a and 3b). This test showed that rain must fall for some minimum amount of time (in this case 500 sec.) to produce the maximum attainable initial burst. After the burst, however, continued rain sustains the strong, steady outflow winds near the base of the downdraft but does not increase the dissipating burst of winds expanding at the head of the outflow . In this way, for long sources of precipitation, the dominant surface winds eventually become the winds near the base of the downdraft. This test suggested why some observed microbursts expand while others do not, and why some remain strong and others

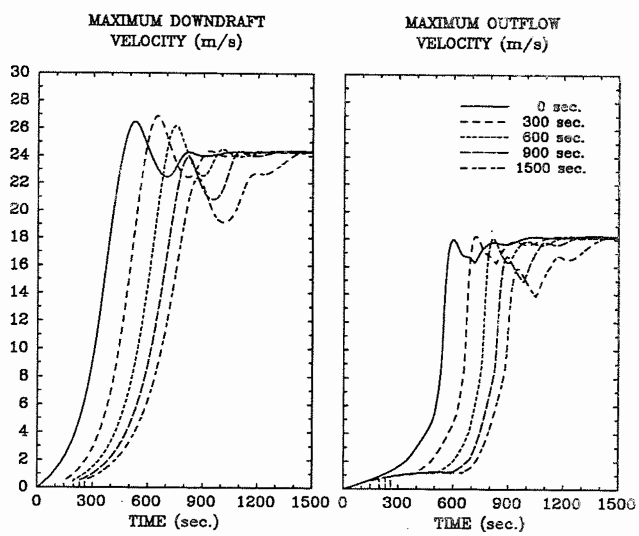

Fig. 2. Evolution of (a) maximum downdraft velocity (b) maximum outflow velocity, where the time until cloud reached its maximum rainfall rate is varied from 0 to 1500 sec., as shown.

quickly decay (Hjelmfelt, 1988) - short periods of precipitation produce only a weakening, expanding burst of winds at the head of the outflow, while in cases with long precipitation sources, strong, steady surface winds occur near the base of the downdraft and do not expand.

4. Effect of Lapse Rate on Microburst Behavior

Many studies (Krueger and Wakimoto, 1985; Srivastava, 1985, 1987) have shown that a lapse rate of temperature near the dry adiabatic favors microbursts, and, although microbursts cannot yet be predicted, this fact has been used as an indicator that microbursts may develop. However, this work suggests that the lapse rate of temperature cannot be used alone to explain microburst strength or predict microburst danger.

Fig. 4 shows how a downdraft evolves with each of 4 subcloud lapse rates when 4 g/kg of rain falls steadily from a cloud base at 4 km (Fig. 4a) or 1 km (Fig. 4b). Although the steepest lapse rate (9.5 K/km) produces the strongest downdraft in both cases, the sensitivity of the downdraft speed to lapse rate clearly depends strongly on the cloud base height. While varying the lapse rate over a wide range (6.5 - 9.5 K/km) produces a difference of 17 m/s in the downdraft speed for the high-based cloud (Fig. 4a), this variation produced only a 2 m/s difference for the low-based cloud (Fig. 4b). (Outflow speeds respond in the same way.) Thus, for low-based clouds, the lapse rate is practically irrelevant, whereas for high-based clouds, it is a dominant factor.

As well as limiting downdraft strength, this model suggests that stable subcloud lapse rates may be responsible for fluctuations in strength that were observed in microburst outflows (Cornman *et al.*, 1989; Biron, Isaminger, and Flemming, 1990; Hjelmfelt, 1988). The observed time-varying pulses could have been due to repeated rainwater gushes from cloud base, but only in some cases (Biron, Isaminger, and Fleming 1990) have pulses been tied to storm evolution. These numerical experiments show that fluctuations in downdraft strength can occur every few hundred seconds, with corresponding pulses of several m/s in

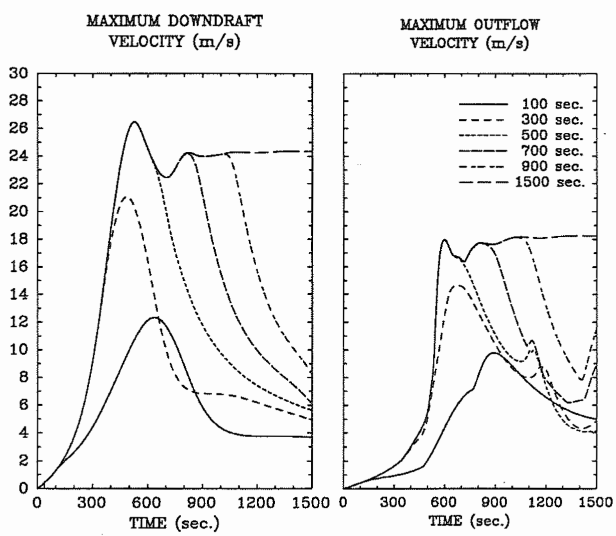

Fig. 3. Evolution of (a) maximum downdraft velocity (b) maximum outflow velocity, where the duration of rainfall rate is varied from 100 to 1500 sec., as shown.

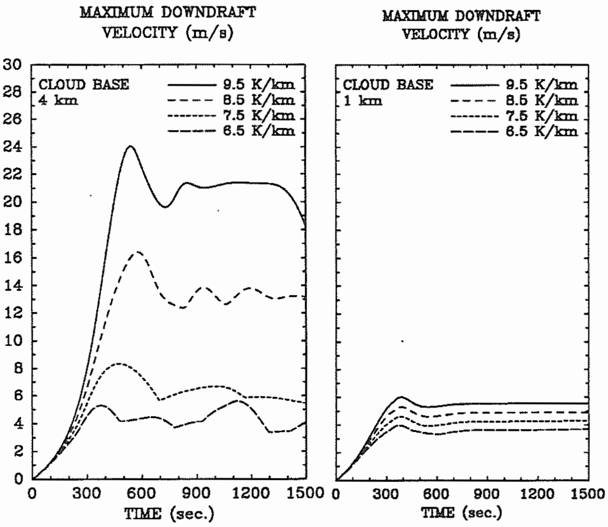

Fig. 4. Evolution of maximum downdraft velocity for several lapse rates, as shown, from a cloud base of (a) 4 km and (b) 1 km.

outflow strength for certain combinations of rainwater mixing ratio and stable subcloud lapse rates *even given a steady source of rain.*

When a 8 g/kg rainwater source falls into a subcloud layer with a lapse rate of 7.5 K/km, a strong downdraft of 17 m/s builds and descends rapidly, but instead of settling to a steady state as it would with a neutral lapse rate, the downdraft strength pulses regularly, every 250 sec (fig. 5a). These pulses occur in the outflow too (fig. 5b), timed such that when one of the downdraft cores nears the surface, there is a burst of 11 m/s outward. This microburst cannot driven by evaporatively-cooled air, since the downdraft air is about 1.5 °C warmer than the environment. The pulses occur by the following process: an initial downdraft core descends when lots of rain, dragging the positively buoyant air with it, reaches the ground, causing an outburst of rain and strong winds at the ground. After this initial burst, the positively buoyant air tries to rise, causing rain to accumulate in the downdraft. But, with more rain falling into the downdraft and overtaking the storage region, the restoring force is overwhelmed, and another burst of winds and rain occurs at the ground, before the rainwater storage begins again. This interaction of precipitation and downdraft dynamics is similar to that described by Kessler (1974) to explain the storage and oscillatory nature of water content in updrafts.

The model suggests that this pulsing behavior does not occur in every case, since a very stable lapse rate prevents a strong downdraft from reaching the surface while a large rainwater mixing ratio would overwhelm any restoring force. This behavior requires a positively buoyant region in the downdraft in the presence of rain, *i.e.* evaporation that does not occur rapidly enough to cool the downdraft air beneath the temperature of the environment. Since the small drops of the distribution evaporate rapidly in the subcloud region, evaporative cooling at lower layers is due to the larger drops of the distribution. This behavior has not been observed in previous axisymmetric microburst models (Krueger and Wakimoto, 1985; Proctor, 1988, 1989) perhaps because they have used parameterized cloud microphysics - Coen (1988) has shown that parameterized microphysics do not accurately

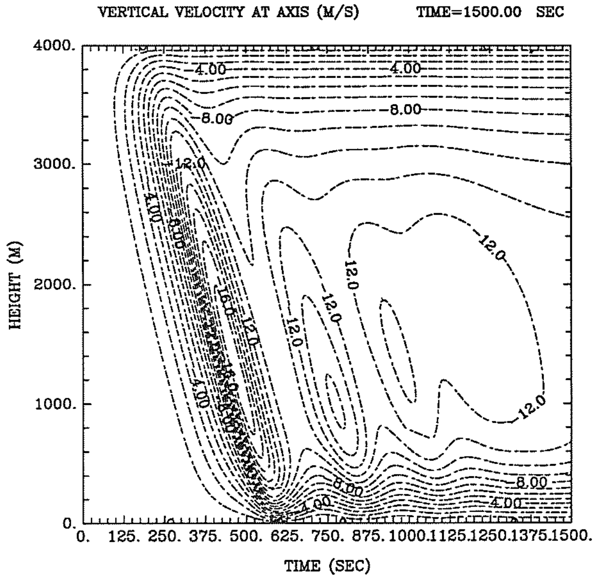

Fig. 5a. Vertical velocity at the axis of the microburst as a function of time. Contours are every 1 m/s. Dashed lines indicate negative contours. (Rainwater mixing ratio = 8 g/kg; lapse rate = 7.5 K/km; Cloud radius = 800 m).

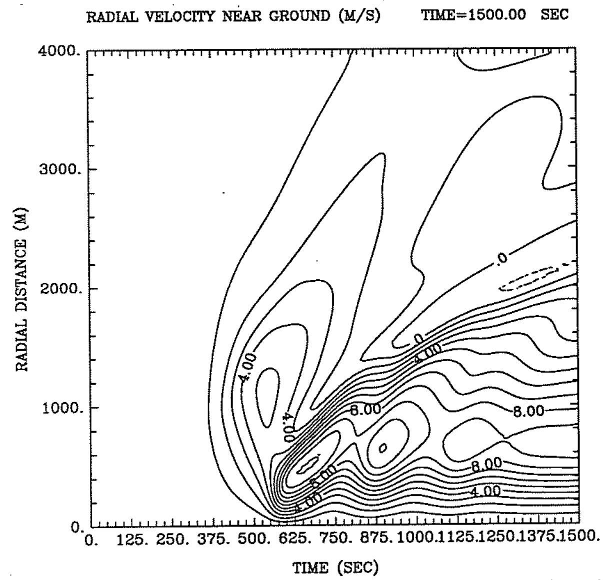

Fig. 5b. Horizontal velocity at a height of 25 m as a function of time. Contours are every 1 m/s. Dashed lines indicate negative contours.

represent raindrop sorting due to size and overestimate the amount of evaporation in microburst downdrafts by numerically redistributing the rainwater into smaller drop sizes, which evaporate rapidly. These oscillations are probably an exaggeration of the truth, however, because drop collisions and breakup will to some degree replenish the concentration of small drops. A more detailed study that can include the interaction of raindrops in a model with more than one dimension is necessary to more accurately determine the effect of microphysics on microburst outflow.

5. Summary and Conclusions

This work sought to explain the unclear time and spatial aspects of microburst behavior using simple, discrete microphysics that treat raindrop sedimentation and evaporation in a nonhydrostatic, anelastic numerical model of the region beneath a cloud. I tested temporal characteristics of the rainwater source to show that, in addition to the well-documented microburst-enhancing effects of large rainwater mixing ratios and steep lapse rates, other characteristics of the rainwater source can strongly influence microburst strength. Specifically, a rainwater source that builds rapidly to its maximum contributes to the burst-like nature of microbursts. Also, tests showed that the duration of rainfall determined whether the dominant outflow was the expanding, dissipating burst of winds at the head of the outflow or a non-expanding, steady flow at the base of the downdraft.

I found that, contrary to past studies, the subcloud lapse rate was not always a dominant factor in determining microburst outflow strength, but that its effect depended on cloud base height - for high-based clouds, the lapse rate was indeed an important parameter, but for low-based clouds, the lapse rate was irrelevant. The subcloud lapse rate may also explain fluctuations in the strength of microburst outflows, but complete understanding of such an effect must await more a detailed treatment of microphysics in microburst models.

6. Acknowledgements

I thank Professor Ramesh C. Srivastava for guidance, insight, and many helpful discussions. This work has been supported by the National Aeronautics and Space Administration through the Graduate Student Researchers Program under Grant NGT-50449 and by the National Science Foundation through Grant ATM 91-05182 (R. C. Srivastava).

7. References

Biron, P. J., M. A. Isaminger and K. J. Flemming, 1990: A case study of the Claycomo, Missouri microburst. Preprints 16th Conf. Severe Local Storms. Amer. Meteor. Soc., 388-392.

Clark, T. L., 1979: Numerical simulations with a three-dimensional cloud model: Lateral boundary condition experiments and multicellular severe storm simulations. *J. Atmos. Sci.*, 36, 2191-2215.

Cornman, L. B., P. C. Kucera, M. R. Hjelmfelt and K. L. Elmore, 1989: Short time-scale fluctuations in microburst outflows as observed by Doppler radar and anemometers. Preprints 24th Conf. Radar Meteor. Amer. Meteor. Soc., 150-153.

Fujita, T. T., 1985: *The Downburst: Microburst and Macroburst.* The University of Chicago Press, 122 pp.

Hjelmfelt, M. R., 1988: Structure and life cycle of microburst outflows observed in Colorado. *J. Appl. Meteor.*, 27, 900-927.

Kessler, E., 1974: Model of precipitation and vertical air currents. *Tellus*, 26, 519-541.

Krueger, S. K. and R. M. Wakimoto, 1985: Numerical simulation of dry microbursts. Preprints 14th Conf. Severe Local Storms. Amer. Meteor. Soc., 163-166.

Proctor, F. H., 1988: Numerical simulations of an isolated microburst. Part I: Dynamics and structure. *J. Atmos. Sci.*, 45, 3137-3160.

Proctor, F. H., 1989: Numerical simulations of an isolated microburst. Part II: Sensitivity experiments. *J. Atmos. Sci.*, 46, 2143-2165.

Soong, S. T. and Y. Ogura, 1973: A comparison between axisymmetric and slab-symmetric cumulus cloud models. *J. Atmos. Sci.*, 30, 879-893.

Srivastava, R. C., 1985: A simple model of evaporatively driven downdraft: Application to microburst downdraft. *J. Atmos. Sci.*, 42, 1004-1023.

Srivastava, R. C., 1987: A model of intense downdrafts driven by the melting and evaporation of precipitation. *J. Atmos. Sci.*, 44, 1752-1773.

PENETRATIONS OF THUNDERSTORMS WITH THE OPERATIONAL SWISS RADIOSONDE

Jürg **JOSS** and Emanuele **ZALA**
Swiss Meteorological Institute, Osservatorio Ticinese, CH-6605 Locarno Monti

Paul L.**SMITH** and Harold D. **ORVILLE**
Inst. of Atmospheric Sciences, School of Mines and Technology, Rapid City, South Dakota 57701-3995

Gilbert **LEVRAT** and Pierre **VIATTE**
Station Aèrologique, CH-1530 Payerne

Paul **RUPPERT**
Meteolabor AG, CH-6020 Wetzikon

1 Cause for the Analyses

The new Swiss radiosonde, equipped with fast response temperature, pressure and humidity sensors, allows on average every 3 seconds a temperature measurement and every 10s a pressure measurement. Routine ascents are made every 12 hours. During the past two years, some 5 soundings penetrating thunderstorms have been observed. Large gradients in temperature and turbulence have been observed in these cases. In fact the changes were so large, that the operator thought the sonde was defective, which is still open for discussion. There is evidence that the sensors are accurate (Sec.4) but the observations go beyond the range of plausible thermodynamic conditions. An explanation could be that variations in nature are more pronounced and more complicated than measured in the past with coarser instruments.

The data of the soundings are being analysed together with the measurements of the two operational Swiss weather radars, performing a full volume scan every 10min. In the most recent and best documented case the sonde encountered a reflectivity of 40dBZ in an updraft of 12m/s, then entered a downdraft (up to -12m/s) in the core of the reflectivity of over 55 dBZ (over 100mm/h of rain rate). This confirms the exceptional severity of the case (in agreement with the meteorological situation recorded on the ground).

2 Sensors of the Radio Sonde

2.1 Pressure

A hypsometer is used to measure pressure: every 10s the temperature of boiling water is measured with a copper constantan thermocouple and the saturation pressure of the water vapor calculated. As the measure of the pressure of the sonde is adjusted at ground level with stationary instruments of high precision, the overall error can usually be kept below 1hPa during the ascent to 10hPa.

2.2 Temperature

A similar thermocouple as above, using wires of 0.05mm diameter is used to measure air temperature every 3s. The time constant is of the order of 0.1s at ground level and of the order of 1s at 10hPa. The radiation error in full sun shine is below 0.1K at ground level and of the order of 1K at 10hPa.

2.3 Humidity

The humidity is measured with a VIZ-hygristor. Between ground level and 12km altitude it shows values close to saturation. Condensation and inertia may cause errors.

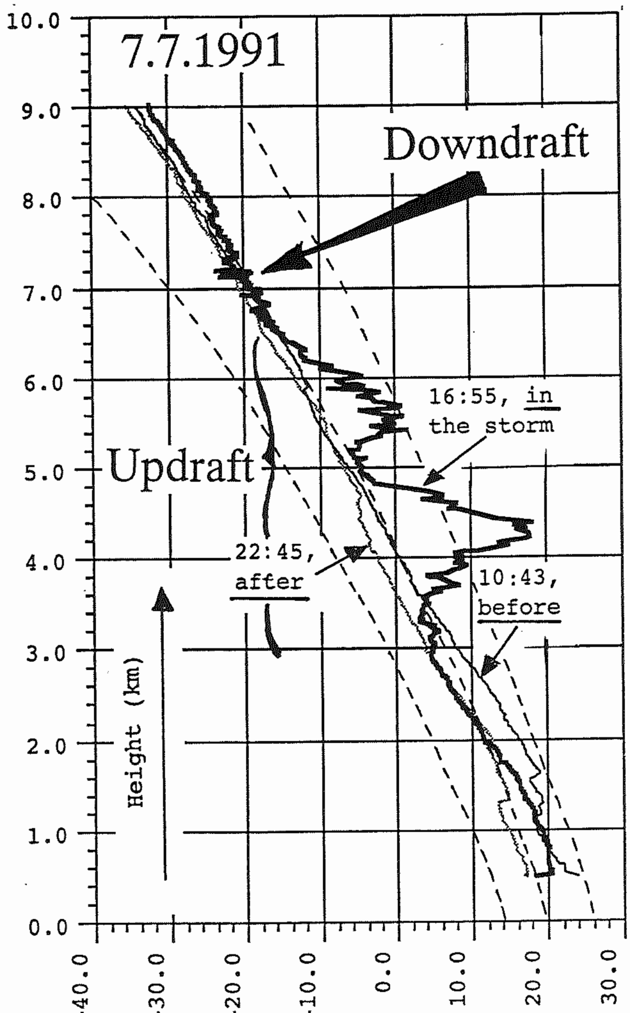

Fig.1: Height [km] versus temperature [C°] of the sonde in the thunderstorm and for comparisons the results of 6 hours before and afterwards. Dashed lines are moist adiabates.

3 Observations

3.1 Overview

The sonde was launched in the afternoon (16:55UTC) of 7 July 1991. Up- and downdrafts with strong gradients of temperature and turbulence happen below 9km; therefore, we restrict the analyses to this part of the atmosphere. Fig.1 shows the height versus temperature for the sonde in the thunderstorm and, included for comparison, the results of soundings 6 hours before and afterwards. Temperature excesses of up to 18C° appear in the updraft region at about 4.4km height (604hPa). As can be seen from Fig.2A, the sonde was floating for about 500s at roughly the same altitude (pressure) above 7.1km in a weak downdraft (arrow in Fig.1). To investigate downdrafts as well as updrafts, time (and not pressure or height) had to be taken as the principal, independent variable. Therefore, Fig.2 shows height, vertical velocity of the sonde, temperature and rate of change of temperature versus time. As the ascending rate of the balloon is of the order of 4m/s (dash-dotted line in FIG.2B), we must subtract this value to obtain vertical air motion.

3.2 Updraft Region

In the main part of the updraft the vertical speed of the sonde reaches up to 16m/s, corresponding to 12m/s of updraft air speed (Fig.2B) in the colder, upper part of the updraft region and up to 12m/s (8m/s for the air) in the warmer, lower part of the updraft. Temperature changes are larger also in the cold part of the updraft, attaining frequently over a degree per second, corresponding to a spatial gradient of temperature of 1/4 K/m (assuming a relative speed of 4 m/s of the balloon to the air).

3.3 Downdraft Region

Compared to the updraft region, the air in the downdraft is more turbulent and temperature changes are somewhat smaller. This may be explained by better mixing of the air. While the updraft part extends over more than 3km (where the speed of the air has the same sign as the speed of the balloon relative to the air), the downdraft region extends only over a small fraction of a kilometer (where the speed of the air is compensating the balloon speed). Of course time and space variations may be a factor in the apparent extent of these regions.

3.4 Before and afterwards, neighboring soundings

To allow comparison of the results in the storm with "normal" conditions, the two adjacent soundings were added in Figs.1and 3. As expected, we find in both cases (6 hours before and afterwards) a much smoother lapse rate of the temperature. As indicated by comparing geopotential heights, the thunderstorm sounding between 960 (491m) and 150hPa (14126m) was on average 2.2 degrees warmer than 6h before or after. The segment between 700 (3153m) and 500hPa (5891m) was on average even 8 degrees warmer than 6h before or after. Compared to the soundings of Stuttgart, München, Lyon, Nîmes and Milano the thunderstorm sounding in Payerne was 1.3 degrees warmer (960/150hPa).

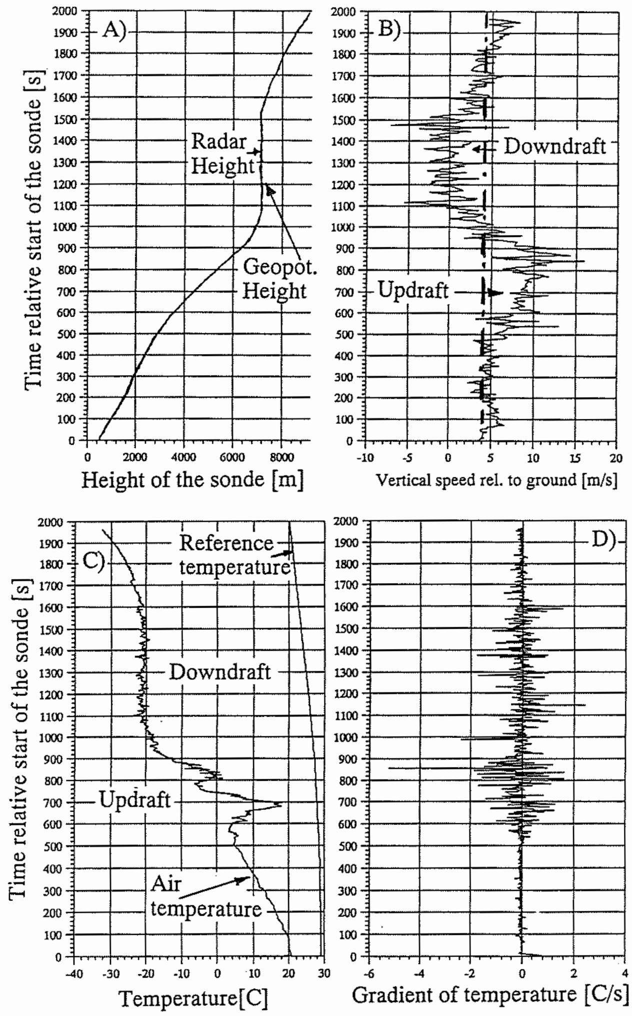

Fig.2: Height, vertical velocity, temperature and rate of change of temperature versus time.

Fig.3: Details for up- and downdraft region before, in and after the storm. Note the difference in scales.

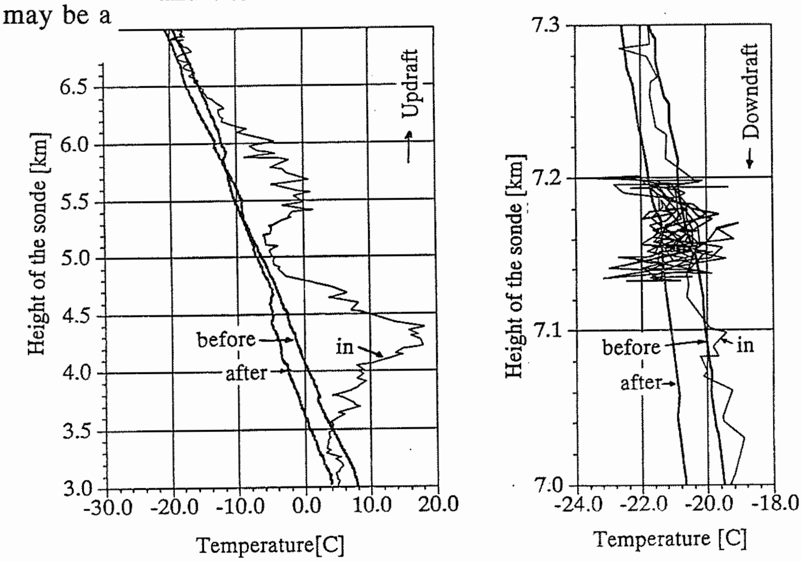

3.5 Radar Observation

Fig.4 gives an overview of the radar reflectivity. The superposition of a zoom on the radar information around the launching station of the sounding and the path of the sonde relative to the launching point indicates that the sonde flew through the region of strongest radar reflectivity. As the wind kept changing direction with height, the sonde remained close to the launch (within 4km horizontal range) in spite of up to 35kt horizontal wind during half an hour.

4 Evaluation of the Measurements

4.1 Continuity of measurements

Successive measurements of the sonde in the storm show a reasonable continuity. Because geopotential height is calculated from the pressure and pressure depends on a measurement of temperature, the continuity of the measured height in Fig. 2A is also evidence for the correctness of temperature measurements: one degree error of the hypsometer-temperature corresponds to an error of hypsometer-pressure of roughly 30hPa, equivalent to 300m of error in height determined with the hypsometer at ground level. (Note that this consideration concerns the temperature- and pressure reading of the hypsometer only, not the temperature of the atmosphere. We use it as evidence that the sonde is able to measure very precise hypsometer-temperature, and therefore, hopefully, also precise air temperature.)

4.2 Agreement with Observations of the Transponder Radar

The height of the sonde was calculated with two, completely independent methods:

- Hydrostatic integration of the PTU-values,
- from the transponder distance and the elevation of the transponder radar antenna.

The agreement of the two values in Fig.2A is excellent and confirms the up- and downdrafts encountered. It also excludes a significant temperature error of many degrees: In the downdraft a systematically higher (40m) hydrostatic-height was found, as compared to the radar-height. If the temperature between ground level (960hPa) and the downdraft (430hPa) had been only 1.7°C lower, we would have found perfect agreement. If the whole difference were attributed to the updraft layer (700~470hPa) the mean temperature would have had to be about 3.5°C lower to bring about agreement. But there may be timing errors in the transponder part of the order of 0.3 microsecond and it will therefore be dangerous to try to calibrate the temperature sensor with the radar height.

4.3 Internal Reference-Temperature

The internal reference temperature for the thermocouples (Fig.2C), calculated from the measured resistance of a copper wire, shows the expected behavior and continuity with slow changes of around 10^{-2}C/s.

4.4 Icing and Electrical Phenomena, etc

Perhaps the weakest evidence for the correctness of the measurements is the fact that we cannot imagine instrumental malfunctioning to produce the observed values. Icing (and resulting errors in the measurement of air temperature) cannot explain the high temperature at 4km altitude (temperatures are well above freezing). Electrically produced errors can be excluded on the basis of simulations in the laboratory: Electrical fields up to the value producing corona discharge on the sonde were investigated and have not been able to produce a deviation from normal anywhere close to the observed ones. Effects caused by sensor wetting, ingestion of precipitation, interference of high frequency etc. have been considered but seem unlikely according to our knowledge of the sonde behavior.

4.5 Contradictory Indications

An observed temperature of 18°C at 604hPa (4.4km altitude) is thermodynamically implausible. Considering the heat of condensation and extrapolating adiabatically to ground level, we would need 32°C at 100% humidity (or 40°C and 60% relative humidity), which is indeed quite impossible.

The temperature interpolated from above or below and from 6h before or afterwards is of the order of 0°C. Modeling-results indicate 10K excesses in the cloud compared to the environment in strong, convective situations with temperature conditions similar to the Swiss conditions. In general these differences show up at the -5°C level where significant icing (riming) is occurring, so that the heat of fusion is also contributing to the temperature differences.

An updraft of 12m/s or a downdraft of -12m/s is not spectacular. The measured vertical speed in the updraft is 5-15m/s. But for the measured temperature difference between the cloud and its surroundings (up to 18°C) we expect vertical velocities of up to 45 m/s (Sulakvelidze, 1967). However, we do not know what the maximum speed was, because we measured the speed at the location of the sounding and not necessarily in the core of the storm.

More extreme (less expected) were the high gradients of temperature (over 100 times compared to average, vertical gradients in a saturated air) and wind shown in Figs.2 and 3.

5 Concluding Remarks

Instrumental considerations make it hard to explain a temperature error of more than 3 degrees. At the moment of writing the paper we are still trying to find the reason for the (apparently anomalous) observed data and searching for explanations without violating well established physical laws.

6 Appendix: Brief description of the Synoptic situation

Surface: Uniform pressure distribution over the alpine region (~1020hPa). Depression with center at 7° W 48° N with center pressure at 1010hPa. Cold front from Scotland over Belgium and eastern France until Gulf of Lion.

Upper levels: Well defined cutoff trough with center over southeast England (-17° C at 500hPa). Axes reach from southeast England over Bordeaux until Gulf of Lion. Slightly cyclonic curvature over the western part of Switzerland. Jet from Massive Central until Ireland, so that the region of interest (Payerne) is locate under the right jet entrance. The Omega block over Middle Europe prevents an advancement of the cutoff low over Central Europe.

Local situation: Typically unstable conditions. The soundings show a very high θ_w around 18°C at 850hPa and around 17°C in the upper levels. Warm and relatively moist air from the Westerly Mediterranean had been advected during the days before the event, so that a θ_w over 18°C was found in the whole region situated on the northern slope of the alps and some thunderstorms had already been observed in the region.

During the daytime (7.7.91) a relatively strong insolation was recorded. The automatic station of Payerne measured more than 6 hours of insolation. The maximum temperatures where about 29°C at ground level. The mountain stations measured also high values of T and U (MLS at 2000m 18.2°C/99%, NAP at 1400m 22.8°C/79%, CHA at 1600m 20.4°C/73%). The condition was favorable for strong thunderstorms.

A hypothetical explanation of the 1800UTC sounding: The wet-bulb potential temperature of the sounding was around 18°C at 850hPa and 17°C in the upper levels, 6 hours before and 6 hours after 1800. The thunderstorms were connected with a typical prefrontal squall line: The prefrontal pressure-fall, the unstable thermodynamic conditions, the cyclonic curvature, the right jet entrance and the diurnal insolation contributed to the formation of the line squall. Moreover it often happens that the moist and unstable air remains entrapped between the alps and the french pushing front (Swiss meteorologist call it the "sandwich-effect").

The 1800 sounding shows in the lower part (500-3000m) winds blowing from northwest. This is confirmed by the surrounding automatic stations (CHA 320°, NAP 316°, MLS 280°). Between 3000 and 5000m it blows from east-northeast, and above it assumes the direction of the general circulation. As a hypothetical explanation we propose that the radiosonde went through the frontal part of the squall line (gustfront, warm updraft between 3000 and 6000 meters and downdraft). The ascending core of the warm inflow would have to have a θ_w of 18-32°C, but the greatest observed values were in the mid 20's.

Other problems: The windspeed in the lower part of the gust front (around 7kt) seems to be a little small. Indeed the automatic station of Payerne measured 12kt with gusts over 30kt. But it's possible that behind the front the winds fell rapidly.

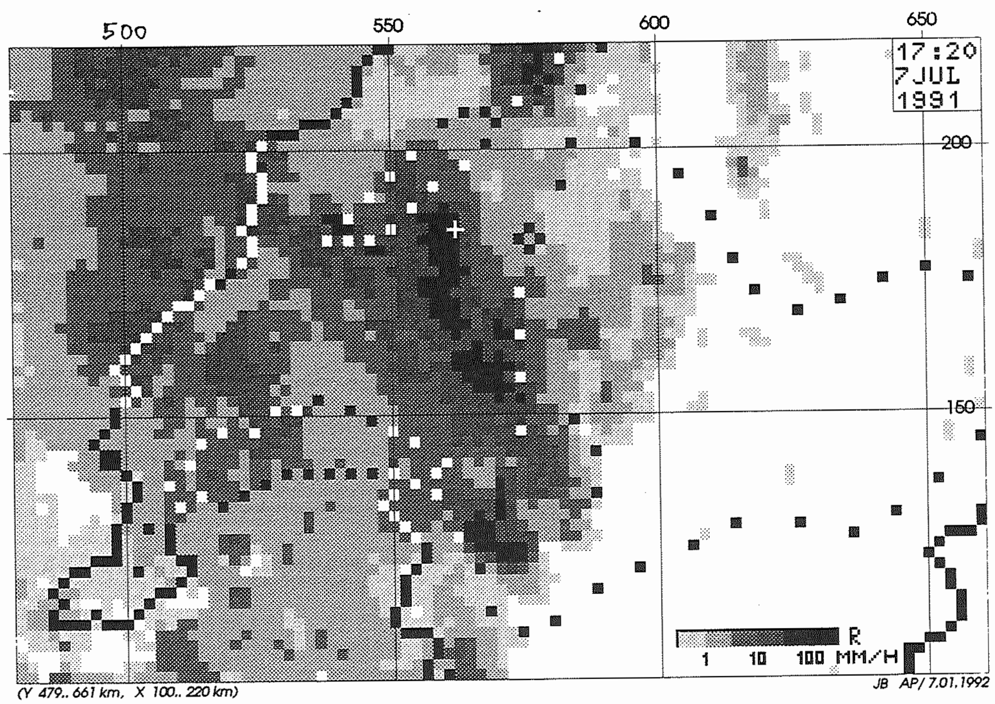

Fig.4: Results of the operational Swiss radars. The volume scan (17:20, 7 JUL, 1991) was performed between 17:10 and 17:16. The range of the rain rate is divided in seven equal steps on a logarithmic scale, the lowest step indicating intensities <0.3mm/h and the highest one intensities >100mm/h. The values indicate the maximum rain rate estimated in a column vertical above the pixel. The size of the pixel is 2 x 2 km^2, the radio sonde was launched from the location marked with a white cross.

The Effects of Radiation on the Dynamics of a Numerically Simulated Tropical Mesoscale Convective System

Takmeng Wong and Graeme L. Stephens

Department of Atmospheric Science, Colorado State University, Fort Collins, CO. 80523

1 Introduction

Tropical Mesoscale Convective Systems (MCS's) are known to exert a large influence on the radiation budget of the tropical atmosphere through the mutual interactions between radiation and cloud hydrometeor fields (such as cloud droplets, rain drops, snow, and graupel particles; Wong *et.al.*, 1992 a and b). These changes in radiation fields can, in turn, modify the dynamics of the tropical MCS's through internal feedback processes (i.e., cloud radiative heating/cooling). For examples, many recent papers have pointed to the importance of the infrared radiative processes in modulating the circulation of these MCS's (i.e., Chen and Cotton, 1989 and Dudiha, 1989). Furthermore, radiative heating of the MCS can also significantly alter the large scale heating profile (Houze, 1982). In this preliminary study, we investigate the role of radiation in shaping the dynamic circulation of tropical cloud system through numerical experiments with a tropical MCS that occured during the Equatorial Mesoscale Experiment (EMEX) using the Colorado State University Regional Atmospheric Modeling System (CSU-RAMS). Section 2 gives a brief description of the numerical mesoscale cloud model used in this study. It is followed by a discussion on the set up of the numerical experiments. The preliminary results obtained from the numerical experiments associated with the tropical MCS are presented in section 3. Section 4 gives a summary and some further comments on this work.

2 Dynamical mesoscale cloud model

The numerical cloud model used in this study is the Colorado State University Regional Atmospheric Modeling System (CSU-RAMS). As described by Cotton and Tripoli (1978), Tripoli and Cotton (1980, 1982), and Cotton *et al.* (1982, 1986), this model is non-hydrostatic, fully compressible and includes a full set of dynamical, thermodynamical, and microphysical equations for water and ice phase particles. The model predicts all three components of the velocity, the ice-liquid potential temperature (Tripoli and Cotton, 1981), the dry air density, and the mixing ratios of different bulk hydrometeor species including cloud water, rain water, ice crystal, graupel, and aggregates. The size distribution of these bulk hydrometeor quantities are prescribed in the model. Parameterization of subgrid-scale turbulence is also contained in the model using a simple first order closure scheme in which eddy exchange coefficients for heat and momentum are calculated as a function of fluid deformation and Richardson number.

3 Experimental Setup

For this study, the cloud model is formulated on a two dimensional (2-D) grid of 500×32 points which represents a domain of 500 km in the horizontal and 21 km in the vertical. Previous works on the tropical MCS's (i.e., Xu and Krueger, 1990, Nicholls and Weissbluth, 1988 and Tao *et al.*, 1987) have demonstrated the validity of 2-D cloud simulations for studying the physical processes associated with these cloud systems. The horizontal resolution chosen to resolve convection in the tropical MCS is 1 km (eg Nicholls, 1987) and the vertical grid is stretched slowly from 400 m near the surface to 1 km at top of the model to minimize gravity wave refraction due to rapid changes in vertical spacing (Nicholls, 1987). A weak dissipative layer is applied to the highest 8 km of the domain to reduce reflection from the upper rigid walls. The kinematic and thermodynamic/microphysical variables in the model are set up on a staggered grid system (Tripoli and Cotton, 1982). Rigid walls are used as vertical boundaries. Frictional effects are neglected at the bottom boundary but fluxes of latent and sensible heat from the ocean surface are included in the model by specifying a constant temperature and moisture gradient. The lateral boundaries include a mesoscale compensating region (MCR, Tripoli and Cotton, 1982) to provide a large-scale balance adjustment of circulation generated within the interior of the model domain. The Klemp-Lilly (1978) radiation boundary condition is also applied as the lateral boundaries of the fine-mesh to allow propagation of gravity waves through the fine mesh/MCR walls and to minimize the reflection of these gravity waves back to the model domain. The cloud model is initialized at approximately 0516 LST on 2/3/87 at latitude 9 S and longitude 139 E using sounding data obtained from Darwin, Australia and integrated forward in time for 6 hours with a 10 seconds timestep. To study the dynamic response of radiative heating in a mesoscale cloud system, two numerical experiments were performed. In the 'full-physics' run, all processes including radiation were turned on in the model simulation. The results of this simulation are described in more detail by Wong *et.al.*, 1992b. In general, this run seems to capture many features of the observed EMEX tropical cloud cluster. In the second set of simulation, all conditions were the same as the 'full-physics' run with the exception that radiative processes were turned off in the model. The dynamic responses to the radiative heating are studied by examining the time series of the model fields between these two simulations.

4 Results

In this section we will describe some of the preliminary results obtained from the numerical experiments with the EMEX cloud cluster system.

Figure 1 shows a time history of the peak upward vertical velocity in the model domain for the 'full-physics' run (labelled 'rad' in the figure) and the 'no-radiation' run ('norad'). The two profiles start off with very similar time series in the first 90 minutes of the simulation. After this time the two peak upward vertical velocities curves begin to diverge from each other. The 'full-physics' run seems to have significantly stronger peak upward vertical motion than the 'no-radiation' case. Furthermore, the difference between these two cases can be as large as 50% of the value of the 'full-physics' run according to the figure. Since the peak upward vertical velocity is an indicator for intensity of cloud cluster system (i.e., strong peak upward vertical velocity usually leads to stronger in-cloud circulation), Fig. 1 suggests the presence of radiative processes can have significantly influences on the circulation of this tropical MCS through cooling at top and heating at base of the cloud system.

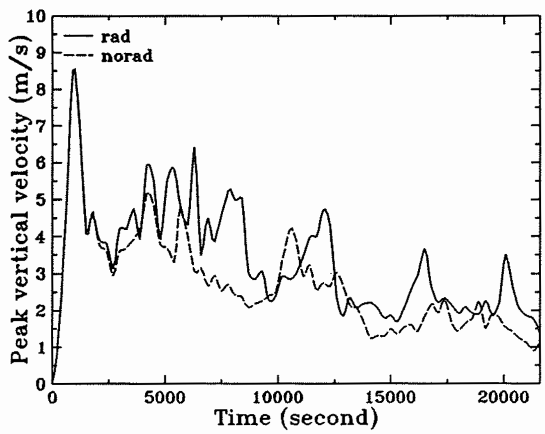

Figure 1: Time series of the peak vertical velocity (m/s) in the cloud model for the 'full physics' case (labelled as 'rad', solid line) and the 'no-radiation' case ('norad', dashed line).

This increase in cloud circulation intensity can further enhance the growth of the cloud hydrometeor field. Figure 2, 3, 4 show the time series of the domain integral of the total (solid plus liquid water), the solid water, and the liquid water hydrometeor field for the 'full-physics' run and the 'no-radiation' case. These figures clearly demonstrate the significant effect of radiation on the cloud hydrometeor fields. The 'full-physics' run seems to produce approximately 30% more cloud hydrometeor than the 'no-radiation' case. These figures also suggest that the radiative-dynamic-microphysics interaction may enhance longevity of tropical MCS by continuously sustaining cloud circulation.

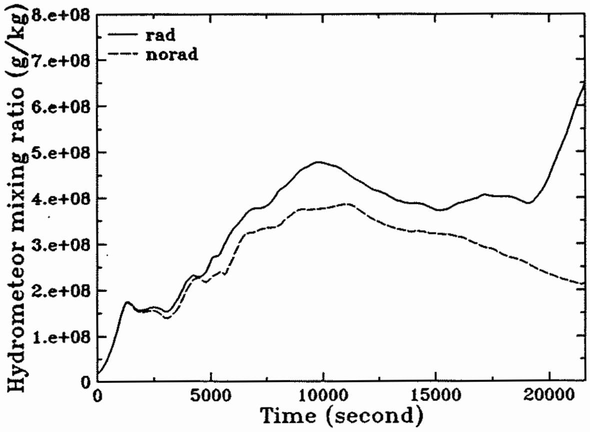

Figure 2: Time series of the domain integrated hydrometeor mixing ratio (g/kg) in the cloud model for the 'full physics' case (labelled as 'rad', solid line) and the 'no-radiation' case ('norad', dashed line).

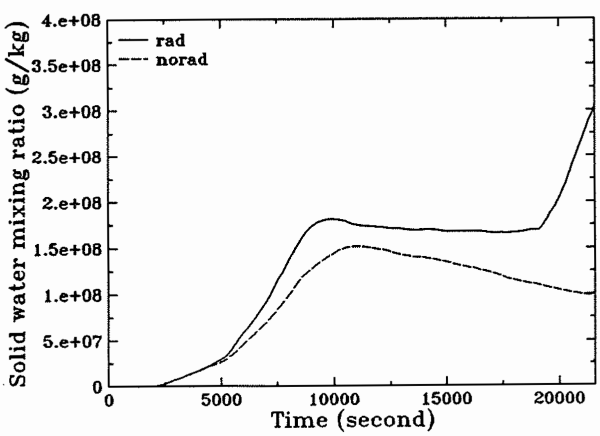

Figure 3: Time series of the domain integrated solid water mixing ratio (g/kg) in the cloud model for the 'full physics' case (labelled as 'rad', solid line) and the 'no-radiation' case ('norad', dashed line).

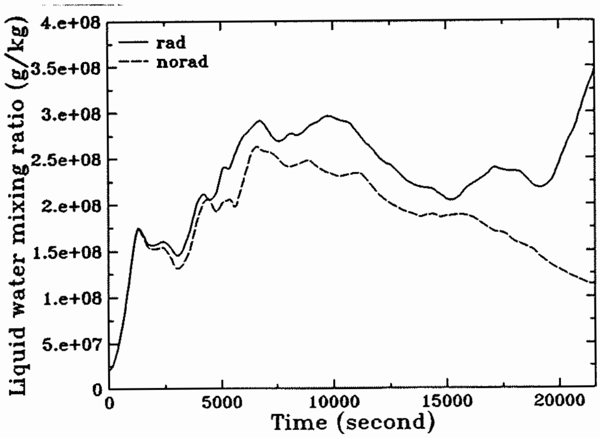

Figure 4: Time series of the domain integrated liquid water mixing ratio (g/kg) in the cloud model for the 'full physics' case (labelled as 'rad', solid line) and the 'no-radiation' case ('norad', dashed line).

Radiation also have impacts on the surface precipitation field. Figure 5 shows the time series of the domain integral of the surface precipitation field for the 'full-physics' run and the 'no-radiation' case. The 'full-physics' run again produces approximately 20% more surface precipitation than the 'no-radiation' case. This increase in surface precipitation arises from to the increase in the intensity of the cloud circulation and also the increase in the generation of the cloud hydrometeor fields as shown on the previous figures.

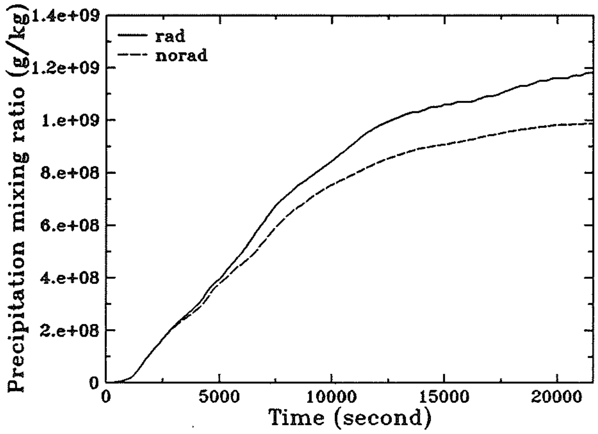

Figure 5: Time series of the domain integrated surface precipitation mixing ratio (g/kg) in the cloud model for the 'full physics' case (labelled as 'rad', solid line) and the 'no-radiation' case ('norad', dashed line).

5 Conclusions

This paper reports on a preliminary investigation of the role of radiation in shaping the dynamic response of tropical cloud system through numerical experiments with a tropical MCS that occured during the Equatorial Mesoscale Experiment (EMEX) using the Colorado State University Regional Atmospheric Modeling System (CSU-RAMS).

The preliminary findings from these experiments are :

1. the effect of radiation is to increase the maximum peak upward vertical velocity in the model simulation by an average of 50%. This also indicates that radiative effects can intensify circulation in the tropical MCS through cooling at top and heating at base of the cloud system.
2. Radiation also appears as an increase in the total cloud (solid and liquid water) hydrometeor field.
3. the effect of radiation can also modify the surface water budget by increasing surface precipitation.

More detailed studies are now underway by the authors to understand the effect of radiation on the tropical MCS.

Acknowledgments

This research was supported in part by NSF grant ATM-8812353, NSF grant ATM-8617856, and NASA grant NAG-5-1122.

REFERENCES

Chen, S., and W. R. Cotton, 1988: The sensitivity of a simulated extratropical mesoscale convective system to longwave radiation and ice-phase microphysics. *J. Atmos. Sci.*, **45**, 3897-3910.

Cotton., W. R., and G. J. Tripoli, 1978: Cumulus convection in shear flow: Three dimensional numerical experiments. *J. Atmos. Sci.*, **35**, 1503-1521.

Cotton., W. R., M. A. Stephens, T. Nehrkorn, and G. J. Tripolie, 1982: The Colorado State University three dimensional cloud/mesoscale model-1982, Part II: An ice parameterization. *J. Rech. Atmos.*, **16**, 295-320.

Cotton., W. R., G. J. Tripoli and R. M. Rauber, 1986: Numerical simulation of the effects of varying ice crystal nucleation rates and aggregation processes on orographic snowfall. *J. Climate Appl. Meteor.*, **25**, 1658-1680.

Dudhia, J., 1989: Numerical study of convection observed during the Winter Monsoon Experiment using a mesoscale two-dimensional model. *J. Atmos. Sci.*, **46**, 3077-3109.

Houze, R. A., Jr., 1982: Cloud clusters and large-scale vertical motions in the tropics. *J. Meteor. Soc. Japan*, **60**, 396-410.

Klemp, J. B., and D. K. Lilly, 1978: Numerical simulation of hydrostatic mountain waves. *J. Atmos. Sci.*, **35**, 78-107.

Nicholls, M. E., 1987: A comparison of the results of a two-dimensional numerical simulation of a tropical squall line with observations. *Mon Wea. Rev.*, **115**, 3055-3077.

Nicholls, M. E., and M. J. Weissbluth, 1988: A comparison of two-dimensional and quasi-three-dimensional simulations of a tropical squall line. *Mon. Wea. Rev.* **116**, 2437-2452.

Tao, W.-K., J. Simpson, and S.-T. Soong, 1987: Statistical properties of a cloud ensemble: A numerical study. *J. Atmos. Sci.*, **44**, 3175-3187.

Tripoli, G. J., and W. R. Cotton, 1980: A numerical investigation of several factors contribution to the observed variable intensity of deep convection over Florida. *J. Appl. Meteor.*, **19**, 1037-1063.

Tripoli, G., J., and W. R. Cotton, 1981: The use of ice-liquid water potential temperature as a thermodynamic variable in deep atmospheric models. *Mon. Wea. Rev.*, **109**, 1094-1102.

Tripoli, G., J., and W. R. Cotton, 1982: The Colorado State University three dimensional cloud/mesoscale model-1982. Part I: General theoretical framework and sensitivity experiments. *J. Rech. Atmos.*, **16**, 185-220.

Wong, T., G. L. Stephens, P. W. Stackhouse, Jr., and F. P. J. Valero, 1992a: The radiative budgets of a tropical mesoscale convective system during EMEX-STEP-AMEX Experiment. I: Observations. Submitted to *J. Geophys. Res.*

Wong, T., G. L. Stephens, P. W. Stackhouse, Jr., and F. P. J. Valero, 1992b: The Radiative Budget of A tropical Mesoscale Convective System during EMEX-STEP-AMEX Experiment. II : Model Results. Submitted to *J. Geophy. Res.*

Xu, K.-M., and S. K. Krueger, 1990: Evaluation of cloudiness parameterizations using a cumulus ensemble model. *Submitted to Mon. Wea. Rev.*

A 3-D MODEL FOR HAILSTONE TRAJECTORIES IN THUNDERSTORMS USING NONSTATIONARY FIELDS

Nesvit E. Castellano[1], C. M. Scavuzzo[1], Olga B. Nasello[1], G. M. Caranti[1] and Laura Levi[2]

[1]*Facultad de Matemática, Astronomía y Física.*
Universidad Nacional de Córdoba, Argentina
[2]*CONICET, Buenos Aires, Argentina*

1. INTRODUCTION

It is widely recognized that the fastest mechanism for growth within a cloud is accretion of supercooled droplets and that this is the process involved in the production of hail inside a cloud. Ice particles called the embrios increase their sizes quickly through accretion to sizes of up to several centimeters. Nevertheless not every particle in a cell become a hailstone. Some of them are carried aloft too soon by the strong updrafts to regions with little water concentration others become too heavy for the moderate updraft were they are located and fall off too soon from the cloud also without becoming large particles. A main motive for the present study is to find the optimum conditions in space and time from which these particles can develop to the sizes that can be potentially harmful. This is a complex process that can be understood only when it is studied in its various aspects such as the coupling of the microphysics (accretion, particle density and shape, aerodynamical forces) with the macrophysics (wind fields, mixing, etc.) in a complete manner. Zones more favourable to the initiation and growth of these particles can be determined in this way, data which is of great importance when it comes to defend crops and properties from damage caused by hail.

The fact that hail collected at the ground present a texture in its structure prompted investigators to try to correlate the cloud regions where the particle probably went through with that structure. This was thought could lead to the use of the hailstones themselves as probes of the clouds they grew in. Therefore trajectories studies were considered important to establish this correlation. Early studies (Musil, 1971) employed one dimensional wind fields. The doppler radar techniques allowed the estimation of the tridimensional wind field with reasonable resolution which led to the computation of more accurate trajectories, (Paluch (1978) , Heymsfield (1983), Foote (1984), Knight *et al.*, (1986), Miller *et al.*, (1990)). Trajectories in computer simulated clouds were also used (Xu, 1983). In the evaluation of these previous investigations it is important to note that while some authors employed stationary wind fields in general associated to a mature stage of the cloud. (Paluch (1978), Knight *et al.*, (1986), Xu (1983)), others worked with time dependent fields (Heymsfield (1983) and Miller *et al.*, (1990)). Also, the particles were considered to fall with different drag regimes such as a constant drag coefficient (Paluch (1978) or that obtained from a relation between the Best and Reynolds numbers fitted experimentally (Miller *et al.*, 1988). Moreover, most authors use the terminal velocity assumption i.e. they consider the particles attached to the air in the horizontal direction and falling with terminal velocity in the vertical direction.

The present work is aimed at comparing the trajectories and final sizes of hailstones calculated with and without a realistic equation of motion, stationary and non-stationary wind fields and the detailed drag forces on the particles. The wind field is generated in a computer model (Scavuzzo *et al.*,, 1991), which allowed all these cases to be studied.

2. CLOUD MODEL

The cloud model (Scavuzzo *et al.*,, 1991), is of the deep convection type and was designed to be machine efficient since it can simulate 1 hour of cloud evolution in a region of $16 \times 16 \times 16$ Km without resorting to the help of any predetermined symmetry, in about 2 hours on a relatively small workstation. Finite differences are used on a stagger grid of $\Delta x = 500m$ in time steps $\Delta t = 10s$. The diagnostic equation for the pressure perturbation is solved using a pseudospectral method and periodic boundary conditions on the lateral sides of the region. The model computes the liquid water concentration, temperature, pressure, and the three componentes of the air velocity as function of space and time. The tests carried out so far have shown a satisfactory performance of the model in the first stages of cloud evolution. A single cell simulation was used in this work to keep the analysis simple. Fig 1 shows a cut on a (x,y) plane at 4 km altitude. Fig 1 a) shows contours of the vertical wind component superimposed on vectors of the horizontal wind component of the central portion of the cloud (13×13 points). Fig 1 b) shows contours of the liquid water content in a larger (23×23 points) region. The latter quantity increased with height up to about 8 g/m^3.

The temperature profile had a lapse rate of 9 °C /km, starting at 28 °C at the ground. Maximum values for liquid water concentration and air velocity where around 6–8 g/m^3 and 20–25 m/s respectively.

3. THEORETICAL BACKGROUND

Previous work on simulation of trajectories of hydrometeors inside a cloud, (Heymsfield 1983, Knight *et al.*, 1986, Miller *et al.*, 1990) obtain the particle positions from the terminal velocity assumption.

In the present work two equations of motion are solved numerically. The corresponding to the terminal velocity assumption and the following one:

$$m \frac{d^2 \vec{x}_p}{dt^2} = \vec{F}_D - m\vec{g}, \tag{1}$$

where $\vec{x_p}$ and m are the vector position and mass of the particle, $\vec{F_D}$ is the drag force and $\vec{g}$ is the acceleration of gravity. Equation (1) is an improvement over the terminal velocity assumption since it does not assume instantaneous response. Since the drag caused by the change in momentum of the accreted droplets was considered negligible, the only drag force included corresponds to the aerodynamical one on a sphere of radius r

$$\vec{F}_D = \left(\frac{C_D\, R_e}{24}\right) 6\pi\eta r(\vec{V} - \vec{V}_p), \tag{2}$$

where $\vec{V}$ and $\vec{V_p}$ are the air and particle velocities, C_D is the drag coefficient, R_e is the Reynolds number and η is the dynamic viscosity of the air.

In this work two expressions are used for the drag coefficient. One is a simple power law suggested by Caranti *et al.*, (1991) in the context of simplifying calculations relative to Doppler radar analyses and is valid for medium range graupel, hail and water drops up to several mm

$$C_D = 6.23 R_e^{-0.347} \tag{3}$$

The other is an expression suggested by Beard (1980)

$$R_e = 20.52[(1 + 0.0901\, X^{1/2})^{1/2} - 1]^2, \tag{4}$$

where $X = C_D\, R_e^2$ is the Davies (Best) number.

Hailstones grow in these calculations both from vapor diffusion and accretion of a cloud of monodisperse droplets of radius 10 μm with a collection efficiency as given by Beard and Grover (1974). At this stage the accretion of ice crystals is not taken into account in the model. The hailstone density is calculated using the criteria given in Levi and Lubart (1991) (pag. 201).

For the runs with stationary fields the wind corresponded to that of the mature stage while for the runs with time dependent fields the wind was taken at one minute intervals and keeping it constant at intermediate times.

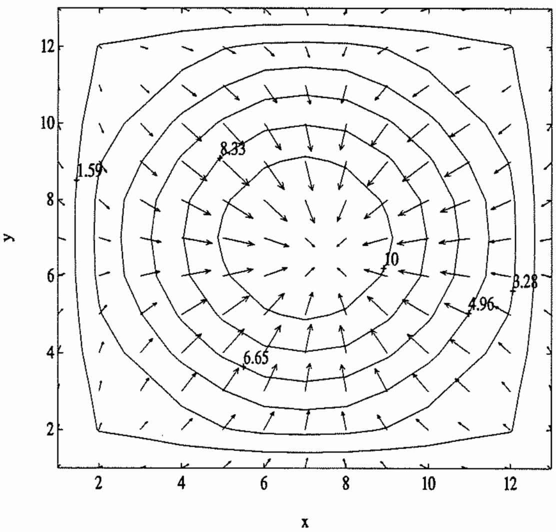

Figure 1 a). The wind field at 4 km altitude. Contours correspond to the vertical component (m/s) and arrows to the horizontal component. 13 × 13 grid points sorrounding the center of the cloud.

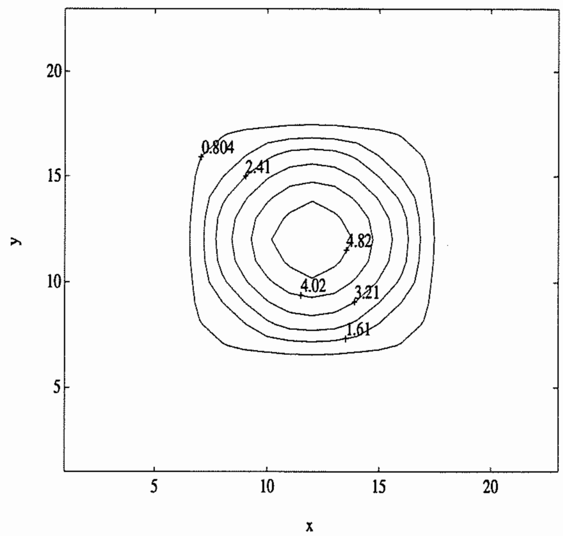

Figure 1 b). Contours of Liquid Water Content in g/m^3 at $z = 4$ km in a region of 23 × 23 grid points.

The hailstones trajectories studied were those corresponding to spherical embrios (frozen drops) with radius $r_0 = 0.25, 0.5$ and 1.0mm and density $\rho_0 = 0.9$ g/cm^3. Initially the embrios are seeded along a square grid on constant altitude planes and the trajectories are followed until the particles reach the 0 °C isotherm.

To help in the data analysis the parameter $HPR(z_0, r_0, r_f)$ was used as defined by Xu (1983):

$$HPR(z_0, r_0, r_f) = \frac{N(z_0, r_0, r_f)}{N(z_0, r_0)} \qquad (5)$$

$N(z_0, r_0, r_f)$ is the number of hailstones whose embrios were released at altitude z_0 with initial radius r_0 and reached final radius larger or equal than r_f . $N(z_0, r_0)$ is the total number of embrios with initial radius r_0 in a specific sector of the plane z_0.

The motion equation (1) and the corresponding to the terminal velocity assumption were solved by finite differences using a time increment of $\delta t = 0.1$ s, which yieldeds table solutions.

4.RESULTS

Results shown are those of embrios starting in the region of the cloud illustrated in Fig.1 a), in a square grid of 13 points per side giving a total of 169 particles to be followed per horizontal plane. The planes used were those of $z = 4, 5, 6, 7$ km. Planes with $z < 4$ km were not studied since at $T_a > -15$°C, it is difficult to freeze drops with $r_0 <$ 1mm (Mason (1971)) and recirculation was not taken into account. The main reason to chose the central square in Fig.1 a) was the observation that embrios starting outside this region evolved into small particles, which cannot be considered hailstones.

As an example of the numerous trajectories calculated, Figure 2 shows by couples trajectories of particles, starting at the same point, growing in time dependent and independent wind fields. The first couple of particles start with a radius of 1 mm at 4 km altitude and at about 0.5 km to the west and 1.5 km north from the center of the cloud while the second couple start with the same size at 7 km altitude and at the same horizontal position. Final radii for the first couple are 5.87 mm and 4.06 mm and for the second 1.57 mm and 2.34 mm according to whether the wind field is time independent or dependent respectively. The difference observed shows the importance of using the appropriate cloud fields in this kind of work.

Figure 3 shows a group of particles all starting with a radius of 0.25 mm at 4 km altitude along a line through the center of the cloud to the west of it. Since the wind field (see Figure 1) is similar to that of an electronic lense, focusing - defocusing effects could be observed. Figure 3 illustrate the effect in which particles sparsely released at one level in this wind field focus together in a smaller region as they fall, even though the final sizes are different.

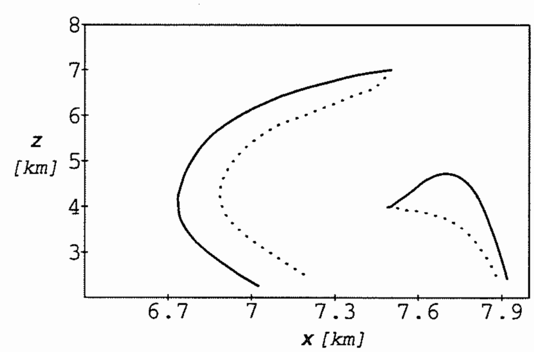

Figure 2. Trajectories projected on the plane y=9.5 km of particles with initial size of 1 mm released at 4 and 7 km altitude. Solid line motion in a stationary wind field. Dashed line trajectories in a time dependent wind field. Scales are in km and the center of the updraft is at $x = y = 8$ km.

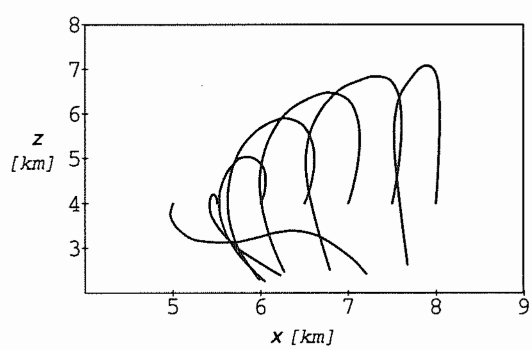

Figure 3. Trajectories projected on the plane through the center on the cloud ($y = 8$ km) of particles with initial size of 0.25 mm released at 4 km altitude on this plane. Scales are in km.

On the other hand, the results obtained using the equation of motion (1) and those using the terminal velocity assumption show a definitely different behaviour. Figure 4 shows in a horizontal cut at $z_0 = 4$km the contours of equal fractional difference of the final radius arising from the two calculations, $(r_{f1} - r_{f2})/r_{f1}$ where subscripts 1 and 2 refer to the former and the latter procedures, for embrios of 0.25 mm. It is observed that the final size of particles starting near the core of the updraft computed using (1) are larger than the other while the reverse is true for particles starting at the periphery. This is a general result observed for the other embrio sizes considered and other altitudes.

Table 1 summarizes the most representative results obtained.

Cases B and C correspond to trajectories inside a stationary cloud when the motion is that described by (1) with drag coeficients given by (4) and (3) respectively. Cases noted by C^* are also using (1) and (3) but for a time dependent cloud.

The quantities $HPRS$ and $HPRL$ are hail production rates $(HPR(z_0, r_0, r_f))$ associated to final radii $r_f = 3$ mm corresponding to the specific sectors shown in figure 1 a) and b) respectively. The time it takes for a hail particle to grow to a final radius $R_{f\max}$ is represented by t_{R_f}.

A comparison of the B and C cases in Table 1 show that the use of (1) together with (4) (B) systematically yield final radii larger than (1) and (3) (C) by as much as 35%. There is no systematic difference between cases B and C as far as the global parameter HPR and the time for maximum radius t_{Rf} are concerned. This is a consequence of the fact that when using (4) the maximum size for particles released at the periphery is smaller than using (3) causing that in some cases less particles cross the threshold of $r_f = 3$mm. A similar reasoning explain the similarity of HPR values when the largest stones are produced. In both cases particles grow far larger than the threshold giving values near 100%.

In general it is observed that the parameter HPR given the same initial radius, diminishes as the initial altitude increases. This is more pronounced for smaller r_0 and the maximum in HPR is found for the plane $z_0 = 4$ km.

The maximum radius attained by the hailstones, $R_{f\max}$ present a similar behaviour to that of HPR since for $r_0 = 0.25$ mm it diminishes in 90% when the initial altitude goes from 4 to 7 km, while for $r_0 = 1$ mm the decrease is about 50%. It should be noted however that the maximum in $R_{f\max}$ is not always associated to $z_0 = 4$ km. Clearly, as a limiting case one may consider a very large particle that can not be lifted by the wind. Since the particle simply falls it will be better to release it at high altitudes where it will be able to traverse most of the cloud. This behaviour can be observed for a 1 mm embrio where the maximum radius the particle attains is, on some conditions, for a release at 5 km and not at 4 km as for the other two sizes. The maximum radius is approximately ten millimeters irrespective of initial embrios sizes.

The time it takes for a hailstone to grow from a given size r_0 increases inversely to the final size $R_{f\max}$. Nevertheless, the largest stone (case $B5$) did not spend the shortest time inside the cloud.

The hail grown in a time dependent cloud ($C*$) reach smaller final sizes and take longer times than the corresponding stationary cloud cases. In some occasions the differences can be as high as 30%. This is not generally true as Fig 2.).

5. DISCUSSION AND CONCLUSION

From the above analyses it is clear that the region of the cloud most favourable for the initiation and growth of hail is situated at or at the immediate vicinity of the main updraft in accord with previous studies. Another striking feature is that the observed final size corresponding to the same initial altitude is almost independent of the initial size of the embrio. This is a fact other authors have also drawn attention, and suggest that the maximum size is related to the kind of cloud they evolve in and not on the particular trajectories. The present result also show that given an initial embrio radius r_0, the largest hailstones spend less time in the cloud. However, it is not observed, as suggested by Xu (1983), that the largest stone grows in the shortest time.

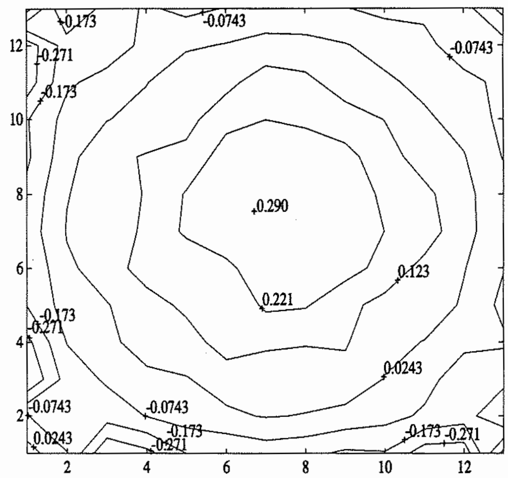

Figure 4. Contours of equal fractional difference (see text) between the final radii($r_f(x_{initial}, y_{initial})$) obtained by using the proper equation of motion (1) and by assuming terminal velocity. Coordinates are in grid points as in Figure 1 a).

Table 1

Case	z_0 *km*	r_0 *mm*	$HPRS$	$HPRL$	$R_{f\max}$ *mm*	t_{R_f} *min*
$B1$	4	1.00	0.98	0.36	12.9	11.2
$B2$	5	1.00	0.98	0.35	12.8	9.7
$B3$	6	1.00	0.67	0.20	7.7	9.5
$B4$	7	1.00	0.16	0.05	4.9	9.5
$B5$	4	0.50	1.00	0.46	13.3	10.8
$B6$	5	0.50	0.90	0.28	8.8	9.5
$B7$	6	0.50	0.16	0.05	5.1	10.0
$B8$	7	0.50	0.00	0.00	3.0	14.0
$B9$	4	0.25	0.98	0.46	11.5	10.2
$B10$	5	0.25	0.33	0.09	6.1	9.8
$B11$	6	0.25	0.06	0.02	3.4	13.3
$B12$	7	0.25	0.00	0.00	1.4	23.8
$C1$	4	1.00	0.98	0.38	9.0	7.7
$C2$	5	1.00	0.98	0.36	10.2	7.0
$C3$	6	1.00	0.67	0.19	7.1	7.3
$C4$	7	1.00	0.08	0.02	4.4	9.5
$C5$	4	0.50	1.00	0.49	10.2	7.8
$C6$	5	0.50	0.65	0.19	7.2	8.0
$C7$	6	0.50	0.08	0.02	4.4	10.8
$C8$	7	0.50	0.00	0.00	2.3	18.3
$C9$	4	0.25	0.96	0.35	9.3	8.2
$C10$	5	0.25	0.16	0.08	5.1	9.8
$C11$	6	0.25	0.00	0.00	2.8	38.0
$C12$	7	0.25	0.00	0.00	1.2	29.0
$C1^*$	4	1.00	0.82	0.25	7.5	8.0
$C2^*$	5	1.00	0.90	0.28	9.7	8.7
$C3^*$	6	1.00	0.65	0.19	7.0	9.2
$C4^*$	7	1.00	0.25	0.07	4.6	10.8
$C5^*$	4	0.50	0.98	0.36	9.9	8.8
$C6^*$	5	0.50	0.49	0.14	5.3	10.3
$C7^*$	6	0.50	0.02	0.01	3.1	15.5
$C8^*$	7	0.50	0.00	0.00	2.3	19.3
$C9^*$	4	0.25	0.90	0.40	7.0	9.5
$C10^*$	5	0.25	0.00	0.08	3.8	30.8
$C11^*$	6	0.25	0.00	0.02	3.5	37.5
$C12^*$	7	0.25	0.00	0.00	1.0	32.5

The general behaviour of the results indicate that although the cloud model does not incorporate the complete microphysics it is all the same adequate to describe the growth of hydrometeors. It also allows to draw the following conclusions with respect to the study of hailstone trajectories:

The solution of the equation of motion (1) or the use of the terminal velocity assumption can give very different results. It is observed that (1) predicts larger stones for embrios released near the cloud core up to 30%. This can be understood by noting that the particles would not follow faithfully the air motion and stay a longer time in the high liquid water region. On the other hand, the fact that at the periphery the behaviour is reversed can be understood by noting that the terminal velocity assumption would allow particles to easily reenter the cloud and so be able to grow more.

The use of stationary wind fields can produce an overestimation of the maximum sizes achieved by hail and underestimate the residence time of these particles inside the cloud. Although this is in general true, in some cases especially in the outer rim and high altitudes the reverse is observed as seen in Figure 2.

Acknowledgements: We would like to thank Luisa Lubart for supplying her programs on onedimensional trajectories. This research was supported by CONICOR and CONICET, Argentina.

REFERENCES

Beard K. V. and Grover S. N.,1974: "Numerical Collision Efficiencies for Small Raindrops Colliding with Micron Size Particles". *J. Atmos. Sci.*, 31, 543-550.

Beard K. V., 1980: "The effects of Altitude and Electrical Force on the Terminal Velocity of Hydrometeors". *J. Atmos. Sci.*, 37, 1363-1374.

Caranti G. M., Comes R. and Krehbiel P. R., 1991: "On the Relation of the terminal Velocity of Hydrometeors to environmental Condition and Particle Size and Density", in press.

Foote G. B., 1984: " A Study of ail utilizing observed storm conditions". *J. Climate Appl. Meteor.*,23, 84-101.

Heymsfield A. J., 1983:" Casse Study of a Hailstone in Colorado. Part IV: Graupel and Hail Growth Mechanisms deduced through Particle Trajectory Calculations". *J. Atmos. Sci.*, 40, 1482-1509.

Knight C. A. and Knupp K. R.,1986: "Precipitation Growth Trajectories in a CCOPE Storm". *J. Atmos. Sci.*, 43, 1057 -1073.

Levi L. and Lubart L., 1991: "Analysis of hailstone from a severe storm and their simulated evolution". *J. Rech. Atmos.*, 26, 191-211.

Mason B. J., 1971:"The Physics of Clouds". *Oxford University Press.*

Miller L. J., Tuttle J. D. and Knight C. A., 1988: " Airflow and Hail growth in a severe northern high plains supercell". *J. Atmos. Sci.*,45, 736-762.

Miller L. J., Tuttle J. D. and Foote G. B., 1990: " Precipitation production in a large Montana hailstorm: Airflow and particle growth trajectories". *J. Atmos. Sci.*,47, 1619-1646.

Musil D. J.,1971: " Computer Modeling of Hailstone in Feeder Clouds". *J. Atmos. Sci.*, 27, 474-482.

Paluch I. R.,1978:" Size Sorting of Hail in a Three - Dimensional Updraft and implications for Hail Suppression". *J. Appl. Meteor.*, 17, 763 - 777.

Pflaum J. C. and Pruppacher H. R., 1979:"A wind Tunnel investigation of the growth of graupel initiated from frozen drops". *J. Atmos. Sci.*, 36, 680 -689.

Scavuzzo C. M., Comes R. A. and Caranti G. M.,1991:"A simple 3-D Cloud Model". *J. Computational Physics.* in press.

Xu J., 1983: " Hail growth in a three - dimensional cloud model". *J. Atmos. Sci.*, 40, 185 - 203.

Three-dimensional Numerical Modeling of the Formation of an Organized Precipitating Convective System

Ryohei Misumi[1] and Takao Takeda[2]

[1] National Research Institute for Earth Science and Disaster Prevention, Japan

[2] Water Research Institute, Nàgoya University, Japan

1. Introduction

Generally a cumulonimbus cloud finishes its life within a few tens minutes, but its special type persists for a long time. In Japan, such a long-lasting precipitating convective clouds are often observed among many other short-lived clouds. It is very strange that only several convective clouds are long-lasting in spite that many other convective clouds are short-lived in the same situation. This indicates that long-lasting clouds form through the interaction of many other short-lived cells. The purpose of this modeling is to make clear how a long-lasting convective cloud form in a convective-cell ensemble.

2. Numerical model

The numerical domain is 150km×150km×15km, and mesh sizes are 2km x 2km x 0.5km. Air motions are anelastic and the Coriolis force is neglected. Microphysical processes are represented very simply by almost same way as Kessler-type parametarization.

The initial atmosphere is horizontally homogeneous and potentially unstable up to 10.75km level. Initial wind velocity is zero in y-direction and vertical wind shear is given only in x-direction. As initial disturbance, psitive temperature deviations (that is, thermals) less than 1.5 K are given at random in the region at 0.25km level. The arrangement of thermals are changed in two types, as shown in Fig.1.

The value of parameters in each case of computation are shown in Table 1.

Table 1. Values of parameters in each case

case	Vertical wind shear (ms^{-1}/km)	Initial disturbance
A	2	D1
B	2	D2
C	1	D1

Numerical computation was made for 120 min in each case.

3. Behavior of convective cells

Horizontal distribution of vertically integrated precipitating water in case A is shown in Fig.2. Many precipitating cells formed and decayed until the end of the computation. All the cells are classified into three types according to their behavior and structure.

1) S-type cell

S-type cells are short-lived. They have downshear-tilting updrafts and downdrafts locate to the downshear side of the updraft. The downdraft cut the surface flow which supplies warm and moist air into the updraft. Typical one is shown by M in Fig. 2

2) La-type cell

La-type cells are long-lasting. They have upshear-tilting updraft and downdraft locate to the upshear side of the updraft. Thus the updraft does not cut the surface flow from downshear side and the updraft is maintained quasi-steadily. Typical one is shown by C in Fig.2

3) Lb-type cell

Lb-type cells are long-lasting. They have downshear-tilting updraft, but downdraft does not cut the surface flow because this type of cells move in upshear-direction very quickly and surface flow comes from upshear-side relative to the cells. Typical one is shown by N in Fig. 2

4. Formation of long-lasting cells

1) La-type cell

The feature of La-type cells is upshear-tilting updraft. Its formation process is that updraft root moves in the downshear direction with help of the other cells. There are three patterns in this process as schematically shown in Fig. 3. In pattern I the updraft root moves with outflow diverging from one short-lived cell. This patten occurred only in case B, in which ambient vertical wind shear is weak. In pattern II the updraft root moves with the help of short-lived cells which form successively. This pattern occurred in case A and case C, in which precipitating cells are sufficiently adjacent to each other. In pattern III the updraft root moves together with the cold outflow diverging from a pre-existing La-type cell.

2) Lb-type cell

Figure 4 shows schematically the maintainance of a Lb-type cell. Its updraft is sustained by strong convergence caused by the cold air which moves very fast in the upshear direction. Cold air pool is formed by the evaporative cooling of water precipitating from pre-existing convective-cell ensemble and by the advection of the cold air from developed cells. The existence of other developed cells is indispensible for the formation and maintenance of Lb-type cells.

5. Formation of organized convective band

Figure 2 shows that precipitating-water is distributed in bands at 105 min. These bands are maintained quasi-steadily by replacement of short-lived cells. There were two of patterns in the formation of a band. In the first pattern a line of new cells were triggered along gust front. In the second pattern, the space between two cells were filled with new cells which were triggered by collision of two gust fronts. They are maintained along the edge of the low-level cold air pool.

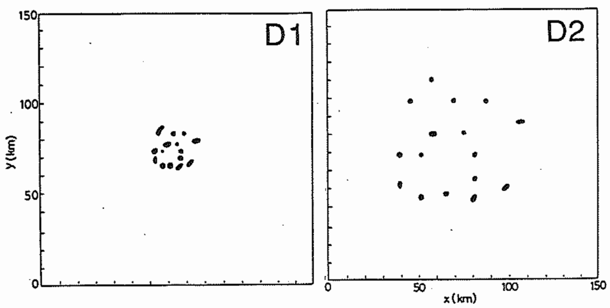

Fig. 1. Horizontal distribution of initial temperature deviations at 0.25km level. Areas where temperature deviations are larger than 0.5K are shaded.

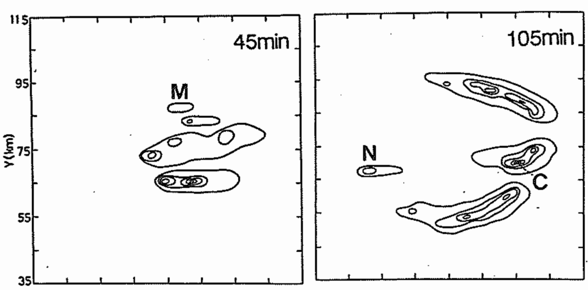

Fig. 2. Horizontal distribution of initial temperature deviations at 0.25km level. The outermost contour indicates the content of 1 kg/m^2, and contours are drawn every 5 kg/m^2.

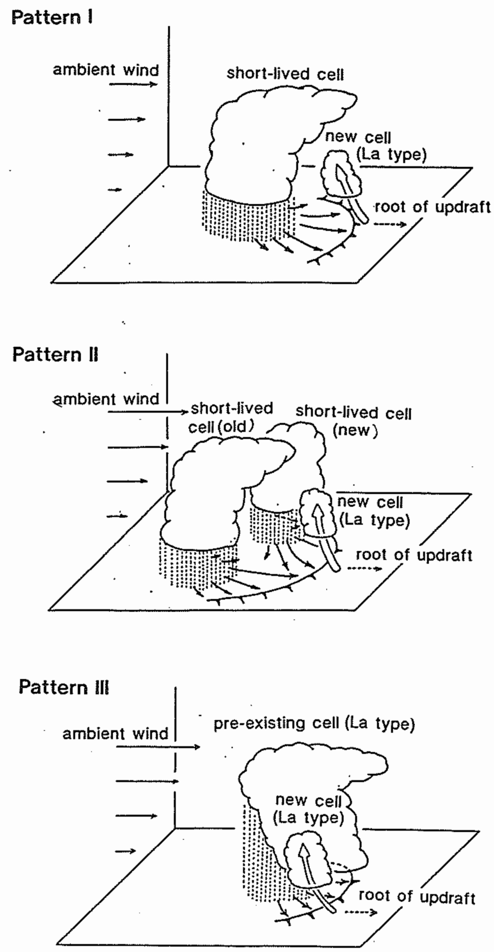

Fig. 3. Three patterns of the role of the other cells in the formation of upshear-tilting updraft.

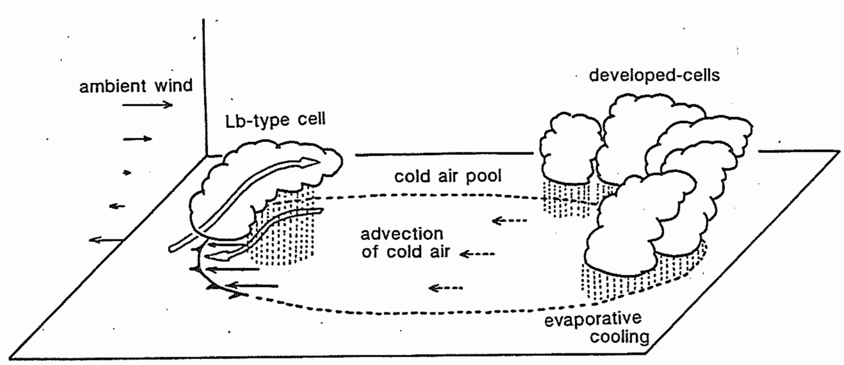

Fig. 4. Schematic representation of the maintenance of a Lb-type precipitating convective cell.

STUDY OF CONVECTIVE STORM SERIES AND PRECIPITATED HAIL IN SOUTH ARGENTINA

Laura Levi[1], Luisa Lubart and Jorge Lässig[2].

[1] Servicio Meteorológico Nacional, CEFA, Buenos Aires, Argentina.
Consejo Nacional de Investigaciones Científicas y Técnicas (CONICET).
[2] Univ. Nacional Comahue, Fac. Ingeniería.

1. INTRODUCTION

The High Valley of Río Negro and Neuquén is located leeward the Andes chain at about 40°S, 65-70°W. In normal atmospheric conditions, dry westerly winds blow into the Valley after crossing the mountain chain where the Pacific air humidity is deposited. As a consequence, the region is usually dry, though the possibility of irrigation is favorable to agriculture development.

Despite these general climate conditions, convective events occur in the region during summertime, determining an average of 5 hailstorm days per year. Since the Valley cultivation mainly consists of fruits the quality of which is very sensitive to hail impacts, a research group of Comahue University has addressed its attention to the study of hailstorms and their effects in the Valley.

In the present work, the period from 10 to 19 February 1990, characterized by the occurrence of various severe hailstorms and nearly daily convective events, is analysed, to obtain relations between different meteorological and microphysical parameters. To this purpose, a 1DTI cloud model is applied and hailstone trajectories are simulated in the updraft.

2. SYNOPTIC SITUATION

The weather conditions in the High Valley for the studied period must be related to the end of a singular synoptic situation which was established in central Argentina from the beginning to the middle of February 1990 (Nuñez et al., 1991). This situation was characterized by the presence of a blocking high located on the Atlantic Ocean, near the continental coast, at about 40-45°S, 50-55°W. This hindered westerly winds and the passage of cold fronts from the south, determining the prevalence on the continent of northeasterly winds carrying moist air from the Atlantic Ocean. After 12 Feb, the anticyclon slowly moved westward so that its effects on the continent were weakened. Due to this situation and to the presence of a nearly permanent trough at 500 hPa along the chilean coast, with a related ridge on the west of the Argentine territory, precipitations above the average for the season occurred since the beginning of February in central Argentina, but only since 10 February in the High Valley. In this region the convective activity gave place to hailfalls on 10, 14, 15 and 19 February.

The surface pressure field for 11 Feb, given in Figure 1, can be considered representative of the synoptic situation during the period 10 to 13 February. This indicates that humid air advection should have occurred from the N-NE, according to the general anticyclonic circulation.

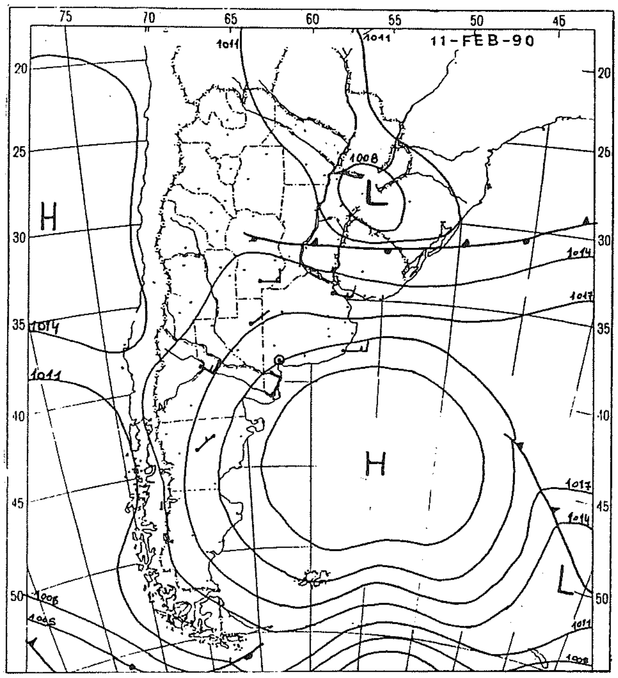

Figure 1. *February 11, surface pressure field.*

The local humid wind direction in the High Valley was, however, from the E and SE, as shown in Fig.2, where the wind direction distributions in the 10-19 and 10-20 Feb periods are given. Actually, both distributions have their mode in the intervals corresponding to easterly and southeasterly winds. However, the latter distribution differs from the former because of the enhanced contribution of westerly or southwesterly winds, this fact suggesting that the last day a new situation was established.

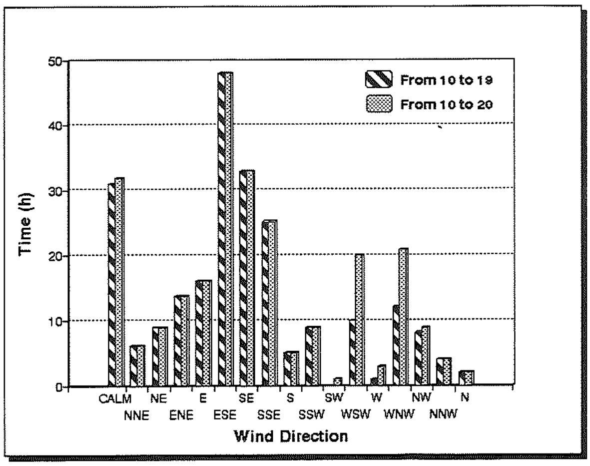

Figure 2. *Wind direction distribution.*

The characteristics of the studied period and the situation change occurring on 20 Feb also appear evident in Figure 3, where the surface air temperature T and dew point Td diagrams from 9 to 21 Feb are plotted. Actually, the high surface humidity is represented in this figure by Td>15°C prevailing from 10 to 19 Feb, while the decrease to Td≃10°C, occurring on 20 Feb, can be correlated with this day change of the wind direction.

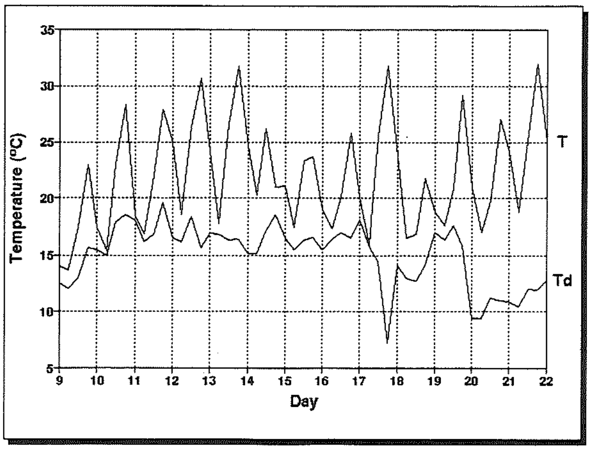

Figure 3. *Temperature T and dew point Td from 10 to 21 Feb.*

3. RADIOSONDE AND HAILPAD DATA ANALYSIS

The 1DTI Hirsch model (Hirsch, 1971), as implemented by Ghidella and Saluzzi (1979), was applied to the morning radiosonde data provided by the Neuquén station. The sounding of 10 Feb, given in Figure 4, can be considered typical of the whole period as for the moderate atmospheric instability and the humidity values that are high at the ground but decrease rapidly with altitude.

In Table 1 the cloud top height HT and the maximum values of the updraft speed Wmax and the condensed water content CWCmax, calculated without removing frozen water, are given for simulated clouds in the period 10-20 Feb Calculations were always performed assuming a wind speed Wo = 4m/s at cloud base.

Table 1. *Top height and maximum values of CWC and W for clouds simulated assuming Wo = 4 m/s.*

Day	HT (km)	CWCmax (g/m³)	Wmax (m/s)
10	12	3.6	26
11	-	-	-
12	12	4.9	26
13	12	3.7	15
14	11.5	4	13
15*			
16	10.5	4.7	26
17	11	3.1	25
18	-	-	-
19	11.5	3.9	30
20	-	-	-

* *No Data*

Notice that a cloud of similar size could be simulated all days except for 18 and 20 Feb when the atmosphere was stable and for 11 Feb when Wo=8m/s would have to be assumed. In several cases it was Wmax>25m/s but this maximum was attained at high levels where T<-30°C and the cloud should have been mostly glaciated.

The main characteristics of the solid precipitation were derived from the analysis of hailpads distributed along the Valley and from the crop damage evaluation. The hailpad network included 116 recording stations in a 1044km² area.

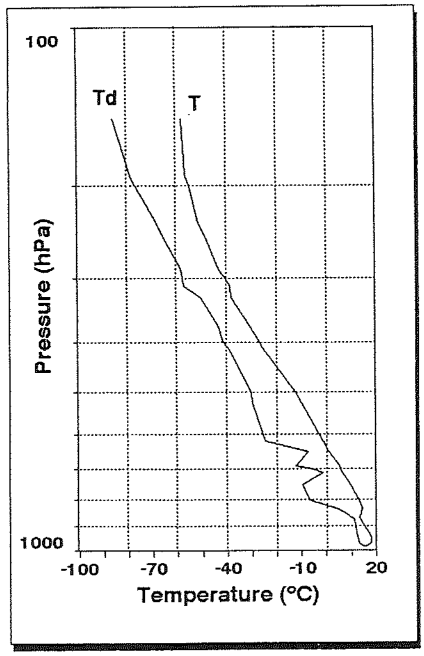

Figure 4. *Sounding taken at 0900 (local time) 10 February 1991 at Neuquén.*

The general hailstorm effects are summarized in Table 2, where an approximate relation is shown between damage evaluation and the results of hailpad analysis. Notice that, due to the type of fruit cultivation of the region, a density of stones on the ground above 1/cm² was sufficient to determine total crop destruction, while the damage was reduced to below 40% when this density decreased to about 0.1/cm².

Table 2. *Damage evaluation and hailfall density.*

Area (km²)	Damage (%)	Hailstone Number	Kinetic Energy (J/m²)
126	100	1650-15000	110-1030
54	90	≃ 2000	≃ 10
54	60	1000-2000	30-100
90	40	500-1000	10-50
18	20	≃ 350	≃ 15
162	5-10	10-375	< 10

Hail size distributions were also derived from hailpad analysis. In approximate agreement with previous results (Mezeix, 1990) these showed that small hail 5 to 10 mm in diameter predominated, while larger stones 20 to 30 mm in diameter were less than 4% in number.

Two hailstone samples, precipitated at 18:00 local time on 10 February and collected near two hailpad stations were available for analysis. The stones were 20-30 mm in diameter, so that they could be considered representative of the largest specimens in the hailpad data distributions.

The observation in natural and polarized light of thin sections of hailstones belonging to both samples indicated that:

1) The embryos and the subsequent main crystal layers were formed by large crystals, several millimeters in size and transparent ice. Consequently, most of the growth should have occurred below the -15°C level.

2) Several stones were formed about frozen drop embryos which could be clearly recognized when hailstone thin sections were observed in natural light, because they were separated from subsequent growth by a thin opaque layer. However, since the large crystals forming the embryo continued in the accreted ice layer, the distinction between the latter and the embryo was not clear when the section was observed between crossed polaroids. This fact indicates that, in the studied storm, large drops of 2-3 mm radius existed and could freeze rather near the 0°C level.

3) Specimens more than 20 mm in diameter usually showed a thin small crystal layer near the stone periphery. This fact suggests that, during the initial upward motion of the hailstones, these arrived up to a cloud region where the temperature was near -20°C before beginning the downward motion and precipitation.

4. HAILSTONE TRAJECTORIES IN SIMULATED UPDRAFT

Hailstone trajectories in simulated updrafts have been studied for 10 February, which was considered of special interest because of the extended area covered by solid precipitation, occurring at 18:00, 22:00 and 24:00, and because the hailpad information for 18:00 hailfall could be completed with that derived from hailstone structure analysis.

In order to calculate the hail trajectories in the simulated 1D updraft a hailstone growth model was applied (Levi and Lubart, 1991), where the particle size, structure, free fall speed and up and down motion are related to the environmental parameters derived from the vertical profiles of T, W and LWC.

Trajectories were initialized at different levels H_o, assuming that accretion occurred about spherical particles of radius R_o and density ρ_o=0.9 g/cm^3. The spherical shape was preserved during growth, so that the drag coefficient CD was derived from the Beard equation (Beard, 1980) for Davies number $X \leq 2x10^5$, while CD=0.55 was used for $X > 2x10^5$. A cloud droplet radius r=10μm was assumed.

For 10 Feb, two simulated clouds were considered: cloud C1, directly derived from the morning sounding, and cloud C2, derived from the same sounding but with an increment of the dew point average in the first 100 hPa so that surface dew point is modified by 2°C, thus taking into account afternoon higher surface humidity.

In Figures 5 and 6 the updraft profiles corresponding to each of these clouds are plotted, together with several possible trajectories, represented as H(R), where H is the trajectory altitude reached at a given particle radius R.

Taking into account the results of hailstone structure analysis, the process was initialized at low levels, where $-5 \geq T > -15$°C.

The trajectories in Figure 5 correspond to R_o=0.5mm and show that, for H_o<5.9km, T_o<-12°C the particles would precipitate to the ground after reaching a maximum level where T varies from -9.4 to -21.6°C. In these cases the final hailstone diameter can reach values between 8 and 16mm, larger diameters corresponding to higher values of H_o. For $H_o \geq 5.9$km, the particles would enter in a cloud region where W increases rapidly with H so that they would rise up to above the maximum updraft level, where T<-30°C and the cloud is mostly glaciated. Since accretion is negligible at these levels, in this case precipitation could only occur if the particle were ejected from the updraft. Some attempts performed assuming R_o=1mm gave similar results as for the relation between hailstone growth levels and final sizes.

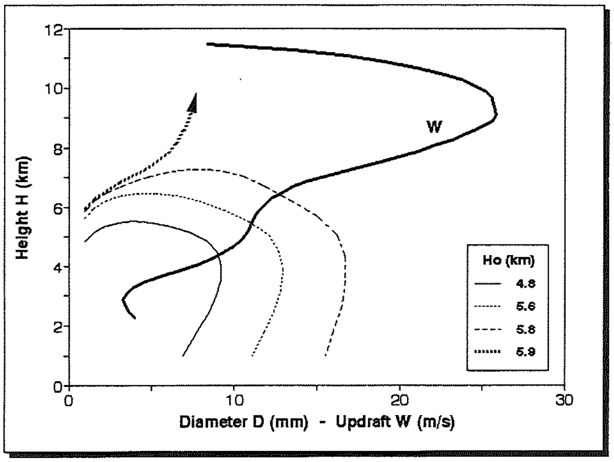

Figure 5. *Updraft profile and hail trajectories simulated using the sounding of Figure 4.*

The trajectories in Figure 6 were obtained assuming R_o=2mm. It can be seen that they are similar to those in Fig.5, as for the attained altitudes, though the larger value of the updraft permits the formation of particles with diameters varying in the range of 20-25mm, corresponding to that of the analysed hailstones. As in Fig.5, the final particle diameter increases with H_o up to the transition value H_o=6.2km, where the upward particle motion could not be reverted and precipitation inside the updraft could not occur. These results show that the morning sounding of the considered day, though indicative of atmospheric instability, could not have

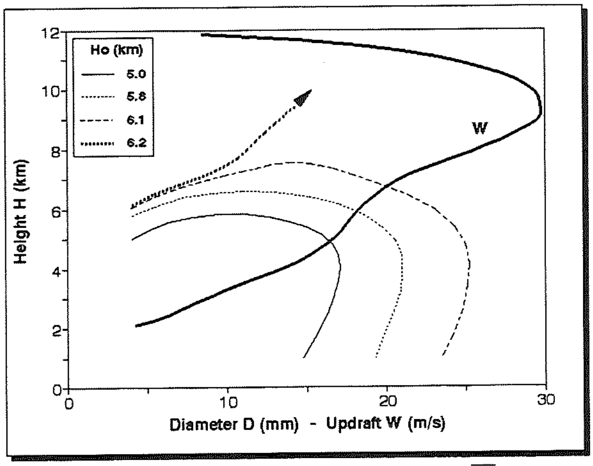

Figure 6. *As in Figure 5 but with increased $\overline{Td}$.*

determined the precipitation of hail more than 10 mm in diameter, but that the humidity increase occurring during later hours was enough to permit the formation of the largest precipitated hailstones.

It is also interesting to observe that, due to the shape of the simulated updraft profile, which increases more sharply at levels above H≃7.5km, the cloud region where hailstones can grow and precipitate has an upper limit at about -22°C. This fact is in semiquantitative agreement with the observed hailstone structure, mainly formed by large crystals. Notice also that the maximum hail diameter is more depending on the shape of the updraft profile than on the maximum updraft value, which reaches about 26m/s, so that it could support hailstones with larger sizes.

5. CONCLUSIONS

The present work has permitted some relations to be established between the development of convective clouds in the High Valley of Río Negro and Neuquén and the meteorological conditions, characterized by the surface pressure field, the local wind direction and the radiosonde data.

It has been shown that the convective clouds simulated by the application of a 1DTI model to the morning radiosonde data corresponded well enough to the observed events. However, as convective activity usually occurred during the afternoon, the observed surface humidity changes had to be taken into account in the simulation.

The application of a hail growth model in the clouds simulated for 10 Feb has shown that up and down vertical trajectories could be obtained and that those for cloud C2, corresponded to the formation of hailstones similar, as for their size and structure, with the largest ones registered on the ground. Thus, the parameters calculated by the simulation could be considered to represent those characterizing the cloud region where such hailstones were grown. This could be a region near the edge of the updraft core where the presence of ice particles was shown in some cases by airborne data (Orville et al., 1990).

The formation of small hail, observed in large number on the ground, could not be simulated in the latter updraft, which can be considered to correspond to the cloud in its mature stage. Thus, it can be expected that the size spectrum of the precipitated stones could only be simulated using a 2D or 3D time dependent model, where the evolution of the updraft and of other cloud parameters could be represented.

Notwithstanding, the present results are encouraging as for the development of further investigations, directed to obtain more reliable relations between synoptic and local conditions in the studied region, where a better farmers' information could be helpful for agriculture damage reduction.

Acknowledgments - The authors are indebted to M.E. Saluzzi and H. Ciappesoni for useful discussions, to E.L. Friera for technical help and to C. Palese and M. Cogliati for data contributions. Financial support of CONICET is acknowledged.

REFERENCES

Beard, K.V., 1980: The effects of altitude and electrical force on the terminal velocity of hydrometeors. *J.Atmos.Sci.*, 37, 1363-1374.

Ghidella, M., and M.E.Saluzzi, 1979: Estudio de un modelo numérico de nube convectiva. *Geoacta*, 10, 111-122.

Hirsch, J.H., 1971: Computer modelling of cumulus clouds during project Cloud Catcher, Report 71-7.

Levi, L, and L.Lubart, 1991: Analysis of hailstones from a severe storm and their simulated evolution. *Atmosp.Research*, 26, 191-211.

Mezeix, J.F., 1990: Further Exploratory Evaluations of Grossversuch IV Using Hailpad Data: Analysis of Hail Patterns and Stratifications by Storm Type for Seeding Effect. *J.Appl.Meteor.*, 47, 401-417.

Nuñez, J.M., M.Giachino, M.E.Saluzzi and N.L.Di Lorenzo, 1991: The problem of the nowcasting in the River Plate Basin, Part I, measurement and treatment of data by radar and the employment of numerical analysis. *Proc.of the 25° Int.Radar Conference - Paris - France*, 25-29.

Orville, H.D., F.J.Kopp, U.S.Nair, J.L.Stith and R.Rinehart, 1990: On the origin of ice in strong convective cells. *Proc.of the 1990 Conference on Cloud Physics - S.Fco. - Cal*, 16-20.

ANALYSIS OF A MESOSCALE CONVECTIVE SYSTEM PRODUCING HAILS AND HEAVY RAINS OVER THE JIANG-HUAI RIVER BASIN IN CHINA

Yeh Jia-Dong[1], Fan Bei-Fen[1], Tang Xunchang[2], Du Jingchao[2], and Song Hang[2]

1 Dept. of Atmospheric Science, Nanjing University, Nanjing
2 Jiangsu Meteorological Bureau, Nanjing, China

1. Introduction

From the evening of 3 May 1988 to the early morning next day, a severe convective storm system developed in region of Jiang-Huai river basin in East China. The storm system formed in northern portion of Jiangsu and Anhui provinces. During the ensuing 8-10 hours of its lifetime as the storm system propagated southward, a series of severe weather events such as heavy rainfall, hails and severe wind gusts produced. The peak values of daily rainfall amount come up to 90-97 mm, and the heavy rainfall area in which the daily amount is more than 50mm located at the region of Jiang-Huai river basin in a long and narrow zone of about 600x100 km. The heavy rainfall is abrupt with a duration of about 1-3h. Maximum rain fall density in the center region of heavy rains is up to 35-46 mm/h. At the same time hails have been observed in several sites of Moncheng, Fengyang, Xuyi and Xinghua. Strong surface wind gusts were also found in more sites with a peak value of 24 m/s. This paper concentrates on the analyses of large scale weather conditions favorable for generating the storm system, the surface mesoscale flow field, and radar echo structure of the convective storms. Then a brief discussion of the storm system generation and organization mechanisms, and its propagation characteristics is given.

2. Large scale circulation situation

Early in the May 1988, the northern portion of Asia is controlled by polar vortex, the polar frontal zone progress southerly to 45^{o}-60^{o}N. Circulation in midlatitude of the East Asia is prevailing west flow, and a series of short wave troughs propagate eastward constantly. At 0800 LST 3 May, a trough in westerlies is propagating eastward rapidly with a speed of about 30 km/h through Mongolia plateau, and spreading southward to the regions of Northeast China and North China. At 2000 LST when the severe convective storm initiating, The northern portion of Jiang-Huai river basin is affected by the tail of the trough (Fig.1). The air flow in 500 hPa level at this time has transformed into WNW direction. Cold air mass begin to intrude into Jiang-Huai river basin at mid-levels of troposphere. However, southwest air flow is still prevailing in lower level characterized by a strong low-level advection of heat and moist air providing an abundant supply of moist static energy.

Coordinating with the propagating eastward of 500 hPa trough and spreading southerly, the surface cold air mass in Mongolia region is also strengthened in its moving course eastward, resulting in a cyclone formed from the low-pressure disturbance. Pressure in the cyclone center descents to 990 hPa at 0800 LST 3 May. The cyclone spreaded southerly in East Asia affects the regions of Northeast China and North China. The tail of cold front sweeps easterly across the northern portion of Jiang-Huai river basin, and interacts with a warm shear line associated with the West China inverted trough, providing a large scale weather situation favorable for the development of severe convective storm system.

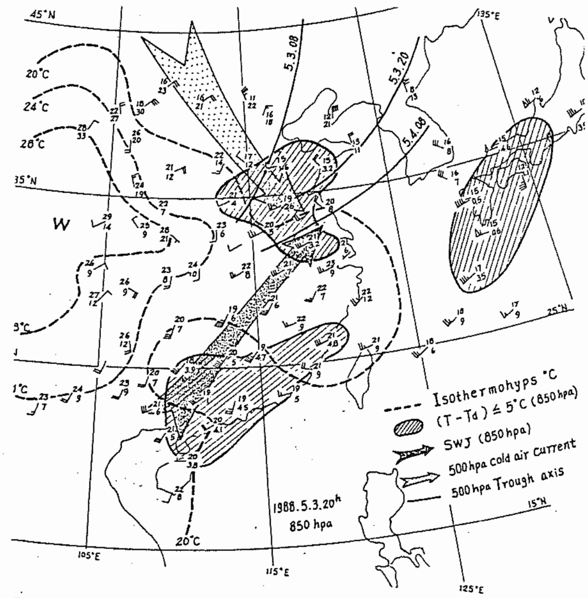

Fig.1. Large scale circulation situation in the 850 hPa and 500 hPa levels.

Low-level SW jet stream: Early in May the West Pacific subtropical high ridge on 500 hPa level locates at 19^{o}N, the ridge top represented by 588 isobar pushes westward to 98^{o}E. At the lower levels over the South China and Jiang-Huai river basin, the West Pacific subtropical high establishes itself far enough westward to drive warm-moist air northeastward over these areas. This circulation especially favors the development of low-level SW jet laden with warm moist air. At 2000 LST, the SW jet moves northward and strenthens with a peak value of 18m/s. The SW LLJ axis has veered to a more southwesterly direction, the southern component of jet stream is enhanced evidently and exhibits the flow becomes increasing convergent along the jet. The Jiang-Huai river basin region is in the left-exit zones which is favored zone for upward motion and severe weather occurrence. Accompanying the strenthened of jet and convergence of moist air, a rich water vapor region is formed in Jiang-Huai river basin and Shandong peninsula at 2000 LST (Fig.1). The dew-point deficits at Jinan, Xuzhou and Nanjing are 1.6^{o}, 2.6^{o} and $3.2^{o}C$ respectively. On the surface, the affect of SW jet is also evident. Under the influence of the lasting SW warm-moist air flow, a sustained temperature increasing is found from 29 April to 3 May. The temperatures in several sites approach to the highest levels in the historical records. As an example, the peak value of temperature in 3 May in Nanjing is up to 32.2 C. The sounding data over Jiang-Huai river basin region exhibit that a deep layer from surface to 350 hPa level (0-8.5 km MSL) is conditionally instable, the CAPE reaches up to about 53 J/kg in Fuyang at 20 00 LST just before the initiation of the convective storm system. Low levels beneath 700 hPa is controlled by warm-moist SW air flow, the dew-point deficits are about $3\text{-}8^{o}C$. The air is drier on the 500 hPa level under the influence of northern cold flow, the dew-point deficits reach up to $10\text{-}19^{o}C$. Once a suitable trigger factor occur under the instabilized stratification condition, strong convective overturning will immediately break out.

3. Mesoscale surface flow field

The initial forcing of the severe con vection system is attributed to the movement southerly of dry-cold air in the middle troposphere over northward-moving moist warm low-level air. This creates a region of conditional unstable air as described above. Low-level thermal advection, in addi tion to creating a narrow tongue of warm-moist air as shown in Fig.1 contributes to surface convergence. Thus , a narrow zone of conditionally unstable air with a mesoscale surface convergence triggers deep convection. The mesoscale surface convergence is obvious in the surface flow field (Figure is omitted). Eastern wind prevails in most area portion of Jiangsu province under the influence of the West-China inverted trough, south-west of it in the regions of southern Anhui province and flanks of Changjiang River (Yangtze River) is prevailing southwestern wind. In addition to the influence of favorable topography of Dabieshan Mountain, a southern flow pushes into Caohu Lake Plain east of Dabieshan Mountain and arrives to a hilly land south of Benbu and Fengyang. At 2000 LST the surface southern winds in Lujiang and Dinyuan are SSW 6.3 m/s and SSE 4.3 m/s, respectively. Surface mesoscale convergence of wind speed and direction is evident in the region of south flank of Huaihe river accompanying a warm-moist tongue with peak values of $31.4^{o}C$ and 32.7 hPa for temperature and vapor pressure in the warm-moist tongue, respectively. In there the southern air flow encounters the eastern air flow came from Jiangsu province to form a mesoscale convergence zone, in addition to the favorable topographic effect of hilly land, especially favors to trigger severe convective weather occurrence, Results in this region become an important convective storm originating source.

The low-level mesoscale convergence is not only a trigger factor, but also is an important organization mechanism of severe convective system. Analyses of hourly surface rainfall associated with the severe storm system and of surface air flow field reveal that the convective precipitation region is closely related with the surface mesoscale convergence zone. At 2000 LST the surface mesoscale convergence center is in the region north of Huaihe river with a peak value of divergence of $-6.1\text{x}10^{-3}s^{-1}$. An isolated severe thunderstorm develops violently in Moncheng with an hourly rainfall amount of 46.2 mm and produces hails. After 2000 LST, several isolated abrupt convective precipitations occur in Huaibei, Xuzhou and Guoyang with hourly rainfall amounts of 20.6, 17.7 and 27.9 mm, respectively. Since 0000 LST 4 May, cold air flow strengthens and pushes souther'y to a line along Benbu, Baoyin and Sheyang. The convective precipitation region is organized in a mesoscale band with peak hourly rainfall values of 41.3, 25.8 and 20.8 mm that is aligned by a mesoscale surface convergence zone in which the peak divergence values are of $-8.4\text{x}10^{-3}s^{-1}$ and $-8.7\text{x}10^{-3}s^{-1}$ in Sihong and Guannan as shown in Fig.2a. After that time, the convective precipitation band moves southerly following the strengthened surface mesoscale convergence zone (Fig.2b,c), and produces hails in Xinghua. At 0400 LST 4 May, the surface mesoscale convergence zone has arrived to the south flank of Changjiang River, the peak values of divergence in convergence zone reach to $-9\text{x}10^{-3}$, $-14.4\text{x}10^{-3}$ and $-12.1\text{x}10^{-3}s^{-1}$(Fig.2c). The corresponding hourly rainfall band is following the convergence zone to a belt along Changjiang River from Nanjing, Zhenjiang, to Hai-an as shown in Fig.2c. Thus it can be seen the severe convective storm producing heavy rains and hails is triggered by a mesoscale convergent air flow in low-level under the favorable large scale circulation situation, heat and moisture environment, and local topographic conditions. It is then organized to a mesoscale convective system along the surface convergence zone and propagates southerly under its forcing. So the propagation mechanism of the convective system seems to be a forced propagation, remember the evaporation effect of raindrop in lower layer is probably weak since the air in the low level is moist as found from the sounding data.

4. Radar echo structure characteristics

Several isolated strong convective echoes developed in the region of Huaihe river basin from 1900 LST to 2200 LST 3 May and produced local abrupt convective rainfall as mentioned above. After 2200 LST, since the cold air flow intrude into this region and the surface mesoscale convergence zone intensify, a series of convective

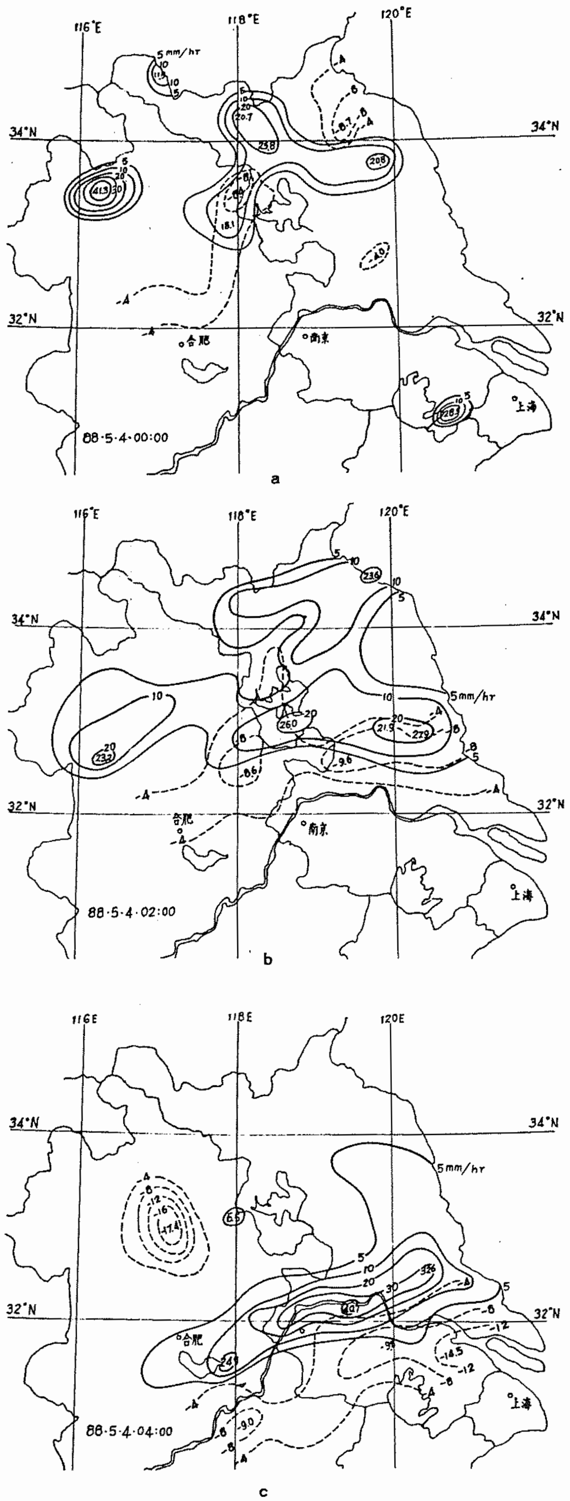

Fig.2. Surface mesoscale convergence zone and convective precipitation band with the hourly rainfall amount larger than 5 mm. The solid line denotes the contour of hourly rainfall amount in mm/h, and the dashed line is the contour of surface divergence value (unit is $10^{-3}s^{-1}$) in the convergence zone.

echoes develop and organize to form a mesoscale convective system following the surface mesoscale convergence zone. Fig.3 shows the CAPPI radar echoes at varied levels represented as a portion of the convective system. It can be seen from Fig.3 that the anvil cloud regions produced by the severe convective storms B and C, and several smaller convective cells including the decaying storm cells A developed by 1930 LST 3 May have merged at higher levels as shown in Fig.3c,d to form a mesoscale convective cluster with an area of about 300x200 km. The severe convective storms B and C are in mature stage by 2200 LST 3 May. The echo top of strong echo region with reflectivity of 45 and 65 dBZ in these two storms reach up to heights upper than 18 km and 15 km levels, respectively (Fig.3c,d). The RHI echo structures of these two severe storms are shown in Fig.4b,c,d and Fig.5. Storm B initiated at about 2000 LST. The radar echo top of it at the mature stage reaches up to 19 km (MSL), and the width of strong echo region with reflectivity of 65 dBZ is about 14 km which top is up to 16 km height. Hail falling from the severe storm B have been observed in Xuyi. When the storm approaches to the Hongzehu Lake the storm is intensified under the influence of warm-moist air over lake. The severe storm B is consisted by 3-4 cells having various intensity and life-cycle stages, which looks like a multicell severe storm. Sounding data taken at 2000 LST 3 May in Xuzhou and Fuyang showed that the vertical shears of horizontal wind are about $2.7x10^{-3}s^{-1}$ and $2.2x10^{-3}s^{-1}$ from surface to 14 km height, which is favorable for the development of multicell severe storm. Storm C located at the place of 120 km west of storm B, is another lasting vigorous severe convective storm. The sustained time period of its echo top exceeded 17 km is longer than 2.5 hours.The reflectivity of strong echo center is also reaches to 65 dBZ and produced hails in the region of Fengyang. Storm C is also consisted by 2-4

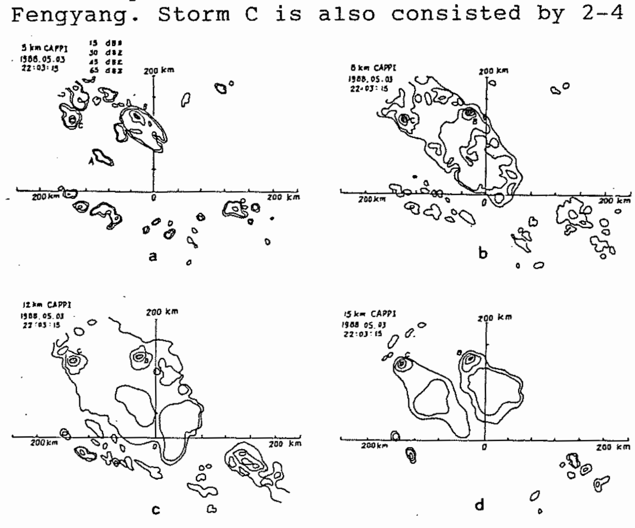

Fig.3. CAPPI radar echoes of the severe convective storms B and C at varied levels. The contours denotes the reflectivity of 15, 30, 45, and 65 dBZ, respectively. The origin is in Nanjing.

convective cells and has evident structure characteristics of multicell severe storm in aspects of echo intensity, lasting range of life-cycle, and hail shooting. After 0030 LST 4 May the reflectivity in strongest echo center is still maintained at the level of 65 dBZ (Fig.5c,d).

The stratiform anvil cloud region of mature storm is located at a layer with the cloud base from 4 to 6 km height, and the top of it from 10 to 14 km. The depth of stratiform anvil cloud is about 5-10 km. The main part of it is in the levels above $0^{o}C$ level. In the lower portion of the anvil cloud region from 5 to 8 km height, a radar echo belt with reflectivity exceeding 30 dBZ has been found (Fig.4 and 5). It appears to be caused mainly by the aggregates as found in the stratiform region of MCC (Yeh et al., 1991). A weaker echo region is also presented between the stratiform anvil cloud region and convective region similar to that found in MCS in the United States (Smull and Houze, 1985; 1987; Yeh et al., 1987). Forthermore, the sounding data in the region of Jiang-Huai river basin at 20 00 LST exhibit that the environmental atmosphere is conditionally instable under 9 km height MSL and is moister with dew-point deficits of $4-10^{o}C$ in the layer of 7-10 km MSL. Thus the upper divergent flow caused by convection should be in more higher levels as 10-15 km MSL to form the anvil cloud, which is hard to explain the fact of that the stratiform anvil cloud mainly concentrates at the layer of 5-10 km MSL. Observations of a squall line system have shown that a deep layer of convergence exists between 6.0 and 10.0 km height in tailing stratiform region. The inferred vertical motion field from the divergence profile showed that, above 6.5 km, a deep layer of ascent is inferred that is similar to that found in the stratiform region of tropical and midlatitude MCSs (Srivastava et al., 1986). Numerical simulation of a deep convective system has shown that convective latent effects will be able to cause a mesoscale warm center which can promote the formation of mesoscale convergence and ascent motion in the middle layer of troposphere (Fan et al., 1990). Thus, the resultant stratiform anvil cloud caused by the mesoscale ascent motion is active in dynamics and can usually last a longer range of time after the convection decaying.

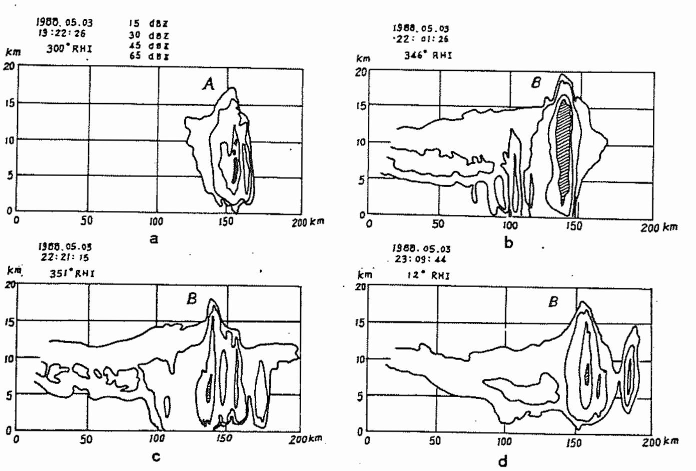

Fig.4. RHI radar echoes of the severe convective storm B and an earler developed storm A. The contours are same as in Fig.3.

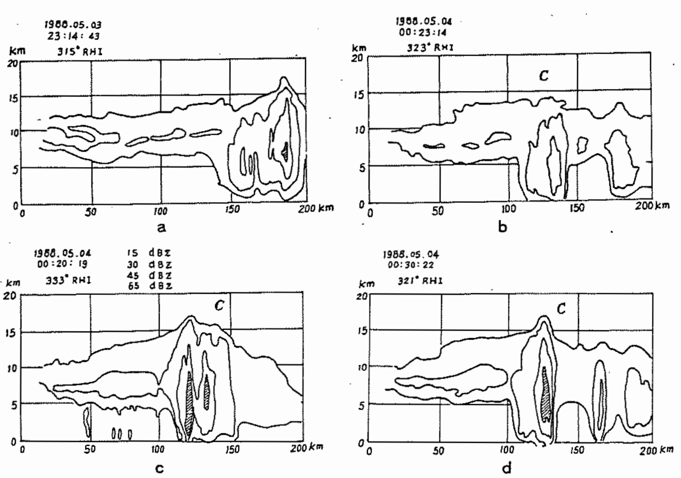

Fig.5. Same as Fig.4 except for the storm C.

This research is supported by the Natural Science Foundation of China in the number of 49070244.

REFERENCE

Smull, B.F.,and R.A.Jr.Houze, 1985: A midlatitude squall line with a trailing region of stratiform rain: Radar and satellite observations, Mon. Wea. Rev., 113: 117-133.

Smull, B.F., and R.A.Jr.Houze, 1987: Dual-Doppler radar analysis of a midlatitude squall line with a trailing region of a stratiform rain, J. Atmos. Sci., 44: 2128-2148.

Srivastava,R.C., T.J.Matejka, and T.J.Lorello, 1986: Doppler radar study of the trailing anvil region associated with a squall line. J. Atmos. Sci., 43:356-377.

Fan Bei-Fen, Yeh Jia-Dong, W.R.Cotton, and G.J.Tripoli, 1990: Numerical simulation of microphysics in meso- -scale convective cloud system associated with an MCC, Adv. Atmos. Sci., 7: 154-170.

Yeh Jia-Dong, Fan Bei-Fen, M.A.Fortune, and W.R.Cotton, 1987: Comparison of the microphysics between the transition region and stratiform region in a mesoscal convective complex, Preprints to the Third Conference on Mesoscale Processes, Vancouver, B.C., Canada, 21-26 August, 1987, 188-189.

Yeh Jia-Dong, Fan Bei-Fen, W.R.Cotton, and M.A.Fortune, 1991: Observational study of microphysics in the straiform region and transition region of a midlatitude mesoscale convective complex, ACTA METEOROLOGICA SINICA, 5: 527-540.

Relationship between mass, pressure and momentum fields in the stratiform region of a fast–moving tropical squall line.

J–P Lafore and J–L Redelsperger

CNRM (Meteo–France and CNRS)
42 av. Coriolis 31057 Toulouse Cedex, FRANCE

1. Introduction:

Tropical fast–moving squall lines (SL hereafter) are mesoscale convective systems organized in a line of convective cells (the convective part), perpendicular to their propagation speed and followed by a wide stratiform anvil extending backward (the stratiform part).

Most of previous numerical and theoritical studies focused up on strong convective region at the leading edge of squall lines. On contrary there are little works addressing the interaction between the convective region and its associated trailing stratiform region. The importance of this latter region has been progressively established from observations gathered over the last three decades. Three major features characterize these stratiform parts: first, an unsaturated warm mesoscale descent at low levels (Zipser, 1969), second, a mesoscale ascent characterizing the active middle and upper layers (Gamache and Houze, 1982), and third a "mesoscale rear inflow" at mid-level (Smull and Houze, 1987).

However, the understanding of the mechanisms responsible for the development and maintenance of the observed structure of the stratiform region and its interaction with the convective scale, is less clear. To study these interactions and to simulate explicitly the mesoscale circulation in the stratiform part, we have developed a full ice phase parameterization.

2. The model and the case studied

The three-dimensional time dependant non hydrostatic cloud model depicted in Redelsperger and Lafore (1988) (RL hereafter), has been used in its 2D version for the present study. The size of the domain is 400 km by 23 km, with a regular horizontal mesh of 1250 m and 45 levels distributed on a variable mesh to resolve the low level shallow structures. The treatment of cloud microphysical processes uses the bulk physical concept, as described in Caniaux *et al.*(1992). The microphysical scheme treats the transfer between six prognostic variables: water vapor, cloud liquid water and cloud ice moving with the air velocity, and rainwater, aggregates and graupel as precipitation categories.

The case studied is the SL observed on 23 June during the COPT81 experiment. The initial conditions are the same as those used by RL for their 3D simulation. The model initiation is obtained by perturbing the initial homogeneous environment with a cold pool.

3. Importance of the ice phase parameterization

Many observed features (Chalon *et al.*, 1988) have been reproduced such as the mesoscale ascent and downdraft (Fig. 1c), the weak "rear inflow" jet (Fig. 1b), the bright band due to melting of ice particles, the "reflectivity trough" in the transition zone (Fig. 1a), the cold pool (fed by convective scale downdrafts) spreading at the ground, and the unsaturated warm mesoscale descent at the system rear (Fig. 1d). The full ice phase parameterization appears to be important in the formation of this well-developed wide spread trailing stratiform region, as confirmed by the "warm simulation" depicted by figure 2.

Without any ice phase parameterization, even after 8h of simulation, the system did not succeed to develop an extended trailing anvil (Fig. 2a): the wind perturbations induced by the system (Fig. 2b) and descent at the system rear (Fig. 2c) stay localized and limited to the convective region. It is a quasi-steady pattern which is similar to the one temporarily obtained after 3h by the simulation including the ice processes.

4. A comprehensive diagnostic study of the pressure field

To study the development and maintenance of the simulated stratiform part, we here chose to analyse the budget of the cross-system momentum equation, instead of the along-system vorticity one. The pressure field becomes therefore an important parameter to look at.

4.1 The pressure field

The pressure deviation from the hydrostatic domain-scale mean state is shown by Fig. 3a. The basic pattern of its structure consists of four principal extrema; either a low pressure (L) centred at 3 km associated with the convective region, overlying a surface high (H), and at the system rear, the opposite structure with a mesohigh (h) at 3 km and a mesolow (l) at low levels. The resulting main feature is a front-to-rear mid-level pressure gradient of about 1 hPa over 150 km. Previous numerical studies on large domains (Nicholls, 1987; Lafore and Moncrieff, 1988) produce similar structures.

The comparison with the pressure field corresponding to the "warm simulation" (Fig. 3b) enlightens the basic differences between the two simulations, as the four pressure extrema have very different localisations. The low-level centres H and l stay close to each other (30 km), whereas the mid-level ones L and h are separated (from each other) of 100 km at 8h.

The interpretation of the pressure field and of its evolution is a difficult task because it is intimately related to the momentum flux. To lend insight into this question, we developed a diagnostic analysis of the pressure fields.

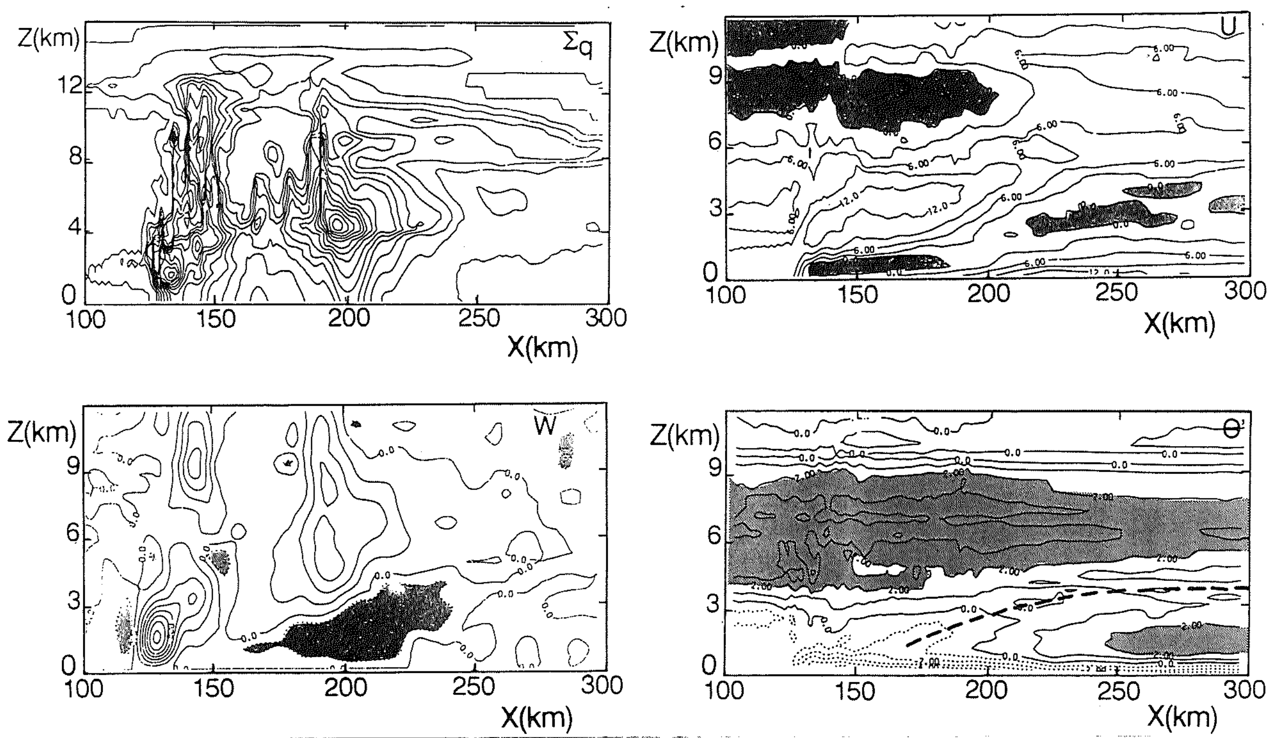

Fig. 1: Simulated 1 hour averaged fields (7 to 8h time period) for (a) the total liquid and ice water content (the contour interval is $0.1 g kg^{-1}$ and the maximum value is $1.45 g kg^{-1}$), (b) the wind velocity relative to translation speed of the model frame ($-12 m s^{-1}$) (contour interval of $3 m s^{-1}$), (c) the vertical velocity (contour interval is $20 cm s^{-1}$ for upward velocities (solid lines) and $10 cm s^{-1}$ for downward velocities), (d) and the temperature perturbation (the contour interval is $1°C$, minimum and maximal values are -5.5 and $4.5°C$).

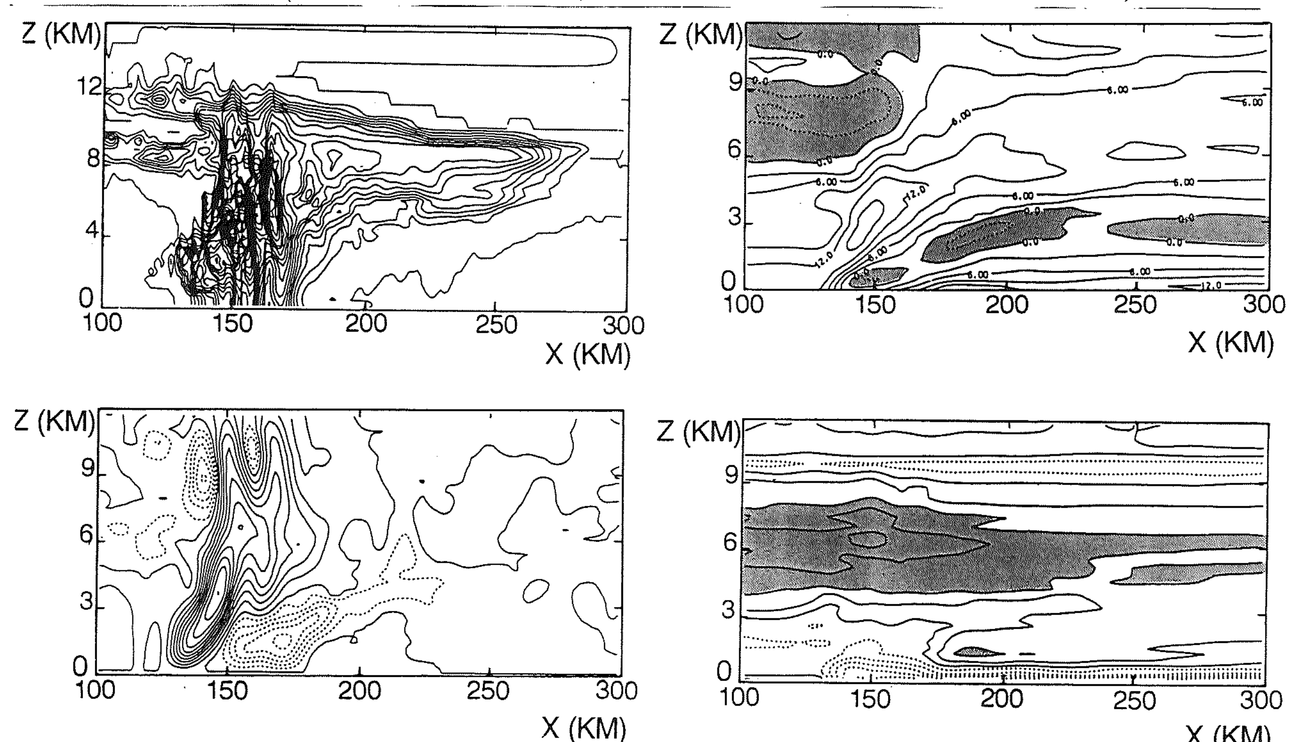

Fig. 2: As Fig. 1 but for the experiment without the ice phase parameterization.

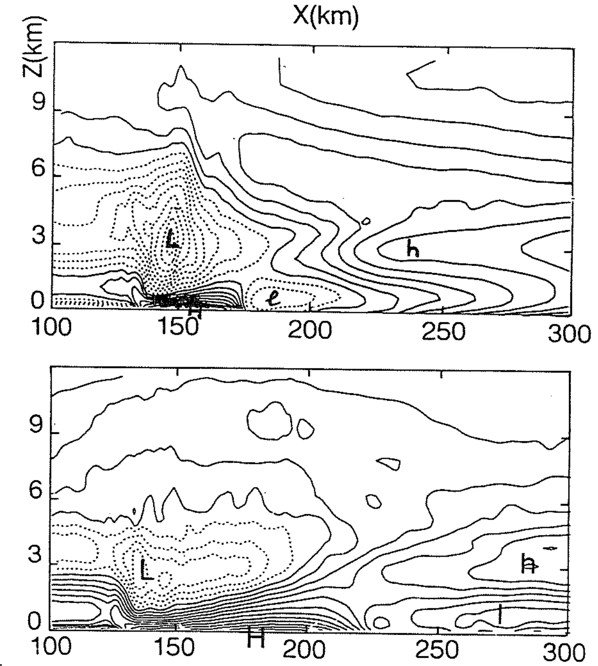

Fig. 3: Cross sections of the pressure deviation p' (contour interval 0.1 hPa) at 8h for experiment with (a) and without (b) the ice phase parameterization.

4.2 The diagnostic pressure equations

The diagnostic pressure is based on a balance equation similar to the hydrostatic balance, but derived from the model equations. To find the pressure at a reference level, we define the mean pressure deviation over the domain depth H as:

$$\overline{p'}^H = \frac{1}{H}\int_0^H p' dz \tag{4.1}$$

Owing to the use of the continuity equation, a diagnostic equation for $\overline{p'}^H$ can be derived by vertically integrating over the domain height H, the u momentum equation;

$$\frac{\partial^2 \overline{p'}^H}{\partial x^2} = -\frac{1}{H}\frac{\partial^2}{\partial x^2}\int_0^H \overline{\rho} u^2 dz + \frac{1}{H}\frac{\partial}{\partial x}\int_0^H \overline{\rho} D_u dz + f\frac{\partial \overline{\rho V}^h}{\partial x} \tag{4.2}$$

as vertical velocity w vanishes at the ground and at the model top. The term D_u represents the parameterization of the subgrid processes.

Using the hydrostatic equation together with Equ. (4.2), it is possible to diagnose a pressure p'_D. It is convenient to note it in a synthetic form:

$$p'_D = p'_D|_{Dyn} + p'_D|_{Corio} + p'_D|_{Mass} \tag{4.3}$$

allowing to identify three contributions to the pressure; either a dynamical one $p'_D|_{Dyn}$, the effect of the Coriolis term $p'_D|_{Corio}$ and the contribution of the mass fields $p'_D|_{Mass}$. Figure 4 illustrates the result of the diagnostic pressure computed at mid-level ($z = 3km$) during the 7-8h time period corresponding to the mature stage. It clearly appears that the diagnostic pressure p'_D is a good approximation of the model pressure p'_{NH}.

4.3 The coriolis and dynamic contributions

Figure 4 shows that for this tropical case, the coriolis contribution $p'_D|_{Corio}$ to the pressure field is negligible. On contrary the dynamical contribution $p'_D|_{Dyn}$ is important. For instance it increases the pressure jump across the system of 0.35 hPa at the 3 km level. Therefore the front-to-rear mid-level pressure gradient of 0.77 hPa over 200 km is due for 41% to dynamical processes.

The dynamical contribution $p'_D|_{Dyn}$ is proportional to the mean pressure $\overline{p'}^H$, which can be physically explained by its diagnostic equation (4.2). Indeed neglecting the second order coriolis and subgridscale terms, this equation allows to write a kind of Bernouilli equation but without any hypothesis such as the stationarity one:

$$\overline{p'}^H + \frac{1}{H}\int_0^H \overline{\rho} u^2 dz \approx Ax + B$$

This relation is confirmed by Fig. 5, with a trend A of 0.15 hPa over 200 km. Except the linear trend A, the mean pressure $\overline{p'}^H$, is the mirror image of $\overline{KE_h}^H$. It physically means that intense gradients of pressure can be generated to oppose to the horizontal changes of kinetic energy $\overline{KE_h}^H$, resulting of the momentum vertical transports occurring in the system. Therefore the momentum transport and effects of larger scales are important to increase the intensity of the pressure doublet $L-h$ at mid-level.

4.4 The contribution of the mass fields

The proposed diagnostic equation also allows to analyze the contribution of the full buoyancy field to the pressure field, by separately identifying the effects of the temperature, of the vapor mixing ratio and of the cloud water and precipitation drag fields. As we will show during the conference, all above mass fields are important to explain the pressure basic pattern, and it is impossible to neglect one of them. In particular, the mid-level

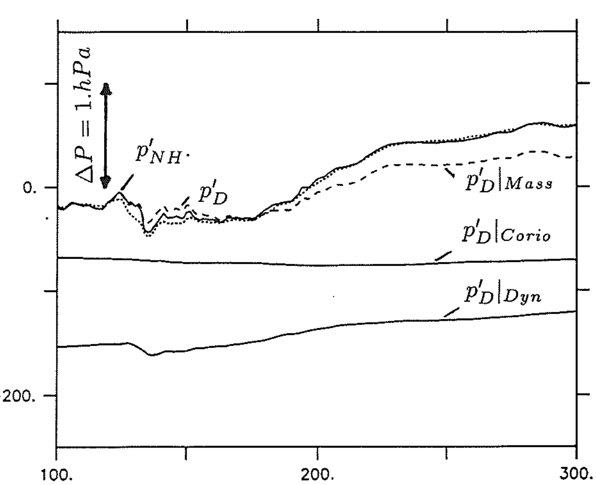

Fig. 4: Diagnostic pressure analysis performed during the 7 to 8h period, at level z = 3 km. The cross-line variations of four pressures or contributions are shown; p'_{NH}, p'_D, $p'_D|_{Mass}$, $p'_D|_{Corio}$ and $p'_D|_{Dyn}$.

system scale pressure jump is mainly due to the fact that averaged on the vertical, the system generates more buoyant air at its rear. This result is due to the widespread rear anvil injecting large amount of water vapor behind the system and to the adiabatic warming underneath the rear anvil.

5. Connection with the cross-line momentum field and conclusion

To analyse the combined effects of momentum transport and pressure induced momentum changes, Fig. 5 shows the cross-line momentum budget during the mature stage. The mid-level front-to-rear pressure gradient appears fundamental to explain the vertical circulation in the stratiform part. A strong convergence zone (Fig. 5c) is induced at mid-level of the stratiform part when the zone of front-to-rear pressure (Fig. 5b) gradient stretches farther than the zone of front-to-rear momentum change by advection (Fig. 5a). In other words the mid-level high pressure center (h on Figs. 3) induced by the system at its rear, prevents the progression by advection of the mid-level front-to-rear flow coming from the convective part, and forces its mesoscale ascent in the anvil and the unsaturated, warm mesoscale descent underneath.

6. References

Caniaux, G., J.-L. Redelsperger, and J.-P. Lafore, 1992: A numerical study of the stratiform region of a fast-moving squall line. Part I: General description, and water and heat budgets. To be submitted to *J. Atmos. Sci.*.

Chalon,J.P., G.Jaubert, F. Roux, and J.P. Lafore, 1988: The West African squall line observed on 23 June 1981 during COPT81: Mesoscale structure and transports. *J.Atmos.Sci.*,**45** 2744-2763.

Gamache,J.F., and R.A. Houze,Jr., 1985: Further analysis of the composite wind and thermodynamic structure of the 12 September GATE squall line. *Mon. Wea.Rev.*, **113**, 1241-1259.

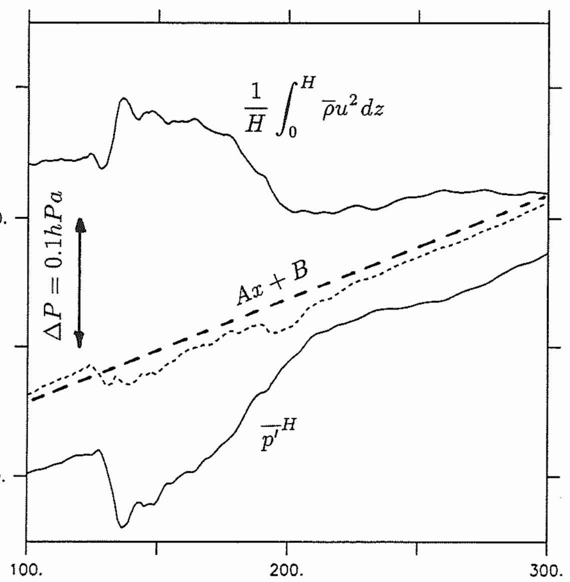

Fig. 5: Relation between the mean pressure $\overline{p'}^H$ and the mean horizontal kinetic energy $\frac{1}{H}\int_0^H \overline{\rho}u^2dz$. Their sum (dotted line) is close to a straight line as suggested by the Bernouilli-type equation.

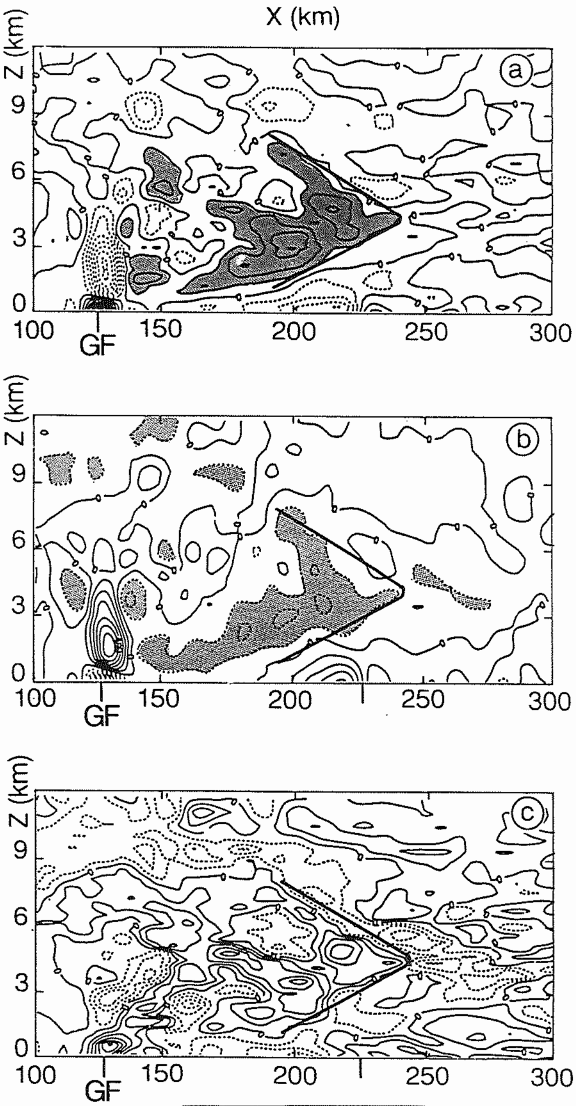

Fig. 6: Two-dimensional cross-line momentum budget during the 4-5h time period, for (a) the advection term, (b) the pressure induced term and (c) the Eulerian evolution. The contour interval is $1.10^{-3}ms^{-2}$ for (a) and (b), and half of (c). Zones with values of the advection term and pressure induced term, greater than $1.10^{-3}ms^{-2}$ and lower than $-1.10^{-3}ms^{-2}$ respectively, are shaded.

Lafore, J.P., and M.W. Moncrieff, 1989: a numerical investigation of the organization and interaction of the convective and stratiform regions of tropical squall lines. *J.Atmos.Sci.*,**46**,521-544.

Nicholls, M. E., 1988: A comparison of the results of a two-dimensional numerical simulation of a tropical squall line with observations. *Mon. Wea. Rev.*,**118**, 3055-3077.

Redelsperger, J.L., and J.P. Lafore, 1988: A three-dimensional simulation of a tropical squall line: convective organization and thermodynamic vertical transport. *J.Atmos.Sci.*,**45**,1134-1356.

Smull, B. F., and R. A. Houze, Jr., 1987: Rear inflow in squall lines with trailing-stratiform precipitation. *Mon. Wea. Rev.*,**115**, 2869-2889.

Zipser, E. J., 1969: The role of organized unsaturated convective downdrafts in the structure and rapid decay of an equatorial disturbance. *J. Appl. Meteor.*,**8**, 799-814.

A NUMERICAL STUDY OF THE MOMENTUM BUDGET OF A SQUALL LINE

Ming-Jen Yang and Robert A. Houze, Jr.

Department of Atmospheric Sciences
University of Washington, AK-40
Seattle, Washington 98195

1. INTRODUCTION

Mesoscale budget studies are useful in determining the interaction between a mesoscale convective system (MCS) and its environment. Studies of the momentum transport by lines of convection in the tropics (LeMone 1983; LeMone *et al.* 1984) and midlatitudes (Gao *et al.* 1990) have shown that the momentum transport is generally countergradient in the normal-line direction and downgradient in the along-line direction.

A typical structure for a squall-line MCS is leading-edge convection followed by a horizontally uniform stratiform precipitation area (Zipser 1969; Houze 1977; Smull and Houze 1985). The momentum balance and transport within these two regions may be quite different. The objective of this study is to decompose the momentum budget and flux into processes associated with convective and stratiform regions of a midlatitude squall line. This study is based on a numerical simulation of the intense squall line that occurred on 10-11 June 1985 during the Oklahoma-Kansas Preliminary Regional Experiment for STORM-Central (called PRE-STORM for short; see Cunning 1986).

2. MODEL

The model used in this study is a two-dimensional version of the Klemp-Wilhelmson compressible cloud model (Klemp and Wilhelmson 1978; hereafter KW) which includes the cloud microphysical bulk parameterization as described by Lin *et al.* (1983). The basic-state environment is assumed constant in time and horizontally homogeneous. Large-scale motion, surface fluxes, and radiation are neglected. Stretched grids are used in both vertical and horizontal directions (similar to Fovell and Ogura 1988; hereafter FO) in order to optimize resolution. In the vertical, the grid size of the lowest layer is 140 m; the grid size of the highest layer is 550 m; and the model top is at 21.7 km. A total of 455 grid points are used in the horizontal. The central 315 points comprise a fine mesh with 1-km resolution, and the total horizontal domain size is thus 4,814 km. The top and bottom of the domain are rigid lids. Since sound waves exist in the compressible equations, a time-splitting scheme is used to provide numerical efficiency by treating sound wave modes (2 s time step) and cloud-scale gravity wave modes (6 s time step) separately.

The initial temperature and moisture profiles for the simulation were from the 2331 UTC 10 June sounding from Enid, Oklahoma (Fig. 1a). This sounding showed the environmental conditions 4 h before the squall line passed the station. The initial normal-line wind profile is in Fig. 1b. The convective available potential energy indicated by this sounding was 3,323 J kg^{-1}, higher than the average value for springtime severe storms in this region (Bluestein and Jain 1985). However, the wind shear is so strong that a model storm cannot survive if it is initiated with the observed wind profile. Therefore, a similar approach to that of Fovell and Ogura (1989) is taken, *i.e.*, a reduced shear (3×10^{-3} s^{-1} in the lowest 2.5 km, no shear above 2.5 km) is used to initiate the storm. Once the cold pool of the storm is strong enough to act against the wind shear (model time ~6 h), the background wind is slowly changed back to the observed profile. A 5°K thermal similar to that used by KW is put in the central domain to initiate convection. The thermal is centered at 1.4 km AGL with horizontal radius 10 km and vertical radius 1.4 km.

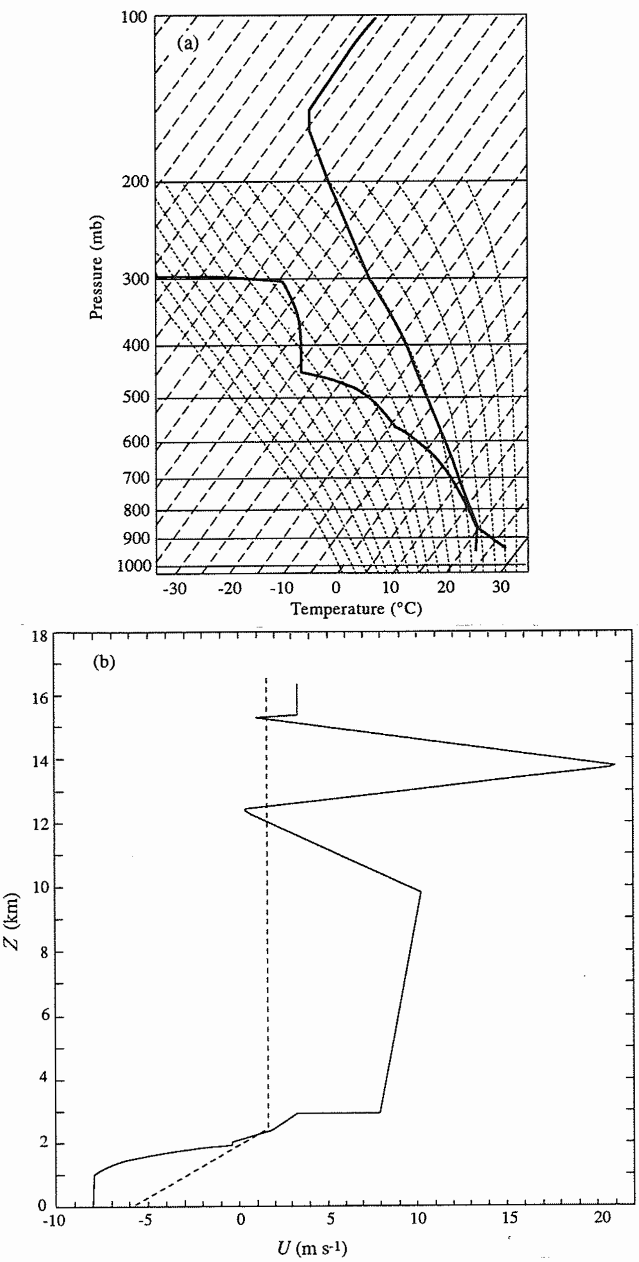

Fig. 1 Initial sounding used in the model simulations. (a) The temperature and dew-point temperature profiles (dark lines) are plotted in skew-T format. Curved lines are moist adiabats. (b) Observed line-normal wind profile is the solid line, and the reduced wind-shear profile used to initiate the storm is the dashed line.

Model verification shows that the cloud model can reproduce many realistic aspects of the squall line, which are known from observations (*e.g*., Johnson and Hamilton 1988; Biggerstaff and Houze 1991). Specifically, the model simulated the storm-relative front-to-rear (FTR) flows in both upper and lower levels and the rear-to-front (RTF) flows in between (Fig. 2a), the upshear tilt of the updrafts (Fig. 2b), a precipitation-induced high at the gust front and a wake low (not shown), the leading convective rainfall followed by a transition zone, and the trailing stratiform precipitation. Thus, we proceed to an examination of the momentum budget of the model storm.

3. METHODOLOGY

Since the computational domain moves with the squall line so that the model storm is always in the fine mesh, the horizontal momentum equation used in the model is:

$$u'_t = -cu'_x - (u'u')_x - (\rho_o wu')_z / \rho_o - c_p \theta_{vo} \pi_x + D_{u'} \qquad (1)$$

where x and z are the horizontal and vertical coordinates. When used as subscripts, x and z denote partial derivatives. u' is the system-relative horizontal flow, c is the domain translation speed (usually the squall-line propagation speed), w is the vertical velocity, ρ_o is the basic-state density, c_p is the specific heat at constant pressure, θ_{vo} is the basic-state virtual potential temperature, π is the nondimensional pressure, and $D_{u'}$ is the sub-grid scale turbulence term (the detailed definition of each symbol is given in KW). From the model output, each term in (1) can be directly calculated.

In order to understand how each physical process contributes to the balance of the u-momentum equation during the lifetime of the model storm, three characteristic 30-min periods (at model times 376-406 min, 556-586 min, and 736-776 min) were chosen to represent the three stages of the storm: developing, mature, and decaying. Then each

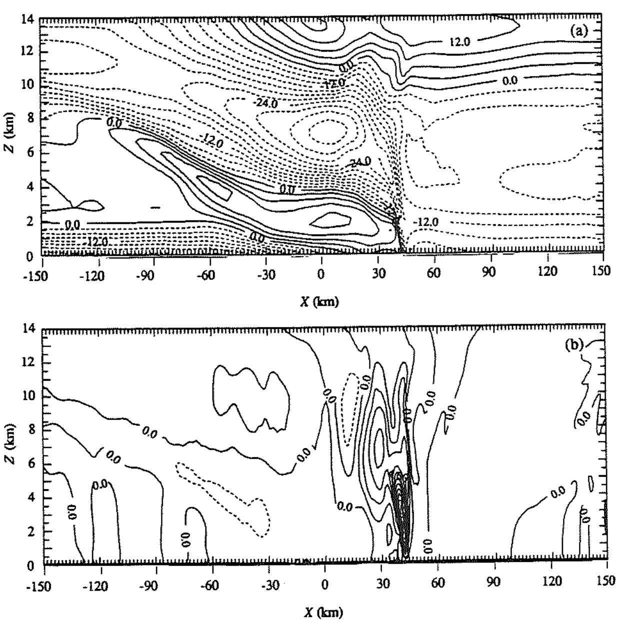

Fig. 2 Time-averaged wind fields at the mature stage (model time 556-586 min). (a) Horizontal storm-relative flow contoured every 3 m s^{-1} with negative values dashed. (b) Vertical flow contoured every 1 m s^{-1} with negative values dashed. The convective region is between x = 12 and 43 km, and the stratiform region is between x = –50 and 11 km. Storm motion is from left to right.

term in (1) is averaged over the 30-min period with a 2-min data interval. The reason for the time average is that an individual convective or precipitation cell has a regeneration time scale (~10 min) shorter than that of the convective and mesoscale structures in which we are most interested, and the small-scale structures associated with individual precipitation cells can be smoothed out by taking the time average over a period longer than that of the cell regeneration period (FO). In addition to the time average, a horizontal average was also taken of each term in (1) over two regions: one over the entire convective rainfall region, and the other over the whole stratiform precipitation region (the distinction between the convective and stratiform precipitation regions was based on the time-average surface rainfall rate).

4. HORIZONTAL MOMENTUM BUDGET

In general, the vertical profiles for u momentum at the three life cycle stages are of a similar shape. The profiles differ mainly in their magnitudes and heights of their maxima and minima. Fig. 3a shows the vertical profiles for the terms in the u-momentum budget of the convective region during the mature stage. The horizontal pressure gradient produces FTR acceleration throughout the whole troposphere except at very low and high levels. Horizontal advection is roughly out of phase with vertical advection. Sub-grid scale turbulence is the smallest effect. The net acceleration is RTF in lower levels (below 4.5 km) and FTR above. The vertical profile of the u momentum in the stratiform region during the mature stage (Fig. 3b) is different from that in the convective region. The pressure gradient produces RTF acceleration throughout the entire troposphere except at lower levels (below 2 km). Horizontal advection oscillates in the vertical but is again strongly out of phase with vertical advection. Sub-grid scale turbulence is again the smallest term. The net acceleration is FTR in lower and upper levels, and RTF in between, which is consistent with the flow pattern in the stratiform region.

5. IMPACT OF MOMENTUM FLUX ON MEAN FLOW

In this section, we examine the effect of momentum transport on the horizontal (line-normal) mean flow in the convective and stratiform regions. Fig. 4a shows the area-averaged horizontal wind profiles in the convective region at the three life cycle stages, while Fig. 4b displays the corresponding mean momentum flux profiles. Consistent with the upshear tilting of the updraft and downdraft in the convective region, the momentum flux within the whole troposphere is negative during these three stages except in the midlevels at the mature stage. The direction of the vertical momentum transport is indicated by

$$\overline{u^* w^*} = -K \frac{\partial \overline{u'}}{\partial z} \qquad (2)$$

where

$$u' = \overline{u'} + u^*, w = \overline{w} + w^* \qquad (3)$$

In (2) and (3), the overbar denotes an area average, while the asterisk denotes the departure from the average. By the mixing length theory, $\overline{u^* w^*}$ is said to be downgradient if K is positive, and countergradient if K is negative. Fig. 4a and b shows that initially the momentum flux is mostly downgradient in the convective region, becomes more countergradient in the mature stage, and is mostly downgradient again in the decaying stage. Fig. 5 is the same as Fig. 4 except for the stratiform region, and the results inferred from it appear to be consistent with Gao *et al.* (1990). However, their 00 UTC profile was subject to large-scale environmental variation which is excluded in our study. In contrast to the result in the convective region, the momentum transport in the stratiform region is mostly countergradient at first and then becomes more and more downgradient as the system ages. The different momentum transport characteristics between convective and stratiform regions have not been indicated in previous studies. The reason for this difference will be explored by calculating the momentum flux from the model result for each region and each life cycle period. In this way, we shall isolate the main mechanism for the production of momentum flux of the indicated sign. This work is in progress.

6. CONCLUSION

In this study, we have examined the momentum budget of a numerical simulation of the 10-11 June 1985 squall line and separated the processes occurring in the convective region of the storm from those occurring in the stratiform region. In the u-momentum budget of the convective region, the pressure gradient produces FTR acceleration within the whole troposphere, except at very low and high levels. Horizontal advection is roughly out of phase with vertical advection. Sub-grid scale turbulence is the smallest effect. The net acceleration is RTF in lower levels (below 4.5 km) and FTR above. In the stratiform region, the pressure

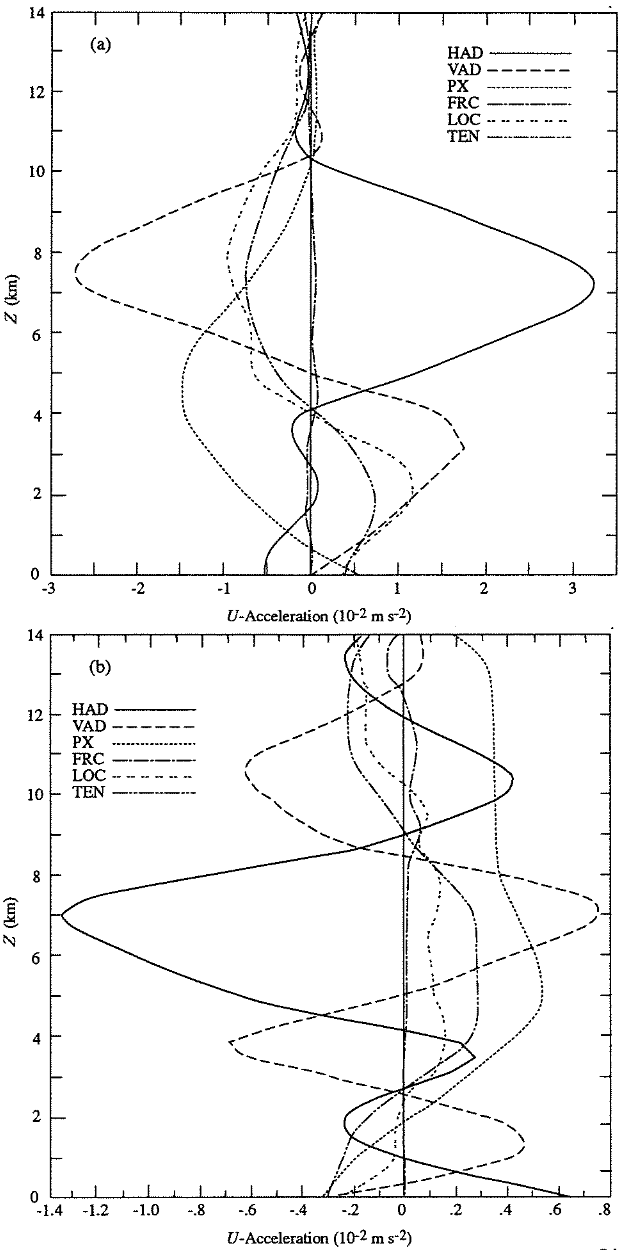

Fig. 3 The vertical profiles of each term in the u-momentum equation averaged over (a) the convective and (b) the stratiform region. LOC denotes the local time rate of change term (u'_t), TEN the apparent tendency term ($-cu'_x$), HAD the horizontal advection ($-(u'u')_x$), VAD the vertical advection ($-(\rho_o wu')_z/\rho_o$), PX the pressure gradient force ($c_p\theta_{vo}\pi_x$), and FRC the sub-grid scale turbulence ($D_{u'}$), respectively.

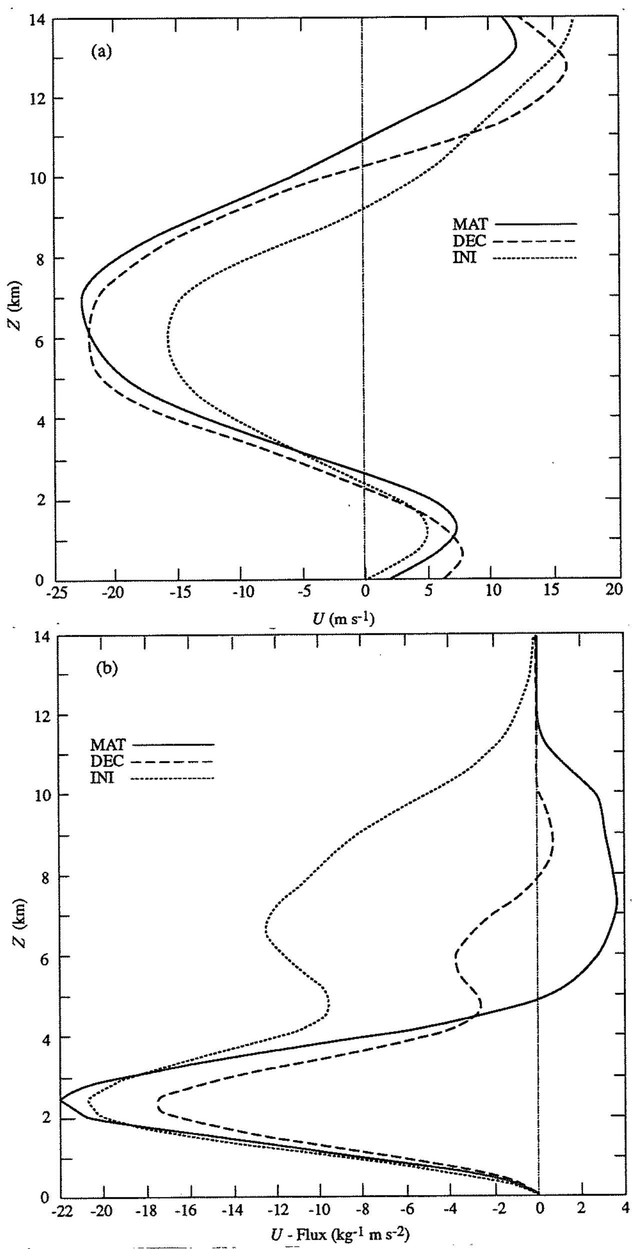

Fig. 4 The vertical profiles of the area-averaged horizontal wind (a) and momentum flux (b) in the convective region at three life cycle stages. INI denotes the initial stage, MAT the mature stage, and DEC the decaying stage, respectively.

gradient results in RTF acceleration within the whole troposphere except at low levels (below 2 km). Horizontal advection oscillates in the vertical but is again strongly out of phase with vertical advection. Sub-grid scale turbulence is again the smallest term. The net acceleration is FTR in upper and lower levels and RTF in between.

Initially, the momentum flux is mostly downgradient in the convective region, becomes more countergradient in the mature stage, and is mostly downgradient again in the decaying stage. However, in the stratiform region, the momentum transport is mostly countergradient initially, and becomes more and more downgradient as the system ages. The different momentum transport characteristics between convective and stratiform regions have not been addressed in previous studies. This will be our next phase of research.

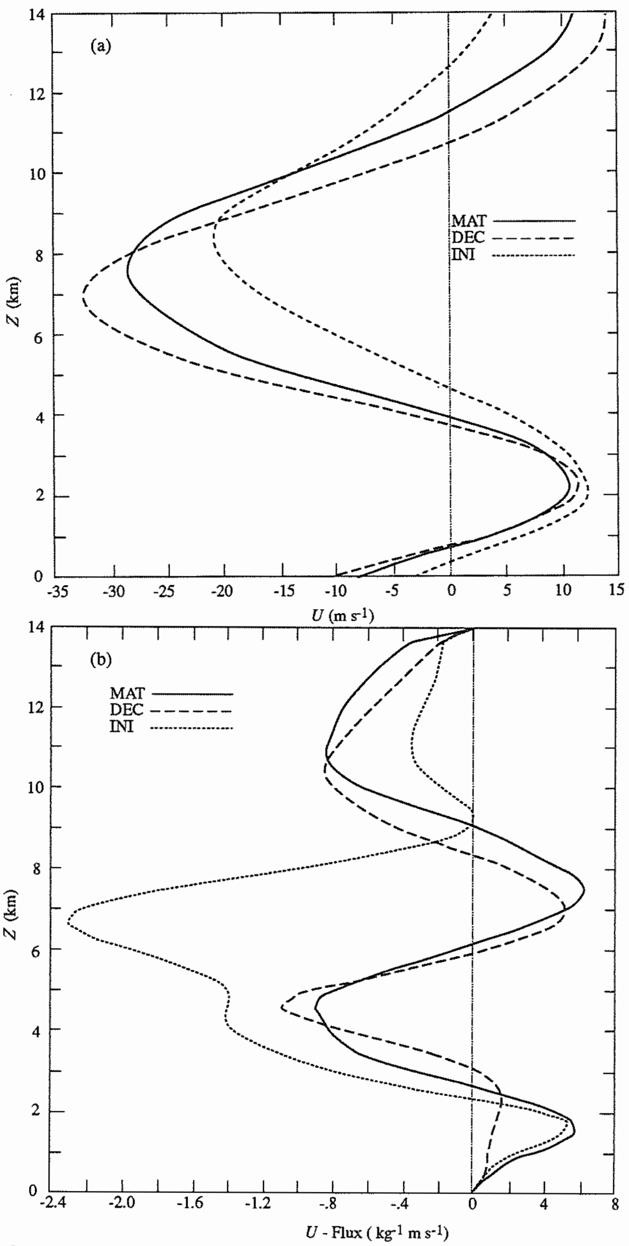

Fig. 5 The same as Fig. 4, except for the stratiform region.

Acknowledgments: The cooperation of Professor Robert G. Fovell has been vital to this study. G. C. Gudmundson edited the manuscript and K. M. Dewar assisted with the figures. The computations were made on the Cray Y-MP computer of the National Center for Supercomputing Application at the University of Illinois at Champaign-Urbana. This research was supported by the National Science Foundation grant ATM-9101653.

REFERENCES

Biggerstaff, M. I., and R. A. Houze, Jr., 1991: Kinematic and precipitation structure of the 10-11 June 1985 squall line. *Mon. Wea. Rev.*, **119**, 3034-3065.

Bluestein, H. B., and M. H. Jain, 1985: Formation of mesoscale lines of precipitation: Severe squall lines in Oklahoma during spring. *J. Atmos. Sci.*, **42**, 1711-1732.

Cunning, J. B., 1986: The Oklahoma-Kansas Preliminary Regional Experiment for STORM-Central. *Bull. Amer. Meteor. Soc.*, **67**, 1478-1486.

Fovell, R. G., and Y. Ogura, 1988: Numerical simulation of a midlatitude squall line in two dimensions. *J. Atmos. Sci.*, **45**, 3846-3879.

Fovell, R. G., and Y. Ogura, 1989: Effect of vertical wind shear on numerically simulated multicell storm structure. *J. Atmos. Sci.*, **46**, 3144-3176.

Gao, K., D.-L. Zhang, M. W. Moncrieff and H.-R. Cho, 1990: Mesoscale momentum budget in a midlatitude squall line: A numerical case study. *Mon. Wea. Rev.*, **118**, 1011-1028.

Houze, R. A., Jr., 1977: Structure and dynamics of a tropical squall-line system. *Mon. Wea. Rev.*, **105**, 1540-1567.

Johnson, R. H., and P. J. Hamilton, 1988: The relationship of surface pressure features to the precipitation and the air-flow structure of an intense midlatitude squall line. *Mon. Wea. Rev.*, **116**, 1444-1472.

Klemp, J. B., and R. B. Wilhelmson, 1978: The simulation of three-dimensional convective storm dynamics. *J. Atmos. Sci.*, **35**, 1070-1096.

LeMone, M. A., 1983: Momentum flux by a line of cumulonimbus. *J. Atmos. Sci.*, **40**, 1815-1834.

LeMone, M. A., G. M. Barnes and E. J. Zipser, 1984: Momentum flux by lines of cumulonimbus over tropic oceans. *J. Atmos. Sci.*, **40**, 1815-1834.

Lin, Y. L., R. D. Farley and H. D. Orville, 1983: Bulk parameterization of the snow field in a cloud model. *J. Climate Appl. Meteor.*, **22**, 1066-1092.

Smull, B. F., and R. A. Houze, 1985: A midlatitude squall line with a trailing region of stratiform rain: radar and satellite observations. *Mon. Wea. Rev.*, **113**, 117-133.

Zipser, E. J., 1969: The role of organized unsaturated convection downdrafts in the structure and rapid decay of an equatorial disturbance. *J. Appl. Meteor.*, **8**, 799-814.

A STUDY OF SPRING RAIN, MOLD RAIN AND TYPHOON RAIN IN THE OCEANIC ENVIRONMENT OF XIAMEN ISLAND

Shaocai Yu, Zhemian Cheng, Xiaopin Cai and Xiaojiang Cheng

1. Xiamen Municipal Research Institute of Environmental Protection No.56, Hu-bin Southern Road, Xiamen 361004, P.R. China
2. Xiamen Meteorological Observatory, Xiamen 361004, P.R. China

1. TRODUCTION

Several researchers have indicated that acid precipitation is widespread in Europe, in the northeast United States and in Southern China [Galloway et al., 1982; Zhao et al., 1988; Yu et al., 1991]. There are several studies that have attempted to relate rainfall acidity to meteorological condition. Gorman (1961) examined the influence of such environmental factors as precipitation amount and intensity, evaporation, temperature, wind speed and direction on the concentrations of major ions in inland water. Raynor and Hayes (1982) reported that concentrations of major ions in precipitation are determined by season and by local and synoptic weather conditions including synoptic type, precipitation type and rate, and wind direction and speed. In this paper, we study spring rain, mold rain and typhoon rain in the oceanic environment of Xiamen Island by using sequentially sampling in short time during 1990, and try to identify some relationships between the pH value of the precipitation and meteorological parameters including surface wind direction and speed, preciitation amount and type, cloud type, coming direction of precipitation and the synoptic weather pattern of surface and high altitute (850mb) during rain observed by radar and satellite. Satellite and radar observations have been used to reveal features of mesoscale precipitation system developed over various parts of the world [Houze and Hobbs, 1982].

2. EXPERIMENTAL

2.1. Outline of Xiamen Island

Xiamen, is an island located on the southeast China coast, and the city lies at 117°53'-118°12' east longitude and 24°25'-24°46' north latitude, to the west of the Taiwan Strait and consists of Xiamen Island proper, Gulanyu and coastal part of the norther bank of Jiulong Rive (See Fig.1). Xiamen has a subtropical oceanic climate. The windscale is between 3 and 5. There are only 10-12 foggy days during the year. Xiamen also lies in the typhoon track and four or five typhoons may pass annually.

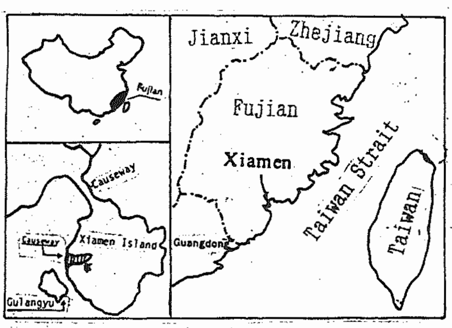

Figure 1. Map of Xiamen (* Sampling Site)

2.2. Sampling and analysis methods

Sampling: To investigate the gradual changes in chemical composition during rain, several secrupulously washed polythlene containers were exposed to the atmosphere just prior to the onset of precipitation simultaneously and were retrieved immidiately after collected volume of rainfall was fitted for requesting and then several containers were exposed to the atmosphere to collect rainwater again, and collecting process was repeated again untill the end of rain. These samples were collected sequentially on precipitation intensity and time rather than a volume basis. The atmospheric concentrations of SO_2 and NOx were measured during sampling. The pH of each of the subsamples was measured shortly after collection.

Analytical Methods: Anion ion concentrations (SO_4^{2-}, NO_3^-, F^-, Cl^-) were determinated using IC; Cation ion concentrations(Na^+, K^+, Ca^{2+}, Mg^{2+}) were determinated using atomic absorption spectrophotometer; NH_4^+: using classic colorimetric method.

3. Results and Discussion

3.1. Statistics of the pH of precipitation in Xiamen

The rain in the oceanic environment of Xiamen Island where its atmospheric quality reach the National Atmospheric Quality 2rd Standard is very acidic, especially for spring rain and mold rain (Yu et al., 1990). We have observed 404 events of rain between 1983-1989 and have collected 1050 rain samples. Figure 2 shows the frequency distribution of pH of 404 rain events.

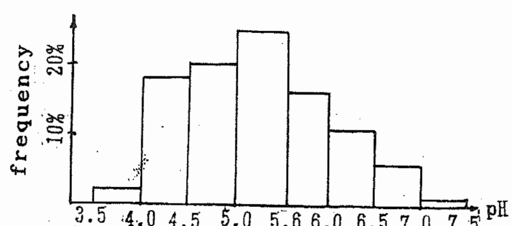

Fig.2 Frequency distribution of pH in rain of Xiamen during 1983-1989

3.2. Case Studies

Spring rain, mold rain and typhoon rain are major rain patterns in Xiamen. The major precipitation systems occuring in the Xiamen area are: the propagating-frontal systems from February to late April, the rainfall associated with a return flow around the high pressure systems in springtime, the quasi-stationary frontal systems from May to mid-June for mold rain, the showers, thunderstorms and typhoons in the summer time. We'll present results of some case studies to illustrate the cause of acid rain of the different weather patterns in Xiamen.

a. Spring rain

The "Spring rain" period in Xiamen is from February to April, and the spring rain is usually very acidic. Four spring rain events were sequentially sampled, and variation of pH in sequential samples with sampling time and meteorological parameters are presented in table 1. Surface synoptic system were low pressure, low pressure, stationary front and low pressure for April 11, 15, 16 and 19 respectively. High-altitute synoptic system (850mb) were SWly frontal trough, Wly shear, Wly shear and SWly frontal trough for April 11, 15, 16 and 19 respectively. The precipitation cloud of April 16 first comed from southwest, southeast and east (1938 LST) and covered Xiamen Island completely and move eastward (2141 LST) as shown in radar echo maps (Fig. 3). The precipitation cloud of April 19 comed from west (1240 LST), covered the Xiamen Island in 1339 LST and then moved southeastly in 2154 LST as shown in radar echo map and the satellite image (Fig. 4). Fig. 5 illustrates the synoptic scale map at 0800 and 2000 LST on April 19, 1990. The frontal system and the accompanying precipitation system moving from South China may have been influenced by the pollution of South Chinese mainland where acid rain is heavy (Zhao et al., 1988, Yu et al., 1990). The atmospheric concentrations of SO_2 and NOx in Xiamen During April were 0.034-0.100 mg/m^3 and 0.015-0.08 mg/m^3 respectively, and couldn't make spring rain in Xiamen so acidic. This suggest that the spring low pH rainfall in Xiamen Island was caused by Long-tansport of pollution from southern Chinese mailand.

Table 1. Variation of pH of sequential springrain samples with sampling time and meteorological parameters

	Sampling time (1990)	pH	Precip. amount	Type of Precip.	Direction Speed	Precip. cloud	Site of Cloud
1	April 11,1300-1350	4.23	11.5	R	SW/4.0	≡Cb	W/E
	1350-1400	4.64	1.0	$\dot{\nabla}$/:	SW/4.0	≡Cb	W/E
	1400-1510	4.30	1.5	$\dot{\nabla}$/:	SSW/3.3	≡Sc	W/E
	1510-1520	4.39	1.1	$\dot{\nabla}$/:	SSW/3.3	≡Sc	W/E
2	April 15,1600-2000	4.20	7.0	$\dot{\nabla}$/:	E/3.0	Sc,Fn	W/E
	2000-2110	4.94	4.2	$\dot{\nabla}$/:	NNE/5.0	Sc,Fn	W/E
	2110-2130	4.70	4.4	$\dot{\nabla}$/:	NNE/4.0	Sc,Fn	W/E
	2130-2215	4.78	10.8	$\dot{\nabla}$/:	NE/4.0	Sc,Fn	W/E
	2215-2230	5.03	1.0	$\dot{\nabla}$/:	NE/2.0	Sc,Fn	W/E
	2230-2320	4.83	1.0	$\dot{\nabla}$/:	NE/2.0	Sc	W/E
3	April 16,1700-1945	4.41	3.7	R/:	E/4.0	Sc,Fn	W/E
	1945-2000	4.37	3.2	$\dot{\nabla}$/:	E/5.0	Sc,Fn	W/E
	2000-2135	4.70	3.3	$\dot{\nabla}$/:	E/5.0	Sc,Fn,Cb	W/E
	2135-2150	5.12	3.2	$\dot{\nabla}$/:	ENE/6.0	Sc,Fn,Cb	W/E
	2150-2205	5.10	3.2	$\dot{\nabla}$/:	ENE/6.0	Sc,Fn,Cb	W/E
	2205-2215	5.44	2.4	$\dot{\nabla}$/:	ENE/6.0	Sc,Fn,Cb	W/E
	2215-2230	5.30	2.0	$\dot{\nabla}$/:	NE/5.0	Sc,Fn	W/E
	2230-2300	5.11	1.6	$\dot{\nabla}$/:	NE/5.0	Sc,Fn	W/E
4	April 19,0950-1425	4.32	3.3	$\dot{R}$/:	WSW/2.0	≡	W/E
	1425-1435	4.17	8.3	$\dot{R}$/:	WSW/2.0	≡	W/E
	1435-1445	4.36	1.7	$\dot{R}$/:	WSW/2.0	≡	W/E
	1445-1515	4.11	1.1	$\dot{R}$/:	W/3.0	≡,Cb	W/E
	1515-1530	4.24	1.2	$\dot{R}$/:	W/5.0	≡,Cb	W/E
	1530-1755	3.97	1.8	$\dot{R}$/:	W/4.0	Sc,Cb,Cu	W/E
	1755-1815	3.98	1.4	$\dot{R}$/:	W/4.0	Sc,Fn	W/E
	1815-1830	4.22	1.2	$\dot{R}$/:	WNW/3.0	Sc,Fn	W/E
	1830-1900	4.39	1.7	$\dot{R}$/:	WNW/3.0	≡	W/E
	1900-1930	4.30	1.3	$\dot{R}$/:	WNW/3.0	Sc,≡	W/E
	1930-2125	3.86	1.2	$\dot{R}$/:	WNW/3.0	Sc,≡	W/E
	2125-2130	3.96	1.0	$\dot{\nabla}$/:	W/4.0	Cb,Cu	W/E
	2130-2400	3.80	0.3	$\dot{\nabla}$/:	W/3.0	Cb,Sc	W/E

Note: Units of precip. amount and ground wind speed are mm and m/s respectively; $\dot{\nabla}$, $\dot{R}$ and : present shower, thunderstorm and continual rain respectively. Site of cloud present its position to Xiamen in prior and after rain

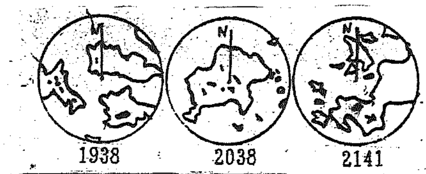

Fig 3. Radar echo maps on April 16, 1990

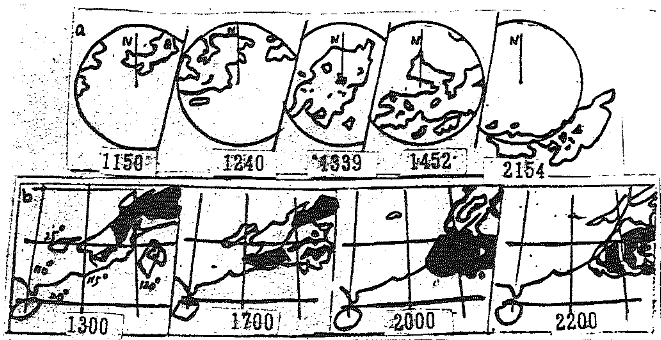

Fig 4. (a) Radar echo maps
(b) The satellite image on April 19,1990

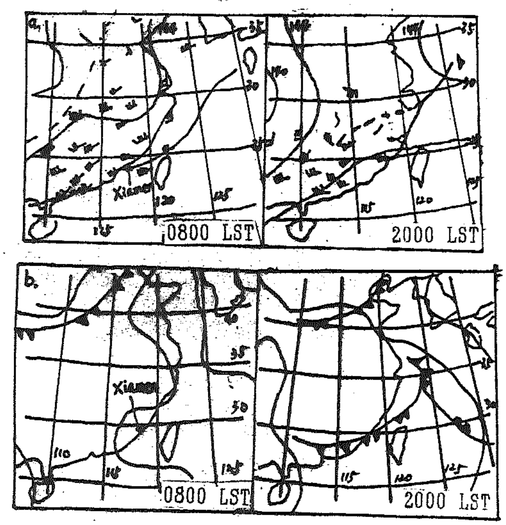

Fig 5. (a) The high-altitute synoptic maps
(b) The surface synoptic maps on April 19, 1990

b. Mold Rain

The "mold rain" period in Xiamen is from May to middle June, and the mold rain is also very acidic. Three mold rain events were sequentialy sampled and results were presented in table 2. All rain types are showers accompanied by continual precipition. Surface synoptic systems were cold front, the rear of the high pressure and the rear of the high pressure for May 17, May 18-19 and June 6 respectively, and high-altitute synoptic system (850 mb) were Wly trough-line, southwestlies at the head of the trough and southwestlies at the head of the trough for May 17, May 18-19 and June 6 respectively. A cyclonic storm producing in south china ocean in the moring of May 18 (0800 LST) only influenced Xiamen Island by its periphery and then move eastward as shown in Fig. 6. The sequential samples of rain caused by precipitation cloud from northwest were not as acidic as those caused by precipitation cloud from west and southwest (See table 2).

Table 2. Variation of pH of sequential mold rain samples with sampling time and meteorological parameters

	Sampling time (1990)	pH	Precip. amount	Type of precip.	Direction speed	Precip. cloud	Site of cloud
1	May 17, 1100-1455	4.68	26.0	$\dot{\nabla}$/:	WNW/1.3	Cu,Cb	NW/SE
	1455-1515	5.44	3.7	$\dot{\nabla}$/:	W/2.0	Cu,Cb	NW/SE
	1515-1525	5.53	2.1	$\dot{\nabla}$/:	WSW/2.0	Cb	NW/SE
	1525-1535	5.59	4.0	$\dot{\nabla}$/:	NE/1.0	Cb	NW/SE
	1535-1540	5.06	1.2	$\dot{\nabla}$/:	NE/1.0	Cb	NW/SE
	1540-1550	5.02	2.7	$\dot{\nabla}$/:	SE/2.0	Cb	NW/SE
	1550-1600	5.29	2.5	$\dot{\nabla}$/:	SE/2.0	Cb	NW/SE
	1600-1610	5.03	4.4	$\dot{\nabla}$/:	c/0	Cb	NW/SE
	1610-1615	4.68	1.4	$\dot{\nabla}$/:	E/1.2	Cb	NW/SE
	1615-1625	4.35	1.5	$\dot{\nabla}$/:	ENE/1.2	Cb	NW/SE
	1625-1800	4.37	6.2	$\dot{\nabla}$/:	NW/5.0	Cu	W/E
	1800-2100	4.91	1.0	$\dot{\nabla}$/:	ENE/1.7	Cu,Sc	W/E
	2100-2145	5.48	1.3	$\dot{\nabla}$/:	NNW/1.7	SC	W/E
	2145-2205	5.32	3.0	$\dot{\nabla}$/:	N/1.7	Sc	W/E
	2205-2225	4.96	2.7	$\dot{\nabla}$/:	ENE/1.7	Sc	W/E
	2225-2245	4.98	1.7	$\dot{\nabla}$/:	NNE/1.7	Sc	W/E
	2245-2300	4.97	1.2	$\dot{\nabla}$/:	NNE/1.7	Sc	W/E
2	May 18, 0730-0830	4.65	1.3	$\dot{\nabla}$/:	NE/3.0	Sc,Fn	W/E
	0830-1200	4.63	2.0	$\dot{\nabla}$/:	ESE/2.0	Sc,Fn	W/E
	1200-1700	4.78	1.6	$\dot{\nabla}$/:	ENE/2.0	Sc,Fn	W/E
	1700-1830	4.48	2.8	$\dot{\nabla}$/:	ENE/2.0	Sc,Fn	W/E
	1830-2230	4.42	1.5	$\dot{\nabla}$/:	ENE/3.3	Sc,Fn	W/E
	2230-0700*	4.71	13.5	$\dot{\nabla}$/:	NNE/3.7	Sc,Fn	W/E
	May 19 0700-0720	4.93	3.2	$\dot{\nabla}$/:	ENE/2.7	≡	W/E
	0720-0740	5.55	3.0	$\dot{\nabla}$/:	ENE/2.0	≡	W/E
	0740-0800	5.23	1.1	$\dot{\nabla}$/:	ESE/1.7	≡	W/E
	0800-0830	4.41	4.0	$\dot{\nabla}$/:	ESE/2.0	≡	W/E
	0830-0900	4.40	2.9	$\dot{\nabla}$/:	ESE/2.0	≡	W/E
	0900-1200	4.43	1.4	$\dot{\nabla}$/:	WNW/1.3	≡,Sc,Fn	W/E
3	June 6, 1820-1835	5.39	4.6	$\dot{\nabla}$/:	ESE/5.0	Sc,Fn	SW/E
	1835-1900	4.65	3.0	$\dot{\nabla}$/:	ESE/1.0	Sc,Fn	SW/E
	1900-1930	4.33	2.3	$\dot{\nabla}$/:	ESE/4.0	Sc,Fn	SW/E

Note: the same as notes in Table 1. * May 19,0700.

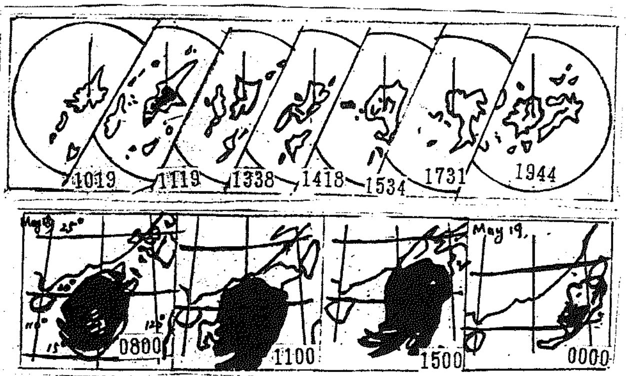

Fig 6. (a) Radar echo maps on May 17, 1990
(b) The satellite image on May 18- 19,1990

C. Typhoon Rain

The "Typhoon rain" period in Xiamen is from middle June to September . Several typhoon rain events were sequentially sampled and results were presented in table 3. The precipitation cloud of June 24 and July 30-31 rain moved from the south, and their synoptic systems of surface and high-altitute were the periphery of typhoon. July 1, and August 1 surface synoptic systems were stationary front, and belt of convergency respectively, and their high-altitute synoptic systems were frontal trough, and belt of convergency respectively. The precipitation cloud of August 20 rain moved from east ocean as shown in radar echo maps in Fig.7 and the pH of its six sequential rain samples ranged from 5.74 to 5.93, higher than 5.6. This was reasonable because the east of Xiamen is Taiwai Strait where there is not any pollution sources. September 8-9 surface and high-altitute synoptic system was the periphery of typhoon. Table 3 shows that two rains which precipitation cloud moved from southwest were more acidic than those which precipitation cloud moved from other directions, and the August 1 rain was most acidic in all typhoon rains.

From Table 1,2 and 3, we can get the conclusion that the subsample pH of every event of rain were fluctuated with sampling time and didn't decrease cntinuously. The single rain event didn't caused by a single precipitation cloud band but by many precipitation bands as shown in radar echo maps ,and every band may not be the same as each other. The fluctuation of the pH of every rain event showed the results of radar and satellite observation. Subsample pH of every rain even had strongly relationship with coming direction of precipitation cloud.

Table 3. Variation of pH of sequential typhoon rain samples with sampling time and meteorological parameters

	Sampling time (1990)	pH	Precip. amount	Type of precip.	Direction speed	Precip. cloud	Site of cloud
1	June 24, 1730-1850	4.83	23.9	$\dot{\nabla}$	SW/7.0	Sc,Cb	S/SE
	1850-1930	4.94	2.5	$\dot{\nabla}$	SW/6.0	Sc,Cb	S/SE
	1930-2030	5.08	3.5	$\dot{\nabla}$	SSW/6.0	Sc,Cb	S/SE
	2030-2040	5.73	4.4	$\dot{\nabla}$	SW/7.0	Sc,Cb	S/SE
	2040-2230	4.62	3.7	$\dot{\nabla}$	SW/4.0	Sc,Cu	S/SE
2	July 1, 1015-1040	5.19	7.3	$\dot{\nabla}$/:	SSW/6.0	Sc	SW/NE
	1040-1050	5.36	14.0	$\dot{\nabla}$/:	SSW/6.0	Sc	SW/NE
	1050-1100	5.36	6.8	$\dot{\nabla}$/:	SW/6.0	Ns	SW/NE
	1100-1110	4.99	2.6	$\dot{\nabla}$/:	SW/6.0	Ns	SW/NE
	1110-1140	4.63	2.2	$\dot{\nabla}$/:	SW/7.0	Sc, Fn	SW/NE
	1140-1255	4.95	18.4	$\dot{\nabla}$/:	SW/6.0	Ns	SW/NE
	1255-1315	5.23	1.8	$\dot{\nabla}$/:	SW/5.0	Fn,Sc	SW/NE
	1315-1500	4.33	1.6	$\dot{\nabla}$/:	SW/4.0	Fn,Sc	SW/NE
3	July 30, 0800-1600	5.19	14.7	R	ESE/9.6	Sc,Fn	S/WNW
	1600-2020	6.11	6.8	$\dot{\nabla}$	NEN/7.3	Sc,Fn	S/WNW
	2020-2130	6.41	2.8	$\dot{\nabla}$	NNE/7.3	Sc,Fn	S/NW
	2130-2330	6.05	5.0	$\dot{\nabla}$	ENE/10.0	SC,Fn	S/NW
	2330-0530*	5.39	40.4	$\dot{\nabla}$	ENE/9.7	≡,Fn	S/N
	July 31, 0530-0800	5.49	15.5	$\dot{\nabla}$	ESE/10.3	Fn,Sc	S/N
	0800-0830	6.21	3.2	$\dot{\nabla}$	ESE/11.3	Fn,Sc	S/NNE
	0830-1130	8.25	1.2	$\dot{\nabla}$	SSE/11.7	Fn,Sc	S/NE
	1130-1610	5.48	6.6	$\dot{\nabla}$	SE/9.0	Cu,Ac	S/NE
	1610-1640	4.97	12.7	$\dot{\nabla}$	SE/6.3	Cu,Ac	S/NE
4	Aug.1, 0725-0750	4.97	2.9	$\dot{\nabla}$	SSW/3.7	Ns,Fn	SW/NW
	0750-0810	4.91	2.5	$\dot{\nabla}$/:	SSW/3.7	Ns,Fn	SW/NE
	0810-0830	4.69	2.5	$\dot{\nabla}$/:	SW/2.7	Ns,Fn	SW/NE
	0830-0900	4.70	3.0	$\dot{\nabla}$/:	SW/2.7	Ns,Fn	SW/NE
	0900-0930	4.45	2.0	$\dot{\nabla}$/:	SW/2.7	Ns,Fn	SW/NE
	0930-1000	5.78	5.9	$\dot{\nabla}$/:	SSW/2.0	Ns,Fn	SW/NE
	1000-1030	4.80	3.6	$\dot{\nabla}$/:	SSW/2.0	Ns,Fn	SW/NE
	1030-1100	4.67	2.7	$\dot{\nabla}$/:	S/1.7	Ns,Fn	SW/NE
	1100-1200	4.61	2.3	$\dot{\nabla}$/:	SE/2.3	Ns,Fn	SW/NE
5	Aug.20, 1050-1900	5.80	37.1	$\dot{\nabla}$	WNW/10.0	Sc,Ac	E/W
	1900-2030	5.93	6.7	$\dot{\nabla}$	WNW/13.0	Fn,Ns	E/W
	2030-2100	5.83	5.2	$\dot{\nabla}$	WNW/13.0	Fn,Ns	E/SW
	2100-2200	5.80	8.3	$\dot{\nabla}$	WNW/8.0	Fn,Ns	E/SW
	2200-2240	5.77	5.4	$\dot{\nabla}$	WNW/5.7	Fn,Ns	E/SW
	2240-0800	5.74	16.7	$\dot{\nabla}$	WNW/7.3	Fn,Ns	E/SW
6	Sept.8, 0800-1550	5.69	32.3	$\dot{\nabla}$	NNE/11.0	Sc,Fn	NNW/E
	1550-1650	4.85	12.5	$\dot{\nabla}$	WNW/6.0	Sc,Fn	NW/E
	1650-1730	5.20	10.9	$\dot{\nabla}$	WNW/9.0	Sc,Fn	NW/E
	1730-1830	5.15	2.9	$\dot{\nabla}$	SE/10.7	SC,Fn	NW/E
	1830-2300	5.70	7.7	$\dot{\nabla}$	SSE/7.7	Sc,Cu	NNW/SE
	2300-0940+	5.55	29.3	$\dot{\nabla}$	SSE/6.7	Sc,Cu	NE/SW
	Sept.9, 0940-1120	4.92	5.2	$\dot{\nabla}$	SSE/5.3	Sc,Cu	NE/SW
	1120-2100	4.82	10.6	$\dot{\nabla}$	S/11.3	Sc,Cu	NE/SW
	2100-0830++	4.92	11.8	$\dot{\nabla}$	SSW/8.7	Sc,Cu	NE/SW

Notes: the same as notes in Table 1.* July 31,0530;+ Sept.9,0940; ++ Sept.10,0830.

Fig 7. Radar echo maps on August 20-21, 1990

3.3. Composition of Subsample Rain

Table 4 presents volume-weighted concentrations of anion and cation ions and pH in three type of rain.The calculated Cl^-/Na^+ ratios of 1.24 and 1.06 on an equivalent basis in our mold rain and typhoon rain respectively are close to the Cl^-/Na^+ ratio of 1.16, the accepted seawater value [Lebowitz and de Pana, 1985]. Seawater spray dominates the concentrations of Cl^- and Na^+ at coastal sites.But the calculated average Cl^-/Na^+ ratio of 2.23 in spring rain which is larger than 1.16 suggests that spring rain in Xiamen wasn't influenced by sea water spray at coastal site, and this is consistent with their precipitation cloud moving from west e.g. the south Chinese mainland (See table 1). Figure 8 shows that the concentrations of SO_4^{2-} didnn't decrease continuouslly but fluctuated during rain progression, and the pH and other ion concentration have the same fluctuation in sequential samples of rain . Result of table 1,2 and 4, and Fig.8 suggest that precipitation cloud of spring rain, mold rain and typhoon rain which moved from south Chinese mainland were already acidic itself, and that the rainwater acidification in Xiamen Island was mainly caused by long-transport of pollutants from south Chinese mainland, and not by local pollution source.

ble 4. Volume-weighted concentrations of ions and pH in Xiamen (ueq/l)

	pH	F^-	Cl^-	NO_3^-	SO_4^{2-}	Na^+	NH_4^+	K^+	Ca^{2+}	Mg^{2+}
ring rain	4.43	4.40	14.45	13.90	60.65	6.48	49.52	4.98	23.72	3.67
ld rain	4.72	9.83	12.10	4.59	55.90	9.75	21.15	2.79	8.75	2.16
phoon rain	5.13	8.61	25.42	3.59	39.41	23.9	13.19	2.80	22.18	9.40

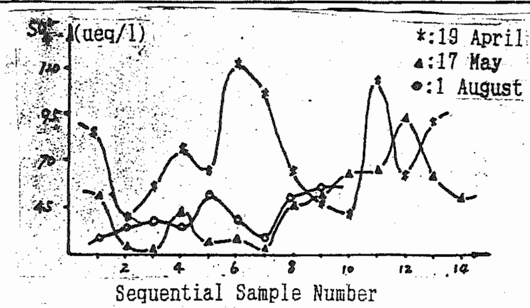

Fig 8. The change of SO concentrations in sequential samples with sampling time in three rain

3.4. Multivariate regression analysis

To investigate the relationship between pH and inorganic ion contents in every type of rain , multivariate progressive regression mold(MPRM) was used.The following regression equation can be gotten for 31 sequential springrain samples within 90% confidence limit by MPRM (n=31):

$$[H^+]=6.199+3.394[NO_3^-]+0.765[SO_4^{2-}]+1.540[Na^+] -0.870[NH_4^+] -7.533[Mg^{2+}],\ r=0.948 \quad (1)$$

For 33 sequential mold rain samples, SO and NH were first chosed and then Cl^- and F^- in MPRM analysis.The following regression equation can be gotten within 85% confidence limit by MPRM (n=33):

$$[H\ ]=18.069+0.526[F^-]+0.665[Cl^-]+0.779[SO_4^{2-}] -0.561[NH_4^+] -2.386[K^+],\ r=0.863 \quad (2)$$

For 43 sequential typhoon rain samples, SO_4^{2-} and Ca^{2+} were first choosed and then F^- and NO_3^-. The following regression equation can be gotten within the 90% confidence limit by MPRM (n=43):

$$[H^+]=2.147-0.215[F^-]+0.289[NO_3^-]+0.362[SO_4^{2-}] -0.261[Ca^{2+}] \quad r=0.806 \quad (3)$$

Equation 1,2 and 3 show that the main ions which influence the pH of spring rain , mold rain and typhoon rain were different. But SO_4^{2-} was the same inluencing ion of their pH.

4. Conclusion

The following conlusions are drawn from this study:

(1) the acidity of rain in Xiamen Island was strongly correlated with the coming direction of precipitation cloud . Maritime rainwater caused by precipitation cloud from east and south ocean were not acidic, with pH values near 5.70 , but rainfall from west, northwest and southwest were acidic, especially from southwest. The major influencing ionsof Spring, mold and typhoon rain were different, but SO_4^{2-} was the same influencing ion.

(2) The pH of sequential sample of rain didn't decrease continuously with sampling time but fluctuated. This was caused by different cloud band, the acid rain in Xiamen associated with the coming direction of precipitation cloud suggest that acid rain in Xiamen may be caused by long-transport of pollutant from southern Chinese mainland.

(3) Sequentially sampling of rain water revealed much composition variation within storms,which can not be determined using event or weekly data, and precipitation clouds were observed by radar and satellite . We think this method is useful in studying acid precipitation.

Acknowledgment:Thiswork was supported by Xiamen Municipal Science Commission.The authors would like to thank Prof. Tang Xiaoyan and Prof. Bi Mutian of Peking University and also thank Mr.Wu Zilin, Mr. Lin Hangzhon and Mr. Gao Chentie of Xiamen EPA

REFERENCE

Gorman E. 1961, Factor influencing supply of major ions to inlandwaters with special reference to the atmosphere. Geol.Soc.Am.Bull. 72,795-840.

Galloway J.N, Liken G.E, Keene W.C and J.M. Miller, 1988 The composition of precipitation in remote areas of the world. J.Geophy.Res., 87,8771-8786.

Lebowitz L. G. and de Pana R. G. 1985. Chloride and Sodium content in Northeast United States Precipitation. J. Geophys. Res., 90, 8149-8154

Houze R.A.Jr.and P.V. Hobbs. 1982. Organization and structure of precipitation cloud systems. Adv. Geophys., 24.225-315.

Raynor G.S. and J. V. Hayes, 1982, Variation in chemical wet deposition with meteorological conditions.Atmospheric Environment. 16,1647-1656.

Yu S.,Bi M., Li X.,Yao R.,and X. Tang, 1991. Organic acids in precipitation from Baiyun Mountain, Guanzhou and in cloudwater from Miaoer Mountain, Guangxi. Acta Scientiae Circumstantiae. 11(1), 25-30.

Yu S. Cai X. and X. Cheng ,1990, Initial study about cause of oceanic acid rain in Xiamen Island. Atmospheric Environment. 5(4),43-44 (in China)

Zhao D.,Xiong J., Xu Y.and W.H. Chan, 1988 Acid rain in southwestern China. Atmospheric Environment. 22,349-358.

A RADAR-BASED MICROPHYSICAL STUDY OF TROPICAL SQUALL LINES

Charlotte A. DeMott and Steven A. Rutledge

Department of Atmospheric Science
Colorado State University, Fort Collins, Colorado 80523

1. INTRODUCTION

The occurrence of squall lines has been observed over every populated continent as well as over the oceans. The importance of these storms to annual rainfall budgets and their potential for disaster has lead to many studies concerning their development and behavior. Most of these studies have taken place on the North American continent, where many types of observing systems (i.e., radars, sounding networks, raingauges, etc.) are already in place and others are easily assembled. In tropical latitudes, squall lines and associated cloud clusters have receieved attention because of their vital role in the atmosphere's global circulation. Detailed observations of tropical squall lines, and tropical precipitating systems in general, are not as numerous as in the mid-latitudes primarily due to the scarcity of observing stations and the difficulties involved in assembling observing systems over large tracts of unpopulated land and open ocean.

The Tropical Rainfall Measuring Mission (TRMM) has proposed the launch of a satellite to map tropical rainfall amounts and distributions. Data collected from this effort may then be used to infer large-scale heating rates in the tropics. The TRMM satellite will be equipped with a variety of active and passive sensors, the data from which will be used to compute rainfall amounts from a variety of retrieval algorithms. As with any remote sensing method, some sort of ground truth is necessary for comparison of retrieval results. TRMM has therefore selected several validation sites for which extensive ground-based analysis of the precipitating systems particular to that area will be made. One of the chosen validation sites is Darwin, Australia, which was also the setting for the Down UNder Doppler and Electricity Experiment (DUNDEE).

Since many of the rainfall retrieval algorithms are sensitive to hydrometeor type and distribution, this study will focus on some preliminary analyses related to this topic. Although this is only a preliminary analysis, such information is important to the development and validation of TRMM rain retrieval algorithms.

2. THE DUNDEE DATA SET

The DUNDEE was conducted in and around Darwin, Australia during the rainy summer seasons of 1988-1989 and 1989-1990. The primary observing systems consisted of the MIT and NOAA TOGA 5 cm Doppler radars, a lightning detection network, a NOAA 50 MHz profiler, rawinsondes, and a surface mesonetwork (Rutledge *et al.*, 1992). The DUNDEE observing network is shown in Figure 1.

During the summer months, the Darwin area is subject to two primary circulation regimes. The first, called the "break period" is characterized by deep easterly flow, high values of convective available potential energy (CAPE), a northwesterly component of storm movement, and strong convection. The second regime, the "monsoon", is associated with westerly flow up to 850 mb, low CAPE, generally southeasterly movement, and less vigorous and shallower convection compared to the break period. Both of these regimes produce squall lines consisting of regions of convective and stratiform precipitation.

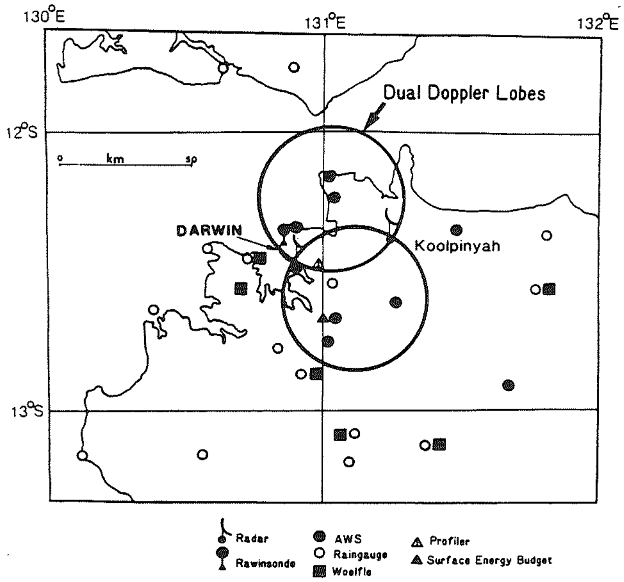

Figure 1. Location of observing facilities used in DUNDEE (from Rutledge, *et al.*, 1992).

In this study stratiform regions from one monsoon (12 January 1990) and two break period systems (5 December 1989 and 22 January 1990) are analyzed. Vertical profiles of radar reflectivity and hydrometeor fallspeed obtained using the Extended Velocity Azimuth Display (EVAD) technique (Matejka and Srivastava, 1991) are used to infer properties of stratiform microphysics. Variations in the inferred microphysical properties and a dual-Doppler analysis of one storm are presented to address the question of steadiness in the wind fields in the stratiform region.

3. RESULTS

The EVAD technique estimates hydrometeor fallspeeds averaged over a 30 km (radius) cylindrical volume centered on the radar. In stratiform regions vertical air motions are typically less than particle fallspeeds, so hydrometeor terminal velocities are initially set equal to the vertical component of motion detected by the radar. The vertical motion field, which is estimated from the convergence/divergence profile, is then used to adjust the terminal velocity estimates. The average radar reflectivity in a cylinder is also a product of the EVAD analysis.

Figures 2 through 4 present profiles of radar reflectivity and hydrometeor terminal fallspeed at several times for each squall line. For reference, CAPE values on 12JAN90, 5DEC89, and 22JAN90 were 400, 750, and 1000 J/kg, respectively. There are several similarities common to each storm. Each case exhibited a well defined radar bright band located at approximately 5 km. Above this level, reflectivities decreased from an average of 20 dBZ to less than 10 dBZ at the upper levels of the cloud deck. This is a feature common to stratiform regions and it has been suggested (i.e., Leary and Houze, 1979) that aggregation and riming of falling

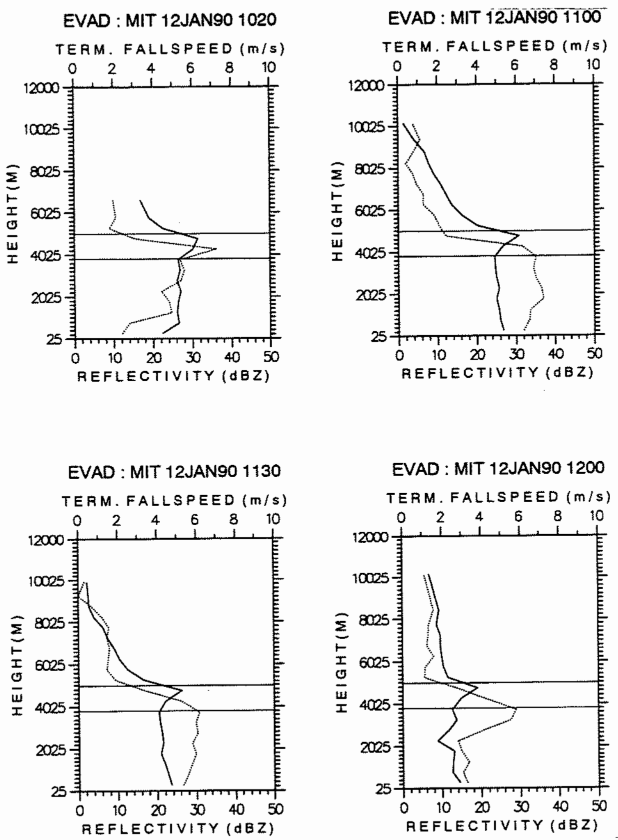

Figure 2. Reflectivity (heavy solid line) and particle terminal velocity (dotted line) as determined using the EVAD technique on 12JAN90. Top thin horizonal line is the freezing level, bottom horizontal line is subjectively determined base of the radar bright band. All times are UTC.

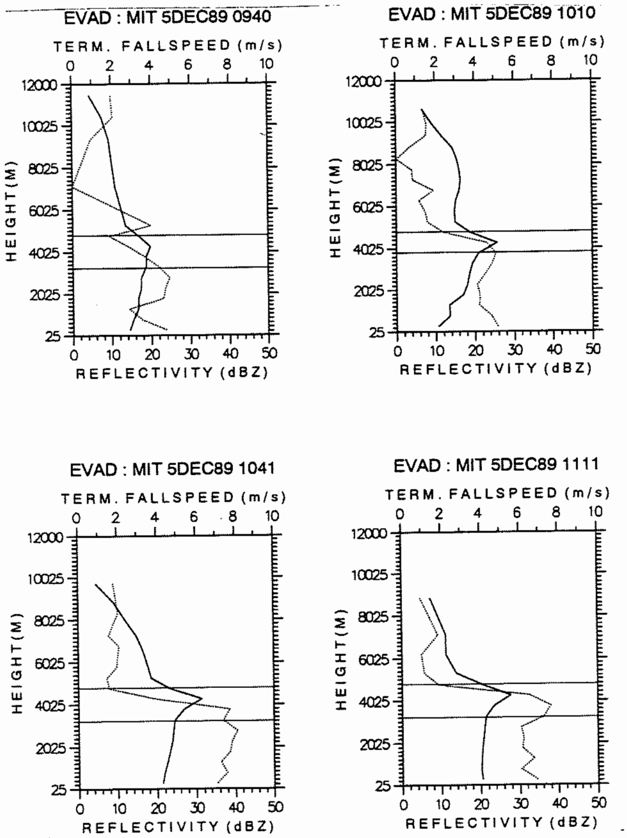

Figure 3. As in Fig. 2, but for 5DEC89.

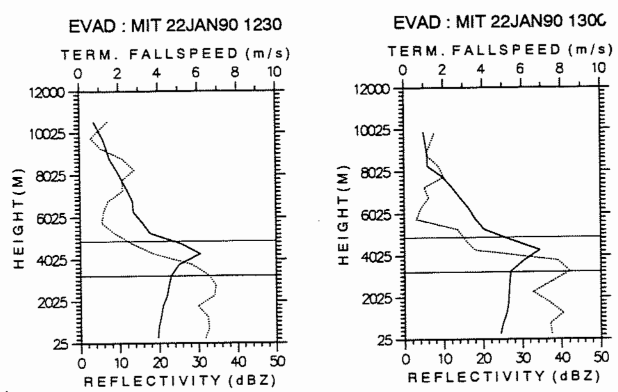

Figure 4. As in Fig. 2, but for 22JAN90.

ice crystals are responsible for the enhanced reflectivity values just above the melting layer. As these ice crystals descend below the melting level, they convert to water-coated ice and raindrops. Complete melting normally occurs within a few hundred meters of the 0°C level. As the melting ice particles collapse to drops, their densities increase and praticle drag decreases, resulting in greater fallspeeds, as is observed in the EVAD velocity profiles. Finally, below the bright band reflectivities decrease as 1) fully melted raindrops assume smaller oblate spheroidal shapes, 2) the concentration of hydrometeors per unit volume decreases as terminal fallspeeds increase, and 3) drops evaporate in the drier subcloud air.

In addition to these general similarities of the EVAD profiles, there are features unique to each storm type. One such difference is the depth of the bright band. The subjective analysis technique described in Leary and Houze (1979) was used to determine the depth of the bright band for each storm system. The height of the 0°C line (shown in Figures 2-4) in each case is within 200 m of 5 km. The subjectively determined bottom of the bright band is also shown. For each case, the height of the base of the bright band is nearly constant, except for the earlier time periods of the 5DEC89 case. Of the three cases studied, this case exhibited the most variability in its reflectivity and fallspeed profiles. Analysis of profiler- and EVAD-derived vertical air motions (Cifelli and Rutledge, 1992, this preprint volume) reveal that vertical air velocities in the stratiform region of this storm also experienced large variations in both sign and magnitude Generally, however, it should be noted that the base of the bright band in the 12JAN90 case extends down to approximately 3825 m, while those in the two break period cases generally extend down to 3225 m. This difference results in a bright band depth of 1.2 km for the monsoon case and 1.6 km for the break period cases.

Willis and Heymsfield (1989) studied microphysical data collected with an aircraft in a midlatitude MCS bright band. Their observations indicated that, while most ice particles melt within a few hundred meters of 0°C, a few large, and not completely melted, aggregates were observed well below this level. These authors attribute the existence of the radar bright band at depths well below 0°C to the presence of these few unmelted aggregates. From these observations and the observed greater depth of the bright band in the break period storms, it is reasonable to conclude that break period storms are producing larger aggregates above the melting layer than are being produced in the monsoon case. Some possible explanations for this behavior will now be presented.

Since aggregation of ice crystals requires crystals of varying sizes, any process that broadens the crystal size distribution should enhance aggregation. Stratiform vertical motions presented in Cifelli and Rutledge (1992, this preprint volume) show that the break period cases have stronger

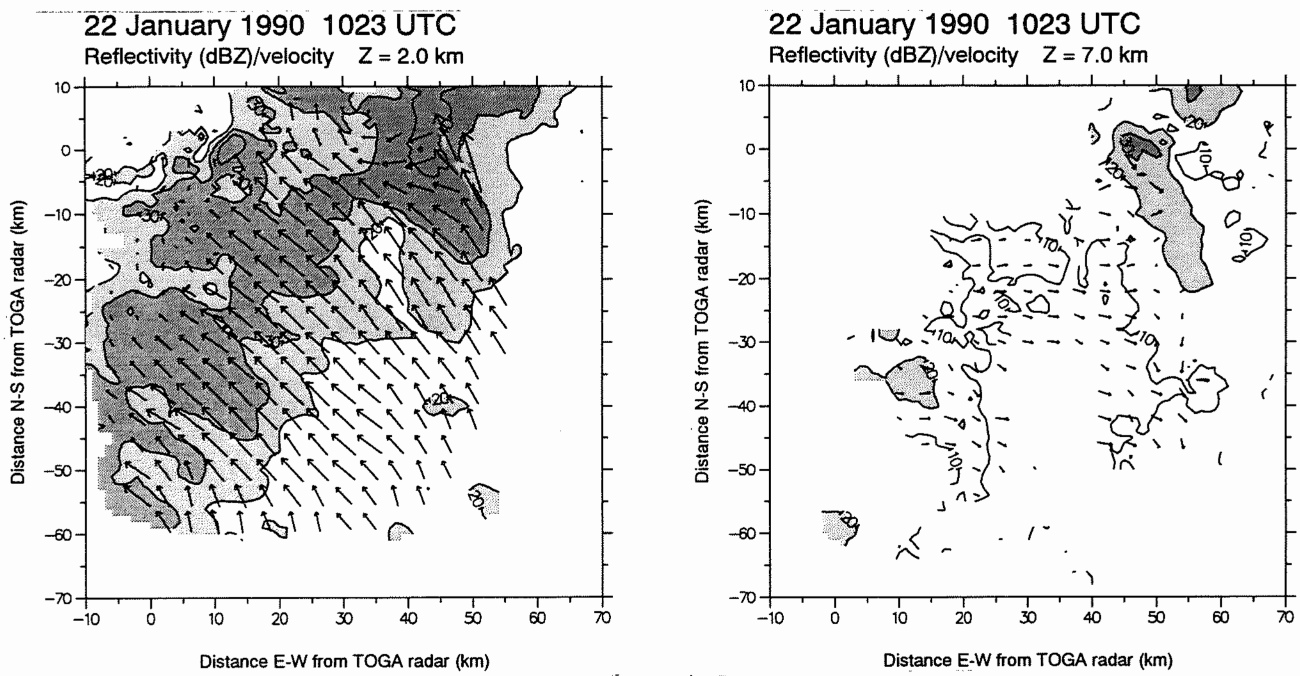

Figure 5. Radar reflectivity and dual-Doppler derived winds speeds at 1023 UTC at 2.0 km (left panel) and 7.0 km (right panel). Reflectivities ≥20 dBZ (light shading) and ≥30 dBZ (dark shading) are shown.

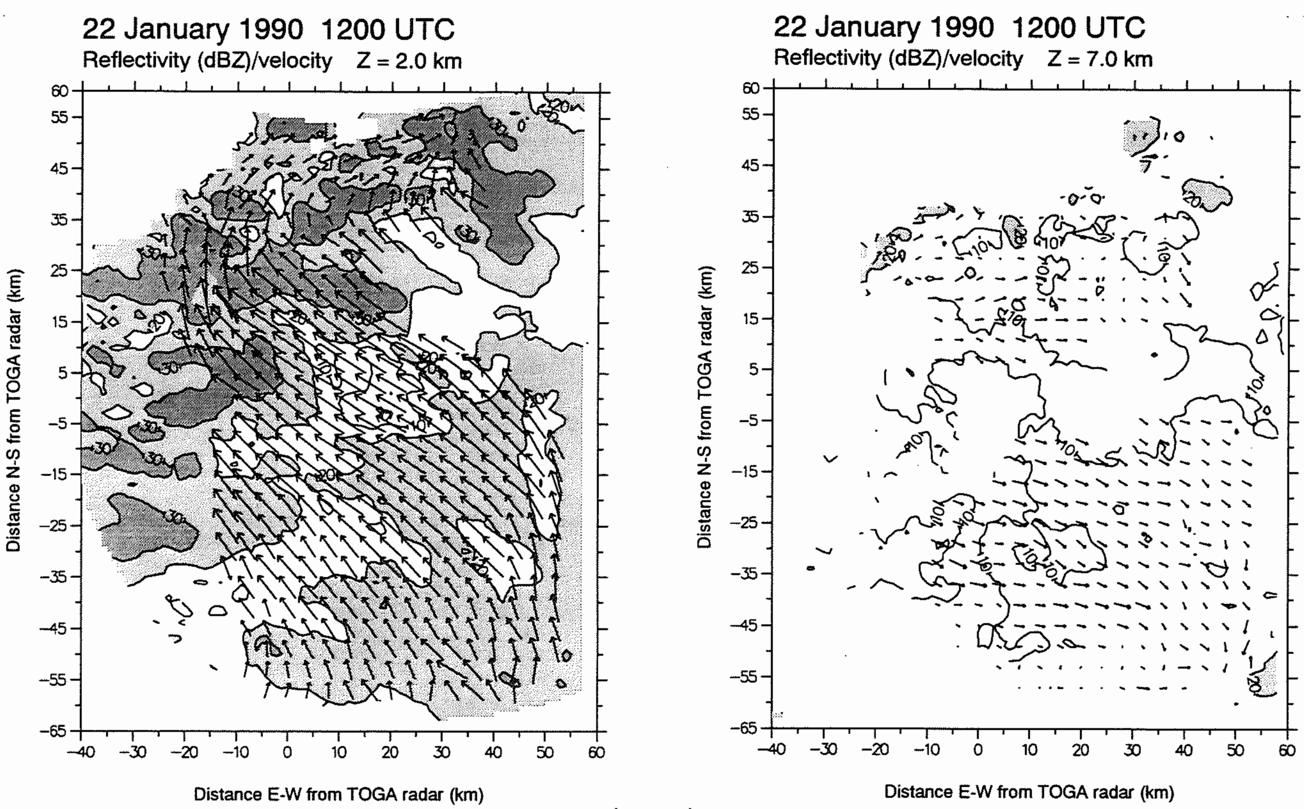

Figure 6. As in Fig. 5, but for 1200 UTC.

mesoscale ascents above the the melting layer than are observed in the monsoon case. This greater vertical velocity should promote greater depositional growth, and therefore larger ice crystals. Furthermore, Petersen (1992) has performed one-dimensional calculations which indicate that the differences in updraft velocity between the two storm types (break period and monsoon) lead to mixed phase microphysical processes in the break period case above 0°C, with maximum liquid water contents occurring between -5 and -12°C. In these simulations, mixed phase microphysical processes were not predicted in the monsoon case. Not only should the presence of liquid water enhance depositional growth of ice at the expense of water, it would also allow for growth by riming. The greater fallspeeds associated with rimed crystals would allow them to make more collisions with slower moving crystals, thereby enhancing aggregation. Furthermore, Willis and Heymsfield (1989) indicate that collisions between aggregates and liquid water drops is a primary mechanism for developing the large aggregates that are slow to melt once they fall below the melting level.

If the situation described above is accurate, one would expect the size of the ice particles to be reflected in the fallspeeds above the melting layer, with lower fallspeeds found in the monsoon case. Examination of Figures 2-4 reveals that the fallspeeds exhibit a much larger variation with height than the reflectivities and, consequently are of little use in estimating crystal size. However, if a crude approximation of the mean fallspeed above the melting layer is made, it is possible to estimate particle sizes by a power law relationship that relates fallspeed to crystal size. Locatelli and Hobbs (1974) report several such relationships for various types of ice crystals. To use such a relationship, one must first have an idea of what type of ice particle is being observed. Particle types were therefore estimated from the types of ice crystals observed by Houze and Churchill (1984) in the stratiform region of a winter monsoon cloud cluster. These authors observed small graupel particles and larger unclassifiable particles. Using this information and assuming a mean hydrometeor fallspeed of 1 m/s, a mean crystal size of about 1.75 mm is obtained. This diameter is significantly larger than the majority of those observed by Houze and Churchill (1984), who reported that fewer than 10% of the observed hydrometeors had diameters of this size. It is suspected that this discrepancy is a manifestation of the EVAD technique, which, because of the reflectivity weighting, is biased towards larger hydrometeors in the fallspeed calculations (Matejka and Srivastava, 1991).

In spite of this limitation, the reflectivity and fallspeed data are still useful for the purpose of examining temporal variations in the stratiform region. A cursory inspection of the EVAD profiles reveals that the reflectivity and fallspeed profiles vary over both height and time. Such variations may be the result of the natural variability of the stratiform region, or it is possible that decaying convective elements have drifted into the stratiform region. Rasmussen and Rutledge (1992) have noted occurrences of convective elements drifting into the stratiform region of tropical squall lines as the main line begins to tilt over. It is quite possible that the residual updrafts and ice particles from these elements may at times influence the EVAD analyses.

The variations in hydrometeor distribution and fallspeed raise questions concerning the steady state assumptions that have been applied to the stratiform regions of squall lines for 2-D kinematic modeling purposes (i.e., Rutledge, 1986). Clearly, there are variations in the microphysical makeup of these storms occurring on the order of less than an hour. Such variations are important when integration times used to model these systems are on the order of several hours.

To further investigate how well these systems meet the steady-state model assumptions, dual-Doppler analyses of several 22JAN90 storm volumes have been performed. Figures 5 and 6 are CAPPIs of the storm at two levels at 1023 and 1200 UTC. Examining the 2 km CAPPIs at each time reveals that the wind field is essentially perpendicular to the convective line over a large area. At 7 km, the flow is not exactly perpendicularly oriented to the line, but does have a strong line-normal component at both times. At both levels and times, departures from line normal flow are infrequent. Therefore, it appears that, at least to a first approximation, the winds in the stratiform region of this particular storm are nearly two-dimensional and steady state. The implications for 2-D kinematic modeling of these storms based on EVAD and dual-Doppler analyses will be summarized in the next section.

4. CONCLUSIONS

Radar data from three DUNDEE squall lines have been presented. Results from EVAD analysis of these data suggest that the stratiform regions of the two break period squall lines may contain larger ice particles than the monsoon case. Both storm types appear to exhibit considerable temporal variations in stratiform ice particle size and concentration. Dual-Doppler results suggest that horizontal wind fields in at least some of these storms may meet the two-dimensional and steady state assumptions invoked in some modeling applications.

Obviously, the variability observed in ice hydrometeor quantities raises the question of how feasible it may be to simulate characteristics of a given squall line under the above assumptions. Perhaps a better approach to this problem, and one more in line with TRMM goals, is to consider "average" monsoon and break period storms. Since the TRMM satellite will pass over a given area only twice per day and will take one month to make an observation of that area at every hour in a day, the first concern in any ground truth effort should be determining typical, or average, rainfall characteristics. While any given squall line in the DUNDEE area may be subject to drifting convective elements which will alter their microphysical makeup for a period, when averaged over time and over several storms, a representative hydrometeor profile may be obtained. It is precisely these representative hydrometeor distributions and rainfall characteristics that TRMM wishes to determine and are, therefore, begin pursued in our research.

5. ACKNOWLEDGEMENTS

This research was supported by the NASA/TRMM grant NAG-5-1592-S-02.

6. REFERENCES

Cifelli, R., and S. A. Rutledge, 1992: Stratiform vertical motion structure in tropical storms. *Preprints, 11th International Conference on Clouds and Precipitation. Montreal, August 17-21, 1992*, this volume.

Houze, R. A., Jr., and D. D. Churchill, 1984: Microphysical structure of winter monsoon cloud clusters. *J. Atmos. Sci.*, **41**, 3405-3411.

Leary, C. A., and R. A. Houze, Jr., 1979: Melting and evaporation of hydrometeors in precipitation from the anvil clouds of deep tropical convection. *J. Atmos. Sci.*, **36**, 669-679.

Locatelli, J. D., and P. V. Hobbs, 1974: Fall speeds and masses of solid precipitation particles. *J. Geophys. Res.*, **79**, 2185-2197.

Matejka, T., and Srivastava, R. C., 1991: An improved version of the Extended Velocity-Azimuth Dislay analysis of single Doppler radar data. *J. Atmos. and Oceanic Tech.*, **8**, 453-466.

Petersen, W. A., 1992: Cloud to ground lightning in the trailing stratiform regions of tropical MCSs. M.S. Thesis, Colorado State University, Ft. Collins CO 80523, 151 pp.

Rasmussen, E. N., and S. A. Rutledge, 1992: Squall line evolution. Part I: kinematic and reflectivity structure. Submitted *J. Atmos. Sci.*

Rutledge, S. A., 1986: A Diagnostic modeling study of the stratiform region associated with a tropical squall line. *J. Atmos. Sci.*, **43**, 1356-1377.

Rutledge, S. A., and R. A. Houze, 1987: A Diagnostic modeling study of the trailing stratiform region of a midlatitude squall line. *J. Atmos. Sci.*, **44**, 2640-2656.

Rutledge, S. A., E. R. Williams, and T. D. Keenan, 1992: The Down Under Doppler and Electricity Experiment (DUNDEE: overview and preliminary results. *Bull. Amer. Meteor. Soc.*, **73**, 3-16.

Smull, B. F., and R. A. Houze, Jr., 1987: Dual-Doppler radar analysis of a midlatitude squall line with a trailing region of stratiform rain. *J. Atmos. Sci.*, **44**, 2128-2148.

Willis, P. T., and A. J. Heymsfield, 1989: Structure of the melting layer in mesoscale convective system stratiform precipitation. *J. Atmos. Sci.*, **46**, 2008-2025.

THREE-DIMENSIONAL NUMERICAL SIMULATIONS OF EFFECTS OF COLD WATER SURFACE ON EVOLUTION AND PROPAGATION OF HAILSTORMS

Huang Meiyuan   Kong Fanyou   Xu Huaying
(*Institute of Atmospheric Physics, Chinese Academy of Sciences, Beijing 100029, PRC*)

1. INTRODUCTION

Observations found that large water area, such as lake, river, or even large area of rice field, can usually modify the propagation and intensity features of convective hailstorms developing in summer afternoon. These significant modifications of hailstorm activity, attributed to uneven underlying surface properties, arise large difficulties to the nowcasting of local severe weather based on extrapolation of weather radar and satellite images.

In this paper a fully elastic three-dimensional hailstorm numerical model[1] is used to investigate the impacts of semi-unbounded cold water surface on the evolution, propagation, and precipitation or hail shooting features of hailstorms. Special emphasis will be given to variations of propagation path of the simulating storms and their physical reasons.

2. MODEL DESCRIPTION

The model used here is the one developed by the authors (Kong et al. 1990,1991)[1-3]. The dynamic framework of the model is similar to that of Klemp and Wilhelmson(1978)[4], but this model contains more detail bulk-water parameterized microphysics, including not only four warm cloud microphysical processes but also seventeen ice phase processes, so that it can be used to simulate the more realistic storms in the atmosphere. Because it is desirable to include the effects of cold water surface, a parameterized surface layer is contained.

The temperature deficiency of the water surface is assumed constant in time and position. Here in this paper it is 10°C. The model domain is 35km in the both horizontal directions and 18.5km in the vertical, with the grid interval of 1km in the horizontal and 0.5km in the vertical.

3. SIMULATION RESULTS

In order to make the simulations more valid and realistic, an environmental sounding profile taken near an intense, quasi-steady thunderstorm activity which was observed on 19 July 1977 over South Park, Colorado, and presented by Knupp and Cotton(1982)[5] is used in the simulations, though the actual storm took place over a mountain area and without evidence of water surface effects. In this storm environment wind veered from northerly at low level to southerly at mid and upper level, and the convection system as a whole propagated northward.

Three simulation cases are runned. Among them, WC0 is a contrast case since no water surface is included in it. The storm's intensity, penetrating height, and propagation direction are basically consistent with observation result. Other two, WC1 and WC2, are the horizontally uneven cases in which semi-unbounded cold water surfaces with different area and orientation are embedded in the model's lower boundary. In this abstract, however, only the simulation results of WC1 and their comparison with WC0 are briefly presented. For WC1, the initial disturbance center is about 9km away from water area, and the orientation of coast line is characterized by a very small angle with low level ambient wind.

3.1 Change of Storm's Propagation Path

Figure 1 depicts the pathes of maximum mixing ratio of total hydrometeor and the areas of the total mixing ratio greater than 4 g/kg at 2.25km level for the modeling storms of WC1 and WC0. The water area for WC1 case is also shown in the figure. WC1 is simulated for 96min. In WC0, which uses a mono land surface at its lower boundary, the storm at first propagates northward by east, splits apart into two cells after 48min. The right moving cell propagates northeastwards, gradually by east, while the left one turns to northwest. The two cells all keep developing, their intensities and scales increase.

When the cold water surface, shown in Figure 1, is embedded (WC1), the storm's propagation path is significantly modified. It can be seen from Figure 1 that in its early developing stage (before 32 min) the simulating storm in WC1 first turns slightly to the water area, then turns to in parallel with the coast line and moves northwards. Again the storm's hydrometeor field splits apart at about 48 min, starting from low level. Unlike WC0, however, the splitting right branch tends to move along the water-land interface (coast line) though its intense core slightly invades into water surface after 64 min. In addition, its high value area of hydrometeor is smaller. The splitting left cell still propagates northwestwards, but more northerly (after 56 min) and much faster compared to that in WC0.

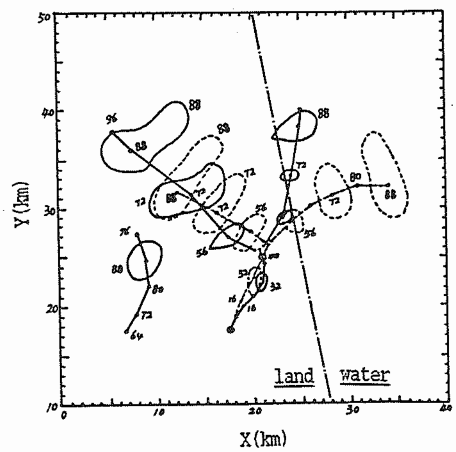

Figure 1. Propagation path of total hydrometeor center and outlines of q_t greater than 4g/kg of simulating storms at 2.25km level. Solid line is for WC1 and dash for WC0, labelled figures represent times in min.

3.2 Evolution and Structure of Simulating Storm

Figure 2 depicts the three-dimensional outlines of WC0 and WC1 storms at 80 min. The two splitting storms in WC0 have comparable hydrometeor fields in intensity and scale. After 80 min the right cell is even more extensive in its mid and lower portion, when a small secondary cell forms behind. In the case with water surface embedded at lower boundary, WC1, however, the horizontal scale and penetrating height of

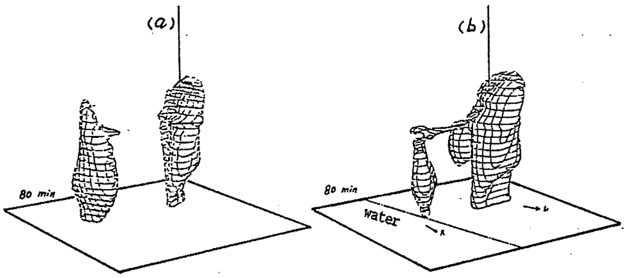

Figure 2. Distribution of total hydrometeor within the modeled storms in WC0(a) and WC1(b), as viewed from the northeast. The contoured surfaces represent the q_t=4g/kg surface, the arrow point out the brief propagation directions of the cells.

the right cell are far smaller than those of the left cell, and weaker than the right one in WC0 as well. On the other hand the left branch is more vigorous than the one in WC0. Another remarkable difference of WC1 with WC0 is that the departure degree of the two splitting storms for WC1 is relatively smaller.

Figure 3 shows the time variations of the maximum updraft speeds of the left and right storms for both cases. It should be noted that, since before 56 min the main storms do not entirely split apart, the curves over 0-56 min in the figure represent variations of the single, unsplitted main storms.It is seen that the hailstorm in WC0 has a some weaker right cell. This phenomenon is coincident with the result presented by Klemp and Wilhelmson (1978)[6] in that a counterclockwise turning ambient wind shear, like that used in this simulation, favors development of the left-moving storm but prohibits the right one. If compared WC1 with WC0, however, it can be found that with water surface effect the right cell in WC1 is further weaker, the maximum updraft speed is only two-thirds of that in WC0; The left cell, in contrast, is more vigorous than that of the case without water surface influence.

Apart from increasing the peak updraft speed of the left cell, the water surface effects lead

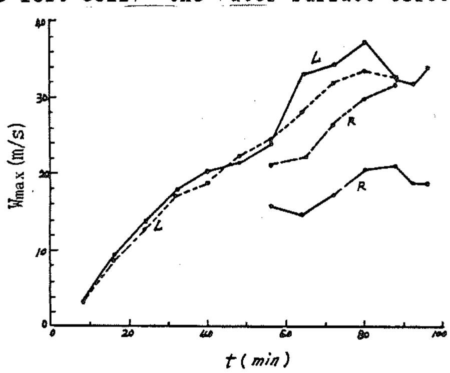

Figure 3. Time variation of the maximum updraft speed for the left cell (labelled with 'L') and right cell (labelled with 'R') in WC1(solid line) and WC0(dash line).

the cloud top to rise and the maximum solid (ice phase) precipitation amount to even increase by about 50%. The peak of the right cell's updraft speed falls down largely, by one thirds, and its liquid and solid precipitations all decrease. Compared to WC0, the WC1's accumulative total precipitation over 88 min period increases 41.5%, mainly attributed to the solid part of left cell (active over land). In other word, one effect of cold water area is to make hailstorms, developing and propagating within near-coast area, to produce much heavier hail shooting. The result is basically coincident with observations.[1]

3.3 Precipitation Distributions

The ground total (liquid plus solid) accumulative precipitation distributions over 88 min period for case WC0 and WC1 are depicted in Figure 4, in which solid precipitation accounts for over 70% of the total amount. It is evident in the figure that the right cell of the case WC1 with water surface effects only produces very small amount of precipitation, mainly distributing along coast area. In contrast, the left cell produces a far more extensive and intensive precipitation area, which even overtake the contrast case, WC0, to a large extent. The left precipitation area extends far northwestwards and spreads out at the northern flank near water area as well.

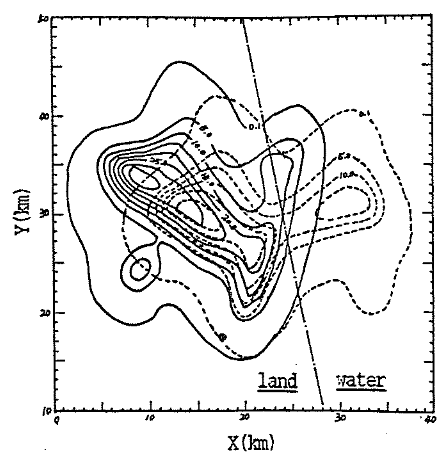

Figure 4. Distribution of accumulative total precipitation during 88 min of simulation time, with contours labelled in mm.The solid and dash lines represent WC1 and WC0, respectively.

REFERENCES

[1] Kong,F.Y.,1991: Three-dimensional numerical simulations of hailstorms, Ph.D dissertation, Institute of Atmospheric Physics, 155p.

[2] Kong, F.Y., M.Y. Huang, and H.Y.Xu, 1990: *Chinese J.Atmos.Sci.*, 14,437-450.

[3] Kong, F.Y., M.Y. Huang, and H.Y. Xu, 1991: *Chinese J.Atmos.Sci.*,15,78-88.

[4] Klemp,J.B., and R.B.Wilhelmson,1978: *J.Atmos. Sci.*,35,1070-1086.

[5] Knupp, K.K., and W.R. Cotton, 1982: *J.Atmos. Sci.*, 39,343-358.

[6] Klemp,J.B., and R.B.Wilhelmson,1978: *J.Atmos. Sci.*,35,1097-1110.

CLIMATOLOGY OF THE PRECIPITATION IN THE LAST 40 YEARS IN THE CHACO-PAMPA REGION

Mirta A. Giachino and José M. Núñez

Servicio Meteorológico Nacional, Buenos Aires, Argentina.

1. INTRODUCTION.

In the works of Hoffmann, 1970 and Krepper et al, 1991, it is possible to see a positive tendency in the depth of the annual precipitations and the displacement of the isohyets to the W.,in the pampa region during the last decades, in particular and with more intensity since the 1950s.

The analysis of the annual, mensual and seasonal of the pampa region rain records, Núñez, 1987, Malaka, 1990, shows that the larger percentage in the annual quantity of rain corresponds to the summer season.

2. REGION CHARACTERISTICS.

The region is a plain with the only exception in the center-south of the Buenos Aires province where two range hills of medium height about 500 mts., extends NW-SE. The geographical position of the meteorological stations and its general data may be to see in the Fig. 1 and Table 1. The first year of the rain records was 1951 and the last one, 1990. The area of the study is 1.607.466 Km², approximately.

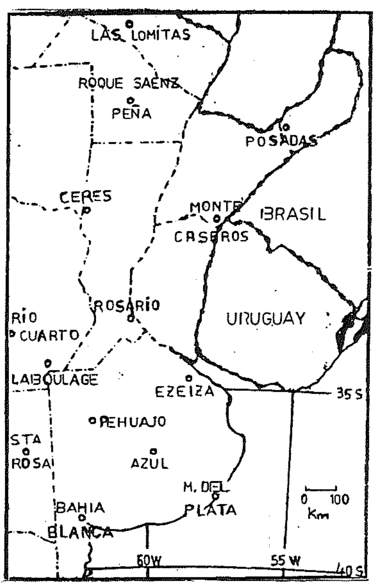

Fig.1. Position of the meteorological stations.

3. ANALYSIS OF THE MATERIAL.

The rain regimen in the pampa region was analysed in Núñez et al, 1986, that it appears as predominant convective. If considerate all the Chaco-Pampa region we note a similar situation.

To show the more relevant rain aspects in the Fig. 2 and Table 1, Syners, 1975, is possible to observe the positive tendency in the aumengtation of the rain, between Ezeiza and Bahía Blanca, and also between Ezeiza and Posadas, but with a gradient feeble. Also the pentadyc moving averages rainforce that behavior. In both extremes of the region the jump of the tendency (negative to positive) was detected, around 1970 year, but not in Ezeiza.

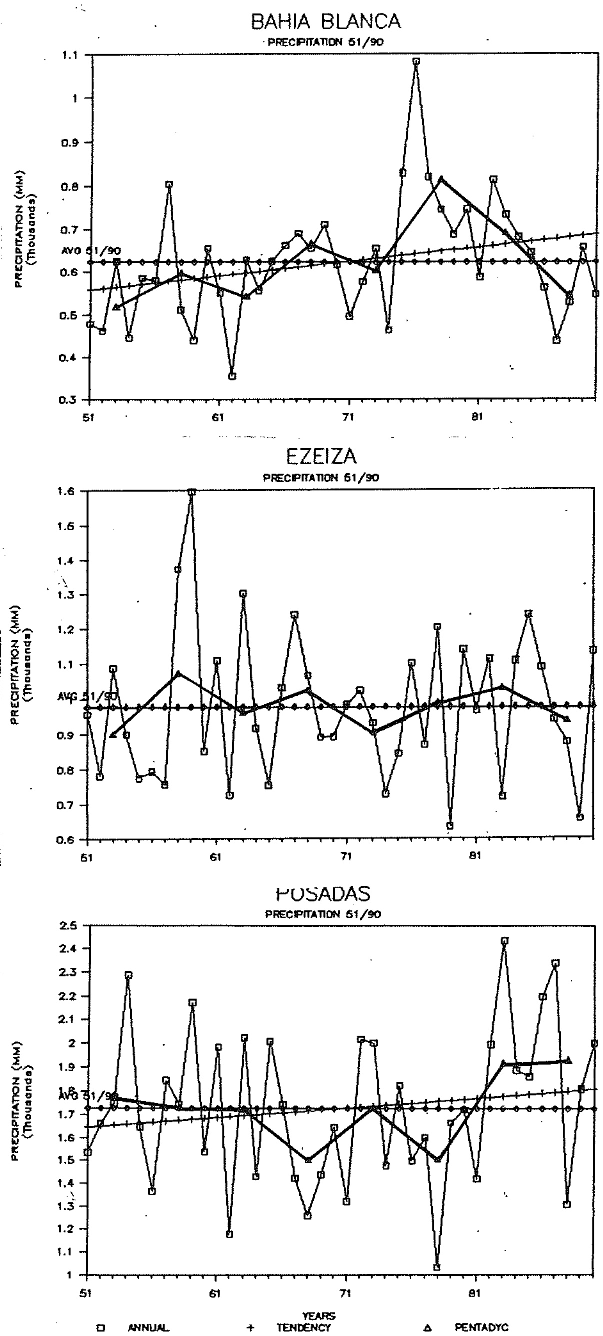

Fig.2. Precipitation annual course in Bahía Blanca, Ezeiza and Posadas corresponding to the period 1951-1990. Smoothing curve at apply pentadyc moving averages (▬), general tendency in the period (—), and annual average for the period 1951/90 (◊).

If we take another baseline, from Posadas, with positive tendency to the South, in Rosario with negative and in Santa Rosa again with a firm positive tendency.

The bar diagram, Fig. 3, indicates the annual distribution of the precipitation, with values above the normal in both extreme points starting from 1980, the inverse occur for Rosario.

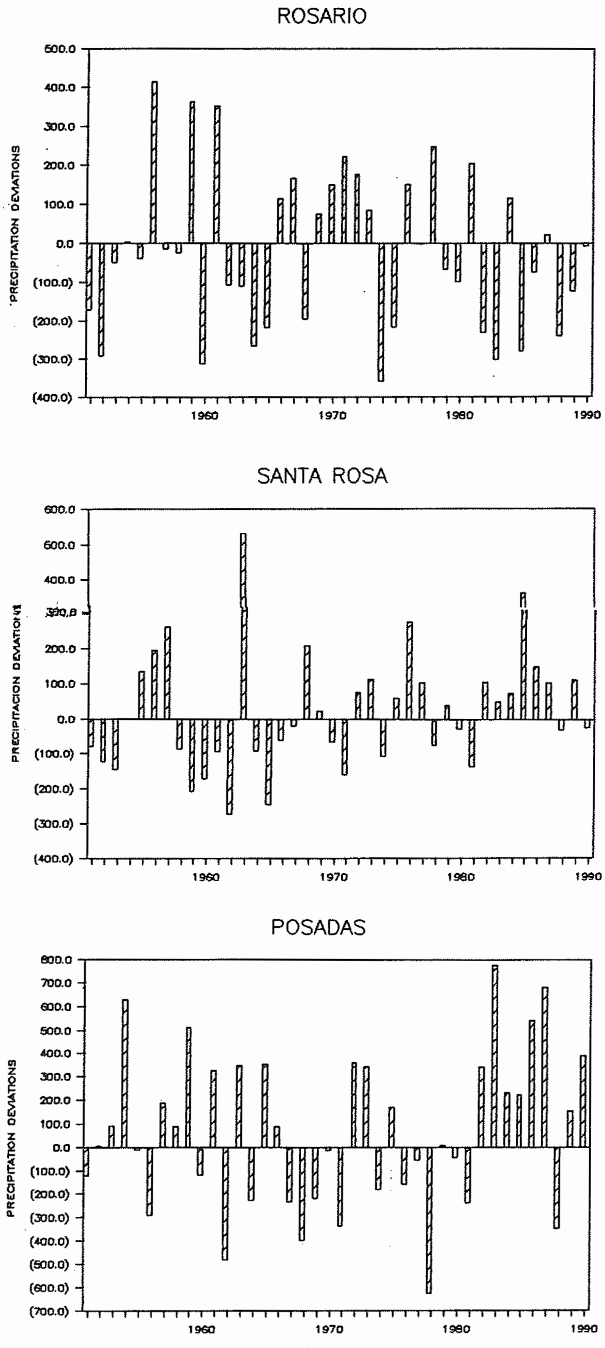

Fig.3. Bar diagram for Posadas, Rosario and Santa Rosa. Precipitation deviation with respect to the normal in the period 1951-1980.

4. CONCLUSIONS.

The analized stations period shows, except for two in the central part of the region, that for the 40 years period 1951-1990, a positive tendency for the increase of the annual precipitation.

The jump in the average is to note that begin positive in the year 1970 and more clearly starting from 1980 in the extreme parts of the region and negative in its middle part. A more detailled analysis in the trend of the mean (annual), suggest changes positive to negative and viceversa in all the stations with periods between 3 to 16 years with more duration of the positive quantities above the normal.

Table 1

Name and geographical position of the meteorological stations. mann test, significance level α_o: 0,05.

STATION	φ(S)	ω(W)	U(n)	U(t)
BAHÍA BLANCA	38°44'	62°10'	2,073	0,049
CERES	29°53'	61°57'	1,074	0,0011
EZEIZA	34°39'	58°32'	-0,534	0,0352
LABOULAGE	34°08'	63°22'	0,742	0,0464
LAS LOMITAS	24°42'	60°35'	0,034	0,0506
PEHUAJO	35°52'	61°54'	0,538	0,0402
POSADAS	27°22'	55°58'	0,56	0,04
RÍO CUARTO	33°07'	64°14'	0,748	0,0469
ROSARIO	32°55'	60°47'	-0,564	0,0427
SANTA ROSA	36°34'	64°16'	2,219	0,040

5. AKNOWLEGMENTS.

We wish to thank for her collaboration to Miss Teresa Ibarzábal, Technical in Climatology.

REFERENCES:

Hoffmann, J.A.J., 1970: Características de las series de precipitación en la República Argentina, Meteorológica, 1, 166-190. Bs.As. Argentina.

Krepper C.M. y Scian B.V., 1991: Climatología de la precipitación en la región pampeana: 1-Variabilidad decádica, tendencias y eventos extremos. Congremet VI., 23-24 Nov. Bs.As. Arg.

Malaka I., 1990; Boletín Climatológico. Vol. II- Nº 2, Febrero, pp. 24-28, SMN.

Núñez J.M. y Malaka I. 1986: Estudio aerológico y de las precipitaciones en la región semiárida de la pampa. I Congreso Interamericano de Met., Brasilia, 20-24 Oct. Brasil.

Núñez, J.M., 1987: Acerca del régimen de las precipitaciones en la región semiárida de la pampa. II Congreso Interamericano de Meteorología, Nov. 30, Dic.4, Bs.As., Argentina.

Snyers, R., 1975: Sur l'analize statistique des séries d'observations. Technical note Nº 143, WMO.

THE APPLICATIONS OF CLOUD AND PRECIPITATION STUDY ON IDNDR

Wang Ang-Sheng, Fan Zhen, Liang Bi-Jun*, Xin Miao-Xin and Yang Yi

Institute of Atmospheric Physics, Academia Sinica, Beijing 100029, China
*The Academy of Posts and Telecommunications Sciences, Beijing, 100083, China

The United Nations has designated the last decade of this century as "International Decade for Natural Disaster Reduction" (IDNDR), calling on every country to take concerted actions to mitigate losses form natural disasters. The call has reflected the strong desire and common will of mankind to fight against natural disasters. The IDNDR will produce significant and profound effect upon the progressive cause of mankind.[1] Cloud and Precipitation Physics, as a science, it will have more important action on IDNDR. As the scientists on this field, we wish ICCP and our colleagues pay more attention on IDNDR.

1. INTRODUCTION

Natural Disaster is the chief common enemy of mankind, and is posing a serious threat and challenge to the people all over the would. Nature has nurtured mankind, on the other hand, natural disaster also restrict the development of human society. Natural disasters have caused mankind casualties and sufferings since ancient times. According to relevant statistics, natural disasters have affected over 800 million people and caused hundreds of billion dollar damages to property in the past 20 years.[1]

The resolution No.169 adopted by 42nd United Nations General Assembly (1987)[2] and the "Resolution of International Decade for Natural Disaster Reduction" and "The International Program of Action of International Decade for Natural Disaster Reduction" adopted by 44th United Nations General Assembly (1989)[3] are important resolution for all countries in our world. As the responsing to the call of the United Nations, about 100 National Committees for IDNDR were established in the world until 1991. China National Committee for INDNR was established in 1989. It consists of 32 Ministries or Departments of our Government. The chairman is Vice-Premier Tian Ji-Yun. During recent years, a volume of INDDR actions was done in all world. Many scientific societies and a lot of scientists engage above works on IDNDR.

Due to closely relationship between Cloud and Precipitation Physics with Natural Disasters, for example heavy rain, flood, drought, typhoon, hail, windstorm, lightning and so on; there are a lot of applications of cloud and precipitation physics on IDNDR. In this paper, authors present the applications in our country, and hope our colleagues pay more attention on IDNDR.

2. ON THE STRATEGY OF DISASTER REDUCTION

China is one of the few countries with frequent natural disasters and serious losses, causing direct economic loss of 50-80 billion Chinese yuan (about 5 RMB yuan=1$) per year due to natural disasters; and 52.5 billion yuan in 1989, 61.6 billion yuan in 1990, over 80 billion yuan in 1991. The strategy of disaster reduction is one of the most important problem on this field.

On the base of above necessary and the relationship closely between cloud physics and natural disasters, some Chinese scientists presented their strategical suggestion. Prof. Wang Ang-Sheng wrote his first suggestion to Chinese Government in 1975 after Henan flood disaster. Since 1975, a lot of strategical studies on disaster reduction was done by Prof. Wang and his colleagues. After 1989, his idea was received by many scientists and Chinese Government. Now, his results were applied on IDNDR in China. Prof. Wang's strategy of serious natural disaster reduction is consists of General strategy, Disaster situation strategy, Information strategy and organization strategy and so on.[4]

One of above important results is that National Centre of Natural Disaster Reduction will be established and we are developing a large disaster reduction system in all China.[4]

3. THE APPLICATION ON HEAVY RAIN DISASTER REDUCTION

Heavy rain and flood is one of

main disasters in China. In 1991, the Heavy rain and flood disaster over Huaihe River and Taihu lake etc. regions. General direct losses were more than 50 billion yuan (TMB). This is the most terrible disaster since 1949. Some studies of this heavy rain disaster were done by our colleagues on cloud physics.

The emergence, development and precipitation etc. processes of heavy rain clouds were analyzed and studied by using radar, satellite, weather map etc. data. Several new phenomena and results were found in larger region and longer time, specially for Mei-rain front in which terrible heavy rain in larger region and longer time was formed usually. For example, some convective clouds in the stratus clouds are useful for heavy rain forming and falling in this region.

At some time, heavy rain disaster reduction was studied by using radar, satellite, rainfall, weather map and other data. A new project of heavy rain disaster reduction was decided just now after 1991 heavy rain and flood disaster. One system of heavy rain disaster reduction is establishing in China. Many studying works on cloud and precipitation physics will be applied in these project and system in our country.[5]

4. ENHANCEMENT RAINFALL FOR DROUGHT DISASTER REDUCTION

Today, although people can't directly prevent serious natural disaster, then disaster reduction is possible. In all disaster reductions, weather modification is an initiative disaster reduction. Enhancement rainfall is an important method for drought disaster reduction.

It is well known that the drought is a main disaster in China. The losses of drought in our country are more than 10 billion RMB yuan/year. Due to enhancement rainfall can reduce local drought disaster, since 1958 it is applied widely in China by using aircraft or rocket or gun. A lot of research works on cloud and precipitation was done for enhancement rainfll during recent ten years. Those basic studies on cloud physics are useful for artificial rainfall very much.

For example, a volume of aircraft observations by using of FSSP -100, 2D-C and 2D-P etc were done in China during recent 10 years. Some research results presented droplet or ice crystal concentration, temperature, average or peak value of LWC, Cloud condensation nucleus concentration and aerosol particle number concentration etc. data in northern part of China. Chinese scientists used these data and their studies to direct Chinese artificial rainfall and obtained several successes on this field.[6] Some results of enhancement rainfall show that 5-20% rainfall were increased.

5. HAIL SUPPRESSION FOR HAIL DISASTER REDUCTION

The same as enhancement rainfall, hail suppression is an important method for hail disaster reduction in China. Because of hail damage is a serious natural disaster, the losses of hail damage are about 2-3 billion RMB yuan/year, So hail suppression are widely applied in China during last 30 years.[7]

A volume of research result on hailstorm or hailstone etc. was done by Chinese scientists on cloud physics. Those basic studies presented the characteristics and life cycle of hail storm, the merging of cells and the formation of hailcloud, five kinds of Chinese hailstorms, lightning feature of hailstorm or thunderstorm, numerical simulation of hailstorm, the microphysical characteristics of hailstone, four kinds of ice crystals and air bubbles in hailstone and so on.

Some research results on hailcloud physics are applied in hail suppression. For example, the identification of hail cloud with radar and lightning data was applied widely in northern part of China from 1972 until today; the observations by using different kinds of radars are a main method on hail suppression, and obtain the best successes. The better result of hail suppression was reduced 60% hail damage over 2,000 km , according to statistical result during about 10 years.[7]

6. THE APPLICATION ON TYPHOON DISASTER REDUCTION

One of the early experiments on weather modification was typhoon disaster reduction in 1947. A lot of dry ice was seeded in typhoon clouds and hope to reduce typhoon disaster. In 60s, some experimentS on typhoon disaster reduction were done in U.S.A., although their results were not successful.[8] This work is very important, so scientists engaged much more works in this field.

Although artificial reducing typhoon is difficult, the studies of the formation, development and weakness of typhoon cloud system are very important and useful. A lot of observational data by using different kinds of radars, satellites, ships and aircrafts provided good research conditions for cloud and precipitation physics on typhoon. It is well known that typhoon is one of main disasters in China, a lot of studies of typhoon cloud and its physical process etc. was done by Chinese scientists. The characteristics and developments of typhoon cloud system were applied in forecast, warning and disaster reduction etc. by using of radar, satellite or other data. Since 1991, one project of typhoon disaster reduction in China was done, it will be useful for reducing typhoon disaster in near future.

7. THE APPLICATION ON SEVERE CONVECTVE STORM DISASTER REDUCTION

Severe convective storms cause serious disaster in local region, for example, the tornado, lightning, thunder, local heavy rain and great wind etc. When environmental condition is very dry, severe lightning usually causes forest fire. In 1987, the forest fire of North-Eastern region of our country was caused by frequently lightnings and very dry environment etc. Some local heavy rain are main cause of landslides and mud-rock flows in China, severe convective storm causes several local serious disaster.[9]

The application of cloud and precipitation physics on severe convective storm disaster reduction is widely. Due to a volume of cloud physics observations by using radar, aircraft, satellite, lightning and other instruments, the laws and mechanisms of severe storms, several methods of forecast, warning and disaster reduction were presented. For example, Nowcasting systems which was used to warning severe convective storm are established in Beijing, Shanghai, Wuhan and Guangzhou etc. cities. They are very useful for severe storm disaster reduction in China.

As mentioned above, we can see that, a lot of research results on cloud and precipitation physics were applied in natural disaster reduction and IDNDR. At same time, the development of natural disaster reduciton and IDNDR prometes the research works on cloud and precipitation physics. So, we suggest that ICCP and our colleagues pay more attention on IDNDR.

REFERENCES

[1] Tian Ji-Yun, 1991: Act to carry out Activities of Decade for Natural Disaster Reduction in China. Natural Disaster Reduction in China. Vol.1.No.1 P3-5.

[2] The resolution No.169 adopted by 42nd United Nations General Assembly, 1987. Disaster Reduction in China (Chinese). Vol.1.No.1 P11-12.

[3] The International Program of Action of International Decade for Natural Disaster Reduciton, 1989. Disaster Reduction in China (Chinese). Vol.1.No.1 P12-14.

[4] Wang Ang-Sheng, 1991: A brief discussion on the strategy of serious natural disaster reduction. Natural Disaster Reduction in China. Vol.1.No.2 P12-15.

[5] Sun Guang-Zhong, Wang Ang-Sheng and Zhang Pei-Yuan, 1990: Natural Disaster in China, P1-280, Academic Book and Periodical Press, Beijing.

[6] Wang Ang-Sheng and Huang Mei-Yuan, 1990: The studie of drought, development of air water resources and artificial rainfall. Advances in Earth Sciences, 1990.No.3.

[7] Huang Mei-Yuan and Wang Ang-Sheng, 1980: The Introduction of Hail Suppression. Scientific Press, Beijing, P1-280.

[8] W.N.Hess, 1974: Wearther and Climate Modification. John Wiley & Sons,Inc., P1-584

[9] Wang Ang-Sheng, Ruan Zhong-Jia, 1986: The cloud and Rain on the Earth. Meteorological Press, Beijing, PI-264.

APPARATUS, TECHNIQUE AND RESULTS OF GROUND STUDIES OF HAILSTONE PHYSICAL CHARACTERISTICS

M.I.Tlisov, A.A.Zagidulin, B.M.Khuchunaev, L.M.Fedchenko

High-Mountain Geophysical Institute, Nalchik, 360030, RUSSIA

The ground investigations of hail show that physical characteristics of hail experience sufficient space-time changes. To study the hailfall characteristics in detail it is neccessary to measure and to sample the hailstones in many points of hail streaks during the falling out of hail. For this purpose in t the framework of Complex Hail Experiment the hail network was situated in the research polygon with total area of 3.5 $x10^3 m^2$. There were 13 automatic hail samplers, 6 special hail recorders, 600 hailpads and 40 pluviographs (Fig.1).

fall beginning, running time and date.

Hail recorders provided for the registration of the amount and energy distribution of hailstone in real time. Registration method consisted in the characteristics detection of electric pulses from each hailstone with subsequent classification on 10 levels in accordance with kinetic energy from $2x10^{-3}$ to $2x10^{1}$ J of falling hail with size from 0.5 to 5.0 cm.

The hail recorder registrates the hail flow over the sixteen 2-min intervals and provides for the memory of hail amount, date, running time, the be-

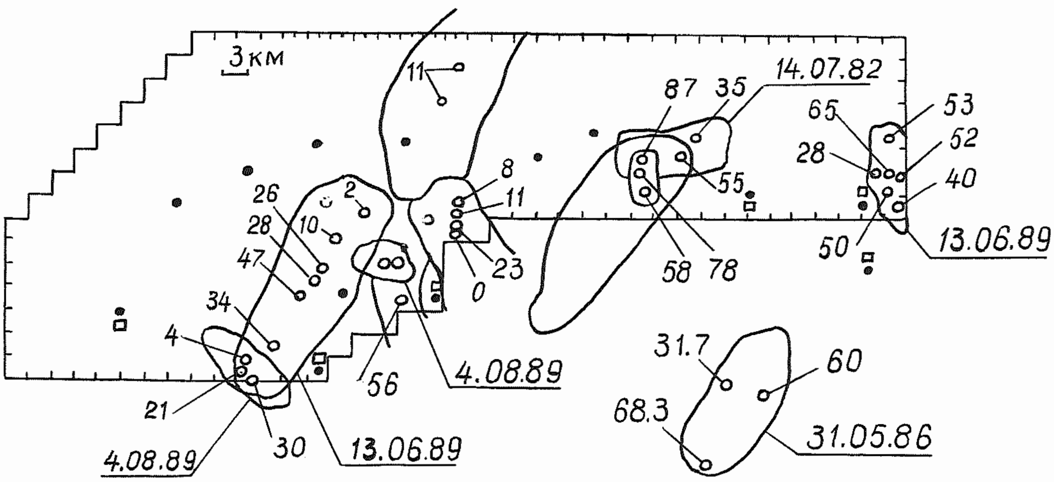

Fig.1 Hail network; • - hail samplers, ▫ - Hail recorders, 53- drop embryo part.

Hail samplers ensure the identification of solid and wet precipitation in real time, the accumulation and conservation of hail in cooled volumes, the detection of physical characteristics and the physical-chemical analysis of hailstones.

The hail samplers containe the hopper with receiving surface area of 0.1m², where there is a plate directing the rain-hail flow into the switch-on unit representing the balance, one beam of which is the string tautened on the frame, and the other is the counterpoise with the connection to the program block and cooling thermal chamber for collection, time sharing and conservation of hail in 5 samplers with total volume of 6 l.

The program block during 1.5-3 min provides for the hail distribution into 5 samplers and the recording of hail-

ginning of hailfall, the number of time interval of distribution and energetic level.

The hail recorder includes the sensor rack, electron block and control panel which are connected electrically. The sensor rack includes 6 cylindrical receivers forming the receiving surface with area of 0.1 m². At the base of the receivers there are the piezoceramic elements. Electron block containes the MC-0513 computor and analog-digital converter.

The density of hailpads on the area of $2.5x10^3 km^2$ was one hailpad per 10 km² and on the area of $9x10^2 km^2$ was one hailpad per 2.5 km².

From 1983 till 1989 72 hailfalls were registrated by our hail network. The main characteristics of these hailstorms are given in the table.(Adirat P.et al., 1985). From the table one can see that

	SWITZERLAND	South Africa	Canada	North Caucasus Russia
Period of the most activity of hailstorms	June-July	November-December	July-August	June
Repetition of maximum sizes of hailstones, mm	50% < 9 80% < 13 0.1% > 40	60%<9 79% < 12 86% < 15 91% < 18	68% < 7 92% < 10 98% < 13 99% < 15	11% < 7 22% < 10 43% < 15 77% < 20 99% < 30 0.9% > 30
Kinetic energy of hailstones, J m^{-2}	68% < 20 81% < 50 91% < 100 3% > 200	30% < 1 72% < 10 91% < 100	49% < 10 81% < 50 91% < 100 0.3% > 600 max 900	40% < 10 70% < 50 81% < 100 97% < 500 3% > 1000 max 1000
Hail streak length, km	< 50	the most of 10-19	85% < 30 97% < 80 0.3% > 150	37% < 10 80% < 30 98% < 60 2% > 60
Hail streak width, km	from 2 to 10-12	the most of 5-9	68% < 3 97% < 6 90% < 15 max 35-30	17% < 3 53% < 6 80% < 15 94% < 24 max 27-30
Hailfall area, km^2	80% < 10 90% < 50	46% < 10 67% < 25 84% < 50 8% > 100 max 350	53% < 15 79% < 50 96% < 300 1% > 1000 0.5% > 1500	34% < 25 55% < 50 98% < 300 1.5% > 1000
Total kinetic energy	$4.5 \times 10^5 \div 2.5 \times 10^{10}$	$2.0 \times 10^6 \div 8.8 \times 10^{10}$	$9.7 \times 10^7 \div 5.0 \times 10^{10}$	$4.0 \times 10^7 \div 2.0 \times 10^{11}$
Total amount of hailstones	$10^8 \div 10^{11}$	$10^9 \div 10^{12}$	10^{12}	$10^9 \div 10^{13}$

TABLE. The hailstorm features in Switzerland, South Africa, Canada and Russia.

the values of total kinetic energy vary from 10^7 to 10^{11} J, the hailstone amount - from 10^8 to 10^{13} and the maximum value of kinetic energy of hailstones per one square meter in some cases increases to 10^3 Jm^{-2}.

The maximum repetition accounts for the values of maximum diameter of 15-20 mm, arithmetic-mean diameter of 6-8 mm, kinetic energy of 10Jm^{-2}, the concentration of 2000 - 3000 m^{-2}. In 50 cases from 100 D_{max} 18 mm, E_k 30 J m^{-2}, N 1500 m^{-2}. In 70% of all cases of hail fallout there is no damage because of E 50 Jm^{-2} (Tlisov et al.,1989).

It is seen from the table that the limits of characteristic changes of hail falls on the North Caucasus and in Canada are very similar but the part of the most severe hailstorms on the North Caucasus is larger than in Alberta.

In the framework of Complex Hail Experiment the special investigations on the detection of ratio change of embryo types on hail streaks were carried out. The hailstone samples from 31 hailfalls we analysed. In 9 hailstorms the sampling was made in different places of hail streak, two samples had a time resolution (Fig.1). From Fig.1 one can see that the maximum part of drop embryos in all cases observed near the right margin of hail streak where the density of kinetic energy was maximum. It is interesting to note that the bimodal size distribution of hailstones can be observed in these places more frequently.

REFERENCES

1. Admirat P., Goyer G.G.,Worriw L.,Carte E., Roos D., Lozowski E.R.,(1985), A comparative study of hailstorms in Switzerland, Canada and South Africa, J. Climatol.-15, 35-51.
2. Tlisov M.I., Taumurzaev A.Kh., Fedchenko L.M., Khuchunaev B.M.,(1989), Kinetic characteristics of hail and agriculture crops losses, 5th WMO Conf. on Weath. Modif. Appl. Cloud Phys., Beijing, 1, 339-340.

THE STORAGE AND PROCESSING TECHNOLOGICAL STUDY OF IMAGE INFORMATION SYSTEM ON SEVERE CONVECTIVE CLOUD

Liang Bi-Jun, Wang Ze-Yan and Wang Ang-Sheng*

Academy of Post and Communications Sciences, Beijing, 100083, China
* Institute of Atmospheric Physics, Academia Sinica, Beijing, 100029, China

ABSTRACT

Due to there are a lot of image and information data in severe storm observations by using radar, satellite and other instruments, the storage and processing technological study of image information plays an important role in our research works.

The studies of distribution image-information system and their storage, processing technology have been described in this paper.

Authors present the basic theory and mathematical method of image information storage and procession which are applied to a realtime operating image database. Same cases of above works are given in the paper.

1. INTRODUCTION

In the studies on Cloud and Precipitation Physics, there are a volume of observational data which are image or picture, for example, radar, satellite, aircraft etc. data.[1,2] When we use these data, the storage and processing technological study of image information system on Cloud and Precipitation Physics is necessary by use of computer specially on severe convective cloud.

Due to atmospheric disasters are the most serious disaster in all world, the Forecast, Nowcasting, Warning and disaster reduction of atmospheric disasters are very important.[3] In China, radar system is one of all important observational systems. As a case, the storage and processing technology of radar image system on severe convective cloud was studied and applied.

The basic theory and mathematical method of image information storage and procession which are applied to a real-time operating image data-base and same cases are given in the paper.

2. BASIC THEORY AND METHOD

When the Radar image information into the center computer would be displayed and conformed to every kinds of image data for technical requirements. The image can be expressed with a two-dimension matrix:

$$P_{ij} = \begin{pmatrix} P_{11}, & P_{12}, \ldots\ldots, & P_{1n} \\ P_{21}, & P_{22}, \ldots\ldots & P_{2n} \\ \ldots\ldots & P_{ij} & ,\ldots\ldots \\ P_{m1}, & P_{m2}, \ldots\ldots, & P_{mn} \end{pmatrix} \quad \langle 1 \rangle$$

Here, P_{11}, P_{12}, ..., P_{ij}, ..., P_{in}, express the data of brightness points, subscript i, j are its coordinates, values are color codes.

To study the mutuality of several images, we can use some operational rules oof spacial set theory as processing. Provided to use a multidimensional spacevector for a image, this expression of vector will be adaptable to structure of relationship data base for storage and processing images.

Hence, the expression with vector is:

$$P_n = [P_{11}, P_{12} \ldots, P_{ij}, \ldots, P_{mn}] \quad \langle 2 \rangle$$

Formula <1> and <2> are the same meaning mathematically.

One of the key of Distribution Image Information System is storage of the image information to the real-time data-base. If a storied information of image is defined as a logical record, the Jth image of N records can be expressed as follows:

$$P_J^N = [P_{J11}^N, P_{J12}^N, \ldots, P_{Jmn}^N] \quad \langle 3 \rangle$$

Here, P_{J11}^N, P_{J12}^N, ..., P_{Jmn}^N are the items of the records, each one expressed a image.

M logical records are defined as a file. These files are separated into two types. One kind of files are made of N records are called data file and another kind of files are called inquiry files which is make of logical condition of these logical records.

If data file is made of M records,

then file is expressed as follows:

$$F_1^M = [P_{i1}^N, P_{i2}^N, \ldots P_{in}^N] \Big| \in Tm\ , Ni\ , s\ , A \quad \langle 4\rangle$$

Here, T_m: limit time of forming file.
Ni: the number for expressing the difference between record number of forming files.
S: type of files.
A: collecting image from different terminals.
P_{i1} , P_{i2} ,... P_{im} : M logical records of data base.

The Hth inquired file is expressed as follows:

$$L_H^C = [H, A, S, C] \in RC \quad \langle 5\rangle$$

The RC express the logical condition of every logical record. H, A, S, C express the time, place, image type, characteristic saparetely, the items of inquired file are made of them.

The data base will be made of all kinds of files, i.e the data base is set of those files:

$$D = \{ F_N \} \Big| \in T,\ I \quad \langle 6\rangle$$

Here T: The time to establish the data base (for example 0-24 hours).
I: The type of files.

After a data base is established, various images collected by the distribution system are cast the space of database according to certain rules.

In the application of image information, it is necessary to produce some new files, such as the J times amplification of local image, compressing image information, composition of the N images and displaying the N images continuously etc. There are several models for processing the image data as follows:

The first model: J times amplification of local image:

First step: Define a new victor set Y for local image processing.

Suppose a image is a vactor P of N-dimensions space set, its dimension is equal to m*n, then

$$Y \triangleq \{Yi \mid i \in R\} \Big| \in X_o,\ Y\ ,\ J$$

$$\forall \quad i = 1,2,3,\ldots, m*n \quad \langle 7\rangle$$

Here X_o: eginning point coordinate of amplified local image.
Y : the rectangular subset, its value to set 1 inside the subset, zero for others.

J : the amplified index, sufficient and necessary condition for J is:

$$J = 2 \hat{}\ W. \quad W = 2,\ 4,\ 8,\ldots 2 \hat{}\ n$$

Second step: To find the set intersection P between original image vector and new vector Y, P is the image taken out:

$$Pf \cap Y = \{Pi \mid Pi \in Pf \text{ and } Pi \in Y\}$$

$$\triangleq \{Pf' \mid d_1 = a*b\} \quad \langle 8\rangle$$

$$\forall \quad i = 1,\ 2,\ 3,\ \ldots,\ a*b$$

Where: d1=a*b, dimension of local image.

Third step: dimension of set vector P'f in local image is amplified from a*b to m*n, i.e, local image is amplified J times. Suppose: Z_1, Z_2 , ..., Z_{W-1} are (W-1) zero sets, to find the mulitype set of P'f and (W-1) zero set.

$$P'f * Z_1 * Z_2 * \ldots * Z_{W-1} \triangleq$$

$$\{P''f \mid d_o = m*n\} \quad \langle 9\rangle$$

Forth step: Put the value to zero points in the P''f set by interpolation method.
If $P''f = \{Pfo \mid d_o = m*n\}$

$$Pf_l \triangleq \{Pfl \mid d_o = m*n\ P'f_l = Pfo\ ,$$

$$P''f = F[Pf(i-1) + Pf(i+1)]\} \quad \langle 10\rangle$$

$$\forall \quad i = 1,2,3 \ldots m*n$$

1. Linear interpolating expression as follows:

$$P''f_l = aPf_o(i-1) + bPf_o(i+1) \quad a,b \in R \quad \langle 11\rangle$$

2. Noneliner interpolating expression as follows:

1) Two times intpolation:

$$P''f_l = [aP^2f_o(i-1) + bP^2f_o(i+1) + abPf_o(i-1)Pf_o(i+1)]^{\frac{1}{2}} \quad \langle 12\rangle$$
$$a,b \in R$$

2) N times intpolation:

$$Pf_l = [\sum_{K=1}^{n} ak\ P^n f_o(i-1) + bK\ P^n f_o(i+1) + \ldots\ldots\ldots]^{\frac{1}{n}} \quad \langle 13\rangle$$
$$a,b \in R$$

Second model: N images are displayed simultaneously on screen.

Suppose there are N images, Jth image in multidimensional space set is expressed by $\{P_J^N\}$, dimension d_o=m*n. where: $N = 2^W$, $W \in R$.

First step: to reduce dimensions of{P }from d_o to d_1=a*b

P_J^N ={P_{io} | d_o = m*n }   original image

$P_J^N \hat{=}$ {P_{i1} | d_1 = a*b, P_{i1}^{N} = P_{io}, $P_{i1}^{N'}$=0 } <14>

∀ i_1 = 1, 2, 3,.......,a*b

Second step: to obtain set union in multidimentional space set:

P_1^NU P_2^NU P_3^N.....U P_n^N = {P_{si} | ∈ d,x,x_{on} <15>

∀ i = 1, 2, 3,...,m*n

Where: d: dimension of new image.
x = I*J, I = J = sweeped lines *2.
x_{on} : the starting point of each image.

Third model: composition of N images:
Suppose N image multidimensional space are expressed as N sets:

P_1 = {P_{1i} | ∈ A_1, d_1, x_{o1} }
∀ i = 1, 2, 3,...a*b
P_2 = {P_{2i} | ∈ A_2, d_2, x_{o2} }
∀ i = 1, 2, 3,...b*c
......

P = {P_{ni} | ∈ A_n, d_n, x_{on}}
∀ i = 1, 2, 3,...m*n

Where: A_N - coordinate systems of N images in multidimensional space.
d_n - dimensions of N images.
x_{on} - differental starting point of N images in multidimensional space.
d - dimensions of comsitive image.

Necessary and sufficient condition of composite images are that all image coordinate must be reffered to same dimension and same coordinate starting point. Then, composition of N images can be obtained as:

P_1^NU P_2^NU P_3^N.... U P_n^N= { P | x ,d }

∀ i = 1, 2, 3....,m*n   <16>

x_o: beginning point coordinate of composite image
d : demensions of composite image

Fouth model: compression of image information.

In order to save space of memory or to reduce rate of transmission on channal, it is necessary to compress the information of a image.

Suppose compressed image P in multidimensional space, dimension d=m*n. Original image P_o= {P_{oi}|d_o= m*n }

∀ i = 1, 2, 3..., m*n. The compressed image is:

P_1 = { P_{1i} | d = D P_{1i} = P_{oi} | λ ≥A,

P_{1i}= 0 | λ <A X_o∈P, X_o∈P_1 } <17>

∀ i = 1, 2, 3, ..., D

where: λ - designed threshold value.
D - compressed dimension of space set.
X_o - the left upper point coordinate of the rectangle which refers to image space.

Fifth model: procedure display of N images.
If N images are defined N points in multidimensional space and N image have continuous property in respect of both time and space.

P_1 = {p_1 | ∈ s_1 , t_1 }
P_2 = {p_2 | ∈ s_2 , t_2 }
......

P_N = {p_n | ∈ s_n , t_n}

If above N images are reflected on screen, we will watch displaying procedure of N images continuous from which it can make out the tendency of target development and law P:

P = {P_1 , P_2, ..., P_n} | ∈ t,A,D   <18>

where: t - moving time of target in multidimensional space.
A - started position of each image, it is function of time (t), A=f(t).
D - it is varied with time and positions, dimensions of image at any moment and achieve to forecasting arm.
P(i+1) = F (t,A) P

3. APPLICATION

A practical system has been developed to process the image information for EMIS. There three operating states as:

First: off-line state:
It is used for examine and demonstration. By terms of sample of picture, to operate all programs and various function, to examine operational state of system.

Second: on-line state:
Get into this state, image information from collected terminals is stored into the database on real-time.

Third: Record state:

After three hours, information in database are automatically backed into magnetic tape machine.

The operating function are shown in Fig. 1.

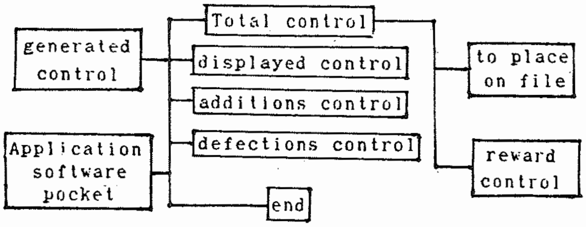

Fig 1

In Fig 2, there are four images displayed on a screen.

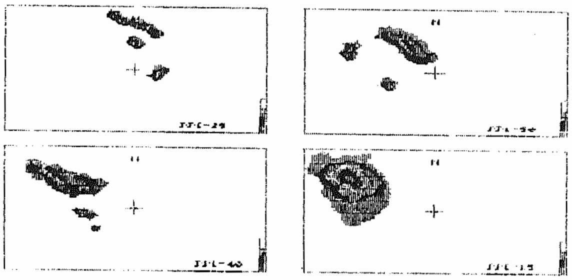

Fig 2

The local amplified image (area S in Fig 2) with 4 times is shown in Fig.3

Fig. 3

4. CONCLUSION:

The image information is one important part used for the EMIS. The image information acquired at remote terminal computers can be transmitted to the central computer by the special method at low rate. For the purpose of the application to the real-time systems, the image information in the centralcomputer must be stored, processed, and displayed in efficiency model.

REFERENCES

[1] Browning, K.A.; 1982: Nowcasting. Academia Press. 1-254.

[2] Teng Fu-Sheng, Liang Bi-Jun, "Organization and Management of image information system",<<Articles Compilation of Computer Managing Information System>> IEEE, Beijing Subdepartment. 1989,9.

[3] T.Pavilidis, The pattern displaying of computer and computation of pattern processing, 1987. Science Press.

Observation and Research on Hail-shooting Physical Parameters

Shi Anying

Hebei Meteorological Research Institute, P.R.China

This paper deals with some parameters of diameter,density,quality,kinetic energy of hail and proportion distribution between quality of hail and precipitation which have been obtained by self-made hailruler,hailpad,hail-rain separator and self-recording hail-rain separator. I get the following results:

1.After statistics analysing on 315 hail spectrums, we found that correlation between quality of hail and diameter can be expressed by $Y=k\exp(\beta x)$.

2.According to $R=N\exp(\beta R')$,the maxi proportion between quality of hail and precipitation is 183,the mini is 14.4,the average is 44.1. In the formula, R is precipitation, R' is quality of hail, N=136.5, β =0.51.

3.Initial time of hail and rain: hail and rain dropped at the same time accounting for 33%, hail ahead of rain account for 7%,rain ahead of hail account for 60%. Terminal time of hail and rain: hail and rain dropped at th same time accounting for 20%, rain ahead of hail account for 26.7%, hail ahead of rain account for 53.3%.

4.The correlation between radar reflectivty factor (Z), flux of hail kinetic energy ($\acute{E}$),and flux of hail quality (M) are $M=45.9\ Z^{0.617}$, $\acute{E}=2118.9\ Z^{0.747}$.

5.Closed cold centre of $-55^\circ C$ on the top of convective cloud may cause heavy hail disaster.

The above mentioned results were obtained under the following conditions:

1.We observed hail-shooting and obtained the parameters of hail in the area of 40-42° N, 114-116° E. Northern of this area is Mongolia plateau, southern is Taihangshan mountain chain and interval basin between mountains. Influenced by northwest air current, annual frequency of hail-shooting is 2 to 11 times counting at 13 stations, the size of disaster area is 736.7km^2.

2.The used apparatus: The structure and parameters of hailpad, hailruler, and hail-rain separator were listed in Reference No.3. Here I point out:the effective observation size of hailpad is 552.25cm^2. According to simulation test, conversion relation between hailhole and real diameter of hail can be expressed by Y=Hx-0.8. Y is real diameter of hail,X is diameter of hail-hole.

3.Observation spots have been distributed in the southern of this area along hail path (NW-SW). 102 Hailpads,hail-rain separator, self-recording hail-rain separater,radar,sounding, pennant have been distributed in 14 stations in size of 8×13.5km^2. Then we used polar-orbiting satellite photographs to set the location of hail cloud and some parameters.

4.Confirm on some parameters:

①Hail spectrum and formula:$P=n/s\cdot t\cdot v$, P is space density of hail, n is quality of hail, s is the size of hailpad (above mentioned), t is hail-shooting duration (S), V is terminal velocity of hail $V=(8/3.\rho_1/\rho_2.g/CD.R)^{1/2}$, ρ_1 is density of hail (take 0.8g/cm^3), ρ_2 is density of surrounding air of hail(takeH5$\times10^{-3}m^{-3}$),g is gravitational acceleration,C_D is resistance coefficient (take 0.5),R is radius of hail. Firstly, we give the formula similar to hail curves,and then calculate constant and take a test of coefficient of correlation. I get 6 kind of formulas in 315 hail spectrums:index function account for 65.7%,rain recombination function account for 7.3%, hyperbola function account for 5.4%, logarithms function account for 2.5%, Γ function 0.3%. According to test of X^2, the distribution of B of index function appeared Gaussian distribution $N(4.26,2.16^2)$.

② Proportion correlation between quality of hail and precipitation.

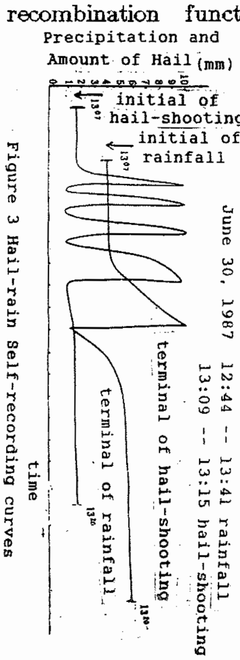

Figure 3 Hail-rain Self-recording curves

Figure 3 is the original note of self-recording hail-rain separate curves. The observation size of hail-shooting is 25 times of rain's. So,we divided quality of hail by 25. I get 44 data.

Also,we have calculated 90 times'data,which were gauged by self-recording hail-rain separator,including total precipitation and amount of hail,initial and terminal time of rain and hail. According to calculation results,I get the above mentioned data.

③The correlation between quality flux of hail (intensity of hail),kinetic energy of hail and radar reflectivty factor.

V_t(terminal velocity of hail)$=V_0\sqrt{D_t}$ $=452ms^{-1}.mm^{-1/2}$,and hail spectrum N(D) was distributed as index spectrum,then radar reflectivty factor (Z) can be shown:D:0→∞

$$Z=\int N(D)D^6dD$$
$$=\int N_0\ e^{-\lambda D}D^6dD$$
$$=N_0\ 6!\lambda^{-7}(mm^6\cdot m^{-3})$$

kinetic energy flux of hail-shooting is:

$$\acute{E}=\int \pi/12\ \rho N(D)D^3V^3dD$$
$$=\pi\rho/12\int N_0\ e^{-\lambda D}D^3V_0\ ^3D^{3/2}dD$$
$$=-\pi/12\ \rho N_0\ V_0^3\Gamma(5.5)\lambda^{-5.5}\ (J\cdot m^{-2}\cdot {}_s^{-1})$$

quality flux of hail-shooting is:

$$M=\int \pi\rho/6\ N(D)D^3V\ dD$$
$$=\pi/6\rho\int N_0\ {}_e^{-\lambda D}D^3V_0\ D^{1/2}dD$$
$$=\pi/6\rho N_0\ V_0\ \Gamma(4.5)\lambda^{-4.5}(mg\cdot m^{-2}\cdot s^{-1})$$

so,it must be : $\acute{E}=aZ^b$ $\quad M=aZ^\beta$

I get the following formula after analysing 13 hail spectrums,calculating the correlation between Z,É and M(the figure was omitted).

$\acute{E}=2118.9E^{0.747}$ (6) $M=45.9Z^{0.607}$ (7)

In these two formulas,the unit of Z is $10^3mm^6\cdot m^{-3}$,the unit of É is $10^{-6}Jm^{-2}\cdot s^{-1}$,the unit of M is $mg\cdot m^{-2}s^{-1}$. The results show that, so long as we get the radar reflectivty factor(Z), we can obtain kinetic energy flux of hail (É) and quality flux of hail (M).

④Correlation between hail-shooting and temperature of cloud top.

This paper deals with a number of polar-orbiting satellite cloud atlas of 15 times' hail shooting,they showed the distribution of temperature,and we find:(a)temperature of cloud top is −55℃,and it only has 1 or 2 cold centres,and heavy hail-shooting has been emerged. The intensity of hail will be increased along with the increasing of temperature gradient, e.g. on June 18,1987, there are 2 cold centres of −55° (cloud top is 13km) in 41° −42° N, 117−118° E and 40° −41° ,115° −116° E, The results are:The hail dropped in 25 counties,it blowed strong wind in 3 counties,and fell thunderstorm in 6 counties. (b)the land size of hail-shooting is about half of cold centre of −55℃.'s (c)the cold centre of cloud top of −40° ∼−35° may cause storm,strong wind in many places,cold centre of over −30℃ may not cause the disaster.

Reference

(1)China Meteorological Press
"Collected Works of Hail-Suppression and Cloud Physics" of 1989.
author: Shi Anying.
(2)No.3,Vol 8 of "PLATEAU METEOROLOGY"of 1989 "Discussion on Distribution Characteristis of Hail Spectrum"
Author:Shi Anying, Sun Yuwen, Tian Zhixi
(3)China Meteorological Press
"Collected Works of Hail-Suppression and Cloud Physics" of 1989
Author:Shi Anying.

HIGH-RESOLUTION THREE-DIMENSIONAL WIND AND REFLECTIVITY FIELDS IN THE EYEWALL OF HURRICANE CLAUDETTE (1991)

Frank ROUX[1], John F. GAMACHE[2] and Frank D. MARKS Jr.[2]

[1]: CRPE (CNET-CNRS), Issy-Les-Moulineaux, FRANCE
[2]: HRD (NOAA/AOML), Miami, Fl., USA

1. INTRODUCTION

Every year from August till October, airborne experiments are conducted by Hurricane Research Division / Atlantic Oceanographic and Atmospheric Laboratory (NOAA), Miami, Fl., USA, with the two NOAA / Aircraft Operation Center WP-3D aircrafts to collect data on hurricanes over the Atlantic Ocean, the Caribbean Sea, the Gulf of Mexico or the Eastern Pacific Ocean. Among the different experiments related to the internal structure of hurricanes and their synoptic environment, the *"Eyewall Evolution Experiment"* is aimed at gathering data on the structure and evolution of the wind and reflectivity fields, on the interactions between the primary (tangential) and secondary (radial and vertical) circulations, on the moisture, heat and momentum transports. These phenomena are important for the intensification and maintenance of hurricane circulation. For this purpose, repeated mappings of the three-dimensional wind field within 80 to 100 km from the eye are conducted with coordinated perpendicular flight patterns with the two NOAA WP-3Ds. As the tail Doppler radar on each aircraft scans perpendicularly to the flight track, these dual-Doppler observations can provide wind fields every 30 to 40 minutes.

A significant improvement in airborne Doppler radar technique has been achieved in July 1991 with the installation of a French made dual-beam antenna on NOAA WP-3D 43. With this new device, the radar beam is electronically switched forward or aft every other sweep. Thus, two independent projections of the air velocity are measured and dual-Doppler observations can now be made with a single aircraft path. A similar approach is F-AST (Forward-Aft Scanning Technique), proposed by Jorgensen and DuGranrut (1991), except that the dual-beam antenna does not suffer the mechanical limitiations of F-AST for high drift angles.

This aircraft equipped with the dual-beam antenna made his first scientific flights over central Florida in August 1991 during the CaPE Experiment (some results can be found in Dou *et al.*, 1992). The two WP-3Ds were also used during the 1991 Hurricane Field Program. This paper presents the wind and reflectivity fields deduced from the observation of the inner region of Hurricane Claudette with the dual-beam Doppler radar on 7 September 1991.

2. HURRICANE CLAUDETTE

1991 was a relatively quiet year with regard to tropical cyclone activity in the Atlantic (Avila and Pash, 1992). Only eight storms occured of which four reached the hurricane status. Claudette was the strongest hurricane of the season, but never threats inhabited regions as it passed its entire lifetime over the ocean. It formed as a moving upper-level trough induced a low-level disturbance about 1000 km SE of Bermuda (at 55°W, 22°N). It became a tropical depression on 4 September, a tropical storm on the 5th and a hurricane on the 6th. At that time, it was slowly moving westward. Claudette reached its maximum intensity on 7 September with a central pressure of 944 hPa and sustained winds of 60 m/s, which made it a category 4 hurricane in the Saffir-Simpson scale. Claudette was a relatively small storm with hurricane force winds (>35 m/s) extending only 40 km from the center. It weakened thereafter and turned to Northwest, then to North. Claudette passed about 200 km ESE of Bermuda on the evening of 8 September. It turned to Northeast on 9 September, to East on the 10th, decreased below tropical storm strength on the 11th and dissipated near the Azores on the 14th.

On 7 September 1991, the two NOAA WP-3Ds flew an *"Eyewall Evolution Experiment"* to determine the structure and evolution of the eyewall and the inner rainbands. As deduced from successive horizontal reflectivity images from the Lower Fuselage radar data, the storm propagated towards NNW at a moderate speed, 160° at 5 m/s. A reflectivity composite for the period 1830-2000 (all times are UTC) shows a partial eyewall at a mean radius of 15 km, an outer convective ring at 40 km and a large spiral band at 100 km (Fig.1). The precipitation field in the inner and outer rings were more intense (reflectivity values larger than 40 dBZ) in the southeastern part, while the maximum values are found in the northern part of the spiral band. During the observation period, the radius of the inner eyewall slowly decreases, while the intensity of precipitation in the outer one increases.

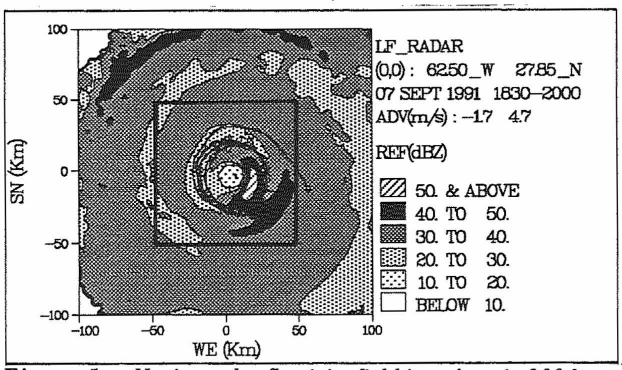

Figure 1: *Horizontal reflectivity field in a domain 200 km on a side, from a lower fuselage radar time composite for 1830-2000, 7 September 1991. The flight track of NOAA WP-3D 43 and the 100x100 km Doppler analysis domain are indicated.*

3. METHODOLOGY

The drawback of the dual-beam antenna (or F-AST) is the horizontal resolution is twice as large as that obtained with the classical dual-aircraft observations. Nevertheless, it is possible to minimize this effect by flying curved trajectories around the region of interest (Fig.2). Of course, the increased resolution in the inner side is balanced by a coarser one in the outer side. Instead of flying simultaneous perpendicular legs with the two aircrafts, an attempt has been made on 7 September 1991 to obtain three-dimensional wind fields from the dual-beam radar data through flying circles of 25 km radius around the storm eye with WP-3D 43. The flight altitude was 3.6 km and the scanning rate was 10 rpm.

Once these Doppler data were replaced in the frame moving with the storm, unfolded and corrected for the aircraft drift, pitch and roll, and for the hydrometeor fallspeed velocity, the

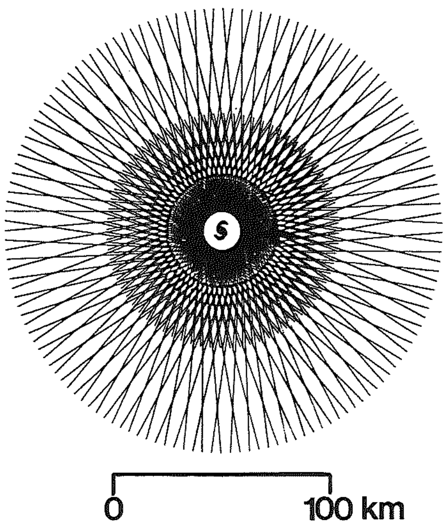

Figure 2 Geometry of the dual-beam airborne Doppler radar scanning for a radius of 25 km and an aircraft speed of 180 m/s (from an original drawing by P. DODGE, NOAA/AOML/HRD)

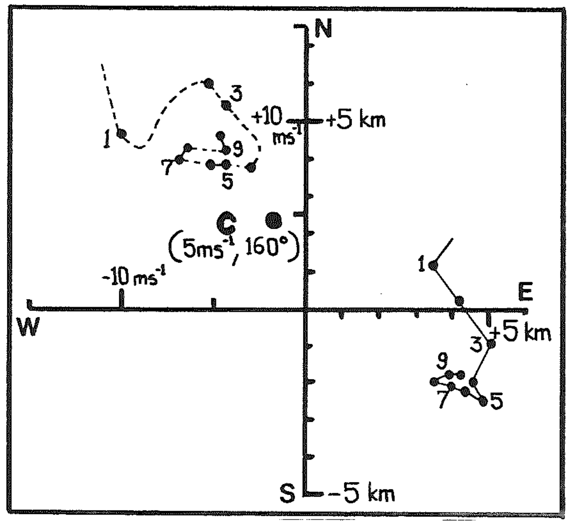

Figure 3: Position of the vortex center with altitude (solid line) relative to the position (62.50°W, 27.85°N), and hodograph of the mean horizontal wind (dashed line). The dot labelled C represents the storm propagation speed. Numbers indicate the altitude in km.

radial velocities were processed through the ABCD -*Analyse de Balayages Coniques Doppler* - method (Roux and Sun, 1990) to deduce the horizontal components in a domain of 100x100 km on a side, extending from 0.5 to 15 km with horizontal and vertical grid spacings of 2 km and 500 m, respectively. The vertical velocity components were derived by downward integration of the continuity equation using the horizontal divergence computed from the horizontal components and corrected with the method proposed by O'Brien (1970).

Although successive three-dimensional wind fields could be deduced from the radar data collected during each of the 6 circles flown by WP-3D 43 around the eye, we will only present here a unique one obtained from the analysis of the radar data from the whole period. The reason for doing this is twofold: first it provides a very complete set to test the method used to process airborne Doppler data, then it allows to derive a mean circulation which will be used as a reference in analyses of the storm evolution.

4. KINEMATIC STRUCTURE

To express the obtained three-dimensional wind fields in the frame moving with the storm, the propagation speed (160°, 5m/s) was substracted to the horizontal components. Other important parameters of the storm circulation are the vertical variations of the vortex center and of the mean horizontal wind (Fig.3). The first one was obtained through the maximisation of the tangential circulation within an annulus comprised between 5 and 30 km radii. The position of the circulation centers varied by as much as 4 km between 1 and 5 km altitudes, making an anticyclonic spiral pattern with increasing altitude.

The mean horizontal velocity components for radii smaller than 40 km gave an estimate of the environmental winds. There is a difference of 8 m/s between the low and mid-level winds and the hodograph also follows an anticylonic loop. This indicates the environmental flow distorted the vortex shape. Similar results were obtained for Hurricanes Norbert (Marks *et al.*, 1992) and Hugo (Roux and Marks, 1991). It can also be seen in Fig.3 that Claudette was moving at a speed slower than the environmental winds with the largest difference below 1 km altitude.

The reflectivity values and the wind components at 5 km altitude, deduced from the tail-Doppler radar data, are displayed in Fig.4. The structures of the inner (10 to 25 km radii) and outer (35 to 45 km radii) convective rings were slightly different. For the first one, the reflectivity values showed a pronounced asymmetry, with a maximum in the southeast and a minimum in the northwest. In the outer ring, although the precipitation were slightly more intense in the southeastern part, distinct maxima are also found around the ring (Fig.4a). These features were related to those obtained for the vertical velocity components (Fig.4b). In the inner ring, there was a large region of upward motions in the South. In the outer ring, maxima and minima are closely associated. They occupy smaller areas, except for the large updraft region in the southern part. Downward motions were observed in the region of low reflectivity values (<10 dBZ) between the two rings in the North.

The horizontal wind was also asymmetric (Fig.4c). The strongest tangential wind (>50 m/s) was found in the northeastern part of the inner convective ring. A comparison between Figs. 4 a, b and c shows that there was an azimuthal shift between the maxima in vertical velocity, radar reflectivity and tangential wind. In the outer ring, two small regions of secondary wind maxima (>40 m/s) were found in the northwestern and southeastern parts. The radial wind component (Fig.4d) shows inflow in the southwestern half of the outer ring and in the southeastern half of the inner one, with the largest values in the vicinity of the vortex center. This structure was due to the storm propagation at a speed slower than the environmental winds, which implied inflow from the back at all levels (Fig.3).

A mean radial cross-section in the southeastern quadrant (azimuth comprised between 90 and 180° from North) gives some details on the vertical structure (Fig.5). The stronger radar echoes and upward motions were found in the inner ring (10<R<25 km) (Fig.5a and b), with secondary maxima in the outer ring (35<R<45 km). The tangential wind maximum (Fig.5c) was associated with the inner ring, but the change in the slope of the 40 m/s contour at R=30 km could be due to the influence of the outer ring. Although it cannot be seen in this mean cross-section, the wind maximum sloped outward with height at angles of 45 to 60° from the horizontal for R<20 km.The radial wind showed inflow below 4 km altitude and above 8 km (Fig.5d). In these upper levels, the radial wind could result from an outflow due to upward motions in the outer ring.

Azimuth-height plots of mean values in the inner convective ring (10<R<25 km) depict its asymmetric structure (Fig.6). The most intense values were found to the right (East) of the storm track: reflectivities up to 40 dBZ at 6 km altitude, winds stronger than 40 m/s at 8 km altitude. In this region, the radial wind was characterized by a relatively strong inflow. The tangential wind

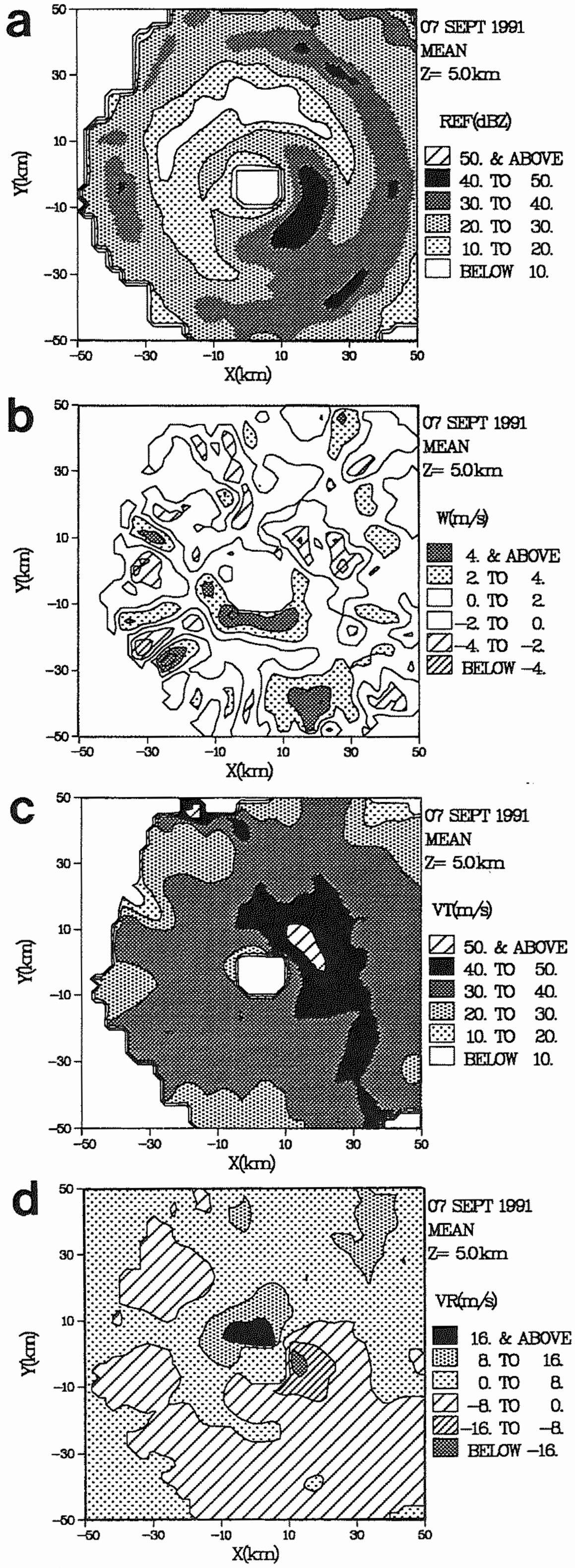

Figure 4: *Horizontal contours of radar reflectivity in dBZ (a), vertical (b), tangential (c) and radial (c) velocity components at 5 km altitude.*

contours showed no significant slope with height. This was probably due to the relatively small wind shear above 2 km altitude (Fig.3). At all levels, there was an azimuthal shift between the maxima of upward motions, reflectivity value and tangential wind. On the left (West) of the track, weaker reflectivity values are associated with downward motions, smaller tangential winds and outflow.

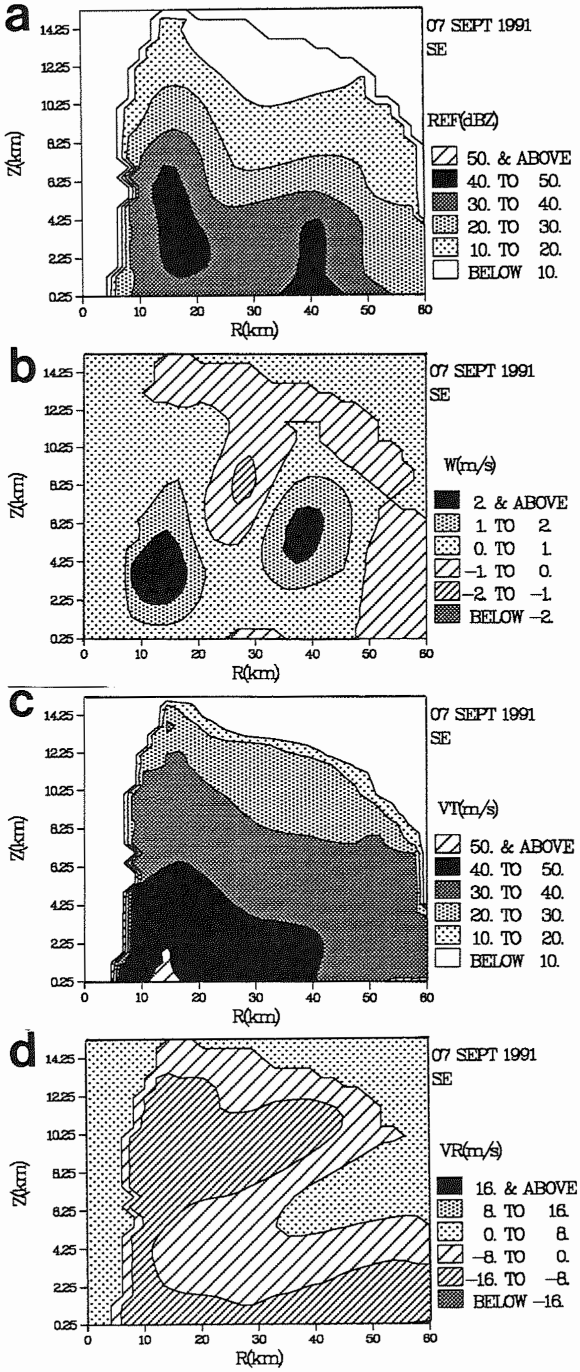

Figure 5 *As Fig.4, except for a mean radius-height cross section for azimuth between 90 and 180° from North.*

5. DISCUSSION

The wind field of a mature Hurricane Claudette was derived from the analysis of Doppler radar data collected when NOAA WP-3D 43 aircraft equipped with the dual-beam antenna flew 6 circles of 25 km radius around the storm eye at 3.6 km altitude. The three-dimensional wind field deduced from the whole data set covered a domain 100x100 km on a side, extending from 0.5 to 15 km in altitude. The main characteristics are:

(i) The storm was moving toward NNW at a speed slightly smaller than the environmental winds.

(ii) The reflectivity field showed two convective rings around the storm eye. The inner one was much more intense in the southeastern part and was associated with a large updraft

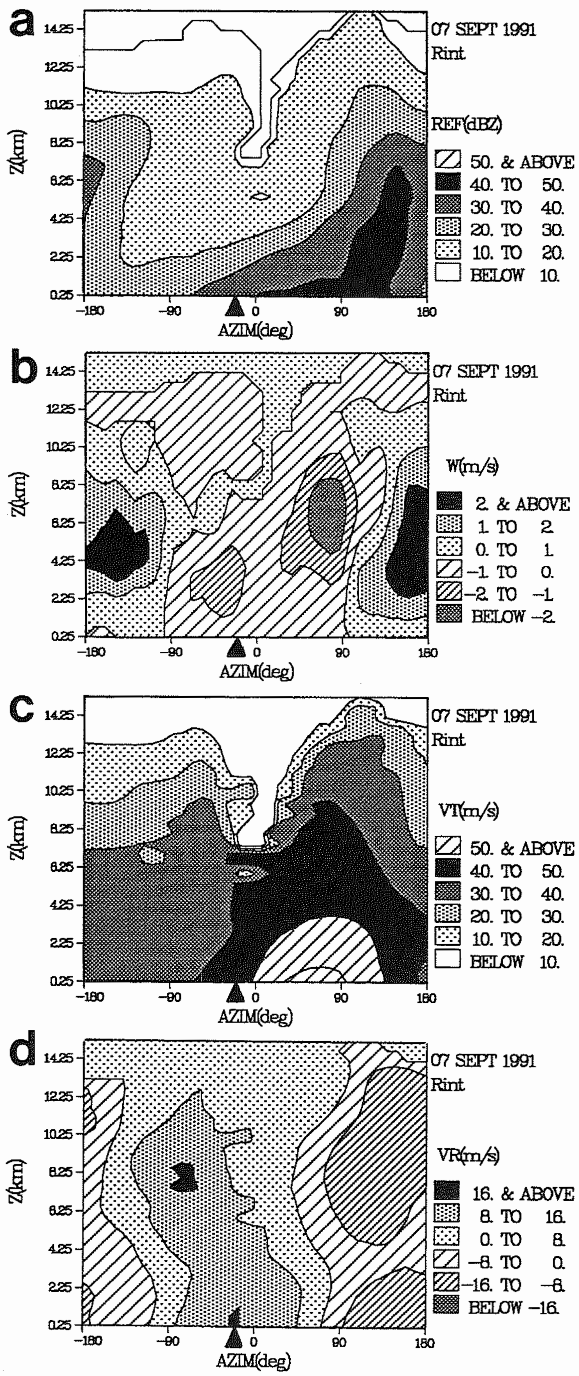

__Figure 6__ As Fig.4, except for a mean azimuth-height cross section for radii between 10 and 25 km. The triangle indicates the direction where the storm is moving to (340°).

region. In the outer ring, maxima and minima of both reflectivity and vertical velocity were observed.

(iii) The tangential wind maximum was associated with the inner ring, but at some distance downwind. Its slope with altitude was small. Secondary maxima were found in the outer ring.

(iv) At all levels, the radial wind showed inflow in the southern part of the domain, and outflow in the North.

The main difference between these results and previous airborne Doppler radar observations of hurricanes (e.g., Alicia: Marks and Houze, 1987; Emily: Marks and Houze, 1991; Hugo: Roux and Marks, 1991; Norbert: Marks *et al.*, 1992) concerns the relatively slow propagation of Claudette which implies environmental air was entering at the back of the storm. While the other storms were characterized by the presence of the most intense precipitation, tangential wind and vertical velocity in their leading part, these features were found in the rear for Claudette.

We must however recall that the results discussed here have been obtained through composing radar data collected during a period of 90 min. Therefore, although this probably allows the main kinematic characteristics to be deduced, it is not possible to infer the details of the air circulation, especially those concerning the vertical motions. A more precise description of the kinematic structure and its evolution will be obtained through independent analyses of the radar data from each circle. We hope to deduce new informations on the inner eyewall contraction and on the outer convective ring intensification, which have been recognized as important phenomena in the evolution of the most intense hurricanes (Willoughby *et al.*, 1982; Willoughby, 1990).

ACKNOWLEDGMENTS

We thank the crews from NOAA/AOC for their excellent job in flying unconventional flight patterns. Frank Roux is grateful to Drs. Stanley Rosenthal and Robert Burpee for permitting analysis of these data in CRPE.

REFERENCES

AVILA, L.A., and R.J. PASCH, 1992: Atlantic Hurricanes. *Weather*, **45** (n°1), 34-41.

DOU, X, G. SCIALOM and Y. LEMAITRE, 1992: Three-dimensional analytical mesoscale dynamic and thermodynamic structure of the stratiform part of a squall line retrieved from airborne Doppler radar data obtained during the CaPE experiment. Preprints, *11th Int. Conf. on Clouds and Precipitation*, Amer. Meteor. Soc., Montréal, Québec, Canada.

JORGENSEN, D.P., and J.D. DUGRANRUT, 1991: A dual-beam technique for deriving wind fields from airborne Dopper radar. Preprints, *25th Int. Conf. on Radar Meteor.*, Amer. Meteor. Soc., Paris, France, 458-461.

MARKS, F.D., Jr., and R.A. HOUZE, Jr., 1987: Inner core structure of Hurricane Alicia from airborne Doppler radar observations. *J. Atmos. Sci.*, **44**, 1296-1317.

----------, ----------, 1991: Kinematic structure of the eyewall of Hurricane Emily (1987) as determined from airborne Doppler radar. Preprints, *19th Conf. on Hurricanes and Tropical Meteor.*, Amer. Meteor. Soc., Miami, Fl., USA, 437-440.

----------, ----------, and J.F. GAMACHE, 1992: Dual-aircraft of the inner core of Hurricane Norbert. Part I: Kinematic structure. *J. Atmos. Sci.*, in press.

O'BRIEN, J.J., 1970: Alternative solutions to the classical vertical velocity problem. *J. Appl. Meteor.*, **9**, 197-203.

ROUX, F., and F.D. MARKS, Jr., 1991: Eyewall evolution in Hurricane Hugo from successive airborne Doppler observations. Preprints, *19th Conf. on Hurricanes and Tropical Meteor.*, Amer. Meteor. Soc., Miami, Fl., USA, 558-563.

ROUX, F., and J. SUN, 1990: Single-Dopper observations of a West-African squall line on 27-28 May 1981 during COPT 81: Kinematics, thermodynamics and water budget. *Mon. Wea. Rev.*, **118**, 1826-1854.

WILLOUGHBY, H.E., 1990: Temporal changes of the primary circulation in tropical cyclones. *J. Atmos. Sci.*, **47**, 242-264.

----------, J.A. CLOS and M.G. SHOREIBAH, 1982: Concentric eye walls, secondary wind maxima and the evolution of the hurricane vortex. *J. Atmos. Sci.*, **39**, 395-411.

THE HEAT BUDGET OF A MIDLATITUDE SQUALL LINE DETERMINED FROM A THERMODYNAMIC AND MICROPHYSICAL RETRIEVAL

Scott A. Braun and Robert A. Houze, Jr.

Department of Atmospheric Sciences, AK-40
University of Washington
Seattle, WA 98195 USA

1. INTRODUCTION

The cumulus-environment interaction is frequently described through budgets for heat and moisture, generally with data collected at scales comparable to, or somewhat larger than, the convective systems. In a recent study, Gallus and Johnson (1991, GJ hereafter) examined the heat budget of the 10-11 June 1985 PRE-STORM[1] squall line using composites of rawinsonde data from the National Weather Service and supplemental sites. The composite data was interpolated to grids with spacing of 0.5° latitude and longitude. This resolution makes it difficult to delineate the convective and mesoscale contributions to the heat budget since convective region velocities can be aliased into the trailing stratiform precipitation region. In addition, this evaluation of the heat budget takes advantage of only a small portion of the data (mainly rawinsondes) from the PRE-STORM network, which was designed to document processes on a wide range of scales simultaneously (Cunning 1986). The ultimate goal of our research is to combine as many of these data sources as possible to obtain a more complete analysis of all the processes contributing to the heat budget than can be obtained from the soundings alone. In particular, we wish to resolve the processes occurring on various scales within the storm. As part of this effort, we present some results of calculations that derive heat budget results for the 10-11 June squall line from dual-Doppler-radar data, which have the resolution to distinguish the separate processes occurring in the convective, transitional, and stratiform regions of the storm. Wind fields have been synthesized previously from the dual-Doppler measurements (Biggerstaff and Houze 1991). Here we apply a retrieval technique to the synthesized wind field to obtain the corresponding temperature and microphysical fields. A heat budget is then formed by combining the synthesized wind field and retrieved thermodynamic and microphysical fields. These calculations indicate the utility of the retrieval technique as a tool for deducing the heating that is associated with convective and mesoscale processes. Although this analysis has the disadvantage that only a small portion of the entire mesoscale convective system can be studied, it has the advantage of resolving the heating down to the scale of the convective motions so that contributions from different regions of the storm (convective, transitional, stratiform) can be deduced. Eventually, results obtained by the retrieval method can be combined with those obtained by other techniques, such as sounding analysis, to obtain a comprehensive study of the heat budget of the storm.

2. RETRIEVAL METHODOLOGY

The retrieval method used for the present analysis closely follows that of Hauser et al. (1988) and Marecal and Hauser (1991). The microphysical fields are obtained by using the bulk microphysical parameterizations of Lin et al. (1983) and Rutledge and Hobbs (1983), and solving two-dimensional, steady-state conservation equations for the microphysical variables.

[1] PRE-STORM is an acronym for Oklahoma-Kansas Preliminary Regional Experiment for the Stormscale Operational and Research Meteorology Program-Central Phase.

Temperature and pressure are determined in a manner similar to the dynamic method of Hauser et al. (1988). For the present case, the Coriolis terms are included in the momentum equations. Since we perform the retrieval for both the convective and stratiform precipitation regions, the temperature and pressure are deduced using the variational approach of Roux and Sun (1990) which was shown by Sun and Houze (1992) to reproduce adequately the temperature field in the stratiform precipitation region.

3. DATA

The three-dimensional wind field used in the retrieval is taken from a composite of dual-Doppler-derived wind fields for the northern portion of the 10-11 June 1985 PRE-STORM squall line during the mature stage of the system. The composite data set has horizontal and vertical resolution of 3 and 0.5 km, respectively (see Biggerstaff and Houze (1992) for details).

An average vertical cross section oriented normal to the squall line was obtained by averaging over a 60-km wide strip perpendicular to the line. Figure 1a shows the mean reflectivity and vectors of the two-dimensional wind in the plane of the cross section, and Figure 1b shows the average vertical velocity. The cross section is characterized by a 60-km wide leading convective line, followed by a region of stratiform precipitation nearly 150 km wide. The transition zone, defined by the low-level reflectivity minimum between $x \approx 35$ and 60 km, separates the convective and stratiform

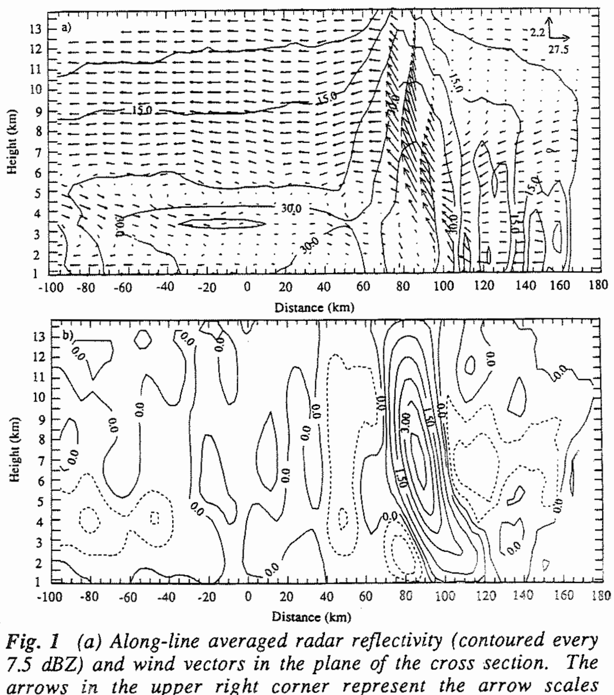

Fig. 1 (a) Along-line averaged radar reflectivity (contoured every 7.5 dBZ) and wind vectors in the plane of the cross section. The arrows in the upper right corner represent the arrow scales corresponding to 2.2 m s^{-1} for the vertical velocity and 27.5 m s^{-1} for the horizontal velocity. (b) Vertical velocity (m s^{-1}) with contours drawn at -0.5, -0.25, 0., 0.25, 0.75, 1.5, 2.25, 3.0, and 3.75 m s^{-1}.

precipitation regions. The velocity field shows strong front-to-rear (FTR) flow in the convective region and above about 5.5 km in the trailing stratiform region. A layer of rear-to-front (RTF) velocity is seen near the melting level in the stratiform rain region. It descends to near the surface in the convective region. Weak RTF flow also occurred at upper-levels ahead of the convective tower, while FTR flow occurred at low levels under the trailing stratiform precipitation. The vertical velocity field is characterized by strong ascent in the leading convective line, but relatively weak ascent in the stratiform region. Substantial descent is present: 1) at midlevels ahead of the convective line, 2) at low levels in the convective region, 3) through the depth of the troposphere in the transition zone, and 4) near the melting level in the stratiform region, particularly in the region behind the secondary band.

The mesoscale ascent above the melting level in the stratiform region is very weak. Comparison of the vertical velocity field to the EVAD vertical velocity analysis of Rutledge et al. (1988) suggests that either the procedure used to obtain the composite field substantially reduced the strength of the mesoscale updraft, or the 60-km wide strip did not sample the mesoscale updraft adequately. In either case, the mesoscale updraft heating will not be well represented in the present results. This is a limitation of the current data set and will require further examination at another time.

4. RESULTS

The retrieved potential temperature perturbation is shown in Figure 2. At low levels, a cold pool extending up to approximately 3.5 km exists as a result of the melting of graupel and evaporation of rain. The lowest temperature perturbations (< –5°K) are located in the vicinity of the convective downdraft. Although the retrieval diagnoses cold air at low levels in the stratiform precipitation region generally well, it is unable to reproduce all of the details of the low-level temperature structure. Comparison of a retrieved stratiform region temperature profile with low-level profiles from rawinsonde data suggests that the cold pool in this region should be somewhat deeper and that lapse rates below the melting level should be steeper. The retrieved melting level is somewhat higher (4.3 km) than the observed level of 3.9 km. However, this difference is less than the vertical grid spacing.

Warm air extends from about 3.5 km up to nearly 10.8 km in the convective region and to about 9 km ahead of and behind the convective region. The cold perturbations above 9-10 km may reflect the transport of low-level air above its equilibrium level. There is a minimum in temperature near x=10 km at storm top, located approximately 70 km behind the top of the convective line. This is in good agreement with the observation of Zipser (1988) that the satellite infrared temperature minimum was located 50-100 km behind the leading convective line during the mature phase of the squall line.

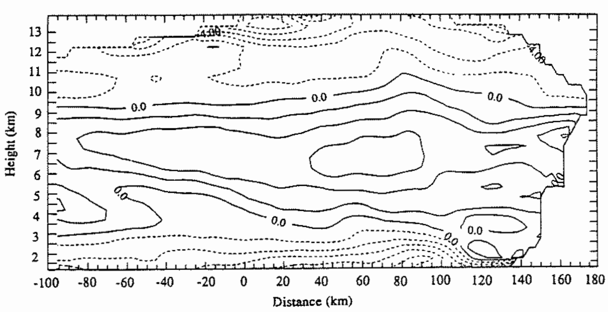

Fig. 2 Retrieved potential temperature perturbation with respect to the pre-squall environment. Contour interval is 1°K. Solid (dashed) contours indicate positive (negative) values.

The heating rate Q_1 is defined following GJ as

$$
\begin{aligned}
Q_1 &= \bar{u}\frac{\partial \bar{s}}{\partial x} + \bar{w}\frac{\partial \bar{s}}{\partial z} \\
&= Q_r + L_v(\bar{c}-\bar{e}) + \left(L_v + L_f\right)\left(\bar{d} - \bar{s}*\right) \\
&\quad + L_f\left(\bar{f} - \bar{m}\right) - \frac{\partial}{\partial x}\overline{u's'} - \frac{1}{\bar{\rho}}\frac{\partial}{\partial z}\bar{\rho}\overline{w's'} \qquad (1)
\end{aligned}
$$

where $s = c_pT + gz$ is the dry static energy, c_p is the specific heat at constant pressure, L_v and L_f are the latent heats of vaporization and fusion, Q_r is the radiative heating rate, and c, e, d, $s*$, f, and m are the rates of condensation, evaporation, deposition, sublimation, freezing, and melting, respectively. The overbars represent averages over 3 km x 3 km x 0.5 km volumes centered on the grid points while the primes denote the deviations from these averages. The last two terms in (2) then represent the horizontal and vertical convergences of the eddy heat flux by unresolved processes. In this study, Q_1 is determined from the left side of (2) and c,e,d, and $s*$ are determined from

$$\vec{V} \bullet \nabla \bar{q}_v = -\delta(\bar{c}-\bar{e}) - (1-\delta)\left(\bar{d}-\bar{s}*\right) \qquad (2)$$

where δ is 1 for $T > 0$°C and zero otherwise, and f and m are determined from the appropriate bulk parameterization terms. No attempt is made to deduce the remaining terms on the right side of (2) explicitly. In the profiles shown below, these terms will be lumped together and determined as a residual (Q_1 – latent heating). Note that this residual may also reflect the amount of error in the retrieval.

The Q_1 field, as determined by the advection of dry static energy, is shown as a two-dimensional line-normal cross section in Fig. 3. Strong heating occurs in the convective updraft with a maximum of 60°K h^{-1} at 6.4 km (464 mb), but relatively little heating occurs in the mesoscale updraft. At midlevels ahead of the convective updraft and at low levels in the convective downdraft, cooling rates greater than 10°K h^{-1} occur. In the transition and stratiform regions, peak cooling rates associated with evaporation, sublimation, and melting occur between roughly 3 and 5 km.

The contributions to the total heating rate, Q_1, of the convective, transition, and stratiform regions can be determined using a decomposition technique similar to that used by Houze (1982). We let

$$Q_1 = \sigma_c Q_{1c} + \sigma_t Q_{1t} + \sigma_m Q_{1m} + \sigma_f Q_{1f} \qquad (3)$$

where $Q_{1c}(\sigma_c)$, $Q_{1t}(\sigma_t)$, $Q_{1m}(\sigma_m)$, and $Q_{1f}(\sigma_f)$ are the heating rates (fractional areas) of the convective region, transition zone, stratiform region, and forward anvil region

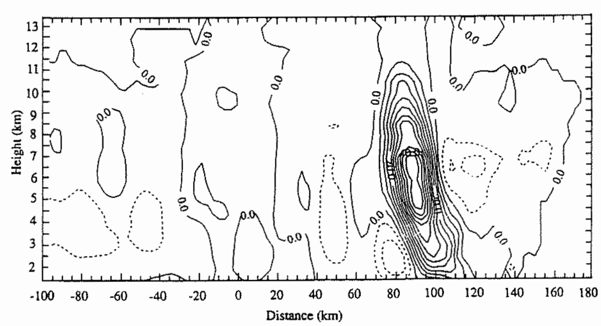

Fig. 3 Apparent heat source, Q_1, contoured every 5 °K h^{-1}.

($x > 135$ km), respectively. Since the heating in the region $x > 135$ km makes only a minor contribution to the total heating (see Fig. 3), a profile for Q_{1f} will not be shown. Profiles for the first three regions are shown in Fig. 4.

In the convective region, except near cloud top, there is net heating throughout the troposphere, with peak heating near 5 km. This differs from the GJ convective profiles in two ways: 1) the profiles of GJ show net cooling at low levels, whereas the results from the retrieval show that heating by condensation at low levels in the convective updraft is stronger than the cooling produced in the convective downdraft; and 2) the peak in the average heating rate determined here occurs 1.5-3.5 km lower than the double-peaked profile of GJ (for 0300 UTC). The lower peak in the heating rate is due partially to the cooling at midlevels just ahead of the convective updraft which was included in the convective region average. Such cooling was apparently not included in the average profile in GJ.

The transition-zone profile is characterized by cooling throughout the troposphere with one cooling maximum located at 3.9 km and a second, weaker maximum near 8.4 km. This is consistent with the double-peaked structure of the transition-zone subsidence found by Biggerstaff and Houze (1992).

Since the mesoscale updraft is poorly represented in the composite analysis, the stratiform region profile differs markedly from that of GJ. In their study, the stratiform region at 0300 UTC is characterized by a strong heating maximum near 450 mb (near 6.4 km) and relatively weak cooling below 700 mb (3 km). Our results show relatively little heating within the mesoscale updraft. On the other hand, substantial cooling occurs through a deep layer from the surface to 6 km with peak cooling at 3.4 km. In GJ, the cooling above 3 km is more than balanced by heating in their main updraft.

In the total heating profile, Q_1, there is heating throughout the troposphere except for shallow layers between 2.5-3.5 km and above 12 km. Below 4 km, the significant cooling by melting and evaporation in the stratiform region and transition zone nearly cancels the heating by condensation in the convective updraft. At mid-to-upper levels, the total heating profile is probably not representative of the actual total heating since the mesoscale updraft is either not sampled adequately or is smoothed out by the analysis procedure (see above).

Figure 5 shows the different components of the total heating according to the terms on the right side of (1). The profile labeled R represents the difference Q_1–'latent heating and should reflect the heating rates associated with radiative processes, the convergence of the eddy heat flux, and any residual errors in the temperature and microphysical retrievals or in the assumption of steady-state conditions. The condensation and deposition profile peaks just under 6 km and decreases rapidly to zero above 7 km. There is additional heating of approximately 0.3°K h^{-1} by the freezing of rain and cloud water between 4.3 km and 9 km decreasing to zero at cloud top. Below 5 km the evaporation and sublimation profile is dominated by the cooling in mesoscale and transition zone downdrafts while above this level, the cooling is largely associated with the subsidence just ahead of the convective updraft as well as with the subsidence in the upper part of the transition zone. Thus, cooling occurs, rather substantially, through the depth of the whole troposphere.

Near 4 km, the curve m in Fig. 5 indicates that the cooling associated with melting hydrometeors has a magnitude approaching that associated with evaporation. Figure 6 shows the spatial distribution of cooling and heating rates by melting and freezing determined from the microphysical retrieval. The most striking feature is the strong cooling by melting (up to –9°K h^{-1}) that occurs in the convective region. It has been previously recognized that a concentrated melting layer occurs in the stratiform region. These results suggest that a similar, and even more intense, melting layer may occur in the convective region. Actually, the high cooling rates in Fig. 6 extend into the transition zone in the retrieval, but this is an artificial result of an inability of the microphysical retrieval to reproduce well the precipitation minimum in the transition zone. The strong cooling rates are associated with the melting of graupel falling from the upper parts of the convective cells in the squall line. The strong melting layer in the convective-

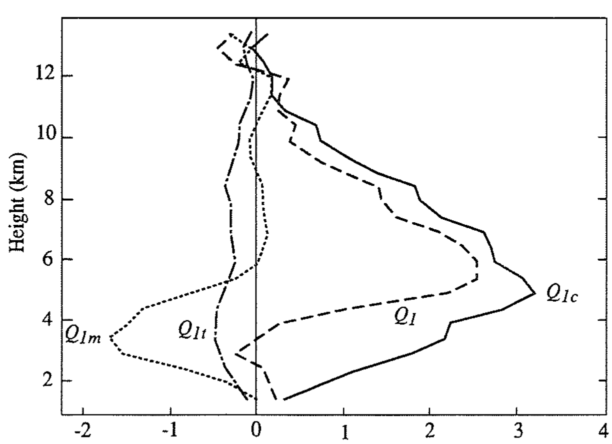

Fig. 4 Vertical distribution of the apparent heat source, Q_1, averaged over the convective region (Q_{1c}), transition zone (Q_{1t}), stratiform region (Q_{1m}), and total domain (Q_1). The profiles have been multiplied by the respective fractional areas to facilitate direct comparison.

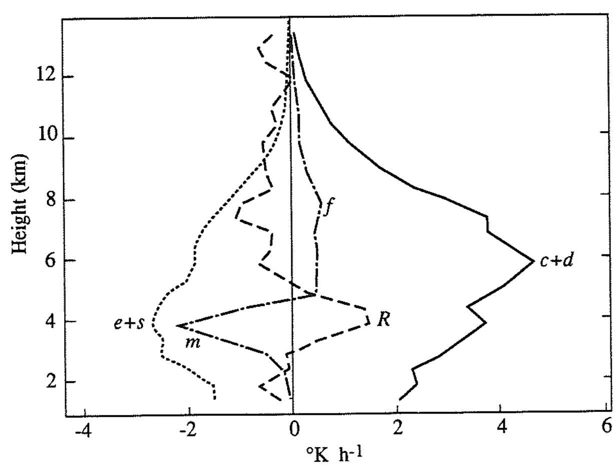

Fig. 5 Vertical distributions of the individual components of the total heating determined from the left side of (2), including condensation and deposition (c+d), evaporation and sublimation (e+s), melting (m), and freezing (f). The profile labeled R is described in the text.

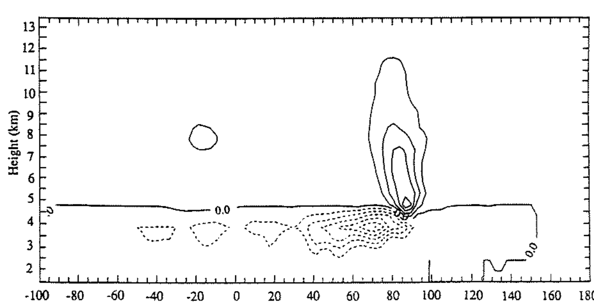

Fig. 6 Heating and cooling rates associated with freezing (solid) and melting (dashed). Contour interval is 1.5°K h^{-1}.

transition region indicates that melting probably played a substantial role in the thermodynamics of this part of the storm by decreasing the potential temperature, and the equivalent potential temperature, of the air parcels descending in the convective downdrafts. This increase in the negative thermal buoyancy can drive stronger downdrafts, as shown by Srivastava (1987). In addition, Szeto et al. (1988) showed that cooling by melting can force significant mesoscale circulations. Melting in the convective-transition region, then, is an additional mechanism for the intensification of the surface cold pool and gust front.

The curve R for Q_1-'latent heating' compares favorably with profiles for radiative cooling and heating by the eddy flux convergence in the "nighttime" simulation of Churchill and Houze (1991). They showed that below the 0°C level, heating due to convective overturning tends to balance partially the cooling by melting and evaporation, while at cloud top, radiative cooling tends to dominate over heating by the eddy flux convergence to produce net cooling.

6. CONCLUSIONS

A thermodynamic and microphysical retrieval was applied to a 60-km wide region of the northern part of the 10-11 June 1985 squall line for the purpose of computing a diagnostic heat budget with data down to the scale of the convective motions. This allowed for a clearer delineation of the convective, transition, and stratiform contributions to the total heating. The retrieval technique enabled us to obtain reasonable estimates of the heating except at mid-to-upper levels in the stratiform region. Of particular interest, we found that the presence of midlevel cooling associated with subsidence immediately ahead of the convective updraft led to a lowering of the peak heating rate in the average convective region heating profile (Q_{1c}). Additional mid-to-upper level cooling occurred within the transition zone. Substantial cooling by melting was found to occur in the rear part of the convective region. This cooling probably acted to reinforce the role of evaporation in the development of the surface cold pool and the gust front.

Acknowledgments: We would like to thank Drs. F. Roux and J. Sun for making the temperature retrieval software available to us, and Dr. M. Biggerstaff for providing us with the synthesized dual-Doppler radar data set used in this study. G. C. Gudmundson edited the manuscript and K. M. Dewar helped draft the figures. This research was sponsored by National Science Foundation grant ATM-610230.

REFERENCES

Biggerstaff, M. I., and R. A. Houze, Jr., 1991: Kinematic and precipitation structure of the 10-11 June 1985 squall line. *Mon. Wea. Rev.*, **119**, 3034-3065.

Biggerstaff, M. I., and R. A. Houze, Jr., 1992: Kinematics and microphysics of the transition zone of a midlatitude squall line system. *J. Atmos. Sci.* (accepted).

Churchill, D. D., and R. A. Houze, Jr., 1991: Effects of radiation and turbulence on the diabatic heating and water budget of the stratiform region of a tropical cloud cluster. *J. Atmos. Sci.*, **48**, 903-922.

Cunning, J. B., 1986: The Oklahoma-Kansas Preliminary Regional Experiment for STORM-central. *Bull. Amer. Meteor. Soc.*, **67**, 1478-1486.

Gallus, W. A., Jr., and R. H. Johnson, 1991: Heat and moisture budget of an intense midlatitude squall line. *J. Atmos. Sci.*, **48**, 122-146.

Hauser, D., F. Roux and P. Amayenc, 1988: Comparison of two methods for the retrieval of thermodynamic and microphysical variables from Doppler-radar measurements: Application to the case of a tropical squall line. *J. Atmos. Sci.*, **45**, 1285-1303.

Houze, R. A., Jr., 1982: Cloud clusters and large-scale vertical motions in the tropics. *J. Meteor. Soc. Japan*, **60**, 396-410.

Lin, Y-L., R. D. Farley and H. D. Orville, 1983: Bulk parameterization of the snow field in a cloud model. *J. Climate Appl. Meteor.*, **22**, 1065-1092.

Marecal, V. and D. Hauser, 1991: Retrieval of thermodynamic and microphysical variables from dual-Doppler-radar measurements in frontal rainbands. *Preprints, 25th Conf. on Radar Meteorology*, 24-28 June 1991, Paris, France, American Meteorological Society, 143-146.

Roux, F. and J. Sun, 1990: Single-Doppler observations of a West African squall line on 27-28 May 1981 during COPT 81: Kinematics, thermodynamics, and water budget. *Mon. Wea. Rev.*, **118**, 1826-1854.

Rutledge, S. A., and P. V. Hobbs, 1983: The mesoscale and microscale structure and organization of clouds and precipitation in midlatitude cyclones, VII: A model for the "seeder-feeder" process in warm frontal rainbands. *J. Atmos. Sci.*, **40**, 1185-1206.

Rutledge, S. A., R. A. Houze, Jr., M. I. Biggerstaff and T. Matejka, 1988: The Oklahoma-Kansas mesoscale convective system of 10-11 June 1985: Precipitation structure and single-Doppler-radar analysis. *Mon. Wea. Rev.*, **116**, 1409-1430.

Srivastava, R. C., 1987: A model of intense downdrafts driven by the melting and evaporation of precipitation. *J. Atmos. Sci.*, **44**, 1752-1773.

Sun, J. and R. A. Houze, Jr., 1992: Validation of a thermodynamic retrieval technique by application to a simulated squall line with trailing stratiform precipitation. *Mon. Wea. Rev.* (April).

Szeto, K. K., R. E. Stewart and C. A. Lin, 1988: Mesoscale circulations forced by melting snow. Part II: Application to meteorological features. *J. Atmos. Sci.*, **45**, 1642 -1650.

Zipser, E. J., 1988: The evolution of mesoscale convective systems: Evidence from radar and satellite observations. *Tropical Rainfall Measurements*, (J. S. Theon and N. Fugono, Eds.), A. Deepak Publishing, Hampton, 159-166.

50 MZ PROFILER OBSERVATIONS OF TRAILING STRATIFORM PRECIPITATION: CONSTRAINTS ON MICROPHYSICS AND IN SITU CHARGE SEPARATION

Earle Williams[1] and Warner Ecklund[2]

[1]Weather Radar Laboratory, Department of Earth, Atmospheric, and Planetary Sciences
Massachusetts Institute of Technology, Cambridge, MA 02139

[2]Aeronomy Laboratory, NOAA, Boulder, CO 80303-3328

1. Introduction

Systematic kinematic and electrical features of squall lines at mid-latitude and in the tropics are increasingly apparent. The deep leading convection and the trailing stratiform precipitation are distinct regions which both extend well into the mixed phase region (0°C ≥ T ≥ -40°C) but exhibit order-of-magnitude differences in electrical activity (i.e., lightning flash rate). The lateral uniformity and quasi-one-dimensionality (in the vertical) of the trailing stratiform component, in both the radar (Houze, 1989) and electrical observations (Chauzy, 1985; Engholm *et. al.*, 1990; Schurr *et. al.*, 1991) lend simplicity to this component of the squall line structure. A valuable new observational tool for exploring cloud microphysics in squall lines are wind profilers, which under certain conditions can provide both the vertical air motions and differential particle motions which are essential in evaluating microphysically-based mechanisms for charge separation.

This paper is concerned with a further examination of a tropical squall line observed in DUNDEE (Down UNder Doppler and Electrical Experiment) near Darwin, Australia (12°S) on December 5, 1989. The analysis makes use of MIT C-band reflectivity data, a 50 MHZ profiler established in Darwin as a collaborative venture between the NOAA Aeronomy Laboratory and the Australian Bureau of Meteorology, and auxiliary electric field measurements beneath the squall line.

2. Reflectivity Observations with the MIT C-band Radar

The MIT C-band Doppler radar, located 26 km ENE of the 50 MHZ profiler performed 10 minute volume scans as the squall line formed to the south and subsequently propagated northward over both radars on December 5, 1989 (Rutledge *et al.*, 1991). The volume scan data were used to construct a time-height plot of radar reflectivity, Z_e, directly over the vertically-pointing 50 MHZ profiler. This procedure provides a reflectivity estimate at specific every 10 minutes. These results are contoured in Figure 1a and show clearly the leading deep convection and trailing stratiform region with accompanying radar bright band.

3. 50 MHZ Profiler Observations

The examination of Doppler spectra from the 50 MHZ profiler for the December 5 squall line in an earlier study (Rutledge *et al.*, 1991) disclosed the presence of a distinct bimodality which is attributable to (1) radar returns from gradients in refractive index (i.e. 'clear air' returns), and (2) precipitation particles (Wakasugi *et al.*, 1985). These two spectral contributions were often of comparable magnitude and this feature was exploited to compare C_N^2 values in the leading and trailing regions of the squall line in the earlier study. The spectral bimodality is further exploited in this study to determine time-height plots of mean vertical air velocity and precipitation fall speed, as shown in Figure 1b and 1c, respectively. In assembling this information, each 100 second-long profile in the time period 0840 to 1145 Z was examined. A vertical velocity was assigned to both the clear-air and precipitation spectral peaks at 1 km height intervals from 2-15 km at all heights where they could be measured. These values were subsequently averaged over 5-minute periods and the values contoured to produce Figures 1b and 1c.

Examination of the vertical air velocity in Figure 1b shows several interesting features. The updraft core aloft at 915-920 Z, which leads by a few minutes the reflectivity core in Figure 1a, attains a peak velocity of 10 m/sec near 10 km altitude. Examination of C-band volume scan data at this time suggests that the convective cell within the squall line closest to the profiler did not pass directly over the profiler, so only the edge of the updraft was probed. The updraft core is 'surrounded' (i.e., to the front and rear) by regions of subsidence. The downdraft aloft at 0930-0940 Z, which reaches 2 m/sec in the altitude range 11-15 km may be the result of the overshooting top. A stronger downdraft is seen directly beneath the deep updraft region in the altitude range 1.5-6 km. A zone of more gentle subsidence (0.1-0.6 m/sec) is prevalent from 1.5 to 12 km altitude at 1000 Z in the transition region from the leading to the trailing stratiform region, and coincides with the zone of minimum radar reflectivity throughout the depth of the cloud. Later in the trailing stratiform region (1015-1100 Z), a weak updraft is prevalent above 5-6 km, with weak subsidence at lower altitudes. This period generally coincides with larger values of reflectivity in the bright band. Weak subsidence is evident at lower levels throughout the stratiform region, but no pronounced changes in air velocity are evident across the melting layer. The cessation of upwelling above the 5-6 km altitude at 1100 Z is associated with a rapid diminishment in bright band reflectivity.

The map of precipitation fall speed in Figure 1c is less complete in the leading deep convection because broad overlapping spectra prevent the separation of air and particle velocities, particularly in the mixed phase region which is likely the site of vigorous charge separation. The largest detected fall speeds are 9-10 m/s beneath 5 km near 920 Z and are attributable to large raindrops or melting graupel. The smallest fall speeds beneath the melting level are observed in the transition region between leading and trailing stratiform regions, and coincide with the zone of deep subsidence and minimum radar reflectivity around 950 Z discussed earlier. Within the trailing stratiform region, pronounced differences in fall speeds across the melting layer are noted, as in many previous studies. Above the bright band, the expected precipitation targets are snow, lightly rimed aggregates, or small graupel. Beneath the bright band, the fall speeds diminish toward the ground, a behavior which may have contributions from the evaporation of rain or the increase of air density. Above the bright band, in the mixed phase region, the particle fall speeds are remarkably uniform in the 1.8-2.2 m/sec range and, surprisingly, appear to be unaffected by the action of subsidence or lifting, as indicated by the air velocity comparisons in Figure 1b. Finally, we note that the fall speeds beneath the leading and trailing regions differ by less than 10%, while the respective radar reflectivities (Figure 1a) differ by about 10 dB. This result emphasizes the great sensitivity of Z_e to particle size and the insensitivity of fall speed to particle size.

4. Electric Field Observations

The electric field at the ground at the MIT C-band radar site was also recorded with a flush-mounted electric field mill of the type used at Kennedy Space Center as the squall line approached and passed overhead. (Unfortunately, no such record was available at the profiler site and we are assuming that the MIT record is representative of conditions at the profiler, admittedly a questionable assumption.) This record is displayed on the same time scale as the radar information in Figure 1d. Positive (negative) values indicate negative (positive) charge overhead. The sudden discontinuities in the record are associated with lightning discharges, which are obviously far more prevalent beneath the leading deep convection than beneath the trailing stratiform region. In general, the DC field shows a prevalence of negative charge overhead beneath the deep convection and a prevalence of positive charge overhead during the trailing stratiform precipitation.

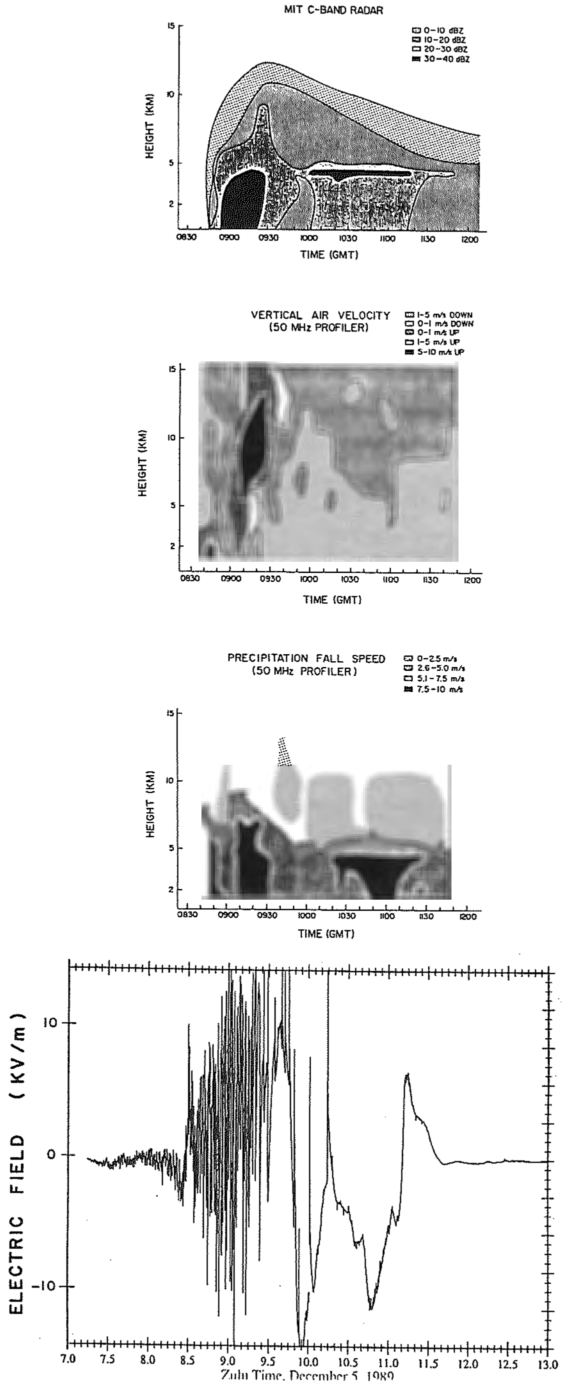

Fig. 1 a) Time-height plot of radar reflectivity, Z_e, over 50 MHZ profiler; b) time-height plot of vertical air velocity over profiler; c) time-height plot of precipitation fall speed over profiler, and d) surface electric field at MIT radar site.

5. Microphysical Predictions for Ice Particle Charging

It is widely believed that ice particle collisions are responsible for charge separation in electrified clouds. Selective charge acquisition by the larger ice particles and the subsequent vertical separation of opposite charges by differential fall speed then establishes the electric field necessary for lightning. It is possible that the requisite conditions are present in both the leading convection and the trailing stratiform region of most squall lines. The differences in particle condition necessary for selective charge separation have not yet been identified. Williams *et al.* (1991) have pursued the idea that the differences in microphysical growth state, controlled by both temperature and the liquid water content via the riming process, are responsible. These ideas show some consistency with laboratory simulations of charge separation during ice particle collisions (Takahashi, 1978). These comparisons are illustrated in Figure 2, for a graupel particle of one size and fall speed in a parameter space of cloud

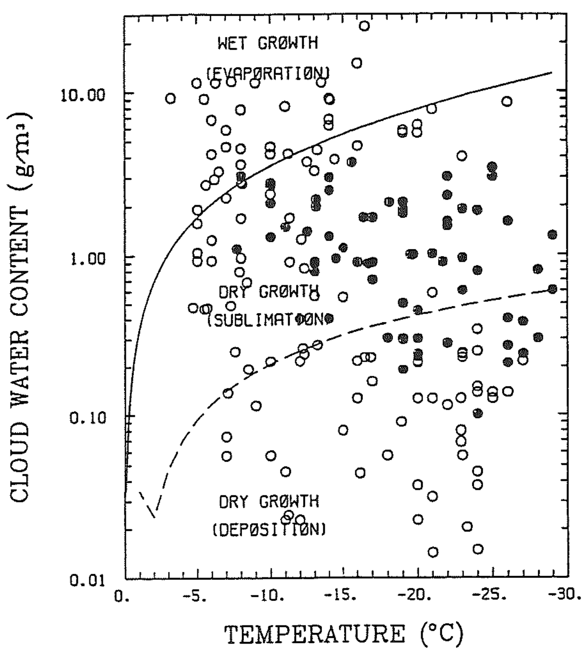

Fig. 2 Microphysical growth states for a simulated graupel particle (3 mm diameter moving at 9 in/sec) on a diagram of liquid water content and cloud temperature. (Taken from Williams *et al.*, 1991.)

temperature and liquid water content appropriate for the mixed phase region of moist convection. When the liquid water content is low and the large ice particles are growing by vapor deposition, positive charge acquisition is predicted. With higher liquid water contents, the particle warms to a temperature which allows sublimation (vapor loss) while growth by riming proceeds, with a prediction for negative particle charging. Finally, at very large liquid water contents, a wet growth condition is attained and the particle charging reverts to positive. The dots in Figure 2 show the results on rimer charging during ice crystal collisions in the laboratory simulation of Takahashi (1978), which show rough agreement with the foregoing predictions.

As a further aid in Section 6 for the interpretation the profiler and electric field observations already noted, the transition between graupel deposition and sublimation and its dependence on graupel size (equivalent spherical diameter) is explored. The same calculations in Williams *et al.* (1991), based on Macklin and Payne (1967), are used in obtaining the results in Figure 3, which show the critical liquid water content necessary for particle sublimation as a function of particle size, and for a range of ambient cloud temperatures.

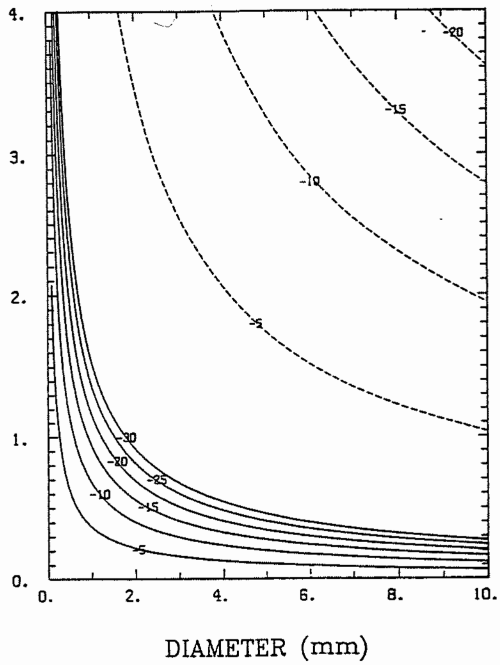

Fig. 3 Critical liquid water content required for graupel transition from deposition to sublimation condition, as a function of particle size and cloud temperature. (Taken from Williams and Zhang, 1992).

6. Interpretation and Discussion

For purposes of comparing the profiler observations and the electric field observations, two assumptions are made with are not entirely defensible. First, the surface electric field at the C-band radar site is representative of the field at the profiler site. We expect this assumption to be more closely adhered to in the case of the stratiform region than for the leading deep convection, based on earlier squall line observations with an array of electric field sensors (e.g. Engholm *et al.*, 1990). Second, we shall assume that the electric field polarity at the ground is largely determined by the polarity of the dominant lower charge in the mixed phase region aloft. This assumption is consistent with the general belief that foul weather polarity field at the ground beneath thunderstorms is caused by the accumulation of dominant negative charge in the lower end of the thunderstorm dipole, and many observations show that this negative charge resides at altitudes above the 0°C isotherm (Williams, 1989). It is also recognized that subsidiary lower positive charge and screening layer/corona layer effects can influence the field polarity at lower levels, but we shall bravely ignore these effects. In support of our second assumption, recent observations of the electric field profile in the trailing stratiform region of a squall line (Schurr *et al.*, 1991) support a correlation between field polarity at the ground and dominant charge polarity aloft.

We now proceed to comparisons in the leading deep convection, the transition region, and the trailing stratiform region, respectively.

Beneath the deep convection (0845-0930 Z), lightning is active and the electric field builds systematically toward positive values (foul weather polarity), between linghtnings, indicative of negative charge overhead. (This detailed behavior is smudged out in Figure 1d by the time compression of the record. The intervals between lightning flashes are seconds, and the field often makes an excursion into negative values at the time of lightning, probably reflecting the presence of positive corona space charge in the boundary layer.) The upward air motions above 0°C at this time support the existence of supercooled water and a mixed phase environment, but without direct measurements of liquid water content, we are unable to characterize unambiguously the microphysical growth state. If the liquid water contents are similar to deep convection at mid latitude (e.g. Musil and Smith, 1989), we can infer that sufficient liquid water content is present to suppress deposition (Figure 3) and the dominant graupel condition is sublimation (Williams *et al.*, 1991; Williams and Zhang, 1992). The results in Figure 3 suggest that liquid water contents of the order of 1 gm/m^3 are needed to suppress deposition and gurantee sublimation.

In the transition region, subsidence is prevalent over a considerable depth of the troposphere and throughout the region associated earlier with mixed phase. With downward air velocity in Figure 1b prevalent from 945-1015 Z, we cannot expect the sustained presence of supercooled water or any of the regimes characterizing mixed phase microphysics as depicted in Figure 2. The descending ice particles may well be sublimating (consistent with diminished reflectivity Z_e throughout the transition region) but not for reasons associated with warming by riming. The major transition in electric field polarity begins at 940 Z and is showing maximum dE/dt at about 950 Z, near the time shown downward air velocity becomes prevalent above 0°C. This observation is inconsistent with the idea that negative ice particle charging is associated with sublimation.

Beneath the trailing stratiform region and associated bright band, the electric field indicates predominantly positive charge overhead, with very infrequent but energetic lightning. (This behavior contrasts with some earlier observations of squall lines in which foul weather field was prevalent throughout (Engholm, *et al.*, 1990)). It is possible that the infrequent lightning is the result of in situ charge separation in the trailing stratiform region. In the present case, we might associate positive charging with depositional growth of the lightly rimed ice particles (Figure 2) in the mixed phase region from 1040-1100 Z when upwelling is present there (Figure 1b), but downwelling is present from 100-1040 Z when the field is also negative. Perhaps sublimation of ice particles is responsible for the electric field trend back toward positive values from 100 to 1015 Z.

The final excursion of electric field back to foul weather polarity is well correlated with the sudden falloff of reflectivity in the bright band and the transition from upwelling to downwelling above the altitude of the bright band. This coincidence suggests that the charging action responsible for positive charge overhead is eliminated by the disappearance of upwelling in the mixed phase region. The final negative charge overhead in this end-of-storm-oscillation (EOSO) may be the result of either residual corona space charge, or the residual upper level charge of the dipole charging process.

7. Conclusion

Comparisons between profiler-observed vertical motions and surface electric field beneath a tropical squall line show some points of agreement with microphysical charging predictions, and other points of disagreement. The simple transition from sublimation in the deep leading convection to deposition in the trailing stratiform convection, which we offered earlier as an explanation for the observations (Rutledge *et al.*, 1991) appears somewhat too simplistic, at least within the context of the assumptions we have made. Upward motion throughout the temperature range ordinarily identified with mixed phase microphysics is not sufficiently prevalent to support depositional growth when positive charge is observed overhead.

The profiler has proven to be a valuable aid in defining the conditions when mixed phase microphysics can be expected to operate. Further measurements of electric field with low-maintenance corona points at profiler sites are recommended to help narrow down on systematic electrical/kinematic behavior in precipitating systems overhead. Profiler observations like those in figure 1 for stratiform regions exhibiting a predominance of negative charge overhead (e.g. Engholm *et al.*, 1990) would be valuable for comparison with the case presented here. Electric field soundings at specific profiler sites would circumvent the need for the questionable assumptions used here in the interpretation of the observations.

References

Chauzy, S., M. Chong, A. Delanney, and S. Despian, The June 22 Tropical Squall Line observed during COPT 81 experiment: electrical signature associated with dynamical structure and precipitation, *J. Geophys. Res.*, 90, 6091-6098, 1985.

Engholm, C., R. Dole, and E. Williams, Meteorological and electrical conditions associated with positive cloud-to-ground lightning, *Monthly Weather Review*, 118, 470-487, 1990.

Houze, R.A., Observed structure of mesoscale convective systems and implications for large-scale heating, *Q. J. Roy. Met. Soc.*, 115, 425-461, 1989.

Macklin, W.C. and G.S. Payne, A theoretical study of the ice accretion process, *Quart. J. Roy. Meteor. Soc.*, 93, 195-214, 1967.

Musil, D.J. and P.L. Smith, Interior characteristics at midlevels in thunderstorms in the Southeastern United States, *Atmos. Res.*, 24, 149-167, 1989.

Rutledge, S.A., E.R. Williams, W.A. Petersen, and E.N. Rasmussen, Radar and electrical study of a tropical squall line near Darwin, Australia during DUNDEE, 25th Conf. on Radar Meteorology, American Meteorological Society, Paris, June 1991.

Schurr, T.J., B.F. Smull, W.D. Rust, and T.C. Marshall, Electrical and kinematic structure of the stratiform precipitation region trailing an Oklahoma squall line, *J. Atmos. Sco.*, 48, 825-842, 1991.

Takahashi, T., Riming electrification as a charge generation mechanism in thunderstorms, *J. Atmos. Sci.*, 35, 1536-1548, 1978.

Wakasugi, S., S. Fukao, S. Kato, A. Mizutani, and M. Matsuo, Air and precipitation particle motions within a cold front measured by the MU VHF radar, *Radio Sci.*, 20, 1233-1240, 1985.

Williams, E. R., The tripole structure of thunderstorms, *J. Geophys. Res.*, 94, 13151-13167, 1989.

Williams, E.R. and R. Zhang, The microphysical growth state of ice particles and the large scale electrical structure of electrified clouds, 9th International Conf. on Atmospheric Electricity, St. Petersburg, Russia, June 1992.

Williams, E.R., R. Zhang, and J. Rydock, Mixed-phase microphysics and cloud electrification, *J. Atmos. Sci.*, 48, 2195-2203, 1991.

Acknowledgements

We thank Steve Rutlege of CSU for earlier collaborative studies on the December 5, 1989 squall line as part of DUNDEE. Bill Jafferis of JFK Space Center provided the electric field mill. We are grateful to the staff of the Darwin Bureau of Meteorology for their assistance in the field program and initial access to Darwin profiler data. DUNDEE was supported by the Physical Meteorology Program at NSF under Contract ATM-8818695 with the assistance of Ron Taylor.

Precipitation and Kinematic Structure of a Bow-Echo Mesoscale Convective System Observed by Airborne Doppler Radar

David P. Jorgensen and Bradley F. Smull
NOAA/NSSL/Mesoscale Research Division, Boulder, CO 80303

1. INTRODUCTION

The tendency for convective storms to organize and propagate as long-lived linear entities has been known for some time. Some of these "mesoscale convective systems" or MCSs, particularly those that have been seen to produce long tracks of strong straight-line surface winds, are characterized by pronounced convex "bulges" in their leading convective lines toward their direction of propagation. Fujita (1978) termed these systems "bow-echoes" because of their appearance on radar PPI displays. Through the analysis of the evolution of radar echoes from several bow-echo cases that produced damaging surface winds, Fujita hypothesized a strong rear inflow jet to be present, with its core located at the apex of the bulge. This strong, concentrated jet was thought to be the source of the damaging surface winds as strong momentum associated with the jet was brought down to the surface near the leading edge of the convective line by convective-scale downdrafts.

More recently, Przybylinski and Gery (1983) have documented the reliability of the bow-echo pattern as an indicator of potentially damaging surface winds. Burgess and Smull (1990) analyzed a particularly severe bow echo over Oklahoma. Research-quality radar observations provided a detailed view of that storm, but only single-Doppler (radial) flow fields were available during its most intense phase. Numerical simulations using the Klemp-Wilhelmson non-hydrostatic cloud model of long-lived convective systems that possess some of the characteristics of bow-echoes have been completed by Weisman (1990). These simulations reveal that, under certain environmental shear and large convective instability conditions, a steady-state convective system evolves after several hours that consists of a 40 to 100 km long bow-shaped configuration of cells. Counter rotating cyclonic and anti-cyclonic eddies (termed "book-end vortices") develop 2-3 km above the surface at the northern and southern ends of this eastward propagating convective line, with an intervening strong rear inflow jet (marked by a line-normal axis of westerly momentum) near its midpoint. In the simulations, the rear inflow remains elevated to near the leading edge of the convective line, where it plunges downward toward the surface and helps to lift surface air that sustains the steady-state updraft.

Motivated by these studies suggesting that strong rear inflow is crucial to the dynamics of bow-echo convective systems, we present and discuss analyses of airborne Doppler radar data that reveal many of these previously hypothesized features.

2. DATA AND ANALYSIS

During the spring of 1991, the National Severe Storms Laboratory conducted a field exercise called the *Cooperative Oklahoma Profiler Studies* (COPS-91) to investigate the electrical and kinematic structure of mesoscale convective systems. Part of this experiment utilized the NOAA P-3 research aircraft equipped with a vertically scanning X-band Doppler radar. During the night of 8 May 1991 an MCS with bow-echo characteristics traversed southern Oklahoma from west to east and was investigated by the P-3. The system evolved from several strong convective storms that initiated along the dryline in the central Texas panhandle about 2300 UTC 7 May 1991. By 0600 UTC 8 May 1991 it had reached south-central Oklahoma. A radar depiction of this system at 0515 UTC is shown in Fig. 1. The MCS contained a roughly north-south oriented leading convective line extending from central Oklahoma

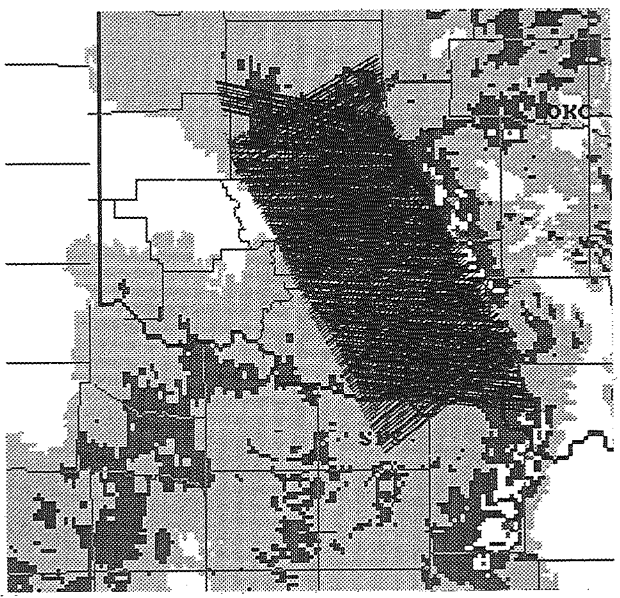

Fig. 1. Radar reflectivity composite at 0515 UTC on 8 May 1991 constructed from base scan PPIs from the National Weather Service network radars at Oklahoma City, Amarillo, Tulsa, and Sephenville, TX. State boundaries are shown as thick solid lines while the county boundaries are shown as thin lines. Shading represents reflectivity levels (in dBZ) as follows: light gray: 18-30; dark gray: 30-41; white: 41-46; medium gray: 46-50; heavy gray: 50-57; black: > 57. The flight track of the P-3 between 0509 to 0533 UTC is shown as the solid line in southwest Oklahoma. Cross hatching represents intersecting beams of the P-3's vertically scanning Doppler radar.

southward into north-central Texas. An eastward bulge in this convective line was evident near the Oklahoma-Texas border. The convective line was moving eastward at about 22 m/s. To the west (rear) of the line was a stratiform rain region with an intruding echo-free "notch" entering southwestern Oklahoma. Identifiable features within the stratiform region were actually moving much slower that the convective line (9 m/s versus 22 m/s) and in a more southeasterly direction. The notch region was also characterized by a "wake-low" marked by a surface pressure deficit several millibars. The P-3 executed flight tracks parallel to and just west of the line, as well as east-west legs through the notch region.

Airborne Doppler radar data were collected using the P-3s Fore/Aft Scanning Technique or FAST (Jorgensen and DuGranrut, 1991). After editing of the raw radial velocity data, wind fields were derived on 1.5 x 1.5 x 1.0 km Cartesian grids.

a. Rear Inflow Structure

The Doppler-derived wind field at 2.5 km immediately to the west of the convective line is shown in Fig. 2. The convective line is just off the analysis domain to the right. Airflow at this level is primarily from the west. Note that the westerly winds strengthen considerably toward the south, while the winds turn to southerly (and even weak southeasterlies) to the north and west. At this level the flow converges along an elongated zone of weaker reflectivity separating the stratiform band and convective line. The core of strongest rear inflow seen at 2.5 km is directed toward the bulge in the leading convective line (cf. Figs 1 and 2).

b. Vortex Structure

The wind pattern in Fig. 2 suggests the presence of a large scale cyclonic vortex centered to the west of the Doppler analysis domain. The existence of this vortex is confirmed by Doppler radar data collected along a later eastbound P-3 flight track across the trailing stratiform region (Fig. 3). Observed winds are consistent with a closed cyclonic circulation centered south of the flight track. In the eastern half of the domain the flow is southerly, but the flow turns to northerlies in the west. Lack of radar return in the notch region limited the Doppler wind analysis. A more complete depiction of the vortex is afforded by the flight level data from two east-west flight legs (Fig. 4). Cyclonic vorticity is clearly evident. In the eastern part of the domain relatively high θ_e air existed in the southerly flow, presumable coming from the convective line. To the west, lower θ_e air was seen associated with drier air entering from the west. A relative minimum in equivalent potential temperature is seen near the center of the circulation. Because ambient equivalent potential temperature typically decreases with height in the low- to mid-troposphere, the presence of a local minimum of θ_e near the vortex center implies descending motion. Decreasing θ_e values toward the west edge of Fig. 4 are consistent with the a mesoscale downdraft maximized toward the rear edge of the stratiform region. This circulation is also suggested by the "notch" in the radar reflectivity pattern of Fig. 1, since descending motion would promote evaporation of hydrometeors and a commensurate reduction of reflectivity.

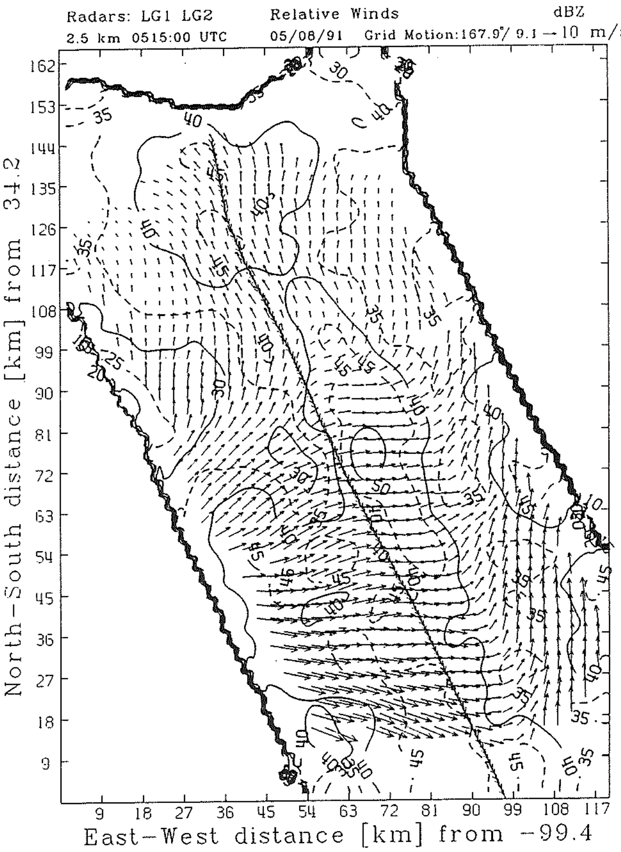

Fig. 2. Ground-relative wind field at 2.5 km AGL for the region just west of the convective line constructed from the P-3's Doppler radar data using the FAST method. Flight track is the solid line and the scale for the wind vectors is shown in the upper right corner of the figure. Contours are X-band radar reflectivity in dBZ.

c. Trailing Region Structure

In the storm's early stages, a sounding was taken at Amarillo, TX at a point about 100 km behind the convective line (Fig. 5). The sounding is shown in Fig. 6. The classic "onion-shaped" profile is seen, indicative of mesoscale subsidence below about 500 mb overlain by mesoscale ascent in the trailing anvil. The wind profile shows a westerly winds of 25 m/s near cloudbase, slightly greater than the line's later motion of 22 m/s. Westerly momentum did not extend to the surface, but rode above the near-surface inversion at 810 mb. This inversion was the result of convective scale outflow, marked by southeasterly winds and comparatively moist low-level conditions. Southerly momentum from 500 mb to 200 mb was probably a result of the convective lines passage as wind observations from the Vici network profiler showed mostly westerly winds above 800 mb prior to line passage.

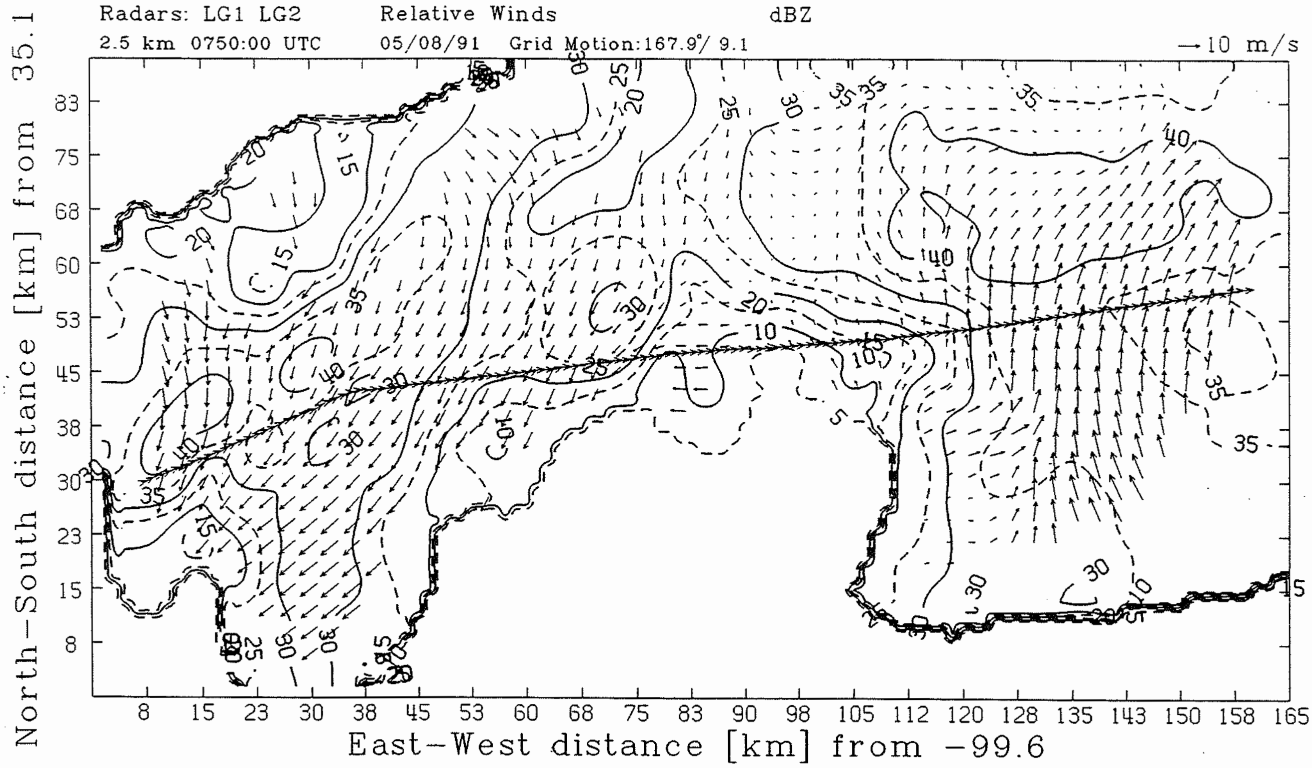

Fig. 3. As in Fig. 2 except for the vortex region about 200 km to the west of the convective line.

3. SUMMARY AND CONCLUSIONS

Analysis of airborne Doppler radar data from a bow-echo MCS reveals similarities to circulation features hypothesized from earlier cases and those produced by a non-hydrostatic model simulations. Those structures include a pronounced eastward bulge in the convective line, a strong elevated rear inflow jet with its core near the apex of the bow, and a trailing region cyclonic vortex with maximum vorticity in low to mid levels. A possible mechanism for the generation of the strong rear inflow is the presence of mesoscale low pressure associated with buoyancy gradients to the systems rear (tilted updrafts) as shown by LeMone (1983). A possible source for the trailing stratiform region vortex is the tilting of environmental horizontal vorticity by the differential vertical motions within the MCS.

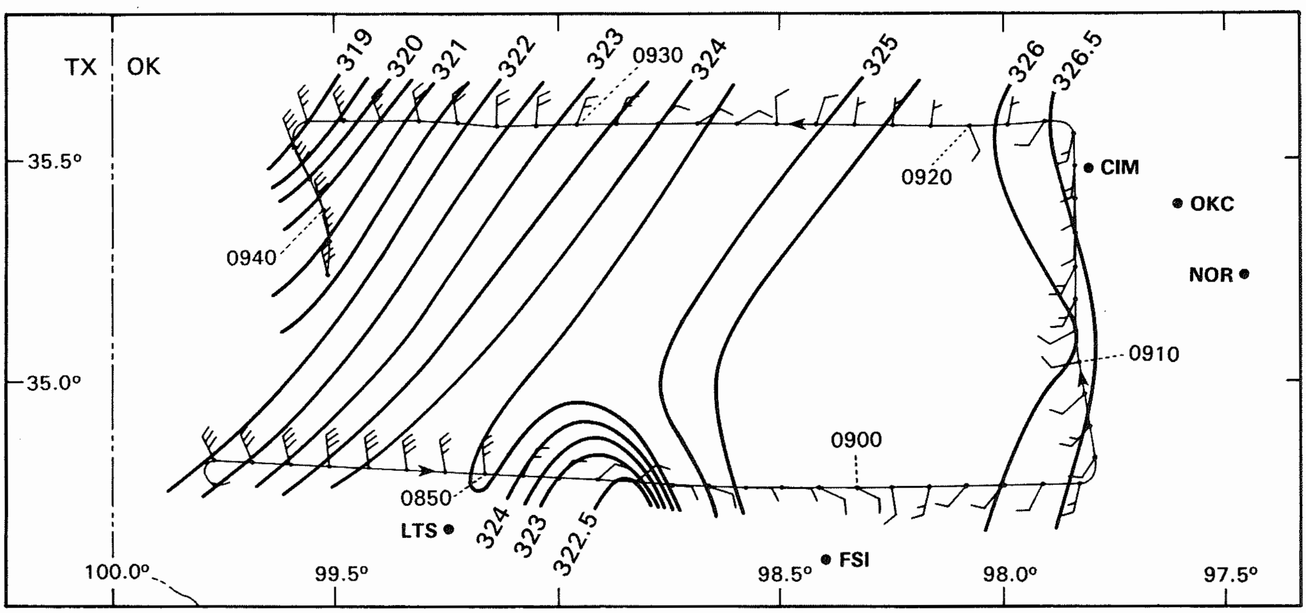

Fig. 4. P-3 flight track at 650 mb (~3.2 km AGL) between 0843 and 0945 UTC. State borders are shown as dotted lines. Wind barbs are in m/s with a full barb equal to 5 m/s. Numbers plotted at intervals along the flight track are equivalent potential temperature (°K). Time marks are shown along the flight track at 10 minute intervals.

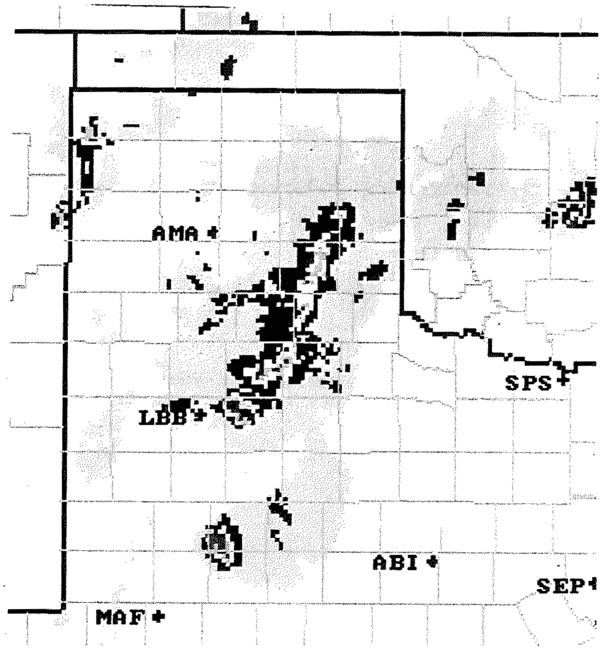

Fig. 5. Radar reflectivity at 0000 UTC on 8 May 1991. Reflectivity shading and map background as in Fig. 1. The location of the sounding in Fig. 6 is at AMA.

Ascending motion within the convective line lofts southerly momentum associated with the pre-storm environment, while descending motion in the trailing region brings down westerly momentum. With time it is hypothesized that an adjustment of mass and momentum occurs in the stratiform region leading to the generation of the surface wake low pressure region. Additional numerical simulations of bow echo evolution could address these mechanisms.

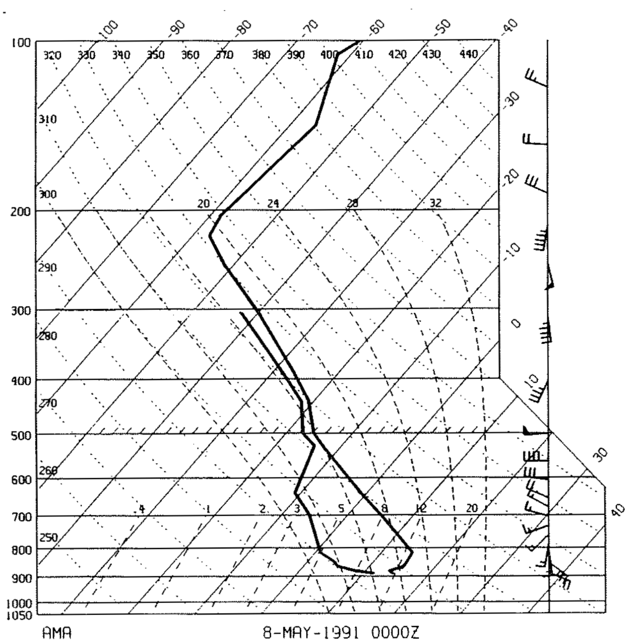

Fig. 6. SkewT–Log P plot of the AMA sounding at 0000 UTC 8 May 1991 just to the west of the convective line. Wind barbs are m/s with 1 full barb equal to 5 m/s.

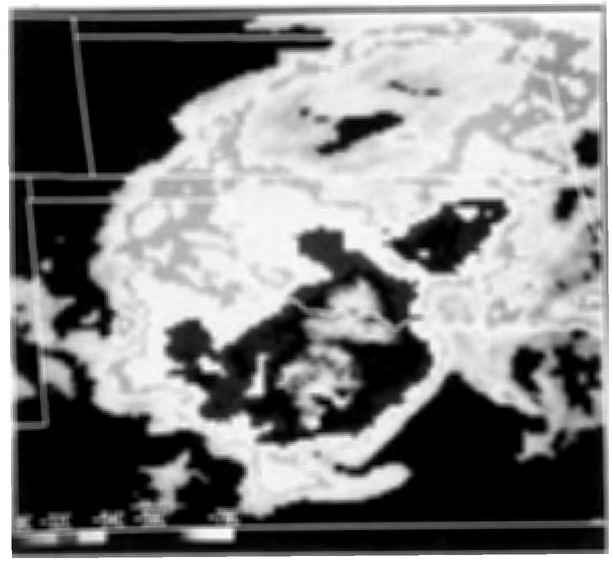

Fig. 7. Infrared satellite photograph depicting the system at 0500 UTC, 8 May 1991. State boundaries are shown in white with the cloud top temperature according to scale at bottom left.

Although "book-end" vortices have been seen in idealized numerical simulations of bow-echo convective systems (Weisman, 1990) the P-3 did not fly far enough south to determine whether a companion anticyclonic vortex existed at the southern end of the line. However, the presence of such a vortex is strongly suggested by the satellite photographs (e.g., 0500 UTC image in Fig. 7), which show a nearly symmetrical trailing anvil with a pronounced notch on its rear (northwest) side.

References

Burgess, D.W., and B.F. Smull, 1990: Doppler radar observations of a bow echo associated with a long-track severe windstorm. *Preprints, 16th Conf. on Severe Local Storms*, Kananaskis Park, Amer. Meteor. Soc., 203-208.

Fujita, T. T., 1978: *Manual of Downburst Identification for Project Nimrod.* Satellite and Mesometeorology Research Paper No. 156., Dept. of Geophysical Sciences, Univ. of Chicago, 104 pp.

Jorgensen, D. P., and J. D. DuGranrut, 1991: A dual-beam technique for deriving wind fields from airborne Doppler radar. *Preprints, 25th Intl. Conf. on Radar Meteor.*, Paris, France, Amer. Meteor. Soc., 458–461.

LeMone, M.A., 1983: Momentum transport by a line of cumulonimbus. *J. Atmos. Sci.*, **40**, 1815-1834.

Przybylinski, R. W., and W. J. Gery, 1983: The reliability of the bow echo as an important severe weather signature. *Preprints, 13th Conf. Severe Local Storms*, Tulsa, OK, Amer. Meteor. Soc., 270–273.

Weisman, M. L., 1990: The genesis of bow echoes: A rear-inflow induced meso-convective structure. NCAR Cooperative Thesis No. 125, 149 pp.

MICROWAVE AIRBORNE MEASUREMENTS OF INTEGRAL LWC IN TROPICAL CYCLONES

A.A.Chernikov[1], A.V.Koldaev[1], Yu.V.Melnichuk[1]

[1] **Central Aerological Observatory, Pervomayskaya 3, Dolgoprudny, Moscow Reg., Russia**

1. INTRODUCTION

The role of clouds in the dynamic structure and evolution of a tropical cyclone is not well understood. The effect of ice microphysics upon the dynamic structure of hurricanes is being studied with the aid of numerical hurricane models. The results indicate, that the presence of ice influences on the storm structure by maintaining mesoscale downdrafts near a $0^{\circ}C$ isotherm, over wide areas beyond an eyewall. The nucleation and growth of ice particles can stimulate cloud development through the release of additional latent heat and may affect on hurricane intensification. For this reason, it is important to measure the space distribution of supercooled liquid water content along azimuthal and radial directions, with respect to the hurricane center, because supercooled LWC zones are mostly suitable for rapid crystal growth.

In earlier work, experimental data on LWC were obtained by airborne 'in situ' probes, providing detailed information along the flight track. To obtain data on the vertical distribution of LWC by means of 'in situ' probes, several aircrafts at different heights are needed. Moreover, the reliability of such measurements in a tropical cyclone cloud system is questional, due to its complicated internal structure.

The experimental measurements presented in this paper were made by means of airborne microwave tomography (Koldaev et al, 1990). This technique permits us to obtain data on integral LWC and supercooled LWC distributions in the tropical cyclones 'Backy' and 'Ed' from board a single aircraft.

2. MEASUREMENTS' TECHNIQUE AND DATA PERFORMANCE

The airborne system consists of two microwave radiometers based on a superheterodyne modulation scheme. It is installed on board the Aircraft Meteolaboratory IL-18 "Cyclone" of Central Aerological Observatory. Characteristics of the radiometers were presented earlier (Chernikov et al, 1991). Each radiometer receives radiation from a definite direction with an appropriate antenna. The first direction was a forward one, along the aircraft track, 30 deg to horizon, the second being in the vertical. The sounding geometry is shown in Fig 1.

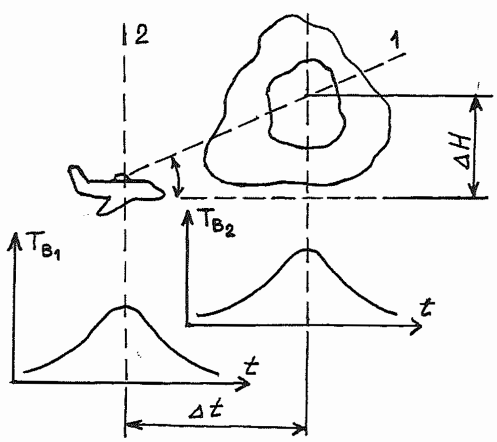

Fig 1. Two-beam sounding geometry. The diagrams below are the records of the first (I) and the second (II) beams, respectively.

As was shown in the paper by Koldaev et al, 1990, this airborne microwave sounding geometry allows one to reconstruct LWC vertical distribution by means of the algorithm of confirming projections. But for a tropical cyclone stratiform cloud system, when layer stratification is very pronounced, liquid water zones height can be estimated without reconstructing algorithms. Indeed, as is shown in Fig 1, a local liquid water zone, due to the sounding geometry, will be found, first, with an inclined beam and, second, with a vertical beam. The time delay between the maxima of the first and the second beams' records is coupled with the height of the zone center by a simple equation:

$$H = H_f + v \cdot \Delta t \cdot tg(\alpha) \quad (1)$$

where H_f - flight level,

v - true aircraft speed,

α - angle of the first beam inclination,

Δt - time delay.

For a cyclone cloud system, we can

assume the existence of a liquid water layer and therefore, can find preferable heights where multiple liquid water zones can be detected. For this reason, it is difficult to distinguish individual zones, and thus, a correlation function needs to be calculated for the first and the second beam records. The time delay is defined from the maximum of this function by solving the following equation:

$$\frac{\partial}{\partial t} \int_{t_2}^{t_1} T_I(t) \cdot T_{II}(t + t')dt' = 0 \qquad (2)$$

Substituting the delay to expression (1), it is possible to estimate the mean height of the liquid water layer. The width of the correlation function at a fixed level, with respect to the maximum will provide information on the layer thickness. The procedure described is more convenient for obtaining information about the vertical structure, while measuring under flight conditions, owing to the very short time required.

It's necessary to point out, that the sounding geometry imposes certain requirements on the piloting mode, because the difference between the aircraft longitudinal axis and flight direction must be less than 5 deg. Otherwise, the two beams' vertical plain doesn't coincide with that of the flight, and defining of mean height of LWC layer is impossible.

3. METEOROLOGICAL CONDITIONS OF FLIGHT EXPERIMENTS AND RESULTS

The aircraft measurements of LWC were made in autumn 1990 during the 5-th Soviet-Vietnamese flight expedition, with a base in Danang (Middle Vietnam) and the flights' region over the South-China Sea, in 'Backy' and 'Ed' cyclones.

The tropical cyclone "Backy" (9016) came to the region under investigation on 27 August. On 28 August a research flight was conducted. The flight started at 03.00 GMT, in the front part of the tropical cyclone cloud mass, along the circulation center transfer track. An undul aircraft return was caused by a technical trouble with the navigation system, from the point 112 deg E, 18 deg N. An extreme integral LWC was registered on the way back, while crossing a rain band. At that moment, the flight height was about 4 km and maximum integral LWC was over 6 kg/m^2. At distances of about 100 km from the circulation center, supercooled liquid water content of about 0.5 kg/m^2 was observed at a 5-km height.

Cyclone "Ed" reached the region under investigations in September. The first attempt to conduct a research flight was made on 15 September. However, the central cloud system was observed beyond the maximum flight range. The second flight started at 06.00 GMT on 16 September. Due to the restriction pointed out in Part 2, measurements by the tomography technique were to be carried out only in case of the flight track oriented along or opposite the wind at the flight level. For this reason, a loop scheme was chosen for the flight around the circulation center. The flight height for all the tracks was between 2 and 4 km. Maximum liquid water content in this flight didn't exceeded 1.5 kg/m^2 and was, on the average, 3 times lower than in the TC 'Backy'. This difference is evidently associated with the azimuthal asymmetry of the tropical cyclones cloud field. Thus, the flight in TC 'Backy' was conducted in the front part of cloud system, while that in TC 'Ed' in the northern, eastern and southern parts.

To investigate LWC distribution asymmetry in TC, an LWC azimuthal plot of the data of both cyclones was constructed (Fig 2).

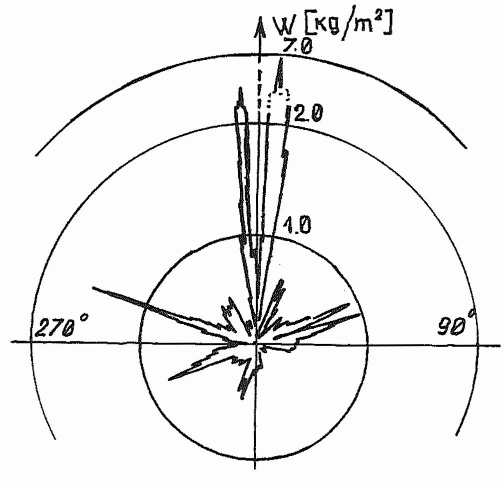

Fig 2. Azimuthal distribution of integral LWC, based on the data from the cyclones 'Backy' (9016) and 'Ed' (9018)

As can be seen from Fig 2, the azimuthal distribution of integral LWC is very inhomogenious, though a satellite IR image doesn't show any sufficient difference in the azimuthal structures. Large LWC values at azimuths near 0°C are associated with the flight through the rain band in TC 'Backy', though the cyclones were at the same evolution stage during both flights, and the flight track in TC 'Ed' also crossed a rain band.

The radial distribution of integral LWC is presented in Fig 3 by the cumulative curves.

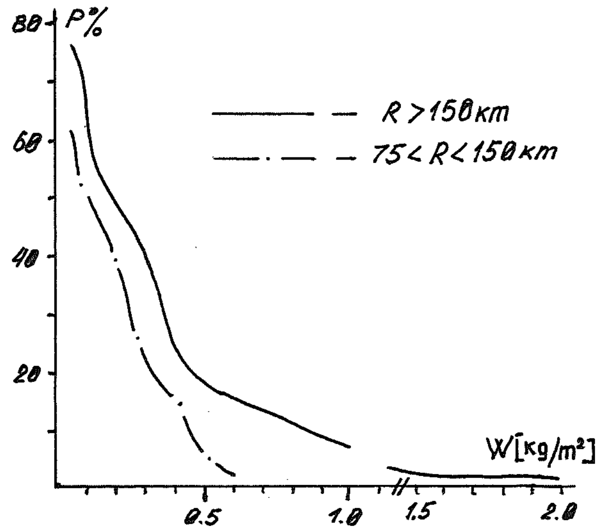

Fig 3. Cumulative distributions of LWC. The solid line presents the distribution within a circle with a 75-km internal radius and a 150-km external radius, the dotted line being for the flight outside a circle with a 100-km radius.

In order to construct the diagrams, we divided the flight track into portions lying inside and outside the circle with a 150-km radius. IR satellite images of both TC show us that the central cloud mass radius was about 300 km, for this reason, the value 150-km was chosen as a mean radius. After that, the probabilities of the existence of integral LWC in a definite range were derived for each flight portion. It is interesting to note that the distributions for the internal and external parts differ very strongly.

4. DISCUSSION

R.Black and J.Hallett (Black R.A., Hallett J., 1986) were the first to study hurricane microphysics at temperatures below $0^{\circ}C$. In particular, their observations were aimed at examining the convective areas of storms where supercooled water occurs in regions having of the likely release of latent heat. They found that, except for the strongest updrafts, hurricane convection cloud systems are largely glaciated at temperatures as low as $-5^{\circ}C$. In these hurricanes, small supercooled LWC was observed everywhere, except an eyewall. The authors have concluded that it is unlikely for a large amount of supercooled water to reach temperatures lower than $-10^{\circ}C$. The same conclusion lead to the cancelling of "STORMFURI" project (Willoughby H.E. et al, 1985).

As it is shown above, we have found in our experiments that at distances of about 100-km from TC circulation center, LWC values of about 0.1 kg/m^2 are characteristic of Ns clouds at middle altitudes, and the value of about 0.5 kg/m^2 frequently occurs at the periferal part of TC cloud system, at distances over 150-km. Our experiments were carried out using microwave remote sensing, and this may be the reason for such large differences in the LWC estimation in the periferal parts of tropical cyclone, because the spacial distribution is strongly inhomogenious, as can be seen from Fig 2, and LWC zones occur more frequently at large distances from the current TC circulation center, as we can see in Fig 3.

Further research to increase our understanding of the space-and-time distribution of supercooled LWC zones at different stages of the hurricane evolution is of great importance.

5. CONCLUSION

For the first time, aircraft measurements of integral LWC in the central part of a tropical cyclone cloud system were made using a microwave radiometric tomography system. These measurements show that supercooled liquid water in cyclonic clouds is localized at distances of 100-150 km apart from the circulation center. Supercooled LWC quantitatively looks like LWC in Ns clouds ($\simeq$ 0.1 $\div$ 0.5 g/m^3). The azimuthal distribution of integral LWC is clearly asymmetric. The detailed examining of LWC in combination with aircraft radar and 'in situ' data will be of great interest for the future studies.

References:

Black, R.A., Hallett, J., 1986: Observations of the distribution of ice in hurricanes. J Atmosph Sci, Vol 43, N 8, pp 802-822

Chernikov, A.A., Koldaev, A.V., Melnichuk, Yu.V., 1991: Remote sensing of liquid water content in tropical cyclones 'Backy' and 'Ed'. Proc 19-th Conf Hurricanes and Tropical Meteorology, Miami, pp 590-593

Koldaev, A.V., Melnichuk, Yu.V., Mironov, A.F., Agapov, Yu.V., Dmitriev, V.V., Nikolski, A.N., 1990: The application of aircraft microwave radiometric tomography in weather modification experiments. Proc 20-th European Microwave Conf, Budapest, Vol 2, pp 1402-1407, Microwave Exhibitions and Publishers Ltd.

Willoughby, H.E., Jorgensen, D.P., Black, R.A., Rosenthal, S.L., 1985: Project STORMFURY: a scientific chronicle 1962-1983. Bul Amer Meteorol Soc, Vol 66, N 5, pp 505-514

STRATIFORM VERTICAL MOTION STRUCTURE IN TROPICAL STORMS

Robert Cifelli and Steven A. Rutledge

Department of Atmospheric Science
Colorado State University
Fort Collins, Colorado 80523

1. INTRODUCTION

Recent studies have suggested that vertical motions in the stratiform regions of tropical Mesoscale Convective Systems (MCS's) occur on the mesoscale (Leary and Houze 1979, Brown 1979, Houze 1989, and Johnson, 1992). Moreover, Houze (1989) has shown that the vertical motion profile in the stratiform region typically consists of a region of mesoscale ascent in the upper portion of the profile and a region of mesoscale descent in the lower portion of the profile. Houze (1989) further argues that these profiles of stratiform vertical motion are persistent features of tropical MCS's.

The purpose of this paper is to compare two separate methods for evaluating the structure and time evolution of stratiform vertical motion profiles at the mesoscale and sub-mesoscale in two tropical MCS's diagnosed from single Doppler radar and wind profiler data. The data were collected during the 1989-1990 DUNDEE (Down Under Doppler and Electricity Experiment) field experiment near Darwin, Australia (Rutledge et al., 1992). Two 5-cm single Doppler radars (MIT and TOGA) were utilized in conjunction with the NOAA/BMRC Darwin wind profiler to sample tropical convection during DUNDEE. The location of the radars and the wind profiler are shown in Figure 1. The two analysis methods include:

1. the Extended Velocity Azimuth Display (EVAD) technique for single Doppler radar data; and

2. a combination of a fully automated data processing technique based on a method described by Sato et al. (1990) and manual editing to analyze precipitation and turbulence components of wind profiler spectral data.

The former method allowed for calculation of the average vertical velocity field in a 30 km range cylinder surrounding the radar, while the latter method provided quasi-two dimensional vertical motion information averaged over a similar time interval but over a much smaller spacial domain than the EVAD technique. A comparison of these techniques provided information on the limitation of single Doppler radar for measuring vertical motions in MCS's and insight into the uniformity of stratiform vertical motion between the sub-mesoscale and the mesoscale. A description of both the EVAD and wind profiler spectral data analysis techniques is provided in the Methodology section of this paper. The first MCS we study occurred on December 5, 1989 and was representative of monsoon break conditions. The second MCS occurred on January 12, 1990 in a monsoonal regime.

2. CASE DESCRIPTIONS

The December 5, 1989 storm formed approximately 80 km south of the Darwin area during the monsoon break period. The MCS formed initially as scattered convective cells and then consolidated into a solid line oriented east-west (Rutledge et al., 1991). The system moved to the north, passing over Darwin, and then out to sea. The maximum vertical extent of radar echos in the convective line was approximately 18 km. The line weakened as it approached the radar baseline and the stratiform region began to develop. The stratiform region was sampled from 1010 to 1120 UTC at approximately one-half hour increments (see Rutledge et al. 1991 for a more detailed description of the storm motion).

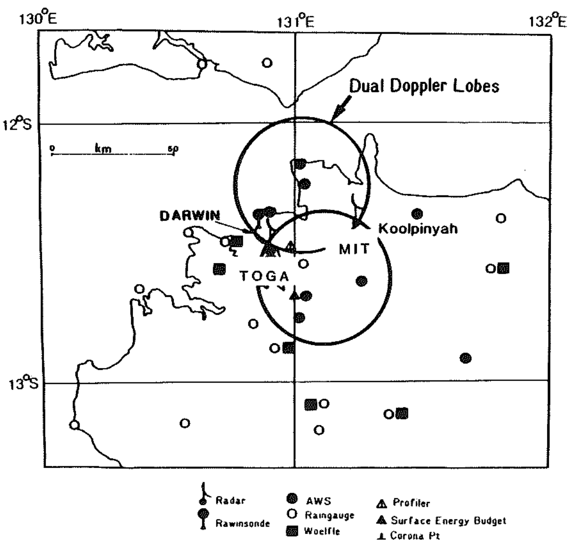

Figure 1. Location of the MIT and TOGA radars and the Darwin wind profiler used during the DUNDEE field experiment.

The January 12, 1990 MCS consisted of a monsoonal rainband with an associated stratiform region which formed in a low CAPE, low shear environment (Keenan and Rutledge, 1992). The system formed as several convex NW-SE oriented monsoon bands embedded in the low-level westerly flow north of Darwin. The bands moved onshore and S-SE across the Darwin area and then merged with cells forming along a sea breeze front east of Darwin. A large stratiform region developed in a NE-SW orientation over Darwin which moved at about 5.5 m/s toward the SE. The stratiform region was sampled from 1100 to 1200 UTC at one half hour intervals.

3. METHODOLOGY

a. EVAD Analysis

The EVAD analysis package was written by Tom Matejka of ERL at NOAA in Boulder, CO. The technique is discussed in Srivastava et al. (1986) and Matejka et al. (1991). The EVAD program package consists of two parts:

1. VAD analysis which generates horizontal rings of radial velocity data for each elevation cone within a specified volume of radar data; and

2. EVAD analysis which calculates divergence, hydrometeor fall-speed, hydrometeor terminal fall speed, and vertical velocity as a function of altitude within a specified volume of VAD data.

We initially scrutinized individual volume scans to determine the suitability of the VAD/EVAD technique for each volume of data. For the two cases analyzed, radar elevation angles ranged from 1-45 degrees. The time required to complete an individual EVAD volume scan was approximately 10 minutes.

The VAD routine utilizes Fourier analysis to calculate radial velocity on horizontal rings centered on the radar. To run the VAD program, a 60 km cylinder radius with a 20 km top boundary was specified. The maximum allowed azimuthal gap within a ring of radar data was set at 30 degrees.

In order to apply the EVAD technique, it is assumed that hydrometeor fall-speed and divergence are horizontally homogeneous within a given vertical layer. The depth of each layer is determined from the radar gate spacing and is constant throughout the EVAD volume cylinder.

The EVAD technique is particularly sensitive to the location of the top boundary of the EVAD cylinder. The altitude of the highest echo from the steepest elevation scan was utilized as the location of the top boundary and it was assumed that the vertical velocity at this point was zero. It was also assumed that the vertical velocity was zero at the altitude of the radar above sea level (bottom boundary). The echo top calculated from the steepest elevation angle scan, as opposed to lower elevation angle scans, was taken to represent the location of the top boundary, since steeper elevation angles provided a minimum of side lobe interference. In both of the MCS's analyzed, the EVAD cylinder radius was 30 km, which allowed for considerable overlap in data coverage between the MIT and TOGA radars (see Figure 1).

b. Wind Profiler Data Analysis

The Darwin wind profiler operates at a frequency of 50 MHZ and is therefore sensitive to both clear air vertical motion and precipitation particle fallspeeds (Carter et al., 1991). In order to extract the clear air motion from the data, a combination of methods was developed to extract the clear air signal from the precipitation signal in the raw spectra.

First, an algorithm to derive both atmospheric turbulence and precipitation parameters was developed based on the method described by Sato et al. (1990). The Sato et al. technique utilizes a Marshall-Palmer distribution to approximate the precipitation component of the spectra and a Gaussian distribution to fit the turbulence component.

Sensitivity analysis with this curve fitting program showed that the algorithm provided reasonable "fits" to double peaked spectra below the melting-level and above about 9 km (AGL); however, in the region between approximately 4.5-9 km, the program usually was unable to distinguish between the clear air and precipitation signal peaks. This was probably due to the existence of rain, snow, and ice hydrometeor species in the mixed phase region of the cloud (Carter et al., 1991). Because the mixed phase hydrometeor species have different fallspeeds, the spectral signals from the turbulence and precipitation components "merged together" and the program attempted to fit both the turbulence and precipitation signal with a single Gaussian curve. In other words, the algorithm was unable to separate clear air vertical motion from the precipitation fallspeed.

Merging of the precipitation and turbulence signals caused a misalignment between the center of the turbulence peak power signal and the center of the Gaussian curve fit (i.e. mean vertical velocity). In these cases, the center of the Gaussian was manually edited so that the mean clear air vertical motion coincided with the approximate location of the turbulence peak power. In general, the precipitation signal decreased significantly above about 9 km so that the program was able to fit the spectra reasonably well with a single Gaussian approximation.

An arbitrary threshold of signal to noise was developed in order to determine if the signal at a particular level represented meteorologically significant data or was part of the noise spectrum. If the ratio of log(signal peak) / log(noise), determined by the curve fitting algorithm, was below about 1.2, it was assumed that the signal was not significant and a vertical velocity value was not determined at this level. Since the signal power decreased gradually with height, there were many borderline cases where the ratio was approximately 1.2. In these situations, continuity of the location and width of the signal with similar signals at lower levels where the threshold was exceeded was used in order to help determine if the level in question had a meteorological significant signal.

The location of the profiler approximately along the baseline between the two radars (see Figure 1) allowed for vertical motion sampling of a particular MCS at a much smaller spacial scale than the EVAD method. In order to compare the EVAD vertical velocity field with the profiler results, individual spectra were averaged over a 10 minute time period centered on the EVAD analysis time. In this way, vertical motions in the MCS at a particular time could be sampled at both the mesoscale and sub-mesoscale. Within the averaged spectral data, individual spectra were scrutinized in order to avoid contaminating the averaged results with spurious spectral power signals (i.e. radio noise, etc).

4. RESULTS

Vertical velocity profiles for the December 5, 1989 break period MCS are shown in Figure 2 (a-d). All four of the profiles shown in Figure 2 were produced in the stratiform region of the MCS, based on inspection of radar reflectivity data. The 1010 UTC and 1040 UTC EVAD profiles (panels a-b of Figure 2) were generated using MIT radar data and the 1100 UTC and 1120 UTC EVAD plots were generated using TOGA radar data. The plots show mostly mesoscale descent throughout the EVAD profiles. The magnitude of the EVAD vertical motion is on the order of 0.1-0.3 m/s.

In contrast to the EVAD data, the wind profiler generally shows upper level ascent and variable regions of ascent and descent at lower levels in the profiles. Peak magnitudes of ascent sampled by the wind profiler ranged from 0.4-0.6 m/s and maximum downdrafts ranged up to 1.2 m/s. With the exception of the 1040 UTC plot (panel b in Figure 2) the overall shape of the wind profiler vertical velocity field at each of the times shown is similar to the EVAD vertical motion field throughout the range of the EVAD profile; however, the wind profiler vertical velocities tend to be of larger magnitude and are more variable than the corresponding EVAD values. This is probably due to the fact that the EVAD generates an average profile over a much larger spacial area compared with the wind profiler.

The wind profiler data also shows a region of upper level vertical motion extending from about 2.5-4.5 km above the top of the EVAD profiles (Figure 2). With the exception of the 1100 UTC plot (panel c in Figure 2), the upper level vertical motion is all positive (i.e. ascent). The location of the base of this upper level ascent region occurred between about 8.5 km (1040 UTC) and 12 km (1100 UTC). The total depth varied during the analysis period, ranging from about 1.7 km (1100 UTC) to 4.7 km (1040 UTC and 1120 UTC).

Vertical velocity profiles for the January 12, 1990 MCS are shown in Figure 3 (a-c). All three plots shown in Figure 3 were generated after the convective line passed southeast over Darwin and are representative of stratiform conditions within the MCS. EVAD's from both radars show similar vertical motion profiles for each of the times indicated in Figure 3. Similar to the December 5, 1989 case, the EVAD profiles show mostly mesoscale descent with peak magnitudes ranging up to 0.3 m/s. Weak updrafts (< 0.1 m/s) occurred in both radar profiles above about 8-9 km at 1100 UTC and 1200 UTC.

The wind profiler vertical motion field shows the same basic structure as the EVAD vertical motion field within the boundaries of the EVAD profile; however, similar to the December 5, 1989 MCS,

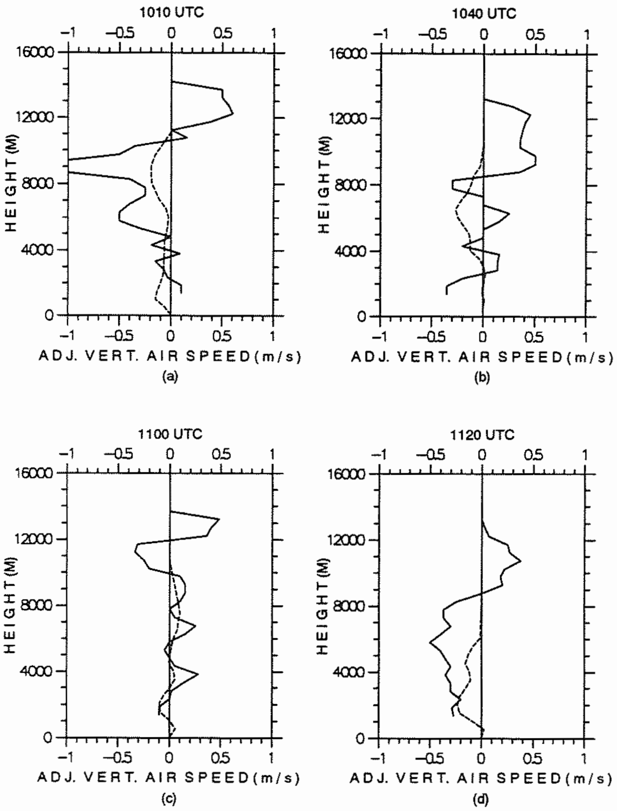

Figure 2. Wind profiler (solid) and EVAD (dashed) vertical velocity profiles for the December 5, 1989 break period MCS. EVAD plots shown in (a) and (b) were produced from the MIT radar. EVAD plots shown in (c) and (d) were produced from the TOGA radar. Analysis times are indicated at the top of each plot.

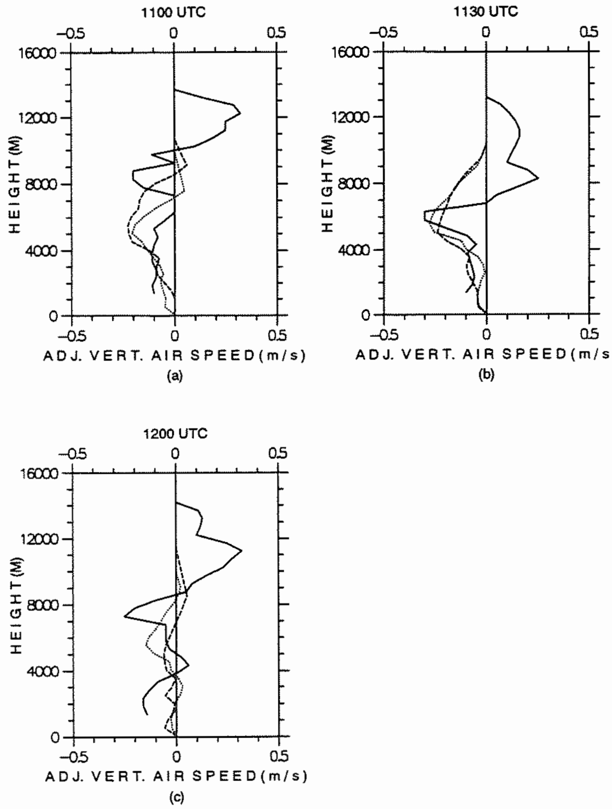

Figure 3. Wind profiler (solid), EVAD-MIT (dashed), and EVAD-TOGA (dotted) vertical velocity profiles for the January 12, 1990 monsoonal MCS. Analysis times are indicated at the top of each plot. Note the horizontal scale change compared with Figure 2.

the profiler detected a significant region of ascent above the top of the corresponding EVAD profile. Peak magnitudes of the upper level updraft were on the order of 0.3 m/s. As shown in Figure 3, the top of the detectable vertical motion in the wind profiler plots ranged from about 2.5 to 3.0 km above the corresponding top of the EVAD profiles. The base of the upper level ascent region in the wind profiler analysis ranged from about 7.0 km (1130 UTC) to about 10 km (1100 UTC). The depth of the upper level ascent zone generally increased from about 3.1 km (1100 UTC) to 5.5-6.1 km (1200 and 1130 UTC, respectively) during the analysis period.

The reason for the relatively low top boundary location in the EVAD profiles compared with the wind profiler vertical velocity field in both of the MCS's studied was probably due to a combination of attenuation of the radar beam and small ice particle sizes in the upper portion of the stratiform cloud (less than the detection threshold of the radar). This combined effect prevented the radars from sampling motions in the vicinity of the cloud-top boundary and produced large gaps in the radar data. Large gaps (i.e. > 30-45 degrees) violated the implicit VAD assumption of a continuous wind field and therefore prevented the processing of many upper level rings of VAD data.

5. CONCLUSIONS

The results of this study indicate that the overall shape of the vertical motion profile generated with single Doppler radar data (EVAD) is similar to the corresponding vertical motion field of wind profiler data within the boundaries of the EVAD profile. Within the limits of the EVAD boundaries, the wind profiler exhibited larger magnitudes and greater variability of clear air vertical velocity than the corresponding EVAD profile.

At upper levels, however, the wind profiler detected a significant region of upper level vertical motion in the stratiform region that was usually "not seen" with the EVAD analysis technique. This upper level vertical motion, ranging from about 2.0-4.5 km above the top of the EVAD vertical velocity profile, was mostly positive (ascent) and was a persistent feature during the time evolution of the stratiform region. In the monsoon case, the depth of the upper level ascent zone generally increased during the evolution of the storm; however, in the break period MCS, the depth of the upper level ascent region was more variable.

The fact that the wind profiler sampled a significant region of vertical motion above the top boundary as observed by the Doppler radars has important implications for MCS heating calculations. The results of this analysis suggest that heating calculations based on single Doppler radar may not provide an accurate representation of the stratiform heat budget.

6. ACKNOWLEDGEMENTS

This work was supported by the grant ATM-9015485 from NSF and the contract NA90RAH00077 from NOAA (Office of Global Programs - TOGA/COARE). Drs. T. Keenan and P. May of BMRC and Dr. T. Matejka of NOAA/NSSL contributed to this research.

7. REFERENCES

Brown, J.M., 1979: Mesoscale unsaturated downdrafts driven by rainfall evaporation: a numerical study. J. Atmos. Sci, 36, 313-338.

Carter, D.A., Ecklund, W.L., McAfee, J.R., Gage, K.S., Keenan, T., and Manton, M., 1991: Results from the first year of observations using the Darwin VHF wind profiler. Preprint, 25th International Conf. on Radar Meteorology, AMS, June 24-28, 1991, Paris, France.

Houze, R.A., 1989: Observed structure of mesoscale convective systems and implications for large-scale heating. Quart. J. Meteor. Soc., 115, 425-461.

Johnson, R.H., 1992: Heat and moisture sources and sinks of Asian Monsoon precipitating systems. J. Meteor. Soc. Japan, 70, 353-372.

Keenan, T.D., and Rutledge, S.A., 1992: Mesoscale characteristics of monsoonal convection and associated stratiform precipitation. Mon. Wea. Rev., in press.

Leary, C.A. and Houze, R.A., 1979: The structure and evolution of convection in a tropical cloud cluster. J. Atmos. Sci., 36, 437-457.

Matejka, T. and Srivastava, R.C., 1991: An improved version of the Extended Velocity-Azimuth Display Analysis of single Doppler radar data. J. Atmos. and Oceanic Tech., 8, 453-466.

Rutledge, S.A., Williams, E.R., Peterson, W.A., and Rasmussen, E.N., 1991: Radar and electrical study of a tropical squall line near Darwin, Australia during DUNDEE. Preprint, 25th International Conf. on Radar Meteorology, AMS, June 24-28, 1991, Paris, France.

Rutledge, S.A., Williams, E.R., and Keenan, T.D., 1992: The Down Under Doppler and Electricity Experiment (DUNDEE): overview and preliminary results. Bull. Amer. Meteor. Soc., 73, 3-16.

Sato, T., Doji, H., Iwai, H., Kimura, I., Fukao, S., Yamamoto, M., Tsuda, T., and Kato, S., 1990: Computer processing for deriving drop-size distributions and vertical air velocities from VHF Doppler radar spectra. Radio Science, 25, 961-973.

Srivastava, R.C., Matejka, T.J., and Lorello, T.J., 1986: Doppler radar study of the trailing anvil region associated with a squall line. J. Atmos. Sci., 43, 356-377.

HORIZONTALLY VARYING EFFECTS OF PRECIPITATION ON THE AIRFLOW IN THE STRATIFORM REGION OF MESOSCALE CONVECTIVE SYSTEMS

Thomas Matejka

Mesoscale Research Division, National Severe Storms Laboratory, NOAA
Boulder, Colorado

1. INTRODUCTION

Besides containing regions of persistent convection, mesoscale convective systems often contain large regions of stratiform cloud and precipitation. These stratiform regions are characterized by well-defined mesoscale circulations. The mesoscale circulations are, at a fundamental level, convectively driven, as suggested by Brown (1979) and Maddox (1980). However, the mesoscale circulations also appear to be accelerated and modified by the diabatic heating and cooling associated with the sustained precipitation processes within the stratiform region itself.

In this paper, I describe the first work in a study designed to examine the energetics of the branches of the mesoscale airflow in mesoscale convective systems. One of the goals of this study is to describe and quantify the effects of microphysical processes on the evolving airflow in the stratiform region. An understanding of this interaction may help us determine to what extent microphysical processes are responsible for the acceleration of the airflows, for halting the acceleration, and for the ultimate dissipation of the mesoscale airflows and the convective system itself.

In this paper, I have concentrated on the cooling of air in the middle-level rear inflow by evaporating rain. I have used Doppler radar data to compare the rates of cooling at different locations within the rear inflow air as this stream traverses the stratiform region.

2. METHOD OF ANALYSIS

Three volumes of data from each of two Doppler radars were analyzed to produce fields of horizontal and vertical air velocity at three times. Horizontal perturbation pressure and horizontal perturbation buoyancy fields were deduced from these data from the time-dependent equations of motion as outlined by Gal-Chen (1978). Horizontal perturbation pressure tendency and horizontal perturbation buoyancy tendency fields were deduced from the same data as outlined by Matejka (1989).

The horizontal perturbation buoyancy state and tendency fields were expressed in terms of virtual potential temperature. Since the effect of horizontal perturbation precipitation weight on the horizontal perturbation buoyancy is small for stratiform precipitation, it was ignored. A field of the substantive derivative of the horizontal perturbation virtual potential temperature $\hat{\theta}_v'$ was computed as

$$\frac{D\hat{\theta}_v'}{Dt} = \left(\frac{\partial\hat{\theta}_v'}{dt}\right)_{U,V} + (u-U)\frac{\partial\hat{\theta}_v'}{dx} + (v-V)\frac{\partial\hat{\theta}_v'}{dy} + w\frac{\partial\hat{\theta}_v'}{dz}. \qquad (1)$$

Here, u, v, and w are the air velocity components in the x, y, and z directions, and t is time. The local time derivative is computed in a frame of reference whose x and y velocity components are U and V. In this study, this frame of reference was taken to be the most stationary frame of reference to reduce errors resulting from courser data resolution in time than in space.

The horizontal perturbation virtual temperature is related to the actual virtual temperature θ_v by

$$\theta_v = \tilde{\theta}_v + \hat{\theta}_v', \qquad (2)$$

where $\tilde{\theta}_v$ is only a function of z and is not recoverable from the equations of motion. The substantive derivative of $\hat{\theta}_v'$ is thus related to the substantive derivative of θ_v by

$$\frac{D\theta_v}{Dt} = \frac{D\hat{\theta}_v'}{Dt} + w\frac{d\tilde{\theta}_v}{dz}. \qquad (3)$$

The first law of thermodyamics is

$$\frac{\delta h}{\delta t} = c_{pd}\pi_0\frac{D\theta_v}{Dt} \qquad (4)$$

$$\pi_0 = \left(\frac{p_0}{p_{00}}\right)^{R_d/c_{pd}}, \qquad (5)$$

where $\delta h/\delta t$ is the rate at which heat is added to the air per mass, c_{pd} is the specific heat at constant pressure of dry air, R_d is the specific gas constant for dry air, p_0 is the hydrostatic pressure of the unperturbed atmosphere and is a function only of z, and p_{00} is 10^5 Pa.

If (4) is applied only in regions in which diabatic heating results from the evaporation of rain, then

$$\frac{\delta h}{\delta t} = -L_v\frac{\delta q_{lv}}{\delta t}, \qquad (6)$$

where L_v is the latent heat of vaporization and $\delta q_{lv}/\delta t$ is the rate at which liquid water mass is evaporating per mass of air. Therefore,

$$\frac{\delta q_{lv}}{\delta t} = -\frac{c_{pd}\pi_0}{L_v}\frac{D\hat{\theta}_v'}{Dt} - \frac{c_{pd}\pi_0}{L_v}w\frac{d\tilde{\theta}_v}{dz}. \qquad (7)$$

The evaporation rates at two points, A and B, can be compared:

$$\left(\frac{\delta q_{lv}}{\delta t}\right)_B - \left(\frac{\delta q_{lv}}{\delta t}\right)_A =$$

$$-\frac{c_{pd}}{L_v}\left[\pi_{0B}\left(\frac{D\hat{\theta}'_v}{Dt}\right)_B - \pi_{0A}\left(\frac{D\hat{\theta}'_v}{Dt}\right)_A\right]$$

$$-\frac{c_{pd}}{L_v}\left[\pi_{0B}w_B\left(\frac{d\tilde{\theta}_v}{dz}\right)_B - \pi_{0A}w_A\left(\frac{d\tilde{\theta}_v}{dz}\right)_A\right]. \quad (8)$$

Since $\tilde{\theta}_v$ is not known, this comparison can only be performed at the same altitude at locations with the same value of w, in which case the last bracketed term vanishes.

Note that this comparison of evaporation rates is derived solely and directly from the air motions. Other researchers have used the first law of thermodynamics along with the equations of motion to derive thermodynamic fields (Roux 1985, 1988; Hauser et al. 1988). However, in those studies, modelled precipitation processes and concentrations were used with the first law to determine the diabatic heating field and $\tilde{\theta}_v$; in addition, a partial steady-state assumption was made. In this study, neither has steady state been assumed nor are there any model assumptions regarding the concentrations or behavior of water. However, the power to deduce diabatic heating and phase change rates is correspondingly restricted as described previously.

3. DESCRIPTION OF THE CASES

Rear inflow at middle levels into the stratiform region frequently occurs in mesoscale convective systems (Smull and Houze 1987). Two cases are shown in Figs. 1–2. Fig. 1 depicts the stratiform region of a squall line that occurred in Kansas on 11 June 1985 and that was observed as part of the Oklahoma-Kansas PRE–STORM Project. Fig. 2 depicts the stratiform region of a mesoscale convective system that occurred in Oklahoma on 4 June 1989 as part of Cooperative Oklahoma P-3 Studies (COPS–89). All analyses were performed in three spatial dimensions; however, for convenience, the analyses have been averaged in the direction in which convection was aligned and displayed as vertical sections perpendicular to the direction of aligned convection. The zone of convection is not included in either analysis region.

In Fig. 1, relative inflow from the rear entered the system between an altitude of 3 and 6 km. This stream of air descended toward the front of the system and, after passing through light precipitation, traversed the broad rainband that was the zone of maximum stratiform precipitation, indicated by the well-defined maximum in radar reflectivity factor in the melting layer at 3.5 km. The 0°C level was at approximately 4.3 km. After traversing the rainband, the rear inflow stream again passed through light precipitation behind the convective line.

A similar situation occurred in Fig. 2. Relative rear inflow occurred from the ground up to 5 km. Again, the rear inflow traversed the stratiform region, which included an embedded rainband.

4. THERMODYNAMIC ANALYSIS

There are two factors that could effect the rate of evaporative cooling of the rear inflow stream: the amount of precipitation falling through the airstream and the degree of subsaturation of the airstream. Subsaturation will be enhanced by descent of the stream, such as was occurring in the two cases.

Figs. 3–4 show the horizontal perturbation virtual temperature field $\hat{\theta}'_v$ in the two cases. For altitudes at and below the melting layer, the axis of minimum $\hat{\theta}'_v$ was aligned closely with the stratiform region rainband. This is particularly clear if $\hat{\theta}'_v$ is examined along streamlines of the rear inflow. This strong negative perturbation, therefore, shows the strong cooling accomplished by the precipitation in the rainband, as opposed to the much weaker cooling accomplished by the lighter precipitation ahead of and behind the rainband.

5. EVAPORATION CALCULATIONS

More insight into the evaporation process can be obtained by examining the substantive derivative of $\hat{\theta}'_v$ for the PRE–STORM case in Fig. 5. Here, it is clear that, in fact, the most intense cooling was occurring when the rear inflow air first entered the rain shaft of the stratiform region rainband. By the time the air had traversed the rainband, the evaporation rate had diminished considerably, probably because the air was no longer so subsaturated. The alignment of the cold axis with the rainband in Fig. 3, then, was a result of cooling on the upwind side of the rainband followed by advection of this cooler air into the center of the rainband.

The evaporation rates can be made more quantitative by applying (8). Points A, B, and C in Fig. 5 are at an altitude of 2.9 km and had vertical air velocities of -0.50 m s^{-1}. The evaporation rate $\delta q_{lv}/\delta t$ at A was 0.0095 h^{-1} greater than at C, At B it was 0.0018 h^{-1} greater that at A. This shows that evaporative cooling was stronger as the rear inflow air entered the region of more intense rain than it was downwind of the rainband.

Points D, E, and F in Fig. 5 are at an altitude of 2.9 km and had vertical air velocities of -0.35 m s^{-1}. The evaporation rate at E was 0.0049 h^{-1} greater than at F, and it was 0.0041 h^{-1} greater at D than at E. This shows that the evaporation rate was greater just as rear inflow air was entering the region of more intense rain than it was in the center of the rainband, probably because the subsaturation had decreased by the time the air had reached the most intense precipitation shaft. However, the evaporation rate was still greater in the center of the rainband than it was downwind of the rainband, where the lighter precipitation and decreased subsaturation apparently prevented strong evaporation from occurring.

6. CONCLUSIONS

Using only time-dependent air velocity fields derived from Doppler radar data, the pattern of evaporative cooling of rear inflow air in the stratiform regions of mesoscale convective systems was deduced. Evaporation was found to be most intense just as the rear inflow air entered the region of relatively strong precipitation associated with the stratiform region rainband. It was weaker in the center of the rainband, probably because of reduced subsaturation. It was weakest downwind of the rainband, probably because of reduced subsaturation and less precipitation to evaporate. The advection of cool air forward displaced the actual region of coldest air to within the rainband.

REFERENCES

Brown, J. M., 1979: Mesoscale unsaturated downdrafts driven by rainfall evaporation: a numerical study. *J. Atmos. Sci.*, **36**, 313–339.

Hauser, D., F. Roux, and P. Amayenc, 1988: Comparison of two methods for the retrieval of themodynamic and microphysical variables from Doppler radar measurements: application to the case of a tropical squall line. *J. Atmos. Sci.*, **45**, 1285–1303.

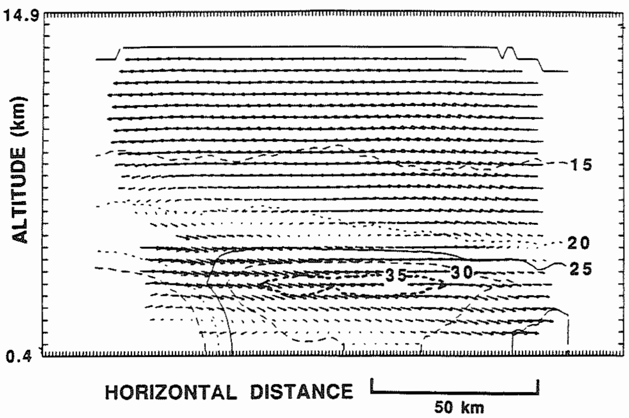

Fig. 1. Vertical cross section perpendicular to the 11 June 1985 squall line showing along-line average radar reflectivity factor (contoured at the minimum detectable signal and every 5 dBZ starting at 15) and along-line average air velocity relative to the most stationary reference frame (arrows, length corresponds to a 5 min displacement). The leading convective line is off the frame to the right.

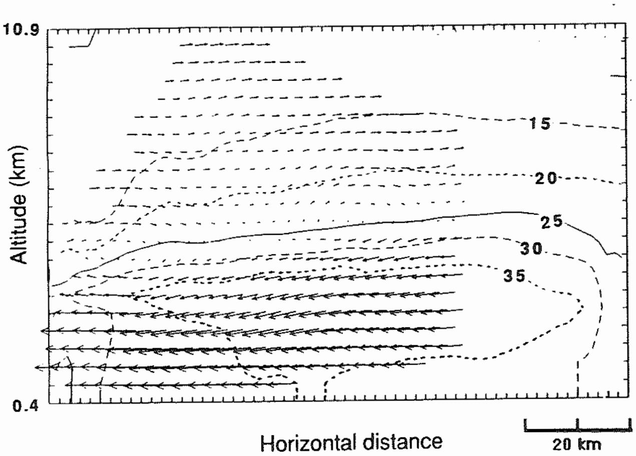

Fig. 2. As in Fig. 1 for the 4 June 1989 mesoscale convective system. The region of convection is off the frame to the left.

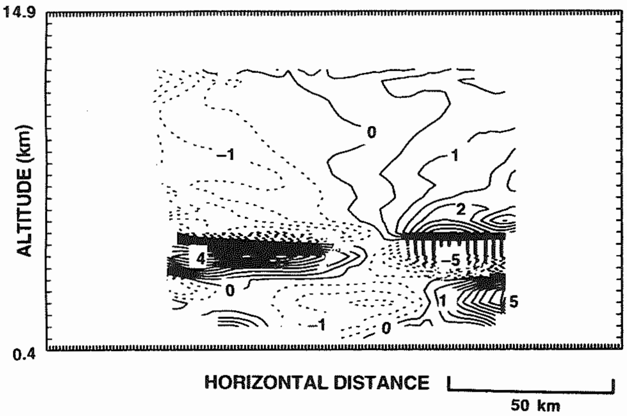

Fig. 3. Vertical cross section perpendicular to the 11 June 1985 squall line showing along-line average horizontal perturbation virtual potential temperature (contoured every 0.5 K).

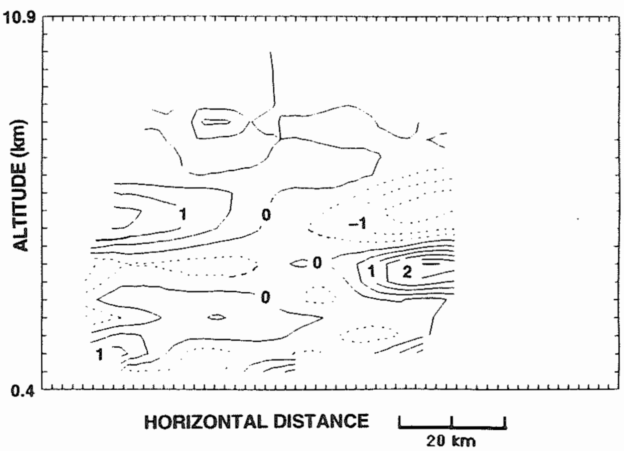

Fig. 4. As in Fig. 3 for the 4 June 1989 mesoscale convective system.

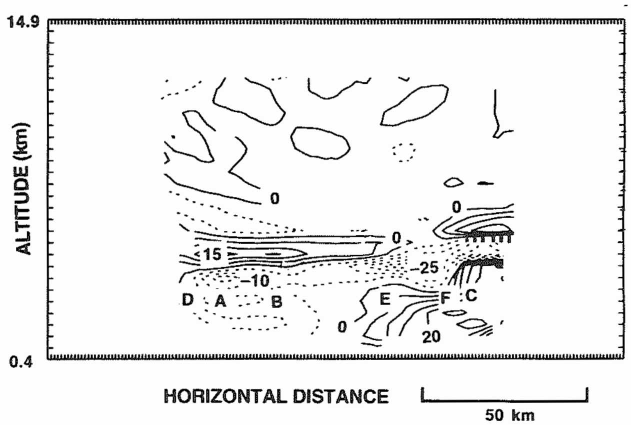

Fig. 5. Vertical cross section perpendicular to the 11 June 1985 squall line showing the along-line average substantive derivative of horizontal perturbation virtual potential temperature (contoured every 5 K h^{-1}).

Gal-Chen, T., 1978: A method for the initialization of the anelastic equations: implications for matching models with observations. *Mon. Wea. Rev.,* **106**, 587–696.

Maddox, R. A., 1980: Mesoscale convective complexes. *Bull. Amer. Meteor. Soc.,* **61,** 1374–1387.

Matejka, T., 1989: Pressure and buoyancy forces and tendencies in a squall line and their relation to its evolution. *Proc., 24th Conf. Radar Meteor.,* Talahassee, Fla., Amer. Meteor., Soc., Boston, Mass., 478–481.

Roux, F., 1985: Retrieval of thermodynamic fields from multiple-Doppler radar data using the equations of motion and the thermodynamic equation. *Mon. Wea. Rev.,* **113,** 2142–2157.

Roux, F., 1988: The West African squall line observed on 23 June 1981 during COPT81: kinematics and thermodynamics of the convective region. *J. Atmos. Sci.,* **45,** 406–426.

Smull, B. F., and R. A. Houze, Jr., 1987: Rear inflow in squall lines with trailing stratiform precipitation. *Mon. Wea. Rev.,* **115,** 2869–2889.

MESOSCALE CONVECTIVE COMPLEXES IN AFRICA AND THE INDIAN SUBCONTINENT

A. Laing and J.M. Fritsch

The Pennsylvania State University
Department of Meteorology
University Park, PA 16802

1. INTRODUCTION

During the past decade, much attention has been given to the distribution, organization and forecasting of mesoscale convection. Much of this interest has focused on the Mesoscale Convective Complex (MCC) (Maddox, 1980). This unique, well organized mesoscale convective system is often associated with severe weather and flooding. The importance of MCCs as major contributors to the warm season rainfall in the United States has been documented by Fritsch et al. (1986) and McAnelly and Cotton (1989). In addition, these systems greatly modify the environment in which they develop (see Augustine and Zipser, 1986; Wetzel et al., 1983 and Cotton et al., 1989).

Large populations of MCCs have been documented in several regions of the world, most notably the Central Plains of the United States (Maddox, 1980; Tollerud and Rodgers, 1991), Central and South America (Velasco and Fritsch, 1987), Australia, China, and the Western Pacific Region (Miller and Fritsch, 1991).

The general characteristics of the regions of MCC development previously documented indicate that equatorial Africa, southeastern Africa and the Indian Subcontinent would be favourable for such development.

This study presents a climatology of MCCs over Africa and the Indian Subcontinent (ISC) and relates the characteristics of these systems to those of MCC populations documented elsewhere in the world. Documentation of the global MCC population will facilitate an estimate of MCC contribution to the global tropospheric energy budget and hydrologic cycle. It is expected that by documenting MCC occurrences in different regions, a better understanding of the nature of their development and their relationship to the large scale environment will be possible.

2. DATA AND METHODOLOGY

Images from METEOSAT and the Indian National Satellite system geostationary satellite (INSAT) were used in this study. Infrared images were available every three hours, starting from 00 UTC; visible images were available at 06, 09, and 12 UTC for Africa and 03, 06, and 09 UTC for the Indian Subcontinent.

METEOSAT imagery for the period January 1986 through December 1987 was used in studying MCCs over Africa. INSAT images for studying MCCs over the ISC were only available for nine months (April to December) of 1988. During the periods 1-8 April and 14 Sept. to 13 Oct. 1988, images were taken at 1730 UTC instead of the usual 1800 UTC. Unlike studies of MCCs in the US, there were no comprehensive storm data reports available to assess the severe weather associated with MCCs in Africa and the ISC.

Values of cloud shield temperature, latitude and longitude were obtained from the digitized satellite images. These values were used as input to a modified version of a computerized MCC program for measuring the satellite-observed characteristics of MCCs (Augustine, 1985). This program computes the area, centroid positions and eccentricity of the -33°C and -54°C cold cloud shields associated with deep convection.

The original definition of the MCC given by Maddox (1980) was modified to accommodate the temporal resolution (every 3 hours) of the INSAT and METEOSAT images. The duration of an MCC was decided in the following manner. If an MCC existed at 1500 UTC and not at 1200 UTC, it was assumed that genesis occurred at the midpoint of the time period, i.e., at 1330 UTC. The shape of the system at the time of observable maximum extent was used to check the eccentricity criterion.

In addition, distortion occurs close to the edge of the satellite image because of the low viewing angle. Therefore, for INSAT, only systems which occurred within the sector bordered by the equator, 40N, 55E and 110E are fully documented. For METEOSAT, documented systems were within the borders of 35N, 35S, 45W and 45E. Systems which occurred poleward of 20 degrees are considered mid-latitude. Since there were several days of missing data and days on which large circular convective systems occurred but one or more images was missing, the number of MCCs documented in this study is slightly conservative.

3. RESULTS

The MCC criteria were satisfied by 195 African systems and 49 ISC systems. Ninety-four African systems occurred in 1986 and 101 in 1987. Thirty-three ISC systems and 26 African systems were classified as mid-latitude. Analyses of their general characteristics are presented.

a. Lifecycle, Duration and Size

The lifecycles of the African and ISC systems are similar to that documented for MCCs in the Americas and Western Pacific Region (WPR) (cf. Fig. 1, Velasco and Fritsch, 1987; Miller and Fritsch, 1991). These systems are predominantly nocturnal. For the ISC, first thunderstorms developed in the late afternoon (≈ 1700 LST) followed by MCC initiation during the early nighttime hours (≈ 2200 LST). Most systems reached their maximum extent between 0000 and 0600 LST. Dissipation usually occurred between 0700 and 1400 LST. Stages of development of African systems were most similar to the US, occurring about 3 h earlier than the ISC, WPR and S. America.

Average duration of the ISC systems was approximately 12 h. For African systems, the average duration was 11.5 h and the modal duration was 9 h. Distributions of system duration are similar to those of the Americas and WPR (Fig. 2).

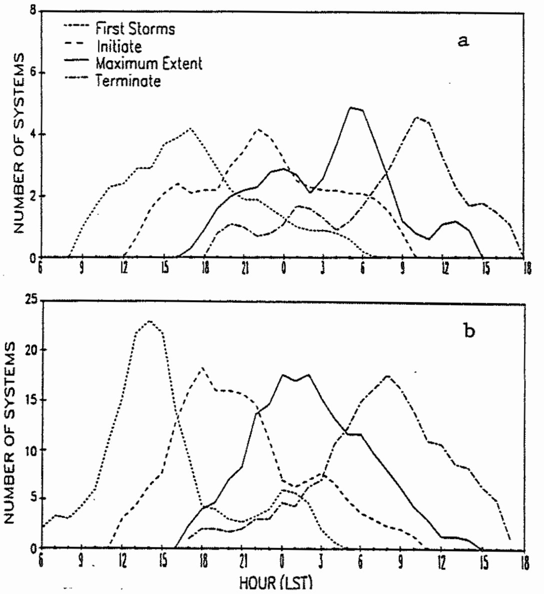

Fig. 1. Frequency distribution of the lifecycle of a) ISC and b) African MCCs. Frequency curves were smoothed with a 3-point running mean.

Most convective systems produced a maximum cold-cloud shield area (-33°C) between 2×10^5 and 3×10^5 km^2. The size distributions of cold-cloud shield areas shown in Fig. 3. are similar. However, the size distributions of mid-latitude South African and South American systems peak at larger values than those for systems in the US, ISC and China.

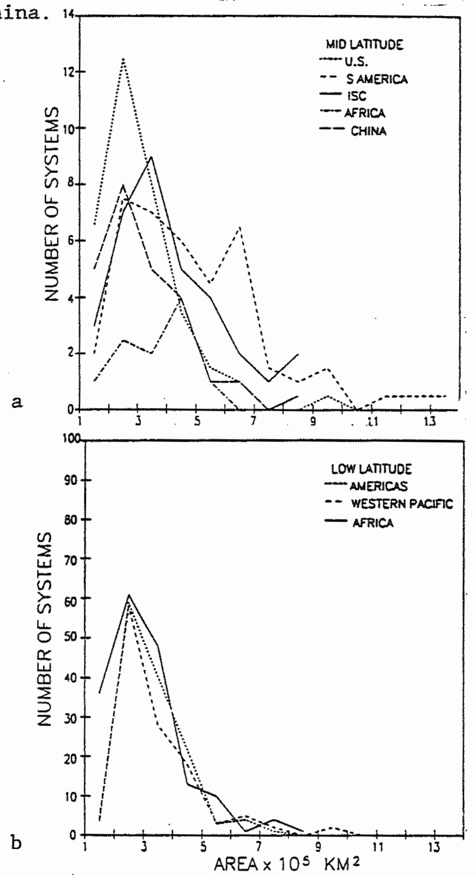

Fig. 3. Frequency distribution of a)mid-latitude and b)low-latitude MCC cold cloud shield maximum area.

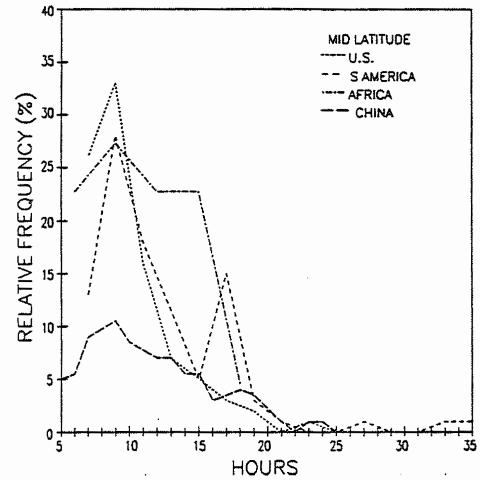

Fig. 2. Frequency distribution of the duration of Mid-latitude MCCs.

b. Seasonal and Geographic Distributions

The development of MCCs in the ISC seems to be associated with the onset and withdrawal of the southwest monsoon. In the early warm season, most systems occur over East India and Bangladesh with little or no activity over the northwestern part of the subcontinent. By mid to late summer (July-Sept), activity has spread northwestward and systems occur over most of the Indian region (Fig. 4). This progression is similar to that of the Indian monsoon (Fig. 5). The monsoon also appears to influence the monthly distribution of MCC activity. Specifically, notice that MCC frequency peaked during the mid to late summer (Fig. 6a). This is in contrast to MCCs in the mid-latitude Africa, Americas and China which have a late spring and early summer maximum.

Systems over the ISC tended to form mainly over land (Fig. 4). This same tendency was observed in most other MCC populations around the world (Velasco and Fritsch, 1987; Miller and Fritsch, 1991). It is also evident that the NE India/Bangladesh region has a distinct sub-population of MCCs. Since the period of study and the total number of systems is relatively small compared to other studies, it is not known if this population is representative of the normal situation. It is important to note, however, that Miller and Fritsch (1991), also found a large population of mesoscale convective systems over Bangladesh and NE India. But, since they used the GMS satellite, the low viewing angle precluded them from making a definitive claim that these were MCCs.

The monthly distribution of all African systems is shown in Fig. 6b. Mid to late summer is the period of maximum activity for the total set of African systems. The mid-latitude systems exhibit a weak maximum around the time of the summer solstice. Although this agrees with all the other mid-latitude populations the sample is too small to make a definitive claim that is statistically meaningful.

The centres of African MCC activity are tied to, but lag the solar maximum, i.e., centres of MCC activity tend to migrate poleward as the warm season progresses. However, as the warm season wanes, MCC activity does not follow the sun equatorward. Rather, the systems simply cease to form. Similar migration characteristics of US MCCs were noted by Velasco and Fritsch (1987).

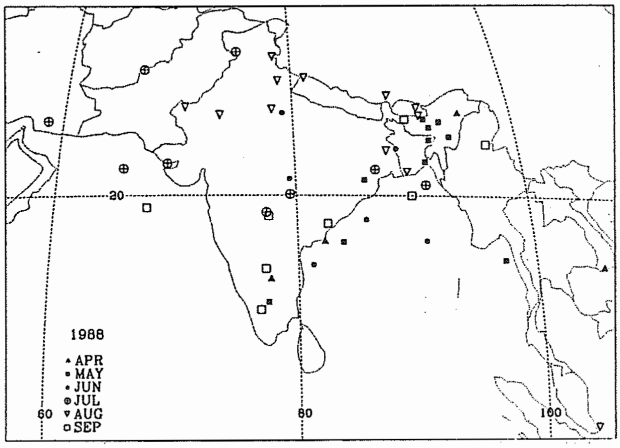

Fig. 4. Geographical and seasonal distribution of MCCs in the Indian Subcontinent. Locations are for the MCC at the time of maximum area.

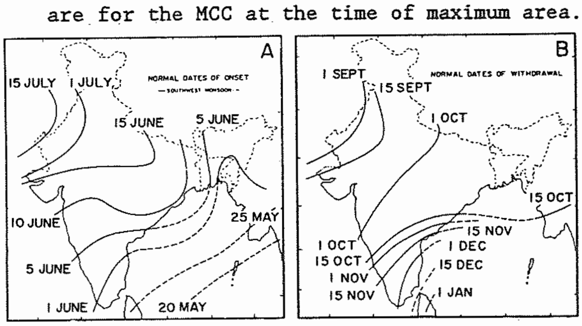

Fig. 5. Mean dates of onset a) and withdrawal b) of the summer monsoon over India. (from Hastenrath, 1991)

Development of MCCs over Africa seems to be confined to certain geographic locations (Fig. 7):
. N Africa between the equator and 18N, and
. SE Africa south of 15S and east of 25E.

Several important observations were made about the regions in which these systems develop. First, most of these systems developed over land or in the immediate vicinity (within 250 km) of the African continent. Second, relatively few systems developed within the tropical rainforest belt of equatorial Africa. Third, most systems developed downstream (relative to mid-tropospheric flow) of mountain ranges. Genesis of MCCs in the tropical easterlies tended to occur west of the north African mountains while MCC genesis in the mid-latitude westerlies occurred east of the South African escarpment. Systems that form over west Africa are not directly induced by orography but seem to be related to the summer monsoonal flow.

c. Tracks

Studies have shown that MCCs generally deviate from the mean flow in the 700-500 mb layer and propagate towards the region with highest θ_e air (Merritt and Fritsch, 1984; Shi and Scofield, 1987). Systems in the NE India/ Bangladesh region generally moved eastward during the April-June period while systems over Pakistan and NW India moved mostly westward during the July-Sept period. The large seasonal and spatial variability of flow in this region makes it extremely difficult to establish any general relationship between the propagation direction and mean flow in the cloud layer. Nevertheless, it is interesting to note

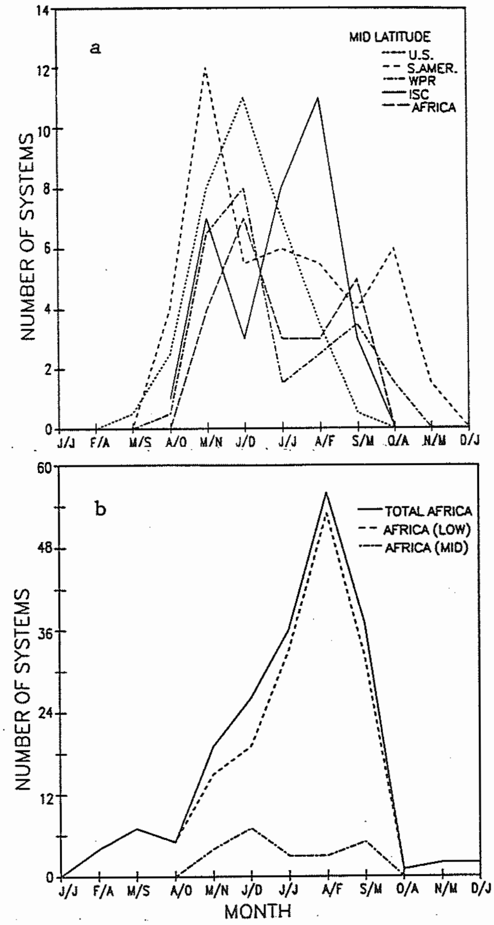

Fig. 6. Monthly frequency of a) mid-latitude MCCs over the US (1978,1981 avg.); S America (May 1981-May 1983 avg.); WPR (1983,1985 avg.); Africa (1986,1987 avg.); ISC (Apr-Dec 1988) b) total set of African MCCs (1986-1987).

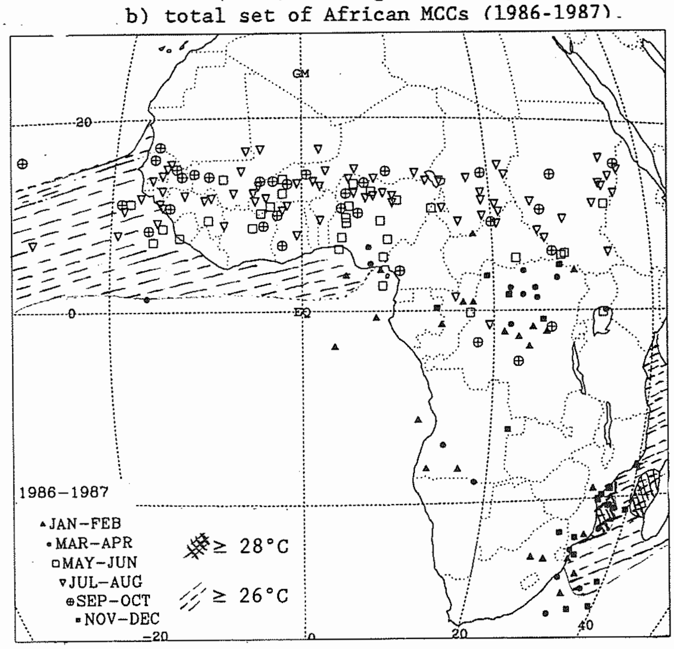

Fig. 7. Geographical and seasonal distribution of MCCs in Africa. Locations are for the MCC at the time of maximum area. Shaded areas show sea surface temperatures ≥ 26 °C for January in S. Africa and July in N. Africa (SSTs from Hastenrath, 1991).

that the monthly mean flow (in the 700 to 500 mb layer) over the northern part of the ISC region switches from a generally westerly direction in the April-June period to easterly in the July-Sept period (Ramage and Raman, 1972).

Low-latitude African systems generally moved to the WSW and systems over SE Africa moved E or NE towards low-level high θ_e air associated with warm sea surface temperatures (Fig. 7).

4. SUMMARY AND CONCLUDING REMARKS

Satellite imagery of Africa, the Indian Subcontinent and the surrounding region reveals the presence of numerous mesoscale convective systems during the warm season. These systems exhibit characteristics (duration, size, diurnal distribution, etc.) that are very similar to the satellite-observed characteristics of MCCs in other areas of the world. Based upon the the similarities of the various populations, the African and ISC convective systems are the same phenomena (i.e., MCCs).

A notable difference between mid-latitude ISC systems and other mid-latitude populations is that the monthly distribution of ISC systems peaks in the mid to late summer, rather than near the summer solstice. This peak corresponds to the maximum spatial extent of the monsoon. ISC MCCs also appear to lead the advance of the monsoon as it progresses northwestward across India.

The African and ISC MCCs seem to play a role in the genesis of tropical storms and depressions. Two ISC MCCs developed into tropical depressions after moving over the Arabian Sea, and the Bay of Bengal. Three west African systems developed into tropical cyclones over the eastern Atlantic ocean. Conversely, just as MCC-generated mesovortices in the Americas have been observed to spawn new convection (Murphy and Fritsch, 1989), the satellite data suggests that a few of the very large systems identified as MCCs over the ISC were remnants of monsoon depressions undergoing various stages of regeneration. The close relationship among MCCs, tropical storms, tropical depressions and MCC-induced mesovortices supports the argument by Cotton et al. (1989) that an MCC is an attempt by the atmosphere to produce an inertially stable and geostrophically balanced system whose radius is larger than the Rossby radius of deformation. Since MCCs in other areas have been observed to develop into tropical storms (Velasco and Fritsch, 1987; Zehnder and Gall, 1991, Miller and Fritsch, 1991), these results may have important implications for understanding the dynamics of MCCs and their potential role in some tropical cyclone formation.

Although there was widespread convection in the Bay of Bengal, Gulf of Thailand, and the equatorial rainforest region of Africa, very few MCCs developed there. The lack of MCCs in some areas where deep convection is frequent and widespread strongly suggests that there are special environmental factors (e.g., magnitude of vertical wind shear, buoyant energy, low level jets, etc.) that are necessary for convection to organize into long-lived mesoscale systems.

Given the worldwide frequency of MCCs, their deep and extensive cloud shields, and the efficiency with which they transport mass and moisture, it is likely that they play a significant role in the global heat and moisture budgets. The present results contribute to the construction of a global climatology of MCCs, and will help to provide a better understanding of their contribution to the global hydrologic cycle.

Acknowledgements

We are grateful to John Augustine for the use of his MCC documentation program, to Dr. Garrett Campbell and Kelly Dean for preprocessing INSAT and METEOSAT data, and Dr. William Rossow for technical assistance. The INSAT images were provided by the Cooperative Institute for Research in the Atmosphere and the METEOSAT images by the NASA Climate Data System. This work was supported by NSF Grant ATM-87-11014.

REFERENCES

Augustine, J.A., 1985: An automated method for the documentation of cloud-top characteristics of mesoscale convective systems. NOAA Tech. Memo. ERL ESG-10, Dept. of Commerce, Boulder, CO, 121 pp. [NTIS PB-85-204246]

Augustine, J.A., and E.J. Zipser, 1986: The use of wind profilers in a mesoscale experiment. Bull. Amer. Meteor. Soc., 68, 4-17.

Cotton, W.R., M.S. Lin, R.L. McAnelly, and C.J. Tremback, 1989: A composite model of mesoscale convective complexes. Mon. Wea. Rev., 117, 765-783.

Fritsch, J.M., R.J. Kane, and C.R. Chelius, 1986: The contribution of mesoscale convective weather systems to the warm season precipitation in the United States. J. Clim. Appl. Meteor., 25, 1333-1345

Hastenrath, S., 1991: Climate Dynamics of the Tropics. Updated edition from Climate and Circulation of the Tropics. Atmospheric Sciences Library. Kluwer Academic Publishers. 488 pp.

Maddox, R.A., 1980: Mesoscale Convective Complexes, Bull. Amer. Meteo. Soc., 61, 1374-1387.

McAnelly, R.L. and W.R. Cotton, 1989: The precipitation lifecycle of mesoscale convective complexes over the Central United States. Mon. Wea. Rev., 117, 784-808.

Merritt, J.H. and J.M. Fritsch, 1984: On the movement of the heavy precipitation areas of mid-latitude mesoscale convective complexes. Preprints, 10th Conference on Weather Analysis and Forecasting, Clearwater, FL, Amer. Meteor. Soc., 529-536.

Miller, D. and J.M. Fritsch, 1991:Mesoscale Convective Complexes in the Western Pacific Region, Mon. Wea. Rev., 119, 2978-2992.

Murphy, J.D. and J.M. Fritsch, 1989: Multiple production of mesoscale convective systems by a convectively-generated mesoscale vortex. Preprints, 12th conference on Weather Analysis and Forecasting, Monterey, CA, Amer. Meteor. Soc. 68-73

Ramage, C.S. and C.V.R. Raman, 1972: Meteorological Atlas of the International Indian Ocean Expedition, Volume 2. Upper Air.

Shi, J. and R.A. Scofield, 1987: Satellite observed mesoscale convective systems (MCS) propagation characteristics and a 3-12 hour heavy precipitation forecast index. NOAA Tech. Memo NESDIS 20, U.S. Dept. of Commerce, Washington, D.C. 43 pp.

Tollerud, E.I., and D.M. Rodgers, 1991: The seasonal and diurnal cycle of mesoscale convection and precipitation in the central United States: Interpreting a 10-year satellite-based climatology of mesoscale convective complexes. Preprints, Seventh Conference on Applied Meteorology, Salt Lake City, Utah, Amer. Meteor. Soc., Boston, Sept.10-13.

Velasco, I., and J.M. Fritsch, 1987: Mesoscale convective complexes in the Americas. J.Geophys. Res., 92, 9591-9613.

Wetzel, P.J., W.R. Cotton and R.L. McAnelly, 1983: A long-lived mesoscale convective system, Part II: Evolution and structure of the mature complex. Mon. Wea. Rev., 111, 1919-1937.

Zehnder, J.A. and R.L. Gall, 1991: Alternative mechanisms of tropical cyclone formation in the Eastern North Pacific. Atmosfera, 4, 37-51.

Analysis of a Tornadic Supercell Using Airborne Doppler Radar

David O. Blanchard
NOAA/NSSL/Mesoscale Research Division
Boulder, Colorado

1. INTRODUCTION

During the spring of 1991, the National Severe Storms Laboratory conducted the COPS-91 (Cooperative Oklahoma Profiler Studies–1991) field program in Oklahoma and the Texas Panhandle. Among its goals were (1) an assessment of the recently deployed National Weather Service (NWS) profiler demonstration network in observational studies of mesoscale convective systems (MCSs), (2) documentation of electrification mechanisms in MCSs, and (3) a detailed study of the dryline.

On the afternoon of 26 May 1991, a thunderstorm developed along the dryline on the Texas Panhandle-Oklahoma border and began to move to the east. Within a short time, the storm had reached severe proportions and large hail and tornadoes were reported. The NOAA P-3 aircraft made multiple passes on the west and south sides of the supercell thunderstorm during and after tornado touchdown, gathering extensive pseudo-dual Doppler radar data. The thunderstorm passed close to the Vici, Oklahoma, network profiler, which was recording vertical wind profiles every 6 minutes.

This paper examines the P-3 Doppler-derived horizontal winds and compares them with the winds from the profiler at Vici. Also, some of the fine-scale circulations and storm structure observed by the P-3 are discussed in the context of current modeling results and understanding of tornadic supercells. Finally, changes in the pre-storm environmental winds are examined.

2. P-3 DATA

The X-band vertically pointing Doppler radar system on the P-3 was recently upgraded to employ the fore-aft scan technique, or FAST (Jorgensen and DuGranrut 1991). This procedure consists of alternatively scanning the P-3's tail radar antenna forward, then aft, about 25° of normal to the aircraft heading. The P-3 has only a single radar and antenna, so the antenna must be mechanically slewed to point in the desired direction. Along a radial, data are collected in bins of 75, 150, and 300 m, depending on the range from the aircraft. The antenna rotation rate (~10 rpm) produces an effective horizontal data spacing of ~1 km at typical P-3 ground speeds (~120 m s^{-1}). FAST allows the P-3 to collect pseudo-dual Doppler radar while following a straight flight track.

The data were processed with a series of programs to edit and transform the slewed radial data into u- and v-wind components. The first step in the editing takes place in radar space. Ground clutter and "2nd trip" contamination is deleted and the aircraft motion is removed from the radial velocity data. Next, the data are examined for aliased velocities and "unfolded." Because the Nyquist interval for this radar is ±12.9 m s^{-1} and the ambient shear for this case is large (> 50 m s^{-1} through the depth of the troposphere), there were multiple folds. This process is repeated for each scan. The next step is to convert the radial data to a Cartesian grid and edit the data in regions that may have been unfolded incorrectly in the first step.

3. PROFILER DATA

The profiler data are from Vici, Oklahoma, which is one of the many NWS profiler demonstration sites currently in operation in the central region of the United States. Data are collected from three beams: one points vertically, and the other two are pointed 15° from the vertical and are oriented toward the north and east. Conversion of Doppler radial velocities along the north and east beams to u- and v-components of the horizontal wind uses the geometry of the beam angles and accounts for the vertical motion using the vertically pointing beam. Besides radial velocity, returned power and spectral variance were also measured and recorded. This information is useful in determining the validity of the derived u- and v-components of the horizontal wind.

3. AIRCRAFT DOPPLER RESULTS

Figure 1 is the result of the pseudo-dual Doppler synthesis of horizontal winds. The winds are storm relative; storm motion was 270° at 8 m s^{-1}.

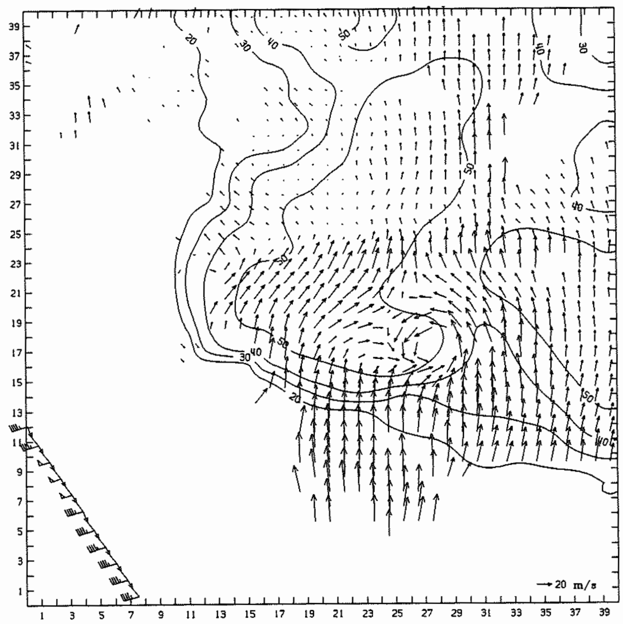

Figure 1. Storm reflectivity and synthesized dual-Doppler winds from the NOAA P-3 aircraft tail radar. Grid is 40 km on a side. Altitude is 1.5 km above ground level (AGL). Aircraft flight track and flight-level (~4.4 km) winds are plotted in the lower left corner. Winds are storm relative using a storm motion of 270° at 8 m s^{-1}*. Scale for wind vectors is given in the lower right corner. Radar reflectivity contours are every 10 dBZ, starting at 20 dBZ.*

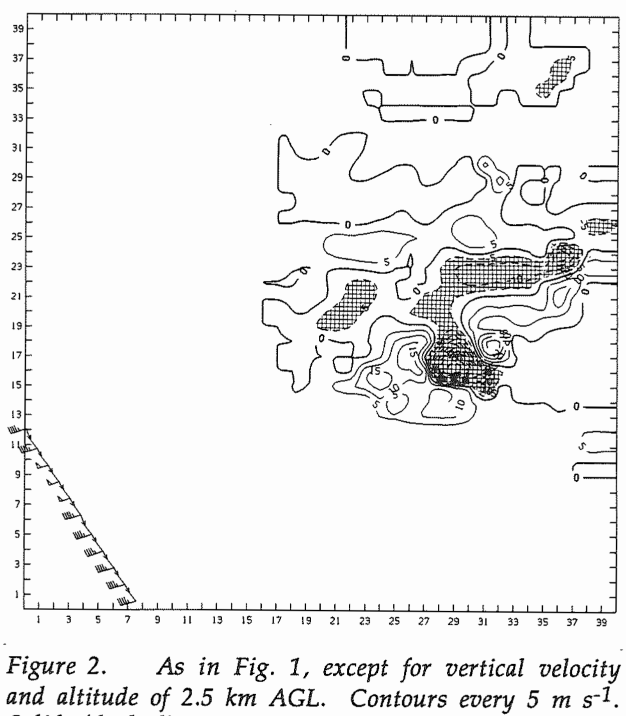

Figure 2. As in Fig. 1, except for vertical velocity and altitude of 2.5 km AGL. Contours every 5 m s^{-1}*. Solid (dashed) contours are updrafts (downdrafts). Zero contour is double width. Downdrafts are hatched.*

It is obvious that a cyclonic circulation is present at $x = 29$, $y = 17$. Wind speeds to the south and southwest of the circulation are ~30 m s^{-1} and greater. The mesocyclone is strongest at this level and weakens aloft, although cyclonic vorticity is present through a deep layer. Reflectivities show a typical "hook echo" in the same region as the mesocyclone. Figure 2 shows the vertical velocities at this level. These velocities were computed through upward integration of the continuity equation and were mass balanced using the O'Brien (1970) technique and assuming that $w = 0$ at the surface. Note the strong downdraft of -40 m s^{-1} adjacent to an updraft of 30 m s^{-1}. The mesocyclone shown in Fig. 1 straddles these two draft structures. Observational and modeling work by Lemon and Doswell (1979), Klemp et al. (1981), and Wicker and Wilhelmson (1992) suggests that tornadogenesis requires the presence of an updraft/downdraft couplet similar to that shown here.

There are uncertainties associated with the strength of these vertical drafts. This is due to two problems with the airborne Doppler data. Owing to ground clutter contamination, winds at the lowest level (0.5 km) were suspect, so low-level divergence is near zero close to the ground. The second problem existed at the upper levels. The radar velocity data were very noisy at the top of the updraft, and good divergence values there are also suspect. Clearly the loss of this information affects the computation of draft strength. The velocities shown here can be considered lower limits, and the actual drafts were probably much stronger.

It is useful to speculate on the cause of the noisy data at high levels. Because the wind structure in the lowest kilometer or two of the atmosphere is strongly sheared in both direction and speed, the relative helicity (Davies-Jones 1984; Davies-Jones and Burgess 1990) is high. Lilly (1986) has shown that high helicity reduces turbulence in the updraft. At the top of the updraft, relative helicity is weaker because there is little shear at this level. As the updraft passes the equilibrium level, it rapidly decelerates and, without the stabilizing effect of helicity, turbulent flow increases. Because the radar averages pulses over many turbulent eddies, the spectral width of the estimate increases, resulting in a noisy mean estimate of the wind. This problem was not noted to such a large degree with other storms on this day. This suggests that the radar was probably working properly and that this thunderstorm was extreme in its draft structure.

4. PROFILER RESULTS

Figure 3 shows the 6-min horizontal winds from the surface to 17 km (AGL) from 2200 to 2348 UTC on 26 May 1991. (The profiler experienced problems after this time, and only 1-h data are available.) The most obvious feature is the almost

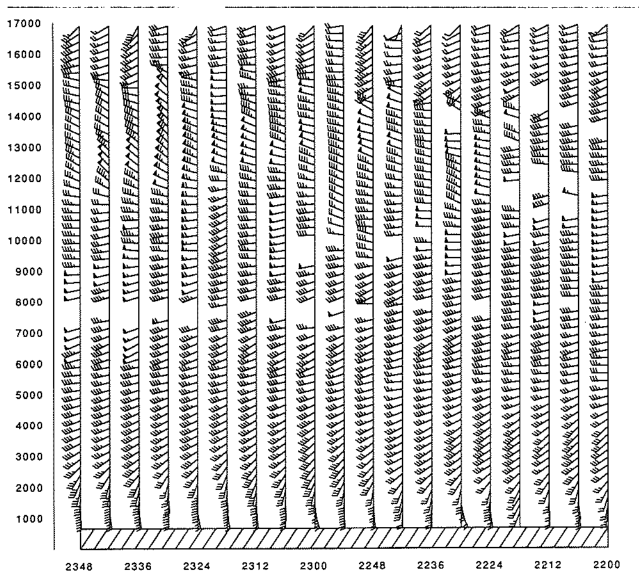

Figure 3. Vertical profile of horizontal winds obtained from the National Weather Service wind profiler at Vici, Oklahoma. Time increases from right to left. Wind profilers are every 6 minutes. Height scale on the left is in meters AGL. Wind barbs conventional; each barb equal to 5 $m\ s^{-1}$, half barbs 2.5 $m\ s^{-1}$, and pennants 25 $m\ s^{-1}$.

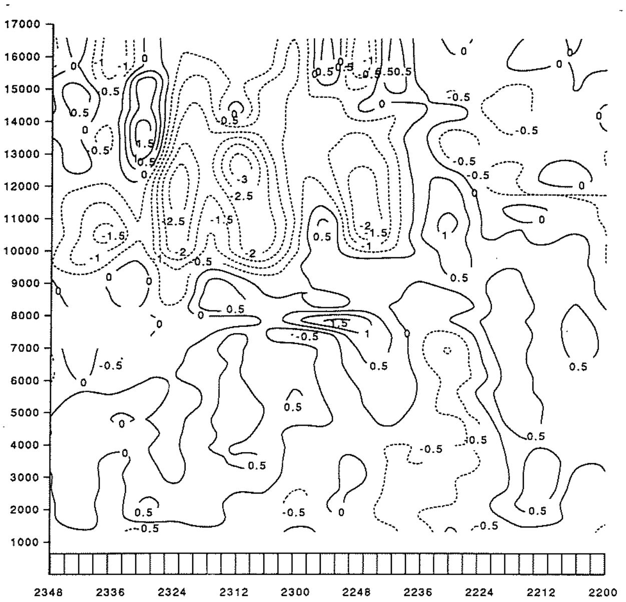

Figure 4. As in Fig. 4, except for vertical velocity. Contours every 0.5 $m\ s^{-1}$; solid contours positive.

unchanging winds through a large portion of the troposphere. The most significant changes occurred in the lowest 1 km where the winds strengthened and backed slightly, and near the tropopause where the winds acquired a more northerly component. The probable cause of the changes at the upper levels is the approaching thunderstorm. A time plot of returned power (not shown) indicates that the anvil passed overhead in the 10–15 km layer starting at 2230 UTC. Downward vertical velocities associated with this feature (Fig. 4) are 2–3 $m\ s^{-1}$. Because the 404-MHz profiler is sensitive to hydrometeors, it is possible that these velocities are the result of ice crystals and hail falling from the anvil. The increasing northerly component could be an artifact of hydrometeors affecting the vertical component of the wind used to correct the horizontal winds. It could also be a basic sampling problem related to inhomogeneities in the anvil between where the north beam is pointing and the vertical beam. For example, at 16-km altitude, the vertical beam and the north beam are 4 km apart and they may be sampling very different vertical velocities. On the other hand, winds from the P-3 Doppler analysis at this altitude show northwest winds on the south side of the anvil, lending credibility to the profiler results.

An interesting updraft in the profiler data originates near the surface at 2212 UTC, and reaches a height of 12 km at 2230 UTC and 16 km at 2242 UTC. A downdraft appears next to the updraft and exhibits the same magnitude and tilt as the updraft. This may be an example of a (gravity) wave passing over the profiler, but it does not appear to be related to the susequent developement of convection.

Another feature of interest is the returned power in the lowest few kilometers (not shown). The region of strongest return indicates the turbulence of the convective boundary layer. The depth of this layer increases during the afternoon, and at about 2212 UTC a convective plume breaks through into the middle troposphere. Satellite images at this time indicate that (moist) convective activity had just developed to the west of the profiler. These data may be useful in forecasting when shallow convection will break through the top of the boundary layer.

5. SUMMARY

A brief analysis has been presented of a tornadic supercell and its environment. The supercell was documented with airborne Doppler radar using FAST while the environment was being sampled every 6 minutes by a vertically pointing Doppler wind profiler within the NWS profiler demonstration network. Synthesis of horizontal winds from the airborne radar showed a well-defined mesocyclone at the lowest levels and cyclonic vorticity aloft. The mesocyclone and the tornado were in a region of strong gradient between an updraft and a downdraft. The strong downdraft is connected to a larger, but weaker region of downdraft to the north and east of the mesocyclone. Because no Doppler data before this time were available, the evolution of these features cannot be documented. Observational and modeling studies suggest that the presence of this downdraft is critical for tornadogenesis. It must be pointed out that the tornado was dissipating when the aircraft arrived. The structure revealed by the radar is that of a post-tornadic storm and differs from most tornadogenesis models and observations that focus on the pretornadic environment.

The profiler at Vici, Oklahoma, was ~35 km south of the mesocyclone. At this distance, the only significant environmental changes are a strengthening and slight backing of the wind in the lowest levels and strongly veered winds near the tropopause. These veered winds may be an artifact resulting from falling hydrometeors, or they may be related to the strongly divergent flow in the thunderstorm anvil. The lack of a strong signal in the low-level environmental winds suggests, in this case at least, that the effects from the storm are not strong at this distance. Possibly other techniques, such as computing the perturbation wind from a moving time average, might provide more information to a forecaster.

Even though the profiler did not note large environmental changes as the storm passed, it is useful for assessing the potential for severe storm development in a sheared, convectively unstable environment. The environmental winds before the tornado show the classic veered profile associated with supercell thunderstorms. This information was used successfully by severe-storm forecasters during the warm season.

Acknowledgements. Thanks are extended to J. Augustine (NOAA/NSSL) for allowing me to borrow his code to retrieve the vertical velocities from the profiler data. Special thanks to D. Van de Kamp (NOAA/FSL) for his efforts to recover the missing profiler data necessary for this case study. The airborne Doppler analysis code is the result of work by B. Smull and D. Jorgensen (NOAA/NSSL)

7. REFERENCES

Davies-Jones, R., 1984: Streamwise helicity: The origin of updraft rotation in supercell storms. *J. Atmos. Sci.*, **41**, 2991–3006.

____________, and D. Burgess, 1990: Test of helicity as a tornado forecast parameter. *Preprints, 16th Conf. Severe Local Storms,* Kannanaskis, AB, Amer. Meteor. Soc., 588–592.

Jorgensen, D.P. and J.D. DuGranrut, 1991: A dual-beam technique for deriving wind fields from airborne Doppler radar. *Preprints, 25th Intl. Conf. on Radar Meteor.*, Paris, Amer. Meteor. Soc., 458–461.

Klemp, J.B., R.B. Wilhelmson, and P.S. Ray, 1981: Observed and numerically simulated structure of a mature supercell thunderstorm. *J. Atmos. Sci.*, **38**, 1558–1580.

Lemon, L.R., and C. A. Doswell III, 1979: Severe thunderstorm evolution and mesocyclone structure as related to tornadogenesis. *Mon. Wea. Rev.*, **107**, 1184–1197.

Lilly, D.K., 1986: The structure, energetics and propagation of rotating convective storms. Part II: Helicity and storm stabilization. *J. Atmos. Sci.*, **43**, 126–140.

Wicker, L.J. and R.B. Wilhelmson, 1992: Numerical simulation of tornadogenesis within a supercell thunderstorm. *Proceedings, Tornado Symposium III* (C. Church, Ed.), Amer. Geophy. Union (in press).

CLOUD CONDENSATION NUCLEI AND THEIR EFFECT ON THE OPTICAL PROPERTIES OF WATER CLOUDS: APPLICATION TO GCMs AND REMOTE SENSING

Graham Feingold* and Andrew J. Heymsfield**

* CIRES, University of Colorado, Boulder, CO 80303
** NCAR, P.O. Box 3000, Boulder, CO 80307

1. INTRODUCTION

Climate studies have established beyond doubt that clouds play an important role in the Earth's energy budget through their effect on the radiation balance (e.g. Cox, 1971). This paper addresses the impact of cloud condensation nucleus (CCN) and cloud droplet spectra on radiative transfer. Their impact is important and could even sway the balance between negative and positive cloud feedback mechanisms one way or the other (Nakajima and King, 1990).

We will present two parameterization schemes which are designed to compute droplet spectra in liquid clouds where droplets grow primarily through condensation, as is the case in marine stratocumulus (e.g., the measurements of Nicholls, 1984). The CCN spectrum plays an important role in determining the cloud droplet spectrum. Calculations of effective radius (r_e) and optical thickness (τ) (or, alternatively, liquid water path, LWP) are of particular interest since water-cloud radiative properties depend almost entirely on these two parameters (Slingo, 1989). Both of the schemes will include CCN spectrum dependence.

2. METHOD

We will predict (i) the droplet concentration (N*) and average droplet radius ($\bar{r}^*$) when the maximum value of supersaturation (S*) is reached; (ii) the average radius ($\bar{r}$) and r_e as a function of time (or height) above the height of S*; and (iii) the resulting cloud optical thickness. The major assumptions are (i) a constant vertical velocity (w), (ii) no entrainment, although provision is made to include entrainment (see Feingold and Heymsfield, 1992); (iii) no horizontal advection of liquid water into, or out of, the parcel and (iv) a constant droplet mixing ratio (N*/ ρ_a) after S* is reached.

We assume the standard equations for droplet nucleation and growth in a parcel rising at a constant w (see, Twomey, 1959). The equation in supersaturation, S, is given by

$$\frac{dS}{dt} = \psi_1(T,P)w \;-\; \psi_2(T,P)\,\frac{dX_L}{dt} \tag{1}$$

where X_L is the liquid water mixing ratio. ψ_1 and ψ_2 are functions of temperature (T) and pressure (P) (e.g., Pruppacher and Klett, 1978). The growth equation for a droplet of radius r is given by

$$r\frac{dr}{dt} = G(r,T,P)\,[S - y(r,T)]\,. \tag{2}$$

$G(r,T,P)$ determines the rate of condensational growth and $y(r,T)$ represents the surface tension and solute correction terms to the saturation field around the droplet. Using (2), and the definition of X_L (the third moment of the drop spectrum, $n(r)$) we may write (1) as

$$\frac{dS}{dt} = \psi_1 w \;-\; \psi_2 4\pi\frac{\rho_l}{\rho_a}\int G(r,T,P)[S-y(r,T)]r\;n(r)\;dr, \tag{3}$$

with ρ_l and ρ_a the densities of water and air, respectively. Twomey (1959) solved (3) analytically for S* (i.e., $dS/dt = 0$) to obtain

$$S^* \;=\; \left[\frac{A(T,P)w^{3/2}}{Ck\beta(3/2,k/2)}\right]^{1/(k+2)}. \tag{4}$$

$A(T,P)$ is given by Twomey (1977) and β is the complete beta function. The number of activated droplets (N*) for a given CCN size spectrum, T, P and w, can be derived from the empirical relation (Twomey, 1959):

$$N^* = C(100\cdot S^*)^k. \tag{5}$$

CCN measurements generally distinguish between continental spectra having high C ($\approx$ 1000 cm^{-3}) and high k ($\approx$ 1), and maritime spectra with low C ($\approx$ 100 cm^{-3}) and low k ($\approx$ 0.5). All reference to "PT" (**P**arameterization **T**womey) will imply use of (4) and (5).

In our parameterization (PFH), we will also use (4). However, to solve (3) we will introduce the mean drop radius, defined as

$$\bar{r} \;=\; \frac{\int rn(r)dr}{\int n(r)dr} \;=\; \frac{\int rn(r)dr}{N}. \tag{6}$$

Also, we approximate G and y using weighted averages, with the weighting determined by the integrand in (3). Equation (3) can then be written as

$$\frac{dS}{dt} \approx \psi_1 w \;-\; \psi_2 4\pi\frac{\rho_l}{\rho_a}\bar{G}(S-\bar{y})N\bar{r} \tag{7}$$

and the maximum supersaturation is

$$S^* \approx \left\{\bar{y}(S^*)^k \;+\; \left[\frac{\psi_1 w}{\psi_2\alpha\bar{G}C(100^k)\bar{r}^*}\right]\right\}^{1/(k+1)}. \tag{8}$$

Eq.(8) can be iteratively solved with rapid convergence. Given S*, we can obtain N^* from (5).

a. Closure of the equations using numerical model calculations

A Lagrangian parcel model (with 100 size-bins of ammonium sulfate CCN) is used to describe the nucleation and condensational growth of droplets (Heymsfield and Sabin, 1989). $\bar{r}^*$, $\bar{G}$ and $\bar{y}$ are expressed in terms of C, k, w, T and P using a multivariate-regression fit to the model data (for a wide range of w, C and k, T and P). The empirical expressions are

$$\bar{r}^* \;=\; a_0(T,P)C^{b(T,P)}k^{c(T,P)}w^{d(T,P)} \tag{9a}$$

$$\bar{G} \;=\; a_1(T,P)C^{f(T,P)}k^{g(T,P)}, \tag{9b}$$

$$\bar{y} \;=\; a_2(T,P)C^{p(T,P)}k^{q(T,P)}w^{r(T,P)}. \tag{9c}$$

The coefficients in (9) can be found in Table 1 (c.g.s. units are used throughout). Equations (5), (8) and (9) form the basis of the PFH scheme.

b. The evolution of $\bar{r}$ with time or height

Following maximum saturation we write (1) as

$$\frac{dS}{dt} = \psi_1 w \;-\; \psi_2\frac{d}{dt}\left[\frac{4}{3}\pi\frac{\rho_l}{\rho_a}\int r^3 n(r)dr\right]. \tag{10}$$

We assume a lognormal form for $n(r)$:

$$n(r) = \frac{N^*}{(2\pi)^{1/2}\ ln\sigma\ r}\ exp\left[-ln^2(r/r_g)/2ln^2(\sigma)\right] \quad (11)$$

with r_g, the geometric mean radius and σ, the geometric standard deviation. From Feingold and Levin (1986) and others,

$$\bar{r} = r_g exp(0.5ln^2\sigma). \quad (12)$$

Assuming that the number mixing ratio (N^*/ρ_a) remains constant and that $\sigma = const. = 1.2$, (10) can be written as

$$\frac{dS}{dt} = \psi_1 w - \psi_2 \frac{4}{3}\pi \frac{\rho_l}{\rho_a} N^* exp(3ln^2\sigma)\frac{d\bar{r}^3}{dt} \quad (13)$$

Setting the left hand side of (13) equal to zero (ie., the quasi-steady value of S) and using an average value for ψ_1/ψ_2 yields

$$\bar{r}(t) = \left[[\bar{r}^*]^3 + \left(\frac{\psi_1}{\psi_2}\right)_{ave.} \cdot \frac{3w(t-t^*)}{4\pi\rho_l(N^*/\rho_a)exp(3ln^2\sigma)}\right]^{1/3}. \quad (14)$$

Observational evidence for the linear increase in LWC implied by (14) is given by Noonkester (1984).

d. Calculations of r_e, τ and LWP

By definition

$$r_e = \frac{\int r^3 n(r)dr}{\int r^2 n(r)dr} = \bar{r}exp(2ln^2\sigma). \quad (15)$$

Twomey's scheme can be extended to provide information on droplet radius by assuming the cloud liquid water content is adiabatic ($LWC_{ad.}$):

$$\bar{r}_{ad.} = \left(\frac{3LWC_{ad.}}{4\pi\rho_l N^*}\right)^{1/3} \quad (16)$$

Calculations of r_e can then proceed from (15). In the case of the optical thickness (in the visible wavelengths),

$$\tau = 2\pi\sum_i\left[\int r^2 n(r)dr\right]_i \Delta z_i = 2\pi\sum_i N^*\bar{r}_i^2 exp(ln^2\sigma)\Delta z_i. \quad (17)$$

The sum is over height intervals Δz_i. LWP can be calculated directly from the adiabatic value.

3. RESULTS

a. Prediction of N^*

Both the PFH and PT schemes are used to generate the predicted S^* and N^* for the entire range of C and k. Fig. 1a shows ratios of the PFH calculated values of N^* to those calculated by the model in $(C;k)$ space for w=50 cm s^{-1} and T=10.4°C. PFH predicts the values of N^* to an accuracy of 20% for most C and k. A comparison of the results obtained by PT (Fig. 1b) shows that the latter produces good estimates of N^* in a narrower band of $(C;k)$ space. Results at different w (not shown here) tend to improve for higher w.

b. The evolution of $\bar{r}$ or r_e with time or height

We use (14) (in the case of PFH) and (16) (in the case of PT) together with (15) to calculate the evolution of r_e with time (or height). A cloud depth of 500 m is considered. Two different $(C;k)$ pairs are used, one, a maritime CCN spectrum, "m" (C=100 cm $^{-3}$, k = 0.7) and the other, a continental spectrum, "c" (C=1000 cm^{-3}, k = 0.9). Figures 2 and 3 show a comparison of the model calculations of the change in r_e with time with the values predicted by PFH and PT, for w=50 and w=100 cm s^{-1}, respectively. In cases with both maritime

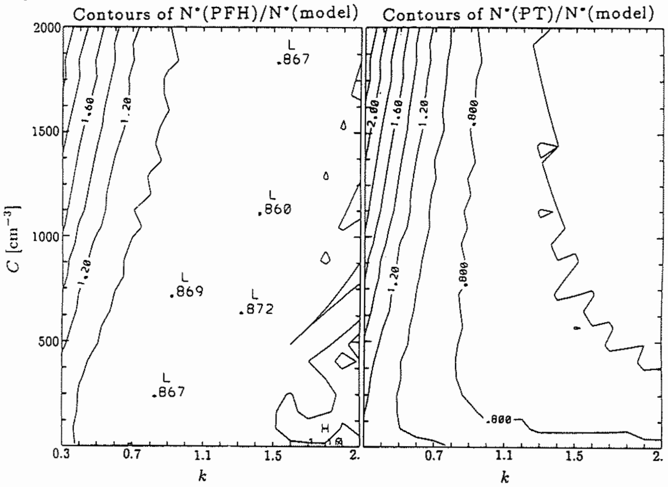

Fig. 1. Contours of the ratio of (a) N^* as predicted by PFH to N^* predicted by the model and (b) N^* as predicted by PT to N^* predicted by the model.

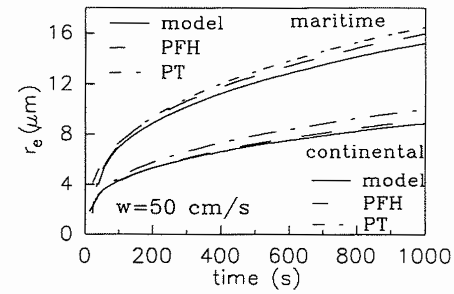

Fig. 2. Comparison between model calculations of $r_e(t)$ and those predicted by PFH and PT for an updraft of 50 cm s^{-1}. The curves marked "maritime" indicate a CCN spectrum with C=100 and k=0.7; those marked "continental" indicate a CCN spectrum (C=1000, k=0.9).

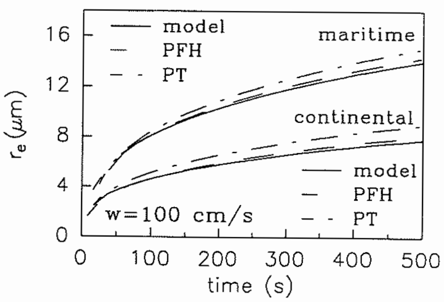

Fig. 3. As in Fig. 2 but for w=100 cm s^{-1}.

and continental CCN spectra, PFH gives excellent predictions of $r_e(t)$. The PT scheme produces good estimates of r_e with some tendency to overpredict this parameter. In both cases, accuracy is only weakly dependent on C, k, and σ.

c. Calculations of τ

Figure 4a presents contours of the ratios of τ as predicted by the PFH scheme to the model calculated values (for the same conditions described in section 3a, and a cloud depth of 500 m). Results are excellent with accuracy generally of the order of 10%. The PT scheme (Fig. 4b) gives good estimates of τ for most physically plausible values of C and k.

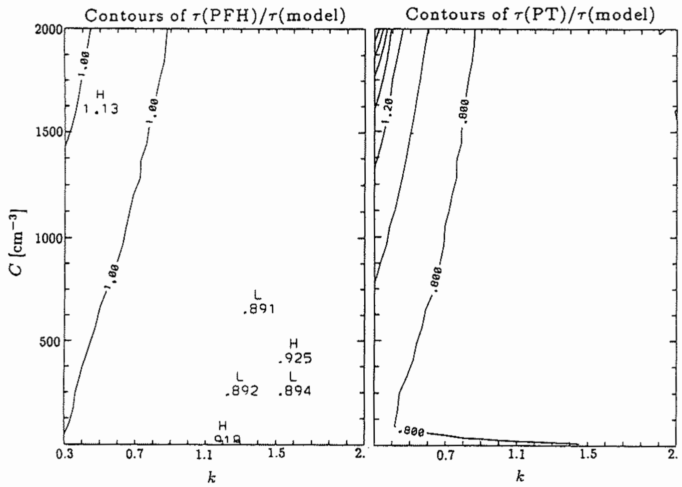

Fig. 4. Contour plots of the ratio of τ as predicted by (a) PFH and (b) PT, to τ calculated by the model for w=50 cm s^{-1}. The cloud depth is 500 m.

4. DISCUSSION

a. Implementation in a GCM

The schemes are formulated in terms of T, P, w, C and k. The first two variables are calculated explicitly in GCMs and pose no problem. The vertical velocity and CCN parameters are more problematic.

1) Vertical velocity

Figure 5 represents the relative error in τ incurred by errors in w of magnitude w_1/w_2. (These are errors which might be associated with sub-grid scale w parameterizations.) For example, if w_1 produces τ_1 and w_2 produces τ_2, then the contours represent values of τ_1/τ_2. The maritime spectrum is considered. We see that errors of up to 34% can be expected for a seven-fold error in w. Information on the sensitivity of r_e to w can be gleaned from Figs. 2 and 3, which show that doubling w from 50 cm s^{-1} to 100 cm s^{-1} incurs errors in r_e of the order of 1.5 μm after 500 m uplift.

2) The CCN spectrum parameters

C and k are not well known but this problem will be alleviated as more data become available. As a first step, GCMs could simply differentiate between maritime and continental C and k. In Fig. 6, we change C to investigate the attendant errors in τ (w is fixed at 75 cm s^{-1} and k at 1.0). Here the errors in τ are more marked; a ten-fold error in C (1000/100) induces errors in τ of the order of 70%, while a two-fold error in C (1000/500) results in an 18% error. The sensitivity of τ to k (holding C at 500 cm^{-3} and w at 75 cm s^{-1}) is shown in Fig. 7; clearly, errors in k are far less important than those in C. Figures 2 and 3 show that like τ, r_e is more sensitive to changes in the CCN spectrum (particularly C) than it is to changes in w.

3) Scaling the integrated liquid water path

Most GCMs perform independent calculations of LWP (Smith, 1990), therefore, the implementation of this scheme in a GCM requires that internal consistency of the total water mixing-ratio calculations be maintained, particularly when LWP is a prognostic GCM variable. The suggested approach is to scale the parameterization-calculated LWP and to adjust the effective radii and/or droplet concentrations accordingly.

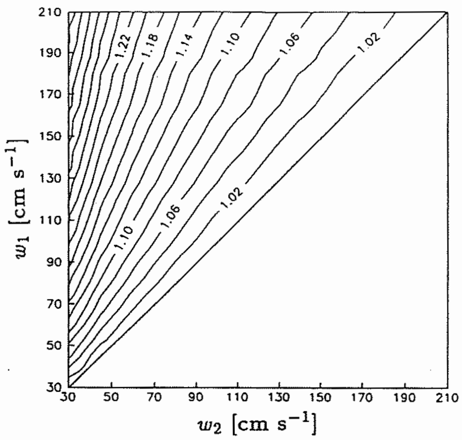

Fig. 5. Contours of normalized τ representing errors caused by overestimating w. The contour values represent the degree of overestimation of τ resulting from an overestimation of w by a factor w_1/w_2. The CCN spectrum is a maritime one.

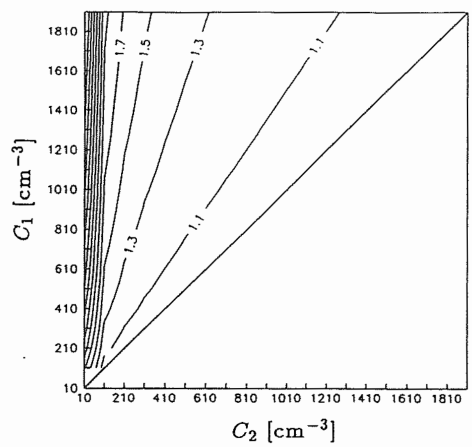

Fig. 6. As in Fig. 5, but for C. w is set at 75 cm s^{-1} and k at 1.

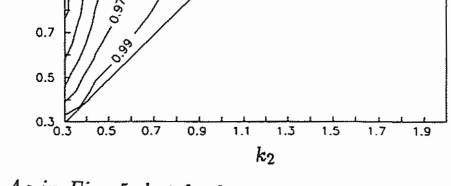

Fig. 7. As in Fig. 5, but for k. w is set at 75 cm s^{-1} and C at 500 cm^{-3}.

b. Potential use in remote sensing applications

The parameterization schemes can be used to infer the r_e profile from remote measurements of τ, T, P and cloud depth. Using an initial guess for w, together with measured T, P and cloud-thickness, and assumed C and k, we can use either PFH or PT to calculate an optical thickness (τ_p) associated with the parameterization. The initial value for w employed in the parameterization scheme is then adjusted iteratively until τ_p converges to the remote measured optical thickness (τ_r). A flow diagram of the procedure is given in Figure 8.

5. SUMMARY

By predicting the effective radius of the droplets, together with the optical thickness (or LWP) the schemes presented here provide the essential information necessary for radiative transfer calculations for water clouds (Slingo, 1989). The importance of the CCN spectrum characteristics (C and k) as well as updraft velocities (w) in determining the optical properties of clouds has been demonstrated. Thus the full potential of these schemes will only be realised when better cloud condensation nucleus measurements are acquired, and sub-grid scale parameterization schemes improve.

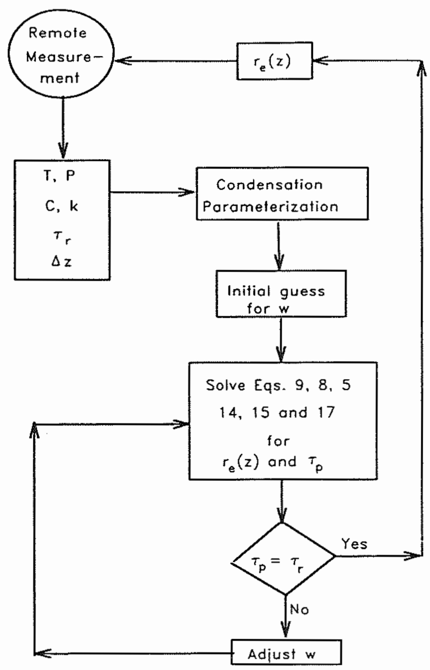

Fig. 8. A retrieval algorithm for the r_e profile. Remote measurements provide values of T, P, C, k and Δz. The parameterization uses these values together with an initial guess for w to calculate the predicted τ (τ_p). This value is then compared with the remote measurement of τ (τ_r). An iterative scheme is used to adjust w until the two agree. At this point, $r_e(z)$, is obtained.

Acknowledgements

One of the authors (GF) was a Rothschild and Fulbright Post-Doctoral Fellow at NCAR when most of this research was completed. Discussions with Drs. W.A. Cooper and P.J. Rasch of NCAR, and Dr. L. Donner of NOAA/GFDL were helpful. Thanks are also due to Larry Miloshevich.

	x_0	x_1	x_2	rval
a_0	$2.124\cdot10^{-3}$	$3.373\cdot10^{-5}$	$9.632\cdot10^{-8}$	0.999
b	-0.321	$-3.333\cdot10^{-4}$	$-9.972\cdot10^{-6}$	0.977
c	-0.464	$9.253\cdot10^{-3}$	$-2.066\cdot10^{-5}$	0.996
d	-0.149	$1.514\cdot10^{-3}$	$4.375\cdot10^{-6}$	0.993
a_1	$6.224\cdot10^{-7}$	$0.281\cdot10^{-7}$	$2.320\cdot10^{-10}$	0.999
f	-0.127	$2.668\cdot10^{-3}$	$7.583\cdot10^{-7}$	0.999
g	-0.214	$9.416\cdot10^{-3}$	$-1.173\cdot10^{-4}$	0.999
a_2	$7.128\cdot10^{-5}$	$-1.094\cdot10^{-6}$	$4.314\cdot10^{-9}$	0.990
p	0.230	$-1.200\cdot10^{-4}$	$1.607\cdot10^{-5}$	0.803
q	1.132	$-9.083\cdot10^{-3}$	$-1.482\cdot10^{-5}$	0.993
r	0.132	$-2.191\cdot10^{-3}$	$3.934\cdot10^{-5}$	0.989

Table 1. The dependence of the regression coefficients on T (°C) given by equations of the form $x_0 + x_1T + x_2T^2$. Range of validity: $-13 < T < 13$°C; $30 < w < 210$ cm s^{-1}; $10 < C < 2010$ cm^{-3}; $0.3 < k < 2$.

REFERENCES

Cox, S.K., 1971: Cirrus clouds and climate. *J. Atmos. Sci.*, **28**, 1513-1515.

Feingold, G., and Z. Levin, 1986: The lognormal fit to raindrop spectra from frontal convective clouds in Israel. *J. Clim. Appl. Meteor.*, **25**, 1346-1363.

Feingold, G., and A.J. Heymsfield, 1992: Parameterizations of condensational growth of droplets for use in general circulation models. *J. Atmos. Sci.*, in press.

Heymsfield, A.J., and R.M. Sabin, 1989: Cirrus crystal nucleation by homogeneous freezing of solution droplets. *J. Atmos. Sci.*, **46**, 2252-2264.

Nakajima, T., and M.D. King, 1990: Determination of the optical thickness and effective particle radius of clouds from reflected solar radiation measurements. Part I: Theory. *J. Atmos. Sci.*, **47**, 1878-1893.

Nicholls, S., 1984: The dynamics of stratocumulus. *Quart. J. R. Met. Soc.*, **110**, 821-845.

Noonkester, V. R., 1984: Droplet spectra observed in marine stratus cloud layers. *J. Atmos. Sci.*, **41**, 829-845.

Pruppacher, H.R., and J.D. Klett, 1978: *Microphysics of Clouds and Precipitation.* D. Reidel, Dordrecht, Holland, 714 pp.

Slingo, A., 1989: A GCM parameterization for the shortwave radiative properties of water clouds. *J. Atmos. Sci.*, **46**, 1419-1427.

Smith, R.N.B., 1990: A scheme for predicting layer clouds and their water content in a general circulation model. *Quart. J. R. Met. Soc.*, **116**, 435-460.

Twomey, S., 1959: The nuclei of natural cloud formation, Part II: The supersaturation in natural clouds and the variation of cloud droplet concentration. *Geofis. Pura Appl.*, **43**, 243-249

Twomey, S., 1977: "The Atmospheric Aerosol", *Elsevier*, 302 pp.

REMOTE SENSING THE SUSCEPTIBLITY OF CLOUD ALBEDO TO CHANGES IN DROP CONCENTRATION

S. Platnick[1] and S. Twomey

[1]NASA Ames Research Center, Moffett Field, CA 94035

Introduction

It is the *cloud sensitivity* (Arking 1991), defined as the change in energy absorbed by the climate system to changes in a cloud parameter, that is meaningful for climate change. Important cloud parameters include the macroscopic (such as cloud amount, or cloud cover fraction, and cloud height and thickness) and the microscopic (cloud liquid water content, drop size, and phase). An important cloud microphysical parameter, not typically incorporated into GCMs, is drop size. Cloud reflectance is partially dependent on drop size which is in turn linked with cloud condensation nuclei (CCN) concentrations present during cloud development. CCN concentrations are variable, having both natural and anthropogenic sources. Among the latter sources are combustion processes that also release CO_2, a major greenhouse gas. The overall effect of increasing CCN is to increase cloud albedo which results in cooling. There is no compensating outcome in the infrared. In light of these concerns, it is useful to define a quantity representing the *sensitivity* of cloud albedo to changes in CCN concentration. This quantity is referred to as *cloud susceptibility*. It is important to appreciate that modification of cloud albedo by CCN does not solely constitute a climate feedback. That is, the effect does not depend on the development of any actual climate change and can occur quite free from any such controversy. In the jargon of climate change, changes in drop size constitute a *climate forcing* mechanism.

As expected, not all clouds are equally susceptible; the determining factors turn out to be cloud optical thickness and drop size. Both can be inferred remotely through solar reflection measurements at wavelengths which are absorbing and non-absorbing for liquid water. Since global susceptibility is of importance for climate, a satellite remote sensing scheme has been developed using the Advanced Very High Resolution Radiometer (AVHRR) aboard the NOAA polar satellites. Channel 3 of the AVHRR, at 3.75 μm, provides the absorbing wavelength. Thermal emission by the cloud, and surface, at this wavelength contaminates the solar reflected signal. Brightness temperature in channel 4, in the thermal infrared, is used to estimate this emission. This study primarily investigates maritime stratus clouds which are expected to be cleaner and so have the greatest susceptibilities to albedo modification. Results for a number of these stratus scenes are presented.

Susceptibility

The ultimate fate for a given wavelength of the incident radiation is partially dependent on the cloud drop density (N) which ranges from tens per cm^3 for very clean air to thousands per cm^3 for continental or polluted air. The final drop density is approximately proportional to the number density of CCN present during cloud formation. Experimental data of CCN versus supersaturation (Twomey and Wojciechowski, 1969) and measurements of both CCN and N by Twomey and Warner (1969) give an approximate linear fit between CCN and drop concentration.

For critical supersaturations below 1%, the difference in CCN concentrations between continental and clean maritime air can easily be greater than an order of magnitude (Twomey and Wojciechowki 1969). Combustion processes are also found to be a abundant source for CCN (e.g., Squires, 1966; Warner and Twomey, 1967). Hobbs et al. (1980) made measurements of elevated CCN in power plant plumes and found order of magnitude increases of cloud drop numbers in clean marine stratus effected by the plume.

Twomey (1974) discussed the following link between pollution and cloud albedo. Since combustion processes are known to be prolific sources of CCN, a cloud forming in a polluted air mass will end up with a larger concentration of cloud drops than for the same cloud developing under identical circumstances in cleaner air. Optical thickness ($\tau \propto r^2 N$) increases which in turn leads to an increase in albedo. But, it is reasonable to assume that clouds forming under the same set of circumstances but with different CCN amounts will have the same supply of vapor available for drop growth. For such a case the liquid water content (W) of the mature clouds can be expected to be equivalent so that drop sizes in the polluted cloud would be smaller than those for the clean cloud. The competing effect of larger N and smaller r gives $\tau \propto N^{1/3}$.

The question then arises as to the significance of the albedo change; clouds formed in clean maritime air having low CCN concentrations are more susceptible than those formed in particle-rich continental air. When A, N, and ΔN are known, a calculation can be made for the change in albedo, but since ΔN is variable it is useful to define a parameter that will characterize the sensitivity of albedo to changes in drop concentration. The derivative dA/dN (approximately equivalent to choosing ΔN=1) represents such a link (Twomey 1989). Since, in general, $A=A(\tau,\varpi_0,g)$, the derivative can be expressed in the form

$$\frac{dA}{dN}=\frac{\partial A}{\partial \tau}\frac{d\tau}{dN}+\frac{\partial A}{\partial \varpi_o}\frac{d\varpi_o}{dN}+\frac{\partial A}{\partial g}\frac{dg}{dN} \tag{1}$$

and under the condition of constant liquid water content will be termed *cloud susceptibility*. Note that all terms are wavelength-dependent. Consider the special case of conservative scattering which is applicable in the visible and where about one-half of solar flux occurs. There ϖ_0=1 and g is approximately constant with radius, so the last two terms in Equation 1 can be neglected. Susceptibility reduces to

$$\left.\frac{dA}{dN}\right)_{W=const}=\frac{\partial A}{\partial \tau}\frac{\tau}{3N}=\frac{4\pi\rho_l}{9W}\tau\frac{\partial A}{\partial \tau}r^3 \tag{2}$$

where either N, or r and W, can be used as independent variables. Of obvious note is the r^3 dependence in the second form. Unless using analytic approximations, numerical calculations for $\partial A/\partial\tau$ will be needed. A calculated susceptibility of 0.01 cm^3 (not uncommon for California marine stratus) indicates that the addition of one drop per cm^3 will increase the albedo by 0.01.

The term $\tau\partial A/\partial\tau$ is given by the two stream approximation as $A(1-A)$ which has a peak at an albedo of 0.5 and an optical thickness of about 13. When multiplied by r^3 (and the term containing liquid water content) the approximation becomes susceptibility. Calculations with a detailed radiative transfer code also give a peak in susceptibility at 50 % albedo for all radii. The two stream approximation can also be used to show albedo changes due to non-differential changes in drop concentration. Consider a cloud having drop concentration N. If N is changed by some factor χ(i.e., $N\to\chi N$) then $\tau\to\chi^{1/3}\tau$ and

$$\Delta A=\left[A(1-A)\left(\chi^{\frac{1}{3}}-1\right)\right]\Big/\left[A\left(\chi^{\frac{1}{3}}-1\right)+1\right]. \tag{3}$$

For instance, at A=0.5, a doubling in N will increase albedo to a value of 0.56. Similar to susceptibility, the peak in ΔA occurs very close to $A = 0.5$ for reasonable χ (< 2).

The important point is that existing cloud microphysics is essential in determining the climate forcing by CCN. Climatologies of cloud albedo may be adequate for understanding the current short-wave energy balance, but *are not* sufficient for estimating changes in the energy balance; cloud microphysics must also be known. Climate modeling of this effect typically assumes that drop concentrations in clean maritime clouds increase by some factor. While changes in other climate modifiers, such as CO_2, may be usefully expressed in this way, the same is not true of drop concentration. For example, pollution is more likely to increase CCN concentrations by some absolute number, say 10 cm^{-3}, over some geographical region. The effect on a cloud that would otherwise have drop concentrations of 10 cm^{-3} can be very different than for a cloud having the same albedo but with N=100 cm^{-3} (and a smaller geometrical thickness). Each will respond differently to the increase in drop concentration (see Equation 3). It is not at all clear that every maritime cloud should have about the same drop concentration, which is one of the underlying assumptions of using a factor increase in N to model albedo modification. So, in addition to albedo, drop concentration must be known, and simple assumptions about the microphysics can be misleading. Any figure of merit for susceptibility will have a two dimensional functional dependence that will include albedo (or optical thickness) and a microphysical variable (e.g., A and N, A and r, τ and r, A and χ); the exact definition is largely irrelevant.

The process defined by susceptibility is the dominant radiation influence of particulate pollution (at least for reasonably clean clouds with typical albedos). Grassl (1982) found little effect in the infrared. Pollution is also a source of carboniferous aerosol which absorbs in the visible. This effect on cloud albedo, considered by Twomey (1977) and Grassl, can only be seen in brightest clouds (albedos greater than about 0.7).

Remote Sensing Susceptibility

Inferring drop radius through near infrared absorption has been used by a number of investigators (e.g., Twomey and Cocks, 1982; Stephens and Platt, 1987) using aircraft borne sensors. None of the investigators made measurements in the 3.75 μm window. In situ cloud measurements typically showed that drop radius was overestimated by 2 μm to 5 μm. Retrieving larger drops implies that the observed ϖ_o is lower than would be expected from calculations based on measured drop sizes. This has been termed anomalous absorption. Stephens and Tsay (1990) give a review of the measurements and comment on proposed causes of the anomaly. Suggested causes include continuum vapor absorption in the windows and cloud inhomogeneities. It is not clear whether radius inferred from a 3.75 μm channel would suffer from a similar anomaly. With much larger liquid water absorption (order of magnitude greater than at 2.2 μm), the mean number of scatterings for reflected photons would be less (about 8 at τ=10 versus 20 for conservative scattering) and photon penetration into the cloud, both vertically and horizontally, would be reduced suggesting that the effect of inhomogeneities would be less. The large liquid water absorption might also tend to mask out any unaccounted for continuum vapor absorption.

Arking and Childs (1985) used the AVHRR for remote sensing cloud drop radii and optical depths. Grainger (1990) used the AVHRR for studying orographic effects on drop sizes. No in situ cloud measurements were used for validation. Emission at 3.75 μm is comparable to, and can even exceed the reflected radiation. Figure 1 shows the ratio of reflected solar radiation to emission in AVHRR channel 3. The two intensities are seen to be equal for drop radii of about 10 μm. While removing emission is certainly an added complication, the large absorption in the channel does give its use one very important advantage - the signal is almost entirely dependent on radius, with very little optical thickness sensitivity except for the thinnest clouds. Shorter wavelengths have substantial optical thickness dependencies over much of the expected radius range. The

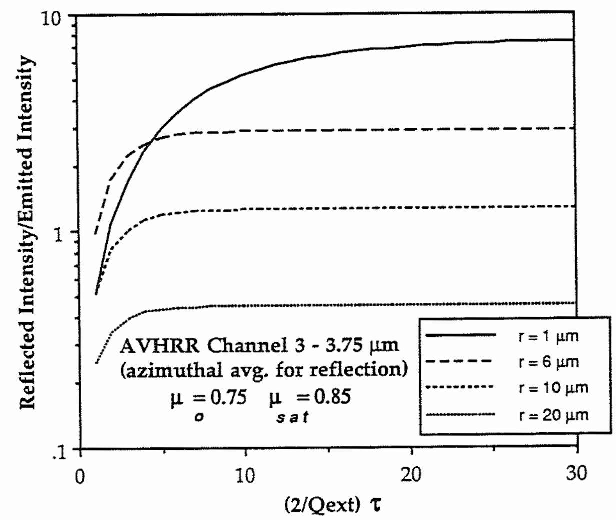

Figure 1 The ratio of reflected solar intensity to thermal emission for AVHRR channel 3. Surface and cloud temperatures are 290 K.

substantial radius information content of a 3.75 μm channel makes it of special interest for remote sensing regardless of it being a major contender for cloud microphysical studies.

Inferring optical thickness and drop radius from satellite reflection and emission data characterizes an *inverse* problem which, in this study, is determined by the best fit between the satellite measurement and *forward* calculations placed into a library file. The library contains bidirectional reflectances for AVHRR channels 1, 2, and 3 (at 0.65, 0.85, and 3.75μm respectively) and effective cloud and surface emissivities for channels 3, 4, and 5 (the latter two channels at about 10.75 and 12.0 μm respectively). The contents of the library includes calculations for all combinations of the following: radii equal to 1, 4, 6, 8, 10, 12.5, 15, 17.5, 20, 25, 30, 35, and 45 μm; τ=1,2,...,60,70,...,150 ; harmonics up to twentieth order for the azimuthally dependent bidirectional reflectance (typically 5 to 10 harmonics are sufficient). Radii are the mean of a normal distribution with a dispersion of 0.2 (giving $r_{eff} \approx 1.08 r_{mean}$). The surface, assumed to be the ocean for this study, is considered Lambertian to diffuse radiation with albedos of 0.06, 0.03, 0.01, 0.0, and 0.0 for channels 1 through 5 respectively. Variations in radiative properties over the finite band of each AVHRR channel is considered in the calculations. In practice, only channels 1, 3, and 4 were needed. Channel 5 was used with channel 4 in a split window technique for inferring sea surface temperature. The effect of the atmosphere on the signal received by the satellite was modeled using the LOWTRAN7 radiation code (Kneizys et al., 1988).

Channels 1 and 2 lack onboard calibration and must, without in-flight techniques, rely on calibrations typically performed several years before launch. In-flight calibrations with scenes of known reflectance shows that the sensor response is modified from the pre-flight calibration (see Teillet et al. 1990). All NOAA-11 channel 1 and 2 data in this study uses the calibration coefficients of Nianzeng et al. (1991). The in-flight calibration made closest in time to the recording of the data being studied is chosen. NOAA-9 and -10 AVHRR data is calibrated in the same way with the Teillet et al. gain values. These in-flight calibrations are made in terms of a reflected intensity. This is converted to albedo using the solar flux data of Neckel and Labs (1984).

A detailed discussion of each topic in this section can be found in Platnick (1991).

Results

A common difficulty in satellite remote sensing is comparison with in situ measurements. As part of the First ISCCP Regional Experiment (FIRE), field observations were made of marine stratocumulus clouds off the coast of southern California in the summer of 1987. Two reports have been published of cloud microphysical measurements taken at times almost concurrent with the pass of a NOAA polar orbiter.

The aircraft measurements by Rawlins and Foot (1990) were taken over the course of several hours on the afternoon of 30 June 1987. Additional data from this flight was obtained from the Meteorological Research Flight of the UK Meteorological Office (Taylor 1991, private communication). A run was made within and above a 300 meter thick cloud. Effective radii of about 9.0 μm were calculated from drop size distributions near cloud top. Optical thickness, estimated from their cloud reflectance data, varied from 15 to 60. We analyzed a NOAA-9 AVHRR LAC image acquired within an hour of the aircraft measurements, for a north-south flight path flown by the plane. In this region, μ_o≈.90 and μ_{sat}≈.50 (corresponding to a resolution of about 3.8 km). Figure 2 shows our retrievals giving radii of 10 μm along the entire path with one pixel showing 8 μm; optical thickness varies from 20 to 70. Agreement between retrieved values of radius and the in situ measurements are within the radius increments available from the library data (at a radius of 10 μm, increments of +2.5, -2.0 μm in radius are possible to resolve with the library). Radius was not sensitive to the exact atmospheric correction. Susceptibilities, using Equation 2 with a cloud liquid water content of 0.3 g/m^3, vary over an order of magnitude, from about 0.5x10^{-3} (units of cm^3 will be assumed throughout this paper) at the northern end of the cloud region to as high as 6.0x10^{-3} at the southern end.

Radke et al. (1989) reported passage through two ship tracks within a stratocumulus cloud layer on 10 July 1987. Radiation and microphysical measurements were taken midway between the approximately 500 meter thick cloud. Drop concentrations were seen to increase from 30 to 50 cm^{-3} outside the track to over 100 cm^{-3} within the track, indicative of larger CCN numbers. We obtained an HRPT NOAA-10 image was for this region (μ_o≈.50, μ_{sat}≈.79 giving about 1.7 km resolution) that was captured twenty minutes before the aircraft measurements were made. Cloud parameters were retrieved along two section lines crossing the tracks. The average retrieved radius, both in and out of the tracks, was typically 3 μm to 6 μm larger than in situ measurements. Microphysical studies in California stratus typically show increasing drop sizes with height (e.g., Noonkester 1984). At the 3.75 μm wavelength, absorption is larger and therefore drop sizes near cloud top contribute a greater influence to the inferred sizes than drops further down in the cloud where in situ measurements were taken. Retrieved susceptibilities are smaller for the ship tracks as expected; 0.5x10^{-3} in-track and 1.0x10^{-3} to 2.0x10^{-3} out-of-track. Susceptibility calculated from the aircraft measurements is similar with 0.20x10^{-3} to 0.65x10^{-3} in-track and 0.70x10^{-3} to 1.45x10^{-3} out-of-track.

Wintertime fog in the central valleys of California is expected to be at the other end of the susceptibility scale, providing another check of the retrieval algorithm. The extensive fog forms in air containing large CCN concentrations from agricultural, industrial, and natural sources. Three NOAA-11 GAC images of valley fog from the winter of 1989/90 were analyzed. Retrieved radius is especially uniform throughout the length of the valleys, typically 6 μm to 8 μm - smaller than for marine stratus as expected and in general agreement with the results of Garland (1971). Optical thickness ranged from 10 to over 100 (larger τ found in the northern part of the Central Valley). Susceptibility was as low as 0.05x10^{-3}, two orders of magnitude less than the larger values found in California marine stratus. This is probably a lower limit since liquid water content is likely to be less than the 0.3 g/m^3 used in the calculation.

Stratus containing ship tracks is expected to have large variations in susceptibility over a small scale, providing a useful test for sensing relative susceptibility; the solar and satellite viewing angles, cloud temperatures, surface properties, and atmospheric influences are similar and so relative retrievals of cloud parameters are more credible then comparisons between distant regions. A dramatic instance of ship tracks was seen in an HRPT NOAA-11 image from 2 March 1990 in a large region centered near 52°N, 140°W. Tracks were seen to be forming in uniform stratus to the west as well as in a thinner stratus region in the center of the image. Resolution was from one to two kilometers. A number of locations in the image have been analyzed including thirteen individual tracks; optical thickness and radius retrievals are summarized in Figure 3 clearly showing smaller radii and larger optical thicknesses in the tracks. Three to five adjacent pixels were typically used to calculate the averages, designated by a single data point. Out-of-track retrievals are taken from the uniform western stratus only. A histogram of susceptibility is shown in Figure 4. Tracks in the thinner stratus show the smaller susceptibilities and smaller optical thicknesses; retrieved radii are about the same for both region of tracks.

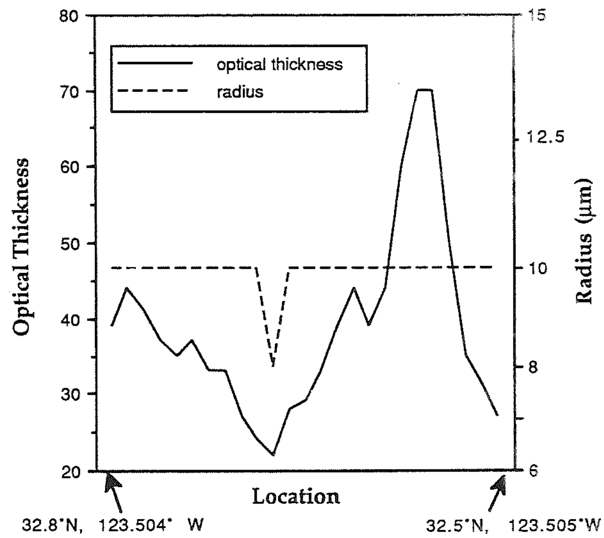

Figure 2 Radius and optical thickness retrieved from a NOAA-9 LAC image, 30 June 1987, along an aircraft flight path taken by Rawlins and Foot (1990) in stratocumulus off southern California.

Marine stratus is quite common, especially near the western coasts of the continents. Two NOAA-11 GAC images in the South Atlantic, off the coast of Namibia and South Africa (4 January 1989 and 19 April 1989 with resolution of 5 to 6 km), were analyzed. Both clouds were extensive and isolated. Retrievals gave 6.0 μm to 9.0 μm radii, optical thicknesses from 3 to 12, and susceptibilities from 0.2x10^{-3} to 0.8x10^{-3}. It is impossible to make any climatological conclusion regarding the microphysics of this stratus, but for the two cases studied, radii and susceptibilities are much less than those typically found in uncontaminated California stratus. Either larger CCN concentrations are found here or the liquid water content of the clouds are much smaller (by a fraction of about 0.15 to 0.30). If these results were generally true, it might explain the lack of ship track sightings in this region even though stratus development is common. A NOAA-11 GAC from 22 January 1989 was analyzed for a region south of Madagascar in the Indian Ocean (33.3°S, 45.71°E). Satellite viewing angles are near nadir giving 4 km resolution. Two likely ship tracks were seen formed in a broken stratocumulus deck. There is an obvious reduction in drop size in the apparent tracks (8 μm versus 12.5 μm to 17.5 μm for out-of-track regions) and larger optical thicknesses (8 to 15 versus 3 to 12 out-of-track). Susceptibilities are also consistent with the expectations for ship tracks, and are comparable to those found in California stratus (to the authors' knowledge, this would be the first report of ship tracks being found in the southern hemisphere).

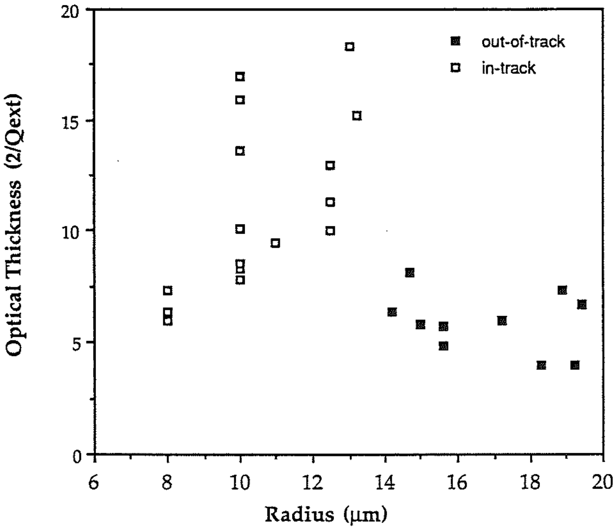

Figure 3 Scattergram of retrieved radius and optical thickness in a stratus cloud containing ship tracks. From NOAA-11 HRPT, 2 March 1990.

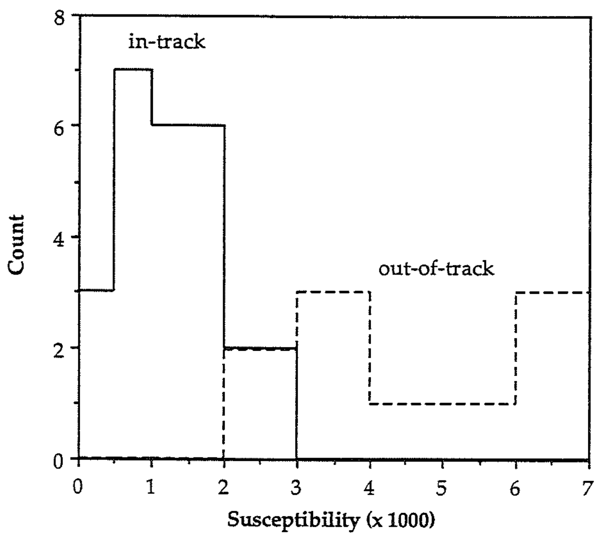

Figure 4 Histogram of susceptibility for the retrievals of Figure 3.

Summary

The retrieved range of susceptibilities (in units of cm^3 and normalized to a liquid water content of 0.3 g/m^3) for the marine clouds studied varied by about two orders of magnitude; from as low as 0.23×10^{-3} in stratus off the west coast of southern Africa to about 20×10^{-3} in thin stratus off the California coast. Susceptibilities for California valley fog were as low as 0.05×10^{-3}, extending the measured range, for all clouds studied, to almost three orders of magnitude. Studies in ship tracks have shown that the tracks are indeed less susceptible than out-of-track regions after having been contaminated with CCN originating from the ship's effluent. Susceptibility, in and out of the tracks, differs by a factor of 2 to 4 and up to as high as 30 for thin stratus. The use of susceptibility extends beyond fog and marine stratus which have been highlighted in this study because of their relative homogeneity for remote sensing purposes.

Acknowlegement. This work was supported by NSF grant ATM-8716637 through the Institute of Atmospheric Physics, The University of Arizona, Tucson.

References

Arking, A., and Childs, J. D., 1985: Retrieval of Cloud Cover Parameters from Multispectral Satellite Images. *J. Climate and Appl. Meteo.*, 24, 322-333.

Arking, A., 1991: The Radiative Effects of Clouds and their Impact on Climate. *Bull. Amer. Met. Soc.*, 71, 795-813.

Garland, J. A., 1971: Some Fog Droplet Size Distributions Obtained by an Impaction Method. *Quart. J. R. Met. Soc.*, 97, 483-494.

Grainger, R. G., 1990: *The Calculation of Cloud Parameters from AVHRR Data.* Ph.D. Dissertation, University of Auckland, New Zealand.

Grassl, H., 1982: The Influence of Aerosol Particles on Radiation Parameters of Clouds. *Idöjárás*, Journal of the Hungarian Met. Service, 86.

Hobbs, P. V., Stith, J. L., and Radke, L. F., 1980: Cloud-Active Nuclei from Coal-Fired Electric Power Plants and Their Interaction with Clouds. *J. Appl. Met.*, 19, 439-451.

Kneizys, F. X., et al., 1988: Users Guide to LOWTRAN 7. *AFGL-TR-88-0177.*

Neckel, H., and Labs, D., 1984: Solar Radiation Between 3000 and 12500 Å. *Solar Physics*, 90, 205-258.

Nianzeng, Che, Grant, B. G., Flittner, D. E., Slater, P. N., Biggar, S. F., 1991: Results of Calibrations of the NOAA-11 AVHRR Made by Reference to Calibrated SPOT Imagery at White Sands, N.M. *SPIE Proceedings*, V1943-21, Orlando, Florida.

Noonkester, V. R., 1984: Droplet Spectra Observed in Marine Stratus Cloud Layers. *J. Atmos. Sci.*, 41, 829-845.

Platnick, S., 1991: *Remote Sensing the Susceptibility of Cloud Albedo to Changes in Drop Concentration.* Ph.D. dissertation, University of Arizona, Tucson, Arizona.

Radke, L. F., Coakley, J. A., and King, M. D., 1989: Direct and Remote Sensing Observations of the Effects of Ships on Clouds. *Science*, 246, 1146-1149.

Rawlins, F., and Foot, J. S., 1990: Remotely Sensed Measurements of Stratocumulus Properties during FIRE Using the C130 Aircraft Multi-channel Radiometer. *J. Atmos. Sci.*, 47, 2488-2503.

Squires, P., 1966: An Estimate of the Anthropogenic Production of Cloud Nuclei. *J. Rech. Atmo.*, 2, 297-308.

Stephens, G. L., and Platt, C. M. R., 1987: Aircraft Observations of the Radiative and Microphysical Properties of Stratocumulus and Cumulus Cloud Fields. *J. Climatol. Appl. Meteorol.*, 26, 1243-1269.

Stephens, G. L., and Tsay, S., 1990: On the Cloud Absorption Anomaly. *Q. J. R. Meteorol. Soc.*, 116, 671-704.

Taylor, J., 1991: Private Communication. Meteorological Research Flight, Farnborough, Hamshire, GU14 6TD, England.

Teillet, P. M., Slater, P. N., Ding, Y., Santer, R. P., Jackson, R. D., and Moran, M. S., 1990: Three Methods for the Absolute Calibration of the NOAA AVHRR Sensors In-Flight. *Remote Sens. Environ.*, 31, 105-120.

Twomey, S., and Warner, J., 1967: Comparison of Measurements of Cloud Droplets and Cloud Nuclei. *J. Atmos. Sci.*, 24, 702-703.

Twomey, S., and Wojciechowski, 1969: Observations of the Geographical Variation of Cloud Nuclei. *J. Atmos. Sci.*, 26. 684-688.

Twomey, S., 1974: Pollution and the Planetary Albedo. *Atmos. Environ.*, 8, 1251-1256.

Twomey, S., 1977: The Influence of Pollution on the Shortwave Albedo of Clouds. *J. Atmos. Sci.*, 34, 1149-1152.

Twomey, S., Cocks, 1982: Spectral Reflectance of Clouds in the Near-Infrared: Comparison of Measurements and Calculations. *J. Met. Society of Japan*, 60, 583-592.

Twomey, S., 1989: Aerosols, Cloud Physics and Radiation. Plenary Lecture 3, *American Association for Aerosol Research*, Annual Meeting, Reno NV.

Warner, J., and Twomey, S., 1967: The Production of Cloud Nuclei by Cane Fires and the Effect on Cloud Droplet Concentration. *J. Atmos. Sci.*, 24, 704-706.

PARAMETERIZATION OF THE RADIATIVE PROPERTIES OF CIRRUS CLOUDS

Qiang Fu and K. N. Liou

Department of Meteorology/CARSS, University of Utah
Salt Lake City, Utah 84112

1. Introduction

The purpose of this paper is to develop a parameterization for the radiative properties of cirrus clouds in both solar and infrared radiation using the single-scattering properties for hexagonal ice crystals. In Section 2, we present a scheme to parameterize the single-scattering properties for randomly oriented hexagonal ice crystals. In Section 3, we briefly describe the δ-four-stream approximation developed for calculating the radiative fluxes and the incorporation of nongray gaseous absorption within clouds. The parameterization results are subsequently compared with data obtained from aircraft observations. In Section 4, a sensitivity study is performed to assess the radiative effects of ice crystal size distributions. Finally, we present a discussion on the significance of the present study in Section 5.

2. Parameterization of the Single-Scattering Properties of Hexagonal Ice Crystals

Based on aircraft observations (Auer and Veal, 1970), the aspect ratio, L/D (length/diameter), of hexagonal ice crystals may be related to the crystal length L. Thus, the ice crystal size distribution can be noted by n(L). For the purpose of radiative transfer parameterization, we may characterize the size distribution in terms of the ice water content (IWC) and the area-weighted mean width by

$$LWC = \frac{3\sqrt{3}}{8}\,\rho_i \int D^2 L n(L)\,dL, \qquad (2.1)$$

$$D_e = \int D^2 L n(L)\,dL \Big/ \int D L n(L)\,dL, \qquad (2.2)$$

where ρ_i is the density of ice and D_e is referred to as the mean effective size.

The extinction coefficient for a given ice crystal size distribution is defined by $\beta = \int \sigma n(L)\,dL$, where σ is the extinction cross section of a single particle. For randomly oriented hexagonal ice crystals in the limits of geometric optics (Takano and Liou, 1989), $\sigma = 3/2D(\sqrt{3}/4D+L)$. Noting the definitions of IWC and D_e and the relationship between D and L based on observations, we find that $\beta \simeq$ IWC $(a+b/D_e)$, where a and b are certain coefficients. The single-scattering albedo, $\tilde{\omega}$, is defined by $1 - \tilde{\omega} = \int \sigma_a n(L)\,dL / \int \sigma n(L)\,dL$, where σ_a is the absorption cross section. When absorption is small, σ_a is approximately equal to the product of the absorption coefficient k and the particle volume, i.e., $\sigma_a \simeq 3\sqrt{3}/8D^2Lk$. Thus, using the expressions for σ and σ_a, we find that $1 - \tilde{\omega} \simeq c + d\,D_e$, where c and d are certain coefficients. For nonspherical particles randomly oriented in space, the phase function can be expressed in terms of the scattering angle, Θ. We may expand the phase function in terms of a series of Legendre polynomials P_ℓ as follows: $P(\cos\Theta) = \Sigma\, \tilde{\omega}_\ell P_\ell(\cos\Theta)$, where $\tilde{\omega}_0 = 1$. Since the phase function is dependent on the ice crystal size distribution, the coefficients $\tilde{\omega}_\ell$ should also be related to the ice crystal size distribution, viz., the mean effective size.

Based on the preceding discussions, the variability of ice crystal size distribution can be largely accounted for in the scattering and absorption calculations if the ice water content and mean effective size are used. The argument is valid in the limit of geometric optics. In view of the observed ice crystal sizes in cirrus clouds (~20-2000 μm), the simple relationships for the single-scattering properties of cloud particles as functions of IWC and D_e should be valid for solar wavelengths (0.2-4 μm). For thermal infrared wavelengths (e.g., 10 μm), the geometric optics approximation may not be appropriate for small ice crystals. However, from aircraft observations, Foot (1988) found that there is a good linear relationship between the extinction coefficient in the infrared spectrum and that derived based upon the large-particle approximation. Based on this observational evidence, the simple relationships described above may also apply to infrared wavelengths. We propose the following general parameterizations for the extinction coefficient and single-scattering albedo of cirrus clouds in both solar and infrared spectrum

$$\beta = IWC \cdot \sum_{n=0}^{2} a_n / D_e^n, \quad \tilde{\omega} = \sum_{n=0}^{3} b_n D_e^n, \qquad (2.3)$$

where a_n and b_n are empirical coefficients. When light is scattered by randomly oriented hexagonal ice crystals, δ-function transmission through parallel planes at $\Theta = 0°$ must be accounted for (Takano and Liou, 1989). Using the similarity principle, the expansion coefficients of the phase function may be expressed by $\tilde{\omega}_\ell = (1 - f_\delta)\,\tilde{\omega}_\ell^* + f_\delta(2\ell + 1)$, where $\tilde{\omega}_\ell^*$ represents the expansion coefficients without the incorporation of the δ-function transmission, and f_δ is the contribution from the δ-function transmission. For the δ-four-stream approximation, the index $\ell = 1,2,3,4$, $\tilde{\omega}_1 = 3$ g, and g is the asymmetry factor. $\tilde{\omega}_\ell^*$ and f_δ may be expressed in terms of the mean effective size D_e as follows:

$$\tilde{\omega}_\ell^* = \sum_{n=0}^{3} C_{n,\ell} D_e^n, \quad f_\delta = \sum_{n=1}^{3} d_n D_e^n, \qquad (2.4)$$

where $C_{n,\ell}$ and d_n are empirical coefficients.

In order to obtain the empirical coefficients a_n, b_n, $C_{n,\ell}$ and d_n, we use the geometric ray-tracing program (Takano and Liou, 1989) to compute the single-scattering properties for wavelengths in the solar spectrum. It has been noted that this program may not be appropriate for small ice crystals in thermal IR wavelengths. Asano and Sato (1980) have developed an exact theory for the computation of light scattering by small spheroidal particles. We have tested and modified this program and found that it can be applied to size parameters on the order of about 30. Since ice is highly absorbing in infrared wavelengths, it is likely that the detailed shape factor may not be critical in scattering and absorption calculations. Therefore, in the infrared spectrum, the optical properties of hexagonal ice crystals whose size parameters are greater than about 30 are computed from the geometric ray-tracing program, while for size parameters that are less than 30 the Mie-type solution for spheroids is employed. In the present computations, 11 ice crystal size distributions from in situ aircraft observations were employed (Table 1). In order to resolve the variation in the refractive index of ice (Warren, 1984) and to account for the gaseous absorption, six and 12 bands are selected for solar and thermal IR regions, respectively (Fu and Liou, 1992). For each spectral band, the complex indices of refraction used are averaged values over the spectral band, weighted by the solar irradiance (Takano and Liou, 1989) in solar spectrum and by the Planck function (T = -40°C) in the thermal IR spectrum.

Table 1. Characteristics of the 11 ice crystal size distributions.

Type	IWC (gm^{-3})	D_e (μm)
Cs*	4.765 e-3	41.5
Ci* Uncinus	1.116 e-1	123.6
Ci** (Cold)	1.110 e-3	23.9
Ci** (Warm)	9.240 e-3	47.6
Ci** (T=-20°C)	8.613 e-3	57.9
Ci** (T=-40°C)	9.177 e-3	64.1
Ci** (T=-60°C)	6.598 e-4	30.4
Ci*** (Oct. 22)	1.609 e-2	104.1
Ci*** (Oct. 25)	2.923 e-2	110.4
Ci*** (Nov. 1)	4.968 e-3	75.1
Ci*** (Nov. 2)	1.406 e-2	93.0

*Heymsfield (1975); **Heymsfield and Platt (1984); ***FIRE (1986).

Figure 1 shows the parameterization results for β/IWC, $\tilde{\omega}$ and g for two spectral intervals: 1.9-2.5 μm and 800-980 cm^{-1}. The formal spectral interval is used as an example for the solar spectrum because the single-scattering properties for this band depend significantly on the size distribution. The latter spectral interval is located in the atmospheric window, where the greenhouse effect of clouds is most pronounced. The present parameterizations for the single-scattering properties in both solar and infrared spectra have accuracies less than ~1%.

3. Parameterization of Radiative Flux Transfer and Comparisons with Observations

For parameterization of radiative fluxes, we use the δ-four-stream approximation developed by Liou et al. (1988). For a homogeneous layer, analytic solution can be derived explicitly for

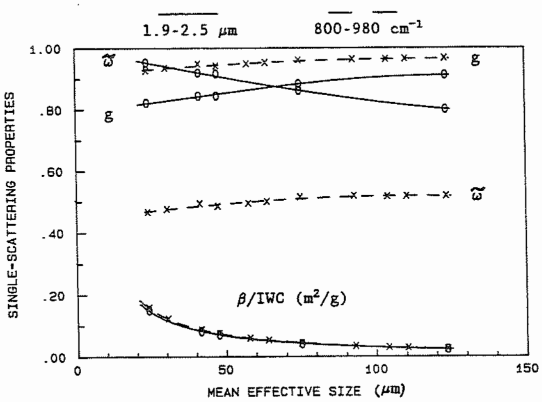

Fig. 1: Comparison of the single-scattering properties computed from parameterization (solid and dashed lines) and the exact method (circles and crosses).

this approximation so that the computational effort involved is minimal. In order to apply this approach to the infrared, we express the Planck function in terms of optical depth in the form, $a' \exp(b'\tau)$, where a' and b' are coefficients determined from top and bottom layer temperatures. Since the direct solar radiation source also has exponential function form in terms of τ, the solution of the δ-four-stream approximation for infrared wavelengths is the same as that for solar wavelengths. For a nonhomogeneous atmosphere, we may divide this atmosphere into N layers in which the δ-four-stream scheme may be applied to each layer. The solution involves the 4xN unknown coefficients, which can be determined by the boundary conditions for the diffuse intensities at the top and bottom of the atmosphere and by matching the diffuse intensities at the interface of the predivided homogeneous layers.

Nongray gaseous absorption, including H_2O, CO_2, O_3, CH_4, and N_2O absorption lines and H_2O continuum, is incorporated in the δ-four-stream scheme based on the correlated k-distribution method (Fu and Liou, 1992). In this method, the cumulative probability function g replaces the frequency ν as an independent variable. Using the optimum number of g intervals to represent the gaseous absorption and to treat overlap within each spectral interval, 121 spectral calculations are required for the entire spectrum. The accuracy of the δ-four-stream scheme coupled with the parameterization for nongray gaseous absorption has been examined with respect to results computed from a line-by-line program. Shown in Fig. 2 is a comparison of IR cooling rates for the midlatitude summer profile when all the constituents are included in the calculations. Discrepancies of ~0.08 K/day are shown in the troposphere. Figure 2 also shows a comparison of solar heatings due to water vapor in the midlatitude summer for different solar zenith angles. The errors in heating rates are less than 0.05 K/day.

The effective upward and downward emissivities ($\epsilon^{\uparrow}$ and $\epsilon^{\downarrow}$) and solar albedo (α) have been derived from aircraft observations by

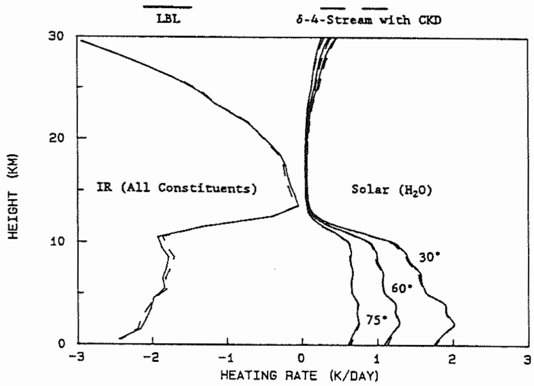

Fig. 2: Comparison of the heating rates computed from the δ-four-stream approximation coupled with the correlated k-distribution (CKD) and a line-by-line (LBL) method.

Stackhouse and Stephens (1991) for the 28 October 1986 FIRE case, which is shown in Figs. 3a-c as a function of the ice water path (IWP). The uncertainties for the observed points are shown by the extent of the vertical and horizontal lines. The model results are also displayed in Fig. 3 for comparisons. In the model simulations, the atmospheric profile used was the average of two soundings from Green Bay at 1400 and 1730 UTC. The cloud was positioned between 8.9 and 11.1 km and the IWP was varied by changing the assumed ice water content (IWC) but keeping cloud positions (cloud top and base) fixed. Ice saturation mixing ratio was assumed in the cloud. The mean effective sizes of 25, 50, 75, 100, and 125 μm were employed in the calculations. These values correspond to five solid lines for $\epsilon^{\uparrow}$, $\epsilon^{\downarrow}$, and α in Figs. 3a-c. The solar zenith angle used was 61.3° and the surface albedo was assumed to be 0.072. The effect of Rayleigh scattering was included in the calculation. Comparing the model results to observed data, we find that the mean effective size is between ~50 - ~100 μm for $\epsilon^{\uparrow}$ and $\epsilon^{\downarrow}$, and ~50 - ~75 μm for α. The mean effective sizes in the cases of effective emissivities are consistent in view of the observational uncertainties. However, the mean effective size in the case of the solar albedo is smaller than that in the case of the effective emissivity. This difference can be explained by the fact that the solar albedo is more sensitive to the size distribution at the cloud top. Based on aircraft observations, the ice crystal dimension shows a trend from smaller sizes near the cloud top to larger sizes at the cloud base (Heymsfield et al., 1990). Figure 3 shows that the mean effective size increases as IWP increases. This is expected because larger IWCs are usually correlated with larger ice crystals. The observed data in terms of cloud emissivities and albedo can largely be explained by the results obtained from model calculations. Further verification of the model simulations would require the reduction of large experimental uncertainties for radiation and microphysical measurements.

4. The Radiative Effects of Ice Crystal Size Distribution

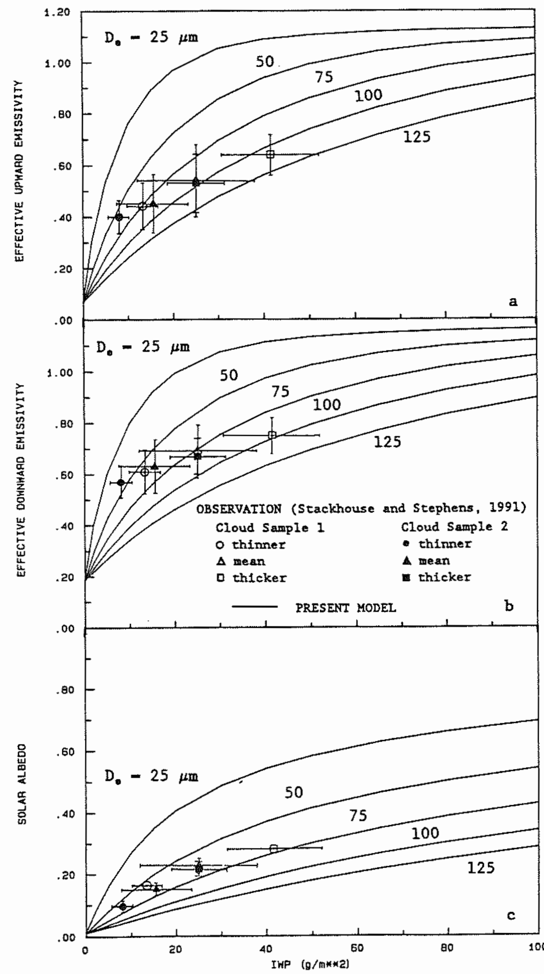

Fig. 3: Comparison of the upward and downward IR emissivites and solar albedo computed from parameterizations and obtained from aircraft measurements during the FIRE cirrus IFO (1986).

Ackerman et al. (1988) carried out a theoretical study to investigate the interaction of infrared and solar radiation with tropical cirrus anvils. Their study was confined to cirrus clouds with a fixed ice crystal size distribution. We examine the effects of ice crystal size distributions on radiative heating within the cloud. The cirrus cloud layer is inserted in the standard atmosphere between 9 and 11 km. A solar constant of 1360 W m^{-2}, a surface albedo of 0.072, and a solar zenith angle of 61.3° were used in the calculations. We also used the mean effective sizes of 25, 50, 75, 100 and 125 μm, covering a realistic range of observed sizes, to investigate their effects on the heating rate. Figure 4 shows the net (solar + IR) heating rate as a function of the mean effective size. The IWC used is 0.015 g m^{-3}, which corresponds to an IWP of 30 g m^{-2} for a typical cirrus cloud. For the smallest D_e of 25 μm, heating rates of about -16 and 32 K/day take place close to the top and bottom of the cloud layer, respectively. Such large differential heating rates between cloud bottom and top (~50

K/day) would have a significant effect on both the entrainment and cloud microphysics (Ackerman et al., 1988). For a D_e of 125 μm, the heating rates at the cloud top and bottom are 2.5 and 5 K/day, respectively. It is clear that radiative heating gradients within the cloud are a function of D_e and that these gradients increase as D_e becomes smaller. As demonstrated by Ackerman et al. (1988), for a given size distribution, larger IWC generates stronger radiative heating gradient. Changes in the heating gradient due to D_e and IWC are thus in opposite directions. Based on observations (Heymsfield et al., 1990), the IWC usually increases with increasing particle size. Therefore, the effects of IWC and D_e may partially compensate each other in actual cirrus clouds. It is well known that the minimum length that an optical probe can measure at this time is about 20 μm. The presence of small particles would reduce the mean effective size, which would generate a steeper lapse rate within clouds.

5. Discussion

A new approach for the parameterization of the broadband solar and infrared radiative properties of ice clouds has been developed. This new parameterization integrates in a coherent manner the δ-four-stream approximation for radiative transfer, the correlated k-distribution method for nongray gaseous absorption, and the scattering and absorption properties of hexagonal ice crystals. There are several new features in the present scheme. First, the ice crystal size distribution consisting of nonspherical particles is effectively accounted for in the parameterization of the single-scattering properties of cirrus clouds. This is especially important in the determination of the solar albedo of cirrus clouds. Second, the IR and solar radiation regions have been treated in a self-consistent fashion using the same parameterization scheme, which is essential to the investigation of the solar albedo effect versus the IR greenhouse effect on the climate system. Third, the present model can efficiently compute the detailed vertical structure of heating rate profile within clouds, which is critical to the understanding of the effects of radiation on cloud formation. The present parameterization for the radiative transfer in the atmosphere involving cirrus clouds is well suited for incorporation in numerical models to study the climatic effects of cirrus clouds, as well as to investigate interactions and feedbacks between cloud microphysics and radiation.

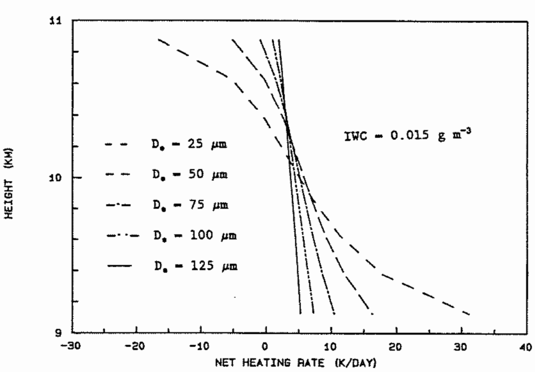

Fig. 4: Heating rates in a cirrus cloud for five mean effective sizes for a given IWC.

Acknowledgments. The research work contained herein has been supported by AFOSR Grant 91-0039, NASA Grant NAG5-1050, and, in part, by NSF Grant 90-24217.

REFERENCES

Ackerman, T.P., K.-N. Liou, F.P.J. Valero, and L. Pfister, 1988: Heating rates in tropical anvils. J. Atmos. Sci., 45, 1606-1623.

Asano, S., and M. Sato, 1980: Light scattering by randomly oriented spheroidal particles. Appl. Opt., 19, 962-974.

Auer, A.H., Jr., and D.L. Veal, 1970: The dimension of ice crystals in natural clouds. J. Atmos. Sci., 27, 919-926.

Foot, J.S., 1988: Some observations of the optical properties of clouds. II: Cirrus. Quart. J. Roy. Meteor. Soc., 114, 145-164.

Fu, Q., and K.-N. Liou, 1992: On the correlated k-distribution method for radiative transfer in nonhomogeneous atmospheres. J. Atmos. Sci. (Accepted).

Heymsfield, A.J., 1975: Cirrus uncinus generating cells and the evolution of cirriform clouds. J. Atmos. Sci., 32, 799-808.

Heymsfield, A.J., and C.M.R. Platt, 1984: A parameterization of the particle size spectrum of ice clouds in terms of the ambient temperature and the ice water content. J. Atmos. Sci., 41, 846-856.

Heymsfield, A.J., K.M. Miller, and J.D. Spinhirne, 1990: The 27-28 October 1986 FIRE IFO cirrus case study: Cloud microstructure. Mon. Wea. Rev., 118, 2313-2328.

Liou, K.-N., Q. Fu, and T.P. Ackerman, 1988: A simple formulation of the delta-four-stream approximation for radiative transfer parameterization. J. Atmos. Sci., 45, 1940-1947.

Stackhouse, Jr., P.W., and G.L. Stephens, 1991: A theoretical and observational study of the radiative properties of cirrus: Results from FIRE 1986. J. Atmos. Sci., 48, 2044-2059.

Takano, Y., and K.-N. Liou, 1989: Radiative transfer in cirrus clouds. I. Single-scattering and optical properties of hexagonal ice crystals. J. Atmos. Sci., 46, 3-19.

Warren, S.G., 1984: Optical constants of ice from ultraviolet to the microwave. Appl. Opt., 23, 1206-1225.

The Sensitivity of Solar Radiative Properties to Cloud Microphysics in Low Cloud Layer Simulations

Zinaida N. Kogan, Douglas K. Lilly, and Yefim L. Kogan

Cooperative Institute for Mesoscale Meteorological Studies
University of Oklahoma, Norman OK

1. Introduction

High sensitivity of the earth's radiation budget to cloud parameters necessitates the development of cloud parameterizations schemes as accurate as possible. In most climate change studies cloud radiative properties are generally assumed to be constant, i.e., either optical thickness or the bulk radiative properties such as the transmittance and reflectivity are fixed (Wetherald and Manabe,1988). The climatic effects of clouds are restricted mostly to those associated with changes in cloud amounts. The same practice is also standard in GCM models. Extensive observations, however, demonstrate (e.g., Feigelson, 1978) that those predetermined cloud properties do not often agree well with either observational data or theory. It is therefore desirable to compare the existing parameterization schemes, improve and/or develop new ones which have a better physical basis and relate the radiative properties more directly to cloud macro- and microphysical properties.

The optical thickness and transmittance of direct solar radiation are probably the most important parameters used in determination of cloud radiative properties. In this paper we will contrast different parameterizations commonly employed for these parameters, using the values obtained from an explicit microphysical model as a benchmark for comparison.

2. Model

The model employed in this study is based on a dynamical framework taken from the 3-D LES model developed by Moeng (1984) and an explicit formulation of cloud physics by Y. Kogan (1991). The model describes the processes of nucleation, condensation, evaporation, and coalescence base on two distribution functions - one for cloud condensation nuclei (19 categories from 0.0076 to 7.6 micron) and another for cloud drops (22 categories on a logarithmic scale from 1 to 128 microns). This allows prediction of the aerosol and drop spectra from activation to drizzle formation. For details related to description of the numerical experiment and the data presented here, the reader is referred to the paper by Kogan et al (1992) in this volume.

3. Results

The exact definition of optical depth (excluding the effects of water vapor) is:

$$\tau_\lambda = \int_0^H \int_0^{r_m?} f(r) Q_{ext}(x)\, \pi\, r^2\, dr\, dz \qquad (3.1)$$

where $f(x,y,z,t,r)$ is the droplet size distribution function, r radius of a droplet, H is the cloud depth and Q_{ext} is the extinction efficiency factor for the given wave length λ. According to Mie theory for spherical droplets and large x ($x=2\pi r/\lambda$), Q_{ext} asymptotes approximately to a constant value of 2. Using this value and making certain assumptions about averaged micro and macro parameters of the cloud, two commonly employed in large-scale models parameterizations for cloud optical thickness can be obtained. The first is given as (Cotton and Anthes, 1989) :

$$\tau_\lambda = 2\, \pi\, \bar{r}^2\, N_c\, H \qquad (3.2)$$

where N_C is droplet concentration, $\bar{r}$ is mean droplet radius, and H is the cloud layer geometrical thickness.

Another parameterization of (3.1) very popular in large-scale models (Stephens, 1984, Slingo, 1989, Cotton and Anthes, 1989) was proposed by Stephens (1978) and employs as parameters the cloud droplet effective radius and liquid water path:

$$\tau_\lambda = (3/2)\, W/r_{eff} \qquad (3.3)$$

where W represents the liquid water integrated over the cloud vertical layer and r_{eff} is the effective radius defined as the ratio of the third to the second moment of the droplet size distribution function. Comparison of the optical depth calculated according to the exact formula (3.1) with parameterizations (3.2)-(3.3) used in GCN and global climate change models will enable us to evaluate the accuracy of the latter parameterizations.

To demonstrate the horizontal inhomogeneities in the 3-D fields as well as to show the potential of the model to reveal them, we show the results from a 3-D LES numerical simulation of a cloud-topped boundary layer during the stage of its transition from convective to a well-mixed quasi-stationary stage. The cloud layer top resides on the inversion level z=1000 m and the cloud layer bottom varies around average height z=796 m .

Fig. 1 shows the isolines of cloud optical thickness in a horizontal cross-section at z=150 m. The cloud optical thickness was calculated according to (3.1) using the drop size distribution function explicitly predicted in the model. Highly inhomogeneous character of this parameter is evident. It varies from 0 to 54 with an average of ~6.2.For comparison Fig.2 shows the liquid water content field at the middle level of the cloud. The gross geometrical structure of both fields is similar, although substantial differences exist on smaller scales. This should be expected, as these two fields roughly represent the third and second moments of the drop size distribution function.

Fig. 3 shows the vertical profiles of optical depth calculated from (3.1) - (3.3). The curve labeled as "model" shows the optical depth parameter calculated using the drop size distribution function from the explicit microphysical model and then horizontally averaged. The profiles parameterized according to (3.2) - (3.3) (labeled as P1 and P2 respectively) need for their calculation the horizontally averaged values of Nc, W, H, and r_{eff}. To obtain these values for large scale models certain assumptions on cloud microphysics have to be made. Usually it is assumed that the

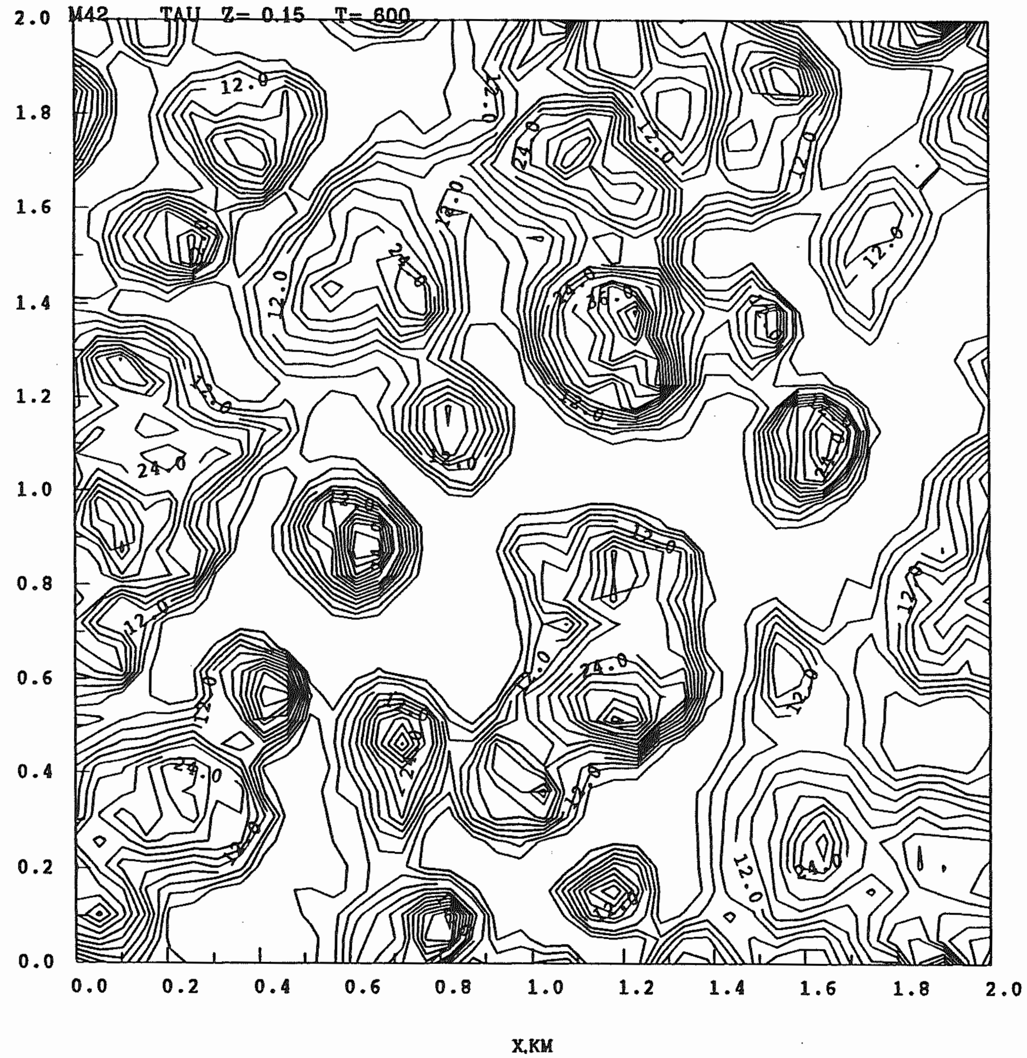

Fig. 1. Isolines of the optical depth in the xy cross-section at the level below the cloud base (z=0.15 km). Time is 600 sec. Contour interval is 3.

cloud is homogeneous and has a prescribed drop size distribution, defined either empirically (e.g., Khrgian-Mazin formula) or analytically (e.g., Gamma distribution). For the present study we mimic this approach by determining the parameters of (3.2) - (3.3) from the high resolution model data of the drop size distribution function f(x,y,z,t,r) and averaging it over the entire integration domain.

As can be seen from Fig. 3, the parameterized expressions can result in 20-40% difference compare to the "model". As an another example, we will show the sensitivity to the averaging procedure of the transmittance of direct solar radiation Tr. For zero zenith angle, its average value is determined as:

$$\mathrm{Tr}\,(z) = \overline{\exp(-\,\tau\,(x,y,z,t)\,)} \qquad (3.4)$$

where the bar means averaging over each horizontal cross section. As such an average can not be obtained without detailed microphysics, it is sometimes replaced by a simpler expression:

$$\mathrm{Tr_p}\,(z) = \exp(-\,\overline{\tau\,(x,y,z,t)}\,) \qquad (3.5)$$

where $\overline{\tau}$ is determined according to (3.2) - (3.3) as explained above. On Fig. 4. we show the vertical profiles of transmittance of direct solar radiation calculated according to (3.4) - (3.5). As Fig. 4 shows, the value of transmittance on the ground calculated from the model data according to (3.4) is about 0.26, which means that the cloud will transmit 26% of the direct solar radiation incident on its top. This transmittance value would correspond to the cloud layer which, if were "smoothed out " from all inhomogeneuties, would have an average optical depth of order of 1.35, and would be still partially transparent for direct solar radiation.

We believe, that this unexpected fact could be in most part explained by those spatial variations of microphysics on the scales of order of hundred meters. The latter are commonly ignored because of the lack of available fine resolution data. It is also interesting to estimate the total amount of solar radiation (direct + scattered), which is transmitted through the Sc-cloud layer in both considerations: for homogeneous one and with the same average parameters, but with spatial variations in microphysics.

These estimates, obtained for the total solar (direct + scattered) radiation, which reaches the surface (Kondrat'yev and Binenko, 1987) show that in the homogeneous cloud layer about 32% of total solar radiation reaches the ground and all of it is scattered, while in the cloud layer, taking into account space inhomogeneities, about 49% of the cloud top incident radiation reaches the ground. In the latter case the direct solar radiation makes up about 26% of the transmitted amount, with the remaining 23% comprised of scattered radiation. We see that the difference in the radiation, which

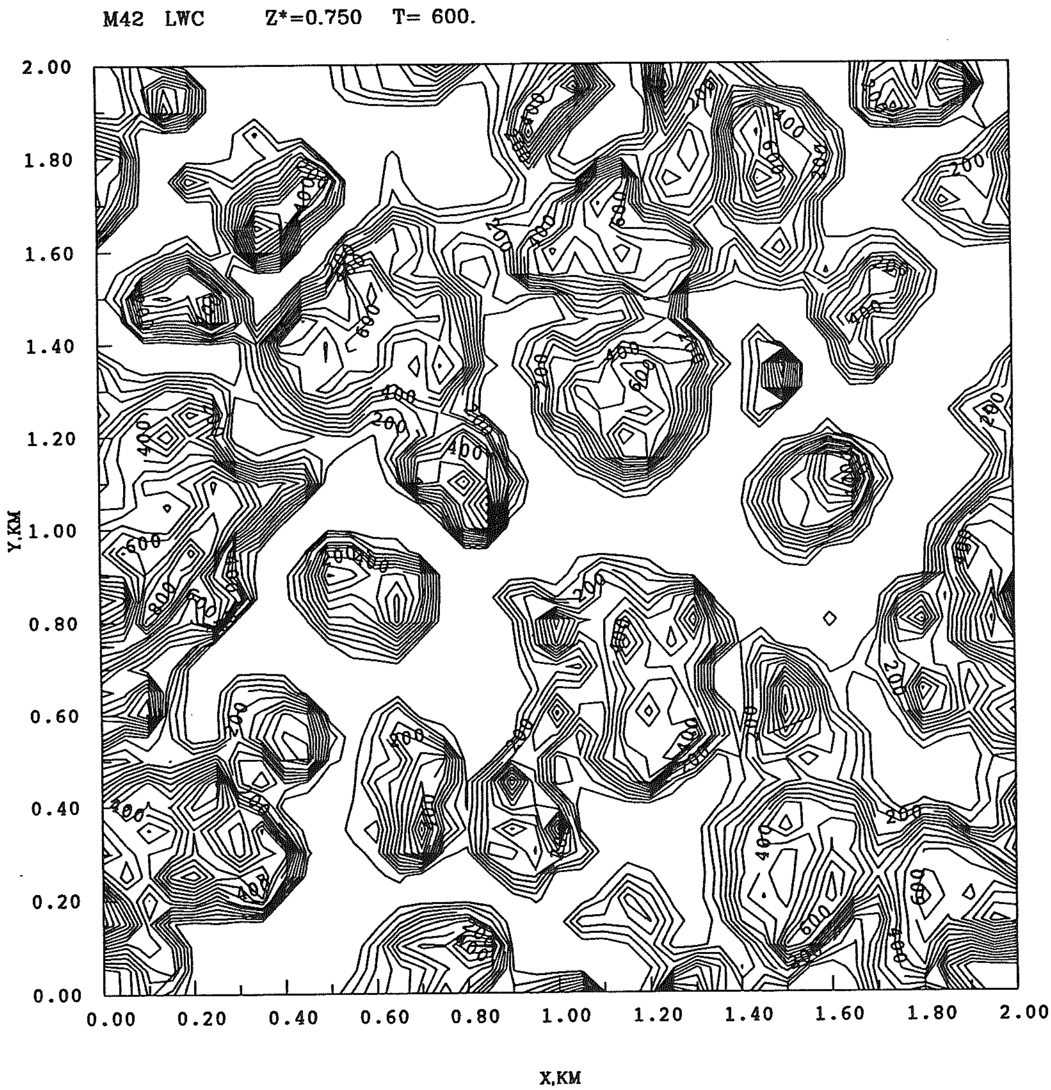

Fig. 2. Isolines of LWC (scaled by a factor of 10^3) in horizontal cross-section at the middle level in the cloud, timeis 600 sec. Contour interval is 50 x 10^{-3} g m^{-3} .

reaches the surface, is not only in the type (direct or scattered) of radiation , but also in its amount. In other words, if we take into account the spatial inhomogeneities in microphysics of Sc-cloud layer while computing the optical depth and transmittance, it will result in a larger transmittance and, consequently, a larger (by 17%) amount of solar radiation which can finally reach the surface through a cloudy atmosphere.

If we use (3.5) for computing Tr with a value $\bar{\tau}$, obtained either from model (~6.2), or from parameterizations (3.2) - (3.3) -- ($\bar{\tau}$ ~ 5 - 12), the cloud layer, however, will be practically opaque to direct solar radiation.

We consider our results as the preliminary ones, which show that the cloud layers, when spatial variations in microphysics are taken into account, can transmit through them part of the incident solar radiation even if they have average high value of optical depth. It happens if they are highly inhomogeneous in space and those variations in microphysics, if they are taken into account, may result in the increased (compare to accepted earlier) transmittance and therefore in the increased magnitude of the heat, which the surface actually gains in the cloudy atmosphere.

We are planning a set of new experiments to verify and confirm our results on more statistics as well as to include the new parameterization schemes not only for optical thickness and then single scatter albedo, but extending to the study of parameterization schemes of radiative transfer in clouds.

4. Conclusions

A sensitivity study has been conducted based on a 3-D high resolution large eddy simulation model with explicit formulation of stratocumulus cloud microphysics. We have shown a sensitivity of cloud optical depth to the employed parameterizations. Sensitivity of cloud transmittance to the spatial microphysical variations has also been revealed. Due to approximations commonly used in parameterizing procedure, in some cases significant differences may result in obtained values of cloud optical depth and transmittance of solar radiation: cloud transmittance of direct solar radiation can be as high as 0.26 instead of zero if spatial inhomogeneities in cloud microphysics are taken into account .

Our preliminary results show that the cloud layers with spatial variations in microphysics being explicitly considered can transmit through them part of the incident solar radiation even if they have as high average value of optical depth as of order of ~ 6.2. That can be explained due to space variations in microphysics which may result in the increased (compared to homogeneous case) transmittance and therefore in the

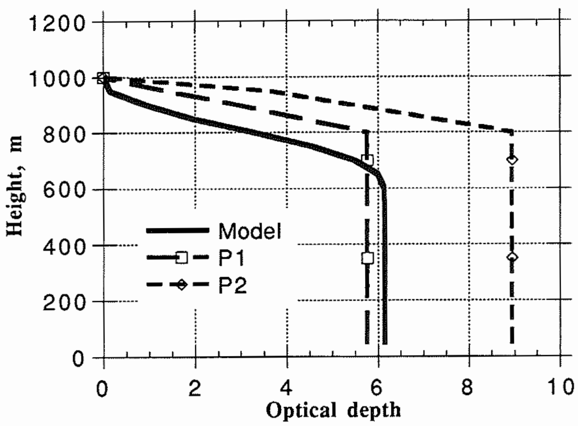

Fig. 3. Vertical profiles of the optical depth parameter obtained from the explicit microphysical model data, and using parameterizations (3.2) -(3.3) (see text for explanation).

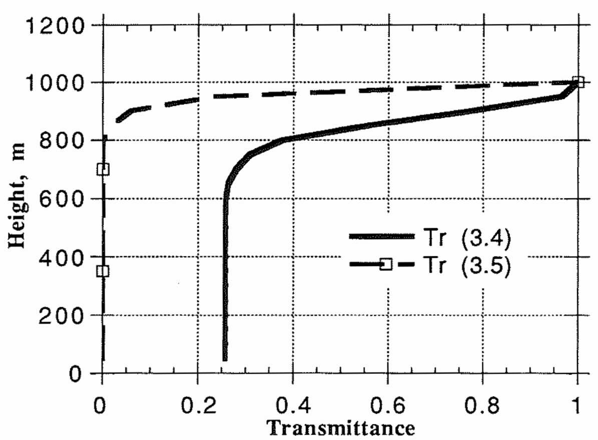

Fig. 4. Vertical profiles of transmittance obtained from the explicit microphysical model according to (3.4) and using averaging procedure according (3.5).

increased magnitude of the heat, which the surface actually may gain through a cloudy atmosphere.

We plan to conduct more experiments to verify and confirm our results on more cases as well as to include the other parameterization schemes for radiative transfer parameters in clouds.

Acknowledgments . The authors would like to thank V.V. Filyushkin for his useful comments. Support for this research was provided by NOAA's Climate and Global Change Program under the Grant NA16RC0117.

References

Cotton, W. R. and R. A. Anthes, 1989: Storm and Cloud Dynamics, Academic Press, Inc., 883 pp.

Feigelson, E.M., 1978: Flows of Sun Radiation and Clouds. Hydrometeoizdat Press, Leningrad, 156 pp. (in Russian).

Kogan, Y. L., 1991: The simulation of a convective cloud in a 3-D model with explicit microphysics. Part I: Model description and sensitivity experiments. *J. Atmos. Sci.*, **48**, 1160-1189.

Kogan Y. L., , D. K. Lilly, Z. N. Kogan, and V. V. Filyushkin, 1992: A 3-D large-eddy simulation model of a stratocumulus cloud layer with explicit formulation of microphysical and radiative processes. The 11th International Conference on Clouds and Precipitation, Aug. 17-21, 1992, Montreal, Canada.

Kondratyev, K.Ya. and Binenko, V.I., 1987: The Cloudiness Effect on Radiation and Climate. Hydrometeoizdat, Leningrad, 210 pp. (in Russian).

Moeng, C.-H., 1984: A large-eddy simulation model for the study of planetary boundary layer turbulence., *J. Atmos. Sci.* , **41**, 2052-2062.

Slingo, A., 1989: A GCM parameterization for the shortwave radiative properties of water clouds., *J. Atmos. Sci.* , **46**, 1419-1427.

Stephens, G. L., 1984: The parameterization of radiation for numerical weather prediction and climate models. *Mon. Wea. Rev.*, **112**, 826-867

Wetherald, R.L., and S. Manabe, 1988: Cloud feedback processes in a general corculation model., *J. Atmos. Sci.*, **45**, 1397-1415.

FIRE CIRRUS AND ASTEX FIELD EXPERIMENTS

David S. McDougal[1] and John T. Suttles[2]

[1]NASA Langley Research Center, Hampton, Virginia 23665
[2]NASA Headquarters, Washington, DC 20546

1. INTRODUCTION

From its inception, FIRE (the First ISCCP Regional Experiment; ISCCP is the International Satellite Cloud Climatology Project) has been designed to be conducted in two phases. FIRE Phase I (1984-1989) was designed to address fundamental questions concerning the relationships of cirrus and marine stratocumulus cloud systems with climate; to validate cloud parameters deduced by ISCCP; and to develop realistic cloud-radiation parameterization schemes used in GCM's (Bretherton and Suomi, 1983;; Cox et al., 1986). FIRE research over those years has led to major improvements in our understanding of the role of these clouds in the global climate system. Perhaps more importantly, FIRE investigations have enabled us to ask the right questions for the second phase of productive research. Based on the results of Phase I, including lessons learned in conducting intensive field programs, FIRE Phase II (1989-1994) will focus on more detailed questions concerning the formation, maintenance, and dissipation of these cloud systems (FIRE Phase II Research Plan, 1989). FIRE is supported nationally by NASA, NSF, ONR, DOE, DOD, and NOAA, and internationally by Portugal, United Kingdom, France, and Russia. The project is managed at the NASA Langley Research Center (LaRC).

2. CIRRUS IFO-II

The FIRE Cirrus Intensive Field Observations-II (IFO-II) was conducted November 13 - December 3, 1991, in southeastern Kansas. The objective of Cirrus IFO-II was to investigate the cloud properties and physical processes of mid-continent cirrus clouds and advected sub-tropical cirrus clouds. The Cirrus IFO-II combined coordinated satellite, airborne, and surface-based observations with modeling activities to study the roles and interactions of processes acting over telescoping scales ranging from the microscale to the large-scale and on characterizing the physical, radiative, and optical properties of cirrus clouds (FIRE Cirrus Intensive Field Observations-II: Operations Plan, 1991). The data will be instrumental in developing parameterizations relating cloud-scale processes to climate-scale variables, and in improving our understanding and utilization of ISCCP data products.

A number of platforms, instruments, and research organizations participated in Cirrus IFO-II (figure 1; table 1). Surface observations were made from Coffeyville and Parsons, Kansas, using upward-looking remote sensors including lidars, wind profilers, Doppler radars, radiometers, and spectrometers. Four aircraft performed in situ and remote measurements above, within, and below the cirrus clouds. Rawinsondes were launched from five sites in the southeastern Kansas region. Special rawinsonde releases from 51 NWS stations in the western and central U.S. were made on three selected intensive mode periods to support NMC and mesoscale modeling analyses to define the large-scale and mesoscale dynamic and thermodynamic fields. The IFO-II instrumentation was intentionally sited within the new NWS wind profiler network that provided FIRE with large-scale horizontal and vertical velocity fields. The IFO-II observations were made in concert with overpassing satellites. Other collaborative experiments participating were the Spectral Radiation Experiment (SPECTRE) and the Surface Radiation Budget (SRB). Approximately 150 researchers from 40 research institutions from the U. S., Russia, Japan, Canada, Germany, and Switzerland participated.

During the 25-day period, observations were performed on cirrus clouds associated with the midlatitude jet stream, including baroclinic leaf, ridge crest, and shortwave phenomena; subtropical jet stream, subtropical storms, and tropical sources; and pre-warm frontal systems. Observations were made of the regional development and dissipation of cirrus cloud systems; remote and in situ sensing of microphysical, radiative, and dynamical cirrus cloud properties; and clear sky conditions. For the first time, cirrus clouds have been measured from aircraft, satellite, and surface-based instruments over a significant part of the diurnal cycle, including sunrise, daytime, sunset and midnight conditions. A summary of the operational aspects are as follows: 118 platforms, instruments, or models participated; operations were conducted every day; 4 aircraft flew 51 missions for 158 hours; 1524 special rawinsondes were released; and 88 satellite overpasses occurred at times and locations when sondes or aircraft were operating. The science team has reviewed the daily mission summaries and has selected the periods November 25-26 and December 5-6 for priority data reduction and analysis.

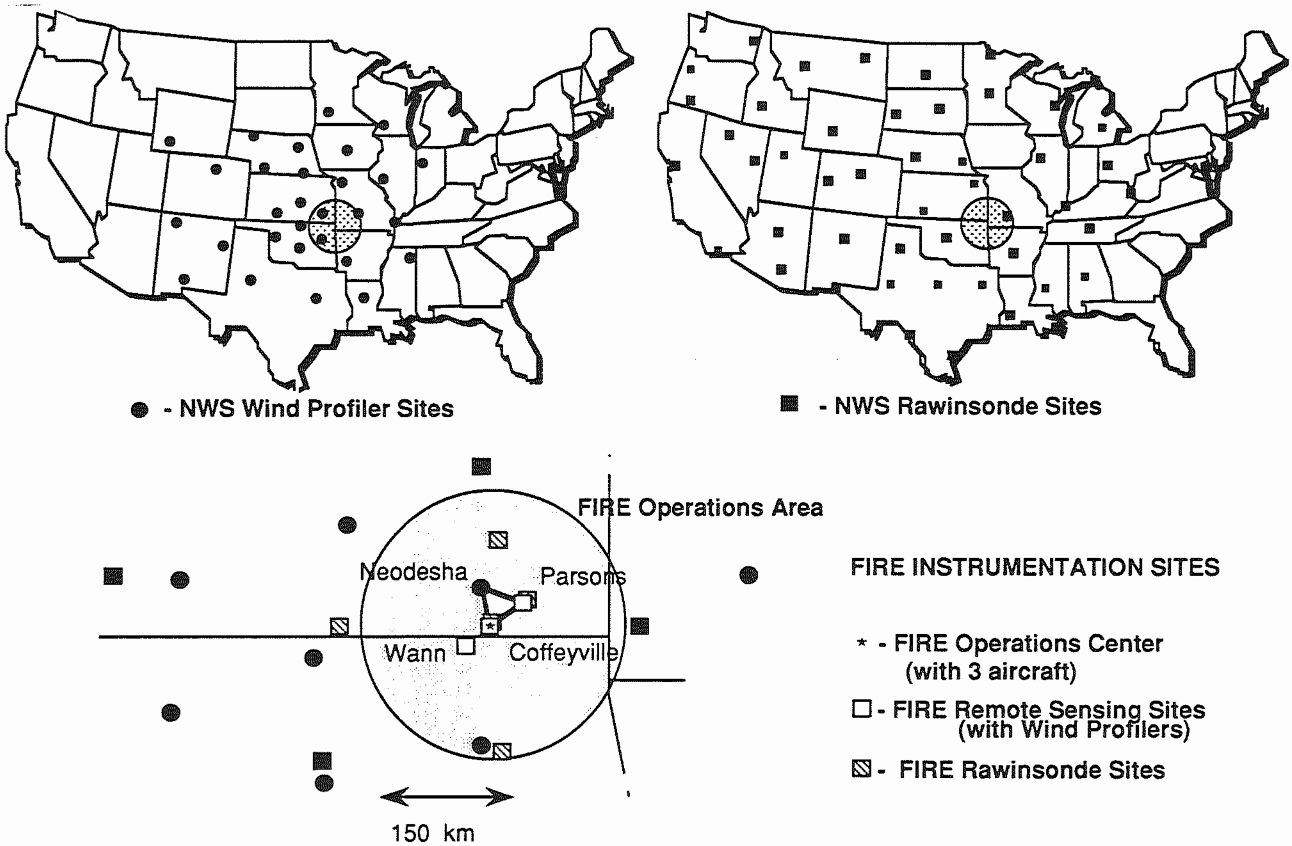

Figure 1 - Location of instruments and platforms for Cirrus IFO-II.

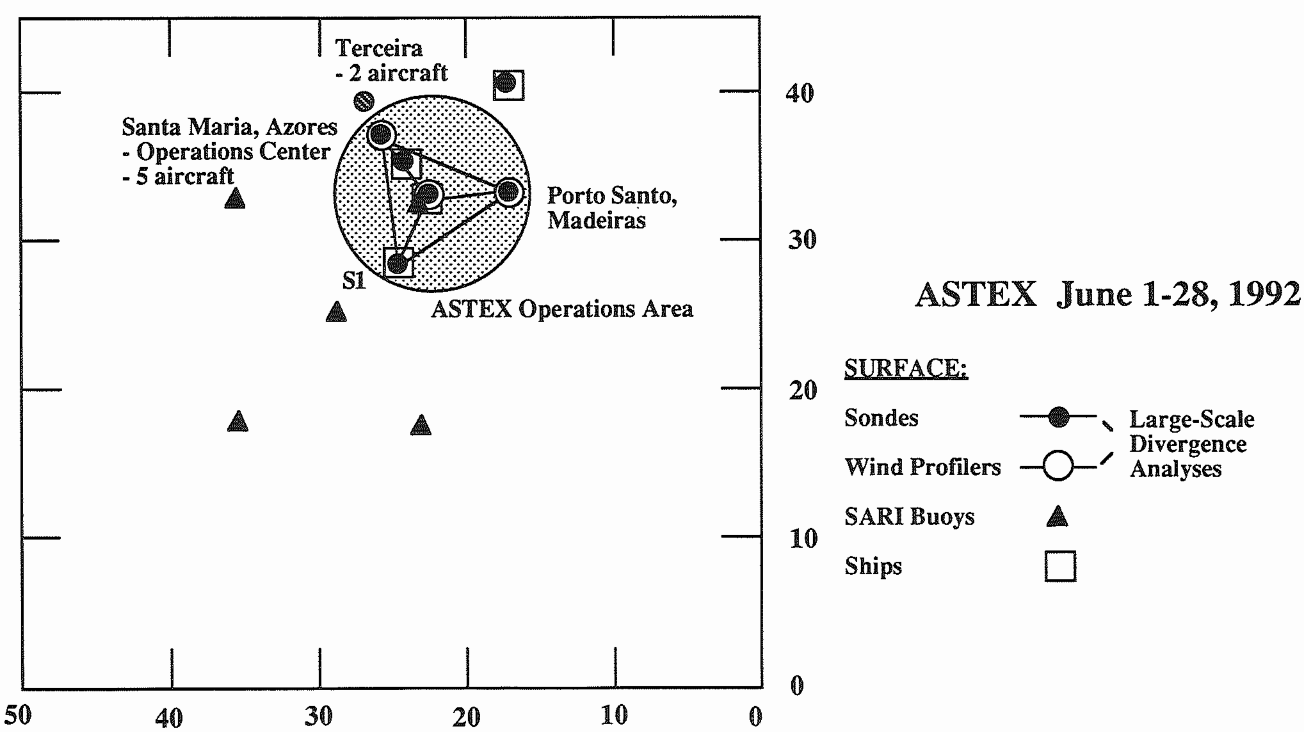

Figure 2 - Location of instruments and platforms for ASTEX.

Table 1 - Platforms, instruments, and organizations participating in Cirrus IFO-II

Platform	Instrument	Organization
SURFACE-BASED		
Lidars	Polarization Diversity Lidar	UUT
	High Spectral Resolution Lidar	UWI
	Volume Imaging Lidar (VIL)	UWI
	CO_2 Doppler Lidar	NOAA-WPL
	Ceilometers	PSU, CSU. NASA-LaRC
	Polarization Lidar	NASA-LaRC
Radars	Doppler Radars	NOAA-WPL, PSU, CSU
Radiometers	Microwave Radiometer	NOAA-WPL
	Whole Sky Imager	AFGL-ASD
	Infrared Scanning Radiometer	AFGL-SMB
	Radiometers	NASA-ARC, MRI, PSU, CSU, IAP
	Sky Imaging System	PSU
	PAMS	NCAR, NASA-GSFC, CSU
	IR Radiometer	UUT
	Sky Camera	NASA-LaRC
	IR Spectrometer	AC
Wind Profilers	Wind Profilers/RASS	PSU, NOAA-WPL, CSU
	NWS Wind Profilers	NASA-GSFC, PSU, NOAA-WPL, NWS
SPECTRE	Mission Planning	NASA-GSFC, UMD
	Raman Lidar	NASA-GSFC
	SIRIS	NASA-GSFC
	Radiometers	UDE, NOAA-ERL, Eppley Labs, ETH, AES, K&S
	HIS (2)	UWI
	RASS	NOAA-WPL
	Dobson	NOAA-ERL
	Trace Gases	NOAA-ERL
	Rawinsondes	NASA-WFF
	Ozonesondes	NASA-WFF
AIRBORNE		
Aircraft	ER-2	NASA-GSFC, NASA-ARC, UWI
	Sabreliner	NCAR, CSU
	King Air	NCAR, UUT, AFGL-ASD
	Citation	UND, DRI
	FAA	KCARTCC
Sondes	NWS Sondes	NASA-GSFC, CSU, NWS
	CLASS Rawinsondes	NASA-GSFC, CSU, NCAR
	Replicator Sondes	NCAR
SATELLITE		
GOES	VISSR, VAS	NASA-LaRC, UWI
AVHRR	GAC, HRPT, HIRS, MSU	NASA-GSFC, UWI, OSU
Landsat	TM	NASA-LaRC, SDSM
DMSP	SSM/I, Imager	AFGL
ERS-1	ATRS	NASA-GSFC, NASA-LaRC
ISCCP	CX	NASA-GISS
MISSION OPS		
Forecasting	McIDAS	UWI
	DWIPS	NASA-LaRC
Modeling	Mesoscale	NASA-ARC, CSU, PSU
	Divergence Analysis	PSU
	Microphysics	NASA-ARC
	Dynamic	NASA-GSFC
	Satellite Analysis	NASA-LaRC, OSU, UWI
Mission Planning		NASA-GSFC
Project Office		NASA-LaRC, STX

3. ASTEX

The Atlantic Stratocumulus Transition Experiment (ASTEX) was conducted June 1-28, 1992, in the vicinity of the Azores and Madeira Islands in the northeastern Atlantic. The objective of ASTEX was to study the type and amount of marine stratocumulus clouds and determine how these clouds are regulated. ASTEX combined coordinated satellite, airborne, island, ship, and buoy observations with modeling activities to investigate the consequences to the atmosphere and ocean of marine stratocumulus clouds and their life-cycle variations, including the important broken cloud regimes (ASTEX Operations Plan, 1992). The data will be used to test several physical mechanisms that might contribute to cloud breakup, to test decisively the physical assumptions underlying the parameterizations used in climate models, and to improve our understanding and utilization of ISCCP data products. ONR is the lead agency for ASTEX and LaRC manages the project.

A large number of platforms, instruments, and research organizations participated in ASTEX (figure 2; table 2). Surface observations were made from the islands of Santa Maria, Azores, and Porto Santo, Madeira, and from the UNOLS ship Malcom Baldrige. Instruments used included Doppler radars, wind profilers, microwave radiometers, short and longwave radiometers, spectrometers, and rawinsondes. Other island measurements included a Doppler sodar, lidar, and tethered balloons. The German ship Valdivia was located about 900 km equidistance from the two islands so as to make an equilateral triangle. Three other research vessels made surface and oceanic measurements within and around the ASTEX triangle. Rawinsondes were released on a 3-hourly basis from the two islands and from three ships. Seven aircraft were used to make observations above, within, and below the low-lying clouds. A network of stationary and drifting buoys was deployed in the ASTEX area. The observations were made in concert with overpassing satellites. ECMWF, NMC, and mesoscale model analyses will be combined with the ASTEX observations to define the large-scale dynamic and thermodynamic fields. Other collaborative experiments participating were the Subduction Accelerated Research Initiative (SARI), Surface of the Ocean Fluxes and Interaction with the Atmosphere (SOFIA), and the Marine Aerosol and Gas Exchange (MAGE). Close to 300 researchers from over 50 research institutions from the U. S., United Kingdom, France, Russia, Spain, Germany, Netherlands, and Portugal participated.

Table 2 - ASTEX platforms, instruments, and organizations participating in ASTEX

Platform	Instruments	Institution
ISLAND		
Santa Maria	Meteorology	PSU
	Radiometers	PSU
	Wind Profilers (405, 915 MHz)	PSU
	RASS (405 MHz)	PSU
	Doppler Radar (94 GHz)	PSU
	Microwave Rad. (9-ch)	PSU
	Ceilometer	PSU
	IR Radiometer	PSU
	Rawinsondes	PSU, PMTC

	Tethered balloon Doppler Sodar Atmospheric chemistry	UUTR INMG URI, DU, UHA, UC-I, ESS
Porto Santo	Meteorology Rawinsondes Tethered balloon Video sky camera Radiometers at MSL &400 m IR Interferometer IR radiometer Wind Profiler (405 MHZ) RASS (405 MHz) Ceilometer	CSU CSU CSU CSU CSU CSU CSU CSU CSU CSU
	IR Radiometer Microwave rad.(3 ch) Doppler radar (35 GHz) Doppler lidar	WPL WPL WPL WPL
SHIP UNOLS Oceanus	Chemistry	URI, DU, UC-I, UA, CIT
NOAA Malcom Baldrige	Meteorology Radiometers Ceilometer IR radiometer Rawinsonde 915 MHz wind profiler 915 MHz RASS micro-wave radiometer Atmospheric chemistry	AOML AOML AOML AOML WPL WPL WPL WPL AOML, CIRES, CSU, UC-I, CFR
German Valdivia	Meteorology Rawinsonde Atmospheric radiation Oceanography	UHB UHB UHB UHB
French Le Suroit	correlation and inertial-dissipative methods tethered balloon "minisodar" (6000 Hz) Doppler sodar (2000 Hz) microwave radiometer (26 & 37 GHz) radiosounding station	UWO CRPE CRPE CRPE CRPE CRPE
BUOYS SOFIA	tethered hydrophone system drifting buoys wave buoy	 CMM, IFREMER, CNES-LA
SARI	Meteorology SST	WHOI WHOI
AIRCRAFT	NASA ER-2 UKMO C-130 NCAR ELECTRA FOKKER F-27 MERLIN IV NADC P-3 U. WASHINGTON C-131	GSFC, ARC UKMO, UC-I, SIO NCAR, URI, DU, UHA, DRI, WFF, UC-I USB, CRPE USB, CRPE NADC, WPL UWA
SATELLITES POLAR ORBITERS	AVHRR, HRPT, GAC, TOVS, HIRS	UWI, OSU, LaRC, INMG
GOES	VISSR, H2O, VAS	UWI, LaRC
METEOSAT	VIS, IR, H2O	LaRC, CNRS, UWI
Landsat	Thematic Mapper	LaRC, GSFC, SDSMT
SPOT	VIS	CNRS
DMSP	Imager, SSM/I, SSM/T1, SSM/T2	SDSMT
ERS-1		CRPE
FY1B	Imager	NPS
ISCCP	CX	GISS
MISSION OPS Modeling	1-D Radiation Turbulence GCM Bulk, High-moment closure, LES LES, 1-D, Turbulent transfer, Mesoscale (LAMPS) Mesoscale Mesoscale 3-D Mixed layer, Radiative transfer, Spectral, LES Regional Satellite analyses	GSFC UWA ECMWF, AR UUT UD ULI, INMG CSU SIO PSU STX, PSU UWI, LaRC, OSU, NPS, LaRC
Forecasting		UWI, INMG, FSU, PSU
Mission Planning		PSU
Project Office		NASA-LaRC, STX, ONR

4. FUTURE PLANS

The data analysis phase for FIRE will include both individual and multi-investigator analyses. End data products for both field experiments are expected to be quantitative measurements of the radiative, physical, microphysical, optical, dynamical, thermodynamical, and meteorological properties of cirrus and marine stratocumulus clouds. The data will be archived at the National Climate Data System located at NASA Goddard Space Flight Center. Once the data has been quality checked and reviewed, it will be released to the scientific community.

In addition, the Pilot Tropical Cirrus Experiment (PTCE) will be conducted in the equatorial western Pacific to study the high and large cirrus cloud shields that pervade over the tropics due to intensive convective activity. The PTCE will be performed in January 1993 as part of the NASA ER-2 and DC-8 aircraft flights during the Tropical Ocean and Global Atmosphere/ Coupled Ocean-Atmosphere Experiment (TOGA/COARE). The PTCE is to be viewed as a target-of-opportunity experiment to take advantage of TOGA/COARE oceanic and atmospheric measurements and as a precursor to a possible FIRE Phase III research program to investigate convective-driven cirrus clouds.

5. REFERENCES

ASTEX Operations Plan, 1992. Available from the FIRE Project Office, MS 483, NASA Langley Research Center, Hampton, VA 23665-5225.

Bretherton, F. P., and V. Suomi, 1983: First International Satellite Cloud Climatology Project Regional Experiment (FIRE) Research Plan, 76 p. Available from the National Climate Program Office, Room 108, 11400 Rockville Pike, Rockville, MD 20952.

Cox, S. K., D.S. McDougal, D.A. Randall, and R.A. Schiffer, 1987: FIRE - The First ISCCP Regional Experiment. *Bull. Amer. Meteor. Soc.*, **68**, 114-118.

FIRE Phase II: Research Plan, 1989. Available from the FIRE Project Office, MS 483, NASA Langley Research Center, Hampton, VA 23665-5225.

FIRE Cirrus Intensive Field Observation-II: Operations Plan, 1991. Available from the FIRE Project Office, MS 483, NASA Langley Research Center, Hampton, VA 23665-5225.

Clouds and two-stream radiative transfer approximation — algorithms and codes

P. J. Flatau, W. R. Cotton, and G. L. Stephens

Department of Atmospheric Science, Colorado State University, Fort Collins, CO.

1 INTRODUCTION

Modern mesoscale and global models require detailed and numerically robust radiative transfer (RT) solvers to study clear sky and cloudy atmospheres. We discuss certain aspects of the two-stream type radiative parameterization. In particular we show how a bulk microphysics scheme can be tied to extinction and scattering efficiencies. The distribution-averaged single scattering properties are calculated using the anomalous diffraction theory (ADT). We show results and suggest a scheme to get analytical expressions for size distribution averaged scattering efficiencies of irregular particles (e.g. cirrus clouds). The radiative transfer (RT) equation is solved using a fast method based on a tridiagonal solver. A new interface to molecular absorption code LOWTRAN7 is discussed. This interface allows definition of the weighted wide band model used by the RT scheme.

2 A simple parameterization of cloud single scattering properties

In many potential applications of light scattering theory the solution to the exact Maxwell equations are of such complexity that the use of exact solutions, if they exist, is impractical. The alternative is to use approximations such as van de Hulst's anomalous diffraction theory (ADT) or Bohren and Nevitt's (1983) approximation (BNA) . One of the advantages of the analytical approximations is that they can be integrated with the typical size distributions of water droplet species used in bulk microphysical models. To get averaged single scattering properties we consider the gamma size distribution which can be written in the form (Flatau et al., 1989)

$$n(r)dr = \frac{N_t}{\Gamma(\alpha)}\left(\frac{r}{r_n}\right)^{\alpha-1}\exp\left(-\frac{r}{r_n}\right)d\left(\frac{r}{r_n}\right) \qquad (1)$$

The r_n is a convenient, but non-measurable, "characteristic" radius.

2.1 Absorption efficiencies

Consider the function

$$\mathcal{K}(w) = \frac{1}{2} + \frac{\exp(-w)}{w} + \frac{\exp(-w)-1}{w^2} \qquad (2)$$

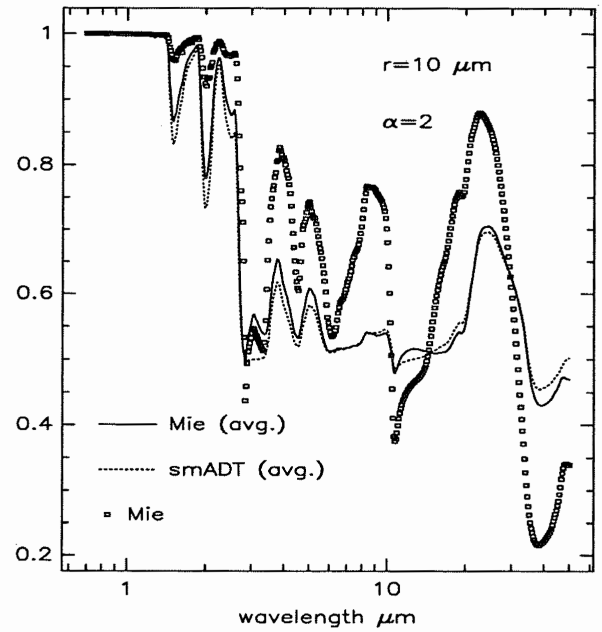

Figure 1: Single scattering albedo as a function of wavelength. Solid lines are Mie calculations for gamma distribution with $\alpha = 2$. The dashed line is the corresponding modified ADT. Square points give values of Mie without averaging for characteristic radius r_n.

and related function $\mathcal{M}(w)$

$$\mathcal{M}(w) = \frac{1}{2} + \frac{1}{\alpha(\alpha+1)}\left[\frac{\alpha}{w(w+1)^{\alpha+1}} + \frac{1}{w^2(w+1)^{\alpha}} - \frac{1}{w^2}\right] \qquad (3)$$

In terms of (2) the absorption factor in the ADT is (Smith, 1982)

$$Q_{\rm abs} = 2\mathcal{K}(4v) \qquad (4)$$

where $\mathcal{K}(v)$ is function of the real argument v. From the definition of the distribution averaged volume absorption coefficient we have

$$\beta_{abs} = 2A\mathcal{M}(4v_n) \qquad (5)$$

Bohren and Nevitt's (1983) results can also be cast in terms of $K(w)$. The absorption efficiency is given as

$$\hat{Q}_{\rm abs} = c\left[2\mathcal{K}(4v) - a^2\mathcal{K}(a4v)\right] \qquad (6)$$

and for the distribution averaged case

$$\hat{Q}_{\rm abs} = cA\left[2\mathcal{M}(4v) - a^2\mathcal{M}(a4v)\right] \qquad (7)$$

where

$$a = \frac{(n^2-1)^{1/2}}{n} \qquad (8)$$

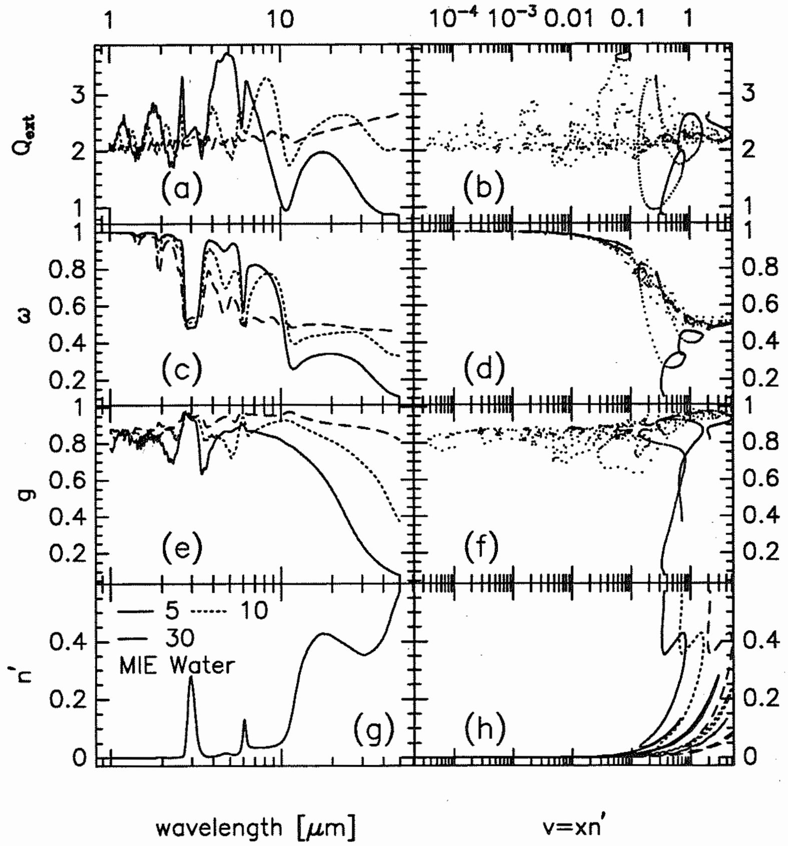

Figure 2: Each panel has three curves. Solid line is for 5μm particle. Dotted line is for 10μm Dashed line is for 30μm. Mie calculations are presented. Left column figures are plotted as a function of wavelength. Right column figures are plotted as a function of v. (a,b) Extinction efficiency. (c,d) Single scattering albedo. (e,f) Asymmetry parameter. (g,h) Complex part of refractive index.

and

$$c = \frac{4n^3}{(n+1)^2 - (n-1)^2 \exp(-4v)} \approx \frac{4n^3}{(n+1)^2 - (n-1)^2} \quad (9)$$

the last approximation holds for n close to 1. Notice that BNA is a correction to ADT. It enhances ADT by a factor c and reduces it by the correction $a^2 K(a4v)$. For $n = 1$ both approximations are equivalent. BNA has proper limits for both small and large v.

2.2 Extinction efficiency

The extinction factor is given by

$$Q_{\text{ext}} = 4\text{Re}\{\mathcal{K}(2(v + iu))\} \quad (10)$$

Notice that it is a function of two parameters u and v. Thus, extinction and other functions depending on extinction, for example single scattering albedo, can not be expected to scale with v only.

$$\beta_{\text{ext}} = 4A\text{Re}\{\mathcal{M}(2w_n)\} \quad (11)$$

2.3 Single scattering albedo

The single scattering albedo is defined as

$$\omega = 1 - Q_{\text{abs}}/Q_{\text{ext}} \quad (12)$$

The distribution averaged single scattering albedo is given in the ADT approximation by $\tilde{\omega} = \beta_{sca}/\beta_{abs}$

$$\tilde{\omega} = 1 - \frac{2\mathcal{M}(4v_n)}{4\text{Re}\{\mathcal{M}(2w_n)\}} \quad (13)$$

Assuming that $\beta_{sca} = 2A$ we get the following approximation

$$\tilde{\omega} = \frac{1}{2} - \frac{1}{(\alpha+1)\alpha}\left[\frac{\alpha}{v_n(v_n+1)^{\alpha+1}} + \frac{1}{v_n^2(v_n+1)^{\alpha}} - \frac{1}{v_n^2}\right] \quad (14)$$

It can be shown that for conservative scattering, $v_n = 0$, gives $\tilde{\omega} = 1$.

2.4 Results — single scattering approximations

In this section we present comparison of calculations based on the corrected (not discussed here) ADT and Mie results. We also exploit the self-similarity predicted by the ADT reasoning; namely, that the Mie results should be similar with respect to the parameter v.

Fig. 1 presents distribution averaged single scattering. Solid lines are Mie calculations for a gamma distribution with $\alpha = 2$. The dashed line is the corresponding modified ADT. Square points give values of Mie without averaging for characteristic radius r_n.

Figure 2 presents results of Mie calculations using the ADT v-scaling. The left column presents Mie calculations plotted against the wavelength. The right column gives the same calculations plotted with respect to the ADT parameter v. Both carry the same information. The results indicate that ADT scaling can be used for extinction, absorption, and single scattering albedo.

3 Towards parameterization of scattering by irregular particles

It is possible to ray trace complex shapes, such as hexagonal ice crystals, and obtain extinction and absorption for all orientations of such an object in the anomalous diffraction approximation. Once this is done functions $\mathcal{M}$ and $\mathcal{K}$ have to be determined empirically by the least square fit. This, in turn, allows one to obtain distribution averaged single scattering properties for scattering by irregular particles. As a step in this direction we developed a general ADT solver (ADSCAT) for convex polyhedra. The convex polyhedra allow one to study common shapes such as, for example, prisms (including hexagonal).

3.1 An algorithm

First we define vertices of a polyhedron $\mathbf{v}_i$, $i = 1, \ldots, n_v$, where $\mathbf{v}$ is a vector. Thus, for example, a cube is described by eight vertices. The vertices are used in a connectivity list which gives set of co-planar faces (polygons) defining the object. This, cube would have six such faces. The object can be arbitrarily rotated by three subsequent rotation of vertices. Once the object has been defined we project vertices on a zy-plane, assuming that incoming light is in the positive-x direction. On the basis of projected vertices we calculate the convex hull of vertices (Eddy, 1977) and the surface of a convex hull. We also define a rectangular grid encompassing the convex hull. For each ray originating on this grid and traveling in x direction we calculate the distance inside the polyhedron using a ray-polyhedron intersection algorithm. Such distance arrays are formed for several orientations of an object.

Finally we perform the ADT calculations (Bryant and Latimer, 1969; Chýlek and Klett, 1991). Figure 4 presents extinction by a hexagonal prism for several orientations defined here by θ. Three size parameters are shown.

4 LOWTRAN7 interface and band structure

Often the information about gaseous transmission is hardwired in radiative transfer codes employed in mesoscale applications; i.e. the band structure, and number of bands are pre-determined. What we propose allows the RT code to be run with arbitrary band structure. It is achieved by a flexible interface to molecular transmission code LOWTRAN7.

The LOWTRAN7 is based on recent line-by-line calculations (FASCODE/HITRAN) and includes completely re-defined narrow band (NB) transmission models as well as new scaling co-

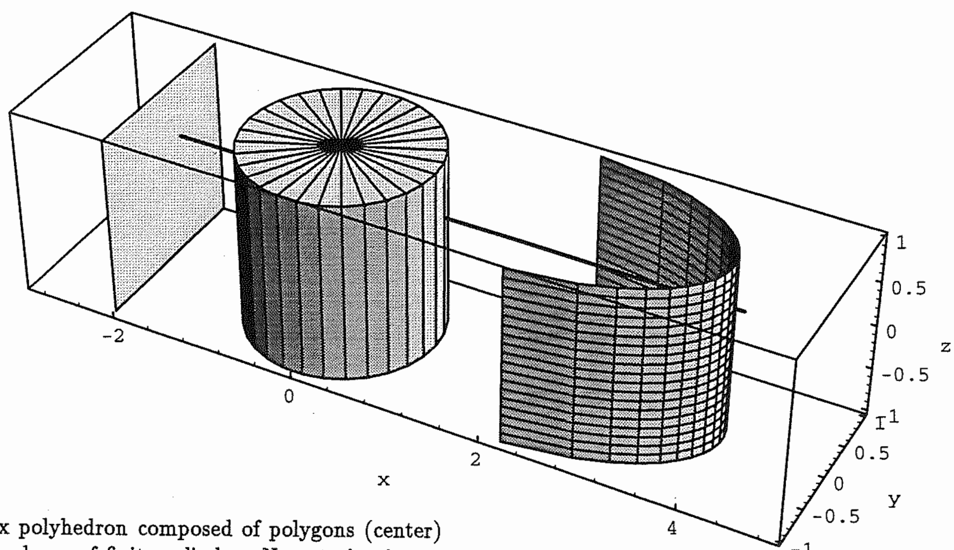

Figure 3: Convex polyhedron composed of polygons (center) approximates the shape of finite cylinder. No rotation is applied. To the right the shadow of the polyhedron is presented. It is calculated by projecting vertices and calculating their convex hull. To the left, distances inside the polyhedron are shown.

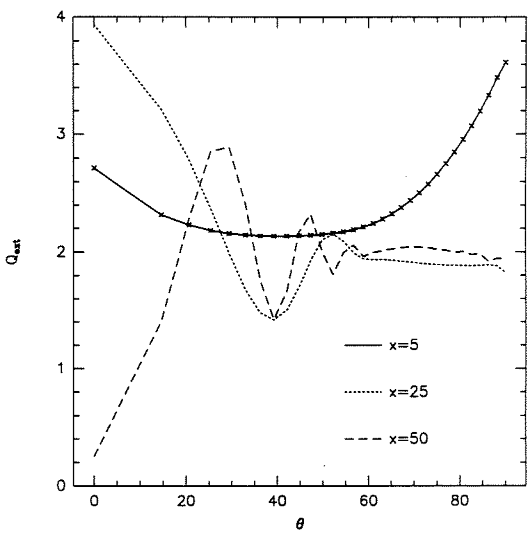

Figure 4: Extinction by hexagonal prism for several orientations defined here by θ. Three size parameters are shown.

efficients. LOWTRAN (Kneizys et al., 1988) calculates the transmittance and/or radiance of the atmosphere from $0 \mathrm{cm}^{-1}$ to $50000 \mathrm{cm}^{-1}$. Band models and band model absorption parameters developed by Pierluissi (Pierluissi et al., 1989) are included in the LOWTRAN 7 model.

Transmission for each absorber amount is obtained for several bands defined by the user. This transmission is optionally solar- or blackbody-weighted averaged. The bands are divided into narrow regions in which solar and/or Planck functions are assumed to be constant.

On input to the driver code one has to define: absorber, band type, averaging type (solar, black, or none), and the version of LOWTRAN. In addition the number of bands, number of divisions of absorber amount, initial band wavenumber, end band wavenumber, initial absorber amount, and maximum absorber amount have to be specified.

```
 1   |MNY v2.0
 2   |COMPILED with mxban,u,iv,pre=     10   250 10000     4
 3   |

 4   |yn=              .79820      .86580      .93620      .96810
 5   |ym=              .05880     -.10340    -1.63380    -1.95370
 6   |vv1[cm-1]=      11700.       8300.       4800.       2800.
 7   |vv2[cm-1]=      12500.       9300.       5900.       3340.
 8   |Flux [W/m2        58.3        72.8        56.7        10.7

 9    .10000E-03  .99979      .99788      .98986      .99562
10    .13434E-03  .99976      .99751      .98812      .99485
11    .18047E-03  .99971      .99706      .98608      .99395
12    .24245E-03  .99965      .99654      .98371      .99289
13    .32570E-03  .99959      .99592      .98094      .99165

14    ......

15    7.4438      .86959      .48055      .40553      .26686
16    10.000      .84798      .44026      .38229      .23349
```

Table 1: Example results from the LOWTRAN7 weighted broadband interface

4.1 Some results

An example (part) of results from the solar-averaged, wide band, LOWTRAN7 data are presented in Table 1. Line 1 defines the version of BANPAC, line 2 specifies the gaseous component, line 3 defines temperature and pressure, line 4 gives minimum and maximum absorber amount. These are logarithmically split between these two extreme values. Line 5 specifies number of bands. Lines 6 and 7 give solar-weighted scaling coefficients. Lines 8 and 9 specify band width in wavenumbers. Line 10 gives solar flux in the band. Rows 11 to the end have 5 columns. The first column is absorber amount, and the next four columns give transmission. Such tables are used in the RT code and are selectable by the user.

ACKNOWLEDGMENTS

The research presented in this report has been supported in part by Air Force grant AFOSR-91-0269.

References

Bohren, C. F. and T. J. Nevitt, 1983: Absorption by a sphere: a simple approximation. *Appl. Opt.*, **22**, 774—775.

Bryant, F. D. and P. Latimer, 1969: Optical efficiencies of large particles of arbitrary shape and orientation. *J. Coll. Inter. Sci.*, **30**, 291—304.

Chýlek, P. and J. D. Klett, 1991: Absorption and scattering of electromagnetic radiation by prismatic columns: anomalous diffraction approximation. *J. Opt. Soc. Am. A*, **8**, 1713—1720.

Eddy, W. F., 1977: A new convex hull algorithm for planar sets. *ACM Transactions on Mathematical Software*, **3**, 398—403.

Flatau, P. J., G. J. Tripoli, J. Verlinde, and W. R. Cotton, 1989: The CSU-RAMS cloud microphysics module: General theory and code documentation. Technical Report 451, Colorado State University, Fort Collins, Colorado 80523.

Kneizys, F. X., E. P. Shettle, and L. W. Abreu, 1988: Users guide to LOWTRAN 7. Environmental research papers AFGL-TR-88-0177, Air Force Geophysics Laboratory, Hanscom AFB, MA 01731, 137.

Pierluissi, J. H., C. E. Maragoudakis, and R. Tehrani-Mohaved, 1989: New LOWTRAN band model for water vapor. *Appl. Opt.*, **28**, 3792–3795.

Smith, C. B., 1982: Inversion of the anomalous diffraction approximation for variable complex index of refraction near unity. *Appl. Opt.*, **21**, 3363—3366.

van de Hulst, H. C., 1957: *Light scattering by small particles.* Dover Publications, Inc., New York.

Estimation of Cloud Geometrical Thickness Using 0.9μm Water Vapor Absorption Band

Tadahiro Hayasaka[1], Masayuki Tanaka[1] and Teruyuki Nakajima[2]

[1] Center for Atmospheric and Oceanic Studies, Faculty of Science, Tohoku University, Sendai 980, Japan

[2] Center for Climate System Research, University of Tokyo, Tokyo 153, Japan

1. Introduction

We have developed an algorithm to estimate the geometrical thickness of clouds by measuring reflected solar radiation in the spectral region of 0.9μm water vapor absorption band. This algorithm is based on a principle that reflected photon path length increases with increasing geometrical thickness for the same liquid water path (LWP). We used the data obtained by aircraft measurements in the Western North-Pacific Cloud-Radiation Experiment in January of 1991 conducted as a part of Japanese World Climate Research Program (WCRP).

2. Absorption of Solar Radiation and Cloud Geometrical Thickness

In the spectral region of gaseous absorption band, reflected solar radiation above clouds is affected by the magnitude of gaseous absorption and the photon path distribution of the reflected radiation. The photon path distribution is determined by phase function, optical thickness and geometrical thickness of clouds. In other words, it is determined by droplet size distribution, vertical distribution of liquid water content and the geometrical thickness. Consequently, it is possible to estimate the geometrical thickness of the cloud layer by measuring reflected solar radiation in the absorbing spectral region if parameters other than geometrical thickness are known. We retrieved the cloud geometrical thickness by using total absorption in a radiance from nadir in the spectral region of water vapor 0.9μm absorption band, and using LWP obtained by a 37GHz microwave radiometer (Fujiyoshi et al., 1992) and droplet size distribution by PMS-FSSP droplet spectrometer (Ishizaka, 1992).

3. Instruments and Observational Details

We have developed an airborne spectrometer for a wavelength range from 0.4μm to 1.1μm. This spectrometer consists of a concave grating to disperse the solar spectrum and a plasma-coupled device array of 1024 elements as a detector. The plasma-coupled device, which is based on the photoelectric effect similar to photo-diode, has a large dynamic range by changing the exposure time. Incident light from nadir and zenith, and that through a quartz diffuser of the aircraft roof are introduced to the spectrometer by rotating mirror. Data were sampled with the maximum rate of 3Hz and converted into 12 bit digital value and recorded by a cassette magnetic tape.

Aircraft measurements of stratocumulus clouds in winter season were carried out over the sea to the Southwest of Japan. The winter stratocumulus clouds form a typical cloud system frequently observed in the Western North-Pacific around Japan, where cold airmasses from the Asian Continent drive convection and form fairly uniform cloud system at the top of planetary boundary layer over the warm current. The amount of low clouds is large particularly in January and February, as compared with middle and high cloud amounts, because this area is covered by large anticyclones. The prevailing stratocumulus cloud cover varies from entirely broken to almost overcast. Observed cloud top height and cloud bottom height were about 4000~8000ft. Cloud top was rather flat whereas cloud base was frequently seen complicated with some broken cloud like cumulus under stratus, since the cloud was formed by convection at the top of the planetary boundary layer under anticyclonic condition. Almost all of clouds observed in this area consists of water droplets except for few cases in a supercooling condition with frost seen on the aircraft window. One aircraft took level flights at about 1000ft or 2000ft above the cloud top for measuring radiation; the other aircraft obtained the temperature and humidity profile and fine structure of clouds, penetrating the cloud layer and the boundary layer.

4 Application to Sample Data

We examined an accuracy of cloud geometrical thickness estimated by the algorithm with a model atmosphere based on the data of January 16, 1991. We assumed 6-layers model atmosphere with four cloud layers and one clear atmospheric layer above and below the cloud. The LWP was vertically distributed as 4 : 3 : 2 : 1 from the top at 2km to the bottom of the cloud. The water vapor mixing ratio was assumed as 100% and 80% relative humidity for each layer except for the layer above the cloud. The water vapor above the cloud was adjusted so as to fit the calculated total absorption of solar radiation in the 0.9μm water vapor band to the observed one.

Assuming the plane-parallel atmosphere, the reflected radiance from nadir was calculated with a discrete ordinate method (Nakajima and Tanaka, 1986). Gaseous absorption of the reflected radiance was calculated for the spectral region from 11500cm^{-1} (0.8696μm) to 10100cm^{-1} (0.9901μm) with an exponential-sum fitting parameters proposed by Asano and Uchiyama (1987). Total absorption by water vapor and droplets was evaluated with an equivalent width defined as the width of a rectangular band whose center is completely absorbed, having the same absorption area (Goody and Yung, 1989).

Figure 1 shows the relationship between equivalent width and geometrical thickness of the cloud with LWP of 2.5, 10.0 and 40.0mg/cm^2. Solid lines indicate the results with 100% relative humidity in the cloud layer and subcloud layers and dotted lines show those with 80% relative humidity. The equivalent width shown here is for the light absorption by cloud and subcloud layers, i.e., the equivalent width by the layer above cloud was subtracted from the total equivalent width. It is indicated that the retrieved value of cloud layer thickness is quite sensitive to the assumed relative humidity. An uncertainty of 100~120m for clouds with 400m geometrical thickness is shown with 20% uncertainty in relative humidity assumed in the algorithm. This uncertainty in geometrical thickness retrieval is corresponding to the uncertainty of LWP about 100%. On the other hand, 50% uncertainty in water vapor amount above the cloud affects about 10% in the equivalent width by cloud and subcloud layers, which cause 100m uncertainty in geometrical thickness retrieval in this example.

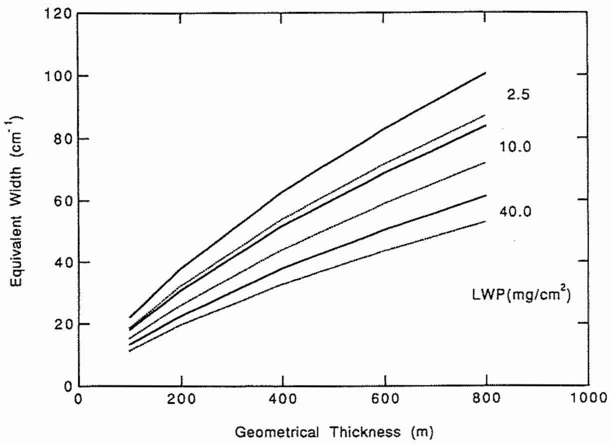

Figure. 1. The relationship between equivalent width and geometrical thickness of cloud with LWP of 2.5, 10.0 and 40.0mg/cm^2. Solid lines indicate the results with 100% relative humidity in cloud and subcloud layers and dotted lines show those with 80% relative humidity.

5. Retrieved Cloud Geometrical Thickness

The retrieved cloud geometrical thicknesses are summarized in Table 1. A homogeneous part of the cloud was selected for the analysis in each flight leg, and the respective data used in the analysis were averaged for the indicated time interval. In the analysis, the relative humidity was assumed as 80% for all data based on the aircraft measurements of dew point temperature. The retrieved geometrical thickness is in fairly good accordance with the geometrical thickness observed by eyes (indicated by 'Eye-Obs.' in Table 1) with slight underestimation by our method. In the case of January 27, however, we had a large discrepancy between two methods. On this day, the observed cloud type was convective stratocumulus and the irregularity and inhomogeneity of cloud top and bottom were conspicuous much more than the other days. The cloud top height observed by eyes may be larger than the geometrically averaged height of the cloud top and the bottom height observed by eyes may be smaller than the geometrically averaged bottom height. Consequently, the geometrical thickness is apt to be overestimated by eye observations. On the other hand, on January 16 and 18 observed were rather thin stratus clouds which have large amount of liquid water content per unit volume. The cloud of January 14 was systematically arrayed stratocumulus, though the convection was not so strong.

6. Concluding Remarks

We have developed an algorithm to retrieve cloud geometrical thickness by using water vapor absorption band, and applied this algorithm to the data obtained by aircraft observations. The retrieved thicknesses of stratus were in fairly good accordance with those observed by eyes, though the retrieved thickness of inhomogeneous stratocumulus was underestimated compared with that observed by eyes. This result may be ascribed to a difficulty in determination of average top and bottom heights of inhomogeneous cloud by eyes.

As a future problem, we should combine the geometrical thickness retrieved with cloud top height retrievals by using thermal channels from satellite. Such simultaneous retrievals of cloud top and bottom heights are fairly promising not only for the study of atmospheric radiation budget, but also for the study of cloud dynamics and microphysics, including formation and dissipation processes.

Acknowledgements

We would like to thank Prof. T. Takeda and Dr. Y. Fujiyoshi and Dr. G. Liu for providing the LWP data, and Dr. Y. Ishizaka for providing the droplet size distribution data. Personnel and the flight facility of Nakanihon Air Service Co. are acknowledged for their efforts during the experimental periods. This research was supported by Funds for the World Climate Research Program (WCRP) from the Ministry of Education, Science and Culture, Japan.

References

Asano, S. and A. Uchiyama, 1987: Application of an extended ESFT method to calculation of solar heating rates by water vapor absorption. J. Quant. Spectrosc. Radiat. Transfer, 38, 147-158.

Fujiyoshi, Y., T. Hayasaka, Y. Ishizaka, T. Takeda and M. Tanaka, 1992: Horizontal distribution of cloud liquid water content and the radiative properties of clouds. (in preparation)

Goody, R. M. and Y. L. Yung, 1989: Atmospheric radiation: Theoretical Basis. Oxford Press, New York, 519pp.

Ishizaka, Y. 1992: Private communication.

Nakajima and Tanaka, 1986: Matrix formulation for the transfer of solar radiation in a plane-parallel scattering atmosphere. J. Quant. Spectrosc. Radiat. Transfer, 35, 13-21.

* * *

Date	Time	LWP(mg/cm2)	EQW(cm-1)	Retrieved(m)	Eye-Obs.(m)
JAN. 14	11:41:35-11:43:05	13.7	51.1	577	} 600
	11:44:24-11:45:54	12.2	49.4	540	
JAN. 16	13:33:04-13:34:30	16.0	48.0	434	} 400
	13:34:59-13:36:50	18.9	39.8	338	
JAN. 18	13:49:48-13:51:00	24.2	31.8	289	300
JAN. 27	13:15:14-13:15:47	14.3	69.0	510	800

Table 1. Liquid water path (LWP) and equivalent width (EQW) observed in the flight legs of the presented time intervals, and the cloud geometrical thickness retrieved with an algorithm in this study (Retrieved) and that observed by eyes (Eye-Obs.).

EFFECTS OF VARIATIONS OF CLOUD MICROPHYSICAL PROPERTIES ON CLOUD REFLECTANCE

Peter R Jonas

Pure and Applied Physics Department, UMIST, PO Box 88, Manchester, United Kingdom

1. INTRODUCTION

It is well known that the microphysical properties of clouds exhibit variability in the horizontal and vertical directions on scales as small as a few meters. However, in calculating the optical properties of clouds, many authors have assumed that the variations in the microphysical properties may be neglected. Although, when applying parametrizations of cloud radiative properties in climate models it unlikely that such variability can be represented, it is important to know the uncertainties which apply to the calculated properties and which arise from this cause. The range of channels now becoming available from satellite remote sensing instruments also offers the possibility of combining the observations from several channels to obtain more detailed information on cloud properties than is possible from observations at one wavelength. In this paper, the results are presented of calculations of the reflectance of layer clouds making different assumptions concerning the microphysical structure of the clouds.

2. THE MODEL

The use of a Monte–Carlo model to investigate the effects of random variability of cloud microphysical properties has been described by Jonas (1992). The version of the model used here has been extended to include absorption by liquid water. In the present calculations, the droplet concentration is assumed constant at 320 cm^{-3} so that variations in water content are reflected in variations in the droplet size distribution. The variations with water content of the scattering coefficient and phase function, were obtained by interpolation from the results of Deirmendjian (1969) for a several droplet spectra and are shown in Figures 1 and 2 for two wavelengths, 0.45 and 3.90 μm.

In the calculations reported here, the reflectance of layer cloud has been obtained by following the passage of photons through a layer of prescribed thickness and calculating the number and direction of the photons emerging from the top of the cloud. In all cases, the liquid water content is assumed to increase linearly with height above cloud base, in accordance with aircraft observations of stratocumulus (eg. Nicholls and Leighton (1986)). In order to model the effects of the cellular structure of stratocumulus, it was assumed that the structure consisted of a series of identical hexagonal cells consisting of a "core" region, in which the water content increased with height at 1 g m^{-3} km^{-1} surrounded by a "wall" region, of constant width, in which the water content was a fraction of that in the core region at the same level. In addition to the thickness of the cloud layer, the cell radius (R_{cell}), the half thickness of the wall (R_{wall}) and the fractional water content in the wall (f_{wat}) were prescribed. Following the observations of Nicholls (1989), the ratio R_{wall}/R_{cell} was set at 1/6 unless otherwise indicated.

In all examples reported here, the cells ware aligned with one edge along an azimuth of 0°. The cells were also assumed to be vertical and to have identical properties. The initial positions of the photons were uniformly distributed over the top surface of the layer while the initial direction of travel was determined from the prescribed solar zenith angle.

The model was used to calculate the directional reflectance of the cloud layer (the ratio of the number of photons emerging from the top of the layer to the incident number) and the reflectivity of the layer when viewed at different zenith angles and zero azimuth angle. The reflectivity was calculated from the number of photons emerging in a given direction. It is estimated that the error in the directional reflectance is ±0.015 while the errors in the reflectivities are around ±0.1.

The model was checked by setting f_{wat} to 1.0, when the results of Jonas (1992) for layer cloud were reproduced. If the water content was set independent of height, the results of McKee and Cox (1974) were also reproduced.

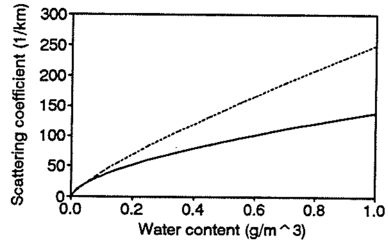

Figure 1. Scattering coefficient as a function of water content at 0.45 μm (solid) and 3.90 μm (broken) calculated from the results of Deirmendjian (1969).

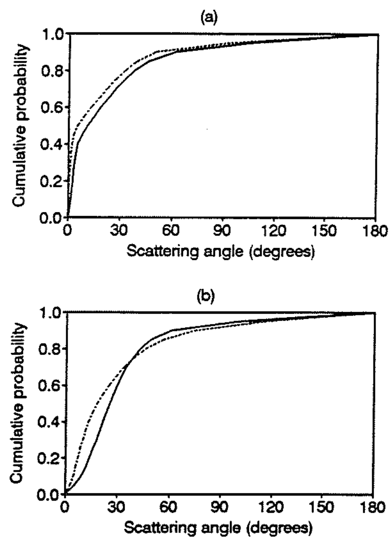

Figure 2. Phase functions at 0.45 μm (a) and 3.90 μm (b) for water contents of 0.01 g m^{-3} (solid) and 0.2 g m^{-3} (broken).

3. RESULTS

Directional reflectance

Figure 3 shows the calculated directional reflectance of horizontally uniform clouds (f_{wat} = 1.0) at 0.45 μm, with no liquid absorption, and at 3.90 μm, with strong absorption. It is apparent that while the reflectance increases rapidly with cloud depth at 0.45 μm, this is not the case at 3.90 μm due to the strong absorption at cloud top where, even in the thinnest cloud (100 m) the water content reaches 0.1 g m^{-3}. At both wavelengths, the reflectance increases significantly with increasing solar zenith angle, although the effect at the shorter wavelength is less marked for thick clouds.

The effects of cellular cloud structure on reflectance are indicated by Figure 4 in which the reflectance is shown for 300 m deep clouds with cells having R_{cell} = 600 m and R_{wall} = 100 m. At 0.45 μm, the effect of the reduced water content and drop size in the wall regions

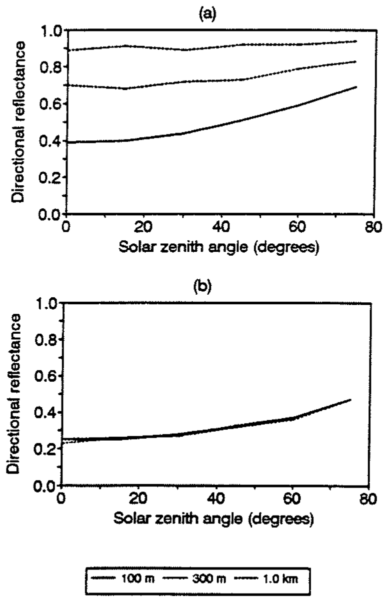

Figure 3. Directional reflectance of horizontally uniform cloud layer at 0.45 μm (a) and 3.90 μm (b) for layers 100 m, 300 m and 1.0 km deep.

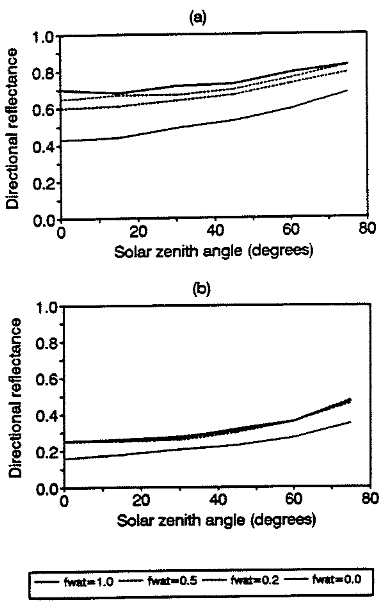

Figure 4. As Figure 3 except for a 300 m deep cellular cloud layer with values of the wall fractional water content (f_{wat}) of 1.0, 0.5, 0.2 and 0.0.

is significant for a 50% reduction in water content. Further reduction of the water content in the walls leads to further decreases in the reflectance so that for broken cloud (f_{wat} = 0) it is 30% lower than for uniform cloud. Calculations (not shown) indicate that the effects are similar for other cloud depths although, for thicker clouds, the reduction in reflectance occurs at lower water content in the walls. However, it is also apparent from Figure 4 that, at 3.90 μm, there is no significant reduction in reflectance until the water content in the walls is less than about 20% of the core value. Due to the strong absorption, the effects on the directional reflectance of layer cloud due to the thickness of the cloud, or to its cellular structure, are much less at 3.90 μm than at 0.45 μm. It is only for very thin or broken cloud that variations in reflectance are to be expected at 3.90 μm.

Reflectivity

The reflectivity of the clouds has been calculated as a function of viewing zenith angle for the 300 m deep cellular cloud layers described above, and results are shown in Figures 5 and 6. The sign convention adopted here is that a positive viewing angle corresponds to back-scattered radiation; in all cases the viewing azimuth angle is 0°. The departures from symmetry about the 0° axis in Figures 5a and 6a are an indication of the errors in the individual points.

At 0.45 μm, the reduction in the reflectance as f_{wat} is reduced, for 0° solar zenith angle, is seen to result from a reduction in reflectivity over a broad range of viewing angles in the range ±50°, while there is little change in the reflectivity at grazing angles. With a solar zenith angle of 45°, although there is also a reduction in reflectivity over a wide

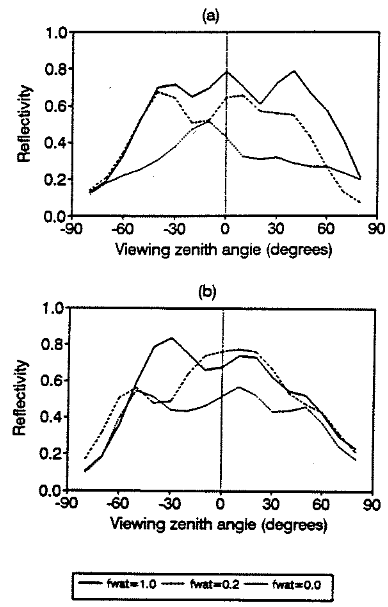

Figure 5. Reflectivity at of a 300 m deep cellular cloud layer at 0.45 μm as a function of viewing zenith angle for different values of the wall fractional water content (f_{wat}). Solar zenith angles are 0° (a) and 45° (b).

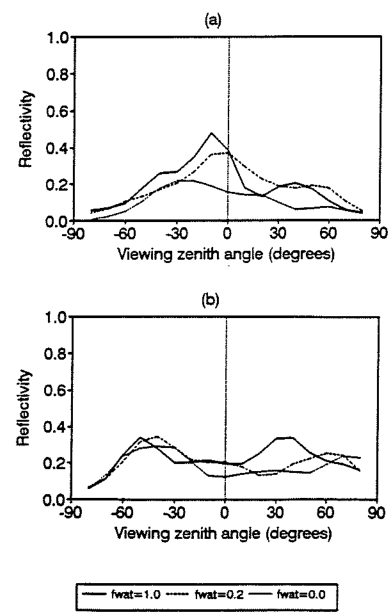

Figure 6. As Figure 5 except at 3.90 μm.

range of viewing angles, the effect is greatest in the region of the weak forward scattered peak at −40°. At 3.90 μm, the trend in the results is similar to that at 0.45 μm, but the magnitude is much smaller. As far as the resolution of the present calculations will allow, it appears that the reduction of the wall fractional water content has little effect on the direction of the peaks in the scattered intensity, although their relative magnitude is reduced as the value of f_{wat} is reduced.

Comparison with observations

Coakley (1991) suggested that the variations in cloud reflectivity with viewing angle and at different wavelengths which were obtained from satellite observations during the FIRE could be explained, qualitatively, in terms of cellular structure within the stratocumulus layers.

Using simplified relations between the satellite viewing angle and the solar zenith angle appropriate to two satellites for the experimental period (Figure 7), the reflectivity, as might be measured by a satellite, was calculated for 300 m deep layer clouds for the four values of f_{wat} used earlier. These represent uniform, broken, and two types of cellular cloud. Differences between the reflectivities of the different layer types were also obtained for each wavelength. The effects of changing f_{wat} were large, as might be anticipated from Figure 3. An attempt was made, therefore, to match the calculated layer reflectivities and reflectivity differences to Coakley's observations at 0.63 μm and 3.7 μm by choosing different values of f_{wat}. The aim was to reproduce the main observational findings:

(i) The reflectivity increases at 0.63 μm as viewing angle increases.
(ii) The reflectivity at all angles is lower at 3.7 μm than at 0.63 μm.
(iii) At 0.63 μm the difference between the reflectivity of continuous and broken cloud shows no systematic variation with viewing angle.
(iv) At 3.9 μm the difference between the reflectivity of continuous and broken cloud is negative for negative viewing angles, and increases systematically to positive values as the viewing angle is increased.

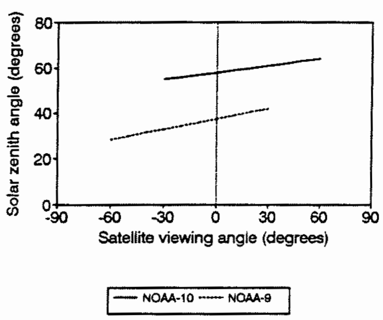

Figure 7. Assumed approximate relationship between satellite viewing angle and solar zenith angle for two satellites during the FIRE field experiment.

The main features of the observations were only reproduced simultaneously for both wavelengths if it was assumed that the continuous layer cloud was comprised of cells with a value of f_{wat} between 0.5 and 0.2. (The best agreement at a single wavelength was obtained with f_{wat} = 0.5 at 0.45 μm and with f_{wat} = 0.2 at 3.90 μm.) The calculated results for f_{wat} = 0.2 are shown in Figure 8. For comparison, Coakley's results have been re-plotted in the same format in Figure 9. It is interesting that the aircraft observations of Nicholls (1989) suggest the water content in the downdraught regions of stratocumulus was around one third of the value in the updraught regions, at least close to cloud top.

4. CONCLUSIONS

The results of Monte-Carlo modelling of radiative transfer through layer clouds show that the reflectance of the clouds can be significantly reduced, especially at 0.45 μm, by the effects of a cellular structure within the clouds when the water content in the cell walls is

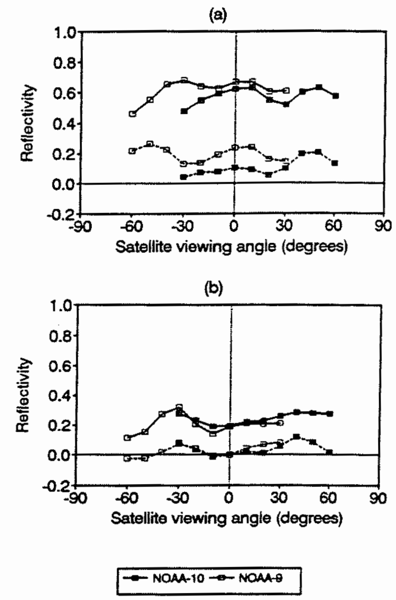

Figure 8. Reflectivity at 0.45 μm (a) and 3.90 μm (b) for cellular cloud layers with f_{wat} =0.2 (solid) and the difference (cellular − broken) calculated as a function of satellite viewing angle assuming the relationship between satellite viewing angle and solar zenith angle shown in Figure 7.

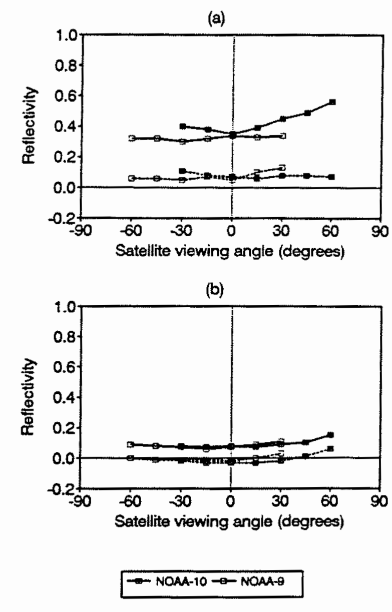

Figure 9. Coakley's (1991) observations of layer cloud reflectivity at 0.63 μm (a) and 3.7 μm (b). The solid line shows the observations for unbroken layers while the broken line shows the difference between unbroken and broken layers.

less than about 50% of that in the core regions. Examination of the reflectivity of stratocumulus clouds and broken clouds, in different directions, shows that information on the cellular structure may be derived from satellite measurements of reflectivity at several wavelengths. The remote determinations of structure appear realistic but further calculations, covering a range of wavelengths, types of cloud structure and microphysical properties, are required to determine the full potential of such techniques.

5. REFERENCES

Coakley, J. A., 1991: Reflectivities of uniform and broken layered clouds, *Tellus*, **43B**, 420–433.

Deirmendjian, D., 1969: *Electromagnetic scattering on spherical polydispersions*, Elsevier, New York.

Jonas, P. R., 1992: Some effects of spatial variations of water content on the reflectance of clouds, *Ann. Geophys.*, **10**, (in press).

McKee, T. B. and S. K. Cox, 1974: Scattering of visible radiation by finite clouds, *J. Atmos. Sci.*, **31**, 1885–1892.

Nicholls, S., 1989: The structure of radiatively driven convection in stratocumulus. *Q. J. R. Meteorol. Soc.*, **115**, 487–511.

Nicholls, S. and J. Leighton, 1986: An observational study of the structure of stratiform cloud sheets, Part 1: Structure. *Q. J. R. Meteorol. Soc.*, **112**, 431–460.

RADAR-BASED RETRIEVAL OF SOLAR AND INFRARED IRRADIANCES IN THE STRATIFORM REGION OF TROPICAL CLOUD CLUSTERS

by
Dean D. Churchill
Rosenstiel School of Marine and Atmospheric Science
University of Miami
4600 Rickenbacker Causeway
Miami, FL 33149

1. INTRODUCTION

Flux convergence of solar and infrared radiation in optically thick tropical clouds is an important source of mesoscale diabatic heating (Webster and Stephens 1980; Houze 1982; Churchill and Houze 1991). The transfer of radiation through tropical cloud clusters affects the surface energy budgets of the underlying ocean (Webster 1990), while the diabatic heating in the clouds influences the general circulation (Hartmann et al. 1984).

It is very difficult to measure radiative heating in clouds. The heating rates are proportional to the vertical gradient of net irradiance; hence, the numerical values of heating rate depend on small differences in the vertical of net irradiance, which in turn are often the small differences between upwelling and downwelling radiation. Thus measurements are prone to error. Furthermore, in the tropics, the greatest radiative heating and cooling rates are found at altitudes of 12 to 18 km (Churchill 1988; Wong et al. 1990). Many research aircraft cannot fly inside these clouds, either because they cannot reach the altitudes required (such as a P3 aircraft), or for safety considerations (such as an ER-2). Consequently most estimates of radiative heating in tropical clouds are determined from numerical simulations.

To help advance the study of radiative transfer through cloud clusters, a technique has been developed to retrieve upwelling and downwelling solar and infrared irradiances, as a function of height and distance, in the stratiform regions of tropical cloud clusters. The heating rates were then determined by vertical finite differences, on a 300 m grid, and horizontal variations in fluxes entering the oceans were determined.

2. RETRIEVAL METHODOLOGY

The retrieval technique uses vertically scanning airborne weather radar, mounted on the tail of a P3 aircraft to observe the precipitation structure of the cloud. The structure of non-radar-reflecting cloud particles was inferred from flight-level (low-to-mid troposphere) microphysical measurements and infrared satellite imagery.

Solar irradiances were retrieved using a multiple-scattering radiative transfer model, in which the optical depths associated with precipitating and non-precipitating hydrometeors was inferred from radar, satellite, and cloud physics measurements. The model incorporates solar scattering from hydrometeors and air molecules; solar absorption by hydrometeors, ozone and water vapor; and infrared absorption and emission from hydrometeors and water vapor. A single broad band in the solar (0.3 to 2.8 μ) and a single band in the infrared (3.5 to 50.0 μ) were retrieved to compare against "ground-truth" measurements obtained from Eppley pyradiometers. The detailed description of the physics of the retrieval is given by Churchill (1992).

A key component of the retrieval scheme is to use the cloud and precipitation particle sizes, measured by Particle Measurement System (PMS) probes, to infer a relationship between cloud optical depth associated with precipitation (τ_p), and radar reflectivity, Z. The function, which relates the sixth moment of the particle diameters to the second moment, has the form

$$\tau_p = aZ^b \tag{1}$$

where a and b are constant coefficients. This is analogous to the relationships used to infer cloud water or ice mass content from radar reflectivity (which relate the 6th moment of the particle diameter to the 3rd moment).

3. VERIFICATION AND RESULTS

To verify the accuracy, the retrieved irradiances were compared with flight-level measurements of solar and infrared irradiances in two cloud clusters observed by a NOAA P3 aircraft during the Equatorial Mesoscale Experiment (EMEX) (Webster and Houze 1992).

Fig. 1 shows the results from one leg of flight through a cloud cluster over the Arafura Sea, north of Australia, on 2-3 February 1987 (EMEX flight 9). Details of the synoptic-scale, mesoscale and convective-scale setting of this cloud cluster are given by Mapes and Houze (1992), and Churchill (1992).

Panel a shows a time-height cross section of radar reflectivity obtained from the P3 aircraft. The solid black line shows the altitude of the aircraft. Panel b shows the observed upwelling, downwelling and net solar irradiance, determined from Eppley pyradiometers mounted on the top and bottom of the P3 fuselage. During the first three minutes of this sequence, the P3 was under a convective cell that reached to about 14 km. During this period, the downwelling solar radiation was less than 100 Wm^{-2}. After flying out from under the cell, the solar irradiance increased rapidly up to 270 Wm^{-2}, even though the P3 maintained constant flight altitude.

The retrieved solar irradiance (panel c), which responses primarily to variations in the radar structure, shows similar values. Throughout the time sequence, the retrieved values differed from the observed by a bias of 10 - 15 Wm^{-2} in the upwelling and downwelling irradiances. The observed and retrieved net irradiances agreed to within 3 Wm^{-2}, with a root mean square difference of 13 Wm^{-2}. The retrieved solar heating rate (not shown) had values of 4 to 10 deg day^{-1} concentrated near the top of the system. These values of heating rates were qualitatively consistent with model simulations of heating rates in other tropical cloud clusters (Churchill and Houze 1991).

A similar analysis for observed and retrieved infrared irradiances is presented by Churchill (1992). He found that retrieved infrared irradiances agreed with observed values in this flight leg to within 12 Wm^{-2}.

4. CONCLUSIONS

Retrieval of solar and infrared irradiances in the stratiform region of a cloud cluster has been accomplished by running radiative transfer simulations initialized with cloud and precipitation information provided by microphysical and radar reflectivity measurements.

Generally good agreement, to within the measurement error of the pyradiometers, was obtained between the observed and retrieved net irradiances. Since the retrieved solar heating rates are reasonable, it is concluded that this retrieval technique provides a method for quantifying the irradiances, as a function of height and distance, along the flight track of the P3. This allows estimates of solar and infrared heating in the clouds to be made, and allows estimates of radiative fluxes at the ocean surface to be inferred. Results from this type of study may contribute to a better understanding of the role of radiation in the hydrological cycle of tropical cloud clusters.

Acknowledgements: Funding for this research was provided by the Rosenstiel School of Marine and Atmospheric Science, University of Miami. Graphical assistance was provided Jean Carpenter.

5. REFERENCES

Churchill, D. D., 1992: Vertical retrieval of solar and infrared irradiances in the stratiform regions of EMEX cloud clusters. *J. Appl. Meteor.*, in press.

Churchill, D. D., and R. A. Houze, Jr., 1991: Effects of radiation and turbulence on the diabatic heating and water budget of the stratiform region of a tropical cloud cluster. *J. Atmos. Sci.*, **48**, 903 - 922.

Hartmann, D. L., H. H. Hendon, and R. A. Houze, Jr., 1984: Some implications of the mesoscale circulations in tropical cloud clusters for large-scale dynamics and climate. *J. Atmos. Sci.*, **41**, 113 - 121.

Houze, R. A., Jr., 1982: Cloud clusters and large-scale vertical motions in the tropics. *J. Meteor. Soc. Japan*, **60**, 396 - 410.

Mapes, B., and R. A. Houze, Jr., 1992: An integrated view of the 1987 Australian monsoon and its mesoscale convective systems. Part I: Horizontal structure. *Quart. J. Royal Met. Soc.*, in press.

Webster, P. J., 1990: The role of hydrological processes in ocean-atmosphere interaction. In *Proceedings of US - PRC International TOGA Symposium, 1988.* China Ocean Press, Beijing. 263 - 294.

Webster, P. J., and G. L. Stephens, 1980: Tropical upper-tropospheric extended clouds: Inferences from Winter MONEX. *J. Atmos. Sci.*, **37**, 1521 - 1541.

———, and R. A. Houze, Jr., 1991: The Equatorial Mesoscale Experiment (EMEX): An Overview. *Bull. Amer. Met. Soc.*, **72**, 1481 - 1505.

Wong, T., P. Stackhouse, G. Stephens, and F. Valero, 1990: A comparison of cloud radiation fields obtained by *in-situ* aircraft measurements and a numerical simulation of a tropical mesoscale convective system. *Preprints 1990 Conference on Cloud Physics*, American Meteorological Society, Boston, J46 - J50.

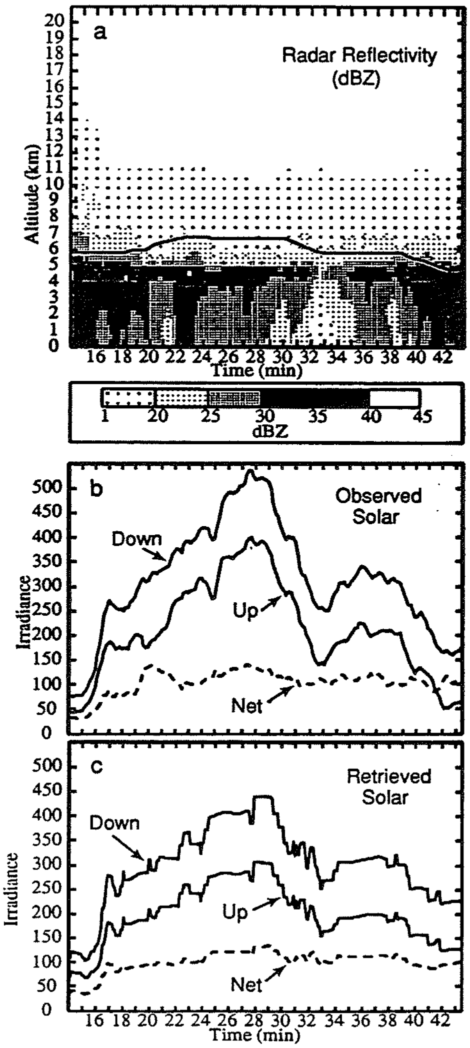

Fig. 1. Time-height cross sections along path of P3. Time is in minutes after 00 UTC 3 February 1987. (a) Time-height cross section of radar reflectivity (dBZ). The solid line shows the flight path of the P3. (b) Observed downwelling, upwelling, and net solar irradiance (Wm^{-2}). (c) Retrieved downwelling, upwelling and net solar irradiance (Wm^{-2}).

IMPROVEMENTS IN THE F_N METHOD FOR RADIATIVE TRANSFER CALCULATIONS IN CLOUDS

R. D. M. Garcia[†] and C. E. Siewert[‡]

[†]CTA/IEAv, 12225 São José dos Campos, SP, Brasil

[‡]Mathematics Department, NCSU, Raleigh, NC 27695-8205, USA

1. INTRODUCTION

In 1985 we applied the F_N method to solve a collection of radiative transfer problems (including one for a cloud) posed by the Radiation Commission of the International Association of Meteorology and Atmospheric Physics (Lenoble, 1977). Among the methods that were used to solve these test problems, the F_N method has proved to be one of the most successful, as demonstrated by the quality of the results published in the literature (Garcia and Siewert, 1985).

The version of the F_N method that we used in 1985 incorporated several computational improvements not available in previous versions of the method (Devaux and Siewert, 1980; Devaux, Siewert and Yuan, 1982); however, about three years ago, while trying to solve a problem for a cloud, with very strong scattering anisotropy, illuminated by an azimuthally dependent incident distribution, we detected numerical instabilities that precluded the application of the method to this class of problems. Since then we have focused our efforts on improving the numerical aspects of the method in order to obtain an accurate tool for solving highly anisotropic, azimuthally dependent, radiative transfer problems.

The purpose of this paper is to review the F_N method for computing the radiance and the flux in a cloud and to report our latest results on computational methods that we hope will end up in extending the range of applicability of the method to more demanding calculations.

2. STATEMENT OF THE PROBLEM

We let $I(\tau,\mu,\varphi)$ denote the intensity (radiance) of the radiation field and utilize the equation of transfer for a plane-parallel medium (Chandrasekhar, 1950) to model our cloud. We write

$$\mu\frac{\partial}{\partial\tau}I(\tau,\mu,\varphi)+I(\tau,\mu,\varphi) = \frac{\varpi}{4\pi}\int_{-1}^{1}\int_{0}^{2\pi}p(\cos\Theta)I(\tau,\mu',\varphi')\mathrm{d}\varphi'\mathrm{d}\mu' \quad (1)$$

where $\tau\in[0,\tau_0]$ is the optical variable, $\mu\in[-1,1]$ and $\varphi\in[0,2\pi]$ are respectively the cosine of the polar angle (as measured from the *positive* τ axis) and the azimuthal angle which describe the direction of propagation of the radiation and ϖ is the albedo for single scattering. In addition, the phase function $p(\cos\Theta)$ is represented by a finite Legendre expansion in terms of the cosine of the scattering angle Θ, *i.e.*

$$p(\cos\Theta)=\sum_{l=0}^{L}\beta_l P_l(\cos\Theta), \quad (2)$$

where the coefficients $\beta_0=1$ and $|\beta_l|<2l+1$, $l\geq 1$, are computed from the phase function for a single particle (Mie scattering) averaged over the size distribution of the cloud particles. We point out that to describe cloud phase functions in an adequate manner a large number of terms is usually required in Eq. (2). This is due to the strong scattering anisotropy that is characteristic of clouds; for example, an expansion with $L=299$ was used in our previous work (Garcia and Siewert, 1985) to represent the Cloud C1 phase function defined in the IAMAP report (Lenoble, 1977).

We assume that the cloud is illuminated uniformly by a radiation beam with direction specified by (μ_0,φ_0) and so we seek a solution to Eq. (1) that satisfies the boundary conditions, for $\mu>0$ and $\varphi\in[0,2\pi]$,

$$I(0,\mu,\varphi)=\pi\delta(\mu-\mu_0)\delta(\varphi-\varphi_0) \quad (3a)$$

and

$$I(\tau_0,-\mu,\varphi)=0. \quad (3b)$$

A convenient way of treating the azimuthal dependence of the problem is to use a Fourier decomposition to reduce the original problem to a series of azimuthally independent problems (Chandrasekhar, 1950; Garcia and Siewert, 1985). Here we can use the decomposition

$$I(\tau,\mu,\varphi)=R(\mu,\varphi)\delta(\mu-\mu_0)e^{-\tau/\mu} + \sum_{m=0}^{L}I^m(\tau,\mu)\cos m(\varphi-\varphi_0), \quad (4)$$

where, for $\mu>0$,

$$R(\mu,\varphi)=\pi\delta(\varphi-\varphi_0) - \tfrac{1}{2}\csc\tfrac{1}{2}(\varphi-\varphi_0)\sin\tfrac{1}{2}(2L+1)(\varphi-\varphi_0) \quad (5a)$$

and

$$R(-\mu,\varphi)=0, \quad (5b)$$

and the addition theorem for the Legendre polynomials, to show that the problem stated by Eqs. (1) and (3) can be reduced to the problem of solving, for $m=0,1,\ldots,L$,

$$\mu\frac{\partial}{\partial\tau}I^m(\tau,\mu)+I^m(\tau,\mu) = \frac{\varpi}{2}\sum_{l=m}^{L}\frac{(l-m)!}{(l+m)!}\beta_l P_l^m(\mu)\int_{-1}^{1}P_l^m(\mu')I^m(\tau,\mu')\mathrm{d}\mu' \quad (6)$$

subject to the boundary conditions, for $\mu > 0$,

$$I^m(0,\mu) = \tfrac{1}{2}(2-\delta_{0,m})\delta(\mu-\mu_0) \tag{7a}$$

and

$$I^m(\tau_0,-\mu) = 0. \tag{7b}$$

It is clear that once we solve the problem stated by Eqs. (6) and (7) for $m = 0,1,\ldots,L$ we obtain the Fourier components $\{I^m(\tau,\mu)\}$ and consequently the radiance $I(\tau,\mu,\varphi)$, as expressed by Eq. (4). Finally, expressions for the partial and net fluxes can be obtained by substituting Eq. (4) into the definitions

$$q_\pm(\tau) = \int_0^1 \int_0^{2\pi} \mu I(\tau,\pm\mu,\varphi)\mathrm{d}\varphi\mathrm{d}\mu \tag{8}$$

and

$$q(\tau) = \int_{-1}^1 \int_0^{2\pi} \mu I(\tau,\mu,\varphi)\mathrm{d}\varphi\mathrm{d}\mu \tag{9}$$

and evaluating the required integrals.

3. THE $\mathbf{F_N}$ METHOD

The F_N method was introduced in the field of radiative transfer by Siewert (1978). It has also been used extensively in other fields such as neutron transport theory, rarefied gas dynamics, kinetic theory and neutral particle transport in plasmas (see the survey by Garcia, 1985). Here we only sketch the essential ideas of the method as applied to our problem; the complete description of the method can be found in the literature (Garcia and Siewert, 1985; Garcia, 1985).

We can summarize the procedure followed by the method in the steps:

a. Deduce a set of singular integral equations and constraints for the unknown exit distributions $I^m(0,-\mu)$ and $I^m(\tau_0,\mu)$, $\mu > 0$, by means of an integral transform applied to Eq. (6);
b. Approximate the unknown exit distributions with a polynomial basis orthogonal in $[0,1]$;
c. Use a collocation scheme to match the number of equations to the number of unknowns;
d. Solve the resulting system of linear algebraic equations for the unknown coefficients of the approximation introduced in step b;
e. Compute the exit distributions, and
f. Repeat the procedure to compute internal distributions.

Highly accurate results obtained with the F_N method for the five test problems posed in the IAMAP report (Lenoble, 1977) have been published (Garcia and Siewert, 1985). By way of comparing our F_N solution with a solution developed with another widely used approximate method for solving the equation of transfer — the spherical harmonics (SH) method (Benassi, Garcia, Karp and Siewert, 1984) — we concluded that, although conceptually more complex and somewhat more difficult to implement, the F_N method is more efficient than the SH method in the sense that, for a given level of accuracy, it requires a lower order of approximation and consequently less computer time than the SH method.

4. RECENT IMPROVEMENTS IN THE METHOD

In this section, we discuss the results of our ongoing work on computational aspects of the F_N method. As stated in the Introduction, we have undertaken the task of developing a numerically stable method for radiative transfer calculations in clouds described by realistic phase functions.

a. Determination of the Discrete Spectrum

The first computational difficulty we encountered when we applied the method to more challenging problems was the determination of the so-called discrete spectrum, *i.e.* the discrete eigenvalues related to Eq. (6). In the context of the F_N method, the discrete eigenvalues belong to the set of points that define the collocation scheme referred to in Section 3. They are also required by other methods for solving the equation of transfer, as for example the method of elementary solutions (Case and Zweifel, 1967; Kuščer and McCormick, 1991), also known as the singular eigenfunction expansion method or Case's method.

The discrete spectrum is composed of the zeros in the complex plane cut from -1 to 1 along the real axis of the dispersion function

$$\Lambda^m(z) = 1 + z\int_{-1}^1 \psi^m(\mu)\frac{\mathrm{d}\mu}{\mu - z} \tag{10}$$

where the characteristic function is

$$\psi^m(\mu) = \frac{\varpi}{2}(1-\mu^2)^{m/2}\sum_{l=m}^{L}\frac{(l-m)!}{(l+m)!}\beta_l g_l^m(\mu)P_l^m(\mu) \tag{11}$$

and the Chandrasekhar polynomials $g_l^m(\xi)$, with the starting value $g_m^m(\xi) = (2m-1)!!$, satisfy, for $l \geq m$,

$$\begin{aligned}(2l+1-\varpi\beta_l)\xi g_l^m(\xi) = (l-m+1)g_{l+1}^m(\xi) \\ + (l+m)(1-\delta_{l,m})g_{l-1}^m(\xi).\end{aligned} \tag{12}$$

For years, the argument principle (Ahlfors, 1953) was considered the standard tool for computing the number of zeros of the dispersion function defined by Eq. (10). However, during an implementation of the argument principle to compute the number of zeros of Eq. (10) for all m for a problem defined with the $L = 299$ phase function mentioned in Section 2, we found that argument-principle calculations suffer from severe numerical limitations when applied to problems with strong scattering anisotropy and azimuthal dependence (Garcia and

Siewert, 1989). We then went on to propose an alternative method based on Sturm sequences (Wilkinson, 1965) that we found to be very stable and efficient. In addition, we also proposed the use of a bisection procedure based on a Sturm sequence in order to compute estimates for zeros of Eq. (10) with magnitudes just greater than 1 and to refine estimates of all the zeros of Eq. (10). Our procedure was found to be much more effective than previously used procedures based on Newton's method, mainly because it avoids the need of computing the dispersion function and its derivative accurately at each iteration step. This, as discussed in detail in our work (Garcia and Siewert, 1989), can be a terribly difficult, if not impossible, job.

b. Computation of the g-polynomials

The second computational difficulty that we resolved recently has to do with the computation of the Chandrasekhar (or g-) polynomials. In the past, it was thought that these polynomials could be computed in an accurate manner by using Eq. (12) in either the forward or backward direction. This technique is good for problems with a moderate degree of scattering anisotropy, but it may fail when the scattering is highly anisotropic.

Fortunately, we were able to devise an effective method for computing the Chandrasekhar polynomials on the real axis (Garcia and Siewert, 1990). As a matter of fact, we worked with a normalized version of the Chandrasekhar polynomials which is defined in a slightly different way than the definition we use in this paper. However, for our purposes here, this distinction is not important. Our method consists in using forward recursion of Eq. (12) when $|\xi| \in [0,1]$, a combination of backward and forward recursion of Eq. (12) plus the solution of a linear system when ξ is a discrete eigenvalue and a Darboux formula when ξ is not a discrete eigenvalue and $|\xi| \notin [0,1]$. A numerical study confirmed that the proposed method is capable of computing the Chandrasekhar polynomials accurately for problems with highly anisotropic phase functions (Garcia and Siewert, 1990).

c. Computation of the $\mathrm{T}^m_{\alpha,l}$ Integrals

We recall from Section 3 that the procedure followed by the F_N method makes it possible to reduce the original problem [Eqs. (6) and (7) of Section 2] to the problem of solving one linear system (or two, if internal radiances and fluxes are desired). In order to compute the matrix elements of these linear systems (Garcia and Siewert, 1985), the integrals

$$T^m_{\alpha,l} = \int_0^1 \mu(1-\mu^2)^{m/2} P_\alpha(2\mu-1) P_l^m(\mu)\mathrm{d}\mu \qquad (13)$$

must be evaluated for $m = 0,1,\ldots,L$, $l = m, m+1,\ldots,L$ and $\alpha = 0,1,\ldots,N$, where N is the order of the F_N approximation.

A recursive scheme for computing the required $T^m_{\alpha,l}$ was reported by Devaux, Siewert and Yuan (1982). Later this scheme was found to be unstable as $m \to \infty$ and an alternative recursive scheme was proposed (Garcia and Siewert, 1985). More recently, however, we have found that, although slightly superior to the previous scheme, the new scheme is also unstable as $m \to \infty$.

Our basic approach to overcome this problem was to look for ways of reducing the dimensionality of the calculation. We note that the problem is defined in a tridimensional space (the α-l-m space) and that the above mentioned recursive schemes (Devaux, Siewert and Yuan, 1982; Garcia and Siewert, 1985) work in bidimensional spaces (α-l and l-m respectively). In our study (Garcia and Siewert, to appear), we were able to deduce a 7-term recursion relation that works in the α-space, thereby allowing the entire calculation to be reduced to several one-dimensional calculations. Our final formula to compute the required $T^m_{\alpha,l}$ can be written as

$$A^m_{\alpha,l}T^m_{\alpha-3,l} + B^m_{\alpha,l}T^m_{\alpha-2,l} + C^m_{\alpha,l}T^m_{\alpha-1,l} + D^m_{\alpha,l}T^m_{\alpha,l} + E^m_{\alpha,l}T^m_{\alpha+1,l} + F^m_{\alpha,l}T^m_{\alpha+2,l} + G^m_{\alpha,l}T^m_{\alpha+3,l} = 0 \qquad (14)$$

where the coefficients $A^m_{\alpha,l}, B^m_{\alpha,l},\ldots,G^m_{\alpha,l}$ are rational numbers that depend only on α, l and m.

We have concluded from the numerical implementation of our scheme that, although Eq. (14) can be used in the backward direction without loss of accuracy for almost the entire α-range, quite often the $T^m_{\alpha,l}$ integrals saturate and roundoff errors start to propagate when $\alpha \to 0$. When this is detected, we stop using Eq. (14) in the backward direction and switch to forward recursion to complete the calculation.

d. Computation of the A_α and B_α Functions

We are presently involved in evaluating the performance of existing methods (Garcia and Siewert, 1985) for computing the basic functions $A_\alpha(\xi)$ and $B_\alpha(\xi)$, for $\alpha = 0,1,\ldots,N$, for problems with highly anisotropic phase functions. In the F_N method, these functions are needed to compute the coefficient matrices of the linear systems referred to in Section 3.

We have found that the two-term inhomogeneous recursion formula for $A_\alpha(\xi)$ [Eq. (71) of Garcia and Siewert, 1985] is not sufficiently accurate for the $L = 299$ *cloud* phase function, the reason being that the scheme used for computing the inhomogeneous term $V_\alpha(\xi)$ [Eqs. (69) and (70) of Garcia and Siewert, 1985] is subject to the propagation of roundoff errors. In order to overcome this problem, we are considering the alternative of using a three-term recursion formula for $A_\alpha(\xi)$ [Eq. (66) of Garcia and Siewert, 1985] in the backward direction; however the calculation of the starting values for backward recursion of the three-term formula will require the evaluation of the characteristic function $\psi^m(\mu)$ in an accurate manner, which can be a difficult problem *per se*.

5. CONCLUSIONS

In the past few years, we have been able to introduce significant improvements in the computational aspects of the F_N method for problems with highly anisotropic phase functions. New methods for determining the discrete spectrum, for computing the Chandrasekhar polynomials and for computing the $T^m_{\alpha,l}$ integrals were discussed in this paper. We are confident that in the near future we will be able to resolve the standing problem of computing the $A_\alpha(\xi)$ and $B_\alpha(\xi)$ functions in an accurate manner. Once this difficulty is resolved, we will be ready to apply the F_N method with confidence in the solution of general radiative transfer problems for clouds.

ACKNOWLEDGEMENTS

This work was supported in part by the CNPq of Brazil, the North Carolina Supercomputing Center and the U. S. National Science Foundation.

REFERENCES

Ahlfors, L. V. 1953. *Complex Analysis.* New York: McGraw-Hill.

Benassi, M., R. D. M. Garcia, A. H. Karp and C. E. Siewert. 1984. A high-order spherical harmonics solution to the standard problem in radiative transfer. *The Astrophysical Journal* **280**: 853–864.

Case, K. M., and P. F. Zweifel. 1967. *Linear Transport Theory.* Reading, Mass.: Addison-Wesley.

Chandrasekhar, S. 1950. *Radiative Transfer.* London: Oxford University Press.

Devaux, C., and C. E. Siewert. 1980. The F_N method for radiative transfer problems without azimuthal symmetry. *Zeitschrift für angewandte Mathematik und Physik* **31**: 592–604.

Devaux, C., C. E. Siewert and Y. L. Yuan. 1982. The complete solution for radiative transfer problems with reflecting boundaries and internal sources. *The Astrophysical Journal* **253**: 773–784.

Garcia, R. D. M. 1985. A review of the Facile (F_N) method in particle transport theory. *Transport Theory and Statistical Physics* **14**: 391–435.

Garcia, R. D. M., and C. E. Siewert. 1985. Benchmark results in radiative transfer. *Transport Theory and Statistical Physics* **14**: 437–483.

Garcia, R. D. M., and C. E. Siewert. 1989. On discrete spectrum calculations in radiative transfer. *Journal of Quantitative Spectroscopy and Radiative Transfer* **42**: 385–394.

Garcia, R. D. M., and C. E. Siewert. 1990. On computing the Chandrasekhar polynomials in high order and high degree. *Journal of Quantitative Spectroscopy and Radiative Transfer* **43**: 201–205.

Garcia, R. D. M., and C. E. Siewert. To appear. On computing a class of integrals basic to the F_N method in radiative transfer. *Journal of Quantitative Spectroscopy and Radiative Transfer.*

Kuščer. I., and N. J. McCormick. 1991. Some analytical results for radiative transfer in thick atmospheres. *Transport Theory and Statistical Physics* **20**: 351–381.

Lenoble, J. (ed.) 1977. *Standard Procedures to Compute Atmospheric Radiative Transfer in a Scattering Atmosphere.* Boulder, Co.: National Center for Atmospheric Research.

Siewert, C. E. 1978. The F_N method for solving radiative transfer problems in plane geometry. *Astrophysics and Space Science* **58**: 131–137.

Wilkinson, J. H. 1965. *The Algebraic Eigenvalue Problem.* Oxford: Oxford University Press.

APPLICATION OF THE DISCRETE ORDINATES METHOD TO 3-D CLOUD RADIATIVE TRANSFER

A. Sánchez[1], W. F. Krajewski[2] and T. F. Smith[3]

[1]Escuela de Ingeniería Mecánica, Universidad de los Andes, Mérida, Edo, Mérida, Venezuela
[2]Iowa Institute of Hydraulic Research, The University of Iowa, Iowa City, Iowa 52242
[3]Department of Mechanical Engineering, The University of Iowa, Iowa City, Iowa 52242

1. INTRODUCTION

Earth's energy balances, global circulation patterns, and climatic variations are examples of studies in which quantitative understanding requires modeling of the three-dimensional aspects of cloud radiation. Proper interpretations of satellite sensed data of radiant intensity for extraction of information related to cloud properties, ground temperature, and rainfall require a radiative transfer model.

Three-dimensional studies of cloud radiative transfer are limited. Studies of radiative properties of broken cloud fields (Stephens 1988; Welch and Wielicki 1989; Kobayashi 1989) are examples. The work cited used the Monte Carlo approach or an extensive mathematical formulation for solving the radiative transfer problem. Modeling of convective clouds and rainfall (Mugnai et al. 1990; Adler et al. 1991) considered three-dimensional cloud structures but only one-dimensional radiative transfer.

The objective of this paper is to apply the discrete-ordinates method to examine three-dimensional cloud radiative transfer. The outgoing intensity for application to remote sensing studies is calculated. Although the real shape of clouds can vary widely, and is best described by fractals (Mandelbrot, 1983), cubical arrays are commonly used (McKee and Cox, 1976; Welch and Wielicki, 1989) to study the radiative characteristics and properties of clouds. The cloud field as illustrated in Fig. 1 consists of an array of cubic clouds of dimensions L_1 separated a distance L_2 with a height L_3. The cloud field is irradiated with direct collimated solar energy. The ground is diffusely reflecting and opaque. Thermal effects are neglected.

2. THE DISCRETE ORDINATES METHOD

Several authors have presented formulations of the discrete-ordinates method (Carlson and Lathrop 1968; Stamnes et al. 1988; Gerstl and Zardecki 1985; Fiveland and Jamaluddin 1989; Kim and Lee 1989). The discretized form of the radiative transfer equation is obtained by subdividing the entire three-dimensional domain into cubical control volumes and discretizing the direction of propagation of the radiant intensity. Typical control volumes are shown in Fig. 2, where control volume P with differential volume $\Delta V = \Delta x\ \Delta y\ \Delta z$ is of interest. Control volume P is surrounded by six adjacent control volumes labeled W (west), E (east), S (south), N (north), F (front), and B (back) with associated interfaces of w, e, s, n, f, and b. Each control volume is homogeneous, and nonhomogeneities are accounted for by assigning different radiative properties to the control volumes. For unpolarized radiation, the radiant intensity in direction i for control volume P is

$$I_i^P = \frac{\frac{|\mu_i|}{\Delta x} I_i^{xr} + \frac{|\delta_i|}{\Delta y} I_i^{yr} + \frac{|\gamma_i|}{\Delta z} I_i^{zr} + \alpha\ S}{\frac{|\mu_i|}{\Delta x} + \frac{|\delta_i|}{\Delta y} + \frac{|\gamma_i|}{\Delta z} + \alpha\ \beta} \tag{1}$$

where the direction cosines μ_i, δ_i, and γ_i are for the x-, y-, and z-directions. Superscripts r designate the interface from which the radiant energy originates for the indicated coordinate. The intensities arriving at the end-faces (which become the reference intensities for the neighboring control volumes) are recovered from

$$I_i^{xe} = [(I_i^P + (\alpha-1)\ I_i^{xr}]/\alpha \tag{2}$$

Expressions for I_i^{ye} and I_i^{ze} can be written by replacing x with y and z. The finite-difference weighting factor α is taken as unity. The radiant source S for inward scattering and a collimated source are

$$S = \frac{s}{4\pi} \sum_{j=1}^{K} w_j\ I_j^P\ \Phi_{ij} + \frac{s}{4\pi}\ I_c^P\ \Phi_{ic} \tag{3}$$

In Eqs. (1-3), β is the extinction coefficient, s the scattering coefficient, Φ_{ij} the phase function for scattering between the i and j discrete directions, K the number of discrete directions in a spherical space, and w_j the quadrature weight for the j direction. The direct intensity I_c^P at point P is

$$I_c^P = I_c \exp(-\int_0^{\zeta} \beta\ d\zeta^*) \tag{4}$$

where ζ is the location of point P and I_c the direct solar intensity at the boundary from direction $\bar{\omega}_c$. The sensed intensity as measured by a radiant sensor placed at P is the sum of the intensity from Eq. (1) plus the direct intensity from Eq. (4), recognizing that the direct intensity is only added when the sensed intensity is sought for the direction $\bar{\omega} = \bar{\omega}_c$.

The boundary condition for Eq. (1) is that the intensity is zero at all boundaries except along the ground surface where it is given by

$$I_i^+ = \frac{\rho_d}{\pi} \left[I_c^- + \sum_{j=1}^{K/2} w_j\ \eta_j\ I_j^-\right] \tag{5}$$

η_i is the cosine of the angle between the normal to the surface (boundary) and the direction of propagation j. The summation in Eq. (5) is over

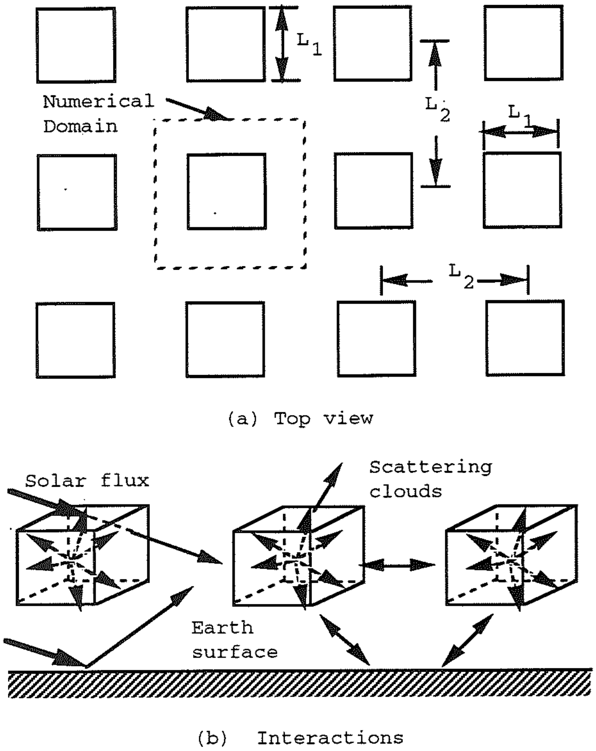

Figure 1 Geometry for the cloud field.

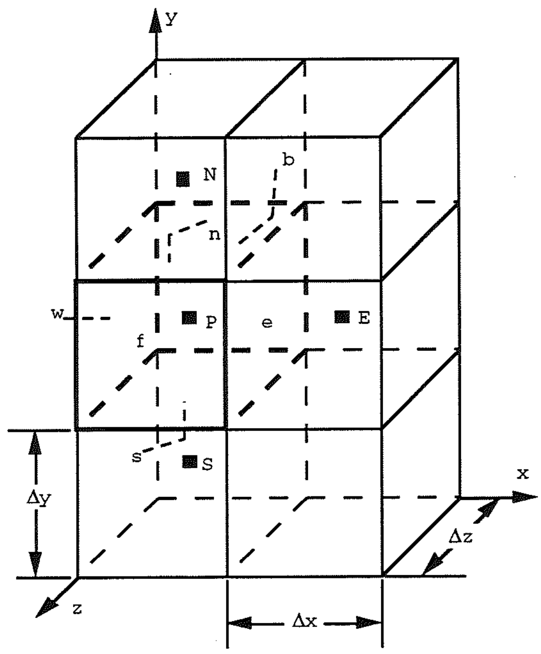

Figure 2 Control volumes.

only the four octants above a boundary that lie within the medium.

The dependency of all radiant energy and property quantities on wavelength and spatial location is understood.

The quadrature set selected is the Level Sequential-Odd quadrature. The discrete ordinates are referred to as S-N, where the total number of directions is $K = N\ (N + 2)$. Quadrature sets were generated from a computer code and agree with those listed by Fiveland (1991).

To evaluate the radiative properties, it is necessary to calculate from the theory for the scattering of spherical particles (Dave, 1964; Bohren and Huffman, 1983), the extinction and scattering cross-sections as well as the phase function based on the wavelength, the refractive index, and the particle radius; to obtain the radiative properties for the polydispersion according to standard equations; to expand the phase function in a series of Legendre polynomials; to apply δ-M scaling to the phase function to find the transformed properties (Wiscombe, 1977; Stamnes et al., 1988; Kim and Lee, 1990a); to apply the modified δ-M scaling to eliminate any negative values from the phase function (Kim and Lee, 1990b), and to renormalize the phase function so that energy is conserved (Wiscombe, 1977; Kim and Lee, 1990a).

The calculation of I_c^P in Eq. (3) is based on some location within control volume P, which may not be at the center of control volume. This location is obtained by spatially averaging the direct beam attenuation over the control volume.

The cloud field in Fig. 1 presents periodicity in x- and z-directions. A mirror technique is applied to take advantage of the periodicity. Hence, the intensities going out of a boundary (for a given iteration) are placed as intensities coming into the opposite boundary (boundary condition for the next iteration) for the direction being modeled.

Intensities from Eq. (1) contain enough information to evaluate S required to apply Eq. (1) to any sensor direction (μ_d, δ_d, and γ_d). Intensities in the sensor direction are calculated by evaluating the boundary intensities from Eq. (5), S from Eq. (3), and then applying Eqs. (1) and (2) to obtain the desired output intensities.

Further details of the model are described by Sánchez et al. (1992).

5. RESULTS AND DISCUSSION

The clouds have dimensions of 1 × 1 × 1 km and are placed 1 km above the ground with an albedo of 0.3. Radiation scattering by the cloud particles is described by a Henyey-Greenstein phase function with an asymmetry parameter (g) of 0.86. The cloud cover CC is defined as

$$CC = (L_1/L_2)^2 \tag{6}$$

The cloud cover is modified by changing the dimension L_1, while L_2 and the altitude of the clouds remain constant. The model was implemented with different grid configurations ranging from a 1 × 10 × 1 uniform grid (for clear sky, CC = 0.0 and, for all covered sky, CC = 1.0) to an 11 × 10 × 11 non-uniform grid (for CC = 0.9) on the reduced numerical domain depicted in Fig. 1. Solar radiation irradiates the clouds at $\theta_c = 60$ deg and $\phi_c = 0$ deg. The output of radiation sensed by a satellite (with a very narrow field of view) placed at $\theta_d = 53.13$ deg and a given azimuthal angle is determined. The cloud optical thickness ($\beta\ L_1$) is 10.

For this application, with large optical thickness and highly anisotropic phase function, a "Henyey-Greenstein modified δ-4" option was selected. The original as well as the scaled phase functions resulting from these calculations

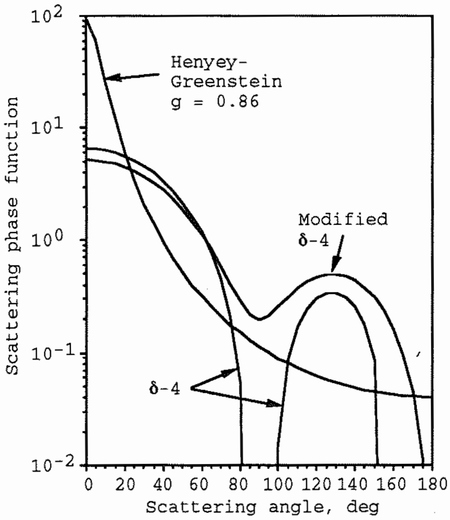

Figure 3 Phase function for cubic cloud.

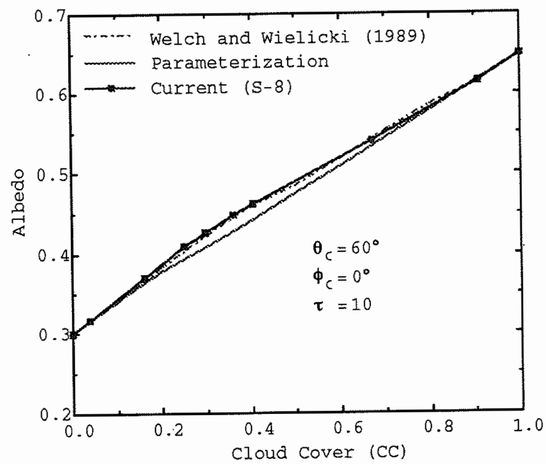

Figure 4 Total albedos for ground albedo of 0.3.

are shown in Fig. 3. Note that the modified δ-4 model does not give as small of values for the phase function for scattering angles near 90 and 180 deg as for the δ-4 model.

Cloud albedos calculated with an S-8 implementation of the discrete-ordinates model are compared in Fig. 3 with the corresponding values calculated by Welch and Wielicki (1989). An empirical parameterization (Welch and Wielicki, 1989) of the albedo based on the limiting values for clear sky and the clouded sky is also represented in the same figure.

Results for cloud albedos presented in Fig. 3 show excellent agreement with the Monte Carlo results from Welch and Wielicki (1989). Equally good is the agreement between the parameterized albedos and those calculated here. The parameterization, however, does not capture the behavior of the albedos in the region of inter-mediate cloud cover. The albedos are very susceptible to the discretization in the vertical direction when the full three-dimensional problem, with periodic boundaries, is solved. In general, ten layers in the vertical direction are needed.

Dimensionless intensities (I/I_c) in the direction of the satellite are displayed in Figs. 5 and 6 for CC = 0.36, θ_c = 60 deg, ϕ_c = 0 deg, and θ_d = 53.13 deg. The parameters in both figures are the same with the exception of ϕ_d = 0 deg in Fig. 5 and ϕ_d = 45 deg in Fig. 6.

The dimensionless intensities in Figs. 5 and 6 show the potential of the model to applications of satellite sensed intensities. In these figures, the maximum intensity is always directed in the direction of the longest line of sight for the satellite. The original cubic clouds (represented by a dotted square in Fig. 5 and 6) are lost in the satellite image. Also, when comparing these two figures, it is evident that changing the relative position between the satellite and the other components of the system can drastically change the perceived image.

The dimensionless solar intensity reflected by the ground is on the order of 0.048, which is not captured in either figure. The "clear corridors" in Fig. 5 indicate a dimensionless intensity near 0.06 (compared with 0.048) indicating the interaction between the base of the clouds and the ground.

6. CONCLUSIONS

The discrete-ordinates method was applied successfully to simulate radiative transfer in a three-dimensional, broken cloud field. The results obtained point to the importance of the three-dimensional aspects of radiative transfer modeling. This has serious implications for the interpretation of remote sensing images of clouds and estimation of rainfall.

ACKNOWLEDGMENTS

The authors wish to acknowledge partial support for this study from the grant NA89AA-D-AC195, National Oceanic and Atmospheric Administration: Global Change Program. The senior author would also like to recognized the financial support received from Universidad de los Andes and Fundación Gran Mariscal de Ayacucho, both of the Republic of Venezuela.

REFERENCES

Adler, R. F., Yeh, H-Y. M., Prasad, N., Tao, W-K., and Simpson, J., "Microwave Simulations of a Tropical Rainfall System with a Three-Dimensional Cloud Model," *J. Appl. Meteor.*, Vol. 30, pp. 924-953, 1991.

Bohren, C. F. and Huffman, D. R., *Absorption and Scattering of Light by Small Particles*, John Wiley and Sons, New York, 1983.

Carlson, B. G. and Lathrop, K. D., "Transport Theory, The Method of Discrete-Ordinates," *Computing Methods in Reactor Physics*, Eds. H. Greenspan, C. N. Kelber, and D. Okrent, Gordon and Breach, New York, pp. 171-266, 1968.

Dave, J. V., *Subroutines for Computing the Parameters of the Electromagnetic Radiation Scattered by a Sphere*, Report No. 320-3237, IBM Scientific Center, Palo Alto, California, 1968.

Fiveland, W. A., "The Selection of Discrete Ordinate Quadrature Sets for Anisotropic Scattering," *Fundamentals of Radiation Heat Transfer*, Eds. W. A. Fiveland, A. L. Crosbie, A. M. Smith, and T. F. Smith, ASME HTD-Vol. 160, pp. 89-96, 1991.

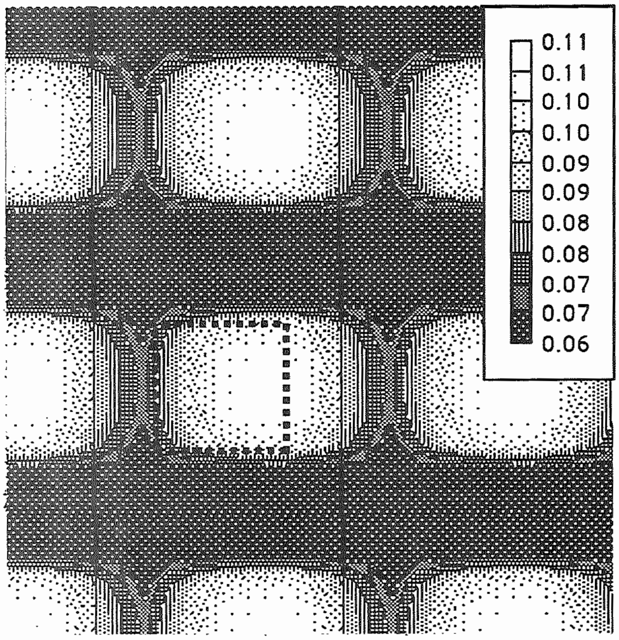

Figure 5 Dimensionless sensor intensities for $\phi_d = 0°$.

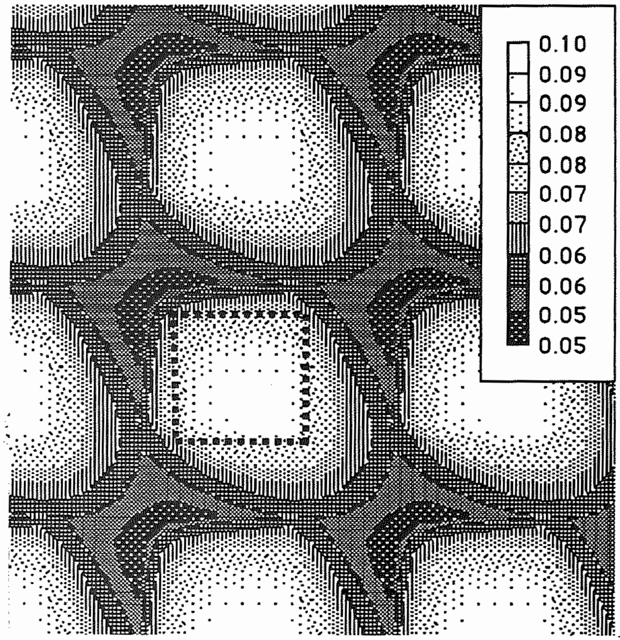

Figure 6 Dimensionless sensor intensities for $\phi_d = 45°$.

Fiveland, W. A. and Jamaluddin, A. S., "Three-Dimensional Spectral Heat Transfer Solutions by the Discrete-Ordinates Method," *Heat Transfer Phenomena in Radiation, Combustion, and Fires*, Ed. R. K. Shah, ASME HTD-Vol. 106, pp. 43-48, 1989.

Gerstl, S. A. W. and Zardecki, A., "Discrete-Ordinates Finite-Element Method for Atmospheric Radiative Transfer and Remote Sensing," *Applied Optics*, Vol. 24, pp. 81-93, 1985.

Kim, T. K. and Lee, H. S., "Radiative Transfer in Two-Dimensional Anisotropic Scattering Media with Collimated Incidence," *J. Quant. Spectrosc. Radiat. Transfer*, Vol. 42, pp. 225-238, 1989.

Kim, T. K. and Lee, H. S., "Scaled Isotropic Results for Two-Dimensional Anisotropic Scattering Media," *J. Heat Transfer*, Vol. 112, pp. 721-727, 1990a.

Kim, T. K. and Lee, H. S., "Modified δ-M Scaling Results for Mie-Anisotropic Scattering Media," *J. Heat Transfer*, Vol. 112, pp. 988-994, 1990b.

Kobayashi, T., "Radiative Properties of Finite Cloud Fields over a Reflecting Surface," *J. Atmos. Sci.*, Vol. 46, pp. 2208-22114, 1989.

Mandelbrot, B. B., *The Fractal Geometry of Nature*, W. H. Freeman and Company, New York, 1983.

McKee, T. B. and Cox, S. K., "Simulated Radiances for Finite Cubic Clouds," *J. Atmos. Sci.*, Vol. 33, pp. 2014-2020, 1976.

Mugnai, A., Cooper, H. J., Smith, E. A., and Tripoli, G. J., "Simulation of Microwave Brightness Temperatures of an Evolving Hailstorm at SSM/I Frequencies," *Bull. Amer. Meteor. Soc.*, Vol. 71, pp. 2-13, 1990.

Sánchez, A., Krajewski, W. F., and Smith, T. F., *A General Purpose Radiative Transfer Model for Application to Remote Sensing in Multi-Dimensional Systems*, IIHR Report No. 355, Iowa Institute of Hydraulic Research, The University of Iowa, Iowa City, Iowa, 1992.

Stamnes. K., Tsay, S-C., Wiscombe, W., and Jayaweera, K., "Numerically Stable Algorithm for Discrete-Ordinate-Method Radiative Transfer in Multiple Scattering and Emitting Layered Media," *Applied Optics*, Vol. 27, pp. 2502-2509, 1988.

Stephens, G. L., "Radiative Transfer Through Arbitrarily Shaped Optical Media. Part I: A General Method of Solution," *J. Atmos. Sci.*, Vol. 45, pp. 1818-1836, 1988.

Welch, R. M. and Wielicki, B. A., "Reflected Fluxes for Broken Clouds over a Lambertian Surface," *J. Atmos. Sci.*, Vol. 46, pp. 1384-1395, 1989.

Wiscombe, W. J., "The Delta-M Method: Rapid Yet Accurate Radiative Flux Calculations for Strongly Asymmetric Phase Functions," *J. Atmos. Sci.*, Vol. 34, pp. 1408-1442, 1977.

Infrared Attenuation by Water Clouds and Fogs

Eric P. Shettle
Code 6522, Naval Research Laboratory, Washington, DC 20375, USA
Petr Chylek and Peter Damiano
Atmospheric Science Program, Dept. of Physics & Oceanography
Dalhousie University, Halifax, Nova Scotia, B3H3J5, CANADA

1. Introduction

The cloud radiative properties in the infrared region of the spectrum is an important factor in any study concerning the climate, climatic change and cloud radiation feedback. Although the radiative transfer formalism together with the Mie scattering and absorption provide means to calculate the cloud's emittance at any wavelength for given size distribution of the spherical particles, such calculations are time consuming and presently are unsuitable for the use in climate or numerical weather prediction models. Consequently simple parametrizations in the form of the cloud's bulk properties (like liquid water content) have been sought (e.g., Paltridge 1974; Platt 1976; Chylek and Ramaswamy 1982) and used in climate modeling (e.g., Ramanathan, 1983).

With the realization that the cloud radiation feedback (e. g., Schneider 1972; Stephens et al. 1990) may modify predicted change of climate a need arises for a more accurate treatment of the cloud's IR radiative characterisitics. A simple expression is needed which would still allow a study of changes connected with the evolution of the cloud's microphysical properties such as the droplet size distribution.

We have developed a simple analytic approximation for the infrared attenuation and emittance of clouds and fogs composed of water spheres, based on a polynomial approximation to the Mie extinction and absorption efficiencies. The attenuation coefficients can be obtained in simple analytic form as a function of the liquid water content and two parameters characterizing the size distribution of the water droplets, such as its effective radius and effective variance.

The coefficients representing the approximation can be precalculated and stored in a form suitable for use in climate modeling, numerical weather prediction, and radiative transfer calculations. The resulting accuracies are within a few per cent when compared with exact Mie calculations and integration over the size distribution, while the computational burden is reduced by several orders of magnitude.

In an earlier paper (Chylek, Damiano, & Shettle 1992, subsequently referred to as CDS), we have applied this approach to the absorption and emittance by clouds in the infrared. The present work will briefly review the formalism developed in that paper and show how their results can be generalized to the other parameters characterizing the radiative properties of clouds. In particular we will discuss the extinction and scattering coefficients as well as the asymmetry parameter, which describes the angular scattering by the cloud.

2. Commonly Used Approximations for Attenuation

The attenuation coefficients, k_{atn} for a size distribution of cloud droplets is given by:

$$k_{atn} = \pi \int r^2\, Q_{atn}(r)\, n(r)\, dr \qquad (1)$$

where the subscript 'atn' represents: ext, scat, or abs for the extinction, scattering, or absorption coefficient respectively; r is the droplet radius; Q_{atn} is the extinction, scattering or absorption efficiency; and n(r) is the droplet size distribution.

a. Small Particle Case

The extreme small particle case is the Rayleigh limit where the size is much smaller than the wavelength, $r << \lambda$. In this case the absorption efficiency, Q_{abs}, is linear function of the particle size and that the absorption coefficient, k_{abs}, is equal to the liquid water content, W, times a function of the refractive index of water, m, (van de Hulst 1957):

$$k_{abs} = W \cdot f(m) \qquad (2)$$

Similarly in this case, the scattering efficiency, Q_{scat}, is proportional to the fourth power of the radius and the scattering coefficient, k_{scat}, is equal to the 6^{th} moment of the size distribution, M_6, times a function of the refractive index of water:

$$k_{scat} = M_6 \cdot g(m) \qquad (3)$$

For cloud drops where the characteristic sizes are on the order of micrometers, these approximations, Eq. (2) & (3), are only applicable in the microwave region, (Falcone et al. 1979).

For the IR spectral region, a similar linear dependence for the attenuation efficiencies, has been noted for values of the radius less than some r_{max}, where the value of r_{max} varies between 5 and 13 μm, depending on wavelength within the spectral region of interest (Platt 1976; Chylek 1978; Pinnick et al. 1979; Chylek and Ramaswamy 1982):

$$Q_{atn} = a_{atn}(\lambda) \cdot r \qquad (4)$$

where $a_{atn}(\lambda)$ is an empirically derived parameter (e.g. Fig. 1). This leads to an expression for the attenuation coefficients:

$$k_{atn} = [\, 3a_{atn}(\lambda) / 4\rho \,] \cdot W \qquad (5)$$

where ρ is the density of water.

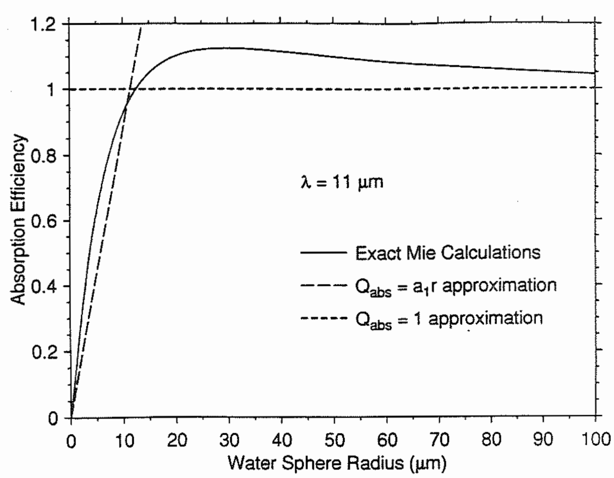

Fig. 1 - The exact absorption efficiency, for λ=11 μm, compared with the limiting approximations: a linear function of radii for small droplet radii, [Eq. (4)] and by a constant Q_{abs} = 1 for the case of large droplets.

The advantage of expression (5) for the absorption coefficient, k_{abs}, is its simplicity. The obvious disadvantage is the fact that we are limited to the small size of droplets for which the approximation is expected to be valid.

b. Large particle case

At least some water clouds and most cirrus have particles large enough to violate the requirement on which the relation (5) is based. Especially when cirrus cloud particles are modeled by equivalent spheres, the effective radius of spheres is usually found to be far above the limits of applicability of the simple approximation for the absorption efficiency and the absorption coefficients represented by eqs. (3) and (5). The effective radius is usually between 20 and 100 μm. For these large particles a different approximation to the Q_{atn} as calculated by Mie theory seems to be appropriate. As the Q_{atn} approaches a large particle asymptotic limit, we can assume for large spherical particles: $Q_{atn} = a_{atn}$, where the a_{atn} will be constants. For the extinction, a_{ext} will be 2, and for both scattering and absorption the constants will be near 1, with $a_{abs} \approx 2 - a_{scat}$, (e.g. see Fig. 1). Using these approximations in the attenuation integral, Eq. (1) leads to:

$$k_{ext} = [\, 3a_{ext} / 2\rho \cdot r_{eff} \,] \cdot W \tag{6a}$$

$$k_{scat} \approx k_{abs} \approx [\, 3a_{ext} / 4\rho \cdot r_{eff} \,] \cdot W \tag{6b}$$

where r_{eff} is the effective radius of the size distribution, n(r), which is defined (e.g., Hansen and Travis 1974) as the area weighted mean radius. This is equivalent to the ratio of the 3^{rd} to the 2^{nd} moment of the size distribution: $r_{eff} = M_3 / M_2$.

3. Polynomial approximations

We propose to develop a simple approximation for the IR properties of clouds composed of spherical particles or represented by effective spheres. Any useful approximation should retain a simple form so that it can be used in parametrization of radiative processes in numerical weather prediction and climate models. For computational convenience it is also desirable that the approximation retains an analytic form when integrated over representative size distributions. At the same time a more physically rigorous approach than that presented in the previous section is desirable.

As noted by CDS, the absorption efficiency Q_{abs} as calculated using the Mie scattering formalism for a moderately absorbing medium does not show significant oscillations as a function of droplet radius. It can be expected that such a curve can be accurately approximated by a N^{th} degree polynomial with a not too high value of N for radii smaller than some value r_{max}. The scattering and extinction efficiencies can be expected to exhibit some oscillations, which are generally broad enough for cloud droplets in the IR, that a polynomial could still reasonably approximate the values.

For the case of water clouds the extinction efficiency, Q_{ext} can be written in the form:

$$Q_{ext} = \sum_{n=0}^{N} b_n r^n \tag{7}$$

where the b_n are expansion coefficients which can be determined at the required wavelengths by least squares polynomial fit to the Mie calculations over a range of the droplet radius from 0 to r_{max}, and tabulated for subsequent use, (Fig. 2 shows an example of a 10^{th} order polynomial fit to the

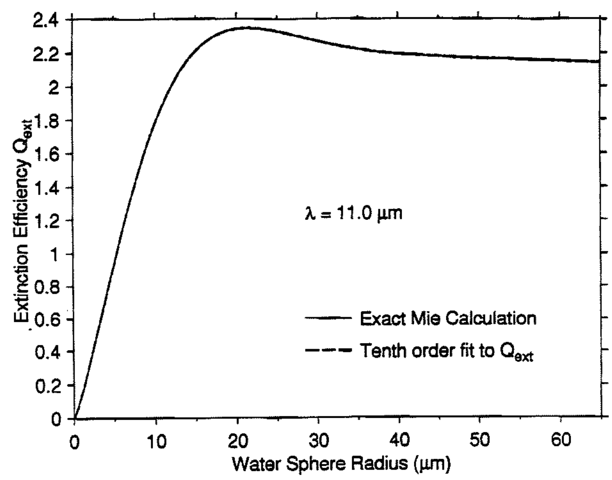

Fig. 2 - A comparison of the exact extinction efficiency, for λ=11 μm, with a 10^{th} order polynomial, [Eq. (7), with N=10].

extinction efficiency for λ =11 μm). Substituting this expansion (7) into the extinction coefficient integral, Eq. (1) leads to a simple expression for the extinction coefficient:

$$k_{ext} = \pi \sum_{n=0}^{N} b_n M_{n+2} \tag{8}$$

where M_n is the n^{th} moment of the size distribution. A similar expression can be written for the scattering efficiency, k_{scat}, and CDS have developed a analogous expression for the absorption efficiency.

To fully characterize the cloud properties for radiation modeling, it is necessary to develop an equivalent expansion for the asymmetry parameterr, g, which is the cosine weighted average of the angular scattering (or phase) function, P(θ), for the particles:

$$g = \iint (\cos\theta) P(\theta) d\Omega \Big/ \iint P(\theta) d\Omega \tag{9}$$

From the definition of the asymmetry parameter, Eq. (9), it follows that the proper weighted average, g, of the asymmetry parameter as a function of droplet size, g(r), is given by

$$\text{or:} \quad g = \pi \int g(r) r^2 Q_{scat}(r) n(r) dr \,/\, k_{scat} \tag{10}$$

This suggests the product $g(r)Q_{scat}(r)$, in Eq (10) be approximated by a polynomial expansion analogous to Eq (7):

$$g(r)\, Q_{scat} = \sum_{n=0}^{N} d_n r^n \tag{11}$$

which when substituted into Eq. (10) leads to:

$$g = \left[\pi \sum_{n=0}^{N} d_n M_{n+2} \right] \Big/ k_{scat} \tag{12}$$

Fig. 3 shows the 10^{th} order fit to $g(r)Q_{scat}(r)$, [Eq. 11, with N=10], for λ=8 μm.

As noted by CDS the factors of πM_n can be rewritten as proportional to a product of the liquid water content, W, and a constant, C_n. They have tabulated these C_n, for a number of commonly used size distributions. Using these results in the expressions, Eq. (8), and (12) leads to:

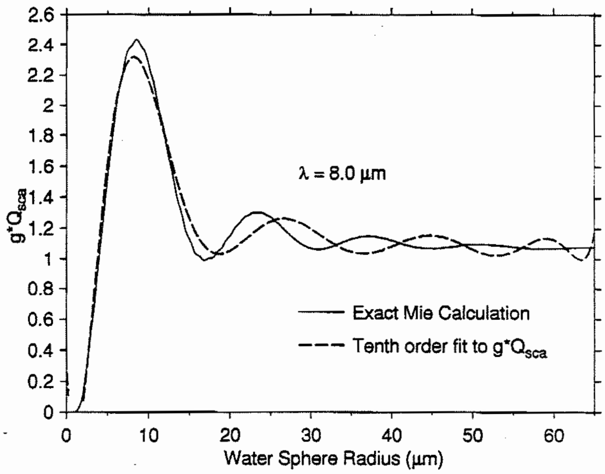

Fig. 3 - A comparison of the 10^{th} order polynomial fit of $g(r)Q_{scat}(r)$, [Eq. (14), with N=10], with the exact calculations for a wavelength of 8 μm.

$$k_{ext} = \frac{3W}{4\rho}\sum_{n=0}^{N} b_n C_{n+2} \quad (13)$$

$$k_{scat} = \frac{3W}{4\rho}\sum_{n=0}^{N} c_n C_{n+2} \quad (14)$$

$$g = \left[\frac{3W}{4\rho}\sum_{n=0}^{N} d_n C_{n+2}\right] \Big/ k_{scat} \quad (15)$$

The expressions, Eq. (13) to (15), along with the similar summation previously developed by CDS are the basic results, where the coefficients $a_n(\lambda)$, $b_n(\lambda)$, $c_n(\lambda)$, and $d_n(\lambda)$ which can be determined at the required wavelengths by least squares polynomial fits to the Mie calculations over a range of the droplet radius from 0 to r_{max}, and tabulated for subsequent use. CDS found the absorption efficiency could be well approximated by 10^{th} order polynomials for wavelengths between 3 and 25 μm, with r_{max} of 100 μm. Because of the broad oscillations which occur in $Q_{scat}(r)$ and $Q_{ext}(r)$ at wavelengths where water is a weak absorber, we have found it necessary to restrict r_{max} to 65 μm, to generally retain accuracies of a few percent at all wavelengths of interest, with 10^{th} order polynomials. While for many wavelengths accuracies of better than a percent could be obtained with lower order polynomials over this size range, for uniformity we have used 10^{th} order for all wavelengths.

By limiting the valid size range to radii less than 20 μm, and relaxing the accuracy requirement, exceptable results can be obtained with a second order polynomial, (N=2). By using the fact, noted by CDS, that the first three C_n can be expressed in terms of the effective radius and the effective variance of the cloud size distribution, Eq. (13)-(15) can rewritten as:

$$k_{ext} = \frac{3W}{4\rho}\left[\frac{b_0}{r_{eff}} + b_1 + b_2 r_{eff}(1+v_{eff})\right] \quad (16)$$

$$k_{scat} = \frac{3W}{4\rho}\left[\frac{c_0}{r_{eff}} + c_1 + c_2 r_{eff}(1+v_{eff})\right] \quad (17)$$

$$g = \frac{3W}{4\rho}\left[\frac{d_0}{r_{eff}} + d_1 + d_2 r_{eff}(1+v_{eff})\right] \Big/ k_{scat} \quad (18)$$

4. Numerical Results

The derived expressions Eq. (13)-(15) or Eq. (16)-(18), can used to calculate the cloud attenuation coefficients, and the asymmetry parameter, as a function of the cloud liquid water content, and the parameters defining the shape of the droplet size distribution. These expressions are relatively simple compared to carrying out the Mie scattering calculations and integration over the size distribution.

To test the validity of these approximations, we compare the results for exact Mie scattering calculations the water cloud and fog models used in LOWTRAN 7 (Kneizys et al., 1988). The characteristics of these models are summarized by Shettle (1989) and will not be repeated here except to note that r_{eff} for the different models ranges from 3 to 20 μm, which includes typical sizes of most cloud distributions.

The results of the comparisons for the 10^{th} order polynomials, [Eq. (13)-(15)], with the Mie calculations is summarized in Table 1. For most of the cloud models, the polynomial approximation reproduces the exact results to within 1 to 2%, with the exception of the radiation fog model where the rms error is as large as 10%. Figures 4 and 5 compare the exact and fitted values of k_{ext} and g, as a functions of wavelength for the radiation fog model.

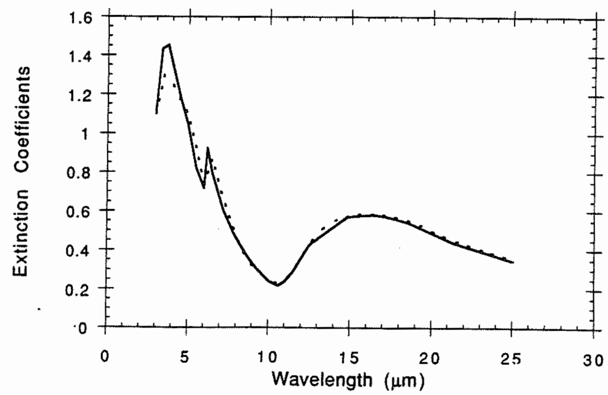

Fig. 4 - A comparison of the 10^{th} order polynomial fit for the extinction efficiency, [Eq. (15)], with the exact results for the radiation fog model as a function of wavelength.

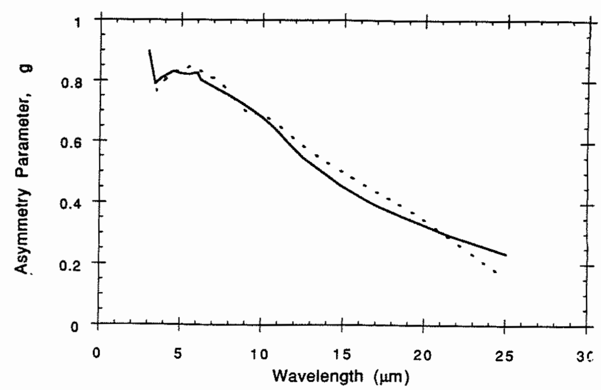

Fig. 5 - A comparison of the 10^{th} order polynomial fit for the asymmetry parameter, [Eq. (17)], with the exact results for the radiation fog model as a function of wavelength.

Table 1 - RMS Percent Error in the 10th Order Polynomial fits							
Parameter	Cumulus	Alto-Strat	Stratus	St-Cumulus	Nimbo-St	Advec.Fog	Rad. Fog
Extinction	0.49	2.03	0.55	1.55	0.25	0.31	4.82
Scattering	0.65	2.38	0.70	1.85	0.33	0.43	6.50
Absorption	0.16	1.17	0.57	0.60	0.19	0.15	2.64
Asym. Par.	0.12	0.47	0.16	0.51	0.07	0.07	10.16

Table 2 - RMS Percent Errors in the Quadratic Fits						
Parameter	Cumulus	Alto-Strat	Stratus	St-Cumulus	Nimbo-St	Rad. Fog
Extinction	3.05	8.75	5.16	9.21	4.47	15.41
Scattering	4.30	10.76	6.74	11.50	5.81	35.09
Absorption	1.79	4.19	2.27	4.04	2.71	6.76
Asym. Par.	0.62	2.59	1.32	3.27	0.83	35.84

The errors in the quadratic fits [Eq. (16)-(18)], compared with the exact calculations for the different models is summarized in Table 2. The advection fog model (with $r_{eff} = 20\ \mu m$) is omitted since many of the particles in the size distribution exceed the upper limit, ($r_{max} = 20\ \mu m$) for validity of the fit. The fits are generally better than 10%, except for the radiation fog model again, where the rms errors were 35% for the scattering coefficient and the asymmetry parameter.

5. Discussion

We have shown that the IR radiative characteristics of most water clouds and fogs can be approximated with simple 3 term formulae, [Eq. (16)-(18)]. These formulae can be written in terms of the cloud liquid water content, the effective radius & the effective variance of the size distribution, and several wavelength dependent coefficients which can be precalculated and stored. Where greater accuracy is required and/or wider range of cloud droplet sizes is necessary, a higher order polynomial approximation can be used, [Eq. (13)-(15)]. The constants for the higher order terms, the C_n, depend on the details of the size distribution used, (see CDS). Chylek, Damiano, Ngo, & Pinnick 1992 have shown that over a limited spectral region, such as the 8 to 12 μm atmospheric window, the wavelength dependent polynomial coefficients can be replaced by a polynomial expansion in wavelength.

6. Acknowledgements

The reported research was supported in part by the Atmospheric Environment Service and the National Science and Engineering Research Council of Canada. Parts of this work were completed while the second author, (PC), was at the Naval Research Laboratory, under the U.S.Navy - ASEE Summer Faculty Research Program.

References

Chylek, P., 1978: Extinction and liquid water content of fogs and clouds. *J. Atmos. Sci.*, **35**, 296-300.

Chylek, P., P. Damiano, D.Ngo, & R.G.Pinnick 1992: Polynomial Approximation of the Optical Properties of Water Clouds in the 8 to 12 μm Spectral Region, to be published in *J. Appl. Meteor.*, **31**.

Chylek, P., P.Damiano, & E.P.Shettle 1992: Infrared Emittance of Water Clouds, to be published in *J. Atmos. Sci.*, **49**.

Chylek, P., and V. Ramaswamy, 1982: Simple approximation for infrared emissivity of water clouds. *J. Atmos. Sci.*, **39**, 171-177.

Falcone, V.J., L.W.Abreu, and E.P.Shettle 1979: *Atmospheric Attenuation of Millimeter and Submillimeter Waves: Models and Computer Code*, AFGL-TR-79-0253, (Available from NTIS, ADA 084485).

Hansen, J. E. and L. D. Travis, 1974: Light scattering in planetary atmospheres. *Space Sci. Rev.*, **16**, 527-610.

Kneizys,F.X., E.P.Shettle, L.W.Abreu, G.P.Anderson, J.H.Chetwynd, W.O.Gallery, J.E.A.Selby, and S.A.Clough, 1988: *Users Guide to LOWTRAN 7*, AFGL-TR-88-0177, (available from NTIS AD A206773)

Paltridge, G. W., 1974: Infrared emissivity, shortwave albedo and the microphysics of stratiform water clouds. *J. Geophys. Res.*, **79**, 4053-4058.

Pinnick, R. G., S. G. Jennings, P. Chylek and H. J. Auvermann, 1979: Verification of a linear relation between IR extinction, absorption and liquid water content of fogs. *J. Atmos. Sci.*, **36**, 1577-1586.

Platt, C. M. R., 1976: Infrared absorption and liquid water content in stratocumulus clouds. *Quart. J. Roy. Meteor. Soc.*, **102**, 553-561.

Ramanathan, V., E. J. Pitcher, R. C. Malone and M. L. Blackman, 1983: The response of a spectral general circulation model to refinements in radiative processes. *J. Atmos. Sci.*, **40**, 605-630.

Schneider, S., 1972: Cloudiness as a global climate feedback mechanism: The effects on the radiation balance and surface temperature of variations in cloudiness. *J. Atmos. Sci.*, **29**, 1413-1422.

Shettle, E.P., 1989: Models of Aerosols, Clouds, and Precipitation for Atmospheric Propagation Studies, pg 15-1 to 15-13, in AGARD Conference Proceedings CP No. 454, *Atmospheric Propagation in the UV, Visible, IR, and mm-Wave Region and Related Systems Aspects*, (available from NTIS N90-21919)

Stephens, G. L., S. C. Tsay, P. W. Stackhouse and P. J. Flatau, 1990: The relevance of the microphysical and radiative properties of cirrus clouds to climate and climatic feedback., *J. Atmos. Sci.*, **47**, 1742-1753.

van de Hulst, H. C., 1957: *Light Scattering by Small Particles*. Dover, 1981 edition, 470 pp.

RADIATIVE TRANSFER MODELING FOR CIRRUS CLOUDS DURING THE 'FIRE 91' FIELD EXPERIMENT

S. Kinne[1] and T.P. Ackerman[2]

[1]NASA-Ames, Moffett Field, CA, USA 94035-1000
[2]Pennsylvania State University, University Park, PA, USA 16802

1. INTRODUCTION

The recent FIRE 91 field experiment provided an unique opportunity to validate atmospheric models. This paper concentrates on the radiative transfer modeling aspect: How well can simple models simulate radiative properties of the atmosphere? Or more specifically, how well can they translate directly or indirectly measured properties of the atmosphere into radiative fluxes?

The quality for radiative transfer modeling is evaluated from a comparison of broadband, both solar and infrared, fluxes at the surface. Measured fluxes are compared to calculated fluxes, which are based on in-situ measurements (e.g. cloud particle probes, radiosondes) and remote sensing data (e.g. sunphotometer, radar).

The radiative transfer model and the available data will be addressed first, before comparisons for cloud-free cases and cases involving cirrus clouds are given. Since the data-analysis, at this time, is still underway, only a couple of initial comparisons will be presented.

2. MODEL

The radiative transfer calculations are based on a four-stream code at solar wavelengths and on a two-stream code for the infrared. The spectral region has been discretized into 8 solar and 12 infrared bands. Absorption by atmospheric gases is based on the AFGL database.

The selected method, the selected spectral resolution and the selected absorption approximation can notably affect calculated results (Fouquart et al., 1991; Luther et al., 1988). To quantify such 'scheme related error', selected cases will be repeated by using a) other methods (e.g. discrete ordinate method, adding-doubling method), b) other spectral resolutions and c) other data sets for the gas-absorption.

3. DATA

In-situ measurements and remote sensing techniques, provide information about atmospheric properties (e.g. atmospheric variables, atmospheric gases, and particles, their optical properties and vertical distribution). The 'FIRE 91' field experiment, during late autumn in the US state of Kansas, provided a multitude of simultaneous measurements for the same location. Here, only those measurements are listed, that are used in this study:

1. Vertical profiles of atmospheric variables (e.g. temperature, humidity) are defined by frequent NOAA radiosonde launches. Model-calculations for times between launches are based on a linear time-interpolation.

2. Cloud optical properties are provided by in-situ airborne NCAR particle probes and remote sensing data from the ground, including the PSU radar system and the PSU sun-photometer; the latter providing optical depths values for optically thin clouds, including cirrus.

3. Cloud structural data are provided by the PSU radar, the UofU lidar system and VCR visual video images.

4. Downward hemispheric broadband solar and infrared fluxes at the surface are provided by PSU radiometers.

Measurements 1, 2 and 3 provide the input to the model. The output of the model is compared to measurement 4.

All measurements carry a measurement error, which might be reduced by dual measurements of the same property. Estimates on how these 'data related errors' affect calculated fluxes will be given.

4. COMPARISON

Comparisons between measured and calculated fluxes will show a combination of 'scheme related errors' and 'data related errors'. Here, only two initial comparisons are given for solar broadband downward fluxes at the surface, for a cloud-free case and a cirrus cloud case.

Figure 1 presents the solar flux comparison for a cloud-free day on 12/4/91.

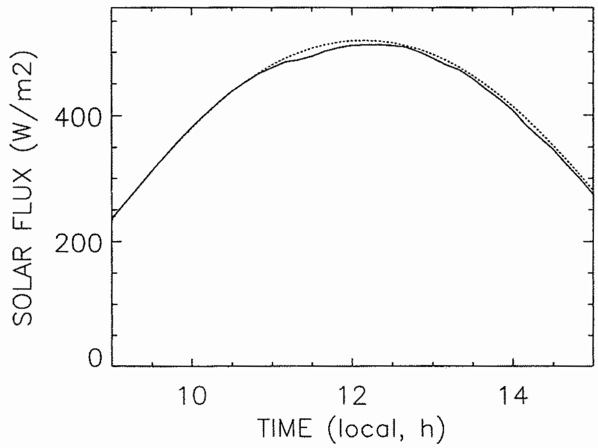

Figure 1. Comparison of downward solar fluxes at the surface for a cloud-free day (12/4/92) of measurements (solid line) and calculations (dotted line) for 10 minute averages.

The agreement of the fluxes in Figure 1 is encouraging and the deviations are smaller, than expected from error analysis. The slightly larger calculated data, during noon and afternoon, may be attributed to a, so far, insufficient incorporation of atmospheric aerosol in the model.

Figure 2 presents the solar flux comparison for a cirrus day on 12/5/91.

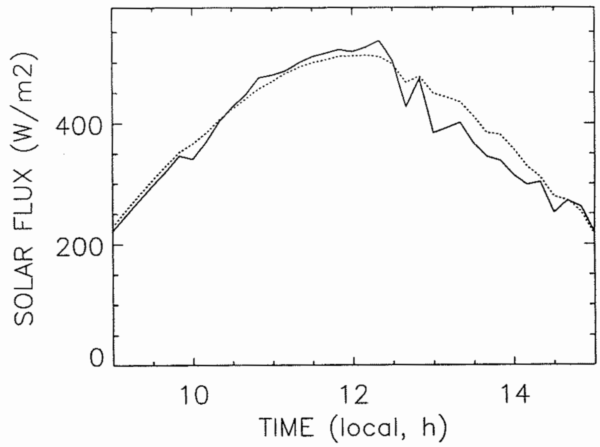

Figure 2. Comparison of downward solar fluxes at the surface for a cirrus day (12/5/92) between measurements (solid line) and calculations (dotted line) for 10 minutes averages.

Cirrus optical depth were small in the morning (τ <.2), however, increased in the afternoon (τ >.7). Although, the flux comparison shows a general agreement, there are significant differences. The measurements suggest larger cirrus cloud optical depths and/or less forward scattering by cirrus particles (the model assumes a solar asymmetry factor of .85). The large deviations for the afternoon also show, that an analysis using 10-minute averages, seems insufficient, suggesting comparisons with higher time resolutions for (cirrus) cloud cases.

5. CONCLUSION

Calculated radiative quantities have been compared to actual measurements, to detect measurement errors, but, more importantly, to detect insufficiencies in the model. An improved representation of atmospheric conditions in radiation models becomes more necessary with the increasing availability of remote sensing information (e.g. satellites). Only then may we be able to relate observed changes to possible effects on climate.

REFERENCES

Fouquart, Y., B. Bonnel and V. Ramaswamy Intercomparing Shortwave Radiation Codes for Climate Studies, J.Geophys.Res. 96, 8955-8968, 1991.

Luther, F.M. et al. Intercomparison of radiation codes in climate models (ICRCCM): Longwave clear-sky results. Workshop summary. Bull.Am.Met.Soc. 69, 40-48, 1988.

WAVELET ANALYSIS OF MARINE STRATOCUMULUS

Steven M. Gollmer and Harshvardhan

Department of Earth and Atmospheric Sciences
Purdue University, West Lafayette, IN

Robert F. Cahalan

Laboratory for Atmospheres, Goddard Space Flight Center, Greenbelt, MD

Jack B. Snider

NOAA/ERL/Wave Propagation Laboratory, Boulder, CO

1. Introduction

The presence of inhomogeneities have an effect on the radiative properties of clouds. Since general circulation models use an assumption of plane-parallel homogeneous clouds for calculating radiative properties, it is important to study the biases introduced by making this assumption. Studied by Cahalan (1992), Kobayashi (1991) and Stephens (1988) this bias can change the reflectance of a cloud by as much as 5% in marine stratocumulus (Cahalan 1992), which are assumed to be fairly uniform.

Simple parameterizations of this inhomogeneity involve incorporating the principles of self-similarity (Cahalan 1989; Schertzer and Lovejoy 1987). This self-similarity is based on the analyses of cloud distributions (Cahalan and Snider 1989; Lovejoy 1982) and states that features of various scales within clouds have common parameters. A method of extracting relationships between scales is addressed here and uses a new technique called wavelet analysis. This technique is used as a basis for a model which is developed from an analysis of liquid water data. This data was obtained from a microwave radiometer used during the marine stratocumulus phase of FIRE (First ISCCP Regional Experiment) (Albrecht et al. 1990). This analysis also provides a method of looking at the effect of inhomogeneities on cloud reflectance.

2. Wavelet analysis and wavelet model

Wavelet analysis, which has been developed over the last few years, provides a new method of analyzing self-similar structures (Arneodo et al. 1988). Though it does not provide any additional information about the data, it does provide an efficient means of organizing the features of the data. A basic wavelet, Ψ, is a function which is square integrable and admissible. These two properties insure that the wavelet has a finite extent and is represented as a small wave (Chui 1992). Once a basic wavelet is defined, it can be adjusted to any spatial scale by incorporating a magnification factor. This magnification factor does not change the shape of the wavelet, but stretches or shrinks its spatial extent. A wavelet transform of the data can be obtained by convolving the data with a wavelet and this transform contains information related to the spatial extent and shape of the wavelet. To extract features over a range of scales a series of convolutions are done on the data where the magnification factor of the wavelet is changed before each convolution.

One particular type of wavelet series which is beneficial to this study is the orthogonal wavelet series. These wavelets are not continuous functions but are defined as a series of coefficients which are orthogonal to a translation of itself (Daubechies 1988). The orthogonality property of these wavelets not only involves translations but also magnifications by factors of two. A specific combination of coefficients determines a basic wavelet from which a wavelet series, $\Psi_{j,k}$, can be generated. The wavelet series obeys the relationship

$$\Psi_{j,k}(x) = 2^{j/2}\,\Psi(2^j x - k) \qquad (1)$$

where j and k are members of the set of integers and are the level of magnification and the translation respectively. By expanding data on this wavelet series the data can be represented in a multiresolution form (Strang 1989). For any particular spatial scale, j, there exists a series of values, $W_j(k)$, which represent variability of the data on that particular spatial scale. Since the spatial scale decreases by a factor of two with an incremental increase of j, the number of values in the series, W_{j+1} is twice the number in W_j. On the largest scale of the analysis, which corresponds with the smallest value of j, an additional series is obtained, V_j, which contains the average value of the data on that scale. The series, V_j, can be further decomposed into W_{j-1} and V_{j-1} by applying the wavelet transform an additional time.

Since wavelet analysis extracts features of a particular spatial scale, it is similar to a windowed Fourier transform and acts like a band pass filter (Daubechies 1989). With an orthogonal wavelet series the effectiveness of the filter is determined by the number of coefficients, where $2n$ coefficients are used to set the first nth moments at the boundary of the window to zero. By using a moderate number of coefficients, data can be resolved into various spatial scales with very little spectral leakage between scales.

A simple application of wavelet analysis involves using it as a filter. By decomposing a time series on an orthogonal wavelet basis, the values of any particular spatial scale, W_j, can be set to zero. The result of an inverse wavelet transform on this modified data set will be similar to the original data with that particular spatial scale removed.

A second application involves developing a model based on wavelet analysis of data taken from the marine stratocumulus portion of FIRE. Segments of the FIRE liquid water data were decomposed into a number of series, W_j, using a 20 coefficient basic wavelet. Comparisons of these series demonstrated a correspondence of variability between adjacent scales. To capture the changes of the variability in the data, the standard deviation over an 8 point running window was done at each scale of the analysis. Correlation between the standard deviations of adjacent scales was present and indicated that there was a coupling between variability at adjacent scales. This coupling is related to the dissipation of energy from larger scales to smaller scales and, therefore, also has a connection with the power spectra of the data. Coupling constants were calculated for each of the scales and were found to depend on the time of day.

The analyzed data also showed a relationship between variability and liquid water amount on the largest scale. An 8 point running window standard deviation was performed on W_j along with an 8 point running window mean on V_j. These running window values correlated and provided coupling constants which also contained a diurnal cycle.

From this analysis, a model was developed which relates small scale features of the liquid water amount to the large scale features. Since the analysis showed correlation between variability of adjacent scales and between mean liquid water and variability on the largest scale, a procedure for generating the series W_j through W_{j+m} from V_j was developed. The distribution of values in W_j from the wavelet analysis were symmetric about zero but were more kurtose than a Gaussian distribution. In spite of this, a Gaussian distribution was chosen to generate the values of W_j through W_{j+m} because of its simplicity and its presence in most natural processes. Since the distribution is symmetric about zero, the values of W_j can be generated from a Gaussian distribution by specifying only a standard deviation. The standard deviation is determined by the statistical properties of the next largest scale and the coupling constant between these scales. For the wavelet based model the lowest resolution mean, V_j, is used to generate the lowest resolution variability, W_j. A value for the xth point in W_j is generated by

$$W_j(x) = \frac{C_{jj}\,R_G}{2l}\sum_{i=-l}^{+l} V_j(x+i) \qquad (2)$$

where C_{jj} is the coupling coefficient between the standard deviation of W_j and the mean of V_j, R_G is a random number that is normally distributed and l is the half width of a window centered at x. To generate the remaining series of W_{j+1} through W_{j+m} a similar procedure is used where $C_{j+1,j}$ is the coupling between the standard deviation of W_j and W_{j+1}. Since W_j has half as many points as W_{j+1}, two values are generated in W_{j+1} before the window is shifted in W_j. Once all of the values of W_j through W_{j+m} have been generated, an inverse of the wavelet transform is performed on each of the levels. This process integrates the features at every scale into a single time series.

3. Application

A segment from the FIRE liquid water data set was used to calculate the dependence of reflectance on inhomogeneity. The data consists of values averaged over one minute time periods and each value corresponds with a spatial resolution of 300 m assuming a mean cloud advection speed of 5 m/s. The segment of data chosen had a length of 512 minutes beginning at 10Z July 15, 1987 which corresponded with the local night and early morning. The liquid water amount at this time was fairly uniform and the resultant clouds had a thickness ranging from 350 to 500 m as calculated by Albrecht et al. (1990). The average liquid water amount was 183 g/m^2 and this corresponds with an optical thickness of 27.5 assuming a water droplet distribution with an effective radius of 10 μm (Stephens 1978). The power spectra of this data segment had a slope of −1.29, which is smaller than the predicted −5/3 of the inertial subrange. Figure 1a is a plot of this data's power spectra and this will be used as a comparison for wavelet manipulations on this data.

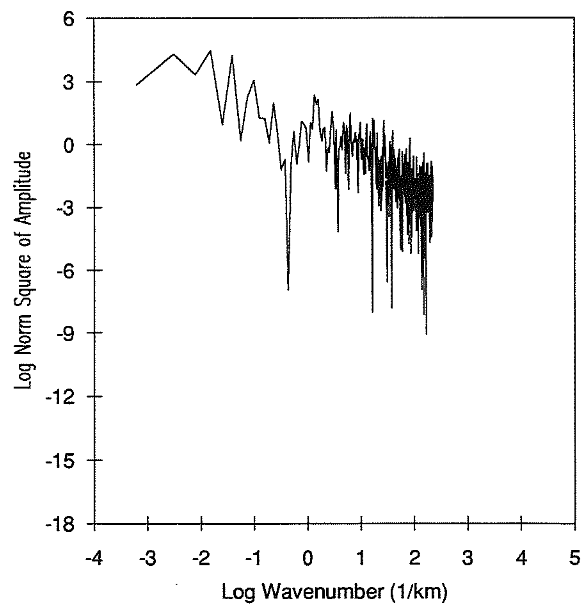

Figure 1(a). Power spectra of liquid water column amount from July 15 2:00 − 10:32 local time. This data represents a resolution of 300 m assuming an advection speed of 5 m/s. The best fit to the slope of the spectra is −1.285. This is not as steep as the theoretically predicted slope of −5/3.

The goal of the wavelet analysis was to determine if a wavelet model could produce reasonable small scale liquid water distributions based on the larger scale features. To aid in the discussion of the procedure that follows the original data set is designated as V_0, which will represent the average value of the data at the one minute time scale or 300 m spatial scale. V_0 is extended to the 37.5 m scale, V_3, by applying the inverse wavelet transform three times. This new data series, which is 4096 points long, contains no information on spatial scales higher than 300 m and, therefore, has very little spectral contribution above $2\pi/300$ m^{-1} wavenumbers (Figure 1b). The spectral component that does exist above this threshold is the result of spectral leakage from the wavelet analysis. The wavelet

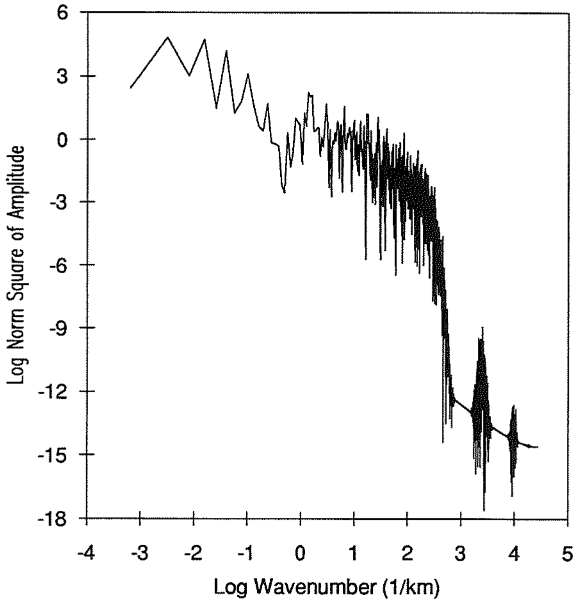

Figure 1(b). Power spectra of expanded resolution on data used in Figure 1a. This wavelet method extends the resolution to 37.5 m without adding any information of the smaller scale. Because this method has spectral leakage there is an introduction of some higher wavenumber components.

model, which generates higher wavenumber components, is initialized with V_{-2} so that several predicted resolutions of the model can be compared to known resolutions of the data. When this initialization data, which has a spatial resolution of 1.2 km, is extended to V_3, it contains a spectral component (Figure 1c) which is reduced from that observed in Figure 1b. The coupling coefficient between the mean of V_{-2} and the standard deviation of W_{-2} was determined along with the coupling between the standard deviations of W_{-2} and W_{-1}. These values were 0.052 and 0.620 respectively and were used along with the initialization data to generate the higher wavenumber components. Assuming that the processes in the cloud are self-similar, the value of 0.62 was not only used for the coupling, $C_{-1,-2}$, but also for any higher couplings, $C_{j+1,j}$. Combining V_{-2} along with the model generated values W_{-2} through W_2 by use of the inverse wavelet transform a new data series is generated which contains features on the spatial scale of 37.5 m. The power spectra of this series (Figure 1d) is similar to the original data set and has a slope of -1.36.

The original data and model results were used in a two-dimensional Monte Carlo radiative transfer program to generate reflectances. Each value in V_3 was converted to an optical thickness and then used to initialize the Monte Carlo program. Since each value in V_3 has a spatial resolution of 37.5 m, the aspect ratio of elements within the cloud were set to 8 assuming that the average cloud depth was 300 m. A Henyey-Greenstein phase function with an asymmetry parameter value of 0.85 was used. A solar zenith angle of

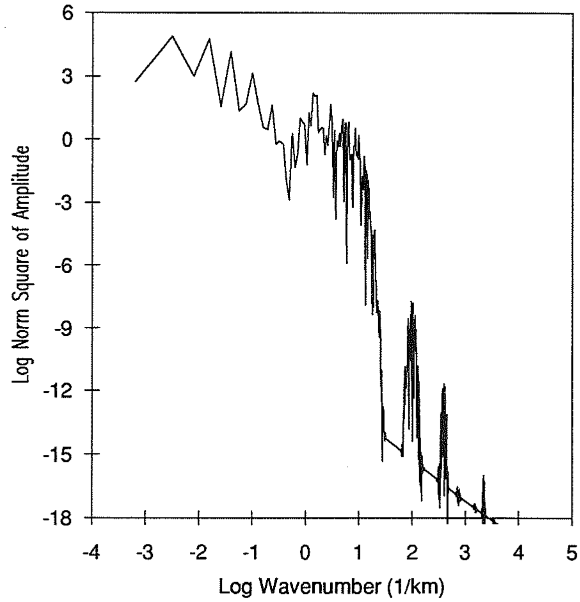

Figure 1(c). Power spectra of expanded resolution on model initialization data. This data is a result of a low-pass filter on the data used in Figure 1a and only retains information on scales larger than 1.2 km. The wavelet method again introduces higher wavenumber components because of spectral leakage.

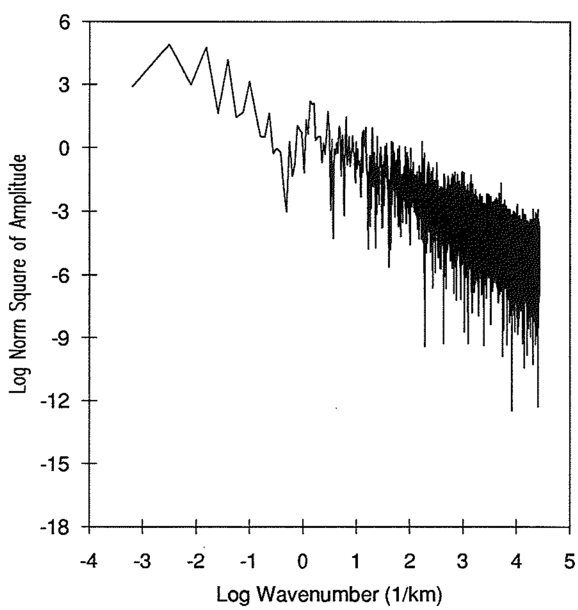

Figure 1(d). Power spectra of model results generated from data used in Figure 1c. This data represents a resolution of 37.5 m. The best fit to the slope of the spectra is -1.358.

60° (early morning) was used where the sunlight was incident perpendicular to the inhomogeneities within the cloud.

A plot of reflectance versus various levels of inhomogeneity is given in Figure 2. The level

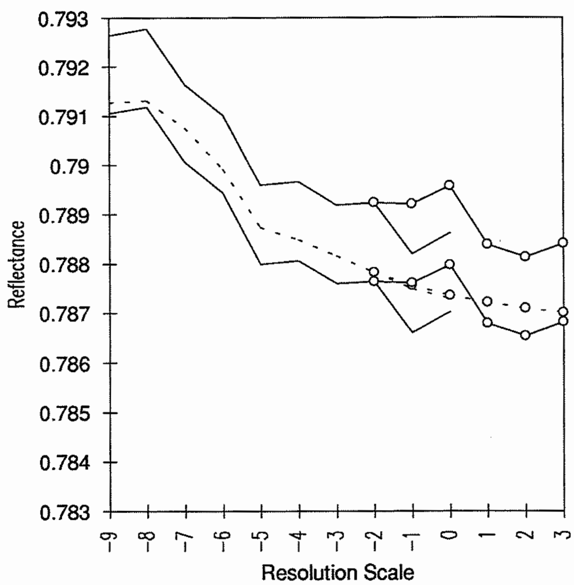

Figure 2. Reflectance of a cloud with various amounts of inhomogeneity. The ordinate goes from a homogeneous cloud (τ = 27.5) at the left to a cloud with inhomogeneities incorporated on the spatial scale of 40 m on the right. The solid lines represent the 95% confidence intervals of the Monte Carlo results while the dashed lines are the IPA results. The untagged lines are based on low-pass filter results of the original data and the 'o' tagged lines are from the wavelet model.

of inhomogeneity is determined by performing a low-pass filter on the original data and the model results. The homogeneous cloud corresponds to the single value of V_{-9} expanded to V_3, where all the values of W_{-9} through W_2 are set to zero. Other levels of inhomogeneity are obtained by retaining the values of W_{-9} through W_j which contain the information of the variability of the data. The two solid lines of the plot are the upper and lower bounds of the Monte Carlo 95% confidence interval. The dashed line is the independent pixel approximation,IPA, (Cahalan 1992) of V_3 and is calculated using a 16 stream discrete ordinates solution.

4. Conclusions

The Monte Carlo results of Figure 2 illustrate a reduction in reflectance as inhomogeneity is introduced. The IPA is contained within the bounds of the Monte Carlo results except for V_0 of the wavelet model. This may indicate that higher order effects of cloud inhomogeneity are becoming important. This may not be significant since this is the only value that does not lie within the confidence interval. The reflectance does not decrease with the initial addition of inhomogeneity because the large scale variability of the data was fairly small.

The IPA results give a better indication of whether the original data and wavelet model values agree. For the two overlapping scales the IPA results are very close and show that the model's reflectance is only slightly larger than the actual data's reflectance. The IPA also shows that the model's reflectances follow a similar trend as the original data for increases in inhomogeneity.

The results obtained through this study demonstrate the utility of wavelet analysis. Its ability to filter data allows features of various scales to be compared. The wavelet model tends to produce values which are consistent with the original data. Though being far from refined, this model may be useful for incorporating high resolution features within liquid water distributions using self-similar relationships between scales.

Acknowledgments. This research was in part supported by funding provided by NSF Grant ATM-8909870. This research was initiated while S.G. attended the Goddard Space Flight Center under the University Space Research Association's (USRA) Graduate Student Program in the Earth System Sciences.

REFERENCES

Albrecht, B.A., C.W. Fairall, D.W. Thomson, A.B. White, J.B. Snider and W.H. Schubert, 1990: Surface-based remote sensing of the observed and the adiabatic liquid water content of stratocumulus clouds. *Geophys. Res. Lett.*, 17, 89-92.

Arneodo, A., G. Grasseau and M. Holschneider, 1988: Wavelet transform of multifractals. *Phys. Rev. Lett.*, 61, 2281-2284.

Cahalan, R.F., 1989: Overview of fractal clouds. *RSRM '87: Adv. in Remote Sensing Retrieval Meth.*, A. Deepak Pub., 371-389.

Cahalan, R.F. and J.B. Snider, 1989: Marine stratocumulus structure. *Remote Sens. Environ.*, 28, 95-107.

Cahalan, R.F. et al., 1992: Albedo of fractal stratocumulus part I: Independent Pixel Approximation. (In preparation).

Chui, C.K., 1992: *An Introduction to Wavelets*, Academic Press, Inc., 264 pp.

Daubechies, I., 1988: Orthonormal bases of compactly supported wavelets. *Commun. on Pure and Appl. Math.*, 41, 901-996.

Daubechies, I., 1989: Orthonormal bases of wavelets with finite support - connection with discrete filters. *Wavelets*, Springer-Verlag, 38-66.

Kobayashi, T., 1991: Reflected solar flux for horizontally inhomogeneous atmospheres. *J. Atmos. Sci.*, 48, 2436-2447.

Lovejoy, S., 1982: Area-perimeter relation for rain and cloud areas. *Science*, 216, 185-187.

Schertzer, D. and S. Lovejoy, 1987: Physical modeling and analysis of rain and clouds by anisotropic scaling multiplicative processes. *J. Geophy. Res.*, 92, 9693-9714.

Stephens, G.L., 1978: Radiation profiles in extended water clouds. II: parameterization schemes. *J. Atmos. Sci.*, 35, 2123-2132.

Stephens, G.L., 1988: Radiative transfer through arbitrarily shaped optical media. part II: group theory and simple closures. *J. Atmos. Sci.*, 45, 1837-1848.

Strang, G., 1989: Wavelets and dilation equations: a brief introduction. *SIAM Rev.*, 31, 614-627.

VALIDATION OF CLOUDS SIMULATED BY AN EXPERIMENTAL MESOSCALE SPECTRAL MODEL AT NMC FOR THE TAMEX IOP-11

Shi-Keng Yang[1] and H. M. Henry Juang[2]

[1]Research and Data Systems Corporation, CAC/NMC/NOAA
[2]General Science Corporation, DD/NMC/NOAA

1. INTRODUCTION

Different from the simple enhancement of the horizontal resolution, Juang and Kanamitsu (1991) are experimenting with a high resolution regional spectral model (RSM) at the National Meteorological Center (NMC), which embeds a global spectral model in the operational Medium Range Forecast model (MRF). The RSM not only uses fields integrated by MRF as boundary conditions, but also as the basic field for the model domain. The synergism is that a more stable regional forecast system with basic time-dependent field can achieve better forecasts. To maintain the same characteristics, the physics package, including cloud parameterization, is unified for both models. This cross-scale utilization of the parameterizations, thus requires a validation, as some were empirically developed under certain scale constraints.

In this study, we focus on examination of cloud and precipitation of the RSM. An Intensive Observation Period (IOP), IOP-11 June 19 and 20, 1987, from Taiwan Area Mesoscale Experiment (TAMEX) was selected. This period distinguished itself with diurnal land/sea breeze associated clouds and precipitation. With a high central mountain ridge along the island, the sophisticated topography of Taiwan poses a good test for any cloud parameterization.

Cloud analyses from U.S. Air Force Real-Time Nephanalysis (RT Neph), containing multiple cloud parameters, are used. Other supplemental data are also incorporated.

2. NMC REGIONAL SPECTRAL MODEL

This RSM (Juang and Kanamitsu, 1991) was recently developed based on the operational NMC Global Spectral Model (GSM). Every three hours, the output from the GSM include the base fields and lateral boundary conditions for the RSM. The RSM specifies primitive equations on sigma coordinates with 18 vertical layers. It includes all the model physics as implemented in GSM, such as PBL physics, vertical and horizontal diffusion, Kuo-type cumulus parameterization, Slingo (1987) type diagnostic cloud, large scale precipitation and Fels and Schwarzkoph (1990) longwave radiation, etc.

Instead of recomputing, this version of the RSM's radiation fluxes are obtained from GSM. Semi-implicit time integration is also used. A polar projection true at 60° latitude with 20 km horizontal grid spacing is utilized.

For this study, a computing domain of 55 x 55 horizontal grid points with 30 waves in both directions are used. This resolution, about 20 km, makes it possible to resolve mesoscale phenomena.

3. U.S. AIR FORCE REAL-TIME NEPHANALYSIS

The U.S. Air Force Real-Time Nephanalysis (RT Neph) (Kiess and Cox, 1988) is currently one of the only two operational global cloud analyses. The observational data are mostly from the two operational Defence Meteorological Satellite Program (DMSP) satellites with supplementary data from the NOAA polar orbiting satellites. Also included are the conventional surface cloud observations. Eight times a day, the analyses are projected onto a polar stereographic map true at 60°N and 60°S latitude with a resolution of 40 km. Each grid includes total cloud amount and up to four sets of layered cloud amount, cloud tops and bases, and cloud types. In this study, we compact the data into 0.5° x 0.5° latitude/longitude coordinates.

4. SYNOPTICS OF TAMEX IOP-11

The dominating systems on June 19, 1987 were a low pressure center located at 30°N and 125°E northeast of Taiwan moving northeast and a high pressure center south of 20°N and 135°E moving northwest (Fig. 1). Tropical depression Ruth was moving to the north of Hai-Nan Island. The Taiwan area was covered with wind from the south and southeast. There was no clear frontal system on the surface analysis until 24 hours later, when a stationary front formed from the low center and stretched to the southwest quadrant about 2° north of Taiwan. During this period, the only precipitation was from air-mass thunderstorms scattered around the domain. The situation was very favorable for the development of land/sea breezes.

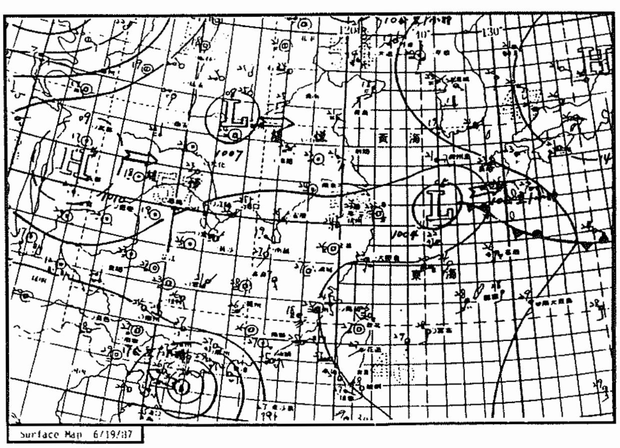

Fig. 1. Surface analysis for 00Z, June 19, 1987, TAMEX IOP-11.

5. FORECAST RESULTS AND COMPARISON

A 24-hour forecast by the RSM was initiated from 00Z on June 19, 1987. Forecasted 3-hourly accumulative precipitation fields are shown in Fig. 2a-c. At 03Z (11 LST, Fig. 2a) the precipitation occurs over a large region of the Taiwan Strait, northwestern part of the island, and offshore of the east coast. The intensity of the western cell is one-third stronger than that off the east coast (5.26 mm/3 hours versus 3.85 mm/3 hours). Compared to the GMS images (Fig. 3a-c), which show that a fair amount of lower-level cloud prevails around these regions, the model output appears to have reasonable coverage, but with higher cloud tops.

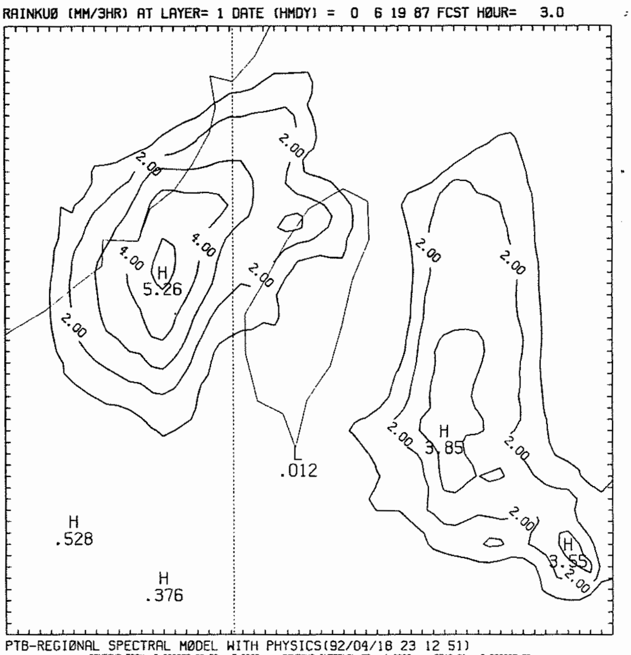

Fig. 2a. Cumulative 3-hour precipitation from RSM, 00Z-03Z, in mm/3 hr.

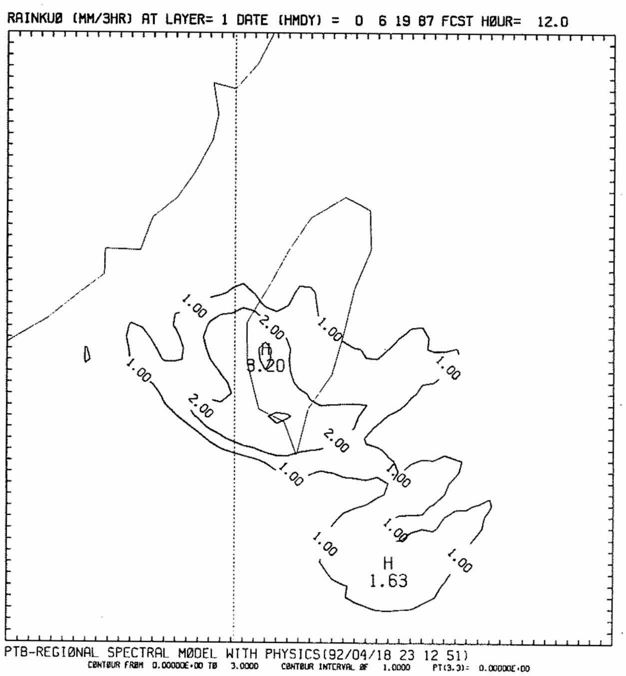

Fig. 2b. Cumulative 3-hour precipitation from RSM, 09Z-12Z, in mm/3 hr.

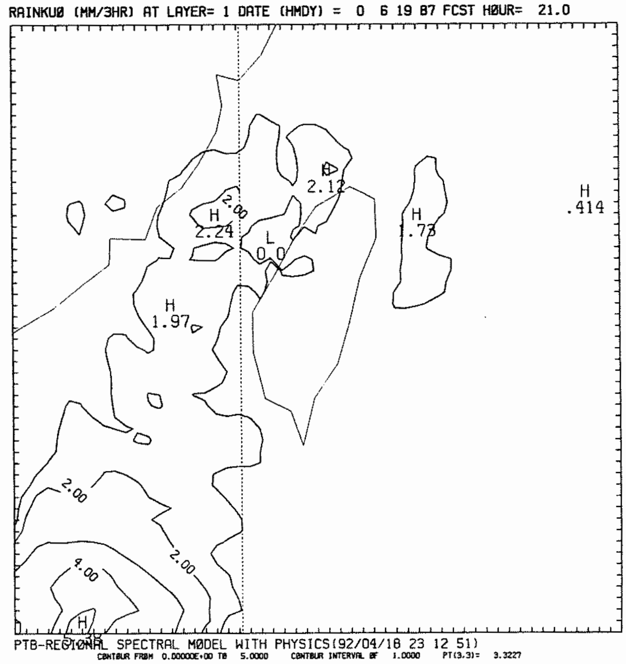

Fig. 2c. Cumulative 3-hour precipitation from RSM, 18Z-21Z in mm/3 hr.

Since the RSM uses a Kuo-type convective scheme, any cloud formed is precipitated out immediately. One can, thus, compare the precipitation with the convective cloud amount.

Cumulus cloud amount from RT Neph, Fig. 4a-b, shows more extensive coverage than the RSM forecasts. Because the display is on a 0.5° x 0.5° latitude/longitude coordinate, it is much coarser than the satellite images and the cloud patterns are less organized.

From the RSM forecast, as the eastern cell dissipated as time passes, the western cell moves southeastward to cover the southern portion of the Island. At 12Z (20 LST), Fig. 2b, the center of the precipitation moves onshore with an intensity of 3.2 mm/3 hour. This illustrates the change from land breeze to sea breeze, part of the expected diurnal cycle. As at 03Z, the model forecast has larger precipitation coverage than the satellite shows; however, it is clear that the center of the precipitation agrees very well.

Changing from 03Z to 12Z, Fig. 4b, RT Neph cloud over Taiwan Strait dissipates as the model and GMS image shows. Most regions do not show any significant change. And, at 21Z (not shown), all data in this domain are flagged for older than 6 hours.

At 15Z and 18Z, (not shown), the RSM does not predict precipitation around the region. At 21Z, precipitation recurs over the Taiwan Strait and stretches southward (Fig. 2c). Also, off the northeast shore of the island, a small cell is forming, while from GMS (Fig. 3c), this is the only region where cloud is forming.

6. SUMMARY REMARKS

In this preliminary diagnostic study, the forecasted precipitation and cloud fields from the experimental NMC RSM are examined for TAMEX IOP-11.

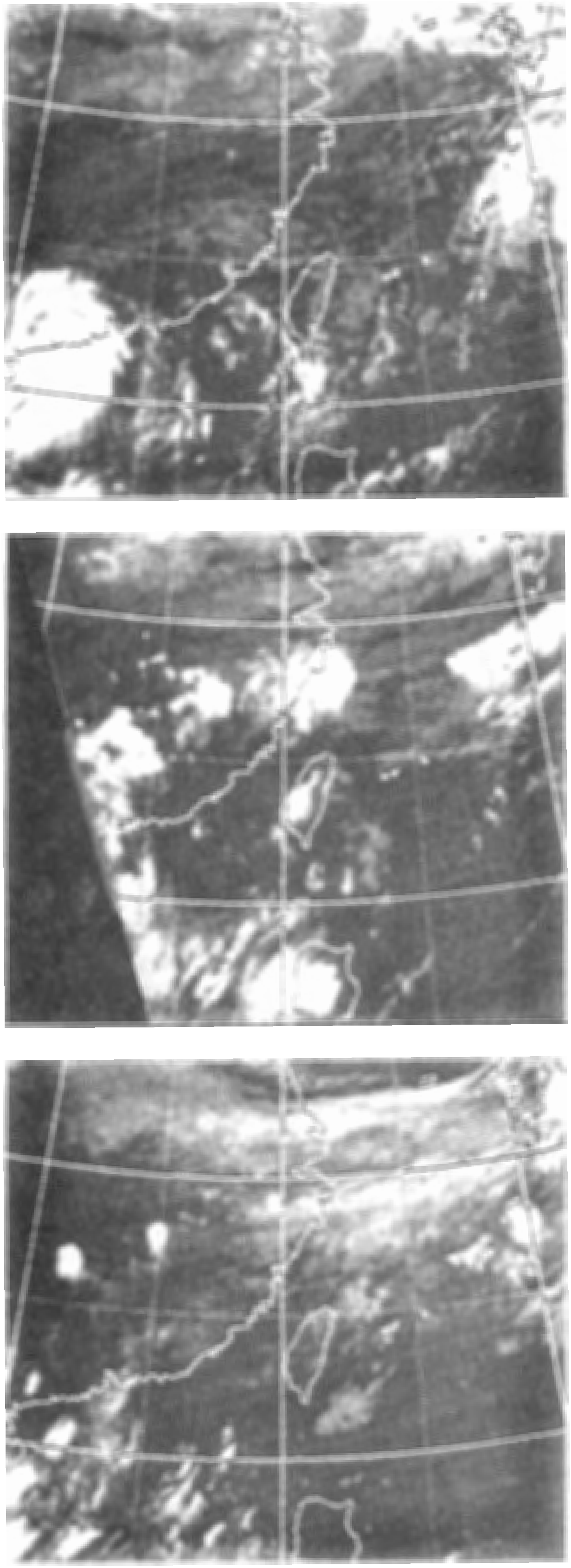

Fig. 3. IR image from GMS for (a) 03Z, (b) 12Z, and (c) 21Z, June 19, 1987.

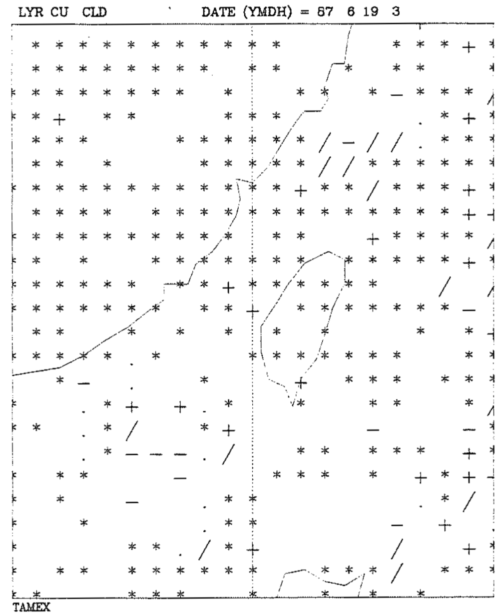

Fig. 4a. Cumulus cloud amount from RT Neph for 03Z, June 19, 1987; "." < 0.2; 0.2< "-" 0.4; 0.4 < "/" < 0.6; 0.6 < "+" < 0.8; 0.8 < "*" < 1.0.

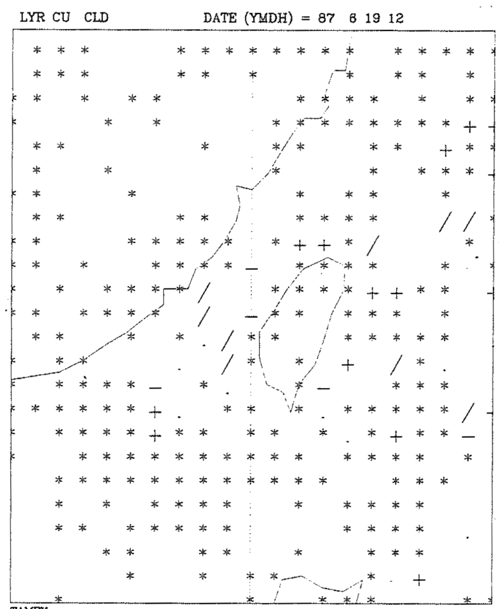

Fig. 4b. Same as in Fig. 4a, but for 12Z, June 19, 1987.

The result shows that the RSM-forecasted precipitation patterns agree reasonably well with GMS images for the first 18 hours. The land/sea breeze cycle is well simulated by RSM.

As we compare the 3-hour cumulative precipitation with satellite snapshots, the model has a larger area coverage of precipitation than the satellite images shows. The intensity of precipitation is stronger than from the observations, which could also be an effect of the higher model resolution.

Compared to GMS images, RT Neph also appears to have much larger cloud coverage and a less organized pattern. As RT Neph was originally designed to identify cloud existence instead of accurately estimating cloud fraction, it is possible to overestimate cloud (Lowther, 1991).

To have more complete validation in the future, one could include the radiation data so that cloud top height can be examined. Radar data from TAMEX can also be utilized to examine the precipitation rate as well as the surface observations.

7. REFERENCES

Cunning, J. B., 1988: Taiwan area mesoscale experiment: daily operations summary. NCAR/ TN-305+STR, 361 pp.

Fels, S. B. and M. D. Schwarzkopf, 1975: The simplified exchange approximation—a new method for radiative transfer calculations. ***J. Atmos. Sci.***, 1475-1488.

Juang, H.-M. H. and M. Kanamitsu, 1991: Regional spectral modelling at NMC. ***AMS 9th Conference on Numerical Weather Prediction***, Denver, CO, October 14-18.

Kiess, R. T. and W. M. Cox, 1988: The AFGWC automated real-time cloud analysis model. AFGWC/ TN-88/001, AFGWC, Air Weather Service, Offutt AFB, NE.

Kristjansson, Jon Egill, 1991: Cloud parameterization at different horizontal resolutions. ***Quart. J. Roy. Met. Soc.***, 117, 1255-1280.

Lowther, R. P., M. T. Surmeier, R. W. Hartman, C. R. Coffin, and A. J. Warren, 1991: RTNEPH total cloud cover validation study. USAFETAC/PR--91/020, USAF Environmental Technical Applications Center, Scott Air Force Base, IL, 62225-5438.

Schwarzkoph, M. D. and S. B. Fels, 1990: The simplified exchange method revisited: an accurate, rapid method for computation of infrared cooling rates and fluxes. ***J. Geophys. Res.***

Schwarzkoph, M. D. and S. B. Fels, 1985: Improvements to the algorithm for computing CO_2 transmissivities and cooling rates. ***J. Geophys. Res.***, 10541-10550.

Sela, J. G., 1982: The NMC spectral model. NOAA Technical Report NWS 30, Silver Spring MD, 36 pp.

Slingo, J. M., 1987: The development and verification of a cloud prediction scheme for the ECMWF model. ***Quart. J. Roy. Met. Soc.***, 899-927.

SIMULATION OF THE TWOMEY EFFECT

W.R. Cotton[1], R.L. Walko[1], G. Feingold[2], Z. Levin[3], S. Tzivion[3]

[1]Colorado State University, Dept. of Atmospheric Science, Fort Collins, CO 80523

[2]CIRES, University of Colorado Boulder, CO 80309-0449

[3] Univ. of Tel-Aviv, Dept. of Geophysics & Planetary Sciences, Ramat Aviv 69978, Israel

1 INTRODUCTION

Twomey (1974, 1977) proposed that air pollution results in the formation of greater numbers of cloud condensation nuclei (CCN) which results in higher concentrations of cloud droplets, which, in turn, increase the reflectance of clouds. This effect is believed to be most influential for optically thin clouds; clouds having shallow depths or little column-integrated liquid water content. It has also been suggested (Albrecht, 1989) that enhanced CCN concentrations will suppress the rate of formation of drizzle drops. This will result in a positive feedback into the CCN-albedo link since reduced drizzle will result in clouds with higher drop concentrations, larger liquid water paths, and, hence, more reflective clouds. Recently Charlson et al.(1992) made a rough, back-of-the-envelope, type of calculation that a 15% increase in global mean droplet concentrations in marine stratus and stratocumulus clouds results in a radiative cooling effect comparable (and opposite in sign) to current estimates of greenhouse warming.

A number of questions must be answered before this hypothesis can be placed on a sound scientific basis:

(1) Are CCN concentrations increasing globally and particularly over the pristine ocean areas where shallow cumulus are prevalent?

(2) Are cloud droplet concentrations in shallow cumuli climatologically changing with time?

(3) What clouds are susceptible to changes in albedo due to CCN concentration increases?

(4) Is the areal coverage of susceptible clouds great enough to cause a significant change in global albedo and global mean temperatures?

The focus of this study is on (3) which is both a cloud microphysics problem and a cloud radiation problem. It is clear that we must make quantitative estimates of (3) before we can estimate the global climatic impacts of anthropogenic releases of gases and particulates contributing to CCN production.

The approach we are taking is to introduce an explicit cloud microphysics scheme into the Regional Atmospheric Modeling System (RAMS) developed at Colorado State University. RAMS is then set up as a large eddy simulation (LES) model in which the major energy-containing eddies are explicitly resolved. The simulated cloud microphysics/macrophysics data are then used by a sophisticated radiative transfer model to evaluate the impacts on cloud albedo.

In the following sections we describe the design and implementation of the LES version of RAMS, the explicit microphysics model, and the planned numerical experiments.

2 THE RAMS LES MODEL

The RAMS is a multi-purpose modeling systems that has been applied to LES over inhomogeneous land surfaces (Hadfield et al., 1991, 1992; Walko et al., 1992) and to the simulation of a variety of cloud types such as Thunderstorms (Tripoli and Cotton, 1986), mesoscale convective systems (Tripoli and Cotton, 1989a,b; Chen and Cotton, 1988; Schmidt and Cotton, 1990; Tripoli and Cotton, 1989a,b; Chen and Cotton, 1988; Schmidt and Cotton, 1990), orographic clouds (Cotton et al.,1986; Meyers and Cotton, 1992), and cirrus clouds (Heckman and Cotton, 1992). In all the cloud applications a bulk microphysics scheme is used in which only the mixing ratios of each hydrometeor species is predicted.

In this investigation RAMS is set up as a non-hydrostatic LES model. Prognostic equations include those for the three velocity components (u,v,w), liquid water potential temperature (θ_ℓ; Tripoli and Cotton, 1981), perturbation Exner function π, and total water mixing ratio (r_t). The predictive equations for the microphysics variables will be described in Section 3.0.

In the bulk microphysics model cloud liquid water is a diagnostic variable, but in the explicit microphysics version condensate is treated in 25 bins describing the droplet spectrum. In order to calculate vapor deposition and evaporation, the cloud supersaturation and sub-saturation must be calculated. This is computed from the predictive variables as

$$S^* = \left(\frac{r_t - r_\ell}{r_s(T)} - 1\right), \qquad (1)$$

where $r_s(T)$ is the saturation mixing ratio calculated from the Clausius-Clapeyron equation and the diagnosed cloud temperature from θ_ℓ, and r_ℓ is the total liquid water mixing ratio. An alternative approach is to diagnose S^* from the quasi-steady value, by assuming a balance between adiabatic ascent (cooling) and the depletion of vapor due to condensation on droplets. Our experiments have shown that this gives good predictions of S^* in core regions of the cloud (see also Kogan, 1991), whereas near the cloud boundaries, a correction term related to the tendency of r_t needs to be applied. The advantage of this approach is that it produces a smoother S field than that obtained from Eq. (1).

Since θ_l is an extensive variable, it changes due to sedimentation of precipitation. Therefore, sedimentation of the sum total of precipitation elements in the microphysical bins effects the prediction of θ_l. Likewise, sedimentation alters total water r_t. Therefore the explicit microphysics feeds back into the LES dynamics through adjustments in total water and θ_l, which implicitly includes condensation and evaporation, and through water loading and radiative feedbacks.

The model includes explicit feedback of bulk cloud properties on radiative heating/cooling based on the radiation parameterization developed by Chen and Cotton (1983). This model uses an effective emissivity approximation for longwave heating. As noted by Heckman and Cotton (1992) the number of computations in this scheme is proportional to the square of the number of vertical levels, so it is quite computationally expensive for high resolution models. The shortwave scheme considers absorption, scattering, and reflection in clear and cloudy air, with cloudy air effects based on Stephens' (1978a,b) empirical model. In addition to its computational expense, this radiation scheme does not include any explicit dependence on the simulated droplet distribution. It only responds to the bulk liquid water paths calculated by the model. A new two-stream model is under development which will respond to variations in drop size spectra and be computationally faster as well. Keep in mind that this radiative scheme is only used to calculate radiative heating/cooling as it impacts the cloud dynamics. A detailed diagnostic model developed by Graeme Stephens' group will be used to determine the impacts of the cloud microphysical structure on cloud albedo.

Sub-grid-scale turbulence is parameterized by using the Deardorff (1980) scheme based on a predicted turbulent kinetic energy field.

The LES model is set up over a 100 × 100 × 80 grid point domain, with horizontal grid spacing of 50m and vertical spacing of 50 m. Additional refinements in the entrainment interface zone are possible by spawning a fine nest.

The lower boundary condition is a surface layer parameterization based on the Louis (1979) scheme, with specified sea surface temperatures. The top boundary is a rigid lid with a Rayleigh friction, wave-absorbing layer in the top-most grid points. Lateral boundaries are cyclic, which assumes we are simulating a horizontally-homogeneous cloud field.

The model is initialized with a horizontally-homogeneous sounding of temperature, relative humidity, winds, and large-scale subsidence, derived from specific case studies. In order to excite large-eddy turbulence, the initial low-level temperature field is randomly perturbed by 0.1 K.

3 THE EXPLICIT MICROPHYSICS MODEL

The explicit microphysics model that has been implemented in RAMS is the moment-conserving scheme for solving mass transfer among a number of discrete bins developed by Tzivion et al. (1987), Feingold et al. (1988), and Tzivion et al. (1989). In this model the mass mixing ratios and number concentration (spectral density) is predicted for each bin. Processes contributing to variations in droplet spectral density are nucleation, vapor deposition/evaporation, and collision-coalescence as well as advection, sedimentation, and turbulent transport. For stratocumulus simulations, a total of 25 bins are used which cover the size range from 3 μm to 1000 μm (see Table 1). Since we are primarily concerned with non-precipitating stratocumulus clouds and clouds with only light amounts of drizzle, the above size range should be adequate. Moreover, drop breakup should be minimal for these clouds, so neglect of drop breakup physics is justifiable.

Table 1: Discrete Model Bin Number, Droplet Diameter, and Mass

Bin number	Diam (microns)	Mass (μg)
25	1008.00	536.27
24	800.05	268.13
23	635.00	134.07
22	504.00	67.03
21	400.03	33.52
20	317.50	16.76
19	252.00	8.38
18	200.01	4.19
17	158.75	2.09
16	126.00	1.05
15	100.01	.52
14	79.38	.26
13	63.00	.13
12	50.00	.065
11	39.69	.033
10	31.50	.016
9	25.00	.0082
8	19.84	.0041
7	15.75	.0021
6	12.50	.0010
5	9.92	.00051
4	7.87	.00026
3	6.25	.00013
2	4.96	.000064
1	3.94	.000032
0	3.13	.000016

Procedures for calculating the evolution of drop spectra are described in the above-cited references. A new nucleation scheme had to be developed for use in RAMS (Feingold and Heymsfield, 1992). In this scheme the dry hygroscopic aerosol particles are assumed to be distributed in a log-normal size distribution,

$$n(a) = \frac{N_a}{(2\pi)^{1/2}\, ln\sigma_a\, a}\, exp\left[-ln^2(a/a_g)/2ln^2(\sigma_a)\right], \quad (2)$$

N_a is the total aerosol concentration, a_g and σ_a are the mean radius and standard deviation of the aerosol, respectively. The concentration and mixing ratio of the aerosol are added to RAMS as prognostic variables. The standard deviation of the distribution is assumed to be constant. Feingold used the Heymsfield and Sabin (1989) Lagrangian parcel model to calculate the parameters of the activated cloud droplet spectrum which is also assumed to have a log-normal distribution. Thus,

$$r_g = b_0 N_r^{b_1} a_g^{b_2} w^{b_3} \quad (3)$$

and

$$\sigma_r = c_0 N_r^{c_1} a_g^{c_2} \sigma_a^{c_3} w^{c_4}. \quad (4)$$

where r_g and σ_r are the mean radius and standard deviation of the activated cloud droplet distribution, and a_g and σ_a are those of the dry hygroscopic aerosol distribution. The activated distribution is then added to the discrete bin model and the concentration and mixing ratio of the dry aerosol are reduced accordingly.

Starting with an initial sounding of dry, hygroscopic aerosol particles, we can then rather simply consider vertical and horizontal transport of the aerosol by the explicitly represented large eddies, and simulate the depletion of those aerosol by nucleation. Moreover, we can simulate the interaction between rising plumes of air depleted in CCN and air streams entrained into the cloud containing environmental concentrations of CCN that are characteristic of above-boundary layer air. Thus it should contain the essence of Kogan's (1991) 19-bin representation of the CCN spectrum, but at great savings in computer memory and computation.

4 SUMMARY AND CONCLUSIONS

Two very powerful models have been combined to simulate the response of stratocumulus cloud albedo to variations in ambient CCN concentrations. The RAMS allows accurate large eddy simulation of a horizontally homogeneous field of marine stratocumulus clouds under a variety of environmental conditions. The University of Tel-Aviv explicit microphysics model affords the opportunity to accurately simulate the evolution of droplet spectra in a cloud of horizontally and vertically varying updraft speeds and supersaturations as well as a varying environmental CCN spectra.

Plans are to exercise the combined models for a number of test cases observed during the FIRE I stratus experiment and ASTEX in order to evaluate the ability of the model to simulate observed macroscopic and microscopic features of marine stratocumulus clouds. Once we have performed credible "control" runs we then plan to vary initial CCN soundings in order to examine variations in cloud albedo for clouds of varying optical depths.

5 ACKNOWLEDGMENTS

We thank Brenda Thompson for her help in processing the manuscript. This research is supported by the National Institute for Global and Environmental Change (NIGEC) under Research Agreement No. NIGEC 91-S01. NIGEC is sponsored by at cooperative agreement between the U.S. Department of Energy and The Regents of the University of California.

6 REFERENCES

Albrecht, B.A., 1989: Aerosols, cloud microphysics, and fractional cloudiness. *Science*, **245**, 1227-1230.

Charlson, R.J., J.E. Lovelock, M.O. Andreae, and S.G. Warren, 1987: Oceanic phytoplankton, atmospheric sulfur, cloud albedo and climate. *Nature*, **326**, 655-661.

Chen, C. and W.R. Cotton, 1983: A one-dimensional simulation of the stratocumulus-capped mixed layer. *Boundary-Layer Meteorol.*, **25**, 289-321.

Chen, C. and W.R. Cotton, 1983: Numerical experiments with a one- dimensional higher order turbulence model: Simulation of the Wangara Day 33 Case. *Boundary-Layer Meteorol.*, **25**, 375-404.

Chen, S., and W.R. Cotton, 1988: The sensitivity of a simulated extratropical mesoscale convective system to longwave radiation and ice-phase microphysics. *J. Atmos. Sci.*, **45**, 3897-3910.

Cotton, W.R., G.J. Tripoli, R.M. Rauber, and E.A. Mulvihill, 1986: Numerical simulation of the effects of varying ice crystal nucleation rates and aggregation processes on orographic snowfall. *J. Clim. Appl. Meteor.*, **25**, 1658-1680.

Deardorff, J.W., 1980: Stratocumulus-capped mixed layers derived from a three-dimensional model. *Boundary-Layer Meteor.*, **18**, 495-527. Feingold, G., and A.J. Heymsfield, 1992: Cloud condensation nuclei and their effect on the optical properties of water clouds: nucleation and condensation. Preprints, 13th Int. Conf. on Nucleation and Atmospheric Aerosols, Salt Lake City, August 24-28.

Feingold, G., S. Tzivion, and Z. Levin, 1988: Evolution of raindrop spectra. Part I: Solution to the stochastic collection/breakup equation using the method of moments. *J. Atmos. Sci.*, **45**, 3387-3399.

Hadfield, M.G., W.R. Cotton, and R.A. Pielke, 1991: Large-eddy simulations of thermally forced circulations in the convective boundary layer. Part I: A small-scale, circulation with zero wind. *Boundary-Layer Meteorol.*, **57**, 79-114.

Hadfield, M.G., W.R. Cotton, and R.A. Pielke, 1992: Large-eddy simulations of thermally forced circulations in the convective boundary layer. Part II: The effect of changes in wavelength and wind speed. *Boundary-Layer Meteorol.*, 58, 307-327.

Heckman, S.T., and W.R. Cotton, 1992: Mesoscale numerical simulation of cirrus clouds–FIRE case study and sensitivity analysis. Submitted to *Mon. Wea. Rev.*.

Heymsfield, A.J., and R.M. Sabin, 1989: Cirrus crystal nucleation by homogeneous freezing of solution droplets. *J. Atmos. Sci.*, **46**, 2252-2264.

Kogan, Y.L, 1991: The simulation of a convective cloud in a 3-D model with explicit microphysics. Part I: Model description and sensitivity experiments. *J. Atmos. Sci.*, **48**, 1160-1189.

Louis, J.F., 1979: A parametric model of vertical eddy fluxes in the atmosphere. *Boundary-Layer Meteorol.*, **17**, 187-202.

Meyers, M.P., P.J. DeMott, and W.R. Cotton, 1992: New primary ice nucleation parameterizations in an explicit cloud model. Accepted *J. Appl. Met.*

Schmidt, J.M. and W.R. Cotton, 1990: Interactions between upper and lower tropospheric gravity waves on squall line structure and maintenance. *J. Atmos. Sci.*, **47**, 1205-1222.

Stephens, G.L., 1978a: Radiation profiles in extended water clouds. Webster Theory. *J. Atmos. Sci.*, **35**, 2111-2122.

Stephens, G.L., 1978b: Radiation profiles in extended water clouds. II: Parameterization schemes. *J. Atmos. Sci.*, **35**, 2123-2132.

Tripoli, G.J., and W.R. Cotton, 1981: The use of ice-liquid water potential temperature as a thermodynamic variable in deep atmospheric models. *Mon. Wea. Rev.*, **109**, 094-1102.

Tripoli, G.J. and W.R. Cotton, 1986: An intense, quasi-steady thunderstorm over mountainous terrain Part IV: Three-dimensional numerical simulation. *J. Atmos. Sci.,* **43**, 896-914.

Tripoli, G., and W.R. Cotton, 1989a: A numerical study of an observed orogenic mesoscale convective system. Part 1. Simulated genesis and comparison with observations. *Mon. Wea. Rev.,* **117**, 273-304.

Tripoli, G., and W.R. Cotton, 1989b: A numerical study of an observed orogenic mesoscale convective system. Part 2. Analysis of governing dynamics. *Mon. Wea. Rev.,* **117**, 305-328.

Twomey, S., 1974: Pollution and the planetary albedo. *Atmos. Environ.,* **8**, 1251-1256.

Twomey, S., 1977: The influence of pollution on the short wave albedo of clouds. *J. Atmos. Sci.,* **34**, 1149-1152.

Tzivion, S., G. Feingold, and Z. Levin, 1987: An efficient numerical solution to the stochastic collection equation. *J. Atmos. Sci.,* **44**, 3139-3149.

Tzivion, S., G. Feingold, and Z. Levin, 1989: The evolution of raindrop spectra. Part II: Collisional collection/breakup and evaporation in a rain shaft. *J. Atmos. Sci.,* **46**, 3312-3327.

Walko, R.L., W.R. Cotton, and R.A. Pielke, 1992: Large eddy simulations of the effects of hilly terrain on the convective boundary layer. *Bound.-Layer Meteorol.,* **53**, 133-150.

Cloud Optical Depth Estimates from Satellite Measurements

Jiujing Gu,[+] Robert Pincus,[◊] Philip Austin,[+] and Malgorzata Szczodrak[+]

[+]Programme in Atmospheric Sciences, #217 1984 West Mall, University of British Columbia, Vancouver BC V6T 1Z2 Canada
[◊]Geophysics Program AK-50, University of Washington, Seattle WA 91895 USA

1. Introduction

Operational satellites have been used for some time to produce estimates of cloud optical depth (e.g. Arking and Childs, 1985; Rossow et al., 1989). Data from the First ISCCP Regional Experiment (FIRE, Albrecht et al., 1988) has made it possible to begin to test these optical depth estimates using a variety of surface and aircraft based measurements. Minnis et al. (1992) compare optical depth retrievals from geostationary imagery with surface data, while cloud retrievals made using higher resolution airborne sensors (Nakajima et al., 1991) show close agreement with in-cloud microphysical measurements. These initial results are encouraging; it appears that operational satellite observations may have the resolution and sensitivity needed to provide cloud microphysical information on time and space scales important to studies of the character and life-cycle of marine clouds.

Below we examine the performance of an optical depth retrieval scheme for simultaneous collocated observations of the NOAA 9 polar orbiter and GOES-6 geostationary satellite for five FIRE days. These cases include uniform, relatively thin stratocumulus layers, and thicker clouds with more complex vertical and horizontal structure. Despite differences in scene geometry, instrument sensitivity and calibration, the two satellites produce very similar optical depth distributions for the five cases, with values that agree with in-situ aircraft measurements.

2. Retrieval Method

We estimate cloud optical depth from satellite measurements of reflectance using the two step technique described in Minnis et al. (1992). First we compute the reflectance of the cloudy atmosphere R_{comp} as a function of the cloud optical depth τ, the cosines of the solar zenith and satellite viewing angles μ_0 and μ, and the azimuthal separation of the sun and satellite ϕ. Then, for a satellite measurement with given values of μ_0, μ, and ϕ, we find the value of τ such that the observed value of the reflectance $R_{obs} = R_{comp}(\tau, \mu_0, \mu, \phi)$.

2.1 Radiative Transfer Calculations

In our theoretical calculations we treat the atmosphere as three horizontally uniform plane parallel layers overlying an ocean surface. The cloud occupies the middle layer. Rayleigh scattering and absorption by water vapor occur in all three layers; absorption by ozone occurs in the uppermost layer. The sea surface reflects isotropically with an albedo dependent on solar zenith angle.

a. Scattering by Cloud Droplets

We approximate the cloud as a collection of spherical droplets of pure water and compute the single scattering properties from Mie theory using the program of Wiscombe (1979). The droplet sizes follow the log-normal distribution of Hanson and Travis (1974). We supply the complex index of refraction (Hale and Querry, 1973) and, at each droplet radius r, the size parameter $x = 2\pi r/\lambda$. The Mie calculation provides, among other quantities, the single scatter albedo ω, the scattering phase function $P(\Theta)$, and the moments al of the Legendre polynomial expansion of $P(\Theta)$. These quantities are integrated over the droplet size distribution to find the average properties of the cloud layer.

For all our retrievals we make the Mie computations at wavelength $\lambda = 0.65\ \mu m$, using effective radius $r_{eff} = 8\ \mu m$ and variance $v = 0.05$. We discuss the sensitivity of the optical depth retrievals to variations in effective radius below.

b. Gaseous absorption, Rayleigh scattering

We treat absorption by ozone using the exponential sum fitting of transmissions (ESFT) method with coefficients from Wiscombe et al. (1984), and specify a ozone column mass path of 0.32 g/m^2 in the upper layer. Water vapor absorption is treated using the k-distribution technique (Chou, 1986), with weights derived from LOWTRAN-7. We use scaled water vapor amounts for these runs taken from the McClatchey mid-latitude summer profile and are 3.09, 0.24, and 1.80 g/m^2 in the bottom, middle, and top layers respectively.

We estimate the Rayleigh scattering optical depth τ_R of each layer with the parameterization of Paltridge and Platt (1976). The total Rayleigh optical depth of our model atmosphere at 0.65 μm is 0.0492, with 91% of the scattering occurring in the top layer.

c. Calculation of Reflectance

For each atmospheric layer we find the total optical depth as the sum of the optical depths due to gaseous absorption, Rayleigh scattering, and scattering by cloud droplets ($\tau = \tau_G + \tau_R + \tau_D$), and the single scatter albedo as the weighted average $\omega = (\tau_R + \omega_D\tau_D)/\tau$. In the top and bottom layers we use a Rayleigh scattering phase function, and in the cloud layer the phase function from our Mie calculations.

We use the discrete ordinate method (Stamnes, et al., 1988) to find the pattern of intensity $I(\mu, \phi)$ for a specific value of τ and μ_0. We make our calculations using 48 streams (values of μ) and 48 values of ϕ evenly spaced between 0 and 180 degrees. For the GOES VISSR (visible infrared spin scan radiometer) we compute the intensity at 0.65 μm; for the NOAA AVHRR (advanced very high resolution radiometer) we integrate the results over the sensor band (0.59 to 0.70 μm). We normalize the intensity by the total solar flux seen by each sensor to find the reflectance $R_{comp}(\tau, \mu_0; \mu, \phi)$. We repeat this calculation for a set of unevenly spaced τs between 1 and 64, and for a set of values of μ_0 (20 evenly spaced between 0.05 and 1 for the GOES retrievals, 10 between 0.6291 and 0.9135 for the NOAA-9). The final look-up tables have more than 500,000 entries describing the reflectance as measured by each satellite at discrete values of τ, μ_0, μ, and ϕ. We can estimate the reflectance at arbitrary values of ϕ, μ_0, μ, and τ by linear interpolation along the table in the coordinate order listed.

Figure 1 shows model estimates of a superset of these calculations: both the AVHRR channel 1 and AVHRR channel 3 (3.7 μm) reflectances calculated for a series of cloud layers of differing optical depths and effective radii at $\mu = 0.6$, $\phi = 111$ degrees, and $\mu_0 = 0.8$. The dashed lines indicate reflectances computed at constant optical depth while the solid lines are computed at constant effective radius (in μm). The lines are nearly orthogonal and indicate the insensitivity of the visible reflectance to the effective radius in the range $4\ \mu m < r_{eff} < 16\ \mu m$. By assuming $r_{eff} = 8\ \mu m$ in our technique we slightly overestimate the optical depth of clouds with droplets at smaller radii. Note that as the cloud becomes optically thicker, small changes in reflectance correspond to larger changes in optical depth. An absolute change of $\Delta\tau = 5$, for example, produces absolute reflectivity changes of $\Delta R = 0.06$ at $\tau = 20$ and $\Delta R = 0.014$ at $\tau = 48$.

2.2 Satellite Measurements

To compare our radiative transfer calculations with the satellite measurements we first convert the raw sensor counts for each pixel to reflectance values using the calibrations reported in Kaufman and Holben (1992) for the AVHRR and Minnis et al. (1992) for the GOES.

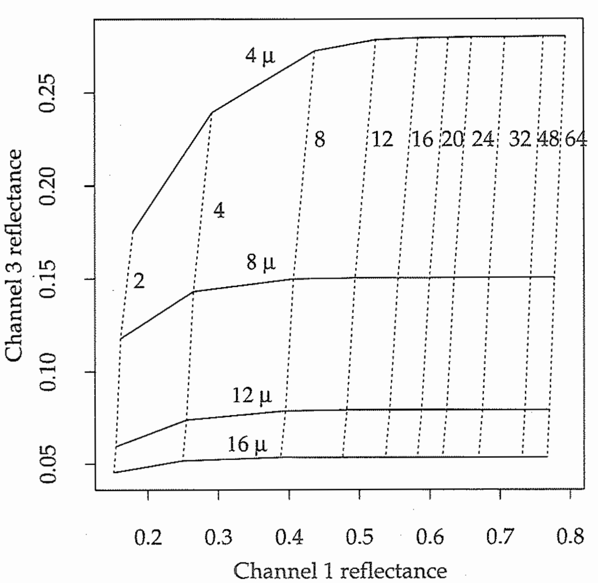

Figure 1: AVHRR channel 1 (visible) reflectance as a function of AVHRR channel 3 (near-IR) reflectance for various values of τ and r_{eff}.

a. Cloud Detection

Because we have used the plane parallel assumption in our model calculations, we feel justified in estimating optical depths only for those portions of a satellite image which are entirely filled with clouds. For AVHRR images we use the Coakley and Bretherton (1982) spatial coherence method, applied to the AVHRR 10.7 μm channel 4, to determine the mean and standard deviation of 2x2 pixel arrays. Figure 2 shows examples of these plots for July 7 and July 14; fully cloud pixels are well defined on the FIRE days used here by standard deviation in the cold "foot" below 0.1.

The 4x8 km spatial resolution of the GOES infrared pixels prevents clear identification of fully cloudy regions using the Coakley-Bretherton technique. We retrieve optical depths for those pixels with reflectance values greater than some threshold (typically 0.2). Side-by-side examination of the AVHRR and GOES images are made to insure that similar pixel selections are used in the comparisons.

b. Estimation of Optical Depth

For each pixel determined to be cloudy we use the time of day, day of year, and subsatellite position to compute the angles μ_0, μ, and ϕ. Once these angles have been specified, the modeled reflectance is a function of τ alone. We find the cloud optical depth by varying τ until

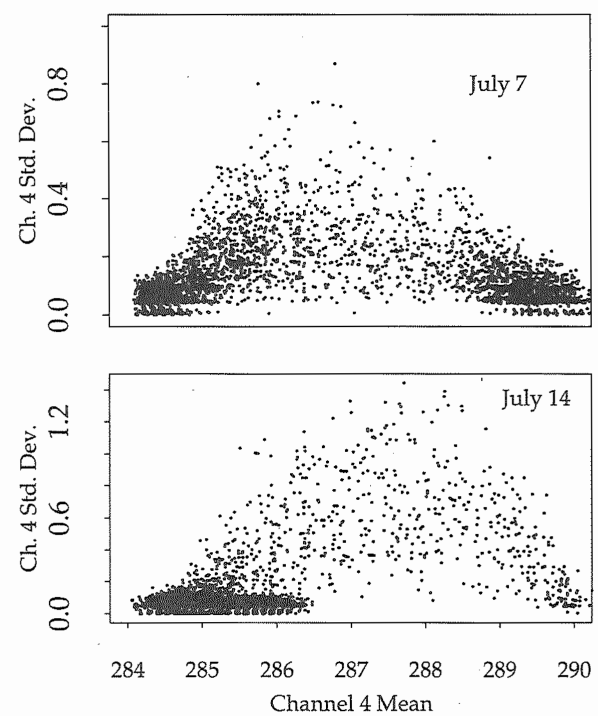

Figure 2: AVHRR Channel 4 mean vs. standard deviation for each 2x2 pixel subregion for July 7 and July 14. Variations in cloud top height appear as a wider cold foot for the July 14th image.

the equation $R_{obs} - R_{comp}(\tau) = 0$ is satisfied.

3. Results

Figure 3 shows histograms of cloud optical depth for fully cloudy pixels on July 7 and July 14, 1987. Results for three other days (June 30, July 10 and July 16) follow the pattern of these two cases. In each, there is close agreement between the GOES and NOAA 9 estimates of the mode optical depth, with the GOES retrieval showing a slightly broader distribution with a higher number of large optical depth pixels.

The cloud layers on July 7 and July 14 had distinctly different characters. In the fully cloudy region of the July 7 scene, lidar mapping runs made by the NCAR Electra at 1100 PDT (roughly 4 hours before the NOAA 9 overpass) show a flat cloud top with fluctuations of less than 50 m about a mean value of approximately 725 m. Four hours later, temperature variations between fully cloudy pixels measured by the AVHRR channel 4 were about 1 K (c.f. Figure 2), which, given a mean lapse rate of 7 K/km, would indicate at most 100 m cloud-top height variations at the time of the AVHRR-GOES optical depth retrieval. Profiles of optical depth at 1100 PDT were made by the multi-channel radiometer (MCR) on board the ER-2 (Nakajima et al., 1991), and they agree closely with the GOES and NOAA-9 mode optical depth estimate of $\tau = 10$. The MCR optical depth estimates show no values beyond $\tau = 17$, and some pixels with $\tau < 3$, in contrast with the approximately 1% of the pixels with $\tau > 20$ retrieved by the two satellites.

For the July 14 case, AVHRR measurements of the temperature of fully cloudy pixels span 2.25 K (Figure 2), which indicates possible cloud-top excursions of as much as 300 m. NCAR Electra soundings taken between 2-4 hours prior to the AVHRR overpass show optical depths ranging from $\tau = 8$ to $\tau = 40$, with excursions in both cloud top and cloud base heights of 150 m (Austin and Wang, 1992). The increased vertical and horizontal structure on this day is reflected in the broad, positively skewed optical depth histogram.

Figure 4 shows an optical depth retrieval for a 95 x 120 pixel subregion of the July 14 scene which permits a closer look at the differences in the satellite retrievals for large optical depths. The 10 bit AVHRR reflectance is potentially 16 times more sensitive than the 6 bit GOES values. The optical depth range between 38 and 41, for example, is spanned by 8 raw AVHRR counts for the viewing geometry of this image. The same optical depth range is spanned by 1 raw VISSR count, effectively increasing the size of the optical depth bins for the GOES retrieval by a factor of eight.

4. Summary

We have estimated optical depth from GOES and AVHRR radiance measurements for five collocated scenes during FIRE. We find good agreement between the estimates, especially in the mode optical depth, although the GOES estimates a higher number of thicker pixels than the AVHRR. The retrieved mode and variance of the optical depth distribution show agreement with independent in-situ and remotely sensed estimates of optical depth made by FIRE aircraft. The GOES retrievals are less sensitive at higher optical depths due to the limited resolution of the GOES sensor.

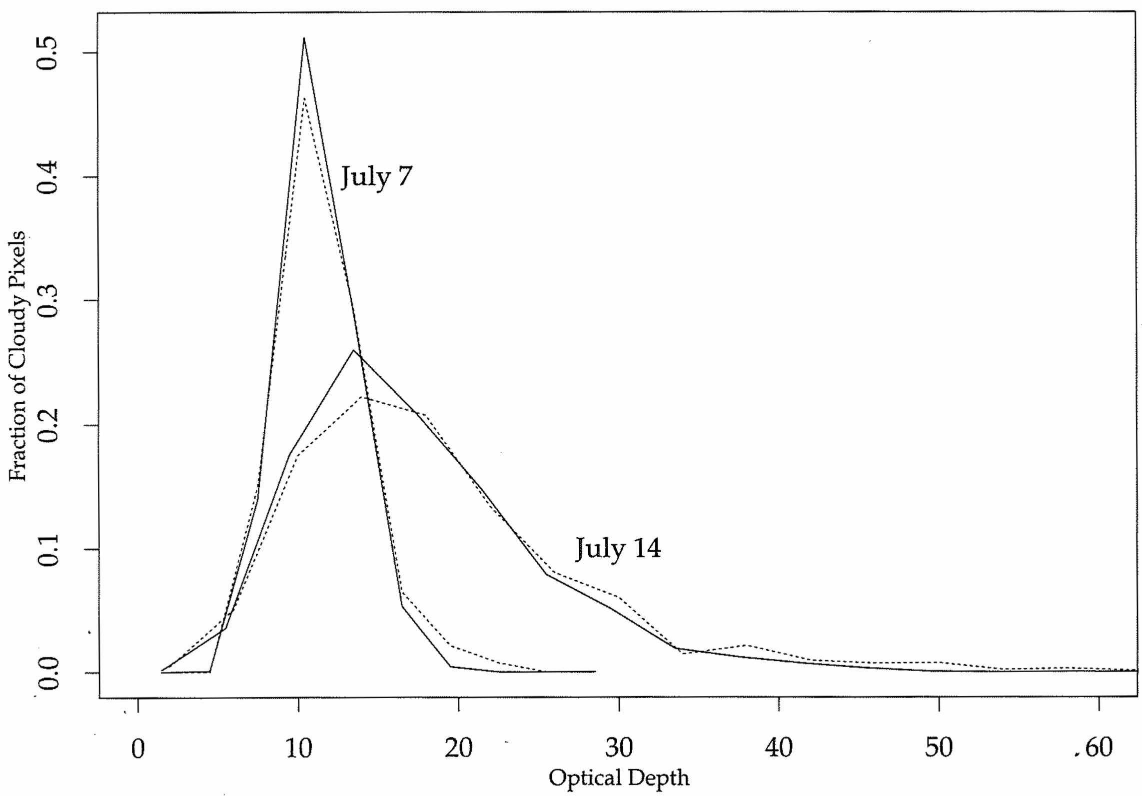

Figure 3: Histograms of optical depth from collocated AVHRR (solid) and GOES (dashed) images for July 7 and July 14, 1987.

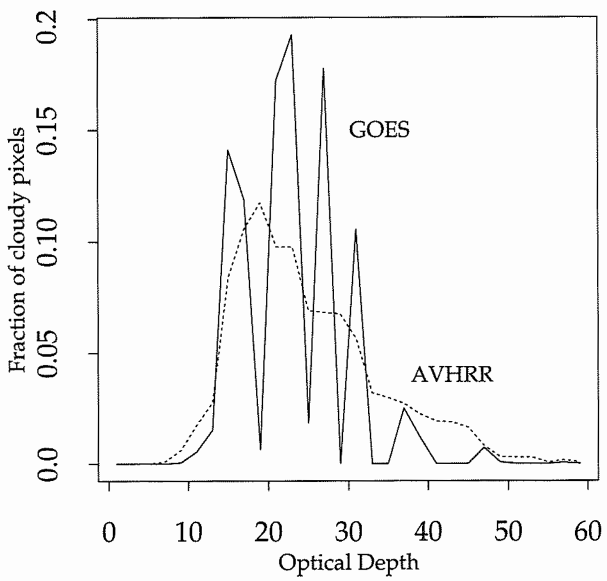

Figure 4: Histograms of AVHRR and GOES retrieved optical depths for a small, optically thick subregion on July 14. The lower resolution of the GOES sensor is apparent.

The temporal and spatial resolution provided by these satellite estimates are useful for process studies of fully cloudy marine boundary layers; work is continuing on a more complete description of the retrieval sensitivity to viewing geometry and cloud character, and on comparisons with collocated Landsat and MCR optical depth estimates.

5. Acknowledgments

The GOES and NOAA 9 data, as well as navigation and calibration software, were graciously provided by the NASA Climate Data System and the Climate and Radiation Branch, NASA Goddard Space Flight Center. We would like to thank Warren Wiscombe for providing the radiative transfer programs and Ming Dah Chou for the k-distribution water vapor coefficients. Scott Katz and Marc Michelson provided valuable tools for satellite image display. This work was supported by the National Science and Engineering Research Council of Canada, and by a NASA Graduate Fellowship in Global Change.

6. References

Albrecht, B.A., D. A. Randall and S. Nicholls, 1988: Observations of marine stratocumulus during FIRE. *Bull. Amer. Met. Soc.*, **69**, 618-626.

Arking, A. and J. D. Childs, 1985: Retrieval of cloud cover parameters from multispectral satellite images. *J. Clim. App. Met.*, **24**, 322-333.

Austin, P. and Y. Wang, 1992. Microphysical variability and drizzle formation in FIRE clouds. *Proceedings* of the 11th International Conference on Clouds and Precipitation. Montreal, Canada, 1992.

Chou, M. D., 1986: Atmospheric solar heating rate in the water vapor bands. *J. Climate Appl. Meteor.*, **25**, 1532-1542.

Coakley, J. A. and F. P. Bretherton, 1982: Cloud cover from high-resolution scanner data: detecting and allowing for partially filled fields of view. *J. Geophys. Res.*, **87**, 4917-4932.

Hale, G. M. and M. R. Querry, 1973: Optical Constants of Water in the 200-nm to 200-μm Wavelength Region. *Appl. Opt.*, **12**, 555-563.

Hansen, J.E. and J. B. Travis, 1974. Light scattering in planetary atmospheres. *Space Sci. Rev.*, **16**, 527-610.

Kaufman, Y. J. and B. N. Holben, 1992. Calibration of the AVHRR visible and near IR bands by atmospheric scattering, ocean glint and desert reflection. Submitted to *J. Appl. Meteor.*

Minnis, P., P. W. Heck, D. F. Young, C. W. Fair all and J. B. Snider, 1992: Stratocumulus cloud properties derived from simultaneous satellite and island-based instrumentation during FIRE. *J. App. Met.*, **31**, 319-339.

Nakajima, T., M. D. King, J. D. Spinhirne and L.F. Radke, 1991: Determination of the optical thickness and effective particle radius of clouds from reflected solar radiation measurements. Part II: Marine stratocumulus observations. *J. Atmos. Sci.*, **48**, 728-750.

Paltridge, G. W. and C M. R. Platt, 1976. Radiative processes in meteorology and climatology. Elsevier Scientific Pub. Co., Amsterdam, 318 pp.

Stamnes, K., S.C. Tsay, W. Wiscombe and K. Jayaweera, 1988: A numerically stable algorithm for discrete-ordinate-method radiative transfer in multiple scattering and emitting layered media. *J Appl. Opt.*, **27**, 2502-2512.

Rossow, W. B., L.C. Gardner and A. A. Lacis, 1989: Global, Seasonal cloud variations from satellite radiance measurements. Part I: sensitivity of analysis. *J. Climate*, **2**, 419-458.

Wiscombe, W. J., 1979: Mie scattering calculations - advances in technique and fast vector speed computer codes. NCAR Tech. Note TN-140+Str, National Center for Atmospheric Research, Boulder Colorado.

Wiscombe, W. J., R. M. Welch and W. D. Hall, 1984: The effects of very large drops on cloud absorption. Part I: parcel models. *J. Atmos. Sci.*, **41**, 1336-1355.

ALBEDO AND TRANSMISSION FIELDS OF SCALE INVARIANT CLOUD MODELS, APPLICATIONS TO REMOTE SENSING AND RADIATION BUDGETS

A. B. Davis,[3,4] S. Lovejoy,[1] and D. Schertzer[2]

[1]Physics Department, McGill U., 3600 University St., Montreal, Quebec, H3A 2T8, Canada
[2]LMD (Boîte 99), Université M. & P. Curie, 4 Pl. Jussieu, Paris Cedex 05, 75 252, France
[3]Atmospheric Environment Service, 2121 Transcanadian Hway, Dorval, Qc, H9P 1J3, Canada
[4]Now at NASA/GSFC, Climate & Radiation Branch (Code 613), Greenbelt, MD 20771, USA

1. MOTIVATION AND OVERVIEW

The idea of using scale invariant structures (fractals and multifractals) in cloud modeling is motivated by the large body of empirical evidence that atmosphere lacks a clear-cut characteristic scale—the elusive "meso-scale gap"—from the synoptic to Kolmogorov's dissipation scale; see Lovejoy *et al.* (1992) for a systematic study of scaling energy spectra (of satellite imagery) in the range 160 m to 4000 km. Atmospheric scaling studies received a boost with the publication of Lovejoy's (1982) non-trivial area/perimeter relation for clouds and rain; but attention is now shifting from such simple (single exponent) scaling approaches to more general ones, capable of accommodating multiple scaling and several analysis techniques have been developed and applied to various geophysical signals. For an instance of special importance to us, the Earth's VIS and IR radiation fields have been shown to exhibit multifractal behaviour (Gabriel *et al.*, 1988; Lovejoy and Schertzer, 1990; Tessier *et al.*, 1992). See, e.g., Schertzer and Lovejoy (1991) for a review of multifractal formalism and a survey of its application to geophysics, in general, and meteorology, in particular.

There are also theoretical reasons for the introduction of scaling concepts in cloud modeling: cloud structure—even formation—is intimately related to the turbulent dynamics of the lower atmosphere while our understanding of turbulence is now largely based on scale invariant constructs (power-law structure functions and spectra, fractal and multifractal models of intermittancy, etc.). Unsurprisingly, King *et al.* (1981) find scaling power spectra in *in situ* cloud liquid water content (LWC) probings; see also Durouré and Guillemet (1990) for box-counting results on similar datasets. We will therefore model clouds with mono- and multifractals for the purposes of radiative transfer investigations, using both analytical and numerical approaches to model the processes involved in the multiple scattering.

Firstly, we are interested in the cloud's overall response to external illumination in both reflection and transmission; in particular, their dependence on cloud optical thickness and the kind of variability model used determine its internal structure. When the model is stochastic, we can expect these radiative properties to fluctuate from one realization (e.g., meteorological situation) to the next and we must turn to ensemble-averages. In the optically thick regime—where the nonlinear effects are most important—we find systematically diverging ratios with respect to the predictions of the standard (homogeneous) models, on the one hand, and between the various ways of modeling the physics of matter-radiation coupling, viz., kinetic-type versus diffusion-type approaches. We also find that, on average, photon free paths are no longer exponentially but algebraically distributed hence shorter total optical paths are to be expected. This means that systematic biases are introduced by applying homogeneous model calculations to real (inhomogeneous) clouds, e.g., as in GCM parameterizations for radiation or in the course of reducing remotely sensed fluxes or radiances to physical cloud properties. For instance, we can argue that absorption, hence heating rates, will be strongly affected by intermittent internal variability due to the much enhanced photon free path distributions.

Secondly, we have successfully simulated fully resolved reflected, transmitted and internal radiation fields for a specific highly variable multifractal cloud model. In particular, we find that power- and singularity spectra for the albedo fields, as well as a range of "apparent" absorption that all compare favorably with their empirical counterparts. Moreover, the most apparently homogeneous models are those that exhibit the greatest differences in overall response when compared to their inherently homogeneous counterparts. Finally, the internal fields show how the strong systematic effects observed in the spatially averaged responses are mediated by net horizontal fluxes that are in fact quite small w.r.t. their vertical counterparts.

2. THE SCALING PROPERTIES OF VARIOUS OVERALL RESPONSES TO EXTERNAL ILLUMINATION

2.a. *The Standard Asymptotic Radiative Scaling Law*

If we restrict our focus the visible part of the solar spectrum, we can neglect absorption in the cloud; it is uniquely described by its overall (angularly and spatially integrated) transmittance T, equivalently, its albedo R=1-T. There is no direct contribution to atmospheric heating but T is a crucial component of the energy budget of the surface. For a plane-parallel cloud model of constant density (or LWC) ρ, geometrical thickness L, total scattering cross section κ, and asymmetry factor g, we can define its effective optical thickness for isotropic scattering

$$\tau^* = (1\text{-}g)\tau = (1\text{-}g)\kappa\rho L \tag{1}$$

which is also known as the "transport" optical thickness. For the two-flux model, a precise treatment of the radiative boundary conditions yields

$$T_{\mathrm{p}}(\tau^*) = \frac{1}{1+b\tau^*} \tag{2}$$

In practice, this is a 1D diffusion problem. The subscript "p" stands for "plane-parallel" and b is an $O(1)$ numerical factor. If $\tau^* \gg 1$, we find the standard (or "normal") scaling result

$$T_{\mathrm{p}} \approx \tau^{*-1} = \frac{1}{1\text{-}g}\tau^{-1} \tag{3}$$

Notice how the phase function (g) can only affect the prefactor, not the exponent. [We have also neglected the boundary layer effects related to the geometry of slant collimated illumination so, in essence, we assume $\tau \gg \max\{1/b(1\text{-}g),\mu_0\}$, μ_0 being the vertical cosine of the Sun.]

Davis (1992) shows that the radiative scaling in eq. (3) is representative of a rather large class of cloud models which includes not only homogeneous slabs but also horizontally bounded cases, clouds with strong (discontinuous) internal variability but only on a narrow range of scales. Even models with variability on all scales but lacking long-range spatial correlations—namely, random binary mixtures which are the (discrete) spatial equivalent of white noise—are in this class. more precisely, eq. (3) still applies in the "singular" limit where the low density value in the binary mixture vanishes, inasmuch as a kinetical-, rather than a diffusion-type theory is used to model the matter-radiation interaction. See, on the one hand, Boissé (1990) or Titov (1990) and references therein for kinetical (transfer) approaches and, on the other hand, Stauffer (1985) for a review of diffusion results obtained at the "percolation" threshold in probability of occurrence of a low density cell. [At percolation (and beyond), a large but very sparse cluster of low density cells spans the whole system and diffusion (equivalently, conduction) theory tells us it will channel all of the radiant energy flux (equivalently, current) in the singular (so-called "RSN" or random superconducting network) limit; for systems of infinite size, anomalous diffusion scaling laws are obtained when the same, rather restrictive, conditions are meet.]

2.b. *An Anomalous Radiative Scaling Law*

In sharp contrast to the homogeneous or somehow "weakly" inhomogeneous situations described in the above, fractal or multifractal distributions of density are not only discontinuous but highly singular; they also exhibit power-law energy spectra and long-range correlations. The simple deterministic example provided in fig. 1 is known as a Sierpiński gasket; its fractal dimension D is readily found by using the basic mass/size relation in eq. (5) below. Let N_λ be the number of filled cells when the system's size is

$$\lambda = L/l_0 \tag{4}$$

i.e., the ratio of the outer size (L) of the cloud to the homogeneity scale (or grid constant, l_0). In the present case, λ is 2^n (n=0,1,···,7) and

$$N_\lambda = \lambda^D \tag{5}$$

with D = log3/log2 = $\log_2 3$ = 1.585··· by virtue of the "cascade" construction. Notice that this value is less than the dimension of space d=2 in which the fractal is embedded. A homogeneous cloud would of course yield D=d and

$$C = d\text{-}D \tag{6}$$

is known as the "codimension" of the set. In particular, the probability of any of the λ^d cells to belong to the fractal (i.e., ρ_λ>0) is

$$\Pr(\rho_\lambda>0) = N_\lambda/\lambda^d = \lambda^{-C} \tag{7}$$

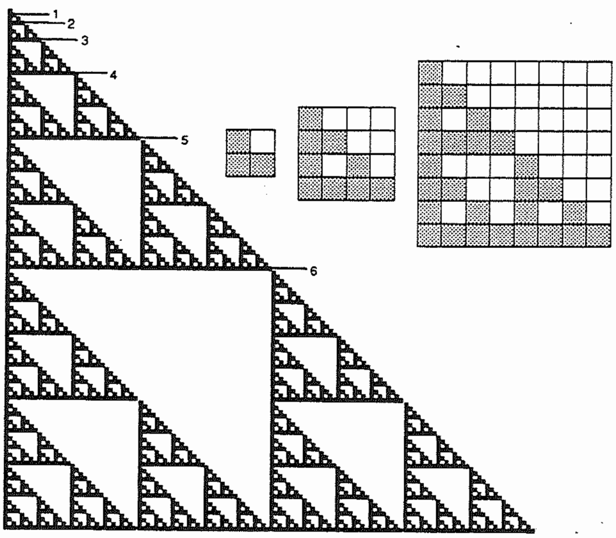

Figure 1: The prototypical monofractal cloud model with fractal dimension D=1.585··· after 7 cascade steps; the first 3 steps are seen in the inset.

The radiative properties of the cloud model in fig. 1 were investigated numerically by Davis *et al.* (1989, 1990a) using the more atmospherically relevant theory of radiative transfer, not its d-dimensional diffusion (or Eddington) approximation. More precisely, extensive Monte Carlo simulations of standard (continuous angle) radiative transfer and of different versions of Lovejoy *et al.*'s (1990) discrete angle (DA) transfer were performed, all with isotropic phase functions and normal illumination conditions. For instance, when the structure in fig. 1 is replicated horizontally, an inhomogeneous but plane-parallel model is obtained for which the authors find the spatially averaged transmittance to scale as

$$\overline{T}_\lambda \approx \overline{\tau}_\lambda^{-\nu_T} \tag{8}$$

with $\nu_T \approx$ 0.4–0.5 < 1—the scaling is "anomalous"—and where

$$\overline{\tau}_\lambda = \tau_0\, \lambda^{1-C} \tag{9}$$

is the spatially averaged optical thickness; τ_0 being that of the filled cells (it was kept constant at a value of 2). At any rate, the novel radiative scaling in eq. (8) is sufficient to explain Wiscombe *et al.*'s (1985) cloud "albedo paradox" that arises when homogeneous radiation theory is applied to real cloud reflectancies in view of independently observed optical thicknesses; see Davis *et al.* (1990a) for a more detailed discussion. A further application of the radiative scaling ansatz in eq. (8) can be found in the radiative aspects of dynamical modeling where spatial details are not of interest.

2.c. *Anomalous "Mean Field" Exponents*

Apart from being deterministically distributed, the multiplicative weights used in the generation of the density field in fig. 1 are either 0 or (nominally) 1. These are unnecessary and unrealistic restrictions. As soon as the latter is relaxed, one goes from monofractals to multifractals and from eq. (7) to

$$\Pr(\lambda^\gamma \le \rho_\lambda < \lambda^{\gamma+d\gamma}) \sim \lambda^{-c(\gamma)}\, d\gamma \tag{10}$$

where γ is a given "order of singularity" (recall that λ>>1) and c(γ), its associated "codimension function" which is non-negative by definition. Multifractals are extremely "spiky" and integrals through them are dominated by a single order of singularity. This means that one can use a multifractal p.d.f. similar to (10) for optical thickness τ_λ too. Applying such a variability model to the homogeneous result in eq. (2), Davis *et al.* (1991a) find that the ensemble averages, <·>, combine into

$$\langle T_{p,\lambda}\rangle \approx \langle\tau_\lambda\rangle^{-\nu_{Tp}} \tag{11}$$

with an analytical expression for the "mean field" exponent which is again independent of g and always less than 1; this is simply a scaling consequence of Jensen's integral inequality: $\langle f(x)\rangle \ge f(\langle x\rangle)$ for any convex $f(x)$ and any p.d.f. So the mean behaviour of a multifractal ensemble of plane-parallel media emulates that of clouds with scaling internal variability.

A priori the result in eq. (11) is purely statistical but it can in fact be interpreted as an "independent pixel" (IP) estimate *à la* Cahalan (1989) for a spatially variable medium; basically, one solves the 1D diffusion for each column (net horizontal fluxes are explicitly neglected). In particular, Davis *et al.* (*ibid.*) find ν_{Tp} = (2-$\log_2 3$)/(1-C) ≈ 0.7 for the prototypical medium in fig. 1. In summary, we have in this case

$$1 = \nu_T(\text{homo.}) > \nu_{Tp} > \nu_T > \nu_T(\text{diff.}) = 0 \tag{12}$$

The last exponent has been confidently anticipated due to the fact that the monofractal is so sparse that it can be viewed as a singular "RSN" binary mixture with every cell almost surely empty. Davis (1992) shows that the hierarchy of exponents found in eq. (12) for this example is entirely consistent with the general principles of inhomogeneous radiation transport; in particular, the singular one-dimensional and d-dimensional diffusion limits that arise in DA similarity theory can be invoked (see Davis *et al.* (1990b) for some of the details and §3.c below for a further illustration).

Finally, the multifractal p.d.f. in eq. (10) can also be applied to direct transmittance

$$T_d(\tau) = \exp(-\tau) \tag{13}$$

which, like $T_p(\tau)$, is a convex function of τ. Accordingly, one finds $\nu_{Td} < \infty$, which is the value that can be (formally) associated with the standard Bouger-de Beer extinction law in (13). In short, one can expect algebraically, not exponentially, decaying geometrical photon free path distributions, hence severely perturbed order-of-scattering statistics, in the sense of lower means. A direct consequence of this inhomogeneity effect is that absorption is likely to be much weaker in multifractally structured clouds models than in their homogeneous counterparts; in turn, this could impact the current problem of cloud "absorption anomaly" in the solar IR spectrum (Stephens and Tsay, 1990).

3. THE RADIATION FIELDS FOR A MULTIFRACTAL, AND SOME OF THEIR INTEGRATED PROPERTIES

3.a. *The Adopted Density- and Associated Radiation Fields*

We now turn our attention to log-normal multifractals in d=2. Although this type of stochastic model was first introduced in turbulence theory (Kolmogorov, 1962; Obukhov, 1962) to account for the intermittancy of the dissipation field, we will simply use it as an extremely variable benchmark for computational radiative transfer. Moreover we consider a single realization but, as it turns out, we obtain a vivid illustration of the general principles of inhomogeneous radiation transport, all physical transport theories combined. For such a model one uses independent log-normally distributed multiplicative weights to randomly modulate the originally uniform density field each time a sub-cell ("sub-eddy") is created in the (turbulent) cascade. This translates to a Gaussian distribution for the γ's in eq. (10) and the weights are normalized in such a way that their ensemble average is unit (our spatial average $\overline{\rho}$ turned out to be 1.52). In these circumstances, the c(γ) in eq. (10) is given by

$$c(\gamma) = \frac{1}{4C_1}(\gamma + C_1)^2 \tag{14}$$

where C_1 is called the "codimension of (the singularities that contribute most to) the mean (of the process)." See Schertzer and Lovejoy (1987), for the description of a two-parameter

Figure 2: Exceedance sets of the adopted multifractal medium for three remarkable orders of singularity associated with widely separated thresholds in density value:

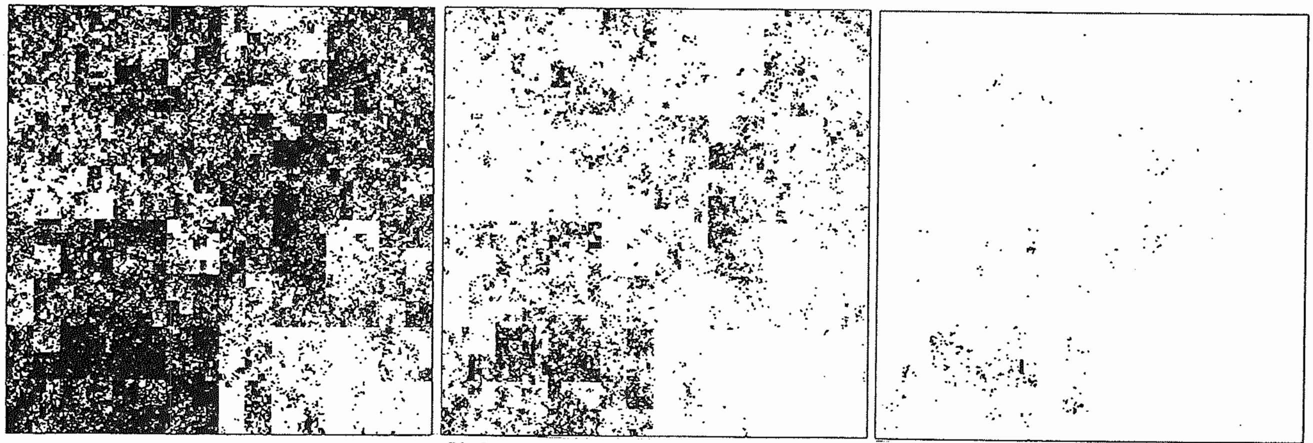

(a) $\gamma = -C_1 = -0.5$ (or $\rho_\lambda = \lambda^\gamma = 1/32$), these negative singularities (or "regularities") fill space, their $c(\gamma)$ vanishes in eqs. (10) and (14).

(b) for $\gamma = 0.0$ (or $\rho_\lambda = \lambda^\gamma = 1 = \langle\rho_\lambda\rangle$), these "neutral" singularities live on a set with $c(\gamma) = 0.125$ for $C_1 = 0.5$ in eqs. (10) and (14).

(c) for $\gamma = C_1 = +0.5$ (or $\rho_\lambda = \lambda^\gamma = 32$), these are the singularities that dominate the mean of the process and they have $c(\gamma) = C_1$ according to eq. (10).

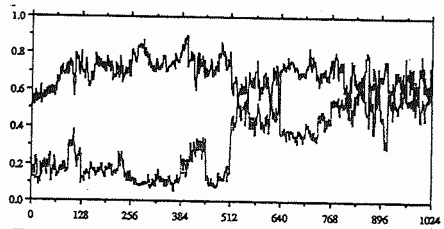

Figure 3: $R(y)$ and $T(y)$ for the $\bar{\tau}$=12.2 multifractal.

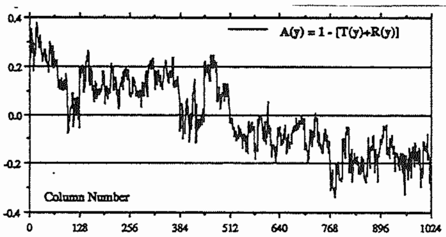

Figure 4: "Apparent absorbance" for the data in fig. 3 ($\bar{\tau}$=12.2). In reality, we are measuring the (column average of the) divergence of horizontal flux which enters, as a characteristic "pseudo-source/sink" term, in Stephens' (1986) Fourier transformed transfer equation for horizontally inhomogeneous plane-parallel atmospheres.

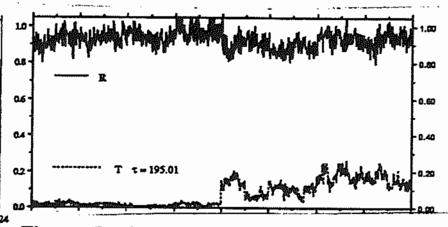

Figure 5: Same as fig. 3 but for the thickest ($\bar{\tau}$=195) multifractal, illustrating the narrowing of albedo range (smoothing) for more massive clouds by the enhanced multiple scattering.

Figure 7: Row-averaged (absolute) horizontal and (algebraic) vertical fluxes. The average flux (or DA "radiance") for all four directions in the adopted DA scheme is also plotted, for comparison.

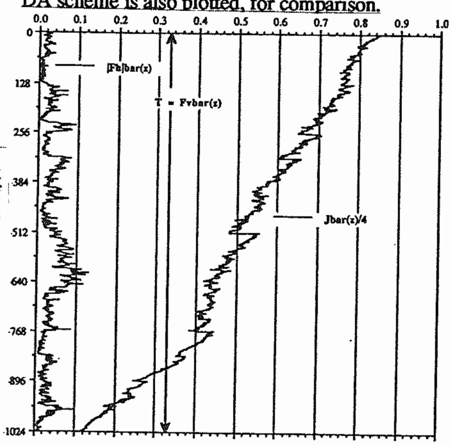

(α,C_1) class of "universal" multifractals that continuously span the gap between monofractals (α=0) and the Gaussian (α=2) models described by eq. (14).

We choose C_1=0.5 in eq. (14) and made 10 steps into the cascade process, dividing by 2 each time, as in fig. 1. We therefore end up with $\lambda=2^{10}=1024$ and figs. 2*a,b,c* illustrate the variability of the final density field using three very distinct thresholds in density value. Finally, the nominal density field is multiplied everywhere by a numerical factor which we can conveniently denote "κ," as in eq. (1). We then numerically solved the DA transfer equations for normal illumination (from the top in fig. 2) with $\log_2\kappa=-7(+1)-3$, hence $\bar{\tau}=\kappa\bar{\rho}\lambda$ ranging from 12.2 to 195, by factors of 2. [For all of the numerical technicalities, we refer to Davis (1992).]

3.b. *Simulated and Observed Radiation Measurements*

Detailed (grey-scale) illustrations of the various components of the internal DA radiation fields are given by Davis *et al.* (1991b) who also discuss them at length, on physical grounds. In particular, they find scaling (power-law) energy spectra for the simulated 1D albedo fields that compare favorably with their observed (e.g., Lovejoy *et al.*, 1992) counterparts. The authors also anticipate a steady improvement of the validity of the diffusion approximation as $\bar{\tau}$ increases since the photons will tend to stream less and scatter (random walk) more; this last finding is totally compatible with King *et al.*'s (1990) empirical evidence for an extensive "diffusion domain" deep inside marine StCu. We can complement these results with another simulated remote sensing experiment.

This time we try to account for the fate of the incoming radiant energy on a per column basis. Fig. 3 shows the run of local albedo $R(y)$ and transmission $T(y)$ with the horizontal coordinate y for $\bar{\tau}$=12.2 while fig. 4 illustrates 1-$R(y)$-$T(y)$, the apparent absorbance field $A(y)$. Interestingly, the values obtained for $A(y)$ are not unlike those obtained in real atmospheric probings, according to the compilation by Fouquart *et al.* (1990), cf. their Table 1. Our range (±30%) is not positively skewed like theirs—the overall average must vanish identically by conservation—but the most negative values observed in Nature may have remained unpublished, due to what may have been perceived as excessive uncertainty (Y. Fouquart, p.c.). Granted that such radiometric experiments are not easy, we nevertheless view the variance in the observations as a straightforward effect of internal variability, not as evidence of true absorption in clouds.

3.c. *Smoothing and "Channeling" via Multiple Scattering*

Perhaps our most striking result is that the greatest differences in overall response w.r.t. the predictions of homogeneous or even IP calculations occur for the highest values of $\bar{\tau}$, simultaneously with a very powerful smoothing in the albedo field of the density fluctuations (via enhanced multiple scattering). This paradox—the most apparently smooth (homogeneous looking) clouds have the most non-standard overall responses—is illustrated in figs. 5–6. [A good example of clouds that are at once relatively featureless visually and highly variable in terms of LWC is provided by arctic stratus (Tsay and Jayaweera, 1984).] On the one hand, fig. 5 is similar to fig. 3, the very same medium is used, only uniformly made 16 times more opaque. Notice the considerably narrower range of values for the $R(y)$ field, largely due to the fact that albedo is saturating at unit; see Davis *et al.* (1991b) for a preliminary scaling representation of the extreme and intermediate cases. On the other hand, fig. 6 gives $\overline{T}(\overline{\tau})$ for three different modalities of calculation: eq. (2) for homogeneity, IPs, and full-fledged numerical DA transfer. We notice how the responses are in the same hierarchy as obtained for the exponents in eq. (13), after taking the "-" sign used in eq. (11) into account.

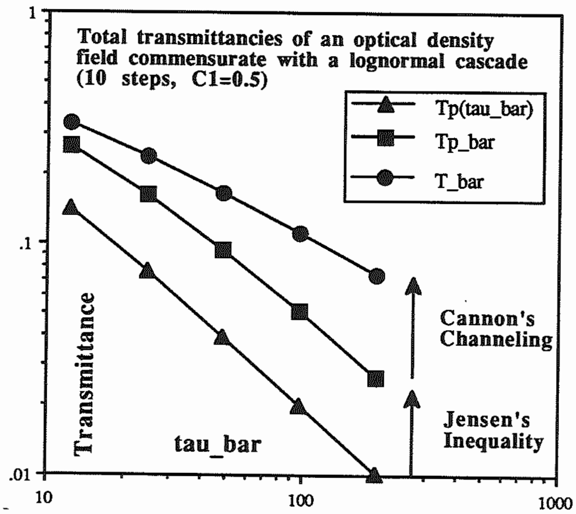

Figure 6: T as a function of (average) optical thickness and three different approaches to the multifractal radiation transport problem. Note that a diffusion calculation is likely to yield a somewhat higher T.

There are good reasons for such inequalities to apply. Firstly, IPs will always yield a higher transmittance than eq. (2) because of Jensen's inequality for convex functions. Secondly, the difference between IPs and the Monte Carlo result is of course entirely traceable to the allowance (in the numerics) for net horizontal fluxes. Fig. 7 gives, as a function of depth and for $\overline{\tau}$=12.2, the row-average of the absolute value of the net horizontal flux, also illustrated is the vertical counterpart (but no absolute values are called for) and it remains constant with depth, equal to T, due to the absence of true absorption. Notice how the greatest horizontal fluxes occur right above the massive concentration of scattering material that lies to the left of a relatively tenuous region in the lower part of figs. 2*a*,*b*,*c*. Although not large, these horizontal fluxes are clearly responsible for carrying the radiant energy around the concentration and they are relayed by their vertical counterparts to carry it further into the tenuous regions on either side (recall that the medium has been made horizontally periodic) and in fig. 3 we are not surprized to see above-average transmittance on the r.h.s. (of the unit "cell" we are looking at). This is just another way of depicting the basic inhomogeneous transfer mechanism that Cannon (1970) has described as "the 'channeling' of photons into the less opaque regions by increased scattering in the regions of greater opacity," to quote his verbatim exactly.

4. SUMMARY AND CONCLUSIONS

We have reported on our continued investigation into the transport of radiation in extremely variable scale invariant (fractal and multifractal) cloud models which we systematically contrast with their homogeneous counterparts (still widely used in spite of their being totally *ad hoc*). Viewing the radiative scaling behaviour of these homogeneous (or weakly variable) models w.r.t. optical thickness or absorption as "normal," we find "anomalous" exponents hence diverging ratios for the overall radiative responses. We discuss some important consequences of these findings for the cloud "albedo paradox" and "absorption anomaly" problems which, in various ways, are of considerable importance to the atmospheric remote sensing and dynamical modeling communities. Most importantly, the radiative features of multifractals can now be resolved spatially ... with a little help from a friendly supercomputer. Our numerical results are not only reliable, they turn out to be quite realistic in several respects and this gives credence to our predictions for radiative aspects of spatially unresolved fractal—not just fractional—cloudiness.

ACKNOWLEDGMENTS

We thank R. Borde, C. Gauthier, D. Lavallée, F. Schmitt, and Y. Tessier, as well as R. Davies, R. Pierrehumbert, W. Krajewski, A. Marshak, W. Wiscombe, R. Cahalan, W. Ridgeway, P. Gauthier and J.-F. Geleyn for the fruitful discussion. We are grateful to *Météo-France* for the generous portions of time on the C^2VR 's Cray-2. This work was partially supported by DoE's ARM project (contract #DE-FG03-90ER61062).

REFERENCES

Boissé, P., 1990: Radiative Transfer Inside Clumpy Media: The penetration of UV photons inside molecular clouds, *Astron. Astrophys.*, **228**, 483-502.
Cahalan, R. F., 1989: Overview of Fractal Clouds, in *Advances in Remote Sensing (RSRM'87)*, Eds. A. Deepak *et al.*, A. Deepak, Hampton (Va.), pp371–389.
Cannon, C. J., 1970: Line transfer in two dimensions, *Ap. J.*, **161**, 255-264.
Davis, A. B., P. Gabriel, S. Lovejoy, and D. Schertzer, 1989: Asymptotic Laws for Thick Clouds, Dimensional Dependence - Phase Function Independence, in *IRS'88: Current Problems in Atmospheric Radiation*, Eds. J. Lenoble and J.F. Geleyn, Deepak Publ., pp103-106.
Davis, A. B., P. Gabriel, S. Lovejoy, D. Schertzer, and G. L. Austin, 1990a: Discrete Angle Radiative Transfer - Part III: Numerical Results and Atmospheric Applications, *J. Geophys. Res.*, **95**, 11729-11742.
Davis, A. B., S. Lovejoy, D. Schertzer, P. Gabriel, and G. L. Austin, 1990b: Discrete Angle Radiative Transfer Through Fractal Clouds, *Proceedings of the 7th Conference on Atmospheric Radiation* (San Fransisco, July 23–27), A.M.S., Boston, USA, pp320–323.
Davis, A. B., S. Lovejoy, and D. Schertzer, 1991a: Radiative Transfer in Multifractal Clouds, in *Scaling, Fractals and Non-Linear Variability in Geophysics*, Eds. D. Schertzer and S. Lovejoy, Kluwer, Hingham (Mass.), USA, pp303–318.
Davis, A. B., S. Lovejoy, and D. Schertzer, 1991b: Discrete Angle Radiative Transfer in a Multifractal Medium, *S.P.I.E. Proceedings*, **1558**, 37–59.
Davis, A. B., 1992: *Radiation Transport in Scale Invariant Optical Media*, Ph.D. thesis, Physics Dpt., McGill Un., Montreal (Qc.), Canada.
Durouré, C., and B. Guillemet, 1990: Analyse des Hétérogénéités Spatiales des Stratocumulus et Cumulus, *Atmos. Res.*, **25**, 331–350.
Fouquart, Y., J. C. Buriez, M. Herman, and R. S. Kandel, 1990: The Influence of Clouds on Radiation - A Climate Modeling Perspective, *Rev. of Geophys.*, **28**, 145–166.
Gabriel, P., S. Lovejoy, D. Schertzer, and G. L. Austin, 1988: Multifractal Analysis of Resolution Dependence in Satellite Imagery, *Geophys. Res. Lett.*, **15**, 1373–1376.
King, M. D., L. F. Radke, and P. V. Hobbs, 1990: Determination of the spectral absorption of solar radiation by marine stratocumulus clouds from airborne measurements within clouds, *J. Atmos. Sci.*, **47**, 894-907.
King, W. D., C. T. Maher, G. A. Hepburn, 1981: Further performance tests on the CSIRO liquid water probe, *J. Atmos. Sci.*, **38**, 195-200.
Kolmogorov, A. N., 1962: Refinement of Previous Hypothesis Concerning the Local Structure of Turbulence in Viscous Incompressible Fluid at High Reynolds Number, *J. Fluid Mech.*, **13**, 82–85.
Lovejoy, S., 1982: The Area-Perimeter Relation for Rain and Clouds, *Science*, **216**, 185–187.
Lovejoy, S., A. B. Davis, P. Gabriel, D. Schertzer, and G.L. Austin, 1990: Discrete Angle Radiative Transfer - Part I: Scaling and Similarity, Universality and Diffusion, *J. Geophys. Res.*, **95**, 11699-11715.
Lovejoy, S., D. Schertzer, P. Silas, Y. Tessier, and D. Lavallée, 1992: The Unified Scaling Model of Atmospheric Dynamics and Systematic Analysis of Scale Invariance in Cloud Radiances, submitted to *Annales Geophysicae*.
Lovejoy, S., and D. Schertzer, 1990: Multifractals, Universality Classes and Satellite and Radar Measurements of Cloud and Rain Fields, *J. Geophys. Res.*, **95**, 2021–2034.
Obukhov, A., 1962: Some Specific Features of Atmospheric Turbulence, *J. Geophys. Res.*, **67**, 3011–3014.
Schertzer, D., and S. Lovejoy, 1987: Physically Based Rain and Cloud Modeling by Anisotropic, Multiplicative Turbulent Cascades, *J. Geophys. Res.*, **92**, 9693–9714.
Schertzer, D., and S. Lovejoy (Eds.), 1991: *Scaling, Fractals and Non-Linear Variability in Geophysics*, 318pp, Kluwer, Hingham (Mass.).
Stauffer, D., 1985: *Introduction to Percolation Theory*, Taylor & Francis.
Stephens, G. L., 1986: Radiative Transfer in Spatially Heterogeneous, Two-Dimensional Anisotropically Scattering Media, *J. Quant. Spectrosc. Radiat. Transfer*, **36**, 51–67.
Stephens, G. L., and S.-C. Tsay, 1990: On the Cloud Absorption Anomaly, *Q. J. R. Meteorol. Soc.*, **116**, 671–704.
Tessier, Y., S. Lovejoy, and D. Schertzer, 1992: Universal multifractals - theory and observations for rain and clouds, submitted to *J. Appl. Meteo.*
Titov, G. A., 1990: Statistical Description of Radiation Transfer in Clouds, *J. Atmos. Sci.*, **47**, 24–38.
Tsay, S.-C., and K. Jayaweera, 1984: Characteristics of Arctic Stratus Clouds, *J. Climate Appl. Meteor.*, **23**, 584-596.
Wiscombe, W. J., R. M. Welch, and W. D. Hall, 1984: The Effects of Very Large Drops on Cloud Absorption - Part 1, Parcel Models. *J. Atmos. Sci.*, **41**, 1336-1355.

THE CLOUD RADIATIVE FEEDBACK OF A MIDLATITUDE SQUALL LINE SYSTEM AND IMPLICATION FOR CLIMATE STUDY

Hung-Neng S. Chin

Lawrence Livermore National Laboratory, Livermore, CA 94550, U.S.A.

1. INTRODUCTION

Increasing effort has been put into improving climate prediction during the past decades. It is, however, far from accurate due to uncertainties in the model physics. The largest uncertainty is attributed to inadequate understanding of the role of clouds in the climate system. In addition, it is well recognized that upper-level cirrus / anvil clouds play an important role on large-scale climate through cloud-radiation interactions, and that cloud radiative properties are strongly modulated by the microphysical structure of clouds. Small changes in cloud optical properties could have a substantial impact on Earth's radiation budget and temperature. A recent modeling study indicated that cloud radiative effects combined with unreliable estimates of cloud amount and distribution can lead to an uncertainty in the amount of greenhouse warming by a factor of two (Mitchell *et al.*, 1989). This high sensitivity suggests that further understanding of the impact of microphysics on the cloud radiative feedback would improve the representation of cloud processes in the climate system.

In general, the cloud feedback on large-scale systems can be manifest into two aspects; 1) thermodynamic effects, such as cloud heating (Q_1) and drying (Q_2), and 2) radiative effects. The strong dependence of deep convection on large-scale fields simplified the development of cumulus parameterizations for the thermodynamic aspect. However, the parameterization of anvil clouds in large-scale numerical models is still an open research topic. Although the thermodynamic effect of anvil clouds is much smaller than their cumulus counterparts, the large coverage and longevity of anvil clouds can lead to significant influences on large-scale systems through radiative processes.

The emphasis of this study is focused on a midlatitude squall line system and assessment of its feedback on large-scale systems. The computational requirements of the radiation calculation and the necessity of including a larger horizontal domain for capturing an extensive anvil confines the cloud model to be two-dimensional. Among MCSs occurring in many geographic locations, the midlatitude broken-line squall system was chosen for this study due to its two-dimensionality in nature and the fact that it is the predominant type of convection in Oklahoma springtime severe storms. In addition, the future availability of ARM (Atmospheric Radiation Measurement Program) data over the Oklahoma site will allow for verification of the simulated cloud radiative properties in future studies.

The constraint of two-dimensionality limits the simulated convective system from replicating all the observed features, particularly the dissipated stage. As shown in Ogura and Liou's (1980) study, the May 22, 1976, Oklahoma broken-line squall case might dissipate due to unfavorable moisture convergence into the storm area associated with the wind directed along the line. However, this mechanism was completely neglected in the two-dimensional model. The purpose of this study was not focused on replicating the essential dynamics that generated and maintained the broken-line squall system; instead, the motivation was to investigate the quantitative impact of microphysics on the cloud radiative feedback. Therefore, the two-dimensional cloud model is sufficient to explore the dependence of cloud radiative properties on the vertical distribution of condensates.

The main objectives of this study are 1) to study the impact of longwave and shortwave radiation on the thermodynamic and kinematic structure of a midlatitude squall line; and 2) to explore the influence of specifically including the ice phase in the cloud-radiation feedback mechanism for climate models.

2. MODEL AND INITIALIZATION

a. Model description

The model used is an extension of Chin and Ogura's (1989) two-dimensional model. The major differences are the inclusion of ice microphysics and radiation. The model is nonhydrostatic and fully compressible. The dynamic framework of this model is similar to that of Klemp and Wihelmson (1978a). The time-splitting technique significantly improves the computational efficiency of the nonhydrostatic model. Model features include an upper-level sponge damping layer (Bradley, 1984), a planetary boundary layer (Blackadar, 1979), a two-category liquid water scheme (i.e., cloud water (q_c) and rain (q_r); Kessler, 1969), a three-category ice-phase scheme (i.e., cloud ice (q_i), snow (q_s) and graupel / hail (q_g); Lin *et al.*, 1983) and shortwave and longwave radiative transfer schemes (Harshvardhan *et al.*, 1987).

The Coriolis force was neglected in this study to allow the model to be strictly two-dimensional. Open boundary conditions (Orlanski, 1976) were used at the lateral boundaries. A rigid boundary condition was imposed at the upper and lower boundaries with a sponge damping layer placed above 15 km to minimize the reflection of internal gravity waves. The vertical grid was stretched below 3.6 km with a spacing ranging from 200 m near the surface to 600 m at 3.6 km altitude. Above 3.6 km, a constant spacing of 600 m was employed up to the model top at 20.4 km. In the horizontal, a uniform grid spacing of 1.5 km was used for the central 375 km of the domain. Outward from both sides of central region, the spacing was stretched with a constant ratio of 1.15. The horizontal stretching allowed for a larger domain size (3420 km wide) to avoid possible influences from the lateral boundaries and to prevent the model convection from decaying due to a limited moisture supply in a small model domain. In this study, the main attention is focused on the sub-domain with a horizontally uniform grid. As pointed out by Fovell and Ogura (1988), horizontally stretched grids have the effect of relaxing the storm-perturbed airflow back to the initial states. Therefore, the mature modeled system propagates into the same favorable environment that leads to a quasi-equilibrium state without experiencing a dissipating stage. A total of 320 x 37 grid points were employed in this study. Model grids were translated with the simulated squall line system to keep the main features within the central portion of model domain during the course of the simulation. The speed of translation is 18.5 and 22.0 m s^{-1} for ice-free and ice runs (elaborated shortly), respectively.

The shortwave radiation scheme uses the Delta-Eddington two-stream approximation and adding-layer method to calculate the scattering from the direct beam and multiple scattering between layers (Davies, 1982). The longwave radiation scheme was described by Harshvardhan and Corsetti (1974). Modifications were made to distinguish the radiative properties of ice clouds from those of water clouds for shortwave (SW) and longwave (LW) radiation, using the parameterization schemes of Stephens (1978) and Starr and Cox (1985) for water and ice clouds, respectively. The optical properties of mixed-phase clouds were determined by a linear combination of the radiative properties of water and ice clouds. There was no partial cloudiness in the cloud model; each grid point was either completely cloudy or clear. In addition, clouds were treated as gray bodies for the longwave calculation. Cloud optical properties are functions of model predicted condensates. The effect of the size and shape of hydrometeors on optical properties was not included in this study. Cloud water and rain were assumed to have the same effects on optical properties of water clouds, so do cloud ice, snow and graupel / hail for ice clouds. However, the habit of ice particles was partially taken into account by reducing the asymmetry parameter from 0.84 to the measured value (0.7). The solar absorption in the clear sky is due to H_2O and O_3, and its counterpart for longwave cooling is caused by H_2O, O_3 and CO_2. The effects of aerosols on cloud optical properites were not considered in this study.

The model top for calculating radiation fluxes was extended to 1 mb by adding six layers above the cloud model domain. Moisture and temperature profiles for the radiation calculations above sounding levels (150 mb) were given by climatological data from the ICRCCM (Intercomparison of Radiation Codes in Climate Models) version of the AFGL atmospheres (McClatchey *et al.*, 1972). The inclusion of a sponge layer above 15 km also has the effect of smoothing the distribution of moisture and temperature near the cloud model top. The mixing ratio of O_3 through the earth atmosphere was based on climatological data. The CO_2 concentration was assumed to be 320 ppm. The surface albedo was specified as 0.2. The validation of longwave and shortwave radiation for clear sky conditions is shown in Table 1; model results exhibited a very good agreement with ICRCCM data.

Table 1. Comparison of LW and SW fluxes with ICRCCM data for clear sky condition.

Midlat-Summer	LW				SW	
sfc albedo= 0.2, CO_2: 300 ppm	Surface			Top	Surface zen=30°	Surface zen=75°
Unit: W m^{-2}	Up	Down	Net	Up	Down	Down
Model	423.5	340.1	83.4	284.6	950.5	231.6
median* (±range)	423.6 (±5.8)	343.4 (±41.9)	80.3 (±42.2)	285.7 (±26.3)	943.7 (±5%)	235.8 (±10%)

*ICRCCM considers the absorption due to H_2O, O_3, O_2 and CO_2 in SW calculations, but the SW scheme used herein only includes H_2O and O_3.

The radiation was calculated every 5 minutes in this study since sensitivity tests showed that there was no noticeable difference between coarse (5 minute) and fine (2.5 minute) resolutions. Constant time steps of 12 and 3 seconds (non-sound and sound wave calculation, respectively) were used throughout the model integration. A total of 585 and 930 seconds (CRAY-2 CPU time) were taken for 8 hour integration of ice-free and ice simulations with radiation, respectively. The radiation calculation accounts for 31% of the total CPU time in the ice simulation.

To distinguish the convective region from the stratiform region in a tilting convective system, the partitioning criteria of Churchill and Houze (1984) was used along with two additional conditions to identify the convective region associated with tilted updrafts aloft and new cells initiated ahead of organized squall lines. A grid column with little or no surface precipitation is considered convective if cloud water is present ($q_c \geq 0.1$ g kg^{-1}) below 4 km ($\approx$ the melting layer), or if the maximum updraft exceeds 3 m s^{-1}. Otherwise, it is included in the stratiform region.

For the heat budget, the collective heating effect of the cloud ensemble, (Q_1), is expressed, in units of °C hr^{-1}, by (Yanai *et al.*, 1973)

$$Q_1 = \overline{\pi}\left[-\frac{1}{\overline{\rho}}\frac{\partial(\overline{\rho}\cdot\overline{w'\theta'})}{\partial z} + \overline{D_\theta}\right] + \overline{M_\theta} + \overline{Q_R}, \tag{1}$$

where overbars indicate horizontally averaged values and primes deviations from the horizontal mean. Meteorological variables are in conventional notation. π is the non-dimensional pressure, Q_R the radiative heating rate, M_θ the heating rate of microphysic contribution to potential temperature (θ) and D_θ the effect of sub-grid scale turbulence.

The horizontal sub-domain used for the averaged heat budget was chosen in a way consistent with Gallus and Johnson's (1990) observational study; namely, a region with 200 km wide upshear (west) from the leading edge (defined by -1 K isotherm of potential temperature deviation from the base state at the lowest grid level).

b. Initialization

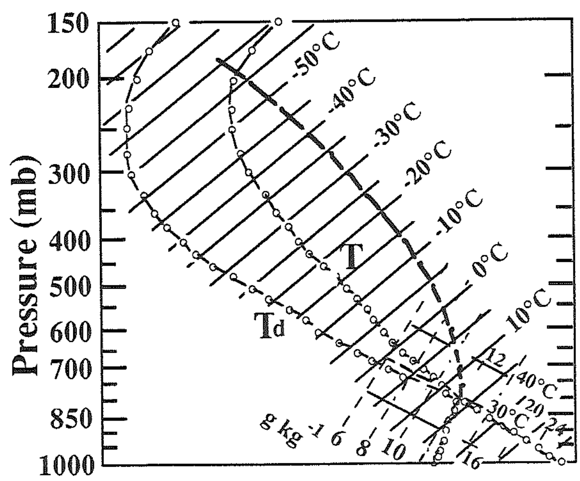

Fig. 1. The modified atmospheric sounding for the broken-line type of squall line systems.

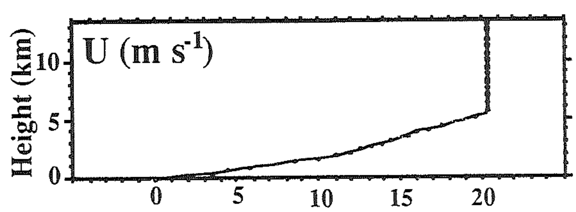

Fig. 2. The base state wind (normal-line component) profile used in this study.

Initial conditions were based on a composite midlatitude squall line sounding for broken-line type systems (Bluestein and Jain, 1985) with temperature and moisture profiles modified to represent a mixed layer below 800 mb, as is often observed in pre-storm conditions (Fig. 1). The imposed base state wind (normal to the line) was depicted in Fig. 2. A constant wind is specified above 5.5 km for simplicity. The CAPE (convective available potential energy) value and bulk Richardson number (Weisman and

Klemp, 1982) of the initial conditions are 2742 J kg^{-1} and 69, respectively. Surface temperature and vapor mixing ratio were specified as 1 °C and 1 g kg^{-1} larger than the initial sounding at the lowest grid (i.e., 33.6 °C and 13.1 g kg^{-1}).

The model was initialized with a warm, moist bubble in an otherwise horizontally homogeneous sounding. This bubble was 15 km wide and 3.4 km deep, and centered at 1.7 km above the ground. Maximum perturbations of potential temperature and vapor mixing ratio were 2 K and 4 g kg^{-1}, respectively.

3. DESIGN OF EXPERIMENTS

All experiments, which were conducted to examine the effects of microphysics on the cloud radiative feedback, were integrated for eight hours of physical time. Fixed surface conditions (temperature and vapor mixing ratio) were used to eliminate the complication of cloud-ground interaction. A total of six model experiments were conducted as listed in Table 2. To identify the influence of the phase of condensates on cloud radiative properties, simulations without the ice-phase (hereafter referred to as ice-free runs) and simulations with both liquid and ice water (ice runs) were performed in group A (ice-free) and B (ice).

Table 2. Summary of numerical experiments.

Experiment	Microphysics	Radiation
A1	ice-free	no
A2	ice-free	LW
A3	ice-free	LW + SW
B1	ice	no
B2	ice	LW
B3	ice	LW + SW

4. RESULTS

a. Simulation without radiation

Both ice-free and ice runs exhibited quasi-steady solutions with a succession of convective cells initiated ahead of the leading edge during the course of simulations. Significant upshear (westward) tilting of the convective core occurred after 3.5 hour.

The influence of the ice phase on thermodynamic feedback is indicated in Fig. 3, where the radiation was not considered during the simulation. The ice simulation predicted a maximum cloud heating rate (~ 8 °C hr^{-1}) comparable to that of the ice-free run, except for the finer structure and deeper anvil heating between 8 and 12 km. Both experiments exhibited a similar dynamic structure for the simulated squall line system (not shown). The altitude of double-peaked heating maxima for the ice run (between 6 and 9 km) is in good agreement with the observed heating profile of the broken-line system during the mature stage (Gallus and Johnson, 1990).

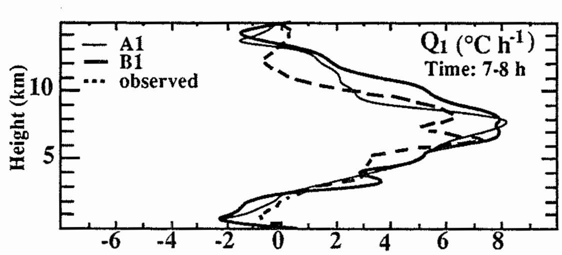

Fig. 3. Temporally-horizontally averaged heating profiles. (Observed profile adapted from Gallus and Johnson, 1991)

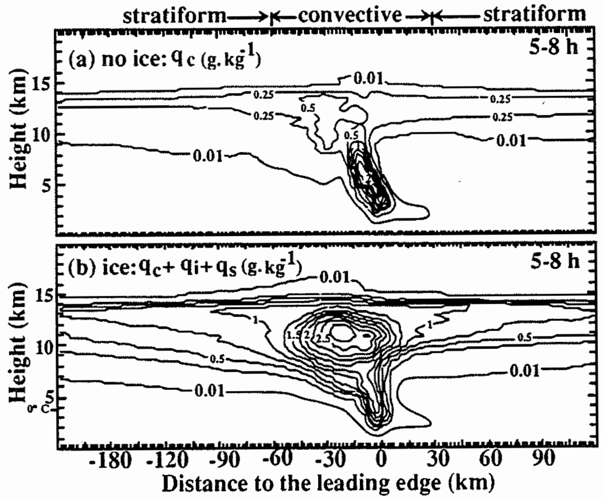

Fig. 4. Time averaged cross-sections of cloud structure. (a) mixing ratio of cloud droplets from run A1. (b) total mixing ratio of cloud droplets, ice crystals and snow from run B1.

To diagnose optical properties of water and ice anvils, temporally averaged temperature, moisture and condensate distributions were constructed from the model simulated squall line system. The ice simulation produced an anvil with a larger vertical and horizontal extent (Fig. 4). The optical properties for water and ice anvils (Fig. 5) were calculated using time-space (3 hours and 200 km) averaged vertical profiles of anvil structure, located between 8 and 14 km within the stratiform region of Fig. 4. The total water content of the ice anvil is about four times its counterpart in the water anvil; the liquid water content within the ice anvil accounts for a negligibly small portion (≈ 0.4 %) of total water. The optical depth (τ) of the water anvil is, however, much larger than that of the ice anvil. The greater optical thickness of the water anvil produced significant differences in solar radiative properties, particularly in the cloud albedo and transmittance. The absorption of solar radiation in the water anvil is about twice as large as in the ice anvil.

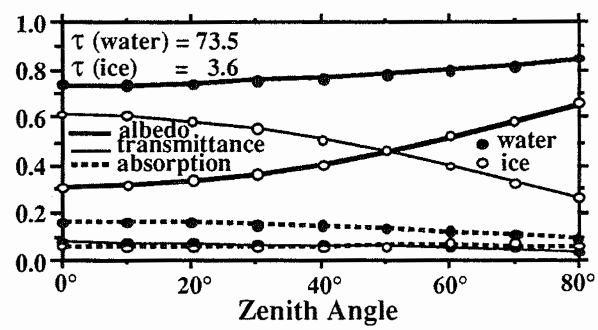

Fig. 5. Cloud albedo, transmittance and absorption of shortwave radiation for varied zenith angles.

The time-space averaged structure was also used to calculate radiative heating profiles for longwave (LW) and shortwave (SW) radiation (Fig. 6). The longwave heating profiles for both water and ice anvils are very similar with the heating near the bottom and cooling near the top of anvils. The higher altitude of maximum longwave cooling for the ice anvil (≈ 1 km) is consistent with the cloud heating profile (Q_1). The profile of longwave heating through the anvil is favorable for the creation of local instability that would intensify vertical motion and condensational deposition. In contrast, the water and ice anvils have distinctly different shortwave heating rates. Shortwave heating, particularly for the water anvil, tends to produce a multi-layer structure through the anvil due to the more stable stratification in the middle. On the contrary, shortwave heating can also provide more buoyancy to counteract its stabilizing effect. The overall feedback of shortwave radiation on the squall line system is shown in the next section.

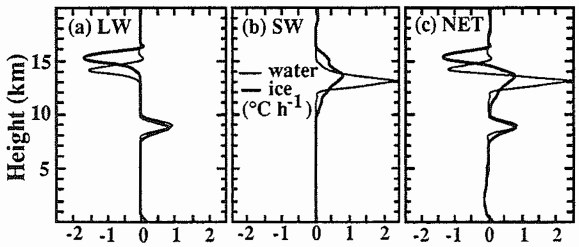

Fig. 6. Heating rates of water and ice anvils. (a) longwave. (b) shortwave at 0° zenith angle. (c) sum of (a) and (b).

b. Simulations with radiation

Further investigation of cloud-radiation feedback for the squall line system is shown in this section. Table 3 shows time and space averaged (8 hours and 200 km) surface precipitation rates for both ice-free and ice simulations. The stratiform precipitation accounts for a negligibly small portion of the total surface precipitation due to the very dry environment below 2 km. The relatively larger ratio of stratiform to total precipitation for the ice simulations reflects the fact that the ice phase enhances anvils due to the small terminal velocity of snow particles. Further, the destabilizing effect of longwave radiation can be seen in not only convective, but also stratiform regions of both ice-free (A2) and ice (B2) simulations. The extra heating near the bottom of anvils leads to a larger increase (16 ~ 20%) of surface precipitation over the stratiform region than in the convective region (4 ~ 6%).

Table 3. Temporally and horizontally averaged surface precipitation rate (mm hr^{-1}).

	ice-free			ice		
	A1	A2	A3	B1	B2	B3
convective	9.77	10.34	9.65	11.82	12.25	11.77
stratiform	0.05	0.06	0.08	0.37	0.43	0.38
total	9.82	10.40	9.73	12.19	12.68	12.15

Table 4. Temporally and domain averaged condensation rate (°C hr^{-1}) within the anvil.

	ice-free			ice		
	A1	A2	A3	B1	B2	B3
stratiform	0.25	0.27	0.29	0.47	0.49	0.46

Table 5. Numerical simulation statistics

	ice-free			ice		
	A1	A2	A3	B1	B2	B3
maximum cooling (K) behind gust front	-12.5	-12.7	-12.6	-15.0	-15.6	-15.4
gust front speed (s m^{-1})	18.9	18.9	18.7	22.4	23.8	22.5

The most interesting feature seen in Table 3 is the distinct feedback of the shortwave radiation for both ice-free (A3) and ice (B3) simulations. The stabilizing effect of shortwave radiation is seen in the convective regions of both simulations. This consistent result is due to the fact that the radiative heating is much smaller than the net cloud heating over the convective region. The shortwave heating becomes a dominant process within the anvils (compare Fig. 6 with Table 4), particularly in the water anvil. Thus, the buoyancy contribution of shortwave heating suppressed the stabilizing effect in the water anvil. This feature is in sharp contrast to the ice anvil. In summary, the inclusion of radiation has small influence on the total energy budget and the dynamic structure of the simulated squall line system. With fixed surface conditions, the kinematic properties of the simulated system, such as cold pool intensity and gust front speed, is altered very little by the radiation (Table 5).

5. Summary and discussion

Results indicate that the phase of ice particles has little impact on the thermodynamic feedback for simulated squall line systems although it does have the effect of enhancing the intensity of anvils. Further, the similar longwave properties of both water and ice clouds lead to a consistent feedback that strengthens the modeled convective systems. The distinct contrast of shortwave properties between water and ice clouds exhibit an opposite feedback on the stratiform region of simulated squall systems. These shortwave differences, however, have a relatively minor effect of weakening the modeled convective system in the convective region since the shortwave heating is much smaller than thermodynamic heating associated with the phase change.

These results also suggest that the phase of condensates plays an important role in the cloud radiative feedback for upper-level anvils. Condensed moisture representation should be appropriately partitioned between liquid and ice in general circulation models to improve the radiative processes of clouds on large-scale climate. As a whole, the inclusion of radiation only qualitatively altered the intensity of the simulated squall systems without affecting its essential dynamic structure. With fixed surface conditions, the kinematic characteristics of squall systems were rarely influenced by the radiation. The translucent nature of ice clouds would, however, have a different impact on the surface radiation budget than its water-cloud counterpart. Thus, the surface heating is expected to be stronger for ice clouds. Further investigation of cloud-ground interaction is being undertaken.

6. ACKNOWLEDGEMENTS

The author wishes to express the appreciation to Dr. R. G. Fovell for his valuable discussion at the ice parameterization scheme and to Dr. K. E. Grant for providing the radiative transfer model and valuable discussion. Discussions with Drs. M. M. Bradley and C. R. Molenkamp were also helpful to improve this work. This work was conducted under the auspices of the U.S. Department of Energy by the Lawrence Livermore National Laboratory under Contract W-7405-Eng-48.

7. REFERENCES

Bluestein, H. B., and M. H. Jain, 1985: Formation of mesoscale lines of precipitation: Severe squall lines in Oklahoma during the spring. J. Atmos. Sci., 42, 1711-1732.

Chin, H.-N. S., and Y. Ogura, 1989: Supplementary modeling study of a tropical convective band. J. Atmos. Sci., 46, 1440-1447.

Gallus, W. A. Jr., and R. H. Johnson, 1991: Heat and moisture budget of an intense midlatitude squall line. J. Atmos. Sci., 48, 122-146.

Starr, D. O'C., and S. K. Cox, 1985: Cirrus clouds. Part I: A cirrus cloud model. J. Atmos. Sci., 42, 2663-2681.

Stephens, G. L., 1978: Radiation profiles in extended water clouds. II: Parameterization schemes. J. Atmos. Sci., 35, 2123-2132.

A LABORATORY STUDY OF THE UPTAKE OF SO_2 AND HNO_3 BY SNOW CRYSTALS

S.K. Mitra, C. Diehl, and H.R. Pruppacher

Atmospheric Physics, Johannes Gutenberg-University, Mainz, FRG

1. Introduction

Much of the NO and NO_2 which enters the atmosphere is ultimately removed by wet deposition as HNO_3 (Crutzen, 1979; Liu, 1980). Because HNO_3 is a strong acid the rates and mechanisms of its removal have important consequences for receiving ecosystems and waters (Galloway et al.;1981). Similarly wet deposition is importantly involved in the removal of SO_2 which arrives at the earth's surface as H_2SO_3 or H_2SO_4, both strong acids. It has been well etablished that due to the high solubility in water of HNO_3 and SO_2, the latter in conjunction with the presence of oxidants such as H_2O_2 and O_3, water clouds and rain are significant sinks for the gases. On the other hand, little is known on the capability of snow to remove those gases. Field studies however, have demonstrated that the melt water of freshly fallen snow does contain significant amounts of $SO_4{}^{2-}$ and $NO_3{}^-$. This indicates that falling snow crystals are able to take up SO_2 and HNO_3 from the vapor phase, although some of the $SO_4{}^{2-}$ and $NO_3{}^-$ ions may have become part of the snow crystal melt water by means of sulfate and nitrate particles which became attached to the crystals.

In Table 1 some observations of the concentrations of $SO_4{}^{2-}$ and $NO_3{}^-$ in the melt water of freshly fallen snow are listed. Most observers found that the snow was acidic with a pH between 3 and 5. Comparison with rain water also showed that the concentration of $SO_4{}^{2-}$ and $NO_3{}^-$ in the melt water of freshly fallen snow was up to 5 times as high as the concentration of these ions in rain water (Georgii, 1965; Raynor and Hayes, 1983), indicating the efficient scavenging capability of snow.

In order to seperate out the contribution of scavenged vapors to the impurities found in snow from the contribution of aerosol particles laboratory studies are necessary. Such studies have thus far only been carried out for the uptake of SO_2 by ice. Thus, Sommerfeld and Lamb (1986) and Chapsaddle and Lamb (1989) measured the adsorption isotherm for SO_2 on ice between -3 and -30°C with SO_2 in the ppbv and ppmv range. Apart from showing the expected increase of the volume of gas adsorbed on the surface with increasing partial pressure of the gas, it was found that the amount of adsorbed gas was a strong function of the surface temperature of the ice. Particularly between -10 and 0°C, the volume of adsorbed gas increased sharply with increasing temperature. This behavior was interpreted as an

Table 1

Field observations of the concentration of $NO_3{}^-$ and $SO_4{}^{2-}$ in the melt water of freshly fallen snow

Observer	Observation site	Concentration (mg/liter) $SO_4{}^{2-}$	$NO_3{}^-$
Raynor & Hayes (1983)	Brookhaven, N. Y.	2.4	3.1
Georgii (1965)	Taunus Mts. FRG, 800 m	10.5	4.5
Tranter et al. 81986)	Cairngorms Mts. Scotland, 1080 m	2.65	2.92
Colin et al. (1989)	Vosges Mts. France, 700 m	7.10	8.85
Kapoor & Paul (1980)	Kashmir, India 2655 m	1.90 to 4.60	0.88 to 1.82
Huebert et al. (1983)	Niwot Ridge Colorado, 3000 m	1.20	1.43

independent verification of the presence of a semi-liquid layer at the surface of ice which is obviously able to accommodate substantial amounts of foreign gas over and above the amount expected from the theory of adsorption on a solid. Unfortunately the experiment was carried out with ice spheres rather than actual snow crystals. Iribarne et al. (1983) and Lamb and Blumenstein (1987) studied the entrapment of SO_2 in ice during the riming process i.e. during the collision of supercooled drops containing dissolved SO_2 with an ice surface. They showed that substantial amounts of SO_2 became transferred to the ice surface by riming. Again no snow crystals were used for this investigation. Valdez and Dawson (1989) showed that during the deposition of water vapor to a flat ice surface the amount of inorporated SO_2 was found to increase linearly with the amount of vapor converted to ice.

In order to explain their results they assumed that SO_2 becomes dissolved in that quasi-liquid layer on the surface of a growing ice surface. Due to the low rate at which SO_2 can diffuse in this layer its diffusional transport away from the advancing ice front prevents most of the SO_2 from escaping the liquid layer.

2. Experimental set up

In order to improve our understanding of the uptake of foreign gases by ice we have carried out some laboratory experiments on the uptake of SO_2 and HNO_3 by snow crystals.The experimental set up of our study with SO_2

has already been reported and discussed in detail by us (Mitra et al.;1990) and shall therefore be not repeated anymore. For the sake of comparison some of our results shall however be presented here. As was with SO_2, two types of experiments were carried out with HNO_3: (1) a study of HNO_3 adsorption onto the surface of laboratory grown dendritic snow crystals containing initially less than 1 x 10^{-6} mol liter $^{-1}$ (≈ 0,06 mg/liter) NO_3^-, and (2) a study of the uptake of HNO_3 during the growth of dendritic snow crystals in humid air mixed with HNO_3. As HNO_3 vapor source we used a 65% solution of supra-analytically pure HNO_3 through which dry nitrogen was bubbled. Experiment-2 was carried out inside a specially constructed diffusion cloud chamber in which near -15°C dendritic snow crystals were allowed to grow. Experiment -1 was carried out inside a horizontal flow chamber located in the walk-in cold chamber. In this arrangement nitrogen gas, prehumidified at ice saturation was allowed to flow at a speed of 10 to 50 cm sec^{-1}, and was mixed downstream with the nitrogen carrying HNO_3. This gas mixture was allowed to flow through a teflon chamber inside of which dendritic snow crystals of about 1 cm diameter was situated on a teflon net. Dew point and temperature were carefully monitored and

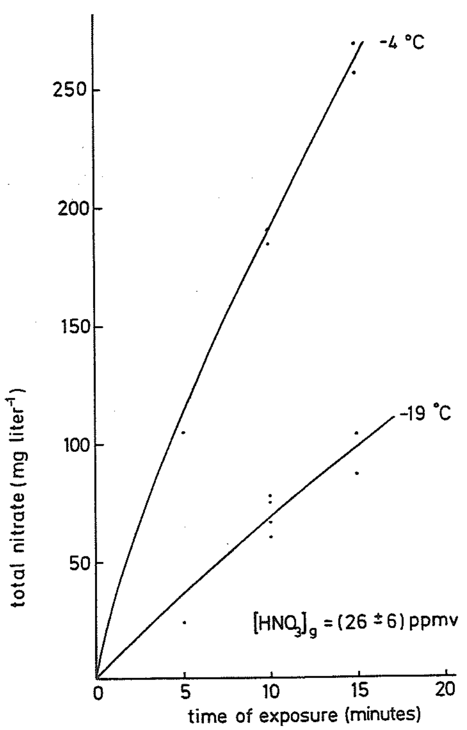

Figure 1 Concentrations of nitrate in snow crystals after exposure to HNO_3 for various lengths of time corrected for a initial concentration of HNO_3 in crystal = 0.06 mg liter $^{-1}$.

the concentration of HNO_3 in the gas phase determined by means of a gas wash bottle containing soda solution acting as a scrubber.

The NO_3^- content in the scrubber was measured by an ion chromatograph. After exposure the snow crystal were droped into a premeasured soda solution where the crystal melted and the amount of taken up NO_3^- was determined by ion chromatograph.

3. Results

In Figure 1 the uptake of HNO_3 by dendritic snow crystals is shown after they have been exposed to HNO_3 gas for varios lengths of time. We notice that even after 15 minutes of exposure saturation has not yet been reached. We also see that the uptake at -4°C is much higher than at -19°C, supporting the notion of the presence of a semi-liquid layer at -4°C which is capable of accomodating substantial amounts of gas. Comparing this result for HNO_3 with that for SO_2 at 30 ppmv (Figs. 2 and 3) we notice that after 15 minutes exposure the amount of nitrogen measured as nitrate in the crystal is at both temperatures about 250 times, larger than the amount of sulfur measured as sulfate in the crystal if during the uptake of SO_2 no H_2O_2 was present in the ice. In fact, the comparison shows that, extrapolated to the ppbv range, adsorption of SO_2 on snow crystals without the presence of an oxidizing agent contributes only negligibly to the sulfur content of snow crystals, in contrast to a significant uptake of HNO_3 in this concentration range (an appropriate Figure will be shown at the conference). If, however, an oxidizing agent is present during the adsorption of SO_2 by the snow crystal the uptake of SO_2 by adsorption is significant even in the ppbv range (an appropriate figure will be shown at the conference).

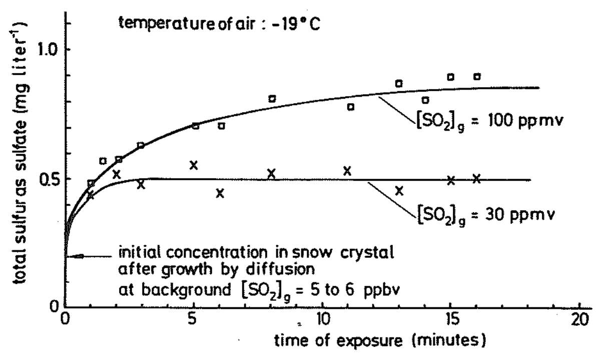

Figure 2 Concentration of sulfur as sulfate in snow crystals after they had been exposed to SO_2 for various lengths of time at -19 °C. Initial concentrations of sulfur as SO_4^{2-} in crystal = 0,2 mg $liter^{-1}$. (from Mitra et al., 1990).

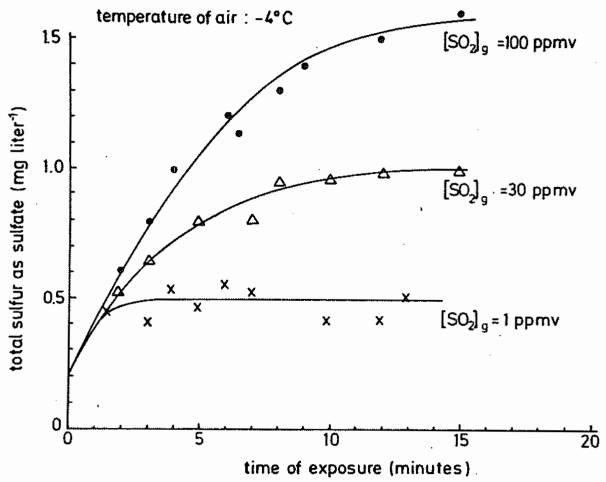

Figure 3 Same as Fig. 2 but for -4 °C.

In order to test in how far the taken up NO_3^- is localized on the ice surface the adsorption study was repeated with equal sized hemisperical ice pellets instead of snow crystals. These were exposed to HNO_3 vapor in concentration of 35 ppmv for 30 minutes. Subsequently different volume fractions were removed from these pellets by washing them with highly purified deionized water at + 4°C. The results of this experiment are summarized in Table 2. We notice that after about 54 % of the volume was washed off only 8 % of the initially present NO_3^- remained. This demonstrates that by far the major portion of the taken up HNO_3 is surface bound. Nevertheless it was highly surprising to find that a still measurable amount of NO_3^- penetrated the inside of the pellets. We suggest as explanation to this observation that after dissolving small amounts of HNO_3 in the semi-liquid layer

Table 2

Concentration of NO_3^- in 20 equal sized ice pellets after exposing than to 35 ppmv HNO_3 for 30 minutes at -19 °C followed by the removal of various volume fractions from the pellets by washing them with pure deionized water of + 1 °C.

Total initial ice volume (cm³)	Total NO_3^- concentration in ice (mg/liter)	per cent ice volume left (%)	per cent NO_3^- remaining in ice left (%)
3.9	20.8	46.2	15
3.6	19.4	36.1	10
3.6	18.4	27.8	8

the equilibrium melting temperature becomes locally depressed, increasing the thickness of the liquid layer which, in turn, allows more HNO_3 to dissolve, and so on, until a new equilibrium has been established. By bulk diffusion a small portion of the adsorbed NO_3^- ions may then have moved from the liquid layer into the ice structure via an interstitial diffusion mechanism, considering that the distances between the nitrogen atom and the 3 oxygen atoms of NO_3^- are between 1.19 and 1.33 A each, thus allowing NO_3^- to fit well into the cavities of the ice lattice.

Direct evidence for the actual incorporation of ions into the ice lattice is given by Fig. 4. We notice that in the absence of H_2O_2 only negligible amounts of sulfur became incorporated into the snow crystals during their growth in an SO_2 atmosphere. However, in the presence of a few ppbv of H_2O_2 the incorporation of sulfur as SO_4^{2-} became quite significant. Studying the sulfur content of the crystals as a function of growth time showed that the concentration remained the same irrespective of the growth time. This demonstrates, in excellent agreement with the results of Valdez et al. (1989) for a growing plane ice surface, that the mass of sulfur incorporated into the snow crystal is proportional to the mass of water vapor converted to ice. It thus appears that also the SO_4^{2-} ion can, in small amounts, be built into the ice crystal lattice, although during growth, the major portion of SO_4^{2-} will remain inside the semi-liquid layer which is constantly moving outward on the surface of the growing crystal. Unfortunately no verification of this consideration can be derived from the freezing potential studies of Workman and Reynolds (1956), Lodge et al. (1956), de Micheli and Iribarne (1963) and of Gross (1965), since their studies did not include sulfate or nitrate solutions. However, they clearly indicated that, with the exception of NH_4^+ solutions, ice preferentially accepts negatively charged ions into its lattice.

We are studying at present the uptake of HNO_3 during the diffusional growth of ice crystals. Results of this study will be presented at the conference.

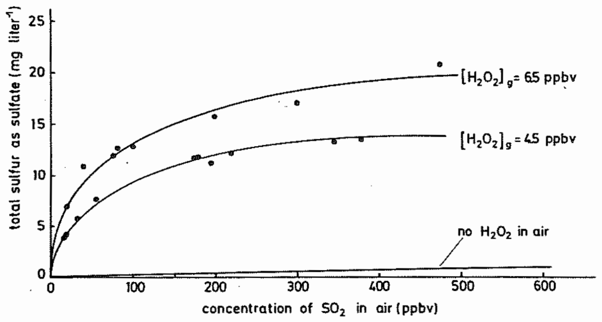

Figure 4 Concentration of sulfur as sulfate in snow crystals grown at -15 °C by vapor diffusion in an atmosphere of SO_2 in air (from Mitra et al., 1990).

References

Clappsaddle, C., and D. Lamb, 1989: The sorption behavior of SO_2 on ice at temperatures between -30 and -5°C. Geophys. Res. Letters, 16. 1173 - 1176.

Colin, J. L., Renard, D., Lescoat, V., Jafrezo, J. L., Gros, J. M., and B. Strauss, 1989: Reationship between rain and snow scidity and air mass trajectory in France. Atmos. Environment; 23, 1487 - 1498.

Crutzen, P. J., 1979: Ann. Rev. Earth Planet, Sci.,7, 443 - 472.

De Micheli, S. M., and J. V. Iribarne, 1963: La Solubilitè des electrolytes dans la glace. J. Chim. Phys., 767 - 774.

Galloway, J. N., and G. E. Likens, 1981: Atmos. Envir. 15, 1081 - 1085

Georgii, H. W., 1965: Untersuchungen über Ausregnen und Auswaschen von Spurenstoffen durch Wolken und Niederschlag. Ber. Deutsch. Wett. Dienst, Nr. 100.

Gross, G. W., 1965: The Workman-Reynolds effect and ionic transfer processes at the ice-solution interface. J. Geophys. Res., 70, 2291 - 2300.

Huebert, B. J. , Fehsenfeld, F. C., Norton, R. B., and D. Albritton, 1983: Scavenging of nitric acid vapor by snow. Precipitation scavenging. Dry Deposition and Resuspension. Elsevier. 293 - 300.

Iribarne, J. V., Barrie, L. A., and A. Iribarne, 1983: Effect of freezing on sulfur dioxide dissolved in supercooled drops. Atmos. Envir., 17, 1047 - 1050.

Kapoor, R. K., and S. K. Paul, 1980: A study of the chemical components of aerosols and snow in the Kashmir region. Tellus, 32, 33 - 41.

Lamb, D., and R. Blumenstein, 1987: Measurement of the entrapment of SO_2 by rime ice. Atmos. Envir., 21, 1765 - 1772.

Lodge, J. P., Baker, M. L., and J. M. Pierrad, 1956: Observations on ion separation indilute solutions by freezing. J. Chem. Phys., 24, 716 - 719.

Mitra, S. K., Barth, S., and H. R. Pruppacher, 1990: A laboratory study on the scavenging of SO_2 by snow crystals. Atmos. Envir., 24 A, 2307 - 2312.

Raynor, G. S., and J. V. Hayes, 1983: Differential rain and snow scavenging efficiency compiled by ionic concentration difference in winter precipitation. Precipitaion Scavenging, Dry depositions and Resuspension. Elsevier, 249 - 262.

Sommerfeld, R. A., and D. Lamb, 1986: Preliminary measurements of SO_2 adsorbed on ice. Geophys. Res. Letters, 13, 349 - 351.

Tanter, M., Brimbelscombe, P., Davies, T. D., Vincent, C. E., Abvehams, P. W., And I. Blackwood, 1986: The composition of snowfall, snowpack and melt water. Atmos. Environ., 20, 517 - 525.

Valdez, M. P. and G. A. Dawson, 1989: Sulfur dioxide incorporation in ice depositing from vapor. J. Geophys. Res. 94., 1095 - 1103.

Workman, E. J., and S. E. Reynolds, 1956: Electric phenomena occurring during freezing of aqueous solutions. Phys. Rev. 78, 254 - 259.

A CHEMICAL CLIMATOLOGY FOR CLOUD WATER AT WHITEFACE MOUNTAIN, NY

Volker A. Mohnen

Atmospheric Science, SUNY, Albany NY USA 12222

1. INTRODUCTION

The Atmospheric Sciences Research Center has initiated in 1978 cloud chemistry measurements at the summit of Whiteface Mountain (1487 meters). Initially the cloud chemistry experiments were carried out on an exploratory basis to design and test cloud collectors and sampling strategies, but since 1982, activities have been substantially increased with the objective to better understand the physical, chemical and meteorological factors that influence the inorganic chemical composition of cloud water and to establish a chemical climatology for cloud water (Mohnen and Kadlecek, 1989).

2. CLOUD PHYSICAL DATA

The data sources considered for estimating cloud frequencies for the "warm" season (May 1-October 31) at Whiteface Mountain are the U.S. Air Force Real-Time Nephanalysis (RTNEPH) archives, and site-specific mountain cloud measurements (optical cloud detector (OCD) (Mallant et al., 1989) readings and relative humidity measurements). Investigation of low-cloud characteristics using RTNEPH data base 1985-87 show a median cloud base height within the Appalachian Mountain region of between 800-1000 m (Fig. 1). The specific results for Whiteface Mountain are shown in Figure 2. Direct observations of cloud base height reveals a median cloud base height of 1100 m at Whiteface (Fig. 3).

Cloud droplet size distribution and cloud liquid water content (LWC) have been measured using an FSSP and a gravimetric technique based on droplet collection on a special filter cartridge (Valente et al., 1989). The data from Whiteface Mountain suggest a relationship between size distribution mode and LWC as shown in Figure 4. Extensive studies of droplet size distributions have been made at Great Dunn Fell in Great Britain (Caruthers and Choularton, 1986); these results provide additional evidence for a droplet-LWC relationship and for a similarity in size distribution statistics for the prevailing cloud types at Whiteface Mountain, namely stratus and stratocumulus.

The hourly averaged cloud LWC for 1987-88 are summarized in Table 1:

Table 1

LWC	1987	1988
Mean	0.39	0.44
Standard Deviation	0.22	0.40
Median	0.36	0.36

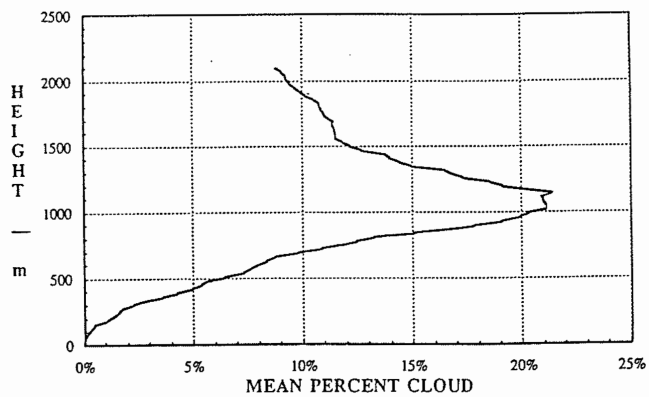

Fig. 1. Mean probability of low cloud (< 2.1 km) as a function of elevation for the northern Appalachian Mountain range (Virginia to Canada), summer 1986 (adapted from Bailey et al., 1989).

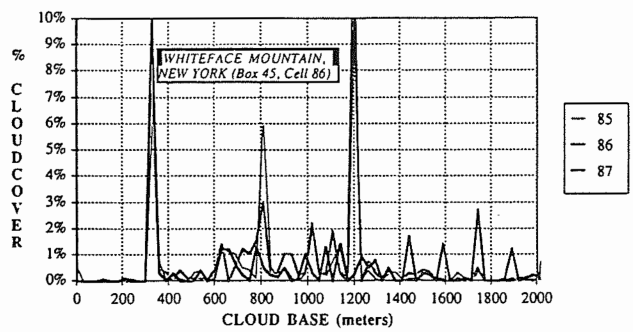

Fig. 2. Frequency of occurrence for cloud base heights for the RTNEPH grid cell (47 km by 47 km) nearest Whiteface Mountain, NY, over three consecutive summers. Dominant cloud base heights were at 330 m (ground fog), 800 m, and 1200 m (adapted from Bailey et al., 1989).

3. CLOUD SYNOPTIC DATA

Six synoptic-type cloud events characterize most of the cloud chemistry observed at Whiteface Mountain. Four are associated with the main sectors of a cyclone (Table 2):

The post-cold frontal type (3) and warm-sector synoptic type (4) make up almost two thirds of total cloud hours (Table 2).

Trajectories were obtained from a mixed-layer model (Heffter, 1980; Kahl and Samson, 1988) and used to describe the fraction of hours within each cloud event that the air was located

Table 2

Synoptic Type	1986-88 Average
1 - pre-warm frontal clouds associated with low-level easterly winds	16.5%
2 - northwest-sector-of-cyclone clouds occurring in direct response to intensifying circulation at low levels	5.8%
stationary front	0.3%
cut off low aloft (SW to NW)	3.4%
cut off low aloft (S to E)	1.4%
3 - post-cold-frontal clouds resulting from destabilization of the atmosphere due to cold advection	32.4%
4 - warm-sector synoptic type clouds representing the southeast (SE) sector of the cyclone with characteristics such as high dew points, evening convection, and a potential for nighttime orographic cloud	30.7%
5 - easterly low-level flow associated with circulation around high pressure off the coast	4.0%
6 - cap cloud of mountain cloudiness in which no important synoptic scale features were apparent, while local airport observations had high cloud bases	5.5%

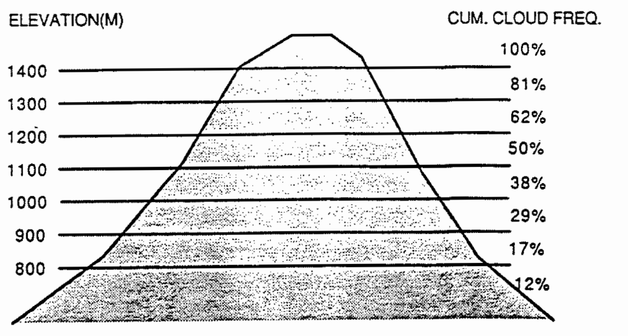

Fig. 3. Cumulative percent of cloud hours with cloud base heights less than the given elevation at Whiteface Mountain, NY, for June-October 1986-1987 from field observer data. (Total cloud impaction frequency at the summit = 42% of all hours.)

in each of the sectors of interest (NW/N, E, SW) over 36 hours and a variable that describes the length of the trajectory path.

4. CLOUD CHEMICAL DATA

The hourly chemical data are aggregated into events and subevents for both precipitating and non-precipitating clouds to reflect changing meteorological conditions. A statistical model, ANOVA, is used for the primary analysis of cloud water chemistry as function of air mass type/origin (Vong et al., 1990). ANOVA allows the determination of class differences with associated probabilities for individual chemical species. Table 3 presents the means for each cloud type and synoptic class.

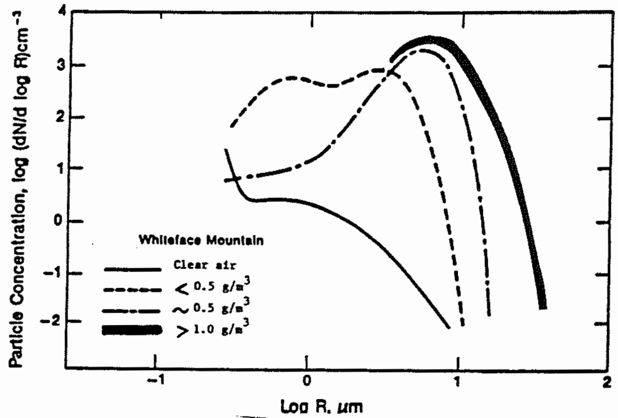

Fig. 4. Cloud droplet size distributions from Whiteface Mountain, NY, calculated by integrating over individual size distributions and grouping the distributions into categories by LWC (< 0.5, 0.5-1.0, > 1.0 g/m^3) and by clear air (adapted from Mohnen, 1987).

Warm-Sector (4) and cap clouds (class 6) events had cloud water concentrations that were significantly higher than concentrations of post-cold front (class 3), pre-warm-frontal (class 1), easterly (class 5) and other (class 2) clouds. Warm-sector events with trajectories from the Ohio Valley had higher concentrations than warm-sector events with any other trajectory, but the differences were not significant. The other major ions H^+, NH_4^+ and NO_3^- were very similar to the SO_4^- ion with respect to synoptic type, trajectory and cloud type. Higher ion concentrations are anticipated because the concentrations of precursor substances SO_2 and aerosol sulfate as well as the oxidants H_2O_2 and O_3 are significantly higher in warm sector air masses arriving at Whiteface Mountain. Higher ion concentrations in cap clouds are due to their stationary nature which enhances scavenging of gases, aerosols and oxidants. Substantial variation remained within each synoptic class which is to be expected because important variations in gas phase and aqueous phase chemical processes, scavenging, etc. can not be described in the synoptic-trajectory classification scheme. For example, the height of the sampling site above cloud base affects LWC and therefore aqueous phase concentrations.

The elevational variation in cloud water concentration was measured simultaneously at two Whiteface Mountain locations: WFM-1 (summit, 1483 m) and WFM-2 (1250 m). The results are shown in Table 4 for the four major ions.

Table 4. Ion Concentrations (μeq/L) for Simultaneously Collected Cloud Water Samples from Precipitating and Nonprecipitating Clouds for 1987-1988.

Ion	Average	Std Dev	Average	Std Dev
H^+	122	165	218	331
SO_4^{2-}	79	102	151	217
NO_3^-	48	66	85	120
Cl^-	3	4	7	10
NH_4^+	74	88	142	186

The mean concentrations for all four ions at the lower site are nearly twice those recorded at the summit. Figure 5 presents the differences in SO_4^- concentration for the simultaneous samples from the two sites (calculated as $[SO_4^{2-}]$ at WFM-2 minus $[SO_4^{2-}]$ at WFM-1). By converting the original concentrations to differences between the two sites, the variation associated with synoptic meteorology is removed from the results, thereby allowing the elevational effect to emerge. Despite the large variability at each site displayed in Table 4, during 92% of the sampled hours the site at lower elevation received cloud water with higher concentrations of SO_4^{2-} than the summit. Similar results are obtained for the other three ions.

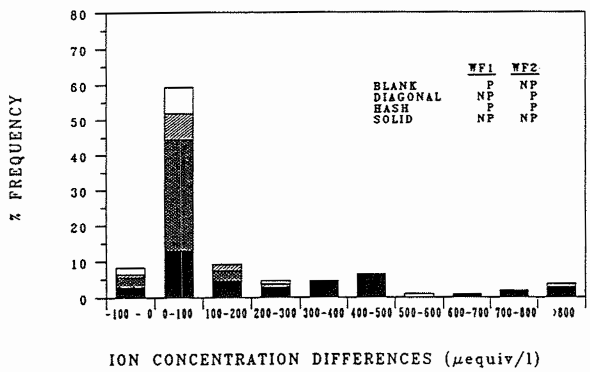

Fig. 5. Frequency of occurrence of the differences in SO_4^{2-} concentrations for the two Whiteface sites (calculated as $[SO_4^{2-}]$ at WF2 minus $[SO_4^{2-}]$ at WF1) for simultaneous, hourly samples. Includes Precipitating (P) and Nonprecipitating (NP) clouds (Vong et al., 1990).

5. CLOUD CHEMISTRY AND ATMOSPHERIC TRACE SUBSTANCES

The analysis of atmospheric gases and aerosols measured during cloudy and clear air conditions showed a similar strong relationship to synoptic conditions as was found for cloud water only. The results of the statistical analysis is shown in Table 5 confirming again that pollutants such as aerosol sulfate, sulfur dioxide, and ozone are highest in the warm sector.

Hydrogen peroxide does exhibit a correlation with ozone only at high ozone concentrations, i.e., above 60 ppb ozone as shown in Figure 6. There are, however, a few "outliers", which all occurred during an event of July 18-20, 1987. During this time, Whiteface was in the warm sector with southerly flow. The sudden rise in H_2O_2 concentration, ozone and SO_2 between midnight and 7 AM represents a clear example of long range transport and is not a result of local H_2O_2.

6. SUMMARY

Air mass type and trajectory have been found to explain significant variability in observed cloud water chemical concentrations. Southwesterly trajectories were consistently associated with high chemical concentrations of SO_4^{2-}, NO_3^-, H^+ and NH_4^+ in cloudwater associated with the warm sector of a cyclone, lower concentrations occur during easterly (marine) flow or post frontal cloud events. It is concluded that synoptic-trajectory classes can be used to describe differences in the transport and mixing of aerosol and gases that lead to differences in ion concentrations observed for individual cloud events and subevents.

7. REFERENCES

Bailey, B.H., M.J. Markus and P. Samson, 1989. Appalachian cloud climatology based on real-time nephanalysis archive data. MCCP Report prepared by Associated Weather Services, Inc., for the Mountain Cloud Chemistry Project, Albany NY.

Caruthers, D.J. and J.W. Choularton, 1986: The micro-structure of hill cap clouds. Quarterly J. Royal Meteorological Society, 112, 113-129.

Heffter, J.L., 1980. Air Resources Laboratory Atmospheric Transport and Dispersion Model (ARL-ATAD) NOAA Tech. Mem. ARL-81, Air Resources Laboratory, Silver Spring, MD.

Kahl, J.D. and P.J. Samson, 1988: Trajectory sensitivity to rawinsonde data resolution. Atmos. Environ. 22, 1291-1299.

Mallant, R.K.A.M., K. Elsholz and B. Bailey, 1989: Fog detection with a low-cost, forward-scattering device, pp. 221. In: Proceedings of the Symposium on the Role of Clouds in Atmospheric Chemistry and Global Climate, Jan. 30-Feb. 3, 1989, Anaheim, CA. American Meteorological Society.

Mohnen, V.A., 1987. Droplet size spectra from Whiteface Mountain Report to MCCP management, State University of New York, Albany NY.

Mohnen, V.A. and J.A. Kadlecek, 1989: Cloud chemistry research at Whiteface Mountain. Tellus, 41B, 79-91.

Valente, R.J., R.K.A.M. Mallant, S.E. McLaren, R.S. Schemenauer and R.E. Stogner, 1989: Field intercomparison of ground based cloud physics instruments at Whitetop Mountain, Virginia. Atmos. Oceanic Technol. 6, 396-406.

Vong, R.J., B. Bailey, M. Markus and V.A. Mohnen, 1990. Factors governing cloud water composition in the Appalachian Mountains. Tellus 42B, 435-453.

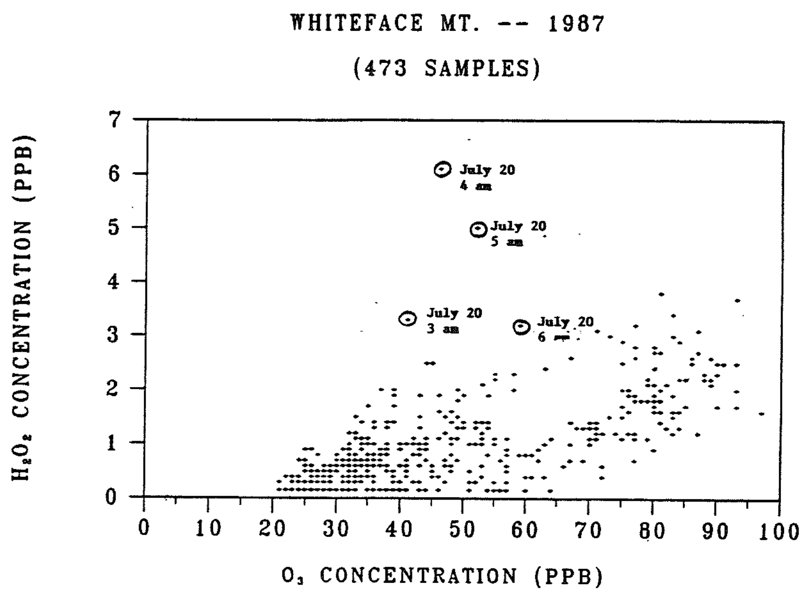

Fig. 6. Gas phase hydrogen peroxide concentration versus ozone concentration. Note that outliers for July 20 are associated with long-range transport (pre-warm front, southwest sector).

Table 3. **Means of Cloud Water SO_4^{2-} Concentrations (μeq/L) for Synoptic-Trajectory Classes and Cloud Types for 1986-1988, Back-transformed from a Cube Root Scale[a]**

Synoptic-Trajectory Class[b]										Mean Over All Hours	Cloud type[c] mean	
Location	wf[1]	o[2]	cf[3,a]	cf[3,b]	ws[4,c]	ws[4,d]	ma[5,e]	ma[5,f]	cap[6]	(NP & P)[c]	P clouds	NP clouds
Whiteface-1 NY	110[d] (175)[e]	16 (72)	20 (59)	76 (217)	286 (158)	218 (67)	60 (24)	281 (17)	537 (23)	128 (912)	77 (327)	165 (585)

[a]Vong et al. (1990).
[b]Synoptic Trajectory Classes: wf[1] -- pre-warm-frontal; o[2] -- "other" synoptic types; cf[3,a] -- post-cold-frontal, NW/N trajectory; cf[3,b] -- post-cold-frontal, not NW/N trajectory; ws[4,d] -- warm sector, Ohio trajectory; ws[4,c] -- warm sector, not Ohio trajectory; ma[5,e] -- marine flow, E trajectory; ma[5,f] -- marine flow, not E trajectory; cap[6] -- cap cloud.
[c]P, precipitating; NP, nonprecipitating.
[d]SO_4^{2-} concentration in cloud water; mean values (μeq/L)
[e]Number of hours (in parenthesis) for synoptic-trajectory classes and cloud types.

Table 5. Cloud Chemistry According to Synoptic Classification.

	Aqueous Phase [μeq/L] SO_4^{2-}	NO_3^-	H^+	NH_4^+	Aerosol [$\mu g/m^3$] Sulfate	Gases [ppb] H_2O_2	SO_2	Ozone
Warm Sector	203 (668 max)	130 (632 max)	134 (1288 max)	181 (652 max)	7.18 (32 max)	0.85 (2.8 max)	2.4 (18 max)	57 (133 max)
Warm Sector with stagnation upwind	214 (1112 max)	190 (1344 max)	335 (1412 max)	226 (920 max)	13.61 (32 max)	1.48 (3.8 max)	2.3 (20 max)	70 (135 max)
All Other Sectors	78 (547 max)	61 (752 max)	320 (1778 max)	80 (770 max)	3.37 (45 max)	0.61 (6.1 max)	0.8 (14 max)	42 (127 max)

The influence of entrainment-induced variability of cloud microphysics on the chemical composition of cloudwater

Chris J. Walcek, Elvira Brankov and Jennifer L. Carlstead

Atmospheric Sciences Research Center
State University of New York, 100 Fuller Rd., Albany, NY 12205 U. S. A.

1. INTRODUCTION

Numerous observations of clouds show that liquid water content, temperature and updraft velocity exhibit considerable variability and are all positively correlated over spatial scales of 10's of meters of less (e. g. Hill and Choularton, 1985). Much of this variability results from the heterogeneous nature of entrainment of dry, cloud-free air into a moist plume of cloudy air. Without entrainment, air within a cloud updraft rises adiabatically, and thus contains a high condensed water content, temperature, and upward velocity. When cooler and dry stagnant air is entrained into a rising cloudy parcel, its upward velocity is immediately reduced, and its condensed water is evaporated, leading to cooling. Observations of fine-scale cloud structure suggest that each point in a cloud has undergone a particular entrainment history, with some points undergoing considerable greater entrainment than other points. Points with the highest degree of entrainment have the lowest water contents, temperatures, and upward velocities.

Classical, 1-dimensional models (Warner 1970) of cloud dynamics assume that air entrained into a cloud uniformly dilutes into the entire cloud volume at the level where entrainment occurs. More sophisticated 2- and 3-dimensional cloud models use eddy diffusion coefficients to characterize entrainment of noncloudy air into a cloud updraft. This approximation usually produces clouds that contain relatively undiluted air near the center of the cloud, and regions of successively greater dilution and entrainment towards the outer edge of the cloud. As noted previously, measurements show that entrainment is far from a continuous or uniform process. Observations show nearly random variations of water content along a particular horizontal cloud cross section, with regions of nearly-adiabatic air lifted from below cloud base interlaced with numerous more heavily entrained regions characterized by significantly lower water contents, temperatures and vertical velocities.

Most models of cloudwater chemistry cannot resolve the fine structure of entrainment-induced fluctuations of parameters such as liquid water content, and implicitly assume that entrainment of air from outside a cloud leads to a uniform mixture of momentum, heat, buoyancy, trace chemicals and water substance within the numerical grid volume simulated by the model. Fig. 1 shows schematically the approximation that most models of cloud chemistry make by neglecting the fine-scale structure of cloud microphysics. In this study, we calculate the chemical composition of a cloudy "parcel" by subdividing the parcel into a distribution of mixtures of dry environmental air and initially adiabatic cloudy air. The resulting cloud chemical model simulates the chemical composition of numerous cloudy parcels composed of varying degrees of entrained dry environmental air. We then compare the acidity and sulfate formation rates aggregated over numerous parcels with a simpler model that assumes that entrainment produces a single, uniform cloudy parcel characterized with a single water content, temperature, and chemical composition.

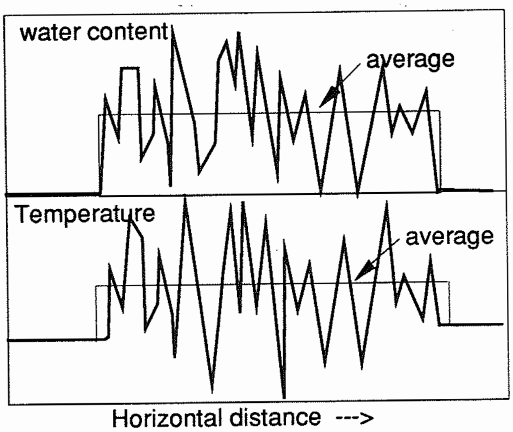

FIG. 1. Schematic of the typical variation of water content and temperature within a cloud traverse. In this study, we compare and contrast chemical properties of clouds that use averaged meteorological conditions with chemical properties calculated using fluctuating meteorological conditions within cloudy parcels.

2. ENTRAINMENT AND MICROPHYSICS

In this study, we assume that small-scale variations in cloud liquid water content are caused by discrete fluctuations in the degree of entrainment experienced by the turbulent "swirls" of cloudy air as they mix with their surrounding environment. Higher water content regions of turbulent swirls represent regions that have been relatively "protected" from mixing with dry, cloud-free air, while small regions also become intertwined within cloudy air that actually contain no condensed water since the entrainment of larger amounts of dry air has totally evaporated the liquid water in the originally cloudy air.

For the following analysis, we assume that the amount of entrainment that a particular point of cloudy air has experienced can be quantified in terms of the entrainment fraction (f_o) of dry, noncloudy air that is present in a mixture of air lifted adiabatically from cloud base:

$$f_o = \frac{m_e}{m_c + m_e} \tag{1}$$

where m_c is the mass of air lifted from below cloud base within a discrete volume of cloudy air, m_e is the mass of air entrained into the discrete cloudy volume element. The sum $m_c + m_e$ is the total cloudy mass. At any point in a cloud, $0 \le f_o \le 1$. Points in a cloud where $f_o = 0$ correspond to those regions that have been lifted adiabatically from below cloud base to a particular level in the cloud without any mixing. Regions where $f_o = 1$ correspond to areas of purely dry environmental air outside the cloud that may be entrained into the cloud, and not actually mixed with the cloudy air on the microscale.

Conservation of water substance will constrain the total water content (q_{tot}) of a parcel of cloudy air, and the vapor plus liquid water content of a mixture of air will equal the mass-weighted proportion of water in the air originating below cloud base (q_{vcb}) and water entrained into the parcel (q_{ve}) at a level above cloud base

$$q_{tot} = q_l + q_v = f_o q_{ve} + (1-f_o) q_{vcb} \qquad (2)$$

For this application, q_{ve} will be an externally-specified parameter, determined by the relative humidity and temperature of the layer of air into which the cloudy parcel rises. The water vapor mixing ratio in the mixture of clear and cloudy air (q_v) will be saturated at the local cloud temperature T_c, or if all the condensed water is evaporated, q_v will be limited by the total water content in the mixture:

$$q_v = \min(q_{vsat}(T_c), q_{tot}) \qquad (3)$$

As air is entrained into the adiabatic cloudy updraft, evaporation of water will lead to cooling. Conservation of energy will then determine the final mixture temperature

$$L(q_{li} - q_l) = C_p(T_i - T) \qquad (4)$$

where T_i is an initial estimate of the parcel temperature, calculated by neglecting evaporation,

$$T_i = f_o T_e + (1-f_o) T_{ad} \qquad (5)$$

Similarly, q_{li} is an initial estimate of parcel water content,

$$q_{li} = (1-f_o) q_{lad} \qquad (6)$$

In (5) and (6), T_{ad} and q_{lad} are the temperature and liquid water content of an air parcel lifted adiabatically from cloud base. Equations (1-6) determine a closed set of constraints from which one can iteratively ascertain the temperature and condensed water content after specifying f_o, the adiabatic cloud temperature and water content, as well as the relative humidity and temperature of air outside a cloud that is entrained into the cloudy updraft.

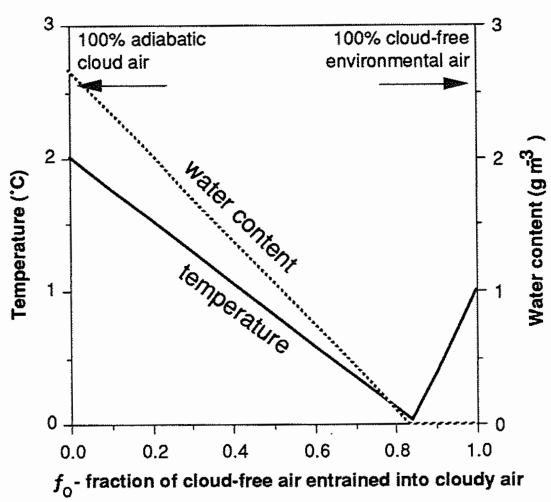

FIG. 2. Water content and temperature of a parcel composed of a mixture of air lifted adiabatically from cloud base mixed with varying proportions of dryer, midtropospheric air. f_o=0 corresponds to parcel lifted adiabatically from cloud base at 900 mb; f_o=1 corresponds to air outside of cloud at 750 mb. Meteorological conditions specified in Table 1.

Fig. 2 shows the water content and temperature of various mixtures of cloudy air lifted adiabatically from cloud base at 900 mb mixed with dry environmental air at 750 mb. The meteorological assumptions in this analysis are shown in part 1 of Table 1. Due to evaporation, many cloudy mixtures become colder than either the cloudy or clear air outside the cloud. Also, liquid water decreases nearly linearly from its adiabatic value as outside air is entrained into the cloud. Liquid water totally evaporates from the mixture of clear and cloudy air when the mixture is ~83% outside air and 17% adiabatic cloudy air. At mixtures with higher proportions of outside air, the temperature approaches the environmental temperature.

For the following analysis, we assume that any volume of cloudy air contains a random distribution of varying degrees of entrainment which can be approximated by assuming a uniform distribution of f_o. For the case shown in Fig. 2, the mean water content of a 50-50 mix of cloudy and clear air is 1.14 g m^{-3}, approximately 42% of the adiabatic water content.

3. AQUEOUS CHEMISTRY

We now consider the effects of entrainment on the concentrations of several soluble trace species and chemical reactivity of SO_2 with O_3 and H_2O_2 in cloudwater.

In cloudwater, the following ion balance will be continuously maintained:

$$[H^+] + [NH_4^+] = 2[SO_4^=] + [NO_3^-] + [HSO_3^-] + [HCO_3^-]$$

where the bracketed quantities represent concentrations of these ions in cloudwater (moles liter^{-1}). Concentrations of these ions can be derived from the following equilibrium and solubility relationships:

$$
\begin{array}{lll}
SO_2(g) & \leftrightarrow SO_2H_2O & \\
SO_2H_2O & \leftrightarrow HSO_3^- & + H^+ \\
CO_2(g) & \leftrightarrow CO_2H_2O & \\
CO_2H_2O & \leftrightarrow HCO_3^- & + H^+ \\
NH_3(g) & \leftrightarrow NH_3H_2O & \\
NH_3H_2O & \leftrightarrow NH_4^+ & + OH^- \\
HNO_3 & \leftrightarrow NO_3^- & + H^+ \\
O_3(g) & \leftrightarrow O_3(aq) & \\
H_2O_2(g) & \leftrightarrow H_2O_2(aq) & \\
H_2SO_4(\text{part}) & \rightarrow SO_4^{2-} & + 2H^+
\end{array}
$$

Superimposed on these rapidly-established equilibria are the following irreversible reactions oxidizing SO_2. Temperature-dependent rate expressions for these reactions are taken from Jacob et al., 1989.

$$
\begin{array}{ll}
S(IV) + H_2O_2 & \rightarrow H_2SO_4 \\
S(IV) + O_3 & \rightarrow H_2SO_4
\end{array}
$$

For this preliminary assessment of the effects of entrainment, we consider only the instantaneous rate of SO_2 oxidation, based on an initial specification of the concentrations of all relevant pollutant concentrations. Pollutant concentrations within mixtures of clear and cloudy air (C_{mix}) are given by

TABLE 1: Meteorological and Chemical Conditions

parameter	in undiluted cloud	in entrained air
	Part 1 - meteorological conditions	
Temperature	2 °C	1 °C
Pressure	750 mb	750 mb
Liquid water content	2.66 g m^{-3}	0
Relative humidity	100%	80%
	Part 2 - chemical conditions	
SO_2	1 ppb	0 ppb
H_2SO_4	1 ppb	0 ppb
HNO_3	0.5 ppb	0 ppb
NH_3	1 ppb	0 ppb
O_3	50 ppb	50 ppb
H_2O_2	0.1 ppb	0.1 ppb

$$C_{mix} = C_o f_o + (1-f_o)C_{cb} \qquad (7)$$

where C_o is the concentration of trace gas in the air entrained into the cloud, and C_{cb} is the concentration of trace gas in the air lifted from cloud base. Concentrations of various trace species are listed in Part 2 of Table 1. We assume that air lifted from below cloud base is relatively polluted, while air outside the cloud at 750 mb contains only oxidants H_2O_2 and O_3. CO_2 concentration is 350 ppm.

Fig. 3 shows the concentration of various ions in cloudwater as a function of the fraction of noncloudy air entrained into the parcel. For highly soluble ions ($SO_4^=$, NO_3^-, H_2O_2), as the liquid water content decreases, concentration of these ions in cloudwater increases. This effect is somewhat moderated by the entrainment of air which has no sulfate or nitrate into the parcel at higher entrainment fractions. The HSO_3^- concentration decreases with increasing entrainment because this ion's concentration is inversely proportional to the hydrogen ion concentration, and also because less SO_2 is available to dissolve as the mixture becomes cleaner as greater amounts of clean air are entrained into the cloudy parcel. While not shown on this figure, the concentration of dissolved O_3, remains constant for all entrainment fractions.

Changes in the liquid water content, temperature, and dissolved trace species concentrations will all affect the rate at which SO_2 is oxidized into sulfuric acid. As shown in Figs. 2-3, these parameters will be different at each location in a cloud depending on the degree of entrainment experienced by a particular point within a cloud. Fig. 4 shows the instantaneous SO_2 oxidation rate as a function of the fraction of dry environmental air entrained into a cloudy parcel. Oxidation rates are proportional to the liquid water content, and do not occur in mixtures where the water is totally evaporated. Due to its strong dependence on hydrogen ion concentration, the oxidation rate due to ozone exhibits a nonlinear dependence on the entrainment fraction.

If we assume a uniform distribution of entrainment mixtures within a particular cloudy volume, we can compute the mean temperatures and concentrations of the parameters that influence SO_2 oxidation rates by averaging the data shown in Figs. 2 - 3. Using the data in Fig. 2, the mean

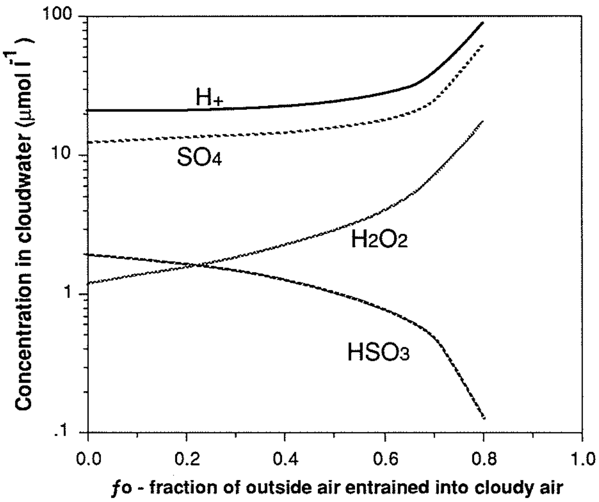

FIG. 3. Concentration of various ions and dissolved trace gases in cloudwater (moles liter^{-1}) at 750 mb as a function of the proportion of dry midtropospheric air entrained into a parcel lifted adiabatically from cloud base. Meteorological and chemical conditions specified in Table 1.

water content and temperature of a 50-50 mix of adiabatic cloudy air and dry environmental is 1.14 g m^{-3} and 1°C. We can compute the mean SO_2 oxidation rate from these averaged meteorological and chemical parameters. A more exact method of computing SO_2 oxidation rates entails actually calculating the SO_2 oxidation rate within each "microparcel" of the cloud, and averaging the rate over the distribution of these different entrainment regions.

In Fig. 4, the average SO_2 oxidation rate for a uniform distribution of entrainment fractions (i. e. a 50-50 mix of cloudy and clear air) is 0.37 ppb h^{-1}. If we only used the average temperature and pollutant concentrations to compute SO_2 oxidation rates, the mean oxidation rate is 0.30 ppb h^{-1}. Thus, averaging of the small-scale microphysical structure leads to an underestimate of the actual SO_2 oxidation rate by a factor of 1.23. The magnitude of the error introduced by averaging the small-scale cloud variability is a function of the

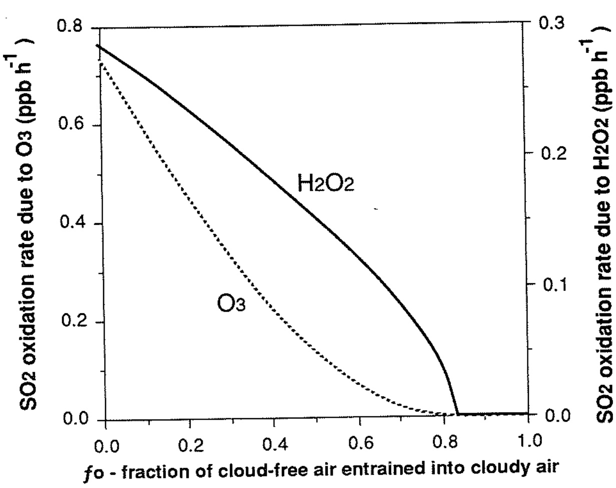

FIG. 4. SO_2 oxidation rate within cloudwater as a function of the proportion of midtropospheric air entrained into a parcel lifted adiabatically from cloud base. Meteorological and chemical conditions specified in Table 1.

mean cloudwater pH and the amount of H_2O_2 relative to O_3 in the cloud. We now present results for a wide range of conditions. We assume that ammonia always equals sulfate and HNO_3 is 1/2 of the sulfate. SO_2 is always 1 ppb.

Fig 5 shows the ratio of the "true" SO_2 oxidation rate to the approximate SO_2 oxidation rate over wide range of sulfate and H_2O_2 concentrations. The "true" oxidation rate is calculated by averaging the SO_2 oxidation rate within each cloudy entrainment mixture. The "approximate" oxidation rate is calculated using only the mean of the meteorological and chemical concentrations within a heterogeneous mix of chemical and meteorological regions in a cloud. For both methods of estimating SO_2 oxidation, the temperature, water content, and pollutant concentrations are identical, but in the more exact method, these chemical and meteorological parameters are allowed to fluctuate about the mean according to the hypotheses outlined in Section 2-3. This figure shows that errors of up to a factor of 1.6 can occur at relatively low H_2O_2 concentrations under moderately polluted conditions.

Under very clean conditions (sulfate < 0.1 ppb), the chemical composition of the cloudwater is determined by equilibrium with CO_2 only, and thus the variation of acidity with water content and entrainment fraction shown in Fig. 3 is minimal. Since cloudwater composition does not fluctuate across the spectrum of entrainment fractions, the SO_2 oxidation rate is a fairly uniform function of the amount of entrainment experienced at any point in a cloud. At high H_2O_2 concentrations (H_2O_2 > 0.1 ppb), H_2O_2 is the dominant oxidant of SO_2, and as shown in Fig. 4, this oxidation rate is fairly linear function of the amount of entrainment experienced by any point in a cloud. Thus, there is little error introduced by averaging the microstructure of the cloud. Under very highly polluted conditions and low H_2O_2 concentrations, the error decreases with increasing sulfate since H_2O_2 becomes more important in the oxidation of SO_2 as acidity (proportional to sulfate) increases.

4. CONCLUSIONS

Depending on the chemical composition of the cloudy air and the air entrained into the cloud, we find that significant errors can be introduced into calculations of in-cloud SO_2 oxidation rates if the small-scale microstructure of the cloud is ignored. Individual regions of cloudy air that are exposed to a high degree of entrainment will have considerably lower liquid water contents and higher acidities. The chemical formation rate of sulfates in these parcels is significantly lower than other regions of the cloudy that experience less entrainment. Differences in the acidity across the spectrum of cloudy mixtures can lead to a significant bias in the estimate of sulfate formation rates, especially when O_3 oxidation is the dominant sulfate production pathway. These results suggest that existing cloud chemical models that ignore small-scale (10's of meters or less) entrainment-induced fluctuations of liquid water content can under some conditions significantly underestimate sulfate formation rates due to the nonlinear relationship between sulfate formation rate and cloudwater acidity, which is predominantly influenced by liquid water content and entrainment.

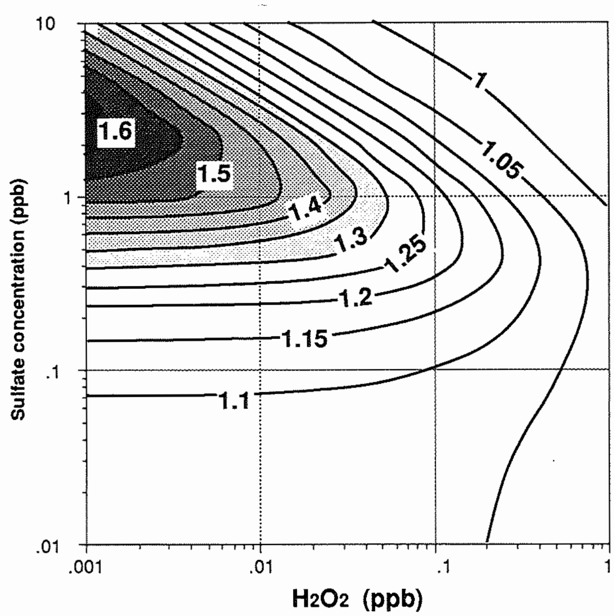

FIG. 5. Ratio of the SO_2 oxidation rate calculated over a uniform distribution of mixtures of various entrainment fractions relative to the SO_2 oxidation rate calculated using only the mean temperature, water content, and pollutant concentrations of athe same distribution of cloudy entrainment mixtures.

Acknowledgements. The authors are grateful to the U. S. National Science Foundation for providing partial support for the research presented here.

REFERENCES

Jacob, D. J., 1986: Chemistry of OH in remote clouds and its role in the production of formic acid and peroxymonosulfate. *J. Geophys. Res.*, **91**, 9807-9826.

Hill, T. A. and T. W. Choularton, 1985: An airborne study of the microphysical structure of cumulus clouds. *Quart. J. R. Met. Soc.*, **111**, 517-544.

Warner, J., 1970: On steady-state one-dimensional models of cumulus convection. *J. Atmos. Sci.*, **27**, 1035-1040

A 2-D SPECTRAL MODEL SIMULATION ON THE SCAVENGING OF GASEOUS AND PARTICULATE SULFATE BY A WARM MARINE CLOUD

Andrea I. Flossmann

Institute for Atmospheric Physics, Joh. Gutenberg University, D-6500 Mainz, F.R.G.

1. INTRODUCTION

The production of sulfate in clouds is known to contribute significantly to the acidification of precipitation. Sulfate enters the cloud constituents not only through the scavenging of sulfate containing aerosol particles but also through the uptake of SO_2 from the gas phase and subsequent oxidation mechanisms in the liquid phase. All these different processes are known to be dependent on the size of the aerosol particle as well as on the size of the cloud constituent.
In an attempt to shed light on the various occuring and interacting processes in cloud chemistry, we have developed a scavenging model including spectral warm microphysics and scavenging of particulate and gaseous pollutants (Flossmann *et al.*, 1985; Flossmann *et al.*, 1987).
We have evaluated this scavenging model in a two dimensional framework for the simple case of a warm precipitating cloud in a marine environment and have studied its scavenging properties for an idealized aerosol particle spectrum consisting only of $(NH_4)_2SO_4$ particles and NaCl particles (Flossmann, 1991).
In order to make a first estimate on the relative contribution of gaseous sulfate as compared to the particulate sulfate we have extended this model to include the gas uptake of SO_2 and the subsequent oxidation. As oxidizing agents only H_2O_2 and O_3 are considered which are simultaneously scavenged from the gas phase. To keep the system as simple as possible no further processes are considered, however, more complex studies are planned for the future.

2. THE PRESENT MODEL

As discussed in detail by Flossmann and Pruppacher (1988) the basic dynamic framework employed in the present study is a two-dimensional slab-symmetric version of the three-dimensional model developed by Clark and Coworkers (e.g. Clark, 1977, 1979). The detailed microphysical and scavenging model is discussed in Flossmann *et al.* (1985) and the extension to the scavenging of two different types of aerosol particles is described in Flossmann (1991). The calculation of gas scavenging in the framework of the warm spectral microphysics is extended from Flossmann *et al.* (1987) to include now, apart from the S(IV) and S(VI) species, also the processing of H_2O_2 and O_3. The following chemical reactions are considered for pH<5.5:

$$[S(IV)]_l = [SO_2 \cdot H_2O] + [HSO_3^-]$$

$$[S(VI)]_l = [SO_4^{2-}] + [HSO_4^-]$$

Drops smaller than 30µm are assumed to be in Henry' equilibrium with the environmental SO_2 concentration:

$$[S(IV)]_l = K_h (1 + K_1/[H^+]) c_g$$

For an explanation of the symbols and the value for the Henry's constant and the dissociation constants see Flossmann *et al.*(1987).
For the drops larger than 30µm a time dependent mass transfer is considered:

$$d[S(IV)]_l/dt = 3\ D_g/a\ (c_g - c_s)/d_g$$

Parallel to the SO_2 also H_2O_2 and O_3 are taken up by the cloud drops. For drops smaller than 7µm Henry's equilibrium is assumed for H_2O_2 while for the larger drops also the time dependent mass transfer is considered. Due to the low Henry's constant, O_3 is for all drop sizes assumed to be in Henry's equilibrium.

H_2O_2 and O_3 act as oxidizing agents transforming $[S(IV)]_l$ to $[S(VI)]_l$:

$$-d[S(IV)]_l/dt=(k_1[H^+][H_2O_2][HSO_3^-])/(1+k_2[H^+])$$

and

$$-d[S(IV)]_l/dt=k_3[SO_2\cdot H_2O][O_3]+k_4[HSO_3^-][O_3]$$

(Seinfeld, 1986). In presence of $(NH_4)_2SO_4$ the equation for electroneutrality is

$$[NH_4^+]+[H^+]=[HSO_3^-]+[HSO_4^-]+2[SO_4^{2-}]$$

this results in a cubic equation for $[H^+]$ (see Flossmann *et al.*, 1987) from which we calculate the pH:

$$pH=-\log[H^+]$$

3. INITIAL CONDITIONS

The model was initialized with a warm cloud sounding taken at Day 261 (18 Sept. 1974) of the GATE campaign at 12 GMT. Our 2-D model domain was oriented in the north-south, as this was the main wind direction. In the lower 2km the wind was southerly as well as above 6km. In between the wind was northerly. The initial aerosol particle spectrum was assumed to be of maritime type consisting of a superposition of three log-normal distributions. The small modes were assumed to consist of $(NH_4)_2SO_4$ particles and the large mode was set to hold only NaCl particles. The particle spectra were assumed to decrease exponentially with height taking into account that practically no NaCl exists above 2.5km.
The SO_2, H_2O_2 and O_3 concentrations were assumed to 0.5ppb, 0.5ppb and 30ppb, resp., uniformly in the entire computational domain in agreement with marine observations.
The model covers a domain of 10km in the vertical and 20km in the horizontal. The grid spacings were dz=200m and dx=400m resulting in 52*52 grid points, and the time step was dt=5sec.

4. RESULTS

The calculations started at 12 GMT. After 26 min of model time a cloud had formed. After 14 min of cloud life time the first rain drops fell from cloud base and after 19 min of cloud life time the first rain reached the ground. The evolution of the dynamical variables of the cloud as well as the microphysical and aerosol scavenging properties were discussed in detail in Flossmann (1991).
In addition to the mass of ammonium sulfate and soldium chloride also the newly considered chemical species were followed in the air, inside the drops in the cloud, and inside the drops which have arrived on the ground. The model also determined the rate at which S(IV) was converted to S(VI) in the cloud drops and the rate at which the pH of the cloud and rain water changed. The relative importance of sulfate formation due to scavenging of particles and due to the uptake and oxidation of SO2 was studied.

5. REFERENCES

Clark, T.L., 1977; A small scale dynamic model using a terrain-following coordinate transformation. *J. Comput. Phys.*, **24**, 186-215.

Clark, T.L., 1979; Numerical simulations with a three dimensional cloud model. *J. Atmos. Sci.*, **36**, 2191-2215.

Flossmann, A.I., 1991; The scavenging of two different types of marine aerosol particles calculated using a two-dimensional detailed cloud model. *Tellus*, **43B**, 301-321.

Flossmann, A.I., W.D. Hall, and H.R. Pruppacher, 1985; A theoretical study of the wet removal of atmospheric pollutants. Part I. *J. Atmos. Sci.*, **42**, 582-606.

Flossmann, A.I., H.R. Pruppacher, and J.H. Topalian, 1987; A theoretical study of the wet removal of atmospheric pollutants. Part II. *J. Atmos. Sci.*, **44**, 2912-2923.

Flossmann, A.I., H.R. Pruppacher, 1988; A theoretical study of the wet removal of atmospheric pollutants. Part III. *J. Atmos. Sci.*, **45**, 1857-1871.

Seinfeld, J.H., 1986; Atmospheric Chemistry and Physics of air pollution. John Wiley Publ., 738pp.

A FIELD STUDY OF THE EFFECTS OF CLOUDS ON CONDENSATION NUCLEI POPULATIONS

T.W. Choularton, K.N. Bower, M.W. Gallagher and J.D.Stancliffe
Physics Department, UMIST, P.O. Box 88, Manchester UK

1. INTRODUCTION

A hill cap cloud which frequently envelopes the UMIST field station on Great Dun Fell has been used as a natural flow through reactor to study (a) The modification of an existing aerosol size distribution by aqueous phase cloud chemistry as the airstream passes through the cloud and (b) The new nucleation and loss by scavenging of very small condensation nuclei which are too small to act as cloud condensation nuclei.

The results of the field experiments are compared to the predictions of a numerical model of these processes in the hill cap cloud. This model has also been used to predict the influence of the aqueous phase cloud chemistry in the hill cap cloud on the radiative properties of stratocumulus clouds forming downwind of the cap cloud.

2. THE CAP CLOUD MODEL

The aim is to consider the effect aqueous phase cloud chemistry has in modifying the cloud condensation nucleus (CCN) spectrum, and to examine the consequences this might have for the microphysical and hence radiative properties of clouds subsequently forming on these modified CCN distributions.

A cap cloud chemistry model is used to investigate the modifications made to the CCN spectrum. A simple 1-D adiabatic model of cloud development is then used to examine the resulting changes made to the cloud droplet effective radius parameter R_{eff} in a typical Stratocumulus (Sc) type cloud.

CAP CLOUD CHEMISTRY MODEL

The model of Bower and Choularton (1991) considers (i) chemistry within specific cloud droplets, (ii) the finite take-up of soluble gases, (iii) limited NO_x chemistry (as HNO_3) and (iv) the effects of dry air entrainment. Only the direct aqueous phase oxidation of S(IV) to S(VI) is considered. Since gas phase oxidation pathways of NO_x are considered to be more efficient than any known aqueous phase oxidation pathways, the gas phase oxidation of NO_x to HNO_3 is assumed to have already occurred prior to entering the cloud parcel in the model.

(a) The Dynamics Model

The complete model computes the microphysical and chemical development of a representative cloud condensation nucleus (CCN) spectrum of embryo cloud droplets as they are subjected to adiabatic cooling, as the air parcel in which they reside travels up and over a hill.

To determine updraughts to be used in the microphysical model, a model of airflow over hills of moderate slope is required. The model used is that of Carruthers and Choularton (1982). This calculates the airflow perpendicular to the long axis of a bell shaped ridge defined by a Hill Function :-

$$f(x) = H \times \left(1 + \left(\frac{x}{L}\right)^2\right)^{-1}$$

x is the horizontal displacement from the ridge axis, H is the height of the hill and L is the half width at half height.

The atmosphere above the ridge is divided into three layers. The cap cloud forms in Layer 1 which approximates to the turbulent boundary layer (assumed to have neutral stability). Layer 2 is a stable capping inversion layer, which is capped by Layer 3 a less stable layer, which is assumed to represent the remaining atmosphere. To calculate the airflow Helmholtz's equation for inviscid flow is solved in each of the three layers (i=1,2,3).

(b) The Microphysics Model

This is based upon a general 1-D adiabatic growth model in which the updraught profile provided by the dynamics model is a function only of z (the cloud parcel follows a mean streamline, along which the vertical and horizontal wind components are known).

A CCN spectrum (of mixed origin) is developed from cloud base at 99% relative humidity to the observation site, set at cloud base on the lee-side of the hill in this exercise. The model considers two types of nuclei, NaCl and $(NH_4)_2SO_4$ which represent maritime and continental distributions respectively. The size and concentration of droplets in each category i, are obtained as a solution to the Kohler equation at 99% relative humidity.

$$-0.01 = \frac{\chi}{r_i} - \frac{\chi\,(r_c)_i^2}{3\,r_i^2}$$

where the critical radii $(r_c)_i$ are calculated from the critical supersaturations $(S_c)_i$ using :-

$$(r_c)_i = \frac{2}{3}\,\frac{\chi}{(S_c)_i}$$

$(S_c)_i$ values are obtained from the typical activity spectrum $N_i=G(S_c)_i^k$ for each aerosol type (where activity spectrum constants G and k are dependant upon aerosol type and set to 100 and 0.7, and 600 and 0.5 for maritime and continental CCN respectively).

The initial CCN spectrum is set up so that not all categories become activated in the subsequent adiabatic ascent. This ensures that the number of cloud droplets generated will not be held artificially low, and so prevents the development of unrealistically large droplets (due to the partition of the available liquid water over too few condensation centres).

(d) The Chemistry Model

This considers the oxidation of S(IV)aq by the oxidants O_3 and H_2O_2. Other oxidants (eg. transition metal catalysed O_2) are not presently included on arguments of timescale and ambient cloud water pH values. The model [1] considers the chemical development within each droplet, and does not assume an instantaneous equilibrium between gas and aqueous phases for all species.

Species present in the gas phase include H_2O_2, O_3, SO_2, NH_3, HNO_3 and CO_2. The solubility of each is determined by Henry's Law. The dissociation reactions of the aqueous gases SO_2 NH_3 HNO_3 and CO_2 are also considered. The solubility and dissociation constants of these reactions are temperature dependent and are recalculated after each timestep. Other ions initially present in solution include Na^+ and Cl^- within maritime categories (inactive ions in this model), and SO_4^{2-} in continental droplets, although SO_4^{2-} is subsequently generated in all droplets due to S(IV) oxidation.

Only O_3 and CO_2 are considered to be in instantaneous equilibrium. The soluble gases NH_3, H_2O_2 and HNO_3, and SO_2 are considered to be taken up at a finite rate by the drops. This take-up rate is given by :-

$$\frac{4}{3}\Pi\lambda\left(\frac{8kT}{M_x\Pi}\right)^{\frac{1}{2}} r\;\frac{N_g - N_{ge}}{\left(1+\left(0.7+\frac{4(1-\alpha)}{3\alpha}\;\frac{\lambda}{r}\right)\right)}$$

where M_x is the molar mass of the gas, λ is the mean free path of a gas molecule, k is Boltzman's constant, α is the accommodation or sticking coefficient, N_g is the number of gas molecules per unit volume and N_{ge} the number per unit volume assuming equilibrium with the liquid phase concentration of the species.

The rate of production of sulphate within each drop size category is given by :-

$$\frac{d}{dt}[SO_4^{2-}] = K_H\,[HSO_3^-]\,[H_2O_2] + K_O\,[HSO_3^-]\,[O_3]$$

where [ ] denotes the concentration of aqueous species (moles/dm^3). K_H and K_O are the oxidation rate constants of H_2O_2 and O_3 respectively. These rate constants are pH and T dependent, and are recalculated after each timestep dt using (from Martin and Damschen (1981) and Maahs 1983):-

$$K_H = 5.2\times10^6\exp\left(-3655.3\left(\frac{1}{T} - \frac{1}{298}\right)\right)\frac{[H^+]}{[H^+] + 0.1}$$

$$K_O = 4.39\times10^{11}\exp\left(-\frac{4131}{T}\right) + 2.56\times10^3\exp\left(-\frac{996}{T}\right)10^{pH}$$

The concentration of hydrogen ions within each cloud droplet is determined by the charge neutrality condition :-

$$[H^+] + [NH_4^+] = [OH^-] + 2[SO_4^{2-}] + [HSO_3^-] + [HCO_3^-] + [NO_3^-]$$

After calculating changes due to absorption, partitioning and reaction, species concentration changes due to parcel expansion and entrainment are considered. The chemistry model is entered after each (0.01s) timestep and new aqueous species concentrations calculated. These are then recalculated as a result of dilution due to droplet growth. The new effective CCN mass within each droplet is also calculated (along with mean values of solute molar mass and Van't Hoff factor) before leaving the chemistry module. From this new values of droplet critical radius and hence critical supersaturation can be calculated, enabling the modified activity spectrum to be generated at any point along the parcels trajectory.

N.B. The chemistry model is activated only when the liquid water content exceeds 0.01gm^{-3}, and only for droplets larger than 0.5 μm radius (to avoid the non-ideal behaviour of high ionic strength solutions). This is true on both the upwind and lee sides of the hill near to cloud base.

THE STRATOCUMULUS CLOUD MODEL :-

A simple 1-D adiabatic growth model is used (as in the cap cloud model), but the updraught W is prescribed and set at a value of 0.5m/s (typical for Sc). The input CCN spectrum is either (i) as input to or (ii) as modified by the cap cloud model. The subsequent development of the CCN spectrum is carried out as in the cap-cloud micro-physics model, and an effective radius parameter R_{eff} is calculated at each timestep. This radius (used extensively when considering the radiative effects of clouds, to parameterise the droplet size distribution) is defined as:-

$$R_{eff} = \sum_i n_i r_i^3 \Big/ \sum_i n_i r_i^2$$

where n_i and r_i are the number concentration and radius of droplets in category i respectively. (NB. The updraught used is considerably lower than the updraught normally generated in the cap-cloud model (~ 2-3m/s), and leads to much lower values of peak supersaturation above cloud base. Hence, for similar CCN input distributions fewer categories are generally able to activate in the Sc cloud.

RESULTS FROM THE MODEL :-

A series of model runs were undertaken to assess the sensitivity of the modification of the CCN spectrum emerging at cloud base on the lee-side of the hill (2-D model)

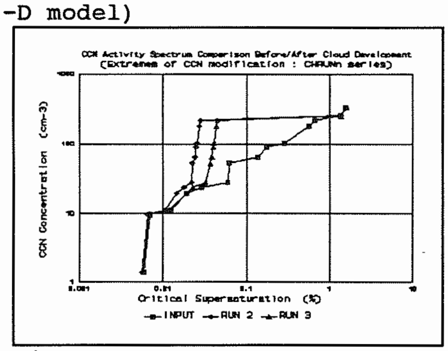

Figure 1

to (i) variations in the chemical input to the model (Table 2), and (ii) to variations in the microphysical input to RUN2 (which generates the largest CCN spectrum modification)

Table 2 :- Gas Phase Input Concentrations (ppbV) (CHRUN series)

Species Conc'n	Run 1	Run 2	Run 3	Run 4	Run 5	Run 6	Run 7	Run 8
SO_2	5	5	2	2	2	2	0	0
NH_3	1	1	1	1	1	1	0.5	0
H_2O_2	1	1	0	0	0.3	0.3	0	0
O_3	30	30	15	15	30	30	15	15
HNO_3	0	1	0	1	0	1	0	0

Figure 1 illustrates the extremes in CCN modification achieved in Runs 2 and 3 and how these compare with the input CCN spectrum (NB. the control runs of 7 and 8 produced spectra which were coincident with the input spectrum). Figure 2 shows the range of CCN modifications produced by runs 1-6.

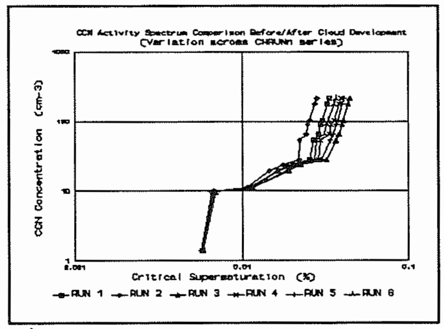

Figure 2

(NB. Standard Model Input :-
cloud base = 400m, T = 278K, p = 990mbar, Ug = 15m/s CCN spectrum : 14 categories (8 maritime, 6 continental) constants G and K as set above,
maritime to continental concentration ratio :- 75 % to 25%.)

Varying the cloud base temperature by ±10K in Run 2 (which produced the maximum CCN modification above) produced less significant changes in the CCN than induced by the effects of chemistry (not shown).

The effects of increasing the number of CCN categories were insignificant in each case, except to smooth the modified CCN distributions obtained. In Figure 3, dN/dlogR verses R plots of both the maritime and continental contributions to the CCN spectra at 99% RH, prior to and following modification by the cap cloud for run 2 with increased (24) CCN categories (14 maritime and 10 continental), are shown. It can be seen that the main effect of modification is to produce a bimodal CN spectrum, when the results are combined with the unactivated sections of the CCN distributions (not shown) which occur to the left of the modified regions.

Figure 4 shows the effective radius profiles generated within the Sc cloud model using both unmodified and the

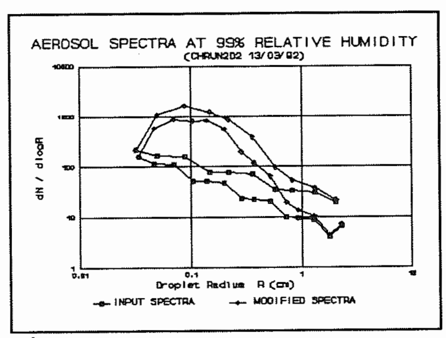

Figure 3

modified CCN distribution of run 2 as input. This models the development of Sc cloud on either side of a hill enveloped by cap clouds. The modified distribution is seen to generate R_{eff} values which are lower than the unmodified case by up to 2μm near to cloud top. This occurs as a result of the increasing ease with which the smaller (and hence most modified) CCN categories are able to activate in the Sc model. The result is reproduced irrespective of the actual modified CCN distribution used as input, and has important consequences for the radiative and hence climatological properties of such clouds.

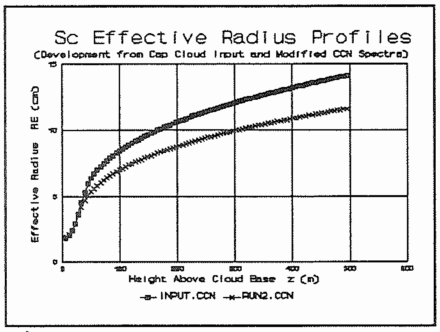

Figure 4

3. THE FIELD EXPERIMENTS

Upstream of the hill cap cloud, below cloud base, the aerosol size distribution was measured in the size range 0.1 um to 2.0 um using a Knollenberg Axial Scattering Spectrometer Probe (ASASP-X). The total concentration of particles in the size range 0.01 um to 0.1um was measured using a Condensation Nucleus (CN) counter. A cascade impactor was used to measure the size resolved chemical composition of the aerosol particles. At the hill summit measurements were made of the cloud droplet size distribution and liquid water content of the hill cap cloud. Samples of cloud water were collected using a passive cloud water collector for later analysis by ion chromatography. At this site measurements of the gas phase sulphur dioxide concentration were made. At the downstream site, below cloud base, the set of measurements from the upstream site was repeated.

4. RESULTS OF THE FIELD STUDIES

Only a fraction of the available data has been analysed at the time of writing. In the case studies analysed no evidence has been found of the fresh nucleation of small particles. Generally the data from the CN counters showed that significant loss of small particles occurred.

Figure 5 shows typical aerosol size distributions from the ASASP-X from upwind and downwind of the hill. This shows a loss of particles smaller than about 0.35 um diameter and substantial growth of larger particles. This size roughly corresponds to the

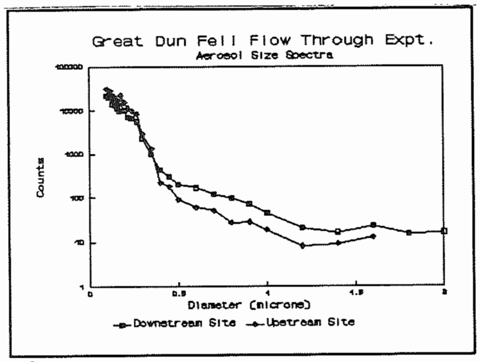

Figure 5

smallest particles that are predicted to be activated during this particular case study. The growth of the larger particles was due to the aqueous phase generation of sulphate. In this case the hydrogen peroxide concentrations were very low so ozone was the principle oxidant.

5. CONCLUSIONS

1. The passage of an airstream through a cap cloud has a marked effect on the aerosol spectrum and can generate a bimodal spectrum.

2. The smallest particles may be generated by gas to particle conversion or lost due to Brownian capture on cloud droplets

3. The effects of CCN modification (eg. in hill cap clouds) lead to a reduction in the critical supersaturations required for activation of the smallest categories (previously unactivated) in less vertically dynamic clouds such as Sc. This leads to the activation of a greater number of droplets in Sc cloud formed on a modified CCN spectrum.

The partition of the same amount of liquid water amongst an increased number of cloud droplets leads to a reduction in the average droplet size, and also of important radiative parameters such as the cloud droplet effective radius R_{eff}. This has important climatological consequences. Slingo 1990, showed that a reduction of R_{eff} from 10μm to 7.9-8.4μm within a G.C.M. was able to completely offset the mean global warming predicted to occur as a result of doubling global CO_2 concentrations.

6. REFERENCES :

Bower,K.N. and Choularton,T.W. *Atmos.Environ*. 25 (1991) 2401-2418.
Carruthers,D.J. and Choularton,T.W. *Q.J.R.Meteorol.Soc*. 108 (1982) 603-624.
Martin,L.R. and Damschen,D.E. *Atmos.Environ*. 15 (1981) 1615-1621.
Maahs,H.G. *J.Geophys.Res*. 88 (1983) 10721-10732.
Slingo,A. *Nature*. 343 (1990) 49-51.

7. ACKNOWLEDGEMENTS

This work was supported by the Natural Environment Research Council and the UK Department of the Environment on contract PECD 7/10/199.

MICROPHYSICAL AND CHEMICAL ASPECTS OF CLOUD FORMATION AT LOW TEMPERATURES

Dennis Lamb

Department of Meteorology
The Pennsylvania State University
University Park, PA 16802, USA

1. INTRODUCTION

The formation of clouds at low temperatures has become a particular concern in recent years. In the upper troposphere, for instance, cirriform clouds are known to contribute to the earth's climate in uncertain ways (Ackerman et al., 1988; Ramanathan and Collins, 1991), while cirrus is thought to help remove water and other trace substances from specific layers of the atmosphere via sedimentation (Danielsen, 1982). In the lower stratosphere, the formation of both ice and chemically enriched clouds in the polar regions has been linked to the depletion of ozone (Toon et al., 1986). The impacts that a possible future fleet of high-speed civil aircraft may have on the chemistry and clouds of the stratosphere are currently debated (Douglas et al., 1991). Noctilucent clouds that form in the particularly cold regions of the atmosphere near the mesopause apparently arise as a consequence of methane oxidation and have been identified as a possible indicator of man's influence on his global environment (Thomas et al., 1989). Such concerns seem to be growing and emphasize the need to understand the processes of cloud formation at a fundamental level.

Cloud formation at low-temperatures differs in several regards from that at higher temperatures. The relatively low temperatures are often associated with substantially lower pressures, so gas-kinetic effects may need to be included in the traditional treatments of aerosol activation and cloud particle growth as the molecular mean-free paths increase in magnitude. At low temperatures, certain trace gases, such as nitric acid, tend to condense out of the air and contribute appreciably to the condensed phase (Toon et al., 1986; Elliott et al., 1990). The presence of such trace chemicals may alter the threshold conditions for phase nucleation and aerosol activation, as well as affect the particle growth rates. A proper understanding of cloud formation at low temperatures demands that we scrutinize our traditional assumptions and introduce appropriate new phenomena into our theoretical treatments when needed.

This paper represents an initial attempt to expand our traditional theories of cloud formation to include the effects of multicomponent chemical equilibria. By way of a specific example, I explore the thermodynamic and kinetic influences that nitric acid (HNO_3) has on aqueous particles, as might apply to the formation of polar stratospheric clouds (PSC). An overview of the microphysical aspects of the problem is presented first, followed by a treatment of the chemical role that nitric acid plays in the activation of sulfuric acid aerosol particles. Subject to verification, it is concluded that the liquid-phase sorption of a soluble trace gas may enhance the formation of clouds under some low-temperature conditions.

2. MICROPHYSICAL CONSIDERATIONS

A fundamental consideration of polar stratospheric cloud formation is the process by which the background sulfate aerosol particles serve as nuclei for the condensation of water vapor and nitric acid vapor (Toon et al., 1989). At issue early in the sequence of events is whether or when the sulfate particles become activated and so form liquid droplets that may grow spontaneously as solution droplets that are relatively rich in nitric acid. At some point these solution droplets may freeze and form crystalline nitric acid trihydrate (NAT) particles (Type I PSC). Once the temperature of the air parcel falls below the local frost point, possibly because of radiational cooling or adiabatic uplift, water ice presumably deposits on the NAT particles. These various stages in the evolution of the cloud particles all involve microphysical processes that may be affected by the chemical composition of the particles and the air parcel at the time of cloud formation.

The microphysical process of particle activation, the main aspect of the problem to be treated in this paper, involves both the kinetics of vapor deposition and the thermodynamics of aqueous-phase equilibria that vary with the ambient conditions and depend on droplet size. As a way of seeing how these various aspects are interrelated, consider an individual droplet of radius r_p in an environment containing specified, but possibly time-varying concentrations of water vapor ($n_{w\infty}$, molec m^{-3}) and a condensable trace gas ($n_{g\infty}$, molec m^{-3}). At this early stage, when the droplet is of submicron size, it is appropriate to ignore any bulk motions of the air around the particle or ventilation effects.

The mass growth rate of the particle due to the simultaneous deposition of water vapor and trace gas from the environment is a first step to be considered. As with the classical theory of drop growth ascribed to Maxwell (Pruppacher and Klett, 1978, p. 414), it can be assumed that the distributions of the vapors about the drop adjust instantly to any changes in the ambient conditions and that the movement of the drop boundary condition can be ignored. Gas- and surface-kinetic effects are readily accounted for by introducing appropriate mass accommodation or "sticking" coefficients, α_w and α_g, and a free-molecular distance, Δ, extending approximately one mean-free path from the drop surface. The mass growth rate contributed to the drop by each condensable vapor i is of the form

$$\frac{dm_i}{dt} = 4\pi m_i' D_i' r_p [n_{i\infty} - n_i(r_p)] \quad , \tag{1}$$

where m_i' is the molecular mass, and the modified diffusion coefficient

$$D_i' = \frac{D_i}{\dfrac{r_p}{r_p + \Delta} + \dfrac{4D_i}{r_p \alpha_i v_i}} \quad . \tag{2}$$

Here, D_i is the ordinary diffusion coefficient of species i in air and v_i is the mean molecular speed. Particle growth is for all practical purposes controlled by the differences in vapor concentrations between the environment and immediately over the particle surface. Each difference, $[n_{i\infty} - n_i(r_p)]$, is driven in large part by the instantaneous magnitude of $n_i(r_p)$, so this variable needs to be considered in some detail.

The particle surface boundary condition for each species, the function $n_i(r_p)$, is assumed to be the gas-phase concentration in equilibrium with the respective component in the aqueous phase. Actually, $n_i(r_p)$ pertains to the surface state of the particle, so that the curvature and temperature of the particle must be accounted for as well as its bulk chemical composition and phase. Because the equilibrium vapor concentration depends on the composition of the particle, the set of rate equations become coupled -- the deposition of one vapor species alters the composition of the particle, which then causes the equilibrium vapor concentrations and deposition rates of the other species to vary. The particle growth rate thus becomes a complicated function of the chemical equilibria within the aqueous phase.

The equilibrium vapor concentration may be related to bulk, rather than surface properties through appropriate transformations. First, let us assume that all of the vapors behave as ideal gases, so that the vapor concentration of species i can be related at will to the respective partial pressure P_i through $n_i = P_i/kT$, where k is Boltzmann's constant and T is the temperature. Latent heating effects on the particle temperature are likely to be small at the low deposition rates expected at low temperatures, so to first approximation the surface temperature is taken equal to that of the ambient air. The positive curvature of the particle surface can be expected to enhance the equilibrium vapor pressures of all volatile components above those pertaining to the bulk-composition parameters (Kelvin effect). The presence of other solution-phase components lowers the equilibrium vapor pressures of the given component by a generalization of Raoult's Law, so the equilibrium concentration of component i is given by

$$n_i(r_p) = n_i^{\circ}(T) \bullet \gamma_i X_i \bullet \exp(\frac{2\sigma}{n_c k T r_p}) \quad , \tag{3}$$

where $n_i^{\circ}(T)$ is the equilibrium vapor concentration over a pure, flat surface of component i, γ_i is the activity coefficient of i in the bulk solution, X_i is the mole fraction of i, σ is the composition-dependent surface free energy of the particle and n_c is the molecular density of the condensed phase.

Insertion of Eq (3) into Eq (1) allows the mass accumulation rates of each component to be calculated. The composite mass growth rate of the particle can then be determined from the individual growth rates:

$$\frac{dm_p}{dt} = \sum_i \frac{dm_i}{dt} \quad . \tag{4}$$

Integration of these sets of equations in principle allows one to calculate the particle mass m_p as it experiences various environmental conditions.

3. CHEMICAL INFLUENCES

The trace chemical composition of the environment in which a given particle is embedded determines to a large extent the composition and hence growth characteristics of the particle. The treatment summarized in the previous section provides a framework for separating the chemical and microphysical effects on the particle growth. If we think in terms of water vapor and trace gas saturation ratios, $S_{Ki} = n_i/n_i^{\circ}(T)$, then Eq. (3) may be viewed as a generalized Köhler Theory expression (Pruppacher and Klett, 1978, p. 141) and written in the form

$$S_{Ki} = a_i \cdot \exp(\frac{C_K}{r_p}) \quad , \tag{5}$$

where $a_i = \gamma_i X_i$ is the activity of component i in solution and

$$C_K = \frac{2\sigma}{n_c kT} \quad . \tag{6}$$

The chemical influences on the system are embedded in σ, but mostly within the set of interdependent activities a_i.

The separation shown here to exist between the chemical and microphysical aspects of the problem permits the chemical activities to be expressed in terms of bulk thermodynamic data found in the literature. Here, since the particle is considered initially to be a liquid ternary solution drop containing various proportions of sulfuric acid, nitric acid, and water, the semi-empirical theory of Jaecker-Voirol et al. (1990) is employed. In essence, this theory permits experimental measurements of vapor pressure data in the various binary systems to be combined in a way that is applicable when all three components are present simultaneously in arbitrary proportions. Although both experimental uncertainties and theoretical assumptions are implicit in the results, generally favorable comparisons with empirical data have been made (see Jaecker-Voirol et al., 1990, and references therein). Their formulation in effect allows the activities of each component to be calculated once the particle composition is expressed in terms of the mole fractions X_S, X_N, and X_W for sulfuric acid, nitric acid, and water, respectively.

The detailed consideration of the full ternary solution chemistry is needed here because of the nonlinear interactions that each of the components exerts on the others. The water activity, for instance, is strongly suppressed because of the presence of the sulfuric and nitric acids in the solution drop, as shown in Fig. 1. The water activity is represented by the surface that builds from the base plane toward the corner of the composition diagram denoting pure water (marked by "W"). The negative deviation from

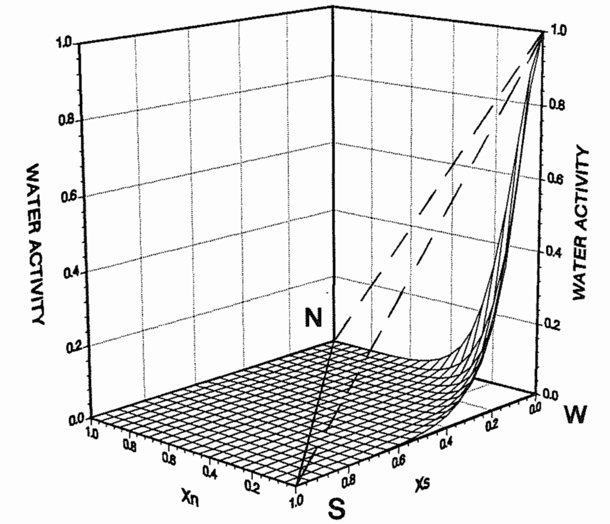

Fig. 1. Activity of water in the ternary system at -80°C as a function of the mole fractions of sulfuric acid (Xs) and nitric acid (Xn). The ideal-solution dependence (Raoult's Law) is provided for comparison as the planar surface outlined by the dashed lines. The area to the left of the N-S line has no significance.

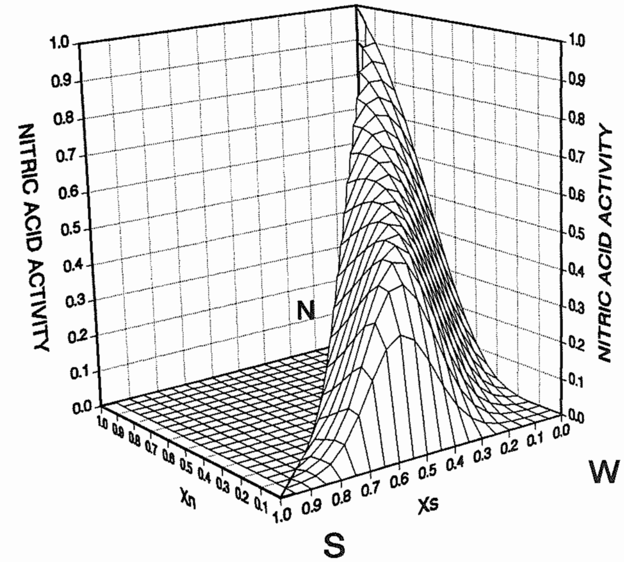

Fig. 2. Activity of nitric acid under the same conditions as in Fig. 1.

Raoult's Law (bounded by the straight dashed lines in Fig. 1) is pronounced and due to the relatively strong bonding between the molecules in solution.

The activity of nitric acid in such ternary solutions is relatively more complicated. As shown in Fig. 2, the nitric acid activity surface on the composition diagram exhibits a ridge line, indicating that nitric acid is relatively insoluble in moderately strong sulfuric acid solutions. This thermodynamic property may affect the behavior of sulfate particles in the stratosphere by limiting the sorption of nitric acid until the particles have cooled sufficiently and gained an appreciable amount of water to dilute the sulfuric acid.

4. COMBINED EFFECTS

The chemical thermodynamic data may be combined with the Kelvin effect via the generalized Köhler Theory expression given in Eq. (5). In typical applications of Köhler Theory to warm tropospheric clouds, the solute content of the particle is considered constant as the relative humidity and particle radius change. A maximum in the equilibrium saturation ratio of water results from the competitive effects of curvature and solute on the equilibrium vapor pressure of water. In the "haze" region, when the particle is smaller than the critical size, the effect of water condensation at increasing humidities is to dilute the solute, causing the water activity to increase to match the ambient saturation ratio. Once activated by growing beyond the critical radius, the particle behavior is increasingly controlled by the Kelvin effect. The effect of trace gases on particle activation is virtually nonexistent at these normally high temperatures because of the exceedingly small chemical saturation ratios found with typical atmospheric abundances. At low temperatures, however, the saturation ratio of nitric acid can become large enough to affect the water activity even with the small mixing ratios found in the stratosphere.

The sorption of ambient nitric acid has a qualitatively different impact on the particle solute content and water activity than does the sulfuric acid. Because the vapor pressure of sulfuric acid is so low at these temperatures, this constituent can be considered to reside almost exclusively in the condensed phase; that is, to first approximation, the total number of moles of sulfate in the particle may be held constant, just as the total solute content of the particles is fixed in traditional Köhler Theory. The nitric acid, however, will have its greatest impact at larger drop sizes, when the sulfuric acid is relatively dilute. Moreover, the nitric acid in solution, by virtue of its significant volatility, will tend to maintain equilibrium with the local environment; that is, the concentration, not the total number of mole of nitric acid in solution will tend to remain constant with drop size. Thus, the composite solute content of the particle increases as the particle grows in size, causing a continuous suppression of the water activity.

The combined influence of a fixed sulfuric acid content and nitric acid equilibrium on the equilibrium activity of water in the ternary solution drop is shown in Fig. 3 for a particle containing 10^{-20} mol sulfate. The vertical axis, S_{KW}, is the saturation ratio of water in Köhler-Theory equilibrium with the particle as a function of the particle radius for various specified ambient saturation ratios of nitric acid, S_{KN}. The traditional Köhler curve, without the influence of a trace gas, is evident in the vertical plane for $S_{KN} = 0$. The presence of the soluble trace gas causes each Köhler curve to become a surface for each given sulfate content. Consistent with the thermodynamic data, the sulfate exerts the greatest influence on the equilibrium surface at small particle radii when the sulfate concentration is relatively large. The nitric acid strongly affects the magnitude of the critical supersaturations and suppresses the water activity at all larger drop sizes. Note that a value of $S_{KN} = 1x10^{-4}$, equivalent to a mixing ratio of about 5 ppb of nitric acid at -85°C, causes the critical saturation ratio of these particles to be depressed nearly to 0.7.

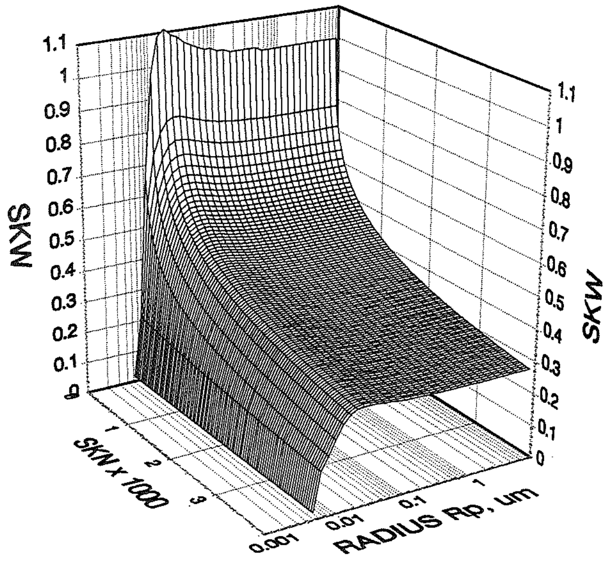

Fig. 3. The saturation ratios of water vapor (SKW) and nitric acid vapor (SKN) needed to maintain growth equilibrium with a solution drop of radius Rp.

5. CONCLUSIONS

This treatment, based on a generalization of Köhler Theory, provides a means to account for the presence of a soluble trace gas (HNO_3) during the activation and growth of a hygroscopic (sulfate) particle. Nitric acid tends to be sorbed by the particle preferentially at large sizes, leading not only to the increased likelihood of activation during environmental cooling by radiation or adiabatic uplift, but also to enhanced growth rates by the simultaneous condensation of water vapor and nitric acid vapor. The effect of the trace gas on the particle thermodynamics and growth kinetics becomes increasingly pronounced at low temperatures where the ambient trace gas saturation ratio becomes relatively large for a given trace gas mixing ratio. Complete treatments of cloud formation in the upper troposphere, lower stratosphere, and particularly near the mesopause should take compounds other than just water vapor into account.

The theoretical basis for a complete treatment of aerosol activation and cloud formation at low temperature is generally available, but much work needs to be done to formalize the concepts and bring the various fragments of understanding into a coherent framework. Work is proceeding with the growth rate calculations for various environmental cooling rates, from which particle sedimentation rates can be derived, of some importance to the issues of stratospheric dehydration and denitrification (Toon et al., 1990). The likely phase changes of the particle from a liquid solution drop to a solid nitric acid trihydrate or ice particle are also important to include. The numerous assumptions and approximations made must also be verified through systematic investigations of gas-particle interactions in laboratory experimentation, as well as through atmospheric observational data.

6. ACKNOWLEDGMENTS

This work was sponsored in part by the National Aeronautics and Space Administration under Contract No. NAG 2-751, and the National Science Foundation under Grants ATM-8919837 and ATM-9115590. Discussions of the ideas in this paper with Jen-Ping Chen and William Brune are greatly appreciated.

7. REFERENCES

Ackerman, T.P., K-N. Liou, F.P.J. Valero and L. Pfister, 1988: Heating rates in tropical anvils. J. Atmos. Sci., 45, 1606-1623.

Danielsen, E.F., 1982: A dehydration mechanism for the stratosphere. Geophys. Res. Lett., 9, 605-608.

Douglass, A.R., M.A. Carroll, W.B. DeMore, J.R. Holton, I.S.A. Isaksen, H.S. Johnston and M.K.W. Ko, 1991: The atmospheric effects of stratospheric aircraft: A current consensus. NASA Reference Publication 1251, January 1991, NASA, Washington, DC, 39 pp.

Elliott, S., R.P. Turco, O.B. Toon and P. Hamill, 1990: Incorporation of stratospheric acids into water ice. Geophys. Res. Letters, 17, 425-428.

Jaecker-Voirol, A., J.L. Ponche and P. Mirabel, 1990: Vapor pressures in the ternary system water--nitric acid-sulfuric acid at low temperatures. J. Geophys. Res., 95, 11857-11863.

Pruppacher, H.R. and J.D. Klett, 1978: Microphysics of Clouds and Precipitation, Reidel, Boston, MA, 714 pp.

Ramanathan, V. and W. Collins, 1991: Thermodynamic regulation of ocean warming by cirrus clouds deduced from observations of the 1987 El Nino. Nature, 351, 27-32.

Thomas, G.E., J.J. Olivero, E.J. Jensen, W. Schroeder and O.B. Toon, 1989: Relation between increasing methane and the presence of ice clouds at the mesopause. Nature, 338, 490-492.

Toon, O.B., P. Hamill, R.P. Turco and J. Pinto, 1986: Condensation of HNO_3 and HCl in the winter polar stratosphere. Geophys. Res. Letters, 13, 1284-1287.

Toon, O.B., R.P. Turco and P. Hamill, 1990: Denitrification mechanisms in the polar stratosphere. Geophys. Res. Letters, 17, 445-448.

Toon, O.B., R.P. Turco, J. Jordan, J. Goodman and G. Ferry, 1989: Physical processes in polar stratospheric ice clouds. J. Geophys. Res., 94, D9, 11359-11380.

CLOUD PHYSICS IN THE STRATOSPHERE:
FREEZING OF SULFURIC ACID DROPLETS TO FORM POLAR STRATOSPHERIC CLOUDS

J. E. Dye, D. Baumgardner and S. Borrmann
National Center for Atmospheric Research, Boulder, Colorado *

1. INTRODUCTION

In recent years there has been increased interest in aerosols in the stratosphere. The dramatic decreases in stratospheric ozone in the Antarctic are now known to be linked to the release of chlorofluorocarbons into the atmosphere and the subsequent heterogeneous reactions occurring on the surfaces of polar stratospheric cloud (PSC) particles. These reactions lead to free chlorine which then can destroy ozone. The most common PSC particles form at the cold temperatures found in the polar stratosphere from the co-condensation of nitric acid and water onto stratospheric sulfate particles and are probably nitric acid trihydrate (NAT) in a crystalline form, although there is still some uncertainty about the composition and phase. Papers on the chemistry, dynamics and physics of the polar ozone problem can be found in Special Issues of the Journal of Geophysical Research (For the Antarctic: Vol. 94, Nos. D9 and D14, 1989 and for the Arctic: Vol. 97, D7, 1992) and in Geophysical Research Letters, Vol. 17, No. 4, 1990 as well as numerous other publications.

Likewise, there has been much interest in possible ozone loss at mid-latitudes by heterogeneous reactions occurring on the stratospheric sulfate particles, particularly during periods with large volcanic enhancements of the stratospheric aerosol (Hofmann and Solomon, 1989). During June 1991 Mt. Pinatubo in the Phillipines ejected large quantities of SO_2 into the stratosphere which has dramatically changed aerosol concentrations and sizes of this region.

In this paper we discuss some of the processes thought to occur with the sulfate particles as temperature decreases and polar stratospheric clouds form. We also contrast the measurements of the sulfate particles made by the Forward Scattering Spectrometer Probe (FSSP) Model 300 during AASE I in late 1988 and early 1989, a period with low sulfate aerosols loading in the stratosphere, with those made after the eruption of Mt. Pinatubo during the Airborne Artic Stratospheric Experiment (AASE II) in late 1991 and early 1992.

The observations presented below were made with the FSSP 300 from the NASA ER-2 aircraft near 20 km (about 60 mb) or during ascent or descent portions of the flight. The FSSP 300 is similar in physical appearance to the standard FSSP 100, but has important operational differences which are discussed in Baumgardner et al., (1992) along with measurement uncertainties. The size range of the instrument is nominally 0.4 to 20 μm diameter, but it is intended as an aerosol probe and is not designed to work in tropospheric clouds which have larger concentrations of particles in the upper size range. The instrument was carefully aligned and calibrated almost daily during both AASE I and II and it's calibraiton was very stable.

2. STRATOSPHERIC SULFATE AEROSOL

The Junge layer of sulfate aerosols is a regular feature of the stratosphere which extends from about 15 to 30 km with a broad maximum in concentration around 20 km during periods without perturbations from volcanic eruptions. There is ample evidence (e.g. Hofmann and Rosen, 1983) showing that in most regions of the stratosphere the particles are supercooled solution droplets of sulfuric acid and water. At typical stratospheric temperatures of 220 to 230 K the sulfuric acid fraction is approximately 75%. However, when temperatures decrease such as near the tropical tropopause and in the regions of polar winter where temperatures can be 195 K or colder, the droplets deliquesce and grow in size to maintain equilibrium between the ambient water vapor pressure and the vapor pressure over the solution droplets. The expected change in sulfuric acid fraction as a function of temperature is shown in Fig. 1 based on the work of Steele and Hamill (1981). By heating the inlet of their

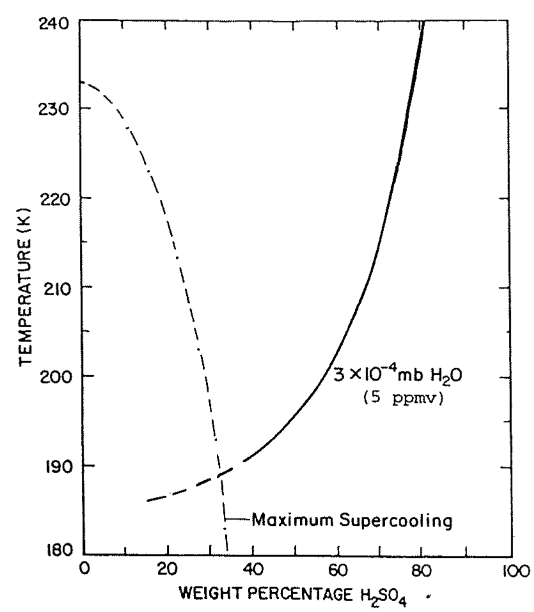

Fig. 1. Weight composition and maximum supercooling of sulfuric acid droplets as a function of temperature.

* The National Center for Atmospheric Research is sponsored by the National Science Foundation.

dustsonde Hofmann and Rosen (1983) demonstrated that at temperatures of 210 to 220 K the boiling point of the stratospheric aerosol was consistent with the weight percent of sulfuric acid calculated by Steele and Hamill.

3. MEASUREMENTS FROM AASE I

In many studies of polar stratospheric clouds, it has been assumed that the sulfuric acid droplets would be frozen well before 195 K, the approximate temperature at which nitric acid saturation over nitric acid trihydrate (NAT) is reached and PSCs can form. However, measurements from the FSSP 300 strongly suggested that most of the sulfuric acid droplets were deliquescing and remaining liquid to temperatures of at least 193 K (Dye et al, 1992). Furthermore, they speculated that homogeneous freezing of the sulfate droplets might play a role in the formation of PSCs. If the sulfate droplets were in fact liquid rather than frozen, the droplets would probably not be effective nuclei for PSC particle nucleation until they froze. The dashed line in Fig. 1 shows the maximum supercooling as a function of weight percentage of sulfuric acid which Hallett and Lewis (1967) predicted based on depression of the freezing point of water by sulfuric acid. As the sulfuric acid droplets in the stratosphere cool and become more dilute from deliquescence they can continue to supercool until they freeze homogeneously (or heterogeneously if that happens first). Based on Hallett and Lewis' work and the change in composition given by Steele and Hamill homogeneous freezing would be expected approximately where the two lines in Fig. 1 intersect, which is several degrees colder than that required for saturation of nitric acid over NAT.

The FSSP 300 observations in the Arctic (Dye et al, 1992) showed the first hint of PSC particle formation near saturation of nitric acid over NAT (about 195 K), but the main formation occurred near 191 to 192 K, which correspond to supersaturations >10 for nitric acid over NAT. Fig. 2 shows size distributions illustrating the growth of the sulfuric acid droplets via deliquescence, the initial indication of PSC particles and a size distribution in a well developed PSC for the ER-2 flight of Jan. 24, 1989. Curve A shows the size distribution of the sulfate droplets at 205 K and curve B at 199 K. Curve C at 194 K with small supersaturations of nitric acid over NAT shows the slight enhancements of the largest particles on the tail of the particle distribution which we believe is the formation of a few PSC particles on the largest sulfate particles. This enhancement is more easily seen in the surface area plots. Curve D shows the size distribution at 189 K in the main body of the PSC cloud in which all of the sulfate particles have been activated.

Unlike the Arctic observations which showed that the main onset of PSC clouds did not occur until temperatures considerably colder than that needed for nitric acid saturation (~195 K), similar observations with a standard FSSP in the Antarctic (Fahey et al., 1989) showed that the formation of PSCs occurred very near nitric acid saturation. As there is no way in the stratosphere to melt the frozen sulfuric acid droplets, once the droplets in an air parcel are frozen they will remain frozen. The Antarctic temperatures are much colder (temperatures less than 188 K are common) than the Arctic and the FSSP observations were near the end of the Antarctic winter, thus it is likely that all of the sulfate particles in the Antarctic were frozen during the period of the observations. Dye et al., (1992) speculated that in the Antarctic the already frozen sulfate particles could more readily act as nuclei for NAT particles, thus allowing all of the sulfate particles to be activated to form NAT near nitric acid saturation, as observed. Whereas, in the Arctic only a small fraction of the sulfate were frozen and only this fraction could nucleate NAT near nitric acid supersaturations. Those sulfate droplets which were supercooled had to freeze first in order to be effective nuclei for NAT formation. A complicating factor in this process is the cooling rate of the air mass which governs the rate at which nitric acid becomes available for growth, hence influencing the supersaturation which can develop. See Dye et al, 1992 for further discussion and references.

An alternative explanation to the one described above has been proposed by Hofmann and Deshler (1991). They suggest that the main onset of PSCs in the Arctic may be the result of the larger supersaturations achieved during fast cooling of an airmass which allows the formation of ternary solutions of nitric acid, sulfuric acid and water. Additional observations, particularly of particle composition and phase are needed to resolve this interesting difference between the Arctic and Antarctic.

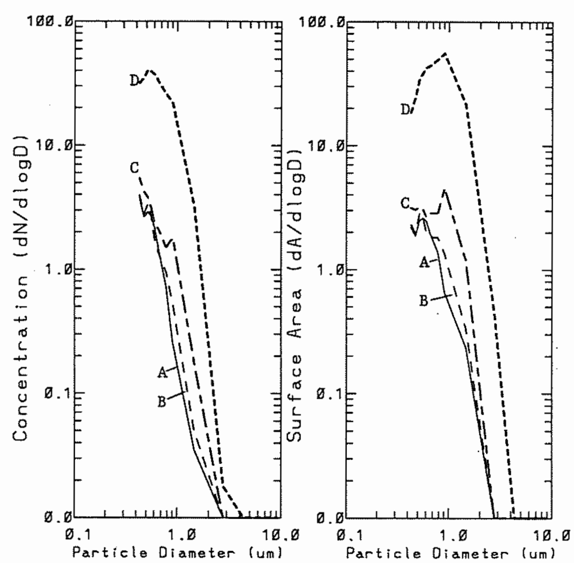

Fig. 2. Particle size distributions for 300 sec averages of FSSP 300 measurements from Jan. 24, 1989. (See text)

4. MEASUREMENTS FROM AASE II — Effects of Mt. Pinatubo

The observations made during AASE I were made during a period considered to be background conditions of stratospheric sulfate aerosol loading. Measurements made during the ferry flight from Wallops Island, Virginia (38°N) to Stavanger, Norway (61 °N) on Dec 31, 1988 are shown in Fig. 3a. Note the very uniform nature of the stratospheric aerosol during this entire flight. All flights which were not in the polar vortex or in PSCs during late 1988 and early 1989 showed similar homogeneity in the FSSP 300 observations.

In June 1992 Mt. Pinatubo in the Phillipines erupted and dramatically changed the stratospheric aerosol loading. Measurements made on Sept. 17, 1991, three months after the eruption of Mt. Pinatubo, are shown in Fig. 3b) for a test flight of the ER-2 flown from Moffett Field, California (37 °N)to 52 °N and back. The character of the stratospheric aerosol is very different than that in 1988. There are regions with concentrations somewhat similar to those in 1988, but there are others where the aerosol concentrations are highly variable with maxima a factor of 10 or more higher. The large enhancement in concentration around 18.0 hr UT is apparently a portion of the Pinatubo plume at the ER-2 altitude which has made its way northward. The plane then flies out of the plume and the concentration decreases. From about 18.4 to 19.25 hr UT the ER-2 descended from about 19.5 to 15.2 km pressure altitude and reascended, which we will refer to as a dip. The maxima concentrations in Fig. 3b occur during the dip. As the plane descends the aerosol concentration first increased then decreased as the plane descended below the aerosol maxima. The lowest altitude was at about 18.8 hr UT. The reverse of this pattern is evident as the plane again ascended. From about 19.3 to 20.2 hr UT the plane was apparently in air unperturbed by Mt. Pinatubo, but by 20.5 hr UT as the plane flies south it reenters the volcanic plume at the higher altitude.

By March 22, 1992 a flight south from Bangor, Maine (45 °N) to about 24 °N and return to Bangor shows that the concentrations measured by the FSSP 300 at 20 km had become relatively uniform (Fig. 3c). The decreases in concentration between 16.5 and 17.0 hr UT were during a dip, where the ER-2 apparently descended below the main layer of aerosol. The concentration of aerosols > 0.4 μm is about a factor of 10 greater and the aerosols > 1 μm diameter are a factor of 30 to 50 greater than late 1988. The fluctuations in the concentration for aerosols > 1 μm in Fig. 3a) are statistical scatter due to the low number count at those sizes. For 120 sec averages the statistical uncertainty at concentrations of 1, 0.1, and 0.01 cm/sec are about 3, 9, and 30%, respectively.

Concentration and surface area size distributions for selected time periods of the time series plots of figure 3 are shown in Fig. 4. All are 600 sec averages which for the 200 m/sec flight speed of the ER-2 corresponds to 120 km of flight track.

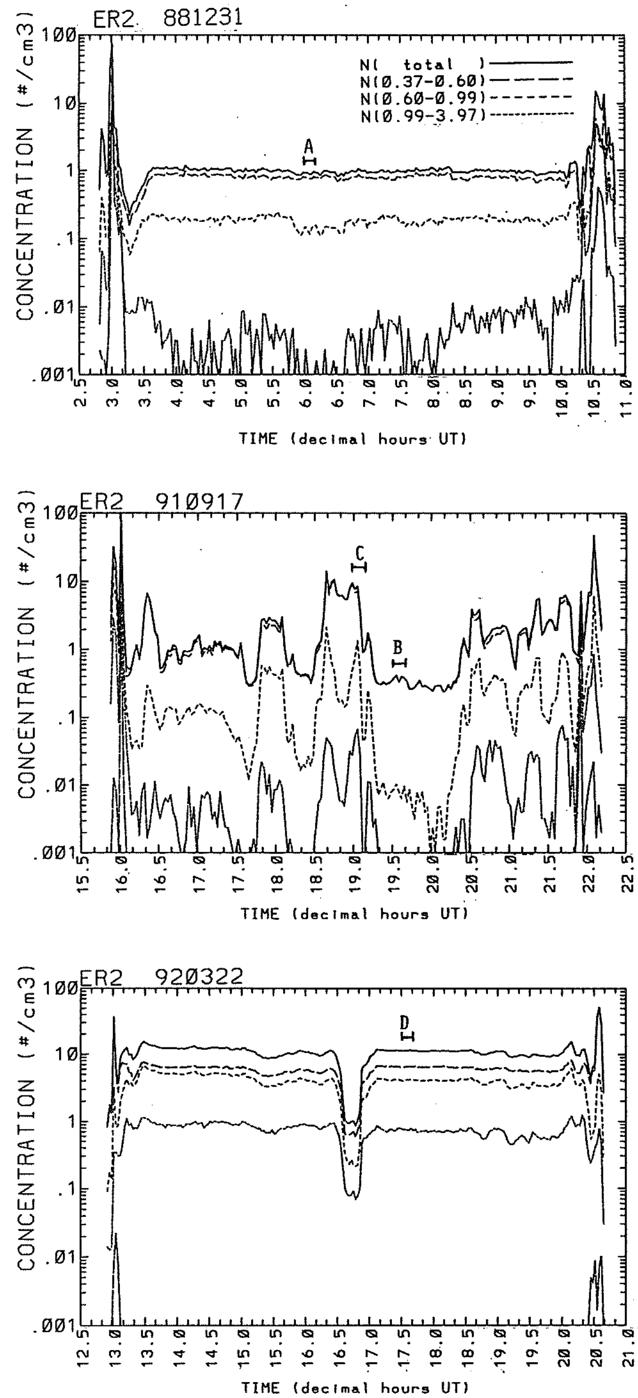

Fig. 3. Aerosol measurements averaged over 120 sec from the FSSP 300 for Dec. 31, 1988, Sept. 17, 1991 and Mar. 22, 1992 from flights of the NASA ER-2 in the stratosphere.

The size distribution labeled A is for the 1988 flight which was thought to be background conditions. B is from a period during the Sept. 17, 1991 flight when the ER-2 is above the volcanic plume from Mt. Pinatubo. Note in the figure that the aerosol concentrations in the undisturbed portion of the stratosphere have decreased since 1988, particularly for the larger particles. Similar distributions to that shown by curve B of Fig. 4

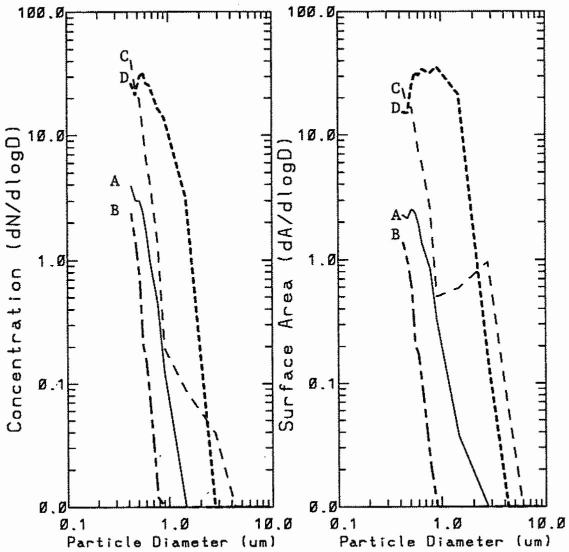

Fig. 4. Particle size distributions averaged over 600 sec for the time periods marked A, B, C, and D in Fig. 3.

also were observed during October, 1991 in what we think were undisturbed airmasses, thus the Sept. 17 data is not anomalous. The decrease from 1988 to 1991 is consistent with faster sedimentation rates for the larger aerosols and suggests that in 1988 the stratospheric aerosols larger than 0.4 μm diameter had not yet reached a steady state background level after the previous perturbation caused by El Chichon.

Size distribution C is an average over the heaviest part of the volcanic plume at a pressure altitude of about 18 km. Note the enhancement of the largest aerosols seen by the FSSP 300 compared to the "undisturbed" plots of A and B and that the particles extend to 4 μm diameter. By the March 22, 1992 flight (curve D in Fig. 3d) the concentration of the smallest particles had decreased somewhat as had the very largest particles, but over most of the size range of the FSSP 300 there were large increases in the number of particles, as growth and coagulation occurred.

The corresponding surface areas derived from the FSSP 300 measurements are shown on the right side of Fig. 4. The modal diameters for distributions A, B, and C are < 0.4 μm, the lower limit of the FSSP 300. However, by March the modal diameter of the surface area is between 0.6 and 1.0 μm diameter. The total surface area for aerosols > 0.4 μm seen by the FSSP 300 in March is 20 to 30 times larger than that from 1988 and 50 to 100 times larger than the surface areas in undisturbed regions observed on Sept. 17, 1991.

5. CONCLUDING REMARKS

A wealth of new information on aerosols in the stratosphere and the physical processes affecting them has been obtained in the short period of a few years. Yet, many questions remain. Some of the more important ones are:

1. At what point do the sulfuric acid droplets freeze? What promotes the freezing of the droplets? Could aircraft flying in the lower stratosphere influence this process and then possibly the chemical reactions occuring in this region?

2. Are the frozen sulfate particles the nuclei upon which NAT particles form or are there other possible mechanisms?

3. What is the composition of the PSC/NAT particles? Are they solid or liquid or a solid solution?

4. What roles do cooling rate and freezing of the sulfate droplets play in the PSC formation process?

5. What is the background level for stratospheric sulfate particles and are anthropogenic emissions influencing

Acknowledgements: This research was aided by support from the NASA Upper Atmospheric Research Program.

REFERENCES

Baumgardner, D., J. E. Dye, R. G. Knollenberg, and B. W. Gandrud, 1991: Interpretation of measurements made by the FSSP-300 during the airborne Arctic stratospheric expedition, in press *J. Geophys. Res.*

Dye, J. E., D. Baumgardner, B. W. Gandrud, S. R. Kawa, K. K. Kelly, M. Loewenstein, G. V. Ferry, K. R. Chan, B. L. Gary, 1992: Particle size distribution in Arctic polar stratospheric clouds growth and freezing of sulfuric acid droplets and implications for cloud formation. in press *J. Geophys. Res.*

Fahey, D. W., K. K. Kelly, S. R. Kawa, A. F. Tuck, M. Loewenstein, K. R. Chan, and L. E. Heidt, Observations of denitrification and dehydration in the winter polar stratospheres, *Nature*, *344*, 321–324, 1990.

Hofmann, D. J., and T. Deshler, Stratospheric cloud observations during formation of the Antarctic ozone hole in 1989, *J. Geophys. Res.*, *96*, 2897-2912, 1991.

Hofmann D. J., and J. M. Rosen, 1983: Stratopspheric sulfuric acid fraction and mass estimate for the El Cichon eruption, *Geophys. Res. Lttrs*, **10**, 313-316.

Hofmann, D. J. and S. Solomon, 1989: Ozone destruction through heterogeneous chemistry following the eruption of El Chichon, *J. Geophys. Res*, **94**, 5029-5041.

Steele, H. M., and P. Hamill, Effects of temperature and humidity on the growth and optical properties of sulphuric acid-water droplets in the stratosphere, *J. Aerosol Sci., 12*, 517–528, 1981.

ON THE AEROSOL-CLOUD INTERACTION: FIELD OBSERVATIONS ON EL YUNQUE PEAK, PUERTO RICO*

T. Novakov,[1] C. Rivera-Carpio,[1] C.F. Rogers,[2] and R.C. Schmidt[1]

[1]Energy and Environment Division, Lawrence Berkeley Laboratory, Berkeley, CA 94720
[2]Desert Research Institute, Reno, NV 89506

1. INTRODUCTION

It has been postulated that increased concentrations of cloud condensation nuclei (CCN), particularly biogenic and anthropogenic sulfate aerosol, should lead to increased concentrations of cloud droplets, resulting in increased short-wave albedo of clouds (see Charlson et al., 1992, and references therein). Estimates of this effect are based on simplifying the assumption that the aerosol-cloud interactions do not change the liquid water content of the cloud. Consequently, the increase in sulfate-induced droplet concentration is expected to be accompanied by a decrease in mean droplet radius and thus in total surface area of the droplets. To assess the magnitude of the aerosol-induced changes in the optical properties of clouds, it is crucial to empirically establish the relationships between cloud microphysical parameters (liquid water content, droplet concentration, and size distribution) and mass concentrations of aerosol species, total aerosol number, and CCN concentration for a variety of cloud types. Such information can be obtained from aircraft measurements and ground-based in-situ measurements on mountain peaks or preferably from both. Ground-based measurements are suitable for studies of processes occurring at or near the cloud base and provide longer-term data time series than are obtainable from aircraft studies. In this paper we report the results on interactions of aerosols with warm clouds from several experiments on a mountain peak in Puerto Rico. These experiments used a full complement of cloud and aerosol measurements and thereby add to the limited previous data sets where investigators attempted to fully characterize the input aerosol, including its cloud nucleating ability and then to compare those data to measured cloud microphysical properties (see, for example, Squires, 1958; Twomey and Warner, 1967; Warner, 1969; Baker et al., 1982; Hudson, 1983).

2. FIELD SITE AND MEASUREMENT CAPABILITIES

Field measurements are performed on El Yunque peak (18°19'N, 65°45'W) at an elevation of ∿1000 m. This peak is located at the eastern end of Puerto Rico, directly exposed to trade winds. The El Yunque site is most commonly impacted by warm cumuli, which often produce rain. Weather systems such as easterly waves or subtropical fronts additionally cause stratiform clouds at the site. Orographic uplift contributes to cloud development. Depending on specific meteorological situations, the measurement site can be below, at, or sometimes well above the cloud base. The aerosol detected at the site is a mixture of natural marine aerosol, long-distance transported continental anthropogenic and natural (i.e. dust) aerosol, and a relatively minor contribution from local biogenic and anthropogenic sources. The chemical composition and concentration of the aerosol varies, depending on the transport of air masses that reach the site. These facts make the El Yunque site suitable for obtaining systematic data to evaluate the effects of the aerosols on cloud microphysical properties.

Measurements at the site include: (1) Cloud drop number concentration and size distribution — measured by a CSASP 100 HV drop spectrometer (Particle Measurement Systems). This instrument operates in three particle diameter ranges — 2-32 μm, 1-16 μm, and 0.5-8 μm. (2) Liquid water content — derived from drop spectra. (3) Interstitial aerosol number concentration — measured with a condensation particle counter (CPC, TSI Model 3022) equipped with an impactor designed to retain the cloud drops (cutoff ≲5 μm). (This counter detects particles with diameters >0.01 μm.) Under clear sky conditions, total aerosol concentration is detected. (4) Backscattering coefficient for visible light — measured with a modified integrating nephelometer operated in the backscattering mode (Novakov et al., 1991). (5) CCN counter (M-1, DH Associates). (6) Total aerosol filter sample collection — collected with a heated inlet sampler. (The slight heating of the inlet air evaporates the cloud drops, which are collected as aerosol particles.)

Parameters 1 through 5 are measured in real time with time resolutions between 1 and 60 sec, depending on the instrument. Four 6-hr filter samples were collected throughout each day. All the above-mentioned measurements give local (volumetric) data.

3. RESULTS

Measurements were performed during July 1991 and during March/April 1992. Analyses of 19 6-hr filter samples collected in July 1991 resulted in an average non-sea-salt sulfate concentration (on the average 80% of total sulfate) of 0.70 ± 0.22 μg m^{-3}. The average nitrate concentration was 0.69 ± 0.10 μg m^{-3}. The dust concentration estimated from the Fe concentration was highly variable, ranging from <1 μg m^{-3} to ∿12 μg m^{-3}. Concentration ratios of Al, Si, and Fe were found to be consistent with average global crustal ratios (Mason and Moore, 1982), indicating the crustal origin (dust) of these particles. Backtrajectory analyses (Harris, 1991) show that these can be traced to the Saharan dust.

Our results on nss sulfate and nitrate concentrations are virtually identical to those found by Savoie et al. (1989) in the marine air on Barbados. The close agreement between these two sets of measurements indicates that the sulfate and nitrate at our site are representative of the marine aerosol, not significantly influenced by the local pollution. We also note that according to the findings of Savoie et al., the marine sulfate aerosol is a mixture of biogenic and long-distance transported anthropogenic sulfate.

During the July 1991 experiment, for six days (out of 14 days) the clouds impacted the site for extensive periods of time. The average nss SO_4^{2-} concentrations corresponding to the periods of cloud impact ranged from $\sim$0.2 to $\sim$1.0 $\mu g\ m^{-3}$. If the sulfate mass concentration is proportional to the CCN number concentration, then the cloud drop concentration should show an increasing trend with SO_4^{2-} concentration. Furthermore, if the assumption of liquid water constancy applies, a decrease in drop size with increasing sulfate concentration should be expected.

Contrary to these expectations, our results show no correlation between average droplet concentration (which ranged from $\sim$140-$\sim$250 cm^{-3}) and an eightfold change in nss SO_4^{2-} concentration. However, both liquid water content and effective and modal droplet radii showed an essentially linear increase with sulfate concentrations. We also note that the droplet concentrations were equally insensitive to large variations in the total and interstitial aerosol number concentrations. These results show that for the days studied, periods of high sulfate loadings do not correspond to high (local volumetric) droplet concentrations. We note, however, that an average nss concentration of 0.7 $\mu g\ m^{-3}$ may correspond to $\sim$270 particles cm^{-3} with a mass-radius of 0.07 μm, assumed to be typical of marine sulfate (as quoted in Charlson et al., 1987). This value is close to the average drop concentration range between 140 and 250 cm^{-3}. It is therefore possible that the droplet concentration is more strongly influenced by sulfate aerosol size rather than its mass concentration.

The results referred to above pertain to the droplet concentrations and size distributions corresponding to different sampling days (and different cloud types), averaged over morning and afternoon cloud impact periods. The sulfate concentrations to which the cloud properties are compared were obtained from 6-hr aerosol samples collected between 0600-1200 and 1200-1800 hours local time.

We have also analyzed the relationships between cloud droplet size distribution and droplet number concentration, measured with 10-sec time resolution on individual days. For the purpose of this analysis, droplet concentrations are used as a surrogate for activated CCN concentrations. For most days in the 1991 experiment, a systematic, approximately linear increase in effective radius with droplet concentration was observed. (For the constant liquid water content assumption, an opposite trend is expected.) Consequently the cloud scattering coefficient and liquid water content should exhibit an even more pronounced but nonlinear increase with droplet or CCN concentrations. For selected data with a narrow spread in the effective radii, a linear dependence of liquid water content on droplet number concentration is observed, similar to that observed by Slingo et al. (1982) from aircraft data.

In the 1992 experiment, the measurement capabilities at the site were complemented with a CCN counter operating at a fixed supersaturation of 0.3%. The CCN counter was equipped with a cyclone separator so that in-cloud measurements correspond to the CCN in the interstitial air. The bulk of the data from this experiment is being analyzed at the time of this writing. Preliminary analyses of the CCN and droplet concentration data show that the CCN concentrations in the precloud air decreased with the onset of the cloud. The difference between the precloud and interstitial CCN was found to be approximately equal to the droplet concentration as expected. However, the CCN concentration in precloud and often in interstitial air exceeded the droplet concentration. At this time we can conclude that only a fraction of available CCN are activated. The CCN that are not activated may be those that are introduced into the clouds after their maximum supersaturation has been generated. A speculative explanation is that the droplet concentration is determined by the CCN introduced into the clouds in their earliest formative stages, i.e. near the eastern Puerto Rican shoreline, where most cumuli first form, and that the unactivated CCN originate from local anthropogenic or natural sources located between the shoreline and the mountain site.

*This work is supported by the Director, Office of Energy Research, Office of Health and Environmental Research, Environmental Sciences Division of the U.S. Department of Energy under contract no. DE-AC03-76SF00098.

References

Baker, M.B., A.M. Blyth, D.J. Carruthers, S.J. Caughey, T.W. Choularton, B.J. Conway, G. Fullarton, M.J. Gay, J. Latham, C.S. Mill, M.H. Smith and I.M. Stromberg, 1982: Field studies of the effect of entrainment upon the structure of clouds at Great Dun Fell. Quart. J. R. Met. Soc., 108, 899-916.

Charlson, R.J., J.E. Lovelock, M.O. Andreae and S.G. Warren, 1987: Oceanic phytoplankton, atmospheric sulfur, cloud albedo and climate. Nature, 326, 655-661.

Charlson, R.J., S.E. Schwartz, J.M. Hales, R.D. Cess, J.A. Coakley, Jr., J.E. Hansen and D.J. Hofmann, 1992: Climate forcing by anthropogenic aerosols. Science, 255, 423-430.

Harris, J., 1991: Personal communication.

Hudson, J.G., 1983: Effects of CCN on stratus clouds. J. Atmos. Sci., 40, 480-486.

Mason, B., and C.B. Moore, 1982: Principles of Geochemistry, Wiley, 46-47.

Novakov, T., C. Rivera-Carpio, R.C. Schmidt and C.F. Rogers, 1991: Measurement of cloud integrated backscattering coefficient with a nephelometer. Geophys. Res. Lett., 18, 1453-1456.

Savoie, D.L., J.M. Prospero and E.S. Saltzman, 1989: Non-sea-salt sulfate and nitrate in trade wind aerosols at Barbados: Evidence for long-range transport. J. Geophys. Res., 94, 5069-5080.

Slingo, A., S. Nicholls and J. Schmetz, 1982: Aircraft observations of marine stratocumulus during JASIN. Quart J. R. Met. Soc., 108, 833-856.
Squires, P., 1958: The microstructure and colloidal stability of warm clouds. Part I. The relation between structure and stability. Part II. The causes of the variations in microstructure. Tellus, 10, 256-261 and 262-271.
Twomey, S., and J. Warner, 1967: Comparison of measurements of cloud droplets and cloud nuclei. J. Atmos. Sci., 24, 702-703.
Warner, J., 1969: The microstructure of cumulus clouds. Part II. The effect on droplet size distribution of the cloud nucleus spectrum and updraft velocity. J. Atmos. Sci., 26, 1272-1282.

The Physical and Chemical Features of Cloud, Precipitation and Aerosol in South China

Dui Wu

Guangdong Institute of Tropical and Oceanic Meteorology
Fujin Rd. 6, Guangzhou Guangdong, 510080 P.R.China

Water content and features of cloud droplet spectra in warm clouds over early summer in the Xinfeng Jing river vally (north-east Guangdong) are first analysed. It is pointed out that the warm cumulus has more moisture than warm stratocumulus, which includes more water in early summer in Guangdong than precipitive As-Ns clouds in North China. Coalescence becomes the main rain trigger for the observed clouds, more easily such in cumulus congestus than in stratocumulus.Cumulus is more of marine type in Guangdong than in Hunan or other provinces.

From the chlorine and sulfate nuclei data, observed in Yongxing (Xisha islands,South China Sea) (16.8N, 112.3E) in May, 1987, it is found that:

1) The average concentration of chlorine ion nuclei is 618 per liter and the average salt content is 57.2$\mu g/m^3$. Both values are between those observed in Putou (29.9N, 122.2E) and Haiyang island (39N, 123.1E); the spectrum type shows quasiunimodal and exporential lapse rate. The average concentration of sulfate ions is 15 per liter, the mean salt content is 23.8 $\mu g/m^3$, and the spectra how multimodal types, wider than those of chlorine ions. The largest dried diameter reaches 59μ;

2) Both concentrations of sulfate ions and chlorine ions decrease as the distances to seaside increase;

3) The distribution of sea-salt nuclei has very good correlations with speed and wave height. Chlorine ion nuclei appear largest value at 14 o'clock. Their diurnal variations are relative to tide.

The data of giant sea-salt nuclei(Cl^-) observed in Guangzhou (22N, 113.3E) area in August and september, 1987, are then analyzed. The main results are:

1) The average concentration of chlorine ion nuclei and the average salt content whose dried diameters are larger than 2μm are 31 per litre and 0.84 $\mu g/m^3$ respectively, the special giant nuclei whose dried diameters are larger than 4 um is 3 per liter, the largest dried diameter reaches 25 μm. They all are much lower than the values observed in South China Sea.

2) The spectrum of concentration shows a one-peak type and power lapse pattern,and the spectrum pattern is narrow, but smooth. The spectrum of mass shows a one-peak pattern, too.

3) The day to day variation of the concentraion of sea-salt nuclei is closely related to synoptic situation. The typhoon may make the concentration of sea-salt particles increase and form the phenomenon called "sea-salt nuclei storm".

The drop-size distribution of shower in Guangzhou is also analyzed. The results show that Type 3 spectra appear with highest frequency and no Type 1 in that area. The average size is larger. The maximum diameter of drops can reach up 6.5mm. The outstanding features are that the minimum diameter of drops is too large, and there are few small drops but much more larger ones. As a result, it is imperfect to describe the spectra with an exponential function. In addition, the results reveal the areal difference of W-I relationship is much smaller than that of Z-I relationship. In Guangzhou area W-I and Z-I relationship of shower are expressed respectinvely as

$$Z = 345I^{1.39}$$

$$W = 0.0569I^{0.88}$$

The evaporating process during the raindrops falling beneath cloud has been tested numerically. The simulation results show that:

1) The temperature of falling drops is lower than that of surroundings because of the evaporation of raindrop heat, and also the fallng drops tend to remain the lower temperature of higher layer;

2) Since the temperature of drops is lower than that of surroubings, the evaporating process during raindrop falling in unsaturated atmosphere is restrained, even the condensing process occures possibly.

Samples from thounders showers controled by subtropical high duing the south-west summer monsoon, observed in Yongxing(Xisha islands, S.C.S.) in May, 1987, reveal that the pH values of all samples are about 7.0, and that the concentrations of chlorine and sodium ions are large,with about 62.5% and 36.1% of the negative ions and positive ions respectively. The ratio of chlorine to sulfate ions is 2.3, different from that observed over mainland of China.

These results may represent the chemical composition of precipitation over South China Sea region for atmospheric and environmantal science.

The samples of showery rain taken in November, 1988 in Yongxing Is. and Shenhang Is. (16.7N, 111.7E), Xisha Islands, (S.C.S.), when northeast monsoon was prevailing, suggest that pH values of the samples are between 5.90-7.45. The concentration of ions is greater than that of thunder showers of southwest summer monsoon. The concentration of chlorine and sodium ions are large, which are about 86.6% and 59.8% of the anion and cation in total, respectively. The equivalent ratio of chlorine to sulfate ion is 7.6, contrasting with sulfate predominance in cation for the mainland of China. The enriching process of K^+, Ca^{++}, Mg^{++} and $SO_4^=$ are in varying degrees. The $SO_4^=$ and F^- of "extraquantity" are from East Asia continent.

An Andersen particle sampler(model 20-709) has been used for the collecting and measurement atmospheric total aerosol samples at Guangzhou, Shaoguan (24.6N, 113.5E), longmen (23.7N,114.3E), Liuzhou (24.6N, 109.8E),Nanning (22.9N, 108.3E), Yangshou (24.7N, 114.3E), and of South China in the winter and summer of 1988. The mass distribution of total aerosol and the distribution of fluorine, chlorine, nitric, sulphuric, sodium, ammonia, potassium, calcium, magnesium ions of water soluble have been analyzed.The results show that in clean regions the distributin of water soluble composition of aerosols mostly exhibit a basic triseak distribution, which has a seak on supergiant particles range, giant particales range and submicron range respectively. This basic distribution is destroied in industry cities and in result the concentration increases fast mainly in giant particles range due to various anthropogenic pollutants that are drained into atmosphere. The sulphuric and calcium ions of water soluble of aerosols are obviously higher in industry cities than those in clean regions and chlorine ions are markedly lost.

In Guangzhou from May 1988 to Apil, 1989, the mass distribution of total aerosol and the distribution of fluorine, chlorine, nitric, sulphuric, sodium, ammonia, potassium, calcium, magnesium ions of water soluble show that the concentration of aerosol is lower in rainy seasons than that in dry seasons in Guangzhou. The concentration of sulphuric and calcium ions that are soluble in water are the largest in every month of the year. The mass distribution of total aerosol exhibits a triseak distribution. On the orther hand, the distribution of water soluble composition is divergent, the magnesium, nitric, potassium and fluorine ions mostly exhibit triseak distribution, and the calcium ions are mainly bimodally distributed, and the chlorine and sodium ions are of quasi-unimodal distribution. The sulphuric ions are enriched greatly in Guangzhou, especially in rainy seasons. The m.m.d is larger in rainy seasons than in dry ones. This is also true to the total aerosol and water soluble composition. The sulphuric is the most important cation in aerosols in Guangzhou, but concentration of nitric ions is very low, different from those observed in rain water. There are free acid in aerosols in Guangzhou · in most of the year, especially in rainy season, causing aerosol to show neutral or weak acidity. It accounts for easy formation of acidrain in Guangzhou.

Ionic compositions of water solubles aerosols observed at the seashore of the Tong Gu Bay in Taishan county (South Guangdong) during Feb. 1989, namely, Cl^-, NO_3^-, $SO_4^=$, Na^+, K^+ and Mg^{++}, are also analyzed. It is found that the dominant ions are Cl^- and Na^+, which are of marine salt aerosol. The same origin is with Mg^{++} ,too. K^+ mainly comes from the continent, and $SO_4^=$ from sea salt mostly. It does reveal, however, the large scale high pollution of sulfate in the continent of East Asia. The study points up high concentration of NO_3^- of 100% non-sea-salt origin. It is obvious that it is related with local farming and household cooking.

参考文献
(References)

〔1〕 吴兑等，西沙永兴岛降水的酸度及其化学组成，气象学报，47(3)，381—384，1989。

〔2〕 A.K.Mukherjee, et al., Rainwater chemistry over sea areas during monsoon season, MAUSAM, 37(2), 173—178, 1986.

〔3〕 H.D.霍兰，大气和海洋化学，初汉平等译，科学出版社，156，1986。

〔4〕 钟晋梁等，我国西沙群岛松散堆积物的粒度和组成的初步分析，海洋与湖沼，10(2)，125—135，1979。

〔5〕 沈志来等，西太平洋热带海域雨水化学组成，大气科学，特刊，328—332，1988。

〔6〕 王润鹿等，本底污染区域监测站降水化学的一些监测结果，气象，14(11)，9—12，1988。

〔7〕 全文哲等，广州地区酸雨现状的研究，中国环境科学，9(2)，123—128，1989。

〔8〕 黄美元等，重庆地区云水和雨水酸度及其化学组分的观测分析，大气科学，12(4)，389—395，1988。

〔9〕 C.T.Nagamoto, et.al., Chemical analyses of cloud water, precipitation and aerosol samples collected in Colorado, conference on cloud physics, American meteorological society, 95—98, 1986.

〔10〕 毛节泰，吴兑等，芜湖冶炼厂大气尘的物理化学特性，大气环境，3(2)，3—6，1988。

〔11〕 A.K.Mukherjee et.al., Chemical composition of rainwater during monsoon season over Pung (Maharashtra) and its relation to meteorological factors, MAUSAM, 36 (3), 267—274, 1985.

〔12〕 S.J.Maske, et.al., Studies on chemical constituents of precipitation over India, MAUSAM, 33(2), 241—246, 1982.

〔13〕 KunioYo shizumi, et.al. , Characterization of atmospheric aerosols in Chi chi of the Ogasawara(Bonin)islands, Atmospheric Environment, 20 (1), 151—156 1986.

(14) Pruppacher, H.R.,and J.D, Klett, 1978, Microphysics of Clouds and precipition, D.Reidel Publishing Company.

(15) Pruppacher. H.R., and R.Rasmussen, 1979, A Wind tunnel investigation of the rate of evaporation of large water drops falling at terminal velocitory in air, J.A.S., 36, 7, 1255-1260.

(16) Borovikov, A.M.,et al., Fizika Oblakov, 1961, (Cloud Physics), Gidrometeor, Izdatel' stvo, Leningrad. (English Translation by Isreal Program for Scientific Translations, Jerusalem, 1963)

(17) A.K. Mukherjee, Krishna Nand, B.Mukhodhyay and S.G. Ghanekar, 1986 Rainwater Chemistry over Indian sea areas during monsoon season, MAUSAM, 37, 2, 1730178.

(18) David.B.Johnson,1982, The role of giant and ultragiant aerosol particles in warm rain initiation, J.A.S., 39 (2), 448-460.

(19) W.E.Rang and J.B. Wong, 1952, Inspection of dust and smoke particles on surface and body collectors, Ind. and Eng. Chem., 44(6) 1371-1381.

(20) Kouichi Hama and Noboru Takagi, 1970, Measurement of sea-salt particles on the coast under moderate winds, Papers in Meteorology and Geophysics, 21(4), 449-458.

ON THE RELATIONSHIP BETWEEN CLOUD DYNAMICS AND CLOUD ACIDITY

T. P. DeFelice[1] and V. K. Saxena[2]
[1] University of Wisconsin-Milwaukee, Milwaukee, Wi, USA 53201
[2] North Carolina State University, Raleigh, NC, USA 27695

1. INTRODUCTION

Simultaneous cloud microphysical, chemical and meteorological data were obtained approximately 2.5 km southwest of the Mt. Mitchell, NC summit atop (2,006 m MSL) a southsouthwest-northnortheast oriented ridgeline during the summers of 1986 through 1988. The site and the general physical and chemical characteristics of the cloud episodes that traverse this site are detailed in Saxena et al. (1989). The most common ionic components of the collected water during the 1986 through 1988 field periods were hydrogen, sulfate, nitrate, ammonium, sodium and chloride. Saxena and Lin (1990) provide further details of the chemical nature of the cloud episodes. A general relationship between pH and wind direction exists for cloudwater samples of cloud systems that traverse our site (e.g., Saxena et al., 1989; DeFelice and Saxena, 1991). The directional dependence of cloudwater pH suggests that back trajectory analysis for the air parcel giving rise to cloud episodes at our site would yield very useful information about the source of the acidic pollution (e.g., Leck and Rodhe, 1989; Saxena and Yeh, 1989). The analysis of the microphysical, chemical and meteorological data suggests a temporal relationship between cloud dynamics and acidity. A relationship of this kind would be useful in determining acid deposition and as a parameterization for cloud dynamical processes within cloud chemistry and global climate models.

Typical cloud only (herein denoted as Type A for convenience) and, cloud and precipitation events (herein denoted as Type B for convenience) sampled at our site have been chosen to illustrate the relationship between cloud dynamics and cloud acidity.

2. RESULTS AND DISCUSSION

Some general meteorological characteristics of the Type A and B events are given in Table 1. This Table also provides the event averaged pH of the collected water.

Type A clouds usually form in 850 mb synoptic scale southwesterly flow into the site, last 3.4 h, have liquid water contents below 0.2 g m^{-3} and average droplet sizes of 8.0 µm. These events may contain extreme (pH≤3.1, e.g., NAPAP, 1987; DeFelice, 1989) and nonextreme cloudwater acidities when the site winds are from 230° and 303° during the first 2 h after their onset, respectively. Among these clouds, it appears that the greater the crossbarrier angle or the faster the windspeed, the less acidic the cloud (all else identical). The crossbarrier angle is taken as the event first 2h averaged wind direction minus the angle of orientation of the terrain upon which the site sits, namely ≈215°.

Type B cloud with precipitation events usually form in westnorthwesterly to northnorthwesterly, and southwesterly 850 mb airflows, last 7h, have an average cloud liquid water content of 0.4 g m^{-3} and average droplet sizes of 13.0 µm. They are accompanied by 250° (±80°) and 142° site winds during the first 2 h after their onset are associated with extreme and non-extreme acidities given the former and latter

Table 1. General characteristics of Type A and B events

Event	pH Ave.	Event Pressure Perturb.[a] (mb)	Ave. Wind First 2 h Speed (m s^{-1})	Ave. Wind First 2 h Direction (°)	850 Mb 24 h Back Trajectory
TYPE A					
7/ 5/86[b]	3.1	+1.1(±0.1)	5(±0.5)	229	SW
8/17/87	3.6	+1.1(±0.1)	10(±0.2)	300	WSW-SW[c]
7/22/88	3.4	+0.3(±0.1)	3(±1.0)	306	WSW
TYPE B					
6/ 3/88	2.9	-0.9(±0.3)	12(±0.3)	292	NNW
6/24/88	3.0	-0.4[d]	5(±0.5)	213	WNW-NW
6/30/88	3.0	-0.7(±0.4)	6(±0.7)	288	WNW
7/23/88	3.9	-0.7(±0.0)	6(±1.0)	142	SW

[a] Pressure perturbation is based on 15 min averages; [b] Reads July 5, 1986; [c] Reads westsouthwest to southwest; [d] +0.6 mb first 3.25 h and -1.0 mb next 5.75 h.

850 mb flows, respectively. Among the Type B events, the faster the windspeed the more acidic the sampled water, and no pH dependence due to the barrier is evident. This may be due to the presence of precipitation. However, they typically relieved periods of high ozone concentrations (DeFelice, 1989). Thus suggesting an in-cloud oxidation of S(IV) to S(VI) by the high O_3 concentrations (e.g., Jacob et al., 1989; Pandis and Seinfeld, 1989a,b to name only a few).

The acidity associated with the dynamically different Type A and B events is contrary to what is expected. NAPAP (1987) indicates that events with clouds and precipitation should have higher pH's than those with only clouds. Upon investigating this descrepancy a relationship between temporal acidity (measured by pH), acid formation, liquid water content (LWC) and the dynamics associated with the cloud system began to evolve. Table 2 shows the slope of the temporal pH versus LWC curve, the general synoptic (primarily at 850 mb, since the site was typically at 815 mb) scale feature associated with, the initial pH and ozone concentrations, minimum ozone concentration, and the average LWC for the events in Table 1. The slope is purposely left in qualitative terms due to the size of the dataset presented. A slope of zero implies that the observed pH, which is determined by the ionic composition of its cloudwater, is produced (i.e., acid enhancement) independently of the rate at which water is made available or consumed (e.g., cloud formation dynamics and condensation, or evaporation and/or change in air-mass, i.e., meteorological dynamics) to yield the observed liquid water content (LWC). A positive slope indicates that the production of acidity is due to the dynamics of the event (namely, near a region of evaporation, near the boundary of two air-masses, or during an event that was accompanied by some precipitation). The greater the slope the more intense the evaporation, the more different the air-mass, or the more intense the precipitation. A negative slope indicates that the production of acidity is due to internal (e.g., the oxidation of S(IV) to S(VI) by ozone) processes, and/ or a change to a more polluted air-mass has occurred. The 7/22/88 and the 8/17/87 events were formed in the same general airflow (implying the same crossbarrier wind angles) with the 8/17/87 episode containing winds that were twice as fast as those of the 7/22/88 event (implying that the former was slightly more dynamic-larger updraft speed, more vapor condensed out, etc). The 8/17/87 event was sampled close to its top (DeFelice and Saxena 1990b) implying evaporation was occurring during sampling. In contrast, the 7/22/88 event was not sampled near its top but it did have higher ozone concentrations. The 7/23 Type B cloud and precipitation event was accompanied by an hour long period of rain during the middle of its duration with cloud only periods before and after its middle. Each of the three events containing large positive pH-LWC slopes had event averaged pH's ≥3.4. The 6/3/88 and 6/24/88 events have a small positive slope. The small negative slope for the 6/30/88 event could be due to the dominance of dynamics since light to moderate intensity precipitation was present throughout its existence (≈5 h), since it was associated with a significant frontal system. The production of acidity due to ozone oxidation remained significant throughout this event and it cannot be ignored. The slope of the 6/30 event remains negative as the ozone concentration remains high, despite the intense precipitation (≈5 h long) and the air inwhich this system has been forming remains as polluted as it was at the beginning of the event. The 6/24 case differs from the 6/30

Table 2. The relationship between the slope of the temporal pH and liquid water content for Type A and B events, and cloud related dynamics and acidity.

Event	pH initial	Ozone[a] initial (ppb)	Ozone[a] min. (ppb)	LWC ($g\ m^{-3}$)	General Weather[b] Feature Causing Event
LARGE POSITIVE SLOPE					
8/17/87	3.8	33	33	0.2	Weak upper level disturbance.
7/22/88	3.7	50	50	0.2	Passing weak surface frontal inversion.
7/23/88	3.3	57	53	0.2	Decaying south-ward moving Low. The Low remaining west of the site.
SMALL POSITIVE SLOPE					
7/ 5/86	3.1	86	83	0.1	Not Available.
6/ 3/88	2.6	97	45	0.6	Closed Low over Virginia.
6/24/88	2.8	94	80	0.3	Thunderstorms delayed start. Shift in air-mass occurred.
SMALL NEGATIVE SLOPE					
6/30/88	2.8	100	81	0.6	Surface front associated with an intensifying Low.

[a] The ozone concentrations are based on 15 minute averages.
[b] 850 mb surface unless otherwise indicated.

episode since a shift to a less polluted air-mass occurred during it. This change in air-mass allowed the dynamics of the 6/24 system to have a relatively greater control on its acidity production than in the 6/30 event. The general 850 mb synoptic features associated with these events support the notion of a relationship bewteen meteorological dynamics and cloud acidity. For example, the the 6/3 event is associated with a large closed low over Virginia, and the 6/30 event was associated with a southwárd bound intensifying low just north of Montreal. While the 7/23 event was associated with a weakening southward moving Low that remained west of the site.

4. REFERENCES

DeFelice, T. P., 1989: The characterization of extrema deposition of air pollutants in Mt. Mitchell State Park: Potential for forest decline and opportunity for cloud deacidification. PhD thesis, Dept. of Marine, Earth and Atmospheric Sciences, NCSU, Raleigh, NC.

DeFelice, T. P., and Saxena, V. K., 1991: The characterization of extreme episodes of wet and dry deposition of pollutants on an above cloudbase forest during its growing season. *J. Appl. Meteorol.*, **30**, 1548-1561.

DeFelice, T. P., and Saxena, V. K., 1990: Temporal and Spatial distribution of ionic composition and acidity in clouds: Comparison between modeling results and observations. *J. Atmos. Sci.*, **47**, 1117-1126.

Jacob, D. J., Gottlieb, E. W. and Prather, M. J., 1989: Chemistry of a polluted cloudy boundary layer. *J. Geophys. Res.*, **94D**, 12,975-13,002.

Leck, C., and Rodhe, H., 1989: On the relation between anthropogenic SO_2 emissions and concentration of sulfate in air and precipitation. *Atmos. Environ.*, **23**, 959-966.

National Acid Precipitation Assessment Program (NAPAP), 1987: Interim Assessment: The causes and Effects of Acid Deposition, J. L. Kulp and C. N. Herrick, eds., U.S. Government printing office, Vol. 1, Washington, D.C., 1-53.

Pandis, S. N., and Seinfeld, J. H., 1989a: Sensitivity analysis of a chemical mechanism for aqueous-phase atmospheric chemistry. *J. Geophys. Res.*, **94D**, 1105-1126.

Pandis, S. N., and Seinfeld, J. H., 1989b: Mathematical modeling of acid deposition due to radiation fog. *J. Geophys. Res.*, **94D**, 12,911-12,923.

Saxena, V. K., and Lin, N.-H., 1990: Cloud chemistry measurements and estimates of acidic deposition on an above cloudbase coniferous forest. *Atmos. Environ.*, **24A**, 329-352.

Saxena, V. K., and Yeh, J.-Y., 1989: Temporal variability in cloudwater acidity: Physico- chemical characteristics of atmospheric aerosols and windfield. *J. Aerosol Sci.*, **19**, 1207- 1210.

Saxena, V. K., Stogner, R. E., Hendler, A. H., DeFelice, T. P., Lin, N.-H. and Yeh, R. J.-Y., 1989: Monitoring the chemical climate of the Mt. Mitchell State Park for evaluating its impact on forest decline. *Tellus*, **41B**, 92-109.

MULTIPHASE CHEMISTRY IN A MICROPHYSICAL RADIATION FOG MODEL.— A NUMERICAL STUDY

Andreas Bott

Institute for Atmospheric Physics, University of Mainz, Postfach 3980, 6500 Mainz, F.R.G.

1. Introduction

In the past years numerous measurements have been performed of the chemical composition of fog and cloud water elucidating that the concentrations of reactants are often much higher in small droplets than in rain water. Since at some locations fog periods sometimes last for several days, it is expected that under certain atmospheric conditions low clouds and fog are mainly responsible for the damages to vegetation or the acidification of lakes.

To improve our understanding of the complex interaction between the chemistry and the thermodynamics in clouds and fog, in the past decade various numerical models have been developed. However, due to the high complexity of the problem, many authors focus the discussion on partial aspects of the whole system such as the detailed description of aqueous phase chemical reactions or the comprehensive study of microphysical processes.

To obtain a better description of the coupled microphysics–chemistry system, in this paper a radiation fog model is presented which treats comprehensively the interaction between thermodynamical and chemical processes in the gas and in the liquid phase. The combined microphysics–chemistry fog model results from the linkage of the radiation fog model of Bott *et al.* (1990) and Bott (1991), the condensed gas phase chemical module of Lurmann *et al.* (1986) and an aqueous phase chemical reaction system which is largely based on the work of Chameides (1984).

2. Model Description

The thermodynamic part of the model consists of a set of prognostic equations for the temperature T, the components u and v of the horizontal wind vector, the specific humidity q and the particle spectrum f(a, r) which is treated as a two–dimensional size distribution with the masses of the total particle and of its dry aerosol nucleus as independent variables. (r is the total particle radius, a is the radius of the dry aerosol nucleus.) The entire particle spectrum is subdivided into 1200 classes of 30 different radii r and 40 different radii a with $0.01 \leq a \leq 2\mu m$ and $a \leq r \leq 40\mu m$.

The time evolution of the particle spectrum is determined by solving a coupled system of 40 droplet growth equations for the 40 different aerosol classes. Hereby the humidification of aerosols as well as their subsequent activation to form cloud droplets are explicitly calculated. This is done with a semi–Lagrangian advection scheme which is based on the area preserving flux form advection algorithm of Bott (1989a, b).

The gas phase chemical reaction set is taken from the condensed mechanism of Lurmann *et al.* (1986). It consists of 112 reactions for 53 different reactants, whereby for 17 short lived species steady state approximations are employed instead of prognostic differential equations. The aqueous phase chemical reaction mechanism is due to Chameides (1984). For the present investigation this mechanism has been extended mainly by including oxidation reactions of S(IV) with O_2 as catalyzed by Fe(III) and Mn(II). The corresponding reactions are taken from Jacob *et al.* (1989).

In the chemical part of the fog model the microphysical particle spectrum is subdivided into three regions with total particle radii ranging between $a \leq r < 5\mu m$, $5\mu m \leq r < 10\mu m$ and $10\mu m \leq r \leq 40\mu m$. Chemical reactions in the aqueous phase are only treated in the second and in the third particle region, (i.e. the small and the large droplet regime, respectively), in the first region (the aerosol regime) the particles are assumed to be chemically inert. However, when aerosol particles become activated, their chemical composition is also accounted for in the liquid phase chemistry of the two droplet regimes. The mass transfer of chemical species between the gas phase and the two droplet regimes is explicitly calculated by solving the corresponding coupled differential equation system. Aqueous phase chemical reactions are calculated as function of the time dependent mean values of the liquid water and the mean droplet radii of the two droplet regimes. The model also considers the effects of turbulent mixing, gravitational settling, condensation and evaporation of particles on the chemical composition of the fog water.

3. Numerical Results

The model simulations are performed on a day in October which is favorable for the formation of radiation fogs. The declination of the sun is $-3°$ and the geographical latitude is $50°$ North. Local times of sunrise and sunset are 6h and 17.30h, respectively. The atmosphere is assumed to be moderately polluted, i.e. the physico–chemical characteristics of the aerosol particles, the initial concentrations and the emission rates of the gas phase chemical species are chosen to be typical for urban regions.

Fog formation starts at 23h in the evening. During the night the fog grows in the vertical up to its final height of 44m at 7h. In the dissipation stage (after 10h) the fog is lifted from the ground and the top of the fog rises shortly up to 55m. This behavior is typical for the dissipating fog. It is explained by the increasing solar irradiance in the morning yielding a relatively large evaporation of the fog water which has been deposited at the ground during the night. Furthermore, the water vapor of the lowest atmospheric layers is transported into upper fog layers by turbulent mixing processes which also become effective after sunrise.

The liquid water content is continuously changing in the two droplet size classes. Typically the values range between 0.05—0.1 g m^{-3} and 0.1—0.15 g m^{-3} in the small and the large droplet regime, respectively. Whenever fog forms in a certain atmospheric layer, the main liquid water mass is initially carried by the small particles. Due to the condensational growth of the droplets, after a while the particles start to leave the small droplet regime and enter the large one because their total radius exceeds 10 μm. Hence, the liquid water content is increasing in the large droplet regime while in the small droplet regime it is decreasing. Furthermore, the gravitational settling of the particles as well as turbulent mixing processes have an influence on the liquid water content in each droplet regime.

From numerical results obtained with the chemical part of the coupled microphysics–chemistry model the following conclusions are drawn:

(1) The chemical constitution of fog water is strongly controlled by the entrainment of fresh air at the top of the growing fog, by the chemical constitution of the activated aerosol particles, by gas phase chemical reactions (in particular the onset of photochemical reactions after sunrise), and by turbulent mixing processes.

(2) Ion concentrations are much higher in small than in large droplets. The concentrations vary between several orders of magnitude as a function of time. The highest values are observed in the initial stage, after the entrainment of fresh air and when the fog starts to dissipate.

(3) The fog water pH varies between 3.0—3.5 and 3.5—4 in small and in large droplets, respectively. Due to the continuous emission of NH_3 at the earth's surface, near the ground the H^+ concentrations are lower than in upper fog regions.

(4) S(IV) oxidation rates in the aqueous phase depend on the size of the droplets. The dominant S(VI) production mechanisms are the reactions with H_2O_2 and the catalytic Fe(III) reaction. In the morning, after the onset of gas phase photochemical reactions, in the large particle size class the reactions of S(IV) with O_3 and the OH radical are important pathways for the sulfate production. In the small droplet regime these reactions are of minor importance.

(5) Fog water deposition by gravitational settling of the particles occurs mainly in the large droplet regime. Nevertheless, at the beginning of the fog the wet deposition rates of chemical species are larger in the small than in the large droplet regime. This is explained by the relatively high concentrations of chemical species in the small droplets. In the mature and in the dissipation stage of the fog, the wet deposition rates of chemical species are increasing in the large droplet regime and are decreasing in the small droplet regime.

References

Bott, A., 1989a: A positive definite advection scheme obtained by nonlinear renormalization of the advective fluxes. *Mon. Wea. Rev.*, **117**, 1006—1015.

Bott, A., 1989b: Reply. *Mon. Wea. Rev.*, **117**, 2633—2636.

Bott, A., 1991: On the influence of the physico–chemical properties of aerosols on the life cycle of radiation fogs. *Bound. Layer Meteor.*, **56**, 1—31.

Bott, A., U. Sievers and W. Zdunkowski, 1990: A radiation fog model with a detailed treatment of the interaction between radiative transfer and fog microphysics. *J. Atmos. Sci.*, **90**, 2153—2166.

Chameides, W.L., 1984: The photochemistry of a remote marine stratiform cloud. *J. Geophys. Res.*, **89**, 4739—4755.

Jacob, D.J., E.W. Gottlieb and M.J. Prather, 1989: Chemistry of a polluted cloudy boundary layer. *J. Geophys. Res.*, **94**, 12,975—13,002.

Lurmann, F.W., A.C. LLoyd and R. Atkinson, 1986: A chemical mechanism for use in long–range transport/acid deposition computer modeling. *J. Geophys. Res.*, **91**, 10,905—10,936.

EXAMINATION OF SOME CLOUD PROCESSES RELATIVE TO SODIUM ACCUMULATION IN POLAR SNOW

Austin W. Hogan

Atmospheric Research
Piermont, NH 03779, USA

1. INTRODUCTION

There is a well established literature describing sodium (Na) concentration in polar snow, firn and glacial ice; there are also numerous papers describing Na compounds as cloud condensation nuclei and Na aerosol concentrations in maritime and continental air. Aerosol Na can be measured in remnants of polar maritime (mP) air intruding on the Antarctic Plateau (Parungo, et al., 1979) with sufficient time resolution to examine marine and continental aerosol components in warm and cold advection stages of a storm (Hogan, et al., 1984); concurrent Na aerosol measurement at the edge of the Ross Ice Shelf and at South Pole by Murphey, et al. (1991) has shown the commonality of Na source and exchange at these two places. Comparison of daily aerosol observations at South Pole with Na concentration measured in recent nearby snow by Legrand and Kirchener (1988) indicates Na accumulation reflects recent aerosol transport history. Hogan and Gow (1992) examined the glaciological Na accumulation record and the tropospheric Na aerosol flux over the plateau. They proposed that aerosol deposition was sufficient to account for the annual mean accumulation of Na in polar snow but was insufficient to account for many of the maximum Na in snow water concentrations measured by Legrand and Kirchener (1988) in individual layers. They hypothesized that rimed snow could account for the greater concentrations found in these layers.

2. RESULTS OF ANALYSIS

Although the boundary layer above the Antarctic Plateau is relatively cloud poor and subsaturated on most days, Alto Stratus and other supercooled liquid water clouds are relatively common coincident with the warmest air which lies .5 to 1.0 km above the ice surface. Strong cyclonic activity about the periphery of Antarctica causes relatively "warm" mP air to be advected over the plateau; Lettau (1969) has shown that these advection events are necessary to provide the water vapor necessary to maintain the growth of the interior ice sheet. Mid-winter surface air temperatures frequently exceed -40C concurrent with these events, with the overlying warm air apparently ice saturated and warmer than -30C in some soundings. Precipitation is not measured at South Pole Station, but snow grains or snow pellets and poor visibility are observed at the surface during these times. Kikuchi and Uyeda (1979) replicated ice crystals at Inuvik coincident with similar temperature structure and found rimed planar and dendritic ice crystals in the lowest 100 m. Although there is no winter analysis of ice crystal type or degree of riming available for the South Pole, it would appear that the snow grains reported are small, heavily rimed crystals.

The several power laws relating ice crystal mass and fall speed to crystal diameter (i.e., Locatelli and Hobbs, 1974; Heymsfield and Kajikawa, 1987; and Mitchell, et al., 1990) have been unified into a calculation scheme by Hogan (1992). This scheme integrates over the snowflake size distribution and facilitates estimation of mass change due to riming. The concentration of antecedent condensation nuclei in snow can be found using the assumption that nuclei mass is conserved and one nucleus is contained in each rime drop. The size distribution of antecedent nuclei is constrained by a supersaturation regulated minimum size and the limited number of "large" particles available in an air parcel.

Calculations estimating the mixing ratio of former nuclei in thick plates (Magono-Lee Class C1h) and radiating assemblages of dendrites (Class P7b) are given in Table 1. These two crystal types were chosen as the Nakaya diagram shows plates and thick plates to occur at temperatures less than -20C, and because the author has observed radiating assemblages of dendrites which appeared to be lightly rimed falling from -30C layers at the South Pole. The calculations were made using the dropsize distributions measured in Antarctic mP clouds by Saxena and Ruggiero (1991).

Lightly rimed (.1 or .3 of surface covered and definable to crystal type according to Harimaya, 1989) crystals of either type have antecedent nuclei concentration of 10^{-9} gm nuclei/gm water, typical of polar snow. Snow grains made by riming the entire area of these crystals have concentrations exceeding 10^{-8} gm/gm, the value of the greatest concentration of Na found in some layers. It is interesting to note that increasing the size of the smallest active nucleus would increase the antecedent nucleus mass concentration, allowing the Na fraction to be greater than 10^{-8} gm Na/gm H_2O. This could result from a reduction in supersaturation, which is quite a plausible explanation for clouds 1500 km from open water over a nearly level ice sheet.

TABLE 1

CONCENTRATION OF ANTECEDENT CONDENSATION NUCLEI IN RIMED SNOWFLAKES

MEDIAN CRYSTAL DIAMETER CM	GEOMETRIC STANDARD DEVIATION	FRACTION OF AREA RIMED	MINIMUM NUCLEUS RADIUS 1e-06CM	MAXIMUM NUCLEUS RADIUS 1e-05CM	MIXING RATIO CCN MASS/ICE 1e-09 G/G
THICK PLATES, MAGONO LEE CLASSIFICATION C1h					
.04	1.25	0.1	2.0	1.6	1.0
.04	1.25	0.3	2.0	1.6	2.6
.04	1.25	1.0	2.0	1.6	4.4
.04	1.25	1.0	2.8	1.6	10.8
.04	1.25	1.0	4.0	1.6	27.2
.04	1.25	1.0	2.0	3.2	5.5
.04	1.25	1.0	2.8	3.2	13.8
RADIATING ASSEMBLAGE OF DENDRITES, MAGONO LEE CLASSIFICATION P7b					
.14	1.4	0.1	2.0	1.6	3.8
.14	1.4	0.3	2.0	1.6	5.1
.14	1.4	1.0	2.0	1.6	5.7
.14	1.4	1.0	2.8	1.6	14.3
.14	1.4	1.0	4.0	1.6	34.4
.14	1.4	1.0	2.0	3.2	7.2
.14	1.4	1.0	2.8	3.2	18.2

3. CONCLUSION

We propose that snow grains formed on columnar or dendritic crystals by accreting rime drops formed at low saturation are responsible for the greatest concentrations of Na found in polar snow. The antecedent nucleus chemistry of polar snows may vary by a factor of more than ten due only to changes in riming and nucleation processes.

BIBLIOGRAPHY

Bromwich, D.H., 1988; Snowfall in High Southern Latitudes, Rev Geophys., 26, 149-168.

Harimaya, T. and M. Sato, 1989; Measurement of the Riming Amount on Snowflakes, J. Fac Sci, Hokkaido Univ., VII, 8, 355-366.

Heymsfield, A.J. and M. Kajikawa, 1987; An Improved Approach to Calculating Terminal Velocities of Platelike Crystals and Graupel, J. Atmos Sci., 44, 1088-1099.

Hogan, A.W., 1992; Snow Mensuration, submitted to J. Atm. Oceano. Tech.

Hogan, A.W., J. Samson, K.Kebschull, R.Townsend, S.Barnard, B. Murphey, and T. Hare, 1984; On the Interaction of Aerosol with Meteorology, J. Rech Atmos., 18, 41-67.

Hogan, A.W. and A.J. Gow, 1992; Particle Transport to the Snow Surface at the South Pole; the Beginning of a Tropospheric History, submitted to Tellus.

Kikuchi, K., and H. Uyeda, 1978; Cloud Droplets and Raindrops Collected and Frozen on the Surface of Natural Snow Crystals in the Arctic Canada, in Ministry of Education, Hokkaido University, Sapporo, Japan, March 1978, pp. 83-102.

Legrand, M. and S. Kirchener, 1988; Polar Atmospheric Circulation and Chemistry of Recent (1957-83) South Polar Precipitation, Geophys Res Lett., 15, 879-882.

Lettau, B., 1969; The Transport of Moisture into the Antarctic Interior, Tellus, 21, 331-340.

Locatelli, J.D. and P.V. Hobbs, 1974; Fall Speeds and Masses of Solid Precipitation Particles, J. Geophys Res., 15, 2185-2206.

Mitchell, D.L., R. Zhang, and R.L. Pitter, 1990; Mass-Dimensional Relationships for Ice Particles and the Influence of Riming on Snowfall Rates, J. Appl. Meteorol., 29, 153-163.

Murphey, B.B., T. Hare, A.W. Hogan, K. Lieser, J. Toman, and T. Woodgates, 1991; Vernal Atmospheric Mixing in the Antarctic, J. Appl. Meteorol., 30, 494-507.

Parungo, F., E. Ackerman, W. Caldwell, and H.K. Weickmann, 1979; Individual Particle Analysis of Antarctic Aerosols, Tellus, 31, 521-529.

Saxena, V. and F.H. Ruggiero, 1991; Antarctic Stratus Clouds:Microstructure and Acidity, submitted to AGU Antarctic Series.

Concentration of heavy metals in precipitation over Hungary

László Bozó
Hungary

Institute for Atmospheric Physics
H-1675 Budapest, P.O.B. 39.
Hungary

1. INTRODUCTION

Since the middle of this century energy generation and industrial production as well as vehicular traffic have caused a serious increase in environmental contamination by trace elements. The airborne heavy metal concentrations have risen remarkably during this period. Heavy metals can accumulate in the biosphere and may be toxic to living organisms. Wet deposition of these elements is an important source to ecosystems so their monitoring in precipitation is of great importance.

2. SAMPLING AND MEASUREMENTS

The Hungarian background air pollution monitoring station (K-puszta) is located in the centre of Hungary (19°33' E, 46°58' N), approximately 70 km southeast of Budapest. The closest city is 25 km southeast (100,000 inhabitants) and there is an ironworks plant approximately 50 km west of the monitoring station.

Wet only collectors have been installed for taking precipitation samples. Samples are collected in polyethylene bottles with funnels. 3 ml 1:1 HNO_3 are added to 1000 ml precipitation collected.

The Pb and Cd content of the samples have been determined by graphite furnace atomic absorption spectrometry at the Institute of Inorganic and Analytical Chemistry of the Budapest University. 20 μl of the solution have been put into the graphite tube and analysed. A Perkin Elmer Model 303 atomic absorption spectrometer with a HGA 74 graphite furnace and deuterium background collector have been used for the analyses. The detection limit for the precipitation samples are 0.1 μg/l (Cd) and 5 μg/l (Pb). The standard deviation of the method is 10 %.

Recently, the measurements of other heavy metals - Ni, V, Zn - have also been started. The samples are collected on the same monitoring station and analyzed by ICP technique.

3. CONCENTRATION OF HEAVY METALS IN PRECIPITATION

Sampling and measurement for the determination of Pb content of precipitation have been carried out since 1983 at K-puszta station. The lowest concentrations can be noticed in June and August and the highest ones in November and March. The average winter and summer Pb concentration in precipitation are 20.9 μg/l and 14.4 μg/l, respectively. The annual variation has a slight decreasing trend (-1.6 μg/l/a).

The Cd measurements were started in 1984. The average monthly variation shows peaks in winter (1.14 μg/l) and minima in summer (0.62 μg/l). The trend of the weighted-by-precipitation annual average values is decreasing (-0.12 μg/l/a).

The monitoring and measurements of Ni, V and Zn content of precipitation were started in July, 1991. Because of this short period we have only limited information on the concentration of these metals in precipitation. The half-year averages of their concentrations (from July to December) are 1.72 μg/l, 1.90 μg/l and 46.0 μg/l, respectively.

4. WET DEPOSITION OF PB AND CD IN HUNGARY

Precipitation is an important component of deposition because of its transfer of material to the surface and - indirectly to the biosphere. The amounts of Pb and Cd deposited by wet deposition can be calculated by using their average concentration and precipitation amount. The lowest wet deposition amounts were detected in July and August both for Pb and Cd. On one hand July and August were among the dryest months in Hungary during the period examined. On the other hand both lead and cadmium have low concentration in precipitation in summer. The yearly average wet deposition of lead and cadmium calculated for K-puszta are 7.98 $mg/m^2/a$ and 0.45 $mg/m^2/a$, respectively.

On the basis of the evaluation of the total (wet+dry) deposition of lead and cadmium it has been found that the wet deposition of these metals are much higher than the dry deposition of them over Hungary.

5. LONG-RANGE TRANSPORT ESTIMATION

A simple trajectory-based long range model has been constructed (Bozó and Horváth, 1992) in order to estimate the average contribution of the Hungarian Pb and Cd sources to the total Pb and Cd deposition over the country. The results of model estimation show that the relative contribution for Pb and Cd are around 30% and 10%, respectively. Similar results have been obtained by the TRACE-model computations carried out at IIASA, Austria (Bozó et al., 1991). This very low relative contribution to the total deposition of Cd can be explained by the fact that the cadmium emission density is low as compared to the nearby countries' emission densities (Pacyna, 1988). Since the atmospheric Pb and Cd are attached to fine aerosol particles it is obvious that the long range transport of these metals plays important role in the deposition of rural areas, even several hundred kilometres far away from the sources. It can be assumed that the "excess" Pb and Cd deposited in Hungary comes from sources outside the country and transported here by advection. On the other hand, the Pb and Cd released from Hungarian sources are deposited not only over Hungary, but at rural areas of the other countries in Europe.

REFERENCES

Bozó L., Alcamo J, Bartnicki J. and Olendrzynski K. (1991): Heavy Metals Contamination in Eastern Europe: Background Load from the Atmosphere, IIASA Working Paper 91-46, International Institute for Applied Systems Analysis, Laxenburg,

Bozó L. and Horváth Z. (1992): Concentration and deposition of lead and cadmium over Hungary. Ambio (in press).

Pacyna J.M. (1988): Atmospheric emissions of arsenic, cadmium, mercury and zinc in Europe in 1982, NILU Report 17/88, Norwegian Institute for Air Research, Lillestrom, 1988.

PREDICTION OF CLOUDWATER TO PRECIPITATION ION CONCENTRATION RATIO BY VERTICAL DOPPLER RADAR

Lukas Mosimann[1] and Matthias Steiner[2]

[1]Atmospheric Physics, ETH, Hönggerberg, CH-8093 Zurich, Switzerland
[2]Dept. of Atmospheric Sciences, AK-40, University of Washington, Seattle, WA 98195, U.S.A.

1. INTRODUCTION

The chemical composition of precipitation is strongly affected by the composition of the air mass in which it forms and by the mechanisms of formation and growth (Collett et al., 1991). Snow crystals grown only by water vapor deposition are relatively clean compared to the surrounding cloud drops (Parungo et al., 1987), leading to high ion concentration ratios of cloudwater to precipitation. However, if cloud drops get captured by falling snow crystals, a process called riming, the ion concentration in the precipitation approaches that of cloud water with the ion concentration ratio reaching about one for graupel (Collett and Steiner, 1991). On the other hand riming of a ice crystal results in a mass increase and thus an increase of its fall speed. Combining these two facts a relation between the fall speed of a snow crystal and the cloud water to precipitation ion concentration ratio is expected.

Physical as well as chemical parameters are measured simultaneously in several case studies. Based on the observations during the winter 1990/91 relationships between the mean vertical Doppler velocity and the degree of riming as well as between the degree of riming and the cloudwater to precipitation ion concentration ratio are obtained. Thus, with the measured Doppler velocity the degree of riming can be estimated, which in turn determines the ion concentration ratio.

2. MEASURING SITE AND INSTRUMENTATION

The data discussed here are taken at Rigi Staffel and Seeboden, two sites located at an elevation of 1620 m asl and 1030 m asl, respectively, on the steep northwestern slope of Mt. Rigi, which stands out as an isolated precursor of the main chain of the Swiss Alps. A detailed discussion of the measuring area and the complete instrumentation is given by Staehelin et al. (1992b).

Snow crystals are replicated every 5 minutes using the Formvar technique described by Schaefer (1956) which allows a careful determination of the crystal shape, size and the degree of riming later under a laboratory microscope. Averaged values of these parameters are computed for each sample (Formvar slide) which contains up to 80 single crystals depending on the snow fall rate and the exposure time. Determination of the crystal shape is based on the classification of Magono and Lee (1966), whereas the degree of riming is expressed on a self defined scale running from 0 (unrimed) to 5 (graupel or fully rimed) as explained by Mosimann et al. (1992).

Vertically pointing Doppler radar measurements using a 3.2 cm mobile Doppler radar system located at the base of Mt. Rigi, approximately 3.5 km WNW of Rigi Staffel, provide information on the vertical precipitation structure and the particle fall velocity. Vertical profiles of radar reflectivity and Doppler velocity are measured up to a height of 14.25 km with a resolution of 50 m in space and one minute in time.

Cloudwater samples are collected with the Caltech Heated Rod Cloudwater Collector (CHRCC). Cloudy air is drawn by a high speed fan across a bank of 3.2 mm stainless steel rods as collection surfaces. Collett et al. (1990) gives a more complete description of the cloudwater collector.

Precipitation is sampled using a thermostated 43 cm diameter polyethylene funnel attached directly to a polyethylene sample bottle. The chemical samples are analyzed for major ions such as e.g. NO_3^-, SO_4^{2-} and NH_4^+.

3. RESULTS AND DISCUSSION

The cloud to precipitation ion concentration ratio at Mt. Rigi has been found to be correlated with the degree of riming observed at the same station (Staehelin et al., 1992a), which is depicted in Figure 1 (above) for NO_3^-. The other major ions show a similar pattern. Only time periods with simultaneous samples of cloudwater and precipitation are taken and the degree of riming is averaged over the corresponding time periods. As found earlier by Collett and Steiner (1991) the ratio reaches one for a degree of riming of 5 since graupel particles consist primarily of captured cloud drops. The less rimed the snow crystals are the more the precipitation differs from the cloudwater leading to high values for the cloud to precipitation ion concentration ratio. The exponential behavior of the relation arises from the definition of the riming scale and the fact, that the composition of a graupel particle is not likely to be changed much by the capture of a few additional cloud drops, while the composition of an unrimed snow crystal may be altered significantly.

Since cloud drops larger than 10 µm in diameter are not involved in accretional growth (Harimaya, 1975) differences between the chemical composition of different cloud drop sizes (see e.g. Noone et al., 1988) imply that the sampling of bulk cloudwater does not accurately reflect the composition of cloud drops captured by the ice crystals. In this sense, we are lucky that the cloudwater collector used in this study has a theoretical

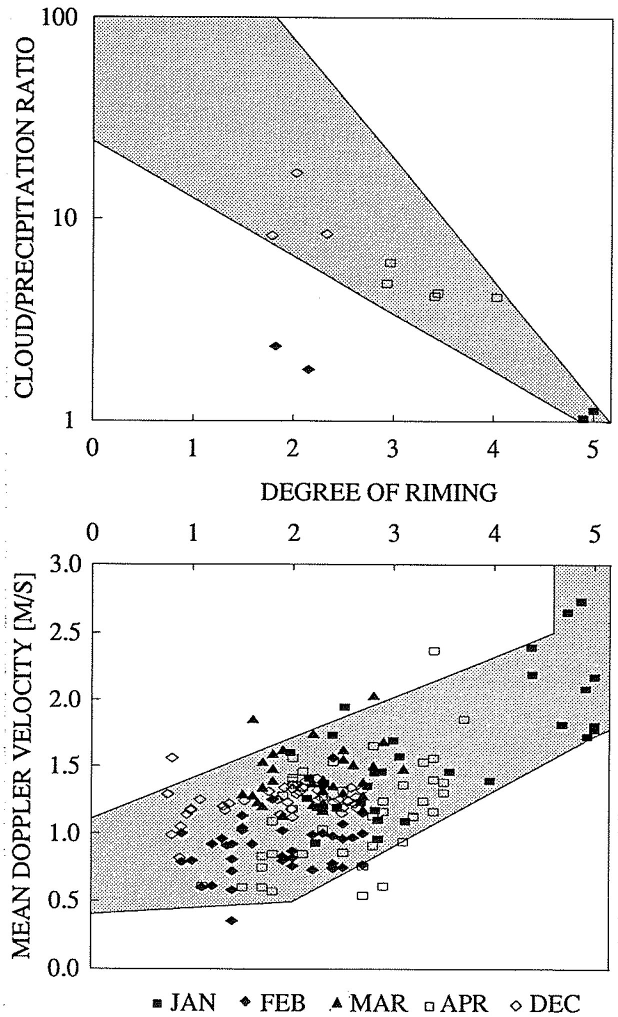

FIG. 1. Relations between the mean Doppler velocity and the degree of riming and between the degree of riming and the cloud to precipitation ion concentration ratio based on the measurements of 5 cases during the winter 1990/91 (see text). The shaded area for the upper graph is constructed to include all reasonable data points, whereas for the lower graph it corresponds to the range discussed in Mosimann et al. (1992).

lower size cut of 8 μm minimizing this problem. More serious is the complication that the precipitation chemistry may reflect the composition of the atmosphere and the cloud at an elevation much higher than the locally collected cloud samples. The influence of the overall background pollution level is kept as small as possible building the ratio of the ion concentration in precipitation and cloudwater (instead of precipitation alone), but nevertheless the influence increases towards lower degrees of riming causing the fanning off of the relation (shaded area).

The data of the case on February 8, 1991 tend not to follow the general relation. This event is marked out by exceptional high aerosol concentrations. Since the pollution level in the precipitation is determined not only by the ion concentration of the frozen cloud drops but also by the collected aerosols and gases the shift of the ratio to lower values is not surprising.

Mosimann et al. (1992) found a relationship between the degree of riming and the mean Doppler velocity measured at the same height (Figure 1, below). Each data point is based on one sample of collected snow crystals and a 5 minutes average of the mean Doppler velocity. In spite of a big scatter the increase of the Doppler velocity with higher degrees of riming is obvious. Since the Doppler velocity is the sum of particle fall speed and vertical air motion, the latter has to be negligible for taking the Doppler velocity as the terminal fall speed of the snow crystal. This assumption seems to be reasonable in stratiform winter precipitation, but nevertheless vertical winds induced by small convective cells or frontal passage as well as supplementation of the vertical air motion by orographic air flow may occur. The few data points lying out of the shaded area may indicate an influence of vertical air motion.

The combination of the two above discussed relations leads to the possibility to predict the cloud to precipitation ion concentration ratio by use of the mean vertical Doppler velocity. Because of various assumptions this new relationship has a rather qualitative character, but nevertheless it provides a further understanding of the mechanism leading to the removal of pollutants of the atmosphere. High Doppler velocities are coupled to a cloud to precipitation ion concentration ratio close to one. For a mean Doppler velocity of 1.5 m/s the ion concentration ratio is expected to be 8 varying in the range from about 10 to 2.

4. CONCLUSION

Using the degree of riming of the snow crystals, the cloudwater to precipitation ion concentration ratio has been connected to the vertically observed mean Doppler velocity. The larger the Doppler velocity of the snow crystals, being the result of more and more captured cloud drops, the closer the ratio gets to one indicating a convergence of the ion concentrations in the precipitation and in the cloudwater. Due to the influence of the naturally occurring variability of the size distribution and different shapes of the snow crystals, the vertical air motion and the background aerosol concentration the presented relationship exhibits a rather qualitative character. Nevertheless, for Doppler velocities larger than 2.5 m/s corresponding to graupel particles the cloud to precipitation ion concentration ratio can be predicted to be one within a reasonable error. The less rimed the snow crystals are the more uncertain the ratio gets, although an increasing tendency is obvious.

5. ACKNOWLEDGEMENT

The authors are grateful to Ruedi Lüthi for operating the vertical Doppler radar as well as to Donat Högl for his technical support. We thank all the members of the measuring team for their help in the field often under adverse conditions. This project is a contribution to the EUROTRAC subproject ALPTRAC. Partial funding was provided through an interdisciplinary program of the Swiss Federal Institute of Technology known as WaBoLu (Wasser, Boden, Luft meaning Water, Soil, Air).

6. REFERENCES

Collett, J.L. Jr., B.C. Daube, and M.R. Hoffmann, 1990: The chemical composition of interccepted cloudwater in the Sierra Nevada. *Atmos. Environ.*, **24A**, 959-972.

---, A.S.H. Prévôt, J. Staehelin, and A. Waldvogel, 1991: Physical factors influencing winter precipitation chemistry. *Environ. Sci. Technol.*, **25**, 782-788.

--- and M. Steiner, 1991: Investigations of the relationship between cloudwater and precipitation chemistry using Doppler radar. Presented at the fifth International Conference on Precipitation Scavenging and Atmosphere-Surface Exchange Processes, 15-19 July 1991, Richland, WA USA.

Harimaya T., 1975: The riming properties of snow crystals. *J. Meteor. Soc. Japan,* **53**, 384-392.

Magono, C., and C.W. Lee, 1966: Meteorological classification of natural snow crystals. *J. Fac. Sci., Hokkaido University*, Ser. 7, 2, No. 4.

Mosimann, L., M. Steiner, and W. Henrich, 1992: Prediction of snow crystal shape and riming by vertical Doppler radar. *J. Atmos. Res.*, in press.

Noone K.J., R.J. Carlson, D.S. Covert, J.A. Ogren, and J. Heintzenberg, 1988: Cloud droplets: solute concentration is size dependent. *J. Geophys. Res.*, **93**, 9477-9482.

Parungo, F., C. Nagamoto, and R. Madel, 1987: A study of the mechanisms of acid rain formation. *J. Atmos. Sci.*, **44**, 3162-3174.

Schaefer, V.J., 1956: The preparation of snow crystal replicas - VI. *Weatherwise*, **9**, 132-135.

Staehelin, J., J.L. Collett, Jr, R. Dixon, W. Henrich, C. Hsu, L. Mosimann, B. Oberholzer, A. Waldvogel, 1992a: Investigations of physical and chemical processes contributing to winter precipitation chemistry using field measurements from Mount Rigi (Switzerland). Proceed. EUROTRAC Symp. 1992, Garmisch-Partenkirchen.

---, A. Waldvogel, J.L. Collett, Jr, R. Dixon, R. Heimgartner, W. Henrich, C. Hsu, L. Li, L. Mosimann, B. Oberholzer, A.S.H. Prévôt, W. Schmid, T. Schumann, M. Steiner, M. Volken, and B. Zinder, 1992b: Scientific goals and performed experiments of the project "Winter Precipitation at Mount Rigi": An overview. *Water, Air and, Soil Pollut.*, accepted for publication.

ON THE INTERACTION BETWEEN CLOUD MICROCHEMISTRY AND MICROPHYSICS

V. K. Saxena

Department of Marine, Earth and Atmospheric Sciences
North Carolina State University, Raleigh, NC 27695-8208, USA

1. INTRODUCTION

Conventionally, microphysics of cloud systems has been considered (e.g. Wallace and Hobbs, 1977; Pruppacher and Klett, 1980; Rogers and Yau, 1989) as the driving mechanism for the behavior of clouds during their life cycles. Precipitation from clouds or their dissipation, the amount, chemical composition and the phase of precipitation elements (e.g. raindrops, snowflakes, hailstones, etc.); concentration, size distribution, and chemistry of aerosols released by dissipating clouds are thought to be controlled by microphysical processes responsible for the formation and growth of cloud droplets and ice particles. The latter have been the central theme of textbooks on cloud physics beginning with the earlier ones (e.g. Mason, 1971; Fletcher, 1966; Byers, 1965). During last two decades, a *silent revolution* has been in progress, the major outcome of which is the formulation of microchemistry of clouds *as the driving force* behind cloud microphysical processes. This has widened the scope of cloud physics. The results of cloud physics research will continue to be useful in planning weather modification and understanding inadvertent weather modification, with the new thrust on unraveling the complexities of global and localized climate change for which the low level stratiform clouds are of particular importance since these control (Twomey, 1991) the shortwave albedo thereby exercising considerable influence on the vertical temperature structure, especially in marine atmospheres.

Because of the global significance of interactions between cloud microchemistry and microphysics, we present in this paper three examples: one each in arctic, marine and continental atmospheres. Results of field experiments highlighting the importance of such interactions are briefly discussed.

2. BASIS FOR CLOUD MICROCHEMISTRY - MICROPHYSICS INTERACTIONS

For the formation of low level clouds which are capable of producing localized cooling effect, there are needed three necessary ingredients: hygroscopic aerosols which are effective cloud condensation nuclei (CCN), moisture, and existence of environmental supersaturation with respect to water. Microchemical processes have been recently shown (Hegg, 1990, 1991) to be responsible for heterogeneous production of CCN within clouds although experimental evidence for such a phenomenon has existed (e.g. Hegg et al., 1990; Saxena et al., 1970) for over twenty years. In humid, clean arctic airmasses, these processes could lead (Shaw, 1989) to production of new H_2SO_4 droplets which constitute highly effective CCN. Abundant gaseous sulfur is provided by oceanic sources, for example, in the form of dimethyl sulfide (Andreae et al., 1985; Charlson et al., 1987; Hegg et al., 1991) as well as anthropogenic sources (NAPAP, 1991). Current evidence suggests (Ayers et al., 1991; Ayers and Gras, 1991) that in clean marine air, a nonlinear relationship exists between DMS production and CCN number concentration. Scenarios of global climate change based on the reduction in the strength of anthropogenic sulfur sources have been presented by Wigley (1989, 1991). The basis for these scenarios is that microchemical processes could alter the microphysical parameters, such as droplet size distribution, in low level clouds and this in turn will change their reflectance.

The reflectance of clouds (i.e. the shortwave albedo) increases as the size of the cloud droplets decreases even if the total column liquid water is conserved. The cloud droplet size distribution is governed by cloud nucleation and growth processes (Pruppacher and Klett, 1980). The cloud optical thickness (δ_v) is dependent (Twomey, 1977) upon the effective mean radius (r_e) of cloud droplets as

$$\delta_v = \int_{Z_b}^{Z_t} \int_0^{\infty} n(r,z)\, 4\pi^2\, Q_{ext}(x,m)\, dr\, dz \simeq \frac{3W}{2r_e}\rho \quad (1)$$

where Z_b and Z_t are cloud base and cloud top height , $n(r,z)$ is the number of droplets of radius r per unit volume at altitude z, $x = 2\pi r/\lambda$, m is the liquid-water index of refraction, Q_{ext} is the Mie extinction efficiency, $\rho = 1000$ kg. m-3 (density of water). At visible wavelengths, $x>>1$ and $Q_{ext} \simeq 2$, such that δv is proportional to the total liquid water content:

$$W = \int_{Z_b}^{Z_t} \int_0^{\infty} n(r,z)\, 4\pi r^3/3\, dr\, dz \quad (2)$$

The effective radius is

$$r_e = \left(\int_{Z_b}^{Z_t} \int_0^{\infty} n(r,z)\, r^3\, dr\, dz \right) \left(\int_{Z_b}^{Z_t} \int_0^{\infty} n(r,z)\, r^2\, dr\, dz \right)^{-1} \quad (3)$$

and the total number of droplets per unit volume at the altitude z is

$$N(z) = \int_0^{\infty} n\,(r,z)\, dr. \quad (4)$$

The total number of droplets are considered as the vertically averaged number:

$$N = \int_{Z_b}^{Z_t} N\,(z)\, dz/(Z_t - Z_b). \quad (5)$$

For constant total cloud water, larger N implies smaller r_e; hence, the optical thickness increases with N.

3. CASE STUDIES

a. *Arctic Atmosphere*

The results of a field experiment conducted during June 1980 to study the arctic stratus clouds have been reported by Tsay and Jayaweera (1984), and Saxena and Rathore (1984). The latter work reported an unusual finding that the concentrations of CCN and CN reached their maxima within the cloud layer. Most satisfactory explanation for this finding has now been advanced by Hegg (1991) on the basis of homogeneous heteromolecular nucleation of H_2SO_4-H_2O droplets. Since gaseous sulfur has been found to be abundant in the arctic region, particle production is not sulfur-limited and the presence of H_2O_2, O_3, OH and possibly other trace substances could play a crucial role in supplying CN which could grow to become CCN. In the following, another example (in addition to the one cited by Hegg, 1991) which demonstrates the importance of microchemistry in shaping up the microphysical features of arctic stratus clouds, is presented.

In Fig. 1 are shown the results of field measurements aboard the NCAR Electra aircraft at a location (74.8°N, 165.6°W) near Barrow, Alaska -- the farthest point to the north within U.S. Three layers of arctic stratus clouds were observed, the base of the lowest layer was 100 m above the ice. In lower cloud layers, the droplet concentrations were around 70 cm^{-3} (Tsay and Jayaweera, 1984). Average CCN concentration within the cloud layers was found to be 400 cm^{-3} (active at 1% supersaturation with respect to water). However, in each cloud layer, the maximum exceeded 900 CCN cm^{-3}. Although there were open leads in the ice over the sea-surface, these did not seem to elevate CCN concentration below the cloud base. These measurements lend support to the emerging view that the majority of CCN are formed in the atmosphere through microchemical processes of the kind proposed by Hegg (1991).

b. *Marine Atmosphere*

In Fig. 2 is shown CCN concentration at 0.85% supersaturation (with respect to water) at three vertical locations during an ascent sounding made by the NCAR (National Center for Atmospheric Research, Boulder, Colorado) Electra aircraft on June 13, 1976 off the California coast (~33°N,125°W). The boundaries of the marine stratus cloud are identified based on the dew point temperature sounding. The top of the stratus cloud was ill-defined and the aircraft flew through the pockets of cloudless air. The CCN concentrations were measured using the spectrometer introduced by Fukuta and Saxena (1979 a,b). The sampling arrangement was such that the cloud droplets were precluded from entering the instrument. Since the measurements were made under identical isokinetic sampling conditions with the same instrument during a single flight, the data are highly consistent. Near the cloudbase, the CCN concentration drops by a factor of two (from 350 CCN cm^{-3} to 180 CCN cm^{-3} active at a 0.85% supersaturation) but near the top, it increases by a factor of three when compared with the below cloudbase concentration. The vertical trend in the CCN concentration is remarkably similar to the one in CN (condensation nuclei) shown in Fig. 4 of Hegg et al. (1990).

In Table 1 are shown typical values of C (concentration at 1% supersaturation) and slope (k) parameters. When the measurements were fitted to the conventional $n = CS^k$ form, where n is in cm^{-3} and S in percent.

TABLE 1

Concentration (C) and slope (k) parameters of the CCN activation spectrum measured off the California coast (33°N, 125°W) on 13 June 1976

S (%) range	0.4-1.6	0.2-1.2	0.2-1.5	0.2-1.2	0.4-1.2
C cm^{-3}	16	410	96	1350	70
k	1.19	1.55	1.63	0.95	2.32

Hudson and Frisbie (1991) have reported that CCN above marine stratus clouds could have continental origin. We have generally found large values of k (cf. Table 1), indicative of the proximity of the CCN source.

c. *Continental Atmosphere*

DeFelice and Saxena (1990) have reported CCN spectrum measurements in Mt. Mitchell (35°44'N, 82°17'W; 2,038 m MSL) State Park made during the summer of 1988. The case reported below, demonstrates that microchemistry-microphysics interactions are of particular significance at the boundary of the cloud airmass. Figure 3 shows the total droplet concentration to vary between 88 and 336 cm^{-3} and the CCN concentration to range between 78-200 cm^{-3} during the cloud event. The observations were made atop a meteorological tower described by Saxena et al. (1989) and Saxena and Lin (1990). The greatest magnitude of the time rate of change of CCN concentration (~300 CCN $cm^{-3}h^{-1}$) occurred between 0845 and 0859 EST implying that the sampling is taking place near the boundary of two airmasses. By the end of the cloud event, the CCN concentration reached the level characteristic of the pre-event airmass. During the entire event, the overall change was less than 200 CCN $cm^{-3}h^{-1}$.

4. CONCLUDING REMARKS

One of the basic mechanisms by which microchemical processes can change microphysical characteristics of clouds is through rearranging the cloud-active aerosols in cloud-forming airmasses. There exist three possible mechanisms for CCN enhancement in the vicinity of clouds. First, when clouds form as a result of mixing airmasses, real-time CCN measurements show (e.g. Saxena, 1980; DeFelice and Saxena, 1990) that CCN concentrations could register an increase around such clouds due to difference in the aerosol content of the two airmasses. Secondly, due to sulfate production by clouds (e.g. Easter and Hobbs, 1974; Hegg and Hobbs, 1979; Hegg et al., 1980), the CCN concentration in the airmass processed by such clouds could be elevated resulting from a shift in the size distribution and chemical composition of the existing aerosol particles. Thirdly, new aerosol particles could be formed in the vicinity of clouds resulting from the modification of supersaturation field as proposed by Hegg et al. (1990), and Hegg (1991). Such results should be evident if simultaneous measurements of CN (condensation nuclei) and CCN are made because the production of new particles is likely to enhance the concentration of both.

Earlier experiments by Radke and Hegg (1972) have suggested that drop evaporation could elevate particle concentration by a factor of two over the entire size distribution and by a factor of five for particles smaller than

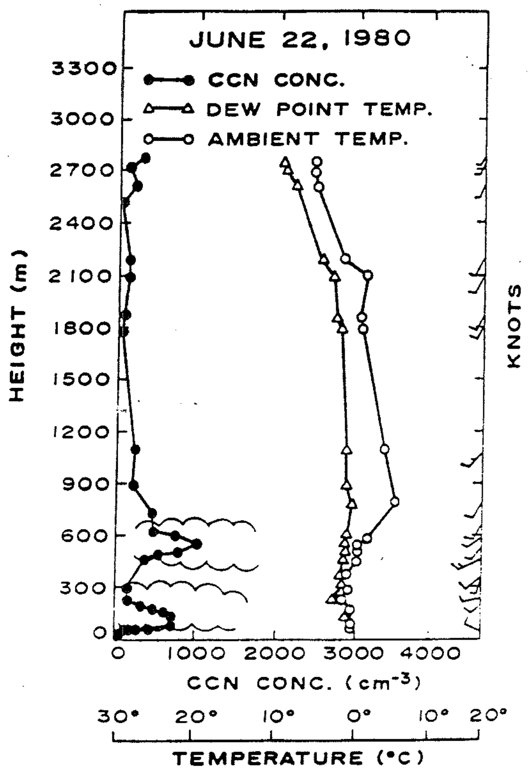

Fig. 1. Number concentration of CCN active at 1% supersaturation as a function of altitude on June 22, 1980. Measurements were made off Barrow, Alaska using the NCAR Electra aircraft. Notice the maximum CCN concentration within the cloudy layers.

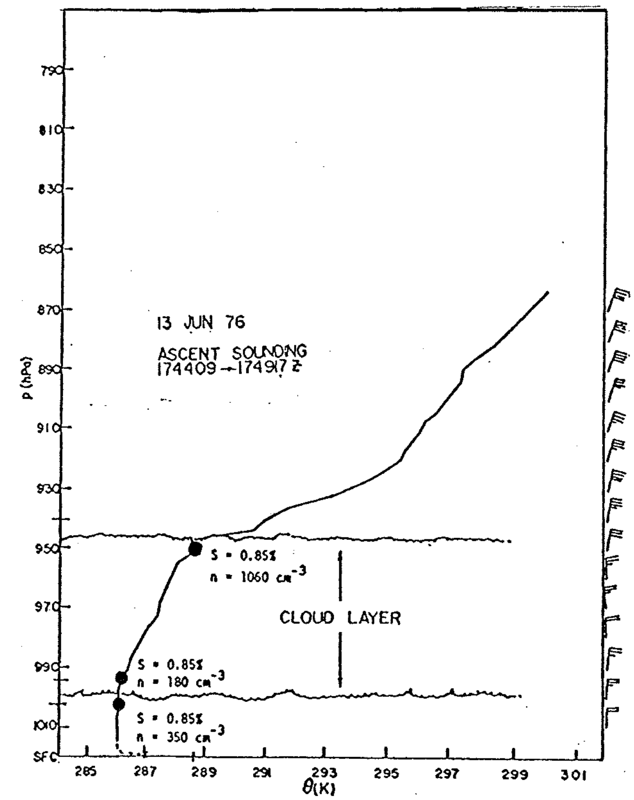

Fig. 2. Potential temperature and wind profiles at (34°N, 127°W) for an ascent sounding on June 13, 1976 during 17:44:09 - 17:49:17 UT. CCN concentrations are shown plotted at three points across the cloudy layer.

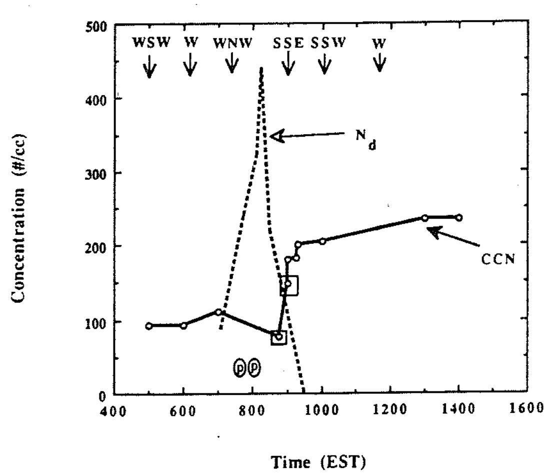

Fig. 3. The temporal variation of cloud droplet concentration (N_d) and CCN concentration during the cloud event of July 22, 1988 at Mount Mitchell, North Carolina in the continental airmass.

0.06 μm in radii. In this paper, we have presented observational evidence in favor of Hegg et al. (1990) and Hegg (1990, 1991).

ACKNOWLEDGMENTS

The support for above measurements was received from the National Science Foundation, National Center for Atmospheric Research and U.S. Environmental Protection Agency.

5. REFERENCES

Andrae, M. O., R. J. Ferek, J. Bermond, K. P. Byrd, R. T. Engstrom, S. Hardin, P. D. Houmere, T. LeMerrec, H. Raemdock and R. B. Chatfield, 1985: Dimethylsulfide in marine air. *J. Geophys. Res.*, **90**, 12,891-12,900.

Ayers, G. P. and J. L. Gras, 1991: Seasonal relationship between cloud condensation nuclei and aerosol methanesulphonate in marine air. *Nature*, **353**, 834-835.

Ayers, G. P., J. P. Ivey and R. W. Gillett, 1991: Coherence between seasonal cycles of dimethyl sulphide, methanesulphonate and sulphate in marine air. *Nature*, **349**, 404-406.

Byers, H. R., 1965: Elements of Cloud Physics. The Univ. of Chicago Press, Chicago, 191 pp.

Charlson, R. J., J. E. Lovelock, M. O. Andreae and S. G. Warren, 1987: Oceanic phytoplankton, atmospheric sulfur, cloud albedo and climate. *Nature*, **326**, 655-661.

DeFelice, T. P. and V. K. Saxena, 1990: Cloud condensation nuclei as tracers of airmass transport and mixing, in Preprints of the 1990 Conference on Cloud Physics, July 23-27, AMS, Boston, pp. 458-464.

Easter, R. C. and P. V. Hobbs, 1974: The formation of sulfate and the enhancement of cloud condensation nuclei in clouds. *J. Atmos. Sci.*, **31**, 1586-1591.

Fletcher, N. H., 1966: The Physics of Rainclouds. The Univ. Press, Cambridge (U.K.), 390 pp.

Fukuta, N. and V. K. Saxena, 1979a: A horizontal thermal gradient cloud condensation nucleus spectrometer. *J. Appl. Meteor.*, **18**, 1352-1362.

Fukuta, N. and V. K. Saxena, 1979b: The principle of a new horizontal thermal gradient cloud condensation nucleus spectrometer. *J. Rech. Atmos.*, **13**, 169-188.

Hegg, D. A., 1990: Heterogeneous production of cloud condensation nuclei in the marine atmosphere. *Geophys. Res. Lett.*, **17**, 2165-2168.

Hegg, D. A., 1991: Particle production in clouds. *Geophys. Res. Lett.*, **18**, 995-998.

Hegg, D. A. and P. V. Hobbs, 1979: The homogeneous oxidation of sulfur dioxide in cloud droplets. *Atmos. Environ.*, **13**, 981-987.

Hegg, D. A., L. F. Radke and P. V. Hobbs, 1990: Particle production associated with marine clouds. *J. Geophys. Res.*, **95**, 13,917-13,926.

Hegg, D. A., P. V. Hobbs and L. F. Radke, 1980: Observations of the modification of cloud condensation nuclei in wave clouds. *J. Rech. Atmos.*, **14**, 217-222.

Hegg, D. A., R. J. Ferek, P. V. Hobbs and L. F. Radke, 1991: Dimethyl sulfide and cloud condensation nucleus correlations in the northeast Pacific Ocean. *J. Geophys. Res.*, **96**, 13,189-13,191.

Hudson, J. G. and P. R. Frisbie, 1991: Cloud condensation nuclei near marine stratus. *J. Geophys. Res.*, **96**, 20,795-20,808.

Mason, B. J., 1971: The Physics of Clouds. 2nd ed., Oxford Univ. Press, London.

NAPAP, 1991: National Acid Precipitation Assessment Program: 1990 Integrated Assessment Rept., U.S. Govt. Printing Office, Washington, D.C., 520 pp.

Pruppacher, H. R. and J. D. Klett, 1980: Microphysics of Clouds and Precipitation, D. Reidel Publishing Company, Holland, 714 pp.

Radke, L. F. and D. A. Hegg, 1972: The shattering of saline droplets upon crystallization. *J. Rech. Atmos.*, **6**, 447-455.

Rogers, R. R. and M. K. Yau, 1989: A Short Course in Cloud Physics. Pergamon Press, New York, 293 pp.

Saxena, V. K., 1980: Some wintertime cloud-aerosol interactions over Lake Michigan. *J. Rech. Atmos.*, **14**, 255-265.

Saxena, V. K. and N.-H. Lin, 1990: Cloud chemistry measurements and estimates of acidic deposition on an above cloudbase coniferous forest. *Atmos. Environ.*, **24A**, 329-352.

Saxena, V. K. and R. S. Rathore, 1984: Transport and formation of summertime cloud condensation nuclei over the Arctic Ocean. In Preprint Volume I: Eleventh International Conference on Atmospheric Aerosols, Condensation and Ice Nuclei, September 3-8, Budapest, Hungary, pp. 292-298.

Saxena, V. K., J. N. Burford and J. L. Kassner, Jr., 1970: Operation of a thermal diffusion chamber for measurements on cloud condensation nuclei. *J. Atmos. Sci.*, **27**, 73-80.

Saxena, V. K., R. E. Stogner, A. H. Hendler, T. P. DeFelice and R. J.-Y. Yeh, 1989: Monitoring the chemical climate of the Mt. Mitchell State Park for evaluation of its impact on forest decline. *Tellus*, **41B**, 92-109.

Shaw, G., 1989: Production of condensation nuclei in clean air by nucleation of H_2SO_4. *Atmos. Environ.*, **23**, 2841-2846.

Tsay, S. C. and K. Jayaweera, 1984: Physical characteristics of arctic stratus clouds. *J. Clim. Appl. Meteor.*, **23**, 584-596.

Twomey, S., 1977: The influence of pollution on the shortwave albedo of clouds. *J. Atmos. Sci.*, **34**, 1149-1152.

Twomey, S., 1991: Aerosols, clouds and radiation. *Atmos. Environ.*, **25A**, 2435-2442.

Wallace, J. M. and P. V. Hobbs, 1977: Atmospheric Science: An Introductory Survey. Academic Press, New York, 467 pp.

Wigley, T. M. L., 1989: Possible climate change due to SO_2-derived cloud condensation nuclei. *Nature*, **339**, 365-367.

Wigley, T. M. L., 1991: Could reducing fossile fuel emissions cause global warming? *Nature*, **349**, 503-506.

FORMATION AND GROWTH OF CLOUD DROPLETS: THE EFFECT OF BINARY HETEROGENEOUS NUCLEATION AND BINARY CONDENSATION

Markku Kulmala, Pekka Korhonen, Ari Laaksonen, Timo Vesala
University of Helsinki, Department of Physics
Siltavuorenpenger 20D, SF-00170 Helsinki, Finland

1 INTRODUCTION

Conventionally the formation and growth of cloud droplets is considered to take place as pure water condensation on different cloud condensation nuclei (CCN). The role of sulphur compounds in forming new particles to act as CCN has been studied widely (see e.g. Charlson et al., 1987; 1990; 1992 and Wigley, 1991). However, in certain humidity conditions also increased concentrations of condensable vapours (such as HNO_3 and HCl) in the atmosphere can activate an increased number of pre-existing aerosol particles to CCN (Kulmala et al., 1992). In the atmosphere nitric acid is formed from NO_x, the emissions of which have increased during the last decades. HNO_3 concentration above polluted areas are many times greater than in backround areas. The continental average is ten times higher than the marine average (Penner et al., 1991). Typical nitric acid concentrations are 0.1 ppbv in marine air and 1.0 ppbv in continental air. In the present study we have investigated the CCN activation size of aerosol particles at different nitric acid concentrations and the dependence of the activation process on the water solubility of the particles.

2 THEORY

Consider an air parcel containing water vapour and aerosol particles, but free of HNO_3. As the relative humidity exceeds 100 %, water starts condensing on a certain fraction of the aerosol particles. We say that this fraction of the particles is activated as CCN. For simplicity, assume that all the aerosol particles are spherical and that their composition is the same regardless of their size. Then the only factor determining whether a particle will be activated or not is its size. The threshold size for activation is now just the equilibrium size for which the saturation vapour pressure is the same as the ambient vapour pressure. The saturation ratio on the surface of larger particles exceeds unity, and they start to grow as water condenses on them.

Next, introduce into the air parcel a small amount of nitric acid vapour. To find the equilibrium size of insoluble particles we must consider the condensation process of a water–nitric acid mixture. With soluble particles the situation is more complicated as the effect of the soluble fraction of the particles must be taken into account.

For insoluble particles we are able to find the size of smallest particle, which can be activated, using the classical binary heterogeneous nucleation theory (see Hamill et al., 1982; Lazaridis et al., 1991). Heterogeneous nucleation takes place when vapour molecules form a critical sized embryo on a CCN. Embryos smaller than the critical size are not stable, and they will evaporize immediately. The critical size corresponds to a minimum in the free energy barrier for droplet formation. For certain binary mixtures the minimum is lower than for either component alone. The size and composition of the critical embroy is the same in the heterogeneous nucleation as in homogeneous nucleation (provided that the ambient conditions are the same), and they can be evaluated using the same method as in the original (sometimes called revised) classical nucleation theory (see e.g. Lazaridis et al., 1991). After nucleation the particles will continue growing without limit as long as there are condensable vapours present.

The essential quantity, which characterizes the free energy barrier is the contact angle, the angle between the surface of the embroy and the surface of the nucleus. The effect of the contact angle on activation size could is presented elsewhere (Lazaridis et al., 1991; Korhonen et al., 1991), and in this study we consider only totally wettable particles.

For soluble particles we are able to find the size of the smallest particle which can be activated using the transition and continuum regime condensation theories (see e.g. Vesala et al., 1990; Vesala, 1991). Although the particle consists of three species, we can use the binary condensation theory since the substance forming the soluble particle is non-volatile. The problems of binary condensation are more complicated than the problems of a single component system. The rigorous general solution of the Boltzmann equation in the transition regime involves considerable mathematical difficulty. We have applied a well-known approach: the mass and heat fluxes are calculated using the continuum regime expressions corrected by Fuchs' and Sutugin's (1970) interpolation formula. The mass transfer of one vapour is ignored when the mass transfer rate of the other is calculated. In dilute vapour mixtures the approximation of independent diffusion has proved to be correct (e.g. Vesala, 1991). The mass and thermal accommodation coefficients are assumed to be unity. The equations for the mass fluxes and for the droplet temperature are solved numerically using the quasistationary assumption by means of fourth order Runge–Kutta method (Majerowicz et al., 1991).

The threshold radius of CCN activation corresponds now to the size of the particle, which can at given ambient conditions continue growing without limit (e.g. reaching the size of at least few microns). Note that particles with sizes under the threshold radius are also capable of growing initially, but they will eventually reach some equilibrium size.

In order to carry out the calculations in practice, one needs physico-chemical data for the mixtures in question. To find the physico-chemical data for three component liquid mixtures is not an easy task. We have chosen sulphuric acid particles to represent the soluble particles, since there is some data available (Jaecker-Voirol et al., 1990) for the H_2SO_4-HNO_3-H_2O system. Sulphuric acid is extremely hygroscopic and thereby these particles are higly soluble.

3 RESULTS AND DISCUSSION

CCN activation due to binary condensation of water and nitric acid vapours on both insoluble totally wettable particles and on soluble non-volatile particles were simulated. In the simulations the saturation ratio for water vapour varied from 1.00042 to 1.01. The nitric acid vapour concentration varies from 0 to 10 ppbv. The temperature was -10 °C and pressure 600 mbar.

The activation size at fixed humidity decreases, when the acid concentration is increasing. The effect is much more significant, when the saturation ratio of water vapour is close to unity (see Fig. 1.). For insoluble particles this effect is always very clear, but for soluble particles at higher supersaturations (S = 1.01) the effect seems to disappear. The activation size of the soluble particles refers to the initial radius (i.e. radius of the soluble particle in zero humidity).

Atmospheric aerosols can be divided in more hygroscopic and less hygroscopic particles (see e.g. McMurry and Stolzenburg, 1989), which will form different size distributions, when the relative humidity exceeds some 85% - 90%. We have calculated the activated fraction of both the more hygroscopic (in our simulation soluble) particles and the less hygroscopic (insoluble) particles at different saturation ratios and nitric acid concentrations. The soluble particles were allowed to grow to their equilibrium size at the relative humidity of 91% and at each concentration of nitric acid vapour. In these conditions the particles do not grow without limit but reach some final equilibrium size. Using this final size the activated fraction of the more hygroscopic particle can be determined, if the size distribution of the particles is available. We used an artificial, but realistic lognormal size distribution with geometric standard deviation of 2.0. The count median diameter for the insoluble particles was 100 nm and for the soluble particles at 91% relative humidity 150 nm. The activated fraction of the insoluble particles increases more rapidly as a function of nitric acid concentration than the activated fraction of the soluble particles (Fig. 2.), and at high acid concentration and low water supersaturations a bigger fraction of the insoluble particles is activated than of the soluble particles. Typically less than 10% of the ambient aerosol particles can be activated at zero nitric acid concentrations (see Pruppacher and Klett, 1978 ; Götz et al., 1991). The increase of the activated fraction due to the presence of nitric acid vapour is therefore significant and the number concentration of cloud droplets can grow considerably, when the acid concentration doubles.

The binary condensational growth of nitric acid – water droplets can take place in the atmospheric conditions used in our simulations, even though pure water droplets at the same conditions would evaporate. Similarly the growth rate of the droplets is higher when the acid concentration is increased (Korhonen et al., 1991). However, the final size of the cloud droplets depends also on the amounts of condensable vapours available. According to the model calculations, the overall effect of activation and condensation will decrease the mean size of cloud droplets, since the increasing number of cloud droplets due to activation will deplete the water and acid vapours sooner and the growth will stop earlier.

4 CONCLUSIONS

Our simulations show that enhanced nitric acid concentrations can affect cloud droplet distributions by increasing the number concentrations and decreasing the mean size of the droplets. This can cause considerable changes to the radiative properties of low clouds. Furthermore, these effects can probably enhance cloudiness. First of all, it is likely that the smaller droplet size will decrease precipitation (Vali, 1991) so that the clouds will have a longer lifetime. Secondly, the cloud formation can take place at smaller saturation ratios of water vapour. Thirdly, with increased HNO_3 concentrations the disappearance of the cloud droplets due to evaporation is slower.

Acknowledgements

Support of this work by the SILMU project of the Academy of Finland is gratefully acknowledged.

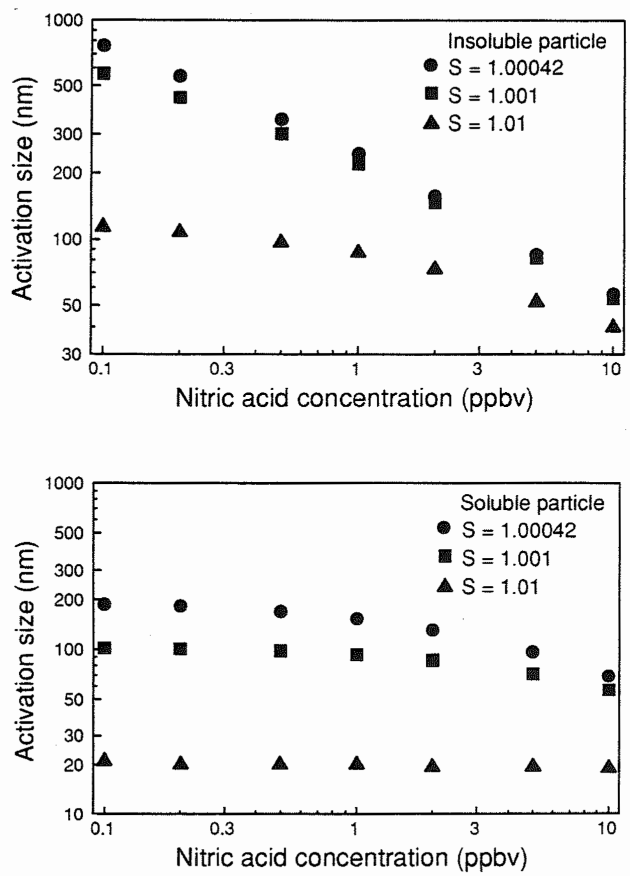

Figure 1: Activation size (radius) of CCN as a function of HNO_3 vapour concentration. Temperature is -10 °C and pressure 600 mbar.

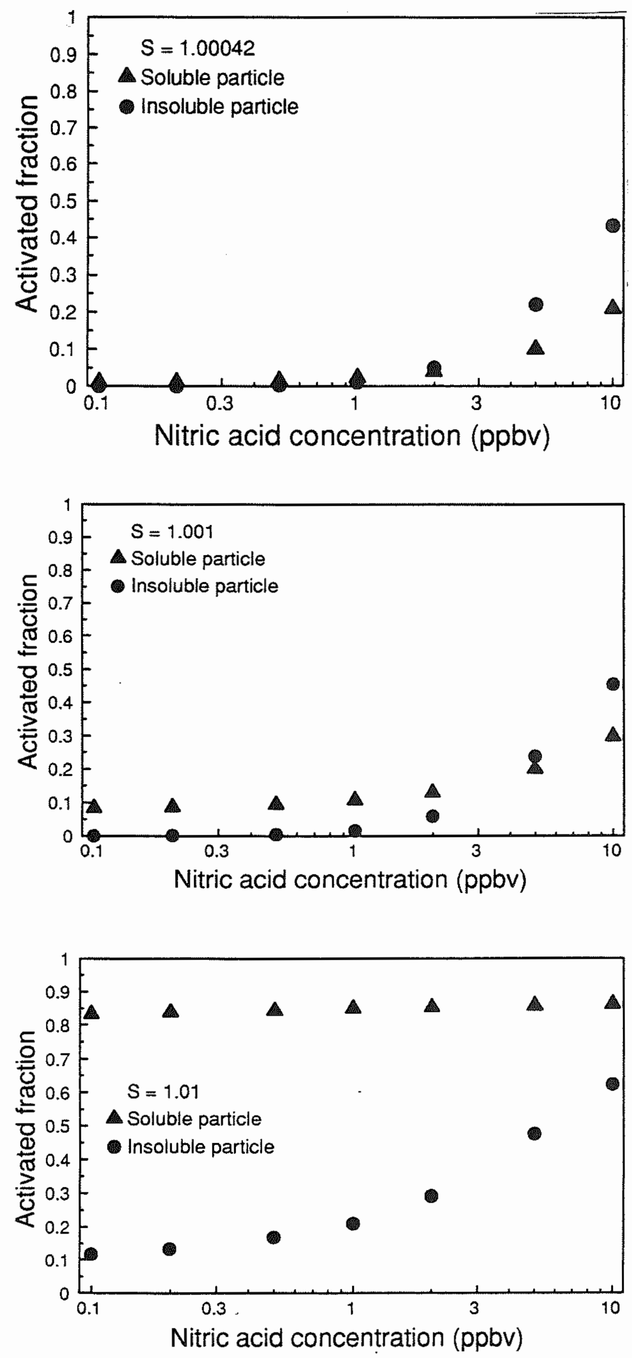

Figure 2: Activated fraction of aerosol particles as a function of HNO_3 vapour concentration. Temperature is -10 °C and pressure 600 mbar.

REFERENCES

Charlson, R.J., J.E. Lovelock, M.O. Andreae, and S.G. Warren, 1987: *Nature* **326**, 655-661.

Charlson, R.J., J. Langner and H. Rodhe, 1990: *Nature* **348**, 22.

Charlson, R.J., S.E. Schwartz, J.M. Hales, R.D. Chess, J.A. Coakley Jr., J.E. Hansen and D.J. Hofmann, 1992: *Science*, **255**, 423-430.

Fuchs, N.A. and A.G. Sutugin, 1970: *Highly dispersed aerosols*, Ann Abor Science Publ., Michigan.

Götz, G., E. Mészáros and G. Vali, 1991:*Atmospheric particles and nuclei.*, Akadémiai Kiadó, Budabest.

Hamill, P., R.P. Turco, C.S. Kiang, O.B. Toon, and R.C. Whitten, 1982: *J. Aerosol Sci.*, **13**, 561-585.

Jaecker-Voirol, A., J.L. Ponche and P. Mirabel, 1990: *J. Geophys. Res.*, **95**, 11857-11863.

Korhonen, P., M. Kulmala, A. Laaksonen, T. Vesala, M. Lazaridis, 1991: *Report Series in Aerosol Science* **19**, 28-32, Finnish Association for Aerosol Research, Helsinki.

Kulmala, M., P. Korhonen and A. Laaksonen, 1992: Enhanced activation of cloud condensation nuclei resulting from NO_x emissions. Report, University of Helsinki, Department of Physics, Helsinki, Finland.

Lazaridis, M., M. Kulmala and A. Laaksonen, 1991: *J. Aerosol Sci.*, **22**, 823-830.

Majerowicz, A., M. Kulmala and P.E. Wagner, 1991: *Report Series in Aerosol Science* **17**, 144-151, Finnish Association for Aerosol Research, Helsinki.

McMurry, P.H. and M.R. Stolzenburg, 1989: *Atmospheric Environment*, **23**, 497-507.

Penner, J.E., C.S. Atherton, J. Dignon, S.J. Ghan and J.J. Walton, 1991: *J. Geophys. Res.*, **96**, 959-990.

Pruppacher, H.R. and J.D. Klett, 1978: *Microphysics of clouds and precipitation*, D.Reidel Publishing Co., Holland.

Vali G. (Ed.), 1991: *Report of the Experts Meeting on interaction between aerosols and clouds* Report WCRP-59, WMO/TD-No. 423, World Meteorological Organization, Geneva, Switzerland.

Vesala, T., M. Kulmala, A. Majerowicz, and P.E. Wagner., 1990: In *Aerosols, Science, Industry, Health and Environment.* Proceedings of 3rd international aerosol conf. Sept. 24-27, Pergamon Press, Oxford, 176-179.

Vesala, T., 1991: Binary droplet evaporation and condensation as phenomenological processes. Ph.D. Thesis. *Commentationes Physico-Mathematicae et Chemico-Medicae* 127, The Finnish Society of Sciences and Letters, Helsinki.

Wigley, T.M.L., 1991: *Nature*, **349**, 503-506.

AIRBORNE OBSERVATIONS SIMULATED WITH A CLOUD CHEMISTRY MODEL

J.P.J.M.M. de Valk, P.G. Duynkerke, and M.H.J. Emond

Institute for Marine and Atmospheric Research, Utrecht University
Princetonplein 5, 3584 CC Utrecht, the Netherlands

1. INTRODUCTION

A realistic simulation of long range transport and transformation processes in the troposphere requires an accurate cloud description to complete it. However, a detailed numerical description of the physical properties of clouds already requires a respectable amount of computing time. The introduction of chemistry enhance this computing demand even further. In order to incorporate a description of clouds in large scale dispersion models a model which can simulate both stratus and cumulus clouds is developed.

This paper gives a qualitative description of the model. Moreover model results are compared to in-situ flight measurements performed and provided by the Atmospheric Environment Service of Environment (AES) Canada and to observations provided by *GEOSENS b.v.*

2. MICROPHYSICAL MODEL

The model consists of two horizontal layers a cloud and a subcloud layer. The upper layer is fully (stratus cloud) or partially (cumulus cloud) filled with a vertically homogeneously mixed cloud with a temperature T_c. The top of the cloud is also the rigid lid of the model. The lower sub cloud layer has a temperature T_a ($T_a > T_c$) and a relative humidity S, see figure 1. The description of the dynamics is restricted to a simple water cycle in which no thermodynamics is considered.

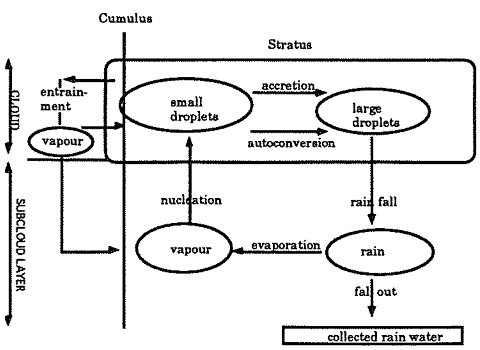

Figure. 1. The water cycle considered in the model for a stratus cloud, at the righthand side of the vertical line, and a cumulus cloud, at both sides of the vertical line. The arrows denote the conversions from one aqueous phase to another.

The considered microphysics copes with three bulk hydrometeor fields, viz. small cloud drops with a fixed drop radius (10 μm), large cloud drops and sub cloud rain drops, the latter two with variable radii. To account for the different chemical development of small and large cloud drops (Hegg and Larson, 1990) a distinction in cloud drop size is made. The physical processes considered are visualized in figure 1. The autoconversion rate (a Kessler (1969) parameterization in warm clouds) is modified to simulate the Wegener Bergeron Findeisen (WBF) process in cold clouds. For clouds with $T_c < 268K$: $\varphi^* = \varphi \times (1 + ICE)$, φ denotes the autoconversion rate and ICE is a function which describes the increased autoconversion due to the WBF process.

3. CHEMISTRY MODEL

The model presented here focusses on aqueous phase chemistry. Gas phase chemistry is omitted. The microphysical development of a droplet influences its chemical composition. To facilitate the comparison of the results to the observations, the considered chemistry is simplified. In the gas phase are SO_2, NH_3, HNO_3, O_3 and H_2O_2 and ammoniumsulfate aerosol are considered. In the aqueous phase the dissociation of SO_2, NH_3 and HNO_3, and the oxidation of $S(IV)$ by O_3 and H_2O_2 are accounted for.

A set of first order coupled differential equations describe both the chemistry and the physics. The set is solved by a multistep Gear method which conserves mass as well as neutrality.

4. INITIALIZATION

In the summer of 1988 the AES of Toronto performed flights above southern Ontario as part of the Eulerian Model Evaluation Field Study (Isaac 1989). The study was prepared under the auspices of the Canadian Institute for Research in Atmospheric Chemistry. For this project, flights were performed between the sites Egbert and Dorset with two aircrafts. We refer to G. Isaac (1989) for a description of the instrumentation. Thirteen cases were selected from the flight data of which model simulations were made. Model input was derived from flight data study.

All the measurements were performed in cumulus clouds. The studied cases could be classified in flights performed in polluted (southerly flow), unpolluted (westerly flow) and night time conditions. An interpretation problem occured as there was no consistent information available about the 'life' time of the studied clouds. We decided to compare measured data with model results obtained after an initiation period of the model of 600 s and two arbitrary times: 1200 s and 1800 s.

In 1990 and 1991 stratus clouds were sampled by *GEOSENS b.v.* The flight strategy was to follow an air mass in westerly wind conditions to determine if a chemical development in the cloud water can be observed. Therefore consequetive tracks perpendicular to the wind direction were flown at down wind locations. The model was initialized with the observations performed at the most westerly track. The observations of the downwind tracks were simulated.

5. RESULTS, DISCUSSION

In figure 2 the model results (ordinate) are compared to the measured aqueous phase concentrations (abscissa) of SO_4^{2-} by the A.E.S.. In each simulated flight two samples were taken simultaneously resulting sometimes in two different measured concentrations for the same simulation result in the figure. In figure 5 a similar graph is presented for the *GEOSENS* data. As several measurements were performed on one track we made two simulations of each track. In figure 5 the averaged values and their standard deviations of both simulations and observations are presented.

The drawn lines denote the one to one ratio of simulated concentrations to measured concentrations. From the small scatter around the drawn lines we conclude that the model performance is very satisfactory.

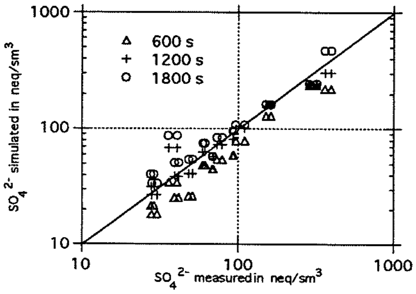

Figure. 2. The SO_4^{2-} concentration measured in neq/sm^3 (abscissa) compared to the simulated SO_4^{2-} (ordinate) for three different simulation times: 600 s, 1200 s, and 1800 s.

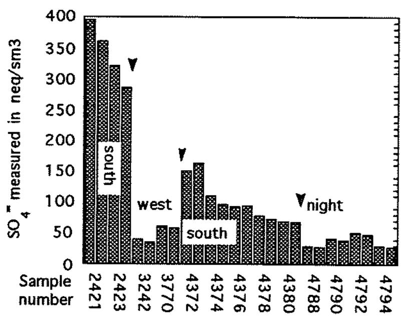

Figure. 3. Histogram of the total $SO_4^=$ concentration measured in neq/sm^3 for each studied sample versus the sample number. The arrows indicate the boundaries for the different conditions.

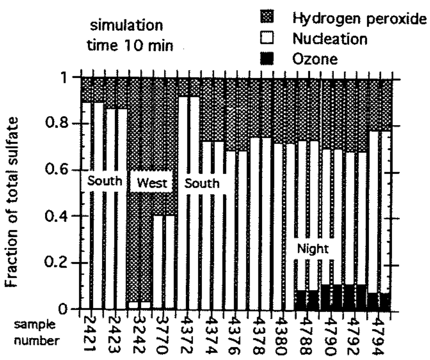

Figure. 4. Histogram of the fraction of the total sulfate contributed by the nucleation process, and the oxidation processes by peroxide and ozone versus the sample number.

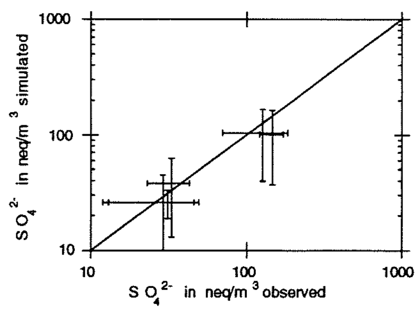

Figure. 5. SO_4^{2-} averaged observed concentration observed in neq/sm^3 (abscissa) compared to the averaged simulated SO_4^{2-} (ordinate) and their standard deviations.

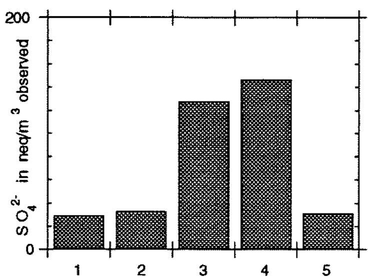

Figure. 6. Histogram of the total averaged SO_4^{2-} concentration measured in neq/sm^3 for each sample: the samples 1, 2, and 5 are measured in summer, and the samples 3 and 4 in winter.

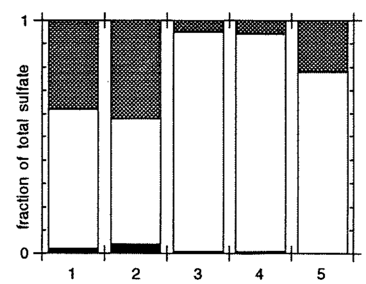

Figure. 7. Histogram of the fraction of the total sulfate contributed by the nucleation process, and the oxidation processes by peroxide and ozone versus the sample number. The numbers refer to the same conditions as in figure 6. For legend see figure 4.

Figure 3 gives the total sulfate measured for each studied sample. In this figure we see that for the flights studied here a southerly flow during day time carries higher sulfate concentrations compared to westerly flows and night time southerly flow conditions. Figure 6 shows the averaged observed total sulfate as observed by *GEOSENS*. Note the difference in total sulfate between winter and summer time conditions. Figure 4 shows the relative fractions of the contributions of nucleation, sulfate oxidation by peroxide and ozone after 10 minutes of simulation time. Clearly visible in figure 4 is the prevailing contribution of nucleation to the total sulfate especially in southerly flows. The second largest factor contributing to the sulfate in cloud water is the oxidation by hydrogen peroxide. These conclusions are confirmed in figure 7 were the averaged relative fractions are shown for flights performed by *GEOSENS* in stratus clouds.

ACKNOWLEDGEMENT

The data with which the model results are compared are the result of the culmination of efforts by a large number of individuals. The author is grateful for all the assistance, discussions and hospatality he had during his stay at the Atmospheric Environment Service in Downsview, Ontario. The author is particulary grateful to Dr. G. A. Isaac, Dr. W. R. Leaitch, Dr. J.W. Strapp, Dr. J. W. Bottenheim, Dr. K. J. Puckett, Dr. L. A. Barrie, Dr. H. A. Wiebe, Dr. K. G. Anlauf, Dr. C. M. Banic, M. D. Couture, A. M. Macdonald, and Dr. G. Raga. The author is also grateful towards *GEOSENS b.v.* for providing the observations.

REFERENCES

Hegg, D.A, and Larson, T.V., 'The effects of microphysical parameterization on model predictions of sulfate production in clouds', Tellus, 42B:272, (1990)

Isaac, G.A, Leaitch, W.R., Strapp, J.W., Anlauf, K.G., Bottenheim, J.W., Wiebe, H.A., and Puckett, K.J., 'Canadian airborne measurements for model evaluation, preliminary results from the 1988 Muskoka field study', *Proceedings of the AMS symposium on the role of clouds in atmospheric chemistry and global climate*, Anaheim, Calif., 1989, pp 225-230

Kessler, E., 'On the distribution and continuity of water substance in atmospheric circulation', *Meteorological monographs*, **10, no 32**,AMS, Boston, (1969), pp 84

SNOW CHEMISTRY AT HIGH ALPINE SITES

M. Schwikowski, U. Baltensperger, H.W. Gäggeler, D.T. Jost

Paul Scherrer Institute, CH-5232 Villigen PSI, Switzerland

1. INTRODUCTION

For the reconstruction of past atmospheric compositions by the interpretation of ice core data from cold alpine glaciers it is important to understand the processes which lead to a certain concentration of a particular chemical trace component in the ice. In the framework of the EUROTRAC subproject ALPTRAC the main objectives of our research are therefore to understand the processes determining the fluctuations of atmospheric trace components at high-alpine sites and to relate the atmospheric and snow concentrations of various chemical components.

2. EXPERIMENTAL

Extensive field studies were performed on Jungfraujoch, Switzerland (3450 m a.s.l.) during March, 1990, and January/February, 1991 in order to investigate the amount of acidic and other species related to anthropogenic activities in alpine precipitation. Snow samples were collected after every snow fall from an exposed Teflon surface as well as from a snow pit at the end of the campaign. In spring, 1991, we performed additional snow pit sampling at three different high-alpine sites (Jungfraujoch: May, Fiescherhorn: May and Weissfluhjoch: March). In order to investigate in-cloud scavenging by snow, air samples were taken in parallel with the snow sampling. A more detailed description of the experimental procedures is published elsewhere (Schwikowski et al., 1990; Baltensperger et al., 1991a). In the obtained air and snow samples the concentrations of Cl^-, NO_3^-, SO_4^{2-}, Ca^{2+}, K^+, Mg^{2+}, Na^+, NH_4^+ were determined. In the snow samples determination of ^{210}Pb, the isotopic ratio $\delta^{18}O$, the pH as well as the conductivity was performed additionally.

3. RESULTS

The concentrations of anthropogenic species (NO_3^-, SO_4^{2-} and NH_4^+) in snow show a pronounced variability. They were lowest in high winter (January and February) and of the same order of magnitude as in polar regions (Clausen and Langway, 1989) indicating that the sampling sites were not reached by air masses from lower polluted regions. In early spring events of increased snow concentrations reflected an increased upward transport of polluted air by thermal convection (see Fig. 1). This was observed for fresh snow samples as well as for snow pit samples. Mean concentrations from four snow pits at three different sites are given in Table 1.

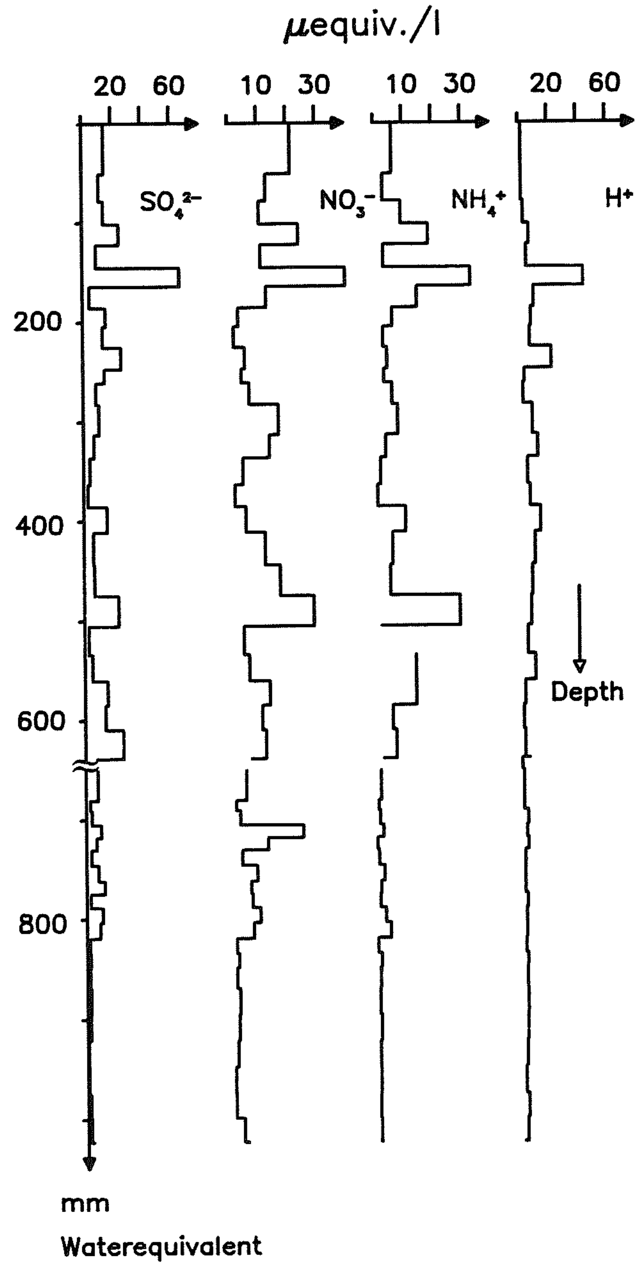

Figure 1: SO_4^{2-}, NO_3^-, NH_4^+ and H^+ profiles in the Jungfraujoch snow pits from February and May 1991. The break at 650 mm waterequivalent indicates that the two pits do not overlap and therefore a few mm of accumulation are missing.

Saharan dust events contributed remarkably to the Ca^{2+} concentration in snow. The corresponding alkaline dust particles showed a high neutralizing potential causing high pH values in the snow samples.

Table 1. Description of the sampling sites and time spans of the snow pit study as well as mean concentrations of some species measured in the snow pit samples (weighted by snow fall height in water equivalents).

	Weissfluhjoch	Jungfraujoch (1)	Jungfraujoch (2)	Fiescher-horn
Elevation (m a.s.l.)	2450	3450		3900
Accumulation [mm weq.]	410	373	639	542
Mean concentrations		[mg/l]		
Cl^-	0.05	0.05	0.05	0.04
NO_3^-	0.52	0.29	0.77	0.47
SO_4^{2-}	0.27	0.20	0.67	0.41
NH_4^+	0.04	0.02	0.15	0.08
Na^+	0.05	0.04	0.03	0.02
K^+	0.03	0.05	0.03	0.02
Mg^{2+}	0.04	0.02	0.02	0.01
Ca^{2+}	0.09	0.43	0.17	0.06

Time Span:		
	Weissfluhjoch:	Nov 90-Mar 91
	Jungfraujoch (1):	~fall 90-Feb 91
	Jungfraujoch (2):	~Mar 91-May 91
	Fiescherhorn:	~Mar 91-May 91

The increased upward transport beginning in March was observed also as a slight diurnal variation of the aerosol concentration with a minimum in the morning and a maximum in the afternoon (Baltensperger et al., 1991b; Baltensperger et al., 1992a). Thus, atmospheric and snow concentrations of anthropogenic species at these high-alpine sites were mainly influenced by transport processes which are related to the meteorological conditions rather than by the source strengths of the precursors (Baltensperger et al., 1991c).

Beside the seasonal variability snow concentrations depended also on the elevation of the sampling site. The lower the site the higher were the concentrations, which again reflects the effect of polluted air masses reaching the site from below. This can be seen from Figure 2, where the SO_4^{2-} deposition patterns at Jungfraujoch (3450 m a.s.l.) and Fiescherhorn (3900 m a.s.l.) and the corresponding $\delta^{18}O$ profiles are shown. The horizontal distance between the two sites is 6 km. To associate single snow samples from both pits the $\delta^{18}O$ measurements in the snow pit samples were used. This was possible by three distinct minima occurring in both $\delta^{18}O$ profiles. In order to compare the deposition patterns of trace species the differing accumulation was corrected for the deeper part of the Fiescherhorn pit by a factor of 0.48 and for the upper part by a factor of 1.57 to adjust the $\delta^{18}O$ profiles. SO_4^{2-} deposition patterns at Jungfraujoch and Fiescherhorn looked very similar with the exception of one sample. The extremely high value on Jungfraujoch was found in both parallel samples taken from the Jungfraujoch pit and has to be explained by polluted air masses from below, reaching Jungfraujoch but not Fiescherhorn. Excluding this outlier the concentrations at Jungfraujoch were about 10% higher than at Fiescherhorn.

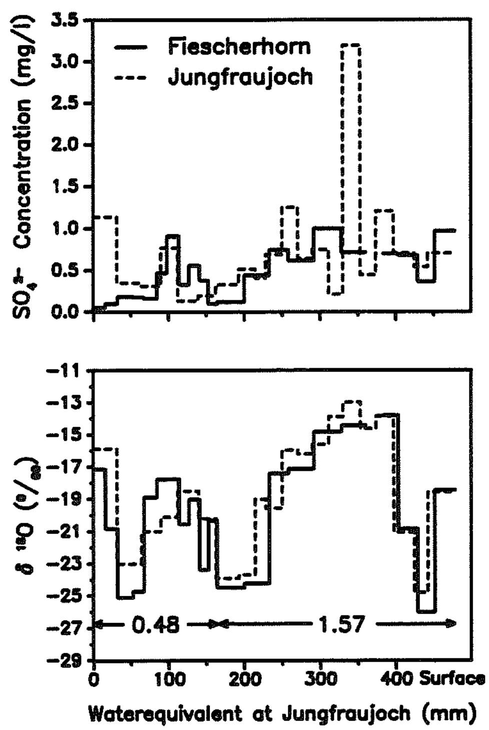

Figure 2. $\delta^{18}O$ (below) and SO_4^{2-} (above) deposition patterns at Fiescherhorn (3900 m a.s.l.) and Jungfraujoch (3450 m a.s.l.).

For the period of 10 January to 18 February 1991 the results of the fresh snow and pit samples were compared regarding the total deposition of trace species and the water accumulation at Jungfraujoch (Table 2). Both methods proved to yield consistent results, provided that the stratigraphy was not disturbed by wind or percolating water (Baltensperger et al., 1992b). The water accumulation is quite similar giving evidence that wind drift, evaporation and occult deposition is of minor importance. The total deposition of the soil tracers Mg^{2+}, Ca^{2+}, Na^{2+} and K^+ was much higher in the snow pit. It seems that dry deposition can not be neglected for these components. This was not the case for SO_4^{2-} and NH_4^+, where the depositions were comparable. NO_3^- and H^+ showed a substantial loss during the snow pack formation. These losses are probably due to evaporation of HNO_3 and neutralization of H^+.

Table 2. Total deposition of various components from snow pit and fresh snow samples for the period 10 January through 18 February 1991 on Jungfraujoch.

	Fresh Snow	Snow Pit	Difference	
	[μeq cm^{-2}]		[μeq cm^{-2}]	[%]
Cl^-	9.4	26	16.6	177
NO_3^-	177	125	-52	-29
SO_4^{2-}	120	111	-9	-8
NH_4^+	25	26	1	4
Na^+	20	40	20	50
K^+	11	27	16	145
Mg^{2+}	14	38	24	171
Ca^{2+}	365	560	195	53
H^+	130	30	-100	77
Accumul. mm weq.	135	154	19	14

Figure 3 shows the snow concentrations of some measured components as a function of the corresponding atmospheric concentrations. Data are from the 1991 campaign as well as the 1990 campaign and the same scale is chosen for all plots. Two data points during a Saharan dust event in March 1990 are excluded (Schwikowski et al., 1992). A reasonable correlation is found only for HNO_3/NO_3^- but not for Ca^{2+}, NH_4^+ and SO_4^{2-}. This correlation and the high efficiency of the scavenging for HNO_3 underlines the importance of gas phase scavenging during snow crystal formation. The absence of a correlation for NH_4^+ and SO_4^{2-} and the low scavenging efficiency indicates that under winter conditions on Jungfraujoch snow crystal growth is much more governed by water vapor diffusion than by supercooled water drops colliding with and freezing on the snow crystals (riming).

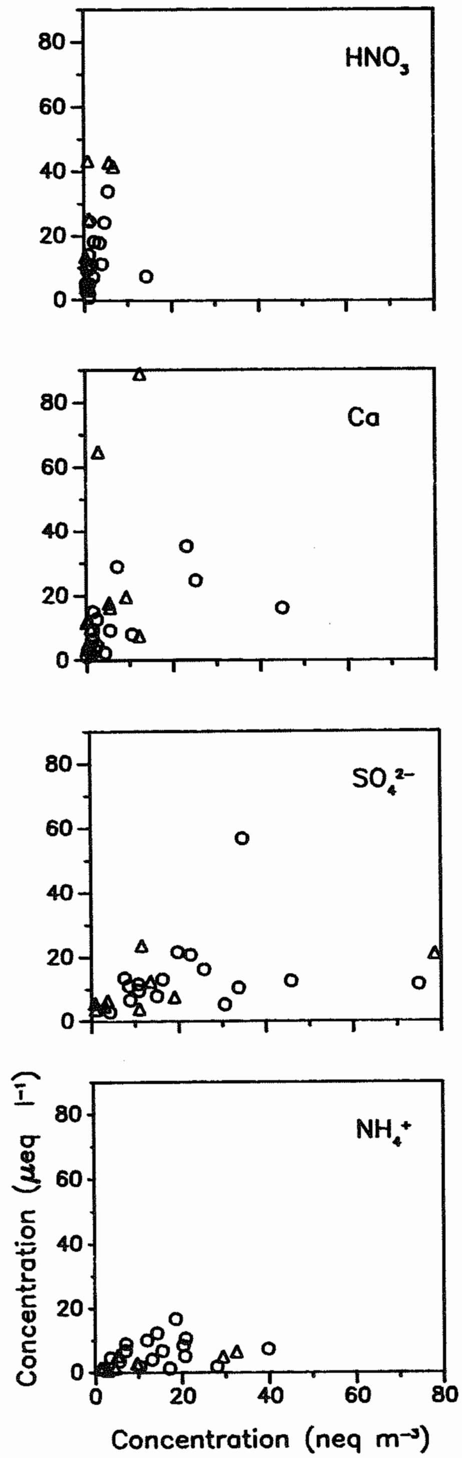

Figure 3. Snow concentrations of NO_3^-, Ca^{2+}, SO_4^{2-} and NH_4^+ as a function of the corresponding atmospheric concentrations of HNO_3, Ca^{2+}, SO_4^{2-} and NH_4^+, respectively. Only HNO_3 was used as atmospheric nitrate species. Cycles represent data from 1990, triangles from 1991.

4. CONCLUSIONS

Snow and atmospheric concentrations of anthropogenic species (NO_3^-, SO_4^{2-}, NH_4^+) were lowest in high winter caused by a decoupling of the atmosphere at high-alpine sites from lower polluted regions.

Dry deposition and evaporation seem to be important processes for certain species during snow pack formation.

$\delta^{18}O$ measurements can be used to associate single snow samples from different snow pits to compare the deposition patterns of trace species.

Distinct correlations between atmospheric and snow concentrations were associated with high scavenging ratios and were found only for NO_3^- where gas scavenging was involved.

5. ACKNOWLEDGEMENTS

This work was supported by the Swiss National Science Foundation. We thank U. Siegenthaler, University of Bern, for the $\delta^{18}O$ measurements, U. Schotterer for technical assistance and the Swiss Army for the helicopter flights. The support of Mr. and Mrs. Kuster and Mr. and Mrs. Bärtschi from the Jungfraujoch research station is greatly appreciated.

6. REFERENCES

Baltensperger, U., Schwikowski, M., Gäggeler, H.W. and Jost, D.T., 1991a. The scavenging of atmospheric constituents by alpine snow. Proc. 5th International Conference on Precipitation Scavenging and Atmosphere-Surface Exchange Processes, Richland, USA, July 15-19, in press.

Baltensperger, U., Gäggeler, H.W., Jost, D.T., Nieveler, U.E. and Schwikowski, M., 1991b. In-cloud scavenging by snow at a high-alpine site. J. Aerosol Sci., 22: 5541-5544.

Baltensperger, U., Gäggeler, H.W., Jost, D.T., Emmenegger, M. and Nägeli, W., 1991c. Continuous background aerosol monitoring with the epiphaniometer. Atmos. Environ., 25A: 629-634.

Baltensperger, U., Gäggeler, H.W., Jost, D.T. and Schwikowski, M., 1992a. Aerosol, radon, thoron and ^{210}Pb measurements with the epiphaniometer at Jungfraujoch. Proc. EUROTRAC Symposium, Garmisch-Partenkirchen, FRG, 23-27 March, 1992, in press.

Baltensperger, U., Schwikowski, M., Gäggeler, H.W., Jost, D.T., Beer, J., Siegenthaler, U., Wagenbach, D., Hofmann, H.J. and Synal, H.A., 1992b. Transfer of atmospheric constituents into an alpine snow field. Submitted to Atmos. Environ.

Clausen, H.B. and Langway, C.C.Jr., 1989. The ionic deposits in polar ice cores. In: The Environmental Record in Glaciers and Ice Sheets, eds. H. Oeschger and C.C. Langway, Jr., pp 225-247 John Wiley & Sons Limited, Chichester.

Schwikowski, M., Gäggeler, H.W., Gloor, M., Keil, R. and Jost, D.T., 1990. Measurements of concentration, chemical composition and size distribution of background aerosol at high Alpine stations. J. Aerosol Sci. 21: S321-S324.

Schwikowski, M., Maupetit, F., Winiwarter, W., Seibert, P. and Tschiersch, J., 1992. A single case of Saharan dust in March 1990. Proc. EUROTRAC Symposium, Garmisch-Partenkirchen, FRG, 23-27 March, 1992, in press.

INFLUENCE OF RIMING ON SNOW CHEMISTRY

Srinivas S.N. Devulapalli and Jeffrey L. Collett, Jr.

Institute for Environmental Studies, University of Illinois, 1101 W. Peabody Dr., Urbana, IL 61801

1. INTRODUCTION

The chemical composition of precipitation is determined through the interaction of various processes including aerosol activation, below-cloud scavenging of particles and gases, aqueous phase oxidation processes, and the mechanism of precipitation formation. Recent experimental observations (Scott, 1981; Borys et al., 1988; Mitchell and Lamb, 1989; Collett et al., 1991) indicate that changes in the degree of accretional ice crystal growth (riming) can affect significantly the concentrations of pollutants that are incorporated into precipitation. Ice crystals grown through water vapor deposition tend to exhibit relatively low ion concentrations. Since cloud drops are efficient scavengers of many aerosol particles and soluble gases, their incorporation into the ice crystal structure through riming increases precipitation ion concentrations.

With the notable exception of the work of Scott (1981) in western Michigan, studies of riming and its effects on precipitation chemistry have been conducted primarily in mountainous terrain. The current study was intended to expand our knowledge about the extent of accretional ice crystal growth and its effects on precipitation chemistry over level terrain where orographic effects don't contribute to liquid water formation. By focusing on precipitation in central Illinois, we also avoided the significant lake effects on winter precipitation formation observed farther to the north and east, including western Michigan.

2. EXPERIMENTAL METHODS

Precipitation samples were collected at 212 m asl at a site four miles south of the small town of Bondville, Illinois. The site, also used as a monitoring location for the National Acid Deposition Program, was selected to minimize effects of local pollutant emissions on precipitation chemistry. Precipitation samples were collected at intervals of 10 minutes to one hour (depending on precipitation intensity) with a 15" polyethylene funnel attached directly to a polyethylene bottle or bag. Snow crystal replicas were made following the technique of Schaefer (1956) by exposing standard 1x3" microscope slides coated with a 2% solution of Formvar in ethylene dichloride. The Formvar solution polymerizes upon contact with water, forming a thin plastic coating over the crystal. Crystal replicas were collected at various intervals depending on precipitation intensity, with the most common collection interval being five minutes. Both the slides and the Formvar solution were pre-conditioned by storage at ambient conditions to prevent melting of the captured snow crystals. Following crystal replication the slides were dried on a bed of silica gel before being brought inside.

Measurements of relative humidity, wind speed and direction, temperature, pressure and precipitation were made at the site with a time resolution of one minute. Precipitation samples were refigerated and transported to the laboratory. Major ion analysis (SO_4^{2-}, Cl^- , NO_3^- , Na^+ , K^+, and NH_4^+) was completed as soon as possible, generally within one to two weeks, using standard techniques of ion chromatography on a Dionex ion chromatograph equipped with a conductivity detector.

3. RESULTS AND DISCUSSION

During the period December 1991 to March 1992 we analyzed six cases of winter precipitation chemistry. Crystal shapes observed during these events were primarily dendrites and plates. Snow crystal aggregates were observed frequently. Little or no riming was observed on crystal replicas collected during five of the six events. Crystal growth during these events was dominated by vapor depositional processes, as illustrated by the crystal replicas in Figure 1. The lack of riming may be the result of either

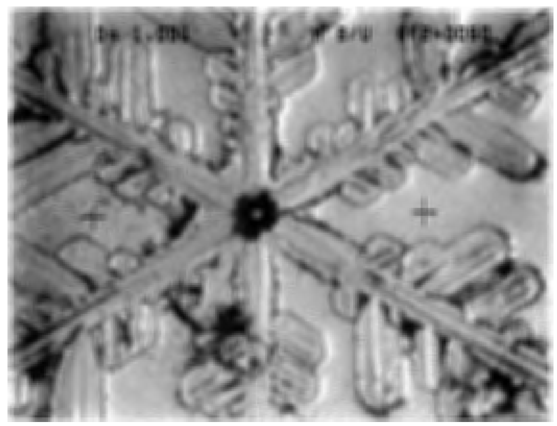

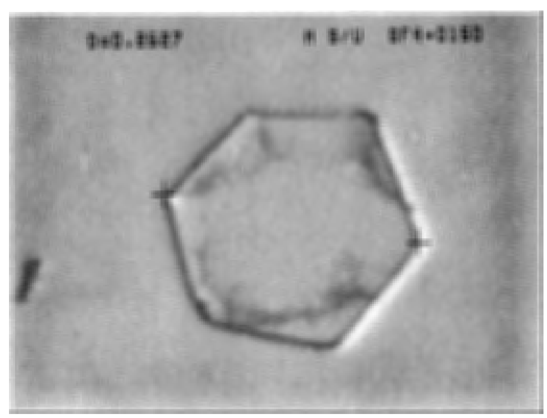

Figure 1. Photographs of Formvar replicas of ice crystals (a dendrite and a plate) collected in east central Illinois. The distance between the markers on each photograph is given in mm in the upper left corner of each photograph.

very low liquid water contents in the precipitating clouds or dominance of the cloud drop spectrum by small cloud drops which are not captured efficiently because of their low inertia. Midwest extratropical cyclones are generally characterized by weak updrafts and very low liquid water contents leading to snowflake growth primarily by vapor deposition and crystal aggregation (Passarelli, 1978).

Snow which fell through the night from March 11 to March 12, 1992, however, exhibited various amounts of riming. Figure 2 illustrates two rimed dendritic crystal replicated during this event. The top photograph depicts a moderately rimed dendrite. The lower photograph depicts a second, more lightly rime dendrite at higher magnification. Measurement of a typical cloud drop (with a diameter of approximately 42 μm) attached to the surface is illustrated. Preliminary analysis of the diameters of cloud drops captured by these crystals (performed at higher magnification than illustrated here in order to improve measurement accuracy) reveal typical sizes between 20 and 45 μm, similar to cloud drop diameters observed on rimed crystals from the Swiss Alps (Collett et al., 1991). The size of the attached cloud drops is of crucial importance for understanding how variations in cloud drop composition with drop size (Noone et al., 1988; Ogren et al., 1989; Collett et al., 1992) affect the degree of incorporation of individual chemical species into the rimed crystals. Species that are found predominantly in drops smaller than those collected by the crystals will not be efficiently removed from the cloud via precipitation.

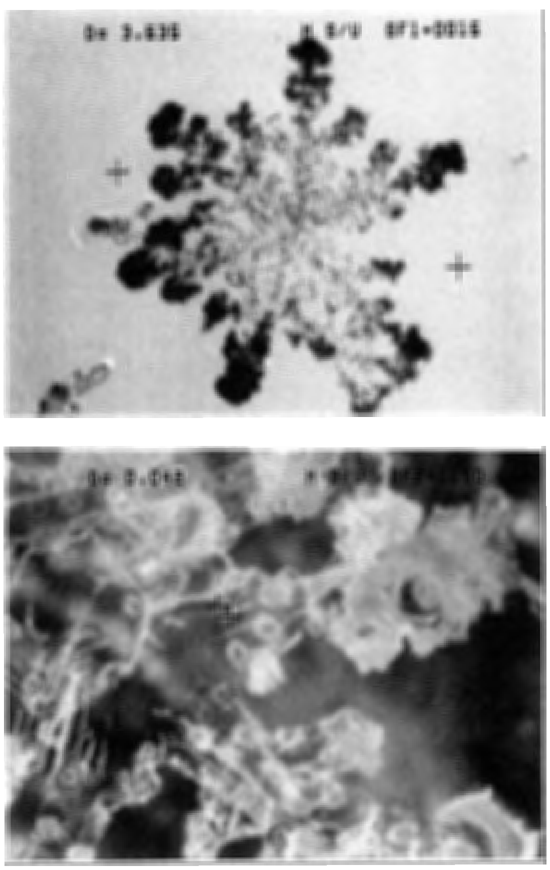

Figure 2. Photographs of Formvar replicas of two rimed dendrites. Dimensions illustrated as in Fig. 1. The size of a typical cloud drop (42 μm) attached to the crystals is shown in the lower photograph.

The extent of riming varied considerably during the course of precipitation on March 11 and 12. Preliminary analysis of the collected series of replicas indicate little riming at the onset or the end of the event, with moderate amounts of riming during the middle portion. Efforts are underway to compare changes in major ion concentrations with changes in the extent of riming to determine whether the period of accretional growth had a significant influence on the precipitation composition. Qualitatively, the expected positive correlation between major ion concentrations and the extent of riming was observed during much, but not all, of the event.

The absence of riming in nearly all snowfall collected in east central Illinois during winter 1991-92 suggests that in-cloud processes probably contributed little to total pollutant wet deposition from these events. Below-cloud scavenging was probably relatively more important here than in areas where direct capture of cloud drops, and the chemical species contained therein, during ice crystal growth is a more common phenomenon.

4. ACKNOWLEDGEMENTS

The authors acknowledge Don Dolske and Mike Snider of the Illinois State Water Survey for providing access to the sampling site and assisting with site set-up. We acknowledge the University of Illinois Campus Research Board for partial funding of the project.

5. REFERENCES

Borys, R.D., E. E. Hindman and P. J. Demott, 1988: The chemical fractionation of atmospheric aerosol as a result of snow crystal formation and growth. *J. Atmos. Chem.*, **7**, 213-239.

Collett, J. L., Jr., A. S. H. Prevot, J. Staehelin and A. Waldvogel, 1991: Physical factors influencing winter precipitation chemistry. *Environ. Sci. Technol.*, **25**, 782-788.

Collett, J., Jr., B. Oberholzer and J. Staehelin, 1992: Cloud chemistry at Mt. Rigi Switzerland: dependence on drop size and relationship to precipitation chemistry. submitted to *Atmos. Environ.*

Mitchell, D.L. and D. Lamb, 1989: Influence of riming on the chemical composition of snow in winter orographic storms. *J. Geophy. Res.*, **94D**, 14,831-14,840.

Noone, K. J., R. J. Charlson, D.S. Covert, J. A. Ogren and J. Heintzenberg, 1988: Cloud droplets: solute concentration is size-dependent. *J. Geophys. Res.*, **93**, 9477-9482.

Ogren, J. A., J. Heintzenberg, A. Zuber, K. J. Noone and R. J. Charlson, 1989: Measurements of the size-dependence of solute concentrations in cloud droplets. *Tellus*, **41B**, 24-31.

Passarelli, R. E., Jr., 1978: An approximate analytical model of the vapor deposition and aggregation growth of snowflakes. J Atmos. Sci., **35**, 118-124.

Scott, B. C., 1981: Sulfate washout ratios in winter storms. *J. Appl. Meteor.*, **20**, 619-625.

Shaefer, V. J., 1956: The preparation of snow crystal replicas-VI. *Weatherwise*, 132-135.

Analyses of Unsolvable Component
in Acid Rain of Guilin by Electron Microscope

Zhang Zheng Cao Yu Hong

Department of Geophysics , Peking University
Beijing 100871, P.R. China

1. INTRODUCTION

Impurities in precipitation come mainly from natural and artificial aerosols and gases which are taken in precipitation elements by rainout in clouds and washout below clouds.

We can divide impurities in precipitation into two parts, soluble in water and unsolvable. People are often concerned with soluble ionic components, such as $SO4^{2-}$, $NO3^{-}$, Cl^{-}, $NH4^{+}$, Ca^{2+}, H^{+} and so on. The reason is that the ionic components can decide acidity and water quality of precipitation and affect conditions of environmental pollution and ecological balance. But some impurities, for example heavy metal elements , which are poisonous or harmful to ecological environment, can present in precipitation as the unsolvable components. Unsolvable components weight occupies a great proportion of the total impurities weight in precipitation. The observational data show that the density of unsolvable components in precipitation may reach 1-3 mg / L. In order to evaluate influence of precipitation for environmental pollution and ecological conditions, it is absolutely necessary to analyse unsolvable components in precipitation (specially acid rain).

In addition, impurities in precipitation which come from rainout in clouds and washout below clouds, should display characteristics of atmospheric aerosols and pollutant gases of ambient enviroments where clouds formed and moved. Because chemistry of unsolvable components is more stable than that of soluble components in precipitation, we can consider unsolvable components as tracer which make a show of pollutant conditions for forming source and moving trajectory of clouds and rains.

2. SELECTION OF OBSERVATIONAL STATION AND TIME

The provinces of Guangdong and Guangxi which are situated in the south part of China, are a serious area where acid rains presented. According to observational data, the spring of every year (from the last ten days of February to the first ten days of April) is a serious season for presenting acid rains. During the period of spring, the characteristics of synoptic situation is that under the controlling of the Northeast monsoon, cold air masses outbreak continually and move in a southerly direction. The synoptic systems which affect the weather conditions for this area, are mainly precipitation processes of cold front.

In order to know the cause of formation for acid rain and adopt the measures of environmental protection, an observational group of acid rain was composed of Peking University and the other universities and environmental research institutes in China. During a period from the 10th of March to the 5th of April, 1988, the observational group made comprehensive investigations into conditions of clouds and precipitations which presented in the provinces of Guangdong and Guangxi.

Guilin City of Province Guangxi which is famous for its scenery in China, is a surface station. The observational data which were got from the stations of surface and mountain and aircraft sounting (below sea level of 4000 meters), included atmospheric aerosols, spectra of cloud and rain droplets, pollutant gases of SO2, NOx and so on, PH, conductivity and chemical components in water of clouds and rains and the other conditions of physics and chemistry for clouds and rains. Analyses of unsolvable components in acid rain of Guilin in this article belong to a part of overall observation.

3. OBSERVATIONAL METHODS

Automotic or manual precipitation collectors which can control time or water volume, sampled continuously for rain water. Rain samples were filtered, and soluble and unsolvable components in rain samples were separated. Using scanning electron microscope (KYKY -1000B) and energy spectrometry (TN

-5500) whose magnifying power is 70,000 times, electron microscope samples which were made by filter paper with unsolvable components of rain water, were analysed. According the measuring results, percentage of weight for the present 12 elements, i. e. Ar, Mg, Al, Si, P, S, Cl, K, Ca, Fe, Ni, and Cr, was chosen as a characteristic distribution of unsolvable components in rain samples. An electron microscope sample was generally measured by three times and three characteristic distributions were got. One characteristic distribution was got from an even part of an electron microscope sample which was composed of fine particles, having a bigger measurement area on the electron microscope sample (about 0.8 mm2) and a less magnifying power about 50 - 200 times. Two characteristic distributions were got from two parts of having forms of particles on the electron microscope sample, choosing a less measurement area (between 10 - 1000 μm2) and a bigger magnifying power 300 -3400 times.

4. RESULTS OF OBSERVATION

We divided four precipitation systems into 11 time intervals of precipitation in which we sampled for rain water. The 11th time interval is the first half of the 4th precipitation system. We did not sample for rain water in the second half of the 4th precipitation system. In the whole 11 time intervals of precipitation, we have got 64 samples for rain water and made completely 64 electron microscope samples with unsolvable components of rain water. Using electron microscope, we sampled 164 times for 64 electron microscope samples and got 164 characteristic distributions of percentage by weight for unsolvable components of rain water.

Two methods which were used for data analyses of unsolvable components in rain water, are averaging method and cluster analysis. Using averaging method, we have got the weight distributions of 12 elements which represented the survey and characteristics for unsolvable components of rain water in four precipitation systems or 11 time intervals of precipitations, separately.

We chose 117 microscope samples whose majority had forms of particles, and divided them into 3 - 10 kinds by cluster analysis. Finally, cluster analysis adopted 9 kinds analysis for measuring data of unsolvable components in rain water. The results got by two analysis methods show:

(1) For total samples which presented in the whole 11 time intervals of precipitation belonged to four precipitation systems, the average weight of three main elements Si (50.07%), Al (18.93%) and Fe (17.35%) come from soil, accounted for about 86 per cent of average weight of total 12 elements. Element K (4.66%) can be considered to come from soil also. The average weight of four elements Si, Al, Fe and K in the earth's crust accounted for about 91 per cent of average weight of total 12 elements. Element Ca which comes from lime and cemet, occupied 3% for average weight of total 12 elements. Elements S and P had a same percentage (2%) by weight. Mg, Ni, Ar, Cr and Cl occupied less percentages by weight than 1%, separately.

(2) If we divided 117 samples into 9 kinds,the results of cluster analysis to weight distributions of 12 elements show:

(A) There is a kind of weight distribution of 12 elements in 9 kinds of distribution. Samples which belonged to the kind of distribntion, made up 57, 63, 75 and 76 per cent of the samples analysed for every system of four precipitations, separately. And the kind of distribution is similar to the total average weight distribution for four precipitation systems. The reson can be considered that four precipitation systems formed and developed in the close synoptic situations, i.e. precipitation processes of cold front.

(B) Some special samples which had characteristic weight distributions of 12 elements, such as samples having higher contents of S. K. Mg or Ni than that of average volume, were got in different precipitation systems. The results present that there were different pollutant conditions of forming source and moving trajectory among four precipitation systems.

5. REFERENCES

Tang Xiao Yan et al., 1990, Environmental chemistry of atmosphere, Publishing House of Higher Education, P.R. China.

Zhang and Sheng, 1990, An analytical sample of streamline fields of upper air and bottom layer effecting acidity of precipitation, Meteorological Monthly, Vol.16, No.4, 3-8.

An Analysis on the Background of Precipitation over the Shita Mountain of Fujian

Deng Jiaquan

(Institute of Meteorological Science,Fujian)

Mo Tianlin

(Department of Atmospheric Sciences,NanJing University)

Keywords:Atmospheric ice nucleus,Chemical composition in precipitation, pH Value, Shita Mountain.

ABSTRACT

The background of precipitation and atmospheric ice nucleus have been observed over the Fujian station of artificial stimulation of precipitation (Shita Mountain) during 1982-1985. The results show that there are no sufficient atmospheric ice nuclei over seeding testing station at seeding temperature window range from -10℃ to -15℃. And that the pH Values are nearly neutral and the chemical compositions of precipitation are very similar to those reported by reference[1].

1. INTRODUCTION

During 1975-1986, We have made the randomized seeding trials of precipitation stimulation for 244 times in Kutian Reservoir region, Fujian Province. Statistical analysis shows that the amount of precipitation after seeding is 23.81% more than that without seeding.

In order to study the background status of precipitation, We have observed the chemical compositions and pH values of precipitation as well as atmospheric ice nucleus over Shita Mountain during 1982-1985.

2. SAMPLING SURVEY

The measuring site was located on Shita Mountain(26° 37'N 118° 33'E) . Its sea level elevation was 1625 m. It was surrounded by many mountains and was covered with the luxuriant vegetation. There was no large industry pollution source within several tens KM.

The improving type of Bigg's cloud chamber and method of millipore filter membrane were used for measuring atmospheric ice nucleus [2, 3].They are explained as follows.The sketch of the improving type of Bigg's cloud chamber is given in Fig. 1. Its containing volume was 3. 8 liters. The diameter of sugar dish for count was 9. 6 cm.The cooling agents used are ice and NaCL or $CaCL_2 \cdot H_2O$. In Fig.1, A Was an equipment for producing fog; B was fog store-house;C was cooling equipment;D was cloud chamber body. The temperatures of cloud chamber were measured by thermal couple. The sugar solution dish in cloud chamber was drawed from chamber top to bottom when air samples were collecting. A certain amount of air samples was transported into cloud chamber via hole for air sample taken in. The original gas in cloud chamber was emited via hole for gaseous emission. The ice crystals can be counted in sugar solution dish. Its mean value can be counted by several times for observation.

The sampling device employing millipore filter membrane consists of air pump, hydrodynamometer and sampling probe(see fig. 2) .Air pass filter film by air pump.Then ice nuclei were remained on film. According to sampling time and the value showed by hydrodynamometer, the sampling volume can be counted. Sampling films were placed in small clean plastic box and then they were activated in laboratory. The cold cloud chamber in laboratory was cylinder. Its diameter was 24 cm and the height 48 cm, and its containing volume was about 22 liters. The cloud chamber was placed in cryopump and its temperature was droped. Vertical and horizontal temperatures in cloud chamber were measured using six thermal couples. Activated condition of each filter film was same in order to compare ice nuclei concentration of each measurement.

The chemical compositions and pH Value of precipitation

During field trials in may in 1982 and 1983, the samples were collected at monitoring station. The pH values and chemical compositions of precipitation were measured respectively.The container used to collect samples was a clean polyethylene basic.Its diameter was 50 cm and the height 15cm. This container was placed on a stand made with iron above 1 m

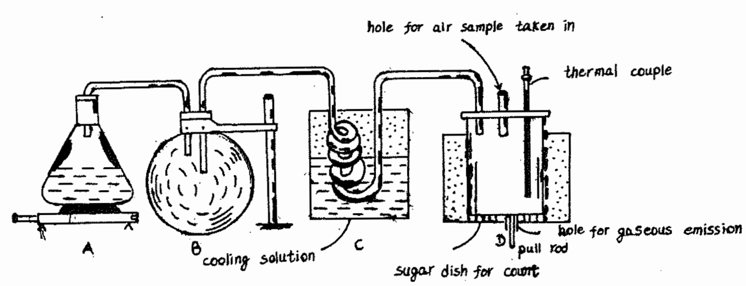

Fig.1 The sketch of the improving type of Bigg's cloud chamber

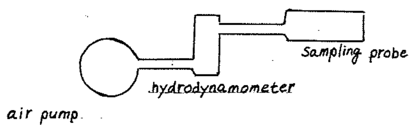

Fig 2. The sketch of sampling equipment with filter membrane

distance from ground for observation station.The container was opened at start of precipitation when the sample of precipitation was collecting each. The sampling time was at 08:00 and 20:00 for continual precipitation, namely the measurements carried out twice a day. For non-continual precipitation,the sample was collected when precipitation was coming to a stop. The pH Values of precipitation were determined on field by acidimeter. The analysis of metal elements,such as Na,K,Mg,Cu,Pb, Zn,Mn,and Ni,in precipitation, was carried out in laboratory using atomic absorption spectrometry(AAS).

3. RESULTS AND DISCUSSION

Analysis and Observation of Atmospheric Ice Nucleus:

The observations of atmospheric ice nucleus have been carried out during April-June in 1983, 1984, 1985 using the improving type of Bigg's cloud chamber, also using millipore filter film method during each May in 1984 and 1985. We have obtained 74 measuring records with an improving type of Bigg's cloud chamer and 413 effective filter-film samples.The results are shown in Table 1. It is seen from the last line of Table 1 that the times of the cloud top temperatures over -20℃ account for 81.3% of the 244 times randomized seeding samples over seeding area during 12 Years and those over -15 ℃ account to 67. 3 %. Thus one of the conditions for artificial seeding clouds is primarily the cloud top temperatures over -20 ℃ for seeding clouds,but specially concentrate on seeding clouds of cloud top temperatures.

Over -15 ℃. It is also seen from the table 1 that the difference on order of magnitude between the ice nucleus concentrations measured with two methods for each temperature range is not occurrence. The concentrations of ice nucleus are 10^{-1}~10^{0} liter $^{-1}$ when activated temperatures range from -10℃ to -15 ℃. Zhao Bailin et al. [4] Have shown that for frontal stratus clouds arrive at the most efficiency of precipitation, it is necessary that the concentration of ice crystals in clouds is more that 10^{2} liter^{-1}.The artificial stimulation of precipitation over Shita Mountain is also mainly seeding for frontal stratus clouds system. Then the difference on order of magnitude between the concentration of atmospheric ice nucleus over Shita Mountain and value computed by above authors is occurrence.The efficiency of natural precipitation will be not situated best. Thus we consider that the artificial seeding cold cloud for the clouds system in rainy season Fujian may rise the efficiency of precipitation for arriving at the aim that precipitation enhancement using artificial seeding. The randomized trials in field have taken 244 samples during 12 Years. Statistical analysis shows that the amount of precipitation after seeding is 23. 81% more than that without seeding with the level of significance 0.05 .It is testified that the trial method used on Kutian is reasonable.

The Observation and Analysis on the Chemical Compositions and pH Values of precipitation

Twenty-four samples of rain water were collected at observing site during May in 1982.The Chemical compositions in rain water were analyzed for fifteen samples. The results are given in Table 2.The metal ions of AL^{3+},Mn^{2+} and Ni^{2+} were not detected. Then they are not given in Table 2. When comparing concentrations of these elements in Table 2 with those[1] reported from the background stations network of atmospheric pollution monitoring for WMO, the concentrations of metal ions are near. There are no differences for order of magnitude. But for the mean Value of SO_4^{2-} ion concentrations , the value of reference[1] is about 50 times more than that obtained from Shita Mountain observation. The pH mean Value of precipitation published in reference[1] is 5.50 .Namely its acidity is about 30 times that the acidity were measured at Shita Mountain.Thus it is seen that Shita Mountain is also a perfect background atmospheric point.We think that the acidic pollutants are less over Shita Mountain and where atmosphere is more clean.

It will be seen from above-mentioned analysis that the concentration of atmospheric ice nucleus is low Shita Mountain area and the background of precipitation is clean. This means than the amount of cloud condensation nucleus(C C N) is also relatively less.

The pH values of precipitation at Shita Mountain during each May in 1982~1984 are given in Table 3. From Table 3, one can see that pH mean value of precipitation at Shita Mountain is decreased year by year. This consists with the trend reported from reference[1] . This may reflect that the background air quality at all East area in China is dropping

Table 1. A Comparison of concentrations of atmospheric ice nucleus measured with two methods

measuring method \ concentration (liter^{-1}) \ activited temperature in cloud chamber	-12 ℃	-15 ℃	-20 ℃	-25 ℃	Period of observation
The improving type of Bigg's cloud chamber	0.3	1.6	5.6	25.4	April~June in 1983,1984,1985
filter film	0.6	2.8	7.0		May in 1984,1985
The probability of cloud top temperature showed by the radar echo over obseravtion site (%)	55.5	11.8	14.0	8.3	1975-1986

table 2. The chemical compositions and pH Value of rain water collected at Shita Mountain during May in 1982

composition	Na^{+}	K^{+}	Mg^{2+}	Zn^{2+}	Cu^{2+}	SO_4^{2-}	HCO_3^{-}	pH
mean content	0.060	0.058	0.029	0.037	0.004	0.030	12.200	6.59

Table3. The pH mean Value of precipitation at Shita Mountain in May yearly

Year	1982	1983	1984
pH mean Value	6.99	6.86	6.58

Table 4. The pH Value of precipitation at Shita Mountain,Kutian and Fuzhou during May in 1983

place name	character ofsample	sampling times	precipi-tation (m m)	pH Value		Status of acidrain					
				mean	variable range	times	a hundred parts for times of precipita-tion	precipi-tation (m m)	a hundred parts for precipi-tation	pH mean Value	pH Variable range
Shita Mountain	non-thunder shower	16	120.2	6.86	6.63~7.45	—	—	—	—	—	—
	thunder shower	3	119.0	6.80	6.50~6.87	—	—	—	—	—	—
	non-thunder shower with dry deposition	6	13.0	6.84	6.40~7.40	—	—	—	—	—	—
Kutian	non-thunder shower	12	64.4	5.75	4.98~6.30	4	33.3	18.9	15.7	5.23	4.98~5.53
	thunder shower	9	93.8	5.47	4.95~7.40	5	55.5	68.3	72.8	5.17	4.95~5.42
	non-thunder shower with dry deposition	9	63.1	6.15	5.20~7.00	2	22.2	12.3	19.5	5.53	5.20~5.40
Fuzhou	non-thunder shower	11	110.0	4.19	3.82~5.70	10	90.9	108.7	98.8	4.18	3.82~5.20
	thunder shower	3	17.6	3.75	3.65~4.02	3	100.0	17.6	100.0	3.75	3.65~4.02
	non-thunder shower with dry deposition	8	45.8	4.43	4.00~7.00	5	62.5	40.8	89.1	4.17	4.00~4.80

year after year.

Contrastion Observation on the pH Values of pecipitation at Various Locality

To approach the pH Values of natural precipitation and precipitation at Various locality, We elect three monitoring Stations,namely Fuzhou (26° 05'N,119° 17'E,sea level elevation 83. 8m),Kutian (26° 35'N,118° 44'E,sea level elevation 361.5m) and Shita Mountain (26° 37'N, 118° 33'E ,sea level elevation 1625m).Their geographical locations are nearer and their trend is near northeast. Fuzhou represents the middle city to be polluted by industry. Kutain represents county town for mountain area.Shita Mountain is elected background contrasting point. When upper air-stream is much the same in May (hith altitude South-West air-stream is predominat) the pH value of precipitation is measured.

The precipitation pH Values measured at three stations during May in 1983 are given in Table 4. From Table 4 it follows that (1) the pH mean Values of thunder shower at three stations are less than that of non-thunder shower. there are a difference between the pH mean values of thunder shower and non-thunder shower at each station.this difference is relative to the population and industry developing cases for city. Namely the more population and industry city contains , the more the difference is. It can be seen from Table 4 that this difference for Fuzhou is the most large, that for Kutian is secondly, that for Shita Mountain is the most little .This may be that the lifting level of pollutants is increased accompanied with convergence up air-stream about ground when thunder shower is forming. Because the more population and industry the area contains, the more the concentration of acidic pollutants is . The pollutants have higher transforming efficiency in thunder shower process. Thus the pH Value of thunder shower over city is lower than that of thunder shower over area with less pollutants or more clean.We think that the decrease of pH Value of thunder shower is relative to the distributional status of pollutants in boundray layer, the transport processes and weather of thunder shower forming. (2) When the pH mean Values of non-thunder shower at three stations compare with those of non-thunder shower with dry deposition, both are nearer at Shita Mountain station and the difference between pH mean Values is lower a order of magnitude than those between pH mean Values at other two stations. Thus acidic and basic polluted particles or aerosols are all less over Shita Mountain.(3)According to the pH Values measured and acid-rain cases at three stations, the pH mean Values of precipitations for thunder shpwer,non-thunder shower or non-thunder shpwer with dry deposition are all the largest at Shita Mountain station,those at Kutian are middle,but those at Fuzhou are the most little. The frequency of acid-rain occurrence is also the most high at Fuzhou, that at Kutian is secondly,no acid-rain appear at Shita Mountain station.

4. SUMMARY

1) The numbers of atmospheric ice nucleus over Shita Mountain is short of the order of magnitude requisite for achieving the most large efficiency of precipitation of frontal stratus clouds. Artificial seeding is necessary for rising the efficiency of precipitation of frontal stratus clouds.

2) According to the chemical compositions in precipitation obtained and a comparison with reference (1) , the atmospheric background over Shita Mountain is clean . The numbers of cloud condensation nucleus (C C N)are less.

3) The pH mean Value of precipitation is nearly neutral.The significant contribution for pH mean Value is native pollution source. The contribution of pollution due to remote area transport is secondary.

4) The background Value of precipitation measured at observation station appear to be almost the same as those published in reference [1].Thus the observation station (Shita Mountain) may become a reference point of background of precipitation in East China

REFERENCES

[1] Hong Shengmao, An analysis on the background air pollution and the acidity and chemical compositions of precipitation in East China, Meteor. Monthly (in Chinese),vol.15,No.9,42-47,1989

[2] Huang Wenjuan, et al.,Concentration of Ice Nuclei on Shita Mountain,Fujian Province ,J.Najing Institute Meteor. (in Chinese),No.1,62-69,1986.

[3] Wu Mingling, et al. , The Measurement and Analysis of Atmospheric Ice-nucleus Concentration on Fujian Shita Mountain, J.Tropical Meteor. (in Chinese), vol.2,No.1 71-78,1986

[4] Zhao Bailin, et al. , The possibility of artificial precipitation enhancement from nimbostratus (I) The problem of ice-water transformation for non-closed system,Acta Meteorologica sinica (in Chinese),vol.33, NO3.382-391,1963.

SO_2 RETENTION COEFFICIENT DURING FREEZING OF MONODISPERSE DROPS

G. Santachiara, F. Vivarelli and F. Prodi[+]

Institute FISBAT-CNR, Bologna, Italy

+ Also at: Dipartimento di Fisica dell'Università, Ferrara, Italy

1. INTRODUCTION

At mid-latitudes precipitation usually forms by the conversion of cloud water to ice by one of two pathways: a) sublimation of water vapour onto ice crystals which grow and fall from the atmosphere or b) riming of ice crystals. The incorporation of gases and vapour by snow crystals during growth by diffusion has been documented by field observations (Huebert et al., 1983; Huang Shi-hong et al., 1988) and laboratory experiments (Valdez et al., 1989; Mitra et al., 1990). Deposition velocities depend not only on the uptake capability of a particular surface for a particular gas but, strongly, on the boundary layer at the surface of the crystal and on thermodynamics. And once a snow crystal has stopped growing, it is capable of further SO_2 absorption, particularly if its surface is at a temperature close to 0°C (Sommerfeld and Lamb, 1986; Mitra et al., 1990).

Riming occurs commonly in cold clouds in which ice particles have grown large enough to sediment significantly with respect to small cloud drops. An analogous situation arises in the case of a stationary surface past which the wind may be blowing supercooled droplets. While rime-ice formation can be very important for removing water mass from the atmosphere, the trace chemicals initially contained in supercooled cloud water are not necessarily removed proportionally. This arises in part from the fact that most substances are very much less soluble in ice than in liquid water.

Experiments provide different results depending on the operating configuration. Iribarne et al. (1983), working with drops in diameters between about 0.5 and 1.0 mm in equilibrium with SO_2 at 18.8 ppm, found that about 25% of SO_2 is trapped by the frozen drops. Drops were allowed to freeze on a thermally massive substrate, so neither geometry nor heat was representative of riming conditions in the atmosphere. Lamb et al. (1987) , to simulate rime-ice formation in the atmosphere, impacted at 2 m s^{-1} supercooled drops with a radius ranging from a few to 10 μm onto thin rods that were made to sweep through the cloud. With $p_{SO_2} \simeq 0.7 \times 10E{-6}$ atm., the entrapped fraction was strongly temperature dependent and varied from about 1% near 0°C to more than 12% at -20°C.

Iribarne et al. (1990) worked with spray - generated droplets having an average diameter 39 μm . In the initial arrangement the droplets fell by gravitation on an ice surface; two other arrangements simulated the riming ventilation. In one series of experiments, the droplets were projected by a gas jet at several m s^{-1} against a target; in another , the droplets were caught by rotating rods. Samples collected by gravitation showed a retention coefficient $\Gamma = S(IV)_{rime} / S(IV)_{eq.} = 0.25 + 0.012\ T_S$: where $S(IV) = SO_2.H_2O + HSO_3^-$; T_S droplet supercooling. The subscript rime and equilibrium indicate S(IV) in the riming sample and S(IV) originally present in the drops in equilibrium with SO_2 in the gas phase. Rime samples showed a large dispersion in the results, the retention coefficient being best represented by an average value Γ=0.62 regardless of temperature. No dependence was found on SO_2 gas phase concentration in the 3-99 ppm range.

The present study was undertaken to clarify the discrepancies evident in the above-cited experiments by employing droplets with a small dispersion and at high concentration.

2. EXPERIMENTAL

The configuration used in our experiments and the droplet impactor are represented in Figs. 1 and 2. A stream of nitrogen is passed through a Collison containing NaCl solution of Super Q water (20 mg l^{-1}). The gas flow at the outlet of

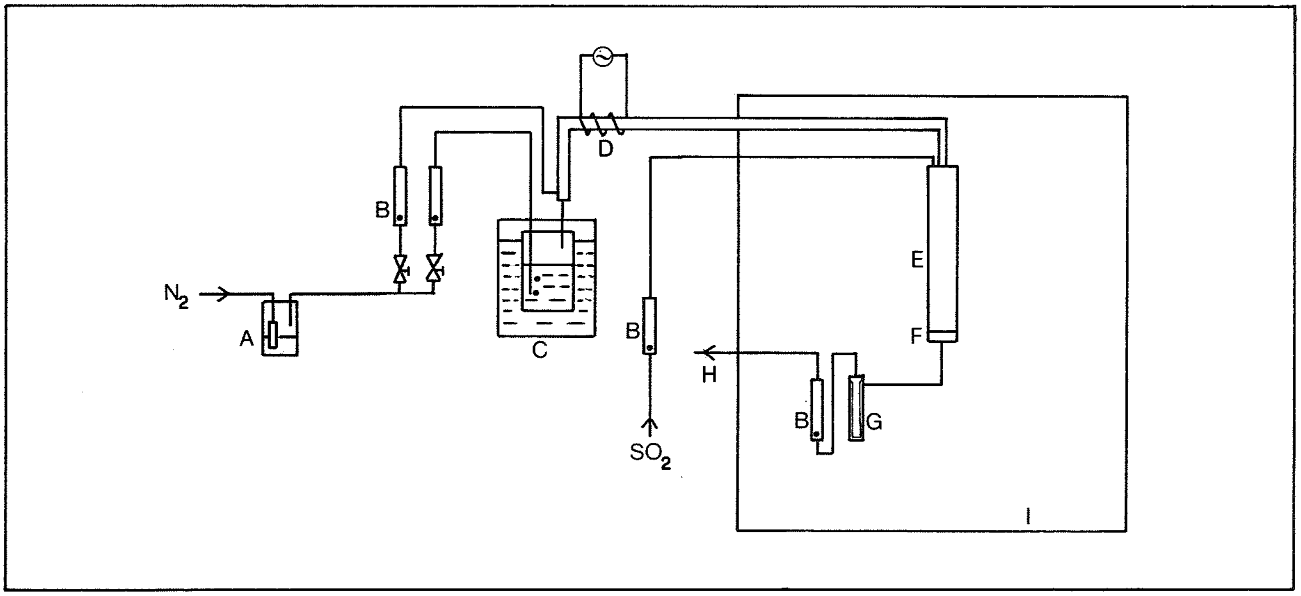

Fig. 1. Diagram of the experimental set-up. A, Collison generator; B, flowmeter; C, thermostated bath; D, reheater; E, droplet chamber; F, droplet collector; G, Bubbler; H, N_2 outlet; I, cold room.

the nuclei generator is split into two streams: one is sent to a bubbler and the other joins the first after the bubbler but before entering the reheater. In the reheater the water is vaporized again and under controlled recondensation produces a cloud of droplets. The size distribution measured with a forward scattering spectrometer probe (PMS Model FSSP-100) is represented in Fig.3 . In addition measurements with a cold glass covered with carbon showed for droplets R = (4.6±0.7)μm. At the generator outlet the droplets pass through a pipe in a chamber situated in a cold room. The chamber measured 45 cm in length and 10 cm in diameter.

The SO_2 source was a compressed gas cylinder of 50 ppm in nitrogen. The concentration of SO_2 fed into the chamber was controlled by a calibrated metering valve. The gaseous stream was also passed through a bubbler containing 40 cc of 5% H_2O_2 solution to measure SO_2 concentration in the carrier gas.

Experimental and theoretical data show that equilibrium of SO_2 with droplets can be expected in a time of the order of 10E-2 s, i.e. a time scale which is short compared to the time necessary for chamber through-put. Temperature of gas at the end of the duct, close to the riming site in a place free of droplets, was measured by thermocouple. At the outlet of the absorption

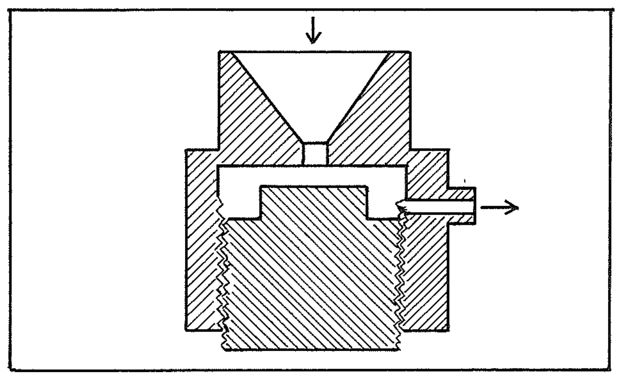

FIG. 2 . Droplet impactor

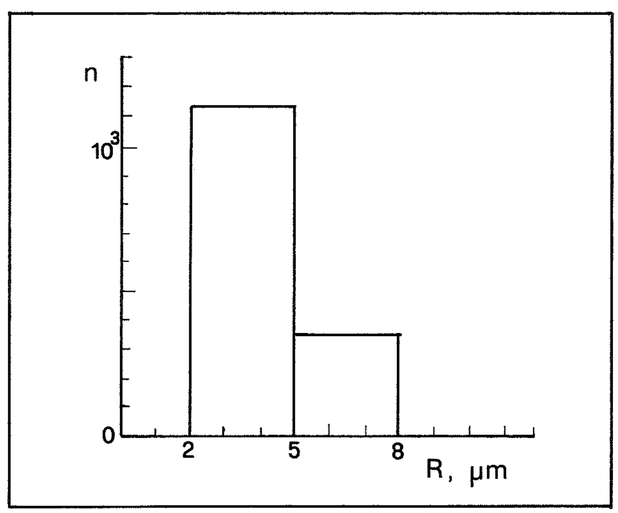

FIG. 3. Drop size distribution; n: total number of droplets per cm^3 in the indicated range.

section, supercooled droplets are captured by an impactor and freeze. The impact velocity of droplets against the surface was about 6 m s^{-1}, and the mass of the deposit was determined with a precision scale (100 μg sensibility).

During the course of an experimental run, a conic deposit of rime is formed, about 1 cm in height. At the end of the experiment, the ice was scraped from the support and allowed to melt in a small closed plastic cylinder with a known volume of 5% H_2O_2 solution to convert S(IV) to S(VI). The concentration of S(VI) in this solution was determined by ion chromatography (Dionex 2000i).

The equilibrium concentration of S(IV) in the supercooled droplets can be calculated from the partial pressure of SO_2 in the gas phase (p_{SO_2}) and the temperature T. Since the pH of droplets in equilibrium with the gas ranged from 2.5 to 3.5, the second dissociation of $SO_2.H_2O$ could be ignored and the total concentration in the droplets S(IV)) is :

$$S(IV) = HSO_3^- + SO_2.H_2O = H\,p_{SO_2} + (H\,K_1\,p_{SO_2})^{1/2}$$

where H is the Henry coefficient and K_1 the first dissociation constant. The temperature dependences of the equilibrium constants were taken from Maahs (1982) to be:

$\log H = 1376 / T - 4.521$ M atm^{-1}

$\log K_1 = 853 / T - 4.740$ M, thus making it possible to calculate Γ.

It is here assumed that measured S(VI) derives from SO_2 entrapped in the ice, not from oxidation of SO_2 due to catalytic activity of Cl^- ion used as nuclei condensation for droplets. This can be justified by the fact that the carrier gas was nitrogen with O_2 impurity of about 2 ppm and that both Cl^- concentration in the droplet and temperature, which influences the reaction rate constant, were low.

3. RESULTS AND DISCUSSION

Results of experiments are reported in Fig.4; runs in each experiment are from 2 to 3. The retention coefficient was measured at SO_2 pressure ranging from 0.19 x 10E-6 atm to 10.9 x 10E-6 atm and at temperature from -3 to -20°C. In these experimental conditions droplets colliding with ice surface have a negligible spreading due to small radius and low impact velocity. Ice density can be calculated from: $\rho = 0.33\,k^{0.6}$, where $k = -\,r\,v_0 / T_D$; r the mean volume radius , v_0 the droplet impact speed and T_D the temperature of the ice deposit(Prodi et al., 1986). For example with r = 4.7 μm and T_D= -15°C, we obtain $\rho \simeq 0.5$ g cm^{-3}. The ice growth is dry. This is confirmed also by the appearance of the ice.

Our data also show that gaseous entrapment is greater the higher the freezing rate, i.e. by large supercooling with higher heat dissipation at the droplet surface. Yet the retention coefficient is independent of supercooling when the scatter of experimental data is taken into account, i.e. entrapped S(IV) is proportional to the S(IV) present in droplet at the beginning of freezing. This agrees with the experiments made under ventilation (jet and rotating arrengements) of Iribarne et al.(1990).

In the solidification of a supercooled water droplet we can distinguish three main stages: the initial , the subsequent freezing and the cooling phase (Macklin et al., 1967). During the first, adiabatic stage, the latent heat of freezing (335 KJ Kg^{-1}) is expended in warming the drop up to

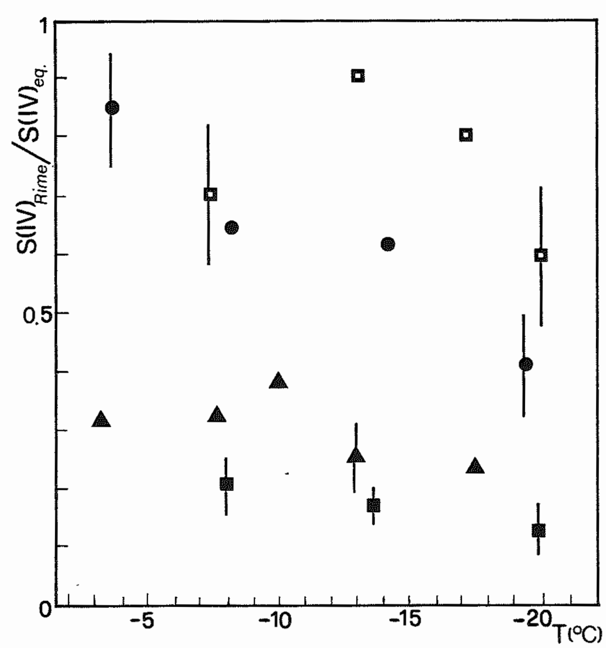

FIG.4. Plot of the fraction of S(IV) entrapped in the rime ice as a function of temperature.

■: p_{SO_2} = (10.9x10E-6)atm ; ▲: p_{SO_2} =(3.3x10E-6) atm ;
●: p_{SO_2} =(1.02x10E-6)atm ; ◘: p_{SO_2} =(0.19x10E-6) atm.

0°C. If m_i and m_w denote the masses of ice and water in the drop and the water at the end of stage one, and we assume that no heat is lost to the envinronment, we have $f_i = m_i / m_w = T_s / 80$. For supercooling from 3 to 20 °C, the f_i range is from 4% to 25% .

The initial stage of freezing is followed by a second one during which the remainder of the water is frozen. Here the freezing rate is controlled by the rate at which heat is conducted into the underlying ice surface and dissipated by forced convection into the environment. During freezing the crystal lattice rejects to a certain degree the foreign chemical species (in the present case $SO_2.H_2O$ and HSO_3^-) because of the complicated steric and electric requirements for the fitting of foreign molecules or ions into the ice crystal (Jaccard and Levi, 1961). So at freezing interface a discontinuity in the concentration of solute gas appears, with a lower value on the solid side and a higher value on the liquid one. As the solid continues to grow, the solute gets pushed towards the liquid fraction. The loss of SO_2 also requires diffusion through the liquid and passage through the surface.

According to the Macklin and Ryan freezing model, when the droplet temperature approaches 0°C due to initial freezing, the S(IV) concentration in the liquid phase is greater than the equilibrium value with respect to the gas-phase concentration, as solubility is lower than at a colder temperature. Given that the higher the initial supercooling the higher the S(IV) liquid-phase concentration (at the same SO_2 gas-phase concentration), more S(IV) is incorporated in the ice during growth. This entrapment depends on the ratio between freezing time and gaseous expulsion time, which is related to liquid diffusivity.

For the dependence of Γ on the SO_2 gas-phase concentration, our data show that Γ increases the lower the concentration, while Iribarne et al., with a broad scatter of results, conclude that no effect of the SO_2 concentration was apparent in the wide range of tested concentrations. For p_{SO_2} = 10.9x10E-6 atm , 3.3x10E-6 atm , 1.02x10E-6 atm , 0.19x10E-6 atm Γ is respectively: (0.16 ± 0.07);(0.29 ± 0.07);(0.65 ± 0.2);(0.74 ± 0.2). This trend can be explained by considering that at the lower concentration the time for drop saturation and for desorption is longer than at higher gas concentrations. This can be explained on the basis of SO_2 equilibrium in air and water (Walcek et al., 1984).

Acknowledgments. The cooperation of Mrs.L.Santoli and Mr.G.Tigli(USL 28-Bologna) in performing the chemical analyses and the assistance of Mr.M.Tercon are gratefully acknowledged.

This study has been supported by the CNR-ENEL Project-Interaction of energy systems with human health and environment-Rome Italy.

4. REFERENCES

Huang Shi-hong, R.A Castillo and V.K.Monhen 1988: Ionic concentrations of rime ice and snow Bergeron Process. *10th International cloud Physics Conference* , Bad Homburg, August 15-20.

Huebert,B.J., F.C.Fehsenfeld , R.B.Norton and D.L. Albritton, 1983: The scavenging of nitric acid vapor by snow. In *Precipitation Scavenging, Dry Deposition and Resuspension*, pp.293-302. Elsevier, Amsterdam.

Iribarne,J.V., L.A.Barrie and A.Iribarne , 1983: Effect of freezing on sulfur dioxide dissolved in supercooled droplets. *Atmos.Environ.*, **17**, 1047-1050.

Iribarne,J.V., T.Pyshnov and B.Naik, 1990: The effect of freezing on the composition of supercooled droplets-II. Retention of S(IV). *Atm.Environ.* **24 A**, 389-395.

Jaccard,C. and L.Levi , 1961: Segregations d'impurités dans la glace. *Z.Angew.Math.Phys.* (ZAMP) , **12**, 70-76.

Lamb,D. and R.Blumenstein ,1987: Measurements of the entrapment of sulfur dioxide by rime ice. *Atm.Environ.* **21**, 1765-1772.

Maahs,H.G., 1982 Sulfur dioxide water equilibria between 0 and 50°C. An examination of data at low concentrations. In *Heterogeneous Atmospheric Chemistry* (edited by Schryer D.R.).pp.187-195. Geophysical Monograph 26, AGU, Washington.

Macklin,W.C.and G.S.Payne, 1967: A theoretical study of the ice accretion process. *Quart.J.R.Met.Soc.* **93**, 195-213.

Mitra,S.K., S.Barth and H.R.Pruppacher,1990: A laboratory study on the scavenging of SO_2 by snow crystals. *Atm.Environ.* **24 A**, 2307-2312.

Prodi,F., L.Levi and P.Pederzoli,1986:The density of accreted ice. *Quart.J.Met.Soc.*, **93**, 195-213.

Sommerfeld,R.A. and D.Lamb , 1986: Preliminary measurements of SO_2 adsorbed on ice. *Geophys. Res.Lett.* **13**, 349-351.

Valdez,M.P. and G.A.Dawson ,1989: Sulfur dioxide incorporation into ice depositing from the vapor. *J.Geoph.Res.* **94**, 1095-1103.

Walcek,C.J. and H.R.Pruppacher, 1984: On the scavenging of SO_2 by cloud and raindrops: I. A theoretical study of SO_2 absorption and desorption of water drops in air. *J.Atm.Chem.*, **1** , 269-289.

A MODEL STUDY OF THE DEPENDENCE OF THE ACIDITY IN CLOUD DROPLETS UPON THEIR SIZES

N.-H. Lin and V.K. Saxena

Department of Marine, Earth and Atmospheric Sciences
North Carolina State University
Raleigh, NC 27695-8208

1. INTRODUCTION

Clouds play an important role of removing and redistributing the atmospheric pollutants. The primary precursors to cloud acidity are sulfur and nitrogen oxides. Experimental results (Noone *et al.*, 1988) have shown the mean solute concentration varying with the sizes of cloud droplets. Theoretical (Hegg and Hobbs, 1979; Jensen and Charlson, 1984) and modeling (Flossmann *et al.*, 1985) studies also suggested that the distribution of pollutants across the cloud droplet spectrum is due to the microphysical processes. Hegg and Larson (1990) indicated that such size dependency may affect the sulfate production rate in the cloud. In this study, a diagnostic cloud chemistry model is developed to simulate the cloud acidity due to scavenging of aerosols and gases by cloud droplets in open and closed systems. A scheme is also developed to calculate the dependency of pH value and chemical composition in cloud droplets upon their sizes. Our model will help identify and quantify the effect of chemical processes on the final acidity of cloud droplets.

2. CLOUD CHEMISTRY MODEL

The cloud chemistry model includes the absorption of trace gases, the oxidation of aqueous phase SO_2, and the scavenging of acidic (H_2SO_4 and HNO_3), neutral ($(NH_4)_2SO_4$ and NH_4NO_3), maritime (NaCl and KCl), and continental ($CaCO_3$ and $MgCO_3$) aerosols. In this study, it is mainly considered that the solution chemistry involves the SO_2, HNO_3, HCl, NH_3, CO_2, O_3 and H_2O_2 gases and the oxidation of S(IV) by O_3 and H_2O_2. The relevant chemical reactions with the equilibrium constants or rate expressions may be found elsewhere (for example, see Easter and Luecken, 1988).

Upon scavenging of atmospheric aerosols, nucleation, aerodynamic impaction, and Brownian diffusion are the dominant mechanisms. For simplicity, it is assumed that all aerosols considered in this study are totally soluble within the aqueous phase, and as a result, at the instant of cloud formation, these are immediately incorporated into the aqueous phase.

a. Model Formulation for an Open System

In an open system, the gaseous concentrations are assumed to be constant. Based on chemical reactions considered in this study, and the theory of electroneutrality, when equilibrium between gas and aqueous phases in cloud droplets is established, the concentrations of all ions in the liquid satisfy the following equation:

$$[H^+] + [NH_4^+] + [CAT^+] + [CAT^{2+}] = [OH^-] + [Cl^-] + [HSO_3^-] + 2[SO_3^{2-}] + 2[SO_4^{2-}] + [NO_3^-] + [HCO_3^-] + 2[CO_3^{2-}] \,, \tag{1}$$

where CAT represents the dissolved but unreacted cations such as sodium, potassium, calcium, magnesium, and so on. The concentrations of the ions in liquid can be expressed in terms of [H+], for example,

$$[NH_4^+] = \frac{K_{ha}K_{a1}}{K_w}[H^+]\, p_{NH_3} \tag{2}$$

In the above equations, K_{ha} and p_{NH3} are the Henry's law coefficient and concentration of the ammonium gas, respectively, and K_{a1} is the first order of dissociation equilibrium constant for $NH_{3(aq)}$. The concentrations of other ions can also be expressed similarly. By replacing the ion concentrations in Eq. (1) except for [H+] with the relationships such as in Eq. (2), a cubic equation of [H+] is formed as follows:

$$A[H^+]^3 + B[H^+]^2 + C[H^+] + D = 0\,, \tag{3}$$

where A, B, C and D are functions of constants p_x and k_x for the species x. The sulfate ion concentration implied in the coefficient B is calculated as follows:

$$[SO_4^{2-}]_t = [SO_4^{2-}]_{t-\Delta t} + (d[SO_4^{2-}]/dt)_{t-\Delta t}\,\Delta t, \tag{4}$$

where Δt is the integrated time. Eq. (3) is solved iteratively for [H+] for each time step. The other ionic concentrations are then calculated.

b. Model Formulation for a Closed System

In a closed system, for an air parcel without mass exchange with the environment, the total concentrations of these gases in both gaseous and aqueous phases are assumed invariable. This is a good assumption when the air parcel is regarded as a reactive chamber and the relative importance of chemical reactions involved can be investigated. If $\overset{0}{p}_x$ represents the initial gaseous concentration and q_x is the aerosol mass concentration of species x, the following relationship shows the conservation of the mass for species x when it dissolves into cloud droplets (Walcek and Taylor, 1986):

$$\overset{0}{p}_x + \frac{q_x RT}{M_x} = p_x + [(x)]LRT \,, \tag{5}$$

where L, R and T are the liquid water content (LWC), the universal gas constant and the temperature of cloud droplets, respectively. The M_x is the molecular weight of x. The $[(x)]$ represents the dissolved gas x. For instance, $[(x)]$ is the sum of $[NH_3(aq)]$ and $[NH_4^+]$ for gaseous NH_3, and the above two states of NH_3 in aqueous phase can be expressed by Henry's law coefficient and equilibrium constant based on the Henry's law and Eq. (2). Therefore, for instance, the gaseous concentration of NH_3 in Eq. (2) is replaced by the following relationship:

$$p_{NH_3} = \frac{p^0_{NH_3} + \dfrac{q_{NH_3}}{M_{NH_3}} RT}{1 + (K_{ha} + \dfrac{K_{ha} K_{a1}}{K_w}[H^+])\, LRT} \tag{6}$$

Similarly, the other gaseous concentrations can be modified based on Eq. (5).

c. Modeling of Acidity in Individual Cloud Droplets

In the above subsections , the cloud water acidity is modeled for both open and closed systems. The pH values are obtained by assuming all cloud droplets of an equal size. However, the solute concentration in individual cloud droplets is dependent upon the cloud formation and growth processes, resulting in the dependence of droplet acidity upon the droplet size.

In Eq. (3), the coefficients A, B, C and D are rewritten by adding the subscript j for representing the cloud droplet of radius r_j. Considering the equilibrium between gaseous and aqueous phases in individual cloud droplets, the Eq. (5) can be rewritten as follows:

$$p^0_x + \frac{q_x RT}{M_x} = p_x + \sum_{j=1}^{m} [(x)_j]\, n(r_j) L_j RT \quad , \tag{7}$$

where L_j is the individual LWC for the droplet of radius r_j. Any terms associated with LRT are rewritten as the sum of the contributions from individual cloud droplets. For instance, Eq. (6) is rewritten as follows.

$$p_{NH_3} = \frac{p^0_{NH_3} + \dfrac{q_{NH_3}}{M_{NH_3}} RT}{1 + K_{ha} \sum_{j=1}^{m} n(r_j)\, L_j RT + \dfrac{K_{ha} K_{a1}}{K_w} \sum_{j=1}^{m} [H^+]_j\, n(r_j)\, L_j RT} \tag{8}$$

where the subscript j denotes the cloud droplet size category of r_j. The relationships for other gases are also modified following the above principle. As a result, the above equation is expanded into m equations for a cloud droplet size distribution which is categorized into m classes. For example, m is 25 for a given cloud droplet size distribution. These 25 sets of equations are simultaneously solved using the iteration method with the least square error within 0.1%.

3. RESULTS AND DISCUSSION

a. Model Simulation of Cloudwater Acidity

The cloud chemistry model is a kinetic model and can be incorporated into any cloud dynamical model. The latter predicts the cloud liquid water content and temperature in clouds as input meteorological and microphysical parameters. In order to test the cloud chemistry model, the temperature and liquid water content are assumed to be constant (288 K and 0.5 g m^{-3}, respectively) and the air parcel is assumed to be a closed system without mass exchange with the surrounding environment. The initial conditions for the gaseous and aerosol concentrations for 9 cases are listed in Table 1.

Table 1. The initial condition for the simulation of acqueous phase chemistry in cloudwater.

Case	1	2[a]	4	5	6	7	8[b]
Gas concentration (ppb)							
CO_2 (ppm)	320	320	320	320	320	320	320
NH_3		1	1	1	1	1	1
SO_2	10	10	10	10	10	10	10
HNO_3		1	1	1	1	1	1
HCl		1	1	1	1	1	1
H_2O_2		1	1	1	1	1	1
O_3	50	50	50	50	50	50	50
Aerosol loading (μg m^{-3})							
H_2SO_4			2				2
HNO_3			2				2
$(NH_4)_2SO_4$				2			2
NH_4NO_3				2			2
NaCl					2		2
KCl					2		2
$CaCO_3$						2	2
$MgCO_3$						2	2

a. Case 3 is the same as Case 2 but H_2O_2 and O_3 are remained in constant.
b. Case 9 is the same as Case 8 but H_2O_2 and O_3 are remained in constant.

The oxidation of SO_2 by H_2O_2 and O_3 is investigated in Cases 1-3. In Fig. 1 is shown the time variation of the pH values, the sulfate ion concentrations produced by the oxidation of S(IV). The curve for the pH value sharply drops from 4.89 to below 3.8 after about 5 min of reaction time, as shown in Fig. 1(a). By contrast, sulfate ions are increased to more than 80 μM. It is found that about 10% of SO_2 is dissolved into the cloud droplets when H_2O_2 is almost consumed for the oxidation of S(IV). Only about 2% of O_3 is involved into the oxidation of S(IV). The pH value and sulfate ion concentration almost remain constant when the concentration of H_2O_2 drops to near zero. It is evident that the oxidation of S(IV) is primarily dominated by H_2O_2. Cases 2 and 3 include the same gases but for Case 3 the entrainment of the H_2O_2 and O_3 is allowed. As a result, more than 95% of SO_2 is oxidized by entrained H_2O_2 and O_3 after 30 min of reaction time in Case 3, as shown in Fig. 2. When SO_2 is almost oxidized, the sulfate ion concentration for Case 3 is more than four times that for Case 2. The final pH value for Case 3 is about 3.2 and is about 0.5 lower than that for Case 2. Obviously, entrainment of pollutants significantly modifies the cloud water acidity.

In Cases 4-7 are explored the influences of scavenged aerosols on the cloud water acidity. The results are shown in Fig. 3. The sulfate and nitrate aerosols are major contributors to the cloud water acidity. Carbonate aerosols increase the pH value, when they are just scavenged by cloud droplets. However, increased sulfate ions by the oxidation of S(IV)

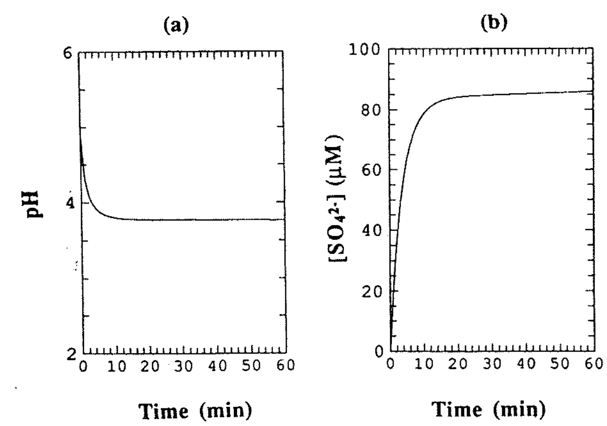

Fig. 1. Results of Case 1. (a) pH value, (b) sulfate ion concentration.

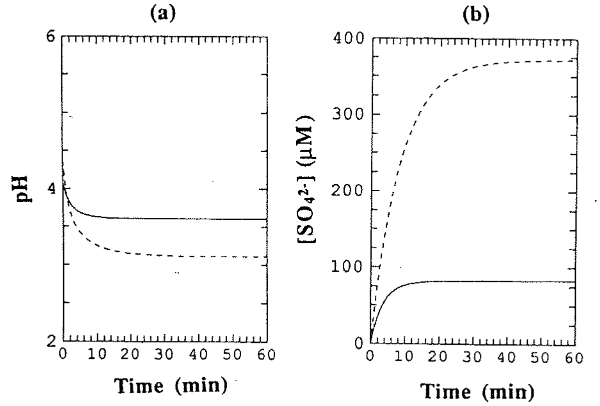

Fig. 2. Comparison of Cases 2 (solid line) and 3 (dashed line). (a) pH value, (b) sulfate ion concentration.

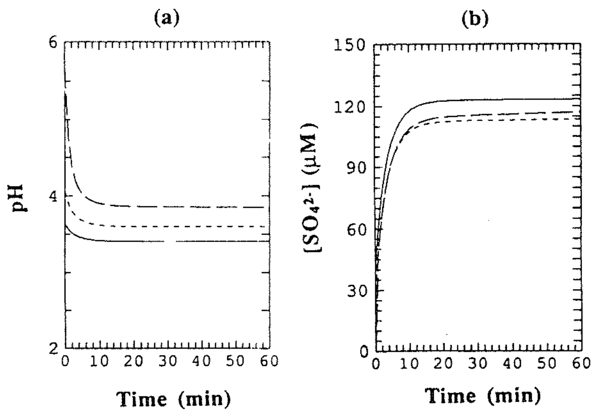

Fig. 3. Comparison of Cases 4 (solid line), 5 (dashed line) and 7 (broken line). (a) pH value, and (b) sulfate ion concentration.

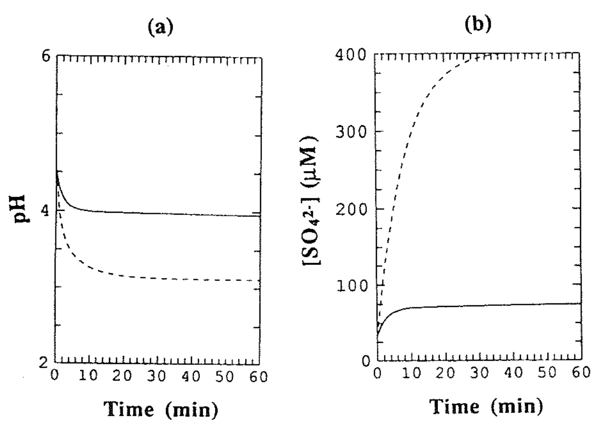

Fig. 4. Comparison of Cases 8 (solid line) and 9 (dashed line). (a) pH value, (b) sulfate ion concentration.

offset the above effect of carbonate loadings. The neutralized ammonium sulfate and nitrate aerosols reveal the moderate effect of acidifying the cloud water. In Fig. 3(b), the sulfate ion production for Case 7 is slightly higher than that for Case 5. This is because the oxidation rate of S(IV) by O_3 at pH=5 is more than 10 times that at pH=4. More sulfate ions are produced when carbonate aerosols are just scavenged by the cloud droplets and increase the pH value to about 5.5 in Case 7. The results of Case 6 for sea salt aerosols are not included in Fig. 3. The chloride sodium and potassium are neutral. When they are scavenged by the cloud droplets, the chloride aerosols can be converted to HCl gas. However, the converted amount is extremely small due to very large Henry's law coefficient of HCl which is in the order of 10^3 M atm^{-1}.

As shown in Fig. 4, the comparison of Cases 8 and 9 is similar to that of Cases 2 and 3, but the former includes the scavenging of aerosol particles. The difference in the pH values for Cases 8 and 9 is significantly larger than that for Cases 2 and 3, resulting from the addition of ammonium and carbonate aerosols in the former cases. The higher sulfate ion concentrations illustrated in Fig. 4 as compared to those in Fig. 2 are due to sulfate loadings.

b. Dependence of Cloudwater Acidity upon Cloud Droplet Size

In this study, the cloud droplet size distributions are prescribed by the Khrgian-Mazin droplet size distribution. The cloud droplet size spectra with respect to 5 liquid water content classes (0.1, 0.3, 0.5, 0.7 and 1.0 g m^{-3}) and 25 droplet size categories (from 0.35 to 32 μm) are evaluated.

For simplicity, the microphysical processes between the cloud droplets are ignored. The cloud droplet size distribution is assumed to be steady during the model simulation (about 10 min). Thus, the solute mass in each cloud droplet for species *i* is assumed to be proportional to the radius of the cloud droplet.

In order to test the dependency of the cloud droplet acidity on its size, the corresponding cloud droplet size distribution for the liquid water content of 0.5 g m^{-3} is used as a representative distribution. The initial condition is assumed the same as that for Case 8. As a result, smaller droplets have higher pH values although the sulfate ion concentrations in them are much higher than in larger droplets, as seen in Fig. 5(a). When the droplet sizes are greater than 2.5 μm, the variation of pH values with droplet sizes is not significant.

The model simulation is also performed for the case in which the carbonate aerosols are excluded. As seen in Fig. 5(a), the result is opposite to the previous one of full inputs. When the droplet sizes are greater than 1.5 μm, the pH values change within only 0.2 unit. The smaller droplets have higher acidity.

By comparing the above two cases, the smaller droplets are found to be most sensitive to aerosol loadings, primarily resulting from their smaller volumes. Although the larger droplets are assumed to have more aerosols dissolved, their resulting pH values are not sensitive to variation in droplet sizes. In Fig. 5(b) are shown the sulfate ion concentrations produced for these two cases. It is found that the concentrations for the case of full inputs are only slightly higher than that for the other case for those droplets of larger than 3.5 μm, whereas, the former is about twice the latter for the smallest droplet. Nevertheless, the pH value for the smallest droplet for the former case is about 4.3 unit lower than that for the latter case. The dilution effect in larger droplets can be seen in these model simulations. The carbonate aerosols significantly neutralize the acid aerosols in the case of full inputs. The sulfate and nitrate aerosols are the dominant species to acidify the cloud droplets, especially for the smallest droplet.

In the above case of no carbonates, the volume-weighed pH value over the cloud droplet size distribution is 3.404. The bulk pH value as calculated in Case 3 is at the same level, but slightly larger than the volume-weighed one. However, when the solute mass is assumed to be proportional to r^2 and r^3, the corresponding pH values are increased to about 3.423 and 3.426, respectively.

For the full model inputs, the simulations are further performed for five LWC classes as described previously. The results are shown in Fig. 6. In general, the higher the liquid water content, the smaller the less acidity in cloud droplets. For the case of the lowest liquid water content, the acidity is significantly higher than those for other cases. However, the acidity in cloud droplets may not be a linear function of the liquid water content, as seen in the case of LWC = 0.5 g m^{-3}. The cloud droplet size distribution is another factor to influence the cloud droplet acidity, because the mixing ratio of aerosols in cloud droplets is strongly dependent upon their sizes.

4. CONCLUDING REMARKS

The cloud chemistry model gives information regarding the dependence of the acidity in cloud droplets upon their sizes, the type of their distribution, and the importance of aerosol loadings. About 10% of gaseous SO_2 is in general consumed for producing the S(IV) and the sulfate ions. However, the addition of aerosols can dramatically alter the acidity in cloud droplets, especially for the smaller droplets. The scavenging of sulfate and nitrate aerosols is the most efficient mechanism to acidify the cloud rather than the oxidation of SO_2. It is feasible to link the developed method with the dynamical cloud model, and thereby, to further investigate the influences of the dynamical behavior of cloud droplets on the solute concentration and the resulting acidity.

5. REFERENCES

Flossmann, A. E., W. D. Hall and H. R. Pruppacher, 1985: A theoretical study of wet removal of atmospheric pollutants. Pt. I: the redistribution of aerosol particles captured through nucleation and impaction scavenging by growing cloud drops. *J. Atmos. Sci.*, **42**, 583-606.

Easter, R. C. and D. J. Luecken, 1988: A simulation of sulfur wet deposition and its dependence on the inflow of sulfur species to storms. *Atmos. Environ.*, **22**, 2715-2739.

Hegg, D. A. and P. V. Hobbs, 1979: The homogeneous oxidation of sulfur dioxide in cloud droplets. *Atmos. Environ.*, **13**, 981-987.

——, T. V. Larson, 1990: The effects of microphysical parameterization on model predictions of sulfate production in clouds. *Tellus*, **42B**, 272-284.

Jensen, J. B. and R. J. Charlson, 1984: On the efficiency of nucleation scavenging. *Tellus*, **36B**, 367-375.

Noone, K. J., R. J. Charlson, D. S. Covert, J. A. Oregen and J. Heintzenburg, 1988: Cloud droplets: solute concentration is size dependent. *J. Geophys. Res.*, **93**, 9477-9482.

Schwartz, S. E., 1984: Gas-aqueous reactions of sulfur and nitrogen oxides in liquid water clouds. In *SO_2, NO and NO_2 Oxidation Mechanisms*. (edited by Calvert J. G.), Butterworth, 254 pp.

Walcek, C. J. and G. R. Taylor, 1986: A theoretical method for computing vertical distributions of acidity and sulfate production with cumulus clouds. *J. Atmos. Sci.*, **43**, 339-355.

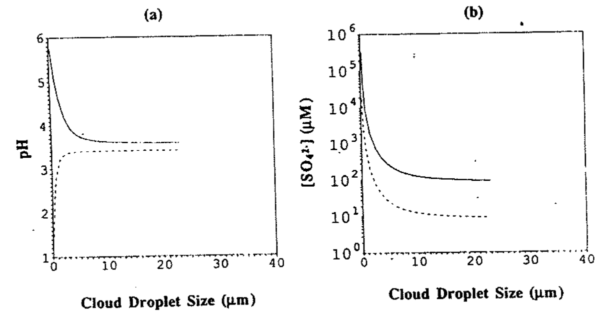

Fig. 5. Comparison of the simulations of cloud chemistry model for the following conditions: (1) full inputs, and (2) excluding the carbonate aerosols. Solid and dashed lines represents the former and latter, respectively. (a) pH values and (b) sulfate ion concentrations as a function of cloud droplet size. In (b), the sulfate concentration for condition (2) is reduced by a factor of 10 in order to differ from condition (1).

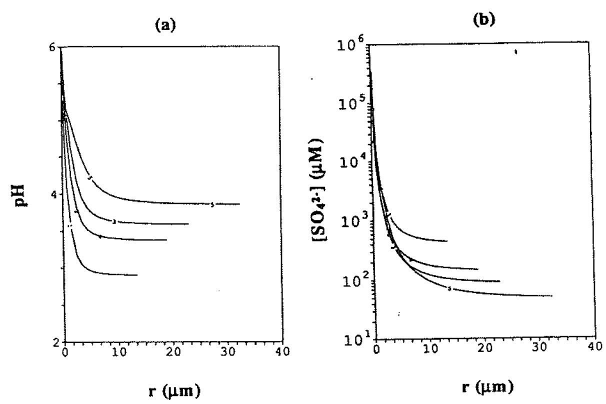

Fig. 6. (a) pH values and (b) ion concentrations as a function of cloud droplet size for five LWC classes.

MEASUREMENTS AND ANALYSES OF CLOUD WATER CHEMISTRY OVER THE SOUTHWEST OF CHINA

Shen Zhilai, Wu Yuxia, Xiao Hui, and Huang Meiyuan

Institute of Atmospheric Physics, Academia Sinica,
Dewai, Beijing, 100029, P.R.China

I. INTRODUCTION

The problem of acid rain has become one of major environmental concern in a global scale. Up to now, most knowledge on the chemical composition of precipitation has been generated by measurements at ground level. Many researcher[Dean,1981; Houghton,1955; Petrenchuk,1966; Scott,1978] have indicated that cloud is of importance for studying of environmental subjects.

Measurement and research on cloud chemistry were conducted first in China by our institute in 1985 in Chongqing area[Huang,1988], following that, several acid rain comprehensive observations both in cloud and on ground had been carried out in Shanghai[Shen, 1989], Guangdong, Guangxi, Sichuan and Guizhou areas. The results of the cloudwater chemistry presented in this paper were mostly from data collected over the Southwest(SW) of China from September through October, 1989.

A Twin Otter aircraft was used for measurement. The regional range of the Southwest of China concerned in this flight observation included Chengdu(the West of Sichaun basin), Chongqing(the Southeast of Sichaun province) and Guiyang(the center and north of Guizhou province) areas. 152 cloudwater samples were obtained with Chengdu's 58, Chongqing's 46 and Guiyang's 48. All of the cloudwater samples were measured for pH and 48, 39 and 41 samples were analyzed for chemistry composition for the three areas, respectively.

II. RESULTS

1. Cloudwater Acidity

Cloudwater in SW of China was acidic with an average acidity of pH≈4.50. Defining pH=5.60 as neutral, the order of frequency occuring acid cloud from high to low was Guiyang, Chongqing and Chengdu (96%, 85%, 78%, respectively).

1989's result indicated that not only had cloud water become acidic, but also the regional range covered with acidic cloud was very large. The minimum of cloudwater pH did not exist over big cities, whereas existed over small cities and towns.

The result of cloudwater collected from 1984 through 1989 over Chengdu and Chongqing areas showed that the average, maximum and minimum values of cloudwater pH dropped down yearly, and there were very low pH of about 4.50 over the two areas in 1989.

2. Chemical Compositions of Cloudwater

(1) Average situation of cloudwater chemistry

It can be seen from Table 1 :

The predominant cation was Ca^{++} and the predominant anion was $SO_4^{=}$. The ratios of $SO_4^{=}/NO_3^{-}$ were 8.4-12.7 which shows that the cloudwater was "sulphur acid-type" over the SW of China.

In cloudwater, the concentration of Ca^{++} was larger than that of NH_4^{+}. The concentrations of Ca^{++} and NH_4^{+} in rainwater were all higher than those in cloudwater. The average pH values in cloudwater were higher than those in ground rainwater, whereas the main ionic average concentrations were larger in rain water than those in cloud water.

The ionic concentrations of cloudwater and rainwater collected in the same period also proved the conclusion, and similar results were obtained in 1985 over Chongqing area[Huang,1988].

The vertical distributions of SO_2, NO_x and NO obtained over Chongqing city in October,1989 showed gaseous pollutant concentrate mostly below 1000m above sea level elevation, i.e. below cloud base.

(2) Variation of ion concentrations of cloud water with height

Main anion concentrations decreased with increasing in height and there was a similar trend for main cation. The highest ion conecntrations were at near cloud base and decreased with increasing in height in cloud.

(3) Regional range of polluted cloud water

The same as the acidification of cloud water over SW of China, the range of cloud water pollution covered not only big cities, but also remote small cities and towns where the concentrations of main chemical compositions were even bigher than those over neighbourhood of big city.

(4) Temporal variation of composition concentrations of cloud water

The total ion concentration increased from 1985's 407.2μeq/l to 1989's 504.9 μeq/l and the pH values of cloud water decreased from 1985's 6.15 to 1989's 4.56, correspondingly. Both anion concentrations($SO_4^{=}+NO_3^{-}$) and cation concentrations ($Ca^{++}+NH_4^{+}$) increased, but the former increased more than the later. The former increased by a factor of 1.2 and the later increased only by a factor of 0.2; correspondingly, the total anion concentration increased by a factor of 0.6 and the total cation concentration increased only by a factor of 0.2.

3. The content of H_2O_2 in Cloudwater

(1) Content of H_2O_2 in cloudwater

The total range of H_2O_2 content in cloudwater over Chengdu, Chongqing and Guiyang were 0.07-116.8μM with an average of 22.8μM. The average

Table 1. Average situation of chemical composition of cloud- and rain-water in 1989, μeq/l

Areas		pH	H^+	F^-	Cl^-	NO_3^-	$SO_4^=$	Na^+	K^+	NH_4^+	Ca^{++}	Mg^{++}	$\Sigma^*(+)$	$\Sigma(-)$	$SO_4^=/NO_3^-$
Chengdu	cloud	4.58 (48)**	26.3	15.6	87.4	24.2	306.9	49.5	31.3	94.6	125.2	24.7	351.6	434.1	12.7
	rain	4.44 (8)	36.3	19.7	42.3	30.4	431.5	22.6	20.8	250.7	192.0	23.0	545.3	523.9	14.2
Chongqing	cloud	4.56 (39)	27.5	12.1	32.6	22.9	192.4	37.3	9.8	40.6	97.3	10.1	222.6	282.3	8.4
	rain	4.03 (22)	93.3	26.7	40.3	43.2	421.8	89.8	15.2	386.6	207.2	13.2	755.3	561.5	9.8
Guiyang	cloud	4.62 (41)	24.0	0.4	16.1	5.3	49.6	17.2	14.1	0	31.9	4.5	91.7	72.4	9.3
	rain	3.99 (9)	102.3	0.0	3.9	9.7	122.4	8.0	14.9	15.8	36.9	3.8	161.7	163.0	12.0

* Σ(+) and Σ(-) represent the sum of concentrations of cation and anion,respectively
** ( ) represents the number of samples

values in upper layer of cloud were higher than those in low layer.

(2) Relationship between H_2O_2 and S(IV) in cloudwater

The range and average of S(IV) concentrations in cloudwater over Chongqing and Guiyang were 1.13-5.73mg/l,2.49mg/l and ND-0.44mg/l,0.043mg/l, respectively. There was a strong anticorrelation of H_2O_2 with S(IV) in cloud water: if H_2O_2 content is high, then S(IV) content is low, and vice versa.

(3) Comparison of H_2O_2 in cloud water and in ground rain water

The range and average of concentration of H_2O_2 in ground rainwater in Chongqing area were 0.16-0.74μM and 0.44μM,respectively, which showed the average value in the ground rainwater was one order of magnitude lower than that in cloudwater.

III.DISCUSSION

1. Importance of Rainwater Acidification Below the Cloud

It was already presened that the concentrations of ions(included H^+) in rainwater were higher than those in cloudwater, whereas it were contrary for H_2O_2 and S(IV). For example, in Chongqing area, H^+ and $SO_4^=$ increased from cloud water's 27.5 and 37.3μeq/l to rainwater's 93.3 and 89.8μeq/l, respectively, while the content of H_2O_2 dropped from cloud water's 19.5μM to rain water's 0.44μM and S(IV) concentration dropped from 2.49mg/l to 1.18mg/l. This means that there is rainwater acidification below cloud, which results possibly from the liquid phase oxidation of S(IV) by H_2O_2 during falling of rain drops from cloud base to ground. It makes H^+ concentration in rainwater higher than that in cloudwater and H_2O_2 consumed. The process contributes importantly to the rainwater acidification below cloud.

2.Interpretation of Spatial and Temporal Variation of Cloudwater Chemistry

The industry(fire power factory) burning coal amount has increased for recent years in the SW of China. These pollution sources exist mostly in suburban(county) and the stacks emitting pollutant are considerely high, which cause a lot of SO_2 to be transported up and around areas. For example, some electric power factory established in 1987 in Chongqing has one of high stacks with 240m, one of 80m and five of 50m. The coal consumption in 1989 was 24% higher than that in 1985 in Chongqing area. The environmental effect of increasing in coal-burning and high stacks was reflected in making heavier about the pollution in the air and the regional acid deposition in the SW,i.e., increase of concentration of SO_2 in the air and concentrations of H^+, $SO_4^=$ and S(IV) in cloud water, as well as the acidity in cloud water and rain water in suburban (county).

REFERENCES

Dean A. et al.,Cloud water chemistry and production of sulfate in cloud, Atmos. Environ., Vol.15,No.9,pp.1597-1604,1981

Houghton H., On the chemical composition of fog and cloud water,J. Met.,12,355-357,1955

Huang Meiyuan, Shen Zhilai and Wu Yuxia, Observations and analyses of acidity and chemical composition of cloud water and rain water in Chongqing area, Scientia Atmospheric Sinica, Vol.12, No.4,389-395,1988

Petrenchuk O.P., et al., On the chemical composi-tion of rain-, snow- and fog-water, Tellus,18, 266-270,1966

Scott W. D., The pH of cloud water and production of sulfate,Atmos. Environ.,12,917-921,1978

Shen Zhilai, Huang Meiyuan, Shao Deming et al., Analysis of acidities and chemical compositions of rain water and cloud water in Shanghai area, Scientia Atmospherica Sinica, Vol.13, No.4,460-466,1989

CASE STUDY ON THE INTERACTION OF SIZE DEPENDENT MULTIPHASE CHEMISTRY AND DETAILED MICROPHYSICS

F. Müller and G. Mauersberger

IFU, Einrichtung für Luftchemie, O-1199 Berlin, Germany

1. INTRODUCTION

A reexamination of the microphysical growth processes (i.e. activation of wet aerosol particles, condensational growth) as well as the cloud chemistry reaction system suggest that both kinds of processes coupled on the basis of joint, the processes governing, parameters. Another common feature of the equations is the particle size dependency of the processes.

Our study is focused on the investigation of the mutually interaction of cloud-microphysical and chemical processes with respect to the chemical composition (characterized by the concentration ratios of the CCN related compounds in the liquid phase) and the chemical "milieu" (characterized by the liquid-phase concentrations, mainly by $[H^+]$) of the developing cloud drops and its size dependency. We are alive to the fact that the consideration of cloud dynamical processes may alter quantitatively our results.

2. THE MODEL

Throughout this study we use a simple closed box model with prescribed meteorological and chemical parameters for the environmental conditions. The model include detailed microphysics and spectral (with respect to droplet size) multi-phase chemistry. Advection and turbulent mixing processes are disregarded during this study.

a. THE CHEMISTRY MODULE

The used chemical module is condensed and directed on the description of the acid formation dynamics. The treatment follows the theory of Schwartz (1988); especially the formulation of the fluxes between gas and liquid phase. In the gas phase the acid related compounds CO_2, H_2O_2, O_3, HCl, SO_2, HNO_3, and NH_3 are included. All mass accommodation coefficients are assumed to be 0.01. Nonequilibrium reactions in the liquid phase are only considered for the sulphate production reactions via H_2O_2 and O_3.

b. THE MICROPHYSICAL MODULE

This module describes the distribution activation of wet particles, condensation and collision with subsequent coagulation and breakup due to hydrodynamic instability. The cloud interstitial aerosol is allowed to remove by collision aerosol scavenging (CAS) using the technic proposed by Beheng and Herbert (1986).

Especially attention is drawn on the time development of the mixing ratio $Q_{d,i}(m)=G_{d,i}(m)/G_w(m)$ of the i-th chemical component in a drop of mass m with the mass density $G_{d,i}(m)$ of the i-th chemical component and the water mass density $G_w(m)$of this drop. The local change of $Q_{d,i}(m)$ writes

$$\frac{\partial Q_{d,i}(m)}{\partial t}=\frac{1}{G_w(m)}\frac{\partial G_{d,i}(m)}{\partial t}-\frac{Q_{d,i}(m)}{G_w(m)}\frac{\partial G_w(m)}{\partial t} \quad (1)$$

The time evolution of the mixing ratio results from a local change of the mass density of this specie (first term on the right hand side) and a change in water mass of the droplet (second term). Activation determines the chemical nature of "new" droplets, i.e. contributes to the local change of the mass density of certain species, namely the electrolytes NH_4^+, Na^+, SO_4^{2-} and Cl^-, as well as to the change of liquid water mass of the droplet. Condensation/ evaporation alters the amount of the drop water mass and keeps the mass density of chemical species in the solution drop constant. Coalescence and breakup are very efficient mixing processes as long as the liquid water content is sufficiently high and the mean radius of the drop distribution has reached a critical size. Both mass density of chemical components and water, respectively, will be changed in time. The uptake of dry cloud interstitial aerosol as well as the chemical processes induce a change of mixing ratio due to a variation of chemical specie mass density.

c. INITIAL CONDITIONS

The environmental conditions are held constant over the whole simulation time at a temperature T=280K, pressure P=900hPa and relative humidity RH=100.1%.

Table 1. Concentration of Gases

CO_2	$3.3\ 10^{+5}$	ppb
O_3	$4.1\ 10^{+1}$	ppb
H_2O_2	1.0	ppb
HNO_3	$5.0\ 10^{-1}$	ppb
NH_3	1.0	ppb
SO_2	2.0	ppb
HCl	$5.0\ 10^{-1}$	ppb

We assume that the aerosol particles consist of an internal mixture of 5% NaCl, 15% $(NH_4)_2SO_4$ and of 80% insoluble matter (SiO_2) with respect to the total aerosol particle mass. This chemical composition is uniform distributed over the aerosol population. The aerosol particles are size distributed along a Deirmendjian distribution (c.f. Pruppacher and Klett, 1978) with the radius for the maximum of the distribution R_0=0.7μm and a total number density of N_0=500cm^{-3}. The initial concentrations of the gases are shown in Table 1.

3. RESULTS

a. EFFECT OF MICROPHYSICS ON THE CHEMICAL MILIEU

In order to study the chemical milieu of a cloud droplet system under the action of microphysical processes we switched off all fluxes of gaseous species between the environment and the droplet surface (this means that throughout this subsection dissociation equilibrium state inside the drop is permitted whereas the uptake of gases and sulphate production reactions are prohibited). Only the electroneutrality equation is solved to calculate $[H^+]$.

$$[H^+]-[OH^-]=\sum_i c_i^- - \sum_j c_j^+ \qquad (2)$$

Here c_i resp. $[H^+]$ denote concentrations in mol/l ($c_i=1000Q_{d,i}\rho_w/M_i$; M_i-molar mass of species i, ρ_w-water mass density). The positive and negative sign on the concentrations c_i refers to positive or negative charged ions. In this case the righthand side of (2) has the form

$$2[SO_4^{2-}]+[Cl^-]-[Na^+]-[NH_4^+] \qquad (3)$$

and is greater than zero since $NH_3 \cdot H_2O$ is being incompleate dissociated. This is the only one reason that the pH differs from the neutrality in this context. Dilution leads to growing of pH (the ratio $[NH_3 \cdot H_2O]/[NH_4^+]$ increases slower than $[NH_3 \cdot H_2O]+[NH_4^+]$ decreases).
For a better understanding Fig. 5 shows the major features we will discuss in the following with the exception of the pH levels. In the case of non-reactive drops the maximum pH level is about 7.0 and the minimum one is above 5.1.

Starting just after nucleation with relative high concentrations of chemical species in the smallest drop size categories (0.1-1μm) and with the lowest concentrations at the large tail of the droplet spectrum (up to about 10-20μm). Under the action of condensation water is added to every drop category with respect to the chemical composition and the mass of aerosol in solution. Small concentrations cause a small dilution effect. As a result of this size dependent dilution effect the concentration distribution of electrolytes reverses over the size range - high diluted small droplets and only less reduction in concentration at the large tail of drop size distribution.

As mentioned earlier coagulation and Chemistrybreakup lead to a redistribution of the electrolytes and the insoluble matter over the whole size range. The uptake of high diluted small droplets forces on one hand a further dilution for the bigger drops, which are very efficient collectors within the size spectrum, and hence a slow increase in pH. On the other hand the transport of relatively concentrated satellite droplets due to breakup of big drops leads to an enrichment of electrolytes in the smallest size categories and hence the ion concentration difference increases. This forces a decrease of pH in this size range. Due to the fact that these processes become the more important the more liquid water is distributed over the drop spectrum the variation of electrolyte concentration due to redistribution dominates the change due to size dependent dilution after a few hundreds of seconds.

The CAS process describes the uptake of cloud interstitial aerosol particles. The fact of the spectral dependency of the scavenging behaviour of droplets is stressed by several investigators (Flossmann et al., 1985; Herbert and Beheng, 1986). In general this process leads to an increase of the $[H^+]$ and hence to a decrease of the pH. The effect of CAS is less important for short simulation times and small collector particles compared with the uptake of chemical species due to nucleation aerosol scavenging (Jensen and Charlson, 1984).

We can conclude that microphysical processes are able to influence the chemical milieu of a size distributed droplet population in the absence of chemical reactions efficiently. Further on the microphysics can not alter the chemical composition of solution droplets but these processes are responsible for drop size dependent changes of the mixing ratio of chemical matter inside the solution drops and for the performance of mixing between the different drop sizes.

b. ACTION OF CLOUD CHEMICAL PROCESSES ON THE COMPOSITION OF CLOUD DROPLET

We leave the experiment with nonreactive solution drops under the action of various microphysical processes of the previous section and will focus our attention to the additional influence of chemical reactions as a size dependent phenomenon. Only the size dependent chemical processes are able to change the internal mixture of the aerosol composition of solution drops. Fig. 1 shows the time evolution of the ratio of $[NH_4^+]$ to $[SO_2^{2-}]$ generated through the aerosol phase.

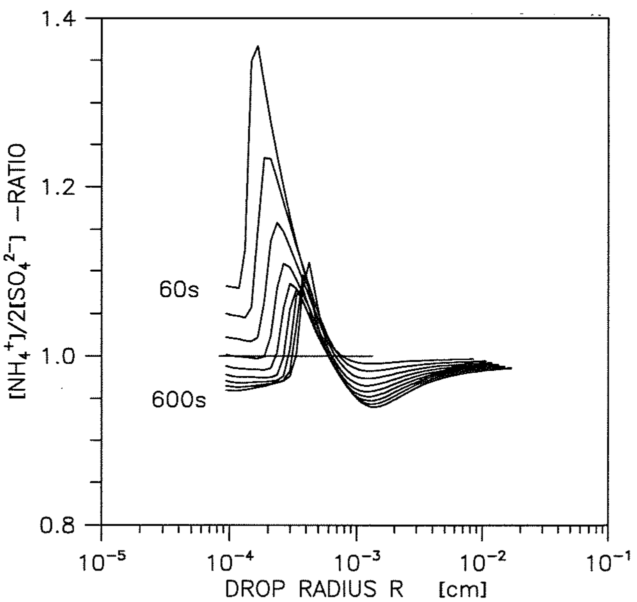

Fig. 1 Change of chemical composition

For the case of $[Cl^-]/[Na^+]$ ratio (not seen here) one can note a general increase of $[Cl^-]$ over the whole size spectrum. This results from the flux of HCl induced by size dependent dilution. The range of maximum increase of $[Cl^-]$ is related to the range of maximum dilution and hence to the pH maximum. The NH_3 flux has a similar behaviour. Since the sulphate production is more uniform over the drop spectrum the $[NH_4^+]/[SO_4^{2-}]$ ratio decrease in ranges of less dilution.

c. THE FRACTION OF MICROPHYSICS AND CHEMISTRY ON THE TIME EVOLUTION OF MIXING RATIOS

In this subsection we will investigate the time evolution of the rates of change of mixing ratios of chemical species due to the chemical processes in the context of their spectral dependent interaction with the microphysics. Exemplarily the Cl^-- ion is chosen to explain our results because it is a part of the chemical reaction system and it exists in the gase-phase, too.

Fig. 2-5 show the major features of the different microphysical processes discussed in the previous section. The decrease of the Cl^- concentrations due to condensation (Fig.2) shows a strong size dependency. In the size range 1-5μm one can note a relative minimum in the rate of Cl^- change which is caused by a minimum of soluble matter in the size distribution and hence by reduced mass growth rates relative to the water mass of the solution drop. Fig. 3 shows very impressive the relative increase of the Cl^- mixing ratio due to breakup in the small droplet size range around 10μm which is related to the maximum in the size distribution of the water mass.

The direct influence of chemical processes is shown in Fig. 4. The HCL gas-liquid system tries to reach a equilibrium

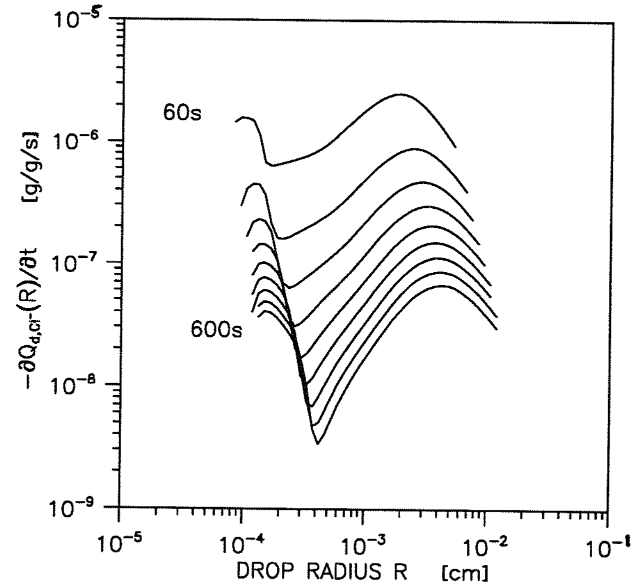

Fig. 2 Rate of change of mixing ratio due to condensation

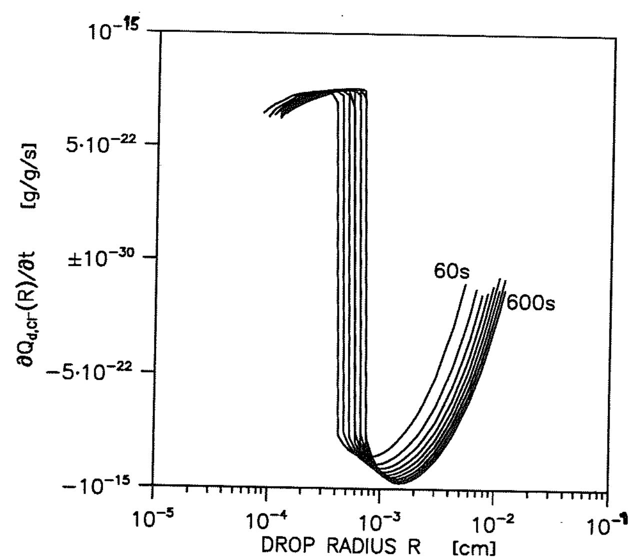

Fig. 3 Same as Fig. 2 but due to coagulation and breakup

whereas the equilibrium concentrations in the liquid phase vary over the droplet size range with the effective Henry coefficient dependent on $[H^+]$. Since the smaller droplets are being more diluted than fopr the bigger ones a new equilibrium is being reached due to flux from the greater to the smaller droplets via the gas phase.

The superimposed effects of microphysics and chemistry are condensed in the time evolution of the size dependent pH in Fig. 5. The size range of the maximum pH in the case of the complex interaction of cloud chemistry and microphysics coincidences with the case of non-reactive cloud drops and is not only related to the minimum in the total electrolyte concentration but also to the minimum in [SiO_2].

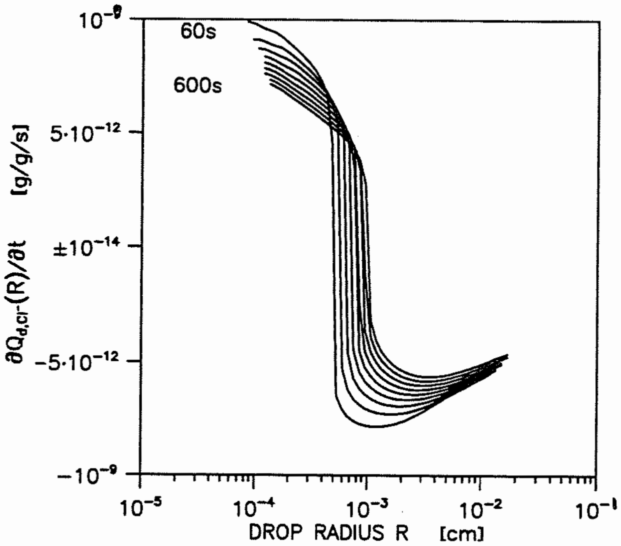

Fig. 4 Same as Fig. 2 but due to chemistry

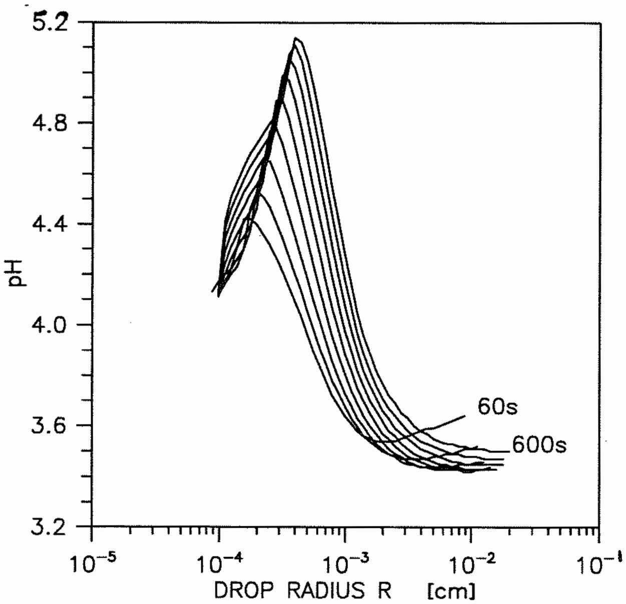

Fig. 5 Time evolution of spectral pH due to chemistry and microphysics

This fact indicates that the [H^+] size distribution and hence the ph is determined by nucleation and subsequent microphysical processes and modified by the chemical reaction system.

4. CONCLUSION

The chemical milieu is determined by microphysics while the chemical composition is a result of nucleation and cloud chemistry.

5. REFERENCES

Beheng, K.D., Herbert, F., 1986: Mathematical studies on the aerosol concentration in drops changing due to particle scavenging and redistribution by coagulation, Meteor. Atm. Phys., 35, 212-219

Herbert, F., Beheng, K.D., 1986: Scavenging of airborne particles by collision with water drops- model studies on the combined effect of microdynamic mechanisms, Meteor. Atm. Phys., 35, 201-211

Flossmann, A.I.; Hall, W.D., Pruppacher, H.R., 1985: A theoretical study on the wet remuval of atmospheric pollutants. Part I: The redistribution of aerosol particles captured through nucleation and impaction scavenging by growing cloud drops, J. Atm. Sci., 42, 583-606

Jenson, J.B.; Charlson, R.J., 1984: On the efficiency of nucleation scavenging, Tellus, 36B, 367.375

Schwartz, S.E., 1988: Mass transport limitation to the rate of in-cloud oxidation of SO_2: Reexamination in the light of new data, Atm. Env., 22, 2491-2499

FORMATE AND ACETATE IN MONSOON RAINWATER IN THE SEMI ARID TRACT OF AGRA

Nandini Kumar, U.C. Kulshreshta, A. Saxena, K.M. Kumari and S.S. Srivastava

Department of Chemistry,
Dayalbagh Educational Institute,
Dayalbagh, Agra 282 005
India

INTRODUCTION

Formic and acetic acids are major chemical constituents of precipitation and cloud water in the global troposphere. They constitute a large fraction of the free acidity in remote regions (*Keene and Galloway, 1984; Keene et al., 1983*) and at Katherine, Australia, 64% of the free acidity of precipitation was contributed by organic acids (*Likens et al., 1987*). In Virginia, USA, this contribution was 16% (*Keene and Galloway, 1984*). In India no studies on organic acid levels have so far been carried out. Their characterization in a semi arid tract would be of additional interest owing to the calcareous nature of the soil and the associated elevated pH values of rainwater and dry deposition.

METHODS

The samples were collected at our institute campus situated in Dayalbagh which is a suburb to the northwest of Agra city. There are a variety of deciduous trees around the campus. Nineteen rainwater samples were collected on an eventwise basis using bottle and funnel collectors. These were clamped to iron stands one meter high, which were placed on the roof of our faculty building (8 m in height). pH was measured immediately after collection and a portion of the sample treated with chloroform for preservation.

Analysis: Analysis for organic anions was performed using Ion Chromatography on a Dionex 2000i/SP Chromatograph (AS4A column) with a conductivity detector. 1.25 mM borax ($Na_2B_4O_7.10H_2O$) was used as eluent and 25 mN H_2SO_4 as the regenerating solution. All standards were prepared from sodium salts of acids.

RESULTS AND DISCUSSION

Table 1 contains means and ranges of different parameters in the nineteen samples analysed. The VWA pH was 7.17 and the total formate and acetate content was 17.9 μeq L^{-1} (VWA). 96.94 $\pm$ 1.9% of the two species was present in the dissociated state. Contributions to free acidity of organic acidity were not estimated because they would be over 100% ; the two acids are present largely in their dissociated forms due to the elevated pH values of the rainwater here and the fact that they are probably present as Na, Ca, K and Mg salts of formic and acetic acid.

These observations are in direct contrast to those at Virginia, USA where the VWA pH of precipitation was 4.17 and maximum contributions to free acidity ranged between 3 and 43% (*Keene and Galloway, 1984*). In general, when the volume of rain recorded was high the levels of both ions were lower. The samples included in this study showed two trends. One type was characterized by F/A (formate-to-acetate) ratios greater than 1.5. This trend could be attributed to the fact that these events were either preceded by antecedent periods or were events prior to which windy/dusty conditions prevailed. These observations led us to hypothesize that besides terrestrial vegetation as sources for formate and acetate, soil also was a contributing factor. The analysis of soil from nearby areas and dry deposition studies revealed F/A ratios of approximately 3. In the other group of samples which were collected either sequentially during prolonged periods of rain or after gaps of only a few hours, lower F/A ratios (<1.0) were observed which indicated the relative dominance of anthropogenic sources over natural sources, including soil. Possible anthropogenic inputs of acetate could be from firewood burning and the alkaline hydrolysis of PAN.

TABLE 1

Parameter	Mean	Range
pH	7.17	5.65 - 7.59
Rain depth (cm)	1.03	0.12 - 3.11
$CH3COO^-$ (μeq L^{-1})*	8.44	bdl - 36.66
$HCOO^-$ (μeq L^{-1})*	8.56	bdl - 71.73
F/A (μeq L^{-1})	1.10	0.36 - 7.38

* Dissociated
bdl- below detection limits

REFERENCES

1. Keene W.C. and Galloway J.N. Organic acidity in precipitation of North America, *Atmos. Environ.* 18, 2491-2497, 1984.

2. Keene W.C., Galloway J.N. and Holden J.D., Jr. Measurement of weak organic acidity in precipitation from remote areas of the world, *J. Geophys. Res.* 88, 5122-5130, 1983.

3. Likens G.E., Keene W.C., Miller J.M. and Galloway J.N. Chemistry of precipitation from a remote terrestrial site in Australia, *J. Geophys. Res.* 92, 13,299 -13,314, 1987.

ACKNOWLEDGEMENTS

We are grateful to the Ministry of Environment and Forests and the Council for Scientific and Industrial Research, New Delhi for providing financial assistance.

Transformation, Deposition and Transport of Air Pollutants in a Frontal System

N.Mölders, A.Ebel, H.Hass, H.J.Jakobs, M.Laube

Universität zu Köln
Institut für Geophysik und Meteorologie
EURAD
Salierring 48
D-W-5000 Köln 1, FRG

A frontal passage is simulated with the EURAD (European Acid Deposition model) with two different cloud moduls to examine the impact of cloud parameterizations on tracer distribution, transformation, scavenging and wet deposition. Focus will be taken on the differences in concentration distribution, on the amount of precipitation and on cloud cover.

The EURAD-model (European Acid Deposition model) simulates the transports, transformations and depositions of chemical tracers on mesoscale regions. In such type of models clouds have to be parameterized as they are of subgrid scale The EURAD-model consists of two submodels: MM4 (Mesoscale Meteorological Model Version 4; Anthes et al., 1987) and the chemical part CTM (Chemistry Transport Model; Chang, et al., 1987; Hass, et al., 1990; Hass, et al., 1991). The meteorological fields prognosed by MM4 (temperature, pressure, wind, water vapor, rain and if the ice parameterization is used cloud water, rain water, ice and snow) serve as input for CTM to predict the transport, transformation and wet and dry deposition.

The first cloud model is a modified Kuo cumulus parameterization. Cumuliform clouds are assumed to occur if sufficient horizontal moisture convergence and instability are present above a grid area. The cloud chemistry, entrainment and scavenging follows Walcek and Taylor (1986). Wet chemistry is calculated for cloud mean values of temperature, liquid water and concentrations. The Kuo type version will be considered as the control experiment.

The second cloud modul tested is a ice parameterization which prognoses water vapor, cloud- rain water and ice. The cold path of precipitation generation follows Cotton et al. (1982). The vertical transport of air pollutants in cloudy columns is done by fluxes. Aquoeus chemistry is determined for every model layer where liquid water occurs, separately.

MM4 is run for a three day episode after the Chernobyl accident (25^{th} to 28^{th} April, 1986) starting and ending at 1200 UTC. The meteorological situation during that time was governed by a cyclone near Iceland and high pressure over northeastern Europe. Over the Alps a frontal system caused heavy rainfalls. It is responsible for the transport of chemical tracers from the planetary boundary la-yer into the free atmposphere. Chemical species having a short life time in the lower la-yers are not transported far away from their sources in the areas of the model where no clouds exist. Once reaching the upper troposphere the gases have longer life times and participate in long range transport.

The cloud parameterizations produce differences in meteorological results (liquid water-, ice content, temperature, vertical mixing, wind, rain and cloud amount) and so changes in aquoeus and gasphase chemistry processes, wet and dry deposition occur. Generally the liquid water content diagnosed by the cloud modul in the control run is higher (up to a factor 10) than that prognosed by the cloud modul including ice. The solubility and transformation are functions of the pH value. The differences in pH for the different meteorological input fields are due to differences in meteorological parameters (especially liquid water), transport (especially vertical transport) and different treatment of chemistry. The sulfat production and the oxidation paths differ between the experiments.

The ice phase is very important for cloud dynamical, rain formation and washout processes. As the ice parameterization considers the washout due to snow there are discrepancies in the washout rates and so in concentration profiles.

The cloud amount and their vertical and horzontal distribution are important for the gas phase as photolysis strongly depends on these parameters. The run with the Kuo-type cloud parameterization delievers too low cloud cover and too few clouds compared to satellite data. The cloud cover distribution and amount of the run with the ice parameterization fits well with the observations. The different cloud distributions and cloud cover change the wet chemistry and wet deposition, the photolysis rates and so the gasphase chemistry.

The cloud base plays a significant role as the gasphase concentrations are changed in the levels below due to decreased photolysis rates and/ or rainout. Wet chemistry, wet removal, decreased photolysis rates and vertical mixing due to entrainment influence the gasphase concentrations and depend on cloud extension. The cloud boundaries strongly between the experiments. The run including ice microphysics prognoses clouds in more than one cloud layer per grid column. Only the lowest cloud is responsible for the wet deposition occuring.

In the control run the accumulated rain is higher than the observations. The run including ice underpredicts the precipitation amount slightly, but fits good in space, location and time with the rain measurements. The differences in the rain data cause differences in both wet and dry deposition as the later one depends on whether a surface is wet or dry.

Discussion

The concentration profiles gained with the ice scheme are more differentiated. The reasons are a more detailled vertical mixing due to clouds, the more precise treatment of wet chemistry, the inclusion of the distinction between washout processes of rain and ice crystals and differences in the vertical transport. The strong deviation of the cloud amount in the two runs is responsible for the differences in gas profiles and in wet deposition. The gas profiles are influenced by the cloud parameterizations as the cloud amount is involved in photolysis rates. The precipitation predicted also influeces dry deposition as the deposition velocities depend on wheather a rain event took place in the last two hours. These investigations are nessecary because dynamical, hydrodynamical and thermal discrepancies may apprecibly affect changes in gasphase- and aquoeus chemistry, transport and deposition.

Acknowledgements

Computational support came from the Research Centre Jülich (KFA), in particular from ICH2 and ICH3. This work was funded by the Ministry of Research and Technology (BMFT) of Germany.

We are grateful to the KNMI who gave access to the precipitation data.

References

Anthes, R.A., E.-Y.Hsie, Y.-H.Kuo: Description of the Penn State/ NCAR Mesoscale Model Version 4 (MM4), NCAR/ TN-282+STR 1987.

Chang, J.S., R.A.Brost, I.S.A.Isaksen, S.Madronich, P.Middleton, W.R. Stockwell, C.J.Walcek: A three-dimensional Eulerian acid deposition model: physical concepts and formulation, J. Geophys. Res., 92, 14681-14700, 1987.

Cotton, W.R., M.A.Stephens, T.Nehrkorn, G.J.Tripoli: The Colorado State University Three-Dimensional Cloud/ Mesoscale Model 1982. Part II: An Ice Phase Parameterization, J.Rech. Atmos., 16 No.4, 295-320.

Hass, H., A.Ebel, H.Feldmann, H.J.Jakobs, M.Memmesheimer: Evaluation studies with a regional chemical transport model (EURAD) using air quality data from EMEP monitoring network, submitted to Atmos. Environ., 1991.

Hass, H., M.Memmesheimer, H.Geiß, H.J.Jakobs, M.Laube, A.Ebel: Simulation of the Chernobyl radioactive cloud over Europe using the EURAD-model, Atmos. Environ., 24, 673-692, 1990.

Walcek, C.J., G.R.Taylor: A theoretical method for computing vertical distributions of acidity and sulfate production within cumulus clouds, J. Atmos. Sci., 43, 339-355, 1986.

A SURFACE-BASED CLOUD OBSERVING SYSTEM

B.A. Albrecht, T.P. Ackerman, D.W. Thomson
M.A. Miller, R.M. Peters

Penn State University
University Park, Pennsylvania 16802

1. INTRODUCTION

The representation of cloud parameters in mesoscale and large-scale models as a function of the variables resolved explicitly by the models remains relatively crude and unreliable. For example, it is unclear how variables such as fractional cloudiness, cloud liquid and ice water content, and droplet or ice particle size should be related to the fields of temperature, moisture, and wind that are resolved by the models. A major obstacle to the development of improved cloud parameterizations has been our inability to observe the large and mesoscale thermodynamic and wind fields (particularly the vertical velocity) while simultaneously observing the micrometeorological or eddy scale characteristics of the cloud field. Recent technological developments in remote sensing now provide the means to overcome many of these long standing observational difficulties and, thus, enable us to improve our understanding of basic cloud processes.

To take full advantage of these developments, we have combined several remote and *in situ* sensors to form a surface-based Cloud Observing System (COS). COS facilitates measurements not only of the dynamical and thermodynamical properties of the clouds but also of their interaction with the large-scale and mesoscale environment in which they exist. The key cloud parameters defined with this system are liquid water content, cloud vertical velocity and velocity variance, and cloud base and top height. At the same time the large-scale wind and thermodynamic structure are defined using other remote sensors and data from conventional radiosondes. Surface radiation measurements are used to evaluate the effect of clouds on the surface radiation energy and momentum budgets. In this paper we describe the components of Penn State's COS and show some initial results obtained from one of the key components of the system -- a Doppler cloud radar operating at 94 GHz.

2. DESCRIPTION OF THE SYSTEM

The suite of instruments that form the Penn State COS is the result of more than a decade's work in design, construction and testing. A summary of the instrumentation that is now in operation is given in Table 1. A key component of the COS is a Doppler 94 GHz (cloud) radar. This radar follows the general design outlined by Lhermitte (1987a,b). It differs from conventional meteorological radars in that it (like the 35 GHz radars described by Pasqualucci et al. (1983) and Hobbs et al. (1985)) is capable of detecting cloud droplets and ice crystals as well as just precipitation. Its relatively small size makes it very portable. The radar is designed to resolve vertical velocities as small as 3 cm/s with a vertical resolution of less than 10 m. For a mean horizontal wind speed of 10 m/s, the 0.25^0 beam width with a 1 second averaging period translates to a horizontal resolution of approximately 10 m at a height of 1 km. The radar will be used to define the updraft and downdraft structure of stratocumulus and to define the height, depth, and internal structure of cirrus and altostratus clouds. In addition, the radar can be used to determine the fall velocity of precipitation-sized droplets. Currently, the radar is operated in a vertically-pointing mode. Cloud layers, and multiple cloud layers of varying depths have all been detected at a range of heights. Initial development and testing of the on-line Doppler signal processor has been completed.

TABLE 1 Components of Penn State's Cloud Observing System

94 GHz Doppler Radar	Vertical Velocity, Cloud Boundaries, Cloud Liquid Water
Array of Three 50 MHz (VHF) Wind Profilers	Wind Speed and Direction, Refractive Structure, Divergence
405 MHz (VHF) Wind Profiler and 905 MHz Wind Profiler	Wind Speed and Directions, Refractive
Radio Acoustic Sounding System (RASS) (for either 50, 405 & 915 MHz profilers)	Low-Level Virtual Temperature Profiles
Microwave Radiometer (20-62 GHz, 9 Freq)	Integrated liquid and vapor, temp and water vapor profiles
Infrared, narrow-beam radiometer (9.15-11.5 μm)	Cloud radiometer, cloud base temperature
Broadband infrared and solar radiometers	Downward irradiance at the surface
Two Laser Ceilometers	Cloud-base height, cloud fraction, lidar backscatter profiles
Video Cameras	Visual record of cloud and sky conditions

Three 50 MHz wind profilers located at the vertices of a triangle ~ 140 km on a side in central Pennsylvania provide winds for the definition of mesoscale kinematic variables (e.g., area averaged divergence and vertical velocities). By using the reflectivity from the zenith and off-zenith beams, these three profilers are also being used to define tropopause heights and the mesoscale variation in those heights. A fourth profiler, operating at 404 MHz, provides winds to about 8 km at a relatively higher (100 m) vertical resolution. In addition it includes an acoustic source so that it can be operated as a Radio Acoustic Sounding System (RASS, Marshall et al. 1972). The processed RASS signals are used to define the lower-tropospheric temperature profile and the boundary layer depth. A fifth profiler, operating at 915 MHz, is used for additional high resolution lower-tropospheric wind and turbulence measurements. It is also equipped for operation as a RASS. During precipitation its vertically-pointing beam provides useful estimates of the full velocity and vertical velocity variations of precipitation-sized hydrometers. Up to ten (5 Doppler and 5 monostatic acoustic sounding sodar systems can be used with COS for low-level wind and turbulence measurements.

A multi-channel (3 water, 6 temperature) dicke-switched microwave radiometer was completed in mid 1990 and has since been used for measurements in the TCM (Tropical Cyclone Movement) and FIRE (First International Satellite Cloud Climatology Program Regional Project) programs as well as in central Pennsylvania. It provides continuous measurements of integrated water vapor and cloud liquid water and coarse estimates of the vertical temperature and moisture structure. Conventional radiosondes are used to define the temperature and moisture structure through the entire troposphere and broad-band radiometers measure surface shortwave and longwave fluxes.

Two Väisälä laser ceilometers (Lonnquist 1988) are used to provide continuous (every 30 s) estimates of the cloud-base height with a vertical resolution of approximately 15 m for bases to a maximum height of about 4 km. These ceilometers also provide backscatter intensity that can be used to define boundary layer depth during clear-sky conditions. Two video cameras (one all-sky) record sky conditions and cloud-base structure and broad-band radiometers provide surface fluxes. An upward looking infrared radiometer with a bandwidth of 9.5 to 11.5 μm is used to estimate the cloud-base temperature of low clouds and the emissivity of cirrus clouds.

The ceilometer, radar, and microwave radiometer are used in combination to define cloud-base and cloud-top heights and the liquid structure of stratocumulus and fair-weather cumulus clouds. Vertical distributions of cloud liquid water will be estimated from the intensity of the backscattered radiation in combination with liquid water path estimates from the multichannel microwave radiometer.

Although the COS is designed to characterize the environment in which the clouds exist, it is recognized that single-point measurements limit this characterization. Thus, work is in progress to integrate COS observations with the Penn State/NCAR mesoscale model. This allows for a more complete description of the mesoscale environment.

3. INITIAL STUDIES

Subsets of the COS instrumentation were used for a number of initial studies. Examples are shown in Albrecht et al. 1990, and Albrecht et al. 1992). Here we show some initial results from the 94 GHz radar to illustrate how it provides a description of cloud top and cloud internal structure. A more complete description of the radar and the data processing procedures is given by Peters et. al. 1992.

Observations from the 94 GHz were made during the FIRE cirrus intensive observations made in Kansas from 10 Nov - 10 Dec 1991. During this deployment the cloud radar, microwave radiometer, ceilometer and surface radiometers, were used to define the structure of cirrus clouds and the effect of these clouds on the surface radiation budget. In addition to the study of the structure of cirrus clouds and the environment in which they exist, this deployment allowed for a critical comparison and calibration of the 94 GHz radar and the microwave radiometer. This instrumentation was operated concurrently with a 35 GHz radar and a microwave radiometer operated by NOAA's Wave Propagation Laboratory. These intercomparisons with *in situ* aircraft measurements and radiosonde measurements are being used to assess the performance of the GHz radar and the microwave radiometer.

Low-level stratus clouds were frequently observed during FIRE. An example of the cloud reflectivity from a low-level stratus deck are shown in Fig. 1. The radar returns indicate cloud top at ~2.2 km. Although the radar reflectivity indicates cloud base of approximately 1.5 km, the cloud base from the ceilometer is at 1.8 km and shows considerably less variability than the lower boundary defined by the radar. The radar returns below the ceilometer cloud base appear to be due to larger cloud particles falling from the stratus deck. We have observed many cases during FIRE and over Pennsylvania where shallow clouds produce precipitation that is not detected visibility but is detected with the radar.

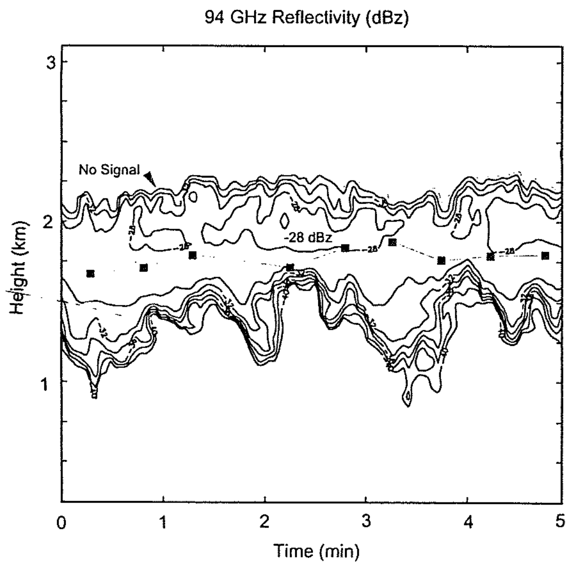

Figure 1. Reflectivity from the 94 GHz radar with cloud-base heights from the ceilometer indicated by solid data points.

Cloud top defined from the 94 GHz and cloud base from the radiometer can be used to define a cloud depth. This depth can be used to calculate an adiabatic liquid water path that can be compared with the liquid water path measured using surface-based microwave radiometers that were operated during FIRE. This basic technique was first demonstrated using data collected from San Nicolas Island during FIRE (Albrecht et al., 1988; Albrecht et al., 1990a). At San Nicolas Island a laser ceilometer, an acoustic sounder, and a microwave radiometer were operated continuously and used to estimate the adiabatic and the liquid water content of shallow stratocumulus.

Components of COS will also be deployed during the international Atlantic Stratocumulus Transition Experiment (ASTEX). During this experiment the 94 GHz Doppler radar, the microwave radiometer, ceilometers, 405 and 915 MHz wind profilers, (with RASS), and IR and visible radiometers, will be deployed on Santa Maria, a small relatively flat island in the Azores, to study boundary layer clouds and the processes that control their type and amount. Similar instrumentation systems will be operated by the Wave Propogation Laboratory and Colorado State University from a small island near Madira (Porto Santo) and from a ship. Measurements from these sites will provide a description of the cloud characteristics in different cloud regimes. The observations from the remote sensors on Santa Maria will also be compared with aircraft observations of cloud microphysical and turbulence variables. Initial results from this experiment will be presented at the meeting.

4. CONCLUSIONS

The measurements from the Cloud Observing System that we are developing, when suitably averaged and combined, will provide a description of the vertical structure of the atmosphere that is analogous to that modeled at an individual grid point in a numerical model. Consequently, the COS offers a unique opportunity to study the interaction of clouds with the large-scale environment in a way that can be translated into state-of-the-art parameterizations. This represents a unique and efficient approach to increasing our understanding of cloud processes and an effective demonstration of how recent technological advances in atmospheric observing systems can be used to improve atmospheric simulations. This approach is very similar to that defined for the Atmospheric Radiation Measurements (ARM) program of DOE.

5. ACKNOWLEDGMENTS

This research was sponsored by the Office of Naval Research (Grant N00014-18-K-0688) NASA (Grant NAG-1-1095), and DOE (Grant DE-F602-90ER61071).

6. REFERENCES

Albrecht, B.A., D.A. Randall, S. Nicholls, 1988: Observations of marine stratocumulus clouds during FIRE. Bull. Amer. Meteor. Soc., 69, 618-626.

Albrecht, B.A., C.W. Fairall, D.W. Thomson, A.B. White, J.B. Snider, and W.H. Schubert, 1990a: Surface-based remote sensing of the observed and adiabatic liquid water content of stratocumulus clouds. Geophys. Res. Letters, 17, 89-92.

Albrecht, B. A., M.A. Miler, and R.M. Peters, 1990b: The development of a surface-based system for observing boundary layer clouds. Preprint, 9th Symposium on Turbulence and Diffusion, AMS April 30-May 3, 1990. Roskilde, Denmark, 70-73.

Albrecht, B.A., T.P. Ackerman, D.W. Thomson, R.M. Peters, M.A. Miller, G.M. Mace, 1992: The development of a surface-based cloud observing system. Bull Am. Meteor. Soc (submitted)

Hobbs, P.V., N.T. Funk, R.R. Weiss, J.D. Locatelli, and K.R. Biswas, 1985: Evaluation of 35-GHz radar for cloud physics research. J. Atmos. Oceanic Technol., 2, 35-48.

Lhermitte, R., 1987a: A 94 GHz Doppler radar for cloud observations. J. Atmos. Oceanic Technol., 4, 36-48.

Lhermitte, R., 1987b: Small cumuli observed with a 3 mm wavelength Doppler radar. Geophys. Res. Letters, 14, 707-710.

Lonnquist, J., 1988: Laser ceilometers gain wide acceptance. Väisälä News, 115-116, 9-13.

Pasqualucci, F., B.W. Bartram, R.A. Kropfli, and W.R. Moninger, 1983: A millimeter-wavelength dual-polarization Doppler radar. J. Climate Appl. Meteor., 22, 758-765.

Peters, R.M. B.A. Albrecht, M.A. Miller and J. Thomas Treaster, 1992: Automated cloud profiling with a 94 GHz radar. Preprints, 11th International Conference on Clouds and Precipitation, Montreal, Quebec, Aug 17-21, 1992.

THE BACKINTEGRATING NEPHELOMETER: AN INSTRUMENT FOR THE MICROPHYSICS OF CLOUD ALBEDO

C. Rivera-Carpio and T. Novakov

Energy and Environmental Division, Lawrence Berkeley Laboratory, Berkeley, CA 94720

1 INTRODUCTION

Current cloud data relevant to radiation studies in general and to cloud albedo studies in particular pertain to two general types of information: radiometric and microphysical. However, data on volume scattering properties of clouds, which are essential to radiation-transfer studies, are essentially non-existent. Such data is needed to test the reliability of single-scattering procedures that use cloud microphysical data, the applicability of approximate radiative-transfer formulations, and to assist in establishing relationships between local radiative fluxes and local and column cloud parameters.

It is thus desirable to measure volume scattering properties of clouds. A volume scattering parameter important in the interaction of solar radiation and clouds is the backhemispheric scattering coefficient σ_{bs}, defined as

$$\sigma_{bs} = \bar{b}\sigma_s ,$$

where $\bar{b}$ is the backscattering fraction for an elemental volume, and σ_s is the scattering coefficient. For optically thin clouds, σ_{bs} is related to the cloud albedo for zenith solar radiation A through the relation (Coakley and Chylek, 1975)

$$A = \bar{\omega}\bar{b}\tau = \sigma_{bs}L ,$$

where $\bar{\omega} = \sigma_s/\sigma_e$ is the volume single-scattering albedo; σ_e, the extinction coefficient; $\tau = \sigma_e L$, the optical thickness; and L, the geometric cloud thickness.

In the absence of direct in-situ measurements, it is necessary to estimate σ_{bs} from Mie theory, using measured drop concentration and size distribution data. However, σ_{bs} can be directly measured in situ by an integrating nephelometer modified for in-cloud use. Novakov et al. (1991) has recently described the instrument and presented some measurement results. The purpose of this paper is to characterize the response and angular truncation measurement error of the instrument, document the truncation measurement error for cloud water droplets, present recent measurement results, and compare those with values calculated from Mie theory using independently measured drop concentration and size distribution.

2 RESPONSE AND ANGULAR TRUNCATION MEASUREMENT ERROR

2.1 RESPONSE

Light scattered toward the photomultiplier is light being scattered through angles varying from θ_1=90° to θ_2=180°$-\Delta\theta^{tr}$, where $\Delta\theta^{tr}$ is the angular extent of truncation of the instrument. Following the argument of Beuttell and Brewer (1949), where the diffused light intensity from the opal glass is assumed to be proportional to the cosine of the angle between the direction of the light and the normal to the glass, it can be shown that the response of the instrument when $\Delta\theta^{tr} = 0$, omitting a constant factor, is equal to the broadband optical backhemispheric scattering coefficient $\bar{\sigma}_{bs}$,

$$\bar{\sigma}_{bs} = \int S_\lambda \bar{\sigma}_{bs,\lambda} d\lambda , \quad (1)$$

where

$$\bar{\sigma}_{bs,\lambda} = \bar{\sigma}_{s,\lambda}\frac{1}{2}\int_{90°}^{180°} \bar{p}_\lambda(\theta)\sin\theta d\theta . \quad (2)$$

In equation (1), S_λ represents the spectral response function of the instrument ($\int S_\lambda \delta\lambda=1$) whereas $\bar{p}_\lambda(\theta)$ in equation (2) is the volume scattering phase function ($1/2 \int_{0°}^{180°} \bar{p}_\lambda(\theta)\sin\theta d\theta=1$).

2.2 ANGULAR TRUNCATION MEASUREMENT ERROR

In practice the construction of the instrument prevents light to be scattered into the backward directions, *i.e.* $\Delta\theta^{tr} \neq 0°$ ($\Delta\theta^{tr} = 10°$ for the LBL version). Therefore, the instrument measures a *truncated* broadband backhemispheric coefficient $\bar{\sigma}^{tr}_{bs}$,

$$\bar{\sigma}^{tr}_{bs} = \int S_\lambda \bar{\sigma}^{tr}_{bs,\lambda} d\lambda , \quad (3)$$

where

$$\bar{\sigma}^{tr}_{bs,\lambda} = \bar{\sigma}_{s,\lambda}\frac{1}{2}\int_{90°}^{180°-\Delta\theta^{tr}} \bar{p}_\lambda(\theta)\sin\theta d\theta . \quad (4)$$

Thus, the truncation measurement error function $\overline{\overline{TE}}$ is

$$\overline{\overline{TE}} \equiv \frac{\bar{\sigma}_{bs}-\bar{\sigma}^{tr}_{bs}}{\bar{\sigma}_{bs}} = \frac{\int S_\lambda \bar{\sigma}_{bs,\lambda}\overline{TE}_\lambda d\lambda}{\int S_\lambda \bar{\sigma}_{bs,\lambda} d\lambda} , \quad (5)$$

where $\overline{TE}_\lambda$, the spectral truncation measurement error, is

$$\overline{TE}_\lambda \equiv \frac{\bar{\sigma}_{bs,\lambda}-\bar{\sigma}^{tr}_{bs,\lambda}}{\bar{\sigma}_{bs,\lambda}} = = \frac{\int_{180°-\Delta\theta^{tr}}^{180°} \bar{p}_\lambda(\theta)\sin\theta d\theta}{\int_{90°}^{180°} \bar{p}_\lambda(\theta)\sin\theta d\theta} . \quad (6)$$

The parameter $\overline{TE}$ is an spectrally-weighted average of $\overline{TE}_\lambda$, which depends on the instrument's angular extent of truncation and on the volume scattering phase function $\bar{p}_\lambda$.

3 ANGULAR TRUNCATION MEASUREMENT ERROR FOR WATER DROPLETS

The magnitude of the angular truncation measurement error depends on the light scattering characteristics of the medium in addition to the extent of angular truncation of the instrument. For the LBL nephelometer version, $\Delta\theta^{tr} = 10°$.

Measurements show that the light scattering phase function of water clouds depend primarily on two main characteristics of the drop size distribution, *i.e.* on the average and spread of the size distribution (see, e.g., Hansen, 1971). Because cloud droplets scatter an amount of light proportional to the square of the radius, it is logical to use the following size distribution parameters. As a measure of average droplet size, the *mean effective radius* defined as

$$\bar{r}_{eff} = \frac{\int r\pi r^2 n(r)dr}{\int \pi r^2 n(r)dr} . \quad (7)$$

And as a measure of droplet size spread, the corresponding *effective variance* defined as

$$\bar{v}_{eff} = \frac{\int (r-\bar{r}_{eff})^2 \pi r^2 n(r)dr}{\bar{r}^2_{eff}\int \pi r^2 n(r)dr} , \quad (8)$$

where $\bar{r}^2_{eff}$ in the denominator makes $\bar{v}_{eff}$ dimensionless. Following Hansen (1971), cloud drop size distributions are modeled using the two-parameter gamma density function

$$n(r) = Cr^{(1-3b)/b}\exp(-r/ab) , \quad (9)$$

which has the property that

$$a = \bar{r}_{eff} \quad , \qquad b = \bar{v}_{eff} \ , \quad (10)$$

i.e. the two parameters in the density function are equal to the physical quantities that characterize the scattering by a size distribution. In equation (9), C is a constant; knowledge of this constant is not required in order to determine $\bar{p}_\lambda(\theta)$.

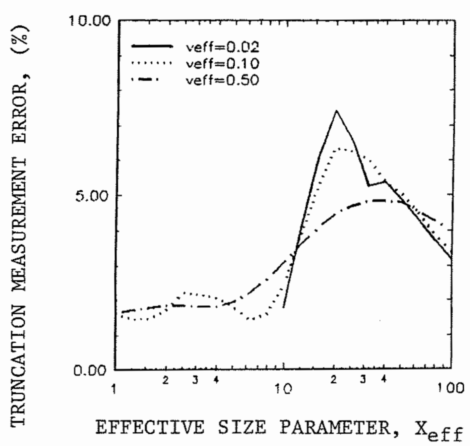

Figure 1 Angular truncation measurement error for water droplets as a function of the effective size parameter for three values of effective size spread; $\Delta\theta^{tr} = 10°$ and m = 1.33.

Figure 1 shows the angular truncation measurement error $\overline{TE}_\lambda$ as a function of the effective size parameter for several values of size spread. These plots illustrate the sensitivity of the measurement error to cloud size spectra characteristics; the measurement error varies between 1.5 to 7.5 percent in a oscillatory fashion. The effect of increasing the size spread is to reduce the magnitude of such variations. Because typical values of effective size parameters for atmospheric water clouds are above 40 (corresponding to $r_{eff} > 5\mu m$ and $\lambda < 0.7\mu m$), these results show that for $\Delta\theta^{tr} = 10.0°$ the measurement error associated with water cloud observations is typically below 5 percent, irregardless of the width of the drop size spectra.

In order to determine the effective truncation measurement error $\overline{TE}$, results for $\overline{TE}_\lambda$ are to be integrated over wavelength using the spectral response function of the instrument, taking into account the wavelength dependence of the backhemispheric scattering coefficient (see equation (5)). However, an upper bound for $\overline{TE}$ can be easily obtained from results for $\overline{TE}_\lambda$. Consider for example an instrument with $\Delta\theta^{tr} = 10°$ and a bandwidth of spectral response between 0.4 µm and 0.7 µm which is used to measure water clouds with $\bar{r}_{eff} > 6.5\mu m$. The lower bound for values of $\bar{x}_{eff}$ here involved is 58 and therefore, from Fig. 1, $\overline{TE}$ <4.7%.

4 REAL-TIME COMPARISON AGAINST MIE ESTIMATES

The nephelometer and a drop size spectrometer (CSASP-100-HV, Particle Measurement Systems, Boulder, Colorado) were installed on a 2.5-m high platform on El Yunque peak (elevation 1067 m, 18°19' N, 65°45' W), located at the easternmost side of Puerto Rico. The horizontal distance between the nephelometer and the spectrometer was approximately 1.0 m. El Yunque is exposed to trade winds generally from the east or northeast and is frequently in clouds. The instruments were operated during a two-week period in July 1991. The CSASP was operated alternatively in either of the two size ranges, 1-16 µm and 2-32 µm. The nephelometer and the drop spectrometer were operated at a time resolution of 10 sec.

An example of the nephelometer computer stored data obtained during a 1-hour timer period on July 19.1991 is shown in Fig. 2. In this figure the variations of the measured backscattering coefficient σ_{bs} (in percentage) are shown as a function of local time. During this measuring period, the air temperature was approximately constant at 22°C. The wind direction was from the northeast, with steady wind speed of about 2 m sec^{-1}.

The variations of the nephelometer response seen in Fig. 2 reflect the horizontal inhomogeneities along the cloud traverse path, which for a 10-sec nephelometer time resolution corresponds to about 20 m. We note that the 10-sec variations in the nephelometer signal did closely track the 10-sec variations in the cloud drop concentrations, indicating that the cloud density at the CSASP intake was essentially the same as in the nephelometer scattering volume.

The cloud drop number concentrations and size distributions obtained from CSASP measurements using the factory calibration were used to calculate the variations in σ_{bs} values. The calculations were for the wavelength of 0.55 μm, which corresponds to the wavelength of maximum photomultiplier response. The Mie-theory-based calculated σ_{bs} values were obtained from the relation:

$$\sigma_{bs}^{(est)} \sim \sum_i b(r_i/\lambda, m) Q_s(r_i/\lambda, m) \pi r_i^2 \Delta n_i \Delta r_i ,$$

where b is the backscattering fraction for a drop with radius r_i and index of refraction m, Q_s the scattering efficiency, λ the radiation wavelength, and Δn_i the drop number density for the radius interval from $r_i - \Delta r_i/2$ to $r_i + \Delta r_i/2$. For simplicity we use the backscattering fraction b, i.e. the proportion of the scattered radiation that goes into the entire backward hemisphere, as an approximation to the nephelometer backscattering fraction, which is lower because of the angular truncation.

Calculated and measured variations in σ_{bs} are found to be in very good agreement. The examples described above demonstrate the feasibility, simplicity, and reliability of direct measurement of optical backhemispheric scattering coefficients of clouds with a backintegrating nephelometer.

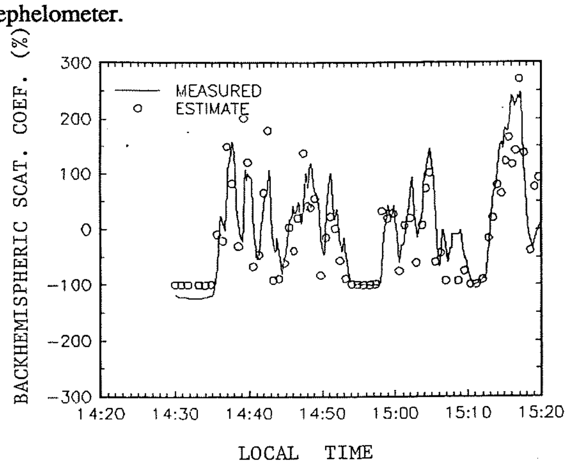

Figure 2 Real-time comparison of nephelometer response against mie-estimates using cloud microphysical data. Backhemispheric scattering coefficients are expressed as a percentage of the corresponding average for the time period of comparison.

5 ACKNOWLEDGMENT

This work was supported by the Director, Office of Energy Research, Office of Health and Environmental Research, Environmental Sciences Division of the U.S. Department of Energy under contract no. DE-AC03-76SF00098.

6 REFERENCES

Beuttell, R.G. and A.W. Brewer, 1949: Instruments for the measurement of the visual range. *J. Sci. Instrum.*, **26**, 357-359.

Coakley, J.A., Jr., and P. Chylek, 1974: The two-stream approximation in radiative transfer: Including the angle of the incident radiation. *J. Atmos. Sci.*, **32**, 409-418.

Hansen, J.E., 1971: Multiple scattering of Polarized Light in Planetary Atmospheres. Part II. Sunlight reflected by terrestrial water clouds. *J. Atmos. Sci.*, **28**, 1400-1426.

Novakov, T., C. Rivera-Carpio, and R.C. Schmidt, 1991: Measurement of cloud integrated backscattering coefficient with a nephelometer. *Geophys. Res. Lett.*, **18**, 1453-1456.

NEW MICROPHYSICS SENSOR FOR AIRCRAFT USE

H. Gerber

Gerber Scientific Inc., 1643 Bentana Way, Reston, VA 22090 USA

1. INTRODUCTION

The following describes a new optical aircraft sensor, Model PVM-100A, for cloud microphysical measurements. This sensor is based on a redesign of the PVM-100 (Gerber, 1991), an optical sensor used for ground-based measurements of integrated particle volume concentration (termed LWC for clouds). The aircraft sensor differs in its aerodynamic shape, and in the addition of two other channels. One of the channels gives the integrated particle surface area concentration (SAC), which combined with LWC gives the "effective droplet diameter" important in radiation/climate modeling (Slingo, 1989). The second channel determines the presence of the ice phase from depolarization effects.

The PVM-100A has a relatively large sensitive volume (1.25 cm^3), and makes in-situ and real-time measurements independent of air speed. These features permit use of the sensor on high-speed research aircraft, provide spatial resolution of microphysics over distances as small as cm, and give results for small hydrometeor concentrations, including ice crystals.

2. PRINCIPLE OF OPERATION

The measurement of LWC and SAC with the PVM-100A is based on earlier findings that light diffracted out of a light beam into the forward direction by larger particles can be weighted as a function of scattering angle to obtain proportionalities with different moments of the particles' size spectrum, such SAC and LWC [e.g., see Hodkinson, 1966; Wertheimer and Wilcock, 1976; Blyth et al., 1984; Gerber, 1984]. More than half a dozen instruments based on this concept have been built by various groups.

The depolarization of the backscattered light of the linearly polarized laser beam in the PVM-100A is a sensitive indicator of the presence of the ice phase, given that water droplets do not cause depolarization unless multiple scattering is important (Sassen and Liou, 1979; Sassen, 1991).

It may also be possible to use the measure of the depolarized backscatter to estimate the total area and volume fractions in a mixed phase cloud. This is done by relating the relatively constant value of the linear depolarization ratio of ice clouds to measurements of SAC and LWC.

3. INSTRUMENTATION

The PVM-100A consists of a probe (Fig. 1) exposed to the airflow outside the aircraft, and an electronic box placed inside. The optical axis of the probe is parallel to its long dimension, and its

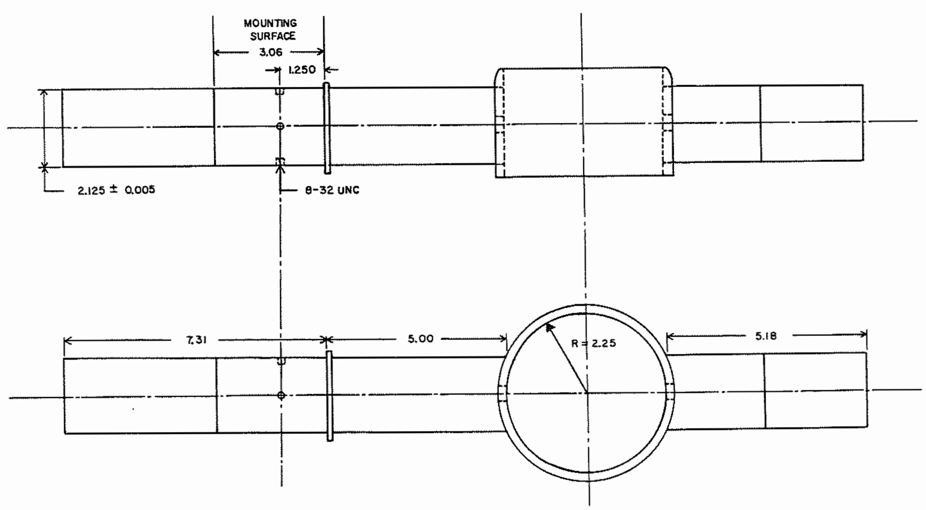

Fig. 1 - Probe of PVM-100A. Top view (upper), front view (lower). Dimensions in inches.

annulus, which contains the scattering volume, faces into the wind direction during use. The probe weighs 3.6 lbs.

The optics of the probe consist of a laser diode light source, collimating optics, and beamsplitter for dividing the scattered light into two components which are weighted to yield SAC and LWC outputs. The weighting is done with spatial filters as described previously (Gerber, 1991). A third detector located in the probes's annulus, and in the plane of polarization of the laser, measures the depolarized backscatter over an angular range of 140 to 170 deg.

The electronics consist of three syncronous detection circuits that output analog voltages proportional to the desired quantities. The reponse of the electronics permit a measurement rate of 0 to 5000 Hz. Calibration consists of an internal light diffusing disk that can be activated with Logic 1.

The leading edge of the probe's annulus contains 140 Watt heaters for icing protection. Additional heaters are used to protect the optics from condensation.

LWC is measured over a range of 0.001 - 10 g/m^3; SAC is measured over 5 - 5000 cm^2/m^3; and the range for the depolarization measurement is yet to be determined.

4. CALIBRATION AT ECN

The PVM-100A was calibrated in the low-speed cloud/wind tunnel at ECN (Netherlands Energy Research Foundation) by comparing its output to gravimetric filter measurements of LWC for various cloud densities and droplet spectra. Co-located FSSP-100 measurements were also made. A schematic of the ECN facility is shown in Fig. 2. Its ability to measure LWC in warm clouds with the filter method over a wide range with an accuracy of better than 10% depends on precisely setting RH to 100% in the cloud to avoid growth or evaporation of droplets in the filters. This is achieved by thermally servoing humidifier temperature to cloud temperature; and by collecting droplets isokinetically in prewetted hydrophobic filters.

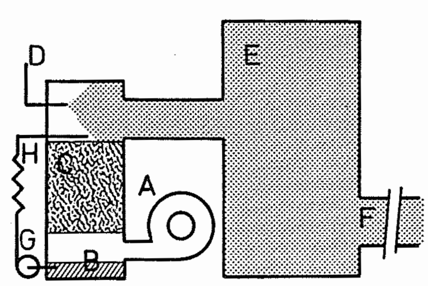

Fig. 2 - Schematic of cloud/wind tunnel at ECN. A (blower), B(water resevoir), C(humidifier), D(fog generator), E(mixing chamber), F(tunnel, 5m), G(water pump), H(heater) [from Mallant (1988)]

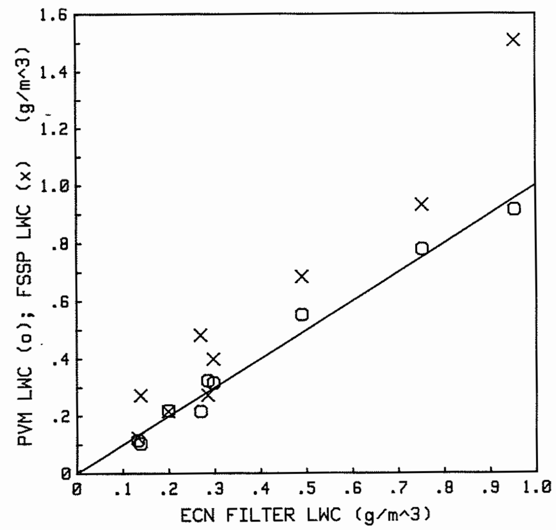

Fig. 3 - Comparison of LWC measurements in ECN cloud chamber with filter method, PVM-100A (o), and FSSP-100 (x).

Figure 3 compares ECN filter, FSSP-100, and PVM-100A LWC measurements for atomizer droplet spectra with mmd ranging from 10.2 um to 30.1 um. The approximately linear relationship between PVM-100A and filter measurements shows that the PVM-100A has the required independence of droplet size over this range of mmd, and the linear relationship can be used to determine the scaling factor for field measurements of LWC with the PVM-100A. LWC values determined by integrating the droplet spectra measured with the FSSP-100 show less of a linear relationship with the filter results, and are as much as 90% larger. For large droplets generated with a paint sprayer (with an unknown number of drops larger than the 95-um limit of largest bin in FSSP-100, and an unknown mmd greater than 40 um), the PVM-100A underestimates LWC, and the FSSP-100 overestimates LWC as compared to the filter measurements.

The SAC channel in the PVM-100A was calibrated using the FSSP-100 integrated droplet surface area data corrected by referencing the FSSP-100 LWC data to the filter LWC:

$$\underset{\text{(corrected)}}{\text{FSSP(AREA)}} = \underset{\text{(measured)}}{\text{FSSP(AREA)}} \times \left(\frac{\text{FSSP(LWC)}}{\text{FILTER(LWC)}}\right)^{-2/3}$$

This approach assumes that correcting for the various possible error sources in the FSSP-measured droplet spectra (see Baumgardner and Spowart, 1990), is equivalent to adjusting the droplet number density uniformly across the spectra. For the present experiment this approach works reasonably well as shown in Fig. 4, where PVM-100A and corrected FSSP-100 total surface areas are compared. The standard deviation of the variability about a linear relationship in Fig. 4 is larger by a factor of about 2 when using uncorrected FSSP-100 data. The linear relationship in Fig. 4 is used to determine the scaling constant for the SAC channel.

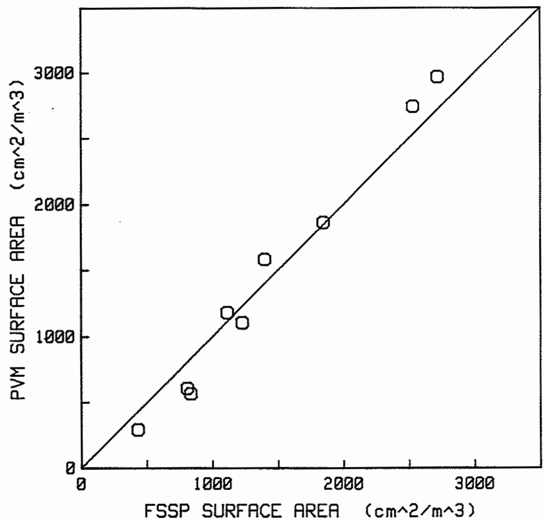

Fig. 4 - Comparison of total droplet area concentration (SAC) measured with PVM-100A and FSSP-100.

5. CONCLUSIONS AND ADDITIONAL EVALUATIONS

The calibration at ECN has shown that the PVM-100A is capable of LWC measurements within an accuracy of about 10% for droplet mmd from 10 um to 30 um in warm clouds. The calibration of the SAC channel is probably less accurate, because it depends in part on the unknown accuracy of the method for correcting the FSSP-100 data.

Additional evaluation of the PVM-100A will consist of placing the instrument in a high-speed icing tunnel where aircraft environmental conditions with repect to temperature extremes and LWC contents can be simulated. Measurements from aircraft are also scheduled.

ACKNOWLEDGEMENTS

Gabor Vali of U. of Wyoming is thanked for his important contribution to the design of the aircraft sensor. Beate Arends and Gerard Cos of ECN for the excellent calibration work, and NSF for partial support of this work under ATM-9207345.

REFERENCES

Baumgardner, D., and M. Spowart, 1990: Evaluation of the forward spectrometer probe. Part III: Time response and laser inhomogeinity limitations. J. Atmos. Oceanic Technol., 7, 666-672.

Blyth, A.M., A.M.I. Chittenden and J. Latham, 1984: An optical device for the measurement of liquid water content in clouds. Q.J.R. Meterol. Soc., 110, 53-63.

Gerber, H., 1984: Liquid water content of fogs and hazes from visible light scattering. J. Climate and Appl. Meteorol., 23, 12-7-1252.

Gerber, H., 1991: Direct measurement of suspended particulate volume concentration and far-infrared extinction coefficient with a laser-diffraction instrument. Appl. Opt., 30, 4824-4831.

Hodkinson, J.R., 1966: "The optical measurement of aerosol" in Aerosol Science, C.N. Davies, Ed., Academic Press, New York.

Mallant, R.K.A.M., 1988: "A fog chamber and wind tunnel facility for calibration of cloud water collectors" in Acid Deposition at High Elevation Sites, M.H. Unsworth and D. Fowler Eds., Kluwer Academic Publishers, The Netherlands.

Sassen, K., 1991: The polarization lidar technique for cloud research: A review and current assessment. Bul. Amer. Meteorol. Soc., 72, 1848-1866.

Sassen, K. and K.-N. Liou, 1979: Scattering of polarized laser light by water droplet, mixed-phase and ice crystal clouds. Part II: Angular depolarization and multiple-scattering behavior. J. Atmos. Sci., 36, 852-861.

Slingo, A., 1989: A GCM parameterization for the shortwave radiative properties of water clouds. J. Atmos. Sci., 46, 1419-1427.

SPECTRAL IMAGING OF CLOUDS USING A DIGITAL ARRAY SCANNED INTERFEROMETER

Philip D Hammer[1], Francisco P J Valero[1], and Wm Hayden Smith[2]

[1]Earth System Science Div., NASA Ames Research Center, Moffett Field, CA 94035
[2]Earth & Planetary Sciences Dept., Washington University, St. Louis, MO 63130

1. INTRODUCTION

Efforts to measure and understand the complex spatial and spectral characteristics of clouds have led to the use of increasingly sophisticated imaging spectrometers. The deployment of the Airborne Visible/Infrared Imaging Spectrometer (AVIRIS) for the remote sensing of cirrus clouds over the wavelengths of 0.4 to 2.5 μm during the most recent FIRE experiment is a case in point.

We are presently developing and validating a new instrument concept, the digital array scanned interferometer (DASI), for Earth remote sensing in the context of global climate change. DASIs have many of the positive characteristics associated with Fourier transform spectrometers and also the capability for spatial imaging. Thus a DASI has the potential of achieving higher spectral and spatial resolution at a specified signal-to-noise level than equivalent aperture grating based instruments such as AVIRIS. Perhaps one of the most notable features of DASIs is their ability to acquire an entire interferogram simultaneously without any moving optical elements. The simplicity of design and operation of DASIs make them particularly suitable candidates for ground and airborne platform based remote sensing instruments.

2. INSTRUMENTAL CONCEPT

The principle of DASI operation is similar to that of scanned interferometers. Detected signals result from two-beam interference. The wavelength spectrum of the incident radiation is obtained by Fourier transforming this recorded interferogram. Unlike a conventional interferometer, the DASI operates with its mirrors fixed in position. The range of path differences between the recombined beams is achieved by means of the configuration of the optical components so that stationary fringes of equal inclination are formed at the image plane. This comprises an interferogram which can be resolved spatially by a detector array. The orthogonal dimension of the image plane is available for spatial imaging. Figure 1 shows a DASI configuration based on a birefringent interferometer to obtain a variable range of path differences across the detector (Okamoto et al., 1986).

The advantages of DASIs may best be understood by comparison with other commonly used spectrometers and interferometers. In general, Fourier transform spectrometers, which include DASIs, have several advantages over grating spectrometers (Connes, 1970), among which are the

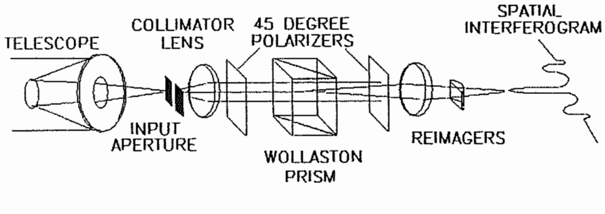

Fig. 1. DASI based on a birefringent interferometer.

following: 1) The throughput or etendue advantage of interferometers over grating instruments is a well known characteristic (Jacquinot, 1960). The enhanced signal-to-noise ratio resulting from the throughput advantage is one of the primary reasons that interferometers are the preferred spectrometer for high resolution infrared spectroscopy. For a given angular field of view and spectral resolution interferometers can pass typically 1 to 2 orders of magnitude more light. 2) Interferometers have a nearly constant efficiency over a very broad spectral range in contrast to the variable efficiency of grating instruments caused by a decrease in the diffracted intensity away from the grating blaze.

DASIs also possess certain advantages over conventional Michelson interferometers, as described by Smith and Schempp (1991) and others cited above (Caulfield, 1976). These advantages include:

1) Simplicity of design and operation - The design and construction of the instrument is greatly simplified since no precision dynamic movement mechanism is needed. Interferograms are acquired with stationary optics. Hence, DASIs are suitable for stable operation over long unattended periods. Compactness, low weight, and low power requirements also stem from these advantages;

2) Capability of observing transient events - the entire interferogram is measured simultaneously. This improves the signal-to-noise ratio and spectral fidelity since there is no distortion of the interferogram due to temporal fluctuations during the observation;

3) Spatial imaging with array detectors - The DASI utilizes the redundant coordinate at the image plane, which is analogous to the coordinate along the length of the slit in a grating spectrometer, for imaging of the field-of-view in one dimension;

4) Enhanced throughput potential - Some DASI optical configurations are field-widened, thus eliminating the aperture size constraint of Michelson interferometers altogether (Smith and Schempp, 1991). In practice the maximum aperture size will likely be constrained by spatial rather than spectral resolution requirements.

Imaging spectrometers currently available such as AVIRIS (Vane, 1987) generally use grating dispersion to obtain spectra. AVIRIS has over 200 contiguous spectral elements from 0.4 to 2.4 μm, with a typical sampling interval of less than 10 nm (100 cm^{-1} at 1 μm). In principle, a DASI can exceed this spectral range and resolution by using a suitable detector array, and achieve enhanced signal-to-noise by virtue of the interferometer throughput advantage described above.

3. POTENTIAL SCIENCE YIELDS

Below we consider the potential applications of DASI instruments to the determination of cloud microphysical properties, which would be within the framework of project FIRE (First ISCCP (International satellite cloud climatology project) Regional Experiment) (Cox, 1987; Starr, 1987). A relatively low spectral resolution (e.g. > 100 cm^{-1}) is adequate since one is observing radiative interactions with solid or liquid phase matter.

Spatially and spectrally resolved atmospheric radiation fields measured by a DASI instrument at visible to near infrared wavelengths (reflected light to 2.5 μm) from a suitable platform (satellite, aircraft or surface) would provide information on cloud attributes including the microphysical properties of the constituent droplets or ice crystals. Specifically, the results we would expect to obtain from analysis of DASI images would be information about particle scattering phase functions, size distributions, condensed water or ice phase presence, cloud optical depths, and macroscopic spatial variability. More generally, obtaining spatial and spectral information simultaneously over a major portion of the solar spectrum can yield substantial returns. For example, having data available over a broad wavelength range from the visible to 2.5 μm extends the range of applicability of particle attribute retrieval algorithms (Twomey, 1977). Also, it is possible in principle to obtain ice and water condensed phase information as well as particle size and optical depth information about the clouds (Pilewskie, 1990). If the instrument's field of view is fixed in space, time dependence information can be obtained as clouds move through the visual field. If the cloud retains its shape and structure, spatially resolved scattering angle information (and thus phase functions) may be obtainable. If the field of view is made to track the cloud the latter approach is a possible way to deal with inhomogeneous spatial variations: specific positions on clouds can be viewed at different angles. Finally, coordination with other measurements (satellite air and ground based) would enable intercomparison studies. A possible airborne platform configuration is shown in Fig. 2.

4. MEASUREMENTS

As part of our instrument development program we have been making ground based measurements of clouds in the wavelength range of 0.4 to 2.3 μm and at moderately low spectral resolution (> 200 cm^{-1}, or > 20 nm at 1000 nm). (Note that a Fourier transform spectrometer yields constant wavenumber spectral sampling intervals). The resulting image cubes reveal the potential science yields from obtaining simultaneous high resolution spatial and spectral information for the analysis of cloud radiative interactions and physical properties.

Two types of 2-dimensional detector arrays are being used to acquire the spectral images. A CCD array of dimensions 390 x 584 pixels covers the 0.4 - 1.0 μm region. For our preliminary measurements we have been orienting the array to obtain 390 spatial elements and 50 spectral elements, giving a nominal resolution of about 300 cm^{-1}, or 30 nm at 1 μm (we have deliberately been oversampling the interferogram; in principle, substantially higher spectral resolution is attainable with this configuration). A short wavelength MCT array of dimensions 256 x 256 pixels covers the 1.0 - 2.5 μm region. Our choice of collimating optics gives a spatial field of view of 5 degrees angular width.

Two dimensional spatial images are acquired by scanning over the field of view, line by line. The spectral information for each image pixel is obtained by Fourier transforming the interferogram associated with that pixel.

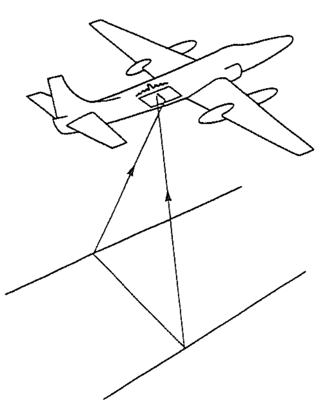

Fig. 2. Nadir viewing orientation of a DASI on an aircraft. The interferogram is recorded along the direction of platform motion. A one dimensional image is recorded in the lateral dimension. Successive time samples result in a multispectral 2-dimensional image.

5. CONCLUSION

The application of DASI imaging spectrometers to remote sensing of clouds at visible and near infrared wavelengths is very promising, based on our preliminary results. The ease of construction and operation due to the absence of actively scanning optical components provides a relatively inexpensive alternative to other interferometer designs. The compactness and flexibility of DASI optical configurations enable corresponding flexibility in the design of collection optics, choice of detectors, and interfacing of data collection systems. Specifically, the spectral and spatial resolutions and ranges we have chosen for our initial measurements as described above could be increased substantially. Some of the features of DASIs we have described are not practically attainable with currently available instruments.

6. REFERENCES

Caulfield, H. J., 1976: "Holographic Spectroscopy", in Advances in Holography, Vol. 2, N. Farhat (Ed)., Marcel Dekker, New York, pp. 139-184.

Connes, P., 1970: Astronomical Fourier Spectroscopy, *Ann. Rev. Astron.* Ap., **8**, 209-230.

Cox, S. K., D. S. McDougal, D. A. Randall, and R. A. Schiffer, 1987: FIRE - The First ISCCP Regional Experiment, *Bull. Amer. Meteo. Soc.*, **68**, 114-118.

Jacquinot, P., 1960: New Developments in Interference Spectroscopy, *Rep. Prog. Phys.*, **23**, 267-312.

Okamoto, T., S. Kawata and S. Minami, 1986: A Photodiode Array Fourier Transform Spectrometer Based on a Birefringent Interferometer, *Appl. Spectrosc.* **40**, 691.

Pilewskie, P., 1990: "Ground-based Remote Sensing of Ice Clouds", Proceedings of AMS Seventh Conference on Atmospheric Radiation, July 23-27, San Francisco, CA, 366-368.

Smith, W. H. and W. V. Schempp, 1991: Digital Array Scanned Interferometers, *Exp. Astron.* **1**, 389-405.

Starr, D. O., 1987: A Cirrus-Cloud Experiment: Intensive Field Observations Planned for FIRE, *Bull. Amer. Meteo. Soc.* **68**, 119-124.

Twomey, S., 1977: Introduction to the Mathematics of Inversion in Remote Sensing and Indirect Measurements, Developments in Geomathematics **3**, Elsevier Scientific Publishing Co., New York.

Vane, G. (Ed.), 1987: "Imaging Spectroscopy II", *Proc. SPIE*, **834**, 2-43.

An Analysis and Visualization System for Two Dimensional Cloud and Precipitation Probe Data From Instrumented Aircraft

Harry T. Ochs III[1], Robert M. Rauber[2], Jack Su[2] and Kenneth V. Beard[1,2]

[1] Illinois State Water Survey, Office of Cloud and Precipitation Research, Champaign, Illinois 61820, USA
[2] Department of Atmospheric Sciences, University of Illinois, Urbana, Illinois 61801, USA

1. INTRODUCTION

PMS probes designed to capture two dimensional images of cloud particles have been mounted on meteorological aircraft for many years. The cloud and precipitation versions of these aircraft instruments have been designed to produce images of cloud particles from large cloud drops through small hail. There have been several programs and algorithms developed for the analysis of this data. These programs have been very successful in analyzing and categorizing cloud hydrometers. They are designed to automatically reject artifacts such as streakers caused by wetting of the probe tips and for sizing and categorizing the various observed cloud particles. Successful algorithms have been developed to size liquid hydrometers in situations where the full two dimensional image is viewed by the probe as well as in situations where only a segment of the two dimensional image has been observed. Other algorithms have been developed to recognize crystal habits in cold portions of clouds. The success of these habit detection algorithms has been more limited since it is often extremely difficult to objectively deduce from a two dimensional snapshot of an ice crystal exactly what its growth habit has been. Broken crystals and aggregation also contribute to the difficulty faced by these identification techniques. In general, for most purposes, the automatic processing of 2-D cloud probe data has been very successful. There are, however, cases where the automatic processing techniques do not produce a satisfactory result. These may occur when the researcher is primarily interested in the microphysical details of cloud development. In some of these cases, the researcher may require a high degree of accuracy in the separation of erroneous streakers from large precipitation drops or in the categorization of ice crystal habit growths. In these cases, the only currently available technique is a laborious hand processing of the two dimensional images. This paper addresses this latter difficulty through the development of a combined automatic data processing system with a very efficient hand editing phase.

2. SYSTEM DESCRIPTION

The software designed to analyze PMS 2-D cloud and precipitation probe data runs under the X11 Release 4 graphical user interface. In addition, the Motif widget set is employed in this system. The system has been designed to run on a Sun work station and the graphical user interface can be displayed on any X Window terminal. The graphical user interface is not dependent on the Motif window manager.

When a new aircraft raw data set is to be analyzed, a utility reads the tape containing the raw data and creates a disk file with the data necessary for the analysis. This utility use a data file which contains information relative to the aircraft from which the raw data was obtained and the necessary specifics on how the raw data was stored. This utility also creates a housekeeping file which allows subsequent programs to readily access any portion of the raw aircraft data.

The four basic modes under which the analysis program operates are 1) automatic analysis, 2) edit analysis, 3) continue edit analysis and 4) examine analysis. The first pass through the data is made using the automatic processing mode of the program. During this pass every 2-D image is identified and typical criteria such as hollow image and image aspect ratio are used to either accept or reject the image. At the same time, each image is sized and if ice crystals are present, habit identifying algorithms are employed. In addition, a best estimate of the time at which each image was observed is computed. All of the information relative to each image is stored in a new analyzed data file.

During the edit analysis phase of the analysis process, images are displayed on the computer screen in as many strips as will fit in the X Window. During this phase and the other graphical phases of the analysis images are displayed with a thin vertical line separating them and sync words, time words and indications for ends of aircraft data records are not shown. Images are not split at the end of screen strips unless the image is too long to fit on one strip. Images that were accepted in the automatic data processing mode are displayed in blue and images that were rejected are red. The user can change accepted images to rejected images or rejected images to accepted images. Images that have been changed to rejected are displayed in orange while images that have been changed to accepted are displayed in green. The user can also change the ice crystal growth habit identified by the automatic analysis program. If the mouse cursor is placed in one of the boxes below each image and the right button is pressed this image is re drawn in the upper left corner of the X Window and the screen is re drawn from this point. This moves the screen display forward in the data. If the left mouse button were pressed the image would be re drawn in the lower right corner of the X Window and the screen is re drawn from this point backwards. This moves the screen display backwards (towards earlier time) in the data. If the edit analysis procedure is exited before the user has viewed every identified image, then the data necessary to restart the edit process is stored. The continue edit analyzed data mode of the program is then used to restart the hand editing of the data at the point where the edit analyzed data mode was terminated.

The examine analyzed data mode allows the user to peruse images which are displayed in the same format as in the edit analyzed data mode of the program. In this mode the analyzed data can not be modified. Several features are available during the examine analyzed data operation. The user can jump to any time during the aircraft flight to see images that were observed at that time. A window can be displayed that contains all of the information relevant to a selected image on the screen. A zoom feature allows any image to be enlarged in a zoomed window and the magnification selected. The display can be constrained to only showing accepted images and the images can be restricted to a range of image sizes.

Once the user is satisfied with the edited data set, additional utilities can be used to plot results such as particle spectra during selected time intervals. These utilities all access the analyzed data file.

3. CONCLUSIONS

We have created a system to significantly improve the efficiency of hand analyzing PMS 2-D aircraft data. This system provides easy and efficient visualization of the data as well as an analyzed data set from which products such as cloud particle spectra can be derived. Using a Sun SparcStation as the client (the machine running the program) the graphical interface has been displayed and used on another Sun, an HP 720 workstation, a Mac II (using Mac X), and a IBM PC clone using Microsoft Windows (800 x 600 resolution and 256 colors) and X terminal software.

Acknowledgment. This research was supported by Grant NSFATM 9020245.

A New Device To Classify Hydrometeors

G. Frank, T. Härtl and J. Tschiersch

Institut für Strahlenschutz, GSF-Forschungszentrum, W-8042 Neuherberg, Germany

1. Introduction:

Type, size (of raindrops) and morphology (of snowflakes) are important properties of hydrometeors, influencing various processes in the atmosphere. For example the below-cloud scavenging of aerosol particles by precipitation is highly affected: snow is much more effective in scavenging than rain (Tschiersch et al. [1990]); snow crystals, showing the influence of riming, seem to be most effective (Staehelin et al. [1992]); the rain drop size distribution (given as a size distribution of the rain event) also determines particle washout (Pruppacher and Klett [1989]).

To acquire the rain drop size spectrum of a rain fall there already exist different methods. Most of them are very time-consuming and the reliability of the statistic depends on the patience of the analysing person (e.g. filter method by Wiesner [1895]). Others are connected with high costs and expensive installation of the equipment. The most established instrument for the analysis of raindrop size distributions, the distrometer by Joss and Waldvogel [1967], is not transportable, because the installation of the top of the instrument has to be even with the ground.

The most direct method of measuring the size of hydrometeors is to analyse them visually, that means by looking at them and comparing them with a well-defined scale. To apply such methods automatically it is necessary to use an image processing system. The advantages of such a system are various and the most important ones are as follows:

- direct measurement of the drop sizes,
- no influence on the falling drops' behaviour,
- transportability of the outdoor system,
- possibility for more advanced work.

For these reasons an image acquiring and processing system has been developed to get pictures of falling hydrometeors and analyse them automatically. The basic aim was to get rain drop size distributions. Furthermore also more advanced analysis can be achieved as for example morphological studies or the determination of the fall velocities and their directions.

2. Characteristics of Falling Hydrometeors:

The size range of hydrometeors, which contributes substantially to the total amount of precipitation varies from 0.3 mm up to about 6.0 mm. Droplets smaller than 0.3 mm are unimportant not only for the total amount of precipitation but also for quantities derived from the rain drop size spectrum such as back scattering cross section, rain intensity and radar reflectivity. Drops larger than about 6 mm in general are unstable and break up during their fall. The velocities of the rain drops are supposed to be the aerodynamical terminal velocities, which result from gravity acceleration and the aerodynamical resistance of the drops. They range from 1.4 m/s for the small drops to 9.0 m/s for the big ones (Gunn and Kinzer [1948]).

There is a large variety in forms especially when the complete spectrum of different hydrometeors as raindrops, hailstones and snowflakes is regarded. While small rain droplets in general show a spherical form, drops of more than about 2 mm are oblate spheroids and finally snowflakes show a large number of different shapes (see Pruppacher and Klett [1989]).

3. Requirements of the System:

To be able to measure during uniform meteorological conditions the sampling time should be short (time scale: 10 minutes). For on-line measurements the processing time has to be as short as possible. This only can be achieved with an optimum in image quality before digitising. Therefore, the main effort has been made particularly in constructing the right lighting for the system.

The best picture would be a binary one containing only two colours, one for the object (raindrop) and one for the background. However, a more realistic aim is to hold the background as homogeneous as possible.

The velocities of the falling raindrops are relatively large. For example a 1.0 mm drop with the terminal velocity of about 4.0 m/s only needs 0.25 ms to cover a distance of its own size. Therefore, to avoid unsharp pictures, which are blurred by motion, it is necessary to use very short shutter times. Otherwise, if well-defined longer shutter times are used, the length of the tracks of the blurred raindrops can give information about their velocity.

Finally, the image acquiring part of the system has to be outdoor and water proof. Additionally, a compact and robust construction, which is easy to transport, is desirable.

4. Instrumentation:

In order to get images of high quality, which are easy to handle with image processing, a special lighting unit has been constructed. Its arrangement is described below.

To record the pictures, a high resolution camera system FA 85-W (water proof version) (by GRUNDIG electronics, Fürth, Germany) with a 2/3"-CCD with 582(V) x 756(H) pixels has been used. It sends out a standard interlaced video signal with 625 lines at 50 Hz (CCIR). The built-in electronic shutter allows shutter times from 1/60 s to 1/10000 s.

The computing system is a common personal computer (IBM standard with INTEL 80386 motherboard) provided with a Variable Frame Grabber Card (ITI VFG VP1400-768 KIT-C2-AT, IMAGING Technology Inc., Woburn, USA). This way a low cost solution has been found without any expensive hardware development.

During the development phase the used image processing software was OPTIMAS (BioScan Inc., USA), for further fastening of the image processing ITI VFG-VP1400-ITEX Library (IMAGING Technology Inc., Woburn, USA) is used.

5. Image Acquisition:

Figure 1 shows the arrangement of the image acquiring system.

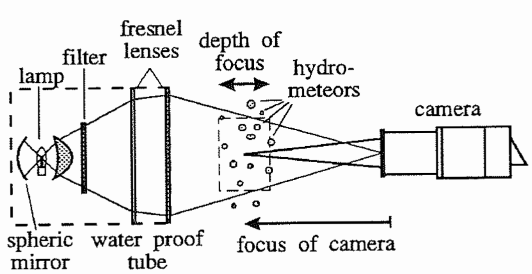

Figure 1: Arrangement of the image acquiring system

The light source is a halogen lamp. By a combination of one concave-convex condenser lens and two fresnel lenses the incandescent coil of the lamp is projected directly into the objective of the camera. By this means a homogeneous illumination without any artefacts generated by the light source is guaranteed. To protect against weathering the whole lighting unit is built in a water proof tube.

The falling hydrometeors are projected onto the light-sensitive CCD-chip in the camera. Depending on the distance from the focus of the camera objective, the drops are projected more or less sharply. It is the task of the image processing to select only droplets which are located in a determined range around the focal plane. This range may be called depth of focus.

The dimensions of the sampling volume are given by the range of sight of the camera (4 cm x 3 cm) and by the depth of focus (6 cm). It amounts to 72 cm^3.

To get sharp pictures of the falling hydrometeors in spite of their relatively high velocities the camera is operated with a shutter time of 1/10,000 s. Moreover for operation without line interlacing a 312 line modification kit is used, because each single hydrometeor only lies on one half picture of the interlaced video signal.

To determine the velocities of the drops shutter times of 1/250 s has been used with the result that one can see the drops with a track in centimetre range. From the length of these tracks one can calculate the drop speeds. Because of the decrease of contrast, which is connected with the longer shutter times, an automatic velocity determination will need the use of a complex combination of image processing filters and has not been done yet. Visual analysis, however, is laborious but possible.

6. Image Processing System:

Figure 2 shows the arrangement of the image processing system.

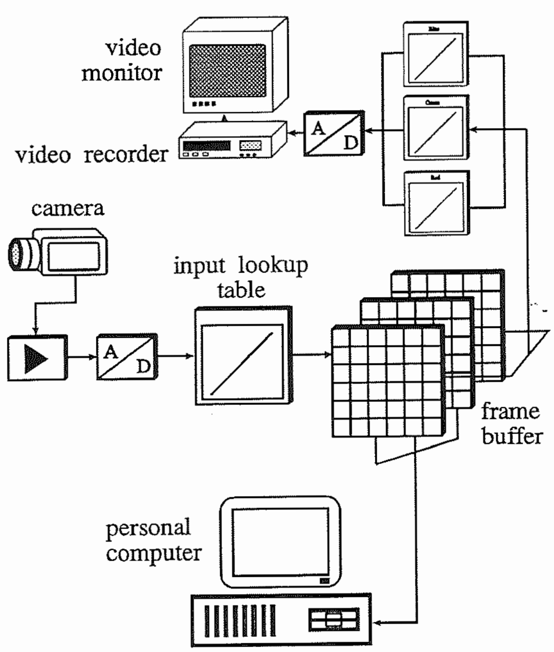

Figure 2: Arrangement of the image processing system.

After amplification and digitisation of the video signal coming from the camera and before storing it in the frame buffer the originally 256-grayscale image is converted to a binary one by means of a so called input lookup table. This tool relates the input gray values to new gray values in real time (for details of image processing methods see e.g. Jähne [1991]). An example of the resulting image is shown in figure 3.

The task of the image processing program is to recognise the objects, measure them and classify them to 59 channels. The lowest channel contains objects with diameter below 0.3 mm, the corresponding diameter range of the following channel increases by steps of 0.1 mm and the highest one is for drops larger than 6 mm.

At the moment the processing time for one image is in the range of about 1-2 seconds. To allow reliable statistics at a time resolution of some minutes during on-line measurements an acceleration of the processing is necessary. Using faster software will solve this problem.

In addition there is the possibility of interactive image processing by using a monitor. If on-line measurements are not possible due to the long image processing times, fast recording of the hydrometeors by a video recorder and afterward classification have been performed.

In the following some examples of first applications of the hydrometeor classifying instrument are given.

7. Examples:

Figure 3 shows the binarised picture of falling water drops, which are generated in the laboratory (the number concentrations in natural precipitation event is much less). The image only consists of two colours. Black drops appear in front of a white background.

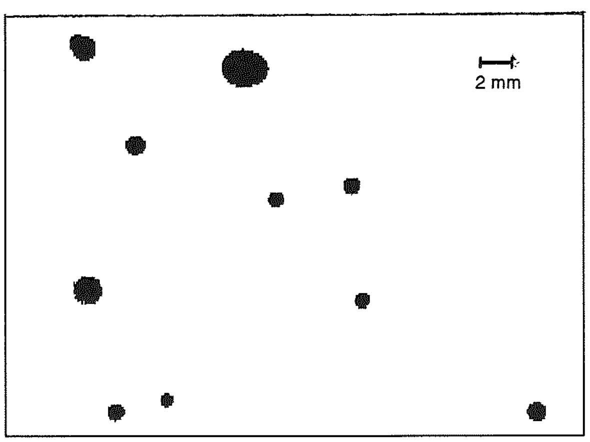

Figure 3: Falling water drops (binarised image). Height of image: 3 cm, width: 4 cm.

As another example figure 4 is showing the image of falling snowflakes. Because of the more complicated and fine structure of the snowflakes the binarisation of their pictures is more difficult. A direct binarisation of the grayscale image by means of only the input lookup table is not possible. One has to use gray morphology operations to get the whole information, which is stored in the image.

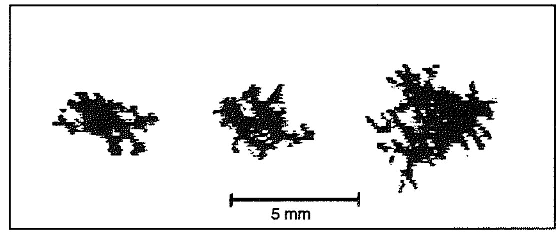

Figure 4: Images of falling snowflakes. (The bad quality of the image is caused by problem in printing grayscale pictures by a printer. The original image holds much more information.)

Figure 5 shows the rain drop size distribution of a drizzle event on 17 December 1991 at Neuherberg. The rainfall intensity was about 0.12 mm/h. The dashed line in figure 5 also shows the corresponding Marshall-Palmer distribution (Marshall and Palmer [1948]), which describes the raindrop size distribution as a negative exponential function given in equation (1).

$$N(d) = N_0 \cdot e^{-\lambda d} \qquad (1)$$

Here N(d) represents the number concentration of raindrops with diameter in an infinitesimal range between d and dd. N_0 is a constant, which for drizzle rain has the value of 30,000 m^{-3} mm^{-1} and

$$\lambda = 5.7 \cdot I^{-0.27} \text{ mm}, \qquad (2)$$

where I is the rainfall intensity in mm/h (Joss and Waldvogel [1969]).

The agreement between the measured drop size distribution and the corresponding Marshall-Palmer distribution in the size range up to 0.6 mm is satisfying.

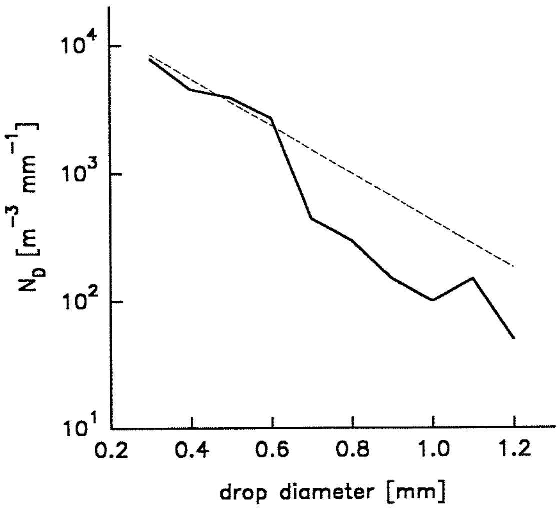

Figure 5: Rain drop size distribution of a rainfall event on 17 December 1991 at Neuherberg.

8. Future Developments:

An instrument to classify hydrometeors under field conditions has been developed. First measurements have shown useful results. Aiming to get an instrument, which is able to do sampling and analysis on-line, the processing speed has to be increased. An extensive calibration, procedure of the system is in progress as well as an intercomparison with other raindrop spectrometers. In the future an automatic snowflake characterisation will be developed.

9. References:

Gunn, R., Kinzer, G.O. [1948]: The Terminal Velocity of Fall for Water Droplets in Stagnant Air. Journal of Meteorology, Vol. 6, 243-248.

Jähne, B., [1991]: Digital Image Processing. Springer. Berlin.

Joss, J., Waldvogel, A. [1967]: Ein Spektrograph für Niederschlagtropfen mit automatischer Auswertung. Pure Applied Geophysics, Vol. 68. 240-246.

Joss, J., Waldvogel, A. [1969]: Raindrop Size Distribution and Sampling Size Errors. Journal of the Atmospheric Sciences, Vol. 26, 566-569.

Marshall, J.S., Palmer, W.McK. [1948]: The Distribution of Raindrops with Size. Journal of Meteorology, Vol. 5, 165-166.

Pruppacher, H.R., Klett J.D. [1989]: Microphysics of Clouds and Precipitation. D. Reidel Publishing Company, Dordrecht.

Staehelin, J., Collett Jr., J., Dixon, R., Henrich, W., Hsu, C., Oberholzer, B., Mosimann, L., Waldvogel, A. [1992]: Investigations of Physical and Chemical Processes Contributing to Winter Precipitation Chemistry Using Field Measurements from the Mount Rigi (Switzerland). in: Proc. EUROTRAC Symp. Garmisch-Partenkirchen, March 23-27th, 1992.

Tschiersch, J., Hietel, B., Schramel, P., Trautner, F. [1990]: Wet Deposition of Aerosol by Rain and Snow. in: AEROSOLS, Science, Industry, Health and Environment, S. Masuda and K. Takahashi, Eds., Vol. 2. 1033-1036. Pergamon Press, Oxford.

Wiesner, J., [1895]: Beiträge zur Kenntnis des tropischen Regens. Sitzungsbericht Akad. Wiss. math.-naturw. Kl., Wien, p. 1897.

Acknowledgements:

This study was partially supported by the CEC under contract no. BI 7-0010.

CLOUD DETECTION BY NOAA WIND PROFILERS

D. C. Law,* P. J. Neiman,** L. S. Fedor,** D. W. van de Kamp*

NOAA/ERL
Boulder, Colorado, USA 80303

1. INTRODUCTION

The National Oceanic and Atmospheric Administration (NOAA) has completed the installation of the 31 profilers in the Wind Profiler Demonstration Network. Previous work (Law, 1991a) showed that returns from precipitation nearly always dominate clear-air returns for the 404.37 MHz (74 cm) NOAA network profilers. Analysis of data from a synoptic-scale trough passage from the four profilers labeled in Fig. 1 illustrates that profiler returns are often due to scattering from hydrometeors in clouds.

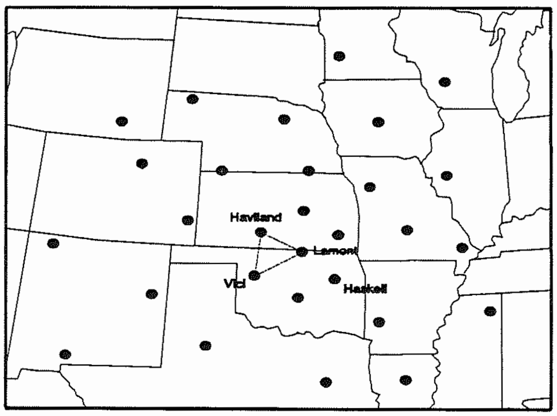

Fig. 1 NOAA wind profiler network.

2. SYNOPTIC OVERVIEW

On 6 December 1990, a northeast-southwest-oriented synoptic-scale (≈2000 km) trough that contained an upper-tropospheric jet stream structure moved southeastward across the Rocky Mountains and Great Plains of the United States. A 300 mb isotach and height analysis at 1200 UTC (Fig. 2) shows the primary jet streak (>60 m s^{-1} centered on Wisconsin) embedded within nearly straight southwesterly flow downstream of the trough axis. At this time the right entrance quadrant of the primary jet streak was situated over a triangular network of wind profilers at Haviland, KS, Lamont, OK, and Vici, OK. A time series of kinematically derived (Bellamy, 1949) jet-stream-level divergence (Fig. 3) calculated from this triangle shows divergence (<5 x 10^{-5} s^{-1}) until sometime between 1400 and 1600 UTC in the right entrance quadrant of the jet and convergence (≈-1 x 10^{-5} s^{-1}) thereafter as the left entrance quadrant migrated over the triangle centroid. The corresponding kinematically derived vertical velocity profiles (Bellamy, 1949) at 1200 and 1500 UTC (Fig. 4; adjusted to satisfy mass balance requirements; O'Brien, 1970) respectively show ascent (≈-2 μb s^{-1}) and subsidence (≈0.7 μb s^{-1}) in the right and left

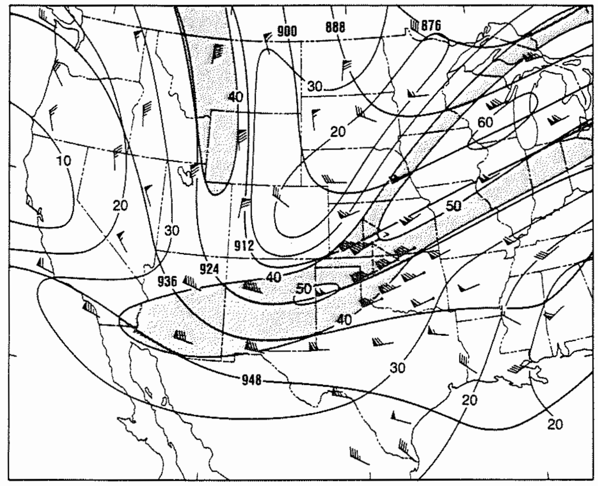

Fig. 2. 300 mb geopotential height (dam, heavy lines) and isotach (m s^{-1}, thin lines) analyses at 1200 UTC 6 December 1990. Wind vector flags 25 m s^{-1}; barbs 5 m s^{-1}; half barbs 2.5 m s^{-1}. Vectors with solid dot heads are wind profiler observations. Thin dashed triangle with vectors, Haviland, KS, Lamont, OK, Vici, OK, profiler network used for kinematic diagnostics; without vectors, same profiler triangle space-time adjusted from 1500 UTC to its estimated position at 1200 UTC.

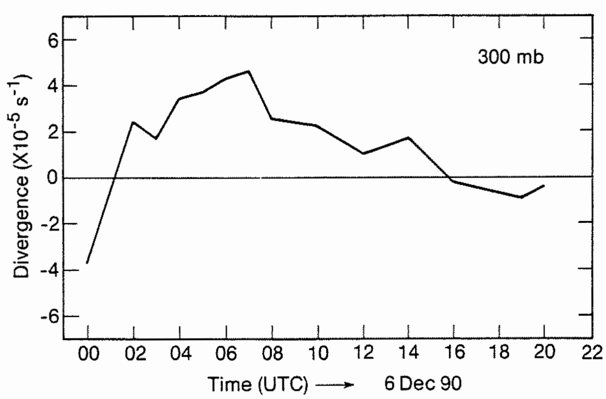

Fig. 3. Time series of kinematic divergence (10^{-5} s^{-1}) at ≈300 mb from the profiler triangle network shown in Fig. 2.

entrance quadrants of the jet at about 300 mb, which is below the core of the jet. Assuming the validity of Taylor's hypothesis (steady-state weather systems propagating at a fixed velocity), these results are consistent with the simple four-quadrant model of divergence and vertical velocity associated with a straight jet (dominated by stretching deformation) and its ageostrophic secondary circulations (Beebe and Bates, 1955; Shapiro, 1982).

*Affiliated with the Forecast Systems Laboratory.

**Affiliated with the Wave Propagation Laboratory.

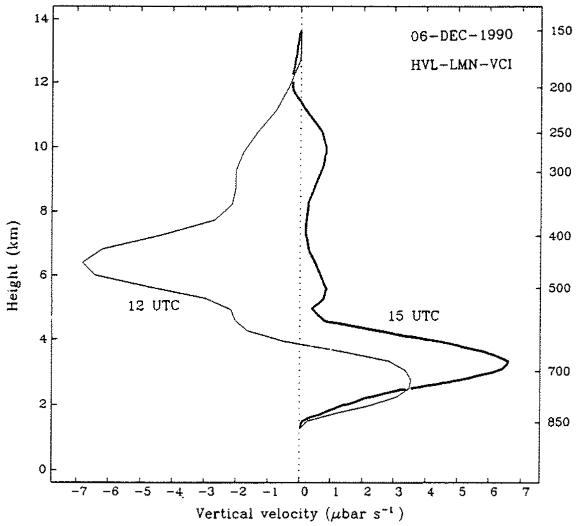

Fig. 4 Kinematic vertical velocity profiles (μb s_{-1}) at 1200 and 1500 UTC 6 December 1990 from the profiler triangle network shown in Fig. 2.

Infrared satellite imagery at 1200 UTC (Fig. 5a) shows -40 °C cirrus cloud tops associated with ascent within the right entrance quadrant of the jet originating in northern Texas and extending downstream over the wind profilers. The jet stream cirrus contained a sharply defined northwestern cloud edge near Haviland that marked the boundary between the ascending and descending branches of the jet entrance circulation; this cloud edge moved southeastward out of the profiler triangle by 1500 UTC (Fig. 5b). The 1500 UTC infrared satellite image also shows midtropospheric clouds with tops at -25 °C (≈500 mb), situated over the profilers. By 1700 UTC (Fig. 5c), the cirrus cloud edge is directly over the Haskell, OK profiler. The 1200 UTC rawinsonde sounding from Norman, OK (Fig. 6), contains a nearly saturated layer between 450 and 300 mb corresponding to the jet stream cirrus.

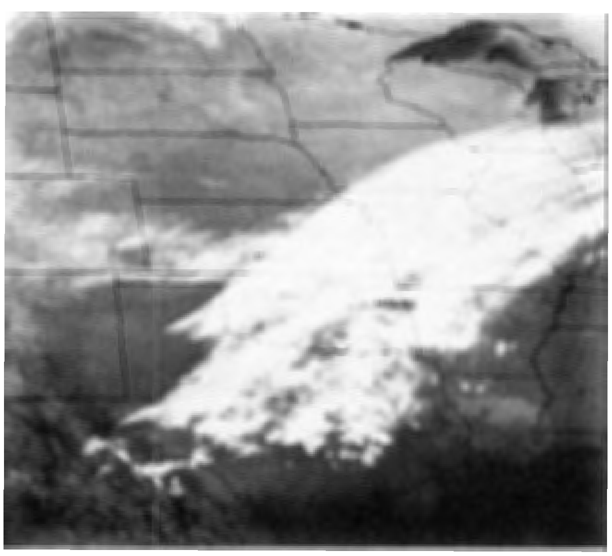

Fig. 5a IR satellite image, 1200 UTC

Fig. 5b IR satellite image, 1500 UTC.

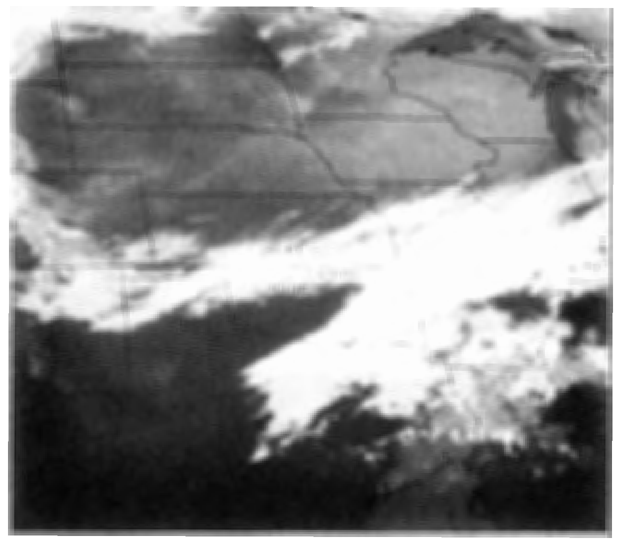

Fig. 5c IR satellite image 1700 UTC.

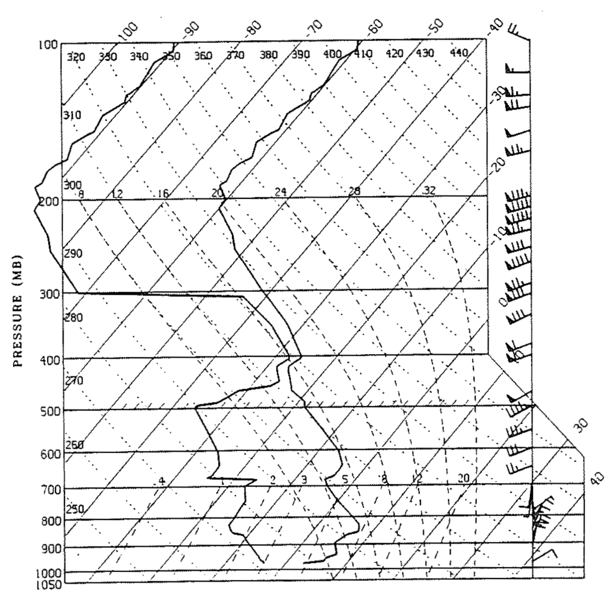

Fig. 6 Skew-T, log-P rawindsonde profiler from Norman, OK at 1200 UTC 6 December 1990.

3. PROFILER CLOUD DETECTION

Assuming a Gaussian-shaped antenna beam, the power (in watts) received by the profiler (Gossard and Strauch, 1983) is

$$P_r = 1.01 \times 10^{-17} \frac{P_t A_e}{\lambda^4} \frac{\Delta r}{r^2} Z \qquad (1)$$

where P_t is the average transmitted power (w), A_e is the effective antenna area (m^2), Δr is the range resolution (m), λ is the radar wavelength (m), r is the range to the target (m), and Z is the radar reflectivity factor (mm^6/m^3) of the cloud. We may rearrange Eq. 1 to express the minimum detectable effective reflectivity factor, Z_{emin} in terms of the minimum received signal power level, P_{rmin}, detectable by the profiler.

$$Z_{emin} = \frac{P_{rmin}\, \lambda^4\, r^2}{10^{-17}\, P_t\, A_e\, \Delta r} \qquad (2)$$

The profiler has an estimated minimum detectable signal power level of 10^{-20} w. If we use the other appropriate profiler parameters in Eq. 2, we find that the profiler is capable of detecting an effective reflectivity factor, Z_e, of 0.0023 (-26 dBZ_e) at 7 km altitude which is sufficient sensitivity to detect the jet stream cloud at about 400 mb described above (Kropfli et al., 1990).

Figures 7a and b show the profiler signal power (no range correction) and vertical velocity, respectively, from 800 to 2000 UTC from Vici. Time increases from right to left with a temporal resolution of 6 minutes. The cirrus cloud is distinguished by higher reflectivity and a positive (downward) velocity of about 0.7 m s^{-1} from 800 to 1200 UTC at 5 to 7 km altitude. This fall velocity is consistent with ice crystal precipitation within the cloud, and sublimation at the cloud base. Although the downward velocities at 6 km altitude cease abruptly at 1200 UTC the reflectivity signature at higher altitude extends to 1300 UTC which corresponds to the passage of the sharp cloud edge evident in the satellite image of Fig. 5a. Later, at about 1700 UTC, the midtropospheric (500 mb) cloud of Fig. 5c is also evident in the profiler data.

Figures 8a and b are the signal power and radial velocity plots from the Haskell profiler. Again, the abrupt cessation in the downward velocities at 1700 UTC corresponds closely with the cloud edge seen in the satellite image of Fig. 5c. Close comparison of the vertical velocities at 1130 to 1230 UTC and the Norman rawindsonde ascent (Fig. 6) shows excellent agreement between the radar-observed cloud layer at 7 to 8.5 km, and the cloud layer inferred from the rawindsonde data at 450 to 300 mb. When interpreted as a cross section, Figure 8b implies that the cirrus cloud was about 4 km thick near the edge.

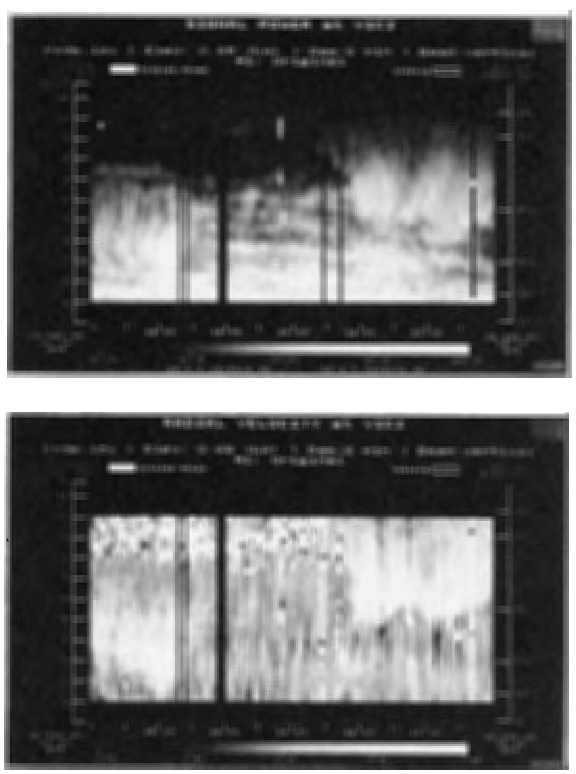

Fig. 7. Profiler data from Vici, OK, 0800 to 2000 UTC showing (a) signal power (dB) and (b) vertical velocity (m s^{-1}).

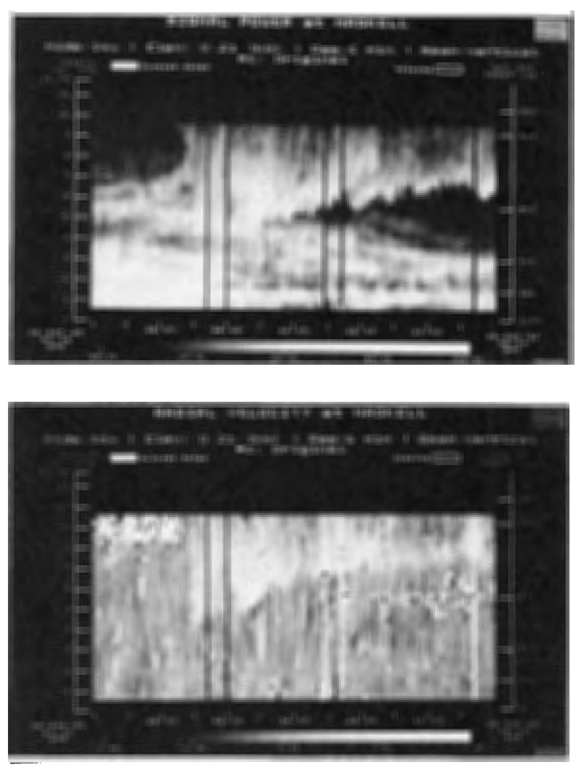

Fig. 8. Profiler data from Haskell, OK, 0800 to 2000 UTC showing (a) signal power (dB) and (b) vertical velocity (m s_{-1}).

4. SUMMARY

Though it would be difficult to determine detailed cloud characteristics from profiler data, the above case demonstrates that profilers are capable of determining the cloud base (or sublimation level of ice crystals) and top under certain conditions. Other work (Law, 1991b) has shown that displays of profiler spectral moment data provide at least qualitative information about precipitation, waves, and turbulence. It now appears that clouds are often the source of profiler signal returns and serve as tracers of wind velocity.

References:

Beebe, R.G., and F.C. Bates, 1955: A mechanism for assisting in the release of convective instability. Mon. Wea. Rev., 83, 1-10.

Bellamy, J.C., 1949: Objective calculations of divergence, vertical velocity, and vorticity. Bull. Amer. Meteor. Soc., 30, 45-49.

Gossard, E. E., and Strauch, R. G., 1983: Radar Observations of Clear Air and Clouds. Elsevier Science Publishing Company, Inc. New York, NY

Kropfli, R. A., B. W. Bartram, and S. Y. Matrosov, 1990: The upgraded WPL dual-polarization 8-MM wavelength radar for microphysical and climate research. Preprint, 1990 Conference on Cloud Physics, July 17-23, 1990, San Francisco, CA. American Meteorological Society, Boston, MA

Law, D. C., 1991a: Effects of precipitation, convection, and waves on NOAA network profilers. Preprint, International Conference on Radar Meteorology, June 24-28, 1991, Paris, France. American Meteorological Society, Boston, MA

Law, D. C., 1991b: Interpretation of wind profiler spectral moment data. Preprint, Seventh Symposium on Meteorological Observations and Instrumentation. Jan 14-18, 1991, New Orleans, LA. American Meteorology Society, Boston, MA

O'Brien, J.J., 1970: Alternative solutions to the classical vertical velocity problem. J. Appl. Meteor., 9, 197-203.

Shapiro, M.A., 1982: Mesoscale weather systems of the central United States. CIRES/NOAA report., University of Colorado, 78 pp.

A NEW LWC-METER FOR SLOWLY FLYING AIRCRAFT

Krzysztof E. Haman, Andrzej M. Makulski and Szymon P. Malinowski

Institute of Geophysics, University of Warsaw, Poland
ul.Pasteura 7, PL 02-093 Warszawa, Poland

1. INTRODUCTION

Airborne hot-wire liquid water content (LWC) meters like Johnson-Williams (JW) or King (CSIRO) probes suffer from errors caused by fluctuations of ambient temperature and airflow velocity (Baumgardner 1983). The lower the cruising speed of the aircraft the greater are these errors. They are particularly troublesome at low LWC values, where they can become greater than 100% . Additionally some hot wire probes suffers from problems with junctions in the low-resistance part of the electric circuitry; even small variations of contact resistance which can be caused e.g. by aging, dirt or mechanical vibrations may easily become a source of considerable false LWC signals. On the other hand, relatively thick sensor of CSIRO probe may show too low collision efficiency for small droplets at low cruising speeds.

In the present paper a new design of a hot-wire device eliminating a great deal of these problems is presented. It is designed for use at low speeds (40m/s or less) on small aircraft, sailplanes etc., particularly at low LWC values. Its preliminary version has been presented at AMS Cloud Physics Conference, San Francisco,1990. The main part of the new sensor (Fig.1) consists of a 5cm long piece of 0.127μm thick alumel wire placed vertically on a small pivoting vane with vertical shaft. One half of the wire is protected against impact of cloud droplets by a thin shielding rod which practically does not disturb the air temperature. The second half of the wire is not protected and collects the cloud droplets. The particular choice of the material and dimensions of the sensor wire is of secondary importance but the use of relatively thin wire improves collision efficiency for small droplets, often prevailing in low LWC clouds. Construction of the shield is identical with that described by Haman (1992) for airborne thermometric device. In order to compensate for reduction of airflow velocity behind the anti-droplet shield, the protected part of the sensor wire is placed inside a sort of Venturi nozzle. It returns the air speed to its undisturbed value and assures identical ventilation for both parts of the wire. The sensor wire is heated by stabilized direct electric current and its two halves form two branches of a Wheatstone bridge (Fig.2). Since both halves of the wire react identically to the fluctuations of ambient temperature and velocity the imbalance of the bridge depends only on the rate of collection and evaporation of cloud droplets by the unprotected branch. The reference branches of the bridge are of relatively high resistance and take negligible current. Let us notice that the low-resistance branch of the bridge has no junctions which could become sources of false LWC signals.

The design of the sensor has been evolving under experience gathered during three years (or rather three flight test series) of its development. The present paper gives details of the last version of the instrument and discusses some problems connected with its exploitation.

2. THEORY OF THE INSTRUMENT

It is easy to see from Fig.2, that if the resistance of of the reference branch of the bridge (R_1 and R_2 in Fig.2) is much greater than that of the sensor wire and takes negligible current the imbalance voltage V of the bridge can be given by formula:

$$V = I\left[R_d(1 - \sigma)R_d - \sigma R_W\right] \tag{1}$$

where: I - heating current; $\sigma = R_1/(R_1+R_2)$; R_d and R_w - respectively resistance of protected and unprotected part of the sensor wire.

Deleting, for space economy, elementary though cumbersome considerations based upon the heat balances of the protected and unprotected parts of the sensor wire as well as assumption of linear dependence between the wire's resistance and temperature, we shall write the final relation between the cloud LWC and output voltage V:

$$V = \frac{I\alpha\sigma R l d E v L}{\pi\kappa Nu - \alpha I^2 R} W \tag{2}$$

where: R - specific resistance of the wire (per unit length) at reference temperature; l - length of the unprotected part of the wire; d - diameter of the wire; E - collection efficiency of the sensor wire for cloud droplets; v - airspeed; L - latent heat of evaporation; κ - thermal conductivity of air; Nu - Nusselt number; W - LWC . It should be noted that Eq.(2) is good if the the bridge in cloudless air is balanced.

3. CONSTRUCTION AND TECHNICAL DATA OF THE INSTRUMENT

The recent version shown on Fig.1 consists of a light, well balanced, pivoting frame (1) turnable around a vertical axle (2) mounted into the support (3). The frame is divided into the upper and lower part. On the upper frontal part of the frame the anti-droplet shield is fastened. It consist of the main triangular rod

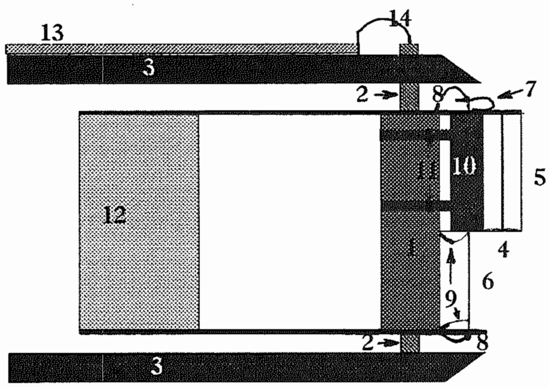

Fig.1. Schematic view of the LWC sensor. See the text for details.

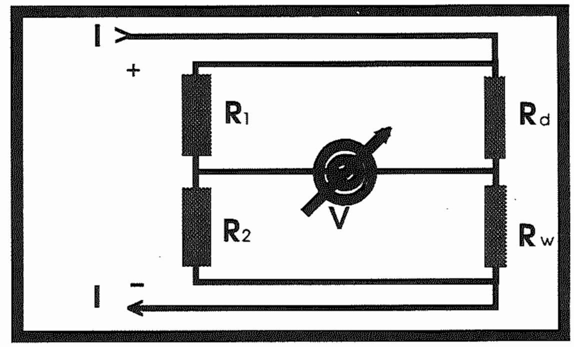

Fig.2. Electric scheme of the LWC-meter. See the text for details.

(4) 1.3mm wide and 25mm long and additional 0.013mm thick wire (5) placed 3mm ahead of the main rod. The sensor wire (6), ca 50mm long and 0.127μm thick, is fixed 7mm behind the main protecting rod so that its lower 25mm remain unprotected. It is made of alumel alloy, has resistance 0.22Ω/cm at room temperature and thermal resistance coefficient $\alpha = 0.0018/K$. The sensor wire is insulated from the frame and stretched by the spring (7). The ends of the sensor wire are soldered directly to the power supply wires (8) but only its central 40 mm form branches of the Wheatstone bridge; the outer ca 5mm segments form thermal protection against parasitic exchange of heat with the frame along the wire. The three signal transmitting connections to the bridge (9) are located in, 20mm up and 20mm down from the center of the sensor wire. They are made of ca 10 mm long pieces of 25μm thick alumel wire; use of the same alloy reduces adverse thermoelectric effects and due to their small diameter the heat flux through the connections is negligible. In case of failure or damage the sensor wire can be easily changed. Its power supply ends and signal connections should be soldered to the proper ends of the permanent cabling of the frame; the latter is made of 0.3mm thick insulated copper wire.

The upper part of the sensor wire is placed between two cylinders (10) 5.5mm thick forming a slot ca 7.3mm wide which acts as a Venturi nozzle; its exact width is precisely adjustable in wind tunnel tests by means of screws (11). To the rear part of the frame a vane (12) on a long (60mm) arm is fixed. It keeps the anti-droplet shield upwind the local, instantaneous airflow. It is important to avoid aerodynamical interactions between the nozzle and the vane; they can create problems by positioning the shield at an incorrect angle with respect to the airflow.

The permanent cabling of the frame is connected to a 5-wire extension cable (13)(leading to the control box) by means of five ca 25 mm long flexible arcs (14) made of 0.15mm thick enameled copper wire. The frame has special bumpers which limit its turn angle to ca ±30°, preventing the connections from becoming twisted.

The sensor wire is heated to about 140 - 160°C with DC stabilized with accuracy better than 1% at preselected level of 1.5 - 1.7A. According to Eq.(2) this gives sensitivity about 15 mV/gm^{-3} at typical cruising speed of 30m/s. The time constant of the instrument is estimated as 0.15s at the same speed. The control box contains among others the reference branches of the bridge (1 kΩ each) with additional high precision potentiometer for balancing the bridge in flight. There is also a LDC panel for readout of the LWC signal voltage and amperage of the heating current.

4. EXPLOITATION OF THE INSTRUMENT

Since small manufacturing differences between individual frames may occur separate regulation of the Venturi nozzle in each case is recommended. It can be made in a wind tunnel by adjusting the slot between the cylinders until the output signal becomes insensitive to variation of air speed in the range of expected flight velocities or to variations of the heating power at constant speed (or both). For precise measurements wet calibration of the instrument is necessary. The instrument should be placed on the aircraft in carefully selected place (preferably on a boom) in order to avoid adverse aerodynamic influences. After take-off balancing the bridge in cloudless air is advisable in order to keep the record in the range of linear response and applicability of Eq.(2).

Despite of generally positive experience with its earlier versions the instrument is still under development and flight and wind tunnel tests, aimed at elimination of some minor drawbacks, are being continued. A version for very low airspeeds (for use e.g. on tethered balloons) with part of the sensor working as a hot-wire anemometer is under consideration.

REFERENCES

Baumgardner,D., 1983: An analysis and comparison of five water droplet measuring instruments. *J.Appl.Meteor.*, 22, 891-910.

Haman,K.E., 1992: A new thermometric instrument for airborne measurements in clouds. *J.Ocean Atmos.Technol.*, in press.

STUDY ON CLOUD FORMATION AND MAINTAINANCE PROCESSES WITH REMOTE SENSING

Zhao Bolin
Department of Geophysics, Peking University, Beijing 100871 China

1. A set of remote sensing instruments of Peking University, which includes an 8mm-1.35cm dual channel (22.235GHz and 35.3GHz) microwave radiometer and a 5mm (54.5GHz) microwave radiometer, has been developed for the Western North-Pacific Cloud Radiation Experiment (WENPEX) of International Satellite Cloud Climatology Project (ISCCP). WENPEX was mainly conducted by Japanese scientists under the leadership of Prof. Takao Takeda. Peking University was invited to take part in this Experiment, and used a set of multifrequency microwave radiometers to observe the cloud marine atmosphere boundary. WENPEX was conducted in winter time from from 1989-91, in Shionomisaki and Amami Oshima, Japan. There were satellite, aeroplane, ship observations as well as ground-based island observation. The result and analysis of Peking University, ground-based observation are presented.

2. The scheme of 8mm-1.35cm dual channel microwave radiometer is shown in Fig.1. Both elevation and azimuth angles scanning are aviable. From the received information of the two frequencies, the total atmospheric vapor content and integral liquid water in cloud can be deduced. See Fig.2 and Fig.3.

3. 8mm microwave radiometer was set under caves and antenna directed at 45^{0} elevation angle. So that it can continues observation when there is rainning. The variation of observed brightness temperature of 8mm microwave radiometer in Jan. 25 1991 is shown in Fig.4.

4. 5mm microwave radiometer remote sensing the temperature profile from surface to 700hpa by elevation angle scanning observation. The variation of temperature

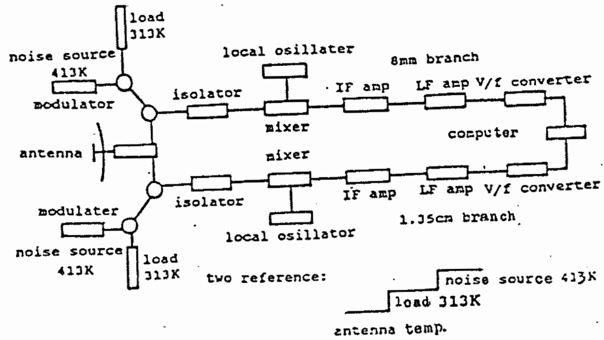

Fig. 1. 8mm-1.35cm dual channel microwave radiometer

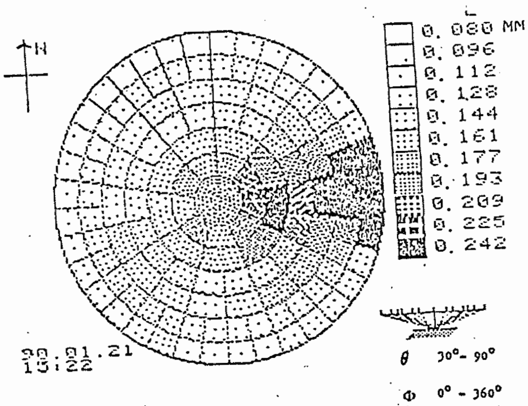

Fig. 2. Distribution of liquid water content of cloud in the whole sky

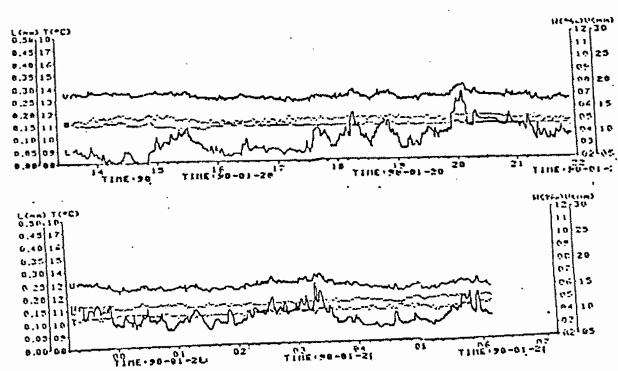

Fig. 3. Diurnal variation of liquid water content of cloud L, total water vapor content U, surface mix ratio W and surface temperature T

profile from radiometer observation in Jan. 16 1991 is shown in Fig.5. The radiosonde data are given also for comparison.

5. In winter, the temperature and humidity profile at 08 Jan. 18 1991 of Amami Oshima radiosonde data is shown in Fig.6. The dry cold air from north west China contient came to the warm sea water, the heating in low part of air due to the warm surface sea eater led to unstability. So that the turbulence was active and convective boundary layer, mixed layer formed. As shown in Fig.6, the potential temperature and mixing ratio are constant with height, that indicated the layer well mixed. At the top of the mixing layer there discontinueties in temperature, humidity, and a strong inversion and sharp decreasion in mixing ratio. Owing to the warm sea surface water, the mixed layer gained heat and humidity flux from sea surface. With one dimension model of cloud topped marine boundary budget, which was introduced by Stage and Businger (1981). The mixed layer depth or cloud top height, the condensation level, cloud base height, the integral liquid water in cloud are main simulation. In Jan. 18 1991 Amami Oshima, under a high pressure, there is a divergence, the mixed layer became thinner, in this period, the stratocumulus transited to cumulus and then disappeared. The initial based on 08 Jan. 18 1991 radiosonde data, divergence set to $0.000015 s^{-1}$. Simulation results are shown in Fig.7. The divergence is only a little larger than entrainment rate. The mixed layer depth became thinner very slowly also and integral liquid water in cloud decreases. The results of simulation coincide with observation data of microwave radiometer.

Stage S.A. and J.A. Businger, 1981, A model for entrainment into a cloud topped marine boundary layer, J. Atmosph. Sci., 38, 2213-2229.

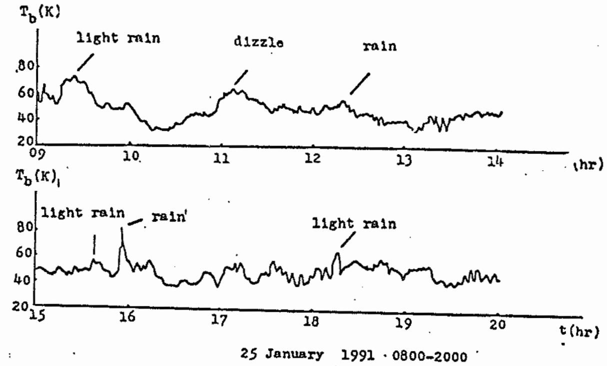

Fig. 4. Variation of 8mm brightness temperature of elevation angle 45°

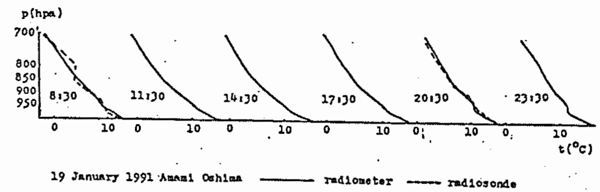

Fig. 5. Diurnal variation of atmospheric temperature profile observed with 5mm microwave radiometer in comparison with that of radiosonde

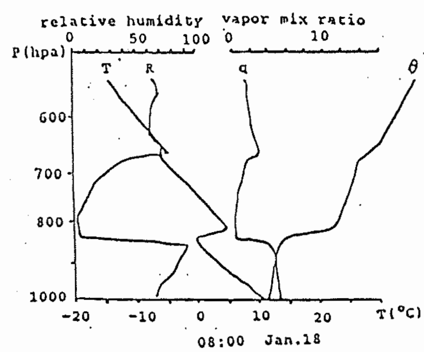

Fig. 6. Profiles of temperature (T), relative humidity (R), potential temperature (θ) and vapor mix ratio (q)

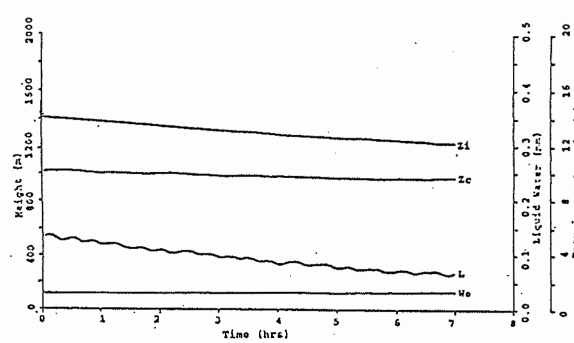

Fig. 7. The evolution of the boundary layer of simulation
(Z_i: depth of mixed layer, Z_c: condensation level, L: integral liquid water and W_e: entrainment rate)

ON CORRELATION, WITH EXAMPLE DATA ON RADAR AND RANGAGE MEASUREMENTS OF RAINFALL

Edwin Kessler[1] and Barbara Neas[2]

[1]Cooperative Institute for Mesoscale Meteorological Studies and
Depts. of Geography and Meteorology, Univ. of Oklahoma, Norman 73019
[2]Biostatistics and Epidemiology, O.U. Health Sciences Center, Okla. City, 73190

1. INTRODUCTION

The coefficient of correlation, which measures interdependence between random variables, diminishes with increasing errors of estimate, and it increases with the range over which the variables are measured. The latter dependency seems not commonly considered. Equations presented here facilitate normalization of correlation coefficients to a standard range for cases where two processes are used to measure the same variable.

Where different physical quantities are correlated, such as rainfall and lightning rate, we may not know about the relationship in advance. On the other hand, with different kinds of observations on the SAME VARIABLE we know that if the measurements are unbiased, the data will cluster along a 45° axis, and if the measurements are perfect, the value of the correlation coefficient is +1.

The second situation described above is close to that which obtains in certain studies of radar meteorology. Rain gage and radar data may be correlated in order to show radar capabilities for measurement of rainfall, e.g., Zawadski, et al., (1986). In this situation, the raingage data are assumed to be more nearly correct, though often not representative of the relatively large regions encompassed by the radar beam.

Many sources of error confound radar measurements, as described, for examples, by Austin (1987) and Brandes and Wilson (1988). In contrast with Zawadski and some others, however, these authors do not evaluate performance with the correlation coefficient, although they do present scatter diagrams and quantities such as the ratio of the average rainfall measured by radar to the average rainfall measured by raingage. Perhaps some authors who do not present correlation coefficients in their studies have encountered problems in use of this measure or are uneasy with it for reasons undefined. In any event, the utility of correlation involving sets of data representing two kinds of measurements of the same quantity is increased by understanding the mathematical properties that are special to such cases, and by normalizing the coefficient to a standard interval of the measured quantity.

2. A SCATTER DIAGRAM

Consider a quantity Z that is measured over the range from a to b through two processes X and Y, associated with error variances K_x and K_y. We assume in the following development that the average of many measurements of the same value of Z by either process is the true average, i.e., that there is no systematic bias. (While this is not a necessary assumption, it corresponds to figure 1.) When a range of values of Z is measured many times through the processes X and Y, the values of X and Y spread across the range of Z as illustrated in figure 1. In this figure, the local standard deviation is constant and the density of data is uniform.

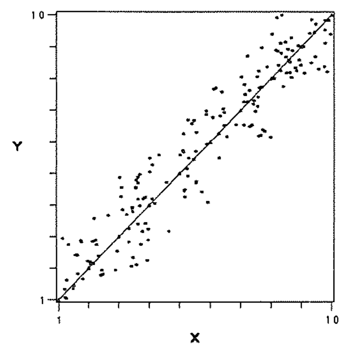

Fig. 1 - Illustrating many observations of the same parameter by processes X and Y.

It is important to realize that the measurements of any particular value of Z are locally uncorrelated. Thus, multiple measurements of a single value of Z simply produce a symmetrical cluster of data centered on a point. In other words, a correlation coefficient attains a magnitude significantly greater than zero only when a range of the object parameter is measured. We now show how the coefficient of linear correlation can be derived from knowledge of the standard errors of estimate and their distribution, the density distribution of the data itself, and the range (b - a).

3. DERIVATION OF EQUATION FOR THE LINEAR CORRELATION COEFFICIENT

One of several equivalent expressions for the correlation coefficient is as follows:

$$r = \frac{\overline{X\,Y} - \bar{X}\cdot\bar{Y}}{[(\overline{X^2} - \bar{X}^2) \times (\overline{Y^2} - \bar{Y}^2)]^{0.5}}, \qquad (1)$$

where the bars indicate average values. These average values pertain to the whole range of the variables, from a to b; they may be determined by integrating formulae for local values. We consider uniform data density and standard deviations initially.

We use L as a subscript to denote local conditions; its absence when a bar is present indicates an average over the whole range from a to b. We also introduce the quantity Z to denote the unknown (true) average of a large number of measurements by either process. Now, since the local correlation is zero, $\overline{X\cdot Y_L} = \overline{X}\cdot\overline{Y_L} = Z_L^2$. The global average, $\overline{X\cdot Y}$ is given by:

$$\frac{1}{(b-a)}\int_a^b \overline{X\cdot Y_L}\cdot dZ = \frac{1}{(b-a)}\int_a^b Z^2\cdot dZ$$

$$= \frac{1}{(b-a)}\cdot\frac{Z^3}{3}\Bigg|_a^b = \frac{(b^3-a^3)}{3(b-a)}$$

Thus,

$$\overline{X\cdot Y} = (b^2 + ab + a^2)/3, \qquad (2)$$

and

$$\overline{X}\cdot\overline{Y} = [\tfrac{1}{2}(b+a)]^2 = (b^2 + 2ab + a^2)/4 \qquad (3)$$

Therefore,

$$\overline{X\cdot Y} - \overline{X}\cdot\overline{Y} = (a-b)^2/12. \qquad (4)$$

The denominator of equation (1) is evaluated here with the assumption that the local variance is constant in the range from a to b, as illustrated in figure 1. Then,

$$\overline{X_L^2} - \overline{X_L}^2 = K_x; \qquad \overline{Y_L^2} - \overline{Y_L}^2 = K_y, \text{ so}$$

$$\overline{X_L^2} - \overline{Z_L}^2 = K_x; \qquad \overline{Y_L^2} - \overline{Z_L}^2 = K_y, \text{ and}$$

therefore

$$\overline{X_L^2} = \overline{Z_L}^2 + K_x; \qquad \overline{Y_L^2} = \overline{Z_L}^2 + K_y. \qquad (5)$$

Then the global averages, $\overline{X^2},\overline{Y^2}$ are given by

$$\frac{1}{(b-a)}\int_a^b (Z^2 + K_{x,y})dZ$$

$$= \frac{1}{(b-a)}\left[\frac{Z^3}{3} + K_{x,y}\cdot Z\right]\Bigg|_a^b,$$

and therefore,

$$\overline{X^2},\overline{Y^2} = [(b^2 + ab + a^2)/3] + K_{x,y}. \qquad (6)$$

Also note that global $\overline{X}^2,\overline{Y}^2$ are given by

$$\overline{X}^2,\overline{Y}^2 = [\tfrac{1}{2}(a+b)]^2. \qquad (7)$$

Therefore,

$$\overline{X^2},\overline{Y^2} - \overline{X}^2,\overline{Y}^2 = [(b-a)^2/12] + K_{x,y} \qquad (8)$$

Then the whole correlation equation, Eq. (1), can be written as follows:

$$r = \frac{(b-a)^2}{\{[(b-a)^2 + 12\cdot K_x]\cdot[(b-a)^2 + 12\cdot K_y]\}^{.5}}. \qquad (9)$$

When the local variances are equal or K is an average value, (9) reduces to

$$r = \frac{(b-a)^2}{(b-a)^2 + 12\cdot K}. \qquad (10)$$

Equation (10) is graphed in figure 2.

Clearly, when K = 0, r = +1, and r diminishes with increasing K, as expected; also, the influence of K diminishes as (b - a) increases. It is also evident that the effect of averaging clusters of points in a local area is to reduce the local variance, K, and hence to increase r. However, if averaging occurs over a large range so that (b - a) is reduced in the averaged data, the correlation coefficient may be practically unaffected, as further discussed in Section 6.

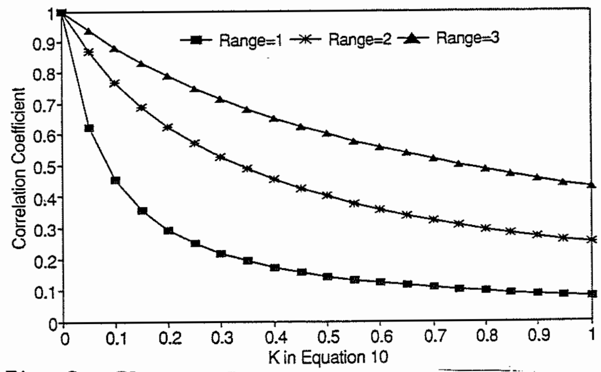

Fig. 2 - Plots of Eq. (10) for various ranges (b-a) and for values of local variance K.

4. CORRELATION COEFFICIENT WITH VARIABLE DATA DENSITY

In many practical cases, the data density is a function of magnitude. For example, light precipitation is much more frequent than heavy precipitation. Errors of measurement are also prone to vary systematically; the average error in measurement of rain is approximately proportional to intensity. Thus, data density, f(Z), and standard error, σ, are, respectively, inversely and directly proportional to magnitude:

$$f(Z) = c/Z; \ \sigma = k\cdot Z \qquad (11)$$

Such distributions become more nearly uniform, like that in figure 1, when logarithms of the data are treated. For such a distribution, the normalized density function is $1/\{Z\cdot[\ln(b/a)]\}$. Then, following along lines presented in section 3 with C defined as the average value of C_x and C_y in the equations for the local standard error or standard deviation, e.g., $C_xZ = (\overline{X_L^2} - \overline{X_L}^2)^{1/2}$,

$$r = \frac{\dfrac{b+a}{2} - \dfrac{b-a}{\ln(b/a)}}{\dfrac{b+a}{2}(1 + C^2) - \dfrac{b-a}{\ln(b/a)}}, \qquad (12)$$

As with equation 10, r is unity when the standard error is zero, and, in the presence of error, r tends to be larger as b - a becomes larger.

5. APPLICATIONS TO RAINFALL MEASUREMENT BY RAINGAGE AND RADAR

a. *Some properties of the distributions*

A paper by Zawadski, et al. (1986), hereafter Za, is illustrative. Figure 3 in the present work is figure 1 in Za; we retain the original caption. The scatter of points about the central line is roughly uniform with rate. Although this log-log plot shows (by eye) some tendency toward increased data density at small rates, the treatment of uniform density in our Section 3 seems roughly applicable, and this treatment is applied below. Notice that the abscissa and ordinate labels are those applicable to the original data. The linear coefficient of correlation (cc) of the data shown in figure 3 is 0.69; this was calculated from the logarithms of these labels. The standard deviation (SD) is 76%; this is an estimated value given by conversion from 0.246 obtained from calculation on the logarithms. (This is not stated in Za, but is confirmed in correspondence with Zawadzki).

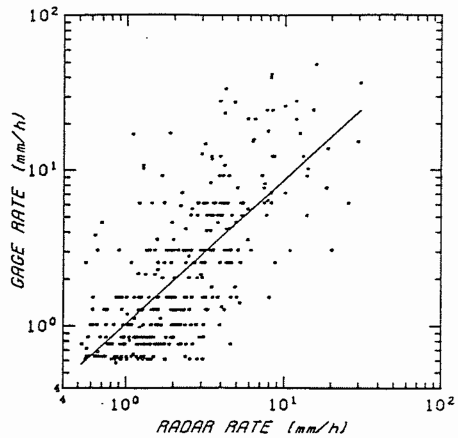

Fig. 3 - Scattergram of radar rates over 1.4 km^2 (from one antenna scan) vs. gage 5-min. rates. The time of the radar scan is approximately centered within the 5-min accumulation period of the gages. Radar rates are obtained 2 km above the gages. (from Zawadzki, et. al, 1986).

Personal communications (Zawadzki, 1990 & 1991), note that the standard deviation as a fraction of a logarithm is difficult to interpret; hence it is presented as a percentage. The correspondence notes that a standard error of the logarithm, expressed as $\sigma_{\log R}$ = logA implies error factors in R, viz., +AR and -R/A. The standard error in logR and the standard error as a percentage are related by Zawadzki through the following equation:

$$\sigma_{\log R} = \log\{1 + [SD(\%)]/100\}. \qquad (13)$$

By this equation, a standard error of 100%, which represents a factor of two, is associated with the logarithm of 2, which is 0.301. Here is a table with some principal values.

Table 1
Estimated correspondence between standard deviation as percentage and standard deviation of logarithm

SD (%)	$\sigma_{\log R}$	SD (%)	$\sigma_{\log R}$
100	.301	50	.176
90	.278	40	.146
80	.255	30	.114
70	.230	20	.079
60	.204	10	.041
50	.176	0	0

Note that with the range b-a given by inspection of figure 3, only two of the parameters SD, r, and (b-a) can be asserted independently if equation (10) is to hold. With SD = 0.246, k = SD^2 = .0605, r = 0.69, then b - a ≈ 1.3. A glance at figure 3 suggests a value more nearly 1.8, but this would be reduced by the low density of data at the higher rates. An alternate approach solves equation 10 for K, given r and b-a. With b - a = 1.8 and r = 0.69, then K would be about 0.35, corresponding to SD above 100%. The difference from 76% may involve the approximation implicit in Table 2. Further investigation of relationships between assumptions of our theory and properties and treatment of real data is indicated.

Why are the calculations in Za made on the logarithms of the rates rather than on the rates themselves? According to Zawadzki (op. cit.), "...If you simply use a linear regression between the rates, the regression line and the correlation coefficient are heavily influenced by the few points with high rates. Given the quasi-exponential decrease of number of points with rate, the linear regression on log-log scales gives roughly the same weight to all rates... weighted non-linear regression on linear scales... is a very lengthy process...[and] for the set of points on which this exercise was performed there was little difference with a linear regression on log-log scales."

Zawadzki's views have been largely confirmed by a computer simulation. This simulation started with a linear distribution such as shown in figure 1. When antilogarithms were taken, the density became inversely proportional to magnitude and the standard deviation increased proportionally with magnitude. The antilogarithmic data are analogous to raw rainfall data, and figure 3 illustrates logarithms of such data.

The simulation involved selection of random number sets and calculation of correlation coefficients for each set. The results illustrated in Table 2 show that the correlation for the simulation corresponding to raw rainfall data was less stable and also lower than that for the data adjusted to constant density and standard error, and Zawadzki's statement is confirmed.

Table 2
Results of Computer Simulation
Fifteen sets of random numbers

	Avg.cc	**σ_{cc}**	**maxim**	**minim**
Linear distribution*	.788	.042	.852	.707
Antilogarithmic dist.#	.600	.176	.855	.308

*Corresponding to logarithms of rainfall data
#Corresponding to raw rainfall data

b. *Effects of averaging*

When averaging over local regions, the effect of averaging is to increase the correlation coefficient. This can be seen in equation (10), and the magnitude of the effect can be estimated from the equation. In a practical case, effects of averaging are illustrated by comparison of figures 3 and 4, both from Za. Notice that both the range and

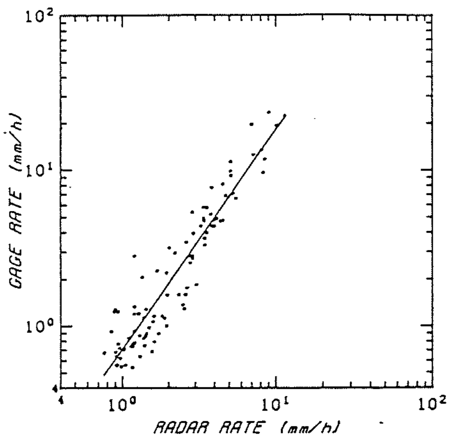

Fig. 4 - Scattergram of radar rates over 36 km² (average from three scans) vs. 35-min gage rates. Radar scans are centered within the 35-min accumulation period of the gages. Gage rates are averages of four gages within the 36 km² area (from Za, 1986).

local variance are diminished in figure 4, and the correlation coefficient is increased from 0.69 to 0.94, according to Za.

If the averaging takes place over the entire field of data, the variance of the entire data set is reduced in the same proportion as the local variance, and the correlation coefficient remains constant. This phenomenon was examined through the simulation study described in the Appendix. The simulation examined correlation coefficients as influenced both by averaging and by the range of sample data. Figure 5 illustrates the effect of drawing samples from an increasing region. At the local level of sampling, the range is 3, and the correlation coefficient is near zero, illustrating the true uncorrelated nature of the local data. When the range of the sample area is increased by 1, the correlation coefficient increases to approximately 0.4. All incremental increases in range illustrate increase of the coefficient toward the value for the entire data set.

The correlation coefficient is only slowly varying when the sampling area increases from an already large area. As means are formed from an

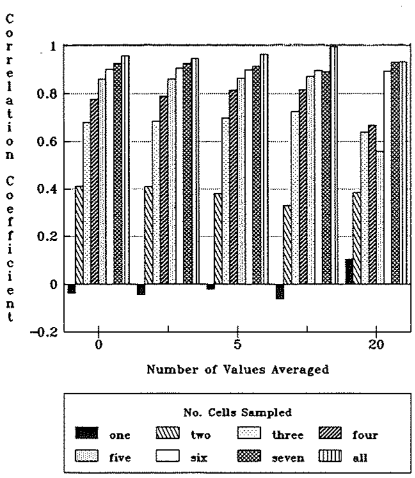

Fig. 5 - Correlation coefficient as influenced by averaging different sizes of sampling areas.

increasing number of observations, fewer numbers are available to associate. As the number of points used to calculate decreases, the coefficient becomes highly variable. In the case illustrated, the coefficient generally decreases. If the original sample is increased so that the sample of means remains constant, then the coefficient also remains constant.

6. CONCLUDING REMARKS

The increase of correlation coefficient with averaging reported in Za is characteristic of averaging over a limited region. Further study should seek to define the averaging process in analytic form, perhaps in terms of a distance divided by a characteristic length of precipitation cells, discussed by Armijo (1966) and Kessler (1966). Use of the correlation coefficient to evaluate radar and raingage should be based in logarithms of observed rates and Eq. (10) should be used to normalize calculated coefficients to a standard range of rainfall intensity, perhaps 1 - 10 mm/hr.

REFERENCES

Armijo, L., 1966: Statistical properties of radar echo patterns and the radar echo process. *J. Atmos. Science*, 23, 560-568.

Brandes, Edward A. and Wilson, James W., 1988: Measuring Storm Rainfall by Radar and Rain Gage, Chapter 11, pp. 171-189 in *Instruments and Techniques for Thunderstorm Observation and Analysis*, E. Kessler, Ed., 2nd Edition, Norman, Okla., Univ. of Okla. Press, 268 pp.

Croxton, Frederick E. and Cowden, Dudley J., 1939: *Applied General Statistics*, Prentice Hall, New York, 944 pp.

Hoel, Paul G., 1971: *Intro. to Mathematical Statistics*, 4th Edition, New York, John Wiley & Sons, Inc., 409 pp.

Joss, Jürg and Albert Waldvogel, 1990: Precipitation measurement and hydrology, Chapter 29a, pp. 577-606 in *Radar in Meteorology*, D. Atlas, Ed., Boston, Mass., Amer. Meteorol. Soc., 806 pp.

Kessler, E., 1966: Computer program for calculating average lengths of weather radar echoes and pattern bandedness, *Journal of Atmos. Science*, 23, 569-574.

Zawadzki, I., 1990 & 1991: Letters to E. Kessler dated October 24 & April 10, respectively.

Zawadzki, I., C. Desrochers, E. Torlaschi, and A. Bellon, 1986: A Radar-Raingage Comparison, pp. 121-124 in *Preprints*, 23rd Conference on Radar Meteorology, Snowmass, Colo. Printed by the Amer. Meteorol. Society, Boston, Mass.

APPENDIX

The simulation for the averaging process discussed in Section 6 involved steps as follows:

1. A population of 50,000 observations for X and Y was created using uniform random number generators. Ten observation cells were created, 1 to 10, where the range of the data for each cell was from its mean -1 to its mean +1. Five thousand observations were created in each cell.
2. A random sample was selected over the entire range or over some specified subset of cells of size 1000. This sample was then divided into ten replicates of 100 observations each.
3. For each sample of 100, the following correlation coefficients were found:
   a. Between X and Y for the individual observations (correlation sample [cs] = 100);
   b. Between X and Y for the means found by averaging two values, cs = 50; five values, cs = 20; 10 values, cs = 10;and 20 values,cs = 5.
4. The mean and standard deviation for the 10 replicates was calculated.

Comparison of Raindrop Size Distribution Measurements by Three Methods

B.E. Sheppard and P.I. Joe

Atmospheric Environment Service of Canada,
4905 Dufferin St., Downsview, Ont., M3H 5T4

1. Introduction

Accurate measurements of drop size distributions (DSDs) are fundamental in cloud physics for the study of the processes that modify the raindrop sizes. Models of the coalescence and breakup mechanism show that a negative exponential DSD will evolve into a three-peaked equilibrium DSD (Valdez and Young, 1985; List et al., 1987). These results are based on laboratory experiments of the coalescence and breakup of colliding drops. Measurements to confirm the multi-peaked spectra are plagued with uncertainties regarding instrument calibration, sampling statistics and sensitivities. Measurements by DSD sensors, each based on a different detection principle, are compared, to ascertain the reliability of the resulting spectra.

2. The Instruments

The instruments are a Joss-Waldvogel Disdrometer (JWD), a Particle Measurement Systems (PMS) 2DGS Spectrometer and an Atmospheric Environment Service (AES) Precipitation Occurrence Sensor System (POSS). They were operated during the summer of 1990 at the King Weather Radar Facility of AES (Crozier et al., 1991). Instantaneous rainfall rates were also measured by an Optical Rain Gauge (Model ORG-505) manufactured by Scientific Technology Incorporated, a tipping bucket and a Belfort Universal Weighing Gauge.

The POSS is a bi-static, X-band, continuous wave radar (Sheppard, 1990a) originally designed as a present weather sensor for automated observing stations. The transmitter and receiver are housed separately and mounted on a frame 45 cm apart. The antennas are oriented 20° from the vertical so that the beam axes intersect midway between them, and about 31 cm above the horizontal plane through the centre points of their radomes.

The POSS measures the Doppler power density spectrum from all raindrops in a volume of air referred to here as the "measurement volume". This volume is a function of drop diameter. Approximately 400 Fast Fourier Transform power density spectra (128 point) are averaged per minute.

The JWD, manufactured by Distromet of Basel, Switzerland has been used for cloud physics research for many years (Joss and Waldvogel, 1967). This probe has a sampling area of 50 cm^2. The channel boundaries were recalibrated to account for non-linearities (Sheppard, 1991b).

The 2DGS (PMS) probe is a shadowing probe manufactured by Particle Measuring Systems, Inc. of Boulder, Colorado. It is similar to the non-greyscale probes except that the shadow of the particles passing through the beam are quantized at four intensity levels of obscuration (0%, 50%, 75% and 100%). The optics are configured such that the probe has a nominal resolution of 150 microns. Thus, the sample width of the sixty-four element photodiode array is 0.96 cm. The distance between the arms of the probe is 22.5 cm resulting in a nominal sample area cross-section of 20 cm^2. The sizing and timing performance of this system has been described elsewhere (Joe and List, 1985). The images were processed with a "center-in" technique to extend the sample volume for large drop sizes.

3. Statistical sampling errors

Statistical sampling errors (Gertman and Atlas, 1977; Joss and Waldvogel, 1969) differ for the three instruments because of their different sampling volumes and the diameter interval of the measurement channels. For the JWD and the PMS, the volume sampled per second is a function of the sampling area and the terminal velocity. For the POSS, it is a function of the combined antenna beam pattern and the FFT processing speed. Random fluctuations in the number of drops n_j of diameter D_j in the measurement volume are assumed to follow a Poisson distribution with a mean $\overline{n_j}$ and standard deviation $\overline{n_j}^{1/2}$. If $\overline{n_j}$ is less than one, the Poisson distribution cannot be applied. The sampling errors for the three instruments are compared by assuming a Marshall-Palmer (M-P) DSD (1948). Figures 1, 2 and 3 compare the sampling errors using a rainfall rate of 4 mm h^{-1} and a one minute averaging period for the JWD, the PMS and the POSS, respectively. The dashed line alternates between $\overline{n_j} + \overline{n_j}^{1/2}$ and $\overline{n_j} - \overline{n_j}^{1/2}$ in successive channels. This curve gives an indication of the multiple peaks that could develop caused by sampling errors alone.

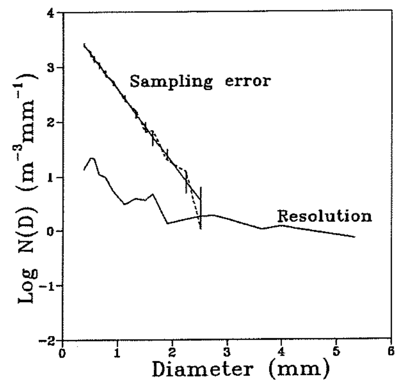

Figure 1: Sampling errors for the JWD.

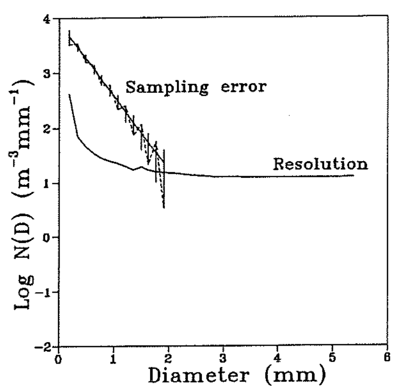

Figure 2: Sampling errors for the PMS.

The DSD corresponding to one count per channel, for a one minute averaging period, is the curve labelled "Resolution". For the JWD, it is irregular because of the non-uniform width of the channels. For the PMS calculations, we have assumed that the "probe active time" is 50% of the elapsed time.

The primary sampling error for the POSS is a bias caused by the large variability in the received power from different locations

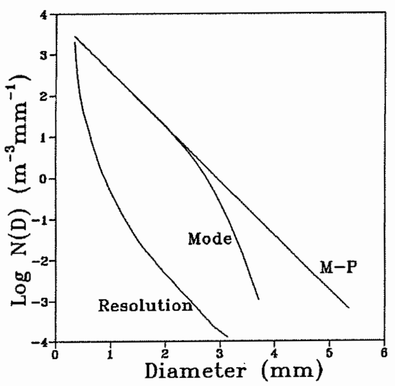

Figure 3: Sampling errors for the POSS.

in the measurement volume due to the combined antenna gains and the R^{-2} factors in the bistatic radar equation. The random fluctuations in the number of drops in the measurement volume are a second order effect. In Figure 3, the curve labelled "M-P" is the DSD retrieved from a synthetic Doppler power spectrum corresponding to a rate of 4 mm h^{-1}, assuming no sampling errors. The curve labelled "Mode" is the most probable DSD that would be retrieved. The underestimation at large drop sizes can be corrected.

The sampling volume of the JWD is approximately a factor of 4 larger than the PMS, assuming the latter is active 50% of the time. The sampling volume of the POSS is one order of magnitude larger than the JWD at small diameters, increasing to 2.5 orders of magnitude at large diameters. Therefore, the POSS has a greater probability of detection of the large drops than the JWD or PMS.

The minimum number concentration, N(D), required to exceed the measurement resolution of the POSS is increasingly less than that of either the JWD or the PMS, respectively, as drop diameter increases. However, below about 0.75 mm, the minimum resolution of the POSS becomes increasingly large. The estimated N(D) at small drop sizes is sensitive to the accurate measurement of the power at the corresponding Doppler frequencies. Errors can occur due to errors in the ambient noise spectrum estimation or low frequency artifact caused by splashing of drops on the sensor.

While a long averaging time may reduce the statistical sampling errors it may "smooth out" details of the evolution of the multimodal nature of the DSD that is of interest to cloud physicists.

4. Results

4.1 Rainfall Rates

The daily integrated amounts from the JWD, the POSS, the ORG, and the Belfort Universal Weighing Gauge were compared to the tipping bucket rain gauge for the experimental period (Fig. 4). The results of a linear least squares fit for each sensor are given in Table 1. The standard error of estimate (SEE) is expressed as a percentage of the average of the daily amounts for the days included in the comparison. The JWD showed the smallest SEE of 25% about the linear fit and the POSS the largest SEE of 46%. These are similar to the Belfort gauge comparison (39%).

Quantitative comparison of DSDs from the three sensors is difficult for several reasons. The data from the sensors were recorded on different systems and clock drifts were unavoidable. Also the sensors were separated by a few metres in order to avoid interference effects.

4.2 Time History

Fig. 5 shows a greyscale presentation of the DSDs from the three instruments. Drop size is represented along the abscissa, time

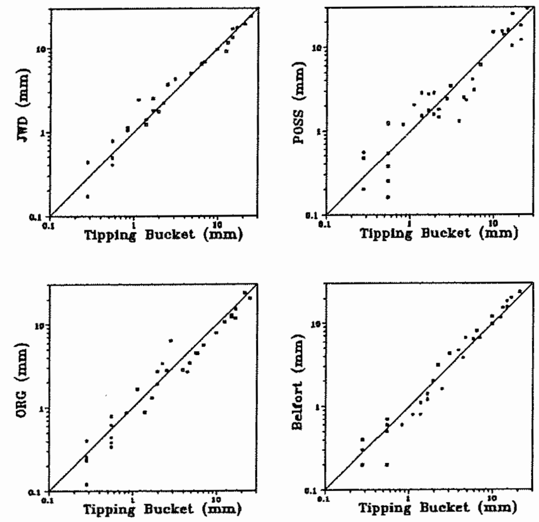

Figure 4: Daily accumulated rain amount for all sensors compared to the tipping bucket rain gauge.

Table 1: Tipping Bucket comparisons.

Sensor	No. of Observations	Intercept (mm)	Slope	SEE (% of mean)
JWD	28	0.34	0.94	15%
POSS	39	-0.01	1.0	46%
ORG	32	0.11	0.88	25%
Belfort	40	-0.17	1.11	39 %

is represented along the ordinate direction and the logarithm of the number concentration is displayed in greyscale. Light shades are large number concentrations and dark shades are low number concentrations. Black represents no particles detected. This type of presentation visually compensates for slight time differences. Exponential distributions are represented as a linear gradation of greyshades (light to dark) from small to large drops.

Several comments can be made for this figure:

- Within this rain event, the DSDs are quite variable. There was no steady-state in the recorded data.
- The POSS is able to observe large drops not evident in the other sensors. The concentration of the large drops is very small.
- Qualitatively, the three sensors are similar. In the mid-range of drop sizes, the DSDs exhibit similar behaviours: concentrations increase and decrease in a similar manner.
- For light rains, the PMS probe appears to be the most sensitive and the POSS appears to be the least sensitive. As a present weather sensor, the POSS detection algorithm is designed to minimize false reports, which in part accounts for missing light rain.
- Large concentrations of small drops are never observed with JWD, whereas they are observed with the other two probes. The presence of the high concentrations of small drops are consistent between the PMS and POSS probes.
- Re-calibration of the JWD channel widths reduces the presence of the multimodal peaks.
- Sometimes N(D) decreases at small drop sizes.

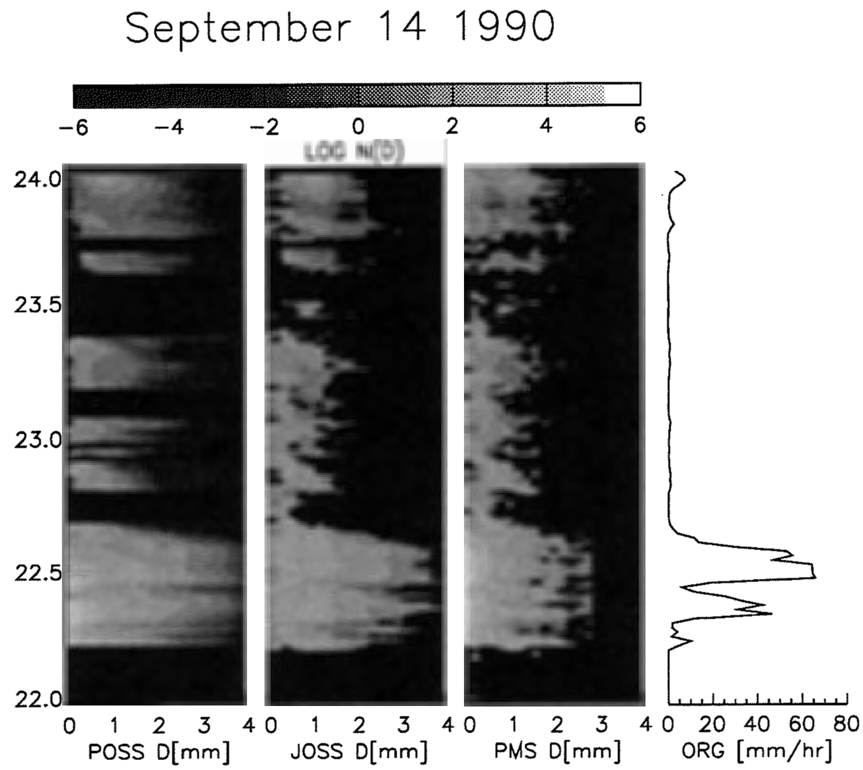

Figure 5: Two hour rain event from Sep. 14, 1990 2200Z to 2400Z.

- The PMS DSDs are not as smooth as the other two sensors which is a result of having the smallest sampling volume.
- Multiple peaks were observed at low rain rates. The PMS data showed greater variability due to smaller sampling size.

4.3 Individual Spectra

Some examples of DSDs have been selected to illustrate specific results of the comparison.

There was generally good agreement between the three sensors with respect to both the diameter sizing and the number concentrations. Fig. 6 shows the expected decrease in N(D) measured by the JWD and PMS at the diameters approximately corresponding to the "Resolution" curves given in Figures 1 and 2.

All of the sensors are capable of resolving "peaks" in the DSD with resolution comparable to those produced by coalescence-breakup models. In the example of Fig. 7, the POSS and JWD detect drops at about 2.5 mm. The minimum at 1.75 mm is below the resolution of the JWD. Fig. 8 shows three modes at diameters less than 2 mm. In this example, the POSS estimate of the diameter of each mode is less than the JWD which in turn is less than the PMS. In addition to the three modes below 2 mm, the POSS is able to detect peaks at 2.4 and 3.1 mm. Calculations indicate that at these two diameters the POSS would underestimate N(D) by about 1.4 and 1.7 decades, respectively.

Fig. 8 compares average DSDs from all 3 sensors during a 4 min period when the ORG reported a rain rate that was essentially constant at 64 to 65 mm h^{-1}. The POSS and JWD agree quite well for D>1 mm but the PMS shows a deficiency of drops in the range of 1 to 3 mm. For D<1 mm the POSS and PMS both show N(D) in excess of the M-P model while the JWD shows a sharp decrease. These features have been seen in other cases.

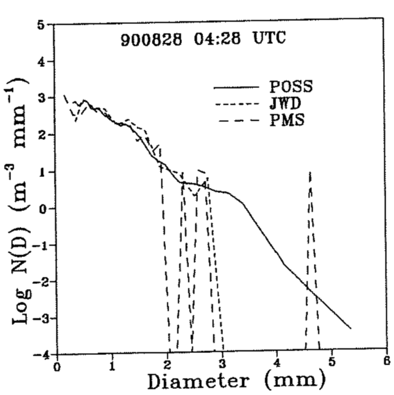

Figure 6: Spectra from Aug 28, 1990 0428Z.

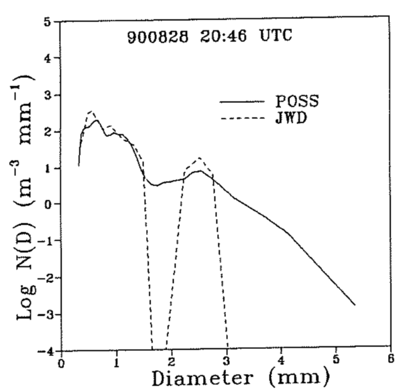

Figure 7: Spectra from Aug. 28 1990 2046Z showing multiple peaks.

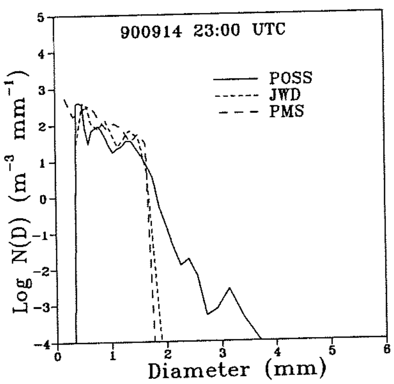

Figure 8: Spectra from Sep. 14 1990 2300Z showing multiple peaks.

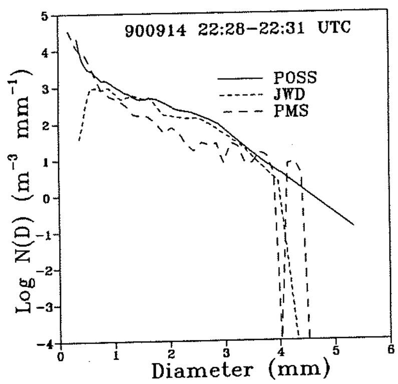

Figure 9: Spectra from Sep. 14 1990 2228Z-2231Z.

5. Discussion and Conclusions

In general, the three DSD meters showed good agreement in a variety of rainfall rates. All are capable of resolving modes in the DSD of the magnitude predicted by the collision-breakup models.

Each method has inherent strengths and weaknesses. The JWD and PMS have smaller sampling volumes than the POSS and therefore have poorer resolution. They also have a lower probability of detection for large drops than the POSS. The POSS is more vulnerable to vertical winds although these are unlikely to be large when averaged over one minute. Motion from human or animal activity near the POSS is another source of error.

Large drops (>3mm) are observed by the POSS in light rain situations. On some occasions, at small drop sizes, the POSS substantially overestimates N(D) when compared to the other two probes. This may be caused by splashing of drops on the radomes which generates low frequency spectral power. The inversion algorithm will estimate a large number of small diameter drops due to this power. Since the experiment reported here, the software that computes the POSS Doppler spectra has been modified to detect and reject the signature of drop impacts in the time domain data. Preliminary results indicate that this has greatly reduced the effects of drop impacts in heavy rain.

Upon occasion, the POSS underestimates N(D) for D<0.5 mm due to overestimation of the ambient noise. Precipitation may reduce the clear air atmospheric noise prior to its onset. This effect is identified by negative spectral components after the start of rain.

6. References

1. Crozier, C.L., P.I. Joe, J.W. Scott, H.N. Herscovitch and T.R. Nichols, 1991: The King City operational Doppler radar: development, all-season applications and forecasting, Atmosphere-Ocean, 29, 479-516.
2. Gertzman, H.S. and D. Atlas, 1977: Sampling errors in the measurement of rain and hail parameters. J. Geophys. Res., 82, 4955-4966.
3. Joe, P.I. and R. List, 1985: Testing and performance of two-dimensional optical array spectrometers with greyscale. J. Atmos. Oceanic Technol., 4,139-150.
4. Joss, J. and. A. Waldvogel, 1967: A raindrop spectrograph with automatic analysis. Pure Appl. Geophys., 68, 240-246.
5. Joss, J. and A. Waldvogel, 1969: Raindrop size distribution and sampling size errors." J. Atmos. Sci., 26,566-569.
6. Joss, J. and A. Waldvogel, 1977: Comments on "Some observations on the Joss-Waldvogel rainfall disdrometer." J. Appl. Meteor., 16,112- 113.
7. List, R., N.R.Donaldson and R.E.Stewart, 1987: Temporal evolution of drop spectra to collisional equilibrium in steady and pulsating rain. J. Atmos. Sci. 44, 3127-3133.
8. Marshall,J.S., and W. McK. Palmer, 1948: The distribution of raindrops with size. J. Meteor., 5, 165-166.
9. Sheppard, B.E., 1990a: The measurement of raindrop size distributions using a small Doppler radar. J. Atmos. Oceanic Technol. 7, 255-268.
10. Sheppard, B.E., 1990b: Effect of irregularities in the diameter classification of raindrops by the Joss-Waldvogel Disdrometer. J. Atmos. Oceanic Technol. 7, 180-183.
11. Valdez, M.P., and K.C.Young, 1985: Number fluxes in equilibrium raindrop populations: A Markov chain analysis. J. Atmos. Sci. 42, 1024-1036.

Remote Sensing of Liquid Water Content with Combined Radar-Radiometer System

Jin-li Liu and Ling Zhang

Institute of Atmospheric Physics, Chinese Academy of Sciences, Beijing 100029, PRC

I. Introduction

Quantitative measurement of liquid water content (LWC) in cloud is significant for improving weather modification and investigating cloud-radiation interaction. Remote sensing of LWC with single radar is currently widely employed in operational works. Owing to the influences of many complicated factors, the accuracy of radar-derived LWC distribution is still difficult to meet application and research needs. Microwave (MW) radiometer has great potential use in LWC measurement. Both theoretical study and field measurement show that a MW radiometer can measure the total amount of LWC in cloud along the antenna path with good accuracy, but it is unable to give the range resolution. A method of LWC and rainfall measurements with combined active-passive (radar-radiometer) MW remote sensing making use of advantages of both radar and radiometer was proposed in the end of 70's (LU and LIN,1980), some successes have been achieved in the studies of the principle and the numerical simulation of LWC measurement with this method (LIN et al.,1984). However, very limited field measurement results have been given so far, which was not enough to show the capability of the method with a reliable statistical analysis. In this paper we intend to discuss the results of field measurements and the statistical analysis of showering precipitating clouds at Xiang-he,Hebei province of CHINA.

II. Observation and Retrieval Method

1. Observation

The observation was made with a combined radar-radiometer system at X-band. The radar and radiometer have co-antenna and operate alternately with waveguide switch, the beam width of antenna is 1.8^0(JING et al.,1982).The sampling time of MW radiometer observation is 10 seconds, and the received radar echo power is digitized and recorded with 150 m range bins along the ray path for LWC measurement.

2. Retrieval algorithm

The main idea of retrieval algorithm of LWC distribution from the simultaneous observation of the combined radar and radiometer system can be briefly described as follow: Firstly, from MW brightness temperature of ray path by the radiometer we may derive the total attenuation (optical depth) τ_0. Then we may derive the distribution of attenuation coefficient $\sigma(r)$ from radar reflectivity along ray path. With the constraint that the integration of $\sigma(r)$ along the path τ_c should equals to τ_0. Finally, through σ-M empirical relation the LWC distribution along ray path M(r) is obtained (LIN et al.,1984) .

III. Results

1. Statistic Results

In the summer of 1990, field observation were made with the improved combined system. During the observation of precipitating clouds, the antenna was vertically pointing and simultaneous rainfall rate R was measured with tipping-bucket rain-gauge with 0.1 mm rainfall resolution. 127 data sets of combined observation of precipitating clouds at different stages were used to retrieve the vertical LWC distribution. The verification of the accuracy of retrieved LWC is very difficult owing to lacking of direct measurement of LWC. As an alternative way, we made comparison of retrieved LWC at surface which was obtained by an extrapolation from the measurement at lowest possible altitude referred to the cloud evolution stage, with measured M at surface through empirical R-M relation. By this comparison, we obtained the relative RMS deviation is 44.8 % for the 127 data sets, and the correlation coefficient between retrieved and measured LWC is 0.937. To show the improvement of present remote sensing of LWC with combined system, we also made LWC distribution with radar observation itself, which is conventional method based on empirical Ze-M relation. The results are that for the same 127 data sets the relative RMS deviation is 119.9% and the correlation coefficient is 0.451.

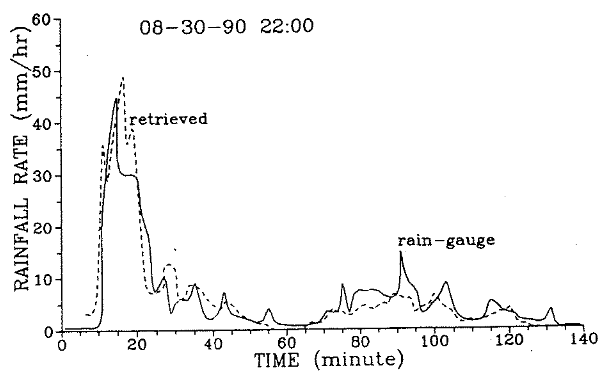

Fig.1 Rainfall rate versus time obtained by retrieved method and rain gauge

Fig.1 shows the observed LWC with combined system on 30 Aug.1990. It is also shown the corresponding rain rates measured by rain-gauge. It can be seen that the variation trends of rain rate distribution obtained from two methods are similar.

2. Temporal and spatial distribution

Although LWC distribution (spatial and temporal) can be also measured by single radar, it was shown that the observed results have a big difference comparing with rian-gauge data, not only in the values of rain rate, but also in the trends of their variation. In contrary, by using combined system we obtained relatively satisfactory LWC distribution, both in spatially and temporally

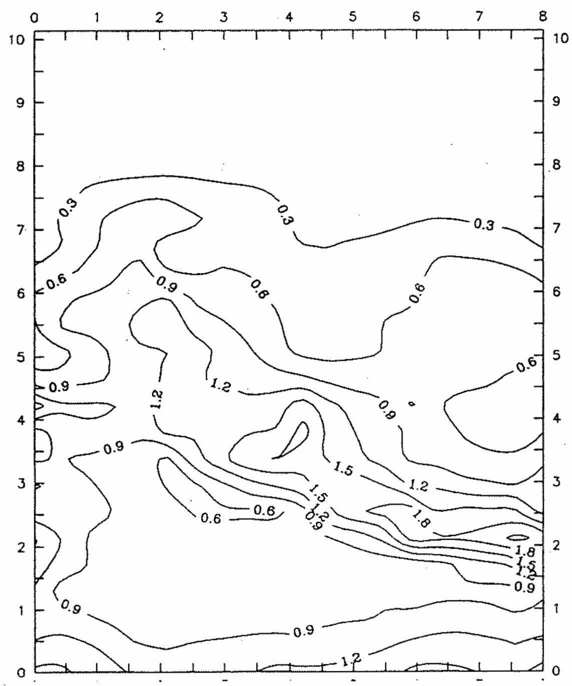

Fig 2. Temporal profile of LWC in Showering precipitating cloud

Fig.2 is a temporal profile of LWC observed by combined system on 30 Aug.1990 in Xiang-he station. It shows that the intensive LWC area (>1.5 g/m^3) located in about 4 km height at 22:11, in next few minutes , this area rapidly dropped down to 2 km . and the corresponding rainfall rate from 11.9 mm/hr rapidly increased to 36.0 mm/hr (see Fig.1).

3. Vertical distribution of LWC

It is known that the vertical structure of LWC in a cloud plays an important role in space-borne rainfall measurements (LIU et al. 1989). For deducing vertical model of LWC in cloud, we did field observation of LWC with combined system in different type and different evolution stages of cloud. Fig.3 is an example of the statistic results for different evolution stage of vertical profile of LWC in showering clouds. It was found that the vertical structure of LWC in initial stage, mature stage and decaying stage are obviously different.

IV. Conclusion and Discussion

1. LWC measurements with combined system is obviously better than with single radar . Comparative study indicates that LWC measurement with single radar has large deviation compared with rain-gauge data. In contrary, LWC distribution (temporal or spatial) measured by combined system are much improved. The advantage of combined method comes from (a) it based on the relation σ-M which is relatively stable and insensitive to the variation of particle size distribution. (b) The absolute calibration of radar is not necessary, it requires only keeping stable during short time-interval which is easy to satisfied. In contrary, single radar method rely on Ze-M relation which is unstable and strongly sensitive to precipitation type and particle size distribution. And it requires absolute calibration of radar .

2. The errors of LWC measurement by combined method had been generally discussed by LIN et al. (1984). It should be emphasized that in this paper only a simplified situation was discussed, i.e., it is assumed that all radar return and MW thermal emission were contributed by water drops. This would results in some errors because of incorrect consideration of the contribution by ice and mixed-phase particles. Further consideration of differentiating the contribution by particles with different phases are needed.

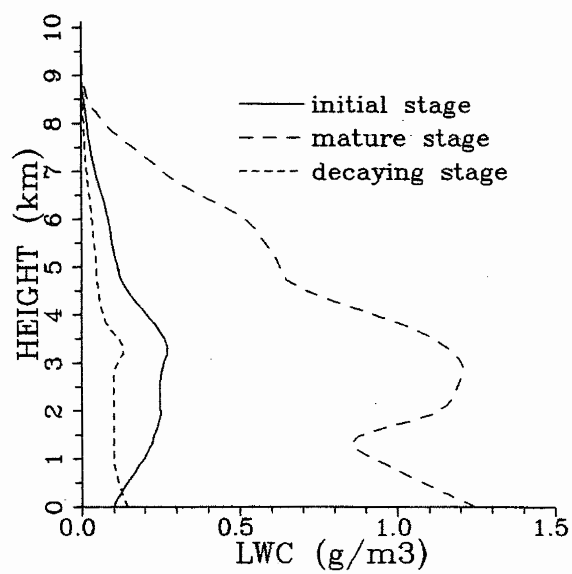

Fig 3. Average vertical profile of LWC in different evolution stages of precipitating cloud

References

Jing Qiyi et al. (1982), A ground-based combined dual-wavelength MW radar radiometer system for measurements of LWC of clouds and rainfall distribution, IAP, Annual Report, Vol.1, 19-28

Lin hai et al (1984), Remote sensing of liquid water content in cloud and rainfall distribution by a combined radar-radiometer system, Scientia Atmospherica Sinica, Vol.8, No.3, 332-340

LIU Jinli, Xiao Jianming and zhang Ling (1989), The Effect of Ice Water Content on Space-borne Microwave remote Sensing, ATMOSPHERIC RESEARCH 24 (1989),5-12

Lu Daren and Lin Hai (1980), Comparison of radar and microwave radiometer in precipitation measurements and their use, Scientia Atmospherica Sinica, Vol.4, No.1, 30-39

Rain Generated Noise in a Container of Water and the Development of a "Wet Disdrometer"

D.Harris, G.L. Austin, C.D. Stow

Physics Department, University of Auckland, Private Bag 92019, Auckland
New Zealand

1. Introduction & Project Description

The possibility of monitoring rainfall over a body of water by analyzing the resulting underwater noise is to be examined.

In the past eight years much insight has been given to the dynamical and acoustical processes involved in individual drop impacts on a free surface of water (Nystuen, 1986, Pumphery *et. al.*, 1989,1990, Medwin *et. al.*,1990). Armed with these insights, one can start to make quantitative predictions (Oguz & Prospereti,1991) that changes in drop-size distribution, rainfall intensity and horizontal wind speed will result in measurably different underwater noise spectra due to the total rainfall for a well defined surface area and time.

Identifying the drop-size distribution, rainfall intensity and wind speed as the principal variables of the problem, their effects on underwater noise are to be studied via Monte Carlo methods. The sound level spectra for rain falling into water are to be simulated and then later refined by observing the real sound levels obtained when a container of water (equipped with hydrophone) is exposed to rain in various meteorological conditions. This, of course, requires simultaneous monitoring of the three principal variables mentioned above(Scrimger *et al.,* 1987).

Drop-size spectra will be obtained using an optical disdrometer (Stow & Jones, 1981). Rain rate will be logged with a high resolution digital electronic raingauge (Stow *et. al.* 1991). And lastly, windspeed is monitored with a conventional 3-cup anemometer. The use of a container in which to listen to the rain means that one can concentrate on the rain noise alone without having to deal with other noise creating mechanisms such as wave-breaking and fauna related noises that one would have in lakes and oceans.

The main advantage of the simulation is that the acoustic effects of rain rate,wind speed and drop-size spectra may be studied independently.

Before the simulaton can be fully realized, however, it requires for its input, a detailed parameterization of the acoustic signals generated by the impact of individual drops of various sizes and impact angle. The signals generated by single drops and how they are studied comprises the experimental portion of this project and are discussed below. Following will be a brief description of the simulation's structure and how it incorporates information from individual drop impacts.

2. Individual Drop Impacts (Experimental)

The acoustic signal due to a single drop consists of an impulse due to initial contact of the drop with the water's surface (lasting up to 100usec) and occasionally is followed by a damped sinusoidal signal due to a bubble which is sometimes entrained by the resulting fluid dynamical processes. A bubble is always entrained by terminal fallspeed raindrops in the 0.4mm to 0.53 mm size range(Oguz & Prosperetti, 1991). Raindrops in this range have the right size and velocity to cause what is known as Regular Entrainment. An example of Regular Entrainment is shown in figure 1. Bubble entrainment outside this range is considerably less probable. Although bubbles are generated for a narrow range of drop sizes, the bubbles radiate with peak pressures typically five times greater than that of the the initial contact impulse and frequencies ranging from 10-20 kHz.

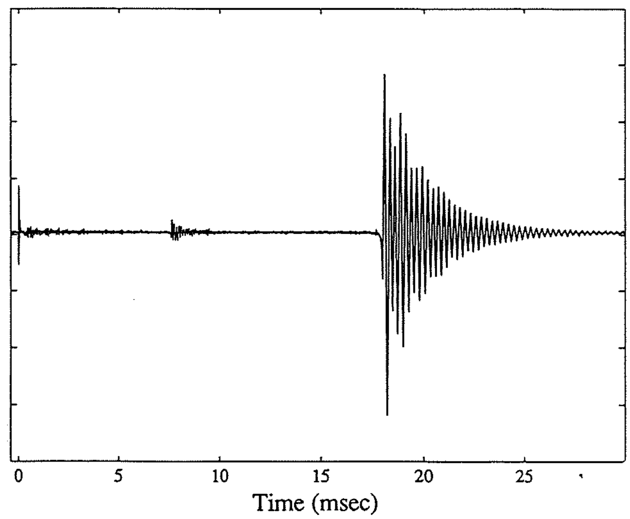

Figure 1-Pressure signal (in arbitrary units) for an artificial rain drop showing Regular Entrainment. The initial impulse is shown at t=0, followed by the encapsulation of a bubble at t=17ms (the small signal at ~7ms is due to a smaller droplet following the main drop and is an artefact of drop production).

The discovery of Regular Entrainment has led to a considerable amount of literature and data concerning the radiative properties of the bubbles formed, as well as effects that oblique impact angles will have on bubble production. This means that most of the data needed for the simulation already exists with a few exceptions, two of which are outlined below and are the main results to be acquired from the experiment with single drops.

Figure 2, below shows the experimental set-up being used. Its important feature is that it uses real rain which thus ensures the drops are falling at terminal velocity and that acoustic signals are obtained for a wide range of drop radii without the need for developing a range of drop makers.

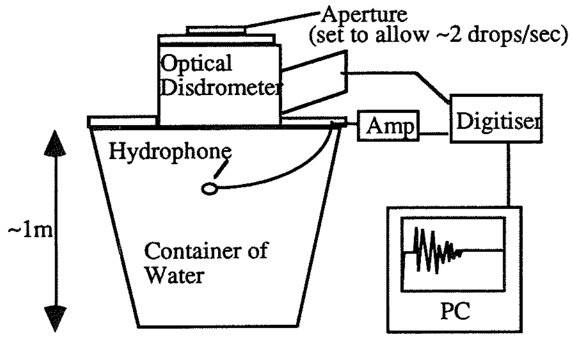

Figure 2- Simplified schematic of individual drop experiment used to simultaneously determine drop' size and the underwater acoustic signal produced on impact with the water's surface.

The optical disdrometer of Stow and Jones (1981) offers ~5% accuracy down to ~0.1mm radius. The feature of this disdrometer most important here is that it is a non-destructive disdrometer. The underwater acoustic signal obtained from a wide-band hydrophone (EDO model 6600) is digitised for signals in the 1 to 40kHz range. A similar set-up will be used to obtain rain (as opposed to individual drop) noise spectra with with the disdrometer placed beside the container; the raingauge and anemometer are placed nearby.

The first result to be acquired concerns bubble noise and has thus far not been well enough documented for the purposes of the simulation. The information needed is the relation between bubble size and the drop-size producing them. This is not a well-defined relationship and takes the form of a distribution, although, in general, frequency increases as drop-size approaches the centre of the regular entrainment range.

The evident importance of bubble noise does not mean that the initial impulse noise is not important. A study of this component of the noise has, however, not been well documented since Franz(1959). This noise is dominant at lower frequencies than that of bubble noise and it thus is also necessary to re-examine its features and verify Franz's results which were obtained using very large drops which are subject to drop shape distortions.This is the second essential result to be obtained from experiments with individual drops.

3. The Monte Carlo Realisation (Theoretical)

The data obtained by analysing individual drop impacts and the pre-existing literature are used to obtain the necessary parameters for the simulation. The parameters are used in the algorithm listed below :

1)Number of drops falling into the container in a specified time is determined for specific rain rate from the drop-size spectrum.

2)Random drop-sizes are generated from Marshall-Palmer and other theoretical or experimental drop-size spectra.

3)Drop speed is determined using the 3rd order regression of Dingle and Lee (1972) and thus allowing the estimation of the impact angle for specified wind speed.

4)Whether or not a bubble is generated is determined. This is dependent on drop size and impact angle (the probability of bubble entrainment decreases with increasing impact angle(Medwin *et. al.*,1990)).

5)If a bubble is entrained its sound level spectrum is determined using existing theory of acoustic bubble phenomena and the results of the individual drop experiment.

6)Sound level due to initial impulse noise is calculated using results from the individual drop experiment.

7)Impulse and bubble noise spectra are incoherently summed.

8)Steps 2 to 7 above are repeated for the number of drops determined in 1.

9)The results of 7 are incoherently summed for all drops and thus the total rain noise sound level spectrum is determined.

4. Acknowledgments

The authors are indebted to the entire Underwater Acoustics group at Auckland University for their technical assistance and guidance particularly Dr. M.D Johns, Prof. A.C. Kibblewhite, & Dr. J.B. Earnshaw. The authors would also like to thank Dr. S.M Tan for his invaluable help in programming the data acquisition software. Special thanks to M.Hollis, M.Camilleri, P.L. Pearce, D.Lodge-Osborne, K.R. George and the rest of the technical staff for their help.

5. References

Dingle, A.N. & Y.Lee, 1972: Terminal Fallspeeds of Raindrops. J. Appl. Meteorol. **11** p. 877-879

Franz, G.J., 1959: Splashes as Sources of Sound in Liquids. J. Acoust. Soc. Am. **31** p. 1080-1096

Medwin, H., A.Kurgan & J.A.Nystuen, 1990: Impact and Bubble Sound from Raindrops at Normal and Oblique Incidence. J. Acoust. Soc. Am. **88(1)** p.413-418

Nystuen,J.A., 1986: Rainfall Measurements Using Underwater ambient noise. J. Acoust. Soc. Am. **79(4)** p. 972-982.

Oguz, H.N. & A. Prosperetti,1991: Numerical Calculation of the Underwater Noise of Rain. J. Fluid Mech. **228** p.417-442

Pumphery, H.C., L. A. Crum & L. Bjorno, 1989: Underwater Sound Produced by Individual Drop Impacts and Rainfall. J. Acoust. Soc. Am. **85(4)** p.1518-1526

Pumphery, H.C. & P.A Elmore, 1990: The Entrainment of Bubbles by Drop Impacts. J. Fluid Mech. **220** p. 539-567

Scrimger, J.A., D.J. Evans, G.A. McBean, D.M. Farmer & B.R. Kerman, 1987: Underwater Noise due to Rain, Hail and Snow. J. Acoust. Soc. Am. **81(1)** p.79-86

Stow, C.D. & K. Jones, 1981: A Self-Evaluating Disdrometer for the Measurement of Raindrop Size and Charge at the Ground. J. Appl. Meterol. **20** p.1160-1176

Stow, C.D, S.G. Bradley, K. Paulson, & L. Couper, 1991: The Simultaneous Measurement of Rainfall Intensity, Drop-Size Distribution and Scattering of Visible Light. J. Atmos. Sci. **30** p. 1422-1435

INSTRUMENTED VEHICLE FOR GROUND-BASED MICROPHYSICAL OBSERVATIONS

R. A. Montañez and F. García-García

Centro de Ciencias de la Atmósfera
Universidad Nacional Autónoma de México
Ciudad Universitaria, D. F. 04510 México

1. INTRODUCTION

In order to have a complete and accurate evaluation of cloud and precipitation phenomena, it is important to observe the entire chain of microphysical events from nucleation, through cloud particle growth evolution, to precipitation occurring at the surface. In recent years, this kind of studies has been improved on with the use of cloud and precipitation particle spectrometer probes, in particular those manufactured by Particle Measuring Systems (PMS) (Knollenberg 1976).

There has been lately a growing interest in the effects of sensor mounting location on airborne measurements of particle concentrations, images and spectra obtained from PMS probes (Baumgardner 1984). It is known that airborne measurements can be significantly affected by airflow distortion depending upon the mounting location and the parameter being measured (Drummond and MacPherson 1985, MacPherson and Baumgardner 1988, Norment 1988), and that these effects are often subtle and difficult to quantify. Greater attention is been paid to these considerations when instrumenting aircraft and using the resulting data.

Although originally designed to be mounted on an aircraft, PMS probes have been modified to operate in a stationary ground configuration to measure some of the microphysical characteristics of precipitation at the ground surface. This system provides a more consistent means of measurement, a larger sample and finer time resolution than manual techniques. A direct application of PMS instruments to surface measurements is limited, however, by the need to know the speed of the particles as they pass through the sampling area, so that they can be properly detected. In the particular case of 2D-probes in relative motion to the sampled particles, the airspeed controls the residence time of a particle in the imaging beam and can thus be used to control the clock rate of the photodiodes. But with a stationary instrument the residence time of the particle is controlled by its terminal velocity and by wind speed. Thus, the resultant images are distorted along the direction of particle motion, since the clock rate of the photodiodes is constant and usually faster than the slow and variable fall speeds of the particles. To remedy this and other problems also related to FSSP's, probes have been fitted with parabolic horns and suction fans to draw particles through the sampling area at a constant speed (see, for example, Humphries 1985). Unfortunately, the errors introduced by aspiration into the measurements are not easily obtained, yet are required before the data can be used quantitatively (Deshler 1988, Norment 1987).

In this article an instrumented van, wich was conditioned with the purpose of performing ground-based, in-motion microphysical observations of fog and precipitation, is presented. The instrumentation includes three PMS spectrometers with related peripheral equipment and a portable weather station. The probes are mounted for operation in a horizontal orientation as on an aircraft, so penetrations into fog clouds and precipitation shafts can be achieved. The particular characteristics of the instrumented vehicle are discussed, as well as the differences in sampling performance of the instruments as compared to ground-fixed ones. The importance of quantifying the effects of airflow distortion due to the presence of the van is also mentioned.

2. DESCRIPTION OF THE EQUIPMENT

Three PMS spectrometers (FSSP-100, OAP-2D-C and OAP-2D-P), a cup anemometer and a wind vane were mounted on a specially designed structure on a Ford Pick-Up truck. The spectrometers were placed for operation in a horizontal orientation, as on an aircraft (Figure 1). Care was taken to place the probes above and ahead of the front of the van in an attempt to minimize airflow distortion caused by the moving vehicle. A thermometer and a barometer were used to monitor the local meteorological situation of the study region. A data acquisition system (DAS) along with a tape recorder and a CRT display were mounted on a rack located in the cargo

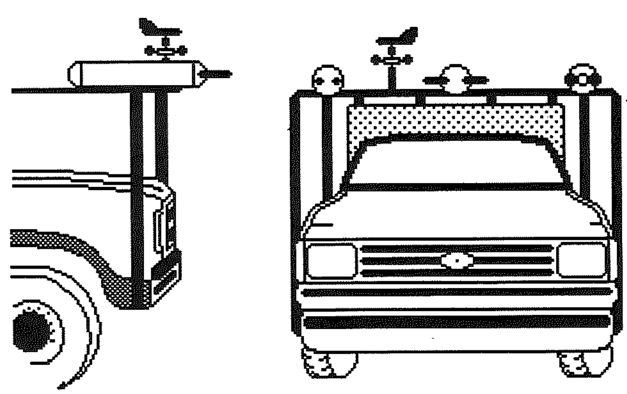

Figure 1. Schematic side and front views of the instrumented vehicle.

compartment of the truck. A power generator was used to drive the electronic and recording systems, thus allowing continuous data collection. A portable computer was placed in the driver's cabin to record the meteorological observations and the sampling velocity. During sampling, the van presents the same driving characteristics as if it were not instrumented. A schematic diagram of the instrumentation disposition is presented in Figure 2.

3. DISCUSSION

The development of the instrumented vehicle allows one to carry out monitoring of fog and precipitation at the ground, from the microphysical point of view, having several applications in radar- and modeling-related studies, characterization of clouds and studies on weather modification.

The ground-based, mobile system described above provides a more consistent means of measurement than manual or photographic techniques, wich present difficulties in making objective observations. The manual collection techniques are tedious and often lack consistency and the desired accuracy. The limited number of samples observed typically represent a small sample volume, and the frequency of observations usually lack the time resolution necessary to document rapidly changing precipitation characteristics. The analysis of such a data set is also painstaking. A great deal of time is usually required to manually measure and categorize the sample. Therefore, to detect the characteristics of the studied system, observations must be taken continuosly and at the proper location.

As compared to the aspirated ground-fixed method of monitoring, the mobile one presents several advantages such as to provide information on the spatial structure of single fog or precipitation events, and an easier data processing. It also allows one to partially overcome the problems of overcounting and dependence in concentration on particle size, such as those reported for aspirated probes (Holroyd 1986, Norment 1987, Deshler 1988). On the other hand, if the probe is used without aspiration, the determination of the sample volume could be erroneous due to the variable particles speeds through the sampling area.

The instrumented van has been and is being presently used in two projects related to fog characterization and precipitation monitoring in Mexico (García and Montañez 1991). From this experience, it is known that a better performance is obtainted when the van is driven on a paved road in order to avoid vibrations that could produce distortions in acquired data. During sampling, it is also convenient to avoid other vehicular traffic in order to produce minimal distortion on the environment. The road must be as regular as possible to allow "soft" driving conditions and to maintain the sampling velocity practically constant. In the above-mentioned case studies, the van was driven at a constant speed of 18 m/s. Also, the experience derived from the knowledge that distortions can be produced when monitoring in airborne or aspirated conditions indicates that an evaluation of the distortions caused by the truck motion and the structure used to mount the spectrometers should be performed. This study is currently under way.

4. SUMMARY AND CONCLUSIONS

A van has been instrumented with the aim of performing microphysical characterization of

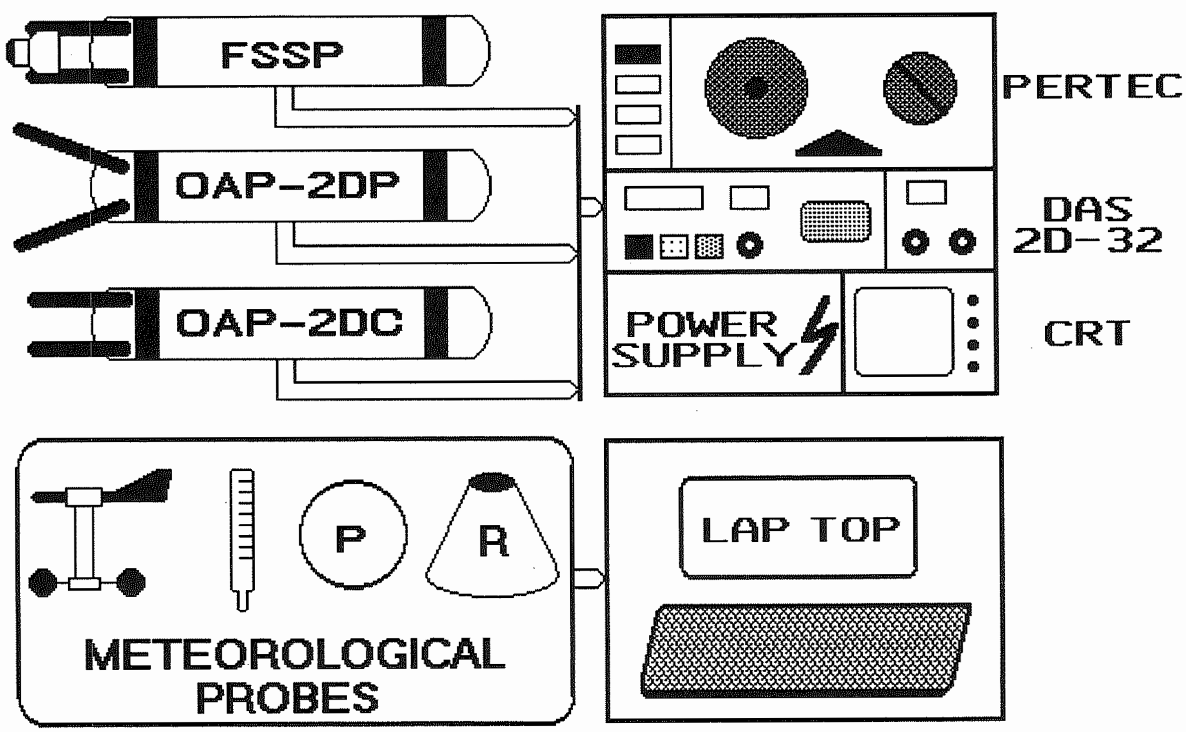

Figure 2. Schematic diagram of the disposition of the instrumentation.

clouds and precipitation at the ground. The equipment includes three PMS spectrometer probes with related peripheral equipment, and a portable weather station with a lap-top computer for meteorological data recording. Sampling can be carried out in motion, as on an aircraft, this having many advantages over traditional, ground-fixed sampling techniques.

The instrumentation is currently being used to perform raindrop size distributions measurements in Mexico City, and there are plans to continue the above-mentioned fog characterization field project in several parts of the country.

Acknowledgements. The authors appreciate the continuous technical support provided by Messrs. J. Escalante, M. García, A. Rodríguez, M. Silva and V. Zarraluqui. Part of this study was sponsored by the Instituto Mexicano de Tecnología del Agua (IMTA) of the Comisión Nacional del Agua, México.

REFERENCES

Baumgardner, D., 1984: The effects of airflow distortion on aircraft measurement. A workshop summary. *Bull. Amer. Meteor. Soc.*, **65**, 1212-1213.

Deshler, T., 1988: Corrections of surface particle probe measurements for the effects of aspiration. *J. Atmos. Oceanic Tech.*, **5**, 547-560.

Drummond, A.M., and J.I. MacPherson, 1985: Aircraft flow effects on cloud drop images and concentrations measured by the NAE Twin Otter. *J. Atmos. Oceanic Tech.*, **2**, 633-643.

García-García, F., and R.A. Montañez, 1991: Warm fog in eastern Mexico. A case study. *Atmósfera*, **4**, 53-64.

Holroyd, E.W.III, 1986: Surface sampling of a snowstorm by a 2D-C probe with and without aspiration. *J. Atmos. Oceanic Tech.*, **3**, 755-758.

Humphries, J.H., 1985: Application of an airborne Optical Array Probe for ground-based microphysical observations. *J. Atmos. Oceanic Tech.*, **2**, 252-259.

Knollenberg, R.G., 1976: Three new instruments for cloud physics measurements: The 2-D Spectrometer, the Forward Scattering Spectrometer Probe, and the Active Scattering Aerosol Spectrometer. *Prepr. Int. Cloud Phys. Conf., July 26-30, Boulder, Colo*. Amer. Meteor. Soc., 554-561.

MacPherson, J.I., and D. Baumgardner, 1988: Airflow about King Air wingtip-mounted cloud particle measurement probes. *J. Atmos. Oceanic Tech.*, **5**, 259-273.

Norment, H.G., 1987: Numerical studies of sampling efficiencies of the ASCME and PMS aspirator hydrometeor measurement instruments. *J. Atmos. Oceanic Tech.*, **4**, 253-263.

-----, 1988: Three-dimensional trajectory analysis of two drop sizing instruments: PMS OAP and PMS FSSP. *J. Atmos. Oceanic Tech.*, **5**, 743-756.

AERODYNAMIC CONSIDERATIONS IN PRECIPITATION COLLECTOR DESIGN

D. J. Hall, J. G. Irwin and S. Upton

Warren Spring Laboratory
Stevenage, Hertfordshire, United Kingdom, SG1 2BX

1 INTRODUCTION

When sampling precipitation for subsequent analysis it is important both to avoid contamination and to collect a chemically representative sample. To achieve the former, precipitation collectors are set well above the ground, typically about 2m, in order to avoid contamination by wind-raised material. Hence they are well exposed to the wind. Over a grass surface (of aerodynamic roughness height 2cm) windspeed at 2m is about 60% higher than at 0.4m (the height of most conventional gauges); as a result undercollection can be significantly greater. Moreover, since these deficiencies are strongly dependent upon windspeed and the falling speed of the precipitation, samples may become unrepresentative, being weighted towards material precipitating at low windspeeds and with high falling speeds. In earlier studies, concerned solely with snow collection (eg Hall *et al*, 1989), we used improved aerodynamic characteristics to reduce displacement and acceleration over the collector, thereby improving collection efficiency. This paper describes further investigations of the fundamental features of wind effects on precipitation collectors.

2 EXPERIMENTAL

Measurements of the aerodynamic properties of various designs of precipitation collectors were made in an open-circuit, fan-driven wind tunnel with a working section 22m long, 1.5m high and 4.3m wide (Hall *et al*, 1993). There is a faired inlet containing four screens and two honeycombs, for flow conditioning and straightening, and a wide angle diffuser at the exit. This is also fitted with a honeycomb to control any fan-generated swirl which would otherwise recirculate back into the tunnel inlet. Most of the experiments reported here were conducted at windspeeds of 3 ms^{-1}. In order to mimic the atmospheric turbulence to which samplers are normally exposed, the wind tunnel roof and floor were roughened using battens of 45mm height and 22mm depth uniformly spaced 600mm apart, fixed along the whole length of the tunnel. This set up a rough-walled channel flow with the highest scales and intensities of turbulence readily manageable in the wind tunnel.

Measurements of the wind flow over the openings of the various precipitation collectors were made using a pulsed-wire anemometer (Bradbury and Castro, 1971). Velocity profiles were measured above the centres of the openings of the collectors and, where they were of sufficient depth, down into the collectors themselves. Fig 1 shows a typical velocity profile. The maximum velocity over the collector opening and the height above the opening at which it occurred were determined by extrapolating curves through the two parts of the profile and taking the values at their point of intersection. This is a somewhat arbitrary definition, but it is a fairly easy point to determine and convenient for rapid assessment of collector performance. It is normally close to the upper edge of the mixing layer at the boundary between the main windflow and the separated flow region within the collector, and so tends to overestimate the velocity increment and displacement a little.

3 RESULTS

3.1 Effect of Aspect Ratio on the Performance of Cylindrical Collectors

The aerodynamic performance of precipitation collectors depends upon their relative depth, the ratio of depth to diameter, and upon other details of their shape (Sevruk *et al*, 1989). Reducing collector depth reduces the displacement and acceleration of the flow over the opening, by decreasing the aerodynamic blockage caused by the collector. One of the problems in assessing performance lies in determining to what extent this is a result of the relative depth of the collector or of the details of its shape. In order to clarify this problem we carried out a preliminary exercise to determine the basic flow characteristics of precipitation collectors, using a series of standard cylinders of varying depth to diameter. The intention was to provide a reference data set against which different collectors could be compared, so that it would be clear to what extent changes in collector shape resulted in improvements or deterioration over the simple form. The cylinders used in the experiments were all straight sided and of 200mm diameter; the heights varied between 10mm and 600mm.

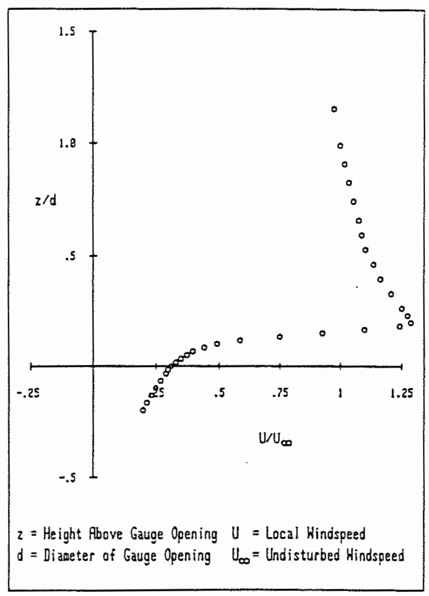

Fig 1. Profile of windspeed over a typical deep cylindrical collector

Acceleration and displacement of the wind flow over the cylinders were measured in the relatively high turbulence flow in which all other measurements were made. In addition some earlier measurements made in low turbulence flow, of about 1-2% intensity compared with the 6% intensity of the present work, were examined. Both showed the same general trends and the same values of displacement to within the level of accuracy of the measurements. There is a difference of about 10-15% between the two sets of acceleration measurements, the lower turbulence measurements showing the higher acceleration. The data show an initial rapid increase in both acceleration and displacement as the aspect ratio of the collector increases. Beyond an aspect ratio of about 0.5, there is an abrupt change in behaviour and though both continue to increase it is at a slow rate. The highest value of the displacement for the high turbulence measurements was about 0.22 and of the acceleration 0.25; it seems likely that these values are close to the maximum that will occur with a cylinder of any aspect ratio.

It is not surprising that some limit to the displacement and acceleration should be reached. There clearly must be some depth of cylinder beyond which the flow at its end becomes a purely 'local' phenomenon independent of the depth. What is perhaps surprising is the relatively small depth of cylinder at which this limit is approached, with an aspect ratio well below unity. It follows that if a precipitation collector is to make use of reduced depth in order to improve the flow over the opening, it must be quite shallow, with an aspect ratio below 0.5 and preferably below 0.2. There are practical difficulties associated with such shallow collectors, for example effective drainage of collected samples and splashing of large raindrops, particularly during heavy rainfall. However, it also follows that, if deeper collectors are preferred for practical reasons, then improvements to the flow over the collector opening must come from improved aerodynamic design.

3.2. Wind Flow over Cylinders and Novel Collector Designs

For comparison with the base data on rectangular cylinders, described above, measurements of flow displacement and acceleration were made over the openings of a number of collectors. The measurements were not intended to be comprehensive but covered a wide variety of different types, including both conventional collector shapes and some novel forms.

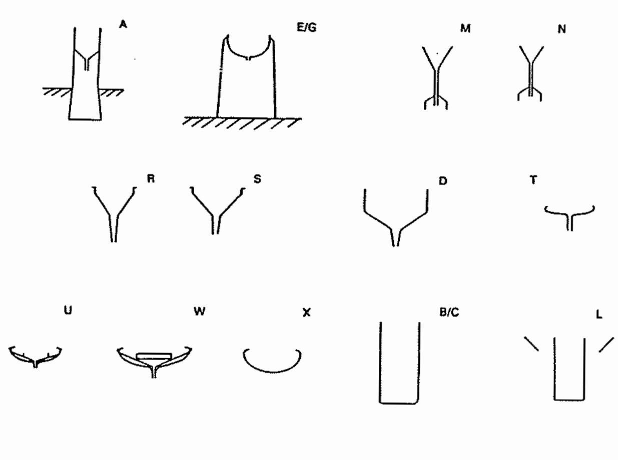

Fig 2. Outline diagrams of collector shapes tested

Diagrams of the outlines of the collector shapes are shown in Fig 2. The approximate aspect ratios of the collectors are listed, along with the measured data, in Table 1. Fig 3 plots displacement against acceleration. The generic types are indicated by the shape of symbol, circles are for cylindrical (or closely so) collectors, diamonds are for funnels and squares for 'bowls' and streamlined shapes. A line, drawn from data for the rectangular cylinders, is included with values of the aspect ratio appended at the appropriate points.

There was a wide variation in the acceleration and displacement over the different collectors that was not merely a function of their aspect ratio. Values of the acceleration ranged between 0.07 and 0.4, and of the displacement between 0.09 and 0.55. When compared with the cylinder of equivalent aspect ratio, the streamlined shapes showed similar levels of acceleration but significantly reduced displacement, the funnels showed greater acceleration but reduced displacement, while the cylindrical shapes showed a very wide spread in both acceleration and displacement.

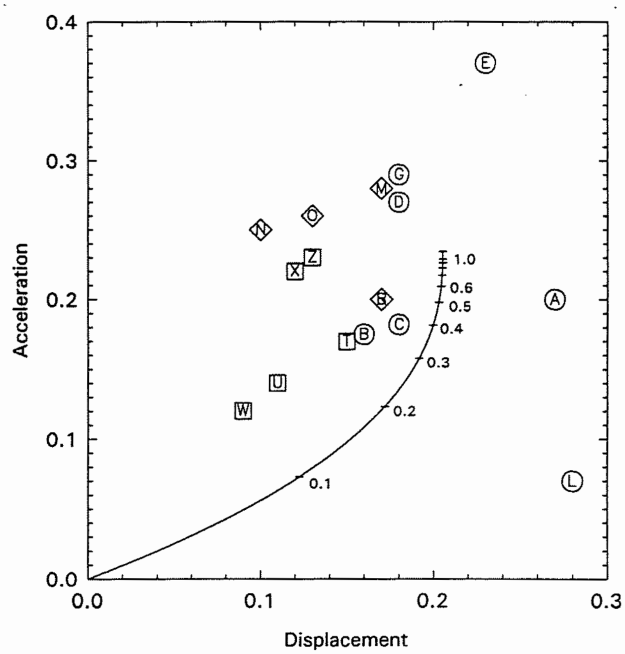

Fig 3. Acceleration against displacement for various collector shapes

Compared with the basic cylinder data, the Met Office gauge (A) showed a higher displacement and slightly lower acceleration. These differences were presumably a result of its being set on the ground and in a shear layer, rather than elevated and in a region of approximately constant velocity as were the basic cylinder measurements. The NILU (B) and proposed ISO gauge (C) produced similar results to one another, with a little less displacement and acceleration than the basic cylinder data. The differences are only just outside the order of accuracy of the experiment. The IoH tipping bucket rain gauge was tested both elevated, E, and on the ground, G (its normal operating position). Setting the gauge on the ground appeared to reduce both the displacement and the acceleration. The displacement was then similar to the standard cylinder measurements, but the acceleration was much greater. The remaining cylindrical gauge tested was the ASTM dust gauge, L, which had a flow deflector around it set at an incidence of 45°. This exhibited one of the lowest values of the acceleration (0.07), but a relatively high value of the displacement, well beyond that of the equivalent cylinder. The main feature of the measurements over the different cylindrical gauges is the confusing picture that they present. The measurement of acceleration and displacement is not a very precise one (partly due to the highly turbulent) and is of about 10% accuracy. However, this is not sufficient to explain the differences between designs that have been observed.

The funnels tested were all of about the same aspect ratio, around 0.8. The two larger funnels, R and S, showed similar levels of acceleration and displacement, not far from the values of the equivalent cylinders. The two smaller funnels, M and N, with a

Table 1. Measurements of Accelerations and Displacements For Various Collectors

Type of Collector	Symbol	Diameter (mm)	Aspect Ratio	Acceleration	Displacement
Met. Office 5" Rain Gauge	A	127	2.68	0.2	0.27
NILU Dust Gauge	B	200	2	0.175	0.16
Proposed ISO Dust Gauge	C	200	2	0.235	0.223
BS Dust Gauge	D	307	0.62	0.27	0.18
Tipping Bucket Gauge(Elevated)	E	200	1.9	0.37	0.23
Tipping Bucket Gauge(Ground)	G	200	1.9	0.29	0.18
ASTM Dust Gauge (45° Shield)	L	150	2	0.07	0.28
UK Rain Funnel (Large)	M	150	0.73	0.28	0.17
UK Rain Funnel (Small)	N	115	0.74	0.25	0.1
UK Rain Funnel (Small + Bottle)	O	115	0.74	0.26	0.13
Large Funnel 1	R	198	0.75	0.2	0.17
Large Funnel 2	S	245	0.6	0.2	0.17
Metal Frisbee	T	227	0.15	0.17	0.15
Snow Collector (Mk II)	U	202	0.32	0.117	0.1038
Snow Collector (Mk III)	W	310	0.29	0.126	0.085
Deep Bowl	X	204	0.44	0.22	0.12
Deep Bowl (+ Cone Insert)	Z	204	0.44	0.23	0.13

steeper side of 60° included angle, showed larger values of the acceleration but similar or lower levels of displacement, the smaller funnel showing the smallest value, of 0.1, distinctly lower than for the other three. Though of different sizes, the two smaller funnels were identical in shape and this variation between them is a little surprising. However, an earlier measurement on a larger funnel, of 200mm diameter as against 115 and 152mm used here, also gave a gave a value of the displacement of 0.11. These variations may simply be due to experimental error, but there could be deeper reasons for the differences. It is possible for Reynolds number effects to occur readily in flows of these scales, but in the present case this seems a little unlikely. The funnels tested also had a variety of shapes of lip to the opening (the larger funnels had vertical edges to the openings, while the smaller funnels had sharp cut edges at the 60° funnel angle) and this is known to affect the resultant flow. The smaller funnels are normally mounted over a shrouded collecting bottle, of about 210mm diameter and 250mm below the funnel opening. This condition is plotted as point O; there was no significant change compared with the isolated funnel.

The results for the streamlined shapes show the clear advantage that can be obtained by carefully shaped collectors, though this seems to be in reduced displacement more than in reduced acceleration. One of the collectors plotted under this heading (labelled 'T') was the inverted frisbee dust gauge, which has some limited streamlining. It had the same displacement but worse acceleration, though the slope of the graph in this region is so steep that the accuracy of the measurement may not be very great. Since this gauge had a distinctly improved collection performance over the conventional deeper cylinders, it appears that this was due to its reduced depth rather than its shape. The performance of the streamlined collectors will be discussed later. Fig 3 also shows that some designs of collector perform distinctly less well than a plain cylinder.

The use of flow deflecting devices around cylindrical collectors was investigated. The results have been reported in detail elsewhere (Hall *et al*, 1993). It was concluded that flow deflectors could reduce the acceleration over a collector opening but could not greatly reduce the displacement. However, with the streamlined collector shapes investigated previously it had proved possible to reduce the displacement quite markedly as a result of reducing the aerodynamic blockage. The acceleration had also been reduced, but not to such a great extent. It seemed, therefore, that a combination of deflector and streamlined collector shape might achieve the desired reduction in both parameters.

The streamlined collector shapes used were the MkII and MkIII snow collectors. These are of similar shapes; the MkIII collector being 40% larger. Most of the experiments were carried out with the MKII collector, which is 227mm in diameter, since its smaller size made the experiments more convenient. Only flat plate deflectors were used, there being insufficient time to investigate more sophisticated designs. In order to minimise the possibility of contaminated particles or water droplets being blow off the deflector into the collector, it is desirable that the deflector should be as far below the collector opening as possible. Ideally it should be tucked quite closely under the outer edge of the collector body but, in practice, it did not prove possible to do this. From an aerodynamic point of view it is desirable that the deflector position should allow a free flow of air between its inner edge and the body of the collector. If the gap is too small the airflow is blocked and the effectiveness of the deflector is reduced.

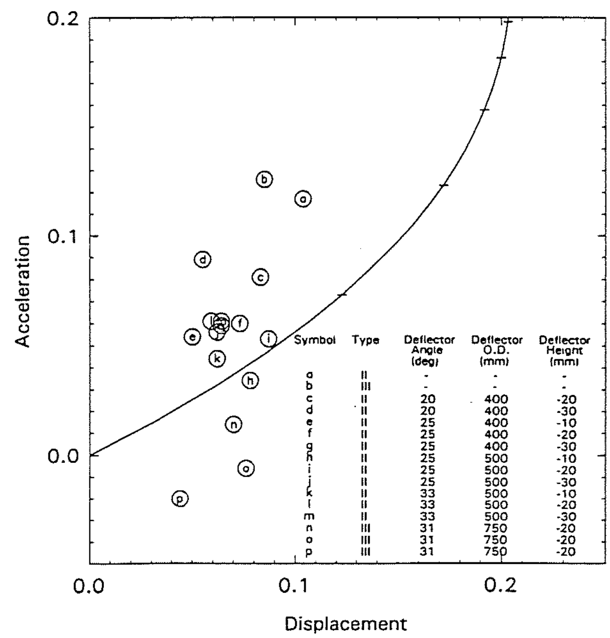

Fig 4. Effect of flow deflectors on streamlined collectors

The results of the experiments are shown in Fig 4, which is of large scale compared with earlier figures. It can be seen that it was possible to reduce the acceleration over the collectors to zero and below. The displacement showed a rather smaller reduction and most of the deflector arrangements produced values of the displacement around 0.06. In fact the true displacement was less than this. The method of determining acceleration and displacement, using the intersect of lines drawn through the two parts of the windspeed profile over the collector, defines approximately the upper edge of the mixing layer which grows over the collector opening rather than the middle of the mixing layer. This error, which is of the order of 0.03-0.05 is not important for the larger values of displacement, but affects these smaller readings more seriously.

The best results were obtained with deflector incidences around 25°-35°. With the MkII collector the best results, h and k in Fig. 4, were with deflectors of 500mm diameter set at incidences of 25°

and 33° respectively with the outer edge of the deflector set 10mm below the top of the collector. This achieved values of the acceleration of about 0.03 and of the displacement of about 0.07. When this arrangement was scaled up pro rata to fit the MkIII gauge, a better performance resulted, n, o and p, which showed some windspeed dependence, the performance improving as the windspeed rose. These changes were presumably due to Reynolds number effects, the performance improved as the Reynolds number increased, whether due to increased size or to increased windspeed. The best condition was obtained with a flat plate deflector of 750mm OD at an angle of 31°, set 20mm below the collector opening (Fig 5). The acceleration, with some variation, was close to zero and the displacement was around 0.04-0.07. What this value of the displacement meant in practice is shown in Fig 6,

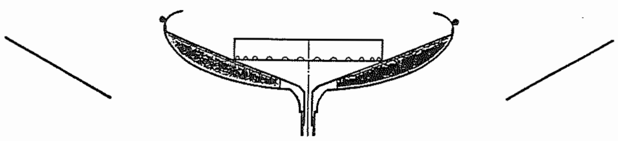

Fig 5. Most effective deflector arrangement, 750mm deflector ring around MkII snow collector

which shows windspeed profiles at five stations along the centreline of the collector opening for condition n, a windspeed of 2.8 ms^{-1}. It can be seen that the mixing layer grew to a depth of about 25mm at the downwind end of the opening and that above this the windspeed profile was nearly uniform at a value close to the reference windspeed of 2.8ms^{-1} (this value in fact varied slightly over the area in which the gauge was placed). Thus as well as could be practicably managed, there was a flat, uniform and unaccelerated flow over the collector opening. This flow pattern should, in principle, produce some over collection as, because of the reduced velocities in the mixing layer, the mean windspeed over the gauge is a little less than the undisturbed windspeed. However, when compared with the flow patterns over conventional gauge designs, this point is a minor one. Flow visualisation of condition n showed that there was a separated flow off the top edge of the deflector, but that the separation line reattached itself back on to the front of the collector before the opening. The collector opening was thus properly exposed to the main windflow, not a separated flow region.

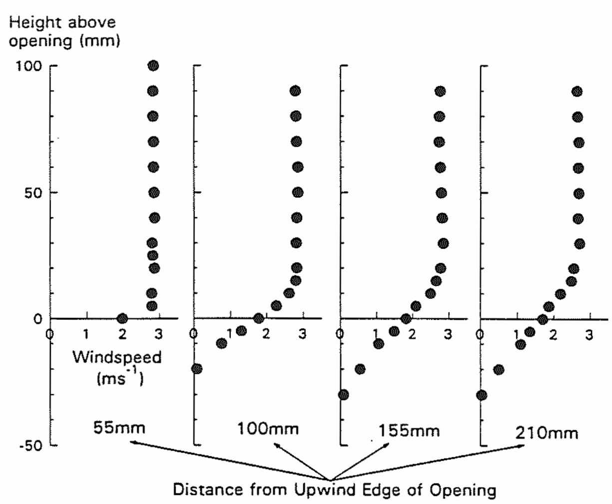

Fig 6. Windspeed profiles over streamlined collector with most effective deflector (750mm diam, 31° incidence)

This sort of design is not entirely satisfactory; there is a possibility of liquid droplets being blown off of the top edge of the deflector into the collector opening. It would be better if the deflector had an attached flow over its upper surface, so that there was no flow separation region near to the body of the collector. This should also lead to a more efficient deflector, which could then be reduced in size and set lower down. However, to be effective at the low Reynolds numbers at which it must operate, it would need careful aerodynamic design probably incorporating a deflector with a slotted-flap and boundary layer control devices.

4 CONCLUSIONS

a) Windflow over the openings of cylindrical precipitation collectors is directly affected by the aspect ratio of the collector. The acceleration and displacement of the flow over the opening, the critical features which affect collection efficiency, are only reduced if the aspect ratio is below about 0.5. Above this value the flow over the opening is not greatly affected by the depth of the collector. Thus quite shallow cylindrical collectors are required if a good collection efficiency is to be obtained.

b) Measurements of the acceleration and displacement of the flow over a variety of existing collector designs have shown a very wide range of values. Funnel shaped collectors show a reduced displacement compared to the equivalent cylinder, but about the same acceleration. Streamlined collector shapes show reductions in both acceleration and displacement, with the greater reduction in the displacement.

c) An investigation of the use of flow deflectors around cylindrical collectors has shown that there is a fundamental problem with designs of this sort, which is that the aerodynamic blockage of the cylindrical collector remains unaffected, as do the flow patterns associated with it. As a result, flow deflectors can reduce acceleration, but not displacement.

d) A combination of a flow deflector and a streamlined collector shape makes possible the reduction of both acceleration and displacement over the collector opening. Using this approach it has been possible to design a collector with a flat, unaccelerated flow over the opening.

5 REFERENCES

Bradbury L J S and Castro I P (1971). A pulsed-wire technique for velocity measurement in highly turbulent flows. *J. Fluid Mech., 49,* 657-691.

Hall D J, Irwin J G, Stone B H and Upton S L (1993). Aerodynamic considerations in precipitation collector design. *Proc. National Measurement System Symposium on Airborne Pollutants Measurement.* Warren Spring Laboratory, 17-18 March 1992.

Hall D J, Upton S L, Campbell G W, Waters R A and Irwin J G (1989). Further Development of a Snow Collector for Use in Acid Deposition Studies. Stevenage: Warren Spring Laboratory, LR 752(PA).

Sevruk B, Hertig J A and Speiss R (1989). Wind Field Deformation Above Precipitation Gauge Orifices. *Proc. Symp. Atmospheric Deposition.* Baltimore, May 1989. IAHS Publication No 179.

Acknowledgement

The funding of this work by the Department of Trade and Industry within their National Measurement System research programme is gratefully acknowledged. This paper is based on a presentation to a workshop within that programme.

USE OF COMBINED REMOTE SENSORS FOR DETERMINATION OF AIRCRAFT ICING ALTITUDES

Marcia K. Politovich[1]
National Center for Atmospheric Research
Boulder CO

B. Boba Stankov and Brooks E. Martner
Wave Propagation Laboratory
National Oceanic and Atmospheric Administration
Boulder, CO

1. INTRODUCTION

At present there is no reliable method for determining the location of aircraft icing conditions other than to examine reports from pilots who have already flown through such areas. There is also no single instrument with the capability of detecting where supercooled liquid water, the substance responsible for aircraft ice accretion, resides in the atmosphere.

Recent developments in remote sensing, combined with improved capabilities for ingest, manipulation and display of information, have made it possible to examine the feasibility of using combinations of sensors to determine the altitude range of icing environments. This study uses a ground-based microwave radiometer in combination with a Radio Acoustic Sounding System (RASS) and a lidar ceilometer to estimate the level at which aircraft icing is expected.

Microwave radiometers have long been used to remotely detect liquid water. Popa Fotino et al. (1986) demonstrated the use of these instruments for detection of icing conditions. They found a strong correlation between integrated liquid water amounts >0.1 mm and reports of icing from pilots within 50 nm of the sensor location. In that preliminary study no attempt was made to determine the altitude range of the hazard.

A later paper by Popa Fotino et al. (1989) described a method by which a first guess of the hazard level could be obtained. The base of the icing environment was assumed to be the lower of either cloud base or the freezing level. The top was either cloud top or the -20°C isotherm. Measurements of icing from a research aircraft corresponded well with these estimates. The method presented in this paper is a further step in delineating the expected icing hazard.

2. SENSORS

Measurements were obtained during the 1990 and 1991 Winter Icing and Storms Project (WISP) in the Denver, Colorado, area. Numerous remote and *in situ* sensors were employed for the study of winter storm structure and evolution (Rasmussen et al. 1992), with particular emphasis placed on conditions leading to aircraft icing.

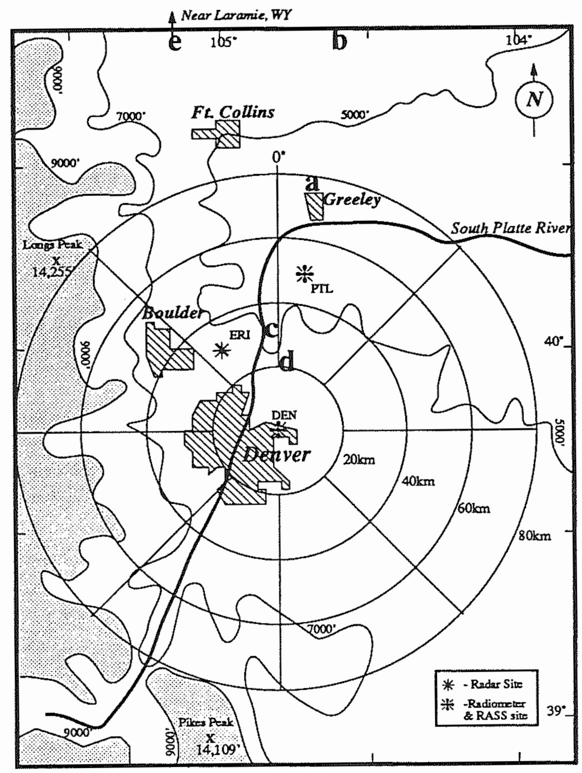

Fig. 1 Locations of facilities used in this study. Letters refer to N2UW soundings listed in Table 1.

The National Oceanic and Atmospheric Administration (NOAA) Wave Propagation Laboratory (WPL) operated dual-channel (20.6 and 31.65 GHz) microwave radiometers at Platteville (PLT) and Denver (DEN) during the WISP field studies (see Fig. 1). The characteristics of these instruments and the retrieval technique used to determine integrated vapor and liquid values are described by Hogg et al. (1983). Measurements were obtained every 2 min.

Temperature profiles were obtained using WPL RASS at PTL and DEN (May et al. 1990). The RASS technique combines an acoustic source with a wind profiling radar to track vertically the acoustic pulse.

[1]The National Center for Atmospheric Research is sponsored by the National Science Foundation.

The speed of the pulse is related to the virtual temperature. The PTL system uses a 49.8 MHz profiler and covers an altitude range of ~3-6 km AGL with 300 m resolution. The DEN system is at 915 MHz with a range of ~0.3-3 km AGL and resolution of 150 m. Soundings and surface measurements were combined and interpolated to provide a continuous profile from ~0.3-6 km AGL. The measurements used in this paper are hourly.

Cloud base height was obtained from a lidar ceilometer operated by the Denver National Weather Service (Schubert et al. 1987) at DEN (Fig. 1).

All the above measurements are available in near real time (a 20-min lag for the radiometer) at the NOAA laboratories in Boulder.

To estimate the top of the icing hazard, a moist-adiabatic approach was used (Stankov et al. 1991). It was assumed that the liquid resided in a single layer which began at the measured cloud base and was produced by adiabatic ascent of saturated air parcels. As the parcels rose the liquid water was calculated; total integrated liquid was summed until the value detected by the radiometer was achieved. This algorithm determined the top of the supercooled liquid, and thus the icing layer.

These estimates were compared with measurements from a K-band radar and a research aircraft. During the 1991 WISP field season, the NOAA WPL K-band radar (wavelength 0.87 cm) was deployed at Erie (ERI) as part of the sensor network. This sensitive radar has a relatively low detection threshold, nearly -50 dBZ at 1 km, and was used to reveal layers of cloud not distinguishable by other remote sensors.

The University of Wyoming King Air (N2UW) was used during both WISP field seasons to document the characteristics of the icing environment and to provide valuable *in situ* data on the cloud structure. The instrumentation is described by Cooper et al. (1984). Liquid water content from either a Forward Scattering Spectrometer Probe (FSSP) or a CSIRO-type hot wire probe were used to define the liquid cloud.

Thirty-five soundings through cloud were obtained by N2UW. Of these, only fourteen were composed of single-layer clouds; the distribution of number of cloud layers observed is shown in Fig. 2a. Profiles of liquid water in these clouds varied, but many layers shared the common characteristic of increasing liquid with height, with the maximum value lying near the cloud top. For these "ideal" profiles, the depth calculated using the moist-adiabatic approach was compared to the observed depth. The distribution of percentage of observed liquid cloud depth is shown in Fig. 2b; the mean value is 64%. The percentages do not show any trend with cloud base or top temperature, nor with total cloud depth. Further analysis of case studies may provide an adjustment, as suggested by Fig. 2b, which can be applied to the moist-adiabatic depth to bring it closer to the true depth of the cloud. One such case study is presented below.

Fig. 2 Frequency histograms from N2UW soundings of liquid clouds.

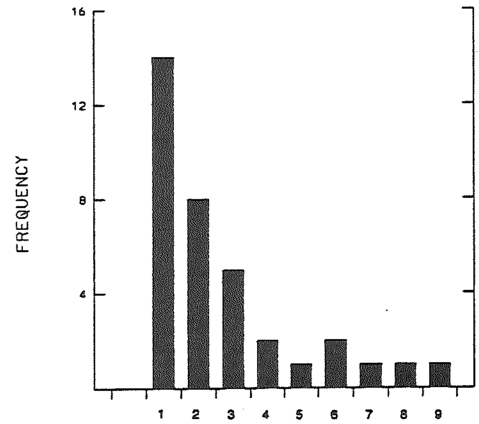

2a) number of cloud layers observed in each sounding

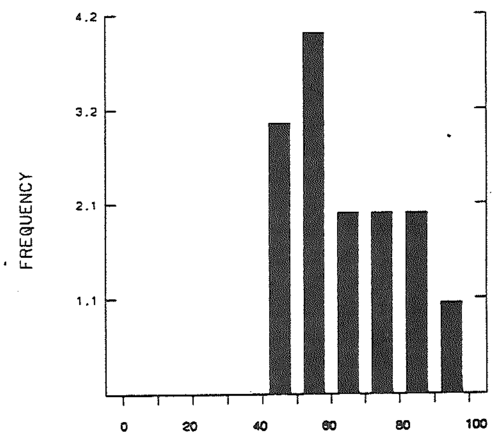

2b) percentage of observed cloud depth represented by the moist-adiabatic calculation for "ideal" clouds (see text)

3. EXAMPLE: 16 MARCH 1991

A 500 mb short wave with a closed circulation moved through the southern portion of the study region aiding in the development of a surface low on the lee side of the Rocky Mountains on 16-17 March 1991. The surface low tracked from southeast to northeast of the Denver area, providing overrunning and wrap-around conditions over eastern Colorado. Low clouds were present in the area through much of the 16th.

N2UW flew two research missions. The first documented the structure of a thin stratus cloud, while the second was conducted later in the storm to investigate the vertical structure of the wrap-around cloud associated with the cyclone. Soundings obtained in cloud are listed in Table 1. Considerable variability in cloud bases and tops is apparent within the temporal and spatial extent of these soundings.

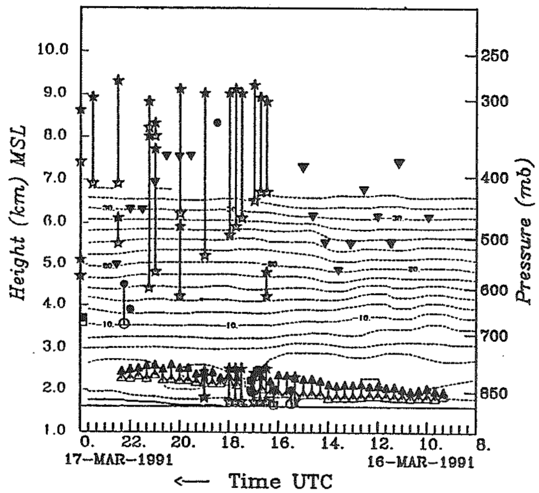

Fig. 3 Time-height profile of RASS-derived virtual temperature (°C) and cloud bases and tops from various sources. Open symbols denote cloud bases, closed symbols are tops. Information from the combined-sensor method for liquid cloud (triangles), K-band radar (stars), research aircraft liquid cloud (squares) pilot reports (circles) and satellite infrared imagery data (inverted triangles) are shown. Lines connecting symbols represent continuous cloud.

TABLE 1

N2UW Liquid Cloud Soundings, 16 March 1991

	time (UTC)	layers	distance from DEN (km)	liquid cloud alt(m), t(°C) base	top
a	1610	1	75	1634, -4.0	1994, -6.6
b	1646	4	121	2315, -3.3	2477, -4.2
c	1703	1	30	1930, -4.7	2224, -5.5
d	1705	2	21	1982, -5.0	2211, -5.8
e	2352	1	175	3544, -10.6	3697, -11.4

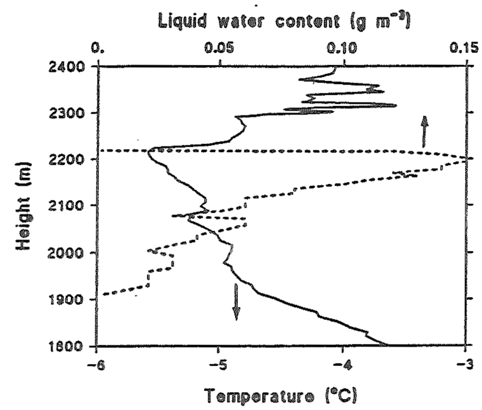

*Fig. 5 Temperature (solid line) and liquid water (dashed line) profiles measured from N2UW during sounding **c**, Table 1.*

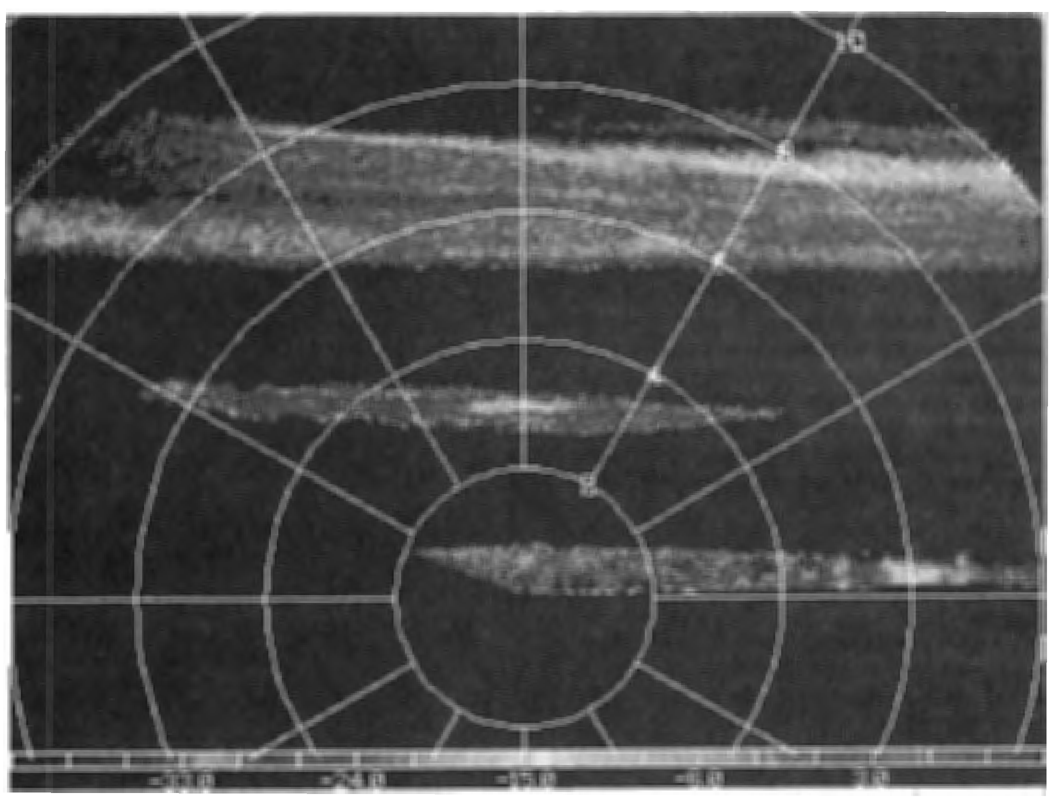

Fig. 4 RHI of reflectivity from the NOAA K-band radar at 1628 UTC, 16 March 1991. The RHI is along the 142° azimuth. Range rings are at 2 km intervals; the scale at the bottom indicates dBZ.

A comparison of cloud analyses is shown in Fig. 3. The K-band radar operated from 1521-1639 UTC, and from 1730 UTC until the end of the event. Top heights of the low level cloud are in good agreement with the liquid cloud top determined from both N2UW and the combined sensor method. Radar measurements of cloud base are slightly lower than those from the ceilometer. Light fog was occasionally reported in the area which cloud account for some of the discrepancy, also, ERI is 25 km distant from and 121 m lower in altitude than DEN. Cloud bases and tops from N2UW (which are for liquid cloud only) and from pilot reports in the Denver area consistent with these measurements of the lowest cloud layer.

The radar-detected cloud top altitude remains fairly constant although the cloud thickens through a lowering of its base. At times, additional layers are evident. A range-height indicator (RHI) display of reflectivity from the K-band radar is illustrated in Fig. 4. Considerable detail of the three cloud layers –low stratus, mid-level altostratus and cirrus – is evident.

Cloud tops from infrared satellite imagery above PLT are also shown in Fig. 3. These indicate upper level cloud at 1000-1500 UTC, and 1930-2330 UTC. Discrepancies between these and the K-band radar measurements could be due to differences in location or errors associated with satellite detection of thin cirrus layers.

Figure 5 shows temperature and liquid water profiles measured from N2UW during sounding **c**. Cloud top is associated with a temperature inversion of nearly 2°C. The maximum liquid water content is 0.15 g m-3, near the top of the cloud. As discussed above, this profile shape was commonly, but not always, observed in stratiform clouds during WISP. A companion paper (Stankov et al. 1992) describes the application of this type of profile to quantify remotely-sensed cloud liquid water.

The microwave radiometer responds only to liquid water, thus its measurements are unaffected by the cirrus, presumably ice crystal layer. Optical and infrared probes generally do not penetrate beyond the first layer of cloud encountered. Therefore, the downward-looking satellite would not have detected the underlying stratus deck while the ground-based ceilometer missed the overlying cirrus. The upper cloud layers detected by the K-band radar and satellite are unlikely to contain significant supercooled liquid water; the bases of these layers are ~-15 to -30°C.

The method used by Popa Fotino et al. (1989) would have placed the top of the icing hazard at near 5 km MSL through the period shown in Fig. 3, which is more than 2 km above the top of the lower stratiform layer likely responsible for any icing. The combined sensor approach used in this paper provides a more realistic estimate of the vertical extent of the icing hazard.

4. FUTURE PLANS

An estimate of the vertical extent of the icing hazard is obtained using measurements from remote sensors. This method shows promise for real-time warning of icing levels in an airport terminal area. To verify the accuracy of these estimates, comparisons of estimated liquid cloud bases and tops obtained during both field seasons of WISP are underway. However, the data sets collected were primarily in shallow stratiform clouds formed in weak upslope conditions. Further measurements should be obtained in a greater variety of weather situations in order to determine the range of conditions under which this method is likely to work.

ACKNOWLEDGEMENTS

This study was funded by Federal Aviation Administration Contract DTFA01-90-Z-02005. Additional support was provided by NOAA and NSF. Jeff Cole analyzed the satellite data.

REFERENCES

Cooper, W.A., W.R. Sand, M.K. Politovich and D.L. Veal, 1984: Effects of icing on performance of a research aircraft. *J. Aircraft, 21*, 708-715.

Hogg, D.C., M.T. Decker, F.O. Guiraud, K.B. Earnshaw, D.A. Merritt, K.P. Moran, W.B. Sweezy, R.G. Strauch, E.R. Westwater and C.G. Little, 1983: An automatic profiler of the temperature, wind and humidity in the troposphere. *J. Appl. Meteor., 22*, 807-831.

May, P.T., R.G. Strauch, K.P. Moran and W.L. Ecklund, 1990: Temperature sounding by RASS with wind profiler radars: A preliminary study. *IEEE Trans. Geosci. Remote Sensing, 28*, 19-28.

Popa Fotino, I.A., M.K. Politovich and J. W. Hinkelman, 1989: Aircraft icing conditions detected by combined remote sensors: A preliminary study. *Preprints, Third International Conference on the Aviation Weather System*, Jan. 30-Feb. 3, Anaheim, 173-177.

Popa Fotino, I.A., J.A. Schroeder and M.T. Decker, 1986: Ground-based detection of aircraft icing conditions using microwave radiometers. *IEEE Trans. Geosci. Remote Sensing, GE-24*, 975-982.

Rasmussen, R., M.Politovich, J. Marwitz, W. Sand, J. McGinley, J. Smart, R. Pielke, S. Rutledge, D. Wesley, G. Stossmeister, B. Bernstein, K. Elmore, N. Powell, E. Westwater, B. Stankov and D. Burrows, 1992: Winter icing and storms project. *Bull. Amer. Meteor. Soc.*, in press.

Schubert, W.H., S.K. Cox, P.E. Ciesielski and C. M. Johnson-Pasqua, 1987: Operation of a ceilometer during the FIRE Marine Stratocumulus Experiment. Colorado State Univ. Atmospheric Science Paper No. 420.

Stankov, B.B., J. A. Schroeder, J. Cole and M.K. Politovich, 1992: Liquid water profiling using combined remote sensors. *Preprints to the 11th International Conference on Clouds and Precipitation*, Montreal, 17-21 August.

Stankov, B.B., J. A. Schroeder, E.R. Westwater and R.M. Rasmussen, 1991: Liquid water profiling using remote sensor observations. *Preprints, Fourth International Conference on Aviation Weather Systems*, 24-28 June, Paris, France, 239-246.

EVALUATING THE USE OF RICHARDSON NUMBER FOR CLOUD TOP HEIGHT ESTIMATIONS

B. Boba Stankov and Brooks E. Martner
NOAA/ERL/Wave Propagation Laboratory
Boulder, Colorado

1. INTRODUCTION

Ground-based vertically pointing microwave radiometers can provide measurements of the total amount of liquid water overhead. Recent studies have examined the possibility of using radiometer data in combination with other remote sensors to determine if the liquid is supercooled and, thus, an aircraft icing hazard or a cloud seeding opportunity (Westwater and Kropfli, 1989; Stankov et al. 1991; Politovich et al. 1992). The studies have focused on using instruments that could be relatively low-cost additions to the NOAA Wind Profiler Demonstration Network and would operate continuously and unattended. The additional required information is the temperature profile, the heights of cloud layer bases and tops, and the height of liquid regions within cloud. Of these, cloud top height has been the most difficult to determine. Information on the height of cloud layers can also be valuable for radiative transfer studies.

Stankov and Bedard (1990, 1992) suggested estimating cloud top height using the profile of Richardson Number (Ri) derived from wind profilers equipped with Radio Acoustic Sounding System (RASS) capability. Boundary layer theory and modeling as well as aircraft measurements (Brost et al. 1982, and Pobanz and Marwitz 1991) suggest that stratiform clouds are often capped by a strong shear layer (low Ri) just beneath a statically stable layer (high Ri). Thus, the Ri profile exhibits a strong inflection at this level which may represent a useful cloud top signature. The wind and temperature data from a wind profiler/RASS provide the parameters for computing profiles of Richardson number.

Stankov et al. (1991) used this idea for a Colorado upslope snowstorm to set the upper limit (cloud top) of a layer over which the radiometer's total liquid value is distributed by various retrieval techniques; the lower limit (cloud base) was provided by ceilometer data. The cloud top estimated by the Ri method agreed well with occasional aircraft reports in this case, as one would expect for a frontal situation with contrasting air masses of opposing motions. The technique might not perform as well for more mundane weather. Until now, there has been no systematic attempt to assess how well the Ri technique approximates the true cloud top height nor of the method's limitations.

In this article we use data from a K-band cloud-sensing radar to evaluate the Ri method for estimating cloud-top heights from RASS or rawinsonde data. Data collected during the 1991 Winter Icing and Storms Project (WISP) are used for the comparisons. Preliminary results are shown here for two cases; studies of additional cases are in progress to develop statistics.

2. INSTRUMENTATION

The NOAA K-band Doppler radar at Erie, Colorado, was used as the verification device for the cloud top height estimations. The short wavelength of K-band (8.7 mm) gives it an advantage over longer wavelength radars for detecting the very small hydrometeors of non-precipitating clouds. The NOAA K-band routinely detects echoes as weak as -30 dBZ at 10 km range (Kropfli et al. 1990). Experience shows that, in the absence of heavy rainfall, it can detect almost all clouds, including continental stratus and most visible cirrus.

Richardson number profiles were computed from data collected with NOAA 915 and 50 MHz wind profiler/RASS units (May et al. 1990) at Denver and Platteville and from National Weather Service (NWS) rawinsondes at Denver and Cross-chain Loran Atmospheric Sounding System (CLASS) sondes launched by the National Center for Atmospheric Research at Platteville. We also include cloud base data from an NWS ceilometer at Denver and cloud liquid content data from 2-channel (20.6, 31.65 GHz) microwave radiometers at Denver and Platteville (Hogg et al.1983). The fact that the instruments were not collocated in this project is a weakness of the study. However, all instruments were within 45 km of each other, and the comparisons are useful if the winter clouds were widespread and fairly uniform. Low level ($\leq$ 2 km) comparisons probably suffer most from the horizontal separations. Future measurements should concentrate instruments at a single site.

3. THE 28 FEBRUARY CASE

Figure 1 shows a time-height cross section spanning 36 minutes of vertically pointing radar reflectivity data on 28 February 1991. An altostratus cloud that thinned with time was located about 2-4 km AGL and cirrus clouds were present above about 6 km. The strongest reflectivity was -3 dBZ in the earlier part of the altostratus echo. The K-band radar measurements provide excellent temporal (2.5 s) and spatial detail (75 m). Profiles of Ri are also shown on the figure. The RASS profile obtained at 2200-2220 GMT is a composite of lower altitude data from the Denver unit and higher level data from Platteville. The sonde profile was from a CLASS launch at Platteville at 2100 GMT, almost an hour before the radar data collection began. The RASS data do show a marked inflection in the Ri profile from a value near 0 at the altostratus echo top to a value of about 6 just above it. This is the anticipated type of cloud top signature. However, the RASS profile also shows a similar, but more pronounced, inflection just below the altostratus. The earlier sonde profile of Ri exhibits 4 sharp inflections, including one

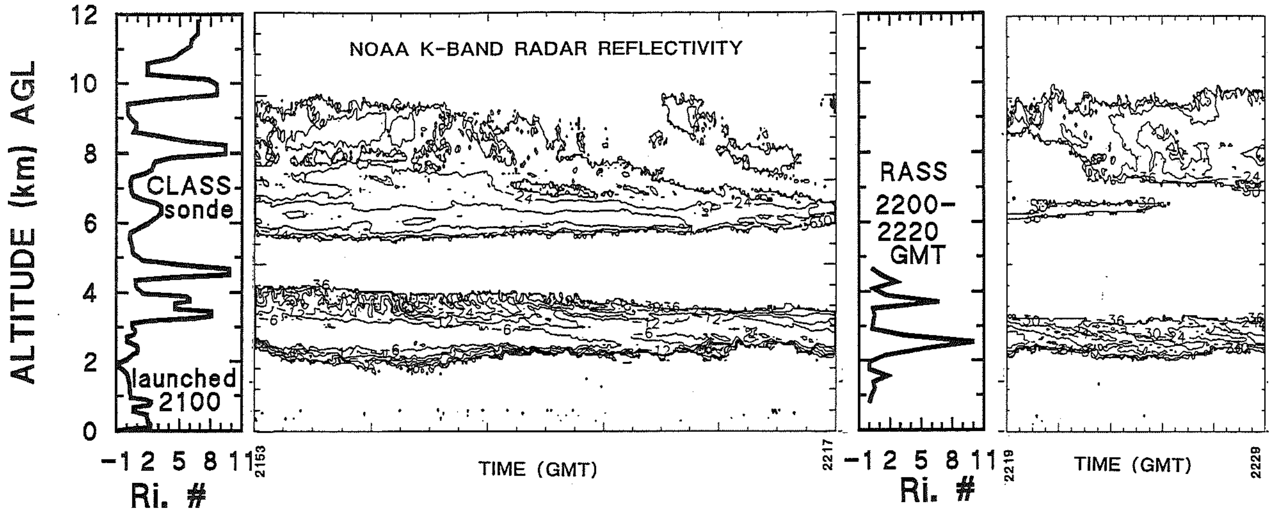

Fig. 1. Time-height display of radar reflectivity factor from the K-band radar on 28 February 1991. The outermost reflectivity contours are -36 dBZ and the contour interval is 6 dBZ. Profiles of Richardson number from RASS and from CLASS sonde data obtained near the time of the radar measurements are also shown.

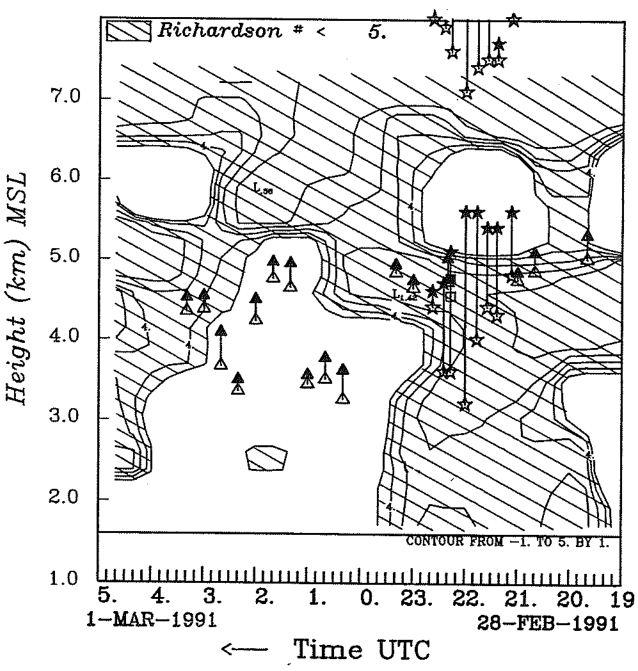

Fig. 2. Composite of cloud height information on a time-height cross section of contoured Ri values computed from Denver + Platteville RASS on 28 February 1991. Hatching denotes regions of Ri $\leq$ 5. Open symbols represent bottoms and closed symbols are tops of layers. Stars are K-band radar echo data, triangles are adiabatic estimates of liquid layer heights, and squares are aircraft measurements of the height of the liquid region.

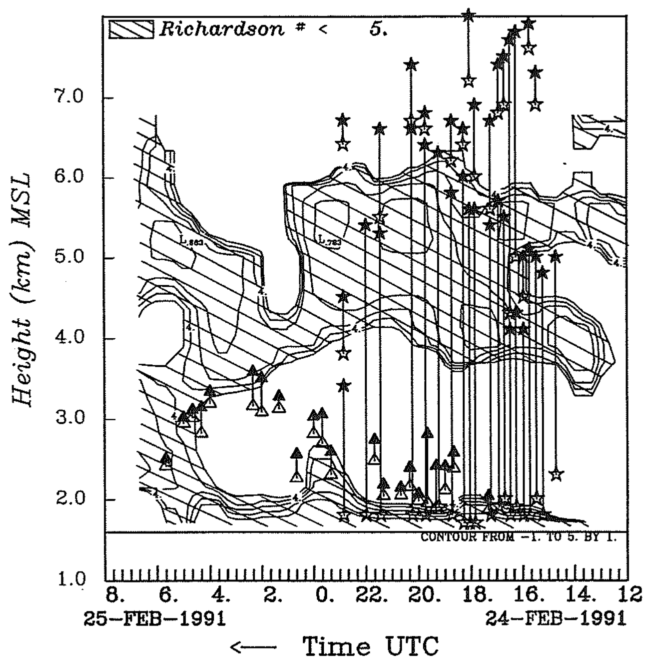

Fig. 3. Same as in Fig. 2, except for 24 February 1991.

near the altostratus top, another near the cirrus top, and two that do not line up with radar echo tops. The two lower Ri peaks on the sonde profile have the same vertical separation as similar peaks on the RASS profile, but are offset by about 1 km in altitude. When considering the apparent discrepancies, one should remember that the various instruments were not collocated.

Figure 2 is a composite of cloud height data from various sources overlain on a contoured time-height cross section of the Ri data computed from the Platteville and Denver RASS units. The figure has been truncated at the top of the RASS coverage, thus omitting the cirrus layers detected by the K-band radar. Estimates of the height of the liquid-bearing part of the clouds (triangles) were obtained by combining ceilometer and radiometer measurements and assuming the cloud water content attained adiabatic levels at each height (Politovich et al, 1992). These agree well with in situ measurements (squares at

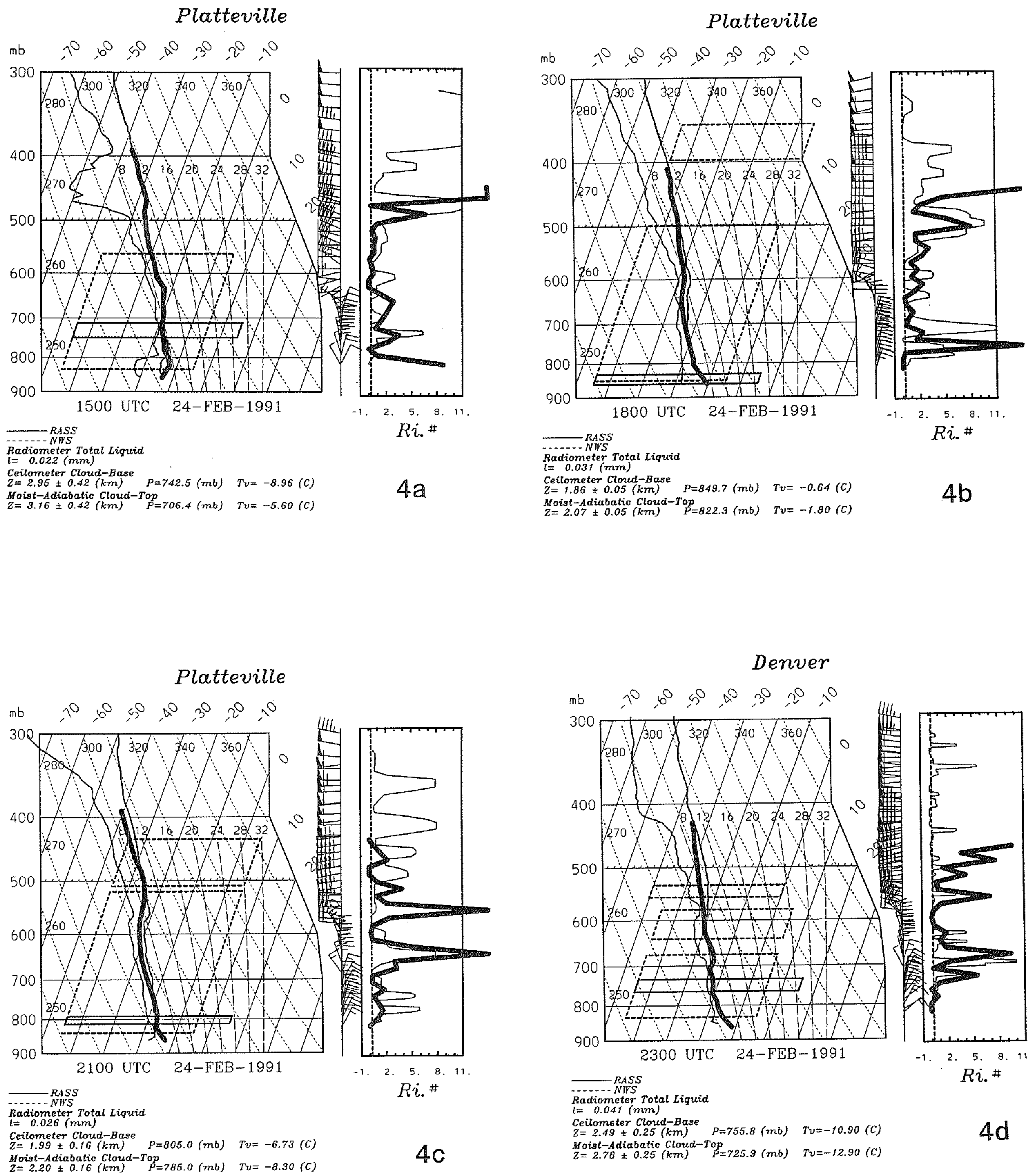

Fig. 4. Profiles of temperature, dew point, wind, and Richardson number on 24 February 1991 at (a) 1500 GMT, (b) 1800 GMT, (c) 2100 GMT, and (d) 2300 GMT. Heavier lines are from RASS; lighter lines are from rawinsondes. Solid parallelograms denote the adiabatic-estimated height of the liquid region in the clouds. Dashed parallelograms show the height span of the cloud layer radar echoes.

about 2220 GMT) by the University of North Dakota Citation research aircraft which spiraled down through the clouds over the radar at Erie and found up to 0.09 gm^{-3} of liquid in the altostratus. The radar echo data (stars) do suggest a weak overall correspondence of the altostratus top level at 5-6 km MSL with an area on the figure where Ri increases sharply with height, as one would expect of the Ri method cloud top signature.

4. THE 24 FEBRUARY CASE

A deeper cloud was present over Erie on 24 February 1991 as shown on Fig. 3 by the radar echo data points (stars) from occasional Range-Height Indicator scans. A layer extended from near the surface to 4-6 km MSL. Thinner cirrus layers (not shown) were detected by the radar above 8 km. The adiabatic estimation technique indicates the liquid portion of the cloud (triangles) was restricted to a narrow layer near the echo base. The top of the lower, deep cloud echo again appears to be loosely correlated with a region where Ri increases sharply with height.

Figures 4a-d show profiles obtained at approximately 3 h intervals during this storm. The heavier lines on the skew-T diagrams and on the Ri profiles are from RASS and the lighter lines are from rawinsondes. Solid parallelograms on the skew-Ts depict the height (actually pressure) span of the adiabatic liquid water region estimation. Dashed parallelograms show the span of the radar cloud echoes at these four times. There appears to be a fairly good alignment of RASS Ri profile inflections from low to high values with radar echo tops in Fig. 4b, but very poor alignment in Fig. 4c, and mixed results in Figs. 4a and 4d. The sonde profiles of Ri have more complicated series of peaks with no clear indications of alignment with echo tops.

5. DISCUSSION

Data from only two of several available WISP cases have been inspected in this initial part of the study. We intend to assess objective statistics of the Ri method's performance using all the data and to determine the conditions under which the technique is most useful. Meanwhile, these first two cases suggest results that may be indicative of the full data set.

Stankov et al. (1991) showed the Ri method accurately estimated cloud top for a strong cold front snow storm in which cold, moist, easterly flow advanced beneath warm, dry, westerly flowing air. The 1991 WISP cases examined here were less dynamic and more complex, and the success of the method appears mixed for these cases. There are situations where a strong inflection from low to high value is present in the Ri profile near the radar echo cloud top. However, frequently there are similar or even more prominent inflections that are not associated with cloud boundaries. These are probably caused by wind shear layers within and outside of cloud.

Thus, while the Ri method is useful in some cases, overall, a high false alarm rate might result from a cloud top algorithm that uses Richardson number information alone. These studies indicate the value of an integrated approach, using measurements from various remote sensors to insure the data are correctly interpreted. Combining the RASS data with additional remote sensing observations, such as liquid height estimations, may offer a more robust approach for estimating cloud top heights for a wide variety of weather. A direct but rather expensive solution would be the installation of sensitive K-band radars at each site.

6. ACKNOWLEDGEMENTS

This research is funded in part by the Federal Aviation Administration contract DTFA01-90-Z-02005 and the Department of Energy's Atmospheric Radiation Measurement (ARM) program. Don Burrows of the University of North Dakota provided data from the research aircraft. At WPL, many people were responsible for data collection; Scott Shaver, Brad Orr and Jannelle Reynolds assisted with data processing. Al Bedard and Judy Schroeder made helpful comments on the manuscript and figures.

7. REFERENCES

Brost, R.A., J.C. Wyngaard, and D.H. Lenschow, 1982: Marine stratocumulus layers. Part II: Turbulence budgets. **J. Atmos. Sci., 39**, 818-836.

Hogg, D.C., F.O. Giurard, J.B. Snider, M.T. Decker, and E.R. Westwater, 1983: A steerable dual-channel microwave radiometer for measurements of water vapor and liquid water in the troposphere. **Climate and Appl.Meteor.,22**, 789-806.

Kropfli, R.A., B.W. Bartram, and S.Y, Matrosov, 1990: The upgraded WPL dual-polarization 8mm wavelength Doppler radar for microphysical and climate research. **Preprints, Conf. on Cloud Physics, San Francisco, CA**, Amer. Meteor. Soc., 341-345.

May, P.T.,R.G. Strauch, K.P. Moran, and W.L. Ecklund, 1990: Temperature sounding by RASS with wind profiling radars: A preliminary study. **IEEE Trans.Geosci. Remote Sensing,28**, 19-28.

Pobanz, B. and J. Marwitz, 1991: Conditions associated with large drop regions. **Reprints, 29th Aerospace Sciences Meeting, Reno, NV**, AIAA, Washington, DC, 2pp.

Politovich, M.K., B.B. Stankov, and B.E. Martner, 1992: Use of combined remote sensors for determination of aircraft icing altitudes. **Preprints, 11th Intl. Conf. on Clouds & Precip.**, Montreal, Canada, 4pp.

Stankov and Bedard, 1990: Atmospheric conditions producing aircraft icing on 24-25 January 1989: A case study utilizing combinations of surface and remote sensors. **Reprints 28th Aerospace Sciences Meeting, Reno, NV**, AIAA, Washington, DC, 10pp.

Stankov, B.B. and A.J. Bedard, Jr., 1992: Remote sensing observations of winter aircraft icing conditions: a case study. **J. Aircraft**, in press.

Stankov, B.B., J.A. Schroeder, E.R. Westwater, and R.M. Rasmussen, 1991: Liquid water profiling using remote sensor observations. **Preprints, 4th Intl. Conf. on Aviation Weather Systems, Paris, France**, Amer. Meteor. Soc., 239-246.

Westwater, E.R., and R.A. Kropfli, 1989: Remote sensing techniques of the Wave Propagation Laboratory for measurement of supercooled liquid water: Applications to aircraft icing. **NOAA Tech. Memo. ERL/WPL-163, NOAA WPL, Boulder, CO**, 28pp.

Techniques to Classify Ice Crystal Images from Aircraft Probes

V. Chandrasekar, A. Benjamin and J. Caylor
Colorado State University
Fort Collins, CO 80523, USA

1. INTRODUCTION

Accurate and automatic classification and analysis of Random Hydrometeor images, obtained from two dimensional probes mounted on aircraft , has always posed a challenging problem. Identification of different hydrometeor types is of great interest, for the basic understanding of various cloud processes. The problems encountered in analyzing and classifying the hydrometeors arise mainly due to the reasons such as, the non spherical random shape of the images, the occurrence of images with gaps due to partial transparency of certain crystals or the diffraction caused by fine crystals, the image being partially present in the sampling area and presence of more than one particle in a single image frame. Since these images are binary in nature, most of the shape and size information is contained in the contour. This paper deals with extracting information on the type of ice crystals and their parameters (size and shape) from raw binary images.

A comparison is made between the available automatic classification techniques and visual method, for hydrometeor images collected from aircraft based data collection platforms. A new classification technique for classifying random hydrometeor images is developed using Fourier descriptors and moment techniques. The feasibility of this technique is analyzed based on simulations and real data, the potential usefulness of this technique is vividly illustrated by examples and comparisons with existing techniques.

The procedures leading to the image analysis can be broadly divided into three parts namely:

a) contour construction from raw binary images,
b) estimation of size shape and orientation parameters of the images and,
c) classification of the image types.

Several authors have addressed the problem of hydrometeor classification using specialized procedures (Rahman et al (1981), Durore (1982) and Holoroyd (1987)). The techniques of Rahman and Durore had more emphasis on the actual image whereas the technique of Holoroyd was based on statistical features. We present a comparative study between the automatic classification technique and manual classification (visual from a video screen display) using data collected by PMS probes through winter storms.

2. IMAGE CONTOUR CONSTRUCTION

The 2-D PMS images are obtained as sequence binary strings composed together to form an image. The binary states of the image are obtained as the particle under observation passes through the sampling area which is formed between a light source and a linear photodiode array. The raw image is initially moved into the image buffer to check for holes due to imperfections in the sampling process.

The gaps in the image is filled according to the following algorithm:

Step 1: a) The image is scanned slice by slice, from the top of the slice beginning at the first slice for "0"s.

b) If (x,y) are the coordinates of the "0", which is same as the position of the pixel in the two dimensional image array. If x is not equal to 1, y is not equal to 32, x not equal to 1 and x not equal to the last slice of the image, then the eight neighboring pixels are, (x-1, y-1), (x-1, y), (x-1, y+1), (x, y+1), (x+1, y+1), (x+1, y) and (x+1, y+1). Since a hole is an interior pixel with the value "0" and is surrounded by pixels of value "1", of the eight neighboring pixels if at least three or more have gray level "1", then the pixel (x,y) under consideration is a hole in the contour and is forcibly made "1".

c) The above steps are repeated till all the "0"s in the image are scanned.

Step 2: In this step the coordinates of the edge pixels are determined scanwise starting from the first scan. Eight connectivity of a pixel is its relation with its eight neighboring pixels (top, left, right, bottom, top left, top right, bottom left, bottom right). Four connectivity of a pixel is its relation with its four neighboring pixels (top, left, right, bottom). An edge pixel is a pixel which has a gray level "1", whose eight connectivity in its neighborhood consists of at least one pixel of gray level "1" and whose four connectivity in its neighborhood consists of at least one pixel of gray level "0".

a) The image is scanned from the first slice for pixels whose value is "1".

b) Check eight connectivity in the neighborhood of the pixel under consideration to determine the number of pixels with gray level "1".

c) Check four connectivity in the neighborhood of the pixel under consideration, to determine the number of pixels with gray level "0", to which the pixel under consideration is connected.

d) Pixels which belong to the top row, bottom row, left column and right column have to be processed separately and the nonexistent rows and columns are not checked for eight and four connectivity.

e) The criterion which determines whether a pixel with gray level "1" is an edge pixel Is that, it should have four connectivity with at least one "0" pixel and eight connectivity with at least one "1" pixel.

f) The above steps are repeated until all the edge pixels are formed.

Step 3: In this step the first two pixels on the contour are determined in the clockwise direction from the edge pixels formed in step 2.

a) The first pixel on the image contour is the first edge pixel formed in step 2.

b) The buffer containing the edge pixels is scanned to determine the pixel which is connected to the first pixel in the clockwise direction. This the second pixel on the contour.

c) A vector VI is formed by these two contour pixels.

Step 4: In this step the remaining edge pixels are connected in the clockwise direction to form the closed image contour.

a) The buffer containing the edge pixels is scanned to determine the pixels which are eight connected to the previous contour pixel.

b) Vectors are formed from each of the above connected pixels with the previous contour pixel.

c) The next pixel on the contour in the clockwise direction is the pixel whose vector cross product with V1 has the least value. Cross product is used since it gives a sense of direction along the contour. To ascertain that the contour is formed in the correct direction, we need to check the cross product of the vectors formed by each of the connected pixels with the previously formed contour pixel. If (x_i, y_i) is the edge pixel whose correct connectivity with the previously formed edge pixel is to be ascertained and if (x_{i-1}, y_{i-1}) and (x_{i-2}, y_{i-2}) are the previously formed edge pixels along the contour in the clockwise direction then

Vector 1 (V1): $a1 = (x_i - x_{i-1})$

$a2 = (y_i - y_{i-1})$

Vector 2 (V2): $b1 = (x_{i-1} - x_{i-2})$

$b2 = (y_{i-1} - y_{i-2})$

Cross product of V1 and V2 is given by

$V1 \times V2 = a1.b2 - a2.b1$

This quantity gives a sense of direction along the contour. The edge pixel (x_i, y_i) is a contour pixel in the correct direction only if the cross product given above has the smallest value.

d) If at a point on the contour there are multiple paths, then the contour formation is along the nearest left path along the contour. The dot products of V1 and V2 is used to determine the path along which the contour formation has to proceed.

$V1.V2 = a1.b1 + a2.b2$

e) If the dot product is the smallest then, (x_i, y_i) is the proper pixel direction along which the contour formation has to proceed.

f) If the contour has extending arms (Dendrites) the path along the contour might come to a dead end, where there are no more connected edge pixels. In such cases the direction along the contour has to be retraced one pixel at a time and the previous steps have to be repeated.

g) Repeat previous steps till the final pixel is formed. A pixel is the final pixel if and only if, (mx = 0 and my = 0) or (mx = 0 and my = 1) or (mx = 1 and my = 0) or (mx = 1 and my = 1), where

$mx = abs\ (x_1 - x_n)$

$my = abs\ (y_1 - Y_n)$

3. ESTIMATION OF SIZE SHAPE AND ORIENTATION

Accurate representation and description of a contour can be accomplished using boundary or shape descriptors such as Fourier and moment descriptors. Chandrasekar et al (1990) have described application of these techniques for analyzing images of raindrops. Let $X(\ell)$, $y(\ell)$ be the points on the contour of our image with arc length ℓ as the independent parameter then the Fourier descriptors (C_n) can be expressed as

$$C_n = \int_0^L u(\ ) \exp\left(-j\frac{2\pi n}{L}\right) d \qquad (1)$$

Fourier descriptors of a contour $n(\ell)$ of order n where n = ... -1, 0, 1, 2 ... can be obtained from the coordinates of the contour. If we approximate the shape of the contour to be elliptical we can get the axis ratio (r) and orientation angle (ϕ) of the particles as

$$r = \frac{\| C_1| - |C_{-1}\|}{|C_1| + |C_{-1}|} \qquad (2)$$

$$\phi = \frac{1}{2}\left[Arg(C_1) + Arg(C_{-1})\right] \qquad (3)$$

The centroid of the image is given by

$$C_o = \sum_{i=1}^{NP} \frac{u(\ell)}{NP} \qquad (4)$$

where NP is the number of points on the contour. For complex images it is difficult to specify a diameter and hence it is easy to specify characteristic maximum dimensions as Maxdf = $|C_1| + |C_{-1}|$. The magnitude of the Fourier descriptors increase with the dimensions of any image. Thus we can use a normalized Fourier Descriptor as

$$C_n' = \frac{Cn}{Maxdf} \qquad (5)$$

If f(x,y) represents a bounded function over a finite boundary of area A, then we can define its moments based on f(x,y). If f(x,y) = 1 then the moments of the region having area A could represent a shape. The order of moments required to characterize an object depends on the complexity of its shape. We can define a set of seven normalized invariant moments referred to as Moment descriptors (Teague, 1980). The central moment of the order (p,q) can be defined as

$$\mu_{pq} = \iint_A (x-\bar{x})^p (y-\bar{y})^q\, dxdy \qquad (6)$$

where the area A denotes the area covered by the image.

If we approximate the image by an ellipse we can obtain the axis ratio (r) and orientation (ϕ) as

$$r = \left\{\frac{\mu_{20}+\mu_{02}-\left[(\mu_{20}-\mu_{02})^2+4\mu_{11}^2\right]^{1/2}}{\mu_{20}+\mu_{02}+\left[(\mu_{20}-\mu_{02})^2+4\mu_{11}^2\right]^{1/2}}\right\} \qquad (7)$$

4. IMAGE CLASSIFICATION

4.1. Fourier Descriptor Method

We have demonstrated in the previous section that we can estimate normalized Fourier descriptors defined by (5). These C_n' can be used in the recognition of images.

In the following we describe recognition of each type of particle based on FDs. The recognition procedure can be easily demonstrated with examples but they are not included for brievity.

a. Recognition of Raindrops

Raindrops are nearly elliptical in shape (Pruppacher and Pitter, 1970), hence they can be characterized by the FD coefficients of order 1 obtained from quantized data. Thus an ellipse fit with C_1 and C_{-1} forms a natural filter to raindrop shapes. It can be shown that for raindrops only FDs of order 1 has a large magnitude and the rest of the Fds have a very small magnitude, the magnitude of higher order Fds is mainly due to the quantizing noise of the digitized image.

b. Recognition of Dendrites

Dendrites are particles which exhibit symmetry and outline periodicity. Such images can also be recognized by Fds. It can be shown that in the FD spectrum of dendrites that only FD5 has a large magnitude when compared to other higher order Fds. The reason for FD5 having a large amplitude can be attributed to the periodicity and symmetry of the star shaped image.

c. Recognition of Aggregates

Aggregates are particles which are made of two or more particles held together. In the case of aggregates the FD2 has a large magnitude compared to other Fds if the aggregate is made of two or more particles other than dendrites. Aggregates of stars have the magnitude of FD5 large, in addition to that of FD2. The reason for FD2 to have large magnitude is due to the fact that an aggregate can be modelled to be made of two or more ellipses. This feature can be utilized in the identification of aggregates from different classes of hydrometeors.

d. Recognition of Hexagonal plates

Images which have hexagonal symmetry can be recognized by Fds. In the case of hexagonal images FD5 is larger than the other higher order Fds, but less than that of stellars.

4.2 MOMENT METHOD

Using normalized central moments we can define a set of seven invariant moments as described in the appendix. These moments will be referred to as moment descriptors (MD1, MD2,...MD7). These are invariant to translation, rotation and scale change (Hu, 1962). The actual expression for the MDs is long and is skipped here for brievity. The seven MDs can be used to classify raindrops, graupels and ice crystals. It has been noticed that for raindrops MD2, MD3, MD4 have smaller amplitudes when compared to MD1. For graupel MD2, MD3 and MD4 have very small magnitude when compared to MD1, however the variation of MD2 to MD4 is different from those for raindrops. Only MD3 and MD4 have significant magnitude when compared to MD1 for dendrites. Thus we can see that MDs can be utilized in classification of 2D PMS images.

5. DATA ANALYSIS AND AUTOMATIC CLASSIFICATION

Holoroyd (1987) developed an automatic classification technique based on statistical parameters such as size, linearity, area, perimeter and image density to classify hydrometeor images. The various categories of classification assigned by Holoroyd are tiny, oriented, linear, aggregate, graupel, sphere, hexagonal, irregular and dendrite. We have used identical classification types for our technique.

In addition to the parameters discussed in the previous section we use parameters FD2 and FD5 defined as

$$FD_{2,5} = \frac{|C_{2,5}|+|C_{-2,-5}|}{Maxdf} \tag{8}$$

We have analyzed the estimation accuracies of the various parameters to study the threshold and dynamic range and the results are skipped here brevity. Based on such analysis and the results of Section 3 we can describe the habit classification algorithm as follows:

Class 1, Tiny: A particle classified as "tiny" if its area A is less than 625 μ^2 (25 diode units 2D-C probe) or 5000 μm^2 (25 diode units 2D-P probe).

Class 2, Linear: If the Axrf of the image is less than 0.40 and its Angf is not in between 30 and 60 degrees, then the hydrometeors is classified as "linear".

Class 3, Oriented: A particle is classified as "oriented" if its Axrf is less than 0.40 and its Angf lies in between 30 and 60 degrees.

Class 4, Aggregate: "Aggregates" are hydrometeors with FD2 greater than or equal to 0.117.

Class 5, Graupel: A particle is classified as a "Graupel" if its Axrf is greater than 0.80 and its Maxdf (half the diameter) is greater than 8.

Class 6, Spheres: A hydrometeor is classified as a "Sphere" if its Axrf is greater than 0.90 and its Maxdf is less than 8.

Class 8, Dendrites: Star shaped "Dendrites" are those hydrometeors with FD5 greater than 0.08 and FD2 less that 0.117. Higher order dendrites are those images with higher order Fds like FD6 or FD7 having values greater than 0.08.

Class 9, Hexagonal Plates: "Hexagonal plates" are those images which have FD5 greater than 0.05 and less than 0.08.

Class 10, Raindrops: A hydrometeor is classified as a "raindrop" if FD2 to FD6 have values less than 0.05.

Class 7, Irregular: Hydrometeors which do not fall in any of the above nine mentioned classes are classified as "irregular".

To determine the feasibility and performance of the classification techniques discussed above, hydrometeor images from winter storms were used to test the algorithms. Data sets were used to assess the performance of the automatic statistical and the new FD technique for classifying hydrometeors. The data that was used was collected by the King air aircraft over winter storms, equipped with a 2D-P probe for particles measuring 200-6400 μm (resolution of 200 μm), and with a 2D-C probe for particles 25-800 μm (resolution of 25 μm).

To quantitatively assess and compare the performance of the various automatic classification techniques, we need to classify the images visually and consider this as the reference for comparison with those of automatic classification techniques. The visual classification is prone to human perception errors, but an effort has been made to classify the images visually to the best possible extent.

A set of thousand images were classified visually. The same set of thousand images were again classified using the automatic classification developed in this paper. The results of the two classifications are summarized in the following table.

Comparison of visual and automatic classification of a 1000 ice crystal image

Hydrometeor	Visual Classification (%)	Automatic FD Classification (%)
Tiny	11	13
Linear	2	2
Oriented	3	3
Aggregates	42	48
Graupels	1	1
Spherical	-	1
Irregular	13	8
Dendrite	20	22
Hexagonal	1	-
Raindrop	7	6

It is evident from the above table that the automatic classification technique described in this paper works as well as the manual visual classification.

6. SUMMARY AND CONCLUSIONS

Analysis and habit classification of hydrometeor images obtained by 2D-PMS probes mounted on aircraft were described in this paper. The shape information of the binary image is contained in its contour and hence a contour formation algorithm was developed. Two image processing techniques namely Fourier and moment descriptors were analyzed to develop parameters that were used in the shape recognition and classification of hydrometeor images. An algorithm to automatically classify images into classes described by Holoroyd (1987) was developed. 2D-PMS data collected in winter storms was used in analyzing the performance of the automatic classification procedure. One thousand images of ice crystals were classified manually from visual displays on video screen and these were compared against automatic classification. The two techniques show good agreement demonstrating the potential of the ice crystal classification technique developed in this paper.

Acknowledgements: This research was supported by the National Science Foundation (ATM-9019596).

7. REFERENCES

Chandrasekar, V., Golestani, Y., Turk, J., and Bringi, V.N., 1990: Fourier and Moment methods applied to two-dimensional raindrop images. J. Atmos. Oceanic. Technol., 7, 197-205.

Durore, C., 1982: "Une nouvelle methode de traitment des images d'hydrometeores donnes par les sondes bidimensionelles." J. Rech. Atmos., 6, 71-84.

Holoroyd, E.W., III, 1987: Some techniques and uses of 2D-C habit classification software for snow particles, J. Atmos. Oceanic. Technol., 4, 498-511.

Hu, M.K., 1962: Visual pattern recognition by moment invariants. IRE Trans. Inf. Theory, IT-8, 179-187.

Pruppacher, H.R., and R. L. Pitter, 1971: A semi-empirical determination of the shape of raindrops. J. Atmos. Sci., 28, 86-94.

Rahman, M.M., Quincy, R., Jacquot, G. and Magee, M. J., 1981a: Feature extraction and selection for pattern recognition of two dimensional hydrometeor images. J. Appl. Meteor., 20, 521-535.

Teague, M.R., 1980: Image analysis via the general theory of moments, J. Opt. Soc. Am., 70, 920-930.

The Utility of a High Resolution Volunteer Snow Observer Network

by

B.C. Bernstein, I. Baker, D. Wesley,
National Center for Atmospheric Research (NCAR)†
Research Applications Program, Boulder, CO 80307
J. Smart, L. Wharton,
National Oceanic and Atmospheric Administration
325 Broadway, Boulder, CO 80303
and **J. Wirshborn**
Mountain States Weather Services, Ft. Collins, CO 80525

1. Introduction

The evaluation of a winter storm event is often done using observations of total snowfall and liquid equivalent. Ironically, during winter field programs, the dataset necessary to compile just such information is often quite sparse, both spatially and temporally. Standard surface measurements of snowfall and liquid equivalent from first order National Weather Service SAO sites are only taken every three hours, and these sites are typically separated by $\sim$ 100 km. To further enhance the number and temporal resolution of snowfall measurements, automated snowgauges have been made available as an option on the National Center for Atmospheric Research (NCAR) Portable Automated Mesonet (PAM) stations. However, these snowguages can be inaccurate, especially in situations where significant winds and/or snow with low liquid content occur.

During the winters of 1990 and 1991, the Winter Icing and Storms Program (WISP) was conducted in northeastern Colorado. This extensive field program was designed to study the structure and evolution of winter storms, with emphasis placed on improving the understanding of the processes which lead to the production and depletion of supercooled liquid water in clouds (which can be a significant hazard to aircraft). As part of this program, a network of approximately 100 volunteer snow observers was implemented. This paper will describe the snow observer network, give some examples of the usefulness of this dataset for both snowfall and icing events which occured during WISP operations, and suggest further uses of such datasets for future winter field programs.

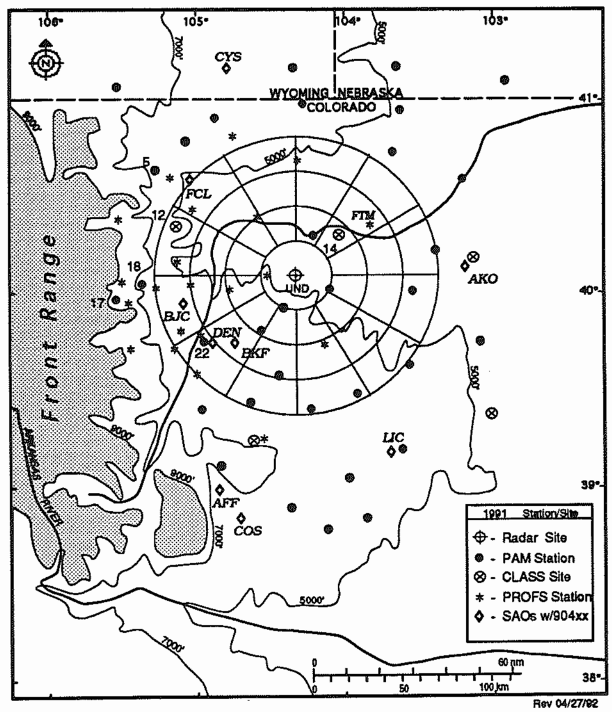

Fig. 1 *The WISP91 Mesonetwork – UND azimuth and range rings and locations of Fort Morgan (FTM), Akron (AKO), Limon (LIC) and PAM 14 (14) R.M. Young snowgauge (numbered PAM sites have snow gauges).*

2. The WISP Volunteer Snow Observer Network

The WISP field program employed a dense array of instrumentation in northeastern Colorado for the winters of 1990 and 1991 (see Figure 1). A detailed description of the WISP90-91 field networks is available in Rasmussen et. al. (1992). To augment the data available from such standard instruments as surface mesonet stations, soundings, radars, aircraft and satellites, a network of approximately 100 volunteer snow observers was developed. The observers, who ranged from meteorologists at NCAR and Colorado State University to high school students from the Colorado eastern plains, recorded values of snow accumulation, snowfall rate, liquid equivalent, crystal habit, degree of riming, and aggregate occurrence and size on simple checklist type forms. The time resolution of the data varied from 30 min to 6 hr. Overall storm data were also recorded, including snowfall period, total accumulations of snow and liquid equivalent, as well as additional information about rainfall, lightning, drifting and general comments about the character of the precipitation event. This information is critical to the evaluation of each WISP event, for without it only a handful of National Weather Service first order stations (which report snowfall and liquid equivalent) and six NCAR Portable Automated Mesonet (PAM) stations equipped with R.M.

† NCAR is sponsored by the National Science Foundation.

Young snowguages would be available for such tasks (see Figure 1).

3. Example cases

3.1 – A Narrow, Intense Snowband

On March 16-17, 1991 a surface low pressure system tracked across the southern extent of the WISP domain. The low moved from southwest to northeast in conjunction with a closed circulation at both 700 and 500 mb, as seen in sounding and wind profiler data (not shown). This system produced widespread snowfall and some freezing rain across the eastern portion of the WISP mesonet, including 3 inches at LIC (Limon, CO) and 2 inches at AKO (Akron, CO) (see Figure 1 for locations). All snowfall measurements in the document are reported in inches to preserve the accuracy of the original measurements.

The main precipitation feature noted in this case was a 80-100 km wide snowband. This band entered the southeastern corner of the network and moved toward the northwest at approximately 17 km/hr (band motions are according to observations by Univ. of North Dakota (UND) radar personnel). A weak extension of this band affected AKO between 1621 and 1815 (all times UTC), during which a volunteer observer reported 0.4 inches of snow. After a 95 minute period of no snowfall, the northern extent of the main snowband swept across AKO between 1950 and 2210. AKO reported heavy snow with 2 inches of accumulation as the band passed (see Table 1). UND radar plots (Figures 2a,b,c) indicate that the band moved to the west of AKO and stalled by 0000 on the 17th, with the band centered near Fort Morgan (FTM on Figure 1). It was near this time that the 700 mb low center passed to the south of FTM. As the low continued to move toward the east, the attendant band weakened and moved eastward at 11 km/hr. The weakened band again passed over AKO between 0540 and 0813, dropping only light snow and little additional accumulation.

Table 1 *Akron, CO National Weather Service (NWS) SAO's for March 16-17, 1991.*

```
AKO SA 1150 W8 X 2F 129/29/26/1611/984/707 26
AKO SA 1247 W5 X 1 1/2F 132/27/26/1312/984
AKO SP 1324 W3 X 1F 1411/984
AKO SA 1349 W3 X 1F 129/28/27/1513/983
AKO SP 1427 E5 OVC 2F 1611/984
AKO SA 1448 E5 OVC 2F 128/29/27/1611/983/203
AKO SP 1520 W2 X 1/2F 1512/9985
AKO SA 1551 W1 X 1/4F 132/29/28/1416/984
AKO SA 1648 W3 X 1/2SF 130/31/30/1416/984/SB21
AKO SA 1845 E10 OVC 6F 32/M/0000/983
AKO SA 1953 W2 X 1/2SF 121/31/29/1306/981
AKO SA 2052 W2 X 1/4S+F 115/31/30/1407/980/808 90401
AKO SA 2147 W2 X 1/4S+F 115/31/29/1109/980
AKO SP 2223 E7 OVC 3S- 1211/979
AKO SA 2248 E9 OVC 7 117/30/29/1209/979/SE42
AKO SA 2350 E9 OVC 10 123/29/27/1108/981/30316 31 90402
AKO SA 0049 E9 OVC 15 132/28/27/1209/983
AKO SA 0150 E5 OVC 15 138/28/26/1108/985
AKO SA 0251 E5 OVC 10 146/28/25/1106/988/220 90402
AKO SA 0349 E5 OVC 10 151/28/26/0000/989
AKO SP 0424 E5 OVC 2 1/2F 1004/991
AKO SA 0448 E5 OVC 2 1/2F 155/28/27/0000/991
AKO SA 0551 E5 OVC 2 1/2S-F 157/29/26/0000/992/SB40/21202 31 90402
AKO SA 0649 E5 OVC 2 1/2S-F 160/27/26/2906/992
AKO SA 0750 E5 OVC 2 1/2S-F 160/27/26/0000/992
AKO SA 0849 E5 OVC 2 1/2F 163/28/25/0000/993/SE13 303
AKO SP 0914 W2 X 1/2F 2908/993
AKO SA 0951 W2 X 1/2F 166/26/25/2808/993
AKO SA 1049 W2 X 1/2F 166/27/26/2708/993
AKO SA 1116 E10 OVC 3F 2810/993
AKO SA 1150 E10 OVC 3F 173/28/28/2909/995/30700 24 20018
```

Fig. 2a *University of North Dakota 0.2° elevation reflectivity plots for 2006 UTC, 16 March 1991. Range rings are every 20 km. For locations of FTM, AKO and PAM 14, compare with Fig. 1.*

Fig. 2b *Same as Fig. 2a, 2202 UTC, 16 March 1991.*

3.1.1 - Mapping the Snowfall

Of the eight NWS stations within the network which report snowfall (904xx groups) and liquid equivalent, only four received any snowfall, and only AKO and LIC reported accumulations. Among the six PAM snowguages in place, only one (PAM 14) received snowfall (2 mm total, excluded from this analysis due to probable innaccuracy of the measurement). Satellite images taken 2 days after the event (not shown) suggest that heavier amounts of snow fell just to the west and southwest of AKO. It is clear from the radar and satellite data that the NWS data does not accurately depict the snowfall which occurred on March 16-17. By adding the volunteer snow observer network data available for this case to the NWS data, the

Fig. 2c *Same as Fig. 2a, 0005 UTC, 17 March 1991.*

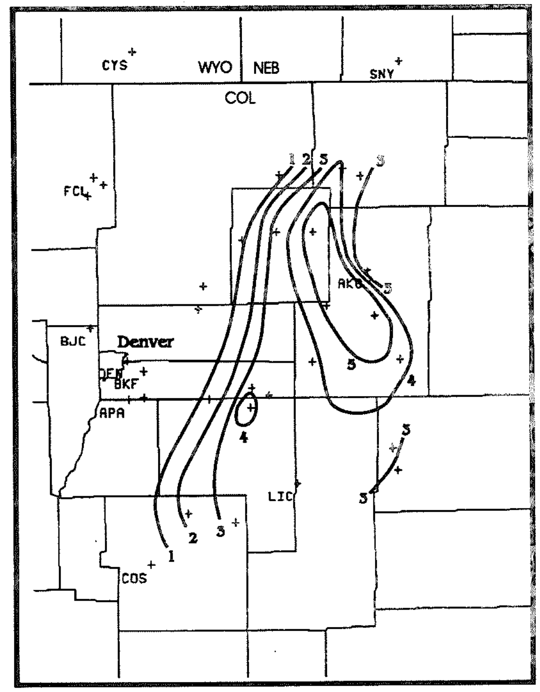

Fig. 3 *Contour map of snowfall (inches) using NWS SAO's and volunteer snow observer network data.*

resolution of the snowfall data increases markedly, and allows for a more accurate mapping of the snowfall (see Figure 3). This analysis is now in much better aggreement with the radar and satellite data. Without the snow observer network, the mesoscale snowfall distribution of this band could not have been resolved.

3.1.2 - Time-series of the Snowband

While spatial resolution of snowfall is important to the evaluation of this event, temporal resolution is equally important. Figure 4 is a time-series plot from an exceptional observer located 3 km west of Fort Morgan. The plot indicates accumulated snowfall, preciptation type and intensity, crystal habit and degree of riming. Between 1820 and 2330 the western half of the snowband passed over this site as its motion stalled. The heaviest snowfall was occurring at and just to the east of Fort Morgan at 2330, as determined by low level UND radar reflectivity plots (Figure 2). Moderate to heavy snow fell for approximately 70 minutes, resulting in one inch of accumulation during the period. This one inch per hour snowfall rate adds credence to the six inch snowfall reports just east of Fort Morgan, where the band persisted for up to six hours.

The time-series of crystal habit and amount of riming, when linked with radar, sounding and aircraft data (WISP conducted many flights along and across snowbands and other features) can give critical "ground truth" data. This information can be used to infer crystal formation zones and temperatures, amount of supercooled liquid water in the cloud, depth of the cloud and particle fall speeds. In the March 16-17, 1991 case, the observation of lightly and heavily rimed crystals during passage of the snowband correlates well with the observation of supercooled liquid water droplets within the band by University of Wyoming aircraft. For the March 6-8, 1990 blizzard, observations of graupel by volunteers were critical in the proper determination of particle fallspeeds for dual-Doppler analysis (G. Stossmeister, personal communication).

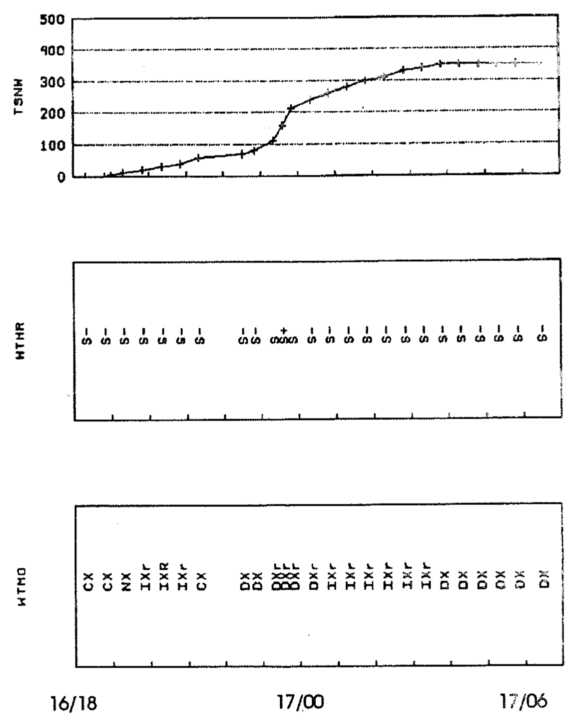

Fig. 4 *Time-series of volunteer snow observer data from 3 km west of Fort Morgan, CO. TOP — total snowfall in $\frac{1}{100}$ inches. CENTER — precipitation type and intensity (sideways). BOTTOM — crystal habit (C-columns, N-needles, I-irregulars, D-dendrites) and degree of riming (R-heavily rimed, r-lightly rimed, no letter-no rime). Plot is from 16 March 1991, 1800 UTC to 17 March 1991, 0700 UTC.*

3.2 Observer network data for other storms

Similar snowfall analyses to those presented in Section 3.1 have been performed for other case studies. Discussion of snowfall mechanisms for these storms is not inluded here. One example is the 30-31 March 1988 storm, which exhibited a strong east-west gradient of snowfall over the foothills and adjacent plains (Wesley and Pielke, 1990). Fig. 5 presents the snowfall distribution for this storm, based primarily on snow observer reports. The tabulation of dominant crystal habit information is shown in Table 2. The habit and riming information was used (along with other data) for specification of likely snow-producing cloud layers in this storm.

Another storm which involved lighter snowfall was the 15-16 January 1991 WISP event, in which the north-south gradient in snowfall was significant. The observer-derived distribution is shown in Fig. 6. In this case, convergence in anticyclonic flow on the south side of the Cheyenne Ridge was responsible for higher accumulation in the western portions of the WISP domain.

4. Conclusions

It is clear that the WISP volunteer snow observer network is a valuable part of the overall WISP mesonetwork. It furthers the insight we gain from remote and in situ instruments by adding "ground truth" observations of the crystals, liquid water and snowfall we could only otherwise infer through the use of radars, aircraft, soundings and satellite datasets. As with any other dataset, volunteer snow networks have their problems. Nighttime cases and windy cases often produce fewer quality observations, and thus less desirable results than those presented here. However, with a dense enough network, and a great deal of patience, quality analysis can be done using this and similar datasets from other projects.

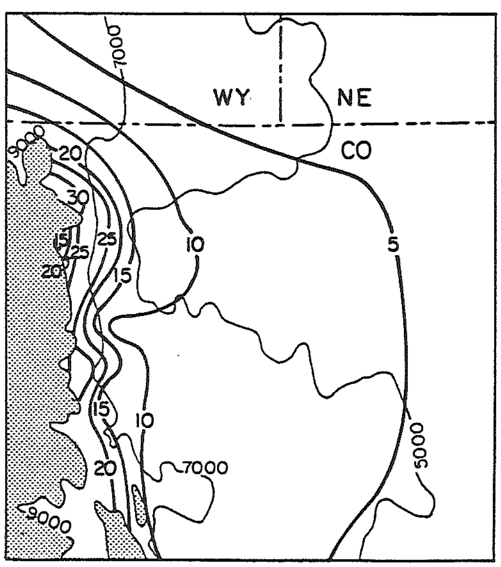

Fig. 5 *Snowfall (inches) distribution for 30-31 March 1988 cold air damming event.*

Table 2 *Snow crystal observations for the spotter network shown in Fig. 5.*

Crystal Type	Total No. Occurrences
heavily-rimed, aggregated spatial dendrites	41
heavily-rimed irregulars	29
graupel	18
rimed, aggregated plates	11
rimed sector plates	9
heavily-rimed stellars	7
unrimed stellars	4
lightly-rimed dendrites	4
unrimed plates	3

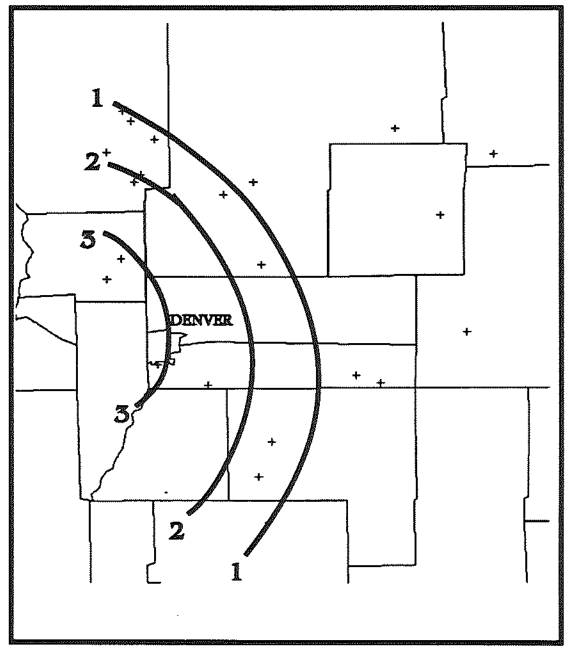

Fig. 6 *Snowfall (inches) distribution for 15-16 January 1991 case.*

Acknowledgments

This work was supported by Interagency Agreement DTFA01-90-Z-02005.

References

Rasmussen, R.M., M.K. Politovich, J.D. Marwitz, J. McGinley, J. Smart, W. Sand, G. Stossmeister, B. Bernstein, R. Pielke, D. Wesley, S. Rutledge, K. Elmore, E.R. Westwater, B.B. Stankov and D. Burrows, 1992: Winter Icing and Storms Project (WISP). *Bull. Amer. Meteor. Soc.* In Press.

Wesley, D.A. and R.A. Pielke, 1990: Observations of blocking-induced convergence zones and effects on precipitation in complex terrain. *Atmos. Res.*, **25**, 235-276.

1991 Winter Icing and Storms Project (WISP91) Data Catalog, 1991: 107 pp. Available from the Research Applications Program, NCAR, P.O. Box 3000, Boulder, Colorado 80307.

A TRY AT UNIVERSAL REGRESSION RETRIEVAL OF THE GROUND-BASED MICROWAVE REMOTE SENSING PRECIPITABLE WATER AND PATH-INTEGRATED CLOUD LIQUID WATER CONTENT

Wei Chong and Lu Daren

Institute of Atmospheric Physics, Chinese Academy of Science
Dewai, Beijing, P.R.China 100029

1. INTRODUCTION

Ground-based dual-frequency (20.6, 31.4 GHz) microwave radiometer(GBDFMR) has played an important part in the measurement of precipitable water vapor Q and path-integrated cloud liquid water content L in the atmosphere and shows a broad prospect. Statistic method is a routine way to retrieve Q and L from measurements of GBDFMR. Usually, some samples of local (typical of an area) radiosonde were used and cloudy samples were made by inserting certain cloud water in some levels of these radiosonde data in a supposed manner.Based on these cloudy samples microwave radiation transfer was calculated to obtain the 'measuements' of GBDFMR. Then relationships between Q, L and the measurements was obtained by statistical regression. Unfortunately, some problems arouse:how can we obtain the relationship in an area where there is no radiosonde station? and how can we use a lot of different local relationships when we take measurement in a vast area?

By using stepwise regression technique a retrieval method is proposed in this paper to try finding universal equations for probing Q and L from measurements of GBDFMR, which can apply all local places, all sea level elevations and all seasons.

2. CLOUD MODEL AND CLOUDY MICROWAVE RADIATION TRANSFER CALCULATION

GBDFMR received brightness temperature T_b at frequency f in the vertical direction is

$$T_b(f)=T_\infty \exp(-\int_0^\infty(\alpha_{H2O}(z)+\alpha_{O2}(z)+\alpha_{cld}(z))*dz+\int_0^\infty T(z) *(\alpha_{H2O}(z)+\alpha_{O2}(z)+\alpha_{cld}(z))*\exp(-\int_0^z(\alpha_{H2O}(z') +\alpha_{O2}(z')+\alpha_{cld}(z'))*dz')*dz \qquad (1)$$

where T_∞ is cosmic background brightness temperature(2.7k), α_{H2O}, α_{O2} and α_{cld} are the volume absorption coefficients for water vapor, oxygen and cloud liquid water,respectively. They are the functions of the densities of these parameters in level z,and therefore are the functions of temperature,humidity and pressure of atmosphere, which can be obtained by using radiosonde data. Unfortunately, no routine information can be used for cloud construction and density of cloud liquid water, so we have to use a way similar to that discribed in the reference (Decker et al., 1978): Using relative humidity threshold as a criterion of exist of cloud. The density of cloud liquid water is related to the thickness of cloud layer itself and distributes as a function of the height above the cloud base in certain manner. Obviously, the number and the configuration of cloud samples vary as the threshold value varies and we can adjust the threshold to get different cloud models based on same radiosonde case.

3.REGRESSION SAMPLES

a. Typical of Areas and Seasons

A set of a priori radiosonde data in typical season(winter, summer) with a total of 2742 cases were selected from eight (typical of climate and sea level elevation) radiosonde stations.They are Beijing (39°48'N, 116°28'E, 55m), Guangzhou (23°08'N, 113°19'E, 7m), Guam(13°33'N, 144°50'E,111m), Yap(9°39'N, 138°05'E, 77m), Lhasa(29°40'N, 91°08'E, 3650 m), Zhangye(38°56'N, 100°26'E, 1480 m), Nagqu(31°29'N, 92°04'E, 4508 m) and Lijiang(26°52'N, 100°26'E, 2394m).

b. Mixing Samples and Cloudy Ratio

A set of mixing samples of radiosonde data with both clear and cloudy situations is used as the regression samples in order to make the expected regression equations. The resulted regression relationship should have the ability of automatically distinguishing clear or cloud days.

The cloudy ratio--the ratio of cloudy days to the total days during a time period in a certain place-- varies largely as the place in the world and the seasons vary. In order to reflect the true condition, climate statistics of cloudy ratio in the two typical seasons is made at the eight stations based on five-year routine surface cloud record. Adjusting the above mentioned relative humidity threshold for each station, we obtain the proportional clear and cloudy samples at each place and in certain season. In this way we construct a set of clear and cloudy mixing samples with a total of 2742 cases including 1244 cloudy cases. The threshold of relative humidity for cloud is selected as 85% in present situation.

4. STEPWISE REGRESSION

a. Predictors

12 variables are selected as the predictors. They are T_{b1}--brightness temperature at 20.6 GHz, T_{b2}--that at 31.4 GHz, T_s--surface temperature (T_{b1}, T_{b2} and T_s are in K), E_s--surface absolute humidity(in g/m^3), P_s--surface pressure(in hPa), CBH--cloud base height (in km), Exist (=0 when it is clear day, =1 when cloudy), E_s/P_s, T_{b1}/T_s, T_{b2}/T_s, $(T_{b1})^2$, and $(T_{b2})^2$.

b. Result of Regression

Table 1. The Regression Coefficients, Compound Correlation Coefficient and Standard Residual S_e for Stepwise Regression Equations

	B_0	T_{b1}	T_{b2}	$(T_{b1})^2$	$(T_{b2})^2$	T_{b1}/T_s	T_{b2}/T_s	R_r	S_e	
Q	-.22489	.10334	-.017461	.00030304	-.00018691		-5.8548	.9998	.0378	(4)
L	- 76.280	-179.32	171.346	.092967		47454.6	-42504.3	.9933	56.63	(5)

* The first column from left is the predictands. The second column is the constant term of the Eqs.

All 12 variables can be introduced into the regression equations both for Q and L when the significance level of F-testing equals 2.0. But, the functions of these variables in the equations are not the same. It is found that Eq.(4) and (5) shown in Table 1 has only five variables and has already had enough accuracy for retrieving Q and L. And there are only three variables (T_{b1}, T_{b2}, T_s) need to be measured and others are their nonlinear combinations. It is weel known that T_s is the most easily avialable variable. So we use the equation (4) and (5) as the universal retrieval regression equations and check these two equations on their accuracies.

5. THE TESTING OF REGRESSION EQUATIONS

a. Standard of Testng

We use RMS as standard of absolute accuracy testing

$$RMS=\left(\sum_{i=1}^{n}(u_i-\hat{u}_i)^2/n\right)^{1/2},$$

and Rel as standard of relative accuracy testing

$$Rel=1/n*\left(\sum_{i=1}^{n}|u_i-\hat{u}_i|/u_i\right),$$

where n is the number of testing samples. u_i is the 'truth' for Q or L and $\hat{u}_i$ the corresponding regression value.

For L we just make the absolute accuracy testing.

b. Testing Samples

Internal Testing Samples:

The data of total amount of 2742 cases at the eight stations and two seasons used for stepwise regression themselves are used as internal testing samples and divided into eight sets according to the stations.

Extrapotation Testing Samples:

1) Temporal Extrapotation Samples, samples from the same eight stations as those for the internal testing samples but in different years or different seasons.

2) Spatial Extrapotation Samples, the samples in different time from following 7 stations: Xian(34°18'N, 108°56'E, 398m), Urumqi(43°47'N,87°37'E,918m), Shanhai(31°10'N, 121°26'E,5m), Kunmin (25°01'N, 102°41'E, 1891m), Chichijima(27°05'N, 142°11'E, 4.1m), Denver(39°45'N, 104°52'W, 1625m) and Washington(39°00'N, 75°00'W, 84m).

Altogether, 21 sets of extrapotation testing samples with total of 1020 cases from 15 stations and (or) in different seasons are taken.

c. Testing Results

For internal samples, the RMS of Q for each out of the 8 set samples are from 0.02 to 0.06 cm and corresponding Rel are from 0.6% to 10.0% and the RMS of L for each out of the 8 set samples are from 30.0 g/m2 to 74.4g/m2 (i.e.0.003--0.0075 cm).

For extrapotation testing samples, among the 21 sets of samples the RMS of Q are in the range 0.011 to 0.096 cm and the Rel is from 0.4% to 6.0% and RMS of L are from 3.3 to 95 g/m2 (i.e. 0.00033 --0.0095 cm).

6. CONCLUSION AND DISCUSSION

Two of the universal retrieval equations for GBDFMR retrieval of the precipitable water Q and column cloud liquid water content L has been obtained in present paper. It is found that the retrieval accuracy of Q from present universal relationship is with fairly fine accuracy, even better than some local statistical regression results (e.g. Wei et al.,1989), The retrieved L also has high accuracy for most of application purposes. The results have shown the feasible and realizable to obtain universal retrieval equations for Q and L.

In present paper, we have not considered the measurement error (errors of T_{b1}, T_{b2}, and T_s etc.), though it is an easy step to do. The samples both for regression and for testing are still limited as concerns 'glouble'. So the tesults are only preliminary.

REFERENCE

Decker M.T.,et al.(1978), Experimental Evaluation of Ground-Based Microwave Radiometric Sensing of Atmospheric Temperature and Water Vapor Profiles. Jour. of Appl. Meteor., Vol.17,1788-1795.

Wei Chong., H.G.Leighton and R.R.Rogers (1989), A Comparason of Several Radiometric Methods of Deducing Path-Integrated Cloud Liquid Water, Atmospheric and Oceanic Technology, Vol.6,No.6, 7001-1012.

The Fluctuating Radar Cross Section (RCS) of Multifractal Scatterers

Mike R. Duncan, [1]S. Lovejoy, F. Fabry, and [2]D. Schertzer

McGill Radar Weather Observatory
Ste Anne de Bellevue, Québec
H9X-1C0
CANADA

[1]Physics Department
McGill University
Montréal, Québec
CANDA

[2]EERM/Météorologie Nationale
Paris
FRANCE

Introduction.

The distribution governing the fluctuations of intensity of echo returns from a fixed pulse volume was formally introduced by Marshall and Hitschfeld (1953) and Wallace (1953). The theory put forth by these authors will be referred to as the 'standard theory'. Other workers at the time also examining the fluctuating returns (Austin, 1952) achieved results consistent with the standard theory. Later verification of the standard theory was put forth by Lhermitte and Kessler (1966). A modification to the standard theory was made by Rogers (1971) who, in a theoretical treatment, included the possibility of gradients in the rainfield affecting the distribution of the fluctuating echo. Schaffner et al., (1980) used the modification of Rogers to measure biases due to reflectivity gradients in the rainfield. Schaffner et al. concluded indirectly that the standard theory was a valid approximation.

Measurements of the fluctuating echo from a fixed pulse volume were recorded using a high pulse repetition frequency (PRF) vertically pointing radar. Each time series of the fluctuating echo consisted of either 3.6 or 7.2 million points. Distributions and power spectra of the time series of echo values were calculated. The distributions show a marked difference from that predicted by the standard theory, and several computed distributions show power-law or 'fat' tails. The power spectra showed two scaling regions consistent with the scales smaller than the wavelength and scale larger than the pulse volume. The intervening scales show a plateau that results from the averaging of the pulse volume. The existence of the scaling regions and the power-law tails of the distribution show the assumptions of the standard theory to be invalid for these measurements.

The standard theory makes two assumptions about the rainfield: That the scatterers be randomly distributed in space and that they be point scatterers. Both of these assumptions can be shown to be violated regularly. The approximation of Rogers (1971) of the effects of gradients in the rainfield likely represents an adequate solution to the problem of gradients in the reflectivity field if the scatterers are assumed to be point scatterers. The dependancy of the standard theory on the assumption of point scatterers has not been examined. The coalescence and breakup of raindrops through collision processes has been studied in great detail (see Prupacher and Beard, 1970 ; Low and List, 1982a,b; List and Fung, 1982; Beard et al., 1983; Chandrasekar et al., 1988). The intermediate products, such as sheets, disks and oblate spheroids, of the drop collision process can have size parameters (at X-band) close to 1 and axis ratios greater than 10:1. Low and List (1982a,b) show how drop collisions can result in intermediate collision products which are very large and short lived. Beard et al., (1983) point out that as many as 10 collisions per second per cubic meter of space may result in only moderate rainfall. Further, Beard et al. mention that the scintillations due to these collisions are clearly visible by shinning a light upwards into a rainy night sky. While a poetic observation, there exists the fact that a vertically pointing radar would also tend to pick up these effects to a certain degree. Gunn and East (1954) made calculations that show the enhanced scattering due to oblate spheroids using the shape factors described by Gans (1912). While not strictly applicable to some of the sizeable collision products, the theory suggests that the preferrentially oriented collision products can greatly enhance scattering.

The term radar cross section (RCS) field is introduced to represent the distribution of cross sections within the pulse volume and in space. Our computations show that the RCS field exhibits scaling behaviour and distributions of echo fluctuations with long tails. This behaviour is not explainable in terms of the standard theory. Modelling of the RCS field, and radar measurements thereof, using a scaling universal multifractal model will be shown to reveal qualitative behaviour consistent with the observed time series (a discussion of universal multifractals in rain processes can be found in Lovejoy and Schertzer, 1990). The scaling of the power spectra and the shape of the distributions that result are a direct consequence of the multiscaling nature of the model. The overall suggestion is that the rainfield exhibits scaling behaviour which extends to the smallest time and space scales.

Instrumentation.

The passage of several precipitation events over the Montreal region were recorded by the vertically pointing radar (VPR) operated by McGill Radar Weather Observatory (MRWO). Two different transmitters were used to collect the vertically pointing data. Table 1 shows a selected list of the vertically pointing data collected at MRWO. The A data set was collected with a 1700 Hz PRF 25 kW pulsed X-band transmitter with a logarithmic receiver which has a noise figure of 10 dB. The rest of the data sets were collected with a 1300 Hz PRF 25 kW pulsed X-band radar with logarithmic receiver which has a noise figure of 4 dB. The vertically pointing radar set up includes a 1.2 m antenna with a sidelobe skirt. The beamwidth of this system is 2°. The transmitter was operated with a 250 ns pulse length (37.5 m) which at 1 km altitude produced a 40m $\times$ 40m $\times$ 37.5m pulse volume.

Table 1: VPR Echo Time Series.

Series	Precip.	Date	PRF (Hz)	Height (km)	# of Points ($\times$ 1024)
A	Conv. Rain	19/09/90	1700	1	7168
B_1	Conv. Rain	26/09/91	1300	1	3584
B_2	Conv. Rain	26/09/91	1300	1.4	3584

The collection equipment for the time series data consisted of a PC-486 computer with 8 MegaBytes of memory and a digitizer card. The digitizer card, which uses an 8-bit flash A/D converter, is triggered by the external radar trigger. After 7,340,032 (limited by computer memory) measurements have been collected, the program dumps the digitized echoes to disk.

Observations and Computation of the Time Series of the Fluctuating Echo.

The Distributions.

The intensity distributions of the echo signal for the vertically pointing radar were computed for the data sets and were found to be far from the expected Rayleigh distribution (Marshall and Hitschfeld, 1953; Wallace, 1953). The Rayleigh distribution is shown in figure 1 with the observed distribution and is represented mathematically as

$$P(I/I_0) = m \exp(m(I - I_0) - \exp(m(I - I_0)))$$

where $m = \log_e(10)$ and I is understood as the log intensity. The distributions observed for the vertically pointing time series showed a log-normal shaped distribution.

The behaviour of the tails of the observed distributions is also significantly different from that predicted by the standard theory. The standard theory predicts that the tails of the distribution governing the magnitude of fluctuations should fall off exponentially as $Pr(p > P) \propto \exp(-\exp(P))$, whereas some of the observed distributions appear to have power-law or 'fat' tails. Table 2 shows some exponents for the power-law tails.

Table 2: Exponents for Power-Law Tails		
A	B_1	B_2
-3.17	-2.59	-2.90

The width of the distributions imply that integrating echoes to produce estimates of reflectivity (Z) will result in uncertainties exceeding the well known 5.6 dB/$k^{1/2}$ (where k is the number of echoes integrated). Simulations using the distribution computed from the observed data indicate that the uncertainty may exceed 8 dB/$k^{1/2}$.

The Power Spectra.

The power spectra show two scaling regions with a plateau between (Figures 2 and 3). The scaling behaviours at high and low frequencies are generally characterized by different scaling exponents. The high frequency scaling regime, High Slope in table 3, represents the physics of the interactions of the scatterers at sub-wavelength scales. Velocities in this scaling regime would be characterized by the drop fall speeds and turbulence. The low frequency scaling regime, Low Slope in table 3, represents the interaction of the pulse volume with the rainfall gradients. Velocities in this scaling regime would be characterized by the advection velocity of the precipitation system. The scaling of the low frequency signal is consistent with the scaling behaviour noticed in the rainfield by Schertzer and Lovejoy (1987), Crane (1990), Lovejoy and Schertzer (1990), and Gupta and Waymire (1990). Correlation times for the different time series are shown in table 3. $\tau_{0.01}$ is the standard representation of the correlation times for radar fluctuation estimates (Sauvageot, 1982).

Table 3: Slopes and Scales of the Scaling Regimes

Data Set	Low Scale (in s)	Low Slope	High Scale (in s)	High Slope	$\tau_{0.01}$
A	4.34	-1.92	0.0104	-1.54	8.5 ms
B_1	7.33	-1.88	0.0124	-1.21	6.1 ms
B_2	7.60	-1.88	0.0136	-1.51	7.9 ms

The plateau region, bounded by Low Scale and High Scale in table 3, is the result of averaging of the rainfield by the pulse volume. By analogy with the continuous cascade model (see next section) the High Scale in table 3 should be 3.21 cm (the wavelength), this gives a velocity of 3.2 m/s for the A time series. The Low Scale in table 3 should represent the pulse volume scale, which implies a turbulent velocity of 8.6 m/s or 31 km/h for series A.

Supporting data for the standard theory was provided by Lhermitte and Kessler (1966). The pulse volumes used by Lhermitte and Kessler were at ranges between 40 nmi and 120 nmi. At 40 nmi (80 km), assuming a 3.3 m circular parabolic antenna and a 10 cm wavelength, the pulse volume would be some 3 km in height and width. The intensity distributions that Lhermitte and Kessler observed were formed from a limited sample of 10^4 points. Assuming that the rain process is multiscaling, a renormalization of our observed distribution to the scales of observation of Lhermitte and Kessler would reveal similar results for the first two decades of probability. The observed distributions differ greatly from the theory in the probability of extreme events or singularities which are very rare but are statistically very significant. The data of Lhermitte and Kessler does not extend to this range of probabilities.

Modelling of the Fluctuating Echo.

The scales present in the power spectra for the observed echoes are used to model the qualitative behaviour of the observed power spectra. Consider a volume (a computer array for current purposes) with discrete elements or pixels. Fill the volume with scatterers. By subdividing the volume into equal sub-volumes we approximate the scales of the wavelength and pulse volume. The intensity resulting from the scatterers in the pulse volume may be computed as follows:

$$I(t) = \sum_i a_i^2 + \sum_{i \neq j} a_i a_j \cos\{(\phi_i - \phi_j)\}$$

Continuous Cascade Model.

We seek a model that exhibits scaling properties in order to emulate the scaling behaviour found in the computed power spectra. Such a model exists and is termed a 'continuous cascade' (see Wilson et al., 1991). What we expect from this model is behaviour consistent with the scaling at high and low frequencies, as well as the representation of the singularites we tentatively associate with enhanced scattering by drop collisions. The continuous cascade is a stochastic process whose ensemble statistics are well documented (Schertzer and Lovejoy, 1987; Lovejoy and Schertzer, 1990) and generically yields multifractal (multiscaling) fields. The continuous cascade has a generator $\Gamma_\lambda = \ln \varepsilon_\lambda$, where λ is a scale ratio < 1 (i.e. λ is the ultimate resolution of the RCS field) and ε_λ is the model of the RCS field. The moments of the RCS field ε_λ are defined as

$$\varepsilon_\lambda^q = \langle e^{q\Gamma_\lambda} \rangle = e^{K_\lambda(q)} = e^{\ln(\lambda)K(q)} = \lambda^{K(q)}$$

where

$$\Gamma_\lambda(\bar{x}) \quad = \quad \int_{S_{1:\lambda}} f(\bar{k})\tilde{\gamma}(\bar{k})e^{i\bar{k}\cdot\bar{x}}d\bar{k}$$

$\tilde{\gamma}(\bar{k})$ is a noise source or 'sub-generator' and $f(\bar{k})$ is a real filter set to $f(\bar{k}) = k^{-D/2}$ where D is the dimension of the space. The resulting power spectrum for ε_λ has the form $S(\bar{w}) \sim w^{-1}$, thus $\Gamma_\lambda(\bar{x})$ is a 1/f pink noise. Thus the RCS field ε_λ is modelled by exponentiated pink noise. The function K(q) is continuous and represents the scaling exponent for ε_λ as a function of q. For universal multifractals

$$K(q) = \begin{Bmatrix} \dfrac{C_1}{\alpha - 1}(q^\alpha - q) & \alpha \neq 1 \\ C_1 q \log(q) & \alpha = 1 \end{Bmatrix}$$

where C_1 is the codimension of the mean of the process (controls the clustering), and α is a parameter which indexes the stable distribution to which the process ε_λ belongs. α and C_1 are two free paramters of the model that control the singularity and correlation of the RCS field. By increasing C_1 the RCS field is spread over sparser sets (clustering becomes stronger). The exponent of the high frequency scaling regime is given by $1 - 2C_1$ (when $\alpha = 2.0$).

The continuous cascades were constructed on 2-dimensional arrays. The pulse volume was then considered to be a column of the array. Thus, one $n \times n$ array would result in n intensity measurements. The natural correlations present in these fields resulted in the n columns representing a time evolution of the scattering in the pulse volume. The power spectra resulting from this model show the qualitative behaviour of the power spectra of the observed echoes. Including the different slopes of the scaling ranges at high and low frequency. The implication of this behaviour is that different scaling exponents can result from the same scaling process. Thus it seems plausible to consider the rainfield as a fully scaling process. It is also possible to extract the wavelength and pulse volume scales from the realized spectra (in analogy to this proceedure the velocities were extracted from the observed power spectra). To date, alpha has been limited to the value 2.0 (log-normal process) and C_1 has been ranged up to 0.125. Figure 4 shows the result of $C_1 = 0.03$. The two scaling regimes and the plateau are clearly visible. The two scaling regimes in figure 4 have slopes -1.36 (low frequency) and -0.94 (high frequency). The visibility of the plateau region is dependant upon the scale of the pulse volume. Availability of computer memory limits the cascade size to 512×512 pixels, with 8 pixels per wavelength and 64 wavelengths per pulse volume. Figure 5 shows the distribution of intensities for the continuous cascade model plotted with the theoretical (Rayleigh) distribution. Comparison of figure 5 with figure 1 reveals that the continuous cascade adequately models the qualitative behaviour of the observed distributions.

Summary and Conclusions.

Observation of the fluctuating echo from small pulse volumes with a vertically pointing radar in continuous precipitation reveals behaviour inconsistent with the standard theory. The existence of scaling processes with long tailed probability distributions makes the standard theory untenable, but remains consitent with observed behaviour in the rainfield. Modelling of the RCS field with continuous cascades, which are multiscaling processes, reveals qualitative behaviour consistent with the distributions and power spectra computed from the observed results. Thus, the RCS field may be considered as a mutifractal and thus, can statistically describe the general scaling of the rainfield at low frequencies and the singularities, tentatively associated with enhanced scattering, at high frequencies.

Some implications of these observations are as follows: Scaling behaviour in the rainfield, noticed by many authors, continues below the scale of the radar wavelength. The width of the distributions for the fluctuating echo suggest that the well known relation for the error on estimates of reflectivity exceed 5.6 dB/$k^{-1/2}$, and may be as high as 8 dB/$k^{-1/2}$. The width of the observed distributions, the existence of scaling regions and the qualitative success of the continuous cascade model suggest a revision of the standard theory is in order.

References.

Austin, P.M., 1952. A Study of the Amplitude Distribution Function for Radar Echoes from Precipitation. Technical Report #17, M.I.T.

Beard, K.V., D.B. Johnson and A.R. Jameson, 1983. Collisional Forcing of Raindrop Oscillations, *Journal of the Atmospheric Sciences*, 40, 455-462.

Chandrasekar, V., W.A. Cooper and V.N. Bringi, 1988. Axis Ratios and Oscillations of Raindrops, *Journal of the Atmospheric Sciences*, 45(8), 1323-1333.

Crane, R.K., 1990. Space-Time Structure of Rain Rate Fields. *Journal of Geophysical Research*, 95(D3), 2011-2020.

Foote, G.B, and P.S.du Toit, 1969. Terminal velocity of raindrops aloft. J. Appl. Metor., 8, 249-253.

Gans, R., 1912. Uber die Form ultramikroskopischer Goldteilchen. *Ann. der Physik*, 12, 881-900.

Gunn, K.L.S., and T.W.R. East, 1954. The microwave properties of precipitation particles. *Quarterly Journal of the Royal Meteorological Society*, 80, 522-544.

Gupta, V.K., and E. Waymire, 1990. Multiscaling Properties of Spatial Rainfall and River Flow Distributions. *Journal of Geophysical Research*, 95(D3), 1999-2009.

Lhermitte, R.M., and E. Kessler, 1966. Estimation of the Average Intensity of Precipitation Targets. Preprints of the 12th Conference on Radio Meteorology, AMS, Boston.

List, R., and C. Fung, 1982. The Effect of Pressure on the Breakup of One Pair of Raindrops. *Atmosphere-Ocean*, 20, 17-27.

Lovejoy, S., and D. Schertzer, 1990. Multifractals, Universality Classes and Satellite and Radar Measurements of Cloud and Rain Fields. *Journal of Geophysical Research*, 95(D3), 2021-2034.

Low, T.B., and R. List, 1982. Collision, Coalescence and Breakup of Raindrops. Part I: Experimentally Established Coalescence Efficiencies and Fragment Size Distribution in Breakup. *Journal of the Atmospheric Sciences*, 39, 1591-1606.

Low, T.B., and R. List, 1982. Collision, Coalescence and Breakup of Raindrops. Part II: Parameterization of Fragment Size Distributions. *Journal of the Atmospheric Sciences*, 39, 1607-1618.

Marshall, J.S., and W. Hitschfeld, 1953. Interpretation of The fluctuating Echo from Random Distributed Scatterers; Part I. *Canadian Journal of Physics*, 31, 962-994.

Marshall, J.S., and W. McK. Palmer, 1948. The Distribution of Raindrops with Size. *Journal of Meteorology*, 5, 165-166.

Musgrove, C., and M. Brook, 1975. Microwave Echo Fluctuations Produced by Vibrating Water Drops. *Journal of the Atmospheric Sciences*, 32, 2001-2007.

Pruppacher, H.R., and K.V. Beard, 1970. A wind tunnel investigation of the internal circulation and shape of water drops falling at terminal velocity in air. *Quarterly Journal of the Royal Meteorological Society*, 96, 247-256.

Rogers, R.R., 1971. The effect of variable target reflectivity on weather radar measurements. *Quarterly Journal of the Royal Meteorological Society*, 97, 154-167.

Sauvageot, H., 1982. **Radarméteorologie**. Eyrolles, Paris, France.

Schaffner, M., R. Rhinehart, and R. Leonardi, 1980. Detection of Nonuuniformities within the Radar Measurement Cell. Preprints, 19th Radar Conference, AMS, Boston, 256-263.

Schertzer, D., and S. Lovejoy, 1987. Physical Modelling and Analysis of Rain and Clouds by Anisotropic Scaling Multiplicative Processes. *Journal of Geophysical Research*, 92(D8), 9692-9714.

Wallace, P.R., 1953. Interpretation of The fluctuating Echo from Random Distributed Scatterers; Part II. *Canadian Journal of Physics*, 31, 994-1009.

Wilson, J., D. Schertzer, and S. Lovejoy, 1991. Continuous Multiplicative Cascade Models of Rain and Clouds. In, **Non-Linear Variability in Geophysics**, D. Schertzer and S. Lovejoy (Eds.), Kluwer Academic Publishers.

Figures

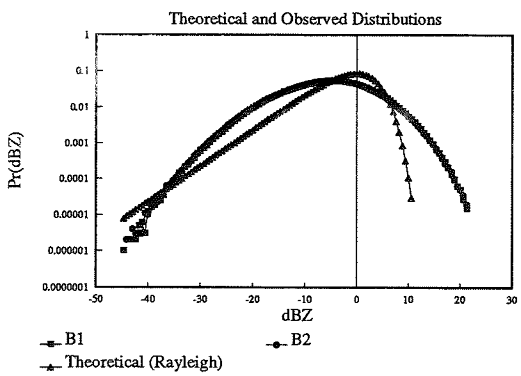

Figure 1: Observed and theoretical distributions.

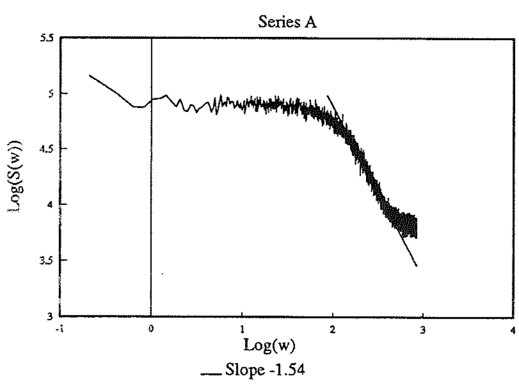

Figure 2: Power spectrum for high frequency.

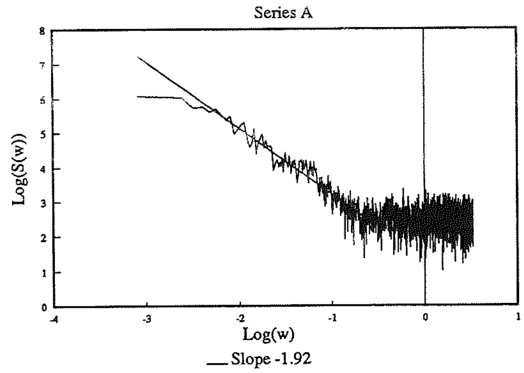

Figure 3: Power spectrum S(ω) for low frequency.

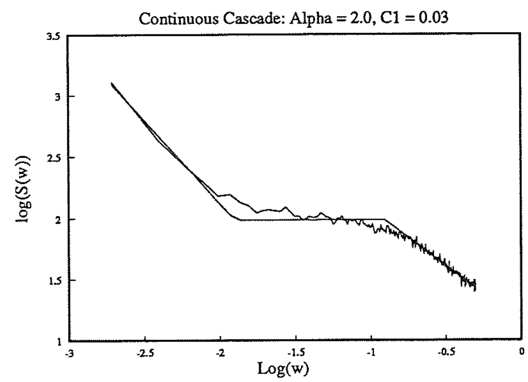

Figure 4: Power spectrum from the continuous cascade model.

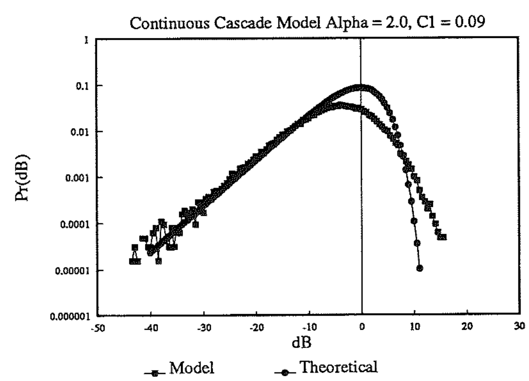

Figure 5: Intensity distribution for the continuous cascade model.

HYDROMETEOR BACKSCATTERING AT MILLIMETER WAVELENGTHS

Orazio Sturniolo[1], Alberto Mugnai[2] and Franco Prodi[1(+)]

[1]Istituto FISBAT, Consiglio Nazionale delle Ricerche, Bologna, Italy
[2]Istituto di Fisica dell'Atmosfera, Consiglio Nazionale delle Ricerche, Frascati, Italy
[(+)]Also with the Dipartimento di Fisica, Università degli Studi, Ferrara, Italy

1. INTRODUCTION

Millimeter-wavelength radars operating in either of the atmospheric windows at about 35 and 90 GHz can provide information on cloud and precipitation, that is not available from measurements taken by conventional radars operating at centimeter wavelengths (Pasqualucci et al. 1983; Hobbs et al. 1985; Lhermitte 1987). For instance, smaller cloud and precipitation particles, as well as lower concentrations of them, can be detected by millimeter-wavelength radars since the hydrometeors, having a larger optical size, are more efficient scatterers than at longer wavelengths. By the same token, greater care should be devoted in interpreting the radar data for the backscattered signal can be largely impacted by the physical properties of the hydrometeors. However, the backscattering from nonspherical and non-homogeneous hydrometeors at millimeter wavelengths has been so far scarcely investigated. To our knowledge, most theoretical work on shapes different than spheres or oblate spheroids has concerned only centimeter wavelengths (see, for instance, Aydin et al. 1984; Bringi et al. 1986), while at millimeter wavelengths detailed calculations have been presented only for atmospheric ice crystals of several shapes (Evans and Vivekanandan 1990). At these wavelengths, the effects of conicity and elongation have not been studied in any detail.

We have recently udertaken both laboratory and theoretical studies on this subject, with particular emphasis on large particles for which the effects due composition and shape are more pronounced. A dual-polarization Doppler scatterometer operating at 8.38 mm has been developed at FISBAT/CNR to measure the backscattering from known water and ice particles (Prodi 1989). In addition, by using the *Extended Boundary Condition Method* (EBCM -- see Barber and Hill 1990), we have computed the backscattering for a large set of both elongated and conical hydrometeors having different composition, size, and shape, and as a function of their orientation with respect to the incident field.

A tiny selection of the computed backscattering cross sections and depolarization ratios at 35.8 GHz for these nonspherical hydrometeors is here presented and briefly discussed. The bulk of our scattering calculations, as well as corresponding laboratory measurements, will be contained in a forthcoming paper.

2. PARTICLE SHAPE AND COMPOSITION

For our backscattering studies, we have considered rotationally-symmetric homogeneous particles composed either of water or pure ice, as well as their non-homogeneous counterparts made of either soft or wet ice. In the latter case, the refractive index (m) has been computed using second order Maxwell-Garnett theory for inclusions of either air or water in ice (see Bohren and Huffman 1983).

To describe the particle shape we have selected the analytical form proposed by Wang (1982), which allows to continuously vary particle conicity and/or elongation. These 'Wang particles' are described by the mathematical function:

$$x = \pm\, r_{ev}\, a\, \{1 - [y \,/\, (b\, r_{ev})]^2\}^{1/2} \cos^{-1}[y \,/\, (\delta\, b\, r_{ev})] \quad (1)$$

where x and y are the horizontal and vertical coordinates of the surface (the rotation, or symmetry, axis is vertical), r_{ev} is the radius of the equal-volume sphere, b ($0 < b < \infty$) is the elongation parameter, δ ($1 \leq \delta \leq \infty$) the conicity parameter, and a is a function of b and δ. For any given b, conicity decreases by incresing δ. Thus, spheres and spheroids are obtained for $\delta = \infty$, b being the axial ratio of the generating ellipse ($b < 1$ and $b > 1$ for oblate and prolate spheroids, respectively; $b = 1$ for spheres). In this study, we have considered elongation values $0.8 \leq b \leq 1.2$. Examples of relevant Wang particles are shown in Fig. 1.

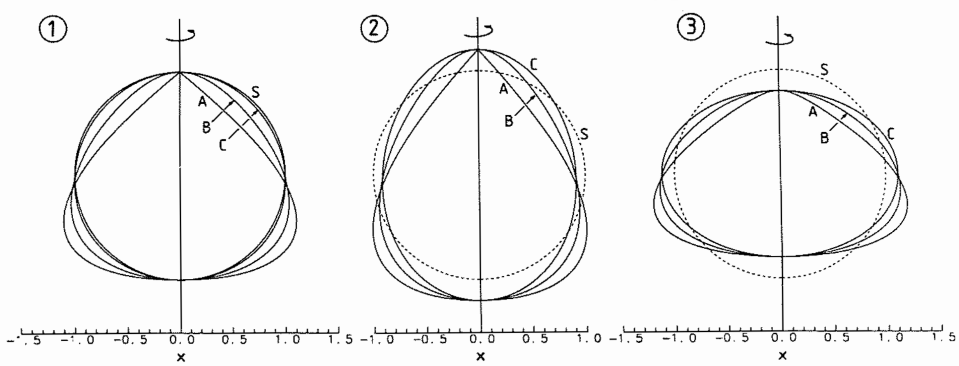

FIG. 1. Examples of Wang particles corresponding to an equal-volume sphere (curve S) having unitary radius: (1) for elongation parameter $b = 1.0$ and conicity parameter $\delta = 1.0$ (curve A), 2.0 (B), 10.0 (C), and ∞ (S: sphere); (2) for $b = 1.2$ and $\delta = 1.0$ (A), 2.0 (B), and ∞ (C: prolate spheroid); and (3) for $b = 0.8$ and $\delta = 1.3$ (A), 2.0 (B), and ∞ (C: oblate spheroid).

3. NUMERICAL RESULTS

In our computations, the symmetry axis of the scattering particle is supposed to be vertical (thus, hydrometeor canting has not been taken into account) while the direction of the incoming radiation is let to vary from an incidence angle (Θ) $\Theta = 0°$ (when the radar is pointing vertically, i.e. for a 90° elevation) up to $\Theta = 90°$ (when the radar is pointing horizontally, i.e. for a 0° elevation).

By means of an EBCM code, backscattering quantities that are of primary importance for interpretation of multiparameter radar observations have been computed: i.e., the backscattering cross sections at horizontal and vertical polarization (σ_H and σ_V, respectively -- the horizontal plane is the plane containing both the symmetry axis of the particle and the direction of the incoming radiation), their ratio (the so-called differential reflectivity, Z_{DR}), and the circular depolarization ratio (*CDR*), which is obtained by means of the backscattering matrix. [No linear depolarization ratio (*LDR*) can be observed for the considered scattering geometry.] As customary, in what follows both Z_{DR} and *CDR* will be expressed in logarithmic units (dB); thus, for a sphere, $Z_{DR} = 0$ dB and $CDR = -\infty$ dB.

Fig. 2 shows the values of σ_H, Z_{DR}, and *CDR* as a function of the angle of incidence Θ for five different soft-ice Wang particles with density equal to 0.6 g/cm^3 ($m = 1.522 - 0.0024\,i$), $r_{ev} = 0.5$ cm, and shapes which can be considered as limiting cases in our investigation. [Note that for $b = 0.8$, the EBCM code converged only for $\delta \geq 1.2$ -- in general, convergence becomes more and more difficult as b departs from unity and/or δ decreases.]

It is evident that for most non-spherical shapes, there are significant variations in the scattering quantities even for limited variations (a few degrees) of the angle of incidence. This is particularly true for conical oblate graupel particles (curve A), especially for low-to-mid radar elevations, and less true for conical prolate particles (curve D) for which both σ_H and Z_{DR} tend to be almost insensitive to Θ. It is also evident that at almost any angle, there is a considerable sensitivity to the shape of the scattering graupel particle. Such sensitivity is maximum for large Θ values (low radar elevations), while tends to disappear for Z_{DR} and *CDR* at low Θ values due to the fact that Wang particles are rotationally symmetric. Generally speaking, by comparing curves for the same b and different δ, one can get an idea of the expected variation due to conicity; vice versa, by comparing curves for the same δ and different b, one can see the effects of elongation. However, we must caution the reader that great care should be taken in this comparison for the effects due to varying b or δ may be highly non-linear -- as the following Fig. 3 will show. Moreover, we must caution the reader that the patterns shown in this figure are only representative of the considered particles; should their composition and/or size change, the curves would look rather different (cfr., following Fig. 4).

Fig. 3 shows the values of σ_H, Z_{DR}, and *CDR* as a function of the conicity parameter δ for soft-ice Wang particles at an angle of incidence $\Theta = 45°$. Results are shown for three different sizes ($r_{ev} = 0.2$, 0.5, and 1.0 cm) and for five different values of the elongation parameter b ($b = 0.8$, 0.9, 1.0, 1.1, and 1.2) which cover the range of variability considered in this paper for such parameter.

For all scattering quantities, variation with particle conicity generally increases with particle size -- note that depending on elongation, it may be considerable even for particles as small as those with $r_{ev} = 0.2$ cm. Often, the values for $\delta \approx 10$ are significantly different from those for very large δ's. Part (1) of Fig. 1 shows both the sphere and the corresponding Wang particle for $\delta = 10$; similar differences (not shown in Fig. 1) are found between oblate (or, prolate) spheroids and corresponding Wang particles with $\delta = 10$. Thus, even slight deformations from the spherical or spheroidal shape can cause backscattering variations that can impact radar measurements. The effects of conicity rapidly increase when δ decreases below about 10. Much larger changes are usually present in the conicity parameter range $2 \leq \delta \leq 10$ -- i.e., for moderately conical graupel particles (cfr., Fig. 1). Below $\delta \approx 2$ (i.e., for highly conical particles) the effects of conicity can become dramatic, causing sometimes, especially at the larger sizes, sharp rises and/or decreases of the plotted scattering quantities.

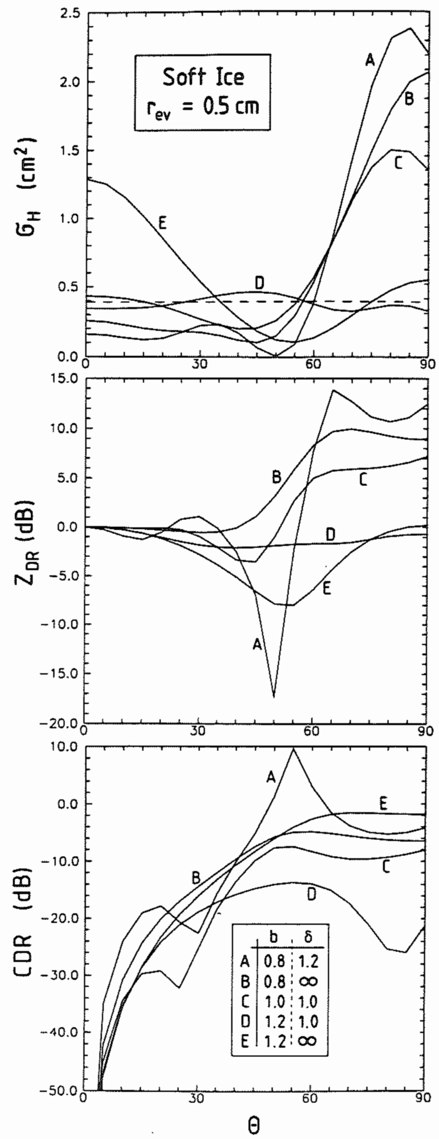

FIG. 2. Horizontal backscattering cross section (σ_H), differential reflectivity (Z_{DR}), and circular depolarization ratio (*CDR*) as a function of the incidence angle (Θ) for 5 different soft-ice Wang particles with $r_{ev} = 0.5$ cm. As a reference, σ_H for the equal-volume sphere is shown as a dashed line.

Fig. 3 can be also used to analyze the effects due to elongation. For small sizes (see results for $r_{ev} = 0.2$ cm), the curves for both σ_H and Z_{DR} are well ordered with particle elongation: for any δ value, σ_H decreases while Z_{DR} increases when b increases. This is not true, however, for *CDR*. For high conicity ($\delta \leq 2$), the curves are still well ordered, but intersect each other when conicity decreases. Nevertheless, a general trend is quite evident for moderately-to-slightly conical particles. In this case, as elongation increases, *CDR* decreases for oblate particles, and then increases again for prolate particles. [Note that *CDR* for $b = 1$ (curve C) is much lower than for oblate or prolate particles -- it rapidly tends to the spherical value ($CDR = -\infty$ dB).]

The variation of the scattering quantities with particle elongation becomes more and more complex as size increases (see results for r_{ev} = 0.5 and 1.0 cm). The curves corresponding to different b values intersect each other; in addition, they may show a sharp maximum or minum, usually for high conicity -- note, however, that Z_{DR} for r_{ev} = 1.0 cm and b = 1.2 has a deep minimum for a rather moderate conicity ($\delta \approx 6$). As a consequence, no general trend can be found for highly, and even moderately, conical large graupel particles. On the contrary, this is usually found for the slightly-to-moderately conical ones; in fact, as elongation increases, results for oblate particles get closer and closer to corresponding "spherical" values (i.e., for b = 1), and then depart again more and more for prolate particles. However, this is not always true -- as Z_{DR} and σ_H for oblate particles clearly show, respectively for r_{ev} = 0.5 and 1.0 cm.

Finally, we want to mention that while we have shown only the results for Θ = 45°, in our analysis we have considered several angles of incidence in order to study the effects due to different radar elevation. It turns out that while the general comments about the variation of σ_H, Z_{DR}, and *CDR* as a function of conicity, elongation, and size basically hold for any angle of incidence, the curves can be quite different depending on the considered Θ value -- as one can guess from previous Fig. 2.

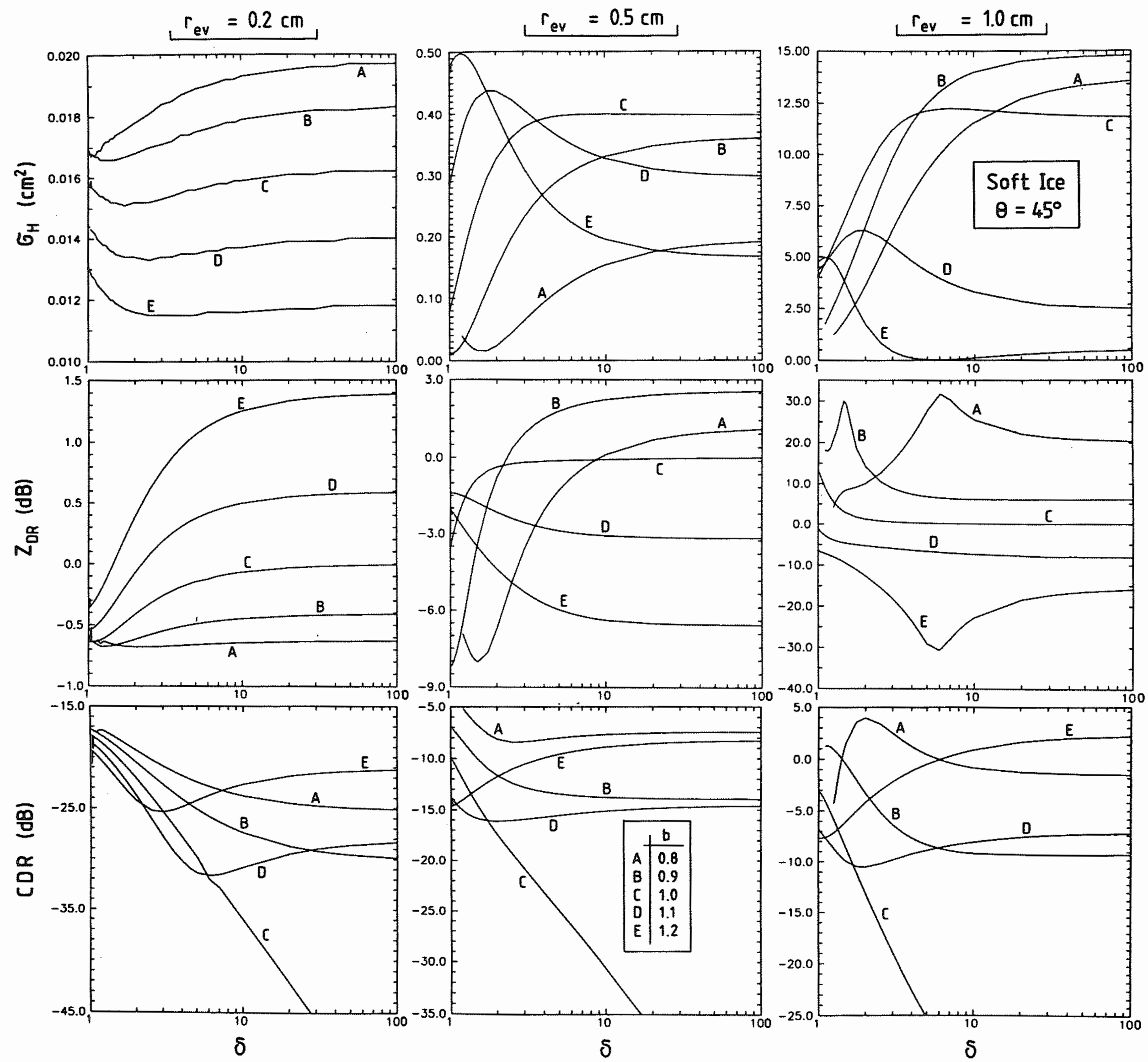

FIG. 3. Horizontal backscattering cross section (σ_H), differential reflectivity (Z_{DR}), and circular depolarization ratio (*CDR*) as a function of the conicity parameter δ for soft-ice Wang particles at an angle of incidence $\Theta = 45°$ and having elongation parameter b = 0.8, 0.9, 1.0, 1.1, and 1.2. The three columns refer to as many different sizes (r_{ev} = 0.2, 0.5, and 1.0 cm).

Fig. 4 shows σ_H, Z_{DR}, and *CDR* as a function of Θ for five different water (m = 4.559 - 2.654 i) Wang particles having r_{ev} = 0.2 cm and shapes which we consider as limiting cases for water drops (i.e., δ is never lower than 2.0, thus avoiding really conical shapes -- cfr., Fig. 1). Falling water drops are usually represented as oblate spheroids. Thus, in this figure it is particularly interesting to compare the results for oblate spheroids (curve B) with those for conical oblate particles (curve A). While σ_H is about the same in both cases, conicity raises significantly both Z_{DR} and *CDR*.

Finally, note that both Fig. 2 and Fig. 4 show that *CDR* is less than -30 dB for incidence angles lower than about 5°. On the contrary, Pasqualucci et al. (1983), by using a 8.6 mm radar at nearly vertical elevation (85°), measure *CDR*'s as high as -14 dB in the melting layer and of about -18 dB just above or below it. In our opinion, this difference may be due to the fact that Wang particles are rotationally symmetric while real precipitating hydrometeors may be not -- *CDR* is very low for rotationally symmetric particles at near nose-on incidence ($\Theta \approx 0°$), regardless of their size and composition.

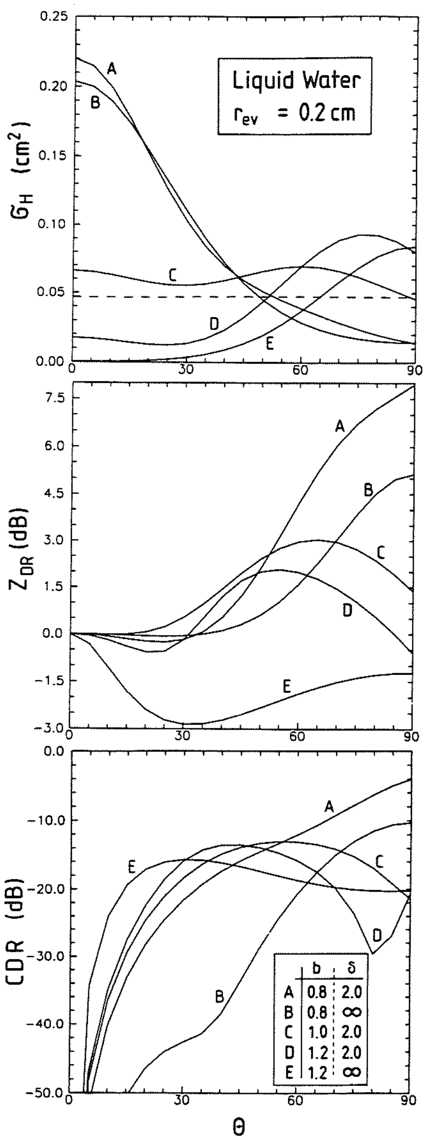

FIG. 4. As in Fig. 2, but for liquid water Wang particles with r_{ev} = 0.2 cm. Note that the lowest δ value is now δ = 2.0, as compared to δ = 1.0 for Fig. 2.

4. CONCLUSIONS

This preliminary study shows that the backscattering of millimeter-wavelength radiation at 35.8 GHz from precipitating soft-ice or liquid-water hydrometeors is quite sensitive to the detailed shape of the particles themselves and to their orientation with respect to the incident radiation. We have in fact analyzed the behaviour of three scattering quantities relevant to radar meteorology (i.e., the horizontal backscattering cross section, the differential reflectivity, and the circular depolarization ratio) for hydrometeors with different -- and, in our opinion, realistic -- degrees of conicity and/or elongation, and have shown that both of these parameters, as well as the elevation of the measuring radar, can impact considerably the considered scattering quantities. Variations can be significant even for small deformations of the particles and/or for small changes (a few degrees) of the direction of incidence of the incoming radiation -- i.e., of the radar elevation.

We believe that these results are of great interest for quantitative interpretations of millimeter-wavelength multiparameter radar measurements of precipitating clouds. Thus, as we have mentioned in the Introduction, we plan to continue this numerical study in conjunction with laboratory measurements taken with a dual-polarization Doppler scatterometer operating at 8.38 mm.

5. REFERENCES

Aydin, K., T.A. Seliga and V.N. Bringi, 1984: Differential radar scattering properties of model hail and mixed-phase hydrometeors. *Radio Sci.*, **19**, 58-66.

Barber, P.W., and S.C. Hill, 1990: *Light Scattering by Particles: Computational Methods*, World Sci. Publ. Co., 269 pp.

Bohren, C.F., and D.R. Huffman, 1983: *Absorption and Scattering of Light by Small Particles*, John Wiley & Sons, 530 pp.

Bringi, V.N., R.M. Rasmussen and J. Vivekanandan, 1986: Multiparameter radar measurements in Colorado convective storms. Part I: Graupel melting studies. *J. Atmos. Sci.*, **43**, 2545-2563.

Evans, K.F., and J. Vivekanandan, 1990: Multiparameter radar and microwave radiative transfer modeling of nonspherical atmospheric ice particles. *IEEE Trans. Geosci. and Remote Sensing*, **28**, 423-437.

Hobbs, P.V., N.T. Funk, R.R. Weiss, J.D. Locatelli and K.R. Biswas, 1985: Evaluation of a 35 GHz radar for cloud physics research. *J. Atmos. Oceanic Technol.*, **2**, 35-48.

Lhermitte, R., 1987: A 94-GHz Doppler radar for cloud observations. *J. Atmos. Oceanic Technol.*, **4**, 36-48.

Pasqualucci, F., B.W. Bartram, R.A. Kropfli and W.R. Moninger, 1983: A millimeter-wavelength dual-polarization Doppler radar for cloud and precipitation studies. *J. Climate Appl. Meteor.*, **22**, 758-765.

Prodi, F., 1989: A scatterometer for laboratory measurements of hydrometeor backscattering at millimeter wavelengths. *Fifth WMO Sci. Conf. on Weather Modification and Applied Cloud Physics*, World Meteor. Organ., Tech. Doc. No. 269, 117-118.

Wang, P.-K., 1982: Mathematical description of the shape of conical hydrometeors. *J. Atmos. Sci.*, **39**, 2615-2622.

THEORETICAL INVESTIGATION OF THE RELATIONSHIP BETWEEN ICE MASS CONTENT AND Ka-BAND RADAR REFLECTIVITY FACTOR

Liang Liao and Kenneth Sassen

Department of Meteorology, University of Utah, SLC, Utah 84112, USA

1. INTRODUCTION

Cirrus clouds have been the subject of increasing scientific study to better understand their impact on climate and atmospheric thermal structure through their radiative effects. In order to establish a model useful to investigate the role of various physical processes in the life cycle of a cirrus cloud, parameterizations to account for microphysical effects on the vertical flux of ice water are required (Starr and Cox 1985). Microwave radars are useful tools for cloud structure investigations and have been used to quantify the presence of hydrometeors. However, the estimation of cloud water content when ice particles are present is more difficult because of the variable shapes of ice particles. The purpose of this study is the development of relationships between the effective radar reflectivity factor and the ice water content in ice clouds through the calculation of regression equations from the size distributions of ice particles obtained from aircraft measurements. Many investigators derived regression equations linking radar reflectivity factor Z and ice water content IWC for different ice clouds from ground-based or airborne radar and airborne particle image data, which are used with empirical particle diameter-mass relations to estimate IWC assuming the ice particles scatter like spheres and the "Rayleigh approximation" of the Mie scattering theory is valid. The accuracy of these Z-IWC equations is limited not only by the measurements of the habits and size distributions of the ice particles but also by the empirical particle dimension-mass relations to estimate IWC in view of the complicated particle shapes of ice particles. Moreover, they are only valid for clouds with particles that are much smaller compared with the radar wavelength. In this study, a theoretical investigation of the relationship between ice water content and effective Ka-band radar reflectivity factor Z_e is presented by utilizing a numerical scheme to calculate scattering parameters that characterize the backscattering for the major shapes of ice particles formed in cirrus clouds.

2. BACKGROUND

a. *Effective Radar Reflectivity Factor*

The average received power $\bar{P}_r$ by radar from particles at range r (see Battan 1973) is

$$\bar{P}_r = \frac{C|K|^2 Z_e}{r^2}, \qquad (1)$$

where Z_e is the effective radar reflectivity factor, K is used to designate $(m^2-1)/(m^2+2)$, where m is the complex index of refraction of particles, and C is the radar constant term. Z_e can also be expressed in terms of backscattering cross section σ of particles as

$$Z_e = \frac{\lambda^4}{\pi^5|K|^2}\iiint \sigma(D,\theta,\phi)N(D,\theta,\phi)dDd\theta d\phi, \qquad (2)$$

where $N(D,\theta,\phi)$ and $\sigma(D,\theta,\phi)$ are the number density and backscattering cross section of particles, respectively, with maximum dimension D and an axial direction (θ,ϕ) with respect to the radar beam. However, σ of a nonspherical particle is not only a function of D, θ and ϕ, but also of the particle axis ratio and the incident wave polarization. Moreover, for Rayleigh scattering, in which the radar wavelength is much larger than the scattering particle, and all the particles are spherical, Z_e is simplified to be a summation of D_i^6 over a unit volume. It is called the reflectivity factor, and designated by the symbol Z. When using Ka-band or shorter wavelength radars for studying ice clouds, some larger particles can no longer be treated as spherical and their dimensions may be beyond the range of the Rayleigh approximation, and therefore Z_e would be more appropriate.

b. *Ice Water Content and Ice Particle Properties*

From in situ aircraft observations, it has been determined that cirrus clouds are largely composed of bullets, columns, plates and their combinations (see Heymsfield and Platt 1984). The computed ice water content IWC from the size distribution of the particles $N(D)$ is

$$IWC = \rho_i \int_{D_{min}}^{D_{max}} V_D N(D)dD, \qquad (3)$$

where ρ_i is the ice particle density and V_D is the volume of the individual particle, which depends on particle shape. The size of an ice particle can be characterized by two dimensions: the particle diameter (d) and thickness (h) for plates, and length (L) and width (d) for columns. The larger dimension of such particles generally varies from less than $10\mu m$ to 1-$2mm$. The dimensional relationships used here for various ice particles were taken from Pruppacher and Klett (1978).

The size distributions of the ice particles are particular important for the calculation of both ice water content and effective radar reflectivity factor. Observations of ice particle size distributions at temperatures ranging from about -20 to $-60°C$ and at precipitation intensities varying between 0.01 and $0.2mm \cdot hr^{-1}$ have been reported by Sato et al. (1981), Kikuchi et al. (1982), Heymsfield et al. (1984), and Sassen et al. (1989), among others. They are strongly dependent on the temperatures and precipitation rate. One of the size distributions analyzed by Sassen et al. (1989) from the cirrus cloud case study of 8 March 1985 is depicted in Fig.1. In each case, the smallest particles are found to dominate with the peak number densities ranging from 20 to $100\mu m$ maximum dimensions.

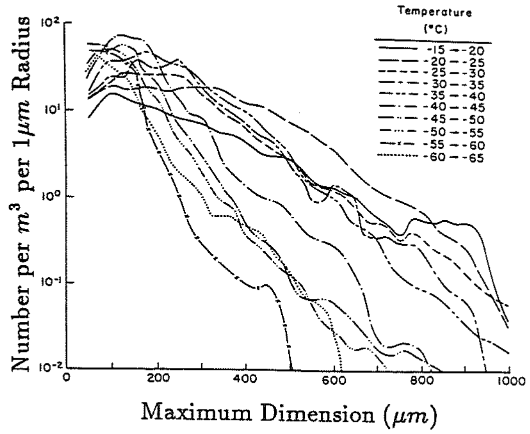

Fig.1. Ice particle size distributions in 5°C temperature intervals from all 2D probe data collected on 8 March 1985.

3. RESULTS

Figure 2 is the radar operating diagram. A horizontal polarization of the radar beam is defined to be parallel to the ground and perpendicular to the scattering plane consisting of the radar propagation direction and zenith direction, while a vertical polarization is in the scattering plane and perpendicular to the radar beam. δ is the zenith angle between the zenith direction and radar beam. In our development of the relationship between ice mass content and effective Ka-band radar reflectivity factor, it is assumed that the ice clouds are composed entirely of ice columns, plates or bullet rosettes with different axis ratios (i.e., all particles used for the computation of Z_e and IWC have the same habit). We use the dimensional relationships of Pruppacher and Klett (1978) for the hexagonal plate (Pla), solid thick plate (Clg), elementary needle (Nla), long solid column (Nle), solid bullet (Clc) with $L < 300\mu m$, hollow bullet (Cld) with $L > 300\mu m$, solid column (Cle) with $L/d \leq 2$ and with $L/d > 2$, hollow column with $L/d \leq 2$ and with $L/d > 2$. The above classification of ice particle shapes is cited from Magono and Lee (1966). The volumes of the ice particle types Pla, Clg, Cle and Clf are based on observational data, while those for the Nla, Nle, and Clc and Cld particles are computed from their geometrical models, because data are absent. In addition, the bullet rosette crystals shown in Fig.3 with a bullet axis ratio of 1/4, is also considered. In order to account for the orientations of particles, which are affected by Brownian and turbulent motions and aerodynamic forcing, it is reasonable to assume that the ice particles are randomly oriented when the largest dimensions of the particles are less than $250\mu m$: otherwise the major axes of the particles are horizontally oriented (see Sassen 1980). Under these assumptions, the effective radar reflectivity factor and the ice water content are computed from eq.(2) and eq.(3). The backscattering cross section σ for the horizontal and vertical polarizations are computed for the various crystal shapes by utilizing a developed numerical scheme consisting of the conjugate gradient and the fast Fourier transform method (CG-FFT), and by using the Rayleigh approxi-

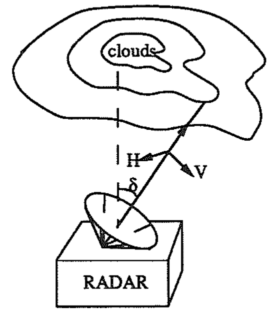

Fig.2 Radar diagram

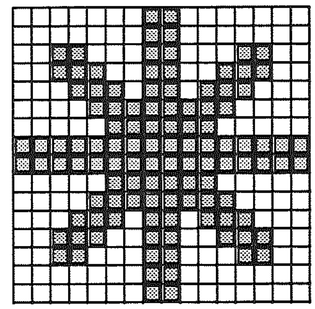

Fig.3 Ice bullet rosette

mation, for the average particle size distributions shown in Fig.1. The scattergram of these calculations are plotted in Fig.4, with each point labeled according to the habit to which it belongs. Fig.4 shows the calculated results for Z_e with horizontal polarization and IWC for $\delta = 0°$. It should be noted that the points labeled "7" are computed under the assumption of that the cirrus is composed of solid bullets$< 300\mu m$ and hollow bullets$> 300\mu m$ in maximum dimension. Hollow bullets and columns are replaced by solid bullets and columns with the same axis ratio and volume in the computation of Z_e and IWC due to a lack of knowledge on how to model hollow particles. However, this has little effect on the development of Z_e-IWC relationships. Applying regression analysis to the entire data set, we fit our data to the following relation to be consistent with previous results (e.g., see Sassen 1987).

$$IWC = AZ_e^B ,$$

where IWC is in units of mg/m^3, Z_e is in mm^6/m^3, and A and B are the constant coefficients. Table 1 summarizes the results of A and B obtained by the least square fitting method for all the predicted points of Z_e and IWC for horizontal (H.) and vertical (V.) polarizations at the different zenith angles (δ). R in Table 1 is the linear correlation coefficient. All computed Z_e and

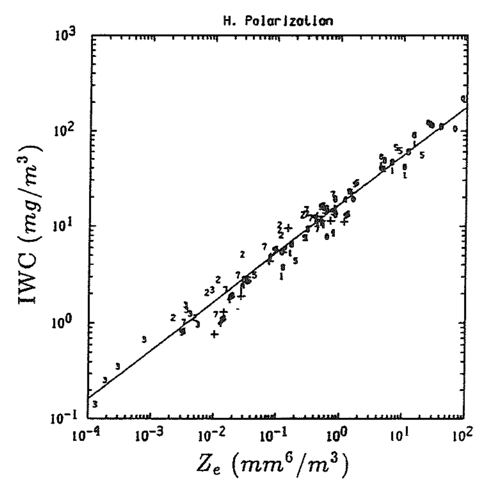

Fig.4. Z_e-IWC relationship at $\delta = 0°$. Value 1 corresponds to Clg particles; 2 to Nle; 3 to Nla; 4 to Pla; 5 to Cle with axis ratio$\geq$0.5; 6 to Cle with axis ratio$\leq$0.5; 7 to Clc&Cld; 8 to Clf with axis ratio$\geq$0.5; 9 to Clf with axis ratio$\leq$0.5; 0 to sphere; symbol + to bullet rosette.

IWC conform very well with the regression lines (Z_e-IWC relationships), since R is always larger than 0.98 for the cases described. In fact, each point in Fig.4 can be thought to be one probability of occurrence for a real cloud, while the regression line is the statistical average. It implies that the Z_e and IWC values from the realistic combinations of ice particle habits ought to have the same regression lines as developed. The Z_e-IWC relationships developed in this way are reliable from the statistical standpoint.

Although the values of Z_e derived from equivalent spherical particles are invariant with the zenith angle and the polarization state according to Mie theory, the Z_e-IWC relationships for nonspherical particles depend slightly on zenith angle and polarization state, as is illustrated in Table 1. Also, we know from the results shown in Table 1 that the Z_e-IWC equations for horizontal polarization do not vary with the zenith angle. This can be explained by virtue of the fact that the dimensions of most ice particles in cirrus clouds are in the range of the Rayleigh approximation, in which the backscattering intensity is mainly proportional to the particle volume and dimension in the polarization direction, and not related to the scattering angle. For the same reason, the relationships for different polarizationss a are almost the same when $\delta = 0°$. It is obvious that the ice water content and the effective radar reflectivity factor differ for clouds consisting of different ice particle habits. Clouds with the elementary needles contribute smaller values of IWC and Z_e, while clouds with higher values are found for solid thick plates, solid columns of larger axis ratio, or spheres. Despite the different ice particle habits, the data tend to have a regular pattern described by regression lines that are closely related to the size distribution of the ice particles.

We now continue to apply this method to obtain Z_e-IWC relationships associated with the measured average size distributions of ice particles expressed by the exponential equation as a function of the precipitation intensity. Our aim is to develop Z_e-IWC relationships for comparison to the Z-IWC relationships computed by Sato et al. (1981) from the instantaneous size distributions of ice particles observed in Antarctica during January 1975 and November 1978. The size distribution

Table 1 Parameters of Ze-IWC relationship

	H. Polarization			V. Polarization		
δ	A	B	R	A	B	R
0°	17.23	0.5070	0.9827	17.23	0.5070	0.9827
15°	17.23	0.5070	0.9827	17.51	0.5064	0.9828
30°	17.23	0.5070	0.9827	18.32	0.5046	0.9830
45°	17.23	0.5070	0.9827	19.54	0.5015	0.9825

is represented by $N_D = N_0 exp(-\Lambda D)$, where D is the melted diameter, $N_D dD$ is the number of ice particles having a melted diameter between D and $D + dD$ in a unit volume of space, and N_0 is the value of N_D for $D = 0$. These expressions are given by Sato et al. for the 1975 data as,

$$N_D = 3.9 \times 10^3 R^{0.59} exp(-1.17 \times 10^{-2} R^{-0.08} D), \quad D \leq 370, \quad 0.0036 \leq R \leq 0.12, \tag{4}$$

and for the 1978 data, as

$$N_D = 9.2 \times 10^3 R^{0.68} exp(-1.37 \times 10^{-2} R^{-0.055} D), \quad D \leq 400, \quad 0.0053 \leq R \leq 0.16, \tag{5}$$

where R is the precipitation intensity in units of $mm \cdot hour^{-1}$ and D is in μm. The assumptions about ice particle habit used here are the same as before, and the sphere volume with a melted diameter D in eq.(4) and eq.(5) is converted into a nonspherical ice particle volume having the same mass. Results of Z_e and IWC computed for the size distributions of both 1975 and 1978 at the different polarizations and zenith angles are shown in Fig.5. As seen from these results, the 1975 and 1978 particle size distributions provide almost the same Z_e-IWC relationship. Hence the Z_e-IWC relationships are obtained from the regression equation based on the composite results from the 1975 and 1978 size distributions. The parameters of these relationships are summarized in Table 2. For the purpose of comparison, the Z_e-IWC relationships from Sato et al. (1981) and the composite Z-IWC relationship derived by Sassen (1987) from these data are also presented in Table 2. Some of the results from Table 2 are also illustrated in Fig.6 for Z_e (or Z) versus IWC.

As seen in Fig.6, these curves are in general agreement despite some difference between Z_e and Z. As discussed before, Z_e and Z differ after taking into account the effects of nonspherical particles no matter whether the scattering is Rayleigh or not since the backscattering intensity from a nonspherical particle with random orientation or major axis perpendicular to the radar beam is always larger than that for a spherical particle with the same volume (see Atlas et al. 1953) in the Rayleigh approximation, this in turn leads to Z_e being greater

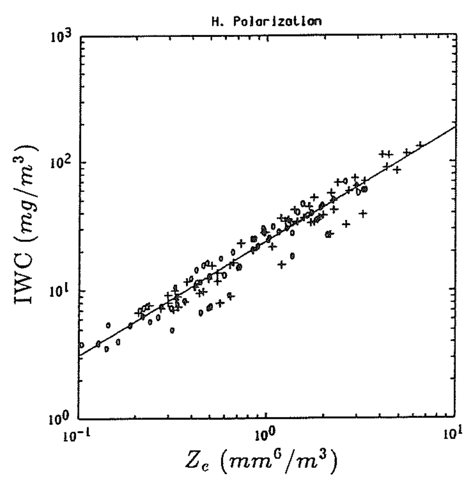

Fig.5. Z_e-IWC relationship at $\delta = 0°$. Points with signs of "0" and "+" correspond to the size distributions of the ice particles of 1975 and 1978 respectively.

Table 2 Parameters of Ze-IWC and Z-IWC relationship

	H. Polarization			V. Polarization		
d	A	B	R	A	B	R
0°	24.14	0.886	0.964	23.14	0.889	0.964
15°	23.16	0.854	0.968	23.90	0.863	0.973
30°	23.26	0.855	0.970	26.27	0.885	0.988
45°	22.22	0.867	0.966	30.22	0.908	0.999
Sato et al.(1975 data)				A: 53.76	B: 0.827	
Sato et al.(1978 data)				A: 49.15	B: 0.90	
Sassen (1987)				A: 37.0	B: 0.696	

than Z for the same size distribution of ice particles with a certain ice water content. This is consistent with the results in Fig.6 in that Z_e is larger than Z for a given IWC. The diameter D of particles in $\sum_{vol} D_i^6$ used by Sato et al. (1981) for the Z-IWC relationship is the melted diameter of the ice particles which is smaller than that of the solid ice particles owing to the difference in densities in the two phases (see Sassen 1987). Consequently, Z calculated from the melted diameter of ice particles is smaller than that for the solid diameter of ice particles. This is another reason that accounts for the difference between Z_e and Z in Fig.6. Results of our analysis indicate that the Z_e vs IWC relationships vary little with the zenith angle and polarization status of the radar beam. The comparison and analysis of the above results imply that the developed Z_e-IWC relationships from the measured ice particle size distributions, after taking into account nonspherical particle effects, are consistent and in agreement with relationships from other sources except for some reasonable discrepancies.

5. CONCLUDING REMARKS

Using measured ice particle size distributions and taking into account typical habits found in ice clouds, theoretical computations of both the effective Ka-band radar reflectivity factor and the ice water content were carried out by utilizing a developed numerical scheme consisting of the conjugate gradient and the fast Fourier transform method (CG-FFT), and the Rayleigh approximation. From the results for the effective radar reflectivity factor and the ice water content, regression equations as a statistical method are employed to develop the Z_e-IWC relationships. The results for different crystal habits correlate very well, and our developed Z_e-IWC relationships compare well with previous Z-IWC relationships using the same data base. This result affirms that Ka-band radar remote sensing can be applied to the assessment of the mean ice mass content and integrated ice mass depth of cirrus and other cold ice clouds.

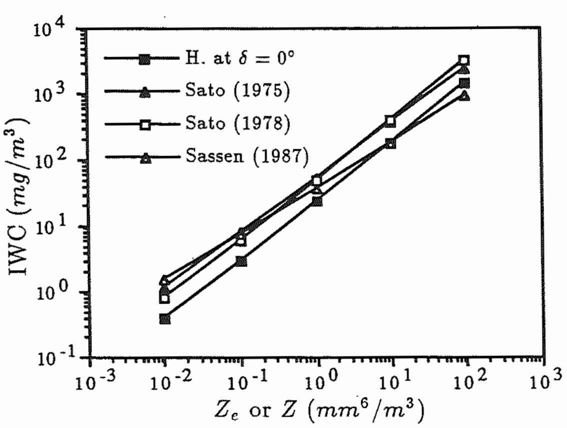

Fig.6. Comparison between Z_e-IWC of H. polarization at $\delta = 0°$ and Z-IWC by Sato et al. and Sassen.

Acknowledgements. This research has been supported by NSF grant ATM-8914348 and Utah Division of Water Resources Contract 90-1039 (under NOAA Agreement NA89RAH09090).

6. REFERENCES

Atlas, D., M. Kerker and W. Hitschfeld, 1953: Scattering and attenuation by nonspherical atmospherical particles. *J. Atmos. Terrest. Phys.*, **3**, 108-119.

Battan, L. J., 1973: *Radar Observation of the Atmosphere.* University of Chicago, 324 pp.

Heysmefield, A. J., and C. M. R. Platt, 1984: A parameterization of the particle size spectrum of ice clouds in terms of the ambient temperature and the ice water content. *J. Atmos. Sci.*, **41**, 846-855.

Kikuchi, K., S. Tsuboya, N. Sato and Y. Asuma, 1982: Observation of wintertime clouds and precipitation. Part 2: Characteristic properties of precipitation particles. *J. Meteor. Soc. Japan*, **60**, 1215-1225.

Magono, C., and C. W. Lee, 1966: Meteorological classification of natural snow crystals. J. Fac. Sci., Hokkaido University, Ser. 7, 2, No.4, 321-335.

Pruppacher, H. R., and J. D. Klett, 1978: *Microphysics of Clouds and Precipitation.* D. Reidel 714 pp.

Sassen K., 1980: Remote sensing of planar ice crystal fall attitudes. *J Meteor. Soc. Japan*, **58**, 422-429.

Sassen K., 1987: Ice cloud content from radar reflectivity. *J. Climate Appl. Meteor.*, **26**, 1050-1053.

Sassen, K., D. O'C. Starr and T. Uttal, 1989: Mesoscale and microscale structure of cirrus clouds: Three case studies. *J. Atmos. Sci.*, **46**, 371-396.

Sato, N., K. Kikuchi, S. C. Barnard and A. W. Hogan, 1981: Some characteristic properties of ice crystal precipitation in summer season at South Pole Station, Antarctica. *J. Meteor. Soc. Japan*, **59**, 772-780.

Starr, D. O'C., and S. K. Cox, 1985: Cirrus clouds. Part I: A cirrus cloud model. *J. Atmos. Sci.*, **42**, 2663-2681.

PRECIPITATION MEASUREMENTS WITH WIND-PROFILING RADARS

W.L. Ecklund[1], K.S. Gage[1], D.A. Carter[1], P.T. May[2] and T.D. Keenan[2]

[1]NOAA/ERL Aeronomy Laboratory, Boulder, CO USA
[2]Bureau of Meteorology Research Centre, Melbourne, AUSTRALIA

1. INTRODUCTION

The technology for measuring atmospheric winds using wind-profiling radars has become widely used in the past decade for atmospheric research, support of field research programs and increasingly for routine monitoring. While the primary motivation for the development of profilers has been directly related to their wind measurement capabilities it has long been recognized that other measurements can be made with the profilers (see, for example, Gage and Balsley, 1978; Gage, 1990; Balsley, et al, 1991). This paper is concerned with the use of wind-profiling radars for precipitation research. This application has been pursued by several authors using profilers operating at several frequencies. In this paper we will consider precipitation measurement using UHF and VHF profilers separately and together.

The Aeronomy Laboratory research program has utilized wind profiling radars for over a decade. Recently tropical dynamics and climate studies have been emphasized and this direction has led to the deployment of a network of VHF radars on island sites in the tropical Pacific (Gage et al., 1991). Because of the need to measure winds to lower altitudes than can be observed using VHF wind profilers, a new generation of UHF wind profilers has been developed (Ecklund et al. 1988, 1990, 1991). The UHF wind profilers are much more sensitive to precipitation than are the VHF profilers and the combination of UHF and VHF profilers enables simultaneous measurement of clear air velocities and precipitation fall speeds (Currier et al. 1992). Related parameters such as size distributions can be inferred from the vertical velocity measurements as discussed in Wakasugi et al (1986) and Gossard et al. (1990) and Rogers et al. (1991).

Precipitation measurements have been made for decades using weather radar using empirical relations between radar reflectivity and rainfall rate. Weather radars typically give precipitation averaged over a large area in a scanning mode. Profilers look nearly vertically and give very good height resolution. They are ideal for determining time series at many heights simultaneously over the radar site. Profilers are useful for monitoring the depth, type and intensity of precipitation. They also have the advantage of simplicity and can be operated unattended for extended periods of time.

In this paper we illustrate the precipitation measurement capabilities of the profilers with examples drawn from observations made with VHF and UHF wind profilers sited in the tropics at the following locations: Darwin, Australia; Hilo, Hawaii; Christmas Island, Republic of Kirabati; and Saipan, Commonwealth of Northern Marianas.

2. TECHNIQUE

Echoes from the clear atmosphere are routinely observed by profilers due to backscattering from turbulent irregularities in radio refractive index. The turbulent irregularities are advected by the wind and produce the Doppler shift measured by the profiler. Turbulent scattering is the primary echoing mechanism that makes possible the routine measurement of atmospheric winds by Doppler radar.

The primary measurements from Doppler wind profilers are derived from the spectrum of Doppler velocities. Doppler power spectra are recorded at about 50 range gates along each of 3 to 5 antenna beams. Dwell time on each beam is typically in the range of 30 sec to 2 minutes in marked contrast to the very short dwell times implicit to rapid scanning Doppler weather radars. In the usual wind profiling mode one of the sequentially sampled beams is directed vertically to measure precipitation fall speed to provide a correction for wind measurements made on oblique beams. For each dwell time an average Doppler power spectrum is calculated.

For operational radars moments are calculated from these approximate 1 minute spectra. These moments are later consensed to obtain 30 minute to 1 hour wind profiles. For research radars the full Doppler power spectra are recorded at each height and for each antenna beam position.

Gossard (1988) has considered the relative sensitivity of radar wind profilers to precipitation at 50, 400 and 1000 MHz. At 1000 MHz they find about equal response from very light rain and clear air. Under these conditions clear air and precipitation peaks can both be used to measure precipitation and background wind. At 50 MHz clear air echoes almost always dominate precipitation echoes, but in moderate to heavy rain the precipitation echo may be detectable in addition to the clear air echo. The use of two profilers operating at widely separated frequencies, e.g. 50 MHz and 1,000 MHz, enables the measurement of a wide range of precipitation types and intensities in addition to wind. Furthermore two vertically-directed profilers operating as above can be combined to measure precipitation fall speeds relative to clear air velocities (Currier et al. 1992).

3. EXAMPLES OF PRECIPITATION ECHOES OBSERVED BY WIND PROFILERS

In this section we illustrate the use of wind profilers for precipitation measurement by presenting several illustrative examples taken from profilers operated in the tropics.

Figure 1 shows widespread stratiform precipitation observed using the 50 MHz profiler located at Darwin (Carter et al., 1991). At this time the profiler was being operated in a vertical-only mode. The stratiform precipitation was observed following the passage of a fairly intense squall line (Rutledge et al., 1989). The figure shows an unusual example of simultaneous snow/ice precipitation echoes above the melting level from 6 - 10km (cf. Chu et al., 1991). The clear air and precipitation echoes are separated by about 1.8 m/s. Below the dark line at 5.8 km, the gain has been enhanced to show the precipitation echoes. Over this height range the clear air echoes are off scale. Below the

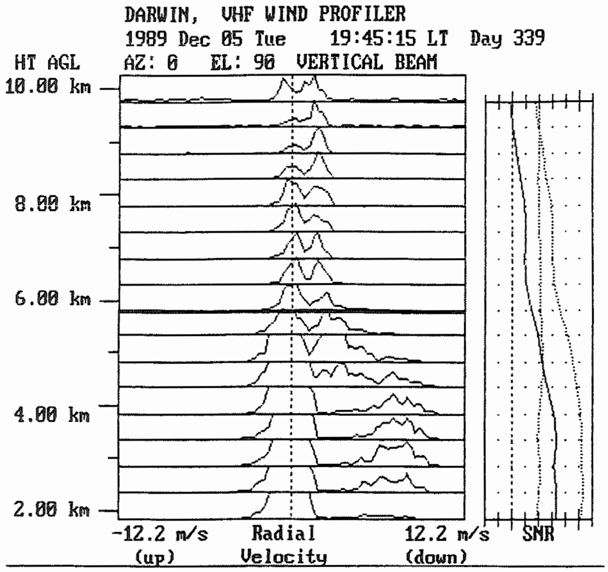

Fig. 1 Example of bi-modal Doppler spectra in widespread stratiform precipitation showing "clear-air" and precipitation echoes observed on the Darwin 50 MHz profiler. Below dark line at about 5.8 km the gain has been increased to show precipitation echoes.

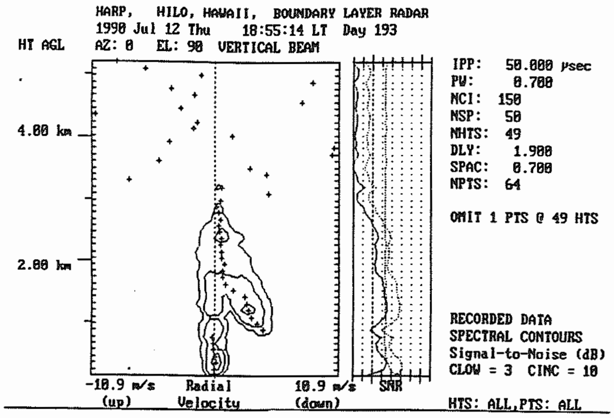

Fig. 2 Warm-rain example of shallow precipitation observed by the 915 MHz profiler used in HARP.

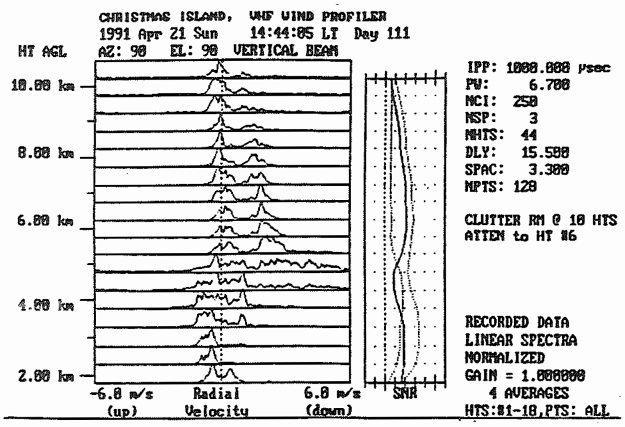

Fig. 3 Example of precipitation echoes seen on the 50 MHz profiler located on Christmas Island, Republic of Kirabati.

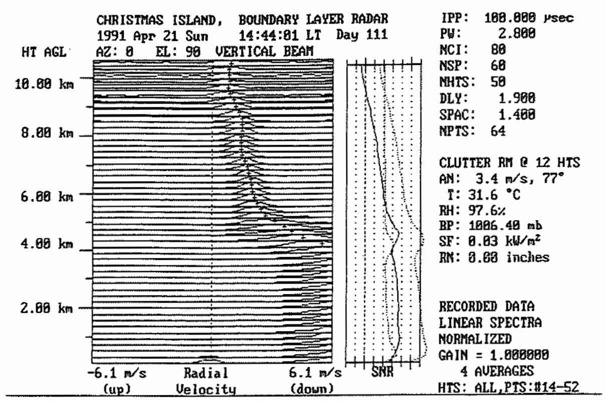

Fig. 4 Preciptation echoes seen on the 915 MHz profiler at Christmas Island at the same time as the observations on 50 MHz profiler in Fig 3. Note the scale has been adjusted for ease of comparison with Fig 3.

melting level the precipitation fall speed increases to about 8 m/s.

The ice crystal fall speed implies that the reflectivity weighted mean melted diameter was large: about 3.5 mm. If the size distribution can be approximated by an exponential distribution (e.g. Gunn and Marshall, 1958), this implies that the distribution is quite flat, with an e-folding scale of about $1.7 mm^{-1}$. Such large crystal sizes and depletion of the small crystals may be consistent with long residence times which may be induced because of the depth of the convection, with convective cloud tops about 18 km high.

During the Hawaiian Rainband Project (HARP) in July and August 1990 a 915 MHz lower tropospheric wind profiler was operated by the Aeronomy Laboratory at a site 20km southeast of Hilo (Rogers et al., 1991b). This experiment was designed to study the morphology of the rainbands that form off the island of Hawaii. During the HARP project both clear air and precipitation echoes were observed by the HARP profiler (Rogers et al., 1992). A sample of the precipitation echoes visible in the vertical beam of the HARP profiler are shown in Figure 2. This example illustrates the clear air and precipitation echoes in a contour format. The precipitation echoes are evident below 2 km in this example.

Of particular interest here is the rapid increase in the reflectivity weighted mean fall speed as the rain falls. Although this is enhanced by the $(diameter)^6$, it nevertheless implies rapid coalescence is occurring in the warm rain regime. The rapid evolution of drop-size distribution with height also has profound implications in the interpretation of weather radar reflectivity data; particularly for rain fall estimation.

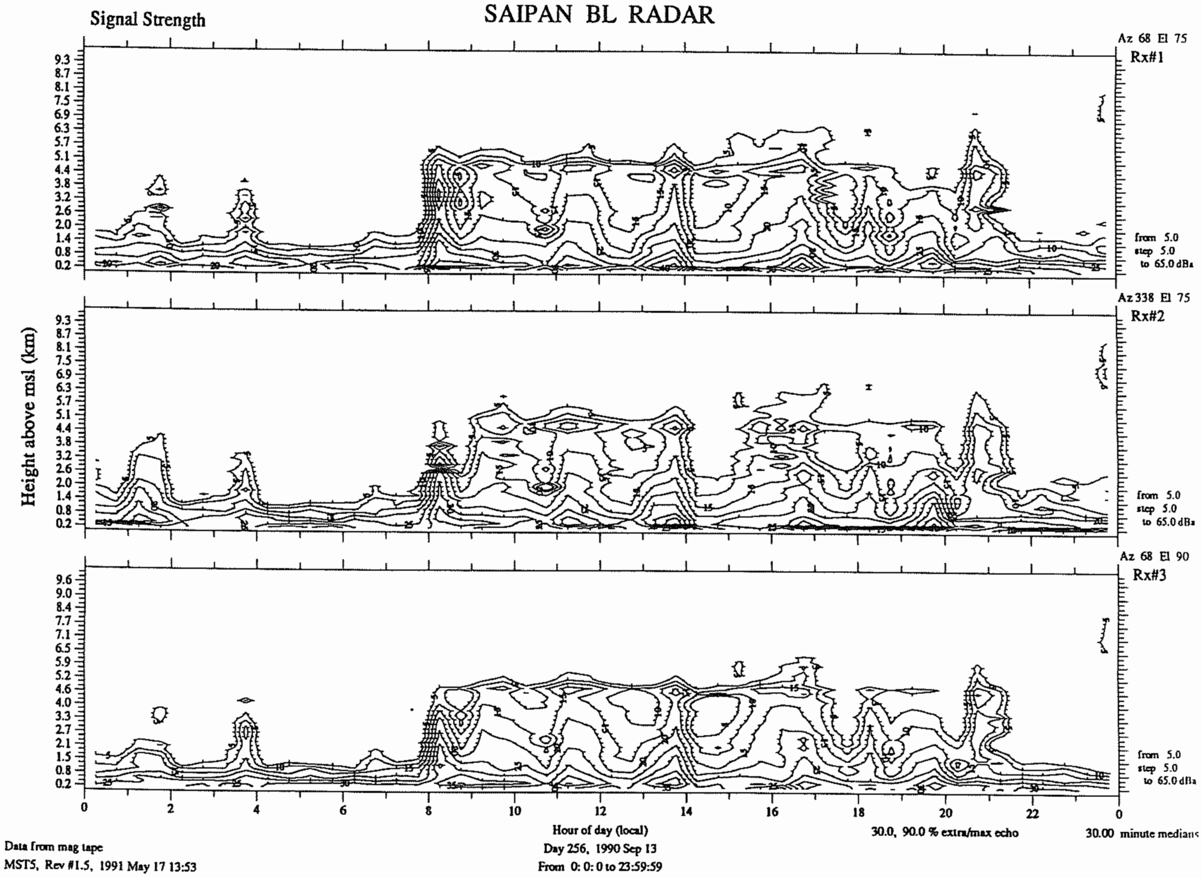

Fig. 5 Time-Height sections of echo strength observed on the three beams of the 915 MHz Saipan profiler on September 13, 1990 during TCM-90. Observations on the vertical beam are shown at the bottom of the figure.

We compare next simultaneous precipitation echoes seen on the vertical beams of the 50 MHz and 915 MHz wind profilers at Christmas Island on April 21, 1991. Deep precipitation echoes were visible for much of the latter half of this day on the 915 MHz profiler. At the time shown in Figure 3, snow/ice precipitation can be clearly seen on the 50 MHz profiler above the melting level. The 915 MHz profiler spectra for the same time are reproduced in Figure 4 with the same scale for the Doppler velocity. Fall velocities seen by the two profilers clearly match very well and the increase in fall velocity with melting is clearly resolved on the 915 MHz profiler below 5km. In this figure the rain below 5km cannot be seen because it is off scale. Note that the 50 MHz profiler sees the clear air velocities as well as the precipitation echoes. Only the precipitation echoes are visible on the 915 MHz profiler. Note also the bright-band peak in signal strength in the melting layer seen by the 915 MHz profiler. The 50 MHz profiler observes a minimum in signal strength at the melting level with an increase above this level. This could be due to the effect of prolonged cooling associated with melting producing a well-mixed layer in the melting region with a capping inversion above. It is well known that VHF wind profilers see strong echoes from stable regions.

Time series of the reflectivity of the 915 MHz systems can also be very useful when utilized with wind data. For example, the wind measurements from both the 915 and 50 MHz wind profilers on Saipan verified to better than 2 m/s when compared with radiosonde data (launched from the profiler site) while the 915 MHz reflectivity data showed significant structure within a mostly stratiform rainband associated with typhoon Flo in 1990. The reflectivity is shown in Fig. 5 and shows the significant bright band echo at the freezing level characteristic of stratiform rain. The stratiform type circulation was confirmed by vertical wind estimates from the 50 MHz profiler. However, there is clearly significant, almost periodic structure in the reflectivity field within the band.

4. CONCLUDING REMARKS

In this paper several examples of precipitation echoes have been reproduced from several tropical locations using wind profilers operating at 50 MHz and 915 MHz. The lower VHF wind profilers are clearly less sensitive to precipitation and can often observe both clear air and precipitation echoes. At 915 MHz the lower tropospheric wind profilers are very sensitive to precipitation. In the presence of deep precipitation their height coverage is greatly extended and it is possible to tell at a glance when precipitation is present simply by examining the time-height cross section of 915 MHz wind profiler data. In the presence of deep stratiform precipitation, the fall speeds of precipitation can be measured on the vertical beam and clearly show the vertical structure of fall speed variations associated with change of phase, evaporation etc. By application of the techniques described in Rogers et al., (1991a), it is possible to measure precipitation rate and drop-size distribution as a function of altitude.

The ability to measure clear air velocities and fall speeds of hydrometeors will have important applications in cloud physics. The ability to monitor the melting level in stratiform precipitation as well as the vertical structure of melting and evaporation should make possible the inference of diabatic cooling rates associated with these processes in convective systems. Simultaneous measurements of vertical motions in such storms should provide valuable insight into the heat balance in these storm systems.

The application of the technology for precipitation measurement considered here will complement the capabilities of weather radars. Only the weather radars can give extensive areal coverage. However, the profilers are ideal for continuous monitoring at fixed locations and because of their ability to resolve vertical structure are ideally suited for climatological studies using long-term data sets.

ACKNOWLEDGEMENTS

We thank Jim Core and Graham Buis (Darwin) and Al Gray (Boulder) for help with installation and maintenance of the Darwin wind profiler. The Darwin wind profiler is operated jointly under a cooperative research agreement with the Australian Bureau of Meteorology Research Centre. We thank Rod Rogers for his assistance in the operation of the HARP 915 MHz profiler, and for help in the interpretation of the results. We also thank Brian Boone, Al Gray and Jim Avery for help with building and installing the Christmas Island 915 MHz profiler and John Bryden for on-going help with operations at Christmas Island. The VHF and UHF profilers at Christmas Island are supported by the U.S. TOGA Project Office. This research was partially supported by the National Science Foundation under Agreement No. ATM-8720797.

REFERENCES

Balsley, B.B., D.A. Carter, A.C. Riddle, W.L. Ecklund, and K.S. Gage, On the Potential of VHF Wind Profilers for Studying Convective Processes in the Tropics, Bull.Amer. Met. Soc., 72, 1355-1360.

Carter, D.A., W.L. Ecklund, J.R. McAfee, K.S. Gage, T. Keenan and M. Manton, 1991, Results from the first year of Observations using the Darwin VHF Wind Profiler, Preprint Vol., 25th International Conf. on Radar Meteorol. Paris, France, 288-291.

Chu, H.-Y., L.-P. Chian, and C.-H. Liu, 1991, The Investigations of the Atmospheric Precipitations by Using Chung-Li VHF Radar, Radio Science, 26, 717-729.

Currier, P.E., S.K. Avery, B.B. Balsley, K.S. Gage and W.L. Ecklund, 1992, Use of Two Wind Profilers for Precipitation Studies, Geophys. Res. Lett., (in Press).

Ecklund, W.L., D.A. Carter, and B.B. Balsley, 1988: A UHF Wind Profiler for the Boundary Layer: Brief Description and Initial Results, J. Atmos. and Oceanic Tech., 5, 432-441.

Ecklund, W.L., D.A. Carter, B.B. Balsley, P.E. Currier, J.L. Green, B.L. Weber, and K.S. Gage, 1990, Field Tests of a Lower Tropospheric Wind Profiler, Radio Science, 25, 899-906.

Ecklund, W.L., D.A. Carter, K.S. Gage, A.C. Riddle, and B.B. Balsley, 1991, Prospects for Lower Tropospheric Wind Profiling in the Tropics, Preprint Volume, 25th Conf. on Radar Meteorology, Paris, France, American Meteorology Society, Boston, MA, 249-252.

Gage, K.S. and B.B. Balsley, 1978, Doppler Radar Probing of the Clear Atmosphere, Bull. Amer. Met. Soc., 59, 1074-1093.

Gage, K.S., 1990, Radar Observations of the Free Atmosphere: Structure and Dynamics, Radar in Meteorology, D. Atlas, Ed., Amer. Met. Soc., 534-574.

Gage, K.S., B.B. Balsley, W.L. Ecklund, R.F. Woodman and S.K. Avery, 1991, A Trans-Pacific Network of Wind-Profiling Doppler Radars for Tropical Atmospheric Research, EOS, 71, 1851-1854.

Gossard, E.E., 1988, Measuring Drop-size Distributions in Clouds with a Clear-Air-Sensing Doppler Radar, J. Atmos. and Oceanic Tech. 5, 640-649.

Gossard, E.E., R. Strauch and R.R. Rogers, 1990, Evolution of Cloud-Drop Size Distributions Observed by Ground-Based Doppler Radar, J. Atmos. and Oceanic Tech., 7, 815-828.

Gunn, K.L.S. and J.S. Marshall, 1958, The Distribution with Size of Aggregate Snowflakes, J. Meteor, 15, 452-461.

Rogers, R.R., W.L. Ecklund, D.A. Carter, K.S. Gage, and S.A. Ethier, 1992, Research Applications of a Boundary Layer Radar, Bull. Amer. Met. Soc., (submitted).

Rogers, R.R., I.I. Zawadzki, and E.E. Gossard, 1991a, Variation with Altitude of the Drop-Size Distribution in Steady Light Rain, Quart. J. Roy.Met. Soc., 117, 1341-1369.

Rogers, R., W. Ecklund, and D. Carter, 1991b, First Results from the HARP Boundary Layer Radar, Preprints, 25th Conf. on Radar Meteor. American Meteorological Society, Boston, pp. 296-299.

THE NASA/JPL AIRBORNE RAIN MAPPING RADAR (ARMAR)

S. Durden, A. Tanner, W. Wilson, F. Li, E. Im, W. Ricketts

Caltech/JPL, Pasadena, CA 91109, USA

1 Introduction

NASA and the Jet Propulsion Laboratory (JPL) have developed an Airborne Rain Mapping Radar (ARMAR). ARMAR is a 14 GHz, multiple-polarization radar, used for support of the Tropical Rain Measuring Mission (Simpson, 1988) and for research in radar meteorology. It operates on the NASA Ames DC-8 aircraft and simulates the geometry of a spaceborne radar by looking downward through clouds and precipitation. In this paper we begin by describing system performance characteristics. We follow with a description of the radar system and test results.

2 Performance Characteristics

In normal operating mode ARMAR scans its antenna beam $\pm 20^0$ from nadir across the flight track and maps the height profile of precipitation reflectivity (Figure 1). This corresponds to a 9 km swath width when the DC-8 is at a 12 km altitude. In Doppler mode ARMAR points its antenna beam at nadir and measures both precipitation fall velocity and reflectivity. In both of these modes ARMAR spends a small fraction of its time measuring brightness temperature in a radiometer mode. In addition to the scanning and Doppler modes, several operating parameters, including chirp length, pulse repetition frequency (PRF), and polarization, can be varied, allowing the radar to be optimized for the weather system to be studied. Like-polarization, cross-polarization, or alternating like- and cross-polarization measurements can be made. Performance characteristics are summarized in Table 1. Table 2 summarizes the expected signal-to-noise ratio (SNR) for return from rain near the top of the rain column (5 km altitude) and for return from rain just above the surface (radar altitude equal to 12 km). A 10 microsecond chirp is used in these calculations; longer chirps provide proportionately higher SNR's. With proper choice of system parameters, rain rates in the range of 0.1 to 80 mm/h should be observable.

ARMAR is a pulse compression radar (Cook and Bernfield, 1967), achieving range resolution through the use of relatively long (5-45 microsecond), large bandwidth (4 MHz), linear frequency chirps. The received data is compressed by correlating it with a replica of the transmitted chirp. One of the major challenges in ARMAR's design was the achievement of very low range compression sidelobes (-55 dB). This was necessary so that the range sidelobes from the surface would not interfere with return from light rain above the surface. The technique used is that of time domain weighting; the transmitted pulse is smoothly tapered between zero amplitude and maximum amplitude at both its start and end.

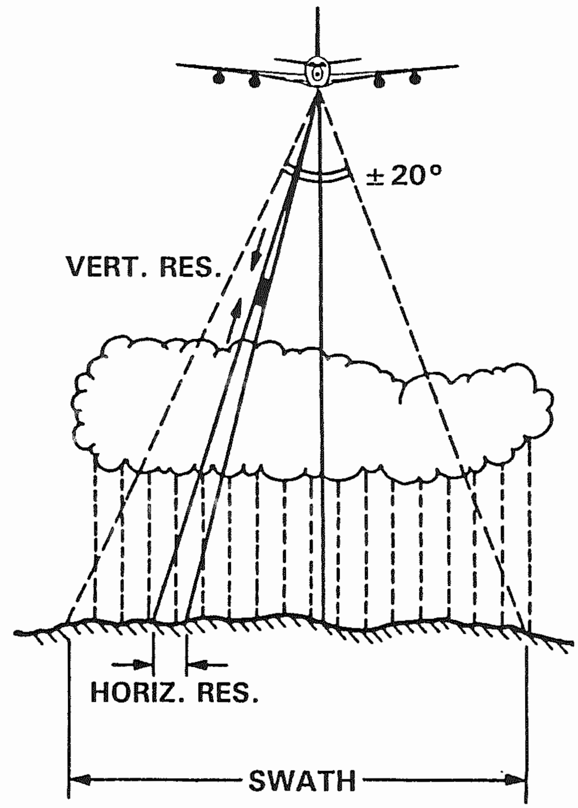

Figure 1. ARMAR flight configuration.

3 System Description

The transmitted chirps are digitally generated under control of the system computer, which sets the frequency, amplitude, length, and inter-pulse spacing of the transmitted pulses. The chirp pulses have a 4 MHz bandwidth and are centered around intermediate frequencies (IF's) near 70 MHz. Up to four separate IF's can be used, increasing the number of independent samples at a given PRF. For Doppler mode, only a single IF is used. The chirp amplitude is shaped in such a way as to give -55 to -60 dB range compression sidelobes, so that range sidelobes from surface return do not obscure return from light rain near the surface. The IF digitally synthesized chirp pulses are upconverted to 14 GHz and then amplified

Table 1: ARMAR SYSTEM PARAMETERS

Performance Characteristics:

Rainrate range	0.1 to 80 mm/h
Vertical resolution	150m
Horizontal resolution	800 m
(at surface, 12 km altitude)	
Swath width (km)	8.7
Frequencies	13.8 GHz
Polarizations	HH, VV, HV, VH

Antenna Characteristics:

Aperture diameter (m)	0.41
Gain (dB)	34
3 dB beamwidth (deg)	3.8
Sidelobe level (dB)	-32
Polarization isolation (dB)	-22

Transmitter Characteristics:

Peak power (W)	200
PRF (KHz)	1-4
No. transmit frequencies	1-4
Pulse duration (microsec)	5-45
Chirp bandwidth (MHz)	4.0

Receiver Characteristics:

System noise temp (K)	700
Sample frequency (MHz)	10
A/D Resolution (bits)	12

Radiometer Characteristics:

Bandwidth (MHz)	40
ΔT (K)	1

Table 2: Expected SNR in dB

RR (mm/h)	SNR (top)	SNR (surf.)
0.1	9.8	3.6
0.5	20.1	13.9
1.0	24.7	18.3
5.0	35.5	27.3
10.0	40.0	29.1
50.0	49.0	11.9
80.0	51.3	-5.8

by a high power traveling wave tube amplifier (TWTA). The amplified chirp ($\sim$ 200 watts) is then sent to the antenna system. The antenna consists of a dual-linearly polarized scalar feed horn which illuminates a precision offset parabolic reflector. The signal is focused by the parabolic reflector and reflected to a flat mechanically scanned elliptical reflector which scans the beam $\pm 20^0$ in the crosstrack direction. Both transmit and receive polarizations can be varied on a pulse by pulse basis, allowing a combination of like- and/or cross-polarization data to be collected. The signal reflected from the rain is collected by the antenna and then amplified by the low noise amplifier (LNA). Following the LNA, the received signal is downconverted to the 70 MHz IF where it is further amplified and filtered. In the final stage, the signal is downconverted to baseband where it is sampled at 10 MHz and digitized by a 12-bit A/D converter. The data are then stored on a high speed tape recorder for processing.

The data processing system takes the recorded data and correlates it with a replica of the transmitted signal to perform pulse compression. For non-Doppler mode data, the average power is calculated and independent samples are averaged. Using calibration loop information and laboratory measurements of the system, these data are converted to reflectivity. For Doppler mode data, the complex compressed signal is used in a pulse-pair algorithm for estimation of the mean velocity.

The radar system is mounted in the cargo bay of the NASA DC-8 aircraft. The antenna beam is directed through an existing opening in the bottom of the DC-8 aircraft. A thin radome covers this observation port, and the entire antenna system is surrounded by a pressure box. The radar RF section (transmitter, receiver) is mounted on a plate which lays on top of the pressure box. A rack for the high-power amplifier and other equipment is mounted in the cargo bay next to the pressure box. The control panel, system computer, tape recorder, and data processing system are mounted in a rack in the DC-8 cabin.

4 Field Tests

During 6-7 February, 1992, the first in a series of winter storms crossed the LA area bringing heavy rains. The total storm accumulation for 6-7 Feb was over 2 inches at JPL. ARMAR was field-tested in a ground-based configuration during this time. The radar and antenna were placed inside the cargo area of a van parked on a hill at JPL. The antenna pointed out the rear of the van toward the south. Because of the location on a hill, a relatively unobstructed view of the LA basin was obtained, allowing horizontal scanning of the antenna over $\pm 20°$ from the south. By placing a plate inclined at 45 degrees in the antenna beam, the beam could be directed upward. Data in both the horizontal and vertical pointing directions were acquired.

Rainfall totals were measured throughout the storm with a raingage, allowing the rainrate at the time of the radar observations to be calculated. A vertically pointing time series is shown in Fig. 2. Here, ARMAR was looking upward, with no scanning. In this image time is zero at the bottom of the image and increases to 11 minutes at the top of the image. The left side of the image is an altitude of 1 km and the right side is an altitude of 7 km. A total of 11 minutes of data is shown, allowing one to see the evolution of the precipitation vertical structure. The bright band can be clearly seen at an altitude of 2 km. Note that its strength varies with time. The raingage

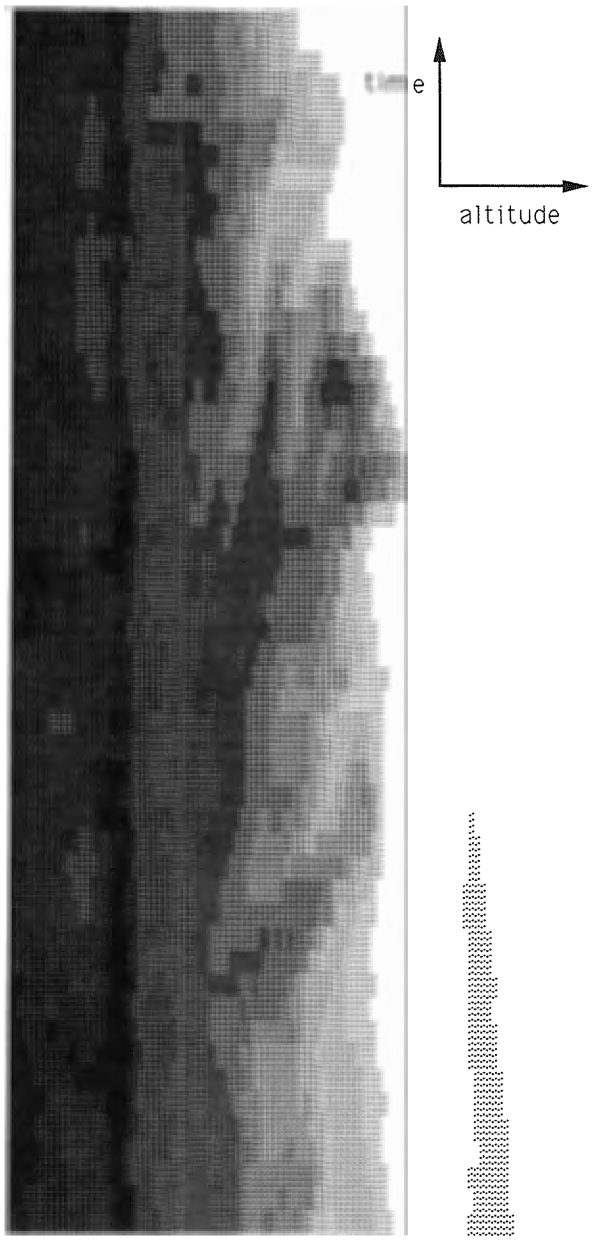

Figure 2. Vertically pointing time series. Bottom of image is time zero, top is 11 minutes. Left side of image is altitude of 1 km, right side is altitude of 7 km. Black corresponds to 40 dBZ, white to 0 dBZ or less.

indicated a rain rate of approximately 5 mm/h. Fig. 3 shows reflectivity and velocity near the start of the data record shown in Fig. 2; the fall velocity for the rain is 5-6 m/s; a jump in the velocity can be seen at the bright band (2 km in range), with the velocity decreasing to 1-2 m/s above the bright band.

Data were acquired for rainrates (as measured by the raingage) between 1 and 13 mm/h. A simple approach for estimating rainrate from radar is the Z-R relation; see, for example, Doviak and Zrnic, 1984. We used the Marshall-Palmer Z-R relation:

$$Z = 200R^{1.6}$$

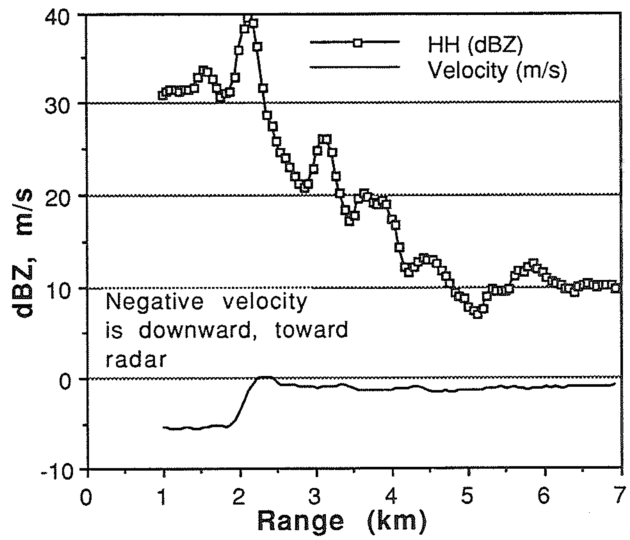

Figure 3. Plot of reflectivity and vertical velocity as a function of altitude for vertical pointing configuration. These data correspond to data in Figure 2 near time zero.

to convert our radar measurements to rainrate, shown in Table 3. Agreement between the raingage and the radar estimates is good except for the 13 mm/h case (as measured by the raingage). This rainfall was probably convective in nature since no bright band was seen and since there were thunderstorms in the area. The lower rainrates were all for stratiform rain. Because the Marshall-Palmer Z-R relation applies only to stratiform rain, the discrepancy at the 13 mm/h rate is not surprising. Table 4 shows brightness temperatures measured by ARMAR in radiometer mode as a function of rainrate.

Table 3: Estimated Rainrate (mm/h)

Raingage	ARMAR
1	1.9
5	3.1
8	7.9
13	5.1

Table 4: 2/92 Radiometer Data

Rainrate (mm/h)	T_B (K)
0	25
1	35
5	44
8	54
13	69

While operating, the radar enters a calibration mode for a small fraction of the time. In calibration mode typically several hundred calibration loop chirps are recorded, along with measurements of a reference load and noise diode. The two latter measurements are used for calibrating the radiometer. The calibration chirps are used for estimating the transmitted power so that reflectivity can be calculated. Shown in Figure 4 is an average of approximately 1500 compressed chirps; each chirp had a length of 15 microseconds. The range compression sidelobes can be seen in this figure to be approximately -55 dB at a range of 300 m and -60 dB at ranges greater than 600 m. In light rain (less than 1 mm/h), the first 300 m of rain above the surface would be obscured by sidelobes from the surface return. Rain more than 300 m above the surface should be measureable. We can also see the radar's intrinsic resolution in the figure. The compressed pulse has a 3 dB width of approximately 60 m. In processing the data a two-fold average in range is used, so the final range resolution is around 120 m.

5 Summary

The 14 GHz channel of ARMAR is complete. Ground-based field tests indicate that performance is as expected. First airborne testing is now planned for May 1992. Future plans call for the addition of a 24 GHz channel.

Acknowlegment

We would like to thank R. Denning, W. Proniewicz, and D. Orozco for their work in developing ARMAR hardware. The research described here was performed by the Jet Propulsion Laboratory, California Institute of Technology, under contract with NASA.

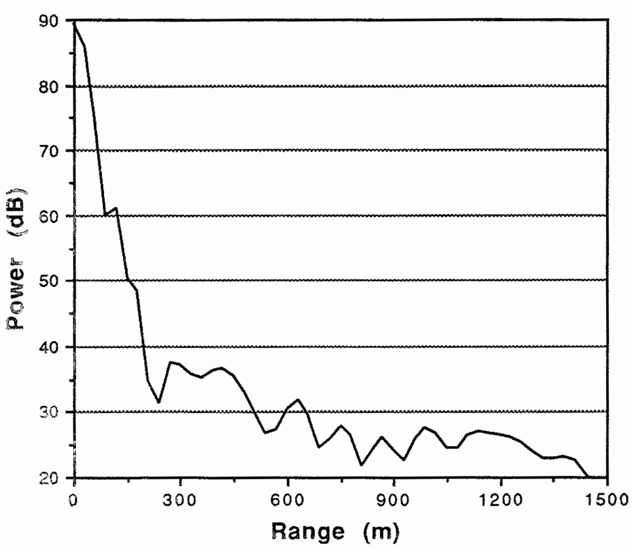

Figure 4. 15 microsecond chirp after pulse compression. Shown is an average over 1500 chirps.

References

Cook, C. E. and M. Bernfield, 1967: *Radar Signals.* Academic Press, New York, 531 pp.

Doviak, R. J. and D. S. Zrnic, 1984: *Doppler Radar and Weather Observations.* Academic Press, Orlando, 458 pp.

Simpson, J. (Ed.), 1988: *TRMM: A satellite mission to measure tropical rainfall*, Report of the Science Steering Group. Govt. Printing Office, Washington, DC, 94 pp.

Vertical Distribution of Clouds Observed at NASA Langley under the ECLIPS and FIRE ETO programs

D. M. Winker

Atmospheric Sciences Division,
NASA Langley Research Center, Hampton, VA USA 23665

1. INTRODUCTION.

Lidar cloud observations have been made on a routine basis at the NASA Langley Research Center since 1987 as part of the FIRE ETO (First ISCCP Regional Experiment Extended Time Observation) program [Cox et al., 1987]. Three other lidar sites are also involved, all located in the US. The purpose of this element of the FIRE program is to produce a set of cloud lidar observations coordinated with satellite overpasses which may be used for comparison of cloud characteristics derived from lidar and from satellite sensors.

NASA Langley has also participated in ECLIPS (the Experimental Cloud Lidar Pilot Study), an international effort involving 16 lidar groups from the US, Europe, Asia, and Australia [WMO, 1988]. ECLIPS is intended to supplement ISCCP (the International Satellite Cloud Climatology Project) with information not readily deduced from passive satellite cloud retrievals, primarily cloud base height, vertical distribution, and optical depth. The data collected by lidar and auxiliary instrumentation may also be used for validation of satellite retrieval algorithms. Here we present preliminary results based on observations conducted under ECLIPS and FIRE ETO.

2. INSTRUMENTATION AND OBSERVATIONS.

The lidar system used for these observations uses the 532 nm linear polarized output of a doubled Nd:YAG laser, an 8" Celestron receiving telescope, and polarization-sensitive receiving optics. Two photomultiplier tubes are used to simultaneously sample backscattered light polarized parallel and perpendicular to the transmitted beam. The signal is digitized at a resolution of 6, 15, or 30 meters, and 8-bit resolution. The laser is operated at a pulse rate between 3 and 10 Hz, with averaged parallel and perpendicular returns being recorded every 15 to 20 seconds. Cloud base and top heights and profiles of scattering ratio and depolarization within cloud layers are routinely derived from the recorded returns. Scattering ratio is defined as (1 + β_c/β_m) where β_c is the volume backscatter cross-section of the cloud particles and β_m is the Rayleigh volume backscatter cross-section.

Both ECLIPS and FIRE ETO lidar observations have been made in conjunction with ground-based measurements of shortwave and longwave fluxes. Rawinsondes were launched from the lidar site during ECLIPS, coincident with about half the AVHRR overpasses, providing detailed profiles of temperature, humidity, and winds. A variety of video and still photography of sky conditions is also available from the ECLIPS observation phases. Observer logbooks are kept, recording WMO cloud codes and other aspects of cloud appearance. Instrumentation used during ECLIPS and FIRE ETO are listed in Table 1.

Observations have been conducted in coordination with overpasses of the AVHRR instruments on the NOAA-10 and NOAA-11 satellites. For the last several years, observations have been made on a schedule of two periods of 5 consecutive working days per month, giving an average of 10 days of observations per month. On observation days, observations are typically conducted coincident with one morning and one afternoon overpass occurring during normal working hours. A single observation lasts one to two hours, centered around the overpass time. Observations are not made during conditions of rain or fog, but otherwise are conducted regardless of whether conditions are clear or cloudy.

ECLIPS activity has been concentrated in two intensive observation phases. At NASA Langley, observations for Phase I were conducted over the period from the middle of October to the middle of November, 1989 and for Phase II for 4 weeks in May 1991. Lidar observations were made continuously over the 4 week period of Phase I. During Phase II, observations were conducted approximately 16 hours per day, timed so that observations were made coincident with all AVHRR overpasses having zenith angles less than 60°.

3. DETECTION OF CLOUD BASE AND TOP.

Cloud bases and tops are identified using a threshhold algorithm. The parallel and perpendicular returns are added together, using an appropriate parallel/perpendicular gain ratio derived from a system calibration. The lidar return is normalized by matching the return in a region of clear air to a simulated return from a molecular atmosphere. A range-dependent threshold is defined, based on the noise in the recorded lidar signal, and a signal excursion above the threshold value for a certain number of successive samples is identified as a cloud. Statistical smoothing is used to eliminate spurious cloud identifications due to noise spikes. Cloud tops are identified as the point where the return drops below the threshold value. In cases of thick clouds, the threshold is redefined to account for attenuation through the cloud.

This algorithm is applied to averaged lidar returns which are recorded every 15 to 20 seconds. All cloud layers apparent in the return are identified, and base and top heights are reported with a resolution of 6, 15, or 30 meters (depending on the sampling rate). We have observed as many as 4 distinct cloud layers in a single return. Because of the short sampling

Table 1. Instrumentation used in ECLIPS and FIRE ETO programs.

Depolarization Lidar:	
	range - 1 to 15 km
	range resolution - 6 to 30 m
	10 Hz pulse rate
	15-second averages recorded
	wavelength - 532 nm
	2 mr field of view
	manually tiltable 5° off-zenith
Vaisala CT12X ceilometer	
	range - surface to 12,500′ (3.8 km)
	range resolution - 15 m
	3-minute averages recorded
Hemispheric downwelling flux measurements:	
	short-wave flux, total and diffuse:
	Licor LI-210 SB pyranometers (0.5-0.6 μm)
	Eppley PSP pyranometers (0.3-3.0 μm)
	broadband long-wave flux:
	Eppley PIR pyrgeometer (3 - 12 μm)
Photography:	
	all sky video - continuous
	narrow field of view video - continuous
	35 mm still photography - intermittent
Meteorology	
	Vaisala rawinsonde
	hourly surface met observations

time, many observations of a single cloud are recorded and the data may be used to investigate the structure of individual clouds.

4. CLOUD HEIGHT DISTRIBUTIONS.

In the past, the vertical distributions of clouds have been estimated from reports by ground observers (Warren et al., 1985), by aircraft observers (deBarry and Möller, 1963), and more recently by passive satellite instruments (Minnis et al., 1990). While having the disadvantage of not being able to sense the tops of dense clouds, lidar has several advantages: continuous monitoring is possible, and it is possible to measure cloud layers which are hidden by thin, lower layers. Further, lidar gives very precise height information.

A lidar system with marginal sensitivity will detect more high clouds at night than during the day, when noise due to skylight is higher. Figure 1 shows scatter plots of the peak scattering ratio observed within a cloud layer, R_{pk}, vs. the base height of the layer. Shown are data from ECLIPS Phase II for all layers above 8 km observed at night (Figure 1a) and observed within two hours of local noon (Figure 1b), when sensitivity would be expected to be worst. At night, cirrus layers with R_{pk} as small as 3 are detected, while most cirrus layers have R_{pk} between 10 and 100. Cirrus layers with R_{pk} less than 10 to 15 have been found to be subvisible (during daylight) to a ground observer. Figure 1b shows that even under the worst lighting conditions detection sensitivity is almost as good as at night with R_{pk} as small as about 5 being detectable. Thus we believe that in normal operation, and in the absence of

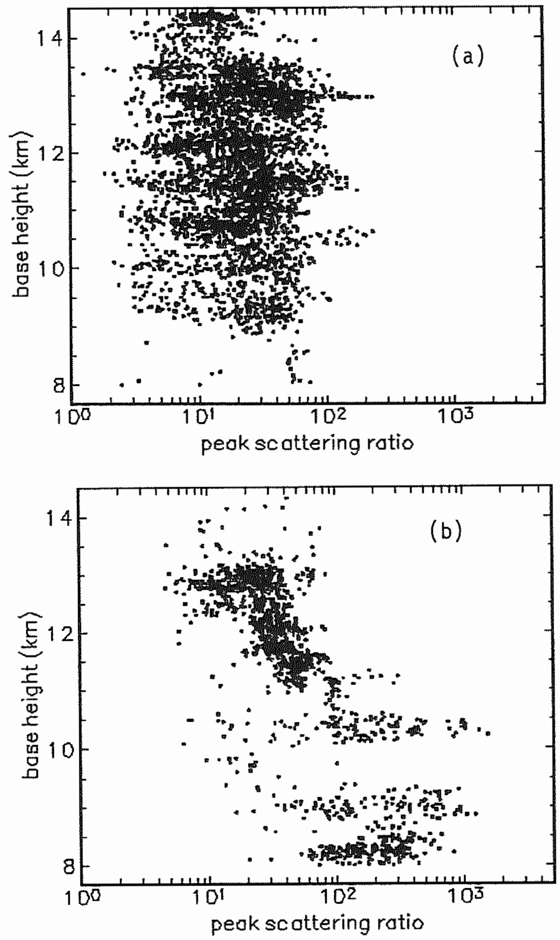

Figure 1. Cloud observations from ECLIPS Phase II. a) all nighttime observations above 8 km; b) all observations above 8 km and within 2 hours of solar noon.

stratus, our system is able to detect the great majority of cirrus, and certainly all the cirrus visible to a ground observer. This is consistent with a sensitivity analysis which was performed, showing system sensitivity is limited more by digitizer quantization error than background noise.

Cloud base height is generally not observable from satellite instruments, therefore a primary objective has been to observe base heights and derive statistics which might be used for parameterization of cloud base height. Figure 2 shows base height statistics for a one year period, by season. About 80% of the observations in spring 1991 were during ECLIPS Phase II, with the rest from ETO observations in April and late March. The lowest altitude at which lidar returns were consistently analyzed for base height during this period was 3 km. Lower base heights are available from the ceilometer operated at the site. The heights of the highest clouds observed follow the seasonal motion of the mean tropopause height, being several kilometers higher in spring and summer than in fall and winter. A minimum in cloud base occurrence often appears in the 4 to 7 km region. This is a real feature and not an artifact produced by the blockage of clouds in this region by dense lower layers. The majority of clouds

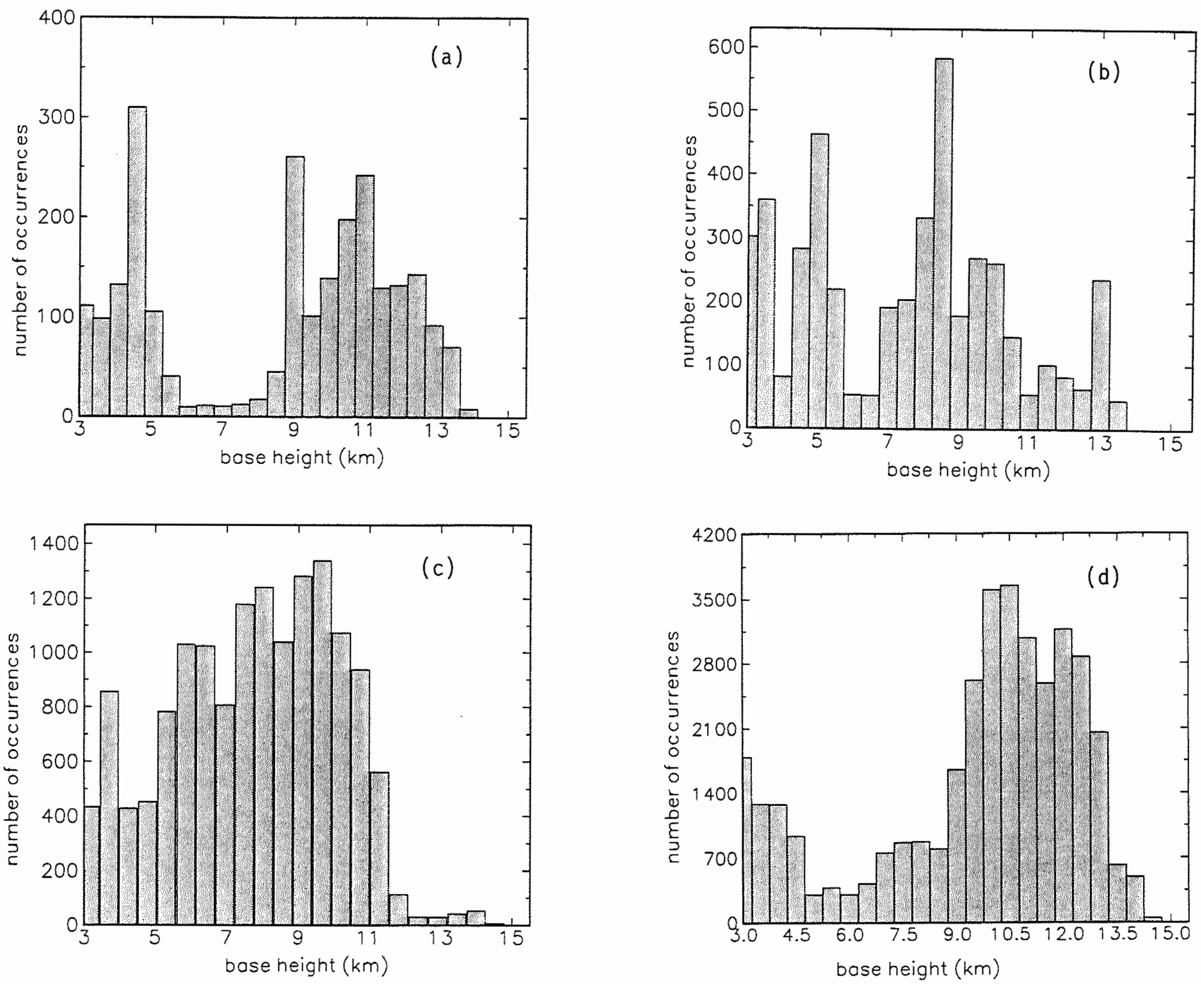

Figure 2. Observed distribution of cloud base heights. a) Summer 1990, 2415 observations; b) Fall 1990, 4598 observations; c) Winter 1990- 1991, 5127 observations; d) Spring 1991, 48,357 observations.

in this altitude region appear to be associated with frontal passages, and few clouds are observed if frontal activity is low on days observations are being conducted.

Except in cases of precipitation and blocking by lower layers, detection of cloud base is unambiguous. Detection of cloud top is not as straightforward. If a lidar return is received from clear air above the cloud or from a higher cloud layer, the top of the lower cloud can be unambiguously identified and this is referred to as the 'true top'. If a clear-air return from above the cloud is not above the background level, it cannot be determined whether the lidar signal was completely attenuated inside the cloud, or whether it was attenuated enough that the return from above the cloud is too weak to be detected. In this case we refer to the 'apparent top'. We have defined a transmittance factor, T_i, to help discriminate between these two cases. T_i is equal to the fraction of the first 50 samples above the reported cloud top which are above background. If the signal has been completely attenuated, signal fluctuations are due only to noise in the background light level and T_i is near 0.5. If T_i is near one, we have some confidence we have detected the true cloud top.

Figure 3 displays cloud layer thickness derived from cloud base and top measurements as a function of cloud base altitude. Only cloud layers having $T_i > 0.75$ are included. Given the high spatial resolution of the lidar, a great many observations were made of very thin layers. While the statistics of low clouds are biased toward small thicknesses, as the thickness of cumulus cannot be measured, very thick cirrus clouds can be accurately measured. The observations of layer thickness greater than 3 km at an altitude of 4 to 5 km all correspond to a single, anomalous, cloud system of a type which has only been observed once.

The lidar often observes multi-layer clouds. About 13% of the profiles from ECLIPS Phase II include 2 or more layers and 1% include three or more layers. Figure 4 shows the distribution of the spacing between multiple layers observed simultaneously in single lidar profiles. Most of the observations fall into three categories. Data points in the lower left quadrant correspond to multilayer stratus, points in the upper left quadrant correspond to multilayer cirrus clouds, and points in the lower right quadrant correspond to the simultaneous observation of stratus and cirrus.

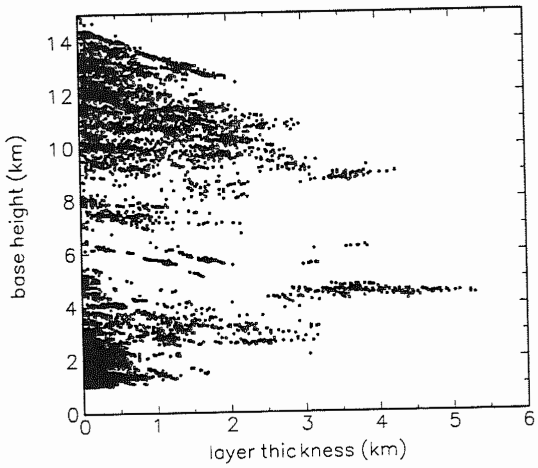

Figure 3. Cloud layer thickness derived from ECLIPS Phase II observations. Only layers having $T_i > 0.75$ are included.

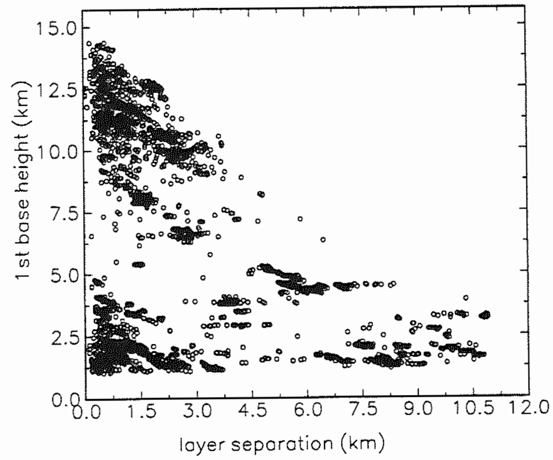

Figure 4. Spacing of simultaneously observed cloud layers derived from ECLIPS Phase II observations.

5. ACKNOWLEDGEMENTS.

I would like to recognize the efforts of Mark Vaughan, who took most of the FIRE ETO data, much of the ECLIPS data and who processed all cloud heights, and of Joe Alvarez, who developed the lidar system used in making these observations and who also took much of the ECLIPS data.

References

Cox, S. K., D. S. McDougal, D. A. Randall, and R. A. Schiffer: 'FIRE - The first ISCCP regional experiment,' Bull. Amer. Meteor. Soc. 68, 114-118, 1987.

deBary, E., and F. Möller: The vertical distribution of clouds, J. Appl. Meteor. 2, 806-808, 1963.

Minnis, P., P. W. Heck, and E. F Harrison: The 27-28 October 1986 FIRE IFO cirrus case study: Cloud parameter fields derived from satellite data, Mon. Wea. Rev. 118, 2426-2446, 1990.

Warren, S. G., C. Hahn, and J. London: Simultaneous occurrence of different cloud types, J. Clim. Appl. Meteor. 24, 658-667, 1985.

WMO: An Experimental Cloud Lidar Pilot Study (ECLIPS), Report of the WCRP/CSIRO workshop on cloud base measurements (CSIRO, Mordialloc, Victoria, Australia, February 29-March 3, 1988), WCRP-14, WMO/TD-No. 251, WMO, Geneva, Sept. 1988.

MEASUREMENT OF ATTENUATION AND RAINFALL BY DUAL RADAR METHOD

R. C. Srivastava and Lin Tian

Laboratory for Atmospheric Probing, Department of the Geophysical Sciences,
The University of Chicago, Chicago, IL 60637

1. INTRODUCTION

Microwave radar has been used for the remote measurement of rainfall for a number of years. The earliest method used an empirical relationship between the radar reflectivity factor (Z) and the rainfall rate (R). Z is proportional to the sum of the 6th powers (in the Rayleigh scattering regime) and R approximately to the sum of the 3.5th powers of the diameters of drops in a unit volume. The rather large difference between the two exponents gives rise to large errors in the measurement of R by this method because of the large variability in the raindrop size distribution as a function of the rainfall rate. Seliga and Bringi (1976) suggested the use of Z and ZDR (differential reflectivity, or the difference in Z at horizontal and vertical polarizations) for estimating R. Estimates by their method are more robust because only the shape of the drop size distribution rather than its magnitude need be uniquely related to R. However, changes in the shape of the distribution, which do occur in Nature, and other factors, lead to errors in R estimated by this method as well.

The microwave attenuation rate (K) is more tightly related to the drop size distribution because it is approximately proportional to the nth powers of the diameters of drops in a unit volume where n is close to 3 1/2. Combinations of Z and K can yield more accurate values of R in spite of variability of the drop size distribution (Atlas and Ulbrich, 1974). However, the measurement of K presents difficulties. Eccles and Mueller (1971) proposed the use of reflectivities measured at S and X bands for the estimation of X-band attenuation. However, this method is subject to errors in the presence of large particles which may be outside the Rayleigh scattering regime at one or both the wavelengths. Other methods for measuring integrated attenuation that have been proposed involve a target of known radar cross-section; in practice, however, such a target may not be available.

In connection with a study of the dual-wavelength detection of hail, Srivastava and Jameson (1978) suggested that attenuation could be derived from measurements of reflectivity by two spaced radars having the same, or approximately the same, attenuating wavelength. The use of the same wavelength removes uncertainties due to variation of reflectivity factor with wavelength. Testud and Amayenc (1989) proposed a similar method for estimating attenuation using a single-frequency dual-beam airborne or space-borne radar and performed numerical simulations to test the feasibility of the method.

Here, we propose the use of two ground-based radars, operating at approximately the same attenuating wavelength, for measuring K and Z, and thereby obtaining a more accurate estimate of R. The use of ground-based radars provides the possibility of testing the method with existing data. In this study, however, we report only on numerical simulations of the method.

2. EQUATIONS

Figure 1 shows schematically two radars scanning a storm on a coplane. The two radars are assumed to have approximately the same wavelength. The radar reflectivity factors measured by the two radars, ζ_1 *and* ζ_2 (each in dBZ), at the point P are related to the true radar reflectivity factor at P, $\zeta(P)$ (also dBZ) by:

$$\begin{aligned}\zeta_1(P) &= \zeta(P) - 2\int_{R_1}^{P} K dr_1,\\ \zeta_2(P) &= \zeta(P) - 2\int_{R_2}^{P} K dr_2\end{aligned} \qquad (1)$$

where r_1 *and* r_2 are the ranges to P from the two radars. Here K is assumed to be in dB per distance. Using similar equations for the points Q, R and S, we can eliminate ζ between the equations to get:

$$\begin{aligned}&\{[\zeta_1(R) - \zeta_1(S)] - [\zeta_2(R) - \zeta_2(Q)]\} - \\ &\{[\zeta_1(Q) - \zeta_1(P)] - [\zeta_2(S) - \zeta_2(P)]\} \\ &= 2\int_Q^R K dr_2 - 2\int_S^R K dr_1 + 2\int_P^Q K dr_1 - 2\int_P^S K dr_2\end{aligned} \qquad (2)$$

From the above, we obtain after some manipulation:

$$\frac{\partial^2(\zeta_1 - \zeta_2)}{\partial\alpha\partial\beta} = 2\frac{\partial}{\partial\beta}\left[K\frac{\partial r_2}{\partial\alpha}\right] - 2\frac{\partial}{\partial\alpha}\left[K\frac{\partial r_1}{\partial\beta}\right] \qquad (3),$$

where α *and* β are the azimuth angles from the two radars. The left hand side of this equation can be measured and the angles and the ranges are also measured. Therefore, in principle, we should be able to calculate K provided the necessary boundary conditions are known. It is to be noted

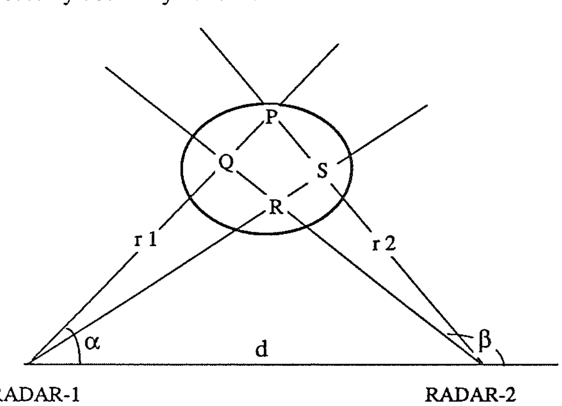

Figure 1: Schematic showing the method of measurement.

that only the derivatives of ζ_1 *and* ζ_2 enter this equation; therefore, radar calibration errors should not affect the determination of K; however, the calibrations would be needed if ζ were also to be determined. We shall now present selected results from numerical simulations performed to test the feasibility of this method for the determination of K.

3. NUMERICAL SIMULATIONS

First, we generate a model storm with given reflectivity and attenuation fields. Then attenuated reflectivities are computed and sampled according to the radar characteristics. This gives the simulated ζ_1 *and* ζ_2 without errors. Inherent errors due to signal fluctuations are then added to these accurate 'measurements' to generate more realistic 'measurements'. The errors are assumed to be uncorrelated and normally distributed with mean zero and known standard deviation.

Once the measurements have been generated, the left hand side of (3) [to be called $M(\alpha,\beta)$] is calculated. With accurate data this is done by interpolating the measured reflectivities on to an (α,β) grid and then performing the necessary differentiations numerically. With noisy data (due to signal fluctuations, for example), measurements over a number of points (taken in the natural radar coordinate system of each radar) are used to calculate surface fits to ζ_1 *and* ζ_2; usually second-degree power-law fits in (α,β) are determined by a least-squares method. The coefficients in the power-law fits yield $M(\alpha,\beta)$. To calculate K, equation (3) is discretized using an 'upstream' method. For boundary conditions, we have assumed $K = 0$ wherever the measured reflectivity is less than 10 dBZ. This can obviously lead to errors if the true reflectivity is large but the measured reflectivity is small because of attenuation.

In the results to be presented below, we assume the model reflectivity to be given by

$$\zeta = \zeta_0 - \alpha_1(x-x_0)^2 - \alpha_2(y-y_0)^2 \qquad (4).$$

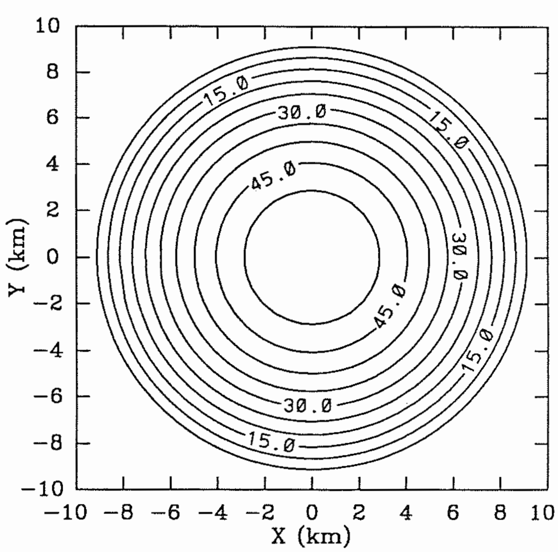

Figure 2a: Contours of radar reflecivity factor for model storm . Minimum contour level is 5 dBZ, the contour interval is 5 dBZ., and the peak reflectivity is 55 dBZ.

Here (x,y) are Cartesian coordinates in the coplane of the radar scan, (x_0,y_0) is the center of the storm where the maximum reflectivity, ζ_0, occurs and α_1 *and* α_2 are selectable parameters which determine the size of the storm. In the results to be presented we have used either a one-celled storm given by equation (4), or a two-celled storm consisting of the sum of two storms given by (4) but with different centers.

The following parameters apply to all the calculations to be presented below:

Wavelength of radars (cm)	3.2
Distance between radars (km)	30
Coordinates of radar #1 (km)	-15,- 30
Coordinates of radar #2 (km)	15, -30
ζ_0 (dBZ)	55
α_1 *and* α_2 $(dBZ\,km^{-2})$	0.6
ζ_{min} (dBZ)	0
range gate width & spacing (km)	0.2
azimuth sampling interval (degrees)	0.5

We assume that the one-way attenuation ($K, dB\,km^{-1}$) is given by the power-law $K = a\zeta^b$ with $a = 2.9\ 10^{-4}$ and $b = 0.72$ (these numbers apply at a wavelength of 3.2 cm). However, it may be noted that it is not necessary to assume any functional relationship between K *and* ζ.

Fig. 2 shows results for a storm cell situated symmetrically between the two radars. Fig. 2a shows contours of unattenuated reflectivity without errors. Fig. 2b is the (attenuated) reflectivity measured by the first radar, again without errors. The reflectivity measured by the second radar (not shown) would be the mirror image of fig. 2b. Note the degradation of the maximum reflectivity and the 'pulling in' of the point of the maximum towards the radar. Fig. 2c shows the attenuation assumed to generate fig. 2b. Fig. 2d shows contours of attenuation ($dB\,km^{-1}$) retrieved from the measured data (that is, fig. 2b, and corresponding figure for radar 2) with superposed measurement errors. The errors were assumed to be normally distributed with mean zero and standard deviation 1.0 dB. It is seen that there is a fair degree

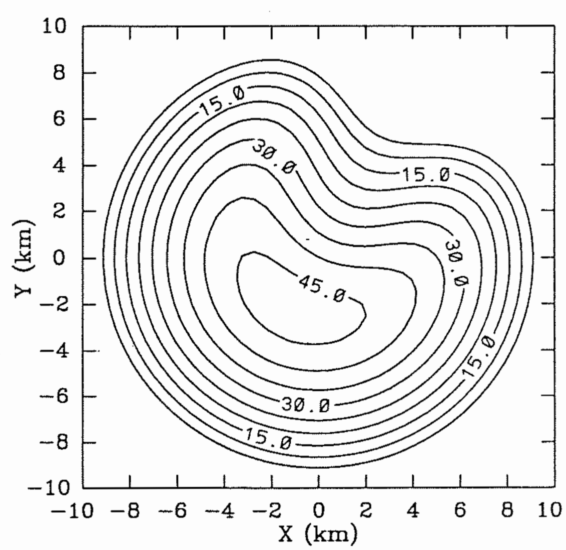

Figure 2b: Contours of attenuated reflectivity measured by radar 1 (no errors). Contour levels as in fig. 2a.

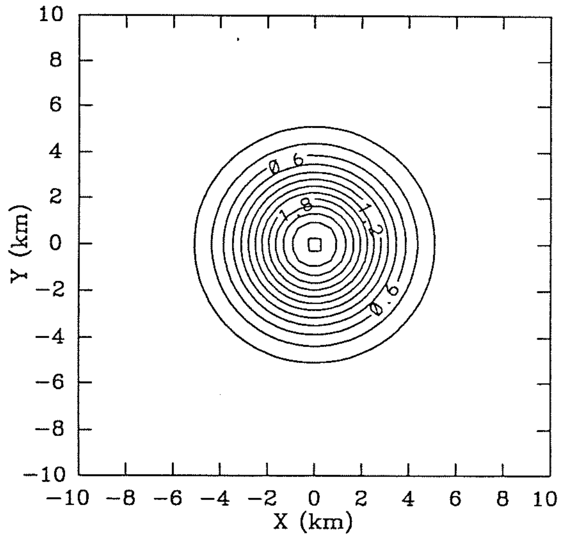

Figure 2c: Contours of assumed specific attenuation for model storm of fig. 2a. The minimum contour level is 0.2 dB/km, the contour interval is 0.2 dB/km, and the maximum attenuation at the storm center is 2.6 dB/km.

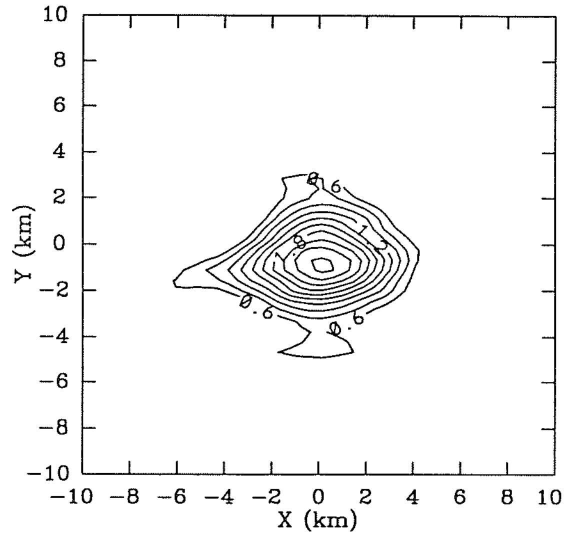

Figure 2d Contours of calculated specific attenuation for model storm of fig. 2b. with additive normally distributed error having standard deviation 1.0 dB. The minimum contour level is 0.6dB/km, the contour interval is 0.2 dB/km, and the maximum attenuation is 2.4 dB/km.

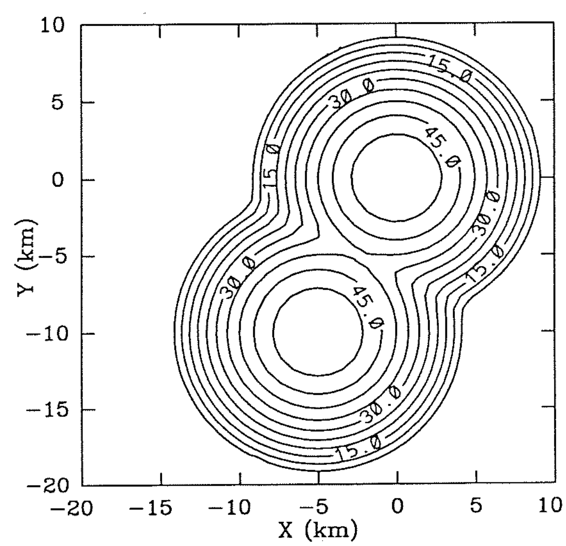

Figure 3a: Contours of radar reflectivity factor for model storm. Minimum contour level is 5 dBZ, the contour interval is 5 dBZ. and the peak reflectivity is 55 dBZ.

of correspondence between the retrieved and assumed attenuation fields. The errors and distortions in the retrieved field occur at low reflectivities. The maximum retrieved attenuation is 2.4 $dB\ km^{-1}$ as against a maximum of 2.6 $dB\ km^{-1}$ in the assumed field.

Fig. 3 shows results for a storm complex consisting of the sum of two equal storms given by eq. (4). The centers of the storms are situated on a radial emanating from radar 1, and their coordinates are (-5, -10) and (0, 0) km. Fig. 3a shows contours of unattenuated reflectivity factor without errors. Figs. 3b and 3c show contours of attenuated reflectivity factors, again without errors, as measured by radars 1 and 2 respectively. Figure 3d shows the assumed attenuation field used to calculate figs. 3b and c. We see that the attenuation generates fictitious high reflectivity centers (see fig. 3b); in place of the two true reflectivity 'cores', we now have four 'cores'. Radar #2 which is situated differently with respect to the storm 'sees' only two reflectivity 'cores'. We also see that parts of the storm become undetectable, especially from the vantage point of radar 1, because of attenuation. Figs. 3e shows contours of the retrieved attenuation field with normally distributed errors with mean 0.0 and standard deviation 1.0 dB added to the measured reflectivities of figs. 3b and c. We see that the retrieved attenuation field generally agrees with the assumed attenuation field. The major deviations occur in regions where attenuation can not be retrieved because the storm becomes undetectable by one or both radars because of attenuation. The maximum retrieved attenuation in the component of the storm with center nearer to radar 1, which does not suffer as much attenuation as the other component of the storm, is 2.2 $dB\ km^{-1}$ which compares favorably with the assumed maximum value of 2.6 $dB\ km^{-1}$

4. SUMMARY AND FUTURE WORK

It has been proposed that microwave attenuation may be estimated from reflectivity measurements by two spatially separated radars having approximately the same attenuating wavelength. A partial differential equation relating the specific attenuation and the measured reflectivities has been derived. A finite difference method has been used to solve the equation for the attenuation. The method has been tested by numerical simulations in which model storms with known reflectivity and attenuation fields have first been used to calculate the attenuated reflectivities measured by two radars without errors. Errors in the measurement of reflectivity have been simulated by adding a random Gaussian variate of mean 0 and a selected standard deviation. For the model storms considered, the assumed and calculated attenuation fields show good agreement even when the standard deviation of the additive normal error was taken as 1.0 dB.

Future work will involve improvements of the numerical method for retrieving the attenuation, further tests of the method through additional numerical simulations, and tests with actual data. We plan to improve methods for smoothing measured reflectivities to reduce noise due to signal fluctuations. We plan to simulate the effects of other errors in radar measurements, such as pointing errors, range

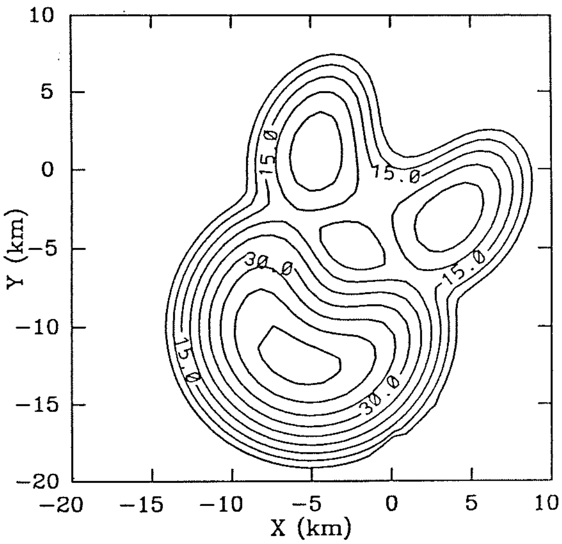

Figure 3b: Contours of attenuated reflectivity measured by radar 1 (no errors). Contour levels as in fig. 3a.

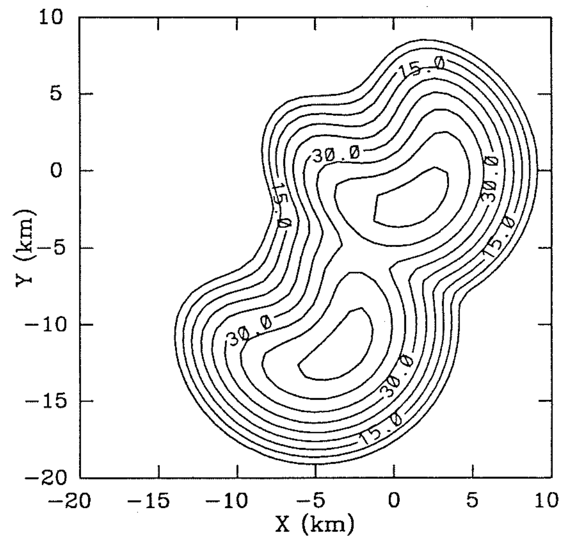

Figure 3c: Contours of attenuated reflectivity measured by radar 2 (no errors). Contour levels as in fig. 3a.

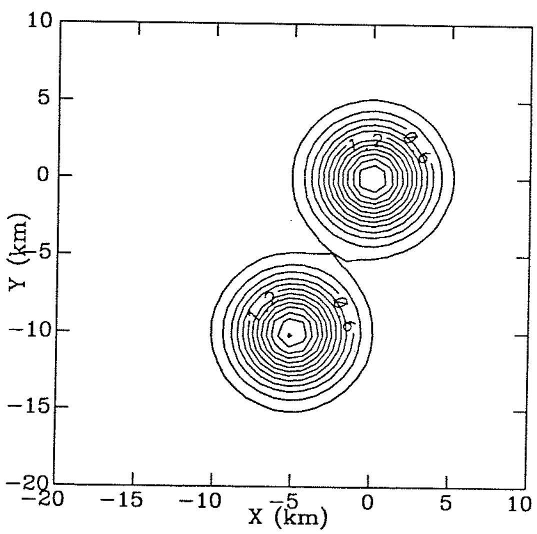

Figure 3d: Contours of assumed specific attenuation for model storm of fig. 3a. The minimum contour level is 0.2 dB/km, the contour interval is 0.2 dB/km, and the maximum attenuation is 2.6 dB/km.

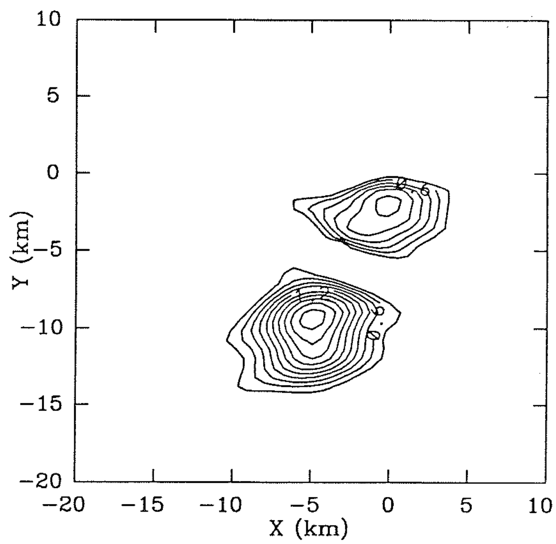

Figure 3e: Contours of calculated specific attenuation for model storm of fig. 3a. with additive normally distributed error having standard deviation 1.0 dB. The minimum contour level is 0.4 dB/km, the contour interval is 0.2 dB/km, and the maximum attenuation is 2.2 dB/km.

measurement errors, pulse-volume filtering effects involving the main and side lobes of the radar antenna. We also plan to use existing data from field experiments in which two 3 and / or 5 cm radars, and perhaps a 10 cm radar were used to observe storms, and aircraft or ground-based sensors were used to measure precipitation.

ACKNOWLEDGMENTS: This research was supported by the National Science Foundation under grant ATM 91 05182. We thank John Valdes for help with the computer work.

REFERENCES

Atlas, D, and C. W. Ulbrich, 1974: The physical basis for attenuation-rainfall relationships and the measurement of rainfall parameters by combined attenuation and radar methods. *J. Rech. Atmos.*, **8**, 175-198.

Eccles, P. J., and E. A. Mueller, 1971: X-band attenuation and liquid water content estimation by a dual-wavelength radar. *J. Appl. Meteor.*, **10**, 1252-1259.

Seliga, T. A., and V. N. Bringi, 1976: Potential use of radar differential reflectivity measurements at orthogonal polarization for measuring precipitation. *J. Appl. Meteor.*, **15**, 69-76..

Srivastava R.C., and A. R. Jameson, 1978: Radar detection of hail. *Amer. Meteor. Soc. Monograph*, **38**, 269-277.

Testud, J., and P. Amayenc, 1989: Stereoradar meteorology: A promising technique for observation of precipitation from a mobile platform. *J. Atmos. Ocean. Tech.*, **6**, 89-108.

94 GHz POLARIMETRIC RADAR SCATTERING FROM ICE CRYSTALS

K. Aydin[1], C. Tang[1], A. Pazmany[2], J. Mead[2], R. McIntosh[2], M. Hervig[3], R. Kelly[3], and G. Vali[3]

[1] Communications and Space Sciences Laboratory
Department of Electrical and Computer Engineering
The Pennsylvania State University, University Park, PA 16803, USA

[2] Microwave Remote Sensing Laboratory
Department of Electrical and Computer Engineering
University of Massachusetts, Amherst, MA 01003, USA

[3] Department of Atmospheric Sciences
P. O. Box 3038
University of Wyoming, Laramie, Wyoming, 82071, USA

1. INTRODUCTION

Millimeter wave radars operating at 94 GHz (3.19 mm wavelength) are being tested for cloud remote sensing applications such as identifying ice crystal habits, estimating ice mass content, and measuring small scale turbulence structures of clouds. Radars at this frequency have the advantage of being compact (e.g., a 1 m diameter antenna has a 0.2° beamwidth) and therefore are highly mobile for use on ground-based (Lhermitte, 1987) or airborne platforms. Scattering from rain at 94 GHz has been measured (Lhermitte, 1987; Richard et al. 1988) and modelled (Aydin and Lure, 1991) earlier. This paper focuses on ice crystals. Results are presented from an ongoing study based on experiments conducted at the University of Wyoming's Elk Mountain Observatory. Researchers at the University of Massachusetts built and operated the 95 GHz polarimetric radar (Mead and McIntosh, 1990). The University of Wyoming group made the in situ measurements and analyzed the ice crystal image data. The Penn State group determined the scattering properties of model ice crystals for comparison with the radar measurements. Another comparative study based on these experiments is also presented in this volume (Hervig et al., 1992).

2. EXPERIMENT

During the month of February in 1991 a series of measurements were made with a 95 GHz polarimetric Doppler radar at the Elk Mountain Observatory (EMO) in Wyoming. The radar transmitter and receiver had 30 cm diameter antennas corresponding to 0.7° beamwidths. Pairs of horizontally (H) and vertically (V) polarized pulses (0.2 μs duration), separated by 140 μs, were transmitted at a rate of 200 Hz. The peak transmitter power was 1 kW. The data presented in this paper represents 20 s averages of measurements obtained from a 30 m range gate centered at 75 m, which was the closest range to the tunnel intake where the in situ measurements were performed, Fig. 1. Operating simultaneously with the radar were several ground based instruments including a Particle Measuring System (PMS) 2D-C probe which recorded two dimensional shadow images of ice crystals as they were forced through the wind tunnel, Fig. 1. The radar was elevated by 12° and pointed to the side of the tunnel to clear the trees and other ground clutter.

The case study presented here is based on measurements obtained on the night of February 18, 1991, when the wind was calm and the air temperature was -15°C. The precipitation was dominated by unrimed stellar and hexagonal plates as shown by the 2D-C images in Fig. 2. The measured size distributions showed peak concentrations at about 200 μm, with maximum sizes ranging from 1900 to 2250 μm. Fig. 3 shows a sample from these distributions. Also worth noting is that specular reflection from the ice crystals were observed with a narrow-beam flashlight only within about 20° from the vertical, indicating a degree of alignment of the planar crystals.

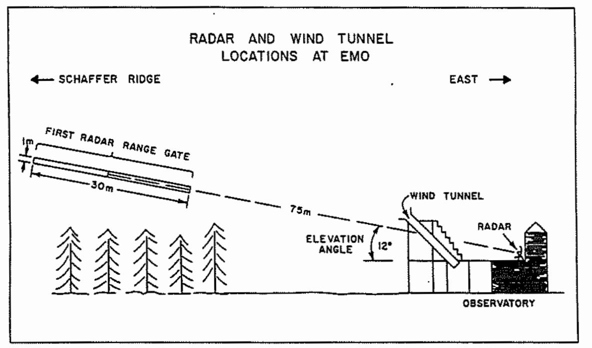

Fig. 1 Side view of the experimental set up at the Elk Mountain Observatory (EMO).

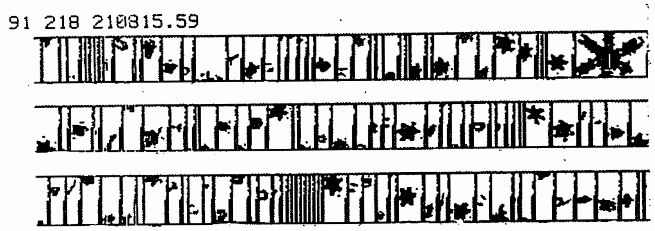

Fig. 2 Typical images from the 2D-C probe obtained on February 18, 1991 at EMO. The vertical extent of each strip is 800 μm.

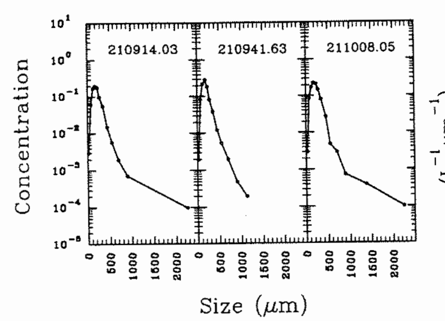

Fig. 3 Sample size distributions derived from the 2D-C images. The size corresponds to the maximum dimension of the ice particle.

3. SCATTERING COMPUTATIONS

Computations of electromagnetic scattering from ice crystals were performed using the Finite Difference Time Domain (FDTD) technique (Umashankar and Taflove, 1982; Luebbers et al., 1991). The accuracy of the calculated field magnitudes and backscattering cross sections are expected to be within 1 dB, based on the technique's performance when compared with Mie series solutions for scattering from spheres.

The model ice crystal shapes were derived using the 2D-C probe images obtained during the experiment. Crystals with sizes (i.e., maximum dimensions) up to 300 μm were chosen as hexagonal plates and the larger ones were modelled as stellar plates with 300 μm hexagonal cores and six branches attached to them, Fig. 4, The ice crystal density was taken to be 0.9 g cm^{-3}, corresponding to a dielectric constant of 3.1307-j0.0111 at 94 GHz (Warren, 1984; Bohren, 1986). A density of 0.85 g cm^{-3} (with dielectric constant 2.9784-j0.0102) was also tested and produced little change in the results. The thickness of the plates could not be obtained from the 2D-C images. Therefore, the following mean relation was used (Auer and Veal, 1970):

$$h = 2.028 d^{0.431} \quad (\mu m) \qquad (1)$$

where h is the thickness (or height) and d is the diameter of the circumscribing circle (or maximum dimension of the ice crystals) in μm.

Information on the orientation of the ice crystals was not available from the situ measurements except for the flashlight observation showing specular reflection only within about 20° from the vertical. The orientation of the particle's axis (i.e., the axis perpendicular to its broad surface and passing through its center) relative to the local coordinate system is determined by the angles θ (from the z-axis which is vertically oriented) and ϕ (from the x-axis). These are two of the three Eulerian angles (Goldstein, 1965) showing the rotation of the particle relative to the local coordinate system. The third angle ψ involves the rotation of the particle around its own axis. Both ϕ and ψ are assumed to be uniformly distributed between 0° and 360°. The angle θ, which varies between 0° and 180°, is chosen to have a truncated Gaussian distribution of the form

$$p(\theta) = I^{-1} \exp[-(\theta-\overline{\theta})^2/2\sigma^2] \,, \qquad 0 \le \theta \le \pi \qquad (2)$$

where

$$I = \int_0^{\pi} \exp[-(\theta-\overline{\theta})^2/2\sigma^2] d\theta$$

$\theta = \overline{\theta}$ corresponds to the peak value (in this study we chose $\overline{\theta} = 0°$) and σ is the standard deviation of the untruncated distribution. The radar elevation angle is measured relative to the horizontal plane (i.e., the xy-plane) in the local coordinate system.

4. COMPARISON OF RADAR MEASUREMENTS AND MODEL RESULTS

The following radar measurands will be used for comparison with the model computations. The effective reflectivity factors Z_{HH} and Z_{VV} at horizontal (H) and vertical (V) polarizations are defined as

$$Z_{HH} = \frac{\lambda^4}{\pi^5 |K|^2} \int \sigma_{HH}(D)\; N(D)\, dD \quad (mm^6\; m^{-3}) \qquad (3)$$

where λ is the wavelength in mm, $\sigma_{HH}(D)$ is the backscattering cross section at H-polarization in mm^2 for a particle of size D, N(D)dD is the number of particles per cubic meter in the size range D to D+dD, $|K| = |\epsilon_r - 1|/|\epsilon_r + 2|$, and ϵ_r is the complex dielectric constant. Z_{VV} can be obtained from (3) by replacing σ_{HH} with σ_{VV}. The commonly used unit for Z_{HH} and Z_{VV} is dBZ, where 10 log Z_{HH} is in dBZ units. The difference

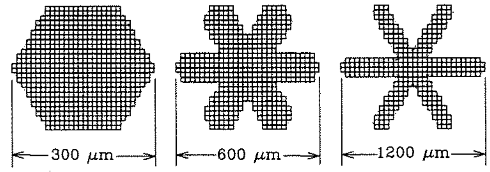

Fig. 4 Model shapes of planar crystals used in the electromagnetic scattering computations. Only three sizes are shown here.

between Z_{HH} and Z_{VV} in dBZ units is defined as the differential reflectivity (Seliga and Bringi, 1976)

$$Z_{DR} = 10 \log Z_{HH} - 10 \log Z_{VV} \quad (dB) \qquad (4)$$

The degree of polarization DP is defined as (Ulaby and Elachi, 1990)

$$DP = \left[(Q^2 + U^2 + V^2)/I_0^2\right]^{1/2} \qquad (5)$$

based on the scattered wave Stoke's vector

$$\begin{bmatrix} I_0 \\ Q \\ U \\ V \end{bmatrix} = \begin{bmatrix} \langle|E_V|^2\rangle + \langle|E_H|^2\rangle \\ \langle|E_V|^2\rangle - \langle|E_H|^2\rangle \\ \langle 2Re(E_V E_H^*)\rangle \\ \langle 2Im(E_V E_H^*)\rangle \end{bmatrix} \qquad (6)$$

where E_H and E_V are the scattered wave field vectors, the triangular brackets denote ensemble average, Re denotes the real part and Im the imaginary part of the expressions following them. The degree of polarization DP will depend on the incident wave's polarization, therefore, a subscript H or V (DP_H and DP_V) is used to indicate this.

Figure 5 shows Z_{HH} over the measurement period of about 7 min. The effect of canting (σ = 20°, 40°, and 60°) on Z_{HH} is less than 0.5 dB. The agreement between the model computations and measurements is very good. One data point at time 10 min 9 s seems to have the largest difference. This may be due to a small number of large crystals or dendrites in the radar scattering volume which may not have been sampled by the 2D-C probe in the wind tunnel (either because they broke up or their concentration was low) resulting in a significantly higher value in the radar measurement. The average value (obtained by averaging Z_{HH} in mm^6 m^{-3} units) of the radar measured Z_{HH} over this time interval is 0.06 dBZ; when the single extreme data point is removed it reduces to -0.34 dBZ. The model produces average values of -0.51, -0.81, and -1 dBZ, corresponding to σ = 20°, 40°, and 60°, respectively. The average differences between the model results and radar measurements are small, ranging from 0.57 to 1.06 dB, and from 0.17 to 0.66 dB when the extreme data point is removed.

Figure 6 shows the time plot of Z_{VV}. It is clear that Z_{VV} is significantly affected by canting. This is to be expected since the V-polarization is sensitive to the vertical dimensions of the particles, which in turn are significantly altered by canting. Note that the model results for σ = 40° and 60° produce much better agreement with the radar measurements. Again the same data point mentioned in the previous paragraph produces the largest discrepancy. The mean value of the radar measured Z_{VV} is -0.05 dBZ, and when the extreme data point is removed it becomes -2.04 dBZ. The model mean values are -7.48, -4.36, and -2.96 dBZ for σ = 20°, 40°, and 60°, respectively. σ = 60° seems to agree the best with the radar data and is different by 2.46 dB. This difference reduces to 0.92 dB after removing the extreme data point.

Figure 7 shows the time series plot of Z_{DR}. The most striking aspect is the variability of the measurements and the flatness of the model results. This may be due to the model canting distribution being size independent. It is very likely that the canting is size dependent and may be the cause of these variations in Z_{DR}, since Z_{DR} is more sensitive to the orientation than the size of the particles in this model.

Figure 8 shows the degrees of polarization DP_H and DP_V. As in the case of Z_{DR}, the model results are fairly flat while the measurements show significant variability over time. Again, this may be due to the size dependence of particle canting. It is also worth noting that the maxima in Z_{DR} corresponds to the minima in DP_H and DP_V, and vice versa. The high Z_{DR} and low DP values may be due to the dominance of large stellar plates, because their long arms (Figs. 2 and 4) can cause higher depolarization (hence lower DP), and their alignment will lead to higher Z_{DR}, since the larger crystals are more likely to have their flat surfaces horizontal.

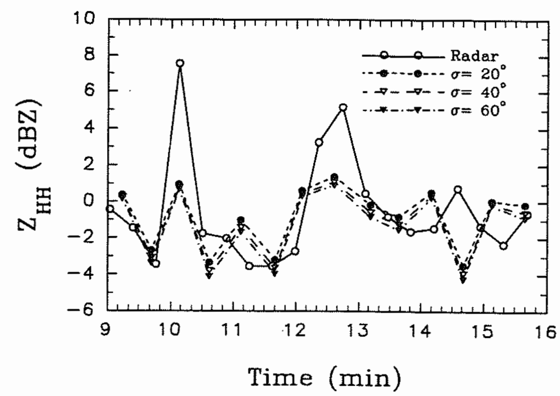

Fig. 5 Z_{HH} as a function of time, obtained from radar measurements and model computations for different values of the canting angle distributions parameter σ. The time corresponds to minutes after 9 PM MST on February 18, 1991.

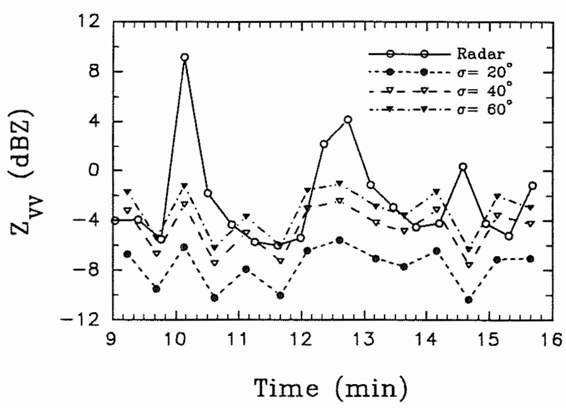

Fig. 6 Z_{VV} as a function of time. (See Fig. 5 for details.)

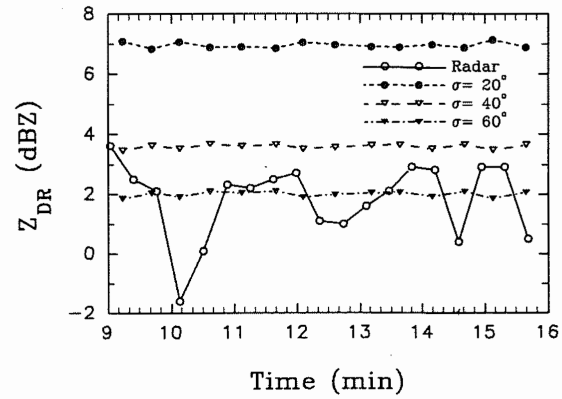

Fig. 7 Z_{DR} as a function of time. (See Fig. 5 for details.)

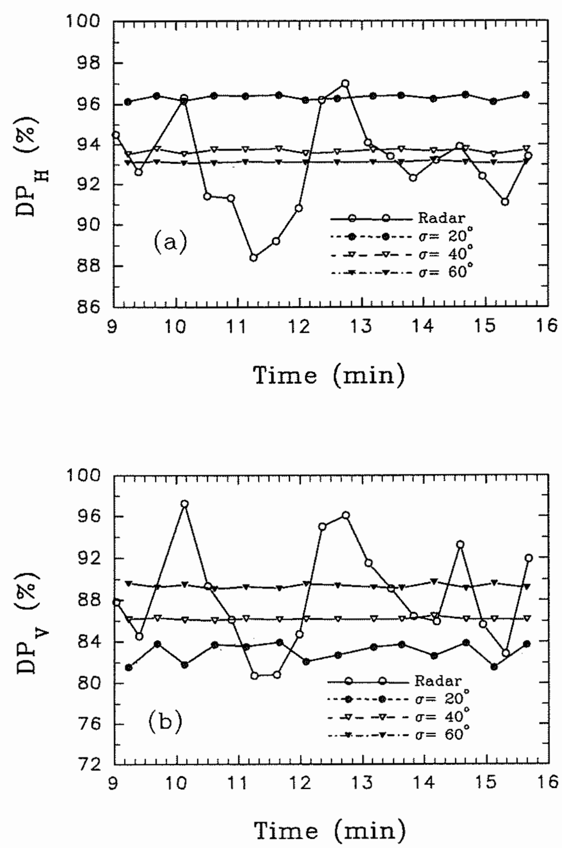

Fig. 8 (a) DP_H and (b) DP_V as a function of time. (See Fig. 5 for details.) The data point at time 9 min 46 s was eliminated due to a data acquisition problem affecting the cross-polar channel.

5. SENSITIVITY OF MODEL RESULTS

The model results were tested to determine their sensitivity to several parameters. The ice crystal density was lowered to 0.85 g cm^{-3}. This caused a decrease in both Z_{HH} and Z_{VV} by an amount less than 0.6 dB, and a slight increase in Z_{DR} (about 0.1 dB). Changes in DP_H and DP_V were not significant.

The thickness of each ice crystal was increased by 33%, while remaining within the bounds of the data presented by Auer and Veal (1970). This lead to an increase in both Z_{HH} and Z_{VV} by about 2 dB (slightly larger for Z_{VV}). The decrease in Z_{DR} was less than a few tenths of a dB. Changes in DP_H and DP_V were not significant.

Finally, the particle size distributions were truncated below 300 μm. This caused reductions in Z_{HH} and Z_{VV} ranging from 0.1 to 0.9 dB, with the larger changes occurring in cases where Z_{HH} and Z_{VV} were low. This is probably a result of the lower reflectivities being due to smaller particles. The decrease in Z_{DR} was less than 0.2 dB and DP_H and DP_V were negligibly affected.

6. SUMMARY AND CONCLUSIONS

Millimeter wave (95 GHz) polarimetric radar measurements were performed in a cloud at the Elk Mountain Observatory in Wyoming on February 18, 1991. The radar provided time series data of the reflectivity factor Z_{HH} and Z_{VV}, and the degrees of polarization DP_H and DP_V from a single range gate centered at 75m. A 2D-C probe was making simultaneous measurements in a closely located wind tunnel. Based on these 2D-C images and other available data in the literature, a model for the observed planar ice crystals was developed. Electromagnetic scattering computations for the model ice crystals were performed using the FDTD technique. A three dimensional canting model was used to simulate the orientation of the ice crystals as they descended. The simulated Z_{HH} and Z_{VV} values compared very well with the radar measurements with a mean difference less than 1 dB. The mean values of the simulated Z_{DR}, DP_H, and DP_V were very close to the measurements. However, unlike the measurements, the simulations did not exhibit much variation over time. This was attributed to the possibility that ice crystal canting could be size dependent; the canting model used for the simulations was size independent.

It was noted that increasing the thickness of the planar crystals by 33% had a significant effect on Z_{HH} and Z_{VV}, but not much on Z_{DR}, DP_H, or DP_V. The effect of decreasing the ice crystal density from 0.9 g cm^{-3} to 0.85 g cm^{-3} was small, less than 0.6 dB on Z_{HH} and Z_{VV}, and negligible on Z_{DR}, DP_H, and DP_V.

It was also observed that Z_{HH} (unlike Z_{VV}) is not very sensitive to the orientation of planar crystals. However, it is sensitive to the change in the thickness of the ice crystal. Hence, it is a good candidate for estimating ice crystal mass with a radar. Such a relationship can be obtained from simulations once their validity is established with several case studies.

7. ACKNOWLEDGMENTS

This research was supported by the National Science Foundation under Grant ATM-8921014 at Penn State and Grant ATM-8921145 at the University of Massachusetts and the University of Wyoming.

8. REFERENCES

Auer, A. H. and D. L. Veal, 1970: The Dimension of Ice Crystals in Natural Clouds. J. Atmos. Sci., 27, 919-926.

Aydin, K. and Y. M. Lure, 1991: Millimeter Wave Scattering and Propagation in Rain: A Computational Study at 94 and 140 GHz for Oblate Spheroidal and Spherical Raindrops. IEEE Trans. Geosci. Remote Sensing, 29, 593-601.

Bohren, C. F., 1986: Applicability of Effective Medium Theories to Problems of Scattering and Absorption by Nonhomogeneous Atmospheric Particles. J. Atmos. Sci., 43, 468-475.

Goldstein, H., 1965: Classical Mechanics. Addison-Wesley Pub. Co., Reading, Massachusetts, 399 pp.

Hervig, M., R. Kelly, R. McIntosh, J. Mead, A. Pazmany, and G. Vali, 1992: A Comparison of Measured and Calculated 95 GHz Radar Volume Backscatter for Ice Particles. 11th International Conf. on Clouds and Precip., Montreal, Canada, Aug. 17-21, (this volume).

Lhermitte, R.,1987: A 94-GHz Doppler Radar for Cloud Observations. J. Atmos. Oceanic Technol., 4, 36-48.

Luebbers, R. J., F. Hunsberger, and K. S. Kunz, 1991: A Frequency-Dependent Finite-Difference Time-Domain Formulation for Transient Propagation in Plasma. IEEE Trans. Antennas Propagat., 39, 29-34.

Mead, J. B. and R. E. McIntosh, 1990: Millimeter-Wave Polarimetric Radars. Pier 3, Polarimetric Remote Sensing, Editor: J. A. Kong, Elsevier, New York, 391-450.

Richard V. W., J. E. Kammerer, and H. B. Wallace, 1988: Rain Backscatter Measurements at Millimeter Wavelengths. IEEE Trans. Geosci. Remote Sensing, 26, 244-252.

Seliga, T. A. and V. N. Bringi, 1976: Potential use of Radar Differential Reflectivity Measurements at Orthogonal Polarizations for Measuring Precipitation. J. Appl. Meteorol., 15, 69-76.

Ulaby, F. T. and C. Elachi, 1990: Radar Polarimetry for Geoscience Applications. Artech House, Inc., Norwood, MA 364 pp.

Umashankar, K. and A. Taflove, 1982: A Novel Method to Analyze Electromagnetic Scattering of Complex Objects. IEEE Trans. Electromagn. Compat., 24, 397-405.

Warren, S. G., 1984: Optical Constants of Ice from the Ultraviolet to the Microwave. Applied Optics, 23, 1206-1225.

RADAR/LIDAR RELATIONS DERIVED FROM A DISTRIBUTION FUNCTION DESCRIPTIVE OF WATER CLOUDS

Vernon G. Plank

Phillips Laboratory, GPAA*
Hanscom AFB, Massachusetts 01731-5000

1. INTRODUCTION

An AFGL (presently Phillips Laboratory) cloud droplet model, based on the Khrgian-Mazin (KM), 1963, distribution function, was used for some 20 years to predict the probable cloud situations along the path trajectories of missiles for "weather-definition" and nose cone erosion purposes. The intimate association of the KM function with visibility theory was recognized and used to provide semi-quantitative equations. The details of the model have been described by Plank (1991). They are too extensive to be reiterated herein. The purpose of the present report is to illustrate certain salient features of this model to show how the cloud hydrometeors of the atmosphere are distributed typically and normally.

The Khrgian-Mazin distribution function specifies the number concentration (N) of cloud droplets in terms of droplet diameter and provides visibility, liquid water content (LWC) and radar/lidar equations (distributed and integrated totals) that are mathematically rigorous and in good accord with previous study findings. The equations are double truncated for application to problems of diameter limitations stemming from natural or instrumental causes.

It should be noted that once a distribution function has been specified, it then follows immediately, by rigorous physics and mathematics, that all size-distributed and total quantities (involving droplet number concentrations and total number, involving summed, projected cross-sectional areas and totals, as is important to visibility, involving cloud liquid water content (LWC), distributed and total, and involving radar and lidar reflectivities, distributed and total) have also been specified for any given single sample. This fact, that all of the quantities cited above are rigorously interrelated by the simple specification of a distribution function is basic to the work herein.

2. DERIVATION OF EQUATIONS

The size distribution properties of cloud droplets in the atmosphere can be reasonably described by the distribution function of Khrgian and Mazin (1963). This is

$$N_D = Q\,D^2\,e^{-\Omega D} \quad \text{No. m}^{-3}\,\text{mm}^{-1} \quad , \qquad (1)$$

where the subscript "D" signifies "distributed by diameter" and where Q (in units of $mm^{-3}\,m^{-3}$) and Ω (in units of mm^{-1}) have discreet values based on the type and liquid water content (M) of the clouds being considered. The equation, as applied herein, is presumed to be descriptive only between the truncation limits D = d (a minimum diameter of physical or instrumental restriction) and D = D_m (a maximum diameter of physical or instrumental restriction). For reasons of comparability among clouds, rain and moist aerosols, the units of d and D in the equation are in mm.

The modal (peak value) diameter of the N_D distribution is

$$D'_N = 2/\Omega \quad \text{mm} \quad . \qquad (2)$$

D'_N is a measurable quantity of cloud distributions, hence, when D'_N is known, Ω is also known, through the above equation.

The total number of cloud droplets in the population described by equation 1 is

$$N = \int_d^{D_m} N_D\,dD \quad \text{No. m}^{-3} \qquad (3)$$

or, on performance of the integration,

$$N = \frac{Q\,\Gamma(3)\,r_N}{\Omega^3} \quad \text{No. m}^{-3} \quad , \qquad (4)$$

where $\Gamma(3)$ is the gamma function of 3 (=2) and r_N is a "truncation ratio" that is the ratio of equation 3 integrated from d to D_m to equation 3 integrated from 0 to ∞.

The liquid water content of the cloud droplets described by equation 1 is distributed with diameter as

$$M_D = \frac{\pi D^3\,\rho_w\,N_D}{6} \quad \text{g m}^{-3}\,\text{mm}^{-1} \quad , \qquad (5)$$

or, from equation 1, and since ρ_w, the density of liquid water, = 1 g cm^{-3},

$$M_D = \frac{\pi \times 10^{-3}\,Q\,D^5\,e^{-\Omega D}}{6} \quad \text{g m}^{-3}\,\text{mm}^{-1} \quad , \qquad (6)$$

where the constant carries length conversion units of $cm^3/10^3\,mm^3 = 10^{-3}$.

The modal diameter of the M_D distribution is

$$D'_M = 5/\Omega = 2.5\,D'_N \quad \text{mm} \quad , \qquad (7)$$

*Presently affiliated with Hicare Company, 77 Union Street, Mansfield, MA 02048 employing equation 2.

The total LWC of all cloud drops of the population is

$$M = \int_{d}^{D_m} M_D \, dD \quad g\ m^{-3} \quad , \qquad (8)$$

which, from equation 6, on integration, gives

$$M = \frac{\pi \times 10^{-3}\, Q\, \Gamma(6)\, r_M}{6\, \Omega^6} \quad g\ m^{-3} \quad , \qquad (9)$$

where $\Gamma(6)$ is the gamma function of 6 (= 120) and r_M , in analogy with equation 4, is the truncation ratio for liquid water content.

The distributed values of the radar/lidar reflectivity factor for the cloud droplets described by equation 1 are expressed by

$$Z_D = D^6 N_D \quad mm^6\ m^{-3}\ mm^{-1} \quad , \qquad (10)$$

or, from equation 1,

$$Z_D = Q\, D^8\, e^{-\Omega D} \quad mm^6\ m^{-3}\ mm^{-1} \quad . \qquad (11)$$

The modal diameter of the Z_D distribution is

$$D_Z' = 8/\Omega = 4\, D_N' \quad m \quad , \qquad (12)$$

using equation 2.

The total reflectivity factor for any given cloud population is

$$Z = \int_{d}^{D_m} Z_D \, dD \quad mm^6\ m^{-3} \quad , \qquad (13)$$

which, from equation 11, results in

$$Z = \frac{Q\, \Gamma(9)\, r_Z}{\Omega^9} \quad mm^6\ m^{-3} \quad , \qquad (14)$$

where $\Gamma(9)$ is the gamma function of 9 (= 40,320) and r_Z is a truncation ratio for the reflectivity factor.

If equations 9 and 14 are solved for Q and equated and equation 2 is also employed,

$$Z = \frac{6.417 \times 10^5\, M\, r_Z}{\Omega^3 \quad r_M} \quad mm^6\ m^{-3} \quad , \qquad (15)$$

which provides the association between M and Z for single samples of KM type.

This equation, ignoring truncation, expresses the dependence of Z on M and Ω for single samples of water cloud populations. The relation might be loosely described as the "Khrgian-Mazin form of an equation of state for water-cloud droplets".

3. MERGER ASSUMPTION; DEPENDENCE OF D_N' ON M

Since, in equation 15, it isn't possible for D_N' to have a finite value when M = 0 , or vice versa, D_N' and M must be functionally related in a manner that will be referred to as a merger relationship.

The droplet sizes in cloud populations will not decrease to actual zero as the LWC decreases. Rather, they will decrease to the sizes of the condensation nuclei (moist aerosols) from which the clouds were first formed.

A convenient reference atmosphere for aerosols is the "dry rural model" of Fenn, et al (1985). This model describes the normal, typical concentration of aerosols in the absence of any special generation sources of particulates, such as sea salt, dust, smoke and industrial pollutants. The features of the model as portrayed by the distribution function of Diermendjian (1964) are illustrated in Figs. 1-5. It is seen that the largest of the aerosols overlap the smallest cloud droplets, that the total number concentration of aerosols is about 10^5 times larger than the numbers for clouds but that the mass concentrations of aerosols is about a hundred times smaller than those for clouds.

In synoptic meteorology, the rule for reporting visibility as restricted or unrestricted is that visibilities smaller than 6 miles (9650 m) are considered restricted whereas those larger than 6 miles are unrestricted. Restricted is not the same as the "unlimited" specification, which occurs at a visibility equal to or greater than about 30 miles (some 48,300 m).

In making the assumption about the D_N' dependence on M , the author reasoned as follows. At an M value of 1.0 g m^{-3} , the corresponding value of D_N' is typically equal to .01 mm (10 μm), see Table 1. This becomes one "tie point" of the assumption. At the restricted/unrestricted boundary of visibility classification in synoptic meteorology, one wishes to define a diameter size for D_N' that

Table 1. Average droplet radius and approximate D_N' and M values for natural clouds. Data from 8 investigators discussed by Plank (1991).

Cloud Type	Ave. Radius $\bar{r}$ μm	Approx. $\bar{D}_N'$ μm	Approx. $\bar{M}$ g m^{-3}
Cumuliform			
Fair weather cumulus--Cu	5.6	7.5	.346
Stratocumulus---------Sc	6.0	8.0	.439
Alto cumulus----------Ac	6.9	9.2	.736
Cumulus congestus-----Cg	7.7	10.3	1.12
Stratiform			
Stratus---------------St	5.7	7.6	.363
Alto stratus----------As	6.3	8.4	.526
Translucidus------- "			
Opacus------------- "		10.0	1.00
Nimbostratus----------Ns	8.4	11.2	1.52

is consistent with the number concentration of the larger aerosols of the atmosphere and that is also reasonably consistent, at the "unlimited boundary", with D_N being neither "ridiculously large" or "ridiculously small", relative to the aerosol distribution. With these considerations in mind, it was presumed that D_N = .001 mm (1 μm) at a visibility of 6 miles. This became the second "tie point" of the basic assumption. Also, it is a point that is amenable to experimental verification.

For these tie points, without expounding the details, D_N becomes dependent on M in the manner

$$D_N' = .01\ M^{.27} \quad \text{mm} \quad . \tag{16}$$

4. THE M VERSUS Z RELATION

When equation 16 is substituted in equation 15,

$$Z = .0802\ M^{1.81} \frac{r_Z}{r_M} \quad \text{mm}^6\ \text{m}^{-3} \quad , \tag{17}$$

or, reversing the equation,

$$M = 4.02\ Z^{.552} \left(\frac{r_M}{r_Z}\right)^{.552} \quad \text{g m}^{-3} \quad , \tag{18}$$

which is the so-called M vs Z relation for water clouds for a Khrgian-Mazin distribution function.

5. THE η VERSUS Z RELATION

The volume reflectivity, η , is the fundamental quantity measured by any "cloud physics radar". It is defined as the summation of the back-scatter return to the receiver, per unit illuminated volume of the radar. It is conventionally expressed in units of cm^{-1}.

Mason (1971) has presented the equation for water hydrometeors,

$$\eta = \frac{.93\ \pi^5}{\lambda^4} Z \quad , \tag{19}$$

where λ is the wavelength of the radar. With units conversion, Plank (1974a), this becomes

$$\eta = \frac{2.85 \times 10^{-10}\ Z}{\lambda^4} \quad \text{cm} \quad , \tag{20}$$

with λ still in cm.

6. REQUIRED η VALUES TO DETECT NATURAL CLOUDS AT DIFFERENT WAVELENGTHS

The average, typical M values for natural clouds were cited in Table 1. For these values, the Z values of Table 2, first column, were determined from equation 18. (Truncation was ignored without substantial consequences.)

The other columns of Table 2 show the values of η (dBη) required to detect the Z values of the first column for radar wavelengths from K-Band to L-Band as computed from equation 20. The lidar values are highly approximate, ref. Plank (1991).

Casually, one would assume that radars of relatively large wavelength, C-Band or larger, would be useless in cloud detection. However, this neglects consideration that numerous radars today are extremely powerful and sophisticated employing chirp and frequency-diversity techniques and long-term averaging of signal from noise. **Clouds have definitely been detected at S and L Band.**

Table 2. Required dBη values for the detection of water clouds with K-Band, X-Band, C-Band, S-Band and L-Band radars, also Lidar.

Cloud Type	Radar Reflectivity Factor Z ($\text{mm}^6\ \text{m}^{-3}$)	Radar Reflectivity Factor dBZ	Required Detection Values: K-Band .86 cm (35 Ghz) dBη	X-Band 1.25 cm (24 Ghz) dBη	X-Band 3.25 cm (9 Ghz) dBη	C-Band 6 cm (5 Ghz) dBη	S-Band 10 cm (3 Ghz) dBη	L-Band 20 cm (1.5 Ghz) dBη	Lidar (Visible-UV) dBη
Cumuliform									
Fair weather cumulus--Cu	.012	-19.2	-112	-119	-135	-146	-155	-167	-38.6
Stratocumulus--------Sc	.018	-17.4	-110	-117	-133	-144	-153	-165	-37.8
Alto cumulus----------Ac	.046	-13.4	-106	-113	-129	-140	-149	-161	-36.2
Cumulus congestus-----Cg	.099	-10.0	-103	-110	-126	-137	-145	-158	-34.9
Stratiform									
Stratus---------------St	.013	-18.9	-112	-118	-135	-145	-154	-166	-38.4
Alto stratus----------As	.025	-16.0	-109	-115	-132	-143	-151	-164	-37.3
Translucidus-------- "									
Opacus-------------- "	.080	-11.0	-104	-110	-127	-138	-146	-158	-35.2
Nimbostratus----------Ns	.17	-7.7	-101	-107	-124	-134	-143	-155	-33.9

7. CONSOLIDATED EQUATIONS

Present empirical descriptions of the size-distribution properties of aerosols, clouds and rain are based primarily on distribution functions that have been developed over time in the separate disciplines of aerosol physics, cloud physics and precipitation physics. The functions are discontinuous across the rather loosely-defined boundaries of the disciplines. Such discontinuities can not be true of the real atmosphere, of course; because perfect continuity of distribution properties is always required in a real atmosphere.

One way of eliminating discontinuities from composite distributions is simply to add the distribution functions that are judged descriptive of aerosols, clouds and rain and also to add the corresponding integrals of the functions that specify the total values of the pertinent quantities.

The totals for representative populations of aerosols, clouds and rain, as well as the summed grand totals for the three hydrometeor types, are noted in Table 3.

Table 3. Representative N, M, Z and Rainrate (R) values for aerosols, clouds and rain under stratiform conditions, also totals.

	N No. m^{-3}	M g m^{-3}	Z $mm^6\ m^{-3}$	R mm hr^{-1}
Aerosols ▲	2.6×10^{10}	5×10^{-6}	9.1×10^{-17}	0
Clouds ■	1.06×10^{8}	.01	1.93×10^{-5}	0
Rain ●	3320	1.0	2.22×10^{4}	20
Total	2.61×10^{10}	1.01	2.22×10^{4}	20
DB Total	104	.043	43.5	13.0

The consolidated distribution curves for N_D, M_D and Z_D are indicated in Figs. 1, 2 and 3, below. Hydrometeor diameter is common to all figures, in mm, bottom scale, and in μm, upper scale. The ordinate scales at the left show the values of the distributed quantities in units of $m^{-3}\ mm^{-1}$; the scales at right are in units of $cm^{-3}\ \mu m^{-1}$.

The figures are presented without comment for the readers reflection. It is unfortunate that space does not permit better description of these quantities and illustrations, reference Plank (1991).

8. REFERENCES

Diermendjian, D., 1964: Scattering and polarization properties of water clouds and hazes in the visible and infrared. Appl. Opt. 3, 187-196.

Fenn, R. W., S. A. Clough, W. O. Gallery, R. W. Good, F. X. Kneizys, J. D. Mill, L. S. Rothman, E. P. Shettle and F. E. Volz, 1985: Optical and infrared properties of the atmosphere. Chap. 18 in Handbook of Geophysics and the Space Environment, A. S. Jursa, Ed., AFGL, 1-80, ADA-167000.

Khrgian, A. Kh. and I. P. Mazin, 1963: Cloud physics. Israel Prog. Sci. Transl., Jerusalem, 392 pp.

Mason, B. J., 1971: The physics of clouds, second edition. Clarendon Press, Oxford, England.

Plank, V. G., 1974a: A summary of the radar equations and measurement techniques used in the SAMS Rain Erosion Program at Wallops Island, Virginia. AFCRL/SAMS Report No. 1, AFCRL-TR-74-0053, Special Report No. 172, 108 pp.

Plank, V. G., 1991: Implications of the Khrgian-Mazin distribution function for water clouds and distribution consistencies with aerosols and rain. PL-TR-91-2293 (in press), 231 pp.

Fig. 1. N_D versus D

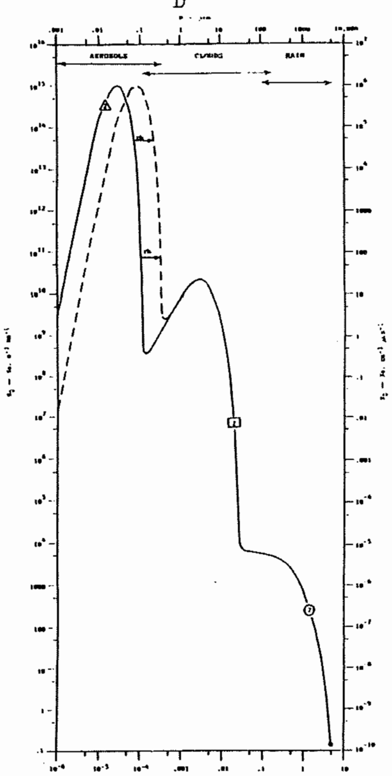

Fig. 2. M_D versus D

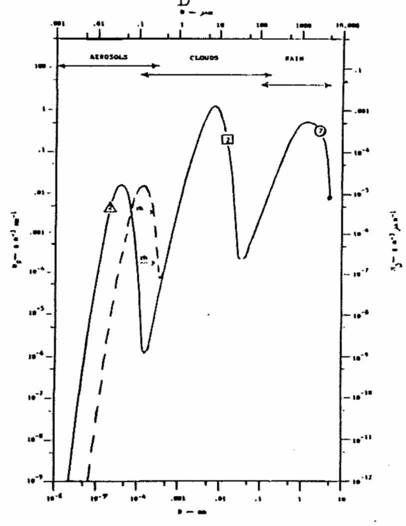

Fig. 3. Z_D versus D

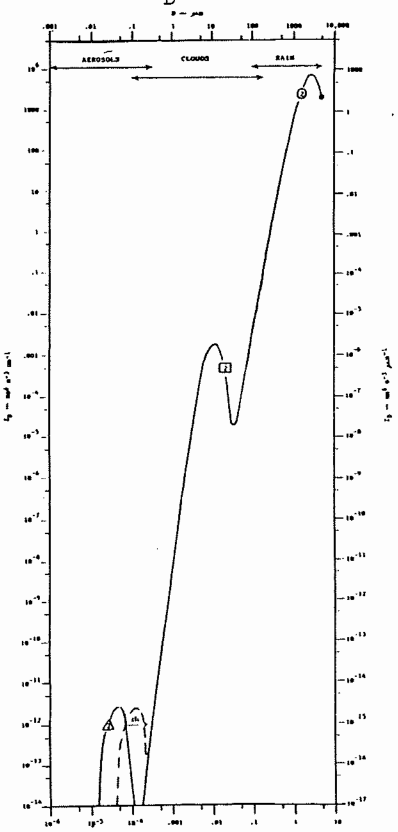

Automated Cloud Profiling with a 94 GHz Radar

Robert M. Peters
Bruce A. Albrecht
Mark A. Miller
J. Thomas Treaster

Dept. of Meteorology
Penn State University
503 Walker Building
University Park, PA 16802

1. INTRODUCTION

A cloud radar operating at a 3 mm wavelength has been developed for use as an integral part of a cloud observing system developed at Penn State University (Albrecht et al, 1991). The need for an instrument of this type was demonstrated during the First International Satellite Cloud Climatology Project Regional Experiment (FIRE) on San Nicolas Island in July 1987. At this experiment a group of instruments were assembled to estimate the adiabatic liquid water content of marine stratocumulus clouds and compare it with the observed liquid water content (Albrecht et al, 1990). The remote sensing instruments used during FIRE included a microwave radiometer, sodar, a wind profiling radar and a laser ceilometer. Calibration data were supplied from aircraft and balloon measurements. The results of this experiment suggest that remote measurements of cloud parameters could not be complete (in the case of thick clouds) without cloud top height and profiles of cloud reflectivity. Beginning in 1987, the 94 Ghz radar described herein was designed to provide these parameters. During the past year construction and testing were completed and the system was successfully deployed at the FIRE Cirrus experiment in Coffeyville, Kansas during November 1991. The ASTEX experiment during June of 1992 made use of the 94 GHz radar, RASS and better surface measurements in addition to the original group of instruments used during the 1987 FIRE experiment.

2. DESIGN CONSIDERATIONS

Sensitivity to radar reflectivity cross section on the scale of cloud drop sizes and a window in atmospheric absorption were the determining factors in choosing this radar's operating wavelength. For cloud physics applications, Doppler capability was also a prerequisite. Furthermore, it was required that components be available on a production basis from microwave equipment manufacturers. A design goal was to produce a "turn-key" radar that could be operated by users having little technical instruction and not requiring constant attendance by an operator. The wavelengths suitable for this use and meeting our design criteria for a cloud radar existed at 8 mm and 3 mm. Based on the pioneering work of Lhermitte (1987), it was decided to construct the radar for the 3 mm wavelength (94 GHz frequency).

3. SYSTEM IMPROVEMENTS

The rapid advancement in the performance of electronic, millimeter wave and signal processing components made it possible to construct a radar meeting our design criteria. Table 1. shows the operating characteristics of the radar.

Table 1. Radar Characteristics

Transmitter:
Peak power - 1.4 KW
Duty Cycle - .005 max
Frequency - 93.95 GHz
PRF - 0 to 20000 Hz
PW - 10 to 2000 nS
Max rise and fall time - 5 nS

Antenna system:
Type - Dual isolated
Gain - 56 dB
Beamwidth - 0.24 Deg.

Receiver:
Mixer Noise figure (DSB) - 4.4 dB
" (SSB) - 7.4 dB
Mixer/preamp gain - 26.7 dB
IF Bandwidth - 20 MHz
STALO - Phase locked Gunn oscillator
COHO - Pulse coherent, quartz stabilized.
Log Output - 0 to -2V.
Log Accuracy - within .5 dB.
Doppler output - I and Q, +/- 1V.

Physical:
Power requirement - 1.5 KW max, 110-240 VAC, 50-60Hz
Footprint (RF unit) - 1M wide, 2M long.

Monitor Data Processing:
Imaging type: 16 to 256 pseudocolor, to 1024 pixel resolution.
Reflectivity data: 512 byte-binary coded disk record.
Imaging Data: "PCX" image format.
Integration rate: 100,000 gates/sec.
Method: Pulse to pulse integration, noise normalized, threshold detected.

Doppler Data Processing:
Data types: reflectivity, Doppler shift, Doppler variance.
Processing rate: Up to 1,000,000 gates/sec.
Method: Pulse pair processing.

As shown on the block diagram in Figure 1., the radar is similiar to most pulse-phase-coherent microwave Doppler radars. Several improvements that were suggested by Lhermitte (1987) were incorporated into the radar. The coherent oscillator, the main source of phase instability in the radar receiver, is commercially manufactured and is quartz stabilized. It also is made phase coherent digitally during the latter part of the transmitter pulse. These features provide a low phase noise and stability approaching that of a much more expensive fully coherent radar.

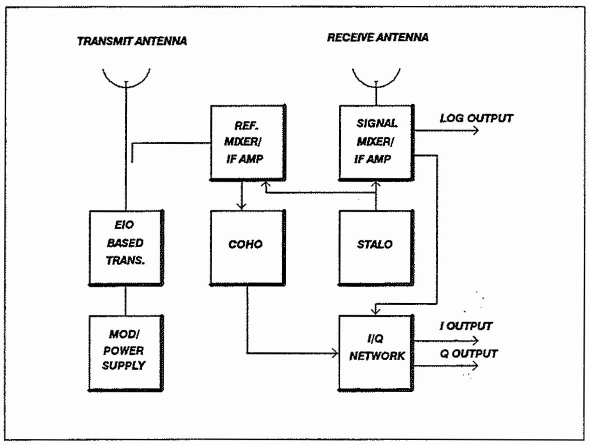

Figure 1. 94GHZ Radar Simplified Block Diagram

The transmitter is based upon a commercially manufactured extended interaction oscillator (EIO) and associated pulse modulator/power supply. The transmitter incorporates fault protection thereby eliminating expensive component failure due to improper operation.

At the present time, an IF bandwidth of 20 MHz is used. In operation, this provides the capability of a 15 m range resolution when used with the appropriate radar pulsewidth and sampling rate. Since T/R switching is not generally available at these frequencies, separate receive and transmit parabolic antennae are incorporated. The risk of expensive component failure and additional receiver loss reinforced this design decision. The low-noise receiver mixer is mounted directly on the receiver antenna. The isolation between the antennae and an absorber lined barrier between them has resulted in a receiver with no desensing due to the transmitter. As no receiver blanking is used and no ground clutter is received (when pointing upward) there is no minimum range where return signals can not be received.

It was decided to incorporate two independent signal processing systems. One based upon reflectivity only and for general purpose use and another for detailed analysis of Doppler moments associated with a much smaller range of heights. The first system provides a color display and archiving of images and reflectivity data in a compact format. It is based upon a '386 type computer and an inexpensive 20 MHz rate analog-to-digital converter that easily interfaces with the computer. Signal integration is accomplished by the computer at a rate of 100,000 gates a second.

The Doppler research system is based upon designs first developed at NCAR (Gray et al, 1989) and produced by Lassen Research Inc. The 100 MFlop signal processing capability of this system provides a greater sensitivity (due to processing speed) and Doppler moments estimation. The host system is also a '386 type computer which is used as an archive and display device. Program development and program storage is accomplished using the '386 computer. Programs are downloaded to the signal processing computer when the systems are initialized.

4. OPERATIONAL ENHANCEMENTS

The radar has proven to be "user friendly" to the cloud research community. In operation, the transmitter frequency requires minor adjustment only during the first 15 minutes of operation. After that time, it can be left to operate unattended. The display of A-scope and false color time sections are processed in real-time and recorded using a standard format. A computer network connection is provided on the display and archive computers so that both data and image files can be transfered from the radar to other computer systems without interruption of radar operation.

The standard image format allows color hardcopy to be produced at the experiment field site in a timely manner so that other operational decisions can be made (such as research aircraft operation schedules and flight altitudes). High quality hard copy is available using desktop publishing grade equipment. The shipping container for the radar also serves as the mounting base. Casters, each individually adjustable for height allow for easy mobility and leveling. A volume scanning capability is planned and will be easily implemented due to the small size of the radar. Also due to its small overall dimension, a radome can be implemented by placing an inexpensive polyethylene tarpalin over the radar. The power requirement for the radar is 700 Watts operating in a non-Doppler mode and 1300 Watts operating with both processing systems. The minimum power requirement and small size provides for inexpensive shipping and operating costs when using the system in remote research sites.

The radar is well calibrated, as all components have been individually calibrated by their respective manufacturers using the best of calibration equipment. Independent measurements have confirmed the radar calibration and the dBz measurements have been shown to be accurate within 1 dBz, (Miller and Peters, 1992).

5. APPLICATIONS

The radar performance has exceeded all expectations with regard to its use as a cloud profiling radar. Most clouds are easily detected with the radar. The capability to accurately distinguish between ice and liquid phase cloud particles could be enhanced with the addition of cross-polarization measurement hardware. The radar has also been used to observe the top of a ground based fog layer. Its ability to profile radar reflectivity and Doppler moments through all cloud layers are major advantages of the radar over laser-based devices. Its use for continuous measurement of cloud and fog heights could also enhance safer terminal area aircraft navigation. The same capability should be useful for monitoring conditions for tropospheric radio propagation since ducting layers often form cloud or fog interfaces. The sensitivity of the radar to very small droplets also is an advantage in detecting low-density rain or snow that is not visible by the eye or conventional radar. Insects also provide a large radar cross-section at the radar's wavelength. The use of insects as tracers possibly could provide measurements of clear-air velocity. Other atmospheric studies could be enhanced by the use of the radar for the study of wave clouds, rotors and the formation of lake effect snow squalls.

Figure 2 shows an example of detected stratocumulus clouds. The minimum detectable signal level (using the monitor data processing system) is shown in Figure 3. An example of detected cirrus clouds is shown in Figure 4.

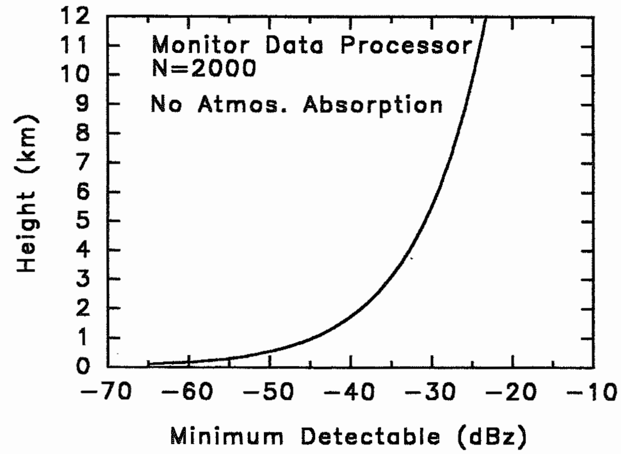

Figure 3. Minimum detectable signal vs. height

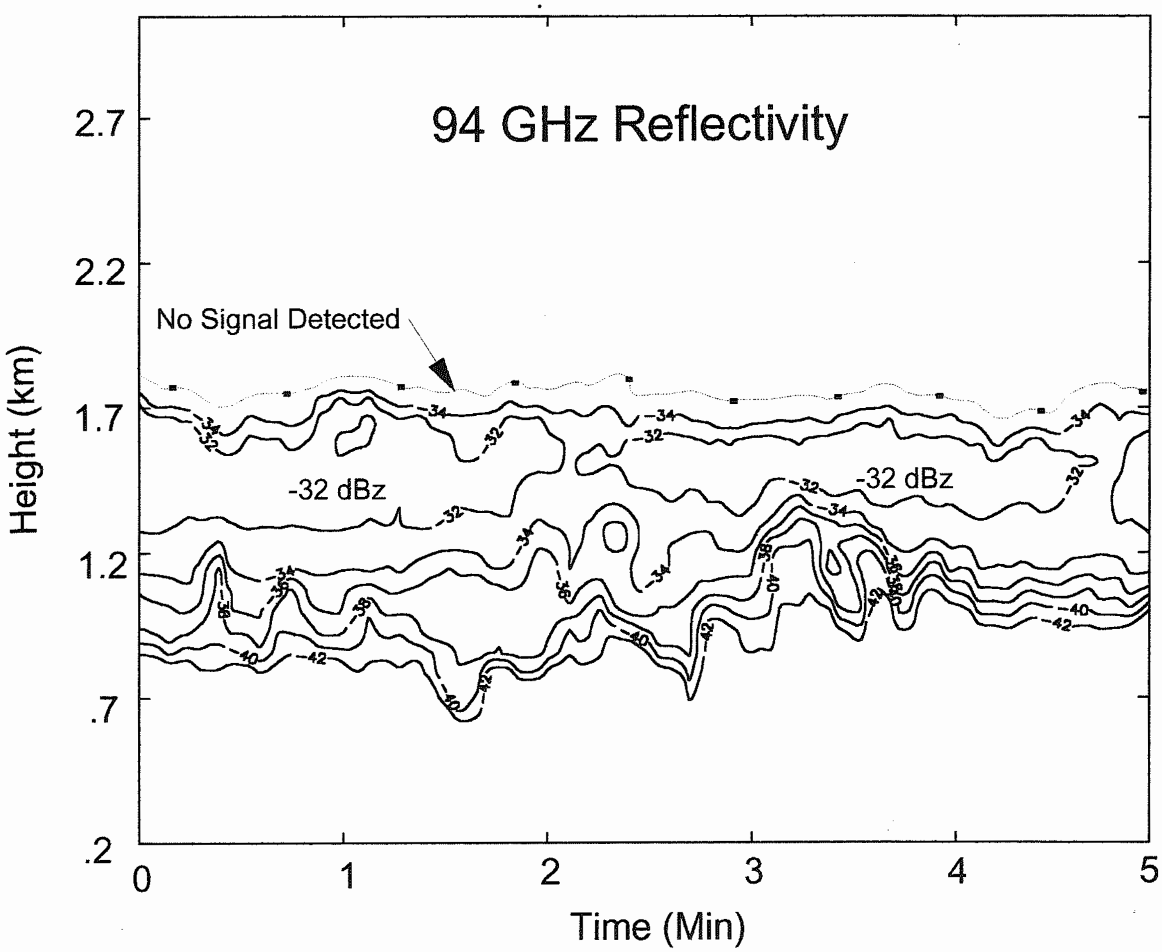

Figure 2. Example of detected stratocumulus clouds

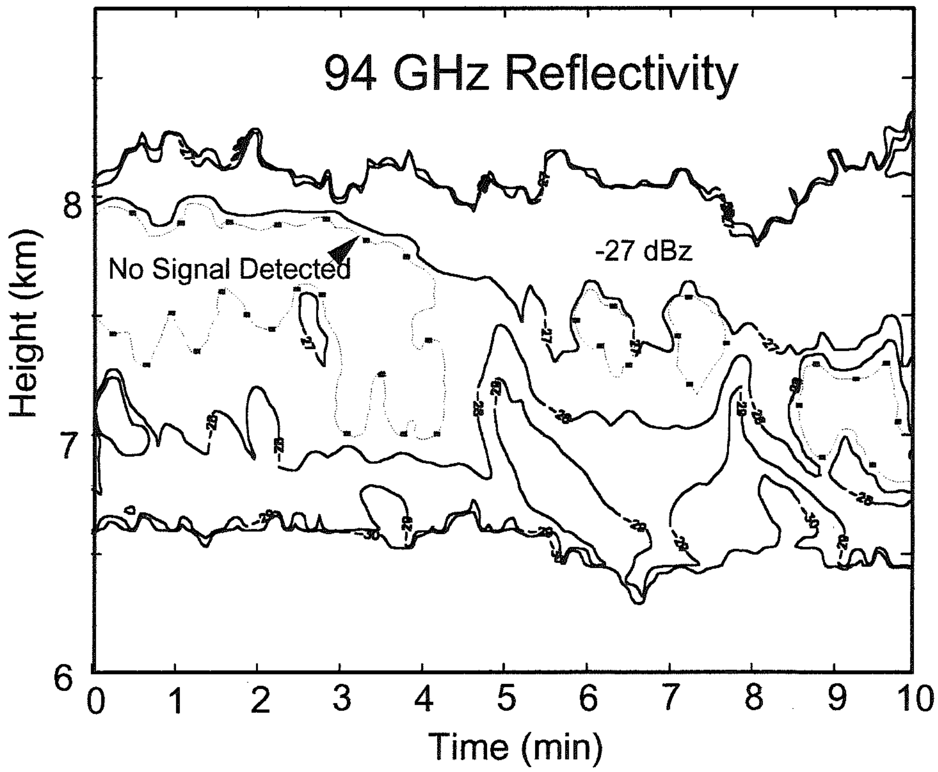

Figure 4. Example of detected cirrus clouds

6. CONCLUSION

The use of radar at 3mm and shorter wavelengths for atmospheric measurement purposes is still in the formative stages, since most applications of millimeter radar up to this time have been for tactical military purposes.

7. ACKNOWLEDGEMENTS

Drs. Thomson and Ackerman have provided invaluable guidance and suggestions during the development of the 94 GHz radar. It was developed under the sponsorship of the U.S. Navy, Office of Naval Research (Grants N00014-86-K-0688 and N00014-91-J-1991), the U.S. Department of Energy (Grant DE-FG02-90ER61071) and Penn State University.

8. REFERENCES

Albrecht, B.A., C.W. Fairall, D.W. Thomson, A.B. White, J.B. Snider, and W.H. Shubert, 1990: Surface-base remote sensing of the observed and the adiabatic liquid water content of stratocumulus clouds. *Geophys. Res. Letters*, **17**, 89-92.

Albrecht, B.A., T.P. Ackerman, G. Mace, D.W. Thomson, M.A. Miller, and R.M. Peters, 1991: A Surface Based Cloud Observing System. Preprint Vol., 7th Conf. on Meteorological Observations and Instrumentation, New Orleans, American Meteorological Society.

Gray, G.R., C.A. Walther, R.J. Keeler, C.L. Frush, and J.R. Vinson, 1989: A new programmable signal processor for NCAR meteorological radars. Preprint Vol., 24th Conf. on Radar Meteorology, Tallahassee, American Meteorological Society.

Lhermitte, R., 1987: A 94 GHz Doppler radar for cloud observations. *J. Atmos. Oceanic Technol.*, **4**, 36-48.

Miller, M.A. and R.M. Peters, 1992: Calibration of the 94 GHz Cloud Radar. Internal report, Department of Meteorology, Penn State University.

RADAR MESUREMENTS OF PRECIPITATION IN VENETO REGION - ITALY : PROBLEMS AND PERSPECTIVES OF SOLUTION

Crespi M., Giaretta P., Monai M.

REGIONE VENETO - DIPARTIMENTO PER L'AGROMETEOROLOGIA
Centro Sperimentale Idrologia e Meteorologia
Teolo, Padova - Italy

1. INTRODUCTION

Veneto Region is in the North-East part of Italy. A C-band weater radar is installed on isolated hills in the middle of the flat plain. Radar suffers particularly from ground clutter problems and, at times, from ANAPROP. For both these types of problem doppler data are better than data obtained in non doppler mode. Anyway, doppler radar data may be affected by second-around target echoes: a comparison between Z and turbulence data and a comparison of Z data obtained with different PRF couples may help in discriminating these echoes. Mountains are present few tens of kilometres apart from radar cause important beam occlusions. A procedure to correct beam blocking effects was activated and used in real time data processing.

2. VENETO REGION WEATHER RADAR

The weather radar of Veneto Region is an Ericsson radar that can be operated also in doppler mode. It is located on the top of Monte Grande Hill, at 475m a.s.l., among the Euganean Hills, 20km away from Padua, in the Po Valley. The operative centre is located in Teolo (province of Padua), in the Experimental Centre for Hydrology and Meteorology (CSIM) of Veneto Region. Figure 1 shows the position of the region and of the radar inside North Italy.

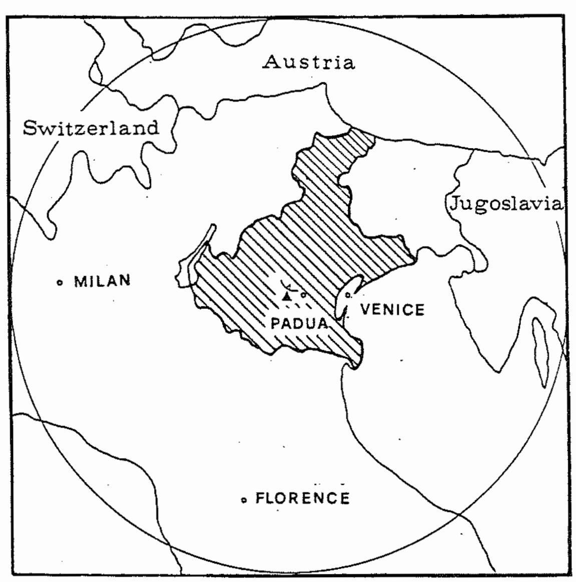

Figure 1: maximum range of coverage of weather radar.

A microwave radiolink assures the communication between the radar and the centre. A computer Digital VAX 8200 is used for radar controlling, data acquisition and management; two Digital VAXstation 3100 are used for radar image displaying and for software development.

3. GROUND CLUTTER AND ANOMALOUS PROPAGATION

For the Veneto Region radar the problem of clutter suppression is much important because of the presence of quite high mountains at distances of only 50km apart from the radar, in the azimuths between NW and NE.

When using radar in normal mode, one of the possible methods of clutter suppression is using a fixed clutter echoes map. This map is a polar volume collected with the radar operating in normal mode in clear day conditions. In such conditions the echoes detected by radar are not due to precipitation, but are clutter echoes. Each polar cell is either affected by an echo with intensity higher than a given threshold Z value (Z-thr) or not; in dependence of this fact one could mark a polar cell as a clutter cell and decide of not using it during radar observation of precipitations. The problem in doing this is the choice of Z-thr. Indeed, a lot of polar cells in the first tens of chilometers from radar are affected by weak clutter echoes due to reflection of side lobes on the ground. This can be true especially for a radar, like the Veneto Region one, placed on the top of a hill surrounded by flat plain. Since side lobes have emission directions considerably different from the direction of the antenna axis, they generate weak echoes also at high antenna elevations. Not using a threshold means to mark a lot of polar cells as clutter cells, even if the contribution of clutter to the echoes returned by them is very low; when using radar in normal mode the choice of the polar cells used for constructing a CAPPI at a given height a.s.l. could be strongly limited to polar cells very high in the atmosphere. Precipitations originating in the lowest layers of the atmosphere (stratiform clouds) may be not observed by the radar and problems of bad correspondence between the nominal height of a CAPPI and the real height of the polar cells used for its construction may arise.

Using radar in doppler mode, clutter suppression takes advantage of the capability of measuring a doppler spectrum, that is the intensity of the signal returned to the radar versus the velocity of the target generating the signal. An automatic suppression of echoes due to beam reflection on the ground, recognizable by means of their speed close to zero, is made. In this way ground echoes contamining the signal returning from a given polar cell are filtered out; only contributions from precipitation are retained. Precipitation can be detected also in the lowest layers of the atmosphere (see Crespi et al., 1991 and Giaretta et al., 1991) . Furthermore the problem of bad correspondence in reciprocal positions of a pixel and the relative polar cell is not present any longer.

Figures 2 and 3 put into evidence such behaviour. They represent reflectivity CAPPIs collected on 20-JAN-92 respectively in normal and doppler mode. Collection times differ only for 2 minutes. The figures show an example of precipitation that does not reach the ground because it evaporates while falling down. In this case in the lowest layers of atmosphere precipitation is not present: this is well shown in the doppler image. The normal image shows a widespread precipitation, that is, in reality confined in the highest atmospheric layers, as it is evident by looking at the vertical sections in figure 3.

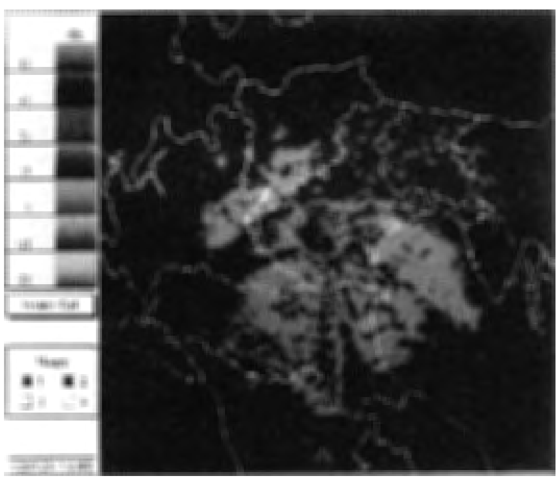

Figure 2: image in normal mode collected on 20-JAN-1992 at 16:00 showing a wide spread precipitation confined in the highest atmospheric layers.

Owing to a near-stationary temperature inversion, anomalous propagation is another serious problem for Veneto radar. Again doppler suppression of stationary echoes is efficient in solving the problem. Anyway, doppler data may be affected by second-around target echoes. Perspective solution involves use of several PRF couples, because in this case precipitation echoes remain in the same positions, while second-around target echoes change their distance from radar; another possible solution is taking into account the values of turbulence measured by radar, that result usually quite high in the areas affected by this type of echoes.

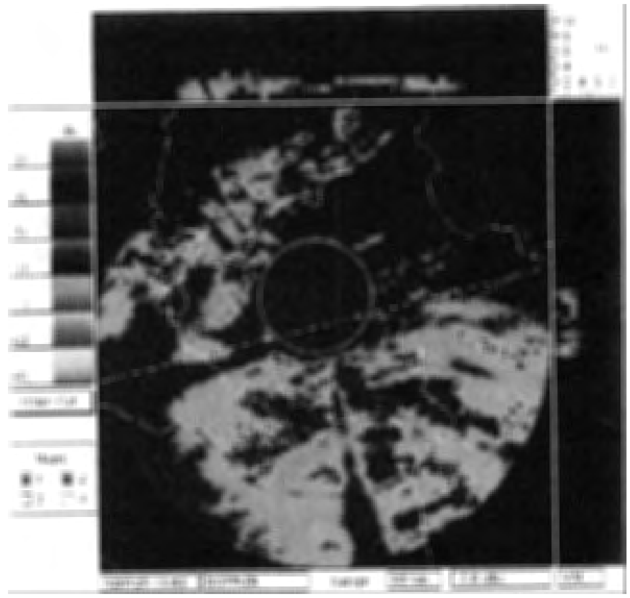

Figure 3: image in doppler mode collected on 20-JAN-1992 at 16:02 showing example of precipitation not reaching ground because of evaporation.

4. CORRECTION OF BEAM BLOCKING EFFECTS

For the Veneto Region radar several azimuth sectors are strongly affected by beam occlusion, starting from distances of about 50km, especially in the azimuths between NW and NE. The procedure developed for correcting beam occlusion effects requires as input (see Crespi et al., 1991):

- the emission diagram of the antenna (ED)
- a model of propagation (MP) of the radar beam in the atmosphere for different antenna elevations
- a digital elevation model (DEM) that decribes the elevation a.s.l. of the ground under the radar umbrella

The emission diagram was provided by the radar constructor; the propagation model used was the effective earth's radius model (see Doviak et al., 1984); the DEM available describes the ground elevation with a resolution of about 230m x 230m. The procedure first uses the ED to subdivide the main lobe of the beam into a series of N sublobes having a limited angular aperture; the emission direction of each sublobe and the fraction of the total main lobe energy associated to each sublobe are computed (respectively d_i and δE_i, i=1,..N). The d_i are computed as a function of antenna elevation (A_e) and azimuth (A_a). Then MP is used for simulating the trajectory of each sublobe in the atmosphere, for each of the A_a and A_e used in normal operations. The simulation is executed for discrete range steps, and for each step the height of the sublobe (H_s) is compared with the corresponding height of the ground (H_g), extracted from the DEM. If, for a given range, the condition $H_g>H_s$ is satisfied for the i-th sublobe then the energy carried by the beam is lowered by an amount equal to δE_i. Application of the procedure leads to a function $F(A_a,A_e,r)$, where r is the range from radar, that gives the fraction of energy carried by the radar beam and not yet occluded at the specified range. The quantity $-10 \cdot \log F_{10}(A_a,A_e,r)$ is the additive term that should be applied to the Z values, expressed in dBZ, measured in real time by the radar to correct the effects of beam occlusion.

5. CONCLUSIONS

A modern radar installed in a complex terrain environment suffers from different problems in measuring precipitation. Some solutions are already operational, others must still be achieved.

6. REFERENCES

Crespi M., Giaretta P., Monai M. (1991): A new procedure to improve rainfall measurements affected by beam blocking. In: Advances in radar hydrology International Workshop, Lisbon (P).

Crespi M., Monai M. (1991): Some remarks on precipitation measurements with a doppler radar. In: 25th International Conference on radar meteorology, Paris, (F).

Doviak R., Zrnic D., (1984) Doppler radar and weather observation. National Severe Storms Laboratory. National Oceanic and Atmospheric Adiministration, Norman, Oklahoma (US).

Giaretta P., Monai M. (1991): Doppler technique: An operational tool for meteorology. In: International Workshop on Multi-parameter radar applied to microwave propagation, Graz (A).

A COMPARISON OF MEASURED AND CALCULATED 95 GHZ RADAR VOLUME BACKSCATTER FOR ICE PARTICLES

M. Hervig[1], R. Kelly[1], R. McIntosh[2], J. Mead[2], A. Pazmany[2], and G. Vali[1]

[1]Dept. of Atmospheric Science, Univ. Wyoming, Laramie, WY 82071
[2]Microwave Remote Sensing Laboratory, Univ. Massachusetts, Amherst, MA 01003

1. INTRODUCTION

In preparation for airborne application, a 95 GHz (3.2 mm wavelength) radar designed and constructed at the University of Massachusetts was used to measure volume backscatter from ice particles of different types in wintertime clouds at the University of Wyoming's Elk Mountain Observatory (EMO) in 1991. Pertinent characteristics of the radar are summarized in Table 1. Cloud volumes were also sampled by a Particle Measuring Systems (PMS) 2D–C probe mounted in an outdoor wind tunnel. Backscatter measurements from the first radar range gate, at 75 m, were compared with backscatter values calculated from particle images and concentrations sampled by the wind tunnel probe. The relative positions of the radar and the tunnel are shown schematically in Figure 1.

Table 1. Characteristics of the University of Massachusetts 95 GHz radar.

Transmitter	
Source	Extended Interaction Amplifier
Center Frequency	94.92 GHz
Modulation	Pulse
Peak Output Power	1500 W
Pulse Width	100 to 2000 ns
PRF	10 Hz to 20 kHz
Polarization	Vertical, Horizontal, ±45°linear
Receiver	
Dynamic Range	75 dB
Noise Figure	9 dB Single Sideband
Noise Floor	-101 dBm at 20 MHz
1st IF Bandwidth	1320 MHz
2nd IF Bandwidth	120 MHz
Outputs	$\lvert V\rvert, I_V, Q_V, \lvert H\rvert, I_H, Q_H$
Antennas	
Reciever	Dual Polarized lens, H and V channels, 0.7° beamwidth
Transmitter	Polarization insensitive lens, 0.7° beamwidth

Figure 1. Schematic view of the radar range gate and wind tunnel used for measurements at the Elk Mountain Observatory.

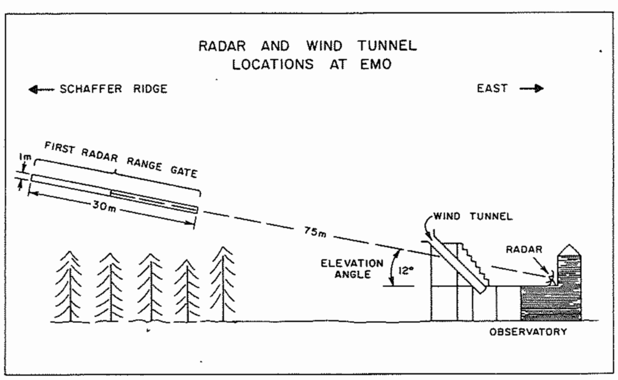

2. BACKSCATTER CALCULATIONS

In order to compare the radar measurements with the calculations from particle images, it was decided to use volume backscatter, rather than radar reflectivity values. In this way, the radar data could be used with no prior assumptions of target composition or density, leaving all such details to the particle calculations. By definition, the volume backscatter is

$$\eta = \sum_{vol} \sigma \quad (mm^2 m^{-3}), \;\; where\ \sigma = 4\pi r^2 \frac{S_s}{S_i}$$

Here, S_i and S_s are the incident and backscattered power densities, and r is the range from the radar to the target.

At a radar frequency of 95 GHz, small precipitation particles and even some cloud particles will be of sizes comparable to the transmitted wavelength. Thus, it was necessary to use the Mie approximation (e.g., Ulaby et al., 1981) for calculating volume backscatter from the particle size distributions. The effects of raindrop size at these short wavelengths were calculated and observed by Lhermitte (1990). Two primary problems were addressed in applying the Mie approximation to wintertime cloud and precipitation particles: 1) Few of the particles were spherical, so actual particle sizes and shapes had to be reduced to an equivalent diameter for the Mie calculations. 2) All but the smallest particles (individual ice crystals, frozen drops, etc.) are likely to be mixtures of ice and air, so that densities different from that of ice had to be incorporated into the Mie calculations.

Density differences were applied to the Mie calculations as differences in the dielectric constant (Polder and van Santen, 1946). In the following discussion, density is represented by the volume fraction, f, which is the fraction of the particle volume filled by ice (the remainder being air). Figure 2 illustrates the size and volume fraction dependence of the Mie backscatter cross–section at 95 GHz, for spherical particles with f=0.1, 0.4, and 0.9. Note the strong dependence on both diameter and volume fraction, especially for diameters above 1 mm.

Particle diameters were derived from each of the 2–dimensional shadow images recorded by the PMS 2D–C probe by 1) fitting an ellipse to the outline of each image, so that the ellipse circumscribed the image, 2) rotating the ellipse around its major axis, and 3) finding the volume of the resulting prolate spheroid. The diameter used for the Mie calculation for each particle was the diameter of a sphere having a volume equal to that of the prolate spheroid.

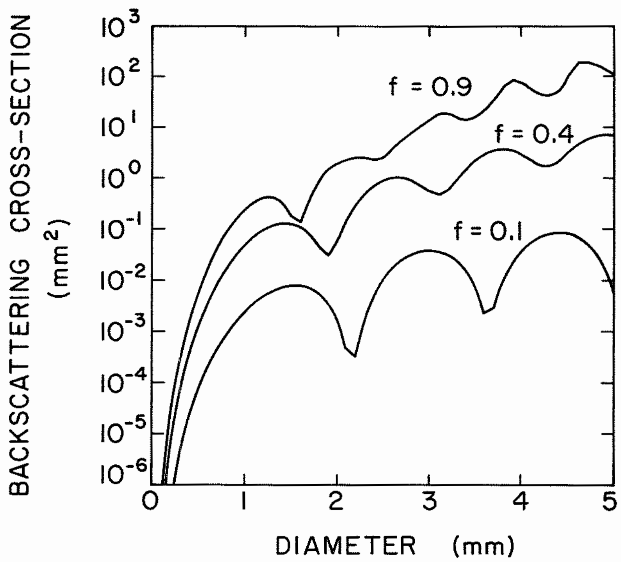

Figure 2. Backscatter cross–sections at 95 GHz for ice spheres with f=0.1, 0.4, and 0.9, as a function of diameter.

Differences in particle density were addressed in two ways. For one set of calculations it was simply assumed that all the particles had f=0.3. Volume backscatter values with this assumption were then compared with the radar measured backscatter values, and the difference used to estimate, or predict, an "average" volume fraction for the full size distribution of particles. These predicted values were then compared with those deduced from visual observations of the particles during each experiment (snow boards and close examination of the 2D–C images).

In the second method, the size distributions of particles were partitioned by size into 2 or more subsets, each having a different f. Values of f were assigned according to the particle type represented by each subset, based on the visual observations and 2D–C images.

In February 1991, concurrent radar and particle image data were collected during 18 different time period, or experiments. Two of those experiments are examined in detail here, and all 18 are summarized in the concluding section.

3. CASE COMPARISONS

3.1 February 23, 1991, 1726–1738 LT

During this experiment the precipitation at EMO was dominated by small graupel. Figure 3 compares the radar volume backscatter with that calculated from the particle images assuming f=0.3. Note that the two sets of values followed each other quite well, both in overall trend and in smaller–scale fluctuations. On average during this period the two sets of values differed by about 5 dB. This difference was applied to the average particle size distribution for the entire period, and the backscatter calculations were repeated, predicting an average volume fraction of 0.6. This value compared quite well with what one would predict for the small graupel that were observed. In addition, the original calculations are repeated with f=0.6 for each particle, and the measured and calculated backscatters agreed within 1 dB.

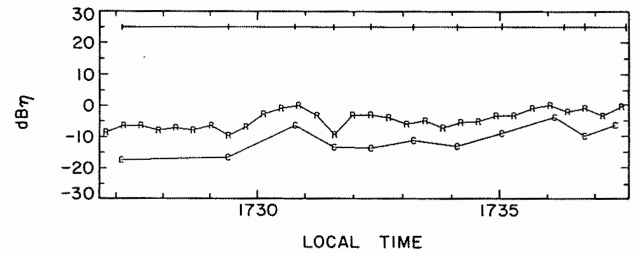

Figure 3. Time traces of measured ("R") and calculated ("C") volume backscatter values for Feb. 23, 1726–1738 LT. Each calculated value represents an average over the time interval shown by the horizontal bar with tics at the top of the window, corresponding to sample volumes of 24–101 L.

3.2 February 18, 1991, 2107 LT

For this observation period the dominant particle types were individual dendritic and stellar crystals, with little or no riming. Typical particle images for this experiment are shown in Figure 4. The average difference between the measured backscatter and that calculated with f=0.3 was about 9 dB, as shown in the time traces of Figure 5. Using an average size distribution, this difference predicted a real particle volume fraction of only 0.1, which was much too small for particles that were essentially solid ice. Partitioning the size distribution into two segments, using f=0.9 for diameters 0–400 μm and f=0.4 for 400–1400 μm, gave an even larger disagreement (about 15 dB). The obvious source of these large errors was the method of finding equivalent diameters. Whereas the prolate spheroid is a good first approximation for aggregates and rimed particles, it is not suited for unrimed, hexagonal planar crystals.

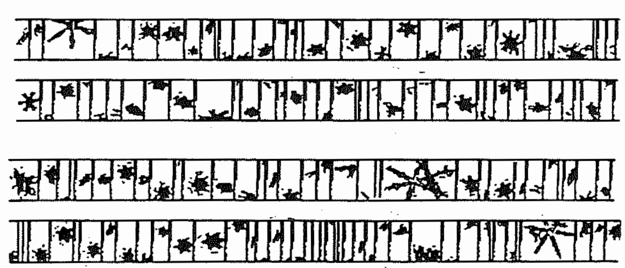
Figure 4. Examples of 2D–C shadow images for the experiment of Feb. 18, 2107–2117 LT. The vertical distance between the horizontal lines of each strip of images is 800 μm.

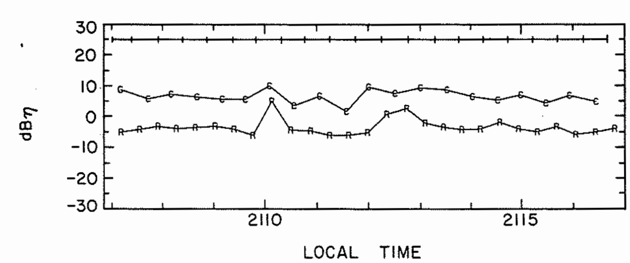

Figure 5. As in Figure 3, for Feb. 18, 2107–2117 LT, with sample volumes of 20 L.

4. SUMMARY AND CONCLUSIONS

Over the 1991 experiments observed crystal types varied widely, ranging from individual, unrimed dendritic and stellar crystals to aggregates of dendrites (rimed and unrimed), snow pellets, and small graupel. During some experiments the crystal types were mixed, and size ranges were partitioned into as many as 3 subsets for the variable–f backscatter calculations.

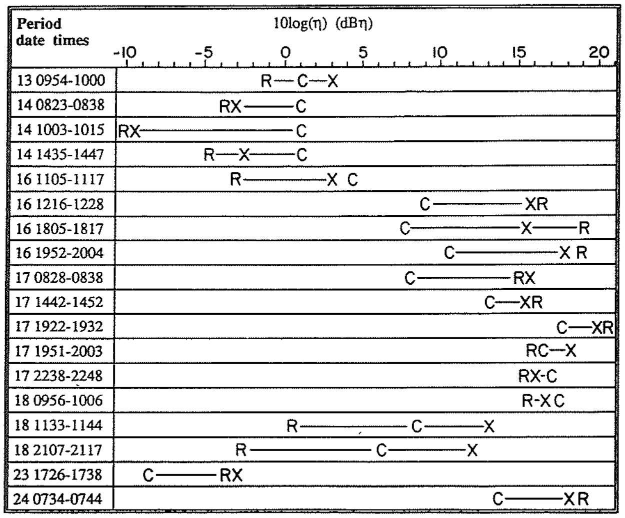

Figure 6. Summary of average measured ("R") volume backscatter values for 18 experiments. Two different calculated backscatter values are shown for each case: those with a constant f=0.3 ("C") and those with diameter subdivided into ranges with different f ("X").

Figure 6 summarizes the radar measurements, the backscatter values calculated with f=0.3, and those calculated with variable f for all 18 experiments. In 13 of the 18 cases, the measured and variable–f backscatter values agreed to within 1–2 dB. In the remaining 5 cases, in which the particle types were of mixed (e.g, graupel plus dendrites) or non–spheroidal shapes (the 18 Feb. case described earlier), the disagreements can be traced primarily to the method used for finding the equivalent particle diameter.

These comparisons show that 95 GHz volume backscatter predicted from measured particle size distributions can compare quite well with those measured by radar, both on average and in variation with time. Agreement between measurement and calculation requires inclusion of both particle size and density in the Mie approximation. To improve the agreement in cases with mixed particle types and for specific non–spheroidal shapes, objective techniques are needed for recognizing particle types and approximating densities from the 2–dimensional shadow images.

5. ACKNOWLEDGEMENTS

This work was supported by the National Science Foundation under grant ATM–8921145.

6. REFERENCES

Lhermitte, R. M., 1990: Attenuation and scattering of millimeter wavelength radiation by clouds and precipitation. J. Atmos. Oceanic Technol., 7, 464–479.

Polder, D., and J. H. van Santen, 1946: The effective permeability of mixtures of solids. Physica, 12, 257–271.

Ulaby, F. T., R. K. Moore, and A. K. Fung, 1981: Microwave Remote Sensing, Active and Passive, Volume I, Artech House, Dedham, Mass., 290–298.

DISCRIMINATION BETWEEN SUPERCOOLED WATER AND ICE BY DUAL WAVELENGTH RADAR: MEASUREMENT ERRORS AND PRECISION

M. Gosset

Université Paul Sabatier, Centre de Recherches Atmosphériques, 65300 Lannemezan, France

1. INTRODUCTION

In previous works (Gosset and Sauvageot, 1991, 1992) it was suggested to use a dual wavelength, 35-10 GHz, radar to discriminate supercooled water from ice in mixed clouds; the principle is explained below:

- on one hand, the equivalent reflectivity of a medium consisting of both droplets and ice crystals can be expressed as a function of both water (M_w) and ice content (M_i), in the following form:

$$Z_e = a_w M_w^{b_w} + a_i M_i^{b_i} \qquad (1)$$

- on the other hand, attenuation by ice being weak, dual wavelength attenuation A_d reduces to a single, liquid water absorption term, given by equation (2):

$$A_d = C_{ad} M_w \qquad (2)$$

These considerations, combined with knowledge about expected range of the parameters (a_w, b_w, a_i, b_i) allow the postulation of a typical behaviour of the observables (A_d, Z_e), which can help to classify a cloud as water only, ice only, or mixed, by measuring both attenuation and reflectivity.

Further, the relation (2) can be used for the retrieval of the averaged liquid water content (M_w) within the volume crossed, from the dual wavelength attenuation A_d measured along a radio path.

So that the method allows quantitative measurement and observation of spatial repartition of supercooled water within a mixed cloud, which is of great interest for a better understanding of cloud microstructure, as well as to be able to provide to pilotes a mapping of icing regions consisting of supercooled water (Politovich, 1989).

In order to explore the possibility of the suggested technique for measuring liquid water with sufficient accuracy, computer-made simulations of dual wavelength signals from modelized mixed clouds, for various radar characteristics, are being performed in our laboratory.

2. MIXED CLOUDS OF INTEREST

This study is focused on dual wavelength technique application for a better knowledge of water phase repartition in straiform mixed clouds, which can be modelized as successive horizontal layers, with water (possibly supercooled) up to the transition level where ice phase appears, and crystals above (this simple scheme being modified according to the dynamical evolution of the cloud). The expected values of water content and reflectivity are small (ranging from 0.01 to 0.5 $g.m^{-3}$, and -15 to 15 dBZ, respectively, in our simulations). Of particular interest are layers where both ice and water phase cohabit. For example, cells of relatively high (up to 0.5 $g.m^{-3}$) supercooled water content embeded by convection in a layer of ice (Fig. 1); or trails of ice crystals, having grown up in the upper part of the cloud and precipitating in a supercooled layer below (Fig. 2).

3. SUPERCOOLED WATER CONTENT MEASUREMENT

3.1. Dual wavelength equation for water content retrieval

The dual wavelength ratio y(r) is defined (Eccles and Mueller, 1971) as the logarithm of the ratio of powers received from range r, at the two frequencies; from the classical radar equation it is obvious to show that its variation between two resolution cells distant from Δr (km) in the radar beam, obeys to the following equation:

$$\begin{aligned}\Delta y &= y(r+\Delta r) - y(r)\\ &= 10 \log \left(\frac{P_X(r+\Delta r)\ P_K(r)}{P_K(r+\Delta r)\ P_X(r)} \right) \qquad (3)\\ &= 10 \log \left(\frac{Ze_X}{Ze_K} (r+\Delta r) / \frac{Ze_X}{Ze_K} (r) \right) + 2\ A_d\ \Delta r\end{aligned}$$

where indices i = X, K refer to 10 and 35 GHz, respectively; A_d ($dB.km^{-1}$) is the averaged, one way, differential attenuation along the path of length Δr.

In clouds consisting of small particles, it is shown that the first term, in the right part of (3), vanishes. Moreover, in the Rayleigh scattering assumption, which is respected in the non precipitating clouds under study, A_d is given by $A_d = C_{ad} M_w$, with $C_{ad} = 1\ dB.km^{-1}/g.m^{-3}$, in the usual range of temperature and for the frequencies considered. So that averaged liquid water content along the path Δr is expressed as:

$$M_w = 0.5 \frac{\Delta y}{\Delta r} \qquad (4)$$

3.2. False indications in water content

In order to detect water contents as small as 0.2 $g.m^{-3}$ (minimum value for a region of a cloud, to be labeled as "hazardous", Politovich, 1989) with good accuracy, various sources of errors in water content retrieval by (4) must be investigated and integrated in the simulation algorithmes.

These include false signal originating from imperfectly matched beams at the two frequencies, which must be analyzed according to reflectivity spatial gradient, mismatching between the two main lobes, level and differencies in side lobes. Another important interfering factor, at low elevation angle, results from terrain obstacles intercepted by the main or side lobes, which may mask the radar beam or create unreliable dual wavelength signal. Further, statistical fluctuations in measured powers will produce some uncertainties in y(r) and then M_W measurement, which depends (Eccles and Mueller, 1971) on the measurement path length Δr, and on the number of independant samples used; it is taken into account to choose the spatial and temporal resolutions, and the best way to process dual wavelength signal, according to the precision needed.

Lastly, the mixed structures of interest, described in section 2, are characterized by rapid change in hydrometeors type (phase and dimension) along the radar beam; non Rayleigh scatterers, even if scarces, and phase transition, will produce variation in reflectivity ratio Z_{eX}/Z_{eK}, and then in y(r), irrespective of attenuation. The error, $\Delta M_W/M_W$ induced, can be significant, since averaged water content is low. Examples are given in figures 1 and 2.

4. REFERENCES

Eccles, P.J., and E.A. Mueller, 1971: X-band attenuation and liquid water content estimation by dual-wavelength radar. *J. Appl. Meteor.*, 10, 1252-1259.

Gosset, M., and H. Sauvageot, 1991: The ability of differential attenuation radar technique to measure water and ice in cold clouds. Proc. 25th Intern. Conf. on Radar Meteorology, Amer. Meteor. Soc., Paris, France, 801-804.

Gosset, M., and H. Sauvageot, 1992: A dual wavelength radar method for ice-water characterization. *J. Atmos. and Oceanic Technol.* (to be published in July 1992).

Politovich, M., 1989: Measurements of hazardous icing conditions. Preprints of the 3rd Intl. Conf. on the Aviation Weather System, Anaheim, CA.

Figures 1 and 2:

Results of simulation of dual wavelength, horizontal sounding. Dual wavelength, horizontal sounding. Dual wavelength ratio, y(r), variations due to the combined effect of non-Rayleigh scattering and phase transition, may affect water content retrieval.

Dashed lines are true water (M_W) and ice (M_i) content; solid line is water content deduced from gate to gate variation, $\Delta y/\Delta r$, of the dual wavelength ratio. Distance between gates is 100 m.

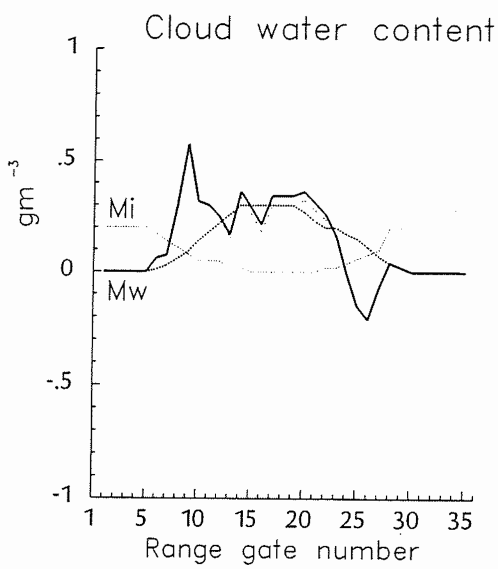

Fig. 1:

Supercooled water cell, embeded by convection in the upper part of a stratiform cloud consisting of a layer of ice crystals.

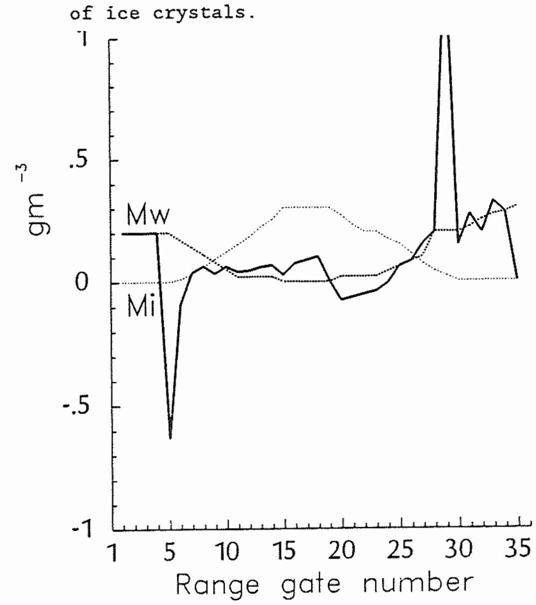

Fig. 2: Trails of ice crystals, generated in the upper part of the cloud and precipitating in a layer of supercooled water.
-see text-

CO_2 LIDAR TECHNIQUES FOR MEASURING THREE IMPORTANT CLOUD PARAMETERS

Wynn L. Eberhard[1], Janet M. Intrieri[2], and R. Michael Hardesty[1]

[1] NOAA Wave Propagation Laboratory, Boulder, CO, USA 80303
[2] Cooperative Institute for Research In Environmental Science, Boulder, CO, USA 80309

1. INTRODUCTION

Lidar has been a valuable tool for observing clouds in research programs. In most cases, a short-wave system has been used, which is defined as a lidar whose wavelength is in or near the visible ($0.3\ \mu m < \lambda\ 1.8\ \mu m$), where absorption by water and ice particles is negligible compared to scattering. A CO_2 lidar operates at a much longer infrared wavelength (commonly 10.59 μm, or at other selected laser lines between 9 and 11.5 μm). Water and ice particles absorb strongly at these wavelengths. This difference in wavelength and scattering properties makes the cloud signals from CO_2 lidar different in some respects from short-wave lidars. We describe our research on techniques to measure three different parameters of clouds that rely on unique characteristics of CO_2 lidar.

CO_2 lidar is also different from most short-wave lidars in some other respects. Our system (Post and Cupp, 1990) uses coherent detection, in which the signal scattered back from the atmosphere is mixed at the detector with a local-oscillator laser beam. This achieves quantum-limited detection, which makes the lidar sensitive to small returns. Coherent detection also enables determination of the Doppler shift to measure the velocity of the light-scattering particles in the component parallel to the beam. The contribution of multiple scatter to cloud signals is very small, which makes quantitative interpretation of the signal easier than many short-wave lidars. Another asset is that coherent CO_2 lidar is fully eyesafe.

2. EFFECTIVE AND MEAN RADIUS OF WATER CLOUD DROPS

We first describe a scheme to measure either the mean r_m or effective r_e radius of a cloud drop size distribution $n(r)$, where r is drop radius and

$$r_m = \int r\, n(r)\, dr \,/\, [\, \int n(r)\, dr\,] \tag{1}$$

$$r_e = \int r^3\, n(r)\, dr \,/\, [\, \int r^2\, n(r)\, dr\,]. \tag{2}$$

The method depends on a fortuitous relationship between a CO_2 lidar's backscatter cross section β and extinction cross section α over the range of drop radii common in clouds. The lidar measures a value of the extinction-to-backscatter ratio

$$S = \alpha/\beta \tag{3}$$

averaged over the penetration depth of the lidar. S is obtained from the apparent backscatter cross section β_a actually measured in the cloud by the lidar, where β_a is β reduced according to

$$\beta_a(R) = \beta(R) \exp(-2 \int_0^R \alpha(R')\, dR'), \tag{4}$$

where R is range and α is the cloud extinction cross section. Integrating β_a in range through the cloud gives

$$\gamma_a = \int_0^\infty \beta_a\, dR\ . \tag{5}$$

If the cloud is optically thick so that extinction drives β_a to negligible magnitude at some distance into the cloud, then (Platt and Takashima, 1987)

$$S = (2\gamma_a)^{-1}\ . \tag{6}$$

For optically thinner clouds, one can sometimes use the change in backscatter from a cooperative target (e.g., an airborne lidar viewing downward at the surface) to obtain the optical depth D of the cloud. In this case

$$S = [\, 1 - exp(-2D)] \,/\, (\, 2\gamma_a\,)\ . \tag{7}$$

Platt and Takashima (1987) suggested using this technique to obtain the mode radius r_p of a size distribution, i.e., the radius of peak number density. They supported their hypothesis using Mie scatter calculations on idealized size distributions at a wavelength of 9.25 μm. We performed more extensive calculations at 10.59 μm and found that the relationship between S and r_p depended strongly on the shape of $n(r)$. The relationship between S and either r_e (Fig. 1) and r_m (not shown here) depends less on the shape of the size distribution, so S gives useful estimates of these two characteristic radii of the drop size distribution.

Figure 2 gives results from the first application of this technique in which our lidar (Post and Cupp, 1990) viewed the sides of fair-weather cumulus in Florida. Although no confirming measurements are available, the magnitudes of r_e are reasonable for this type of cloud, and the values increase with height as expected for a growing convective cloud.

3. DISCRIMINATION BETWEEN ICE AND WATER

A simple method for discriminating between ice and

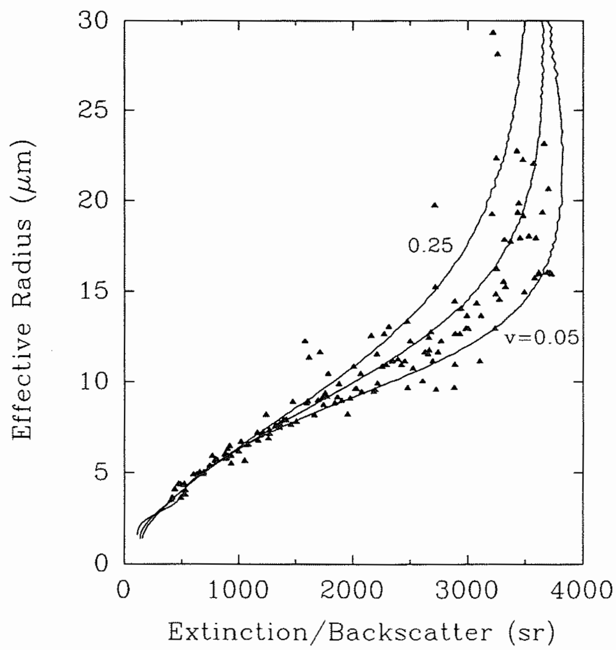

Fig. 1. Calculated relationship of extinction-to-backscatter ratio S at 10.59-μm wavelength versus effective radius r_e for the 156 measured size distributions (triangles) tabulated by Pinnick et al. (1983) and modified gamma size distributions (lines) with non-dimensional width v = 0.05, 0.15, and 0.25 (Hansen, 1971).

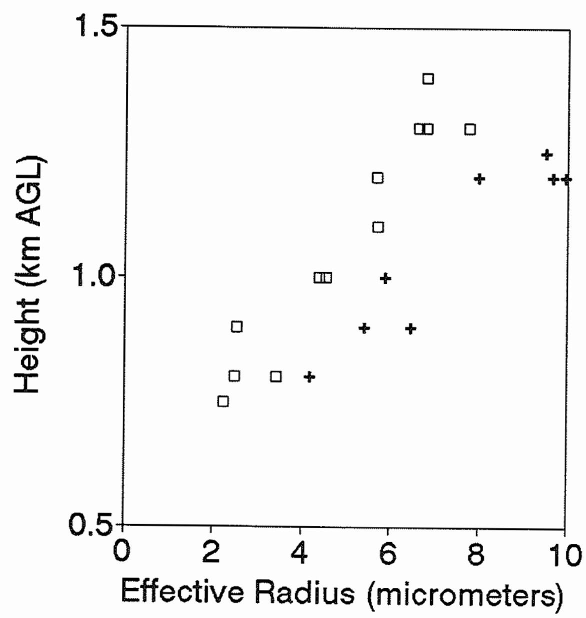

Fig. 2. CO_2 lidar measurements of r_e on the sides of fair-weather cumulus clouds using v = 0.15 from Fig. 1. The squares and crosses designate two different clouds.

water clouds is by measuring the depolarization ratio of the backscatter (Sassen, 1991) by a short-wave lidar. The backscatter from nearly spherical water drops keeps depolarization small (< 3%), although multiple scatter can introduce considerably higher levels of depolarization. For ice, the refraction and internal reflection of rays at non-normal incidence cause depolarization ratios in backscatter of typically 50%. However, ice particles absorb so strongly at CO_2 lidar wavelengths that rays do not penetrate, and backscatter is dominated by reflection (with diffraction) from the surface facing the lidar. CO_2 lidar depolarization ratios even from ice clouds remain small, i.e. ~ 1% (Eberhard et al., 1990; Eberhard 1992), so depolarization does not identify water or ice.

Instead, a dual-wavelength technique shows excellent promise for CO_2 lidar discrimination between ice and water particles. The index of refraction of ice changes with wavelength in a manner quite different from water. This causes β for ice clouds to increase substantially with wavelength between 10.5 and 11.5 μm, whereas β for water clouds decreases slightly. As an example, we have considered a $^{13}C^{16}O_2$ isotope lidar operating simultaneously (or perhaps with alternating pulses with enough averaging to smooth variations from fluctuations in cloud density) at wavelengths of 10.74 and 11.19 μm. The ratio of backscatter $\beta(11.19)/\beta(10.74)$ for water, B_w, is shown in Fig. 3 and for ice, B_i, in Fig. 4. We used modified gamma distributions of different widths, and spherical particles were assumed. B_w depends to a small degree on mean radius of the drop size distribution, and to a lesser extent on width, but is limited to 0.87±0.10 for this set of size distributions. B_i equals 2.83 except for a slight dependence on mean radius and width of the size distribution for very small size distributions. The extinction coefficients at the two wavelengths are also approximately the same, so measurement of B, even at large optical depths, should reveal whether ice or water particles dominate.

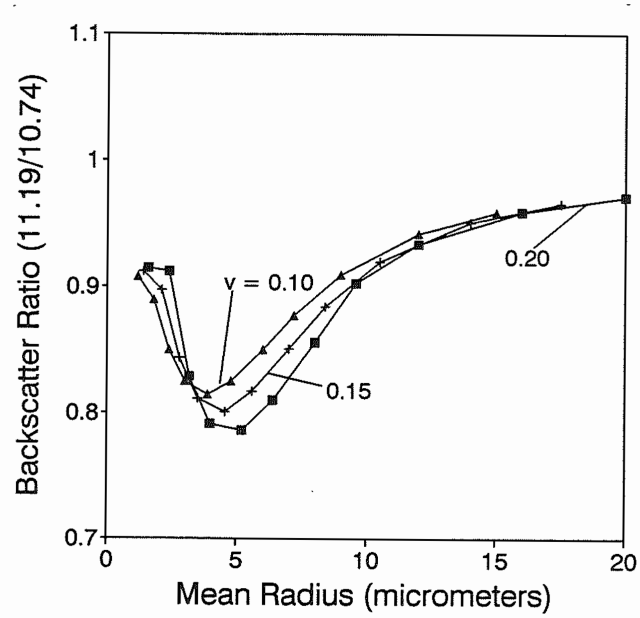

Fig. 3. Ratio of backscatter cross section β at 11.19-μm wavelength to that at 10.74-μm wavelength for water cloud drop size distributions having mean radius r_m and widths v as shown.

This CO_2 dual-wavelength method for discriminating between ice and water clouds requires more complicated hardware than the short-wave depolarization

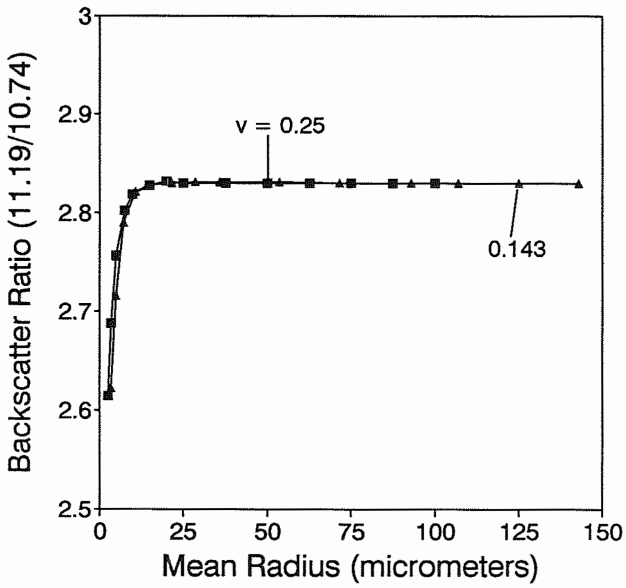

Fig. 4. As in Fig. 3, except for ice particles assuming spherical shapes.

method. However, the CO_2 method has a more rigorous analytical foundation. We are hopeful that the technique can be refined to measure the relative amounts of water and ice in mixed-phase clouds.

Although the Mie scattering assumption may not be very accurate for computing β, we are confident that the errors in the ratio B_i are small, particularly for large particles in the geometrical optics regime. Scattering calculations for cylinders and simple hexagonal particles are planned to verify this.

4. ICE CLOUD ABSORPTIVITY FROM CO_2 LIDAR BACKSCATTER

Another possible technique we are investigating is using CO_2 lidar measurements of β from ice clouds to estimate their volumetric absorption cross section α_a. Mie calculations for a variety of ice cloud size distributions show that the ratio S_a of absorption to backscatter cross sections

$$S_a = \alpha_a / \beta \tag{8}$$

is almost completely independent of particle sizes (Fig. 5). This suggests that a calibrated CO_2 lidar's measurement of β as a function of height h will give $\alpha_a(h)$. By applying the fact that the emissivity ϵ equals the absorptivity, we could thus obtain $\epsilon(h)$. If most of the particles have dimensions larger than 20 μm, the single-scatter albedo equals 0.5 to good accuracy, and the total extinction cross section

$$\alpha = 2\alpha_a \tag{9}$$

to good accuracy. Thus, measurements of β through a cirrus cloud that is not too optically thick would permit an estimate of its total narrow-beam optical depth D.

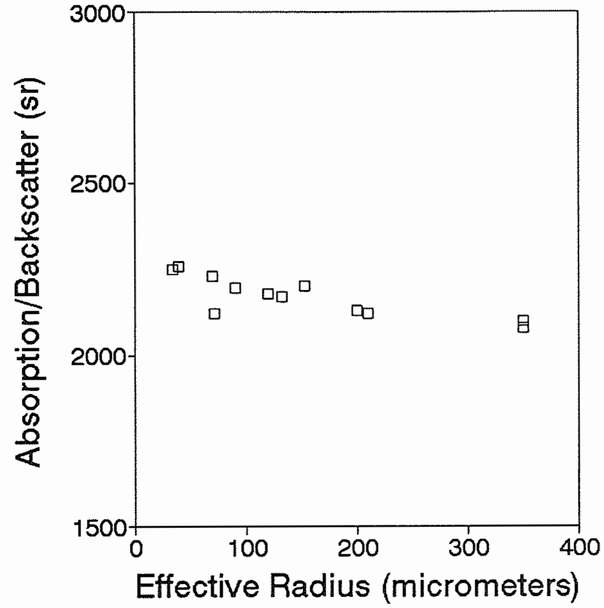

Fig. 5. Ratio S_a of absorption cross section α to backscatter cross section β at 10.59-μm wavelength for size distributions with modified gamma and other shapes (assuming spherical ice particles).

Several major problems must be settled before this technique can be applied. The most critical is that ice particles are decidedly nonspherical, and S_a may depend strongly on particle shape. A second problem occurs when particles become oriented with the long dimension horizontal; specific pointing directions might achieve the desired results in this case. A third problem is correcting the data for extinction in the cloud in determining β. A fourth problem for some applications will be extension from the lidar measurements at a single wavelength to a band of infrared wavelengths and from the narrow-beam values to diffuse values.

We are performing calculations for nonspherical particles to determine if S_a is acceptably stable for real cloud particles. If results are positive, further analytical research will be pursued in an attempt to solve the other problems. Analysis of data from narrow-beam infrared radiometer, radiosondes, and CO_2 lidar during the Cloud Radar and Lidar Exploratory Test (Eberhard et al., 1990) and other field programs can provide experimental justification for the technique.

The Laser Atmospheric Wind Sounder program plans to operate a coherent CO_2 lidar from satellite. If satisfactory techniques can be developed to infer ϵ and α from β for cirrus, they could be applied to obtain excellent value-added information on the optical properties of cirrus over much of the globe.

Acknowledgements

The authors thank M.J. Post and R.E. Cupp for the cumulus measurements, R.G. Pinnick for sharing his tabulations of cloud size distributions, and Mike Jardon, Brent Gordon, and Kathleen Healy for assistance in analysis. This work was funded through grants DE-FG02-90ER61059 and DE-AI06-91RL12089 from the Department of Energy's Atmospheric Radiation Measurement program, NASA Project #4020-CL-378 from the Earth Science and Applications Division, and a grant, titled Cloud Remote Sensing in National Climate Research Programs, from NOAA's Climate and Global Change Program Office.

5. REFERENCES

Eberhard, W.L., 1992: Ice cloud depolarization of backscatter for CO_2 and other infrared lidars. *Appl. Opt.* (in press).

Eberhard, W.L., T. Uttal, J.M. Intrieri and R.J. Willis, 1990: Cloud parameters from IR lidar and other instruments: CLARET design and preliminary results. *Preprints, Seventh Conference on Atmospheric Radiation*, July 23-27, 1991, San Francisco, California, American Meteorological Society, 343-348.

Hansen, J.E., 1971: Multiple scattering of polarized light in planetary atmospheres. Part II. Sunlight reflected by terrestrial water clouds. *J. Atmos. Sci.*, **28**, 1400-1426.

Pinnick, R.G., S.G. Jennings, P. Chylek, C. Ham, and W.T. Grandy, Jr., 1983: Backscatter and extinction in water clouds. *J. Geophys. Res.*, **88**, 6787-6796.

Platt, C.M.R., and T. Takashima, 1987: Retrieval of water cloud properties from carbon dioxide laser soundings. *Appl. Opt.*, **26**, 1257-1263.

Post, M.J., and R. E. Cupp, 1990: Optimizing a pulsed Doppler lidar. *Appl. Opt.*, **29**, 4145-4158.

Sassen, K., 1991: The polarization lidar technique for cloud research: A review and current assessment. *Bull. Amer. Meteor. Soc.*, **72**, 1848-1866.

INITIALIZATION OF STORM-SCALE MOTIONS
IN A NONHYDROSTATIC NUMERICAL MODEL.

Andrew Crook and John D. Tuttle
National Center for Atmospheric Research [1]
Boulder, Colorado 80307

1. INTRODUCTION

As the deployment date for the NEXRAD program approaches, there has been considerable interest recently in the possibility of using Doppler radar data for the purpose of initializing numerical models. The NEXRAD network will provide measurements of reflectivity and radial velocity with high temporal and spatial resolution across the United States. The average spacing of these radars will be approximately 250 km. With this spacing, dual-Doppler coverage with NEXRAD-NEXRAD pairs will be very sparse and of poor quality. (Of course, performing dual Doppler between NEXRAD and a second, nearby, operational radar such as TDWR (Terminal Doppler Weather Radar) is possible.)

The limitation of the NEXRAD measurements to one velocity component has recently prompted several researchers to examine methods of retrieving the cross-beam components of velocity as well as pressure and buoyancy. Techniques for single-Doppler retrieval include the adjoint method (Sun et al., 1991) and a forward assimilation/retrieval method proposed by Liou et al. (1991). Both these techniques attempt to find, simultaneously, the cross-beam velocity components, pressure and buoyancy from measurements of just the radial velocity component. In this study, we take a slightly different approach by first calculating the cross-beam components and then retrieving pressure and buoyancy using the method of Gal-Chen (1978). We consider two methods for calculating the cross-beam velocity. The first technique is a tracking method called TREC (Tracking Radar Echoes by Correlation), which estimates the velocity components by comparing two consecutive radar volumes and finding the translation vector that gives the highest correlation between the two volumes. (The interested reader is referred to Tuttle and Foote (1990) for details of the TREC technique.) Since the method implicitly assumes that reflectivity is a conserved tracer, it works best in the boundary layer where the reflectors are generally small insects and not so well in storms where there are sources and sinks of reflectivity. We shall present one example of a boundary layer flow, specifically that of a gust front emanating from a parent thunderstorm, in which the technique appears to work quite well. The second method is the dual-Doppler technique, in which a nearby radar directly measures a second component of the velocity vector and the third component is obtained from the continuity equation. We are currently evaluating this technique for model initialization as part of a field program in northeastern Colorado called RAPS (Realtime Analysis and Prediction of Storms). In this paper, we present some preliminary results using simulated data of a convective storm.

2. METHOD.

2.1 The numerical model

The numerical model used in this study was developed by T. Clark and collaborators and is described in Clark (1977) and Clark and Farley (1984). The model integrates the finite-difference approximations to the anelastic, nonhydrostatic equations governing atmospheric flow which are cast on a non-orthogonal, terrain-following coordinate system. The finite-difference formulation of the momentum equations employs the Arakawa (1966)-Lilly (1965) second-order algorithm and the second-order-accurate, positive-definite advection transport algorithm of Smolarkiewicz (1984) is used for all scalar conservation equations. The resulting algorithm for the evaluation of the entire system of model equations is second-order-accurate in time and space (Smolarkiewicz and Clark 1986).

2.2 Retrieval using the numerical model

To describe the thermodynamic retrieval method we first write the two horizontal momentum equations in the terrain following coordinate system as,

$$\rho \partial u/\partial t + FX = -\partial(G^{\frac{1}{2}}p)/\partial x - \partial(G^{\frac{1}{2}}G^{13}p)/\partial z \quad (1)$$

$$\rho \partial v/\partial t + FY = -\partial(G^{\frac{1}{2}}p)/\partial y - \partial(G^{\frac{1}{2}}G^{23}p)/\partial z \quad (2)$$

where FX and FY include the effects of advection, Coriolis turning, sub-grid-scale mixing, surface drag and the Rayleigh damping in the upper levels. It also includes the horizontal filters that are used to dampen two delta disturbances. $G^{1/2}$ is the Jacobian of the transformation and $G^{\frac{1}{2}}G^{13}$ and $G^{\frac{1}{2}}G^{23}$ are the two metric tensors. These tensors, which depend on the slope of the terrain, complicate the thermodynamic retrieval by linking the different model levels together. To avoid this complication, we set the tensor terms to zero by assuming that the terrain is flat.

By taking the x-derivative of (1) and y-derivative of (2) an equation for pressure can then be obtained.

[1] The National Center for Atmospheric Research is sponsored by the National Science Foundation

$$\nabla_H^2(G^{\frac{1}{2}}p) = -\partial(FX)/\partial x - \partial(FY)/\partial y$$
$$-\frac{\partial}{\partial t}(\partial(\rho u)/\partial x + \partial(\rho v)/\partial y)$$

where the anelastic mass continuity equation has been used. $\omega = (1/G^{\frac{1}{2}})(w + G^{\frac{1}{2}}G^{13}u + G^{\frac{1}{2}}G^{23}v) = (1/G^{\frac{1}{2}})w$ since we are assuming zero terrain slope.

The procedure for calculating the pressure and buoyancy can be summarized in the following manner;

(1) Given the horizontal wind (u,v) throughout the domain, calculate ω from the continuity equation.

(2) Use the model code to calculate FX and FY.

(3) Calculate the time tendency term $\frac{-\partial}{\partial t}(\partial(\rho u)/\partial x + \partial(\rho v)/\partial y)$. If simulated data is being used, then to obtain the 'true' model pressure it is necessary to use centered time differencing. However, if real data is being used, then sufficient accuracy can be obtained by using forward time differencing.

(4) Calculate the pressure deviation from the Poisson equation using Neumann boundary conditions and then adjust the pressure so it matches the sounding.

(5) Finally, calculate the buoyancy B from the third equation of motion,

$$\rho\partial w/\partial t + FZ = -\partial p/\partial z - (G^{\frac{1}{2}}g/\gamma R_d)(p/T) + \rho g B$$

where FZ includes the effects of advection, Coriolis turning, sub-gridscale mixing and the Rayleigh damping in the upper levels.

(6) The potential temperature deficit can then be derived by subtracting from B the effects of waterloading and virtual temperature.

We will first demonstrate this method using TREC data from a gust front emanating from a parent thunderstorm.

3. INITIALIZATION WITH TREC DATA.

The case to be examined occurred late in the afternoon of 18 July 1991, in northeastern Colorado. As is often the case in Colorado, the first convection formed over the Continental Divide and then propagated eastward over the High Plains. Two particularly strong cells moved off the mountains in the region between Boulder and Fort Collins and produced a gust front that spread generally eastward and southward over the Plains. Figure 1 shows the position of these cells at 2121 UTC and isochrones of the gust front at approximately 20 minute intervals. The gust front propagated at approximately 10 ms^{-1}.

Atmospheric soundings were taken ahead of and behind this gust front at a location just east of Brighton (sounding site is indicated by a solid dot on Figure 1). The two soundings are shown overlaid on Fig. 2. As can be seen, the air behind the gust front is considerably cooler with a maximum deficit of 5°C occurring near the ground. The depth of the cold air is approximately 1.5 km.

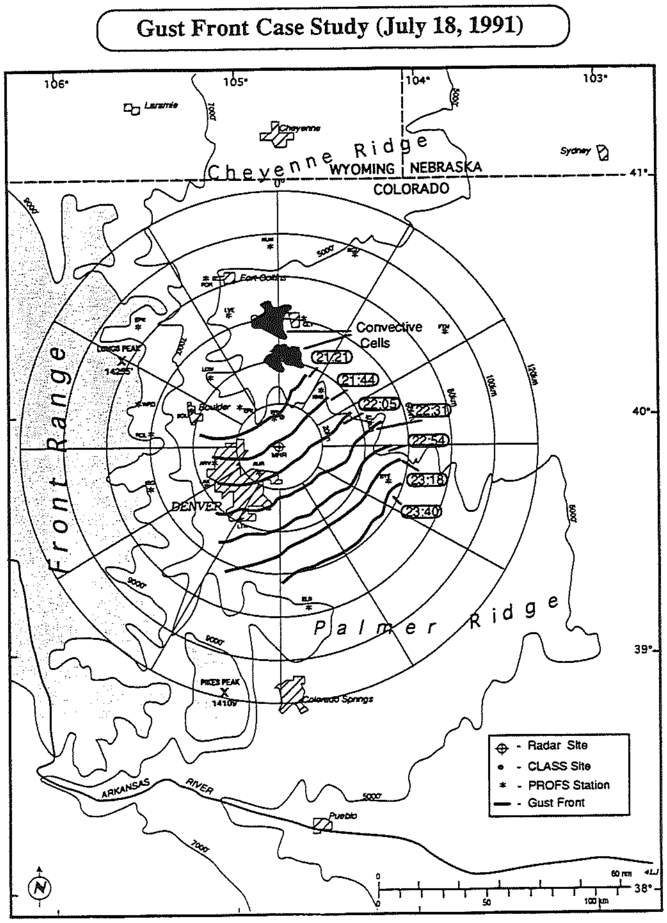

Fig. 1. Gust front case of July 18, 1991. Shown is the parent thunderstorm (the two cells indicated by heavy stippling) at 2121 UTC, and the position of the gust front at approximately 20 minutes intervals. Also shown are the height contours (at intervals of 2000 ft), the Front Range of the Rocky Mountains (light stippling), the PROFS automated weather stations (asterisks), Mile High Radar with 20 km range rings and the CLASS sounding site (heavy dot east of Brighton).

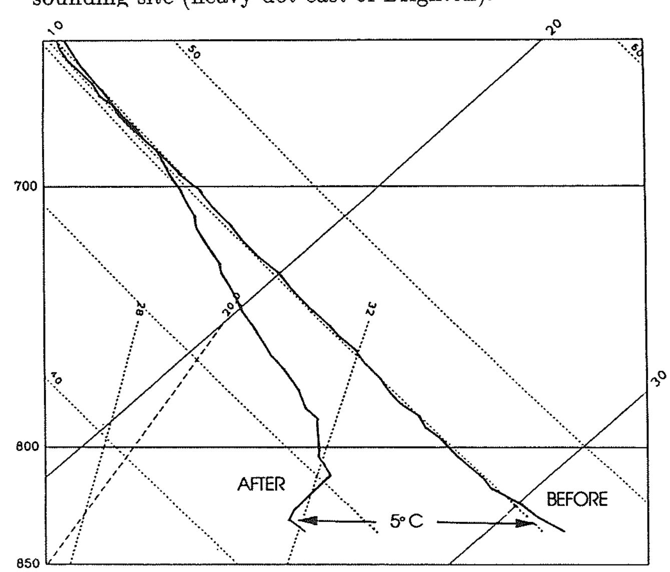

Fig. 2. Thermodynamic profile observed before and after the passage of the gust front. Sounding is only shown below 650 mb. Depth of the cold air is about 1.8 km.

As this gust front moved over the Plains the TREC program was run in real time using consecutive volumes of reflectivity. Once the horizontal velocities were obtained, the procedure outlined above in section 2.2 was followed to give the vertical velocity, pressure and buoyancy. The model has $42 \times 42 \times 34$ gridpoints at 2 km resolution in the horizontal and 300 m in the vertical. To estimate the time tendency terms a least square fit was performed over four consecutive TREC volumes. Tests with idealized data have indicated that even over a 20 minute assimilation window, a least squares fit over that interval can give a reasonable estimate of the tendency terms. This result, however, is unlikely to hold for rapidly developing systems such as thunderstorms.

Figure 3(a) shows the initial wind field just above the surface (z=200 m agl) obtained by the TREC analysis and the deviation potential temperature field from the thermodynamic retrieval. Ahead of the gust front (to the southeast) the flow is northeasterly. Behind the gust front (to the northwest) the flow is northwesterly turning to westerly as the gust front moves off the mountains. The potential temperature field shows that the air is colder behind the gust front by about 3°. This is somewhat less than the temperature drop of 5° measured by the soundings before and after the gust front. However, figure 2 shows that this maximum temperature deviation occurs over a shallow layer near the ground, hence it is not surprising that the low resolution TREC method is not able to capture this layer.

The numerical model was then run forward for 40 minutes. Fig 3(b) shows the velocity field and deviation potential temperature field at that time just above the surface. As can be seen, the gust front has moved south and eastward by about 20 km. This gives a propagation speed of just over 8 m s^{-1} which compares well with the observed speed of 10 m s^{-1}. Note also that the temperature gradient has contracted considerably over this 40 minute period. This is primarily due to the fact that the TREC analysis smooths the velocity field (since it is performed on a grid with 7 km resolution) and hence the temperature field from the thermodynamic retrieval is smoothed considerably compared to reality. When the model is integrated forward the gust front then contracts again towards its natural width. Near the end of the simulation, the scale contraction of the gust front is probably limited by the horizontal resolution of the model.

This case has shown that the pressure and buoyancy in a gust front can be retrieved from single radar data with a reasonable degree of accuracy and that a simulation can then be performed starting from these initial conditions. We now examine the possibility of using dual Doppler measurements to initialize a rapidly developing thunderstorm in a numerical model.

Horizontal Winds From TREC Analysis And Potential Temperature Deviation, T = 0 minutes

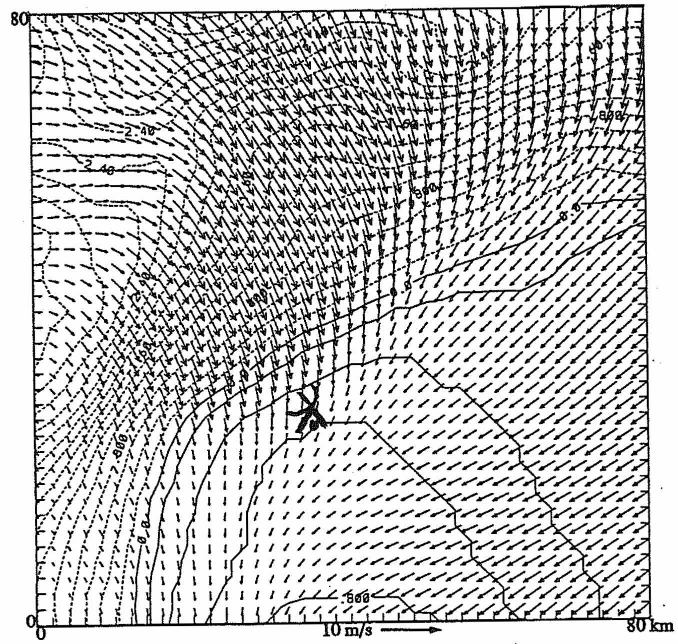

Horizonal Winds And Potential Temperature, T = 40 minutes

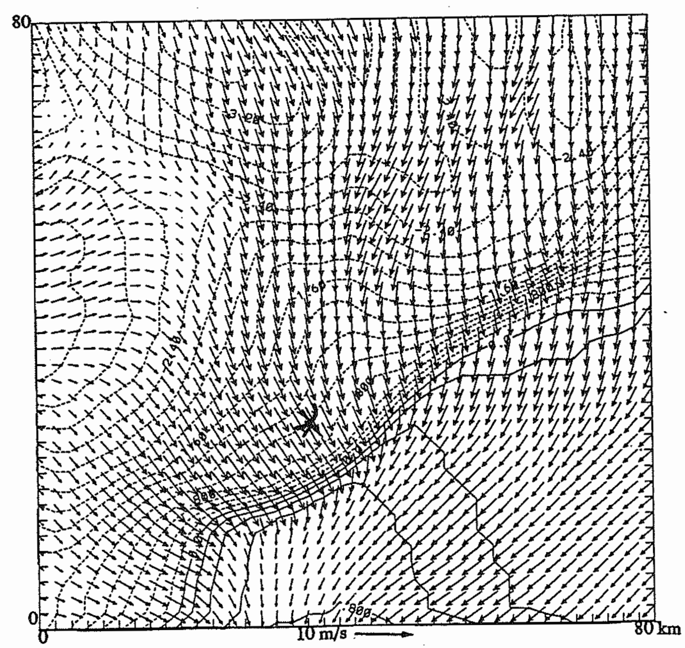

Fig. 3. (a) TREC winds from the July 18 gust front along with the retrieved buoyancy field at 2120 UTC. The position of Mile High Radar is indicated. (b) Velocity and buoyancy fields after 40 minutes of integration.

4. INITIALIZATION WITH DUAL-DOPPLER MEASUREMENTS.

Two major difficulties with storm modeling from radar data are 1) how to initialize the moisture fields and 2) how to initialize the winds outside of the storm where there is generally no data. We have recently been examining the second problem using a method suggested by Lin et al. (1990). They first assumed that outside of the storm, the horizontal divergence $u_x + v_y$ was zero as well as the vertical component of vorticity $u_y - v_x$ (in other words, 2D potential flow.) With these constraints, two separate equations for u and v can be obtained; $u_{xx}+u_{yy} = 0$ and $v_{xx}+v_{yy} = 0$. These equations can then be solved over the data-void region between the storm and the model boundaries (where u and v are specified from a nearby sounding).

We have tested the utility of this method by first running a storm simulation, and then saving the horizontal velocity fields at three consecutive timesteps. The velocity vectors, cloud and dBZ field in a vertical slice through this storm after 30 minutes is shown in figure 4. The velocity field in the regions of reflectivity less than

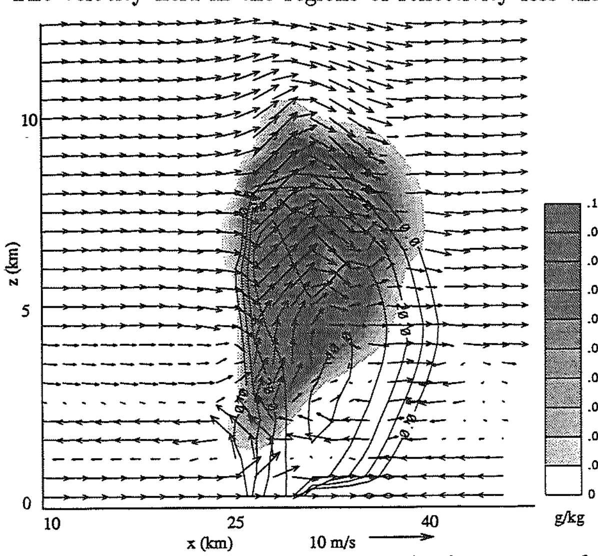

Fig. 4. Vertical slice through the center of a numerical simulated storm after 30 minutes of integration. Cloud water is shown by the gray shading. Reflectivity field is contoured from 0 to 40 dBZ with a contour interval of 10 dBZ.

-10 dBZ and above 2 km (agl) were then removed. The velocity field below 2 km was not removed since we are assuming that boundary layer winds can be obtained with a reasonable degree of accuracy. The deleted regions were then filled with the method described above. The final velocity fields were generally within 10% of the original fields.

The thermodynamic retrieval method described above was then followed using the velocity data at three consecutive time levels and centered time differencing. The 'momentum check' values (Gal-Chen 1978) obtained in these retrievals were generally less than .1 (Momentum checking values of .0 are obtained if the true velocity fields are used, values of .5 are obtained if white noise is used.) The retrieved buoyancies were within 70% of the true values. The degradation of the buoyancy field relative to the velocity field is presumably due to the vertical differencing that must be performed to obtain the buoyancy field.

These tests have tentatively shown that the pressure and buoyancy in a convective storm can be successfully retrieved when the velocity observations are restricted to regions of reflectivity. The next test, that we are currently examining, is a degradation of the time resolution of the data to that of operational radars. Following that is the task of retrieving the moisture fields from reflectivity measurements. Once these (non-trivial) steps have been completed it will be possible to integrate a numerical model forward.

5. CONCLUSION.

Work on the initialization of a numerical model with radar data continues. This paper describes some of the progress we have made in the last year. Some reasonably encouraging results have been obtained in the initialization of boundary layer winds from single Doppler measurements. Inclusion of data from a surface mesonet (if available) should further improve these results.

Real data storm simulations are a much more challenging problem. Results described herein, with simulated data, suggest that the absence of wind measurements outside of the storm (but above the boundary layer) will not be a limiting factor for these simulations. However, other problems such as low time resolution and the question of how to initialize moisture fields are significant and will require considerable research before successful simulations are possible.

6. REFERENCES

Arakawa, A. 1966: Computational design for long term integration of the equations of motion: Two-dimensional incompressible flow. Part 1. *J. Comput. Phys.,* **1**, 119-143.

Clark, T.L., 1979: A small scale numerical model using a terrain following coordinate transformation. *J. Comp. Phys.,* **24**, 186-215.

Clark, T.L. and R.D. Farley, 1984: Severe downslope windstorm calculations in two and three spatial dimensions using anelastic interactive grid nesting: a possible mechanism for gustiness. *J. Atmos. Sci.,* **41**, 329-350.

Gal-Chen, T. 1978: A method for the initialization of the anelastic equations: implications for matching models with observations. *Mon. Wea. Rev.,* **106,** 587-606.

Lin, Y., P.S. Ray and K.W. Johnson, 1990: Simulation of a Convective Storm Using Doppler Radar-Derived Initial Fields. *16th Conference on Severe Local Storms.* Alberta Canada. pp500-503.

Lilly, D.K., 1962: On the numerical simulation of buoyant convection. *Tellus,* **14** 148-172.

Liou, Y-C, T. Gal-Chen and D.K. Lilly, 1991: Retrieval of Wind, Temperature and Pressure from Single Doppler Radar and a Numerical Model. *25th Conference on Radar Meteorology.* Paris, France. pp151-154.

Sun, J., D.W. Flicker and D.K. Lilly, 1991: Recovery of Three-Dimensional Wind and Temperature Fields from Simulated Single-Doppler Radar Data. *J. Atmos. Sci.,* **48,** 876-890.

Tuttle, J.D. and G.B. Foote, 1990: Determination of the Boundary Layer Airflow from a Single Doppler Radar. *J. Atmos. Oceanic Technol.,* **7**, 218-232.

COMPARISON OF TECHNIQUES FOR DERIVING WATER-CLOUD MICROPHYSICAL PROPERTIES FROM MULTIPLE SATELLITE DATA

David F. Young[1], Patrick Minnis[2], Kristina Katsaros[3], Adam Dybbroe[4], and Jennifer Miletta[5]

[1]Lockheed Engineering and Sciences Co., Hampton, VA, USA 23666
[2]Atmospheric Sciences Division, NASA Langley Research Center, Hampton, VA, USA 23665-5225
[3]Departement d'Oceanagraphie Spatiale, IFREMMER/Centre de Brest, Plouzane, France
[4]Geophysik Institut, Copenhagen, Denmark
[5]Department of Atmospheric Sciences, University of Washington, Seattle, WA, USA

1. INTRODUCTION

Accurate representation of cloud microphysical characteristics is essential for proper determination of the cloud radiative exchanges in weather and climate models. Even in the absence of variations in cloud cover or altitude, significant changes in the global mean cloud microphysics may also have profound effects on the Earth's radiation balance. Such changes could offset some of the potential global warming attributed to increases in greenhouse gas concentrations (Charlson et al., 1991). Satellite monitoring of cloud microphysical properties is the most viable approach for observing trends and for providing data for developing and validating cloud physics parameterizations. Current satellite techniques include analyses of microwave radiances to derive cloud liquid water path (LWP) and precipitation rates over marine areas (e.g., Petty and Katsaros, 1990) and spectral differences in reflected solar radiances to estimate effective cloud droplet radii (Coakley et al., 1987), among others. Recently, Minnis et al. (1992) demonstrated the potential for estimating LWP using visible reflectance and for deriving effective droplet radius over oceans using a combination of visible and microwave radiances. This paper further explores those techniques using radiances taken by the Geostationary Operational Environmental Satellite (GOES), the Defense Meteorological Spacecraft Program (DMSP) satellite Special Sensor Microwave Imager (SSM/I), and NOAA-10 Advanced Very High Resolution Radiometer (AVHRR).

2. DATA

Cloud amount, height, and visible (VIS, 0.65 µm) reflectance, ρ, were derived by Minnis et al. (1992) using hourly GOES West 4-km visible and infrared data taken 1-19 July 1987 during the First ISCCP (International Satellite Cloud Climatology Program) Regional Experiment (FIRE) stratocumulus field program. Mean values of the cloud parameters were produced for each hour of data on a 0.5° grid covering part of the Pacific Ocean off the coast of California between 116°W and 126°W and between 28°N and 38°N. To obtain the GOES LWP, W_v, the cloud reflectance data were converted to optical depth, τ_8. The subscript 8 indicates that the optical depth conversion used a bidirectional reflectance model based on adding-doubling radiative transfer calculations for a cloud having an effective droplet radius, r = 8 µm. In the computations, the cloud was located at 950 mb over an ocean surface. An empirical formula from Minnis et al. (1992),

$$\log W_v = 0.109 + 1.60 \log \tau_8, \tag{1}$$

converts the optical depth to cloud LWP.

The DMSP F-8 satellite has equatorial crossing times of 0630 and 1830 Local Time (LT). Total and polarized brightness temperatures were taken at resolutions of ~25 and ~12.5 km for the SSM/I 37 and 85 GHz channels, respectively. These data were analyzed using the algorithms of Petty and Katsaros (1990) to yield liquid water paths, W_{37} and W_{85}, and the normalized 37 GHz polarization difference, P_{37}, which is used to indicate precipitation . Precipitation is usually occurring when $P_{37} < 0.8$ and is absent when $P_{37} > 0.9$. When $0.8 \leq P_{37} \leq 0.9$, precipitation is light if present at all. The LWP data from the SSM/I were averaged on the same grid as the GOES results. The SSM/I data do not uniformly cover the grid during a given overpass. The number of regions with data vary from 53 to 249 for the nine overpasses (3 at 0200 UTC and 6 at 1400 UTC) considered here.

NOAA-10 AVHRR channels 1 (0.67 µm, VIS), 3 (3.73 µm), 4 (10.8 µm, IR), and 5 (12.0 µm) were also taken for the 0730 LT pass over the grid at 1 and 4-km resolutions. Liquid water path, W_m, was also measured using a microwave radiometer on San Nicolas Island during FIRE (Fairall et al., 1990). The 1-minute means were averaged over a 30-minute interval centered at the GOES scan time (Minnis et al., 1992) to obtain W_m.

3. METHODOLOGY

a. *Visible and microwave retrievals*

Following Minnis et al., (1992), the effective droplet radius is approximated as

$$r = 3/2\,(\mathrm{LWP} / \tau_r). \tag{2}$$

Given a value of LWP, a VIS cloud reflectance, and a model of $\rho(\tau_r)$, it is possible to find r from (2) iteratively. Lookup tables of $\rho(\tau_r)$ were derived using Mie scattering in the adding-doubling routine as in Minnis et al. (1992) for r = 2, 4, 6, 8, 12, 16, 32, and 64 µm using an effective variance of 0.1. The values also depend on the solar zenith, satellite zenith, and relative azimuth angles, θ_o, θ, ψ, respectively. The lookup tables provide values of $\tau_r(\rho)$ for use in (2). The SSM/I provides the LWP data. The SSM/I data having $W_{85} > 10$ gm^{-2} were matched with the nearest usable GOES results only for regions containing no land. Since the overpass times of the F-8 are near the terminator, the solar illumination conditions are marginal for retrieval of the optical depths. To obtain a reasonable sample of data, those GOES data having a solar zenith angle $\theta_o < 80°$ and taken within 1.5 hours of the SSM/I overpass were used in this analysis. LWP is also estimated by applying (2) to the GOES data using r = 8 µm. This quantity is denoted as W_8.

b. *Multispectral retrievals*

The AVHRR VIS and IR data are analyzed with the method of Minnis et al. (1987) to obtain cloud fraction, C, and clear-sky and cloud-top temperatures, T_s and T_c., respectively. The channel 3 brightness temperature, T_3, is determined by the combination of solar-reflected and scene-emitted radiation. The observed radiance is approximated as

$$B_3(T_3) = B_3(T_3') + \mu_o E_3[\rho_3 C + (1 - C)\rho_{3s}], \tag{3}$$

where $\mu_o = \cos\theta_o$, E_3 and B_3, respectively, are the solar constant and Planck function at 3.73 µm, and ρ_{3s}, the clear-sky reflectance for channel 3, is estimated to be 0.05. The channel-3 cloud reflectance is $\rho_3(\tau_3(r),\theta_o,\theta,\psi)$, where τ_3 is the channel-3 cloud optical depth for a given effective droplet radius. A set of lookup tables of ρ_3 were developed in the same manner as the VIS model using identical droplet distributions. The emitted component is

$$B_3(T_3') = (1 - C)B_i(T_{3s}) + C[\varepsilon_3 B_3(T_c) + (1 - \varepsilon_3)B_3(T_{3s})], \quad (4)$$

where the channel-3 emittance ε_3 is parameterized using the previously described water-droplet distributions in the calculations. The channel-3 clear-sky temperature is T_{3s}. The VIS optical depth is related to τ_3 by the ratio of their extinction efficiencies. The effective radius for a given scene is determined iteratively by finding the solution to (3) which also explains the observed VIS reflectance.

4. RESULTS

a. *Surface-SSM/I comparisons*

A comparison of nearly simultaneous surface and SSM/I LWP results (Fig. 1) shows that W_m is well correlated (correlation coefficients, R, are noted in the figure) with both W_{37} and W_{85}. A linear fit for the latter yields an offset of 40 gm^{-2}, and a slope of 0.95. The slope and offset for the former are 0.92 and 61 gm^{-2}, respectively. These correlations suggest that the SSM/I results overestimate the LWP but have a precision within the accuracy limits (± 10%) of W_m, except for LWP < 100 gm^{-2}. Some of the discrepancies may be due to scale differences in the two datasets.

b. *VIS-SSM/I liquid water paths*

The plot of W_v (0145 UTC) versus W_{85} (0230 UTC) from 16 July 1987 in Fig. 2 represents the best of nine comparisons of LWP computed using (1) with W_{85}. The best-fit slope is 0.94 and R = 0.85. More typical values of R are 0.5 with slopes varying from 0.2 to 5. Better results are usually obtained using W_8 instead of W_v. The empirical fit tends to give extremely large LWP values for large optical depths. Overall, for a given region, the differences between W_8 and W_{85} are -50 ± 62 gm^{-2} compared to 29 ± 157 gm^{-2} for W_v and W_{85}. Temporal and spatial discrepancies are included in these differences. The W_8 underestimate arises from using a radius smaller than the mean for the area as shown below. The smaller bias for the empirical fit comes at the expense of the large instantaneous overestimates.

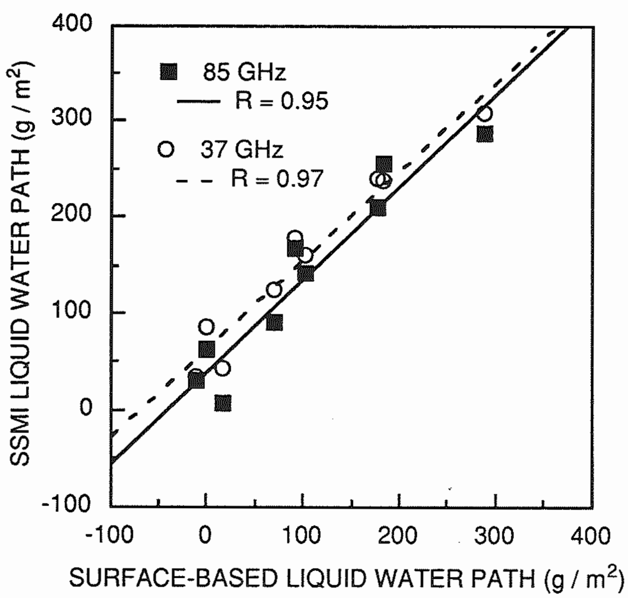

Fig. 1. Comparison of surface-based and SSM/I liquid water path measurements.

c. *VIS-SSM/I effective radius*

Albedo, LWP, and r for 1500 UTC, 16 July 1987 show little correlation in Fig. 3. Cloud amount over the ocean regions is 100% except for a few boxes in the northwestern corner. The largest droplets (Fig. 3c) are found along the northern edges of the cloud field and some of the areas with high LWP (Fig. 3b). The extensive area of maximum albedo (Fig. 3a) includes both low and high values of LWP and r. Smallest droplets are primarily found in the southwestern corner of the grid. Figure 4 shows W_{85} and τ as functions of the derived effective droplet radius for all of the data. Each datum represents a measurement over one region. The droplets generally range in size from 5 - 25 µm with a mean value of 12 µm. Larger or smaller values are probably errors associated with data taken in partly cloudy areas near the edges of the cloud fields. There appears to be no correlation between r and LWP (Fig. 4a), except for a slight tendency for an increase in the minimum radius with LWP. Larger droplets tend to be associated with lower optical depths (Fig. 4b), although there is considerable scatter in the observations.

It is expected that precipitation would primarily occur over areas having large mean droplet sizes and large LWP's. Figure 3d shows the percent of measurements of $P_{37} < 0.8$ in each region. The areas of apparent precipitation are highly correlated with LWP. Excepting the zone in the west-southwestern corner and the cloud edges, the areas of precipitation also correspond closely to the contours of $r > 12.5$ µm. Similarly, at 1500 UTC, 17 July (not shown), areas of precipitation are associated with $r >$ 12.5 µm. However, drizzle was observed at the same time over San Nicolas Island where the derived value of r is 16 µm. There is no indication of rain in the P_{37} data near the island at that time. Large droplets were derived for some small areas on several other overpasses when there was no precipitation indicated in the P_{37} results. Conversely, precipitation was indicated for part of the 12 July afternoon overpass where $r < 12$ µm. Mixed results were also observed the following day. Despite the larger mean droplet sizes, there were no regions with $P_{37} < 0.8$ for the afternoon cases. Precipitation from stratocumulus clouds is usually drizzle so that it is probably borderline in the P_{37} index. Much of the morning data taken have $P_{37} < 0.9$, the high end of the ambiguous range. About half of the afternoon cases have $P_{37} < 0.9$. Although the mean value of P_{37} is poorly correlated with r for all observations (R = 0.2), there appears to be a general increase of r with decreasing P_3, on average.. The mean radius corresponding to P_{37} < 0.8 is 14.9 µm for the morning data. For $P_{37} > 0.9$, the means are

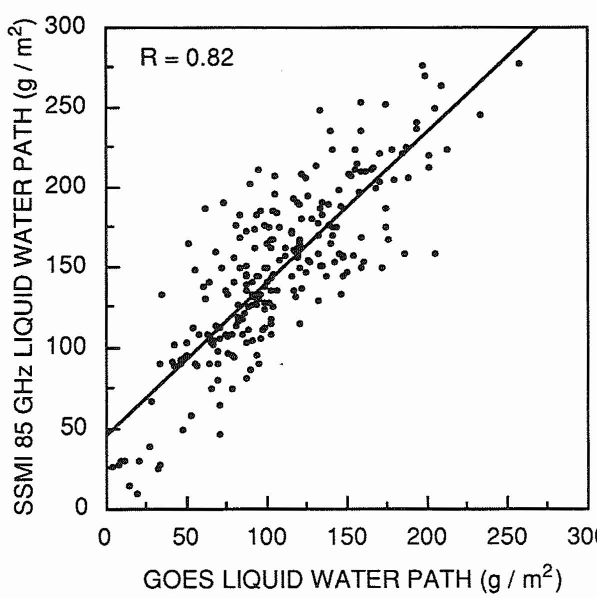

Fig. 2. Comparison of SSM/I 85 GHz and GOES-derived liquid water path from 16 July 1987.

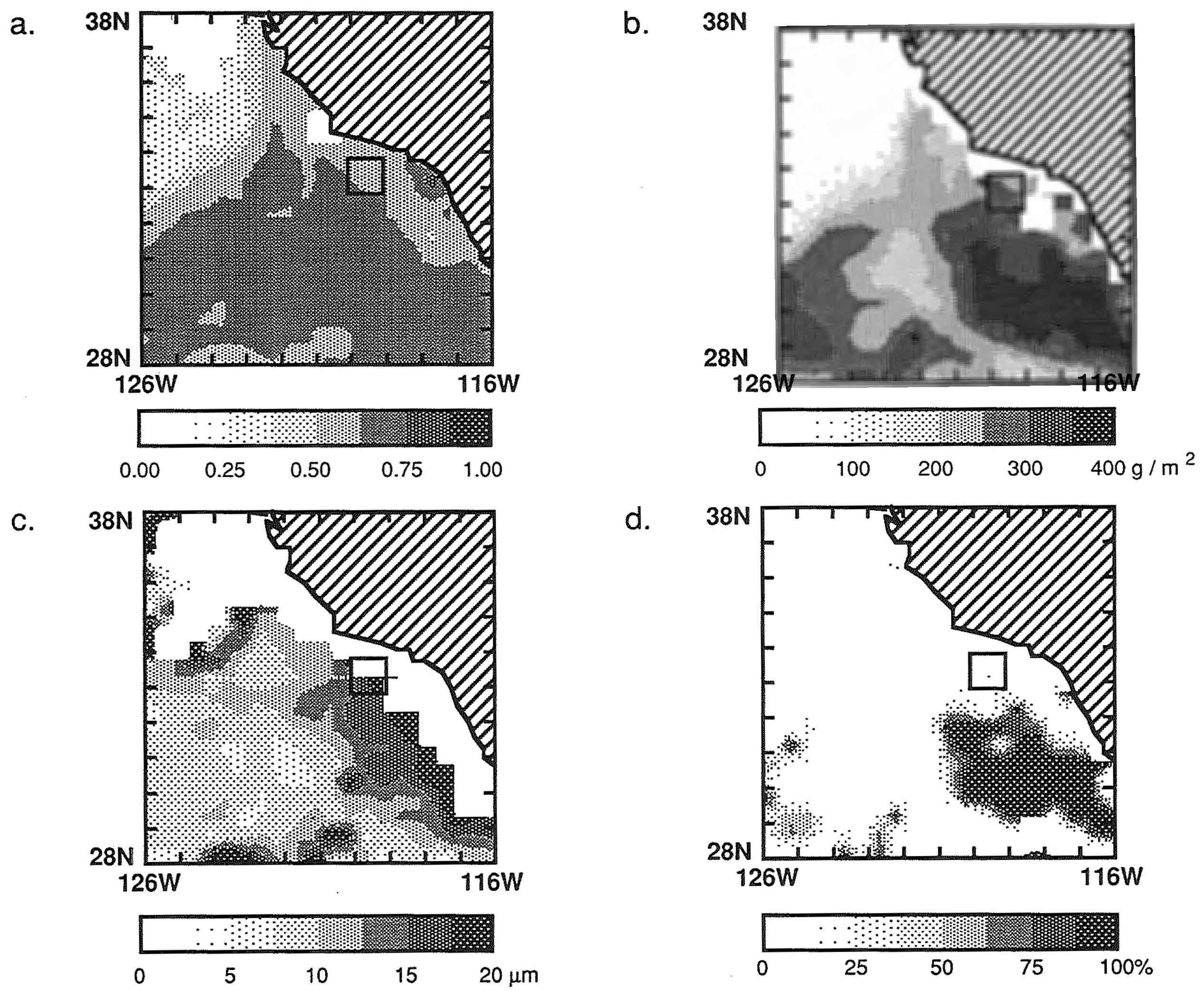

Fig. 3. a) GOES-derived VIS cloud albedo, b) SSM/I liquid water path, c) effective droplet radius, and d) percent SSM/I pixels with p37 < 0.8 from 1500 UTC, 17 July 1987.

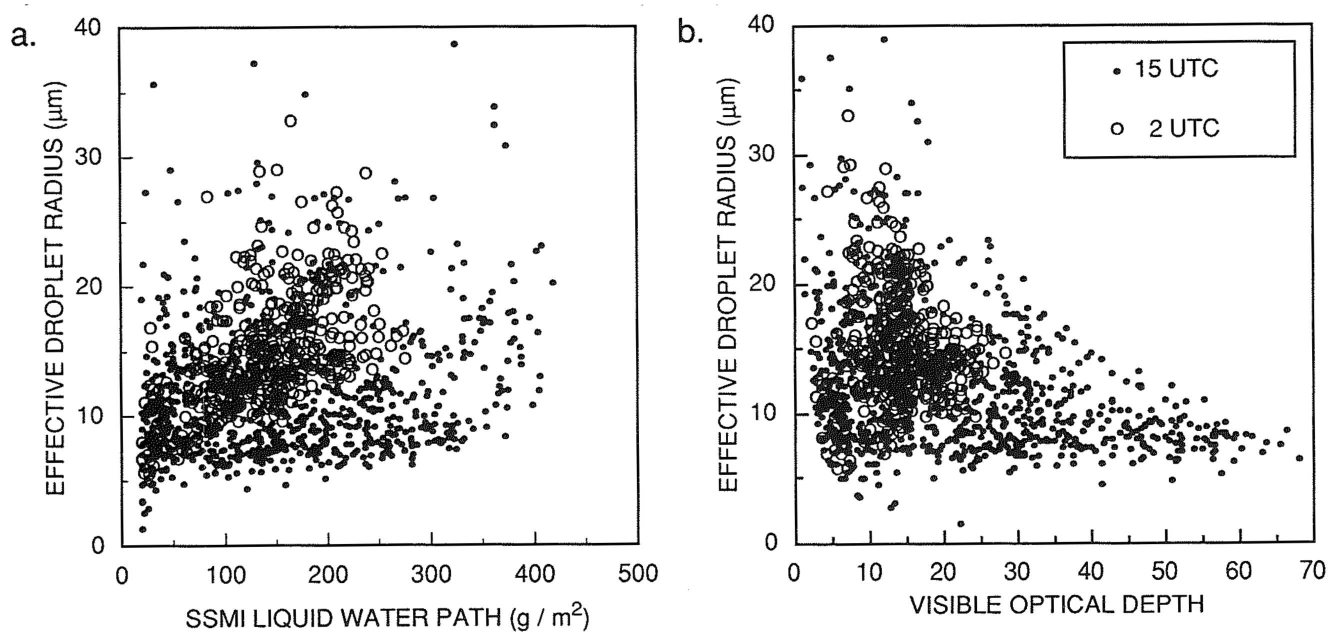

Fig. 4. Effective droplet radius as a function of a) SSM/I 85 GHz liquid water path and b) visible optical depth for 1500 (•) and 0200 (O) UTC.

11.1 and 13.3 μm for the morning and afternoon cases, respectively. Similarly for $0.8 < P_{37} < 0.9$, they are 11.6 and 16.5 μm, respectively. The precipitation index is strongly tied to W_{85} (R = 0.97). Regression analysis shows that $W_{85} > 300$ gm^{-2} for $P_{37} < 0.8$. The largest LWP value during the afternoon was 270 gm^{-2}. Thus, the larger droplets derived for the afternoon cases occur in a diminished LWP environment compared to the morning cases. Whether the afternoon clouds are thin with large droplets or the algorithm is failing to discern a reasonable droplet size in these cases needs further study.

d. *Errors*

There are many potential sources for error in this type of analysis including spatial and temporal sampling differences, LWP algorithm errors, and reflectance modeling assumptions (e.g., the model cloud is plane-parallel) among others. The comparisons in Fig. 2 provide one measure of some of the uncertainty in the SSM/I LWP algorithms. Assuming the island data are correct, it may be concluded that the satellite values tend to overestimate the LWP but have good precision. Assessing the other error sources is not as straightforward.

Aircraft in situ data taken during a few of the days examined here provide a qualitative means of independent confirmation of the satellite results. The University of Washington C-131A aircraft measured effective droplet radii between 5 and 7 μm during a 1-hour flight at 1800 UTC on 13 July 1987 between 31.8°N, 120.5°W and 31.4°N and 121.2°W (Nakajima et al., 1991). The effective radii derived from the satellite data 3 hours earlier are mostly around 8 μm just west of this flight area (Fig. 5). Assuming that r decreases by 25% from 0700 to 1000 LT as seen by Minnis et al. (1992) over San Nicolas Island, the mean GOES-derived radius would be ~ 6 μm at 1800 UTC. Around 1800 UTC, 16 July 1987, the C-131A, flying between 31.9°N, 120.2°W and 31.4°N, 121.2°W, measured r between 7 and 20 μm. Most of the values were between 7 and 8 μm. The early morning satellite retrievals (Fig. 3) show r ranging from 8 to 12.2 μm along that flight path. This range would be 5 to 9 μm if the time-change effect is estimated as above. Further north, the UK C-130 (Rawlins and Foot, 1990) measured values of r varying from 4.1 μm at cloud base to 9.5 μm near cloud center and to 10.2 μm at cloud top on the same day between 1700 and 1900 UTC. Figure 3 shows a mean radius of ~12.3 μm for that same area. Again, the temporal difference correction would yield 9.2 μm for the satellite results.

The differences might also be explained by the apparent biases in the SSM/I LWP values. For the first case above, the mean droplet radius is ~ 6 μm, while $r(85)$ and $r(37)$ are 8.5 and 9.9 μm, respectively. Using the fits derived from Fig. 2 to adjust the LWP values changes the respective radii to 7.1 and 6.7 μm, a much closer comparison. Adjustment for the LWP biases for the other cases also substantially reduces the derived radii. For the second case above, $r(37)$ and $r(85)$ change from 11.3 and 11.1 μm to 9.9 and 9.8 μm, respectively. Likewise, the two mean radii decrease from 13.2 and 12.3 μm to 10.8 and 10.4 μm, respectively, for the third case. The adjusted values are much closer to the observations suggesting that the biases are real for both channels. Given the 3-hour time differences, it is not possible to draw any firm conclusions from these comparisons. It is evident, however, that the effective radii derived here are consistent with the changes from 13 July to 16 July observed in the aircraft data. They are very similar in absolute value, especially if the mean corrections for the diurnal cycle or the LWP biases are applied.

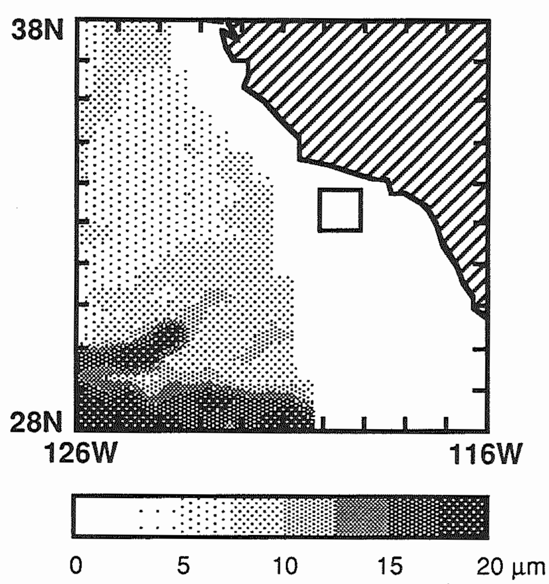

Fig. 5. Effective droplet radii from 1500 UTC, 13 July 1987.

5. CONCLUDING REMARKS

This paper has provided some verification of SSM/I LWP products and of VIS-derived LWP. It has also demonstrated a promising new tool for deriving effective cloud droplet radius by combining data from two different satellites. Additional comparisons of the VIS-SSM/I results with AVHRR-based effective radii are in progress. The spatial limitations of the GOES and the high solar zenith angles inherent in the F-8 orbit restrict the accuracy and utility of this technique. Use of DMSP platforms with different orbits or other satellites such as Meteosat would overcome some of these limitations. Furthermore, the DMSP carries VIS and IR channels in its Operational Line Scanner. Availability and calibration of those data would obviate the geostationary data for this method. It would be possible to derive the cloud properties over any water body during daylight using only the DMSP data. Although the current results are very encouraging, they are limited in scope and cloud type. Further development of the method and verification are needed.

Acknowledgments. Funding for part of the GOES satellite analyses was provided by the Office of Naval Research under Grant USN-N0001491IMP24011.

REFERENCES

Charlson, R. J., S. E. Schwartz, J. M. Hales, R. D. Cess, J. A. Coakley, Jr., J. E. Hansen, and J. D. Hofmann, 1992: Climate forcing by anthropogenic aerosols. *Science*, **255**, 423-429.

Coakley, J. A., Jr., R. L. Bernstein, and P. A. Durkee, 1987: Effect of ship-track effluents on cloud reflectivity. *Science*, **237**, 953-1084.

Fairall, C. W., J. E. Hare, and J. B. Snider, 1990: An eight-month sample of marine stratocumulus cloud fraction, albedo, and integrated liquid water. *J. Climate*, **3**, 847-864.

Minnis, P., E. F. Harrison and G. G. Gibson, 1987: Cloud cover over the eastern equatorial Pacific derived from July 1983 ISCCP data using a hybrid bispectral threshold method. *J. Geophys. Res.*, **92**, 4051-4073.

Minnis, P., P. W. Heck, D. F. Young, C. W. Fairall, and J. B. Snider, 1992: Stratocumulus cloud properties derived from simultaneous satellite and island-based instrumentation during FIRE. *J. Appl. Meteorol.*, **31**, 317-339.

Nakajima, T. M. D. King, J. D. Spinhirne, and L. F. Radke, 1991: Determination of the optical thickness and effective particle radius of clouds from reflected solar radiation measurements. Part II: Marine stratocumulus clouds. *J. Atmos. Sci.*, **48**, 728-750.

Petty, G. W. and K. B. Katsaros, 1990: New geophysical algorithms for the Special Sensor Microwave Imager. *5th Conf. Roy. Met. Soc. and the AMS*, London, U. K., Sept. 3-7, 247-251.

Rawlins, F. and J. S. Foot, 1990: Remotely sensed measurements of stratocumulus properties during FIRE using the C130 aircraft multi-channel radiometer. *J. Atmos. Sci.*, **47**, 2488-2503.

ON THE DETECTION OF CIRRUS CLOUDS FROM SATELLITE MEASUREMENTS

L. Di Girolamo and R. Davies

Department of Atmospheric and Oceanic Sciences, McGill University
Montreal, Quebec, Canada H3A 2K6

1 Introduction

Cirrus clouds remain elusive in terms of cloud-climate feedback. For many years scientists believed that cirrus clouds have a cooling or heating effect at the Earth's surface, depending on their optical properties (i.e. Manabe and Wetherald, 1967; Cox, 1971). Recently, however, Stephens *et al.* (1990) reported that these results were influenced by inadequate treatment of the physics of cirrus clouds and that the effects of cirrus cloud feedback on climate still remain unknown. This reflects our limited understanding of the relationships between the size and shape of ice crystals and the gross radiative properties of cirrus.

Continuous cirrus observations at many spatial and temporal resolutions are required to advance this understanding; satellite observations are one such method. However, satellite detection of cirrus clouds, especially thin cirrus clouds, remains difficult for many cloud retrieval algorithms because of the low optical thickness and variable emissivities these clouds possess. In order to further our capabilities in cirrus detection, we have developed a new technique for the upcoming Multi-angle Imaging Spectro-Radiometer which is scheduled for launch in 1998 on the first platform of the Earth Observing System (Dozier, 1991).

2 The Multi-angle Imaging SpectroRadiometer

The Earth Observing System (NASA, 1991) is a program which will carry out multidisciplinary Earth science studies with the aid of a variety of remote sensing instruments. The Multi-angle Imaging SpectroRadiometer (MISR) (JPL, 1990; Diner *et al.*, 1989) is one such instrument and will provide multi-angle continuous coverage of the Earth at nine discrete view angles. This is achieved by allocating a separate camera for each viewing direction. One camera points at nadir, four point in the forward along-track direction, and four point in the backward along-track direction (0°, ±26.1°, ±45.6°, ±60°, ±70.5°). The optics of each camera are adjusted to give the same cross-track resolution of 240 m in the Local Mode and 1.92 km in the Global Mode. The 360 km swath width and its 705 km sun-synchronous orbit allow complete global coverage every 9 days and a polar coverage every 2 days. Images from each camera will be obtained in a pushbroom fashion in four spectral bands (443, 550, 670, 865 nm). Thus, multi-angle observations of each target area are made within a few minutes, under the same atmospheric conditions.

3 Cirrus Cloud Detection with MISR

(a) Other Cloud Detection Techniques

Many existing cloud detection techniques can be applied to MISR data — including stereo, visible/near IR thresholding and discrimination. Many of these techniques require a large time lag between reception and processing of data in order to choose appropriate thresholds. Moreover, many of these algorithms require some *a priori* information on, for example, atmospheric temperature and humidity profiles. These algorithms typically perform poorly in detecting thin cirrus which have variable emissivity and low reflectance. Therefore to improve our cirrus detection capabilities using MISR, we propose a novel combination of techniques which take advantage of MISR's unique viewing capability. To meet operational considerations, cloud detection must be obtained on a near real-time basis and initial cloud screening must be performed using MISR data alone. The examples cited below are for observations over an ocean surface.

(b) The Predetermined Clear Sky Threshold

In order to obtain near real-time cloud detection, a Predetermined Clear Sky Threshold (PCST) technique is developed. Because no *a priori* information is used, the PCST is defined as the **maximum** contribution to the satellite-measured reflectance from the ocean surface, atmospheric gases, and atmospheric aerosols under clear sky conditions. Using the LOWTRAN 7 (L7) atmospheric model (Kneizys *et al.*, 1988) to obtain radiances, the maximum atmospheric contribution to the top of the atmosphere 0.86 μm radiances corresponds to the L7 sub-arctic winter profile under heavy maritime aerosol concentration. The MISR 0.86 μm channel was chosen because it is less sensitive to changes in atmospheric and oceanic constituents, compared to the other MISR channels. A flat ocean model was used because this state gave rise to maximum reflectance (Preisendorfer and Mobley, 1986).

L7 simulations have shown that the most oblique camera having a relative azimuth angle between 90° and 270° with respect to the sun (that is the side which picks up more of the forward scattering) is best for the detection of cirrus clouds over ocean. Where sun glint is encountered, a less oblique camera can be substituted. With this rule, Figures 1 and 2 show the PCST as a function of solar zenith angle for MISR's 70.5° camera under a relative azimuth angle of 180° and 150°, respectively. Included in these figures, for comparison, is the minimum detectable cirrus cloud optical thickness. This

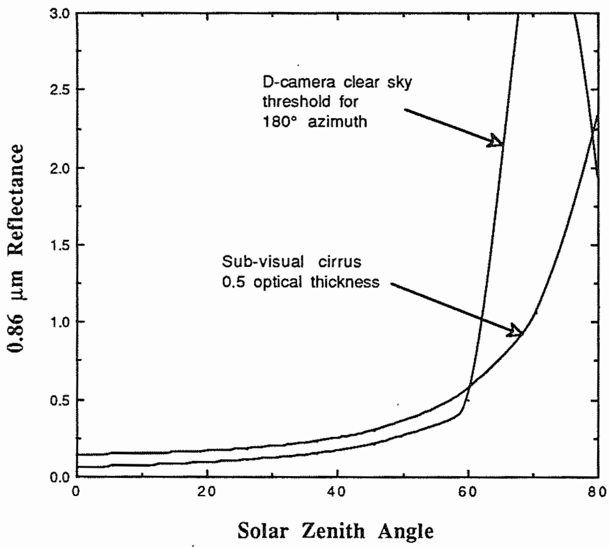

Figure 1. Comparison of thin cirrus cloud (base height = 11 km, thickness = 1 km) with the predetermined clear sky threshold calculated for the MISR-D camera with a RAZ = 180°.

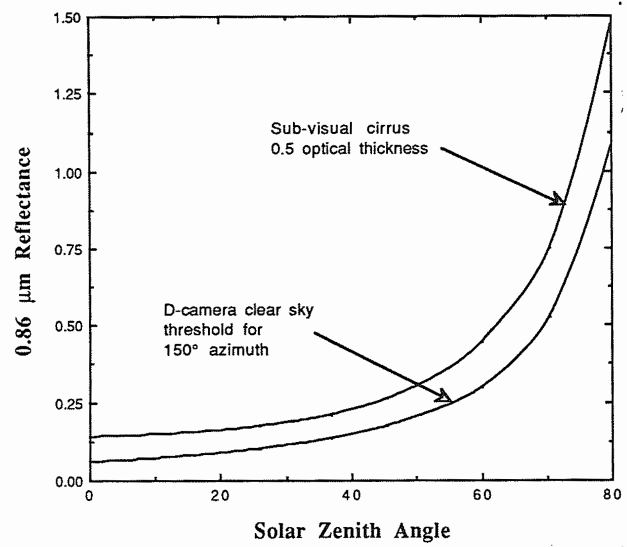

Figure 2. Comparison of thin cirrus cloud (base height = 11 km, thickness = 1 km) with the predetermined clear sky threshold calculated for the MISR-D camera with a RAZ = 150°.

was calculated with no *a priori* knowledge of atmospheric and oceanic state. Thus, conditions giving rise to **minimum** reflectance (i.e. worst case scenario) were assumed. These conditions correspond to the L7 subvisual cirrus profile (Shettle *et al.*, 1988), high clouds, and the tropical atmospheric profile under light aerosol concentrations. The flat ocean model was used because of its simplicity; however, this ocean state does not give rise to minimum reflectance for the direct beam component of low solar elevations (solar zenith > 60°) (Preisendorfer and Mobley, 1986). This does not affect the PCST; instead, it will slightly increase the value of the minimum detectable cloud optical thickness.

A cirrus cloud of visual (0.55 µm) optical thickness of 0.5 is presented in the figures. This cloud is detectable when uncertainty in instrument measurement is included. Note that these results compare extreme scenarios between the clear sky and cloudy atmospheres. If any *a priori* knowledge of atmospheric aerosol concentration, temperature, etc. is known, then threshold values would certainly decrease, improving the ability to detect thinner clouds. Of course, this technique still shares some inherent problems of other algorithms, mainly the misclassification of surface reflectance anomalies (i.e. fog, white caps, ocean foam) as cloud. However when this technique is used in concert with the Band-Differenced Angular Signature technique described below, the problem of misclassification is greatly reduced.

(c) The Band-Differenced Angular Signature Technique.

This section describes a new approach which combines the spectral signature with its angular variation to give the Band-Differenced Angular Signature (BDAS) of the scene. This new approach takes the difference between two solar spectral reflectances as a function of view angle. The resulting angular signature is used to discriminate between low-level and high-level clouds, as well as surface reflectance anomalies. The MISR instrument is ideal for the application of this new technique. MISR's 0.86 µm reflectance is subtracted from the 0.44 µm reflectance. Because a factor of 16 exists between their respective Rayleigh scattering cross-sections (which is the largest difference between all MISR spectral channels), different Rayleigh scattering contributions are expected. The magnitude of this difference will vary between clear and cloudy skies. This is because the cloud masks a large part of the Rayleigh atmosphere from the satellite. Higher clouds will have a larger masking effect than lower clouds. The same is true for thicker clouds. Thus, the BDAS of high thick cirrus clouds is expected to be very different from lower level clouds or from clear skies. Here we focus on detecting cirrus clouds based on the **BDAS pattern alone** (i.e. not on the absolute value of the BDAS or radiance measurement). Inclusion of, say, the absolute value of the BDAS would require further modelling and would certainly improve the detection and classification scheme. This approach is already in its preliminary stage.

LOWTRAN 7, coupled with the flat ocean model, was used for the BDAS simulations. Since the ocean colour contribution and its angular variation with sea surface state is small, the flat ocean assumption introduces little error to the BDAS. The 0.44 µm ocean colour contribution was set at a reflectance R = 0.03 (a typical value). In the BDAS simulations the same atmospheric profile was used for both clear and cloudy skies. L7's tropical atmosphere under light aerosol concentrations was used because it offered minimum TOA band-differenced radiance

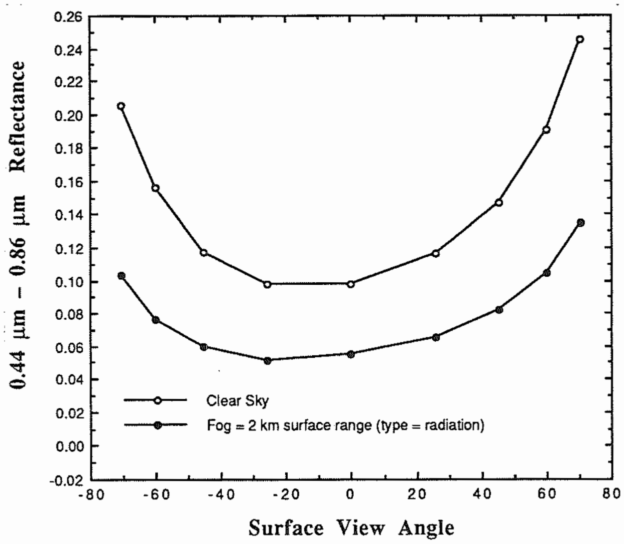

Figure 3. Band-Differenced Angular Signatures for a SZA = 60° and a RAZ = 60°/120°. The atmospheric/oceanic details are in the text.

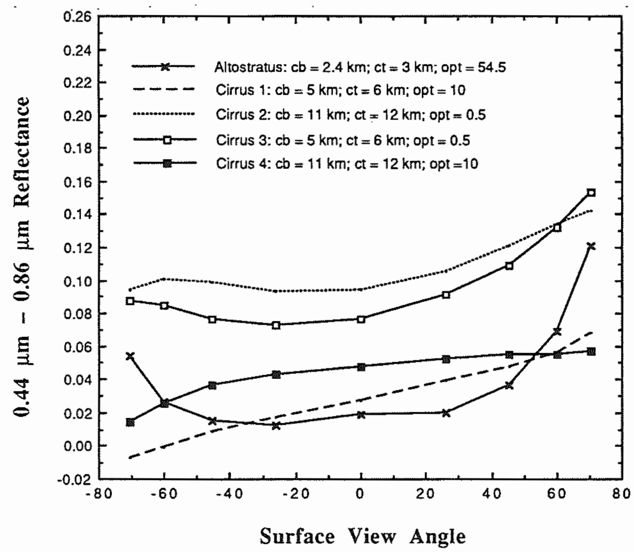

Figure 4. Band-Differenced Angular Signatures for a SZA = 60° and a RAZ = 60°/120°. The atmospheric/oceanic details are in the text. (Cloud models from Shettle *et al.*, 1988; cb = cloud base height; ct = cloud top height; opt = cloud optical thickness @ 0.55 μm)

contribution, thus simulating the worst possible case in using the BDAS for cloud discrimination. The same 0.5 optically thick cirrus cloud detectable by the predetermined thresholds, as well as other cloud forms, were used in the BDAS simulations. All viewing/solar geometries have been examined with the typical results shown in Figure 3 and 4. In these figures, the negative view angles are picking up the forward scatter. Figure 3 shows that clear sky and surface fogs both have a "bowl" shaped BDAS. Thus from their BDAS pattern alone, clear sky and fog cannot be discriminated. Figure 4 shows the BDAS for 5 different clouds. Unlike clear/foggy skies, a distinct feature of cirrus clouds is the decrease in band difference reflectance with increasing viewing obliquity in the forward-scatter direction (surface view angle < 0). As demonstrated in Figure 4, this feature is more pronounced with increasing cloud height and optical thickness. For the lowest thin cirrus, the band-differenced reflectance increases slightly with viewing obliquity. This increase is much more gradual than that of clear/foggy skies. The altostratus cloud with a cloud top height of 3 km is low enough to pick up the "bowl" like pattern of the clear/foggy sky BDAS; thus, it cannot be discriminated against clear sky based on the BDAS pattern alone. However, when coupled with the PCST, clear sky and cloud can be discriminated.

The largest uncertainty in the results probably lies in the LOWTRAN 7 cirrus cloud model. The cirrus ice particles used in LOWTRAN 7 are spherical rather than cylindrical or platelets. The errors brought about when using the spherical assumption over, say, the hexagonal assumption are in the relative change of extinction cross-section (C_e), from 0.44 μm to 0.86 μm, between the two shapes. From Takano and Liou (1989), there is a 1.5% increase from C_e(0.44μm) to C_e(0.86μm) for the spherical particle and no increase for the hexagonal particle. From this, the uncertainty in the use of spherical ice particles over hexagonal ice particles in the BDAS calculations is expected to be small for the cirrus cloud contribution to the total band-differenced reflectance.

4 Summary

This study has developed a new cloud detection technique. This new technique takes advantage of the multi-angle viewing capability of the Multi-angle Imaging SpectroRadiometer (MISR). By combining the spectral and angular information of the radiance emerging from the scene, the Band Differenced Angular Signature (BDAS) is formed. MISR's 0.86 μm reflectance is subtracted from the 0.44 μm reflectance and is plotted as a function of view angle. The resulting BDAS discriminates between cirrus clouds and lower level clouds/fog/clear sky. With the addition of the Predetermined Clear Sky Threshold (PCST), the clear sky scenes are readily identified. Without any *a priori* knowledge of the atmospheric and oceanic conditions, this new method is capable of detecting cirrus clouds as thin as 0.5 visible optical thickness. If *a priori* information of the atmospheric and oceanic conditions is known, as required/assumed by most other cloud detection algorithms, then thinner cirrus clouds would most assuredly be detectable.

References

Cox, S.K., 1971: Cirrus clouds and the climate. *J. Atm. Sci.* 28, 1513-1515.

Diner, D.J., C.J. Bruegge, J.V. Martonchik, T.P. Ackerman, R. Davies, S.A.W. Gerstl, H.R. Gordon, P.J. Sellers, J. Clark, J.A. Daniels, E.D. Danielson, V.G. Duval, K.P. Klaasen, G.W. Lilienthal, D.I. Nakamonto, R.J. Pagano, and T.H. Reilly, 1989: MISR: A Multiangle Imaging SpectroRadiometer for geophysical and climatological research for EOS. *IEEE Trans. Geosci. Rem. Sens.* GE-27, 200.

Dozier, J., 1991: Recommended instruments for the restructured Earth Observing System. *The Earth Observer* 3(6), 1-8.

JPL, 1990: *Preliminary experiment implementation plan for the Earth Observing System (EOS) Multi-angle Imaging SpectroRadiometer (MISR).* Jet Propulsion Laboratory, California Institute of Technology, Pasadena, CA.

Kneizys, F.X., E.P. Shettle, L.W.Abreu, J.H. Chetwynd, G.P. Anderson, W.O. Gallery, J.E.A. Selby and S.A. Clough, 1988: Users guide to LOWTRAN 7. *AFGL-TR-88-0177.*

Manabe, S. and R.T. Wetherald, 1967: Thermal equilibrium of the atmosphere with a given distribution of relative humidity. *J. Atm. Sci.* 24, 241-259.

NASA, 1991: *EOS reference handbook.* NASA Goddard Space Flight Center, Greenbelt, MD.

Preisendorfer, R.W. and C.D. Mobley, 1986: Albedos and glitter patterns of a wind-roughened sea surface. *J. Phys. Oceanogr.* 16, 1293-1316.

Shettle, E.P., F.X. Kneizys, S.A. Clough, G.P. Anderson, L.W.Abreu and J.H. Chetwynd, 1988: Cloud models in LOWTRAN and FASCODE. *CIDOS-88*, October 18-20 workshop, Silver Springs, MD.

Stephens, G.L., S.-C. Tsay, P.W. Stackhouse, and P.J. Flatau, 1990: The relevance of the microphysical and radiative properties of cirrus clouds to climate and climatic feedback. *J. Atm. Sci.* 47, 1742-1753.

Takano, Y. and K.N. Liou, 1989: Solar radiative transfer in cirrus clouds. Part I: Single-scattering and optical properties of hexagonal ice crystals. *J. Atmos. Sci.* 46, 3-19.

On the Retrieval and Analysis of Multilevel Clouds

Bryan A. Baum and Bruce A. Wielicki

Atmospheric Sciences Division, NASA Langley Research Center, Hampton, VA, USA 23665-5225

1 Introduction

An accurate satellite retrieval of cloud properties depends upon the detection and analysis of multilayered, overlapping cloud systems that surface observations show to be common. Multiple cloud layers are often found, for instance, in frontal situations, where cirrus overlays boundary layer convective cloud or low-to mid-level stratus cloud. Surface observers (Hahn et al., 1982) indicate that over ocean in the Northern Hemisphere between 30°N and 60°N, 51 percent of observations are of multilevel clouds. A satellite analysis by Coakley (1983) over the Pacific Ocean finds that more than 50 percent of 500 (250 km)^2 frames exhibit evidence of multilayered cloud systems. The questions addressed in this study are the following: What error is introduced when inferring the cloud pressure from a field-of-view (FOV) that contains some arbitrary amount of transparent cloud overlaying a lower-level black cloud, such as stratus, by making the assumption that there is only a single cloud layer in the FOV, and what may be done to improve the cloud retrieval?

The CO_2 slicing methods (e.g. McCleese and Wilson, 1976; Smith and Platt, 1978; Chahine, 1974) have been shown to provide accurate means of inferring cirrus cloud altitude from passive infrared radiance measurements. The CO_2 techniques have been applied to radiometric data from several instruments, notably the High Resolution Infrared Radiometric Sounder (HIRS/2, hereafter referred to as HIRS), the VISSR Atmospheric Sounder (VAS) (e.g., Menzel et al., 1983; Wylie and Menzel, 1989), and most recently to the High Resolution Interferometer Sounder (HIS) (Smith and Frey, 1990). The methods take advantage of the fact that infrared CO_2 sounding channels spaced closely in wavenumber each have varying opacity to CO_2, thereby causing each channel to be sensitive to a different level in the atmosphere. The techniques have been shown to be effective for single-layered, nonblack, mid- to high-level clouds such as cirrus, but are generally applied operationally to any given cloud occurrence. The CO_2 slicing algorithms are most accurate for clouds that occur in a single, well-defined layer, or for multi-layered cloud cases in which the uppermost cloud layer is nearly black. Significant cloud height retrieval errors may ensue if the HIRS field-of-view (FOV) is contaminated with low cloud. McCleese and Wilson (1976) have shown that the retrieved cloud height for the case of multiple cloud layers is a weighted average of the cloud heights actually present. The weight is approximately proportional to the product of the cloud height and the effective cloud amount. The effect of their result is that the uppermost cloud layer dominates the cloud pressure retrieval. Beyond stating that the higher cloud dominates the cloud pressure retrieval, there is no quantitative information to provide a way of estimating the errors in cloud pressure retrieval one should expect for certain common multilevel cloud situations or any suggestions on how to reduce the errors. In this paper we estimate the magnitude of the errors and use a simple algorithm to reduce the errors in optically thin cloud height retrieval.

2 Data

Bermuda was one of the sites chosen as part of the First Global Surface Radiation Satellite Data Validation Experiment held during April 1989. The purpose of this global experiment was to obtain high-quality Surface Radiation Budget (SRB) observations to serve as validation targets, and later as development tools, for SRB retrievals that are based on satellite data. The data set for this project includes both satellite observations of the region and surface observations including lidar, Navy sondes, and SRB-sponsored sondes to provide temperature and humidity data and measurements of surface radiative fluxes. For this study, we will present results from a scene of cirrus overlaying a boundary layer stratus cloud for a 5° by 5° region centered at Bermuda taken on April 16, 1989, at approximately 6 UTC.

2.1 Satellite Data

The Advanced Very High Resolution Radiometer (AVHRR) instrument is flown on the NOAA series of operational satellites. The Sun-synchronous NOAA satellite has nominal Equator crossing times of 0730 and 1930 local solar time (LST). High-resolution (1.1-km) AVHRR data are used in this study. The AVHRR instrument is comprised nominally of five channels: visible (0.63 μm), near infrared (0.83 μm), and three infrared window channels of 3.7 μm, 10.8 μm, and 12 μm.

The High Resolution Infrared Radiation Sounder (HIRS/2) is one of the instruments that make up TOVS (TIROS Operational Vertical Sounder; TIROS is the Television and Infrared Observation Satellite). The TOVS instrument package is also flown on the NOAA series of satellites. The HIRS/2 instrument receives visible and infrared radiation through a single telescope, and splits the radiation into 19 infrared channels and 1 visible channel by means of a rotating filter wheel. Seven channels are located in the near-infrared region (3.7 to 4.6 μm), 12 channels are located in the infrared region (6.7 to 15 μm), and 1 channel is in the visible light region (0.69 μm). The HIRS FOV is approximately 18 km at nadir but enlarges to approximately 30 km $\times$ 58 km towards the edge of the scan line. HIRS was designed to provide temperature and water vapor sounding profiles, with the result that it has gaps between fields of view and cannot be used for imaging purposes.

2.2 Temperature and Humidity Profiles

During the Bermuda SRB mission, special rawinsonde launchings were used to enhance the standard National Weather Service soundings. For extended time or spatial observations, we use ECMWF (European Center for Medium-Range Weather Forecasting) gridded analyses as the primary source of temperature and humidity data.

2.3 Merging HIRS and AVHRR Data

In Baum et al. (1992), a technique was described in which AVHRR data were collocated with individual HIRS pixels. The HIRS pixel, having a nadir field-of-view (FOV) of approximately 18 km, is much larger than the 1.1-km AVHRR pixel. Further, the individual HIRS FOVs are spaced apart from each other both within a scan line and between scan lines. There is no reason, however, to use only the higher-resolution AVHRR data that are collocated with an individual HIRS FOV. A more logical approach is to use all of the AVHRR data and superimpose the HIRS FOVs over the AVHRR imaging data.

3 Methodology

3.1 HIRS Analysis

First, a set of theoretical optically thick cloudy-sky radiances I^i_{cld} are derived (e. g. Wielicki and Coakley, 1981) that are functions of cloud-top pressure P_{cld}, scan angle, and HIRS channel i. The cloud signal is the change in measured radiance at a particular wavenumber due to the presence of a single layer of cloud that may be optically thin or have partial cloud cover. The cloud signal is given by

$$\Delta I^i_{cld} = I^i_{calc} - I^i_{clear} = \epsilon^i A_{cld}[I^i_{cld}(P_{cld}) - I^i_{clear}], \qquad (1)$$

where the superscript denotes channel wavenumber dependence. Here I_{clear}, I_{cld}, and I_{calc} are the clear-sky radiance, the black-cloud radiance, and the radiance of a partially filled FOV, respectively. The cloud emittance is given by ϵ^i.

The determination of the clear-sky radiance is of great importance. Clear-sky radiances may be calculated from a priori knowledge of the temperature and humidity profiles. These profiles may come from rawinsonde profiles or from gridded temperature and humidity products such as those provided by the National Meteorological Center (NMC) or by the European Center for Medium-Range Forcasting (ECMWF). Another method is to search the scene for nearby "clear" pixels and assume that the surface conditions do not change between the "clear" pixels and the cloud-filled pixels. However the clear-sky radiance is determined, the calculation of the theoretical upwelling radiance will be influenced by the presence of low-cloud contamination.

The cloud-top pressure may be determined using, for example, the radiance ratioing method as discussed in Wylie and Menzel (1989), Smith and Frey (1990), and Smith and Platt (1978). The technique involves taking a ratio of the cloud signals, defined to be the change in upwelling radiance seen by the satellite due to the presence of cloud. For two spectral channels at wavenumbers ν^i and ν^j that are looking at the same FOV, the equation for the ratio G of the cloud signals for two channels is

$$G(P_{cld}) = \frac{I^i_{meas}(\nu^i) - I_{clear}(\nu^i)}{I^j_{meas}(\nu^j) - I_{clear}(\nu^j)} = \frac{\epsilon^i \int_{P_{clear}}^{P_{cld}} \tau(\nu^i, P)\frac{dB[\nu^i, T(P)]}{dP}dP}{\epsilon^j \int_{P_{clear}}^{P_{cld}} \tau(\nu^j, P)\frac{dB[\nu^j, T(P)]}{dP}dP}. \qquad (2)$$

In (2), I_{meas} and I_{clear} are the measured and clear-sky radiances, respectively; $dB[\nu, T(P)]$ is the Planck radiance calculated at temperature $T(P)$ and wavenumber ν; ϵ is the spectral emittance; and $\tau(\nu, P)$ is the fractional transmittance of radiation from the atmosphere at pressure P to the satellite radiometer. For two channels spaced closely in wavenumber, we make the assumption that $\epsilon^i = \epsilon^j$. The function G can be seen to be independent of both cloud opacity and the effective cloud amount. However, G is dependent on the weighting functions of the two channels, the cloud height, and the atmospheric temperature and humidity profile.

In order to calculate the G function, an estimate must be determined for the representative "clear" radiance appropriate for the HIRS FOV. The "clear" radiance may be taken either from a nearby "clear" FOV or from a theoretical upwelling radiance calculated from knowledge of the atmospheric temperature and humidity profiles. The operational approach outlined by Smith and Frey (1990) is to locate representative clear sky radiances from nearby regions and average the clear-sky radiances to form a composite "clear" radiance. In this study, however, we are able to provide additional information for the HIRS algorithm by using the collocated AVHRR data.

3.2 Spatial Coherence

When low clouds (below 700 mb) are present, a rough estimate of cloud pressure can be made using the HIRS 11-μm channel and assuming that the low cloud has an emittance of 1 and fully fills the HIRS FOV. A better way of deriving low cloud properties is to implement the spatial coherence techniques detailed in, for example, Coakley and Bretherton (1982) and Coakley (1983) using the higher spatial resolution AVHRR data. The spatial coherence method is designed to determine the properties of optically thick cloud that covers an areal extent much greater than the individual pixel size, and requires both completely cloud-covered and completely clear fields-of-view. The basic technique employed is to use the local spatial structure of the 10.8-μm field in order to identify the spatially uniform clear-sky and cloud radiances. The method is well suited for analysis of an extensive, optically thick cloud such as stratocumulus that resides in a well-defined layer. The method fails for the case of subresolution clouds in which all clouds are smaller than the FOV, such as trade cumulus, and clouds with variable emissivity such as high, thin cirrus.

For the Bermuda data, we implemented an automated feet detection technique (Coakley, personal communication, 1991) to determine the clear-sky and cloudy-sky radiances. When using 1.1-km AVHRR data, we find that one or at most two feet are determined for each HIRS FOV for this particular case study, with few exceptions.

4 Theoretical Error Analysis

What errors are expected theoretically when a field-of-view (FOV) contains more than one layer of cloud and the upper cloud layer is semi-transparent? For simplicity, we assume that cirrus is present over a black surface, whether it be the actual surface or a lower cloud deck. The upwelling infrared radiation from the Earth-atmosphere system can be modeled for several of the HIRS-2 15-μm CO_2 sounding channels given a knowledge of the background temperature and humidity profiles and also the profiles of trace gases such as CO_2 and ozone. For a single-layered cloud, it is then possible to infer the cloud-top pressure regardless of the cloud's transmittance by using a combination of HIRS channels. For two cloud layers, the upwelling radiances for the HIRS 15-μm channels are determined for the case in which a black cloud is located at a fixed pressure level, such as 850 mb. For these cases, the inferred HIRS cloud-top pressures are determined by assuming that there is no lower cloud.

The effect of lower cloud contamination in a HIRS FOV is given in Fig. 1a for the HIRS 5/6 channel combination and in Fig. 1b for the 6/7 HIRS channel combination. The central wavenumbers for NOAA-11 HIRS channels 5, 6, and 7 are 13.95 μm, 13.66 μm, and 13.34 μm, respectively. Note that no other retrieval errors, such as instrument noise or uncertain clear-sky radiances, are present. In Figs. 1a and 1b, the low cloud is "black" and is located at 850 mb. Channel 7 has a higher transmissivity at the surface than channel 6, which in turn has a higher transmissivity than channel 5. Thus, channel 7 is more sensitive to variations in surface temperature than either channel 5 or channel 6. The "measured" HIRS radiances for the chosen channels are derived from the theoretical upwelling radiance profiles calculated from midlatitude temperature and humidity profiles measured at Bermuda on April 16, 1989, at approximately 6 UTC. Calculations are performed for a range of upper-layer cloud heights ranging from 250 mb to 670 mb and a range of effective cloud amounts. Contours are drawn at 25-mb intervals for the difference between the retrieved cloud pressure and the actual cloud pressure of the upper cloud layer. The difference in retrieved versus actual cloud pressure, a bias, is positive, showing that the retrieved cloud pressure is higher than the actual cloud pressure for all cases. A higher retrieved cloud pressure means that the retrieved cloud heights will be lower than the actual cloud heights. It can be seen from inspection of Figs. 1a and 1b that the cloud retrieval error is greater for the 6/7 channel combination than for the 5/6 channel combination. The error increases for the channel combination that has the greatest transmittance at or near the surface. As an example, we take the case of using the 6/7 HIRS channel combination to examine a HIRS FOV in which a high cloud with an effective cloud amount of 0.5 overlays a black stratus cloud located at 850 mb. From Fig. 1b, we find that the retrieved cloud pressure will actually be approximately 50 mb higher. A 50-mb pressure difference in this case relates to a cloud height error of approximately 1 km. The cloud pressure error can be seen to increase rapidly with decreasing effective cloud amount. Lidar studies (Platt et al., 1987) indicate typical cirrus emittances of 0.1 to 0.35, which would give errors of 75 to 200 mb for the HIRS 6/7 channel combination and 50 mb to 150 mb for the HIRS 5/6 channel combination.

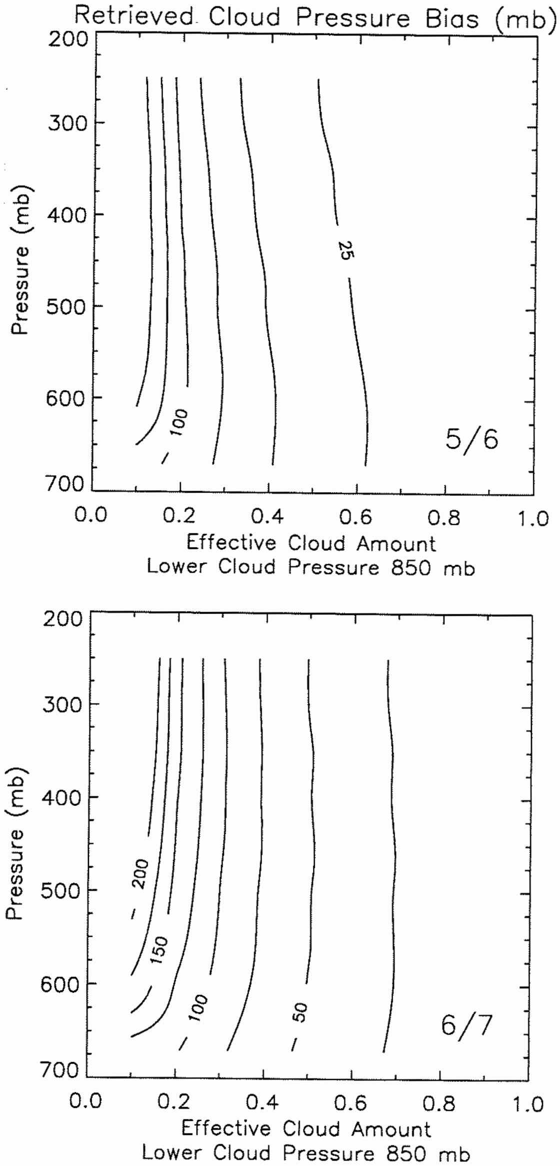

Figure 1: HIRS Pressure Retrieval Bias Error. The cloud pressure bias is defined as the retrieved cloud pressure minus the true cloud pressure.

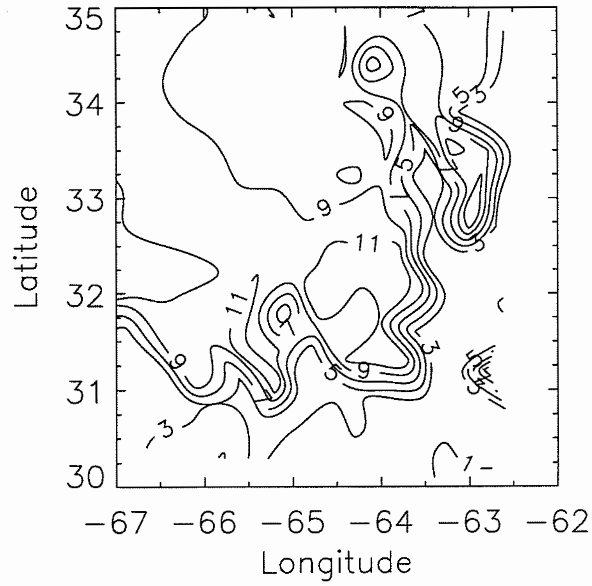

Figure 2: HIRS Channel 6/7 cloud height results for the multilevel cloud scene of April 16, 1989, at approximately 6 UTC, in the vicinity of Bermuda. The cloud heights are uncorrected for the presence of a lower cloud deck located at approximately 1.5 km. Height contours are in km.

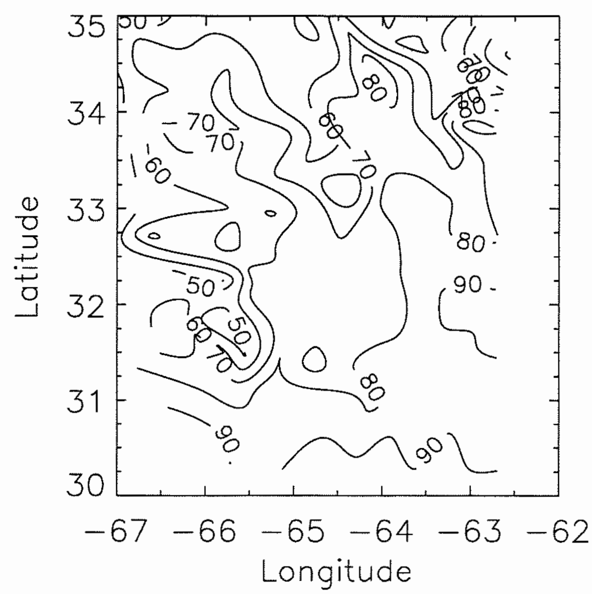

Figure 3: Spatial coherence results for the multilevel cloud scene of April 16, 1989, at approximately 6 UTC, in the vicinity of Bermuda. Radiances are in units of $mWm^{-2}str^{-1}cm$.

5 Bermuda Data

The Bermuda data are used to provide an example of retrieving cirrus cloud heights in a multilevel cloud scenario. The scene chosen for study is of a large stratus cloud deck with cirrus of varying thickness overlaying the lower cloud. The results from HIRS 6/7 cloud height analysis with no correction due to the presence of a lower cloud deck is shown in Fig. 2.

One way of reducing the error in the HIRS cloud pressure retrieval is to incorporate spatial coherence results into the cloud retrieval algorithm to locate the lower cloud deck. The application in the spatial coherence algorithm results in the determination of a clear-sky foot at approximately 95 ± 1 $mWm^{-2}str^{-1}cm$. A contour plot of the retrieved radiances using spatial coherence analysis is shown in Fig. 3. For groups of 1.1-km AVHRR pixels located over the lower cloud deck, the arch feet indicate that the radiance of the lower cloud deck varies between 84 ± 2 $mWm^{-2}str^{-1}cm$.

Our algorithm may be described as a three-step process. First, calculate the HIRS cloud height assuming one cloud layer in the FOV. Second, apply the spatial coherence algorithm to the collocated AVHRR 11-μm data and determine the average radiance of the lower cloud layer. The third step is to recalculate the HIRS cloud height based on the lower cloud deck radiances. The surface in the HIRS algorithm is redefined to be the height of the lower cloud as determined by spatial coherence analysis of the AVHRR data. This approach will most affect the HIRS cloud height retrievals for those pixels that contain optically thin cloud.

The results of recalculating the HIRS cloud heights are given in Fig. 4 for the 6/7 HIRS channel combination. In this figure, the difference is defined as the corrected minus the uncorrected HIRS cloud height in km. The range of height correction falls between 0.25 and 1.5 km for this scene.

This technique by itself cannot determine with certainty that multilevel clouds may be present in a single HIRS FOV. However, there are other textural techniques using the AVHRR data that may provide additional information on the composition of a group of pixels in order to aid classification.

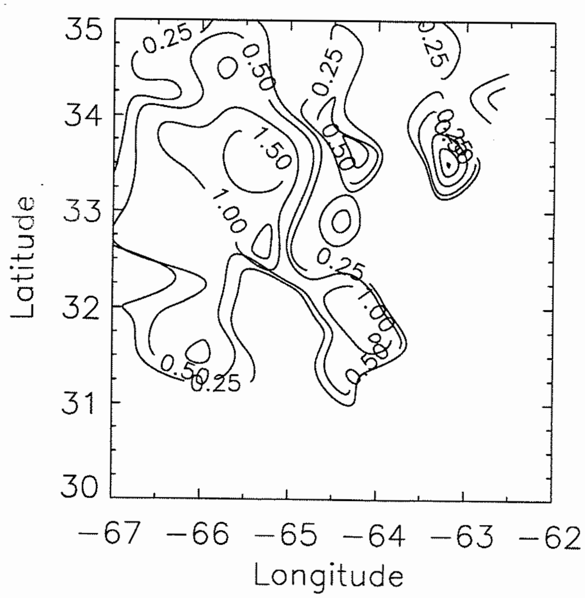

Figure 4: HIRS Channel 6/7 cloud height difference results for the multilevel cloud scene of April 16, 1989, at approximately 6 UTC, in the vicinity of Bermuda. The cloud height differences are defined as the corrected cloud height minus the uncorrected cloud height in km.

6 Conclusions

Significant errors in cloud pressure retrieval, using the conventional sounding channel methods outlined in this study, may be the result if more than one cloud layer is present. Progress in identifying and analyzing multilevel cloud scenes may be made by using the methodology detailed by Baum et al. (1992) for merging data from both the AVHRR and HIRS satellite instruments aboard the NOAA operational platforms. In this study, we show how the spatial coherence algorithm may be used to determine whether low clouds exist in the scene of study, determine the low cloud height, and use that low cloud height in subsequent analysis of the HIRS data. Spatial coherence is one of the simplest textural techniques by which to determine whether multilevel clouds are present. A more complex scheme could be implemented that utilizes more textural features such as that proposed by Welch et. al. (1988).

References

Baum, B. A., B. A. Wielicki, P. Minnis, and L. Parker, 1992: Cloud property retrieval using merged HIRS and AVHRR data. *J. Appl. Met.*, **31**, No. 4, 351-369.

Chahine, M. T., 1974: Remote sounding of cloudy atmospheres. I. The single cloud layer. *J. Atmos. Sci.,*, **31**, 233-243.

Coakley, J. A., Jr., 1983: Properties of multilayered cloud systems from satellite imagery. *J. Geophys. Res.*, **88**, 10,818-10,828.

Coakley, J.A., Jr., and F. P. Bretherton, 1982: Cloud cover from high resolution scanner data: Detecting and allowing for partially filled fields of view. *J. Geophys. Res.*, **87**, 4917-4932.

Hahn, C. J., S. G. Warren, J. London, R. M. Cherrin, and R. Jenne, 1982: Atlas of simultaneous occurrence of different cloud types over the ocean. NCAR Technical Note, TN-201+STR, 211 pp.

McCleese, D. J., and L. S. Wilson, 1976: Cloud top heights from temperature sounding instruments, *Quart. J. Roy. Met. Soc.*, **102**, 781-790.

Menzel, W. P., W. L. Smith, and T. R. Stewart, 1983: Improved cloud motion wind vector and altitude assignment using VAS. *J. Clim. Appl. Meteor.*, **22**, 377-384.

Platt, C. M. R., J. C. Scott, and A. C. Dilley, 1987: Remote sounding of high clouds. Part VI: Optical properties of midlatitude and tropical cirrus. *J. Atm. Sci.*, **44**, No. 4, 729-747.

Smith, W. L., and R. Frey, 1990: On cloud altitude determinations from high resolution interferometer sounder (HIS) observations. *J. Appl. Met.*, **29**, 658-662.

Smith, W. L., and C. M. R. Platt, 1978: Comparison of satellite-deduced cloud heights with indications from radiosonde and ground based laser measurements. *J. Appl. Met.*, **17**, 1796-1802.

Welch, R. M., S. K. Gupta, and K. S. Kuo, 1988: Marine Stratocumulus Cloud Fields Off the Coast of Southern California Observed Using Landsat Imagery, Part II: Textural analysis. *J. Appl. Met.*, **27**, No. 4, pp. 363-378.

Wielicki, B. A., and J. A. Coakley, Jr., 1981: Cloud retrieval usin infrared sounder data: Error analysis. *J. Appl. Meteor.*, **20**, 15' 169.

Wylie, D. P., and W. P. Menzel, 1989: Two years of cloud cc statistics using VAS. *J. Clim.*,**2**, 380-392.

GLOBAL RAIN ESTIMATES USING A COMBINATION OF LOW-ORBIT MICROWAVE AND GEOSYNCHRONOUS IR DATA

Robert F. Adler (1)
George J. Huffman (2)
Andrew J. Negri (1)
Peter R. Keehn (3)

(1) NASA/GSFC, Laboratory for Atmospheres, Greenbelt, MD, USA 20771
(2) Universities Space Research Association, NASA/GSFC, Laboratory for Atmospheres, Greenbelt, MD, USA 20771
(3) Science Systems and Applications Inc., Lanham, MD, USA 20706

1. INTRODUCTION

Knowledge of the time and space patterns of climate-scale precipitation is important in the diagnosis of the global climate system, including understanding the general circulation of the atmosphere. Observations from space are critical in producing global, or semi-global estimates because of the large areas of the globe with inadequate or non-existent surface data. The estimation of mean monthly rainfall from satellite observations, however, immediately faces difficulties related to the inherent limitations of the observations. In order to have a good physical connection between the radiance observed and the instantaneous rainrate, one is drawn to the microwave portion of the spectrum where the radiances are responsive to precipitation-sized particles. However, that choice limits the observations to those from low-orbit satellites, with their inherent sampling limitations (one, or at the most two, views a day with a single satellite). The geosynchronous IR data have the advantage of high time resolution (important for rapidly changing precipitation patterns and for the detection of diurnal signals), but lack a strong physical connection between the remotely-sensed signal and the surface rainfall.

Adler et al. (1992) have applied a simple method to take advantage of the strengths of both the low-orbit microwave and geosynchronous IR observations and combine them into a monthly mean rain estimate. This paper describes the application of that technique to a global data set.

2. THE MICROWAVE TECHNIQUE

The microwave technique used in this global application has been described by Adler et al. (1992). The algorithm is uses the scattering signal produced by precipitation-sized ice particles in clouds to define precipitation areas and assign rain rates. The scattering signature is defined primarily by the 86 GHz frequency on the Special Sensor Microwave/Imager (SSM/I) instrument flying on the polar orbiting Defense Meteorological Satellite Program (DMSP) satellite. Other frequencies (19 through 37 GHz) are used to identify and eliminate surface features (snow on ground, cold ocean, and some desert) that could be misidentified as precipitation.

The scattering by ice produces lowered brightness temperature (T_b) values over rain areas at 86 GHz. Based on cloud model-microwave radiative transfer model calculations, a rain/no rain cutoff of 247 K (1 mm h^{-1}) is selected and a T_b-rain rate relation of $T_b = 251.0 - 4.19R$ is derived.

The result of applying the algorithm to a month of SSM/I data is shown in Fig. 1 in terms of monthly total rain in 0.5^o by 0.5^o latitude-longitude areas. Although the small size of the averaging area produces a noisy field due to the limited number of samples at each grid box, the general pattern is very reasonable, with a clearly defined, narrow ITCZ (Inter-Tropical Convergence Zone), sub-tropical dry zones and the mid-latitude rain maxima.

3. CALIBRATING GLOBAL IR DATA WITH MICROWAVE DATA

a. *Concept*

The microwave technique discussed above should have a small bias because the physical basis for the relation between brightness temperatures and rainrate is fairly direct. However, all microwave instruments currently fly on polar-orbiting satellites, providing relatively sparse sampling in time. On the other hand, even though the physical basis for relating IR data to rainfall is fairly weak, a number of geosynchronous-orbit platforms carry IR instruments and provide nearly continuous coverage around the globe in space and time. Our goal is to use cases of coincident microwave and IR data to compute an IR rainrate relationship that matches (i.e., is "calibrated" by) the microwave rainrate. These calibrated IR rainrate relationships will slowly vary in time and space. The calibrated IR rainrate relationships are then applied to all the geosynchronous satellite data to take advantage of the superior time sampling.

b. *Data*

The SSM/I data were observed by the F8 DMSP, whose ascending equatorial crossing occurs at about 6:30 local time. Histograms of the estimated microwave-based rainrate and the rain totals were collected onto a 0.5^olon x 0.5^olat grid, and averaged to a 2.5^ox2.5^o latitude-longitude grid for pentads (5-day periods). The best way to obtain the microwave-IR matchups for derivation of the calibration relations would be to use the IR sensor on board the same satellite as the SSM/I. Although there is such a companion sensor, the Optical Line Scanner (OLS), the digital data from that sensor is only very recently becoming routinely available. Therefore, "coincident" IR data for this study was provided by the NOAA-10 AVHRR, whose ascending equatorial crossing occurs at about 8:30 local time. Histograms of brightness temperature are provided by NMC/CAC on a 2.5^ox2.5^o grid for pentads for this sensor. These AVHRR histograms are considered a temporary expedient, since the AVHRR swaths are more than 2 hr behind the SSM/I and cover larger geographical regions than the SSM/I.

Finally, global IR data was provided by the Global Precipitation Climatology Project (GPCP) merged GEO-LEO product, which provides histograms of brightness temperature on the same time-space grid as the AVHRR IR.

c. *Calibration*

The SSM/I data display considerably more small-scale variance than the IR data, both due to differences in physical processes responsible for the signals, and deficiencies in the SSM/I sampling. We wish to smooth the SSM/I to account for the sampling, since we expect variations in the calibration ratios to be meaningful only on relatively large space and time scales. Currently, we smooth with an evenly weighted 3x3 grid-cell filter and compute the ratio for a month. Cyclic boundary conditions apply on the east and west boundaries of the grid, and "missing" boundary values are set at the north and south sides. For consistency, the AVHRR data are also smoothed with the 3x3 filter.

The last pre-processing step is to ensure that the monthly averages of SSM/I and AVHRR are constructed from coincident data. We ignore any pentad for which either data set has high rates of missing data.

The calibration coefficients are expressed as the ratio

$$\frac{\text{SSM/I rainfall for month in matched pentads}}{\text{AVHRR rainfall for month in matched pentads}}.$$

The rainfall estimated from the IR data (either the AVHRR on the polar orbiter, or the geosynchronous satellites) uses the Geosynchronous Precipitation Index (GPI) IR algorithm of Arkin and Meisner (1987), which assigns a rainrate of 3 mm h^{-1} to clouds colder than 235 K in the IR.

In practice the ratios are limited to the range [0.2, 5] to prevent unreasonable behavior in regions of small rainfall, where sampling fluctuations may have first order importance. Finally, the monthly average merged GEO-LEO IR rainfall estimate is multiplied by the calibration ratios.

4. RESULTS

Fig. 2 shows the results of the microwave technique in the top panel (2.5 by 2.5 degree resolution). The middle panel displays the GPI IR results using the eight times a day sampling from the geosynchronous satellites. The third panel shows the adjusted or calibrated GPI, with the adjustments being based on the calibration coefficients derived from the SSM/I-based rain estimates and the AVHRR results. The third panel is the result of multiplying the IR-based rain estimates in the second panel by the array of coefficients derived as explained before. The resulting adjusted GPI rain map (bottom panel) has the general bias of the microwave, but the smoothness of the original IR estimate because of the much larger number of samples going into each grid element.

The results of this initial test have been examined relative to ground validation data. Fig. 3 shows results of the three techniques seen in Fig. 2 in comparison to monthly totals in the area of Japan as determined from the operational radar-raingage network of the Japan Meteorological Agency (JMA) obtained from the GPCP. The results of validation over this one area indicates that the adjusted GPI outperforms both the microwave technique (poor sampling) and the GPI (significant cirrus cloud areas being identified as rain). The adjusted GPI has the lowest bias and lowest RMSE of all the techniques. Additional validation using raingage data from Pacific Ocean atolls indicates that the microwave technique is significantly underestimating the rain in that area and that the combined approach fails to improve the results over what is available from the GPI.

5. CONCLUSIONS

The basic approach of using the rain estimates based on the polar orbit microwave data to calibrate the geosynchronous IR-based estimates data appears valid and can be applied on a global basis. The approach is dependent, however, on the quality of the microwave estimates. The technique will be considerably improved when IR data from the same satellite as the SSM/I can be used to derive the calibration relations. Considerably more validation in a number of geographical areas will be necessary in order to completely evaluate the technique

REFERENCES

Adler, R. F., and A. J. Negri, 1992: Estimation of monthly rainfall over Japan and surrounding waters from a combination of low-orbit microwave and geosynchronous IR data. Accepted *J. Appl. Meteor.*

Arkin, P. A., and B. N. Meisner, 1987: The relationship between large-scale convective rainfall and cold cloud over the Western Hemisphere during 1982-84. *Mon. Wea. Rev.*,**115**, 51-74.

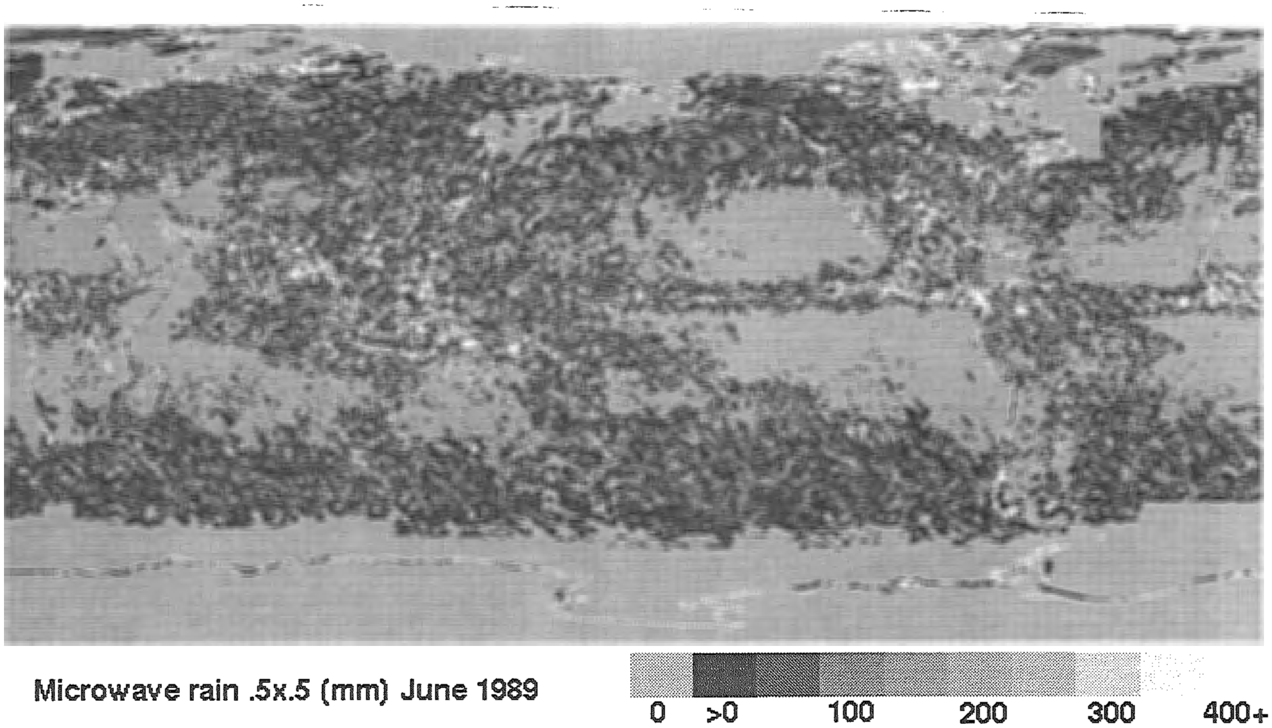

Figure 1. Global rainfall estimates (mm) from SSM/I data as computed by the Goddard Scattering Algorithm for June 1989 on 0.5° by 0.5° lon/lat grid.

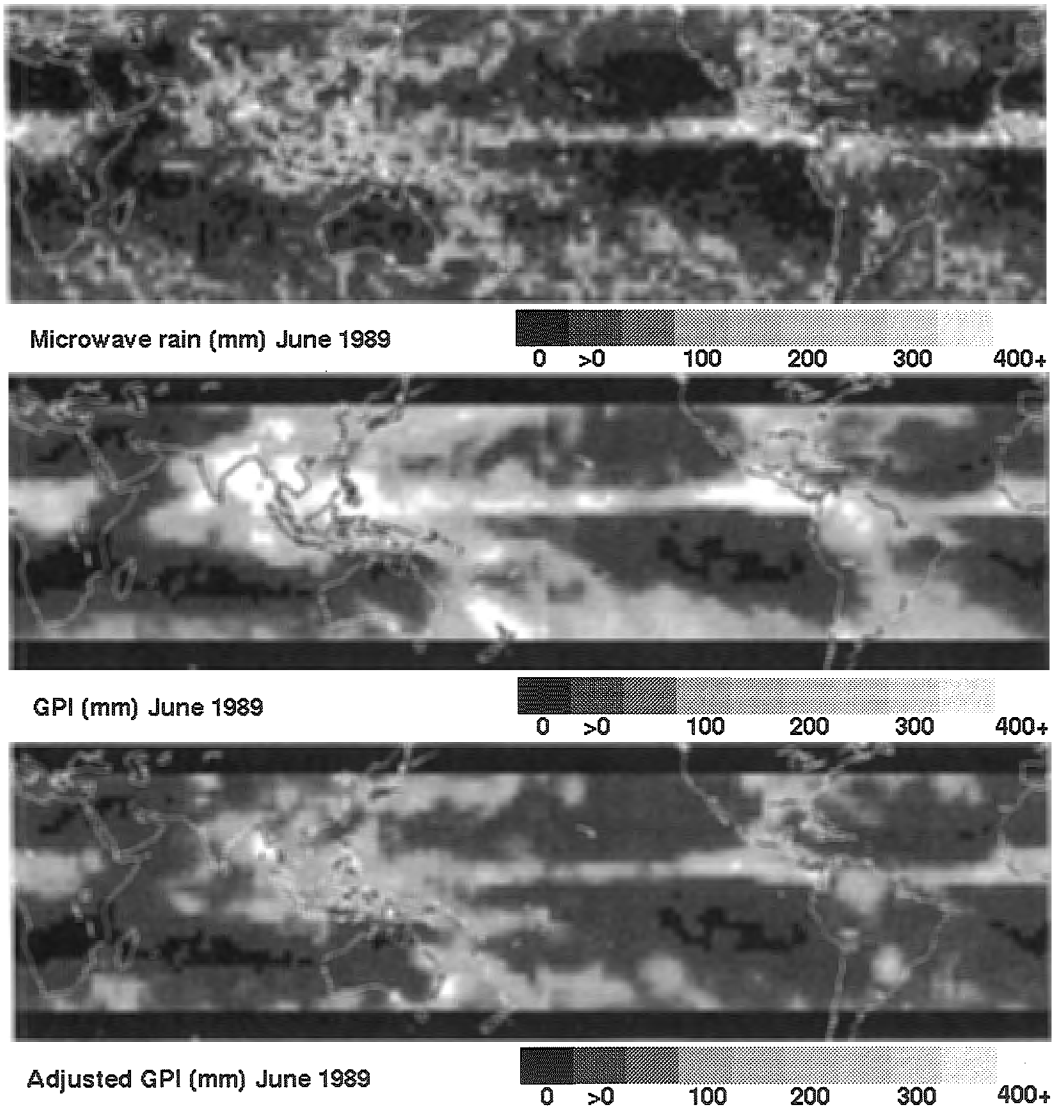

Figure 2. *Global images for June 1989 on 2.5° by 2.5° lon/lat grid of:*

(Top) *Rainfall estimates (mm) from SSM/I (no smoothing, all data) as computed by the Goddard Scattering Algorithm,*

(Middle) *Rainfall estimates (mm) from merged GEO/LEO IR as computed by the GPI, and*

(Bottom) *Adjusted rainfall estimates (mm) from GEO/LEO IR as computed by multiplying the GPI estimates by the calibration ratios.*

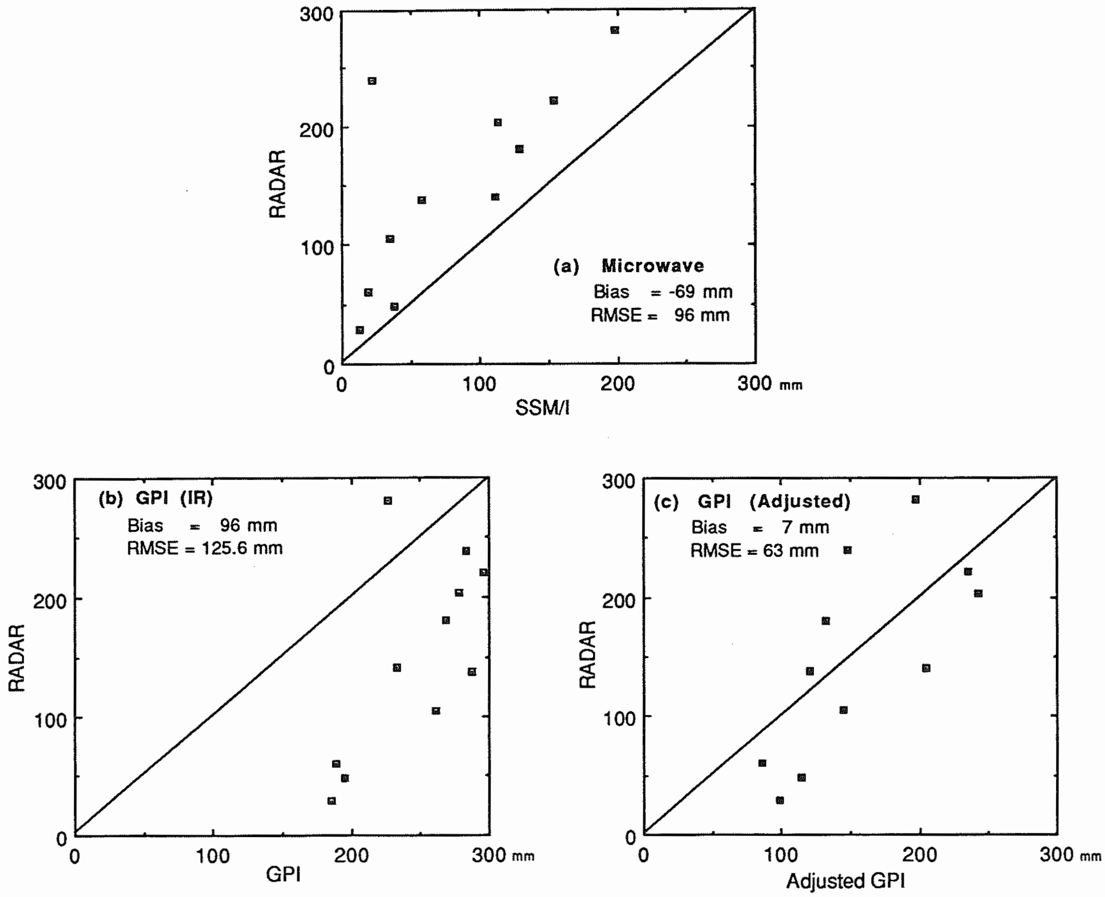

Figure 3. Verification scatter plots for June 1989 on 2.5° by 2.5° lon/lat grid of:

(a) Rainfall estimates (mm) from SSM/I (no smoothing, all data) as computed by the Goddard Scattering Algorithm,

(b) Rainfall estimates (mm) from merged GEO/LEO IR as computed by the GPI, and

(c) Adjusted rainfall estimates (mm) from GEO/LEO IR as computed by multiplying the GPI estimates by the calibration ratios,

versus rainfall totals from the JMA radar-raingage system.

SATELLITE ESTIMATION OF THE TROPICAL PRECIPITATION USING THE METEOSAT AND SSM/I DATA

Isabelle Jobard and Michel Desbois

Laboratoire de Météorologie Dynamique du CNRS,
Ecole Polytechnique, 91128 Palaiseau Cedex, France

I. INTRODUCTION

In tropical regions, the precipitations over land are produced mainly by convective systems or squall lines and are characterised by a high spatial and temporal variability. The methods currently utilized for the estimation from satellite imagery, of cumulated rainfall are simple statistical methods using the thermal infrared channel of geostationary satellite radiometers.

The aim of this present study is to improve these infrared methods by introducing some information on the localization of the precipitation areas which can be derived from the microwave satellite imagery. The procedure which is proposed is based on a classification method using the coincident infrared and microwave satellite measurements and also the full time resolution of the geosyncronous satellite infrared images.

II. SATELLITE DATASETS

The tropical region concerned in this study is the Sahelian region which is a band expanding from 10° N to 20° N in West Africa, where the annual precipitations range from 100 to 1000 mm.

The infrared dataset is composed of the full resolution images (5 km pixel) of the thermal infrared channel and the water vapor channel of Meteosat. It contains the half-hourly images for the two rainy seasons of 1988 and 1989.

The microwave dataset is obtained from the low and high frequency channels (19, 22, 37 and 86 GHz) of the SSM/I radiometer on board the DMSP low orbit satellite which is over-passing the studied region twice a day at 6.00 am and 6.00 pm.

III. A COMBINED INFRARED / MICROWAVE METHOD

The poor time sampling of the microwave dataset is an inconvenience for the estimation of the precipitation because of the high variability of the tropical rainfalls. On the other hand, the microwave radiances and especially the radiances of the high frequency 86 GHz channel, operating in the scattering mode (Wilheit, 1986) are well related to the precipitation rate (Szejwach et al., 1986).

On the contrary, the time sampling of infrared data is sufficiently high but the infrared radiances are only related to the cloud top temperatures and thus, are not related directly to the precipitation rate. The infrared methods assume that all cold clouds having a cloud top temperature below an appropriate threshold, are producing rain. This is acceptable in so far as large-area averages are considered and as the cold cloud occurrences are cumulated over a long time period.

The method which is studied in this paper, takes advantage of both, the good time and space resolution of the infrared satellite radiances, and the rain information retrieved from the microwave images. It combines the infrared and microwave data in order to use the microwave signal to contribute towards the discrimination of the clouds producing rain, among all the cold clouds. A classification method using a dynamic clustering technique allows the coincident infrared and microwave images to be classified into homogeneous classes characterising various types of clouds. This method is described in Jobard and Desbois, (1992-a).

The different time sampling of the infrared and microwave datasets leads to a two-step procedure : first, the classification of the low time-resolution coincident infrared and microwave images is carried out during the learning phase, then in the application phase, the 'rain index' images are computed from the high time-resolution infrared images. The details of this combined infrared/microwave method are given in Jobard and Desbois, (1992-b).

IV. RESULTS

The validation of this combined infrared/microwave method is studied using the ground precipitation measurements given by the dense network of raingauge recorders implemented by ORSTOM on the validation site of Niamey (Niger) for the EPSAT program which intends to improve the Estimation of Precipitation by Satellite over the Tropical Africa. The distribution of the raingauges over the 1° by 1° square site during the season of 1989 is displayed on figure 1.

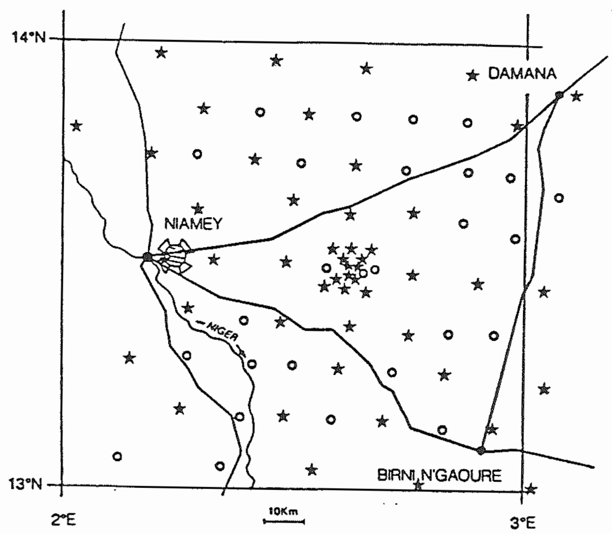

Figure 1. Distribution of the raingauges in the network of the validation site of Niamey, during 1989.

The correlation coefficients between ground measurements of the cumulated areal precipitation and the rain indices produced by the combined infrared/microwave method are compared to the correlation coefficients obtained with a simple infrared method. Several tests concerning additionnal parameters taken into account in the classification procedure, such as the infrared water vapor channel of Meteosat and the microwave low frequency channels of SSM/I, are discussed.

V. CONCLUSION

A method which combines the satellite microwave and infrared radiances for the estimation of tropical precipitations, takes advantage of both, the necessary good space and time resolution of the infrared imagery and the ability to distinguish between the raining and non raining clouds on the microwave images. The first results obtained for the studied tropical african region, indicate an improvement in comparison with the results obtained with a simple statistical infrared method.

REFERENCES

[1] T. T. Wilheit, "Some comments on passive microwave measurements of rain", *Bulletin American Meteorological Society,* Vol 67, N° 10, pp. 1226-1232, 1986.

[2] G. Szejwach, R. F. Adler, I. Jobard and R.A. Mack, "A cloud model-radiative model combination for determining microwave T_B-rain rate relations", *Preprints, 2nd Conference on Satellite Meteorology / Remote Sensing and Applications,* Williamsburg, Va., American Meteorological Society, pp. 444-449, 1986.

[3] I. Jobard, and M. Desbois, "A method combining infrared and microwave satellite radiances for the estimation of the tropical rain", *Preprints, 6th Conference on Satellite Meteorology and Oceanography*, Atlanta, Ga., American Meteorological Society, pp. 264-267, 1992-a.

[4] I. Jobard, and M. Desbois, "A classification method combining IR and MW satellite radiances to estimate the precipitations" *Proceedings of the Third Specialists Meeting on Microwave Radiometry and Remote Sensing,* Boulder, Co., U.S.A., January 14-16, 1992-b.

RETRIEVIENG MICROPHYSICAL PROPERTIES OF CLOUD TOPS BY MULTISPECTRAL ANALYSIS OF AVHRR DATA

Daniel Rosenfeld[1] and Garik Gutman[2]

[1]The Hebrew University, Jerusalem, Israel
[2]NOAA/NESDIS, Washington DC, USA

1. INTRODUCTION

It has been pointed earlier (Pilewskie and Towmey, 1987) that additional information about microphysics and rain processes near cloud tops can be gained by using the information from the reflected solar radiation in several wavelengths in the IR portion of the spectrum. The wavelength of 3.7 micron is strongly absorbed by water, and even more so by ice. In cloud, most of the absorption occurs in the larger particles, while the smaller particles of ordinary clouds scatter the radiation very efficiently, being nearly the size of the wave length. This situation implies that:

1) The extinction distance in clouds for 3.7 micron radiation is much shorter than for the visible light, thus allowing treatment of most clouds as infinitely optically thick at 3.7 micron.
2) Clouds with small droplets scatter and reflect much of the 3.7 micron radiance, thus appearing as bright clouds on satellite images.
3) Increase in the cloud particle size, and/or the presence of large drops or ice crystals near cloud top will reduce the reflectance of the clouds.
4) Clouds which contain much ice appear very dark, as ice absorbs strongly at 3.7 micron and ice crystals are typically much larger than ordinary cloud droplets.

Therefore, the tops of raining clouds with large water droplets and/or ice particles appear dark on the daytime satellite imagery of the 3.7 micron waveband.

The problem of mixed emitted and reflected radiation in this waveband should be treated to determine the 3.7 reflectance, A_3, from observed radiances. In the present study it is done by assuming that the emissivity of optically thick clouds equals 1. The 3.7 reflectance is calculated by:

$$A_3=(L-P)/S$$

where L is the observed radiance, S is the spectral solar irradiance and P is the emitted thermal radiation derived from the thermal channels.

The anisotropy of clouds is accounted for by a radiation-cloud model (Nakajima and King, 1990), which calculates the single and multiple Mie scattering for cloud of spheres with given size distribution and index of refraction. The model calculated bidirectional reflectances have different behavior depending upon the size and phase of cloud particles. Fig.2 shows the dependence of the reflectances at 3.7 micron for water upon the scattering angle, which is the angle between the sun, the target and the sensor.

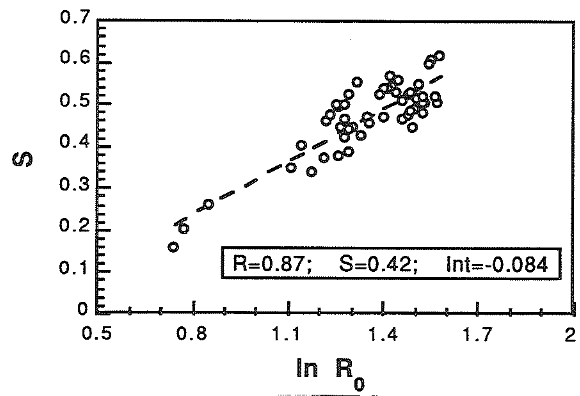

Fig. 1: The dispersion, S, of the lognormal cloud drop size distribution as a function of ln R_0, for measured spectra in precipitating convective clouds in Israel.

The following assumptions are made for the model:

1) cloud drop size distribution is assumed to be lognormal, with the dispersion S of the distribution dependent on the mean geometrical radius R_0 by:

$$S = -0.084+0.42 \ln(R_0)$$

as was found to be best fitted to measured distributions in precipitating convective clouds in Israel, using PMS-1D airborne instrument (see Fig. 1). The measurements were carried out for the Israeli rain enhancement project.
2) cloud tops are assumed homogeneous , flat, and filling the field of view.
3) only optically thick clouds, defined by the visible band and the IR split-window, are considered.
4) atmosphere above the cloud tops is neglected, i.e. no correction for atmospheric radiation scattering and absorption is made.

2. THE DATA

The data used in this study were taken from the AVHRR Local Area Coverage (LAC) NOAA-11 orbits over East Mediterranean. The resolution of AVHRR at nadir is 1.1 km, degrading to several km at large off-nadir views. The NOAA-11 daytime observations are taken in the mid-afternoon. AVHRR has five channels: two in the solar reflective region (Ch1 and Ch2), one centered at 3.7 micron (Ch3) and two in the thermal IR (Ch4 and Ch5). Ch2 is not used in this study because our model calculations did not indicate any significantly different information from that derived using the visible channel. The thermal channels are calibrated onboard the satellite, but a correction was made to account for nonlinearity in the calibration. As for the visible channel (Ch1), there is no onboard calibration. In the present study prelaunch NOAA-11 calibration for Ch1 was used.

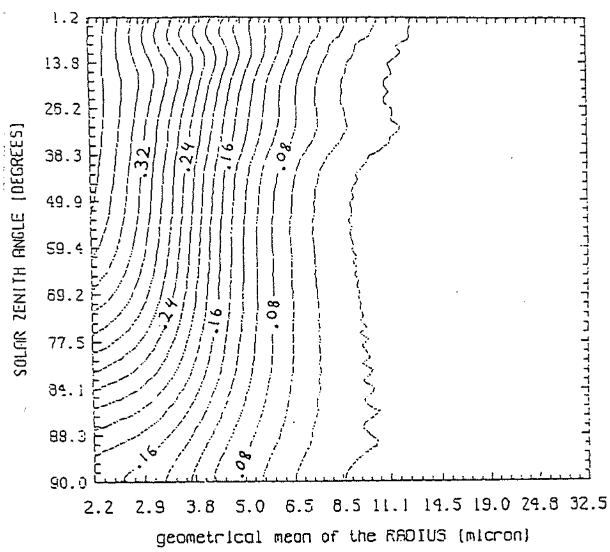

Fig. 2: The reflectance of 3.7 micron radiation from an infinitely thick water cloud as a function of the mean geometrical radius of the droplets, and of the sun-target-sensor angle.

The radar data used in this study were obtained by a C-band radar, operated at a mode of 5 min volume scans. The radar is located near Tel Aviv and is operated by Electrical-Mechanical Services of MEKOROTH, the Israeli national water company, for the Israeli rain enhancement project.

Thirteen case studies of instantaneous observations of cloud systems were selected from the data during the 1990/91 and 1991/92 winter seasons. The small number of cases was due to the infrequent recordings of LAC data by NOAA.

In this study we did not treat situations with multi-layered clouds, because the tops of potentially precipitating clouds may be obscured by overlying non-precipitating clouds. Only observations between 15 and 100 km from the radar on the western half of the radar field of view were considered to ensure the reliability of radar data in terms of distance and absence of false signals (clutter) due to topography.

3. THE ALGORITHM

The algorithm for retrieving the effective cloud droplets radius consists of two steps: 1) detection of optically thick cloud pixels in the satellite image and 2) the model application for retrieving the phase and radius of cloud particles. The first step is the selection of pixels filled with optically thick clouds. The selection was based on thresholding the visible albedo, the Ch4 brightness temperature and the (Ch4-Ch5) temperature difference, as an indication for optically thick clouds in the far IR (Inoue, 1987). All pixels with visible albedo below 40%, or warmer than 7 C, or having (Ch4-Ch5) greater than 1 deg K were rejected because they were suspected to contain optically thin or subpixel clouds. These criteria are site specific, and were empirically specified such that even slightly questionable pixels were rejected. The pixels having Ch3 reflectance below 2% were considered to be definitely clouds with ice particles. In this case no calculation of the radius was done. Note that large radii (greater than 10 micron) typically coincide with very cold tops and thus can be assumed to be all ice. For the rest of the pixels the radius was calculated using an assumption that the cloud contained exclusively water droplets, while the interpretation of the results may involve any possible ice/water ratio. Ch1 reflectance, A_1, was not used for radius calculations because of the lack of sensitivity to particle size.

The actual delineation of precipitating clouds was done by the following procedure. The area under consideration, i.e. with reliable radar data, was subdivided into several nearly equal area regions of 4000 AVHRR pixels, equivalent to boxes with 60 to 80 km on the side, depending on the distance from the sub-satellite trajectory. The number of the pixels with radar precipitation echoes at any height was determined. Then, the number of pixels above different threshold values for the effective radius R_0 were computed for boxes of each of the scenes. Any cloud top property that delineates well the precipitation area should ideally fulfil several conditions:

1) The area having this property is well correlated with the area of the actual precipitation.
2) The slope of the regression should be near unity.
3) The intercept of the regression should be near zero.

The skill to delineate precipitation areas, as determined by radar, was tested this way, using three cloud top properties:

1) the retrieved R_0 at cloud tops;
2) the Ch4 cloud top temperature;
3) the Ch1 visible reflectance.

4. RESULTS

The selected cases were subdivided into two groups: 1) with deep convective systems; 2) with shallow convective systems. The separation was done by noticing that the first type of cloud systems were associated with apparent Cb clouds with anvils, and the coldest cloud tops, T_{min}, below 245 K whereas the second type had temperatures higher than 245 K and no obvious Cb clouds. These two groups had 7 and 6 dates, amounting to 20 and 19 equal area boxes for the cold and warm groups, respectively.

The number of pixels above different threshold values for the effective radius R_0 were compared with the number of pixels determined as precipitating by radar. The skill of R_0 in delineating the precipitating cloud tops was compared with that of cloud top temperature, T, and visible reflectance, A1, as obtained from Ch4 and Ch1, respectively. The relative performance was tested using linear regression analyses. The regression and correlation coefficients are given in Table 1.

The threshold value with the best precipitation delineating skill was determined for each of the three parameters and of the two groups in Table 1, according to the criteria mentioned earlier. The best skills were found for the values: R_0 = 6

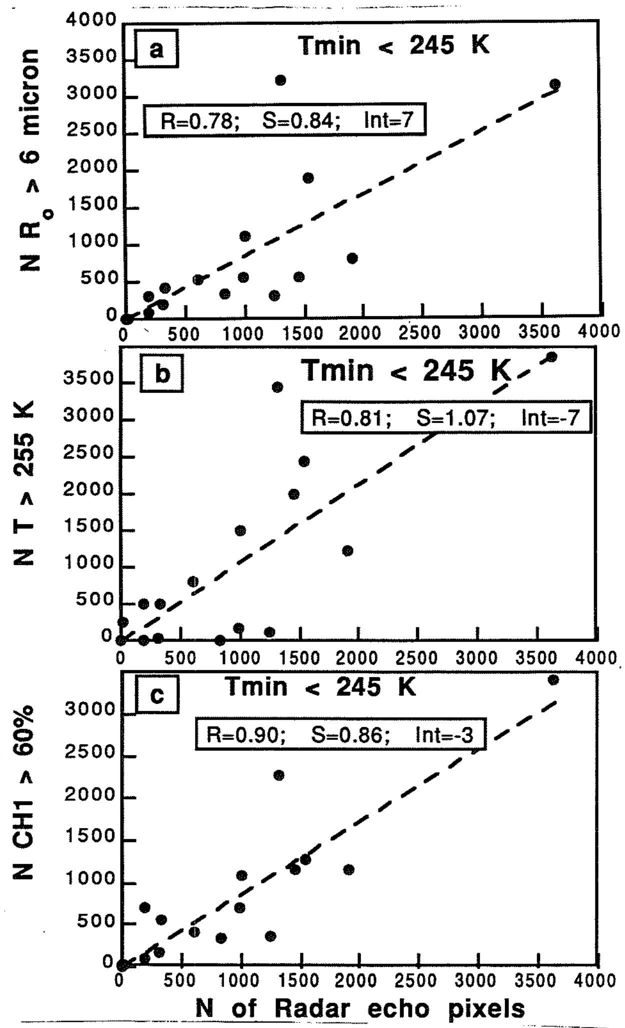

Fig. 3: The number of pixels with precipitation radar echoes in 4000 pixel boxes vs. the number of pixels with: (a) R_0 greater than 6 micron; (b) cloud top temperature colder than 255 K, and (c) Ch1 reflectance greater than 60%, for deep convective systems with cloud tops colder than 245 K.

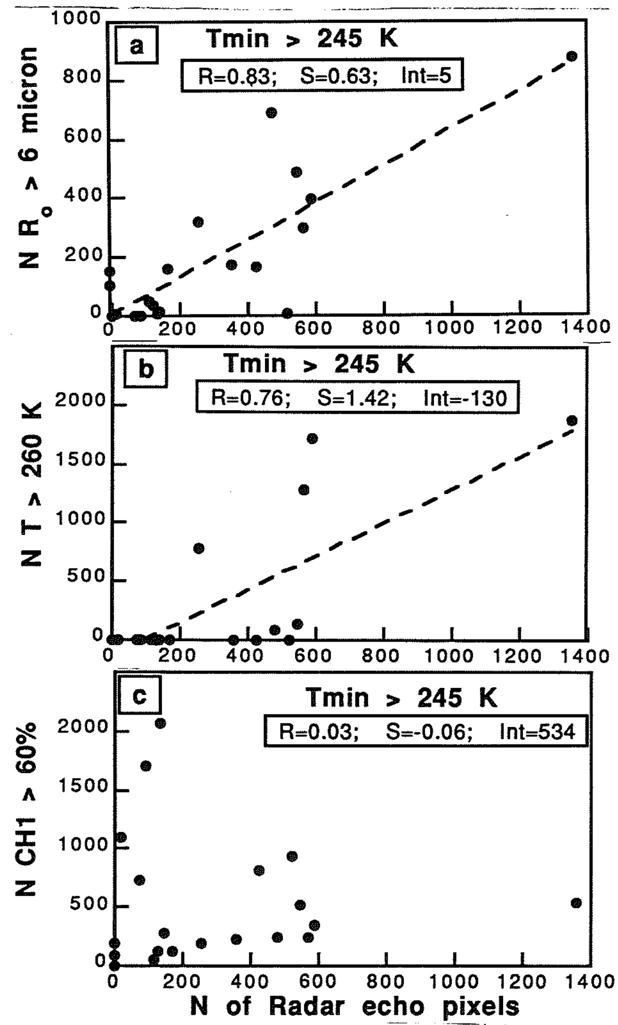

Fig. 4: The same as Fig. 3, but for systems with coldest cloud tops warmer than 245 K, and top temperature colder than 260 K in (b).

micron for both cold and warm top clouds; T = 255 and 260 K for the cold and warm cases, respectively; A_1 = 60% for the cold top clouds. None of the values of A_1 yielded reasonable correlation with the precipitation areas for the warm top clouds. The regression parameters corresponding to these threshold values are denoted in bold type in Table 1 and their scattergrams are given in Figs. 3 and 4. Since no acceptable value was found for A_1 in the warm cases, Fig 4c shows the scattergram with the value of A_1 as adopted from the cold case. This value is indicated by an asterisk in Table 1.

According to Fig. 3 the precipitation areas in the deep convective cloud systems are delineated well by the retrieved R_0. This is found to be the case also for T and A_1. It implies that the addition of Ch3 to the spectral analysis for delineating precipitation areas does not have the potential to improve VIS/IR methods, such as developed by Lovejoy and Austin (1979), in situations of convection with very cold cloud tops, at least in the study area.

In contrast to the above, Fig 4 shows that R_0 has by far the largest skill in delineating the precipitation at the warmer cloud tops. The visible reflectance contained little information about the precipitating properties of the clouds. Cloud top temperature, even at the optimal threshold value of 260 K, failed to delineate the precipitation areas in all but four boxes. In the same conditions, R_0 showed reasonable skill for most of the data points, including the boxes with relatively small precipitation area (less than 600 pixels).

These results can be explained by the fact that tops of deep convective clouds are almost always frozen at temperatures colder than about 245 K (-28 C), and therefore Ch3 does not add much new information beyond that given by the temperature alone. However, cloud tops at warmer temperatures may be either glaciated or supercooled. The occurrence of precipitation processes depends on the presence of ice or large cloud droplets, which can be detected by retrieving R_0.

Table 1:

	WARM, T_{min}>245 K			COLD, T_{min}< 245 K		
	Corr	Slope	Intcpt	Corr	Slope	Intcpt
R_0, micron						
4	0.38	0.93	750	0.79	0.84	110
5	0.83	1.23	251	0.79	0.84	92
6	**0.83**	**0.63**	**5**	**0.78**	**0.84**	**7**
7	0.86	0.33	-12	0.77	0.84	-73
8	0.83	0.24	-12	0.76	0.82	-98
9	0.80	0.16	-6	0.75	0.79	-129
T, Temperature, K						
240	-	-	-	0.74	0.93	-129
245	-	-	-	0.76	0.98	-100
250	0.18	0.00	0	0.79	1.03	-69
255	0.75	0.22	-27	**0.81**	**1.07**	**-7**
260	**0.76**	**1.42**	**-130**	0.83	1.11	116
265	0.56	1.77	530	0.83	1.08	468
270	0.44	1.57	1334	0.79	1.06	884
A_1, Visible reflectance, %						
30	0.25	0.79	1816	0.84	1.12	756
40	0.19	0.57	1407	0.87	1.11	428
50	0.09	0.22	963	0.87	1.03	183
60	*0.03	-0.06	534	**0.90**	**0.86**	**-3**
70	0.01	0.00	126	0.91	0.40	-50
80	0.22	0.02	16	0.79	0.11	-13
90	0.11	0.00	4	0.64	0.03	-3

Cloud tops with retrieved R_0 greater than 6 micron are interpreted by this method as containing precipitation particles. A lognormal distribution with $R_0 = 6$ and $S = 0.67$ yields 14% of the droplets larger than a radius of 12 micron, or a diameter of 24 micron. The existence of drops of at least that size in a cloud is known to be required for efficient warm rain processes as well as for ice multiplication processes. According to Fig. 5, the number of droplets with radius greater than 12 micron becomes significant when R_0 grows from 5 to 6 micron. Indeed, re-examination of Table 1 shows that R_0= 5 micron is also correlated well with the precipitation areas in the warm cases, whereas this correlation deteriorates for R_0=4 micron, in which case, according to Fig. 5, very few drops larger than 12 micron exist.

6. CONCLUSIONS

It was shown that the existing AVHRR 3.7 micron channel can be utilized to facilitate the multispectral analysis of cloud microphysics using satellite sensor data. In the deep tropical convective regimes this channel would not add much information to the IR analysis because precipitating cloud tops are usually very cold. Thus, cloud top temperature alone is a good indication of precipitating clouds in this regime.

However, much of the rain in Israel falls from clouds with tops warmer than 245 K (Gagin and Neumann, 1981). In these conditions there is typically great microphysical diversity at the cloud tops. The microphysical information retrieved with A_3 is therefore instrumental in the inference of precipitation processes at these cloud tops.

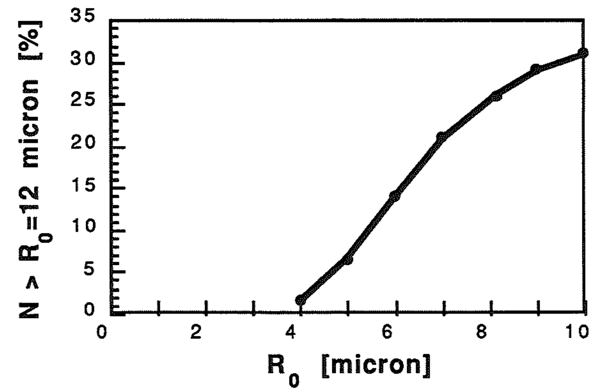

Fig. 5: The percentage of cloud droplets having radius greater than 12 micron, in a cloud with lognormal drop size distribution, as a function of the mean geometrical radius R_0. The dispersion is dependent on R_0 as given in the text.

The suggested methodology should improve the VIS/IR techniques by detecting the existence of large drops and/or ice in the clouds. The ability to infer microphysical information relevant to precipitation processes is instrumental in recognizing clouds as candidates for rain enhancement by seeding. As a result, the potential to monitor rain on a global scale is increased.

ACKNOWLEDGEMENTS

This research was supported by a grant from the United States-Israel Binational Science Foundation (BSF), Jerusalem, Israel. The authors thank E.M.S. for the radar data. The authors are grateful to Dr. Michael King for the use of his Mie scattering and doubling models.
The authors are thankful to Mrs Tsipora Weinberg, who made the model adaptation and calculations of the effective radius for all the data. The authors are also thankful to Mr. Itamar Lensky, who helped in the thresholding of the cloud top parameters.

REFERENCES:

Gagin A. and J. Neumann, 1981: The second Israeli randomized cloud seeding experiment: Evaluation of the results. Journal of Applied Meteorology, **20**, 1301-1311

Inoue T., 1987: An instantaneous delineation of convective rainfall areas using split window data of NOAA-7 AVHRR. Journal of The Meteorological Society of Japan, **65**, 469-481.

Lovejoy S. and G. L. Austin, 1979: The delineation of rain areas from visible and IR satellite data for GATE and mid-latitudes, Atmos. Ocean, **20**, 77-92.

Nakajima T. and M. D. King, 1990: Determination of the optical thickness and effective particle radius of clouds from reflected solar radiation measurements. Part I: Theory. Journal of Atmospheric Sciences, **47**, 1878-1893.

Pilewskie P. and S. Towmey, 1987: Discrimination of ice from water in clouds by optical remote sensing. Atmos. Res., **21**, 113-122.

MULTISENSOR REMOTE SENSING ANALYSIS OF DEEP CONVECTIVE STORMS' STRUCTURE OVER CONTINENTAL EUROPE AND THE MEDITERRANEAN

V.Levizzani[1], M.Setvák[2], J.Kráčmar[2], F.Porcú[1] and F.Prodi[1,3]

[1]Institute FISBAT-C.N.R., Clouds and Precipitation Group, via de' Castagnoli 1, I-40126 Bologna,Italy

[2]Czech Hydrometeorological Institute, Satellite and Radar Dept., pracoviště Libuš, Na Šabatce 17, 14306 Praha 4, Czechoslovakia

[3]Dept. of Physics of the University, via Paradiso 12, I-44100 Ferrara, Italy

1. Introduction

The structure of convective storms has in recent years been intensively and quantitatively studied by means of weather radars in its three components: kinematics, dynamics and microphysics (Houze and Hobbs,1982; Ray,1990; Jameson and Johnson,1990, among other fine reviews). The understanding of the dynamic forcing and interactions is being greatly enhanced by the concurrent advances in three-dimensional time-dependent numerical modeling. On the other hand, there are several areas, including a large portion of central and southern Europe where radar data are not available at all or their quality and/or time repetition is not sufficient for storms studies. This points to the possibility of using widely available satellite cloud top observations for type classification and inference to the internal structure of storms.

NOAA polar orbiters' Advanced Very High Resolution Radiometer (AVHRR) provides data in five spectral bands/channels in the visible and infrared (Ch1:0.58-0.68; Ch2:0.725-1.10; Ch3:3.55-3.93; Ch4:10.3-11.3; Ch5:11.5-12.5 μm) with nadir resolution 1.1×1.1 km. For a selected area, however, only a few satellite passes a day are available, depending on the number of currently operational satellites. METEOSAT geosynchronous satellites' Visible and Infrared Spin Scan Radiometer (VISSR) is operative in the three channels of visible, infrared and water vapor (VIS:0.4-0.9; IR:10.5-12.5; WV:5.7-7.1 μm) with an image repetition period of 30 minutes. The resolution, though, is much lower than for NOAA (approximately 6×9 km in the IR for central Europe). Data from a C-band (5.3 cm) Doppler radar located in Teolo (near Padova in northern Italy, 45.4 N, 11.7 E) have been used for locating active portions of convective storms and relating them to satellite-observed structures. Section 2 describes the datasets and their processing.

The first investigation that needs to be performed is to quantify the lowest spatial detectability of the highest tops of deep convective storms on METEOSAT imagery. This because the latter has a considerably lower spatial resolution than NOAA's, and thus a check must also be run on how much it can distinguish of the finer details of the storms' cloud top structure, which is vital for classification. This is to be done by comparing METEOSAT IR images to the matching ones from NOAA AVHRR Ch4 or Ch5 for those cases in which the temporal deviation is small enough in terms of convective processes. A few preliminary results in this connection are presented in section 3. The influence of each satellite's differing calibration procedures on low-temperature detection was examined. For those cases in which satellite and radar data were available a comparative analysis of both was performed to elucidate the interrelationship of satellite-viewed cloud top patterns and the storm's radar-detected internal structure (section 4). Other cloud top or convective storm-scale features (dynamic and kinematic), detectable on NOAA and/or METEOSAT imagery, are worth studying as a possible source of information on storm structure, and these are discussed in section 5.

2. Data reception and processing

The investigation for the present paper was carried out using data from the year 1991, when many cases of simultaneous images from NOAA and METEOSAT were available.

NOAA AVHRR data over Europe and the Mediterranean throughout 1991 were received, archived and processed at the Czech Hydrometeorological Institute (CHMI) in Praha. HRPT 10-bit data are transformed by the station processor to 8-bit format. Primary processing was carried out at CHMI on PC 486 and consisted of temperature calibration of Ch3 (nighttime data), Ch4 and Ch5, sun elevation correction, Ch3 reflectivity calculation (daytime data) (Setvák,1989), and geometrical correction.

METEOSAT VISSR images for the whole of 1991 were received and archived at FISBAT-C.N.R. in Bologna. The HRPT data in VIS, IR and WV were, and are being, recorded every half hour. Archiving was performed using raw data accompanied by files containing the calibration header. Calibration of brightness temperatures in the IR and WV was then performed on-line when processing the images and was based upon European Space Agency guidelines (ESA,1989). Final processing of the data was performed by using both PCs and the FISBAT-C.N.R.'s SUN 4/330 + AT&T Pixel Machine 964dX.

Data from the Doppler radar in Teolo were available for the convective event of September 12 and consist of 15 minute interval PPI radar reflectivity scans with a maximum range of 240 km and a cell resolution of 2 km. Pre-processing and archiving of the data were done at the radar site and the results transferred via computer-compatible tape to FISBAT-C.N.R., where their final processing was carried out using CHMI software on PC/386: maximum reflectivity, and CAPPI at 2, 5 and 8 km levels were used. Data from the MRL-5 3.1 cm analog radar of CHMI in Praha-Libuš were available for two cases and used only for detecting the radar echo top and reflectivity values of the storms' convective areas at 1.5 and 5 km levels.

The total number of deep convective events examined from the NOAA archive was 13, from 31 May to 27 October; the number of the correspondent satellite passes was 22. For the present study Ch2, Ch3 and Ch4 were analyzed. METEOSAT imagery was available almost continuously throughout the year and, among the events having simultaneous images from the two satellites available, 5 were selected with good timing between NOAA passes (total of 9) and METEOSAT scannings. For the purpose of cross-calibrating cloud top and sea surface temperatures between satellites, 3 of these events with a total of 3 NOAA passes are discussed below in section 3.

The above data analysis proved to be more efficient when applying color enhancement, which enables the distinguishing of fine details of the cloud top structure that are hard to detect using black and white look-up tables. It should be noted that some of the details derived from color imagery discussed below do not clearly show up in the included figures as color illustrations are not accepted.

3. Comparison of METEOSAT and NOAA data

Given the lower geometrical resolution of METEOSAT imagery as compared to NOAA's, some differences in the potential of distinguishing fine details of cloud top structure, as well as deviations in low-temperature sensing of the two types of satellite, can be expected. Then, too, the differing calibration procedures (Lauritson *et al.*,1979; ESA,1989) can lead to more or less significant differences in the lowest temperatures detected over deep convective storms.

The three deep convective storms used in verifying the magnitude of temperature deviations were also chosen because of their proximity to an unambiguously detectable area of cloud-free sea surface having constant black body temperature over a large number of pixels (on both images). This latter comparison served the purpose of comparing the temperature detection in the warm end of IR radiances, which should be less influenced by different calibration procedures. In order to distinguish between the impact of different sensor resolution and the influence of differing calibration procedures, artificial "lower resolution" images were computed from original NOAA AVHRR ones. These "lower resolution" images were 5×7 and 5×8 pixel value averages created from calibrated NOAA AVHRR images, thus simulating METEOSAT resolution for latitudes 40-45 N and 45-50 N, respectively. The longitude of the storms lay in all the cases between 5 W and 20 E, so that excessive METEOSAT pixel deformation caused by the earth's curvature was avoided. Table 1 shows the results for the selected events.

TABLE 1. The comparison of storm minimum temperatures and sea surface temperatures as detected by NOAA AVHRR Ch4 (full and "lower" resolution) and METEOSAT IR.

Date 1991	Time dev. [min.]	NOAA Ch4 AVHRR storm min.T	NOAA Ch4 AVHRR sea T	NOAA Ch4 low res. storm min.T	METEOSAT IR storm min.T	METEOSAT IR sea T
28 Aug	6	202.0	295.0	205.5	209.7	295.0
31 Aug	3	203.5	297.5	206.5	211.0	296.4
27 Oct	3	200.0	292.0	202.5	206.4	291.3

The METEOSAT scanning in all three cases was performed before NOAA's. The accuracy of the black body temperatures is ±0.5K for these NOAA data (due to calibration and consequent rounding to count values), ±0.3K for METEOSAT sea surface temperatures and ±0.8K for METEOSAT storm cloud top temperatures. To avoid as much as possible any influence arising from the choice of the location of the averaging windows over original NOAA images for the production of "lower resolution" images, several shifts of this position were performed to attain the same minimal cloud top temperature.

The sea surface temperatures were found to be the same for original as well as for "lower resolution" NOAA images, and therefore there was no need to include this latter comparison between the two sets of data. It can be seen that the sea surface temperatures from NOAA and METEOSAT are in very good agreement when considering the correspondent accuracy of the measurements.

According to the measured minima of the cloud top storm temperature, it seems that a difference of about 4K can be attributed to the two calibration procedures since it is the same for all three events when comparing "lower resolution" NOAA and METEOSAT values. This is comparable to the results of Negri (1982), which were obtained by means of a different method and by comparison of NOAA and GOES satellites. The rest of the difference between NOAA and METEOSAT is obviously a result of the different ground resolution, and depends on the number of coldest pixels in NOAA imagery as well as on the cloud top temperature gradient around the coldest spots.

These findings, although based on a limited number of investigated cases, should be taken into account when estimating cloud top height of deep convective storms on the basis of METEOSAT IR imagery (or other geosynchronous satellites with comparable resolution). One of its likely impacts can be seen in an underestimation of real temperature differences between the coldest portions of V-patterns and related warm spots (Heymsfield and Blackmer, 1988).

Fig.1 shows the squall line of August 28 over Spain as seen in images from NOAA AVHRR Ch4 (Fig.1a), "lower resolution" NOAA Ch4 (Fig.1b) and METEOSAT IR (Fig.1c). Even if some of the details of the cloud top thermal structure are obviously missing, METEOSAT and "lower resolution" NOAA images still clearly depict the active areas of the storm. This is an important result, as it enables active portions within storms (represented by cold spots or larger cold areas on the upwind side of the highest peaks of cloud top that are displaced over updrafts) to be distinguished. This brings us to considerations on the storm's internal structure as detectable from its cloud top thermal pattern, the topic of the next section.

4. Comparison of radar and satellite data

The comparison of radar and satellite data was made using the multicellar storms of 12 September over northern Italy (Fig.2). Given NOAA AVHRR 1.1×1.1 km and radar 2×2 km resolution, the comparison between radar reflectivity field and NOAA Ch2 and Ch4 imagery was performed first. Simultaneous radar and NOAA scans of the storms between 13:45 and 13:47 UTC were available, so that the influence of the convective evolution while comparing data at different times was avoided as far as possible. Since storm top height as determined from NOAA Ch4 and rawinsonde data from Milano-Linate at 12:00 UTC was about 13.5 km, the 8 km CAPPI reflectivity data were used as most suitable among those available. At the time of comparison the cloud top was sharply defined with several overshooting tops detectable on both NOAA Ch2 and Ch4 and no widespread anvils. The relative position of individual, well-pronounced overshooting cloud tops and the 8 km CAPPI reflectivity cores were found to be in good agreement. Another cold cloud top area detected in NOAA Ch4 was associated with anvil cirrus by means of Ch2 and radar data. This cold area differed from overshooting tops by its substantially weaker temperature gradient and the absence of significant reflectivity cores in the 8 km CAPPI.

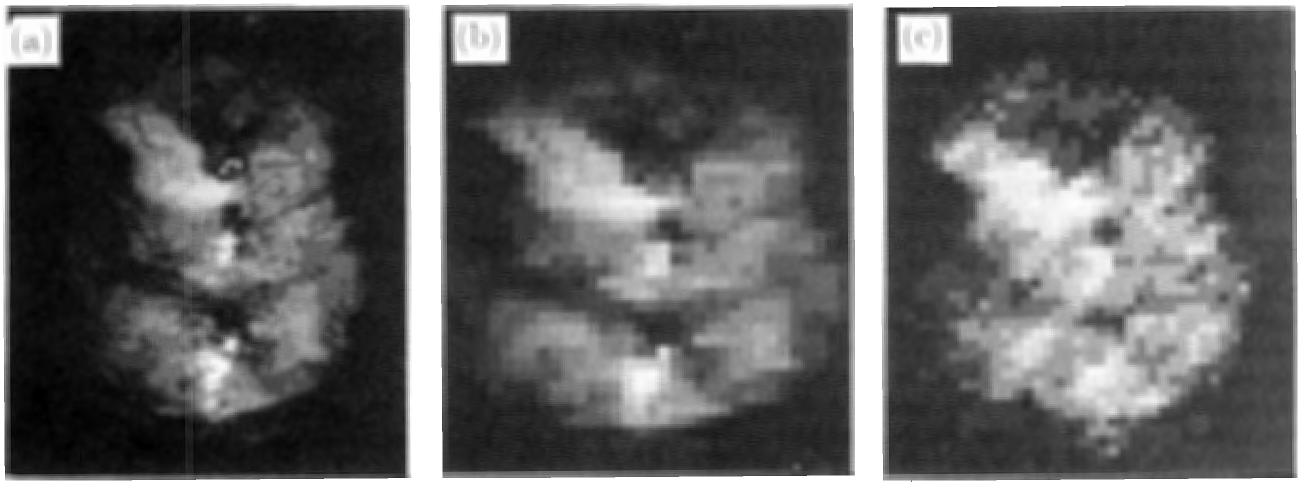

FIG. 1. Squall line over Spain on 28 August 1991: a) NOAA AVHRR Ch4 at 14:58 UTC; b) corresponding "lower resolution" NOAA AVHRR Ch4; c) METEOSAT VISSR IR at about 14:52 UTC.

FIG. 2. Multicellar storm over northern Italy on 12 September 1991: a) NOAA AVHRR Ch2 at 13:45.5 UTC; b) corresponding NOAA AVHRR Ch4; c) 8 km CAPPI radar reflectivity scanned between 13:45 and 13:47 UTC (linear gray scale from dark gray=2dBZ to white=58 dBZ).

The comparison between METEOSAT imagery and radar data for the same events was carried out next between 12:00 and 23:00 UTC. Although the time deviation between radar and subsequent satellite scans was about 6 minutes, the two together allowed analysis of the storms' time evolution, which is impossible in the case of NOAA. The life history of the storms was well described by both observational techniques, although shorter scan periods (5 to 10 minutes) would be desirable for convective analysis. For mature storms, where the size of the cloud top features is above METEOSAT's IR pixel resolution (of the order of 15 km or more), the correspondence of active convective areas in METEOSAT IR and 8 km CAPPI reflectivity cores was found to be satisfactory. For smaller scale and earlier stage of storm development METEOSAT's IR tended to underestimate the storms' intensity, while for later stages with widespread anvils an overestimation of intensity and of active convective area was taking place. Although the overestimation can be qualitatively reduced by taking into account the magnitude and location of the temperature gradients, a storm's classification based only on METEOSAT can sometimes be misleading. This also implies that precipitation estimation techniques based upon the geostationary satellite IR channel, mostly developed for tropical convective storms, might fail when applied to midlatitude storms (Levizzani *et al.*,1990).

METEOSAT IR has proved necessary in correctly inferring a storm's structure in the presence of single radar attenuation behind strong reflectivity cores.

5. Other satellite-derived cloud top features

Apart from the well known correspondence between satellite IR "V-patterns" and the severity of storms (e.g. Heymsfield and Blackmer,1988), there are other cloud top features that, whenever detectable, can be used as indicators of storm dynamics and microphysics.

NOAA AVHRR Ch3 daytime imagery provides information on the microphysical composition of the upper portion of the clouds (Scorer,1990). In many cases either large areas or small scale structures of convective storms can be observed exhibiting increased Ch3 cloud top reflectivity (CH3CTR). Although CH3CTR is presumably a result of the specific microphysical composition of the cloud top layer (Liljas,1984; Setvák and Doswell,1991) and thus resulting from processes going on inside the storm, its nature remains altogether unrevealed.

Ch3 features may also show connections to the mechanisms of meteorological processes on a scale larger than that of cloud microphysics. An example of this is the CH3CTR image of a storm of 31 August over France (not included in the figures) clearly showing its cyclonic rotation (or at least of its top part), which is not detectable in any other AVHRR channel (nor by animation of Meteosat data). For the case examined in Fig.1 the CH3CTR image (not shown) provides the evidence of cloud top outflow streamlines from the line of updrafts in the squall-line over Spain.

Another feature deserving of attention can be found in AVHRR Ch1 or Ch2 for many cases: 3 July over Moldavia and Ukraine, 26 July over Bulgaria and 23 September over the Tyrrhenian Sea and southwestern Italy. It shows around the active part of the storm a series of concentric structures resembling concentric gravity waves on a water surface. There might exist two explanations for this phenomenon: 1) the structures are formed by quasi-steady updraft with pulsing intensity; 2) they appear shortly after a new updraft has penetrated the cloud top equilibrium level and generated gravity waves on it. Unfortunately these patterns are beyond reach of Meteosat full resolution VIS and therefore no time sequence is available to provide an exhaustive answer. According to the time evolution of these storms on METEOSAT imagery, however, the first explanation seems to be more appropriate. If this could be proved (e.g. by the next GOES-I observations), these patterns could serve for satellite recognition of supercell storm candidates.

All these cloud top features have been observed on NOAA HRPT imagery over a wide number of cases in the past. The basic reason for not studying them in detail was the unavailability of METEOSAT HRPT data to these authors, thus preventing the analysis of storm evolution which is necessary for the correct interpretation of cloud top features.

6. Conclusions

The present paper reports preliminary results of a multisensor analysis of deep convective storms over Europe and the Mediterranean. METEOSAT was found to underestimate the cloud top height as derived from brightness temperature due to lower geometrical resolution and different calibration procedures as compared to NOAA. A good agreement was found between NOAA HRPT cloud top data and CAPPI 8 km radar reflectivity cores for the detection of storms active areas, although correspondence was not as good when comparing METEOSAT and radar observations. For the purpose of proper storm classification METEOSAT data have to be combined with NOAA HRPT and radar data. Our study points to the possibility of using next-generation METEOSAT images with their increased spatial, time and spectral resolution for a more satisfactory storm classification and operational monitoring, both required by nowcasting.

Acknowledgments. The authors are indebted to Dr. Karel Hlavatý and Eng. Pavel Hampl of CHMI in Praha for developing the NOAA HRPT data processing software. The Centro Sperimentale per l'Idrologia e la Meteorologia (CSIM) of the Veneto Region in Teolo (Padova) is aknowledged for providing digital radar data. The research was funded by the Gruppo Nazionale per la Difesa dalle Catastrofi Idrogeologiche (GNDCI) of the Consiglio Nazionale delle Ricerche (C.N.R.) and by the Agenzia Spaziale Italiana.

REFERENCES

ESA,1989: METEOSAT high resolution image dissemination. METEOSAT Exploitation Project, 57 pp.[available from ESA/ESOC, Meteosat Exploitation Project, Robert Bosch Straße 5, D-6100, Darmstadt, Germany.

Heymsfield,G.M. and R.H.Blackmer Jr.,1988: Satellite-observed characteristics of midwest severe thunderstorm anvils. *Mon. Wea. Rev.*, **116**, 2200-2224.

Houze,R.A. and P.V.Hobbs,1982: Organization and structure of precipitating cloud systems. *Adv.Geophys.*, **24**, 225-315.

Jameson,A.R. and D.B.Johnson,1990: Cloud microphysics and radar. *Radar in Meteorology*, D.Atlas, Ed., Amer.Meteor. Soc., 323-340.

Lauritson,L., G.J.Nelson and F.W.Porto,1979: Data extraction and calibration of TIROS-N/NOAA radiometers.Tech. Memo. NESS 107, 58pp. [available from U.S. Dept. of Commerce, NOAA, National Environmental Satellite and Information Service, Washington, D.C. 20233, U.S.A.].

Levizzani,V., F.Porcú and F.Prodi,1990: Operational rainfall estimation using Meteosat infrared imagery: An application in Italy's Arno river basin - Its potential and drawbacks. *ESA J.*, **14**, 313-323.

Liljas,E.,1984:Processed satellite imageries for operational forecasting. PROMIS Report, 43 pp [available from Swedish Meteorological and Hydrological Institute, S-60176 Norrköping, Sweden].

Negri,A.J.,1982: Cloud-top structure of tornadic storms on 10 April 1979 from rapid scan and stereo satellite observations. *Bull.Amer.Meteor.Soc.*, **63**, 1151-1159.

Ray,P.S.,1990: Convective dynamics. *Radar in Meteorology*, D.Atlas, Ed., Amer.Meteor.Soc., 348-390.

Scorer,R.S.,1990: *Satellite as microscope.* Ellis Horwood Series in Environmental Science,.

Setvák,M.,1989: Convective storms - the AVHRR channel 3 cloud top reflectivity as a consequence of internal processes. *Proc., Conf. on Weather Modification and Applied Cloud Physics*, Beijing, World Meteor.Org., 109-112.

———— and C.A.Doswell III,1991: The AVHRR Channel 3 cloud top reflectivity of convective storms. *Mon.Wea.Rev.*, **119**, 841-847.

PULSE COMPRESSION TECHNIQUE FOR SPACEBORNE PRECIPITATION RADARS

E. Im, S. Durden, F. Li, A. Tanner, W. Wilson

Caltech/JPL, Pasadena, CA 91109, USA

1. INTRODUCTION AND MOTIVATION

Pulse compression radar systems have been proposed for spaceborne and airborne rain mapping (Im and Li 1989; Li et al. 1988; Wilson et al. 1988) due to the fact that they allow the achievement of high range resolution with relatively low peak transmit power while maintaining acceptable signal-to-noise ratio. For spaceborne rain mapping by radars, there are two major reasons why high range resolution is required. Firstly, it is important that the rain mapping radars provide high resolution vertical profiles of rain backscatter measurements over the entire rain cell for diagnosis of the vertical distribution of latent heat release in the atmosphere and its influence on the global energy circulation (Simpson et al. 1988). Secondly, to reduce the space-time sampling error of the rain maps obtained to a level that is useful for climatological studies (Simpson et al. 1988; Shin and North 1988), the orbiting radars must rapidly scan over a large ground swath. As the result, the available time for collecting independent measurements over a given area is very limited. Under the constraint of limited dwell time, the statistical fluctuations on radar measurements can be reduced by vertical averaging over adjacent range bins. However, to maintain a resulting range resolution that is acceptable for rain profiling, the intrinsic range resolution of each individual measurement must be even finer. To obtain a high range resolution, conventional short-pulsed radars would require extremely high peak power, which is a formidable task for spaceborne systems. The use of pulse compression, therefore, is highly desirable.

A major problem associated with the use the pulse compression technique for the spaceborne rain mapping radars is that the surface clutter contained in the pulse compression range sidelobes may dominate the returns from rain at the targeted range bins due to strong surface reflection. This problem is particularly severe at nadir incidence where the surface backscatter cross-sections are large, and/or at light rain where the backscattered signals from the rain are weak. As will be shown in the next section, the pulse compression sidelobes must be suppressed to the -60 dB level in order to reliably estimate the rain echo power.

For spaceborne rain mapping applications, the suppression of sidelobes that are farther away from the main lobe is of primary interest because the locations of these sidelobes correspond to rain layers near the top of the rain cell. Unfortunately, the existing techniques (see, for example, Harris 1978) hardly address the suppression of these far range sidelobes. At the Jet Propulsion Laboratory, a dual-frequency Airborne Rain Mapping Radar (ARMAR) is being developed in support of the Tropical Rainfall Mission Mission (TRMM) (Wilson et al. 1988). We have recently built and tested the 13.8-GHz linear frequency-modulated pulse compression radar electronics system and the preliminary test results have indicated that the far range sidelobes can be suppressed to the desired -60 dB level in laboratory environment.

2. COMPRESSION SIDELOBE REQUIREMENT

For any radar sensors, clutter can be treated as one of the noise sources. To reliably detect the target reflected signals, all noise sources must be suppressed to certain tolerable level. For a downward viewing pulse compression rain radar, the rain-signal-to-surface-clutter-ratio, abbreviated as SCR, can be shown to be

$$SCR \approx \frac{c\,\eta\,h^2 \cos\xi}{2B\rho\sigma_s^o(\xi)(h-h')^2}\, exp\,\{0.2\,ln10 \int_o^{h'sec\xi} k_p\,dr\} \qquad (1)$$

where c is the speed of light, h is the radar altitude, h' is the altitude of the range bin of interest, ξ is the angle of incidence, B is the radar bandwidth, η is the reflectivity of rain, k_p is the attenuation coefficient of rain (in dB/km), ρ is the pulse compression sidelobe level, and $\sigma_s^o(\xi)$ is the rain-perturbed surface backscatter coefficient pertained within the radar ground resolution area. A flat earth model has been assumed in deriving Eq. (1). At large angles of incidence, the diffused components of the surface scatterers dominate, and $\sigma_s^o(\xi)$ falls off according to $cos\ \xi$ (Ulaby et al. 1982). In this case, the angular dependence of SCR lies upon the exponential term in Eq. (1), and the net result is that SCR increases directly with increasing angle of incidence when ξ is large. As ξ approaches 0, on the other hand, $\sigma_s^o(\xi)$ increases rapidly as the specular com-ponents of the surface scatterers become dominant while the other terms in Eq. (1) remain almost constant. In this case, SCR decreases rapidly with decreasing ξ for small values of ξ, and the pulse compression sidelobe level must be suppressed to a much lower level in order to obtain reasonable SCR. Consequently, the "global" pulse compression sidelobe requirement must be derived based on the nadir viewing geometry.

As listed in the recent research announcement on TRMM (NASA 1990), the TRMM radar measurements will have "minimum signal-to-noise ratio of unity for a rain rate of 0.5 mm/hr for the backscatter from the top of the rain". If we assume $SCR = 1$ to be a minimum requirement, then the minimum required sidelobe level, ρ_{min}, can be deduced as

$$\rho_{min} = \frac{c\,\eta\,\cos\xi}{2\,B\,\sigma_s^o(\xi)\,(1-\frac{h'}{h})^2}\, exp\,\{0.2\,ln10 \int_o^{h'sec\xi} k_p\,dr\}\ . \qquad (2)$$

Equation (2) has been evaluated using the Marshall-Palmer type rain parameters and the Gaussian distributed ocean surface. The numerical results for the 13.8 GHz ARMAR system (B = 3 MHz, h = 12 km) at nadir viewing are shown in Fig. 1. We see that a ρ_{min} value of approximately -60 dB is required at a rain rate of 0.5 mm/hr. For spaceborne radar applications the ratio h'/h approaches zero and it results in a somewhat more stringent requirement on ρ_{min}.

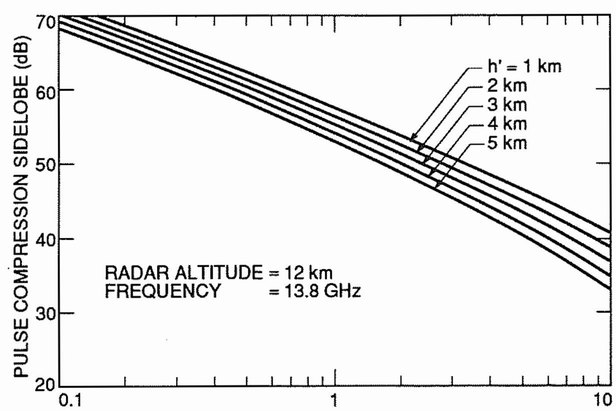

Figure 1. The required pulse compression sidelobe levels for the Airborne Rain Mapping Radar at normal incidence. h' correpsonds to the height of the range bin which contains the rain backscatters.

3. LINEAR FM PULSE COMPRESSION

The ARMAR system uses the linear FM (also commonly known as chirp) pulse compression technique to achieve high range resolution (150 m) and large number of independent samples (≥ 500). Many existing algorithms use either time-domain or frequency-domain weighting to achieve sidelobe suppression at the expense of broadening the main lobe response (Cook and Bernfield 1967). Most of them, however, concentrate on suppressing sidelobes that are "close" to the main lobe. As an illustration, Fig. 2 shows the results when Hamming weighting is applied to a rectangular linear FM pulse with time bandwidth products (*TB*) between 30 and 240. These *TB* values correspond to those being used by the ARMAR system. It can be seen that while the sidelobes close to the main lobe have been substantially reduced, the sidelobes further removed from the main lobe remain at a relatively high level, and the results are inadequate for rain mapping applications.

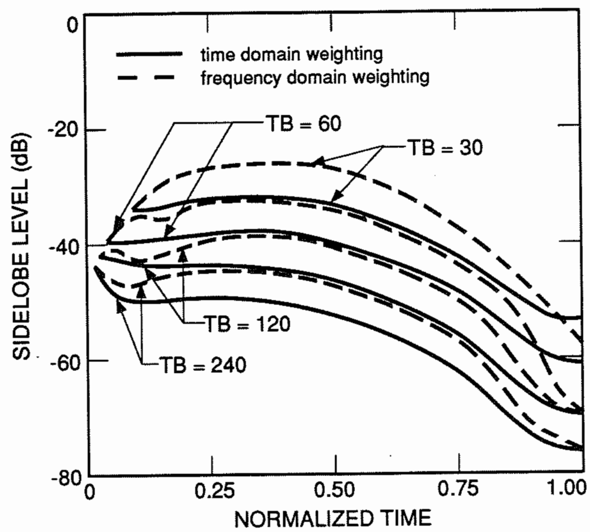

Figure 2. Theoretical compression sidelobe levels of the time-weighted and frequency-weighted rectangular chirp signals with *TB* values of 30, 60, 120, 180 and 240 (B = 3 MHz in each case) using a Hamming weighting function.

In order to suppress the far range sidelobes, a different compression technique is being employed by the ARMAR system. With this technique, the radar pulse signals are amplitude weighted prior to transmission, and the rain reflected signals are matched filtered by the receiver whose impulse responses are matched to the transmitted signals. That is,

$$s_1(t) = s(t)\, w(t) \;, \tag{3}$$

$$h(t) = K\, s^*(-t)\, w^*(-t) \;, \tag{4}$$

$$g_m(t) = K\, s_1(t) \otimes h^*(-t), \tag{5}$$

where $s(t)$ is the rectangular linear FM pulse signal, $w(t)$ is the amplitude weighting function, $s_1(t)$ is the transmitted signal, $h(t)$ is the matched filter response, K is a scaling factor, and $g_m(t)$ is the compressed signal. The symbols (*) and (⊗) are used to denote the complex conjugation and the convolution operations, respectively.

The particular weighting function that the ARMAR system has used is a cosine-taper function of the form

$$w(t) = \begin{cases} 1 & 0 \le |t| \le \dfrac{dT}{2} \\ 0.5\,[1 + cos\{\dfrac{\pi\,(|t| - 0.5dT)}{0.5(1-d)T}\}] & \dfrac{dT}{2} < |t| < \dfrac{T}{2} \end{cases} \tag{6}$$

In Eq. (6), T corresponds to the time duration of the transmitted signal and $(1\text{-}d)$ corresponds to the fraction of the signal being tapered. Notice that Eq. (6) evolves from a Hanning function to a rectangular function as the parameter d varies from zero to one. Figure 3 shows the theoretical sidelobe levels of the compressed chirp signals with a time-bandwidth product value of 120 when this particular compression technique is applied. The results are computed for different values of d. We can see that the sidelobe levels drop rapidly to less than -60 dB with a relatively small reduction on d. These results imply that it is theoretically possible to obtain a low mid-to-far range sidelobe level by paying small penalties on the signal strength and range resolution. For $d \ge 0.6$, the corresponding signal reduction and main lobe broadening are less than 1.32 dB and 30%, respectively.

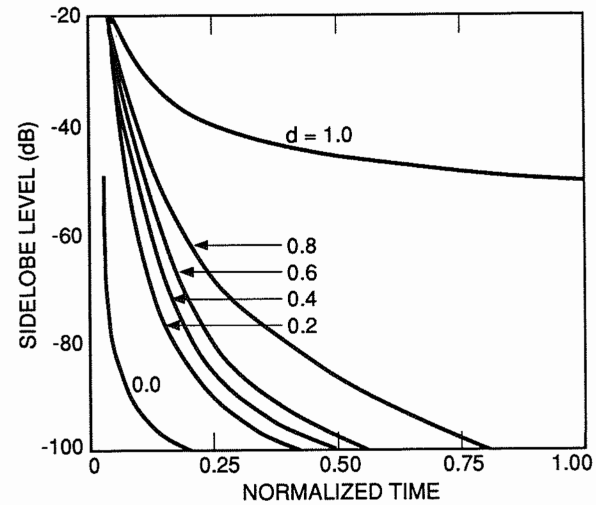

Figure 3. Theoretical compression sidelobe levels of a matched filtered output signal. The transmitted signal with *TB* = 120 is amplitude weighted by the Cosine-taper weighting functions. The parameter (d) corresponds to the fraction of the original pulse not being tapered.

4. PRACTICAL CONSIDERATIONS

After consideration on available technologies, the ARMAR system design uses a digital frequency synthesizer for generation of different chirp signals; a traveling-wave tube amplifier (TWTA) operating in the linear region for signal amplification; and a digital Fourier transform approach for pulse compression. In practice, distortions and nonlinearities in all part of the pulse compression system hardware can contribute distortion lobes which cannot be removed by the weighting technique described in the last section. In this section, we present the simulation results which help to define the permissible levels of hardware induced distortions for the ARMAR system.

The flow diagram of the simulation process is shown in Fig. 4. It consists of five major blocks - frequency synthesis, signal amplitude synthesis, bandpass filter synthesis, quantization, and matched filter synthesis. The digital frequency synthesizer uses the staircase-type frequency increments, or the so-called stepped FM, to approximate the linear time-frequency characteristics of a given slope. In our simulation, we use a frequency resolution of 100 mHz, and a phase continuity control of 1.4°. These values are typical for a commercially available synthesizer. Although typical syn-thesizers can achieve time resolutions of the order of 100 nsec, we choose to make it a varying parameter in order to study the grating lobe effects. We have also added a random phase component every 50 nsec throughout the entire phase history of the synthesized modulation. These random phase comp-onents are assumed to be uniformly distributed over $(-\psi, \psi)$ where ψ is the maximum permissible phase noise level. The output of the frequency synthesizer is a 'quasi-linear' FM pulse with unity amplitude. The amplitude of this pulse is weighted at the second stage of the simulation. At this stage, the pulse envelope is modulated to the desired magnitude by a simulated digital-to-analog converter. After envelope modulation, a band-limited, zero-mean Gaussian distributed amplitude noise is added on the weighted, noise-free pulse envelope. During this process, the maximum allowable standard deviation of the amplitude noise is determined. The output of the envelope synthesizer, denoted as $s_1(t)$ in Fig. 4, is passed through a bandpass filter for out-of-band noise rejection. Two types of filters are simulated at this stage - Butterworth and Chebyshev transfer functions with poles varying from 1 to 10. The filtered output, $s_2(t)$, is sampled at a rate equal to or slight higher than the Nyquist rate. At the same time, the amplitude of $s_2(t)$ is discretely quantized by a simulated analog-to-digital converter. The quantized signal, $s_2(n)$, is then matched-filtered by $h(n)$. In practice, $h(n)$ may not be the exact replica of $s_2(n)$ for various reasons. For instance, $h(t)$ and $s_2(t)$ generated at different times may have different random fluctuations on amplitude and phase. In our simulation, $h(n)$ is assumed to be a different noisy realization of the same noise-free signal. Eventually, the waveform of the simulated matched-filtered output is computed.

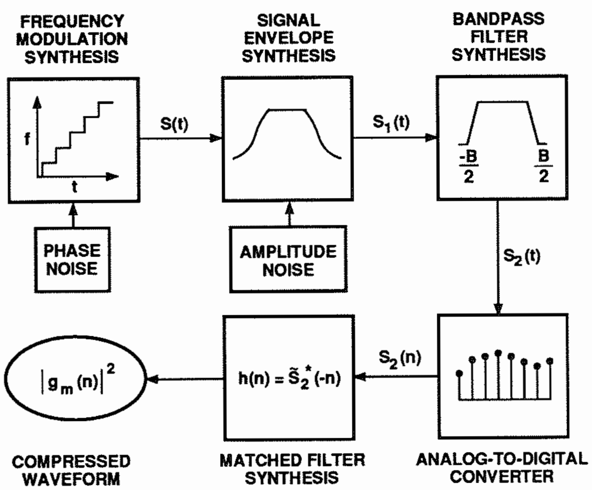

Figure 4. Pulse compression simulation flow diagram.

Through our simulation, we have derived the following set of requirements on the ARMAR hardware.

Synthesizer's time step size:	167 nsec
Attenuator's resolution:	≤ 0.2 dB
Maximum phase noise deviation:	±2°
Standard deviation in amplitude noise:	±2 dB
Bandpass filter characteristics:	3-pole Butterworth ot 3-pole Chebyshev with a 0.5-dB ripple level
A/D converter's resolution:	12 bits

Figure 6(a) shows a compressed signal waveform with TB=120 and d=0.6 when the permissible contributions from all sources as listed above are taken into account. It can be seen that a mid-to-far sidelobe level of -60 dB can still be achieved. Similar results have been obtained for other TB values used by the ARMAR system.

5. INSTRUMENT SETUP AND TEST RESULTS

Figure 5 shows a detailed block diagram of the 13.8 GHz channel of ARMAR. In laboratory testing, the transmitter is directly connected to the receiver through attenuators, and the antenna and T/R switch are absent. The radar is capable of producing programmable chirp waveforms of arbitrary pulse lengths and 3 MHz bandwidth centered about an RF frequency of 13.8 GHz. The desired chirp amplitude and frequency information are stored in a look-up-table, which composed of a 32x1024 bit random access memory. During the transmit cycle, the information is sent to the programmable frequency synthesizer and the digitally-controlled attenuator at a rate of 6.7 MHz. The synthesizer generates a rectangular IF chirp at 100 MHz. The IF chirp is then tapered to the desired pulse shape by the attenuator. The resulting chirp is upconverted to RF by mixing with a 13.7 GHz oscillator. This signal is transitioned into a waveguide where it is again filtered and amplified with a solid-state amplifier to a level of +13 dBm. In laboratory testing, this signal is sent directly to the receiver stage or is amplified by a TWTA to a power level of 250 Watts (+54 dBm). In the latter case, the high output power of the TWTA is sent to a high power load and a small amount is coupled off for the receiver. In both cases the sampled pulse is attenuated down to the level expected in actual operation and sent to the receiver's low noise amplifier. After the signal is amplified and filtered, it is downconverted to an IF of 70 MHz, where it is again filtered and amplified to the proper level. The final stage of the receiver downconverts the signal to baseband, amplifies it, and digitizes it with a high speed A/D converter. Each pulse is stored in a memory buffer, and then read into the microprocessor where it can be recorded on a disk and sent to a desktop computer for pulse compression.

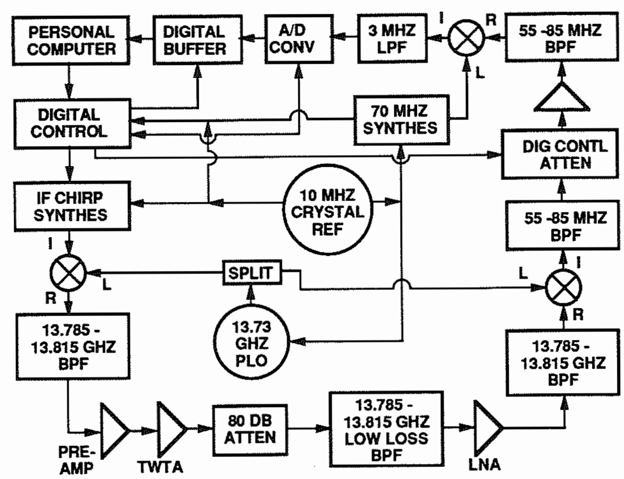

Figure 5. Block digram of the 13.8 GHz ARMAR test model.

Figure 6(b) shows a typical test chirp after compression. This test chirp has a 40-μsec pulse duration, a 3-MHz bandwidth (TB=120), and a d value of 0.6. It can be seen that the test data is very similar to the simulated result shown in Fig. 6(a), and that the mid-to-far sidelobes are suppressed to the desired -60 dB level. Test results obtained for TB values between 72 and 144 are similar.

6. CONCLUSIONS

Pulse compression technique is attractive to spaceborne and airborne radar rain mapping applications because it allows good range resolution for rain profiling without substantial increase in peak transmitted power. In order to capitalize on these advantages, however, the pulse compression sidelobes must be suppressed to a very low level. For a pulse compression rain radar operating at 13.8 GHz, it was shown that a -60 dB compression sidelobe level is required in order to retrieve the rain signal from the imbedded surface clutter. A technique based on matched filtering of the cosine-tapered linear FM signal and the corresponding hardware configuration have been developed for the JPL's Airborne Rain Mapping Radar. Both the simulated and the breadboard test results have indicated that the -60 dB compression sidelobe level is achievable.

Because of the stated advantages, the success of this pulse compression radar system will have far-reaching impacts on the designs of future spaceborne radars for meteorological observations. The development of the ARMAR 13.8-GHz system was completed and the first flight test of the pulse compression module will be conducted in the summer of 1992.

It should also be noted that although this paper was devoted to the problem of pulse compression sidelobes for a 13.8 GHz downward looking rain radar, the described technique, however, is in general applicable to any situations and at other radar

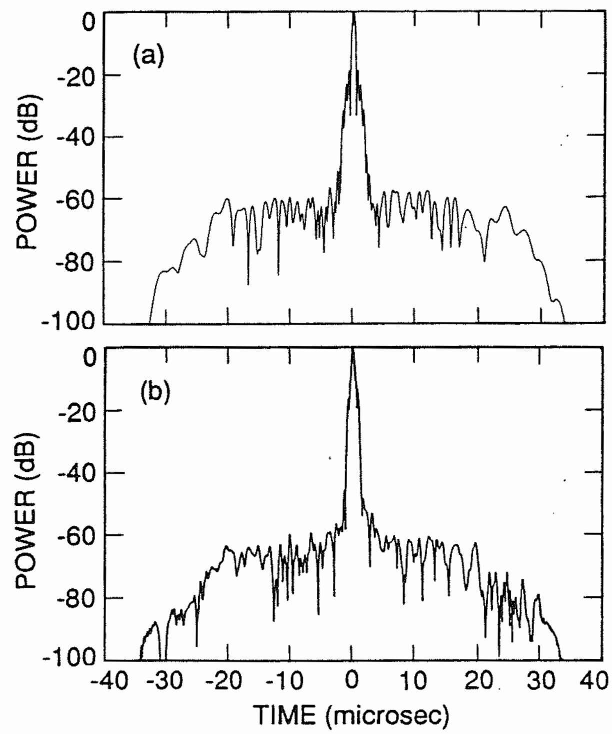

Figure 6. (a) Simulated result of a compressed pulse with TB=120 (T=40μsec, B=3MHz) and with Cosine-taper weighting when permissible contributions from all distortion sources under consideration are taken into account. (b) Test result of the ARMAR generated chirp signal with the same chirp and amplitude characteristics.

frequencies where low mid-to-far range sidelobe levels are required.

ACKNOWLEDGEMENT

We would like to thank R. Denning, W. Ricketts and W. Proniewicz for their help in developing the ARMAR system hardware. The research described in this paper was performed by the Jet Propulsion Laboratory, California Institute of Technology, under contract with the National Aeronautics and Space Administration.

REFERENCES

Cook, C. E. and M. Bernfield, 1967: Radar Signal - *An Introduction to Theory and Application.* Academic, 531 pp.

Harris, F. J., 1978: On the use of windows for harmonic analysis with the discrete Fourier Transform. *IEEE Proc.*, **66**, 51-83.

Im, E., and F. Li, 1989: Tropical rain mapping radar on the space station. *Proc. IGARSS'89*, 1485-1490.

Li, F. K., K. E. Im, W. J. Wilson, 1988: On the design issues for a spaceborne rain mapping radar. *Tropical Rainfall Measurements*, J.S. Theon and N. Fugono, Ed., A. Deepak Pub., 387-393.

NASA, 1990: Tropical Rainfall Measuring Mission (TRMM) Science: Research Opportunities. NASA NRA-90-OSSA-15.

Shin, K.-S., and G. R. North, 1988: Sampling error study for rainfall estimate by satellite using a stochastic model. *J. Appl. Meteor.*, **27**, 1218-1231.

Simpson, J., R. F. Adler, and G.R. North, 1988: A proposed Tropical Rainfall Measuring Mission (TRMM) satellite. Bull. Amer. Met. Soc., 69, 278-295.

Ulaby, F. T., R. K. Moore, and A. K. Fung, 1982: *Microwave Remote Sensing: Active and Passive,* **II**, Addison-Wesley, 498 pp.

Wilson, W. J., G. S. Parks, F. K. Li, K. E. Im, and R. J. Howard, 1988: Airborne Rain Mapping Radar. *Tropical Rainfall Measurements*, J.S. Theon and N. Fugono, Ed., A. Deepak Pub., 229-233.

DIFFERENTIAL ROTATION, CLOUD RADIANCES AND GENERALIZED SCALE INVARIANCE

S. LOVEJOY, D. SCHERTZER* , K. PFLUG
Department of Physics, McGill University, 3600 University St., Montréal, Québec, H3A 2T8, Canada

ABSTRACT

The standard picture of atmospheric dynamics is that of an isotropic two-dimensional large scale and an isotropic three-dimensional small scale, the two separated by a dimensional transition called the "meso-scale gap". Evidence now suggests that on the contrary, atmospheric fields while strongly anisotropic, are nonetheless scale invariant right through the meso-scale. Using visible and infra-red satellite cloud images and the formalism of generalized scale invariance (GSI), we attempt to quantify the anisotropy for cloud radiance fields in the range 1 - 1000 km. To do this, we exploit the statistical translational invariance of the fields by studying the anisotropic scaling of lines of constant Fourier amplitude, and investigate the change in shape and orientation of average structures with scale.

1. INTRODUCTION:

There are two principle approaches to understanding atmospheric dynamics. The first is a statistical, turbulent approach conventionally based on the assumption of a small scale isotropic three dimensional turbulence and large scale isotropic two dimensional turbulence. The second, the "dynamical meteorology" approach starts with a phenomenological classification of structures, and seeks deterministic understanding of corresponding idealized flows. The two approaches have never been satisfactorily reconciled because (until recently) the turbulence approach has not been able to statistically explain the existence of "coherent" atmospheric structures, and the dynamical meteorology approach has not been able to demonstrate its compatibility with ubiquitous power law spectra, and other statistical manifestations of scaling predicted by turbulence theory.

In a series of papers (Schertzer and Lovejoy 1983, 1984, 1985a,b, 1989a,b, 1991, Lovejoy and Schertzer 1985, 1986), we have criticized both approaches and proposed the outlines of a synthesis which can potentially reconcile the statistics with the (coherent) structures, as well as accounting for the observations. The unified scaling model is a synthesis based on the dramatic advances in scaling notions that have occured over the last ten years. Two distinct advances are paramount here. The first, is the recognition that the general framework for scaling *fields* - and hence dynamics - is multifractals rather than fractals (which are only adequate for treating scaling *sets*). Multifractals are complex superpositions of singularities of various orders, and thus intrinisically involve coherent structures of all sizes. The general canonical multifractals (associated with the turbulent atmospheric cascade processes) not only generate such coherent structures on each realization, but have the (realistic) property that high order singularities (corresponding to violent, intense events), exist which will almost surely be absent on an individual realization, but which will (almost surely) exist in a sample of a sufficiently large number of realizations. In meteorological terms, this corresponds to the appearance of different "synoptic conditions" on each realization without any artificially imposed nonstationarity in the basic dynamical mechanism. The discovery of universal multifractals (Schertzer and Lovejoy 1987a,b, 1989, 1991, Schertzer et al 1991), makes multifractals even more appealing as a framework for the dynamics since the properties of the cascades will depend on only three fundamental parameters- most of their details will be "washed out" in the limit of a large number of interacting structures. In recent papers (Lovejoy et al 1992, Tessier et al 1992, Lovejoy and Schertzer 1990), the (isotropic) energy spectra of satellite radiances (as well as multifractal paramters) were systematically studied for the first time, confirming that the scaling accurately holds right through the mesoscale (from at least ≈300m to ≈4000km, see fig. 1).

The second major advance was the discovery of "Generalized Scale Invariance" (GSI) (Schertzer and Lovejoy 1983, 1985a,b, 1988, 1989a, 1991, Lovejoy and Schertzer 1985, 1986), which provides the general framework for defining the notion of scale and scale transformations in scale invariant systems. It answers the question as to what are the minimum (most general) conditions under which the large and small scales of a system can be related to each other only by their respective scale ratios, without reference to their actual sizes. In atmospheric (as in many other geophysical systems), the physical justification for scale invariance is the absence of a well-defined (and strong enough) mechanism that can break the scale invariance symmetry respected by the basic physical laws as expressed in the dynamical equations. Indeed, when analyzed in detail, the standard model's prediction (see e.g. Monin 1972 or Lesieur 1987) of fundamentally distinct dynamics at large and small scale is *not* based on the identification of *any* dynamical scale breaking mechanism whatsoever! It is rather an indirect theoretical inference resulting from the adherence to outmoded restrictive scaling ideas which identify scaling with isotropy, and which deduces a scale break from the evident lack of isotropy (as evidenced particularly by the large scale stratification of the atmosphere). The final inference concerning the distinct dynamics is based on the fact that 2D isotropic and 3D isotropic turbulence are fundamentally different because of the existence of vortex stretching in the latter but not in the former. The overall result of this chain of reasoning is that the standard model predic' very different regimes with different power law energy spectra (k^{-3}, $k^{-5/3}$ respectively), seperated by a sharp (Schertzer and Lovejoy 1985a) "dimensional transition" in the mesoscale. The alternative 2.555... (23/9) dimensional unified scaling model of atmospheric dynamics proposed by Schertzer and Lovejoy 1983, 1985a simply retains the assumption of scaling and dynamical cascades, but drops the ad hoc assumption of isotropy. Rather than requiring energy injection to occur over a narrow range of (large) scales, it is expected to occur in a scaling way over a wide range, corresponding to the observed scaling modulation of the solar radiation by clouds. The primary boundary conditions such as topography are also (multiple) scaling (e.g. Lovejoy and Schertzer 1990b, Lavallée et al 1992), and will not break the scaling of the dynamics.

2. GSI IN REAL AND FOURIER SPACE:

The purpose of this paper is to report on some new results testing the generalized scale invariance of satellite cloud radiances. This summarizes the results of Pflug et al 1992.

GSI has the following basic ingredients:

i) A unit "ball" B_1 which defines all the unit vectors. If an isotropic unit ball exists, we call the corresponding scale the "sphero-scale".

ii) A (semi) group of scale changing operators $T_\lambda=\lambda^{-G}$ which reduces the scale of vectors by scale ratio λ: $B_\lambda=T_\lambda(B_1)$ is the ball of all vectors at scale λ. Virtually the only other

*Laboratoire de Météorologie Dynamique, Tour 15-25, Boite 99, Univerisité Pierre et Marie Curie, 4 Place Jussieu F-75252 Paris Cedex 05, France.

restriction on T_λ is that the B_λ are strictly decreasing ($B_\lambda \supset B_{\lambda'}$;$\lambda<\lambda'$), hence that the real parts of the (generalized) eigenspectrum (Schertzer and Lovejoy 1985b) of G are all >0.

iii) A measure of scale such as some power of the volume of S_λ; the exact definition is somewhat a matter of convenience or convention[5]; although the most obvious is to use the fact that if ϕ^D indicates the ordinary volume operator in a space dimension D, and d_{el}=Trace G, then a convenient "elliptical" scale ϕ_{el} is given by the following relation:

$$\phi_{el}{}^{del}(B_\lambda) = \phi^D(B_\lambda) = \lambda^{del}\phi^D(B_1) = \lambda^{del}\phi_{el}{}^{del}(B_1) \qquad (1)$$

Note that in GSI size is a measure (not metric) quantity and the type of scale invariance is not specified i.e. GSI can apply to fractal sets, multifractal measures or other types of scale invariant systems. When G is a matrix we have "linear GSI", the anisotropy is position independent. Linear GSI can always be regarded as a local approximation to the full (nonlinear) GSI. When the matrix is the identity, we have self-similar scale invariance, when G is a diagonal matrix, we have a "self-affine" system, and when off-diagonal elements are present, we have have differential rotation. In all cases, d_{el} is an important characteristic since it quantifies the overall rate of change of volumes of structures.

Up until now, methods for empirically evaluating G have been limited to estimates of d_{el}. For example, for atmospheric motions, Schertzer and Lovejoy 1983, 1985a obtained $d_{el}\approx 23/9=2.555...$ in (x,y,z) space, and for rain (Lovejoy et al 1987) $d_{el}=2.22\pm0.07$, and also for rain, for space time transformations ((x,y,t) space), 2.5 ± 0.3 (Lovejoy and Schertzer 1991, for a review see Lovejoy and Schertzer 1992). In each case, d_{el} characterizes stratification, $d_{el}=3$ corresponding to isotropic (self-similar) scaling, $d_{el}=2$ to complete stratification into layers. In this note, we report on results of a new "Monte Carlo Differential Rotation" technique which for the first time enables us to empirically estimate the off-diagonal elements of linear GSI.

We illustrate the method on visible and infra red satellite pictures at 1.1km resolution (figs. 2a,b,c). These pictures are from the NOAA 9 satellite and were remapped on regular 256X256 and 512X512 point grids before the analysis was performed. Details of this and the analysis techniques may be found in Pflug et al 1992. We assume statistical translational invariance of the radiance fields; in Fourier space, this implies random phases, hence we examine the modulus of the Fourier amplitudes squared (the spectral energy density, denoted $P(\underline{k})$ at wavenumber $\underline{k}$, see fig. 3a,b,c). If $\underline{x}_\lambda = T_\lambda \underline{x}_1$, then the corresponding Fourier relation $\underline{k}_\lambda = \tilde{T}_\lambda \underline{k}_1$, where the Fourier operator $\tilde{T}_\lambda$ has generator $\tilde{G} = G^T$ (where "T" indicates "transpose"). Furthermore, using a decomposition into quaternions (Pauli matrices), we can obtain the following explicit formula for linear GSI in two dimensions:

$$G=\begin{pmatrix} d+c & f-e \\ f+e & d-c \end{pmatrix}; \qquad \tilde{G}=\begin{pmatrix} d+c & f+e \\ f-e & d-c \end{pmatrix} \qquad (2)$$

$$\tilde{T}_\lambda = \lambda^{\tilde{G}} = \lambda^d\left(1\cosh au + (\tilde{G} - d1)\frac{\sinh au}{a}\right) \qquad (3)$$

$$a^2=c^2+d^2-e^2; \qquad u=\log\lambda$$

When a is real, stratification dominates, whereas when a is imaginary, rotation dominates; these two qualitatively different behaviors have been proposed as a basis for classifying galaxies into barred or spiral types (Schertzer and Lovejoy 1989a).

If T_λ is the real space scale changing operator for second order moments (structure functions), then the corresponding Fourier space operator satisfies:

$$P(\tilde{T}_\lambda \underline{k}) = \lambda^{-s} P(\underline{k}) \qquad (4)$$

where s is an (anisotropic) spectral exponent. Hence in fig. 3, $\tilde{T}_\lambda$ will map one set of isolines of P onto another.

Unlike the vertical or time axis which are stratified with respect to the horizontal, the two horizontal directions display no obvious overall stratification, we therefore took our definition of size to be the square root of the area of the B_λ, hence $d_{el}=2$, d=1. To test linear approximations to GSI, we therefore seek to determine c, e, f, s, the energy density of the unit ball, as well as the shape of the unit ball. In the simplest cases (see fig. 2a,b), a nearly circular ("sphero-scale"), seems to exist, hence we only require an estimate of the corresponding radius (a total of six parameters). In case 3c however, no sphero-scale is apparent; indeed, given the roughly log spiral shape of the cyclone, one does not expect one to exist. In the latter case, we used the following parametrization (this polar coordinate parametrization of the unit ball is the first few terms in a fourier series respecting the fourier symmetry $P(\underline{k})=P(-\underline{k})$):

$$r(\theta) = r_0 + a_1\cos 2\theta + b_1\sin 2\theta + a_2\cos 4\theta + b_2\sin 4\theta \qquad (5)$$

The full details of the parameter estimation scheme are given in Pflug et al 1992; in outline a quadratic error function is defined and the parameters are adjusted for best fit. The only complication is that while it is easy to compute $\underline{k}_\lambda$ give G, λ, $\underline{k}_1$, (by applying T_λ), the inverse, (finding λ given $\underline{k}_\lambda$, $\underline{k}_1$, G) involves solving a transcendental equation and is numerically prohibitive due to the large number of times it must be solved by the regression algorithm. The error in the parameters is therefore only statistically estimated using a Monte Carlo method (hence the name).

3. CONCLUSIONS:

The resulting parameters are shown in table 1, the corresponding "balls" are superposed in fig. 3, showing the fairly accurate fits that are acheived. We may note the following:

a) It has been found (fig. 1, using isotropic spectra) that the parameter s is mostly a function of wavelength of the radiation, this is confirmed here.

b) In the two cases where sphero-scales exist, they are right in the middle of the "meso-scale", the horizontal scale corresponding to the exponential fall-off height for the

	Image 1	Image 2	Image 3
Image type	Infra red, Marine stratocumulus	Visible, stratocumulus	Visible, midlatitude cyclone
Range of scales	1.1X256=281km	1.1X512=563km	2.2X512=1126km
s	2.5±.1	2.18±.05	2.10±.01
sphero scale	3.5±.8km	3.9±.6km	not applicable*
c	-0.43±.08	-0.32±.05	-0.18±.03
f	0.0±.1	-.01±.02	0.00±.02
e	-0.4±.2	0.17±.04	0.04±.05
a	0.2±.3	0.28±.07	0.18±.03
$\lvert\Delta\theta\rvert_{max}$	60±30°	30±10°	10±10°

Table 1: A comparison of the characteristics of the three satellite images discussed in the text. a (see eq. 3) was found to be real in all cases, the total rotation between small and large scale structures is therefore bounded, $\lvert\Delta\theta\rvert_{max}$ providing an estimate of this bound.

*As indicated in the text, no spheroscale is apparent in this case, using eq. 4, in units of pixels in wavenumber space (fig. 2c), choosing an energy density level arbitrarily, near the centre of fig. 2c, we found $r_0=108\pm1$, $a_1=-20\pm1$, $b_1=-23\pm1$, $a_2=17\pm1$, $b_2=-6\pm1$.

pressure field (≈10km). This is totally at odds with the standard view which postulates a qualitative change ("dimensional transition", "meso-scale gap") in the meso-scale; this may be the primary way that the vertical scale height influences the horizontal structure.

c) The primary variation in the scaling parameters seems to be c, e which vary much more than a (which is always positive indicating strafication dominance). This suggests that a is a more fundamental parameter.

d) The cases with the most rotation of structures with scales are the "texture" fields 1, 2. This is not as surprizing at it may seem; computer simulations of fractal clouds show that the anisotropy is indeed asssociated with texture; whereas the cyclone is already nearly a (self-similar, isotropic) scale invariant log-spiral.

Obviously many more pictures must be analysed before more definate conclusions can be reached. The statistics of the parameters should be examined, higher order moments should be studied, and finally multifractal simulations (Wilson et al 1991) should be performed to confirm that the analyzed generator does indeed correspond to the true generator.

References:

Lavallée, D., S. Lovejoy, D. Schertzer, P. Ladoy, 1992: Nonlinear variability and Landscape topography: analysis and simulation. **Fractals in Geography**, Eds. L. De Cola, N. Lam (in press).

Lesieur, M., 1987: *Turbulence in Fluids*. Martinus Nijhoff Publishers, Dordrecht.

Lovejoy, S., D. Schertzer, 1985: Generalized scale invariance in the atmosphere and fractal models of rain. *Wat. Resour. Res.*, 21, 1233-1250.

Lovejoy, S., D. Schertzer, 1986: Scale invariance, symmetries, fractals and stochastic simulations of atmospheric phenomena. *Bull AMS*, 67, 21-32.

Lovejoy, S., D. Schertzer, P. Ladoy, 1986: Fractal characterisation of inhomogeneous measuring networks, **Nature, 319**, 43-44.

Lovejoy, S, D. Schertzer, A. A. Tsonis, 1987: Functional box-counting and multiple elliptical dimensions in rain. *Science*, 235, 1036-1038.

Lovejoy, S., D. Schertzer, 1990: Multifractals, universality classes and satellite and radar measurements of cloud and rain fields. *J. Geophys. Res.*, 95, 2021-2034.

Lovejoy, S., D. Schertzer, 1991: Multifractal analysis techniques and the rain and cloud fields from 10^{-3} to 10^{6} m. *Scaling, Fractals and Non-linear Variability in Geophysics*. D. Schertzer and S. Lovejoy, Eds., Kluwer, Dordrecht-Boston, 111-144.

Lovejoy, S., D. Schertzer, 1992: Multifractals and Rain. **New uncertainty concepts in hydorology and hydrolgical models**, Ed. A. W. Kundzewicz, Cambridge University press (in press).

Lovejoy, S., D. Schertzer, K. Pflug, 1992: Generalized scale invariance and differential rotation in cloud radiances. *Physica A* (in press).

Lovejoy, S., D. Schertzer, P. Silas, Y. Tessier, D. Lavallée, 1992: The unified scaling model of atmospheric dynamics and Systematic analysis of scale invariance in cloud radiances. Submitted to *Annales Geophys.*

Monin, A. S., 1972: *Weather Forecasting as a Problem in Physics*. MIT Press, Cambridge.

Pflug, K., S. Lovejoy, D. Schertzer, 1992: Differential Rotation and Cloud Texture: analysis using Generalized Scale Invariance. *J. Atmos. Sci.*, (in press).

Schertzer, D., S. Lovejoy, 1983: Elliptical turbulence in the atmosphere. *Proceedings of the 4th Symposium on Turbulent Shear Flows*. Karlsrhule, West Germany, 11.1-11.8.

Schertzer, D., S. Lovejoy, 1984: On the dimension of atmospheric motions. *Turbulence and Chaotic Phenomena in Fluids*. T. Tatsumi, Ed., Elsevier North-Holland, New York, 505-508.

Schertzer, D., S. Lovejoy, 1985a: The dimension and intermittency of atmospheric dynamics. *Turbulent Shear Flow 4*. B. Launder, Ed., Springer, New York, 7-33.

Schertzer, D., S. Lovejoy, 1985b: Generalized scale invariance in turbulent phenomena. *P. C. H. Journal*, 6, 623-635.

Scherzter, D., S. Lovejoy, 1987a: Singularités anisotropes et divergence de moments en cascades multiplicatifs. *Annales Math. du Que.*, 11, 139-181.

Schertzer, D., S. Lovejoy, 1987b: Physical modeling and analysis of rain and clouds by anisotropic scaling multiplicative processes. *J. Geophys. Res.*, 92, 9693-9714.

Schertzer, D., S. Lovejoy, 1988: Multifractal simulation and analysis of clouds by multiplicative processes. *Atmospheric Research*, 21, 337-361.

Schertzer, D., S. Lovejoy, 1989a: Generalized scale invariance and multiplicative processes in the atmosphere. *Pageoph*, 130, 57-81.

Schertzer, D. S. Lovejoy, 1989b: Nonlinear variability in geophysics: Multifractal simulations and analysis. *Fractals: Physical Origin and Consequences*. L. Pietronero, Ed., Plenum, New York, 49-79.

Schertzer, D., S. Lovejoy, 1991: Nonlinear geodynamical variability: multiple singularities, universality and observables. *Scaling, Fractals and Non-linear Variability in Geophysics*. D. Schertzer and S. Lovejoy, Eds., Kluwer, Dordrecht-Boston, 41-82.

Schertzer, D., S. Lovejoy, D. Lavallée, F. Schmitt, 1991: Universal hard multifractal turbulence, theory and observations. **Nonlinear Dynamics of Structures.** R. Z. Sagdeev et al, eds., World Scientific R. Z. Sagdeev, U.Frisch, F. Hussain, S.S. Moiseev, N.S. Erokhin eds., World Scientific, 213-235.

Tessier, Y., S. Lovejoy, D. Schertzer, 1992: Universal multifractals: theory and observations for rain and clouds. *J. Appl. Meteo.* (in press).

Wilson, J., S. Lovejoy, D. Schertzer, Scaling, fractals and non-linear variability in geophysics, D. Schertzer, S. Lovejoy eds.,185-208, Kluwer, (1991).

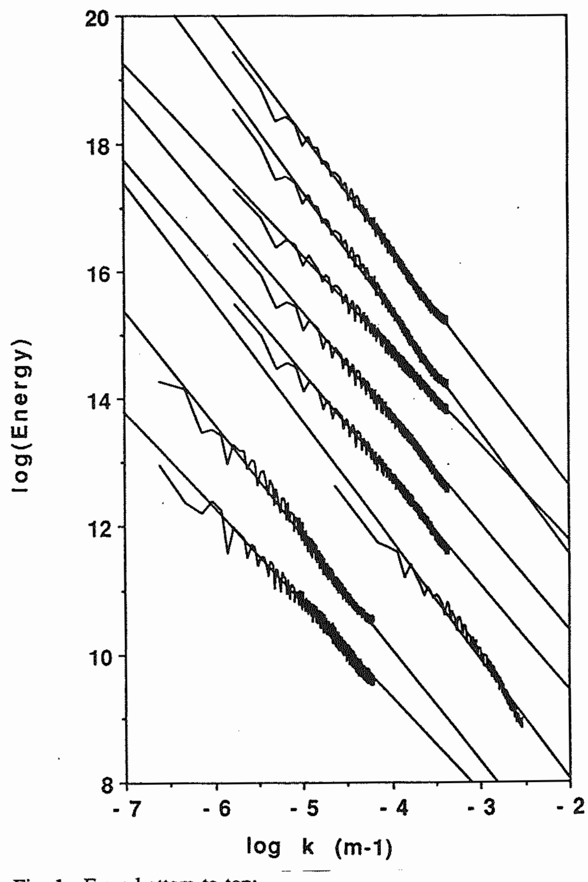

Fig. 1: From bottom to top:
-GOES satellite VISSR pictures at 8 km resolution for visible (0.7 to 1.0 μm) and thermal infrared (10.5 to 12.5 μm taken over a region of the Atlantic west of Spain. Three we could cover the range of scales from 8 km to 4000 km.analyzed three 512 by 512 pixel images were used for each.
-Average of three (MSS) LANDSAT pictures (wavelength of 0.49 to 0.61 μm) over the tropical Pacific. Resolution 160m.
-Average of 15 NOAA AVHRR pictures at 1.1km resolution over the tropical Atlantic, channels 1 to 5 (0.5-0.7μm, 0.7-1.0μm, 3.6-3.9μm, 10.4-11.1μm, 11.4-12.2μm).

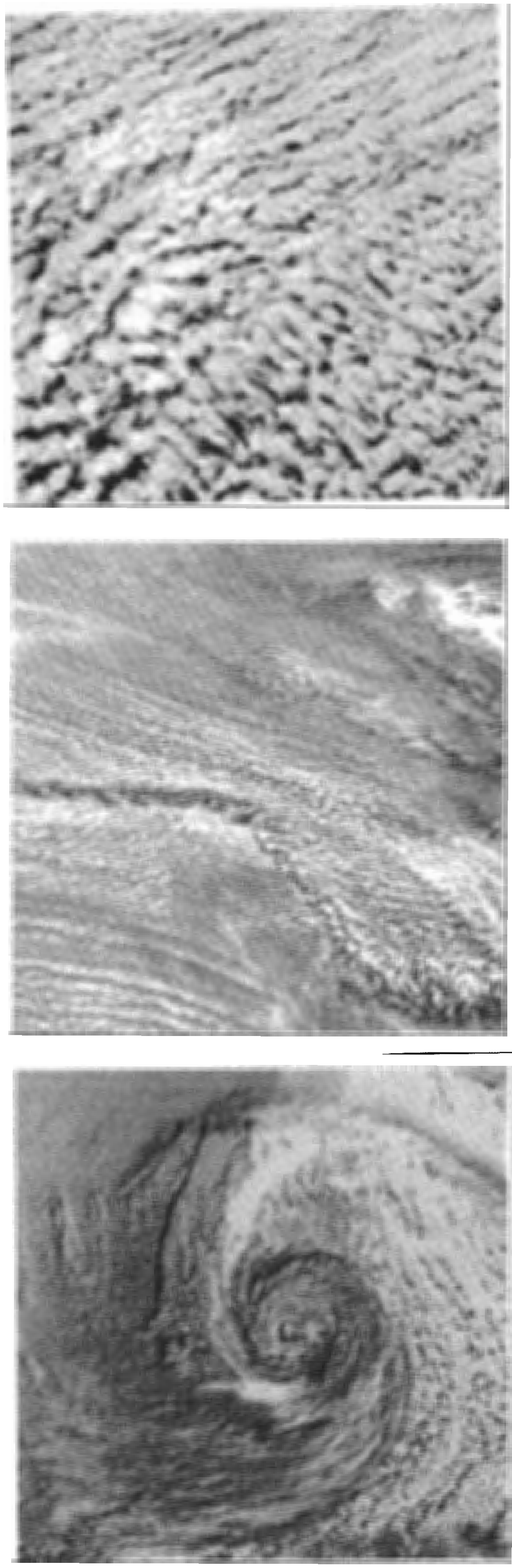

a

b

c

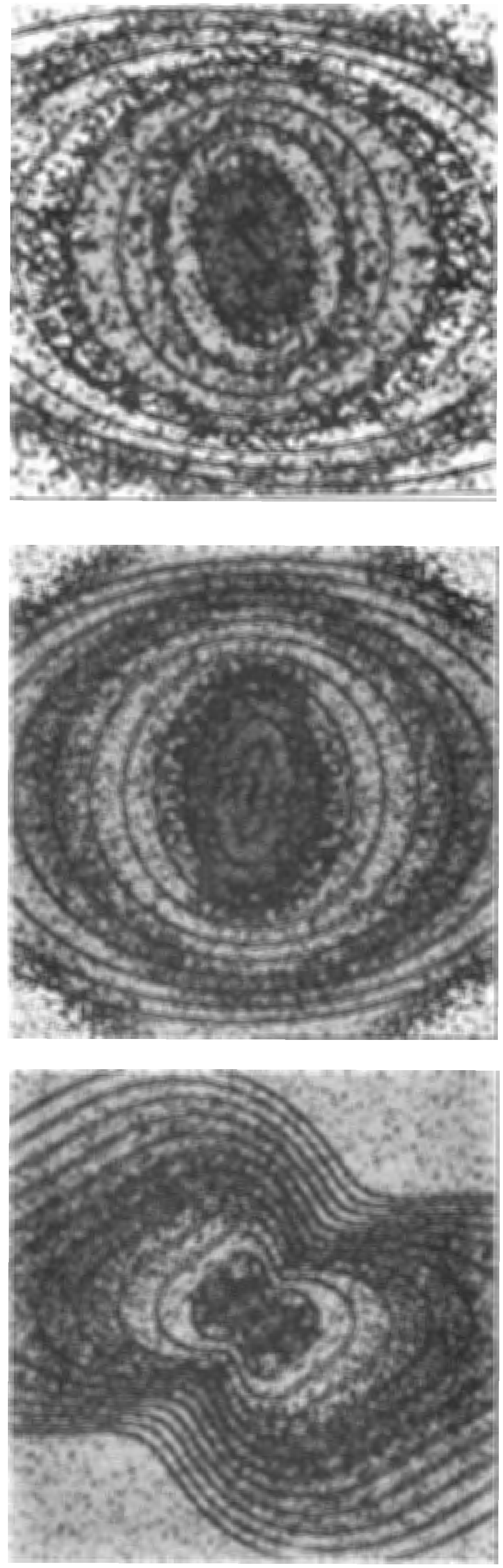

Fig. 2a,b,c: A grey shade rendition of images 1, 2, 3 the radiance fields studied in the text, see table 1 for details.

Fig. 3a,b,c: A colour rendition of the log of the Fourier space energy density of images 1, 2, 3. Superposed are the isolines as deduced from the Monte Carlo Differential Rotation technique using the parameters in table 1.

RETRIEVAL OF PRECIPITATION FROM SATELLITE MICROWAVE MEASUREMENT USING BOTH EMISSION AND SCATTERING

Guosheng Liu and Judith A. Curry

Department of Aerospace Engineering Science, University of Colorado at Boulder, CO, USA 80309-0429

1. INTRODUCTION

Measurements of the global precipitation are of enormous importance for understanding the Earth's energy balance. The latent heat released by precipitation is the largest source of atmospheric heating in the tropics and provides a significant heat source in the temperate latitudes as well. As a regulator of salinity, precipitation also plays an important role in determining ocean dynamics and thermodynamics. The lack of surface-based measurements of precipitation particularly in oceanic regions makes satellite remote sensing indispensable. This study is an attempt to improve satellite rainfall retrievals using the Special Sensor Microwave/Imager (SSM/I). Horizontally polarized brightness temperatures at 19 and 85 GHz are used in the present algorithm, although data at 37 and 22 GHz are also available.

Three different approaches to retrieving rainfall from passive satellite microwave measurements have been utilized: emission-based algorithms, scattering-based algorithms, and retrievals utilizing a radiative transfer model. Emission-based rainfall retrieval algorithms utilize the fact that rain clouds emit more radiation than does the background ocean and cloud-free atmosphere. The principal drawbacks to emission-based rainfall retrieval algorithms are that they saturate at relatively low rainfall rates and also show substantial sensitivity to the assumed freezing level. Scattering-based rainfall retrieval techniques utilize the scattering by ice particles at the rain cloud top, implicitly assuming that a larger amount of ice particles at cloud top is associated with heavier rainfall. Difficulties using scattering-based techniques arise primarily in situations other than deep convective precipitation. Precipitation retrievals using a radiative transfer model have also been presented by several investigators. However, these algorithms require the solution of the radiative transfer equation for every observed datum and require assumptions about the structure of the rain clouds, which are usually unknown.

Owing to the deficiencies of the retrieval techniques described in the preceding paragraphs, we have derived a new SSM/I rainfall retrieval algorithm that combines the emission and scattering regimes. The algorithm is developed using a theoretical study of microwave radiative transfer in plane-parallel rain clouds. Algorithms for rainfall retrieval over ocean and over land using SSM/I data are presented. Validation is made using the surface (radar and rain gauge) data in the region of 25° to 45°N and 120° to 145°E during June and July 1989, corresponding to the first GPCP Algorithm Intercomparison Project (AIP/1).

2. THE PRECIPITATION ALGORITHM

Assuming a plane-parallel horizontally homogeneous raincloud, the radiative transfer equation is solved by an iterative method. The atmosphere is divided vertically into 15 layers and the depth is each layer is 1 km. Three different types of rainclouds are applied to this model calculation: (1) liquid-only raincloud; (2) thin ice-layer topped raincloud; and (3) mixed-phase deep raincloud. Figure 1 shows δT_B ($=T_B - T_{B0}$, where T_B and T_{B0} are the brightness temperatures for rainfall and a "threshold" cloudy situation.) of 19 and 85 GHz versus rainfall rate over ocean for the three rainfall types. It is seen that for rainfall rate less than 12 mm/h δT_B at 19 GHz increases with rainfall rate while δT_B at 85 GHz either does not change much or decreases with rainfall rate. The main feature of this low rainfall range is that the increase in rainfall rate increases the 19 GHz vale of δT_B, "emission regime". For higher rainfall rates, however, the major feature is that the δT_B at 85 GHz decreases with rainfall rate because of the scattering by ice particles near the cloud top, "scattering regime". The algorithm presented in this study will combine the two regimes.

It is seen from Figure 2 that δT_{B19}- δT_{B85} increases with rainfall rate up to 50 mm/h without being saturated, although this relationship is not linear and depends on the rain cloud

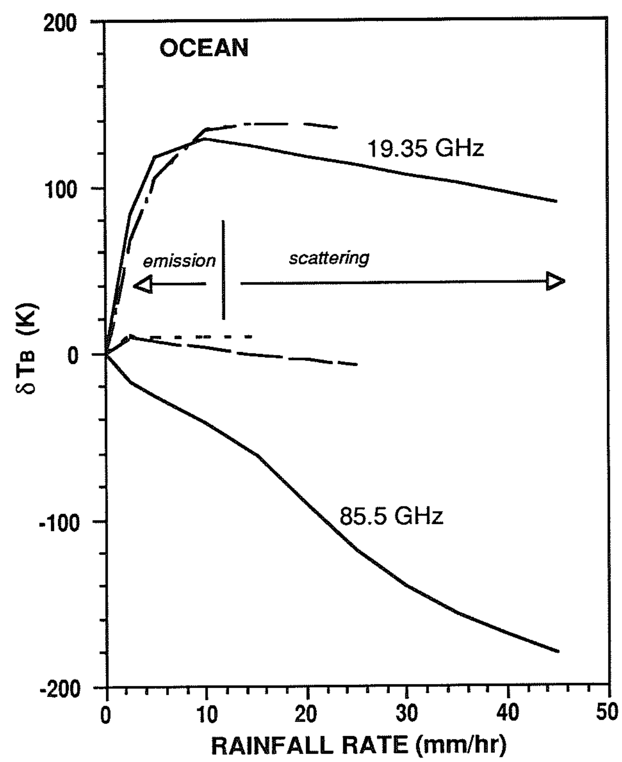

Fig.1 δT_B of 19 and 85 GHz versus rainfall rate over ocean: liquid-only rain cloud (dotted curve); thin ice topped rain cloud (dashed curve); and mixed-phase deep rain cloud (solid curve).

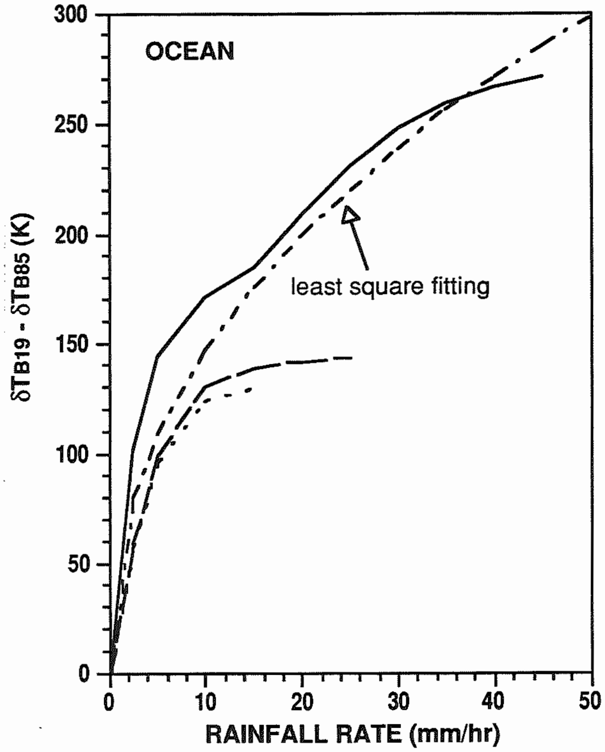

Fig. 2 Values of δT_{B19} - δT_{B85} versus rainfall rate over ocean: liquid-only rain cloud (dotted curve); thin ice topped rain cloud (dashed curve); and mixed-phase deep rain cloud (solid curve). A least squares fitting curve is also shown.

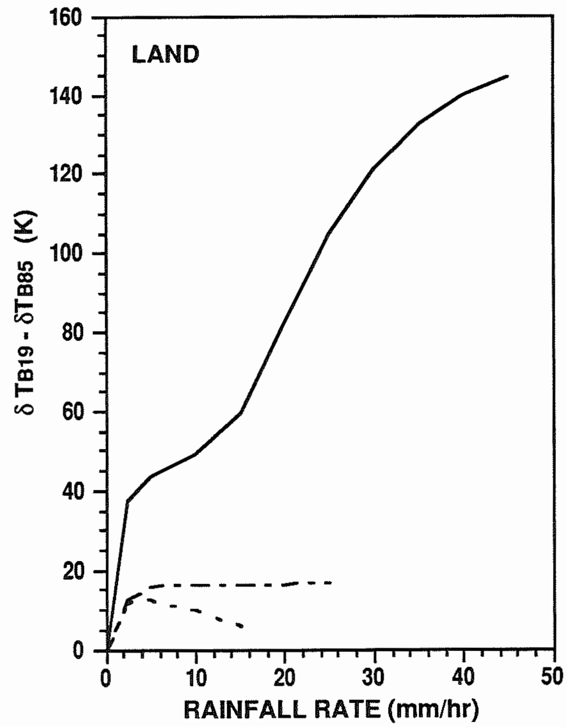

Fig. 3 Same as Figure 2, except for over land.

type. This simple combination, δT_{B19}- δT_{B85}, not only takes advantage of the emission-based method in directly using the radiation of raindrops as a measure of rainfall rate but also picks up the scattering signal due to ice particles to obtain rainfall information for large rainfall rates.

Figure 3 shows δT_{B19}- δT_{B85} versus rainfall rate for rainfall over land. Although there is little signal of rainfall rate for liquid-only and thin ice topped rain clouds, we still can detect the mixed-phase deep rain clouds.

Using the curves in Figures 2 and 3 as a reference, we assume the following form for the rainfall retrieval algorithm:

$$R = \alpha\, (\Delta T_B - \Delta T_{B0})^{\gamma} \ , \qquad (1)$$

where α and γ are coefficients, and $\Delta T_B = T_{B19} - T_{B85}$; $\Delta T_{B0} = T_{B019} - T_{B085}$.

First, let us consider the case of rainfall over ocean. Although the model results showed that ΔT_B-ΔT_{B0} and rainfall rate are relatively linear compared to emission-based algorithms (e.g., *Wilheit*, 1977), the nonlinearity is still significant. A least squares fit of (1) to the curves in Figure 2 shows that α=1.163E-04 and γ=2.276. Because the rainfall rate in one satellite field of view (FOV) is seldom uniform, the nonlinearity of the relationship given by (1) would cause an error in the estimated rainfall rate (*Chiu et al.*, 1990), which is referred to as the beam-filling problem. In order to obtain a better expression of the rainfall rate in terms of ΔT_B-ΔT_{B0} in which the beam-filling problem is also taken into account, we introduce a modification to the algorithm. The following three points are considered here in determining a correction for beam filling:

(1) The rainfall rate equation remains in the form of equation (1). According to the model results (1) is a good expression of the relationship between ΔT_B-ΔT_{B0} and rainfall rate.

(2) The relationship between ΔT_B-ΔT_{B0} and rainfall rate should be closer to linearity than that resulting from plane-parallel models. This is based on the observational results of *Spencer et al.* (1983), which showed that observed brightness temperature tends to be lower for light rainfall rates and becomes higher for large rainfall rates than the model-predicted values.

(3) By comparing the radar observations during the Global Atmospheric Research Program Atlantic Tropical Experiment (GATE) with rainfall rate retrievals from Nimbus 5 ESMR data using the emission-based algorithm, *Short and North* (1990) and *Chiu et al.* (1990) showed that the retrievals were approximately 50% smaller than the radar rainfall.

On the basis of these considerations the modified algorithm in the present study is (1) with α=5.5E-03 and γ=1.6. These coefficients are derived by letting the factor to multiply model-based retrievals be 2 at a rainfall rate of 5 mm/h and decreasing to 1 when the rainfall rate reaches to 50 mm/h.

The coefficients of α and γ for algorithm over land is simply determined by a linear fit to the model results because the relationship between ΔT_B-ΔT_{B0} and rainfall rate shown in Figure 2, is almost linear. The value of coefficients α and γ are determined to be 0.275 and 1, respectively.

Determination of Precipitation Threshold

Figure 4 is a scatter plot of T_{B19}-T_{B85} versus T_{B19} in a 5° latitude x 5° longitude domain obtained using SSM/I data during a 10-day period. The threshold is determined as follows: First, the minimum value of T_{B19}-T_{B85} is determined from a scatter plot as shown in Figure 4. The threshold value (T_{BTH}) is then defined as the brightness temperature of 19.35 GHz at the minimum value of T_{B19}-T_{B85} (T_{B19min}), plus a correction coefficient χ, i.e.,

$$T_{BTH} = T_{B19min} + \chi \text{ K.} \quad (2)$$

Accordingly, ΔT_{B0} is the value of T_{B19}-T_{B85}, where T_{B19}=T_{BTH}. It is noted that ΔT_{B0} is a function of both location and time. Comparing with *Petty and Katsaros* [1990], we find χ=10 K.

A similar approach is used to determine threshold over land.

Sensitivity of Algorithm

Sensitivity tests were made for the influences of freezing level height and surface temperature. Results showed that the current algorithm is much less sensitive to the changes of these parameters than emission-based methods. This is because the brightness temperature difference is used in the algorithm which cancels some of these influences.

3. ALGORITHM VALIDATION

Ocean

Figure 5 compares the retrievals by the algorithm with the observed hourly rainfall rate on islands. The retrievals by the algorithm seem to give a satisfactory agreement with the ground observations. Correlation coefficient is 0.89 and rms error is 2.6 mm/h. Errors in collocation and timing inconsistency may be the main cause of the scatter.

Figure 6 shows comparison with gauge-radar composite (*AMeDAS*) data averaged in a 1.25° x 1.25° domain. The agreement of the SSM/I retrieval and AMeDAS rainfall is obvious (correlation coefficient is 0.85, rms error is 0.62 mm/h), although the SSM/I retrieval seems to systematically overestimate the rainfall rate for the heavier rainfalls. Besides some mismatches of the two data sets (e.g., AMeDAS data are averaged in 1 hour while SSM/I data are from a single pass and navigation error in the SSM/I makes the two data sets subject to different position), the attenuation of the radar echo intensity by both rainfall and beam spreading suggests an underestimation of rainfall rate by the radar, because data used are far from radar site.

Figure 7 shows comparison with emission-based techniques using 19 GHz (*Chiu et al.*, 1990). It is seen from that for a rainfall rate less than 5 mm/h, the two retrievals are in a good agreement. But for larger rainfall rates, the retrievals from the emission-based method are substantially underestimated when compared to the present algorithm. Because the radiation at 19 GHz actually becomes saturated for a rainfall rate larger than 15 mm/h, it appears that the emission-based algorithm is systematically underestimating the larger rainfall rates. In a study of GATE data, *Short and North* (1990) and *Chiu et al.* (1990) pointed out that the retrievals from the emission-based method were approximately half of those by radar observation. This supports the validity of the current algorithm.

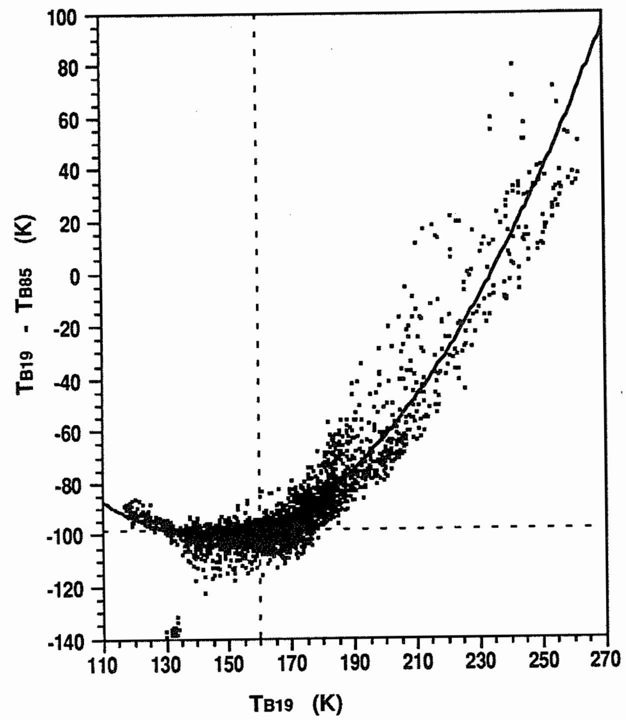

Fig. 4 Scatter plot of T_{B19} - T_{B85} versus T_{B19} from SSM/I data obtained over ocean for the region 25° -30° N and 135° -140° E for the period June 1-10, 1989.

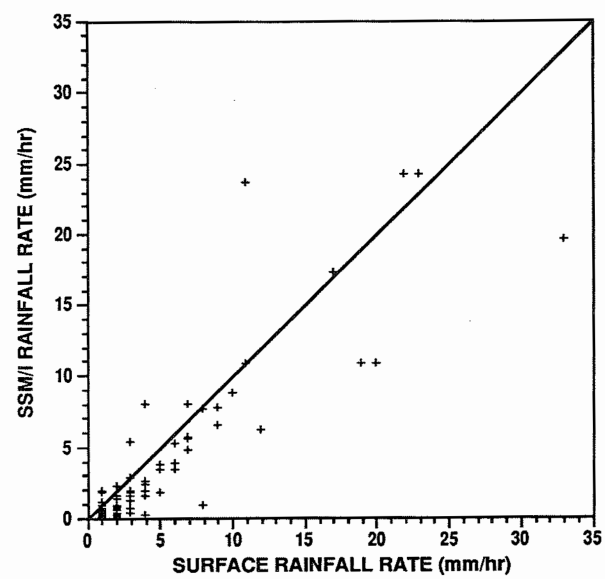

Fig.5 Scatter plot of SSM/I rainfall retrievals versus island surface observations of rainfall rates.

Land

Figure 8 shows the comparison of observed surface rainfall rates with ΔT_B-ΔT_{B0} over land. It is seen that our algorithm (the line in the figure) basically agrees with ground observations in tendency, but the scatter is also significant.

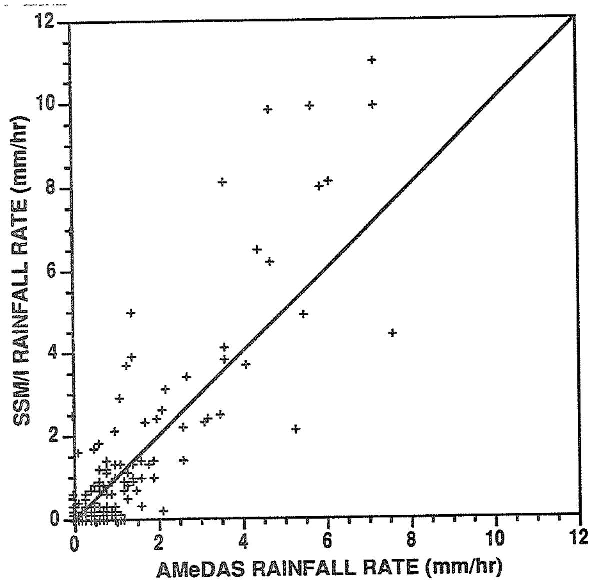

Fig.6 Scatter plot of SSM/I rainfall retrievals versus AMeDAS rainfall rates.

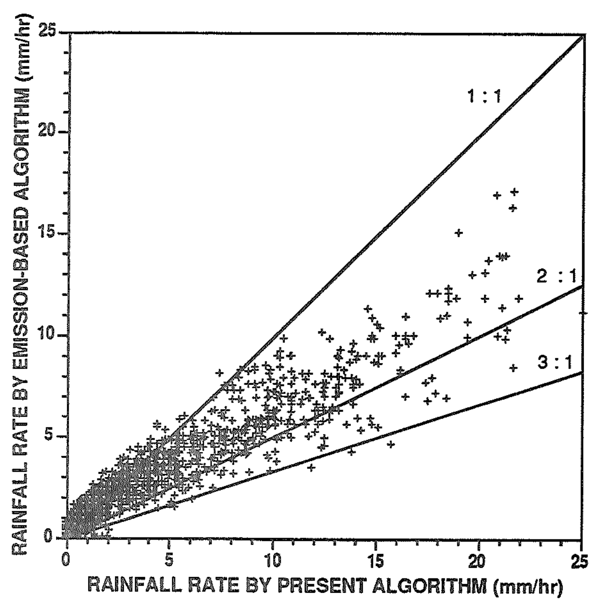

Fig. 7 Comparison of rainfall rates determined by the present algorithm with an emission-based algorithm. The lines indicated by 1:1, 2:1. and 3:1 indicate where the retrievals by this algorithm are equal to 2 and 3 times those obtained by the emission-based algorithm.

For a low rainfall rate (e.g., 1 to 3 mm/h) the value of ΔT_B-ΔT_{B0} varies from -10 to 35 K. There are two reasons for this problem: (1) our algorithm can only pick up scatter signal which is only significant for heavy rainfalls and (2) the uncertainty of land surface emission has the maximum influence when the rainfall rate is small. Therefore our land algorithm would not give reasonable retrievals for shallow rainfall.

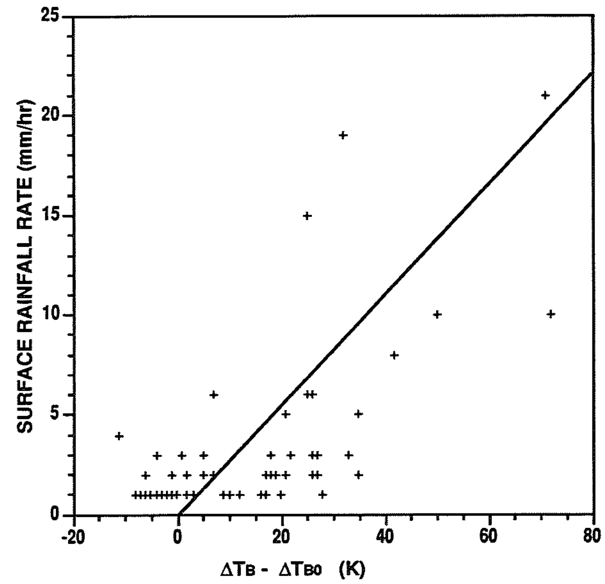

Fig. 8 Comparison with land observed rainfall. The solid line represents the rainfall rates obtained by the algorithm.

4. CONCLUSIONS

An algorithm for precipitation retrieval is presented for rainfall over both ocean and land on the basis of the model calculation. A threshold for discrimination of precipitation and a modification to model results for reducing the influence resulted from the beam-filling problem are included in the algorithm. Sensitivity test shows that this algorithm is not sensitive to changes in freezing level and surface temperature. Comparison with surface rainfall observations shows that the threshold for rainfall over ocean is in a good agreement, while the threshold for rainfall over land cannot sense rainfall rates less than 3 mm/h.

This algorithm is an attempt to combine the emission and scatter regimes of microwave radiation and the result is very encouraging. Besides being physically based, the algorithm has the characteristics of mathematical simplicity. Therefore it is suitable for processing large satellite data sets required for climatological research.

REFERENCES

Chiu, L. S., G. R. North, D. A. Short, and A. McConnell, 1990: Rain estimation from satellites: Effect of finite field of view, *J. Geophys. Res.*, **95**, 2177-2185.

Petty, G. W., and K. B. Katsaros, 1990: Precipitation observed over the South China Sea by the Nimbus-7 Scanning Multichannel Microwave Radiometer during winter MONEX, *J. Appl. Meteorol.*, **29**, 273-287.

Short, D. A., and G. R. North, 1990: The beam filling error in the Nimbus 5 electronically scanning microwave radiometer observations of Global Atlantic Tropical Experiment rainfall, *J. Geophys. Res.*, **95**, 2187-2193.

Spencer, R. W., W. S. Olson, W. Rongzhang, D. W. Martin, J. A. Weinman, and D. A. Santek, 1983: Heavy thunderstorms observed over land by the Nimbus 7 Scanning Multichannel Microwave Radiometer, *J. Clim. Appl. Meteorol.*, **22**, 1041-1046.

Wilheit, T. T., A. T. C. Chang, M. S. V. Rao, E. B. Rodgers, and J. S. Theon, 1977: A satellite technique for quantitatively mapping rainfall rates over the oceans, *J. Appl. Meteorol.*, **16**, 551-560.

ESTIMATION OF CLOUD THICKNESS AND CLOUD BASE FROM SATELLITE DATA

William L. Smith, Jr.[1], Patrick Minnis[2], Joseph M. Alvarez[2], Patrick W. Heck[1], and Taneil Uttal[3]

[1]Lockheed Engineering and Sciences Co., Hampton, VA, USA 23666
[2]NASA Langley Research Center, Hampton, VA, USA 23665-5225
[3]NOAA/Wave Propagation Laboratory, Boulder, CO, USA 80303

1. INTRODUCTION

Downwelling longwave radiation at the surface is sensitive to the cloud-base temperature. The distribution of radiative cooling within an atmospheric layer depends on the vertical extent of the cloud in the layer. These two radiative quantities are important components of the tropospheric radiation balance which impacts the general circulation at various scales. Algorithms and models that explicitly include cloud base or cloud thickness to compute these radiative parameters typically rely on crude assumptions such as constant cloud thickness (e.g., Darnell et al., 1983). The importance of knowing cloud base height has led to the implementation of the Experimental Cloud Lidar Pilot Study (ECLIPS; WCRP, 1988) to develop long-term statistics on cloud-base altitude over various sites. One goal of ECLIPS is to provide a database for development of satellite-derived cloud-base height algorithms so that a global climatology of cloud base can be established. Currently, cloud-top temperature or altitude and cloud optical depth are included in the parameter list of most satellite cloud climatologies, for example, the International Satellite Cloud Climatology Project (ISCCP; see Schiffer and Rossow, 1983). However, research into methods to derive cloud vertical thickness or cloud base height from satellite data has been very limited. Garand (1988) estimated that the cloud base temperature corresponds to the warmest nonclear pixel in a scene. Minnis et al. (1991) estimated cirrus cloud thickness using an empirical fit based on cloud optical depth and cloud radiating temperature. Minnis et al. (1992) found a square-root dependence of boundary-layer stratocumulus thickness on optical depth. This study expands on some of the earlier work to improve the capabilities for estimating the vertical extent of clouds using standard meteorological satellite data. Matched Geostationary Operational Environmental Satellite (GOES) and active surface remote sensing data taken during the first ECLIPS period (October 1989) over Hampton, Virginia, the First ISCCP Regional Experiment (FIRE) Phase II Intensive Field Observations (IFO) over southeastern Kansas (13 November - 7 December 1991), the Bermuda surface radiation budget field experiment (April 1989), and the Atlantic Stratocumulus Transition Experiment (ASTEX) near the Azores (June 1992).

2. DATA & ANALYSIS

GOES visible (VIS, 0.65 µm) data taken every half hour at the nominal 1-km resolution were averaged to obtain an effective 4-km resolution to match the corresponding 4-km x 8-km infrared window (IR, 11.2 µm) radiances. Each scan line of the IR data was duplicated to achieve an effective 4-km resolution. All GOES data within a 28-km square box centered over the surface lidar site were extracted and formed into a bispectral histogram. For cirrus clouds, the histograms were analyzed as in Minnis et al. (1990) and Minnis (1991) to obtain cloud-center temperature, T_c; cloud-top temperature, T_t; cirrus optical depth, τ, based on a hexagonal crystal, cirrostratus scattering model; and cloud-top altitude, $z(T_t)$. The cloud-top radiance is

$$B(T_t) = [B(T) - (1 - \varepsilon_t)B(T_{cs})]/ \varepsilon_t,$$

where T is the observed IR equivalent blackbody temperature, B is the Planck function at 11.5 µm, T_{cs} is the clear-sky temperature, and

$$\varepsilon_t = \varepsilon(2.966 - 0.009141T_c). \qquad (1)$$

The effective cloud emittance, ε, is a function of τ and is based on T_c;. This empirical formula was derived by Minnis et al. (1991) using data from the FIRE-I cirrus experiment and has a limited range of application. During ASTEX, Meteosat VIS and IR histograms were analyzed using the methods of Minnis et al. (1987, 1992) to determine the same properties over marine stratocumulus clouds except that optical depth was derived using a model based on a cloud having droplets with an effective radius of 8 µm.

The NASA Langley 8-inch lidar system, similar to that described by Sassen et al. (1990), was used to measure cloud-base height and thickness (when possible) over Bermuda; Parsons, Kansas; and Hampton, Virginia. The NOAA/WPL 35 GHz Ka-band radar (Kropfli et al. (1990)) measured cloud base and top heights as well as ice water path (IWP) over Coffeyville, Kansas and over Porto Santo during ASTEX. The lidar and radar data were averaged over 20 minute intervals centered at the GOES times to yield cloud base, center, and top heights and thickness: Z_b, Z_c, Z_t, and ΔZ, respectively. Rawinsonde data taken during the experiments were used to relate height to temperature.

3. RESULTS

a. *FIRE-II Cirrus*

Preliminary results from the FIRE-II experiment are presented here. Analyses of the other datasets are in progress. Cloud-top heights derived using (1) are compared with Z_t in Fig. 1. The mean difference of 0.2 $\pm$ 0.5 km for these cases is actually slightly better than that found for the FIRE-I data which were taken during October 1986 over Wisconsin (Minnis et al., 1990b). Figure 2 shows a comparison of optical depth and cloud thickness for the two experiments. Overall, thicker clouds were observed during FIRE-I. Since ΔZ is defined as $Z_t - Z_b$, cloud free areas between layers are included in the thickness. There were quite a few multilayered decks during FIRE-I. Most of the clouds in this initial FIRE-II dataset appear to have been continuous from base to top. This layering discrepancy may explain why the implied slopes for the two datasets are significantly different in Fig. 2 and why the FIRE-I mean cloud thickness is so much greater than the FIRE-II points shown here. The variations in the data are about the same, however. Cloud thickness is plotted against T_c for both FIRE datasets in Fig. 3. The parameterization of Platt and Harshvardan (1988) is included for comparison. The FIRE-II results are similar to the parameterization at the warm end, but ΔZ shows a more rapid decline with temperature than the Platt and Harshvardan (1988) model. In the center of the temperature range, the FIRE-II sampling is too limited. The FIRE-I data, however, show the same tendencies as the model predictions.

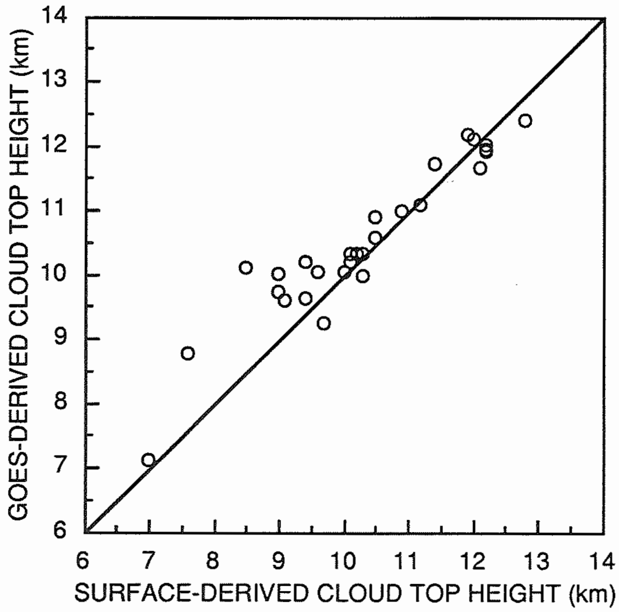

Fig. 1. GOES-derived cloud top heights versus heights derived from lidar and radar measurements.

The empirical model used by Minnis et al. (1991) to estimate cloud thickness,

$$\Delta z = -14.8 + 0.076\, T_c + 0.47 \ln\tau, \qquad (2)$$

was applied to the FIRE-II GOES data. As expected from the previous figures, the resulting cloud depths (Fig. 4) are overestimated by 1 km, on average, by using (2). Thus, a new regression analysis using the initial 28 FIRE-II data points was applied to the same formulation resulting in

$$\Delta z = 7.2 - 0.024\, T_c + 0.95 \ln\tau. \qquad (3)$$

The rms residual of this fit is 0.75 km with a multiple correlation coefficient of 0.76

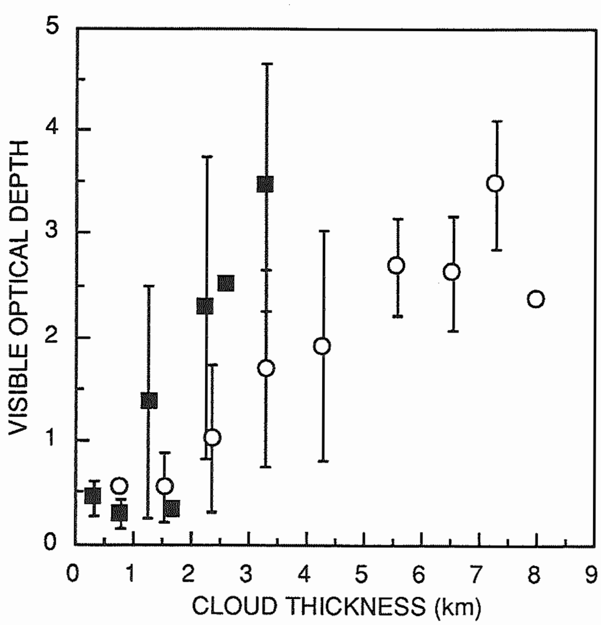

Fig. 2. GOES-derived visible optical depth versus cloud thickness for FIRE I (O) and FIRE II(■).

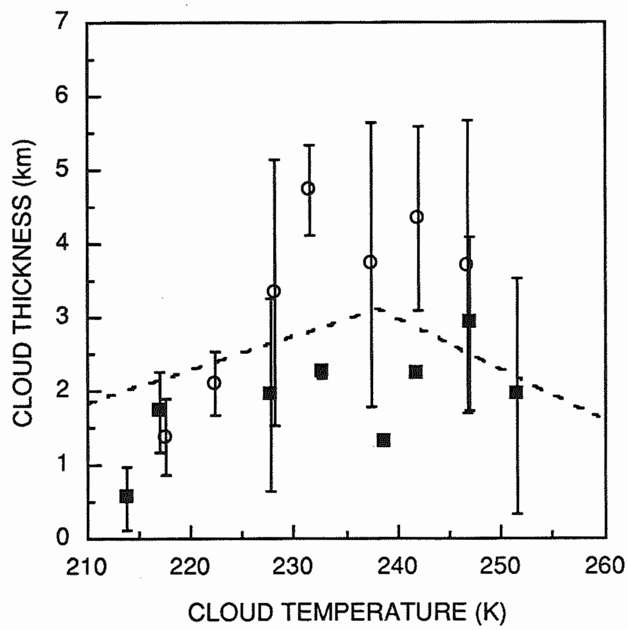

Fig. 3. Surface-derived cloud thickness versus cloud center temperature for FIRE I (O) and FIRE II(■). The dashed line is the parameterization from Platt and Harshvardan (1988).

Subtracting the results of (3) from (1) gives a satellite estimate of cloud base, z_b. Figure 5 shows a comparison of z_b and Z_b for the FIRE-II dataset. The greatest differences are found for the lowest and highest bases. In the former case, the cloud is multilayered with several cloudfree layers between the top and bottom of the cloud decks. Thus, some of the space assumed to be contributing to the optical depth is cloud free. Therefore, the small optical depth of this cloud leads to an underestimate of its thickness and an overestimate of cloud base. The cloud with Z_b = 12.6 km was so thin that it was placed at the tropopause (12.3 km on the sounding) by default resulting in an optical depth of 0.26.

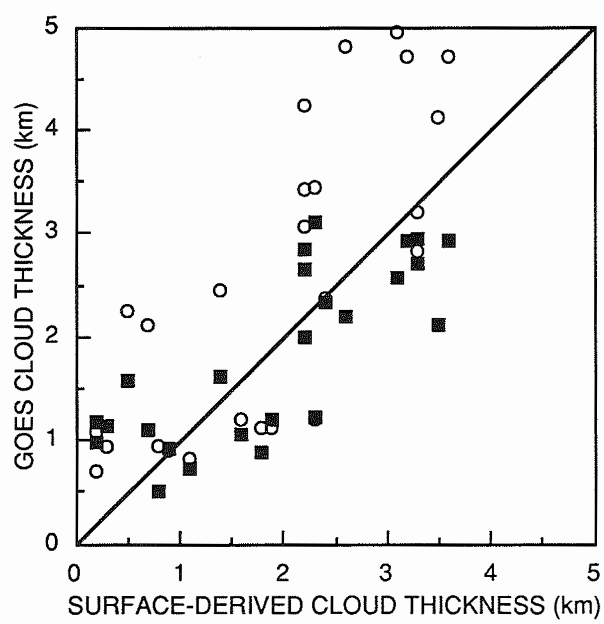

Fig. 4. Comparison of GOES and surface-derived cloud thickness for the FIRE I (O) and FIRE II(■) parameterizations.

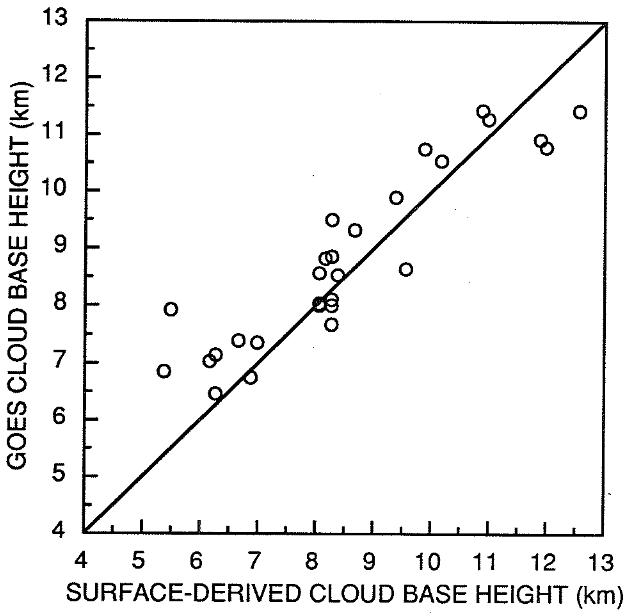

Fig. 5. Comparison of GOES and surface-derived cloud base height.

The lidar operator noted that the cloud was barely detectable visually. The sounding used in this case was 18 hours old when used in the analysis. Thus, the tropopause selection may have been correct, but the altitude may have been misplaced because of the sounding. On average, the satellite overestimates cloud base by 0.2 km with a standard deviation of $\pm$ 0.8 km. At that altitude, the rms error translates to a pressure height uncertainty of $\pm$ 40 mb, only 40% of that assumed by Darnell et al. (1983).

4. DISCUSSION

The empirical formulae derived by Minnis et al. (1992) yield mixed results when applied to an independent dataset. Nevertheless, the problem of cloud depth determination from satellites appears to be tractable. Cloud-top temperatures of semitransparent cirrus clouds can be determined with almost as much precision as the cloud-center temperatures, at least, for the two FIRE datasets. Even though it has not been independently tested, the empirical formula derived here for cloud thickness used in the estimation of cloud-base height shows considerable skill compared to an assumption of constant thickness or to a formula based only on cloud temperature. If it is assumed that the mean cloud thickness is 2.2 km and cloud-top temperature is known exactly, the mean error in cloud-base height is zero, but the rms uncertainty is $\pm$ 1.9 km, nearly three times that of the current fit. The Platt and Harshvardan (1988) parameterization in Fig. 3 yields a mean cloud-base underestimate of 0.4 $\pm$ 1.3 km for the data in Fig. 5. It is clear from Fig. 2 that cloud thickness is closely related to optical depth. Thus, it is not surprising that some improvement is gained by including optical depth in the formulation. Additional datasets will be used to determine if a more stable parameterization can be derived.

Cloud thickness estimates are affected by a number of factors other than temperature or optical depth. As shown above, multilayering of clouds within a gross cloud layer (i.e., low, middle, or high) negates one of the basic assumptions, that the cloud is continuous, in the development of a simple relationship using optical depth to infer cloud thickness. Any property of very thin clouds derived from VIS and IR data will be highly uncertain. The depth of mixed-phase clouds will probably be difficult to ascertain also because of the lack of cues indicating the phase of the cloud. The impact of these and other variables on satellite retrievals will be examined when more data become available.

5. CONCLUDING REMARKS

From the limited results shown here and from previous analyses, it appears that cirrus cloud thickness can be estimated to an acceptable degree of uncertainty using VIS and IR data. However, development of a reliable algorithm will require building a statistically large dataset of actively sensed cloud base and top heights coincident with satellite data. Data from the rest of the FIRE-II experiment and from the other field programs noted here are being analyzed and included in the database. This paper has only examined cirrus clouds. Methods to derive cloud thickness for most other types and combinations of clouds have not yet been researched. Analyses of the field program data are being pursued for low and midlevel clouds.

REFERENCES

Darnell, W. L., S. K. Gupta, and W. F. Staylor, 1983: Downward longwave radiation at the surface from satellite measurements. *J. Clim. Appl. Meteorol.*, **22**, 1956-1960.

Garand, L., 1988: Automated recognition of oceanic cloud patterns. Part I: Methodology and application to cloud climatology. *J. Clim.*, **1**, 20-39.

Kropfli, R. A., B. W. Bartram, and S. Y. Matrosov, 1990: The Upgraded WPL Dual-Polarization 8.6 mm Doplar Radar for Microphysical and Climate Research. Preprints of the Conf. on Cloud Physics, July 23-27, Amer. Met. Soc., San Francisco, CA.

Minnis, P., E. F. Harrison and G. G. Gibson, 1987: Cloud cover over the eastern equatorial Pacific derived from July 1983 ISCCP data using a hybrid bispectral threshold method. *J. Geophys. Res.*, **92**, 4051-4073.

Minnis, P., P. W. Heck, and E. F. Harrison, 1990: The 27-28 October 1986 FIRE IFO Cirrus Case Study: Cloud parameter fields derived from satellite and lidar data. *Mon Wea. Rev..*, **118**, 2426-2446.

Minnis, P, 1991: Inference of cirrus cloud properties from satellite-observed visible and infrared radiances. PhD dissertation, University of Utah, Salt Lake City, 161 pp.

Minnis, P., P. W. Heck, D. F. Young, C. W. Fairall, and J. B. Snider, 1992: Stratocumulus cloud properties derived from simultaneous satellite and island-based instrumentation during FIRE. *J. Appl. Meteorol,*, **31**, 317-339.

Platt, C. M. R. and Harshvardan, 1988: Temperature dependence of cirrus extinction: Implications for climate feedback. *J. Geophys. Res.*, **93**, 11051-11058.

Sassen, K., C. J. Grund, J. Spinhirne, M. Hardesty and J. M. Alvarez, 1990:The 27-28 October 1986, FIRE IFO cirrus case study: a five lidar overview of cloud structure and evolution. *Mon. Wea. Rev.*, **118**, 2288-2312.

Schiffer, R. A., and W. B. Rossow, 1983: The International Satellite Cloud Climatology Project (ISCCP): The first project of the World Climate Research Progamme. *Bull. Amer. Meteor.Soc.*, **64**, 779-784.

WCRP, 1988: An Experimental Cloud Lidar Pilot Study (ECLIPS). WCRP-14, September, WMO/TD-No. 251, 36pp.

Precipitation Data Sets for Validating Remote-Sensing Estimates of Rainfall

Otto W. Thiele

Laboratory for Atmospheres, Goddard Space Flight Center, Greenbelt, Maryland U.S.A.

1. Introduction

Substantial efforts are underway to acquire comprehensive observations of global precipitation to satisfy modeling requirements in connection with climate and global change studies. The only practical way to obtain such observations with the necessary time and spatial scales is through remote sensing with satellites. The immediate approach is to derive precipitation estimates from available satellite data, e.g., visible and infrared radiometers on Geostationary Operational Environmental Satellite (GOES) and National Oceanic and Atmospheric Administration (NOAA) satellites and microwave radiomters on the Department of Defense operational meteorological satellites. Such an effort is in progress under the World Climate Research Program (WCRP) sponsored Global Precipitation Climatology Program (GPCP)(Arkin and Ardanuy, 1989). The GPCP is highly successful in providing very useful data, but there are limitations in the accuracy that can be attained with such indirect methods. A more direct approach for space observations of precipitation, focused on the highly active tropical regions, is being undertaken with the Tropical Rainfall Measuring Mission (TRMM)(Thiele, 1987)(Theon and Fugono, 1988)(Simpson, 1988). This satellite will include, in addition to microwave and visible/infrared radiometers, the first precipitation radar in space for specific measurements of rainfall. However, there are many uncertainties in remote observations particularly in the case of precipitation. Therefore, substantial in situ observations are required to validate and/or calibrate the satellite estimates of rainfall. Already sizable programs have been initiated for validating the space observations both by NOAA and National Aeronautics and Space Administration (NASA). The TRMM validation program already is involved with "ground truth" sites at Darwin, Australia; Kwajalein Atoll, Marshall Islands; Cape Canaveral area of Florida; Phuket and Omkoi, Thailand; Taiwan, Israel, and São Paulo, Brazil.

This paper briefly outlines the techniques used for area rainfall estimation, some information on Darwin rainfall investigations, summary of rain measurement research for radar calibration and some information about a large field experiment to be conducted in the warm pool region of the western Pacific from November 1, 1992, through February 28, 1993. The TOGA/COARE is expected to provide very important tropical Pacific Ocean precipitation data sets for TRMM studies and investigations of tropical convection, surface fluxes, etc.

2. Large Area Rainfall Estimation

The development of tropical rainfall climatologies for representative regions around the globe was one of the first goals of TRMM. However, it was recognized that rain gauge networks would not suffice alone and that precipitation radars would be necessary for large-area coverage and the kind of sampling needed, but techniques for estimating rainfall from radar reflectivity measurements had not advanced much over the last few decades.

To overcome this problem, an early parallel goal of the program was to determine where previously developed techniques could either be improved or replaced with much more accurate radar rain estimates on both short and long time scales. Because of early intensive research activity and related studies to produce higher quality climatologies, only very limited rainfall products have been made available even though data collection from several sites has been in progress for 3 to 4 years. In the meantime, however, requirements for TRMM instrument algorithm developments and climatically related sampling studies have accelerated the need for some level of rainfall products that could be used now (Thiele et al., 1992). Therefore, while the development of more advanced and sophisticated techniques for higher quality rain estimates continues, procedures using more conventional methods have been undertaken in the interim to produce preliminary products to support TRMM scientists having immediate need for such data. There are larger error bars associated with these early versions, of course, and one must pay heed to the caveats associated with the conditions and circumstances involved in the collection and processing of these data which vary from site to site and system to system.

3. Radar Techniques

Most approaches to rainfall estimation from radar reflectivity measurements have depended on the generalized application of a Marshall-Palmer distribution to derive a reflectivity (Z)-rain (R) relationships. However, studies of rainfall probability functions (PDF's) of rain-rate suggest a significant difference in the distribution of rain drop sizes that might be expected in differing rain systems, hence, variable Z-R relationships. Thus, climatologically tuned Z-R's (Atlas et al., 1990) appear to be a necessary requirement for achieving reliable quantitative rain estimates where there are pronounced differences in rainfall morphology that may occur, whether due to a variability of local conditions or seasonal climate changes.

For large spatial averaging over longer time periods, e.g., weekly to monthly, an areal-time integral appears to provide the best results (Rosenfeld et al., 1990). The procedure is to match the radar observed reflectivity (Ze) PDF's and the rain gauge (R) PDF's (Rosenfeld et al., 1992b). This is sometimes referred to as the PDF matching method (PMM). The PDF matching technique assumes that similar rain intensity distributions are produced by all rain storms of the same type. Also, the Z_e-R data must be stratified according to rainfall type or those physical parameters associated with that type, e.g., the depth of the convection.

Short term radar estimation of rainfall, however, requires a direct power law application, but the Z-R relationship must be tuned for the rain drop size distribution associated with different kinds of rain systems or types (Figure 1) and for geometric factors such as corrections for rainge biases, i.e., the beam filling problem (Rosenfeld et al., 1992a)(Figure 2).

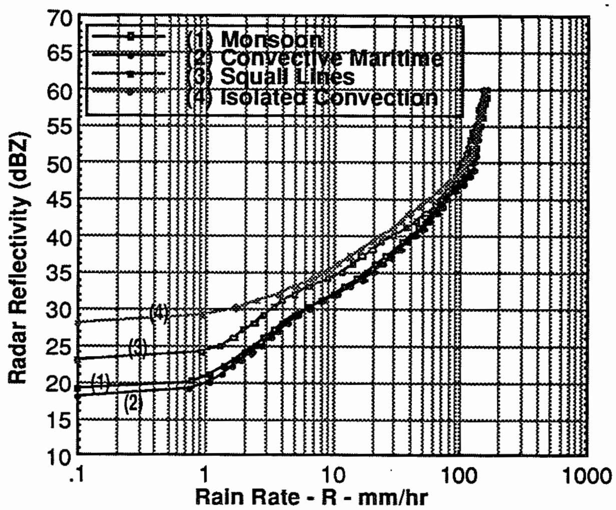

Figure 1. Reflectivity-rain relationships vary substantially for differing rain systems at the lower rain rates (Rosenfeld, 1992a).

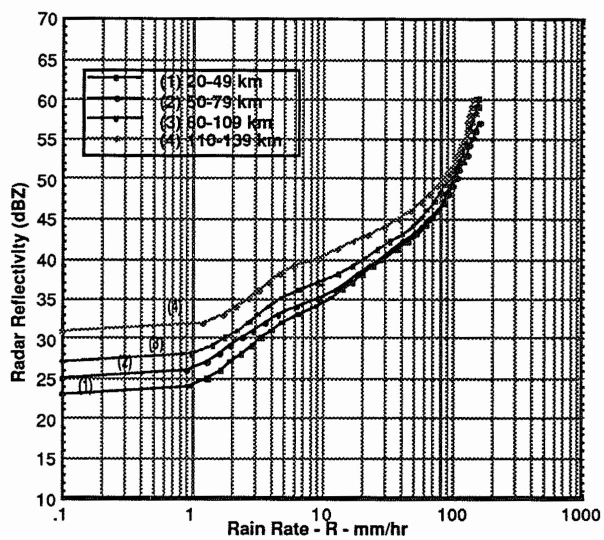

Figure 2. Z-R as a function of range for continental squall lines at Darwin, Australia.

4. Indirect Techniques

Indirect methods of rainfall estimation are also being investigated. Two methods of obtaining corroborative rain data is through inference from mass, heat, and moisture budgets derived from surface wind measurements or rawinsonde data. In one technique, convective outflow at the surface is related to rainfall (Ulanski and Garstang, 1978a, 1978b, 1978c). The downward vertical velocities are integrated over time and space to estimate downward mass transport which in turn can be directly related to rainfall. Over much larger areas, surface fluxes of precipitation are inferred from heat and moisture budgets calculated from upper air soundings describing a large volume of the atmosphere (see, for example, Brummer, 1978). This budget method is one of the few techniques that can provide an estimate of rainfall amount on the largest scales of interest to TRMM.

5. Darwin Rainfall Studies

Extensive investigations of rainfall characteristics and its climatology were initiated in a joint experiment with the Australian Bureau of Meteorology Research Centre (BMRC) at Darwin, Australia, in connection with the TRMM "ground truth" program (Keenan et al., 1987). Darwin is situated in a region where a significant variety of intense tropical convective rain systems occur, especially southern hemisphere monsoons.

The variable rain regimes encountered at Darwin, have been documented more thoroughly than anywhere else because of the intensive investigations occurring there during the rainy seasons of 1987/88, 1988/89, 1989/90, and 1990/91 with the participation of a variety of visiting scientists. This ensured research quality data from the 5-cm Doppler radar and an array of some two dozen recording rain-rate gauges. It is with these data sets that significant progress is being made in analyzing the various rain systems to determine their unique characteristics. For example, large continental rain systems, i.e., squall lines, have the characteristic trailing stratiform rainfall (Figure 3) which maritime monsoon and individual convective cells do not.

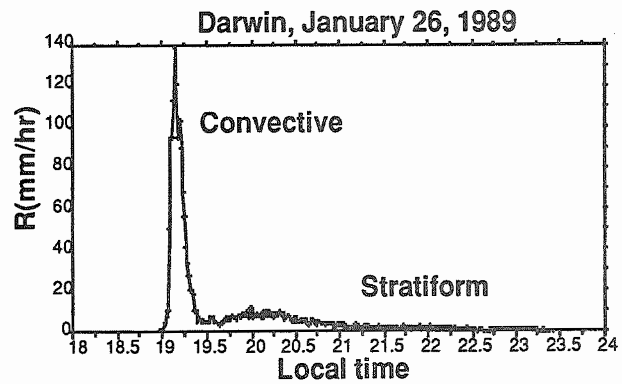

Figure 3. Four and a half-hour time series of rain rate in Darwin, Australia, observed during the passage of a tropical squall line with a trailing stratiform rain area. (Short et al., 1990)

A morphology of the rain systems in the Darwin vicinity have been reported on by Keenan and Carbone, 1989. Figure 4 from the 1987/88 rain season shows the three more prevalent rain systems in the area. A less frequent type not shown is a maritime convective system that forms over the ocean to the northeast and passes over Darwin moving to the southwest.

Routine observations were made with the 5-cm Doppler radar (NOAA/TOGA radar relocated to Darwin after the Equatorial Mesoscale Experiment (EMEX)) essentially during the entire period of the rainy seasons, i.e., from approximately November 1 through March. However, intensive observations were concentrated over three special operating periods (SOP's) each season where special scanning routines were exercised under the direction of a group of visiting scientists from Australia, the United States, and elsewhere. Hourly and daily rainfall products have been derived as well as 20-day averages of each SOP.

The Darwin data with the newer radar rainfall estimation techniques are already providing important verification data for TRMM microwave algorithm development using the microwave radiometer Special Sensor Microwave/Imager (SSM/I) on the Defense Meteorological Satellite Program (DMSP).

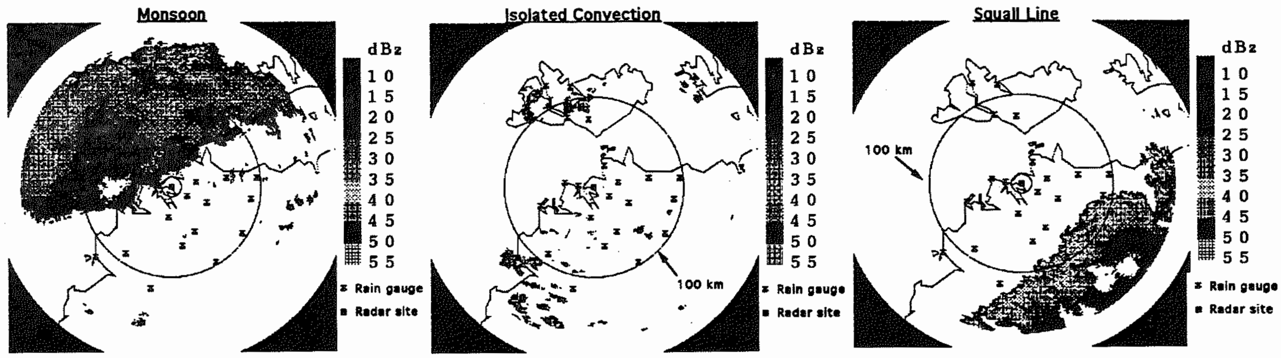

Maritime Monsoon (From the Northwest) | **Individual Convective Cells** | **Continental Squall Line (From the South or Southeast)**

Figure 4. Radar images of three rain system types encountered at Darwin, Australia. Monsoon rains move in from the ocean when the winds turn westerly, convective cells form and dissipate locally with little movement, and the squall lines move northwestward from where they have developed to the southeast of Darwin.

6. Rain Measurement Techniques for Radar Calibration

Extensive research is underway to investigate new rainfall observational techniques, or, where feasible, to improve conventional ones. Rain rate observations of sufficient accuracy are crucial for determining reliable PDF's, a critical step in calibrating the radars.

To examine new surface measurement techniques, a small-scale experimental rain measurement research facility is being developed at Goddard's Wallops Island Flight Facility, Virginia. A polarized multi-frequency microwave attenuation link will be the key component of the facility. Attenuation of horizontally propagating microwave radiation is strongly related to the intensity of intervening precipitation and less sensitive than radar reflectivity-rainfall (Z-R) relationships to rain drop size distribution (Crane, 1985; Ulbrich and Atlas, 1985). The six frequencies employed are two near 8.7 GHz vertically and horizontally polarized, 24, 35, 82, and 245 GHz. The latter two (82 and 245 GHz) were furnished by the Communications Research Laboratory of Japan, participants in this experiment. From these experiments, the intent is to select the most suitable methods for deployment at ground truth sites.

Under the microwave transmission path will be one or more disdrometers and a number of state-of-the-art rain gauges for calibration including a specially designed weighing rain gauge, particularly suited to calibration. Also, at least two new "gauge" techniques will be investigated, i.e., an optical rain gauge and an upward looking Doppler rain gauge. Also located at the Wallops Island Flight Facility is a rain simulation/calibration facility for comparing different kinds of gauges, determining their response times, and for obtaining absolute calibrations at variable rain rates. Higher rain rates exceeding 1,000 mm/hr that the facility is capable of, make it possible to determine the upper limit of certain gauges.

For improved observations over oceans, several approaches are being pursued. One involves an airborne 14 GHz radar being designed for installation on NASA's DC-8 aircraft. This instrument will also make an important contribution to the development of algorithms for TRMM. The NOAA P3's equipped with precipitation radars and particle measurement probes are also expected to make significant contributions over ocean areas. Another approach involves surfaced based techniques, e.g., optical devices for measuring rainfall from ship and buoy platforms and hydrophones for the acoustical detection of rainfall. The latter units can either be tethered below a moored or drifting buoy or anchored to the ocean floor at moderate depths. The optical rain gauge and hydrophone experiments are being accomplished through collaboration with NOAA in connection with similar validation efforts associated with the World Climate Research Program's GPCP.

7. Field Experiments

Another important element for obtaining unique precipitation data sets is through field experiments using specialized observing systems, e.g., aircraft, research radars, augmented surface and sounding observations, etc. While the TRMM validation program will undoubtedly conduct some limited field experiments for algorithm development and for verification of such models as the Goddard Cumulus Cloud Model (GCCM), every advantage is taken of larger field programs that can offer important data.

One such experiment was the Convection and Electrification Precipitation (CaPE) experiment conducted in central Florida during the summer of 1991. A large number of scientists supported by the National Science Foundation (NSF) and NASA participated (Foote, 1991). The experiment included 3 Doppler radars, one of which was equipped with dual polarization and dual frequency (10 cm and 3 cm). Six aircraft and a sailplane were involved with a variety of atmospheric instrumentation which included precipitation radars, radiometers, and particle measurement probes. Also, some 40 automated meteorological observing stations were installed for the experiment and upper air soundings were augmented in the region. Already in place for the TRMM ground truth program were 50 plus recording rain rate gauges. Area rainfall surveillance was provided by the NCAR CP-4 Doppler radar and U.S. Airforce 5-cm weather radar at Patrick Air Force Base, Florida. A detailed precipitation data base from these observations is presently being processed for analysis.

A much larger field experiment in area and scope is the multi-national TOGA/COARE taking place in the western Pacific. Augmented soundings and specially instrumented ocean moorings are already in place in the larger COARE domain centered around the western Pacific warm pool. There will be an intensive operating period (IOP) from November 1, 1992, through February 28, 1993, centered around an intensive flux array (IFA) located at 156°E, 2°S. The IFA will include a dense network of current and surface flux moorings and 13 research ships.

Also 8 instrumented aircraft will be operating in the area. The ships and aircraft will be heavily instrumented to observe all atmospheric and ocean parameters describing surface fluxes and resultant responses to each other. Of primary interest for precipitation will be 4 different kinds of aircraft precipitation radars including one that is designed as a TRMM simulator at 14 GHz. In addition, there will be three shipborne precipitation radars. These observations are expected to provide a unique and comprehensive ocean precipitation data base which will include detailed observations of the vertical structure and microphysical parameters associated with tropical convection in the region.

The main operations base for TOGA/COARE will be located in Townsville, Australia, and the NASA DC-8 and ER-2 will deploy from there. The two NOAA Orion P3's, the National Center for Atmospheric Research (NCAR) Electra, and the United Kingdom (UK) C-130 will deploy from Henderson field, Honiara, Guadalcanal. Ships will be rotated in the IFA vicinity for station times of up to 30 days for each ship. This will provide three 20-day overlap periods for larger area coverage with at least two ships on station. The anticipated Pacific Ocean rainfall data is particularly important for TRMM sampling and statistical investigations, algorithm development, and modeling studies.

8. Conclusions

The establishment of a rather extensive validation program was originated, of course, as a result of the unique TRMM mission objectives and knowledge of the difficulties in obtaining believable measurements of rain from space. However, the scope of efforts involved, e.g., long time series of convective rainfall observations in representative tropical regions, has enormous potential for a broad range of precipitation research. If these efforts can encourage new interests and stimulate wide ranging investigations in this field, which is perhaps one of natures least understood atmospheric phenomenon, then many will benefit including TRMM. Indeed, recent literature already reflects a significant expansion of precipitation research coincident with the start-up of TRMM and its associated ground truth program not only in the atmospheric sciences and hydrology but in statistical and other related fields as well. The unique data sets being acquired offer great opportunity for the study of rainfall characteristics, associated physical processes and data assimilation techniques.

9. Acknowledgment

The author wishes to acknowledge Dr. David Short and David Wolff for their special contributions and constructive criticism in preparing this paper and Janet Wood for organizing and typing the manuscript.

10. References

Arkin, P. A., and P. E. Ardanuy, 1989: Estimating climatic scale precipitation from space: A review. *J. Clim.*, **2**, 1229-1238.

Atlas, D., D. Rosenfeld, and D. Wolff, 1990: Climatologically Tuned Reflectivity-Rain Rate Relations and Links to Area-Time Integrals. *J. of Appl. Meteor.*, **29**, 1120-1139.

Brummer, B., 1978: Mass and energy budgets of a 1 kilometer high atmospheric box over the GATE C-scale triangle during undisturbed weather conditions, *J. Atmos. Sci.*, **35**, 997-1011.

Crane, R. K., 1985: Comparative evaluation of several rain attenuation prediction models, *Radio Science*, **20**, 843-863.

Foote, G. B. (Ed.), 1991: Scientific overview and operations plan for the convection and precipitation/Electrification experiment, NCAR Publication, pp. 145.

Keenan, T. D., G. Holland, and M. Manton, 1987: TRMM ground truth in a monsoon environment: Darwin, Australia. Contributed paper. *Tropical Rainfall Measurements*, A. Deepak Publishing, pp. 528.

Keenan, T. D., and R. E. Carbone, 1989: A preliminary morphology of convective systems in tropical northern Australia, Preprints, *24th Conf. on Radar Meteorology*, Amer. Meteor. Soc., 640-644.

Rosenfeld, D., D. Atlas, and D. A. Short, 1990: The estimation of convective rainfall by area integrals. Part II: the height area rainfall threshold (HART) method, *J. Geophys. Res.*, **95**, 2161-2176..

Rosenfeld, D., D. Atlas, and D. B. Wolff, 1992a: Beamwidth effects on Z-R relations and area integrated rainfall. *J. of Appl. Meteor.*, accepted.

Rosenfeld, D., D. Wolff, D. Atlas, 1992b: General probability matched relations between radar reflectivity and rain rate, *J. of Appl. Meteor.*, submitted.

Short, D. A., T. Kozu, and K. Nakamura, 1990: Rainrate and raindrop size distribution observations in Darwin, Australia. Proceedings of the URSI Commission F Special Open Symposium on Regional Factors in Predicting Radiowave Attenuation Due to Rain, Rio de Janeiro, December 3-7, 1990.

Simpson, J. (Ed.), 1988: TRMM a satellite mission to measure tropical rainfall. Report of the Science Steering Group. NASA Management Publication, pp. 94.

Theon, J., and N. Fugono, 1988: Tropical Rainfall Measurements. A Deepak Publishing, pp. 528.

Thiele, O. W. (Ed.), 1987: On requirements for a satellite mission to measure tropical rainfall, NASA Ref. Pub. 1183, 49 pp.

Thiele, O. W., D. B. Wolff, D. A. Makofski, and B. Fisher, 1992: Tropical Rainfall Measuring Mission (TRMM) data catalog, NASA/GSFC, pp. 80.

Ulanski, S. L., and M. Garstang, 1978a: The role of surface divergence and vorticity in the life cycle of convective rainfall, Part I: observations and analysis, *J. Atmos. Sci.*, **35**, 1047-1062.

Ulanski, S. L., and M. Garstang, 1978b: The role of surface divergence and vorticity in the life cycle of convective rainfall, Part II: descriptive model, *J. Atmos. Sci.*, **35**, 1063-1069.

Ulanski, S. L., and M. Garstang, 1978c: Some aspects of Florida convective rainfall, *Water Resour. Res.*, **14**, 1133-1139.

Ulbrich, C., and D. Atlas, 1985: Extinction of visible and infrared radiation in rain: comparison of theory and experiment, *J. Atmos. and Oceanic Tech.*, **2**, 331-339.

Universal Multifractals: theory and observations for Rain and Clouds

Y. Tessier[1], S. Lovejoy[1] and D. Schertzer[2]

[1] Department of Physics, McGill University, 3600 University St.., Montreal, Qc. H3A 2T8, CANADA

[2] EERM/CRMD, Météorologie Nationale, 2 Ave. Rapp, Paris 75007, FRANCE

1. Cascades processes and multifractals

Rainfall is, without argument, one of the most variable of all natural phenomenon. Just think of long drought, or conversely, think of devastating flood and you will be convinced. Deterministic rainfall models are problematic since the partial derivative equations governing the rainfall dynamic are unknown (we exclude ad hoc deterministic parametrization). Even if they were known, the stochastic approach would still be indispensable because of the strong non- linearity involved and the poor knowledge that we have of the initial and boundary conditions. The usual stochastic models have problems incorporating all the variability on the relevant temporal and spatial scales. This is why different models are used for hourly, daily and monthly precipitation. On the other hand, scaling ideas are seeing rapid advances toward an efficient modeling of rainfall. During the 60's different hypotheses have been investigated (Lovejoy (1981, 1983), Lovejoy and Schertzer (1985, 1991), Lovejoy and Mandelbrot (1985), Lovejoy et al (1992), Schertzer (1987), Hubert and Carbonnel (1988, 1989, 1991), Hubert et al (1992), Gupta and Waymire (1990), Waymire (1985), for a review, Lovejoy and Schertzer (1991). One of the key proposals for this approach was the proposition by Schertzer and Lovejoy (1987) that the variability of rainfall could be modeled by a turbulent cascade process (in first approximation as a passive scalar), thus giving a physical basis to the stochastic modeling. Such processes have the interesting property that they generally give rise to multifractal fields. In the same manner that gaussian noises are generally produced by a linear sum of random variables, cascades processes generally produce universal multifractal by nonlinear mixing of scaling noises. The resulting fields belong to universality classes attractive and stable (i.e. the result is independent of many of the details of the process) which need only three parameters for their description. Hence, the simulation and modeling of such fields is greatly simplified.

In the past seventy years (Richardson, 1922) many phenomenological cascade models of turbulence have been developed. These models rest on the following hypotheses and observations: the dynamics are scaling for a large range of scales. This is true for example of the Navier-Stokes equations for the scale range between the injection of energy (at large scale) and its dissipation (at scales of the order of 1 mm). Another aspect of Navier-Stokes phenomenology which is also likely to be true in rain is the existence of fluxes conserved by the nonlinear dynamics, such as the energy flux and the passive scalar variance flux in passive scalar clouds. The final piece of phenomenology is that the interactions involve mainly neighboring scales (the dynamics are local in Fourier space). These three properties give rise to the cascade phenomenology.

For conservative fields[1] (such as the energy flux) respecting these hypotheses it is possible to define measures with the following properties:

$$\langle \varphi_\lambda^q \rangle \approx \lambda^{-K(q)} \tag{1.1}$$

$$\Pr(\varphi_\lambda \geq \lambda^\gamma) \approx \lambda^{-c(\gamma)} \tag{1.2}$$

where φ_λ is the conservative multifractal field measured at the resolution λ which is the ratio of the external scale (the largest) to the homogenization scale of the process. γ is the order of singularity and $c(\gamma)$ the codimension associated with it. If the observation space (dimension D) is greater than the codimension there is a simple geometrical interpretation: $D(\gamma) = D - c(\gamma)$ and $D(\gamma)$ is the fractal dimension for the singularity of order γ. The K(q) and $c(\gamma)$ functions are related by a Legendre transformation (Parisi and Frisch, 1985). Note that we have supposed that the rain field R is related to the conservative field φ by a relation of the type:

$$\Delta R_\lambda \approx \varphi_\lambda^a \lambda^{-H} \tag{1.3}$$

where H is a scaling parameter and a an exponent. In what follows we will suppose that a = 1. We don't treat the problem of determining H (for details see Tessier et al, 1992) since the method given here is independent of H. The $c(\gamma)$ and K(q) functions for conservative functions follow the following forms (Schertzer and Lovejoy, 1987):

$$c(\gamma) = \begin{cases} \left(\dfrac{\gamma}{C_1\alpha'} + \dfrac{1}{\alpha}\right)^{\alpha'} & \alpha \neq 1 \\ C_1 \exp\left(\dfrac{\gamma}{C_1} - 1\right) & \alpha = 1 \end{cases} \tag{1.4}$$

$$K(q) = \begin{cases} \dfrac{C_1}{\alpha - 1}(q^\alpha - q) & \alpha \neq 1 \\ C_1 q \mathrm{Log}(q) & \alpha = 1 \end{cases} \tag{1.5}$$

The parameter α ($0 \leq \alpha \leq 2$) expresses the degree of multifractality of the process: for $\alpha = 0$ it is a monofractal describe by a β-model (Novikov and Stewart (1964), Mandelbrot (1974), Frisch (1978)), for $\alpha = 2$ we get a lognormal process. C_1 quantifies the sparseness of the mean by giving its codimension.

---

[1] For non conservative fields, it is always possible to find a conservative field with the desired properties by using a fractional integration (power law filter).

2. Estimation of the parameters α and C_1

The best method currently available for estimating α and C_1 is the double trace moment (Lavallée, 1991, Lavallée et al, 1991a). It can be explained in this way:

-Consider a multifractal process $\varphi_{\lambda'}$ where λ is the ratio between the external scale and λ' the homogenization scale. The double trace moment at resolution λ and λ' is defined by:

$$Tr_\lambda(\varphi_{\lambda'}^{\eta})^q = \left\langle \sum_{A_\lambda}\left(\int_{B_\lambda}\varphi_{\lambda'}^{\eta} d^D\overline{x}\right)^q\right\rangle \propto \lambda^{K(q,\eta)-(q-1)D} \quad (2.1)$$

$$K(q,\eta) = K(q\eta, 1) - qK(\eta, 1) \quad (2.2)$$

The sum must be taken over all the set A_λ required to cover the multifractal at the resolution λ and B_λ is the box (resolution element) of size λ^{-1}. $K(q,1)$ is the usual scaling exponent $K(q)$ (eq. 1.5).

The method can be summarized in the following manner: at the finest resolution (λ') of the analyzed field, raise the field to the power η, then calculate a statistical moment of order q (different from 1) for the field at the resolution λ. By taking the slope of $\log\left|Tr(\varphi_{\lambda'}^{\eta})^q\right|$ versus $\log(\eta)$ we obtain the exponent $K(q,\eta)$.

The reason for doing this becomes apparent when it is applied to universal multifractal, then $K(q,\eta)$ is described by:

$$K(q,\eta) = \eta^\alpha K(q,1) = \begin{cases} \dfrac{C_1\eta^\alpha(q^\alpha - q)}{\alpha - 1} & \alpha \neq 1 \\ C_1\eta q \mathrm{Log}(q) & \alpha = 1 \end{cases} \quad (2.3)$$

3. Rainfall spatial variability

The data set we used is the daily rainfall accumulation for a global network of nearly 8000 stations for 1 year (1983). This data set was archived by the National Meteorological Center (NMC) of NOAA. With this database it is possible to study the spatial variability of rainfall including statistical corrections for the sparseness of the network This problem is dealt with by considering that the network itself must be considered as a realization of a multifractal process, since we can see that there are holes in the network at all scales-which is a property of fractal objects. The details of this analysis have been reported in Tessier et al (1992b).

We summarize the procedure in the following manner. Consider that the network has a density ρ_λ (number of stations per unit area) when evaluated at the resolution λ. We will see that ρ_λ is nearly multifractal for scales between 150 and 5000 km. In order to apply the double trace moment method we consider that the network and the phenomenon measured (rainfall R) are statistically independent.Briefly, the measured rainrate at resolution 1 will be the product of the two multifractal densities $\rho_\lambda R_\lambda$. When ρ_λ and R_λ are multiplied, the moments also multiply and the characteristic exponents add. After some simplifications we get:

$$K_R(q,\eta) = K_{meas}(q,\eta) - K_{meas}(q,0) \quad (3.1)$$

where the index 'R' refers to the real field and the index 'meas' indicates the field as measured by the network.

We did this analysis by considering each day as a separate realization. We show (fig. 2) that scale invariance is observed for scale between 150 and 2000 km. On the next graph (fig. 3) it is shown $\log|K(q,\eta)|$ vs. $\log(\eta)$ for different values of q (0.5, 1.5, 2.0). We deduce from this graph that $\alpha \approx 1.35$ and $C_1 \approx 0.16$ by using the straight part of the curve. We observe a scaling break for small and large values of η. For the former, since this region corresponds to weak values of the analyzed field, we conclude that this break occurs when the noise dominates the signal.

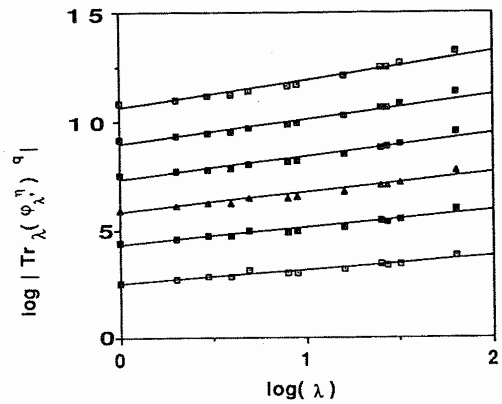

Figure 1: $\log\left(Tr_\lambda(\varphi_{\lambda'}^{\eta})^q\right)$ versus $\log(\lambda)$ for several values of η (from top to bottom, η = 3.2, 2.5, 1.2, 0.35, 0.15) using q = 2.0 for for the spatial distribution of daily rainfall accumulation on a global network.

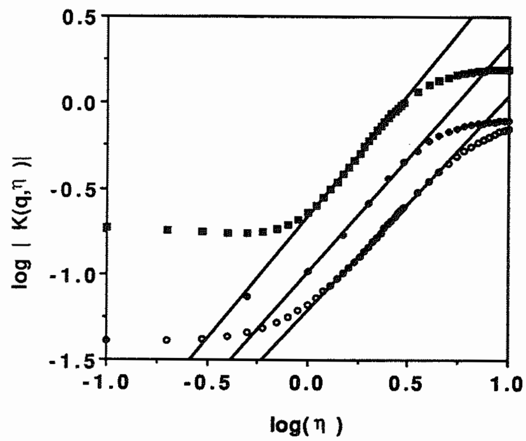

Figure 2: $\log(|K(q,\eta)|)$ versus $\log(\eta)$ for daily rainfall accumulations on a global network after the needed corrections explained in the text. From top to bottom curves for q = 2.0, 1.5 and 0.5 are shown. The regression lines on the different curves give a value of $\alpha = 1.34 \pm 0.09$ and $C_1 = 0.16 \pm 0.03$.

For large values of η, there are two possible explanations as to why eq. 2.3 breaksdown. The first one, expressed by formula (3.2), is that singularities of high enough order are very rare. In fact, a large number of realizations are needed to observe them. But at the same time, they are so intense that statistical moments of order greater than q_s will be under estimated. The critical order for which this occurs is given by:

$$q_s = \left[\frac{D + D_s}{C_1}\right]^{1/\alpha} \quad (3.2)$$

where D is the dimension of the support (D = 2 here) and D_s is the sampling dimension. This concept is introduced to take account of the fact that when many realizations are investigated the dimension of the probability space investigated is augmented by the "sampling dimension":

$$D_s = \frac{\log(N_i)}{\log\lambda} \qquad (3.3)$$

N_s being the number of independent realization used and λ the ratio of the smaller and larger scale used. We considered that we had 365 realizations (one each day) but since we observed a break in the temporal scaling for times of the order of 16 days. We interpreted this break as a decorrelation time. Hence, $N_s = 365/16 = 23$. the scaling range is 150 to 2000 km, $\lambda s = 13.3$, then $D_s = 1.21$ and using $\alpha = 0.5$ $C_1 = 0.6$ wre obtain $q_s = 9.2$. The second possibility, which is not observed due to the smallness of q_s, is that moments of order high enough diverge (Schertzer and Lovejoy, 1987). Theoretically, eq. 2.3 holds up to η given by $\max(\eta, q\eta) = \min(q_s, q_d)$. From this value of q_s we deduce that the break should occur when $\eta \approx 4.6$, for $q = 2$, which is near the observed value.

Studies on radar reflectivities corroborate this result. We group these results in table 1. We could effectively expect that evaluations of α and C_1 for radar reflectivities would be the same as evaluations with raingages because of the semi-empirical relation of Marshall-Palmer type which are often used to relate them. Such relations conserve the value of α. In a relation of the type $Z \propto R^a$ (a = 1.6 for Marshal-Palmer), substitute $Z = \lambda^{\gamma_Z}$ and $R = \lambda^{\gamma_R}$. We have effectively done a linear transformation on the singularities (i.e. $\gamma_Z = a\gamma_R$) an we see that with such a transformation α remains unchanged and C_1 becomes $C_1\alpha^a$. If we use a = 1.6 and $C_{1R} = 0.16$. Then $C_{1Z} = 0.08$, which is approximately verified.

Dataset	Location	α	C_1
Radar[1] reflectivity (horizontal)	Montreal	1.40	0.12
Daily[2] raingages accumulation	Global	1.35	0.16
Radar[1] reflectivity (Vertical)	Montreal	1.35	0.11

Table 1: Evaluations of a and C_1 for the spatial variability of rain. [1]Tessier et al (1992a), [2]Tessier et al (1992b)

4. Temporal variability of rain

We also applied the double trace moment method to the data set described before by considering each station as an independent realization. We used a subset of 4000 stations for duration of 64 days since it was impossible to obtain longer series without missing reports for a sufficient number of stations from this set. We obtained for this set $\alpha = 0.5$ and $C_1 = 0.3$. This result is even more significant since many analyses on independent datasets achieve the same conclusions. This could be seen on table 2 which summarizes the different analysis on the temporal variability of rainfall.

Dataset	Location	α	C_1
Daily[1] raingages accumulation	Global	0.5	0.6
Daily[2] raingages accumulation	Réunion Islands	0.5	0.2
Daily[3] raingages accumulation	Nîmes	0.5	0.6
Daily[4] raingages accumulation	Germany	0.6	0.5
Radar[5] reflectivity	Montreal	0.3 - 0.6	0.6 - 1.2
Radar[6] reflectivity	Montreal	0.6	0.3

Table 2: Evaluations of α and C_1 for the temporal variability of rain.[1]Tessier et al (1992a), [2]Hubert et al (1991), [3]Schmitt and Ladoy (1991), [4]Larnder and Fraedrich (1992), [5]Seed (1989), [6]Tessier et al (1992b)

5. Conclusion

We briefly presented the basis of the multifractal approach which we think is well suited for the analysis of hydrologic and meteorological phenomenon. We explained the double trace moment method which allows us to determine the parameters needed for such a characterization. The necessary corrections to apply the method to inhomogeneous network-sensed data were also presented. The method is even more attractive in that it doesn't require interpolation on the data in order to give the desired information since it respects the geometry of the problem.

The analysis done so far identified important differences between the spatial and the temporal variability of rain. Indeed, the parameters α and C1 takes

the values of a $\approx$ 1.4 and C1 $\approx$ 0.2 in space and $\alpha \approx 0.5$ and C1 $\approx$ 0.6 in time. The difference is even more significant since the generator of the processes is qualitatively very different for values of $\alpha < 1$ and $\alpha > 1$. We also note that these results were obtain by many analyses on independent datasets. It is also important to note that analysis done with radar and with raingages gives a similar answer.

There are many implications and applications of the modeling of rain by multifractal methods. For example, very promising techniques for forecasting and interpolation (objective analysis) which will take into account what is known of the variability of the fields are being developed. By elaborating techniques that exploit the scaling properties, better evaluation of the amount of water in the atmosphere could be done. This will also lead to better analyses and previsions by stochastic multifractal methods. Improvement of data assimilation techniques could also be made with space/time transformations that respect scaling properties. Studies on the evolution of climate could also certainly benefit from a better understanding of the variability of investigated system.

6. references

Frisch, U., P.L. Sulem, and M. Nelkin,. 1978: A simple dynamical model of intermittency in fully developped turbulence. J.Fluid Mech., 87, 719-724

Gupta, V., E. Waymire, 1990: Multiscaling properties of spatial rainfall and river flow distributions, J. Geophys. Res., 92, 9657-9660.

Hubert, P., Y. Tessier, P. Ladoy, S. Lovejoy, D. Schertzer, J.P. Carbonnel, S. Violette, I. Desurosne, F. Schmitt, 1992: Multifractals and extreme rainfall events, soumis à Geophys. Res. Lett.

Hubert, P., J.P. Carbonnel, 1988: Caractérisation fractale de la variabilité et de l' anisotropie des précipitations intertropicales. C.R. Acad. Sci. Paris, 307, 909-914.

Hubert, P., J.P. Carbonnel, 1989: Dimensions fractales de l' occurence de pluie en climat soudano-sahélien, Hydro. Continent., 4, 3-10.

Hubert, P., J.P. Carbonnel, 1991: Fractal characterization of intertropical precipitation variability, Scaling, fractals and non-linear variability in geophysics, D. Schertzer and S. Lovejoy eds., 209-213, Kluwer.

Lardner, C., et C. Fraedrich: Private communication.

Lavallée, D., 1991: Multifractal analysis and simulation techniques and turbulent fields, Ph D. thesis, McGill University, 142pp.

Lavallée, D., S. Lovejoy, D. Schertzer, 1991: Universal multifractal theory and observations of land and ocean surfaces, of clouds, Proceeding of the Society of Photo-optical Instrumentation Engineers (SPIE). p. 1558-07

Lavallée, D., S. Lovejoy, D. Schertzer, 1992: Nonlinear variability of Landscape topography: multifractal analysis and simulation. Fractals in Geography, L. De Cola, N. Lam eds, (in press).

Lovejoy, S., 1981: Analysis of rain areas in terms of fractals, 20th conf. on radar meteorology, 476-484, AMS, Boston.

Lovejoy, S., 1983: la géométrie fractale des régions de pluie et les simulations aléatoires. Houille Blanche, 516, 431-436.

Lovejoy, S., Mandelbrot, B., 1985: Fractal properties of rain and a fractal model. Tellus, 37A, 209-232.

Lovejoy, S., D. Schertzer, 1985: Generalised scale invariance and fractal models of rain, Wat. Resour. Res., 21, 1233-1250.

Lovejoy, S., D. Schertzer, 1991: Multifractal analysis techniques and rain and cloud fields from 10^{-3} to 10^{6}m., Scaling, fractals and non-linear variability in geophysics, D. Schertzer and S. Lovejoy eds., 111-144, Kluwer.

Lovejoy, S., D. Schertzer, 1992: Multifractals and Rain, New Uncertainty Concepts in Hydrology and and Water Resources, Unesco series in Water Sciences, Cambridge University Press, Ed. Z.W. Kunzewicz.

Lovejoy, S., D. Schertzer, A. A. Tsonis, 1987: Functional box-counting and multiple elliptical dimensions in rain, Science, 235, 1036-1038.

Mandelbrot, B., 1974: Intermittent turbulence in self-similar cascades: Divergence of high moments and dimension of the carrier., J. Fluid. Mech., 262, 331-350.

Novikov, E. A., and R. Stewart 1964: Intermittency of turbulence and spectrum of fluctuations in energy-dissipation, Izv. Akad. Nauk. SSSR, Ser. Geofiz, 3, 408-412.

Parisi, G., U. Frisch, 1985: A multifractal model of intermittency. Turbulence and predictability in geophysical fluid dynamics and climate dynamics., 84-88, Eds. M Ghil , R. Benzi and G. Parisi, North-Holland, 84-88.

Richardson L.F. , 1922: Weather prediction by numerical process. Cambridge U. press (Republished by Dover, New York, 1965).

Schertzer, D. S. Lovejoy, 1989: Nonlinear variability in geophysics: multifractal analysis and simulations. Fractals their physical origins and propeties, Pietronero ed. Plenum press, New York, 49-79.

Schertzer, D., S. Lovejoy, 1987: Physically based rain and cloud modeling by anisotropic, multiplicative turbulent cascades. J. Geophys. Res. 92, 9693-9714.

Schmitt, F. et Ph. Ladoy, 1991: communication privée

Seed, 1989:Statistical problems in measuring convective rainfall. ph. D. Thesis, McGill university, 141 pp.

Tessier, Y., S. Lovejoy, D. Schertzer, 1992a: Universal Multifractals: theory and observations for Rain and Clouds, Accepté par le J. Appl. Meteor.,Janvier 1992.

Tessier, Y. , S. Lovejoy, D. Schertzer, 1992b: Multifractal Objective Analysis of Global Rainfall, préparé pour le J. Geophys. Research, Février 1992.

Waymire, E., 1985: Scaling limits and self-similarity in precipitation fields., Wat. Resour. Res., 21, 1271-1281.

Wilson, J., S. Lovejoy, D. Schertzer, 1991 : Physically based cloud modelling by scaling multiplicative cascade processes, Scaling, fractals and non-linear variability in geophysics, D. Schertzer and S. Lovejoy eds., 185-208, Kluwer.

CHARACTERISTIC FEATURES OF CLOUD LIQUID WATER AS DETERMINED FROM SATELLITE MICROWAVE MEASUREMENTS

Guosheng Liu and Judith A. Curry
Department of Aerospace Engineering Science, University of Colorado at Boulder, CO, USA 80309-0429

1. INTRODUCTION

Satellite microwave observation over oceanic regions provides the opportunity of determining liquid water path (LWP) on the global scale. Although efforts to determine LWP from satellite by both statistical and semi-physical methods have been made in the last two decades, some problems still remain unsolved, such as the contamination by precipitating water drops and the influence of horizontal inhomogeneity of the cloud. This study demonstrates a new algorithm to determine LWP that addresses these problems using the data of Special Sensor Microwave/Imager (SSM/I). The SSM/I receives microwave radiation at 19, 22, 37 and 85 GHz, all but 22 GHz being dual-polarized. In the following we will refer these channels as 19V, 19H, 22V, 37V, 37H (i.e., the number is frequency and the character is polarization).

2. LIQUID WATER PATH ALGORITHM

Because of the impact of rain on the LWP retrievals, we divide the clouds into two regimes: nonprecipitating cloud and precipitating cloud, and different retrieval methods are employed for each of them.

Precipitation is determined following Liu and Curry (1992). For the nonprecipitating cloud regime, similar to Takeda and Liu (1987), the cloud emissivity (ε) can be derived from the following equation for each microwave channel:

$$A\varepsilon^2 + B\varepsilon + C = 0 \qquad (1)$$

where A, B, and C are given by

$$\begin{aligned} A &= \alpha T_c \\ B &= T_{B0} - (1+\alpha)T_c \\ C &= T_B - T_{B0} \\ \alpha &\approx 1 - \frac{T_{B0}}{2}\left(\frac{1}{T_a} + \frac{1}{T_s}\right) \end{aligned} \qquad (1a)$$

for the horizontally and vertically polarized channels. T_a, T_s, and T_c are, respectively, mean atmospheric temperature, sea surface temperature and cloud mean temperature.

Using the above equations, LWP can be calculated from each channel by

$$LWP = \frac{1}{\Omega} \log \frac{1}{1-\varepsilon} \cos\theta \quad , \qquad (2)$$

where Ω is a function of frequency and temperature and θ is the incident angle (53°). Among the parameters in the above equations clear-sky brightness temperature T_{B0} and cloud mean temperature T_c.

Clear-sky brightness temperature, T_{B0}, is calculated by a statistical equation derived by the following procedure: First 392 climatological datasets are used to calculated the brightness temperatures for each channel and its corresponding clear-sky brightness temperature. These datasets cover typical atmospheric profiles from equator to 60° N (S), sea surface wind from 0 to 24 m/s. Clouds are assumed in these datasets, their LWP ranges from 0 to 1000 gm^{-2}. A standard regression method is used so that the clear-sky radiation of each channel is expressed by a function of the 5 brightness temperatures: 19H, 19V, 22V, 37H, 37V. The second step is to tune these regression equations using observed real-clear-sky data of SSM/I. This tuning is to minimize the errors caused by some uncertainties such as surface emissivity in the radiative transfer calculation, different footprint size for each frequency, and possible instrument calibration error.

For precipitating cloud regime, clear-sky brightness temperature is calculated in a different way from that mentioned above because contamination by precipitation makes it difficult to obtain a satisfactory regression equation. In this study a monthly mean value is used for T_{B0} in precipitating regime although it also can be calculated from general circulation model (e.g., Curry et al., 1990).

Cloud mean temperature for nonprecipitating cloud is also calculated by a equation derived by a regression method, in which the independents are 19H, 19V, 22V, 37H, 37V brightness temperature and cloud top temperature. The cloud top temperature is determined from International Satellite

Cloud Climatology Project (ISCCP) data. For precipitating regime, the cloud mean temperature is assumed to be the mean of cloud top and surface temperature.

LWP in Nonprecipitating Regime

Figure 1 compares the liquid water path retrievals for nonprecipitating clouds determined for each frequency with different polarization. It is seen that liquid water path retrieved from different polarization at a same frequency agrees quite well with each other except for some disagreement in 85 GHz, which associated with considerable noise in 85V channel. Figure 2 shows the comparison of retrievals from different frequencies. Similar to Figure 1 the agreement is obvious except for 85 GHz. It is noticed that there are larger negative values in 19 GHz retrievals than in 37 GHz. As a result of this comparison, retrievals from 37 GHz horizontal polarization (LWP_{37H}) are used for our algorithm's final liquid water path.

LWP in Precipitating Regime

For precipitating regime, large drop size and inhomogeneity of rainclouds would make the retrieval more complicate. An effort of combining different channels is presented to overcome this problem.

Retrievals for precipitating clouds show substantial disagreement from each frequency, as shown in Figure 3, which is a scatter plot of 37 GHz vs. 19 GHz retrieval. Two major effects could have contributed this disagreement. One effect is drop size (Takeda and Liu, 1987); clouds containing large water drops tend to be overestimated for their liquid water path at 19 GHz and also at 37 GHz when rainfall rate is

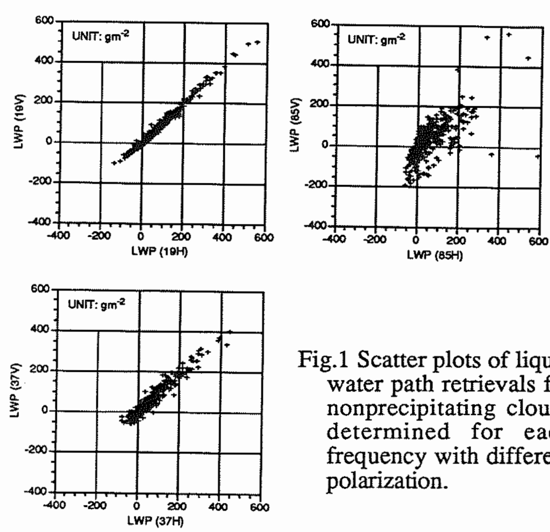

Fig.1 Scatter plots of liquid water path retrievals for nonprecipitating clouds determined for each frequency with different polarization.

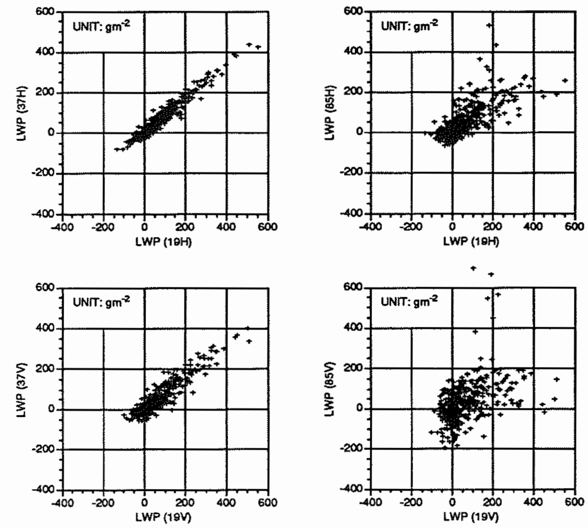

Fig.2 Same as Fig.1 except for different frequencies.

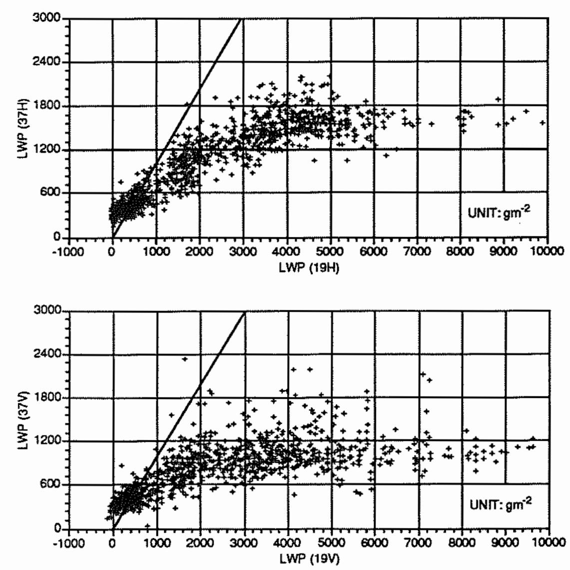

Fig.3 Scatter plots of liquid water path retrievals from 19 and 37 GHz for precipitating clouds.

very small. Another effect is underestimation caused by horizontal inhomogeneity of the cloud/rain field. In Figure 4 are shown the relationship between LWP_{19H} and LWP_{37H} for plane-parallel model result, actual retrieval from SSM/I data, and model results by assuming that the beam-filling effect makes retrieval 50% underestimated for both channels. It is seen that the relationship of the actual retrieval is closer to the 50% underestimation curve than to the plane-parallel model curve, which is consistent with the results of Chiu et al. (1991) and Short et al. (1991) for rainfall studies. To

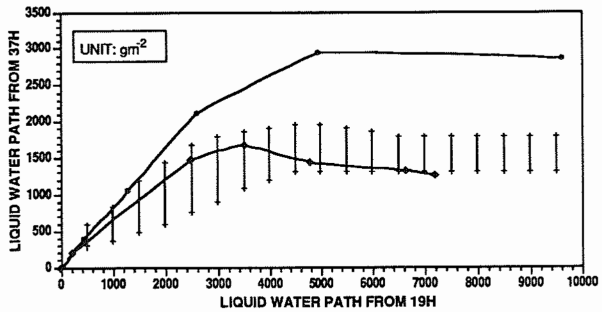

Fig.4 Relationship between liquid water path retrievals at 19 (LWP_{19H}) and 37 (LWP_{37H}) GHz horizontal polarized channels. —●— Plane-parallel model results; —◆— Model results with assuming that the beam-filling effect makes retrieval 50% underestimated. ‡ Actual retrieval range from SSM/I data.

obtain correct liquid water path retrieval, therefore, we need to find a combination of several channels which gives twice the liquid water path amount in terms of plane-parallel model results. The following algorithm meets this requirement:

$$LWP = 0.6\, LWP_{19H} + 0.4\, LWP_{37H} \quad . \qquad (3)$$

Note this combination does not make a gap between non-precipitating clouds and precipitating clouds, because for nonprecipitating clouds $LWP_{37H} \approx LWP_{19H}$.

Large Water Drops

The difference between LWP_{19H} and LWP_{37H} results mainly from the existence of large water drop (precipitating drops). Therefore, it could be an indicator of the size of water drops in a raincloud layer. Figure 5 shows this difference versus rainfall rate derived by a rainfall algorithm (Liu and Curry, 1992). It is seen that $LWP_{19H} - LWP_{37H}$ and rainfall rate is well correlated, which could be interpreted that the heavier the rainfall is the bigger the drop size is.

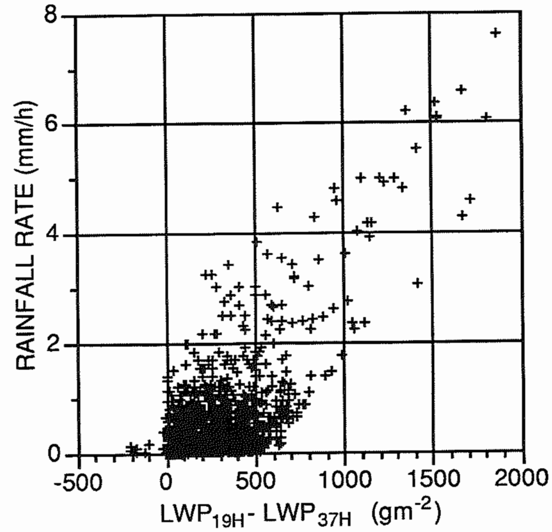

Fig.5 Scatter plot of difference of liquid water path retrievals between 19 and 37 GHz horizontal polarized channels versus rainfall rate.

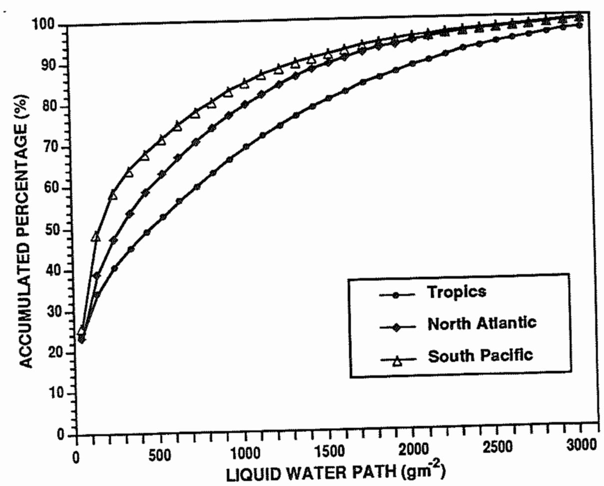

Fig.6 Accumulated percentage of liquid water path for 3 different regions.

3. CHARACTERISTIC FEATURES OF LIQUID WATER PATH

Figure 6 shows the accumulated percentage of LWP less than a certain value to the total liquid water in all LWP bins. Three different regions are examined: (a) Tropics, 10°S - 10°N, 140°E - 170°W; (b) North Atlantic, 40°N - 60°N, 10°W - 50°W; (c) South Pacific, 20°S - 40°S, 70°W - 120°W. More than half of the atmospheric liquid water are in clouds with LWP being less than 750 gm^{-2}. However, the percentage obviously depends on climatological regions, or cloud types. Deep convective clouds in tropics have more liquid water in large LWP portion than shallow stratocumulus in the South Pacific. The stratiform clouds usually associated low pressure systems in the North Atlantic are in between. Figure 7 shows the number ratio of precipitating pixels to all pixels in each LWP bin. It is interesting to see that the LWP at which there is 100% chance to precipitate is almost the same, $\approx$750 gm^{-2}, for the three different regions. That is, a cloud with LWP larger than 750 gm^{-2} is certainly precipitating no matter what type it is.

From figures 6 and 7 it is noticed that more than half of the condensed liquid water in the atmosphere exists in a form of cloud water rather than rain water. This part of condensed water does not heat the atmosphere by releasing latent heat because it eventually evaporates and uses the same amount of latent heat as released during condensation, although it plays an important role in radiative process.

4. SUMMARY

A liquid water path algorithm using SSM/I data is presented, in which all clouds are divided into 2 regimes: nonprecipitating and precipitating clouds and different retrieval method is used for each regime. For nonprecipitating clouds, retrievals derived from all but 85 GHz channel agree with each other very well. LWP_{37H} is used for the final LWP retrieval although there would be no significant difference if any other channel has been chosen. The disagreement of 85 GHz retrievals with other channels could be caused by several reasons such as significant scattering by ice cloud, instrument noise, and different footprint size with other channels. We are still working on these possibilities. If the scattering by ice is dominate of these effects, it is hopeful to get ice information from the difference in retrievals between 85 GHz and other channels. For precipitating clouds, the effects of precipitation and beam-filling can be accounted for in the present algorithm by using a combination of 19 and 37 GHz channels. This is based on that large water drops usually cause overestimation in 19 GHz and beam-filling effect always causes underestimation for all channels. The weighting factor to each channel is obtained by comparing observation and radiative transfer model results. The features of liquid water path in several climatological regions are explored and discussed using this algorithm.

REFERENCES

Chiu, L. S., G. R. North, D. A. Short, and A. McConnell, 1990: Rain estimation from satellites: Effect of finite field of view, *J. Geophys. Res.*, **95**, 2177-2185.

Curry, J. A., C. D. Ardeel and L. Tian, 1990: Liquid water content and precipitation characteristics of stratiform clouds as inferred from satellite microwave measurements. *J. Geophys. Res.*, **95**, 16659-16671.

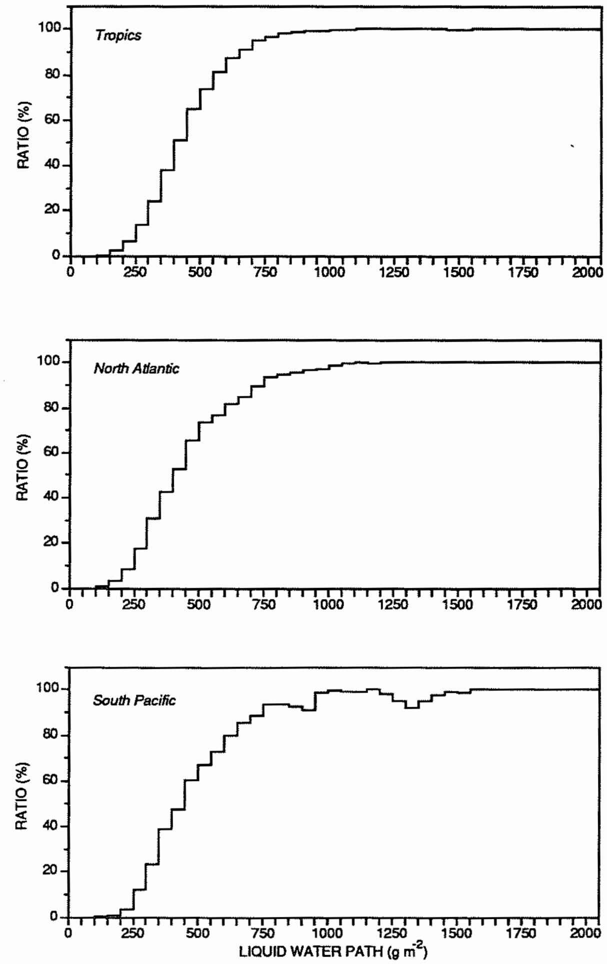

Fig.7 Number ratio of precipitating pixels to all pixels for 3 different regions.

Liu, G. and J. A. Curry, 1992: Retrieval of precipitation from satellite microwave measurements using both emission and scattering. *J. Geophys. Res.* (in press)

Short, D. A., and G. R. North, 1990: The beam filling error in the Nimbus 5 electronically scanning microwave radiometer observations of Global Atlantic Tropical Experiment rainfall, *J. Geophys. Res.*, **95**, 2187-2193.

Takeda T. and G. Liu, 1987: Estimation of atmospheric liquid water amount by Nimbus 7 SMMR Data: A new method and its application to the Western North-Pacific region. *J. Meteor. Soc. JPN*, **65**, 931-947.

FORECASTING RAIN CELL LOCATION USING RADAR DATA

P.J. BRÉMAUD[1] and Y.B. POINTIN[1,2]
Université Blaise Pascal[1], *C.N.R.S.*[2]
LaMP, 12 avenue des Landais, 63000 Clermont-Ferrand, FRANCE

1. INTRODUCTION

For many years, the forecast of precipitation has interested meteorologists and hydrologists. More recently, urban hydrologists have strengthened their requirements for spatially and temporally detailed rainfall forecasts, specially for sewer management or flash-flood warning (Huff et al. 1980, Einfalt et al. 1990). The only practical technique for making high spatial and temporal resolution forecasts is to extrapolate the precipitating cloud echoes which are detected in meteorological radar data. The extrapolation of radar echoes based on their motion as detected in successive radar pictures is only the first step of a precipitation forecast, since the intensity of the extrapolated radar echoes must then be converted into rainfall at the ground (Einfalt 1991, Messaoud and Pointin 1990). This paper is concerned only with this first step of producing the best extrapolating method.

The approaches used until now can conveniently be considered as falling into one of three categories (Collier 1989, Elvander 1976) : cross-correlation techniques (Austin and Bellon 1974), echo centroid (Barclay and Wilk 1970) and more complex methods (Blackmer et al. 1973, Einfalt et al. 1990). We have developed a new forecasting method (called PARAPLUIE), which provides cures for the main defaults of each of these earlier methods.

2. PARAPLUIE : A NEW RAINFALL FORECASTING METHOD

The PARAPLUIE method (Brémaud and Pointin 1992) belongs to the complex method category, and is divided in four steps : a - tracked entity definition, b - tracked entity characterization, c - tracked entity matching for the detection of the different motions and d - forecast by extrapolation. The method is fully automated and an additional procedure is used to distinguish ground echoes from rain echoes and to remove them.

a. *Tracked entity definition*

Contrary to a large majority of complex methods, which use the "T echo" defined by a connectivity property above a fixed given reflectivity threshold technique in order to define their tracked entities (afterwards called "T echoes"), the PARAPLUIE algorithm defines the tracked entities, called "CEL echoes", by the contour constructed at 6 dB below each enclosed reflectivity maximum. This definition of our tracked entities, originally introduced by Crane (1979) for aircraft hazard identification, is illustrated on the figure 1.

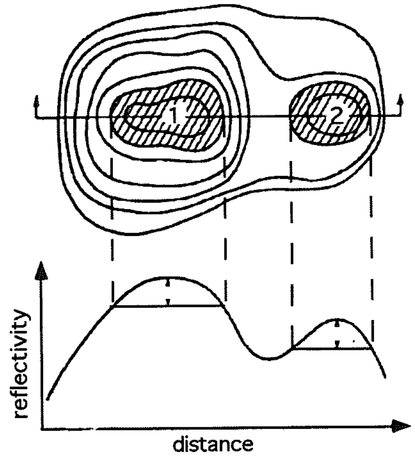

Fig. 1 : illustration of the "CEL echo" detection

There are two main advantages of this "CEL echo" definition. Firstly, in case of critical hydrological weather (convective or frontal situation), the "CEL echoes" are associated with heavy rain cells which are closely related to convective cells. So the accurate forecast of their future position is very important for urban hydrologists. Moreover, the motion of heavy rain cells is often different from the motion of the large rain area within which they are embedded. In that case, the tracking of the large rain area rather than the "CEL echoes" can lead to considerable underestimates of the observed rain over a drainage basin. Secondly, this definition avoids the use of a fixed and arbitrary reflectivity threshold which cannot be appropriate to detect the characteristic motions for every weather situations.

b. *Tracked entity characterization*

In order to recognize which one of the "CEL echoes" of one picture corresponds to the "CEL echo" of the same rain cell in the next picture (the "matching procedure"), we have characterized each "CEL echo" by some characteristic attributes : area, reflectivity distribution characteristics, coordinates of the centroid, elongation of the inertia matrix, inclination of the principal axis of inertia, previous detected motion.

c. *Tracked entity matching and detection of the different motions*

The matching procedure defined in the PARAPLUIE algorithm is based on our experience in tracking rain cells using radar data. We have introduced seven criteria evaluating the confidence we can have in the tested match between any two successive "CEL echoes" :

- two criteria related to the amplitude and direction difference between the tested individual motion and the mean motion established for all the "CEL echoes",
- one criterion of reflectivity difference between the two tested "CEL echoes",
- two criteria of pattern difference,
- one criterion of elongation difference,
- one criterion of inclination difference.

For each tested match, these seven criteria are used with different relative weights to define the unique value of a confidence level which characterizes the likelihood of this match.

Therefore, and in order to obtain realistic trajectories, the test of each matching "CEL echo" pair is stopped whenever the displacement of the centroid is very different from the mean displacement of all "CEL echoes". When the test proceeds, the new position of each "CEL echo" is precisely obtained by a local cross-correlation technique and then all the above criteria are evaluated in order to accept or to refuse the tested match as realistic.

The "CEL echoes" tested in this matching procedure also include the union of "CEL echoes" (Einfalt et al. 1990) in order to account for mergers and splits of such echoes, although these are less frequent than in the case of "T echoes", which can artificially separate because a saddle point reflectivity value may be close to the chosen threshold value.

At the end of this matching procedure, the motion vector assigned to each "CEL echo" is equal to the arithmetic average of all instantaneous speeds of the same rain cell detected on the previous pictures.

c. *forecast by extrapolation*

Through the matching procedure we are able to define with accuracy the motion of the "CEL echoes", i.e. the real motion of the rain cells associated with convective cells. Moreover the high spatial and temporal resolution of the radar data permits us to observe that these structures are very evolutive to such an extent that this dynamical tendency introduces a random noise in the estimation of the motion of the "CEL echoes". So in order to avoid too much dissimilar extrapolation speed relatively to the mean motion really observed, we have chosen to extrapolate the motion of each of the echoes in which the "CEL echoes" are embedded with a speed which is equal to the arithmetic average of the speeds of the "CEL echoes". As illustrated in Fig. 2, these "EC echoes" (for Enclosing Cell echoes) are plotted round each matched "CEL echo" by using a threshold value which is equal to the reflectivity minimum of the less intense "CEL echo". Moreover, an "EC echo" is plotted if a "CEL echo" in one picture is not matched with a "CEL echo" in the next picture; in this case, the plot is centered on the point which corresponds to the centroid of the "CEL echo" translated with the mean motion of all the "CEL echoes".

This definition implies that one "EC echo" can enclose zero, one or more "CEL echoes". The main advantage of this definition is that the multiple mergers of rain cells in strong convective bands can be taken into account by enclosing them in one structure. Indeed, the rain cells in a convective band may have somewhat homogenous motions which can be different from the apparent motion of the entire band. This definition of "EC echo" allows us to find this coherent motion and to forecast with accuracy the location of dangerous hydrological phenomena.

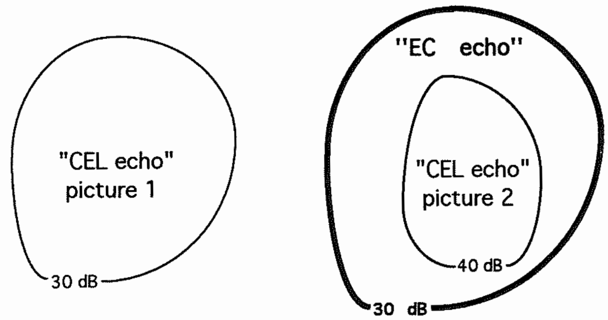

Fig. 2 : "EC echo" round a "CEL echo" of one picture matched with a "CEL echo" of the previous picture.

3. RESULTS

In order to evaluate the real capabilities of the PARAPLUIE method, we have compared it with three other methods on four events (Brémaud and Pointin 1992). The three other methods are the persistence "PERS" (which assumes no motion), the global extrapolation of the entire image "EXTRA" (cross-correlation type technique) and the SCOUT II.0 method (an earlier "complex method"), which is used operationally in Seine-Saint-Denis county (near Paris) for sewer management (Einfalt et al. 1990). The four events studied are characterized by four different weather situations, by different radar data spatial scales and by different time intervals between successive radar pictures. One event has been used to forecast the rain at three different time intervals (5, 10 and 15 min). Each forecasting method is judged by using the values, computed for each prediction time step, of six quality criteria : three "concordance" criteria (Critical Success Index or CSI, Rousseau Index or RI and Cross-Correlation coefficient or CC) and three hydrological criteria. These last criteria, introduced by Einfalt et al. (1990), are defined by :

$$dHS_{-} = \frac{1}{n_{-}} \sum_{i=1}^{n_{-}} (dH_{for} - dH_{obs})$$

$$dHS_{+} = \frac{1}{n_{+}} \sum_{i=1}^{n_{+}} (dH_{for} - dH_{obs})$$

$$dHS = \frac{n_{-} \cdot dHS_{-} + n_{+} \cdot dHS_{+}}{n_{-} + n_{+}}$$

where dH_{obs} and dH_{for} are the equivalent intensity (R) calculated on nine pixel area for the observed picture and for the forecast picture which is deduced, by each method, from the two previous observed pictures. Similarly, n_- and n_+ are equal to the number of pixels where $dH_{for} - dH_{obs} \leq 0$ and to the number of pixels where $dH_{for} - dH_{obs} > 0$, respectively. All these criteria are only calculated on the observed rainy pixels whose equivalent intensity exceeds a fixed threshold value (5 mm·h^{-1}) in order to show how each method is able to forecast the real quantity of heavy precipitation. Therefore, the criterion dHS_- evaluates the underestimation of the observed rain, while the criterion dHS_+ characterizes the overestimation, and the criterion dHS weighs the two first ones against each other.

Since these hydrological criteria do not take into account the false alarms, i.e. a forecasted rain which is not observed, it is important, even for hydrological purposes to consider the results according to concordance criteria. Between these last criteria, the Cross-Correlation coefficient (CC) is the most suited one for hydrology, because its value depends on the concordance of each reflectivity values, in contrary to the Critical Success Index (CSI) or the Rousseau Index (RI) which are calculated from a contingency table of the type "rain/no rain", i.e. independent on the rain quantities. Besides, CSI and RI criteria are, by definition, less sensitive than CC to the number of "rainy pixels" inside the picture. However, the RI criterion is calculated on the same threshold rainy pixels than for the hydrological criteria in order to emphasize the important hydrological events.

For each event and for each forecasting method, the values of each criterion are evaluated at each time step and are reordered in increasing order (or decreasing order for dHS_+) in such a way as to draw the resulting curves from left to right in growing performance (efficiency curves). This implies that the method whose efficiency curve is globally above the efficiency curves of the other methods (or globally below for the criterion dHS_+) can be considered as the best method for this criterion. The use of these efficiency curves avoids the troughs and peaks of the time evolution curves which are due to morphology and intensity changes of the radar echoes from one time step to the next.

These efficiency curves of the CC, RI, dHS_- and dHS_+ criteria, evaluated for a threshold value of 5 mm/h (except for CC which is calculated from all the pixels of both the observed picture and the forecasted picture), appear on Figs. 3a to 3d respectively, for the "Cévennes 88" event. In these figures, the PERS, EXTRA, and PARAPLUIE methods are depicted with dotted line, dashed line and solid line respectively. The "Cévennes 88" event is the most important studied hydrological event (rainfall rate bigger than 125 mm·h^{-1} for more than 24 minutes). The successive pictures of the "Cévennes 88" event, recorded with a time interval of 12 minutes for the first three hours and of 8 minutes for the next three hours, show the formation and the propagation of an intense frontal band.

Since its efficiency curve is globally above the other curves in Figs. 3a to 3c, the PARAPLUIE method gives the best performance according to the CC, RI or dHS_- criteria but all methods globally overestimate the precipitation in the same manner (Fig. 3d). The differences

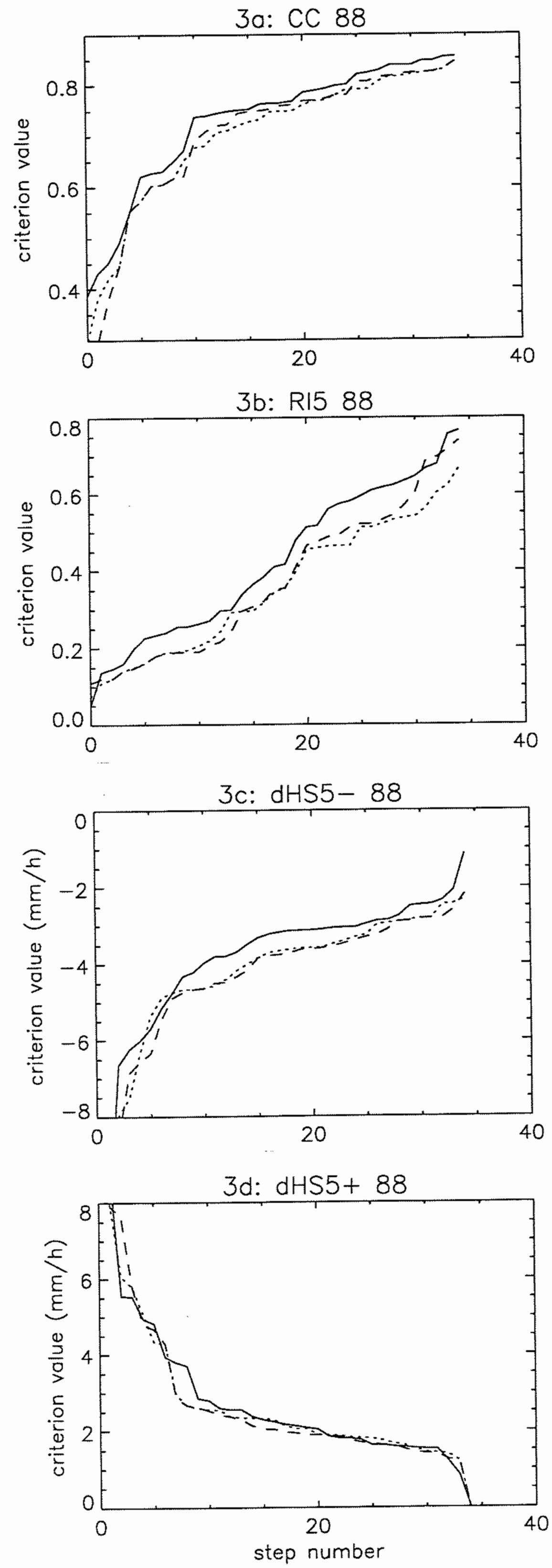

Fig. 3 : efficiency curves of the methods PERS (dotted line), EXTRA (dashed line) and PARAPLUIE (solid line) according to CC (a), $RI5$ (b), $dHS5_-$ (c) and $dHS5_+$ (d) for the event "Cévennes 88".

between the performance of the EXTRA and PARAPLUIE methods are due to the fact that EXTRA detects the motion of the entire frontal band (5 $m \cdot s^{-1}$ towards the east) while PARAPLUIE detects the motion of the rain cells which are embedded within the band (11.5 $m \cdot s^{-1}$ towards the north-north-east). Since these rain cells provide the largest part of the precipitation observed at ground, the worse forecast of their location by the EXTRA method makes it underestimate the real quantity of the observed rain.

The results deduced from the three other events show that the PARAPLUIE method appears globally better than the SCOUT II.0 and EXTRA methods in order to provide against the false alarms, to forecast the location of important hydrological events and to evaluate the quantity of the observed rain at the forecast time (Brémaud and Pointin 1992).

4. CONCLUSIONS

The best way to forecast rainfall at very-short-range is to extrapolate the radar echoes in real time. This forecasting procedure is particularly well suited for urban hydrological purposes, which require spatially and temporally detailed forecast (with less than 1 km spatial resolution and a forecasting time interval of a few tens of minutes). For this last application, we have developed a new forecasting method (Brémaud and Pointin 1992) which focuses on heavy rainfall, since it detects and extrapolates the motion of heavy rainfall cells which are closely associated with convective cells. Indeed both the precipitation forecasting method and the radar data must be adapted to their use, particularly to the desired forecast period, because the meteorological structures associated with rain can have very different spatial and temporal characteristic scales : from 1 km and 30 minutes for the convective cells to 1000 km and 48 hours for the extratropical cyclones, each of these different scale structures having their own motion. So, in order to obtain the best rainfall forecast, the method must detect and extrapolate the motion of that precipitating meteorological structure, whose life duration is about the forecasting time interval and whose motion can be detected on the successive radar pictures. In case of a one hour forecasting time interval, the most suitable method is the one which uses small spatial scale radar data and extrapolates the motion of convective cells.

We have compared our method (named "PARAPLUIE") to three other different methods, one of which (SCOUT II.0) is at present operational for sewer management. The results according to the "concordance" or hydrological criteria show that our method is reliable and performs well whatever the studied event or the used forecasting time interval up to 15 minutes. Thus, the PARAPLUIE method characteristics appear well suited for forecasting time intervals of about 15 minutes to one hour.

ACKNOWLEDGEMENTS

The authors are indebted to Dr. T. Einfalt for discussions and for making some radar data available. The "Cévennes 88" have been obtained by the members of the radar group of the LaMP/OPGC and by all campaign participants. The mathematical tools, which are used in the PARAPLUIE method, have been described to us by Mr. R. Pejoux and Miss D. Chambreuil. The edition of this manuscript owes much to Mr. H. Larsen and Mrs O. Guillot and J. Squarise. We express our thanks to all these persons.

REFERENCES

Austin, G.L., and A. Bellon, 1974 : The use of digital weather radar records for short-term precipitation forecasting. Quart. J. R. Met. Soc., **100**, 658-664.

Barclay, P.E., and K.E. Wilk, 1970 : Severe thunderstorm radar echo motion and related weather events hazardous to aviation operations. ESSA tech. memo. n° 46, NSSL, 63 pp.

Blackmer, R.H. Jr, R.O. Duda and R. Reboh, 1973 : Application of pattern recognition techniques to digitized weather radar data. Final report, contract n° 1-36072, Stanford Research Institute, Menlo Park, California, 89 pp.

Brémaud, P.J., and Y.B. Pointin, 1992 : Forecasting heavy rainfall from rain cell motion using radar data. Submit. to J. Hydrol.

Collier, C.G., 1989 : Short-period forecasting using radar data. In "Applications of weather radar systems. A guide to uses of radar data in meteorology and hydrology", ed. C.G. Collier, Ellis Horwood limited, Chichester, Chapter 6, 136-182.

Crane, R.K., 1979 : Automatic cell detection and tracking. IEEE Trans. Geosci. Electron., GE-17, 4, 250-262.

Einfalt, T., 1991 : Summer 1990 in Seine-Saint-Denis : forecast versus measured areal rainfall values. Atmos. Res., **27**, 151-158.

Einfalt, T., T. Denoeux and G. Jacquet, 1990 : A radar rainfall forecasting method designed for hydrological purposes. J. Hydrol., **114**, 229-244.

Elvander, R.C., 1976 : An evaluation of the relative performance of three weather radar echo forecasting techniques. 17th Conference on Radar Meteorology, Seattle, 526-532.

Huff, F.A., S.A. Changnon and J.L. Vogel, 1980 : Convective rain monitoring and forecasting system for an urban area. 19th Conference on Radar Meteorology, Miami, 56-61.

Messaoud, M., and Y.B. Pointin, 1990 : Small time and space measurements of the mean rainfall rate made by a gage network and by a dual polarization radar. J. Appl. Met., **29**, 830-841.

Forecasting of Cloud and Precipitation Radar Images Using Adaptive Stochastic Models

Andrey V. Belotsercovsky[1], Hiroshi Uyeda[2], Katsuhiro Kikuchi[2]

[1]Hydrometeorological Institute, St.Petersburg 195196, Russia
[2]Faculty of Science, Hokkaido University, Sapporo 060, Japan

1 Introduction

Real-time very-short-term forecasting of near-current cloud and precipitation conditions can be considered as a problem of sequencing corresponded radar images of the region to be surveyed. Radar images forecasting itself can be split into two subproblems which (despite their importance) have not yet been solved. The first is the problem of producing a one-to-one representation of the radar echo using a finite set of parameters in order to replace two-dimensional image forecasting using a set of one-dimensional tasks. The second is the problem of creating a method of one-dimensional forecasting of the parameters' time-series.

Conventional methods of time-series' forecasting implemented in similar cases are based on prior assumptions about the process to be forecasted. The most widely used assumptions are stationarity, normal probability distribution, and negligible values of measurement errors [Box and Jenkins, 1970]. The main advantage of such an approach is that the forecasting procedure is quite simple one to implement. The disadvantage is an attendant lack of realism, because the actual meteorological processes often don't satisfy these assumptions. This can sometimes lead to large forecasting errors.

Conventional methods of radar imagery representation are of two general types. The first is a non-parametric approach wherein an entire image is translated as a single entity using cross-correlation analysis [Bellon and Austin, 1978, Browning, 1979]. In the other approach a representation of a radar echo is created by using a mathematical description of its contour. The contour description method uses either a set of parameters derived from the centroid position and the length of the lines radiating out from the centroid to the contour boundary [Kavvas and Chen, 1989], or individual Fourier transformations of separated functions through which the contour shape can be determined [Ruggiero et al., 1991]. The first way is useful for forecasting key parts of the echo and is important for tracking severe weather; however, it neglets both details of the echo and whole areas covered by the cloud system. The second way is better fitted for nowcasting precipitation movement and is simple enough to run in real time, but has a mathematical disadvantage. The chosen parameters' set doesn't conform to the superposition principle; therefore, each parameter cannot be treated independently from the others in the performance of additional linear extrapolation procedures (in contrast to what usually has been the case).

The objective of this study was to try and implement an approach to real-time radar images forecasting which required no prior assumptions about the process to be forecasted and, though seemingly complicated, is quite reasonable mathematically. In this approach, a radar image is represented by a discrete two-dimensional spatial spectrum. The sequence of radar images of the dynamically evolving meteorological target is considered as a set of Fourier coefficients' time-series. In order to forecast these Fourier coefficients selforganized adaptive stochastic models in state space form are used.

2 Time-series forecasting

Under this approach, time-series of images parameters are forecasted using adaptive stochastic models [Belotsercovsky, 1983, Belotsercovsky et al., 1991]. The framework of the stochastic model is well known as the ARMA model [Box and Jenkins, 1970] and is expressed as the differential equation

$$y_t = \mathbf{Y}_{t-1}^T \Theta_t + \varepsilon_t, \tag{1}$$

where $\Theta_t^T = (a_1^t, ..., a_p^t, b_1^t, ..., b_q^t)$ is a vector of parameters; $\mathbf{Y}_{t-1}^T = (-y_{t-1}, ..., -y_{t-p-q})$ is a data vector; y_t are discrete samples of the process to be forecasted at time t; ε_t is discrete white noise with a zero mean and a dispersion of σ^2; p, q are orders of autoregressive and moving average operators, respectively.

To provide an ability to handle the nonstationary processes the model parameters (unlike the ARMA model) are assumed to be varying over time (random walk)

$$\Theta_t = \Theta_{t-1} + \Omega_t, \tag{2}$$

where $\boldsymbol{\Omega}_t$ is the multidimensional white noise with unknown covariance matrix $\boldsymbol{\Sigma}_t$.

The model parameters vector $\boldsymbol{\Theta}_t$ is updated in real time as a current measurement y_t becomes available

$$\hat{\boldsymbol{\Theta}}_t = \hat{\boldsymbol{\Theta}}_{t-1} + \mathbf{K}_t \mathbf{Y}_{t-1}[y_t + \mathbf{Y}_{t-1}^T \hat{\boldsymbol{\Theta}}_{t-1}] \tag{3}$$

by using a modified extended Kalman filter with the gain vector

$$\mathbf{K}_t = \boldsymbol{\Delta}_t \mathbf{Y}_{t-1}[\mathbf{Y}_{t-1}^T \boldsymbol{\Delta}_t \mathbf{Y}_{t-1} + \hat{\sigma}^2]^{-1} \tag{4}$$

and the inverse covariance matrix

$$\boldsymbol{\Delta}_t = [\mathbf{I} - \mathbf{K}_t \mathbf{Y}_{t-1}^T]\boldsymbol{\Delta}_{t-1} + \boldsymbol{\Sigma}_t. \tag{5}$$

Here $\mathbf{I}$ is the unit matrix $(p+q) \times (p+q)$.

The dispersion of the model's white noise is calculated recursively

$$\hat{\sigma}_t^2 = \hat{\sigma}_{t-1}^2 + \frac{1}{t+1}[(y_t + \hat{\boldsymbol{\Theta}}_{t-1}^T \mathbf{Y}_{t-1})^2 - \hat{\sigma}_{t-1}^2] \tag{6}$$

The influence of past observations on parameter estimates is discounted by adding the covariance matrix of parameters' random walk $\boldsymbol{\Sigma}_t$. The values of this matrix's components and, therefore, the degree of influence exerted by new observations, should be estimated automatically. To achieve this an adaptive feedback loop of the parameters' noise is added. The values of the components of the covariance matrix of the model parameters' random walk are iteratively increasing while the conditional expression of a chi-squared test of the model divergence

$$[y_t + \mathbf{Y}_{t-1}^T \hat{\boldsymbol{\Theta}}_{t-1}]\hat{\sigma}^{-2} > \chi_{1-\alpha}^2, \tag{7}$$

is still true. Here α is value of test significance.

To implement this procedure for forecasting one should not make any prior assumption about the stochastic process to be forecasted. Model parameters follow the current measurement data themselves, tracking the statistical structure transformation of the forecasted process. To some extent, it overcomes nonstationarity and prior indetermination and provides real-time processing ability because of the recursive character of the procedures. It doesn't overburden computer memory because there is no need to retain in memory all samples; only the current last values $(y_t, \hat{\boldsymbol{\Theta}}_{t-1}, \mathbf{Y}_{t-1}, \hat{\sigma}^2)$ and the rules of their development (eq.(3)-(6)) need to be saved.

3 Spectral representation

Using this approach the radar imagery is translated into a complex spatial wave number domain. This way seems most natural because it replaces the image by using a one-to-one parameters' set, which conforms to the superposition principle. This means that an independent treatment of each wave number component used in developing a forecast will not break the mathematical consistence of the linear forecasting problem.

Instead of a radar image $f_{n,m}$ given over the grid $\{n, m\}$, we used spatial spectrum components

$$F_{k,l} = \sum_{n=0}^{N-1} \sum_{m=0}^{M-1} f_{n,m} \exp\{-j(2\pi\frac{kn}{N} + 2\pi\frac{lm}{M})\}, \tag{8}$$

which are considered as objects of forecasting. To reduce the calculation burden an operational wave number domain is compressed by spatial filtering

$$\tilde{F}_{k,l} = F_{k,l} * \begin{cases} 1, & \text{if} k \leq k^*, l \leq l^*, \\ 0, & \text{if} k > k^*, l > l^*. \end{cases} \tag{9}$$

Under these circumstances, the spatial resolution of the forecasting procedure is reduced and thus, fine details of the echo are smoothed out or eliminated. This means that by specifying the value of k^*, l^* one should be able to compromise between the desired spatial resolution and the computational burden.

After the forecasting of spatial spectrum components has been accomplished a forecasted radar image can be retrieved by an inverse Fourier transformation of $\tilde{F}_{k,l}$

$$\tilde{f}_{n,m} = \frac{1}{NM} \sum_{k=0}^{N-1} \sum_{l=0}^{M-1} \tilde{F}_{k,l} \exp\{j(2\pi\frac{kn}{N} + 2\pi\frac{lm}{M})\} \tag{10}$$

Therefore, the forecasting proceeds in a wave number domain using an adaptive stochastic model for each spectral component. The desired number of components, and thus the corresponded number of single stochastic models to be applied, should be specified after taking into consideration computer limitations and the degree of precision desired.

4 Testing

This approach was tested using snow band data collected by Hokkaido University Doppler radar over Rebun Island (Northern Japan) during January 1991 in winter monsoon surges. As an example, a sequence of radar echoes of an evolving snow band taken at one-hour intervals is shown in Fig.1 (panels 1-3).

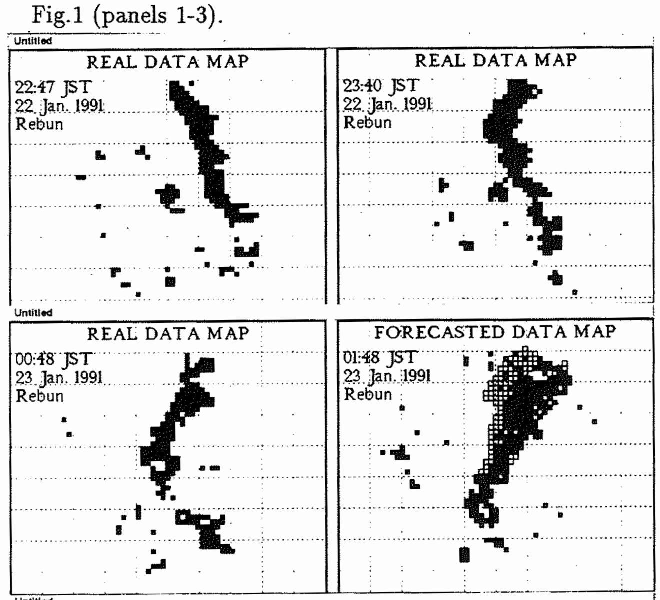

HOKKAIDO UNIVERSITY DOPPLER RADAR
REFLECTIVITY (>23 dBZ), SCALE 120*120 KM, PPI(1.0)

Fig.1. The sequence of radar echoes of the evolving snow band (panels 1-3), the forecasted (panel 4, white squares) and actual (panel 4, black squares) echoes.

This sequence covers the evolution of the shallow, slowly developing convective snow band accompanied by heavy snowfall from the mature state to the beginning of dissipation. The corresponded sequence of two-dimensional spatial spectra is shown in Fig.2.

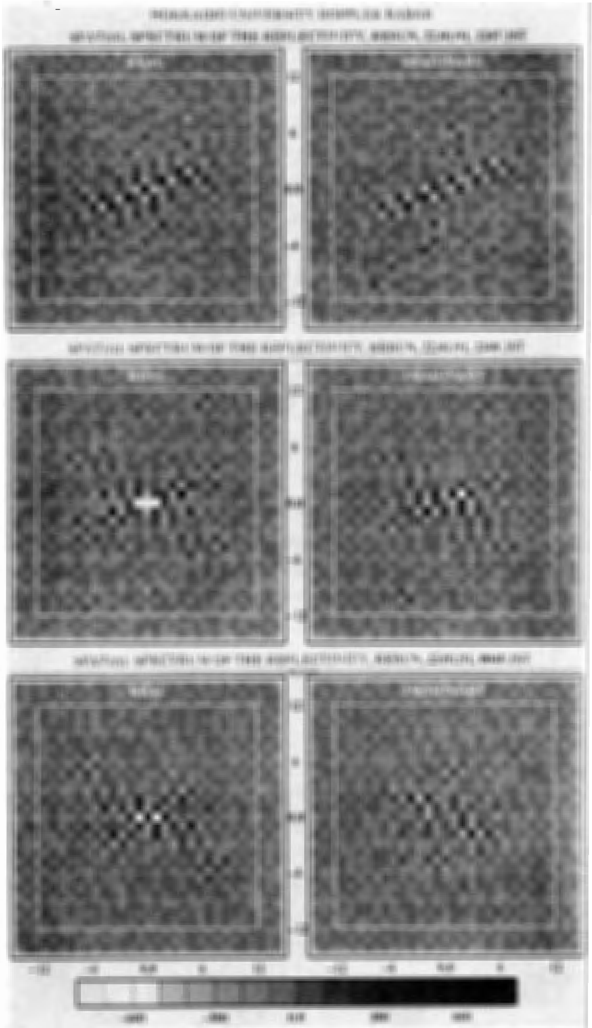

Fig.2. The sequence of two-dimensional spatial spectra of the radar reflectivity (shown in the Fig.1, panels 1-3). The white squares outline the operational low wave number domain.

In Fig.2, the low wave number domain in which the essential spectral components are contained is outlined by the white squares. Using spatial filtering, the operational wave number domain was compressed to the outlined one. As described previously, in our approach the problem of forecasting the radar echo shown in Fig.1 is replaced by the problem of forecasting the spectral components shown in Fig.2. Therefore, a set of 2nd order adaptive stochastic models were applied to each spectral component of the filtered wave number domain. The result, after the forecasted radar image had been converted into a spatial domain using the inverse Fourier transformation, is shown in Fig.1, panel 4. In this panel, the real radar echo overlays the forecasted one. A comparison of the forecasted and actual echoes reveals quite reasonable coincidence considering the shortness of the history for an adaptive stochastic model.

An analysis of this and other cases in which the approach was tested shows same, close coincidence between forecasted and actual echoes when conditions were static or changing at a steady rate; however the degree of coincidence deteriorated if a system's development process was changing (such as in the dissipation of cloud system). The forecasting results worsen for scattered echoes, probably because of contamination of the high spatial wave numbers (needed in these cases) by measurement noise. In particular, a current forecasting error could be used as an indicator of transformations within the cloud system being observed.

5 Conclusion

Preliminary tests suggest that in selforganized adaptive stochastic models the spatial spectral conversion of the radar images to be forecasted may be an attractive tool for automatic real-time short term forecasting. To some extent it overcoms nonstationarity, prior indefinite and mathematical inconsistency problems. In addition, any forecasting error could itself be used as an indicator that a transformation is occurring in the cloud system's development process.

6 Acknowledgements

The authors would like to acknowledge gratefully Messrs. A.Takemoto and N.Osaki for the data acquittance and Mr. N.Takahashi for help over computational matters. This work has been supported under Grant-in Aid for Scientific Research of the Ministry of Education, Science and Culture of Japan.

References

[1] Bellon, A., Austin,G.L., 1978: *The evaluation of two ears of real-time operation of a short-term precipitation forecasting procedure (SHARP).* J. Appl. Meteor., 17, 1778-1787.

[2] Belotsercovsky,A., Uyeda,H., Kikuchi, K., 1991:*An approach to a very- short-term forecasting.* Pre-print of Japan Meteor. Soc., 240.

[3] Belotsercovsky, A., 1983:*On an adaptive algorithm of an optimal filtering and a short range forecasting of meteotological conditions.* Hydrology and Meteorology, XXXII, v.6, 28-34 (in Russian) .

[4] Box G.E.P,, Jenkins G.M., 1970: *Time series analysys. Forecasting and Control,* San Francisco: Holden Day.

[5] Browning, K.A., 1979:*The FRONTIER plan: A strategy fo using Radar Sattelite Imaginary for very short range precipitation forecasting* Met.Mag. 108, pp 161-184.

[6] Kavvas, M.L. and Z. Chen, 1989: *The radar-based short term prediction of the time-space evolution of rain fields.* Geophysics Laboratory Technical Report, GL-TR-89-0103, ADA213802.

[7] Ruggiero,F.H., Heideman, F.K., Doherty, J., 1991:es in operational *An evaluation of three techniques for nowcasting precipitation fields using weather radar* Preprints 25th Int. Conf. on Radar Meteorology, Paris, France.

PROTOTYPE REAL-TIME FORECASTING OF CLOUDS AND PRECIPITATION USING A MESOSCALE MODEL

Greg Thompson and William R. Cotton

Colorado State University, Fort Collins, CO, USA 80523

1. INTRODUCTION

The Regional Atmospheric Modeling System (RAMS), developed at Colorado State University, was used for prototype real-time forecasting during the winter of '91-'92. Simulations were run once a day initialized at 0000 UTC and forecast out to 48 hrs. Two different grid configurations, discussed in the following section, produced real-time forecasts for two experiments. The first configuration was designed to produce forecasts of orographically-forced precipitation for the Colorado region. These simulations were produced daily from mid-November 1991 through the first week of April 1992 on RISC workstations at CSU. The second grid configuration was designed to provide upper-level cloud forecasts, particularly cirrus, to forecasters involved in the First ISCCP Regional Experiment (FIRE) II (13 Nov. - 6 Dec. 1991). These simulations were performed daily on the National Center for Atmospheric Research's (NCAR) CRAY-YMP.

Simulating 48 hrs for the Colorado experiment took 10 to 12 hrs of wall clock time and simulating 24 hrs for the FIRE II experiment took 7 to 9 hrs depending on the machine's load. The following section will describe the grid configurations in more detail. Then, in Sections 3 and 4, one particular day from each experiment will be examined more closely to evaluate the effectiveness of RAMS real-time forecasting.

2. MODEL DESCRIPTION

As mentioned in the Introduction, RAMS was initialized using 0000 UTC data. The dataset used for this was provided by NOAA's Forecast Systems Laboratory's (FSL) Mesoscale Analysis and Prediction System (MAPS). MAPS was used because of its 60km grid spacing and because it incorporates aircraft reports, wind-profiler observations, surface mesonet station observations, surface aviation observations and rawinsondes into its analysis. Each experiment used two interactive nested grids. The Colorado experiment course grid covered the western 3/4 of the U.S. with 100km grid spacing and the fine grid covered Colorado with 25km spacing. There were 24 vertical levels with spacing of 300m at the surface stretching to a constant 1000m near model top. The FIRE II configuration had a course grid roughly covering the same region as mentioned above but with 80km spacing and a 20km fine grid covering all of Kansas and portions of bordering states. For this configuration, much finer vertical resolution was needed so we employed 42 vertical levels with constant 300m spacing up to 9km then slowly increasing to 1000m spacing near 16km. The non-hydrostatic version of RAMS was used for both experiments, however, explicit microphysics was used only for the FIRE II forecasts because of time considerations when running in real-time. Because real-time forecasting could not be accomplished on the CSU workstations when microphysics was included, a replacement for microphysics for the Colorado experiment which allowed precipitation was coded. This scheme assumed that any supersaturation was immediately translated to the ground with a precipitation efficiency based on cloud-top temperature. This provided a crude "dump bucket" method of liquid precipitation but no ice phase. Both experiments used Davies nudging conditions on the lateral boundary regions using NMC's Nested Grid Model (NGM) output in order to provide RAMS with time-dependent lateral boundary conditions.

3. CASE FROM COLORADO EXPERIMENT

On 8 March 1992 a synoptic situation favorable for heavy snow along the Colorado front range was developing. At the surface, an arctic front was approaching from the north while lee cyclogenesis was occurring in the southeastern portion of Colorado. Moisture was being fed into the storm as a strong fetch of air from the Gulf of Mexico protruded northward and westward through Kansas and into Colorado. Aloft, a split flow regime allowed a strong cut-off low to move from Southern California toward the Four Corners region. By 0000 UTC 9 March the arctic front was pushing through Colorado causing an upslope flow regime to develop along the Front Range and snow followed soon after. The snow began in the northern portions of the state first and intensified throughout the nighttime hours. Embedded convection aided in localized heavy snowfall and many communities reported blizzard conditions and occasional lighting. By 1200 UTC Fort Collins reported 33cm of snow while residents in the foothills just west of town reported snowfall amounts as large as 71cm. The surface low at this time had moved into central Kansas and incorporated the arctic front into the system creating a trailing cold front and more classical extra-tropical cyclone. The 500mb cut-off was centered on the Colorado-Kansas border and was beginning to be absorbed in the northern branch of the jet. By 0000 UTC 10 March the whole system had moved into the Great Lakes region leaving Colorado and the Central Plains in a cold arctic air mass dominated by large-scale subsidence.

RAMS simulated this developing storm system very well during this 48 hr time period. The cyclogenesis in southeast Colorado was modeled particularly well as shown in Figure 1. Figure 1 shows the 24 hr predicted mean sea level reduced pressure valid at 0000 UTC 9 March. Here we see a 994mb low in the bottom right corner and the associated cyclonic winds. Elsewhere in the figure, we see a tight gradient between this low and the approaching arctic anticyclone as the arctic front noses down the Front Range in the center of the figure. This is where we see the largest discrepancy between the model and observations. Shown in Figure 2 is the observed mean sea level reduced pressure valid at the same time. Notice the wind indicated a cold front nosing down the 105 meridian to just north of Denver (denoted by DEN). The model, however, advanced the cold front to just south of Colorado Springs (denoted by COS). We attributed the model's faster propagation to the

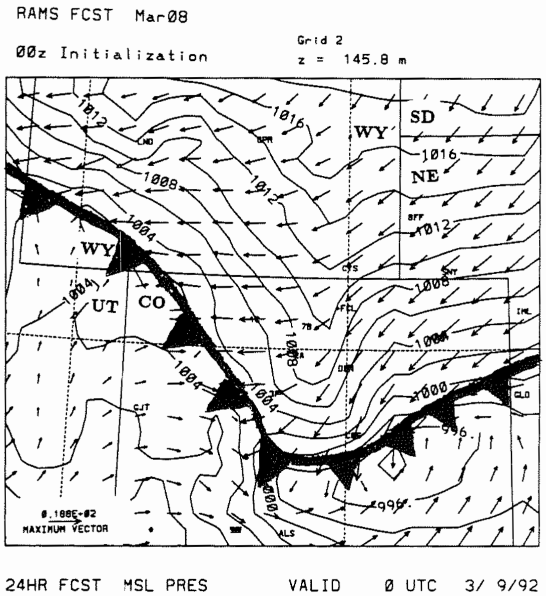

Figure 1. RAMS 24 hour forecast mean sea level reduced pressure valid 0000 UTC 9 March 1992. Dashed lines indicate 40° N and 105° W and select surface stations are plotted by their three letter identifiers. Surface cold front is also drawn in. Contour interval is 2mb.

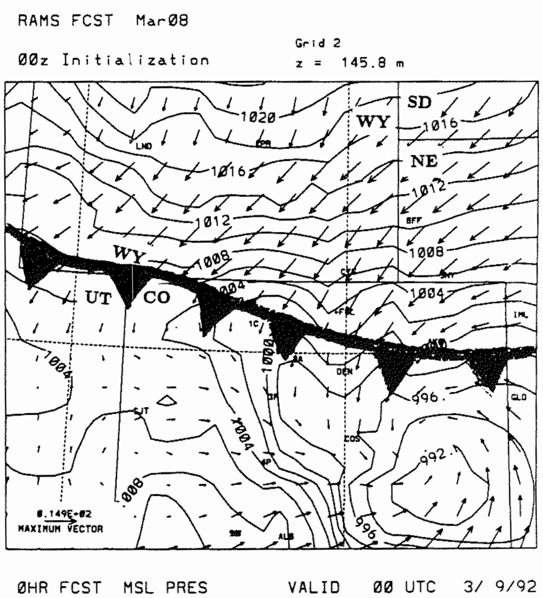

Figure 2. Observed mean sea level reduced pressure valid 0000 UTC 9 March 1992. Other features are the same as in Figure 1.

stronger low-level wind speeds and smoothed terrain. Also notice that the observed central pressure in the low center is 2mb lower than modeled but the model low position corresponds extremely well with observations. The only other major discrepancy between model and observations was in the moisture field upon departure of the storm. The model tended to have too deep a moist layer which remained in place for too long. Further simulations with complete microphysics are currently underway for this and other cases to determine whether this problem stems from the simple "dump bucket" precipitation scheme.

As for precipitation, the model predicted the overall pattern well with the maximum amount predicted and observed to be south and west of Fort Collins. RAMS predicted 2.8cm of liquid water through 1200 UTC 9 March for Fort Collins and the actual reported liquid water equivalent was 3.0cm. Although this prediction was good, other single station observations were as much as 100% in error. This is not hard to imagine considering the crude precipitation scheme and also the embedded convection which this RAMS configuration could not model. Again, further studies are currently underway to improve the predicted precipitation by including explicit microphysics.

4. CASE FROM FIRE II EXPERIMENT

On 26 November 1991, investigators involved in the FIRE II field experiment centered in Coffeyville, KS were delighted to see a broad area of cirrus clouds approaching from the west. The synoptic conditions at 1500 UTC for this day were as follows: a weak surface low extended through the Dakotas with a weak cold front trailing back to the southern portions of Wyoming; a well-defined warm front extended south-east from the low center into north-east Kansas and south-central Missouri; a weak pressure trough existed between the two fronts oriented north-south through west-central Kansas and into the Texas panhandle. This trough was reflected throughout the entire depth of the troposphere as the 200mb chart showed a weak trough in between two equally weak ridges. Also indicated by the 200 and 300mb charts was a NW-SE oriented jet streak entering western Kansas. Some of these features are reflected in the satellite picture valid at 1443 UTC shown in Figure 3. The trough discussed above existed along the western edge of the N-S band of clouds on the right side of the figure.

The real-time RAMS forecast for this event was nothing short of stunning in terms of placement of the upper level clouds. RAMS-predicted non-zero pristine ice and snow mixing ratios (the two active microphysical species) corresponded extremely well with areas of clouds as seen in Figure 3. This agreement can be seen by comparing the satellite photo to the RAMS 15 hr forecast of pristine ice mixing ratio shown in Figure 4. Absolute magnitudes of the mixing ratios show the major weakness of this forecast as they are at least an order of magnitude too low. A possible explanation to this is that the model is initialized with a moisture content that is too low at these upper levels. This may be caused by inaccurate or non-existent moisture measurements by rawinsondes at these altitudes.

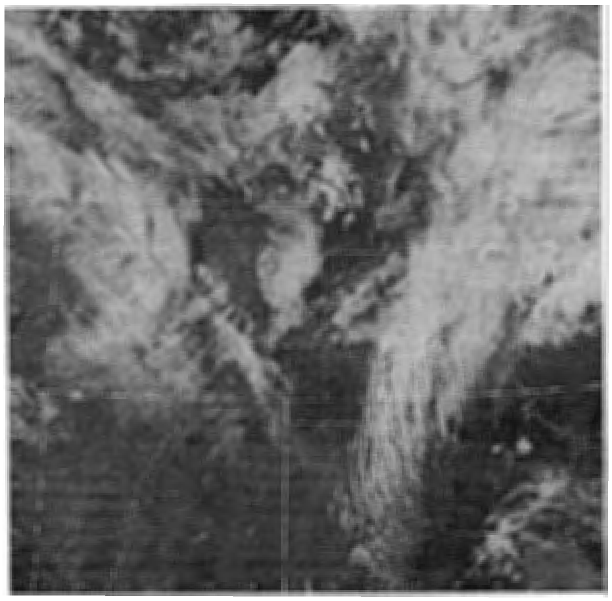

Figure 3. Infra-red NOAA 12 satellite image valid 1443 UTC 26 November 1991. Of particular importance here is the cirrus extending from central Kansas into the Texas panhandle.

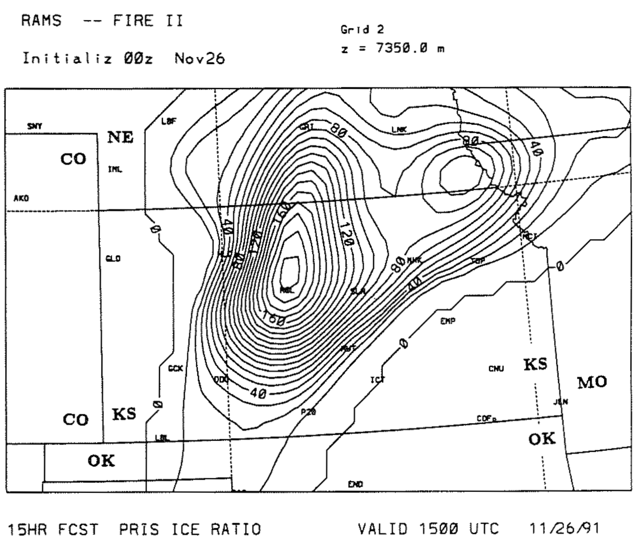

Figure 4. RAMS 15 hour predicted pristine ice mixing ratio at z = 7.35km valid 1500 UTC 26 November 1991. Surface reporting stations are denoted by their three letter identifiers and dashed lines are latitude and longitude lines of interval 5 degrees. Contour interval is 1×10^{-4} gg^{-1}. Notice the similarities between locations and shape of non-zero mixing ratios with respect to Figure 3.

Further compounding this problem is that cirrus dynamics involve weak vertical velocities necessitating long time periods to increase model moisture/condensate to realistic values.

Because of the apparent success of the 24 hr simulation, we decided to repeat the simulation initializing the model 24 hrs earlier and forecasting out to 48 hrs. The result of this forecast was also extremely pleasing in the placement of the upper level clouds. Figure 5 was taken from the 48 hr simulation initialized at 0000 UTC 25 November. It shows the 39 hr RAMS forecast of the same field valid at the same time as Figure 4. Again, we see a strong resemblance to the clouds shown in Figure 3. Once again the magnitudes are an order of magnitude too low. More simulations are planned for this and other cases during the FIRE II field experiment as much should be learned from the analysis of the intensive observations and applied to the modeling studies.

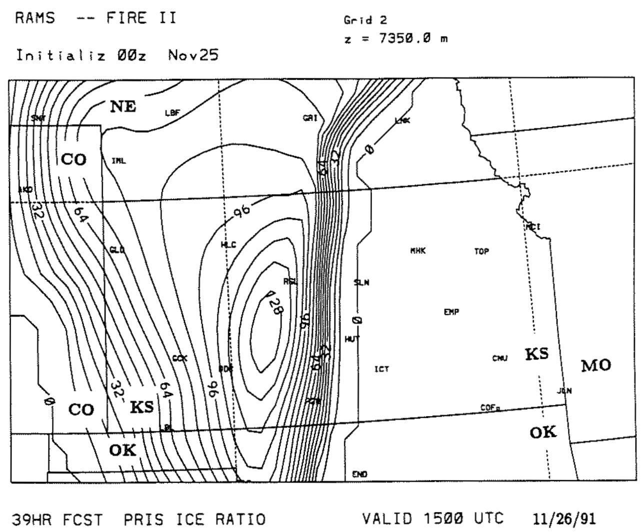

Figure 5. Same as in Figure 4 except for RAMS 39 hour forecast. Contour interval is 8×10^{-6} gg^{-1}.

5. CONCLUSIONS

Initial indications from these two case studies merit optimism in RAMS' ability to forecast mesoscale and synoptic weather in real-time. Many additional simulations are planned for these cases including using the ETA model output as the time-dependent lateral boundary forecast fields in place of the NGM for the 8-9 March case. Furthermore, a statistical analysis of the entire winter forecast period is currently underway using Multivariate Randomized Block Permutation (MRBP) methods as described by Mielke (1991). With the parallelization of the RAMS code in progress, future operational forecasting can include smaller grid spacing and more sophisticated microphysics.

ACKNOWLEDGEMENTS

Thanks are extended to Dr. Craig Tremback for helping modify the RAMS code to enable the ingest of the MAPS and NGM datasets. Paul Schultz of Forecast Systems Laboratory in Boulder was instrumental in providing the MAPS datasets and NGM model output for the duration of the study. Tom Parker provided help in setting up the real-time priority queue for running on the YMP at NCAR. Cray Research provided the grant (#35081185) to use the CRAY-YMP for the FIRE experiment computations. NCAR is supported by the National Science Foundation. The CSU Stardent RISC workstation was purchased under support of the Dept. of Energy, DOE contract #DE-FG02-90ER61066. RAMS was developed under support of NSF and ARO. This research was made possible by the Colorado Agricultural Experiment Station's grant #COL00692 and by the Air Force Office of Scientific Research's grant #AFOSR-91-0269.

REFERENCES

Mielke, P. W. 1991: The application of multivariate permutation methods based on distance functions in the earth sciences. *Earth-Science Reviews*, **31**, 55-71.

IMPLICATIONS OF TROPICAL HIGH CLOUD BEHAVIOR FOR THE GREENHOUSE PROBLEM

Gyula Molnar[1]

Atmospheric and Environmental Research, Inc.
Cambridge, MA 02139, USA

1. INTRODUCTION

One of the greatest uncertainties about future climate changes is associated with the behavior of clouds in response to climate perturbations (e. g., WMO 1987; Cess et al., 1990; Arking, 1991). Cloud/climate interactions could be especially pronounced in low-latitude regions where solar insolation and sea-surface temperature (SST) are high all year long. Consequently, model studies of the surface warming due to the projected increase of atmospheric greenhouse gases should consider possible changes in tropical cloud properties accompanying the greenhouse warming. Another reason for focusing on the tropics is that general circulation models (GCMs) exhibit a very large uncertainty (almost a factor of two) in their predicted tropical greenhouse warming. Recently, Fu et al. (1990, referred to as F90 in the following) used ISCCP analyses to study the relationship between tropical SST variations and changes in properties of deep convective cloudiness (DCC), allowing for some quantification of tropical, oceanic DCC/SST feedbacks. Furthermore, ERBE measurements (Raval and Ramanathan, 1989; Ramanathan and Collins, 1991, referred to as RC91 in the rest of the text) indicate the possible presence of an apparent "runaway greenhouse" on the one hand and a "cirrus limiting factor" on the other.

Before going further, a brief description of definitions warranted. The total greenhouse effect of the atmosphere and clouds, G, is defined as $G = E - F$, where E is the flux emitted by the ocean surface and F is the infrared radiation emitted to space. The atmospheric portion of the greenhouse effect is $G_a = E - F_c$, where F_c is F over clear-sky regions. The difference between G and G_a gives the enhancement of the greenhouse effect caused by clouds, referred to as the cloud long-wave forcing, C_l. The cloud short-wave forcing, C_s, is calculated as $C_s = S(1-\alpha) - S_c$, where S is the solar constant, α is the planetary albedo for the given region, and S_c is the clear-sky solar absorption. The "runaway greenhouse" may be inferred, for instance, from Fig. 2a of RC91, indicating that over the tropical ocean (SST>299-300K), the increase of G with increasing SST becomes very large, about 20-30Wm^{-2}K^{-1}, compared to regions with lower SST (denoted by T_g) values. The "cirrus limiting factor" is RC91's assertion that this "runaway greenhouse" will be limited by formation of highly reflective cirrus clouds, shielding large amounts of solar radiation, limiting SST to temperatures no greater than around 305K.

The "cirrus limiting factor" is found based on comparing periods of colder and warmer tropical Pacific SSTs, whilst the "runaway greenhouse" can be seen from seasonal and spatial variations of the current climate. Consequently, both are related to changes in *insolation*, a forcing different in nature from the greenhouse forcing of CO_2. In addition, since the satellite data cover only a few years at most, the change in anthropogenic greenhouse forcing could not have played a significant role in the results obtained by F90 and RC91. The question arises, therefore, what the implications of these results might be *in the context of the greenhouse problem*. The notion of a possible "runaway greenhouse" for high SSTs is especially disconcerting, since during a greenhouse warming ever larger and larger oceanic areas may reach the threshold of steep G slope. The fact that by the time the "cirrus limiting factor" may halt further warming, the tropical SST could have risen 5-6K above its current value, which implies a global surface temperature increase of about 7-9K because of the high-latitude amplification of the greenhouse signal (cf., IPCC, 1990). Such a global mean surface temperature increase is certainly enough to cause ecological disaster. For the moment, this problem can be addressed only through model simulations. Extending the scope of our earlier related work (Molnar and Wang, 1990) here we use a modeling approach to study the first order, large-scale global change implications of these results.

2. THE CLIMATE MODEL

The 2-dimensional (2-D) seasonal climate model used in this study is an extension of the 2-D annual model of Wang et al. (1984) and includes three latitudinal zones representing the tropical zone (30°S-30°N), southern hemispheric extratropical zone (30°S-90°S), and northern hemispheric extratropical zone (30°N-90°N). Because of the large difference in thermal inertia between ocean and land surfaces, both land and ocean sectors are included within each latitude zone. The model computes the evolution and spatial distribution of atmospheric (18 vertical layers) and ground temperatures from the heat balance for the atmosphere and the subsurface (ocean/land). Due to an improvement over earlier studies, a separate determination of surface air and ground temperatures is possible, through the introduction of a drag law parameterization which determines the surface sensible and latent heat fluxes. In our "standard" CO_2 doubling experiment cloud altitudes are fixed and fractional cloud cover as well as relative humidity and ozone distributions are prescribed according to their observed seasonal cycle. Non-overlapping cloudiness is assumed throughout our calculations. Physically-based meridional (Stone and Yao, 1990) and zonal (Wang et al., 1990) heat flux parameterizations are used, while the vertical dynamical heat flux is parameterized through adjustment (moist adiabatic and baroclinic) processes. The seasonal model uses the same sophisticated radiative parameterizations as the 2-D annual model, i. e., the important atmospheric gases, clouds, and surface characteristics are included. Ice-albedo feedback is parameterized following Robock (1981), and the seasonally varying hemispheric ice and snow extents are in good agreement with observations.

Because data about ocean heat transport and its potential changes are lacking, we use a simple approach: the sum of ocean heat transport and storage for the present seasonal cycle is calculated from the model's surface energy balance with the observed SST cycle prescribed. During a climate change experiment this sum is assumed to remain the same as that of the current climate. Although the model can be run with an interactive ocean that includes a mixed layer and deep ocean, because here we are interested in the relative equilibrium responses, a simple representation of the ocean suffices. This approach has been used in general circulation models (see Chapter 4 of DOE, 1985). The model-calculated seasonal variation of the atmospheric temperature structure, like heat fluxes and planetary and surface albedos, is in good agreement with available observations.

For a more detailed description of the model see Wang et al. (1990)

3. EXPERIMENTS

We address the problem of whether the steep slope of G over large areas of the tropical oceans implies the possibility of a "runaway greenhouse" in the case of CO_2-doubling. Our strategy is the following: Perform a series of CO_2-doubling experiments with tropical DCC, and especially cirrus changes, and analyze the key greenhouse indicators over the tropical ocean. Find the case(s) which reproduces the satellite-derived greenhouse indicators the best, and compare the magnitude of the corresponding tropical SST change(s) to the "standard" (no tropical oceanic cloud/SST feedbacks) CO_2-doubling response. Finally, rerun the experiments with 2% solar constant increases to assess the extent to which changes in the insolation-derived greenhouse indicators of RC91 serve as a proxy for the prediction of the tropical CO_2-doubling signal.

The feedback strengths (in %s) for a given area and time period can be defined as:

$$S = \{ \Delta T_f)/ \Delta T \ -1\}*100,$$

where ΔT_f and ΔT correspond to the surface warming due to CO_2-doubling with and without the individual cloud feedbacks. The feedbacks were implemented into the oceanic box of the models' tropical zone, one by one. We have considered the following three possible cloud/climate interactions:

i) The first interaction studied was the observed positive correlation between DCC fractional cover and SST (F90). The study results suggest that a 3^oC SST rise is associated with an approximately 0.1 increase of the DCC fractional cover. We refer to this relationship as the DCC feedback. Increase of the optically thick DCC fraction has an effect on the planetary albedo, thus we expect a negative feedback. Note that to separate this effect more precisely, we have introduced a separate DCC layer (with visible optical depth of 10) into the model's tropical oceanic control climates (5% fractional cover), and only this is allowed to change during the DCC experiment. Previously (Molnar and Wang, 1990), DCC-changes were represented by equal fractional cover changes in the model's original 3-layer (low-, middle-, high level) cloudiness.

ii) The second interaction considers the possibility that anvil cirrus associated with DCC development may increase in extent, extending thousands of kilometers downwind (RC91). Because RC91 did not provide quantitative results in this regard, we have simply assumed that fractional cirrus cover changes proportionally to the DCC cover changes of F90. The cirrus optical thickness is also parameterized interactively, according to the empirical relationships obtained by Platt and Harshwardhan (1988, referred to as PH88).

iii) Finally, we have addressed the suggestion (RC91; Heymsfield and Miloshevich, 1991) that in addition to its extent, the reflectivity of anvil cirrus will also increase when SST increases. In the original model the cirrus ice particles are assumed to have large (around 25 μm) mean radius. Accordingly, the ratio of their shortwave scattering efficiency and longwave absorption efficiency, β, is prescribed at the value 2. However, as the SST increases, the colder cirrus produced may contain smaller ice particles with much larger β values (Heymsfield and Miloshevich, 1991). We tested this assumption by increasing β to 4, corresponding to a mean particle radius of about 6 μm. (i. e., we use the cirrus treatment as in ii) but change β from 2 to 4).

4. RESULTS AND DISCUSSION

A comparative summary of the model runs performed is shown in Table 1. Note that we have two "control" climates because the "standard" CO_2-doubling case has no cloud feedbacks at all.

Table 1. Summary of cases considered.

Case#: 1: Control climate with separate DCC included

Case#: 2: Same as #1, but cirrus optical depth is parameterized according to PH88

Case#: 3: 2 x CO_2; no cloud feedbacks; #1 as control

Case#: 4: Same as #3, but for 2% solar constant increase

Case#: 5: 2 x CO_2; F90 feedback for DCC cover only; #1 as control

Case#: 6: 2 x CO_2; PH88 cirrus optical depth and F90 cirrus cover; $\beta = 4$; #2 as control

Case#: 7: Same as #6, but for 2% solar constant increase

Case#: 8: Same as #6, but $\beta = 2$

Case#: 9: Same as #8, but for 2% solar constant increase

Table 2 summarizes our most important result: the model-generated tropical oceanic $\Delta G_a/\Delta T_g$ and $\Delta G/\Delta T_g$ values can be compared directly to the observed ones, which are 6.5 $Wm^{-2}K^{-1}$ and about 25 $Wm^{-2}K^{-1}$, respectively, for roughly the same area as in our model (cf. Figs 2a, 2b of RC91). Interestingly, the clear-sky greenhouse slope is close to the observed one for CO_2-doubling in the 'standard' and both in the DCC as well as in the cirrus property change cases (although not so close for the β=2 case). On the one hand, this indicates that the model assumptions about SST-increase induced water vapor changes (fixed relative humidity and moist adiabatic lapse rate) are basically correct. On the other hand, the low $\Delta G_a/\Delta T_g$ values for all cases of solar constant increases may indicate that the observed value was more related to water vapor greenhouse than to insolation changes.

Table 2. The slopes of atmospheric and overall greenhouse effect for the tropical ocean together with the SST(T_g) changes.

	$\Delta G_a/\Delta T_g$	$\Delta G/\Delta T_g$	ΔT_g
Case#: 3	6.226	4.402	1.044
Case#: 4	1.900	0.763	1.280
Case#: 5	5.836	9.685	1.049
Case#: 6	7.660	27.641	0.612
Case#: 7	0.385	20.423	0.842
Case#: 8	3.727	17.900	1.611
Case#: 9	1.146	0.000	0.907

When comparing the overall greenhouse slope, we find that only cases of β=4 are fully consistent with the observations of the 'runaway greenhouse', *both* for CO_2 and insolation increases, strongly suggesting that:

1) Cirrus may indeed become more reflective with increased SST, and

2) Results based on the considerations of RC91 may be assumed to also hold in the context of greenhouse trace gas concentration increases.

Note, however, that the β<4 case cannot be ruled out completely, at least in the CO_2-doubling case.

The annual mean feedback strengths are presented in Table 3, showing that variations in DCC cover imply a small positive feedback, whilst cirrus changes (except Case 7) imply large S values, especially for the tropical zone.

Table 3. Annual mean Feedback Strengths (%) for the northern extratropical (NE), tropical (TR), and southern extratropical (SE) model zones and for the global mean.

	NE	TR	SE	GLOBAL
Case#: 3	0.00	0.00	0.00	0.00
Case#: 4	-0.81	21.89	0.69	7.99
Case#: 5	9.47	6.67	1.73	5.85
Case#: 6	-4.19	-29.32	-1.50	-12.47
Case#: 7	1.96	-5.13	0.65	-1.07
Case#: 8	29.67	64.70	13.59	37.08
Case#: 9	36.38	98.22	18.13	52.86

The suggestion of RC91 and Heymsfield and Miloshevich (1991) seems to be confirmed, since large cirrus particles lead to strong positive S, while β=4 corresponds to an appreciable negative feedback strength. Figure 1 shows the seasonal dependence of the S for the model tropical zone for all perturbed cases.

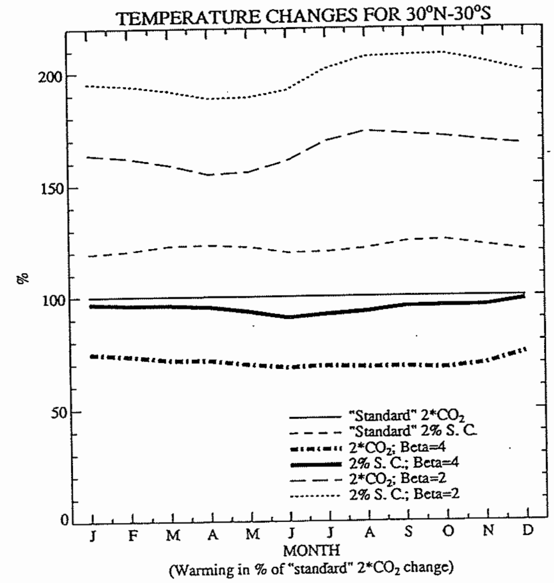

Figure 1: Comparison of the effects of the tropical cloudiness-SST feedbacks, applied individually, relative to the "standard" CO_2-doubling induced surface warming, for the tropical region.

Figures 2 and 3 show these values for the 30-90°N and 30-90°S zones, respectively. Here, the seasonal S variations are pronounced, and even feedbacks that were negative in the tropics can be positive during extratropical winters. The influence of the investigated tropical oceanic feedbacks on the extratropics also shows that their effects on the extratropical regions are lessened, at least on an annual basis.

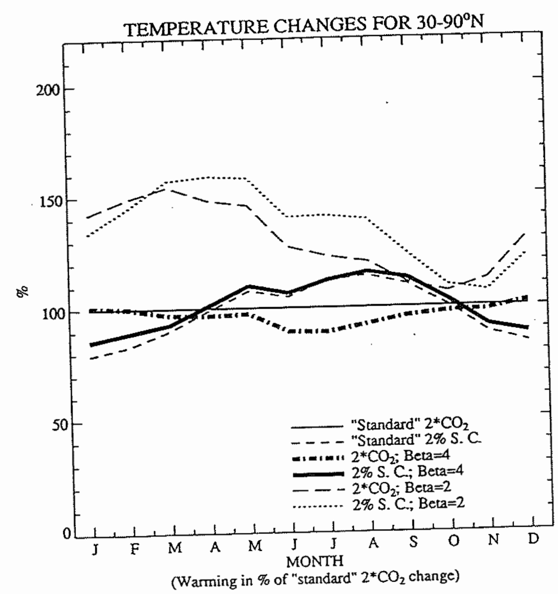

Figure 2: Same as Fig. 1 but for the Northern extratropical zone.

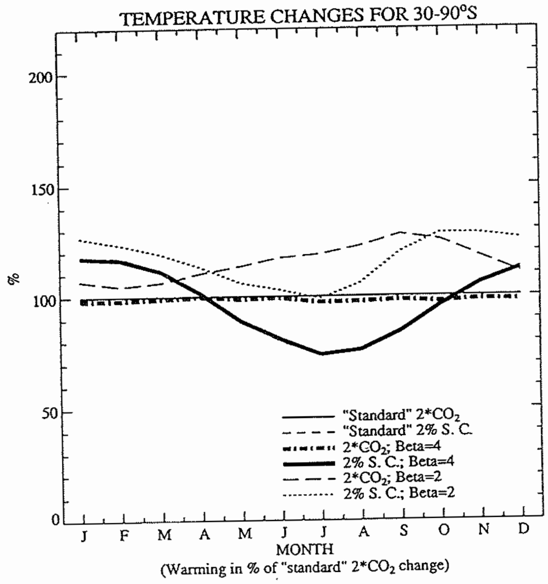

Figure 3: Same as Fig. 1 but for the Southern extratropical zone.

This phenomenon is connected to the efficiency of the meridional heat transport (MHT); as noted earlier, here the physical MHT parameterization of Stone and Yao (1990) was used, which tends to suppress the extratropical response compared to the empirical MHT parameterization of Wang et al. (1984).

In summary, our results indicate:

i) The potential cloud-feedbacks inferred from recent satellite analyses could alter the predicted greenhouse warming significantly, even on a global scale.

ii) Increase of cirrus fractional cover with increased deep convection could induce either a strong positive *or* a strong negative feedback, depending on cirrus microphysical properties. Interestingly, *both* possibilities are more (β=4) or less (β=2) consistent with the observed 'runaway greenhouse', indicating that without further observational studies the effect of the 'cirrus limiting factor' on the predicted greenhouse warming cannot be properly assessed. Nevertheless, these preliminary results imply that greenhouse-effect induced cirrus changes are more likely to lead to a negative feedback, which would even be stronger than have been inferred from the insolation-change related RC91 observations. The opposite is true if the cirrus particles remain large; the implied positive feedback is less for CO_2-increases than for solar constant increases.

iii) These results emphasize the importance of equatorial measurement programs such as TOGA/COARE, and the importance of more accurate in situ and satellite cloud measurements, which, among other things, will provide more accurate climatologies of DCC and cirrus properties.

Acknowledgement.

This research was supported by the the Carbon Dioxide Research Division of the Department of Energy (DE-FG02-86ER60485).

REFERENCES

Arking, A., 1991: The Radiative Effects of Clouds and their Impact on Climate. *Bull. Am. Met. Soc., 71,* 795-813.

Cess, R. D., et al., 1990: Intercomparison and interpretation of climate feedback processes in 19 atmospheric general circulation models. *J. Geophys. Res., 95,* 16601-16615.

Department of Energy, 1985: Projecting the Climatic Effects of Increasing Carbon Dioxide, *DOE Report/ER-0237.*

Fu, R., Del Genio, A. D., and W. B. Rossow, 1990: Deep convective clouds in the tropical Pacific observed from ISCCP radiances. *J. Clim. 3.,* 1129-1152.

Heymsfield, A. J., and L. M. Miloshevich, 1991: Limit to Greenhouse Warming? *Nature 351,* 14-15.

Intergovernmental Panel on Climate Change (Houghton et al. eds.), 1990: Climate Change: The IPCC Scientific Assessment. *WMO, UNEP, Cambridge University Press,* Cambridge.

Molnar, G., and W.-C. Wang, 1990: Interactions between low-latitude marine clouds and sea-surface temperature and their climatic implications. In *Preprints, 1990 Conference on Cloud Physics,* July 23-27, San Francisco, CA, *AMS, Boston,* J61-J63.

Platt, C. M. R., and Harshvardhan, 1988: Temperature Dependence of Cirrus Extinction: Implications for Climate Feedback, *J. of Geophys. Res., 93,* 11051-11058.

Ramanathan, V., and W. Collins, 1991: Thermodynamic regulation of ocean warming by cirrus clouds deduced from observations of the 1987 El Nino. *Nature, 352,* 27-32.

Raval, A., and V. Ramanathan, 1989: Observational determination of the greenhouse effect. *Nature 342,* 758-761.

Robock, A., 1980: The Seasonal Cycle of Snow Cover, Sea Ice and Surface Albedo. *Mon,. Wea. Rev., 108,* 267-285.

Stone, P. H., and M.-S. Yao, 1990: Development of a two-dimensional zonally averaged statistical-dynamical model. Part III: The parameterization of eddy fluxes of heat and moisture. *J. Clim. 3,* 726-740.

Wang, W.-C., G. Molnar, T. Mitchell, and P. H. Stone, 1984: Effects of Dynamical Heat Fluxes on Model Climate Sensitivity. *J. Geophys. Res., 89,* 4699-4711.

Wang, W.-C., G. Molnar, Ko, M. K. W., S. Goldenberg, and N. D. Sze, 1990: Atmospheric trace gases and global climate: a two-dimensional model study, *Tellus, 426,* 149-161.

WMO, 1987: *Clouds in Climate II.* A WCRP workshop on modeling and observations, Columbia, Maryland, Oct. 19-23, 1987.

INCLUSION OF CLOUD MICROPHYSICAL PROCESSES IN THE CSU GENERAL CIRCULATION MODEL

L.D. Smith and D.A. Randall

Department of Atmospheric Science
Colorado State University
Fort Collins, CO 80523. USA.

1. INTRODUCTION

One current challenge in the development of atmospheric general circulation models (GCMs) deals with the parameterization of the various components of the atmospheric hydrologic cycle and their interactions with the other components of the model physics. The driving variables of the atmospheric moisture budget are the cloud liquid (ice) water contents. Condensation (sublimation) from large–scale and convective processes is the chief source of cloud liquid (ice) water. Cloud water may be removed from the atmosphere in the form of precipitation or may evaporate. Cloud water interacts with convection by turbulent mixing and, vice versa, convective systems may act as sources of liquid (ice) water by detrainment at the top of convective columns. Aside from the specific process of formation/removal of cloud water, there also exist mutual interactions between the rates of condensation, evaporation, and precipitation, and the convective circulations. Once cloud water is predicted to form, it directly affects the distribution of cloudiness and its optical properties. It is obvious that the horizontal cloud fraction depends upon the cloud water content. Also, it is strongly dependent upon the intensity of convection. Finally, cloud water interacts with radiation by modifying the optical thickness and infrared emissivity of clouds.

Each of the interactions described above needs to be parameterized in a more realistic fashion in today General Circulation Models (GCMs). The coupling between cumulus convection and associated cirrus anvils is of major interest (Randall, 1989). In this article, we discuss the results of a short experiment made with the one–dimensional version of the Colorado State University General Circulation Model (CSU GCM) in which the detrainment of total water produced by cumulus convection is used as a source of cloud liquid and ice water to a bulk cloud microphysics package. Interactions between the cumulus convection and cloud microphysics schemes are emphasized. The temporal evolution of a few microphysical processes are discussed.

2. THE CLOUD MODEL

The model structure is completely described in Smith and Randall (1992). It is largely based upon the bulk cloud microphysics equations used in Lin *et al.* (1983), and Rutledge and Hobbs (1983). Five prognostic variables for the mass of water vapor, cloud ice, rain, and snow are taken into account. Cloud liquid and ice water amounts are predicted to form through large–scale condensation and sublimation processes plus detrainment at the top of convective cumulus towers. It is assumed that the terminal fall velocity of cloud liquid/ice particles may be neglected compared with the velocity of air, rain, and snow. Rain and snow are assumed to have non–negligeable fall velocities. Interactions between water vapor, cloud water, cloud ice, rain, and snow may be summarized as follows:

Water vapor as a source: Water vapor is a source of both cloud liquid and cloud ice water through instantaneous processes. Cloud liquid water is predicted to form by condensation of vapor when the temperature (T) is equal or greater than 0°C and the air is supersaturated with respect to water. Similarly, cloud ice is predicted to form by sublimation of vapor when T < 0°C and the air is supersaturated with respect to ice.

Cloud liquid as a source: Cloud liquid is a source of vapor by evaporation of cloud droplets when the air is sub–saturated with respect to water. It may be a source of cloud ice by instantaneous freezing if evaporation cooling yields T to become less than 0°C, and some cloud water is still available after saturation with respect to ice is reached. Cloud water is a source of rain through two different mechanisms: (1) autoconversion of cloud droplets to form rain drops; and (2) collection of cloud droplets by rain drops falling through the free atmosphere. Finally, cloud water may also be a source of snow by riming (T < 0°C) or rain (T ≥ 0°C) by collection of snow falling through warm layers.

Cloud ice as a source: As for cloud liquid water, cloud ice water is a source of water vapor by evaporation of cloud ice crystals when when the air is sub–saturated with respect to ice. Otherwise, cloud ice is a source of snow through two different mechanisms: (1) conversion of ice crystals to form snow; and (2) collection of ice crystals by snow falling through the free atmosphere. Instantaneous melting of cloud ice to form cloud water occurs if T is equal or greater than 0°C.

Rain as a source: Rain may only be a source of water vapor by evaporation of rain drops while falling through subsaturated layers.

Snow as a source: As for rain, snow may be a source of water vapor by evaporation while falling through sub–saturated layers for which T < 0°C. Also, snow may be a source of rain by melting if it falls through layers for which T ≥ 0°.

3. RESULTS

3.1 Model experiment

The one–dimensional version of the 17–level CSU GCM is used to test the various cloud microphysics processes and their interactions with the cumulus convection scheme. The GCM employs a "modified–σ" vertical coordinate system so that the planetary boundary layer depth is the thickness of the lowest model layer. The core of the model physics, in terms of the long and short wave parameterizations, and prediction scheme of the cloud fraction and cloud optical properties, is that of the UCLA/GLA GCM discussed in Harshvardhan *et al.* (1989) and Randall *et al.* (1989). Two major modifications to the routinely used version of the model code are: (1) the inclusion of a new cumulus convection parameterization based upon the theory of Arakawa and Schubert (1974), but allowing for a more consistent coupling between cumulus convection and associated stratiform anvils through the detrainment of cloud liquid and ice water (Randall and Pan, 1992); and (2) the replacement of the large-scale condensation scheme with the cloud microphysics package described above. It is important to note that, in the present model version, there exists no coupling between the cloud liquid (ice) water computed by the cloud model and the prediction scheme of the cloud fraction and optical properties.

The initial vertical profile of temperature and water vapor was obtained from a GATE sounding. In testing the cloud microphysics package and its interaction with the cumulus convection scheme, we use of a model time–step of 60s so that the collection rates of cloud droplets and ice crystals by rain and snow, and the falling rates of rain and snow, may be computed using an explicit scheme. An implicit scheme, allowing the use of longer of time–steps, more suitable for GCM experiments, is in development. The GCM experiment is 15–day long.

3.2 Impact of cumulus parameterization

The cumulus convection parameterization yields a detrainment of the total water (water vapor plus liquid plus ice water) to the environment along the sides and at the top of the convectively active layers. It provides a source of cloud liquid and ice water (depending upon the layer temperature) to the microphysics parameterization which is called next. Figure 1 shows the temporal behavior of the detrainment rate of the total water, water vapor, and cloud ice produced by the newly implemented scheme. The diurnal cycle of the convection activity is obvious and shows a maximum at noon. The comparison between Figs. 1.a, 1.b, and 1.c clearly indicates that the entrainment rate of water vapor is maximum at the base of the convective tower above the planetary boundary layer and rapidly decreases upward. The maximum detrainment rate is in the form of cloud ice and occurs at 150 mb at the top of the convectively active column. Some detrainment of water vapor also takes place between 800 mb and 700 mb. The detrainment rate of cloud liquid water (not shown) remains extremely small across the whole atmospheric column. When non–zero, it actually occurs at temperatures below the freezing level and, therefore, may never be a source of cloud water to the cloud microphysics parameterization. The time series of the total detrainment rate also shows an intensification of the cumulus convection at the end of the 15–day run. The corresponding cumulus heating rate is shown in Fig. 2. The cumulus convection yields a warming of the atmosphere below 200 mb and a cooling aloft.

3.3 Impact of cloud microphysics parameterization

The initial atmospheric conditions were such that the model layers which temperatures were above the freezing level never reached super–saturation conditions with respect to water during the 15–day run. Then cloud liquid water and rain were never predicted to form using the cloud microphysics package. The ice phase dominated. Figure 3 presents time series of the net rates of change of the cloud ice (dqci) and snow (dqri) mixing ratios due to the microphysics only. The increase in dqci seen between 600 and 300 mb results because of the instantaneous freezing of the cloud liquid water formed by cumulus detrainment at temperatures less than the freezing level (at present, the liquid and ice phases may coexist in the cumulus convection scheme but may not coexist in the cloud microphysics scheme). Also we observed that most of the frozen cloud water evaporated because the model layers re-

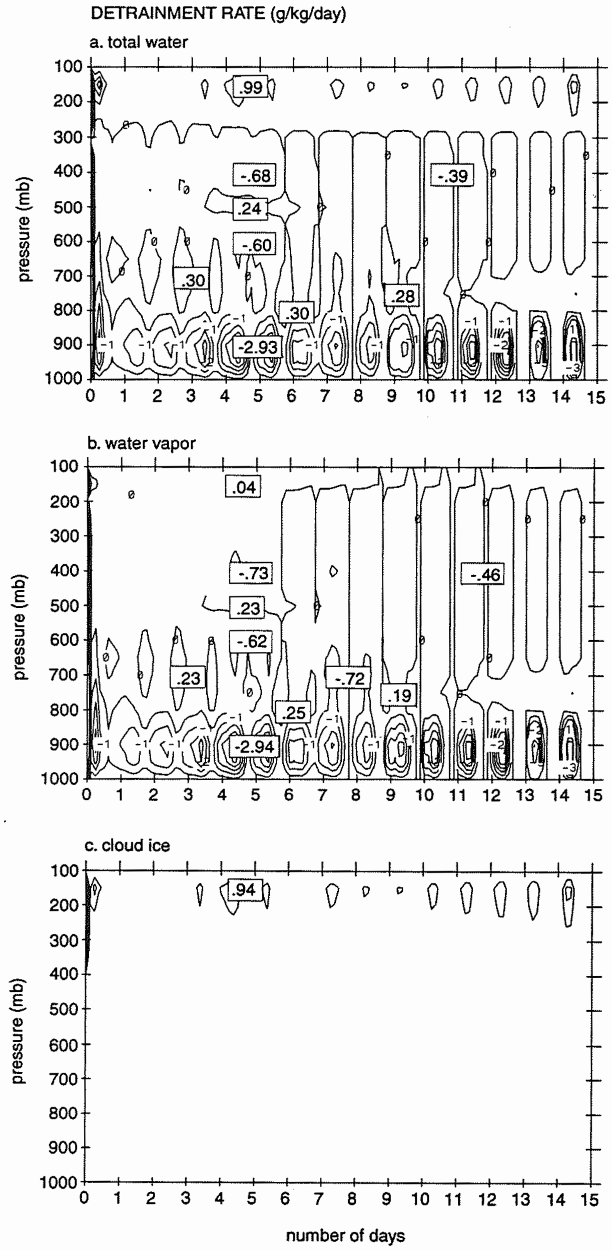

Figure 1: Time series of the detrainment rate of (a) the total water, (b) the water vapor, and (c) the cloud ice amounts from the cumulus parameterization, contour interval every .5 $g\,kg^{-1}\,day^{-1}$.

mained sub–saturated during the whole 15–day run. At 200 mb, dqci remains mostly positive, indicating the dominating process of sublimation of water vapor to ice, except after the fourth day when dqci turns negative for about half a day. It may be shown that the sign change results because of the autoconversion process of cloud ice to snow by collision of cloud ice crystals. It also coincides with a strong detrainment of cloud ice, as shown in Fig. 1. dqri is the largest between 300 and 200 mb. It remains less than zero during the first half of the run because of the dominating evaporation process while snow is falling through the atmosphere. It turns positive at the same time as dqci, i.e. when the air becomes saturated with respect to ice and cloud ice starts to grow at the expense of the water vapor. To illustrate the temporal evolution of one microphysical process, Fig.4 shows time series of the falling rate of snow through sub–saturated layers and its subsequent evaporation rate. In this experiment, we used an explicit scheme to transport snow from the top layer to the surface. The depletion of snow in the layer located at 200 mb where snow is predicted to form by autoconversion of cloud ice crystals and the accompanying growth in the snow mixing ratio in the layers below are well seen. Also it may be shown that, at 200 mb, the minima in the falling rate of snow may be superimposed with the maxima in the autoconversion rate of cloud ice crystals to snow. All the snow is predicted to evaporate before falling through layers which temperature is above the freezing level. No rain is predicted to form through the melting process of snow.

4. SUMMARY

In this article, we present the first results produced by a cloud microphysics parameterization newly implemented in the CSU GCM. Interactions between the cumulus convection and cloud microphysics schemes are discussed. The model satisfactorily reproduces the chief microphysical processes between cloud ice and snow. The coupling between the cumulus detrainment and microphysics processes show promising results in term of the simulation of the life cycles of stratiform anvils and cirrus clouds at the top of deep convective systems. We are presently adapting the present model so that it may be used with longer time–steps for long–term experiments with the CSU GCM. In the near future, we plan to couple the cloud liquid and ice water contents prognosed by the cloud microphysics package with the cloud fraction and cloud optical properties.

ACKNOWLEDGMENTS:

This research was sponsored by the National Science Foundation under the grant ATM–8907414 and the Department of Energy under the grant DEF 02-91ER61218.

REFERENCES

Arakawa, A., and W.H. Schubert, 1974: The interactions of a cumulus cloud ensemble with the large–scale environment. Part I: *J. Atmos. Sci.,* **31,** 674–701.

Harshvardhan, D.A. Randall, T.G. Corsetti, and D.A. Dazlich, 1989: Earth radiation budget and cloudiness simulations with a general circulation model. *J. Atmos. Sci.,* **46,** 1922–1942.

Lin, Y.-L, R.D. Farley, and H.D. Orville, 1983: Bulk parameterization of the snow field in a cloud model. *J. Climate Appl. Meteor.,* **22,** 1065–1092.

Randall, D.A., 1989: Cloud parameterization for climate models: Status and prospects. *Atmospheric Research,* **23,** 345–362.

Randall, D.A., Harshvardhan, D.A. Dazlich, and T.G. Corsetti, 1989: Interactions among radiation, convection, and large–scale dynamics in a general circulation model. *J. Atmos. Sci.,* **46,** 1943–1970.

Randall, D.A., and D.–M. Pan, 1992: Implementation of the Arakawa–Schubert cumulus parameterization with a prognostic closure. Prepared for *"Cumulus Parameterization"*, a Meteorological Monograph. To be published by the American Meteorological Society.

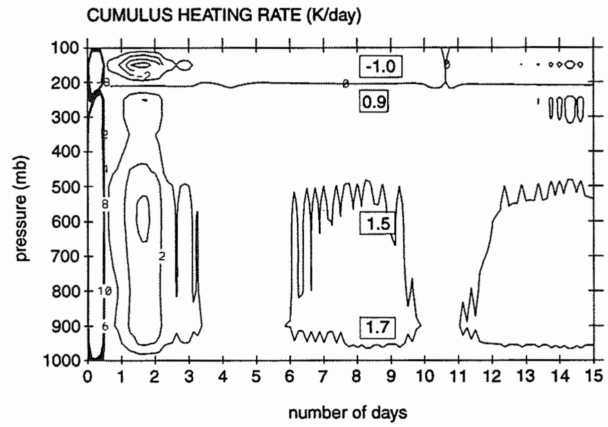

Figure 2: Time series of the heating rate from the cumulus parameterization, contour interval every 1. $\mathrm{K\,day^{-1}}$.

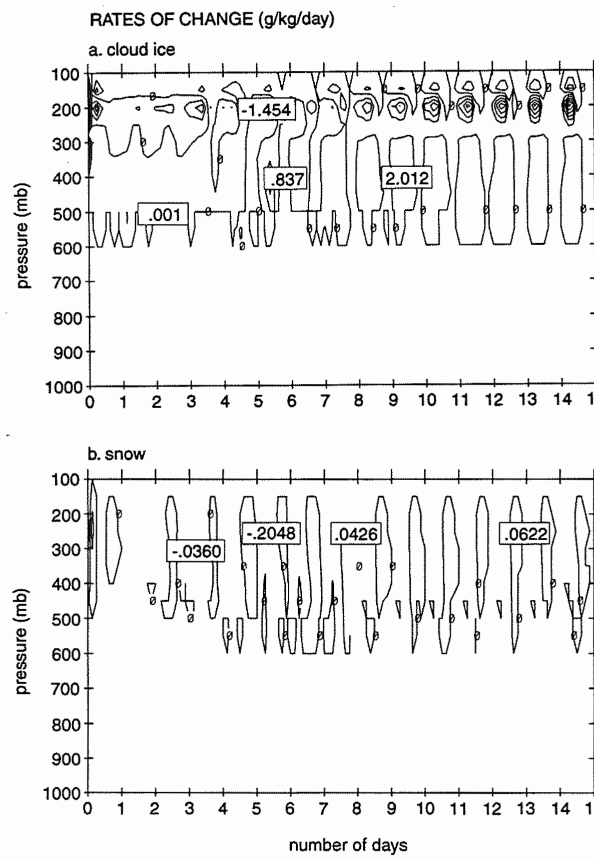

Figure 3: Time series of the rates of change of (a) the cloud ice, and (b) the snow amounts from the cloud microphysics parameterization, contour interval every .5 $\mathrm{g\,kg^{-1}\,day^{-1}}$.

Rutledge, S.A., and P.V. Hobbs, 1983: The mesoscale and microscale structure and organization of cloud bands and precipitation in midlatitude cyclones. VIII: A model for the "Seeder Feeder" process in warm–frontal bands. *J. Atmos. Sci.,* **40,** 1185–1206.

Smith and Randall, 1992: Parameterization of cloud microphysics processes in the CSU General Circulation Model. Atmos. Sci. Pap. 491, Colorado State University, 58pp.

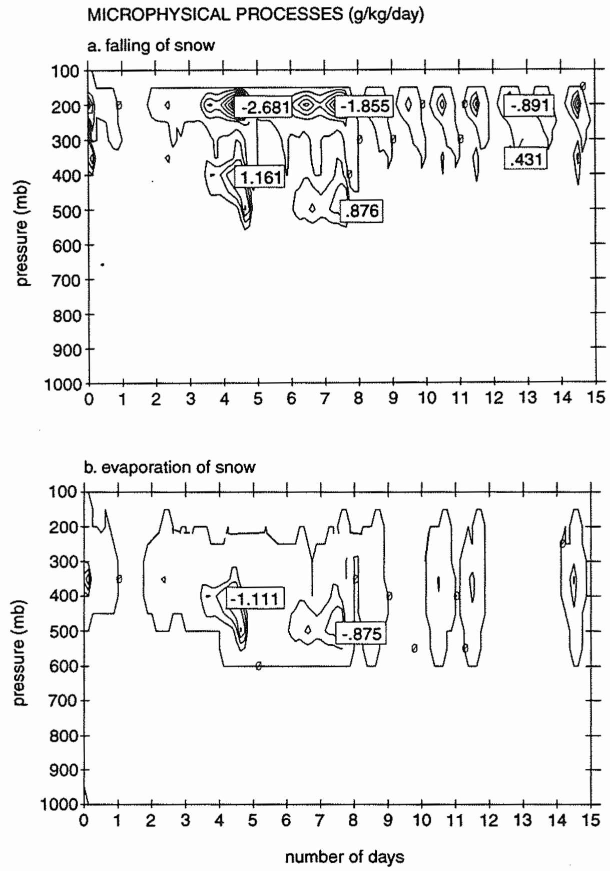

Figure 4: Time series of (a) the falling rate of snow and (b) the evaporation rate of snow from the cloud microphysics parameterization, contour interval every .5 $\mathrm{g\,kg^{-1}\,day^{-1}}$.

COMPUTER ASSISTED AIRCRAFT ICING FORECAST: EXPERIENCES DURING WINTER 1990/91

Werner Fuchs[1] und Klaus-Peter Schickel[2]

[1]German Military Geophysical Organization (GMGO), Geophysikalische Beratungsstelle 202

8542 Roth 2, Germany

[2]German Aerospace Research Establishment (DLR), Oberpfaffenhofen, Institute for Atmospheric Physics

D-8031 Wessling/Obb., Germany

1. INTRODUCTION

Aircraft icing forecast is only possible if meteorological as well as aircraft specific parameters are known. They are:

- Liquid water content = LWC in g/cbm
- Number n and diameter d of the cloud particles (or their median volume diameter MVD in mue m)
- Air temperature T
- Air pressure P
- True Air Speed (TAS) V
- Duration of stay in the icing zone t
- Dimension of the icing profile D
- Angle between flow and profile front edge
- Cargo situation (incidence angle)

In "Computer Assisted Aircraft Icing Forecast" by W. Fuchs (1989) the ice accretion rate is calculated using the method by E. P. Lozowski et al (1979). Unfortunately the parameters LWC and MVD still are not available or just unknwon. But to gain experiences about the quality of this forecast method the following minimum solution was worked out:

Earlier researches by W. Fuchs et al (1985) and H.-E. Hoffmann et al (1990 to 1991) have shown, that the meteorological parameters LWC and MVD in low stratus clouds only depend on the cloud´s temperature, height and vertical extent. So in "Progress in Aircraft Icing Forecast" by W. Fuchs (1990) a first forecast technique was proposed, with limitation on aircrafts penetrating low stratus clouds. In case of success further progress towards a model that will be useful for all aircrafts in any meteorological condition is expected. But to verify the quality of the forecast we need experiences of many flights in icing low stratus. These conditions can be found at the German Army Airfield LAUPHEIM (near ULM), where aircraft equipped for flights under instrument flight rules (IFR), are located. These are CH 53 - helicopters. In contrary to the icing of an aircraft´s wing the icing of the main rotor of a helicopter means to be a complication of the problem. On the other side it is advantageous that the penetration of icing low stratus has been practised at LAUPHEIM successfully for many years, proving that there is no intensified security risk. On 13 days during winter 1990/91 the calculated ice accretionn could be compared with observed icing. But due to technical reasons the observation was limited to subjective reports by pilots concerning routine flight missions. A first simple progress is expected from the use of a camera equipped with flashlight.

2. ICE ACCRETION CALCULATION

The model used by E. P. Lozowski et al (1979) calculates the ice accretion on a non rotating cylindrical rod. To realize the icing hazard of a helicopter the icing of its main rotorblades is important. We simulate the airfoil of CH 53 - helicopter rotorblades by cylindrical rods of 0.03 m in diameter. The endurance to stay in the low stratus cloud is determined by the climb- and descend-rate of the aircrafts. We calculate with 1000 Ft/min during ascent and consider for descend 500 Ft/min. The values for LWC and MVD are calculated by use of empirical formulas by W. Fuchs (1990). There is shown, how temperature, cloud height and vertical extend of the low stratus are considered. The application of these formulas on in situ observations from H.-E. Hoffmann (1990-1991) have shown good agreement. Finally we have to report that our ice accretion calculations (see for example the picture), done by DLR at OBERPFAFFENHOFEN, make use of the meteorological forecasts by our colleagues from GMGO, Geophysikalische Beratungsstelle 201 at LAUPHEIM.

3. RESULTS

During 13 days icing in low stratus has been observed over LAUPHEIM (see schedule). On 91-02-06 our method was not practicable because the stratus cloud exeeded our limits of vertical amount. To show the calculation of ice accretion we chose as example the results of 91-01-23 (see figure). Unfortunately there are no limits between LGT-(=light), MOD-(=moderate) or SEV-(=severe) ICING defined. The aircraft producers are not prepared to this topic. But it is important to solve this problem!

We decided that accretions up to 1 mm are to be defined for TRACES, up to 2 mm for LGT, up to 5 mm for MOD and above for SEV ICING. These values seem to be too small. But it should be first remembered that for helicopter main rotor blades the hazard of ice shedding must be considered, which may affect vibration and/or damage to the tail rotor system. Second the shape of the ice accretion is also very important:

On 91-01-23 a very dangerous ice accretion was calculated at the distance of 10 m to the rotormast, which would affect the airflow around the rotorblade dangerous.

We would get another important experience from the events at 90-11-28. Our model predicted LGT ICING for ascend up to 3100 Ft MSL (mean sea level). During the following horizontal flight between 3100 up to 3500 Ft MSL this flight level had to be left some 15 minutes later due to dangerous increasing icing. This means MOD ICING by definition.

What has happened? The forecaster expected the top of low stratus in 3000 Ft MSL, the real tops were in about 3800 Ft MSL. Because the result of another calculation up to this value predicted again only LGT ICING hazard three rules can be layed down:

- The quality of our aircraft icing forecast depends on the quality of the meteorological forecast.
- Horizontal flights in low stratus can affect MOD ICING even if there is only a LGT ICING hazard for penetrating flights.
- As long as there is no possibility to observe ice accretion at the rotorblades enroute our method cannot be extended to horizontal flights.

4. SUMMARY

The gained experiences can be summarized as follows:

The Computer Assisted Aircraft Icing Forecast, applied on CH 53 - helicopters penetrating icing low stratus clouds, proved to be good. The calculated ice accretion accorded well with the pilots´ observations. The decision to consider ice shapes up to 2 mm as LGT ICING hazard was confirmed. Whether the calculation of LWC and MVD by empirical formulas works better than the use of an extensive cloud climatology can be only discussed after their in situ registration. It became obvious that the calculation of LWC and MVD is more practicable than to use a cloud climatology. In similarity, the question how good calculated and real amounted ice accretion do agree can only be answered by use of extensive technical equipment.

5. REFERENCES

Fuchs, W., Kaluza, J., Schickel, K.-P., Uwira K., 1986: Calculation of Ice Accretion on Cylindrical Rods According to BAIN´s Model and Comparison with Experimental Results, ESA-TT-970 (DFVLR-FB-85-46).

Fuchs, W., 1988: Computer Assisted Aircraft Icing Forecast, Fourth International Conference on Atmospheric Icing of Structures, Paris.

Fuchs, W., 1990: Advances in Aircraft Icing Forecast, Fifth International Workshop on Atmospheric Icing of Structures, Tokyo.

Hoffmann, H.-D., Demmel, J., Horst, H., Löbel, H., 1990: Eine Dokumentation vereisungsrelevanter wolkenphysikalischer Parameter bei Vertikalsondierungen stratiformer Wolken, DLR-Mitt. 90-07.

Hoffmann, H.-E., Demmel, J., 1991: Eine Dokumentation vereisungsrelevanter wolkenphysikalischer Parameter bei Vertikalsondierungen stratiformer Wolken, DLR-Mitt. 91-19.

Hoffmann, H.-E., Demmel, J., 1991: Eine Dokumentation vereisungsrelevanter wolkenphysikalischer Parameter bei Horizontalsondierungen stratiformer Wolken, DLR-Mitt. 91-07.

Lozowski, E. P., Stellabrass, J.R., Hearty, P.F., 1979: The icing of an unheated non-rotating cylinder in liquid water droplet-ice crystal clouds, NRC, LTR-LT-96, Ottawa.

Figure:

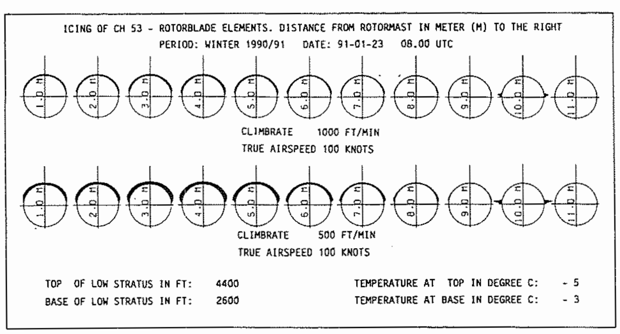

Schedule:

Date	TOP	deg.C.	BASE	deg.C.	LWC g/cbm	MVD mue m	GRADE	REPORT	REMARKS
90-11-07	2600	+ 3	1900	- 3	1.0 - 1.7	35	TRACES	NO ICE	temperature above zero degree
90-11-28	3000	- 3	1900	- 1	1.1 - 1.4	29	TRACES	NO ICE	
90-11-28	3800	- 3	1900	- 1	1.1 - 1.4	32	TRACES	MOD	15 min between 3100-3500 Ft MSL
91-01-16	3400	- 6	2400	- 4	0.9 - 1.1	23	LGT	LGT	
91-01-17	3000	- 8	1800	- 4.6	1.2 - 1.5	36	LGT	NO ICE	
91-01-18	3000	- 5	2300	- 4.9	0.9 - 1.1	24	LGT	NO ICE	
91-01-23	4400	- 5	2600	- 3	0.9 - 1.1	25	LGT	LGT	
91-01-24	4300	- 8	3200	- 5	0.7 - 0.8	18	LGT	NO ICE	
91-01-29	3000	- 7.5	1900	- 7	0.9 - 1.1	23	LGT	TRACES	
91-01-30	3500	0	2300	- 6	0.8 - 1.4	32	TRACES	NO ICE	LGT in DESCENT only
91-02-06	10000	-24	4000	-14					illegal extension of low stratus
91-02-18	2500	- 8.9	1800	- 3	1.0 - 1.1	21	LGT	NO ICE	
91-02-27	3000	+ 2	1800	- 1	1.1 - 1.7	37	NO ICE	NO ICE	temperature above zero degree
91-03-01	3000	+ 1	1900	- 1	1.1 - 1.6	35	NO ICE	NO ICE	temperature above zero degree

Cloud cover and its relationship with relative humidity during a springtime midlatitude cyclone: some implications for climate models

Chris J. Walcek

Atmospheric Sciences Research Center
State University of New York, 100 Fuller Rd., Albany, NY 12205 U. S. A.

1. INTRODUCTION

Microphysical processes occurring within clouds can significantly influence numerous larger-scale dynamic, radiative, and chemical processes occurring in the troposphere (e. g. Walcek et al., 1990). Since clouds are frequently present, it is necessary for accurate models of tropospheric climate or chemistry to account for effects associated with clouds. It is well known that clouds form when the vapor pressure of water exceeds the vapor pressure that would be saturated with respect to liquid water. Within any particular mass of air, fluctuations in temperature or water vapor concentrations can lead to areas where condensation (clouds) can occur even though the water concentration averaged over a larger air mass may not be saturated at the mean air mass temperature.

In large-scale numerical models of the atmosphere, chemical or meteorological properties can only be explicitly resolved over relatively large air masses, typically several hundreds of kilometers horizontally and ~1000 m vertically. It is not unusual to observe significant fluctuations in both temperature and moisture within air masses of this size due to turbulent motions, surface inhomogenieties, terrain and other factors, and these perturbations can result in small areas where clouds are present within the grid elements of these larger-scale models. Even though these clouds are not explicitly resolved by many numerical models, their radiative, dynamic, and chemical effects are significant, and their effects must be estimated. Regional or global-scale meteorology models must parametrize turbulent and cloud-scale processes that occur on scales smaller than the model grid size. In most parameterizations of cloud-scale processes, the heterogeneous (or subgrid-scale) nature of cloudiness is approximated by assuming that a fraction (f) of each grid area is occupied by clouds. This cloud cover fraction is used to apportion cloud effects into a "grid-averaged" forcing within grid areas that contain a mixture of clear and cloudy regions.

Most studies of clouds and their effects on tropospheric processes have concluded that even small cloud amounts can exert a significant influence on larger-scale processes. Under these conditions, the net effect of clouds on any physical or chemical process is strongly proportional to f, the fractional area of cloud coverage. Most models of tropospheric dynamics assume that the fractional area of cloud coverage is determined by the grid-averaged relative humidity. More elaborate treatments (Slingo, 1980) allow stability or resolvable-scale vertical motions to influence cloud coverage under some conditions. Figure 1 shows the functional dependence of cloud coverage within a particular atmospheric layer from a survey of formulations currently used by various researchers. All formulations assume a "critical relative humidity" of between 50-90% above which partial cloudy conditions can occur. Below this critical humidity, all formulations assume totally clear skies. At humidities above the critical humidity, cloud fraction increases by some functional dependence to 100% cover at 100% humidity.

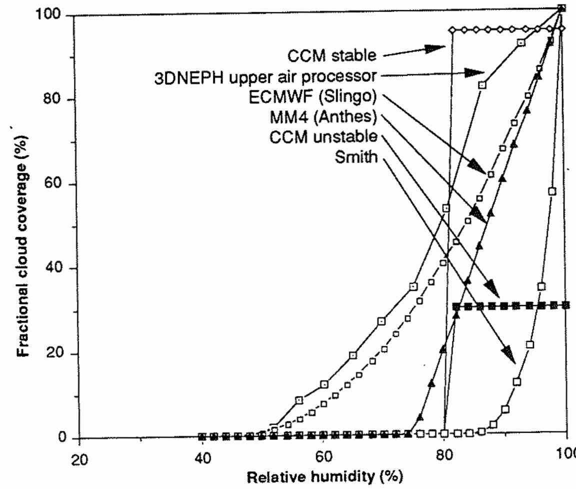

FIG. 1. Fractional cloud coverage as a function of relative humidity at 800 mb according to various formulations used by meso- and global-scale atmospheric models.

Figure 1 shows considerable differences between alternate formulations in assessing cloud coverage within current meteorology and climate models. At 80% humidity, the NCAR Community Climate Model specifies 95% cloud cover (under stable conditions), the British Meteorological Office climate model (Smith 1990) uses 0% cloud cover, while other models specify cloud coverage between these extremes.

In this study, we use observations of both relative humidity and cloud coverage to ascertain the relationship between these two parameters. With a more accurate, observationally-based relationship between cloud cover and relative humidity, the global-scale influence of cloud microphysical processes can be more accurately treated in larger-scale meteorology models.

2. CLOUD COVER OBSERVATIONS

Numerous cloud cover datasets have been collected and analyzed over the past several decades. Hughes (1984) provides a summary of the characteristics of cloud climatologies available in the early 1980's. The earliest cloud climatologies were compiled solely from surface-derived observations, and were often aggregated in time at various latitudes and time of day. Cloud observations in these early datasets were often composed of once-per-day observations averaged over relatively long time frames into seasonal or monthly data at a resolution of 5 - 10° latitude or longitude. Virtually all of the cloud cover datasets reviewed by Hughes (1984) were designed for use in textbooks or climate studies that require relatively coarse temporal and spatial resolutions.

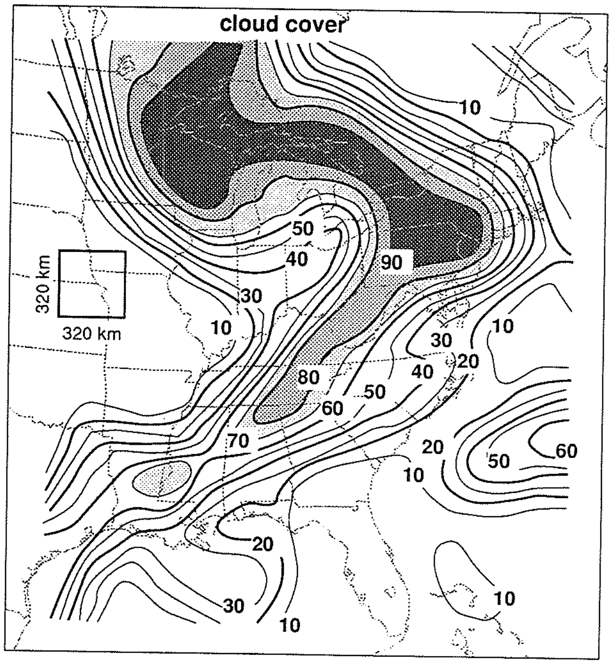

FIG. 2. Cloud cover averaged over (320 km)^2 areas (box shows a sample area) in the layer 800-730 mb at 18 UT, 23 April 1981 according to the U. S. Air Force 3DNEPH compilation of surface reports, aircraft observations, and satellite-derived data.

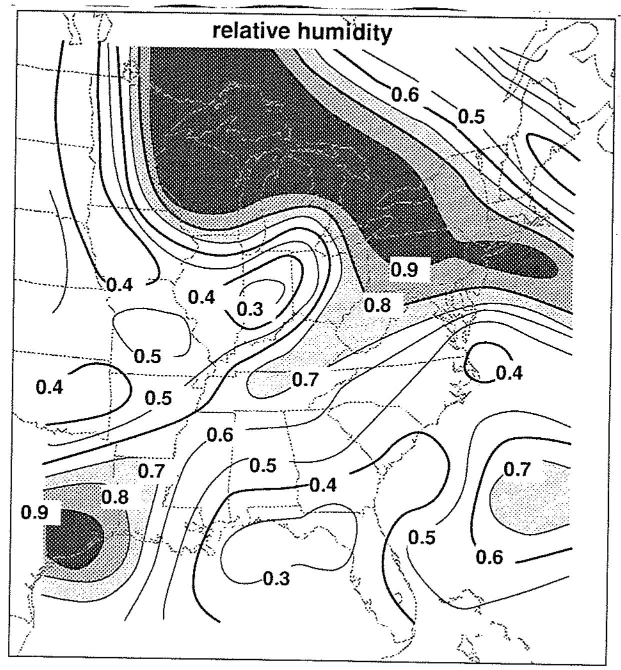

FIG. 3. Relative humidity averaged over (320 km)^2 areas in the layer 800-730 mb at 18 UT, 23 April 1981 interpolated from gridded NMC observations in time and space using a hydrostatic mesoscale meteorology model.

For short-term, regional-scale meteorological and chemical studies, instantaneous distributions of cloud conditions are required throughout a simulation period, updated as frequently as the underlying meteorology is changing. These models cannot readily use cloud cover estimates that are temporally averaged over large areas encompassing numerous meteorological environments. These models must use cloud coverage estimates based on shorter-term observations of cloud coverage.

The United States Air Force Environmental Technical Applications Center has been receiving and storing Air Force Global Weather Central (AFGWC) cloud data since January 1971. From 1971 to 1983, the AFGWC used an operational real-time three-dimensional analysis of cloud cover referred to as 3DNEPH. The 3DNEPH is a global analysis of cloud cover that uses surface-based and aircraft reports, together with visual and infrared satellite imagery to produce 3-D cloud cover information on a routine basis. During periods when satellite or surface data are lacking, clouds are inferred from rawinsonde temperatures and dew points. The data are gridded onto a polar-stereographic global grid with 15 vertical layers between the surface and ~16 km above the surface. Horizontally, the grid size varies from ~25 km near the equator to ~60 km at the poles. The 3DNEPH stores cloud cover information every three hours.

Any cloud cover database will contain a level of uncertainty that is difficult to explicitly evaluate. Numerous unevaluated algorithms are used to consolidate surface-based observations together with visible and infrared satellite imagery. Hughes and Henderson-Sellers (1985) performed an analysis of a later version of the Air Force cloud archive (RTNEPH) for 1979, and although numerous areas of obvious but minor errors were discovered, they found that the RTNEPH observations were generally reliable and in good agreement with known features of tropospheric meteorology. Problems were found when satellite data were gathered over highly variable backgrounds or backgrounds with snow or sea ice. Also, periods of missing data are not uncommon in the data, although they are identified.

In this study, we use five noon-time spring periods analyzed over the northeast U. S. by the 3DNEPH. At noon, we expect the maximum utilization of aircraft and surface reports together with visual and infrared satellite imagery by the 3DNEPH analysis. Fig. 2 shows the cloud coverage within ~(320 km)^2 areas (box shown in Fig. 2) in the layer 800 - 730 mb at noon local time, 23 April 1981. The (320 km)^2 averaging area corresponds to the finest "resolution" of the corresponding meteorology observations used in this analysis. During this five-day period, a relatively intense midlatitude cyclone developed and traversed the domain shown in Fig. 2. At the time of Fig. 2, the cyclone was situated near the center of the domain, and the cloud cover shows a warm frontal region over the Great Lakes, and a cold front extending from Pennsylvania to Texas.

3. STANDARD METEOROLOGY OBSERVATIONS

Temperature and moisture data used in this analysis are taken from observations and spatially and temporally interpolated onto an (80 km)^2 Lambert-conformal grid using a hydrostatic mesoscale meteorology model. Observations are derived from the National Meteorological Center global meteorological analysis and further enhanced using 3-hourly surface observations and 12-hourly vertical rawinsonde soundings. These observations are provided as initial and boundary conditions to the NCAR mesoscale meteorological model (MM4 - Anthes and Warner, 1978). During model execution, observations are incorporated into the model calculations in regions near the observation locations. Differences between observed and calculated temperatures, humidities and wind speeds are continuously minimized through the use of additional tendency terms in the momentum, moisture, and thermodynamic equations which "nudge" the calculation towards the observations. In this manner, model calculations agree closely with observations when and where observations are available, and when no observations are available, the meteorological data are dynamically consistent. Meteorology interpolated and analyzed from observations in this manner provides data of superior temporal and spatial resolution relative to "raw" observations. Vertically, the model encompasses the surface and 100 mb pressure surface (~16 km). The vertical grid size of the meteorology data is ~80 m near the surface, and on the order of a kilometer or more aloft.

Fig. 3 shows the relative humidity in the 800 - 730 mb layer interpolated from observations using the mesoscale meteorology model described above. The temperature and moisture calculations are aggregated into overlapping (320 km)^2 areas, representing a 4x4 average of the smallest grid size (80 km) used by the MM4 model. The domain shown in Figs. 2-3 represents approximately half of the domain simulated by the mesoscale meteorological analysis.

In Figs. 2-3, we have mapped both the cloud cover and humidity data onto the identical 320 x 320 km grid by area-averaging the "raw" temperature, moisture or cloud cover data. Vertically, the cloud cover and mesoscale interpolation model grids are slightly different, and the cloud cover grid was transposed onto the meteorology model pressure-based coordinate using a cloud volume conserving mapping. As a result, a total of 1120 data points at 15 tropospheric levels were available for comparison at any instant in time.

For this analysis, we consider only areas where cumulus convection cannot occur. Local stability ($\partial T/\partial z$) at any point in a sounding is not a sufficient indicator of the presence of convective activity, since convection can often penetrate into atmospheric layers that are absolutely stable with respect to vertical perturbations (Stull, 1991). In order to define areas and layers where buoyancy-induced convection is possible, we provide a 1 m s^{-1} "push" to air with a slightly higher temperature and moisture content from each point on a vertical sounding. In a conditionally unstable environment, the "pushed" parcel will accelerate upwards. Ignoring frictional forces and pressure perturbations, the parcel velocity at levels above the layer where it is perturbed can be obtained by integrating the vertical equation of motion for a parcel rising under the influence of buoyancy accelerations:

$$\frac{dw}{dz} = \frac{1}{w}\left[\frac{(T_{vp} - T_{ve})}{T_{ve}} - q_l\right]g \qquad (1)$$

where w is the parcel vertical velocity, T_{vp} is the virtual temperature of the rising parcel, T_{ve} is the virtual temperature of the surrounding environment through which the parcel rises, and g is the gravitational acceleration. The condensed water content of the parcel (q_l) is the total water content (assumed to remain constant) of the parcel minus the saturated vapor mixing ratio at any level above the impulse level. A grid area has a potential for convective clouds if parcels are capable of rising from any lower layer under the influence of buoyant forces. These areas have been neglected in the following analysis in an attempt to ascertain cloud cover under stable conditions only. Depending on the layer considered, we found between 1000 and 5000 stable grid areas during the five noontime periods considered in this analysis.

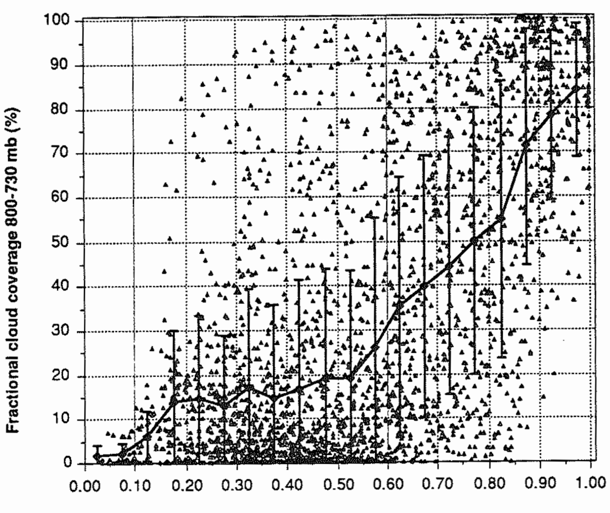

FIG. 4. Fractional cloud coverage as a function of relative humidity at 800-730 mb. Each point represents one (320 km)^2 area in the domain shown in Fig. 2 during 20-24 April 1981. Only grid areas where no buoyant convection can occur are considered. Lines show the mean and standard deviation of cloud cover within 5% increments of relative humidity.

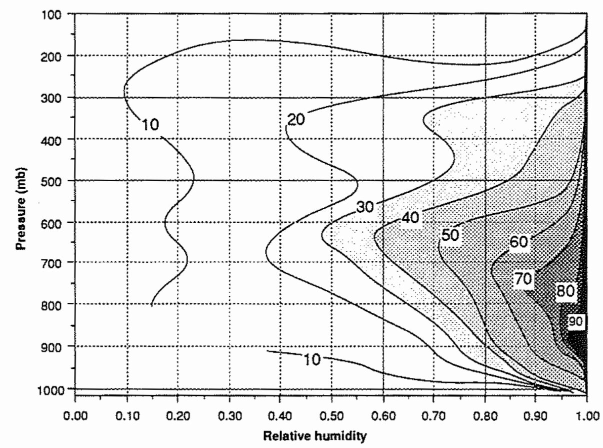

FIG. 5. Fractional cloud coverage as a function of relative humidity and pressure during 20 - 24 April 1981 over the northeast U. S. shown in Fig. 2.

4. CLOUD COVER AND RELATIVE HUMIDITY

Using the observations shown in Fig. 2-3, we now assess the relationship between cloud cover and relative humidity. Data shown in these two figures together with data from 4 additional days comprise several thousand overlapping (320 km)^2 areas where we have concurrent observations of both cloud cover and relative humidity. Fig. 4 shows the 3DNEPH cloud cover in the layer between 800-730 mb plotted as a function of the interpolated relative humidity observations at over 2600 grid areas where there was no potential for convection. A high degree of scatter is immediately evident in this comparison. Much of this scatter can be attributed to the considerable uncertainty in measuring both relative humidity and cloud cover over the large areas considered in this study. In assessing trends in highly uncertain data shown in Fig. 4, we aggregate the observations into 5% relative humidity increments, and then average the cloud coverage within these restricted humidity ranges. Using this averaging technique, trends become apparent in the highly scattered observations. The average and standard deviation of the cloud coverage are shown as a curve with error bars on this figure. As expected, cloud amount increases as humidity increases, and even at humidities between 20 - 40%, there is 10 - 20% cloud cover.

This process is repeated at all tropospheric levels to obtain the average cloud cover within each layer at any particular relative humidity. Fig. 5 shows the average cloud cover within (320 km)^2 stable areas. At a particular relative humidity, cloud amounts are greatest in the 800 - 600 mb layer of the troposphere, a trend that is consistent with earlier approximations (Buriez et al., 1988). The highest cloud amounts occur under high humidities at 900 - 800 mb, but this figure shows that 10-20% cloud coverage occurs at humidities as low as 15%, in contrast to the formulations shown in Fig. 1 which all proscribe zero cloud cover at humidities below 50 - 80%.

These results suggest that fractional area of cloud coverage decreases exponentially as relative humidity falls below 100%, and that there is no clear "critical relative humidity" where cloud coverage is always zero. Based on our analysis of the trends in the average cloud amount shown in Figs. 4 and 5, we suggest the following single-parameter approximation for cloud amount f as a function of relative humidity Rh (Rh<1):

$$f = \exp\left\{ \frac{Rh - 1}{\alpha} \right\} \tag{2}$$

where α is a function of height in the troposphere, and represents the relative humidity depression from 100% at which cloud amount falls off to 37% (e^{-1}). Figure 6 shows the value of α in Eq. (2) that yields the minimum root mean square difference between observed cloud amount and cloud amount calculated using Eq. (2). The best fit to the α values shown in Fig. 6 can be reasonably represented by

$$\alpha = 3\left(1 - \frac{P}{P_s}\right) \exp\left\{ -3\left(1 - \frac{P}{P_s}\right)\right\} \tag{3}$$

where P is the pressure, and P_s is the surface pressure. Using Eq. (2) to calculate cloud cover from relative humidity [both averaged over (320 km)^2 areas] produced cloud cover estimates that on average contained a root mean square difference of 10 - 30 percentage points from the 3DNEPH observations, depending on which level of the troposphere was being considered.

5. CONCLUSIONS

In this study, we have compared satellite observations of fractional cloud coverage within ~(320 km)^2 areas with co-located relative humidity observations over the northeast U. S. during a springtime midlatitude cyclone. Cloud cover observations were derived from the U. S. Air Force 3DNEPH analysis of satellite imagery and surface-based observations. Relative humidity was interpolated from observations using a hydrostatic mesoscale meteorology model. Co-located comparisons of the cloud cover and relative humidity and stability suggest that there is considerable uncertainty in any correlations between these parameters over large areas. Despite a high degree of uncertainty, we find significant correlations between cloud cover and relative humidity when data are aggregated into increments of humidity. These comparisons suggest that cloud coverage decreases exponentially as humidity falls below 100%. Relative to other layers in the troposphere, the middle troposphere (700-500 mb) contains higher cloud amounts at lower humidities, with mean cloud amounts of ~30% near 50% humidity.

Most parameterizations of cloud coverage calculate smaller cloud amounts than reported by the 3DNEPH observations, especially in middle tropospheric levels. These results suggest that current methods of calculating cloud coverage within large-scale climate simulations or atmospheric chemical modeling studies are significantly underestimating the effects of clouds. More importantly, current climate models probably cannot adequately estimate the potentially significant changes in cloud cover that can result from small changes in relative humidity.

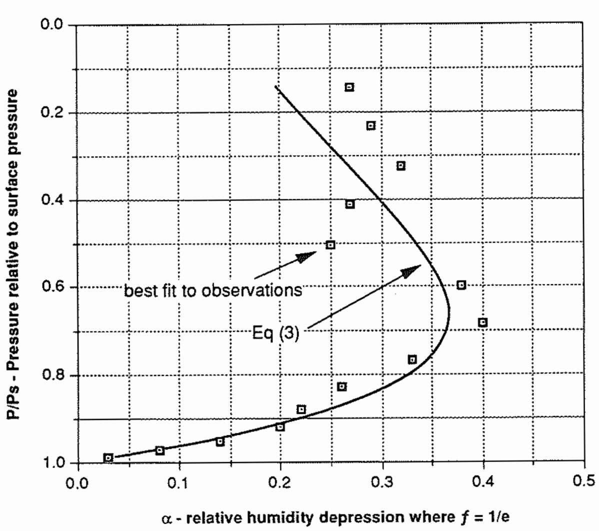

FIG. 6. Vertical variation of the critical relative humidity depression where the average cloud cover is 36.7%. Data points plotted are the values of α in Eq. 2 which yield the minimum RSM difference between 3DNEPH and cloud cover calculated from relative humidity. Curve shows Eq. 3, a reasonable approximation to these data.

Acknowledgements. The author is grateful to the organizations that are supporting portions of the research presented here: the U. S. National Science Foundation; the U. S. Department of Energy; and the U. S. Air Force Office of Scientific Research.

REFERENCES

Anthes, R. A. and T. T. Warner, 1978: Development of hydrodynamic models suitable for air pollution and other mesometeorological studies. *Mon. Wea. Rev.*, **106,** 1045-1078.

Buriez, J.-C., B. Bonnel, Y. Fouquart, J.-F. Geleyn, and J.-J. Morcrette, 1988: Comparison of model-generated and satellite-derived cloud cover and radiation budget. *J. Geophys. Res.* **93,** 3705-3719.

Hughes, N. A., 1984: Global cloud climatologies: a historical review. *J. Appl. Clim. and Meteor.*, **23,** 724-751.

Hughes, N. A. and A. Henderson-Sellers, 1985: Global 3D-nephanalysis of total cloud amount: climatology for 1979. *J. Appl. Clim. and Meteor.*, **24,** 669-686.

Slingo, J. M., 1980: A cloud parameterization scheme derived from GATE data for use with a numerical model. *Quart. J. Roy. Met. Soc.*, **106,** 747-770.

Smith, R. B. N. 1990: A scheme for predicting layer clouds and their water content in a general circulation model. *Quart. J. Roy. Met. Soc.*, **116,** 435-460.

Stull, R. B., 1991: Static stability-an update. *Bull. Am. Met. Soc.*, **72,** 1521-1529.

Walcek, C. J., W. R. Stockwell, and J. S. Chang, 1990: Theoretical estimates of the dynamic, radiative and chemical effects of clouds on tropospheric trace gases. *Atmos. Res.*, **25,** 53-69.

Initialization of cloud water content using a digital filter

Xiang-Yu Huang

Danish Meteorological Institute, Denmark

1. INTRODUCTION

When cloud water content (CWC) is included as a prognostic variable in a numerical weather prediction (NWP) model, a consistent treatment of the condensation-cloud formation-precipitation-evaporation processes is obtained (Sundqvist, et.al., 1989). However, how to initialize CWC is still an open question, because that CWC has seldomly been incorporated into the analysis and data assimilation schemes. The lack of quantified observations makes the subject even more difficult. A preliminary study has been reported by Kristjansson (1991), in which, satellite data and model generated data are used as initial CWC filed. One problem found in Kristjansson (1991) is that the initial CWC field is not in a balance with the rest of the model variables.

Here, an alternative approach is presented, which provides an initial CWC field and leads to a noise-free numerical forecast. This approach is based upon the Diabatic Digital Filtering Initialization (DDFI) developed in Huang and Lynch (1992, hereafter HL92). Since there is a diabatic model integration involved in the DDFI, an initial CWC field can be obtained together with other filtered variables.

2. METHOD: DDFI

The theoretic background of DDFI has been established in Lynch and Huang (1992, hereafter LH92). The high frequencies are removed by applying a digital filter to a time series, X(n), generated by integrating a numerical model from the initial analysis backward and forward in time. In the adiabatic version all the integrations are adiabatic, one backward and one forward (LH92). In the DDFI the backward adiabatic integration is followed by a forward diabatic one (LH92). In the experiment presented here, the filter span and the cutoff period are chosen to be 6h, i.e., 6h diabatic model run is needed for the initialization.

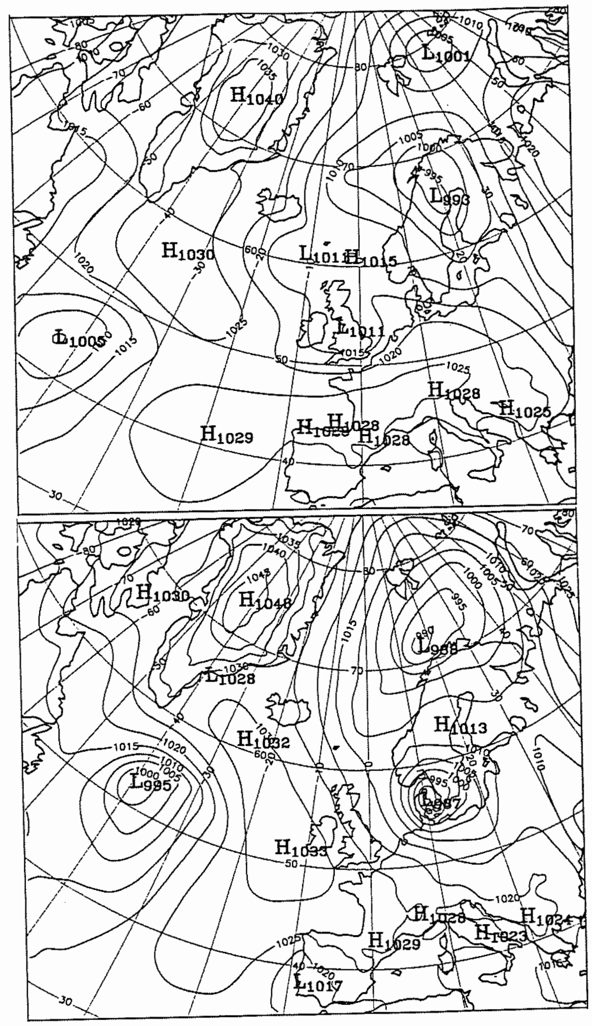

Fig. 1. (a) Sea level pressure analysis in hPa for 00Z, Thursday 5th September 1985 after DDFI; (b) +24h sea level pressure forecast from DDFI analysis. The whole integration area is shown. The low over Denmark in the 24h forecast is also called the September Storm.

The model in use is the HIRLAM model, which is written on premitive equations and has a grid of 110x100x16 points (LH92). The cloud scheme of Sundqvist, et.al. (1989) is used. The case chosen here is the same one used in LH92 and HL92, in which an intense low crossed Denmark and southern Sweden on 5-6 September 1985. The surface pressure field after the DDFI and the subsequent 24h forecast are shown in Fig.1.

It has been shown that DDFI removes high frequency noise completely while keeping the changes to the initial fields and the forecasts reasonably small (LH92 & HL92).

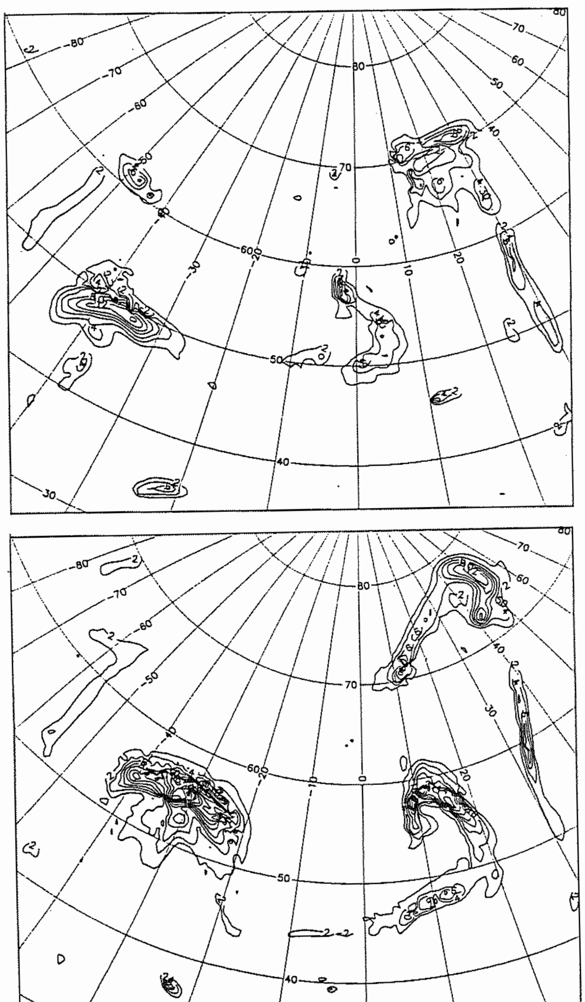

Fig. 2. (a) Vertically integrated cloud water content in g/kg for 00Z, Thursday 5th September 1985 after DDFI; (b) +24h vertically integrated cloud water content forecast from DDFI analysis. The whole integration area is shown. The frontal systems are clearly shown.

3. CWC AFTER DDFI

As the DDFI scheme includes all physics in the diabatic integration, a CWC is obtained as the initial field. In Fig.2, the vertically integrated CWC at initial time (after DDFI) is shown. First of all, it can be seen that the distribution of initial CWC is very good, well in agreements with the weather systems (Fig.1a). For instance, the frontal systems are all displayed correctly. Secondly, the amplitude of the CWC is of the right order of magnitude. The values are probably somewhat small compared with that in the 24h forecast. However, it has to be pointed out that the weather systems are also intensified during the forecast.

The model-averaged CWC as a function of time is shown in Fig.3. The full line is for the forecast from uninitialized analysis. The dotted and dashed lines are for the forecasts from ADFI and DDFI analyses, respectively. We see a significant improvement in the first hours of the DDFI forecast. The gradual increase may be related to the development of weather systems. The rapid increase in the uninitialized forecast may be caused by the noise in the forecast (Fox-Robinovitz and Gross, 1991).

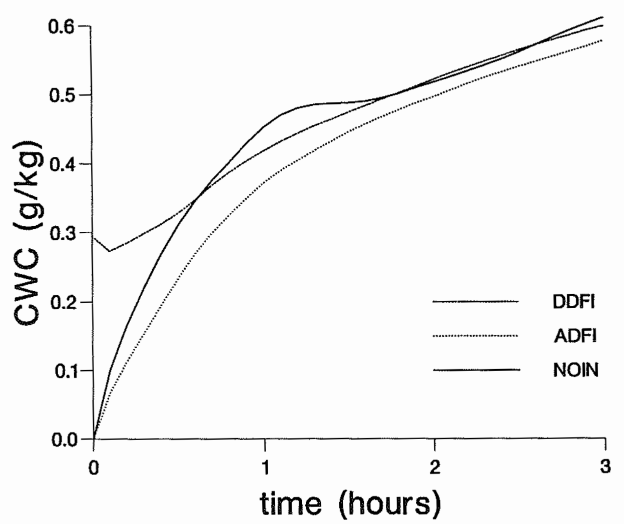

Fig.3. Model averaged cloud water content (g/kg) as a function of time (h). Full line: forecast from uninitialized analysis. Dotted line: forecast from ADFI analysis. Dashed line: forecast from DDFI analysis. Only the initial stage, the first 3h, is shown to emphasize the spinup of the cloud water content.

The model-averaged precipitation rate in the DDFI forecast also shows some improvements compared with the that in the ADFI forecast (FIG.4). However, the initial decrease of the precipitation rate in the DDFI forecast has not been investigated thoroughly. The study of Kristjansson (1991) indicates that a special treatment of humidity field is needed in order to avoid this problem. However, our approach is different to the one used by him. The initial humidity field and CWC field should be in a mutual balance after the DDFI scheme. Further studies on this problem is under consideration.

4. CONCLUSIONS

The diabatic digital filtering initialization scheme used by Huang and Lynch (1992, referred to as HL92) is applied to the HIRALM model which has a consistent parameterization scheme for the condensation/cloud/precipitation/evaporation processes. The model is first integrated adiabatically backward for half of the filter span, in this study -3h. A diabatic integration is then carried out from -3h to +3h to generate the time series, upon which the digital filter is applied. An initial cloud water content field is obtained during the initialization procedure.

The initial cloud water content field obtained is in a very good agreement with the weather situations and has a right order of magnitude, if compared with the cloud water content field in the +24h forecast. Significant improvements in the first a few hours have been observed in the spinup of the model cloud water content field and precipitation rate. However, a decrease in the precipitation rate during the first ten munites has not been understood. Further studies in this direction is considered.

5. ACKNOWLEGMENTS

I wish to thank Professor Hilding Sundqvist and Dr Peter Lynch for constructive discussions. Part of this study was carried out while I was a research fellow at the Department of Meteorology, University of Stockholm and supported by NFR (Swedish National Science Research Council) contract Nos. G-GU 1705-311 and E-EG 2923-302.

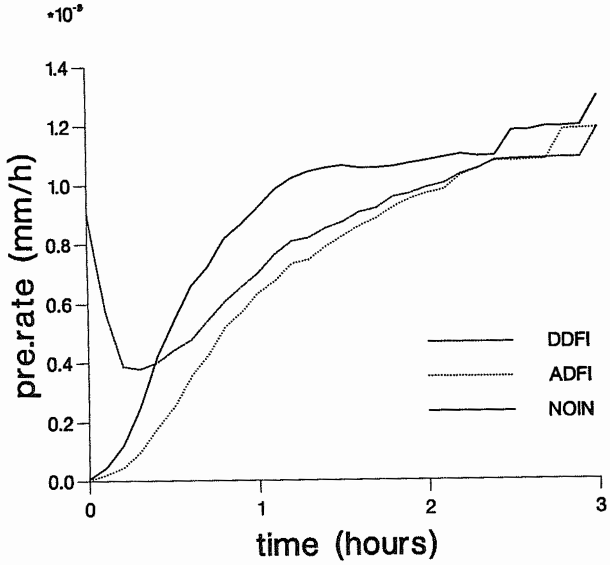

Fig.4. Model averaged precipitation rate (mm/h) as a function of time (h). Full line: forecast from uninitialized analysis. Dotted line: forecast from ADFI analysis. Dashed line: forecast from DDFI analysis. Only the initial stage, the first 3h, is shown to emphasize the spinup of the model precipitation rate.

REFERENCES

Fox-Rabinovitz, M.S. and B.D. Gross, 1991: Diabatic dynamic initialization for the GLA 4-D data assimilation system. In Preprints, Ninth Conference on Numerical Weather Prediction, Denver, CO, October, 1991, American Meteorological Society, 373-376.

Huang, X.-Y. and P. Lynch, 1992: Diabatic digital filtering initialization: Application to the HIRLAM model. Accepted for publication in *Mon. Wea. Rev.*

Kristjánsson, J.E., 1989: Initialization of cloud water in a weather prediction model. In Preprints, Ninth Conference on Numerical Weather Prediction, Denver, CO, October, 1991, American Meteorological Society, 823-824.

Lynch, P. and X.-Y. Huang, 1992: Initialization of the HIRLAM model using a digital filter. *Mon. Wea. Rev.*, **120**, 1019-1034.

Sundqvist, H., E. Berge and J.E. Kristjánsson, 1989: Condensation and cloud parameterization studies with a mesoscale numerical weather prediction model. *Mon. Wea. Rev.*, **117**, 1641-1657.

RAINSAT II: A COMBINED SATELLITE AND RADAR NETWORK RAINFALL OBSERVATIONAL AND FORECASTING SYSTEM

A. Bellon, A. Kilambi and M. R. Duncan

McGill Radar Weather Observatory
P.O. 198, Macdonald College
Ste Anne de Bellevue, Quebec
CANADA H9X 1C0

1. INTRODUCTION

Geostationary visible and infrared data offer a unique opportunity to observe the location and movement of raining clouds at the synoptic scale with a temporal (30 minutes) and spatial (5 km) resolution which is amenable to real-time operational monitoring and nowcasting. Consequently, the RAINSAT system, based on a bispectral method of rain area estimation by Bellon et al (1980), was developed by the McGill Radar Weather Observatory (MRWO) and was in real-time operation in Toronto from 1984 to 1990. An evaluation of its performance has been published by King et al (1989) who concluded that RAINSAT is successful in delineating rain areas in daytime and that the forecasts of these areas are skillful up to 6 hours.

Specifications for an improved version of RAINSAT were first formulated by the Spanish Meteorological Service in 1987. As a result, SIRAM (Sistemas Integracion Radar Meteorologico) was eventually installed by MRWO in 1989 in Madrid. In addition to the Meteosat data, this system also collects data from the Spanish radar network. SIRAM can also receive synoptic information from radiosondes or from numerical weather prediction models, (Fig. 1). The Canadian equivalent, RAINSAT II, sponsored by the Atmospheric Environment Service of Canada, has been running in a µVAX at the Centre Météorologique du Québec (CMQ) in Montreal since early 1991 but is not presently acquiring synoptic data.

2. RAINSAT METHODOLOGY

2.1 *Rain Estimation Technique*

Briefly, infrared measurements provide information on the temperature and hence the height of clouds while the visible brightness is related to cloud thickness. The RAINSAT methodology is based on the simple assumption that clouds which are both high and of large vertical extent are more likely to be raining. Its main strength is its ability to exclude rain from high but relatively thin cirrus clouds and from relatively bright but warm clouds. The radar observation of rainfall rates R is used as ground truth with which satellite data pairs (IR,V) are calibrated and the derived relationship R = f(IR,V) is applied to the surrounding regions scanned by the satellite. Thus, statistical relationships based on a sufficiently large number of radar-satellite comparisons of similar weather conditions are derived as described in Cherna et al (1985) for % probability of rain and in Bellon and Austin (1986) for rainfall rates.

2.2 *Normalization of Visible Data*

It is essential to remove the diurnal dependence of the visible images when they are used as input in a quantitative and objective rain delineation and forecasting procedure as in RAINSAT. For Lambertian surfaces, the brightness is independent of the observer's look angle and the normalization factor is $N(Z) = 1/\sin(Z)$ where Z is the sun angle above the horizon. In order to account for possible deviations from this assumption, the normalization equation is modified to

$N(Z) = (1 + b)/(\sin(Z) + b)$ A value of $b = 0.03$ has been determined by Cherna et al. (1985) from empirical data. Such a small magnitude is an indication that clouds do indeed behave like a Lambertian surface. This normalization procedure is valid until Z = 5 or 10 degrees.

2.3 *Forecast Procedure*

The forecast procedure consists of a linear extrapolation of precipitation patterns, for a duration of 1 to 6 hours, according to the "status quo" assuption, that is, precipitation areas are translated by amounts proportional to a calculated past motion, and without any modifications to their area or intensity distribution. The past motion is determined from the spatial lag of the maximum cross-correlation coefficient γ_{max} when two images separated by a certain time interval are cross-correlated. Since the major portion of forecastability loss is attributed to the unpredictable development and/or dissipation of rainfall patterns rather than to inaccuracies in their forecast motion, it is not essential to devise more complex ways to precisely measure the past velocities of precipitation patterns or of individual storms. The pattern recognition algorithm is applied to 25 subareas of the entire Rainsat map. Each subarea of (400 x 400) km^2 is thus comparable in size with a typical radar coverage. In subareas for which the cross-correlation algorithm cannot be attempted, or for

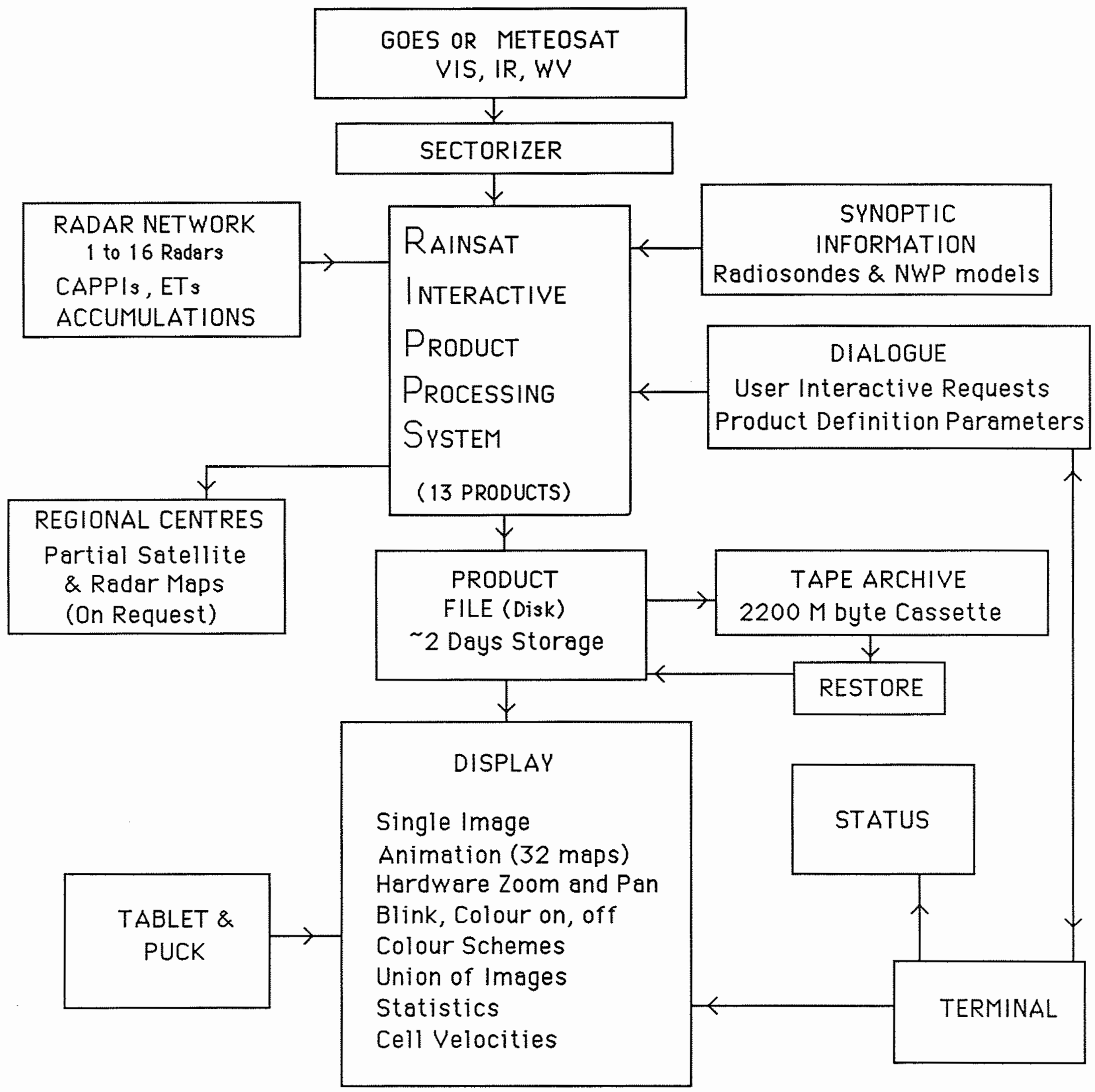

FIGURE 1: RAINSAT II SYSTEM CONFIGURATION

which the computed velocity has been rejected as unreliable, the forecast velocity is obtained by interpolation of velocities from neighboring subareas, or from synoptic data if available.

The (5 x 5) array of velocities is then expanded by linear interpolation to obtain a vector displacement for each of the (512 x 512) pixels of the standard Rainsat map. Using this field of velocities and the current Rainsat image, the forecast map for x hours ahead is obtained by searching, in steps of one hour, for the intensity at the upwind pixel which is expected to reach each (i,j) pixel of the forecast map.

3. SYSTEM CONFIGURATION

A simplified block diagram of the RAINSAT II system is sketched in Fig. 1.

3.1 *Description of Inputs*

The four main sources of input are:

a) Satellite: These data are radiation measurements available at half-hourly intervals from the visible, infrared and water vapour channels of the GOES or METEOSAT geostationary satellites. The sectorizer computer selects from the full earth image only that portion of the data required to completely cover the largest RAINSAT window of approximately (3000 x 3000) km^2. The navigational parameters embedded with the IR information are also required at every cycle in order to recompute the transformation from a satellite to an earth coordinate system.

b) Radar: CAPPI, Echo Top and rainfall accumulation maps processed locally at each of the radar sites are transmitted via telephone lines to the Rainsat central processor RIPPS. CAPPI and ET maps are available every 10 minutes while accumulation maps are sent hourly. These run-length-encoded maps are remapped into the same Lambert conic projection used for satellite data. The RAINSAT at CMQ is expected to receive data from three radars located near Montreal, Ottawa and Quebec City.

c) Synoptic Data: The RAINSAT II system can access synoptic information from a radiosonde network or from the output of numerical weather prediction models. The parameters selected are: temperature, wind speed and direction, dew point temperature and geopotential height at 13 pressure levels from the surface to 50 mb. These data are used to calibrate the IR readings in terms of cloud height, as an initial guess in the module computing rainfall areas displacement and/or as the predicted velocity field in the forecast module.

d) User Input: The DIALOGUE interactive module in Fig. 1 enables the user to enter the parameters defining the various products and to modify the schedule and number of the products to be generated every half hour. DIALOGUE allows access to three types of libraries which contain:
- the bispectral classification schemes
- the parameters used in DISPLAY and
- other user-selectable parameters which affect or define the visible normalization scheme, the rejection criteria for the velocity computation algorithm, the climatological velocities used to supplement the absence of synoptic data, the manual navigation of satellite data, the functioning of automatic display, the smoothing of water vapour images, the removal of spurious lines from raw satellite data, the threshold levels of output maps, the source of synoptic data, (radiosondes or models), the choice of one of the 4 "windows", (Sec. 3.2) and the method of radar data selection over pixels covered by more than one radar.

Other options in DIALOGUE enable the user to update the stations for which point forecasts are to be provided and to indicate the specific products that are to be archived.

3.2 *Description of Products*

All images, except point forecasts, are presented on a (512 x 512) array at 4 km resolution. They are remapped on a Lambert conic projection centred at (45^{o}N, 75^{o}W) and true at the two fixed standard parallels at 39^{o}N and 51^{o}N. In order to allow a longitudinal flexibility in the observation of weather events, the user can relocate the image over 3 different windows centred at 85^{o}, 75^{o} or 65^{o}W longitude. In addition, in order to observe weather systems in the more northerly latitudes of Eastern Canada, a fourth window at 6 km resolution has been introduced to view the visible and IR images and one Rainsat image. It is centred at (50^{o}N, 75^{o}W) with standard parallels at 40^{o}N and 60^{o}N.

A list of the 13 products appears below:

Type #	Group 1		Group 2
#1 -	Visible	#4 -	Rainsat maps
#2 -	IR (InfraRed)	#5 -	Forecast Rainsat maps
#3 -	WV (Water Vapour		
	Group 3		
#6 -	Composite "Radar Only" Rainfall Rate maps		
#7 -	Composite "Radar+Satellite" Rainfall Rate maps		
#8 -	Composite "Radar Only" Echo Top maps		
#9 -	Composite "Radar+Satellite" Echo Top maps		
#10 -	Forecast Composite "Radar Only" Rainfall Rate maps		
#11 -	Forecast "Radar+Satellite" Rainfall Rate maps		
#12 -	Surface Rainfall Accumulation Maps (Radar or Satellite)		
	Group 4		
#13 -	Point Forecasts (from Satellite data)		

Group 1 consists of images which are directly derived from raw geostationary satellite data and remapped into a Lambert conformal projection.

Group 2 consists of products synthesized from a combination of visible and/or IR images in accordance with an assigned classification scheme. The user has the possibility of providing classification schemes that yield satellite maps of probability of rain, rainfall rate, precipitation type, cloud characteristics, severe weather and of any other satellite-derived meteorological parameter. The so-called Rainsat images, (type #4), are thus an indirect inference of a meteorological parameter not directly available with the primary visible and IR maps. The forecast of these images according to the procedure described in section 2.3 constitute type #5.

The composite images which make up group 3 are "composite" in a dual sense:

1- CAPPIs, Echo Top and Accumulation maps from different radar locations are combined into one single image to form a "Radar Only" composite map of the entire radar network (types #6, #8 and #12). When one pixel is under the coverage of more than one radar, the user has the choice of two alternatives; select the intensity from the nearest radar or select the highest intensity.

2- In addition, rainfall rate Rainsat images and IR-derived Echo Top maps are used to complement the "radar only" information over regions which are not under radar coverage. The resultant products are referred to as composite "radar+satellite" maps (types #7 and #9). IR-derived echo top heights are provided for only those pixels in which the corresponding satellite rainfall rate from map of type #4 exceeds a user-specified threshold. This check ensures that IR heights are provided only for raining clouds.

The "radar only" composite maps are forecasted according to the velocity found in the header of each radar picture, (type #10). This velocity is the outcome of a cross-correlation procedure applied to the rainfall pattern within each radar coverage. Beyond radar coverage, the forecast of "radar+satellite" rainfall rate maps is based on velocities obtained from synoptic data or from the Rainsat displacements found in maps of type #5.

Satellite accumulation maps are computed from the half-hourly Rainsat maps (type #4). At every hour mark, a 1-hour accumulation is computed using the three maps which usually cover a 1-hour period. Since the displacement of rainfall patterns during these intervals is much larger than the 4 km grid length of the map, it is essential to use the velocities computed by the forecast module in order to eliminate known quantization effects. From these one-hour accumulations, maps showing an estimate of the total rainfall for periods of up to 24 hours can be easely generated.

Group 4 simply includes the point forecasts based on one rainfall rate Rainsat image (type #4). These consist of forecasts at 16 stations of rainfall rates over 10-minute intervals for the subsequent three hours. "Line" point forecasts are obtained by searching through the current image data along a path originating at the station and proceeding in a direction opposite the computed storm velocity. The resultant total rainfall for the 3-hour period is also provided. "Sector" point forecasts provide the highest rainfall rates that could conceivably affect the station by searching over an area of the image which is equivalent to a 10-minute displacement upwind and, cross-wind, to a 16-degree arc centred on the expected line trajectory.

3.3 *Description of Output*

The user must request at least one satellite rainfall rate map which is based on a Vis-IR classification scheme during the day and on an IR-only scheme at night. The constant availability of this map ensures the computation of the automatic satellite rainfall accumulation maps and of the "radar+satellite" products. For each half-hourly cycle, the user may then request the generation of 7 additional Rainsat images by specifying the classification schemes to be used. Forecasts may be requested for any one of these maps. Usually, the user sets up a number of schedules appropriate for summer or wintertime conditions, for convective or stratiform precipitation, or for any category of his choice for which reliable classification schemes have already been devised. He then simply assigns with DIALOGUE the schedule which generates the types and number of products most suitable for the synoptic situation at hand. Up to 20 products, including the point forecasts, may be generated every half hour. They are stored into a disk file which may retain up to 2 days of data and accessible via the DISPLAY module. A subset of products which the user has selected for archival are stored on a 2200 Mbyte cassette. Run-length encoding of these products has enabled us to store up to 2 months of data in one cassette. A RESTORE command retrieves desired sequences from this medium and returns them into the product disk file for re-examination with the DISPLAY facility. These historical images may also be used as input to programs used for research and development.

The DISPLAY facility consists of a MODEL ONE/85 graphic system from Raster Technologies Inc. which has a 1280 x 1024 pixel colour monitor with 8 bit planes, a high speed DMA access for fast loading of images, a hardware zoom and pan and a digitizer tablet with puck. The high speed programmable 8-bit in 24-bit out colour look tables feature of this system enables the user to select 256 colours from a palette of 16 million colours. The animation feature of up to 32 images is particularly useful in viewing the growth and decay of weather systems and of storms, and in detecting any differential motion from the rest of the precipitation pattern. Two images from different types may be combined into a "union" image. The presentation of the products is complemented with the addition of a geographical background, of a latitude-longitude grid and of velocity vectors.

4. CONCLUSIONS

The RAINSAT system combines precipitation information from a radar network with geostationary satellite imagery in order to generate composite rainfall rate, echo top, accumulation and forecast products. When optimized with a judicious choice of user-selectable parameters through the DIALOGUE module, these products can yield valuable information required to correctly assess or interpret a variety of meteorological situations. Our current efforts are directed at using output from numerical weather prediction models, particularly the field of upward motion, in an attempt to improve the estimate of rainfall areas from visible and IR measurements.

5. ACKNOWLEDGEMENTS

We are grateful to J. D. Steenbergen of AES for his continued interest and support of the Rainsat program and to C. Martinez of the National Meteorological Institute of Spain for encouraging the implementation of the RAINSAT II system in Madrid. We also appreciate the enthusiasm of H. P. Biron, supervisor at CMQ, for suggesting improvements to the operation of the Rainsat system. Portions of the work presented here have also been financed through grants from the National Science and Engineering Research Council of Canada.

6. REFERENCES

Bellon, A., S. Lovejoy and G. L. Austin, 1980: Combining satellite and radar data for the short-range forecasting of precipitation. Mon. Wea. Rev., 108, 1554-1556.

Bellon, A. and G. L. Austin, 1986: On the relative accuracy of satellite and raingauge rainfall measurements over middle latitudes during daylight hours. J. Clim. and Appl. Meteorol., 25, 1712-1724.

Cherna, E. V., A. Bellon, G. L. Austin and A. Kilambi, 1985: An objective technique for the delineation and extrapolation of thunderstorms from GOES satellite data. J. of Geophysical Research, Vol. 90, No. D4, 6203-6210.

King, P., T. Yip and J. D. Steenbergen, 1989: RAINSAT: A one year evaluation of a bispectral method for the analysis and short-range forecasting of precipitation areas. Weather and Forecasting, 4, 210-221.

EFFECTS OF DEEP CONVECTION ON TROPICAL PRECIPITATION AS SIMULATED BY THE CCC GENERAL CIRCULATION MODEL

G.J. Zhang and N.A. McFarlane

Canadian Climate Centre
Atmospheric Environment Service
Downsview Ontario M3H 5T4

1. INTRODUCTION

Cumulus convection is one of the most important energy sources in the tropical atmosphere. Many parameterization schemes have been developed to incorporate the convective effects in general circulation models (Kuo, 1974; Arakawa and Schubert, 1974; and many more). Results from the GCM's using some of these schemes have been diagnosed to examine the role of convection in the atmospheric circulation. Donner et al. (1982) employed the Kuo scheme in the Australian Numerical Meteorology Research Center GCM. Recently Sud et al. (1992) did similar experiments with the Arakawa and Schubert scheme and the Goddard Laboratory for Atmospheres GCM. Their results are considerably different from those of Donner et al. (1982). They attributed some of the differences to the different treatment of subgrid-scale processes including cumulus convection.

In the study reported here, we conducted two experiments using the Canadian Climate Centre's general circulation model (CCC GCM), one with parameterized convection and one without, to study the effect of convection on tropical precipitation. The scheme we used to represent cumulus convection is a bulk mass flux scheme developed in CCC (to be documented). The CCC GCM used in this study is documented by McFarlane et al. (1992).

In both the convection and no convection runs dry convective adjustment is activated when the atmosphere is dry-statically unstable. The large-scale condensation occurs when the atmosphere reaches saturation. The two runs start from the end of March with the same initial condition, and terminate at the end of August. The results over the summer months (JJA) will be used to demonstrate the convective effects.

2. RESULTS

a. Condensation heating and drying

The heating and drying due to condensation with or without convection is significantly different. When convection is included, there is large convective heating and drying in the tropics. But this is to a large extent at the expense of the large-scale condensation. Therefore, it is the difference of the total (large-scale plus convective) condensation heating and drying that measures the effect of cumulus convection. Fig. 1 shows this difference averaged zonally. The heating in the convective run is slightly elevated due to the presence of high clouds (Fig. 1a). However, a more pronounced difference is the latitudinal shift of heating, especially in the tropical region. For instance, in the convection run there is more condensation heating right over the equator whereas there is less heating near 15 ° N. The difference in the total condensation drying (Fig. 1b) shows that in the midtroposphere the latitudes that have less heating also have less drying (for example at 15 ° N) from no convection to convection run. However, in the lower troposphere there is much more drying at almost all latitudes in the convection run. This represents a vertical shift in drying pattern from no convection to convection. More drying in the lower troposphere helps produce a more stable atmosphere in terms of moist static stability.

b. Circulation

The different heating and drying along with other processes with and without convection can certainly produce a different circulation, especially in the tropics. Fig. 2 shows the meridional circulation for the convection (Fig. 2a) and the no convection (Fig. 2b) run averaged over the summer months. Note that stream function contours less than -20×10^{10} kg s^{-1} are not plotted in the no convection run. The Hadley cell in both the runs is well defined. Nevertheless, there are significant differences. In the no convection run it is stronger than in the convection run. Furthermore its centre is located almost right over the equator in the no convection run whereas it is located near 10 ° S when convection is included. Donner et al. (1982) obtained similar results. On the other hand Sud et al. (1992) found that including convection enhances the strength of the Hadley cell and shifts its location from 10 ° S to the equator, opposite to what is found here and in Donner et al. (1982). It is

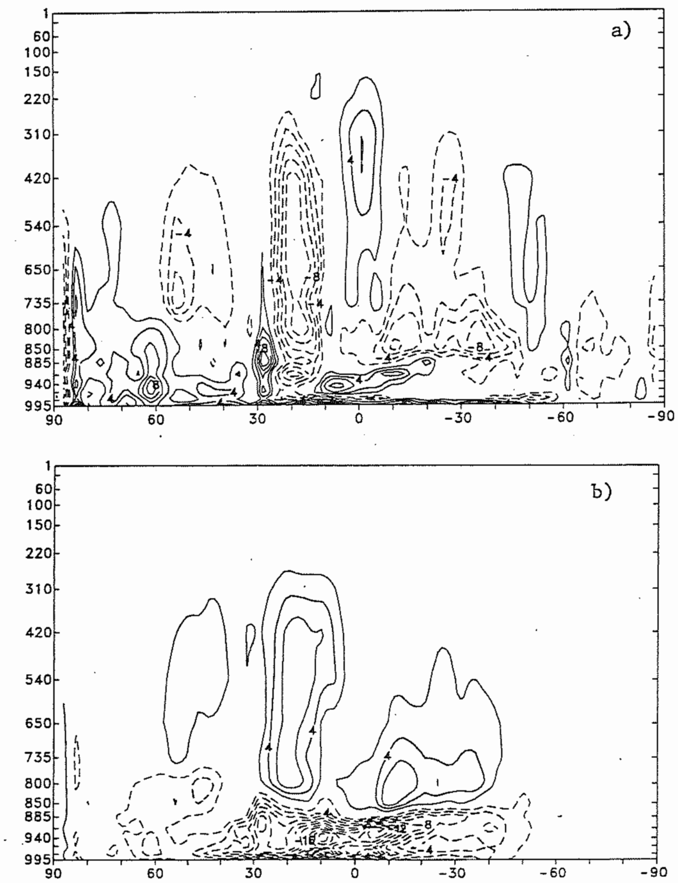

Fig. 1 Difference of the total condensation heating and drying (convection - no convection), contour intervals: a) .1 ° day^{-1} b) .1 g kg^{-1} day^{-1}.

not clear to us what causes this difference (Sud et al. suggested that use of the dry convective adjustment in their study may be a factor contributing to the difference between their results and those of Donner et al., but here we also used the dry adjustment).

c. Precipitation

Fig. 3 presents the global distribution of precipitation in the two runs and their difference in the western Pacific regions. The precipitation maxima are located in the Central American, Indian and Western Pacific monsoonal regions and over the African ITCZ. In the western Pacific, maximum precipitation is located right over the equator in the convection run, corresponding to the rising branch of the Hadley cell. Without convection, the precipitation over the Central America and the tropical Africa is about the same. However, there is less precipitation over the Indian monsoonal region and much more precipitation in the Western Pacific. Moreover, the precipitation maximum in the western Pacific is pushed northward to 15 ° N in the no convection run. This is also consistent with the location of the Hadley cell. Since the largest difference in precipitation with or without convection is in the western Pacific, Fig. 3c shows the difference field of precipitation. It is clear that with convection the precipitation in the Indian monsoonal region and the equatorial western Pacific is enhanced whereas it is reduced significantly in a belt near 15 ° N in the western Pacific.

3. SUMMARY

This study examines the effect of cumulus convection on tropical circulation and its associated precipitation by comparing the results from two climate simulations, one with and one without convection. It is found that with convection the total condensation heating in the tropics is shifted equatorward and the total condensation drying is more concentrated in the lower troposphere. In association with the heating shift, the Hadley circulation also changed its location. In the no convection run its centre is near the equator, with the rising branch locate near 15 ° N. In the

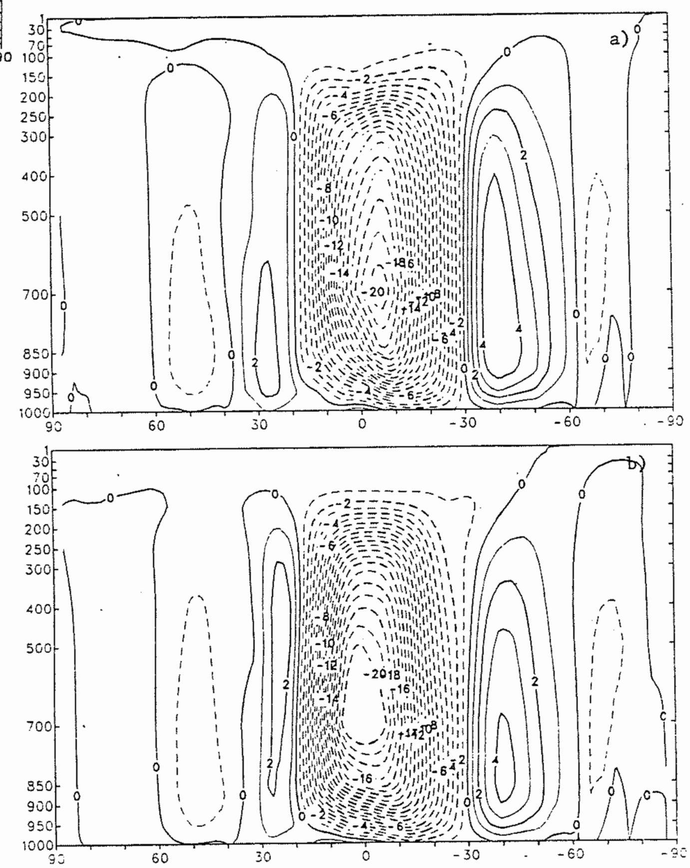

Fig. 2 Meridional mass stream function for a) convection and b) no convection simulations, contour interval: 10^{10} kg s^{-1}.

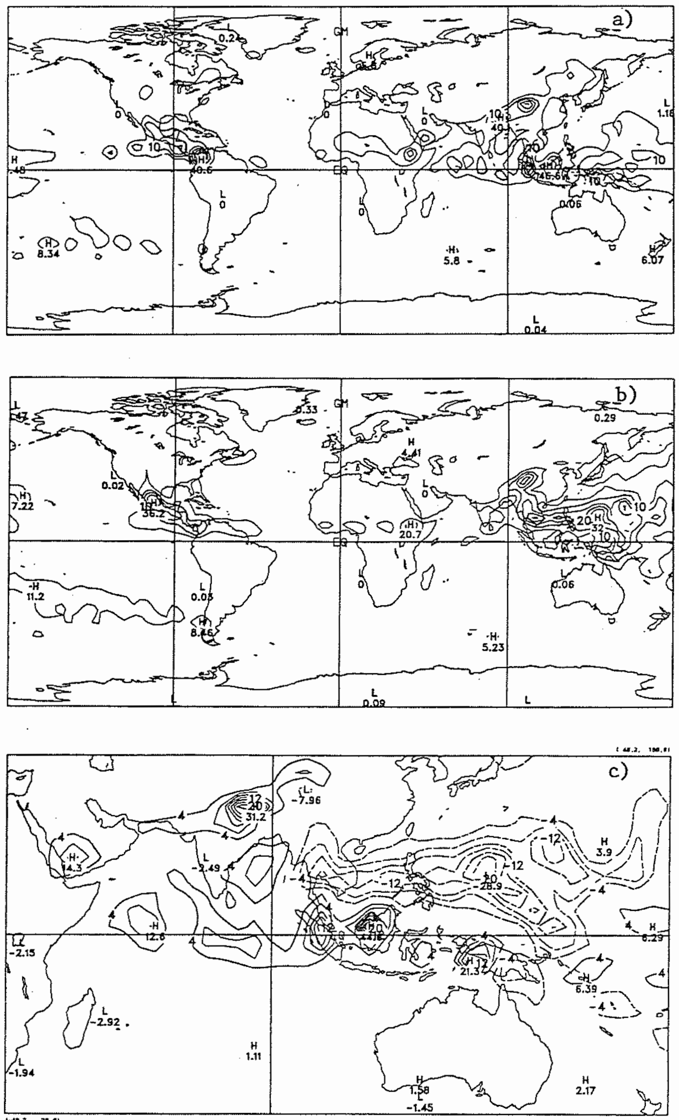

Fig. 3 Total precipitation distribution for a) convection, b) no convection simulations and c) their difference in the western Pacific, contour intervals: 5 mm day^{-1} for a) and b), 4 mm day^{-1} for c).

convection run, its rising branch is located almost right over the equator. Also, corresponding to the more heating in the no convection case, the Hadley cell is stronger. The precipitation distributions with or without convection is considerably different over the western Pacific and the Indian monsoonal regions. They are clearly related to the location of the Hadley circulation. The circulation and precipitation difference with or without convection can be related to the convective stabilization of the tropical atmosphere. Details of this will be presented at the conference.

4. REFERENCES

Arakawa, A. , and W.H. Schubert, 1974: Interaction of cumulus cloud ensemble with the large-scale environment, Part I. J. Atmos. Sci., **31**, 674-701.

Donner, L.J., H.-L. Kuo, and E.J. Pitcher, 1982: The significance of thermodynamic forcing by cumulus convection in a general circulation model. J. Atmos. Sci., **39**, 2159-2181.

Kuo, H.-L., 1974: Further studies of the properties of cumulus convection on the large scale flow. J. Atmos. Sci., **31**, 1232-1240.

McFarlane, N.A., G.J. Boer, J.-P. Blanchet, and M. Lazare, 1992: The Canadian Climate Centre second generation general circulation model and its equilibrium climate. J. Climate, in press.

Sud, Y.C., W.C. Chao, and G.K. Walker, 1992: Role of a cumulus parameterization scheme in simulating atmospheric circulation and rainfall in the nine-layer Goddard Laboratory for Atmospheres general circulation model. Mon. Wea. Rev., **120**, 594-611.

SENSITIVITY OF QUANTITATIVE PRECIPITATION FORECASTS (QPF) TO SPATIAL RESOLUTION USING A MESOSCALE MODEL WITH EXPLICIT CLOUD PHYSICS

Michael P. Meyers and William R. Cotton

Colorado State University, Dept. of Atmospheric Science,
Fort Collins, CO 80523

1. INTRODUCTION

As computer capabilities increase and the availability of observational data continues to grow, numerical forecast models are being run with greater resolution. More powerful computers also enable the models to be run with more complex physics which is especially important for microphysical considerations. With an explicit treatment of cloud microphysics, the models not only can produce quantitative precipitation forecasts (QPF), but can also distinguish between frozen and liquid precipitation, which would be very useful for hydrological purposes.

Meyers and Cotton (1992) applied the two-dimensional version of the Regional Atmospheric Modeling System (RAMS) developed at Colorado State University (CSU) to a prolonged orographic precipitation event which occurred over the Sierra Nevada range in central California on 12-13 February 1986. This well observed case study selected from the Sierra Cooperative Pilot Project (SCPP) (Reynolds and Dennis, 1986) data base documents the microphysical and precipitation evolution of the storm quite well (Rauber, 1992). The simulated results compared well with the observed kinematic structure, microphysical structure and surface precipitation. These simulations demonstrated the feasibility of producing a quantitative precipitation forecast (QPF) with an explicit cloud model. The precipitation distribution of the orographic system was especially sensitive to the model initialization.

This study investigates this topographically complex area, with the 3-D nested-grid version of RAMS. Versions of the model are run at different grid configurations to allow examination of the sensitivity of QPF to increasing the spatial resolution. The increased resolution is attained by adding grid nests to the initial coarse grid. These interactive nested-grid simulations are initialized with an inhomogeneous objective analysis. Comparisons of the kinematic, microphysical, and precipitation structure between simulations and to observations is conducted.

2. NUMERICAL MODEL

The numerical model used in this study is RAMS and is configured similarly as described in Meyers and Cotton (1992). This case is investigated via the three-dimensional nested-grid non-hydrostatic version of RAMS. The horizontal grid spacing in a preliminary model configuration is 50 km with a 45 second timestep on the coarse grid (grid 1), and a 12.5 km horizontal grid spacing with a timestep of 22.5 seconds on grid 2. To maximize vertical resolution in the lower levels, the vertical grid was stretched from 150 m near the surface to 750 m above the barrier. The initialization for this simulation was prepared with an isentropic data analysis package described in Tremback (1990). Data sets used in the analysis included

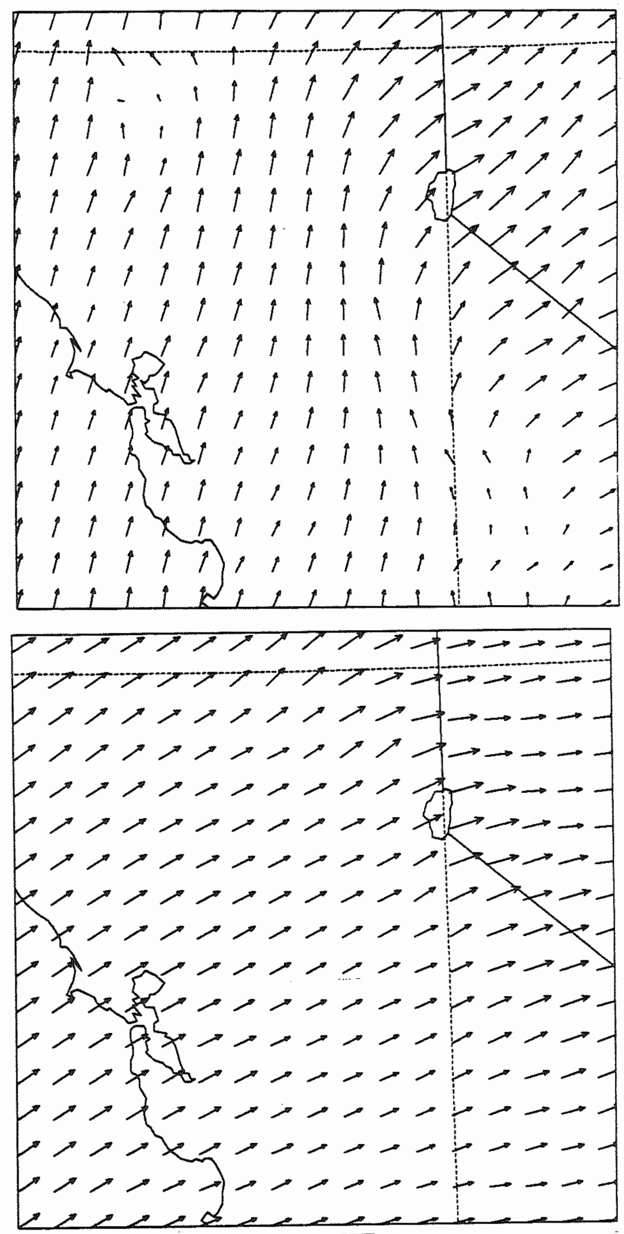

Fig. 1: Horizontal wind vector field at 0.9 km AGL (top) and 3.9 km MSL (bottom) at 1500 UTC of simulation for grid 2. Maximum vector is 32.0 m s^{-1}. The 40°N latitude and 120°W longitude are indicated by the dashed lines.

NMC global analyses and archived rawinsondes. The Barnes objective analysis scheme was then applied to these variables after being interpolated to isentropic surfaces. The first simulation was initialized at 00 UTC on 12 February 1986 and run with only the coarse grid out to 24 h, the second simulation added a finer grid having a 12.5 km grid spacing after 6 hours of simulation and also was run to 24 h.

3. MODEL RESULTS

It is most important to the success of the simulation to accurately predict the kinematic structure. Wind fields at 1600 UTC of the simulation compared well with the observations (Rauber, 1992). Winds at 0.9 km AGL for the grid 2 (Fig. 1a) exhibited a strong south to south-southeasterly component of wind oriented over central California located over the western slope of the Sierra Nevada range. This mountain parallel component of the wind, or "barrier jet" (Parish, 1982) was simulated as strong as 24 m s^{-1}, observed values were about 25 m s^{-1}. The winds veered to southwesterly to the lee of the Sierra crest and strengthened to 32 m s^{-1} indicating downslope flow in this region. The winds at 3.9 km MSL for the fine grid (Fig.1b) exhibited a strong southwesterly moist flow off the Pacific similar to observations. The microphysical structure (not shown) is very similar the observations, however, magnitudes are smaller than observations especially for the coarse grid. The simulated total precipitation for 24 h for the grid 1 is given in Fig. 2a. The distribution exhibits a precipitation maximum (40 mm) close to the observed maximum of 90 mm, but underpredicts it by 50 mm. The overall structure of the distribution is quite smooth compared to the observations lacking small scale variations which are found in the observations. The simulated total precipitation for 24 h for grid 2 shows more small scale variations in the precipitation structure which compares better to the observations than in grid 1. This maximum is slightly northwest and nearly 40 mm greater in magnitude than the observed maximum. Although not perfect both of these runs perform quite well in simulating the observed precipitation structure.

4. CONCLUSIONS

This study has shown the feasibility of using RAMS as a mesoscale QPF model. With the objective analysis of input meteorological data, the simulation evolves more realistically, improving model results. Both the predicted kinematic and microphysical structures were similar to the observations but the maximum values of hydrometeor mixing ratios were underpredicted by the model. The predicted precipitation from the coarse grid was similar in structure but peak values were less than half than observed. The addition of grid 2 produced more small-scale features seen in the observations but maximum values were overpredicted. Model results which employ a larger second grid domain and adding a third grid with 3 km grid spacing will be discussed in the presentation.

5. ACKNOWLEDGEMENTS

Brenda Thompson is thanked for her assistance with the manuscript. This research was supported by the Army Research Office under contract #DAAL03-86-K-0175 and the Air Force Office of Scientific Research under contract AFOSR-91-0269.

7. REFERENCES

Meyers, M.P. and W.R. Cotton, 1992: A wintertime orographic quantitative precipitation forecast with an explicit cloud model. Part I: Two-dimensional sensitivity experiments. *J. Appl. Meteor.*, **31**, 26-50.

Parish, T., 1982: Barrier winds along the Sierra Nevada mountains. *J. Appl. Meteor.*, **21**, 925-930.

Rauber, R.M., 1992: Microphysical structure and evolution of a central Sierra Nevada shallow orographic cloud system. *J. Appl. Meteor.*, **31**, 26-50.

Reynolds, D.W., and A.S. Dennis, 1986: A review of the Sierra Cooperative Pilot Project. *Bull. Amer. Meteor. Soc.*, **67**, 513-523.

Tremback, C.J., 1990: Numerical simulation of a mesoscale convective complex: model development and numerical results. Ph.D. dissertation, Colorado State University, Dept. of Atmospheric Science, Fort Collins, CO 80523.

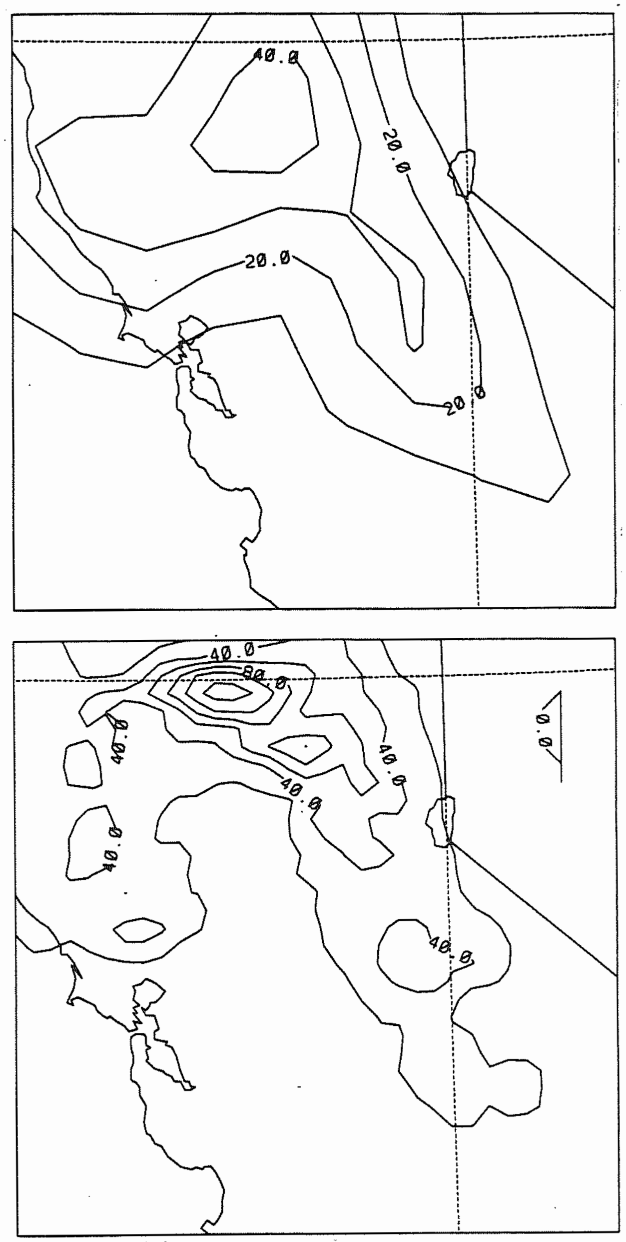

Fig. 2: Total 24 h precipitation (mm) for coarse grid domain which is scaled to the size of the fine grid (top) and for fine grid domain (bottom). Contour interval is 20.0 mm. The 40°N latitude and 120°W longitude are indicated by the dashed lines.

THE SEMI-EMPIRICAL BASIS OF A PROGNOSTIC CLOUD PARAMETERIZATION FOR USE IN CLIMATE MODELS

Kuan-Man Xu and David A. Randall

Department of Atmospheric Science
Colorado State University
Fort Collins, CO 80523, U.S.A.

1. INTRODUCTION

Clouds can directly or indirectly interact with radiative, dynamical and hydrological processes on a wide range of time scales. An accurate representation of clouds is crucial to simulate the various components of the atmospheric hydrological cycle of the climate system (Arakawa 1975; Randall 1989; Randall et al. 1989). However, the understanding of the formative and dissipative processes of clouds is very poor.

There is now an increased effort to improve the cloud formation parameterization with prognostic equations for cloud water species (cloud water, cloud ice, rainwater, snow and/or graupel). This type of prognostic cloud parameterizations generally requires the formulations of (i) the source/sink of the cloud water species and (ii) the fractional cloudiness (e.g., Sundqvist 1978; Smith 1990; Le Treut and Li 1991; Ghan and Easter 1992; Smith and Randall 1992). The fractional cloudiness is basically related to large-scale relative humidity in existing parameterizations, regardless the existence of cloud water/ice (Sundqvist 1978; Smith 1990). Relative humidity is, however, poorly predicted in climate models. Therefore, an improved formulation of fractional cloudiness is necessary.

This study outlines the framework of a prognostic cloud parameterization. One of the key elements of this project is to use prognostic cloud water/ice as a predictor in a semi-empirical (diagnostic) cloudiness parameterization, as an extension of the work of Xu and Krueger (1991; hereafter, XK). This project is coupled with the work of Smith and Randall (1992) who formulate the microphysical source/sink terms of the prognostic cloud parameterization.

The predicted (large-scale average) condensate mixing ratios can be related to those of cloud-scale average through the fractional cloudiness when the condensate mixing ratios of clouds are horizontally uniform, which is approximately true for stratiform clouds. The cloud-scale average condensate mixing ratios are controlled by microphysical and small-scale cloud-dynamical processes. They should be amenable to semi-empirical parameterization. Thus, the formulation of microphysical source/sink terms should be based largely on the cloud-scale and environmental variables, *not* solely on the large-scale average variables which are used in existing parameterizations (Sundqvist 1978; Smith 1990). Utilization of the cloud-scale and environmental variables is the second key element of the proposed parameterization.

A difficulty in developing such a prognostic cloud parameterization arises from the lack of observable cloud-scale data for verifying the parameterization. Fortunately, a cloud ensemble model (CEM), which covers a large horizontal area with a sufficiently small grid size, can provide such a dataset. CEMs have been used to simulate the formation of an ensemble of clouds under a given large-scale condition (Tao and Soong 1986; XK; Xu and Arakawa 1992a, b). This study utilizes a CEM as a tool for verifying the basis of a cloud parameterization.

2. A PROGNOSTIC CLOUD PARAMETERIZATION

A major element of the proposed parameterization is to utilize the cloud-scale and environmental variables, such as the cloud water species, temperature (T) and water vapor mixing ratio (q_v), in formulating the source/sink of the cloud water species. How can we obtain these variables? Let a be the known fractional cloud area (see section 4 for details). The large-scale average condensate mixing ratios are predicted from their respective prognostic equations. Therefore, the cloud-scale average condensate mixing ratios can be obtained from

$$\overline{q_i} = a q_i, \tag{1}$$

where subscript i can be cloud water, cloud ice, snow, graupel and snow. The overbar denotes the large-scale average.

The cloud-scale average T and q_v (q^*) are governed by

$$\begin{aligned} \overline{h} &= a h_c + (1-a)\widetilde{h}, & (2)\\ \overline{q_v} &= a q^* + (1-a)\widetilde{q_v}, & (3)\\ q^* &= q^*(T_c, p), & (4) \end{aligned}$$

where h is the moist static energy, $h \equiv c_p T + gz + L q_v$, c_p the specific heat at constant pressure, g the constant of gravity, L the latent heat of vaporization, q^* the saturation mixing ratio of water vapor, z the height and p the pressure. The tilde denotes the environment (clear area) and the subscript c denotes cloudy regions. Note that $\overline{h}$ and $\overline{q_v}$ are known at a given instant.

Equations (2–4) indicate that q^*, $\widetilde{q_v}$ and $\tilde{h}$ can be obtained if T_c is known. There are four unknowns (T_c, q^*, $\widetilde{T}$, $\widetilde{q_v}$) but only three equations. Therefore this set of equations is not closed. We should not specify T_c in order to solve this set of equations. Thus, another equation involving T_c, q^*, $\widetilde{T}$ or $\widetilde{q_v}$ is required. This is called the *closure assumption*, as commonly used in cumulus parameterizations (Arakawa and Chen 1987). A closure assumption is not just a mathematical equation; it must be physically realistic.

Without considering the effect of condensate loading, the virtual temperature in cloudy regions must be higher than that in the environment. When the loading effect is included, the virtual temperature in cloudy regions is reduced. We expect that *the virtual temperature with condensate loading effect in stratiform cloud regions is approximately equal to the virtual temperature of the environment.* We choose this as the closure assumption. It is expressed as

$$\widetilde{T_v} - (T_v)_c = 0, \tag{5}$$

or

$$T_c(1 + \epsilon q^* - q_l) = \widetilde{T}(1 + \epsilon \widetilde{q_v}), \tag{6}$$

where q_l is the total condensate mixing ratio which is obtained from (1), and $\epsilon = 0.608$. Using the definition of h, subtracting (3) from (2) gives

$$\widetilde{T} = (\overline{T} - aT_c)/(1 - a). \tag{7}$$

Substitution of (7) into (6) yields

$$T_c(1 + \epsilon q^* - q_c) = (1 + \epsilon \widetilde{q_v})(\overline{T} - aT_c)/(1 - a). \tag{8}$$

Then,

$$\begin{aligned} T_c &= \overline{T} - (1-a)T_c(\epsilon q^* - q_c) + \epsilon(\overline{T} - aT_c)\widetilde{q_v} \\ &= \overline{T} - (1-a)T_c(\epsilon q^* - q_c) \\ &+ \epsilon(\overline{T} - aT_c)(\overline{q_v} - aq^*)/(1 - a), \end{aligned} \tag{9}$$

where (3) has been used. Using (4), T_c can be obtained iteratively. Then, $\tilde{h}$ and $\widetilde{q_v}$ can be obtained from (2) and (3), respectively. When $a = 1$, (9) gives

$$T_c = \overline{T}. \tag{10}$$

Le Treut and Li (1991) used (10) as one of the assumptions.

As mentioned in section 1, these cloud-scale and environmental variables are used in formulating the microphysical source/sink terms. This aspect is discussed by Smith and Randall in this Proceeding.

3. VERIFICATION OF CLOSURE ASSUMPTION

Two simulations (with and without geostrophic wind shear) from the UCLA CEM are used in this study; these are identical to those described in Xu and Arakawa (1992b) except with (i) a smaller domain size (128 km), (ii) a smaller grid size (1 km) and (iii) time-independent large-scale advective effects.

Figure 1 shows the scatter diagrams of $\widetilde{T_v}$ vs. $(T_v)_c$ for *stratiform only* and *all types of clouds* (stratiform plus convective) at 7.9 km and 3.5 km. The separation of stratiform and convective clouds is based on the vertical velocity (w) and slightly differs from that used in XK. Convective clouds are assumed to exist at a CEM grid point if either (i) w is greater than 1 $m\,s^{-1}$, (ii) w is twice greater than the average of the adjacent grids or (iii) w at either adjacent grid is greater than 1 $m\,s^{-1}$. A majority of convective clouds is detected by the first criterion.

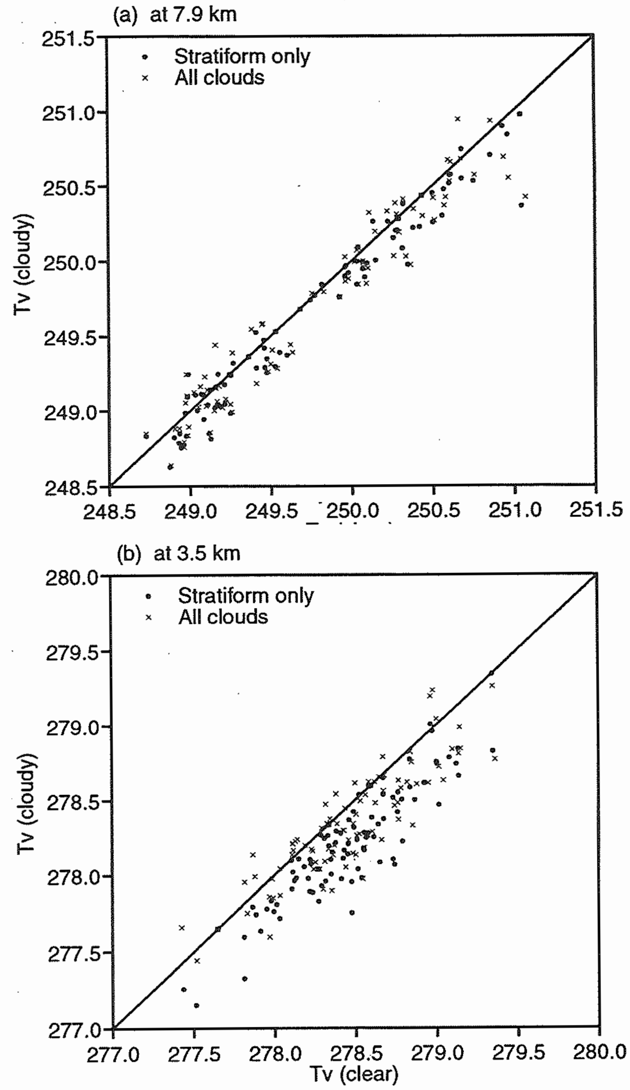

Fig. 1. The scatter diagrams of virtual temperature in clear areas versus virtual temperature in cloudy regions at (a) 7.9 km and (b) 3.5 km. Each data point represents an average over an hour in time and over 64 km in horizontal extent.

Figure 1 reveals that the closure assumption is basically valid. The variances (R^2; see XK for details) explained by the linear relation of (5) are very high; i.e., 96% at 7.9 km and 81% at 3.5 km. Note that $\widetilde{T_v}$ in the lower troposphere (Fig. 1b) is slightly higher than $(T_v)_c$ due to the subsidence warming caused by cumulus convection. The closure assumption is more likely to be valid at any level in the absence of cumulus convection. We have also examined R^2 for a similar relation expressed by (5) except for the temperature. It is found that R^2 is always smaller at any level.

4. DIAGNOSIS OF FRACTIONAL CLOUDINESS

XK showed that the stratiform cloudiness is best predicted on the basis of relative humidity ($\overline{RH}$) while convective cloudiness is related to cloud mass flux (M_c) for diagnostic cloud parameterizations. In prognostic cloud parameterizations the liquid water (+ice) path (LWP) is available. It can be used as a predictor for fractional cloudiness.

Figure 2 shows the scatter diagrams of cloud amount vs. LWP averaged over 64 km at selected levels for both simulations. The cloud amount is highly correlated at most levels for both simulations. The correlation is slightly lower in the upper troposphere (Table 1). This result indicates that the LWP is a good predictor for fractional cloudiness of *an ensemble of clouds* although a large LWP may *not* necessarily correspond to a large areal extent of an individual cloud.

Table 1 compares the correlation and the explained variance (R^2) of cloud amount at selected levels using the LWP and $\overline{RH}$ as the predictors. Except for the upper troposphere (10.8 km), the correlation and R^2 using the LWP are much higher than those using $\overline{RH}$. This suggests that the cloud amount is much better estimated using the LWP than using $\overline{RH}$. The large scatter in the upper troposphere (e.g., Fig. 2a) suggests that some large-scale variables are needed to accurately estimate the fractional cloudiness.

We propose a linear relation of fractional cloudiness using LWP and $\overline{RH}$ as the predictors

$$a = \alpha I + \beta(\overline{RH} - RH_0) \qquad (11)$$

where I denotes the LWP, α, β and RH_0 are determined from linear regressions.

As seen from Table 1b, R^2 at every level is higher when LWP and $\overline{RH}$ are used as predictors than when either of them is used. Because of the high R^2 (Table 1), (11) is a very good relation for estimating fractional cloudiness. It has never been used in existing prognostic parameterizations (Sundqvist 1978; Smith 1990; Le Treut and Li 1991).

5. CONCLUSIONS AND FUTURE WORK

We have proposed a prognostic cloud parameterization which utilizes the cloud-scale and environmental variables for

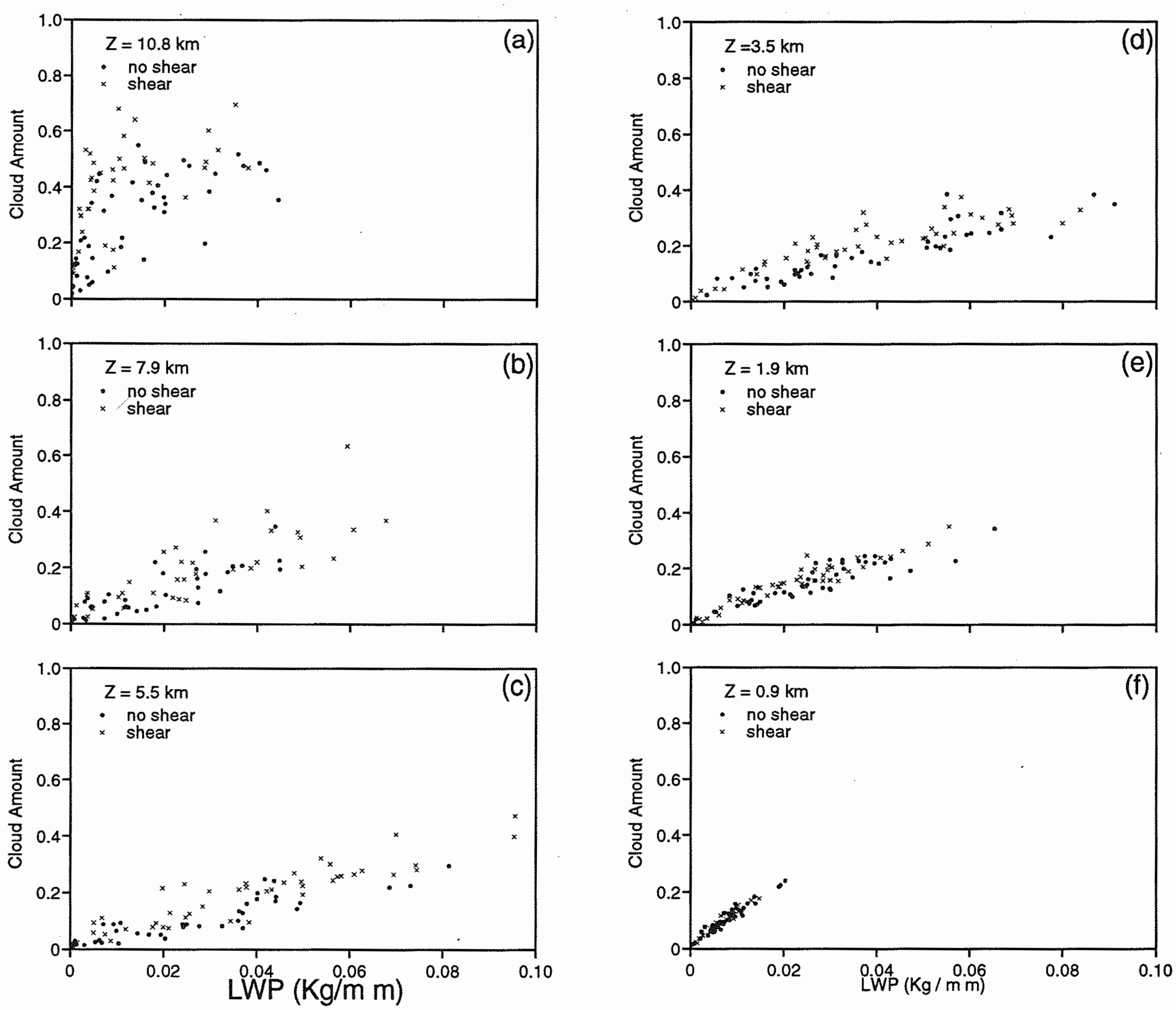

Fig. 2. The scatter diagrams of the cloud amount versus liquid water/ice path (LWP) for both simulations [no shear (dot) and shear (cross)] at (a) 10.8 km, (b) 7.9 km, (c) 5.5 km, (d) 3.5 km, (e) 1.9 km and (f) 0.9 km. Each data point represents an average over an hour in time and over 64 km in horizontal extent.

(a) correlation coefficient

Level	0.9 km	1.9 km	3.5 km	5.5 km	7.9 km	10.8 km
RH	0.34	0.61	0.80	0.71	0.73	0.75
LWP	0.97	0.93	0.90	0.92	0.88	0.61

(b) explained variances (R^2)

Level	0.9km	1.9km	3.5km	5.5km	7.9km	10.8km
RH	0.14	0.34	0.67	0.54	0.50	0.57
LWP	0.93	0.84	0.76	0.83	0.72	0.31
LWP+RH	0.95	0.90	0.88	0.91	0.82	0.72

Table 1. (a) The correlation coefficient between the cloud amount and a predictor (RH: relative humidity; LWP: liquid water+ice path) at selected levels. (b) Same as in (a) except for the explained variances of fractional cloudiness using RH, LWP as the predictor or using both RH and LWP (LWP+RH) as the predictors.

formulating microphysical source/sink terms and uses liquid water+ice path (LWP) as one of the predictors for estimating fractional cloudiness.

To determine the cloud-scale and environmental variables, a closure assumption has been introduced; i.e., the virtual temperature with condensate loading effect in stratiform cloud regions is approximately equal to the virtual temperature of the environment. This assumption has basically been verified using data simulated from a cloud ensemble model. The data have also been used to provide a semi-empirical cloudiness parameterization using LWP and $\overline{RH}$ as the predictors.

Further work includes (i) the refinement of the fractional cloudiness relation with simulations typical of stratiform cloud regimes and (ii) the inclusion of the inhomogeneity of cloudy regions in contributing to the condensation/evaporation. The cloud ensemble simulations will be extensively used in the research, in conjunction with observed data from the Atmospheric Radiation Measurement program.

Acknowledgments: This study was supported by the U.S. Department of Energy's Atmospheric Radiation Measurement program under Grant DE-FG02-92ER61363, and by the National Science Foundation (NSF) under Grant ATM-8907414. The computations were performed at the NCAR SCD. NCAR is sponsored by the NSF.

References

Arakawa, A., 1975: Modeling clouds and cloud processes for use in climate models. *The Physical Basis of Climate and Climate Modelling*, GARP Publ. Ser. No. 16, 181-197.

——, and J.-M. Chen, 1987: Closure assumptions in the cumulus parameterization problem. *Short- and Medium Range Numerical Prediction*, Collection of Papers at the WMO/IUGG NWP Symposium, Tokyo, 4-8 August, 1986, 107-131.

Ghan, S. J., and R. C. Easter, 1992: Computationally efficient approximations to stratiform cloud microphysics parameterization. *J. Geophys. Res.*, (submitted).

Le Treut, H., and Z.-X. Li, 1991: Sensitivity of an atmospheric general circulation model to prescribed SST changes: Feedback effects associated with the simulation of cloud optical properties. *Climate Dyn.*, **5**, 175-187.

Randall, D. A., 1989: Cloud parameterization for climate models: Status and prospects. *Atmos. Res.*, **23**, 345-362.

——, Harshvardhan, D. A. Dazlich, and T. G. Corsetti, 1989: Interactions among radiation, convection, and large-scale dynamics in a general circulation model. *J. Atmos. Sci.*, **46**, 1943-1970.

Smith, L. D., and D. A. Randall, 1992: Parameterization of cloud microphysical processes in the CSU general circulation model. *Atmospheric Science Paper No. 491*, Colorado State University.

Smith, R. N. B., 1990: A scheme for predicting layer clouds and their water content in a general circulation model. *Quart. J. Roy. Meteor. Soc.*, **116**, 435-460.

Tao, W.-K., and S.-T. Soong, 1986: A study of the response of deep tropical clouds to mesoscale processes: Three-dimensional numerical experiments. *J. Atmos. Sci.*, **43**, 2653-2676.

Sundqvist, H., 1978: A parameterization scheme for non-convective condensation including prediction of cloud water content. *Quart. J. Roy. Meteor. Soc.*, **104**, 677-690.

Xu, K.-M., and A. Arakawa, 1992a: The macroscopic behavior of cumulus ensembles simulated by a cumulus ensemble model. *J. Atmos. Sci.*, **49**, (in press).

——, and ——, 1992b: Semi-prognostic tests of the Arakawa-Schubert cumulus parameterization using simulated data. *J. Atmos. Sci.*, **49**, (in press).

——, and S. K. Krueger, 1991: Evaluation of cloudiness parameterizations using a cumulus ensemble model. *Mon. Wea. Rev.*, **119**, 342-367.

APPENDIX

Late Papers

Papers on the pages that follow arrived too late to be included in their proper sessions.

THEORETICAL ASPECTS IN THE DEVELOPMENT OF A MULTILEVEL CLOUD RETRIEVAL ALGORITHM

Robert F. Arduini[1], Bryan A. Baum[2], and Eric O. Schmidt[1]

[1]Lockheed Engineering and Sciences Company, Hampton, VA 23666
[2]Atmospheric Sciences Division, NASA Langley Research Center, Hampton, VA 23665

1. INTRODUCTION

Cloud retrieval algorithms have been developed to estimate cloud parameters such as the height, fractional coverage, optical depth, phase, and particle size from satellite data. Some algorithms involve comparisons of remotely-sensed data and theoretically derived quantities. In general, these algorithms perform best for single cloud layers. However the occurrence of multiple cloud layers is common and their attendant complications provide the impetus to develop second-generation cloud retrieval algorithms, perhaps by combining algorithms and/or datasets. This study addresses some of the theoretical aspects in the radiative transfer modeling of multilevel clouds as they apply to a second-generation cloud retrieval algorithm such as that described by Baum et al. (1992). Theoretical modeling is used to esimate cloud particle size and phase and supplements the retrieval of cloud properties from satellite data.

The primary tools in performing these studies are the radiative transfer codes Lowtran 7 and the Discrete Ordinates Radiative Transfer (DISORT) model. Scattering phase functions for cloud particles are developed from Mie calculations for water droplets and are used to model the optical properties of low- and mid-level stratus clouds. Phase functions for hexagonal ice crystals are used for the overlaying cirrus layers. Theoretical simulations of the upwelling radiance received by the satellite sensors are combined and compared with data from the High Resolution Infrared Sounder (HIRS/2) and the Advanced Very High Resolution Radiometer (AVHRR) during the Surface Radiation Budget Maritime Experiment at Bermuda during April, 1989. These comparisons help to identify some of the sensitivities of the retrieval algorithm to the microphysical cloud parameters.

2. CLOUD/ATMOSPHERE RADIATIVE TRANSFER

Two radiative transfer models are used in this study, one for developing a clear-sky transmittance and optical depth profile, and the other for computing a full multiple-scattering solution to the radiative transfer equation. Lowtran 7 (Kneizys, 1988) is used to develop the clear-sky optical depth profile that includes the effect of atmospheric absorbers at all levels in the atmosphere. In-situ temperature and relative humidity profiles provided by ECMWF (European Center for Medium-Range Weather Forecasting) during the Bermuda experiment proide input to Lowtran 7 which is then used to compute transmittances in 1 km layers in the AVHRR atmospheric window channels.

The code used to compute the upwellng radiances is an optimized form of the discrete ordinate method to solve the radiative transfer equation. This method, first proposed by Chandrasekhar (1960), has been further developed and discussed in the literature by, for example, Wiscombe and Joseph (1977), Stamnes and Swanson (1981), Stamnes and Dale (1981), Stamnes and Conklin (1984), and Stamnes, et al., (1988). We assume that the atmosphere consits of a number of adjacent homogeneous layers. The single scattering albedo and the phase function are constant within each layer, but may vary from layer to layer. The ability to have different scattering properties in each of the atmospheric layers makes DISORT useful in the investigation of the properties of multilevel cloud scenarios. Since the model includes thermal infrared absorption and emission, the model can be used to predict upwelling daytime AVHRR radiance measurements at 3.7 microns where both solar reflection and thermal emission processes are important. Calculations for the AVHRR NIR and IR channels are performed for a central wavelength only.

The situation simulated here is an emitting surface with two overlaying cloud layers. The lower layer is characteristic of a stratus cloud composed of water spheres with a cloud-base height of approximately 1.5 km. The upper cloud layer has its base at about 11 km and is comprised of hexagonal ice crystals. We simulate radiance measurements for 3.7-, 10.8-, and 12.0-micron AVHRR channels. For this study only nighttime conditions have been simulated and so no solar component is considered.

The phase functions for scattering by the stratus cloud particles are generated using Wiscombe's (1979) Mie scattering code for a gamma-distribution of water spheres (see, Hansen and Travis, 1977) having an effective radius of 8 microns and effective variance of 0.2. This distribution has a mode radius of 3.2 microns. The phase functions for the overlaying cirrus clouds were assembled from Takano and Liou's (1989) phase functions for five sizes of randomly oriented hexagonal ice crystals. Distributions typical of cirrostratus, cirrus uncinus and cold cirrus were used.

A major concern in radiative transfer calculations that include scattering is the extreme magnitude of the forward peak in the phase function. This is particularly true for ice crystals. A technique for reducing the number of Legendre terms required to fit the phase function is to truncate the forward peak and then renormalize the phase function, Potter (1970). This also reduces the number of streams required in DISORT. Truncation is applied to the hexagonal ice crystal phase functions used here. The number of Legendre terms is kept to 32.

3. COMPARISON OF SIMULATIONS WITH DATA

The multispectral, multiresolution (MSMR) technique of Baum, et. al (1992) is used to estimate the altitudes of the cloud layers in a multilevel cloud scene taken o April 16, 1989 at approximately 6 UTC during the Surface Radiation Budget Maritime Experiment at Bermuda. The lower cloud consists of a large scale (>300 km) stratus deck at approximately 1.5 km. The cirrus layer is at about 11 km. Using the cloud-height estimates we then simulate the AVHRR radiances in channels 3 (3.7 microns), 4 (10.8 microns) , and 5 (12.0 microns) and compute the brightness temperatures and their differences. By comparing our simulated results with the actual measured results we can obtain estimates of the sizes and phase of the cloud particles. Figures 1 and 2 show some of the typical comparisons for this data set. The simulations shown are for a cold cirrus distribution of hexagonal ice crystals at the indicated temperatures over a stratus deck composed of water droplets having an optical depth 5 at 282 K. The surface is at 295 K. The cirrus optical depth varies from right to left on the curves from 0.01 to 50. The observations are indicated by the symbols on the figures and were chosen from an AVHRR 10.8-micron brightness temperature image of the Bermuda site.

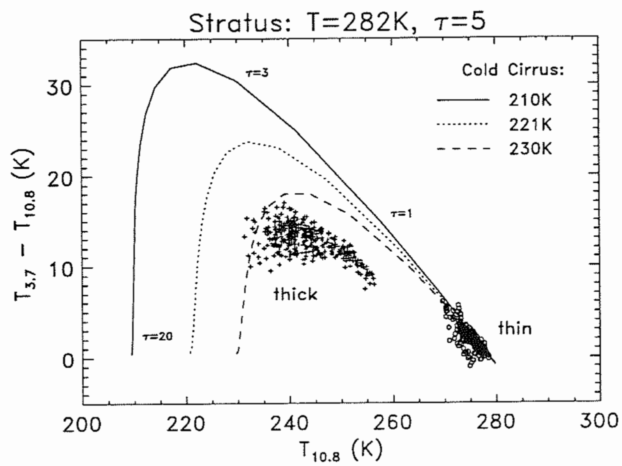

Figure 1. Comparison of simulated and measured brightness temperature differences between AVHRR channels 3 and 4 for multilevel cloud case. 10.8-micron optical depth of the simulated stratus layer is indicated. Observations of thin and thick overlaying cirrus from AVHRR 10.8-micron image of the Bermuda site at 6 UTC, April 16, 1989.

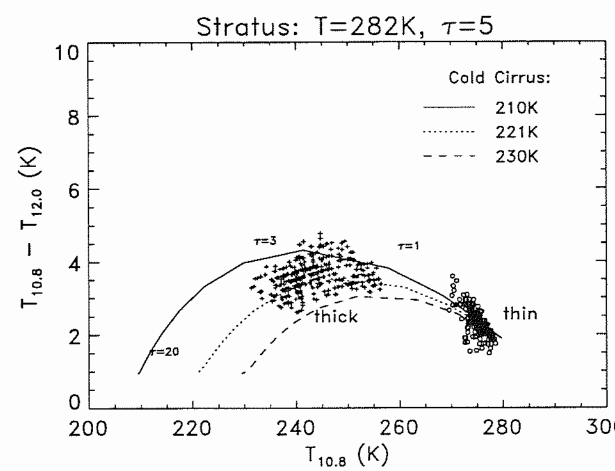

Figure 2. Same as Figure 1, except AVHRR channels 4 and 5.

4. SUMMARY AND CONCLUSIONS

The techniques described here highlight some of the areas that must be carefully accounted for in the development of an advanced cloud retrieval algorithm. This type of algorithm depends on being able to identify the presence of multilevel clouds and to estimate the height of each layer. With this information, our results show that theoretical analyses can assist in the interpretation of the observed brightness temperature differences, that, in turn, can lead to estimates of the size and phase of the cloud particles and the optical depth of the upper cloud layers.

5. REFERENCES

Baum,B.A., B.A. Wielicki, P. Minnis, and L. Parker, 1992: Cloud-property retrieval using merged HIRS and AVHRR data. J. Appl. Met., 31, No.4, 351-369.

Chandrasekhar,S., 1960: Radiative Transfer, Doiver Publications, New York.

Hansen,J.E., and L.D.Travis, 1974: Light scattering in planetary atmospheres. Space Science Reviews, 16, 527-610.

Kneizys,F.X., E.P.Shettle, L.W.Abreu, J.H.Chetwynd, G.P.Anderson, W.O.Gallery, J.E.A.Selby, and S.A.Clough, 1988: User's guide to Lowtran 7, AFGL-TR-88-0177.

Potter,J.F., 1970: The delta function approximation in radiative transfer theory. J. Atmos. Sci., 27, 943-949.

Stamnes,K, and R.A.Swanson, 1981: A new look at the discrete ordinate method for radiative transfer calculations in anisotropically scattering atmospheres, J. Atmos.Sci., 38, 387-399.

Stamnes,K, and H.Dale, 1981: On the discrete ordinate method for radiative transfer calculations in anisotropically scattering atmospheres. II. Intensity computations. J. Atmos.Sci., 38, 2696-2706.

Stamnes,K, and P.Conklin, 1984: A new multi-layer discrete ordinate approach to radiative transfer in vertically inhomogeneous atmospheres. J. Quart. Spectrosc. Radiat. Transfer, 31, No.3, 273-282.

Stamnes,K., S.-C.Tsay, W.Wiscombe, and K.Jayaweera, 1988: Numerically stable algorithm for discrete-ordinate-method radiative transfer in multiple scattering and emitting layered media. Applied Optics, 24, 2502-2509.

Takano,Y., and K.-N.Liou, 1989a: Solar radiative transfer in cirrus clouds: Part I: Single-scattering and optical properties of hexagonal ice crystals. J. Atmos Sci., 46, 3-19.

Wiscombe,W.J., 1979: Mie scattering calculations: Advances in techniques and fast, vector-speed computer codes. NCAR/TN-140_STR.

Wiscombe,W.J., and J.H.Joseph, 1977: The range of validity of the Eddington approximation. Icarus, 32, 362-377.

AERIAL RAINFALL MEASUREMENTS

Willy S Goma
central forecast office
Department of meteorology
P.o box 310095,Lusaka,Zambia

1 INTRODUCTION

Orbiting satellite provide routine observations of the atmosphere,the land surface,and the sea. Data acquired by satellite can be applied to many of the geophysical sciences. Satellite can provide a more frequent data coverage than standard meteorological observations reporting every six , twelve or twenty four hours. These satellite images will be used to locate cloud zones and attempt to determine the amount of rainfall. The process of recording rainfall that has fallen over an area depends upon the type of weather prevailling at that time and its main measuring instrument is the raingauge . Therefore, in oder to account for rain which is unevenly distributed , over or underestimated, or in areas which are poorly instrumented meteosat images are used and estimation of rainfall amount is made . Utilization of satellite imagery information relating to the identification of the intertropical convergence zone severe convective storms, and frontal surface will be discussed.Reference in this presentaion will be made to Zambia which lies between 08 degrees south to 10 degrees in the southern Africa whose rainy season last from november - april. The weather is governed by Zaire air boundary (ZAB) , intertropical converg-ence zone (ITCZ), surface frontal system.

2. REGIONAL CLIMATE

Figure.1.shows the summer mean position of Zaire air boundary (ZAB) , southern intertropical convergence(SITCZ)

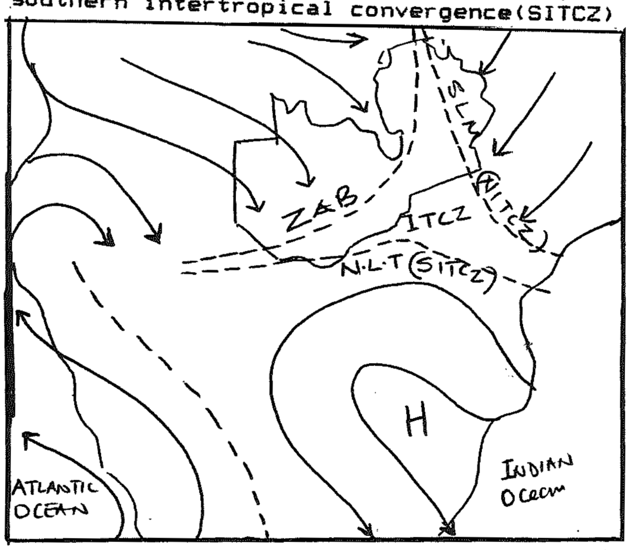

On the satellite picture acontinues inter tropical convergence cloud bands appear across the subcontinent extending into indian ocean . This occurs in December to february. With evidence of satellite images it is now possible to descible and redefine the intertropical convergence zone in more details. In this region of our study,as we experince the movement of cloud frontal towards south africa from the south west, it occassionally links up with the ZAB/ITCZ, to form a broad cloud of disturbed oriented northwest-southeast. In some cases when this cloud band is well -maked,ZAB/ITCZ previously oriented east - west, appears to be more meridional,tending to fall in lines it move, with the cloud band. The cloud band also appear to be more compact, more orgainsed and more active in the region of linkage. The band of disturbed weather takes 3 to 4 days to clear the subcontinent, after which this time the ZAB/ITCZ resumes it normal zonal pattern. When the link-up does not occur, the band of disturbed weather is usually less broad, less orgainsed and less active. The zonal characterist of the ZAB/ITCZ are then more pronounced. Forecasting 48 hours ahead depends on knowing the weather and where the linkage has occured, this is clear from the satellite picture see fig.2

Fig. 2

The intertropical convergence zone, a narrow east -west band of vigorous cumulonimbus convection and heavy precipitation which form along equitorial boundary on the trade winds regimes. These satellite pictures have also on several occasion during rainy seasons facilitated the location of the ITCZ especially when the synoptic data is sparse, and to identification of area where it is active. Satellite pictures have occassionally shown the double structure of the ITCZ see fig.4. However, by using satellite imagery it is posible to interprete and identify tropical storms. It is from these tropical storms where heavy showers come from. Moreover, by utilization of imagery information relating to brightness values to precipitation, then estimation of rainfall is possible from satellite data. More detailed pictures of precipitation amount and distribution wuold be of great beneficial to the meteorologist and hydrologist in poorly instrumented regions for purpose of dairy forecasting, catchment research flood water control etc

3. ESTIMATION OF RAINFALL

Estimation of amounts of rainfall from satellite picture is derived from statistical analysis of several dairy rainfall together with their duration of down pouring. Taking note or the prevailling weather at each time of observation e.g. thunderstorm with showers lasts for shorter period than rain. Therefore apporximate amount of rains will be as follows

$$\frac{\text{Rainfall}}{\text{Time}} = R_{mm}$$

where r_{mm} is estimated amount of rain from the observed convective cloud of cloud band visible on the satellite images. Intensity would be determined by the amount of rains that was falling over an area per minutes / secondes.

Second method, a graduated scale of squred ooxes wil be used by placing it on the satellite picture . This scale on transparent paper will show numbers of boxes which are area and show the coverage of the clouds.Each of the squred boxes when it is raining will be representing R as stated in above method However, in cases where clouds covers an uncomplete squre then the ground rainfall station may either by covered by the clouds or not. Therefore depending upon the location of the raingauge, if it at meteorological station , the weather may be widespread rain or scattered or distant precipitation. If then that tha raingauge was not covered by the clouds then amounts of rain will still be estimated on satellite from those cloud that are covering part of the squre. So rainfall will be as follows;

$$\tfrac{1}{2} \text{ or } R_{mm} = r_{mm}$$

where r is the estimated rainafall in that area of partially covered as shown on satellite image. Or depending on the ration of of cloud coverage the computation will still be dependent on cloud seen on the graduated scale,

$$X_{mm} \text{ of } R_{mm} = R_{mm}$$

where X is ratio of cloud cover in the squre or area concerned as seen on the satellite picture with the graduated scale.

4. CONCLUSION

The operational aspect of utilising the rainfall measurements from the satellite is a technique in a attempt to obtain a method of estimation of rainfall coverage ,intensity and duration in real time or immediary after the rainfall As such it will be possible to assist in events of network checking of readings of rainfall.Finally bearing in mind that estimated rainfall are not to be considered as official readings but as only for rough ideal but that still rainfall readings from from standard raingauges are official ones.

5. REFERENCE

Barret E C (1974) Climatology from satellite page II0-I2,Methuen & Co. Ltd.

Bhaletra Y P R (1973) Lectures notes on general meteorelogy,Published by Zambia meteorelogical department.

U.S.A dept of Commerce (1969) ESSA direct transmission systems users guide page 47-80, supersede APT users guide.

SATELLITE OBSERVATION OF INTERACTION BETWEEN DROPLET AND DUST CLOUDS IN THE CENTRAL ASIA

G.S. Golitsyn[1], D.A. Gillette[2], D. MacKinnon[3], V.V. Smirnov[4]

[1]Inst. atmospheric Physics, Russia Acad. of Sciences Moscow, 10917

[2]ARS/ARL NOAA, Boulder, Co 80303, USA

[3]U.S. Geological survey, Flagstaff, AZ 86001, USA

[4]Inst. experimental Meteorology, Hydrometeorological service of Russia, Obninsk, 249020

1. INTRODUCTION

Space sounding means have been used for a long time and successfully to discover the dust storms, to observe the large-scale dust clouds and to estimate their density (e.g. Grigor'yev and Lipatov, 1974; Fraser, 1976). The North Africa and the Arabian Peninsula regions were rather properly studied with these means.

The paper seeks to study the space time structure of severe dust storms in the Central Asia and in Uzbekistan, Tajikistan, Iran, Afganistan, in particular. The studies have been carried out in September 1989 during american-soviet experiment (Golitsyn, 1992). A complex utilization of the Tajikistan network data, aircraft sounding and space survey by the soviet (Meteor-2/12, TV channel 0,5-0,7 mKm, IR channel 8-12 mKm) and american (NOAA-II, AVHRR radiometer) stations allowed to obtain information on the nature and initial conditions of dust storms in the region, on the character of interaction between droplet and dust clouds.

A detailed information on the methods and results for two dust episodes (15-16 September, when the storm was continuous but moderate in dust intensity, and 19-20 September, when the dust was intensive but comparatively short-period, less than 6 hours) is presented in the collection book edited by academician G.S. Golitsyn (Golitsyn, 1992).

2. INITIAL DUST SOURCE

One of the factors of dust storm effects on soil and atmosphere is the physical-chemical and dispersion composition of dust particles. Then the problem of identifying dust source and recognising soil and meteorological conditions of the process initiation arises.

Fig. 1 presents the diagrammic map of studied sand soils C, highlands B, prevailing trajectories D of air flows preceding the dust episodes, and cloud cover distribution in the region 8 hours before the second dust storm.

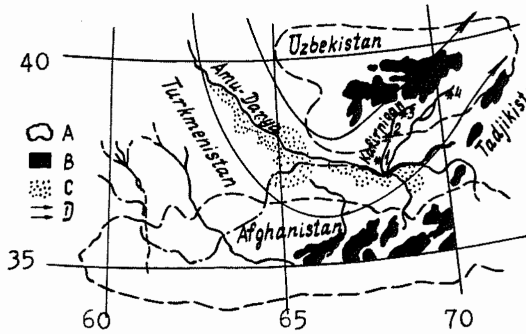

Fig. 1.

The ground sites were organized in the Kafirnigan river valley along the 1-2-3-4 line where 1 - Shaartuz (37°, 68°E), 2 - Isanbai (38°, 68°20E), 3 - Dushanbe (38°36, 68°49E), 4-Altyn-Mazar (the Fedchenko Glacier).

The wind field in this region is complex and variable. According to the satellite data of previous years in the periods of cold air mass intrusion in spring and autumn, the most probable is the situation when northern or northwestern strong air flows firstly turn east along the Gindukush spurs. Then rounding the Pamir mountain system from the west, they move to the north-east across the Kafirnigan and Vakhsh river valleys filling them with dust (Gillette, 1992). As seen from Figs 1 and 2 it has been just this situation which was observed in the studied dust episodes of 15-16 and 19-20 September.

The comparison of Figs 1 and 2a shows that the desert sand plateaux in the northern Iran correspond to the dusty regions. The foothills are cut through by numerous drying valleys (vadi), the sediments in which are the mixture of fine sand particles and clay. They are poorly fastened by plants and eroded during high winds.

At an early stage the dust cloud was between 64-68E and 36-38N. First from the dusting points the wavy streams were stretched to the north-east along the trajectory of powerful cyclonic formation. Some streams were broken passing of about 30-100 km, another crossed the zone of continuous cloudiness which occupied the area limited by 37-50N and 65-77E, the third were generated along the primary dust mass movement.

IR, 01-42 mst 20.09.89

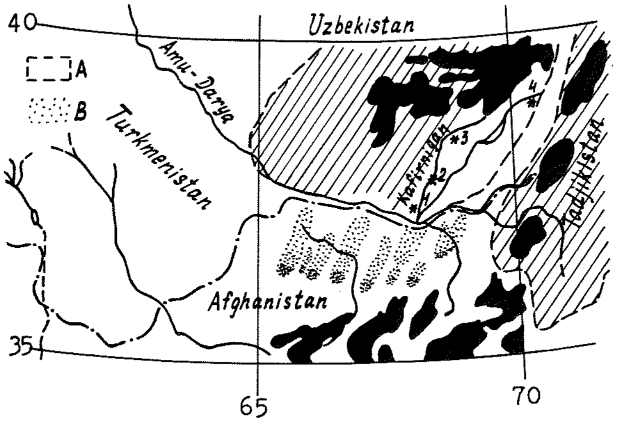

a)

TV, 05-40 mst 20.09.89

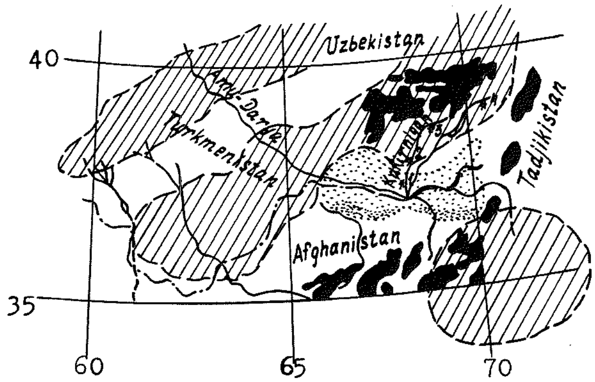

b)

Fig. 2. IR (a) and TV (b) images of droplet A and dust B cloud distribution in the second dust episode.

On the dust cloud evolution

The presence of notable cloudiness in the region studied is the important factor of dust storm evolution within the period of 19-20 September (Smirnov, 1992).

According to the Meteor-2 TV channel data (Fig. 2B) by 0940 LT the dust cloud propagated to the foothills of Tajikistan and eastern Uzbekistan. The northern boundary of a dust cloud, however, was hided by clouds and according to the network data this boundary was not beyond the limits of the southern slopes of the Zeravshan mountain ridge.

The southern boundary of a dust cloud passing along 36°30 is properly identified in the TV images (in the positive - by white short lines, in Fig. 3b - by black lines). Their effect is explained by a high reflecting power of the dust cloud near the source (nearly the same negative blackening density when imaging the stratorain cloud).

So, the dust cloud dimensions from south to north can be estimated as 250--300 km and from east to west by 400--500 km. Nearly similar estimates were obtained from NOAA-II Station radiometers (MacKinnon, 1992).

The total area occupied by the dust cloud can be characterized as significant (about 10^5 km^2) even in weather-climate measures. It is interesting that as opposed to the first dust episode the time of dust cloud existence in the whole observational zone was short (less than 6 hours), though in this case the velocity of a dust front (Fig. 2) was twice as high.

A qualitative model of dust storms in the region

The primary cause of dust storms in the Central Asia is the intrusion of cold air from north-west and north accompanied by surface winds of similar directions. In the narrow spots between mountain systems (Fig. 1) the wind velocity increases up to 15-29 m at the vane level that is quite enough for local soil dusting. The Southern Tajikistan regions are not the source of dust and the local name of dust storms "afghanets" is fully justified. Two types of dust storms are possible: long-term and squally.

The scheme of long-term storms. They originate with intrusing cold fronts of low vertical thickness (of about 1 km or less). In this case the cold air flowing below warm masses, lifts them (Fig. 3a). The developed so-called prefrontal air flows stimulate the surface soil erosion. The lighter particles are entrained upward by a warm flow and reach the height of 3-4 km, where they can exist for several days. The effect is caused by the fact that due to the dust shield the arrival of solar radiation to the Earth surface sharply decreases. The cold lower air is slightly heated and the warm upper air is continuosly being heated and does not lose its buoyancy. The increase of dust content in the surface layer under these conditions is related to particle sedimentation from the upper layers. Since the mean air velocity values in the zone of dust storm were comparatively not large, the principal mass of dust particles seems to be the result of eolithic dust wind erosion, first of all the most fine loess dust (Smirnov, 1992).

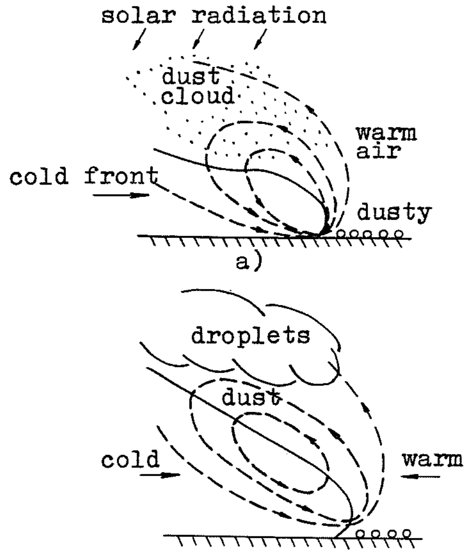

Fig. 3. The schemes of long-term(a) and squall (b) dust storms

The squall "afghanets" appearing with the passage of the cold intrusion front of high vertical depth (upto 3-5 km) and having the surface wind velocity of 20-30 km, raises a lot of large soil particles. However, the zone of convective cloudiness is formed simultaneously. Because of dust particle shield from solar radiation, the life time of a dust cloud decreases and it was observed in the second dust episode. Quantitative constructions will be the subject of future studies.

References

Fraser K.S.(1976) Satellite measurement of mass of Sahara dust in the atmosphere. - Appl. Optics, vol. 15, No. 10, pp. 2471-2479.

Gillette D.A.(1992) Model of transport/deposition of Desert Dust in the Kafirnigan River Valley from Shaartuz to Dushanbe. - A US/USSR experiment on arid aerosol. - S-Petersburg, Gidrometeoizdat, 1992, pp. 50-55.

Golitsyn G.S.(1992) Complex Soviet-American dust experiment, ibidem, pp. 3-6.

Grigor'ev A.A., Lipatov S.V.(1974) Dust storms based on the space investigation data. - L.:Gidrometeoizdat, 31 p. (in Russian)

MacKinnon D.(1992) NOAA AVRR Satellite imagery of the Tajikistan dust storms, ibidem, pp. 25-26.

Smirnov V.V.(1992) Genesis of dust storms in the Southern Tajikistan based on the "Meteor-2-12" satellite and Surface meteoanalysis data, ibidem, pp. 143-154.

GENESIS OF THE ARCTIC FOGS EVAPORATION

N.K.Didenko, V.N.Ivanov, Yu.A.Puzov,
V.V.Smirnov[1], A.A.Grachyov[2]

[1] Institute of Experimental Meteorology, Russia State Committee for Hydrometeorology, Obninsk, 249020
[2] Institute of the Atmosphere Physics, Russia Academy of Sciences, Moscow

1. Introduction

Evaporation fogs, that are very specific for the seas of the Actic water area, are one of the most complex meteorological phenomena. The process of their evolution from the moment of genesis to the dissipation stage essentially depeds on a number of natural factors, the relative contribution and mutual influence of which are studied insufficiently complete, despite various experimental and theoretical investigations [2,4-6]. Such items as the role of the wind sea, concentration and activity of the condensation and crystallization nuclei in the flowing over air mass, existence on the water surface of the layers and films that change the evaporation conditions in the process of the fog microstructure formation still remain unclear. Detailed investigation of the separate factors influence under natural conditions is practically impossible, since they act mutually. In this respect, along with study of the natural fogs formation and evolution processes, laboratory modelling of the evaporation fogs in order to reveal the role and influence of separate meteorological factors in the course of their development is of interest.

The present paper describes a device and methods for the evaporation supercooled fogs modelling under laboratory conditions, preliminary results of investigation of definite processes, that influence the genesis of fogs, specific for the Arctic regions are also given here.

2. Description of the experiment

The device for evaporation sea fogs modelling is based on a thermal pressure chamber (ThPCh) of $100m^3$ in volume and 3m in diameter. The ThPCh contains a metallic cell with an area of $1,5x1,5m^2$ filled with water of 35%. salinity. The water temperature is maintained constant by means of an ultrathermostat of the U15C type, circulating along a closed "cell-thermostat" circle. Modelling of the water surface sea (of 1-2cm amplitude) is realized by a waveproducer and the air humidity change through the vapour overlapping.

The device consists of the

- meters for the water and air temperature of the near water surface part of the fog;
- meter for the fog optical density (base method with employment of the He-Ne laser at the wavelength of λ = 0,63μ);
- "Aspect-10" television analyzer of the fog microstructure, that operates within two ranges: from 2 to 13μ and from 7,5 to 200μ in diameter.

Indication of the fog phase composition is fulfilled through measurements of the linear depolarization ratio in the backscattering signal [3]. The circuit for measurements includes a laser (λ = 0,63μ), a photomultiplier, a focusing system and a polarization filter.

The device allows one to model different conditions (with respect to temperature) for fog formation: the air temperature in the ThPCh changes from positive to -30°C, the water temperature - from -1 to 10°C. Under natural conditions the forgs of moderate and strong evaporation are primarily observed at the air temperature lower than 14°C. In all cases the relative humidity of the air that flows over the water surface is no less than 80%. As this takes place, the water temperature changes in the limits of -2 to 6°C. Taking into account this fact, the range of the device operating temperatures was taken to be as follows: the air temperature - from -12 to -20°C; the water temperature - from -1 to 10°C.

Below you can find the results of modelling and investigation of the moderate (meteorological visibility S_m < 500m) and strong (S_m < 50m) evaporation fogs. As it follows from the experiments, the surface water sea essentially influences the density of the fog being modelled. When the wave producer is switched off the fog optical density for several minutes decreases 3-6 times in dependence on the initial one. Results of the surface water temperature measurements carried out by an AGA-680 thermovisor (λ = 2-5,6 and 7-12μ), indicate a "cold film" formation ($\Delta T_w \simeq$ 1-1,5°C) on the water surface under calm conditions. Apparently, creation of the artificial sea turbulizes as the water surface layer, so the near water surface layer of the air, thus, improving the conditions for the heat and mass exchange from the water surface. Measurements of the temperature of the air near water surface layer in the fog (at the height of 0,05; 0,5 and 1,5m) show, that the temperature mainly changes in the layer of 0-0,05m, where the average temperature gradient attains the value of $3,5\cdot10^2$ degree$\cdot$m^{-1}.

3. Characteristics of artificial fogs

Data on the microstructure of evaporation natural fogs available are extremely insignificant. It is known that down to the temperature of -17°C the fogs are completely of droplet composition, at lower temperatures there is some portion of ice crystals in the fogs. The range of the droplet sizes in the fogs of weak evaporation changes within 1-15μ, of moderate evaporation - from 1 to 20μ and of strong evaporation - from 1 to 35μ. As it follows from the literature data, values of the water content of the evaporation fogs, specific for a cold period, do not exceed 0,25 g$\cdot$m^{-3}. According to the numerical modelling results [2,4], the water content is maximum in the near water surface layer and can attain 0,6g$\cdot$m^{-3} in the dense fogs.

During our experiments the fog characteristics were determined at the level of 0,5-0,7m over the water surface based on the results of the fog microstructure measurements, carried out by means of the "Aspect-10" television analyzer, optical density and backscattering meters. Within the range of the operating temperatures T_o from -12 to -20°C and T_w from -1 to 10°C the fogs with an optical density of τ from 1,8 to ~ 0,03 (S_m from 6,5 to 400m) were modelled. Based on the results of measurements of the linear depolarization ratio in the backscattering signal and data of the analysis of the microparticles form, carried out with the help of the television analyzer, a conclusion was made that down to the temperature of T_o equal to -20°C the fogs being modelled are primarily of a droplet composition.

Fig.1 demonstrates a specific differential spectrum of the artificial fog particles sizes (τ_o = 0,4) in the range of 2,0 - 200μ in the diameter. The root-mean-square diameter of the particles is 5-6μ. The fog water content w was calculated from the measurements data on the optical density and spectrum by the following ratio

$$W=\frac{1}{3}\,\frac{d_3^3}{d_2^2}\,10^2\alpha,$$

where α is the coefficient of the radiation attenuation in the fog, cm^{-1} ($\alpha = \frac{\tau}{L}$, where L = 300cm - length of the radiation path); d_2, d_3 are the root-mean-square and the root-mean-cubic diameters of the droplets size distribution, in μ. The average value of $\frac{d_2^2}{d_3^3}$, calculated from the spectrum measurements data, is 0,125.

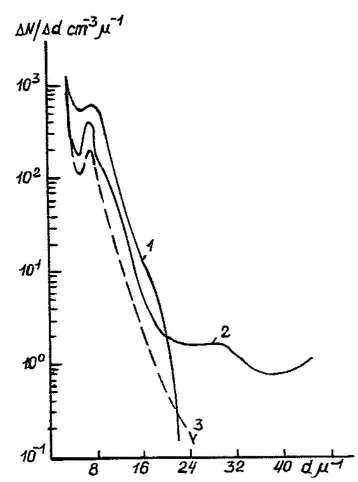

Fig.1 Differential spectrum of the fog particles sizes, τ_o = 0,4 (curve 1) and its deformation when crystallization nuclei (N_c = 50cm^{-3}) are injected: 2 - in 1-1,5 min; 3 - in 8 min after the nuclei injection.

Thus, in the fogs with an optical density of τ = 0,03-1,7 the water content from 0,03 to 1,5g$\cdot$m^{-3} was created. Comparison with the data available on the droplet size distribution for natural water fogs of evaporation demonstrates that the fogs can be satisfactorily modelled by the spectrum.

4. Variability of the fogs microstructure

As it was mentioned above, the evaporation fog, created under laboratory conditions, that is close by its characteristics to the natural fog, is a convenient base for investigation of definite factors influence on the fog microstructure formation process. Investigation of the influence of the crystallization nuclei concentration, available in the fowing over air mass, on such fogs evolution is of interest.

By this goal based on the earlier described device a series of experiments aimed at injection into the fog of the crystallization nuclei AgJ, dispersed through fireworks, was carried out. Concentration of the injected crystalliztion nuclei was chosen proceeding from the conditions of concrete experience and could vary within wide ranges.

The fog was formed at the temperatures of T_o = $-15^{o}C$ and T_w = $10^{o}C$, the fog optical density varying from 1,8 to 0,2 (S_m - from 6,5 to 60m).

In Fig.2 and 3 you can see the curves of the fog optical density variability from the crystallization nuclei concentration in the flowing over air mass and fog initial optical density.

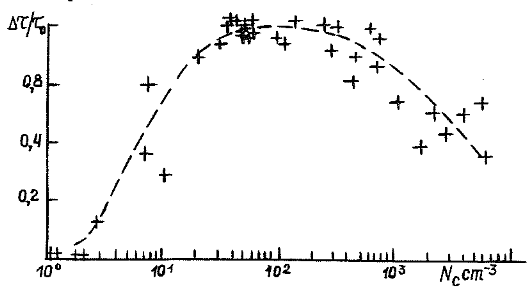

Fig.2 Variability of the fog optical density (τ_o = 0,4 - 1,8) from the concentration of the crystallization nuclei being injected.

The fog optical density variability was characterized by the value $\frac{\Delta\tau}{\tau_0}$ = $\frac{\tau_0 - \tau_{min}}{\tau_0}$, where τ_o is the initial fog optical density, τ_{min} is minimum optical density that is attained when the crystallization nuclei are injected into the fog. As it follows from Fig.2 and 3, optimal nuclei concentration, from the point of view of $\frac{\Delta\tau}{\tau_0}$ maximum value attainment for arelatively short period of time (2-3min), is in the range of 30-300cm^{-3} (τ = 0,4-1,8). At the lower nuclei concentrations within the earlier mentioned range of τ_o the effect of their action was weak, at the higher ones - at the initial moment, due to re-seeding, even turbidity for small values of τ_o, but with subsequent increase of the ratio $\frac{\Delta\tau}{\tau_0}$ up to 0,8 for temporal periods of tens of minutes, was observed.

Constancy of the $\frac{\Delta\tau}{\tau}$ ratio, as τ_o increases (caused by the $\Delta\tau$ increase), is related to that that the intensity of the moisture distillation from the supercooled droplets onto the formed ice crystals increases, as the distance between the droplet and crystal decreases, i.e., as the fog density increases. Therefore, when the fog is denser, the ice crystals can grow faster up to large sizes and fall out earlier than in the case of thin fog. Analysis of deformation of the fog particles spectra, when injecting the crystallization nuclei, indicates that

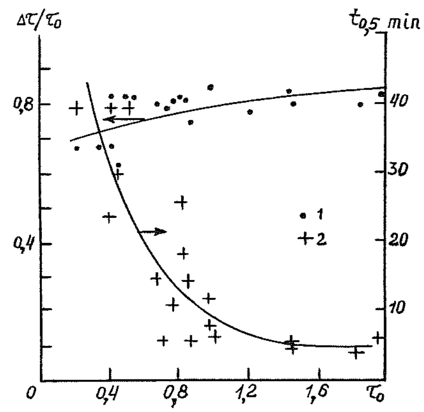

Fig.3 Variability of the fog optical density (1) and life - time of the minimum optical density (2) from the fog initial optical density.

for 1-2 min the spectrum essentially rebuilds: the percent content of small droplets increases as much as 1,5-2 (d = 2-3,6μ), that is related to the partial evaporation of droplets in the spectrum middle part, contribution of particles with d >25μ also increases. In 2-3 minutes in the fog with τ_o 1 the crystals fall out and the minimum optical density is attained. In the fogs of less initial density (τ_o~ 0,2-0,4) the grow and fall out of crystals is slowed down. As this takes place, the dependence of the minimum optical density life-time $t_{0,5}$ on τ, measured by the level τ = 0,5 (τ_o+ τ_{min}) (Fig,3, curve 2) is observed.

Fig.1 shows an example of the spectrum deformation of initial fog particles (τ_o= 0,4, curve 1) in 1-1,5 min (curve 2) and in 8 min (curve 3) after injection of the crystallization nuclei (nuclei concentration N_c ~ 50 cm^{-3}). At the initial moment a decrease of the droplets concentration in the spectrum average part and an increase in the concentration of particles with a diameter more than 20μ (curve 2) were very noticeable. During the experiments formation of crystals was simultaneously observed. Maximum visibility in the fog was achieved in 8 min after injection of the nuclei due to an increase and fall out of large crystals (curve 3).

5. Conclusion

Thus, a possibility of principle to study in detail definite nature factors, that influence the formation and development of evaporation fogs through their modelling under laboratory conditions by means of the device described, is practically supported. The range of the parameters being modelled is as follows: the medium optical density τ = 0,03-1,8 (that corresponds to the meteorological visibility of S_m = 400-6,5m); the water temperature - from -1 to 10^oC; the air temperature - from -12 to -20^oC. An opportunity to change the characteristics of the "flowing over air mass" humidity, the amount of condensation and crystallization nuclei in it and also controlling of the water surface sea intensity is foreseen.

It is shown that the sea, created on the water surface, increases the fog optical density several times and, along with characteristics of the flowing over air mass humidity and "water-air" temperature difference, strongly influences the fog formation and requires a furthe investigation.

The fogs being modelled down to T_o = -20^oC are primarily of a droplet composition. Contribution of the fog droplets with d > 20μ into the size spectrum is negligibly small. As the fog optical density decreases, the percent content of the droplets with d $\sim$ 203μ also increases.

An increase in the crystallization nuclei concentration in the flowing over air mass results in variation of the fog microstructure: as the total concentration decreases, the percent content of the particles with d $\sim$ 2-3μ and d > 20μ increases. As this takes place, one can observe grow and fall out of crystals and a decrease in the fog optical density down to the value of τ_{min} 0,2 τ_0.

References

1. Didenko N.K., Ivanov V.N. (1989). Laboratory modelling of the evaporation fogs.- Proceedings of the Institute of Experimental Meteorology, vyp. 48(138), p.34-41.
2. Khvorost'yanov V.И. (1983). Modelling of evolution of evaporation sea fogs and of influence on them. - Meteorologiya i Gidrologiya, No.12, p.44-52.
3. Kuznetsov V.V., Pavlova L.N. (1981). On the clouds optical features. - Meteorologiya i Gidrologiya, No.10, p.40-43.
4. Matveyev L.T., Soldatenko S.A. (1977). To the theory of formation and forecast of evaporation fogs. - Meteorologiya i Gidrologiya, No.2, p.24-31.
5. Terziyev F.S. (1969). The hydrometeorlogical characteristic of the fogs like evaporations based on an example of the Kola Bay. - Proceeding of the Ucr. RHMI, vyp.77, p.136-143.
6. Saunders P.M. (1964). Sea smoke and steam fog. Qurt.J.of Royal Meteorlogical Society, vol.90, No.384, p.156-165.